Includes interactive eBook with complete content

Musculoskeletal MRI Structured Evaluation

How to Practically Fill the Reporting Checklist

Avneesh Chhabra
Theodoros Soldatos

Wolters Kluwer

Thank you

for purchasing this eBook.

To receive special offers and news about our latest products, sign up below.

Visit LWW.com

Musculoskeletal MRI Structured Evaluation

How to Practically Fill The Reporting Checklist

Musculoskeletal MRI Structured Evaluation

How to Practically Fill The Reporting Checklist

EDITORS

Avneesh Chhabra, MD, DNB
Associate Professor Radiology and Orthopedic Surgery
Division Chief, Musculoskeletal Radiology
UT Southwestern Medical Center
Dallas, Texas
Adjunct Professor
The Russell H. Morgan Department of Radiology and Radiological Science
The Johns Hopkins University School of Medicine
Baltimore, Maryland

Theodoros Soldatos, MD, PhD
Consultant Radiologist
Research Unit of Radiology and Medical Imaging
National and Capodestrian University of Athens
Evgenidion Hospital
Athens, Greece
Former Musculoskeletal Radiology Research Fellow
The Russell H. Morgan Department of Radiology and Radiological Science
The Johns Hopkins University School of Medicine
Baltimore, Maryland

Wolters Kluwer

Philadelphia · Baltimore · New York · London
Buenos Aires · Hong Kong · Sydney · Tokyo

Acquisitions Editor: Ryan Shaw
Product Development Editor: Amy G. Dinkel
Production Project Manager: Bridgett Dougherty
Design Coordinator: Stephen Druding
Manufacturing Coordinator: Beth Welsh
Prepress Vendor: Aptara, Inc.

Copyright © 2015 Wolters Kluwer Health
Two Commerce Square
2001 Market Street
Philadelphia, PA 19103 USA

All rights reserved. This book is protected by copyright. No part of this book may be reproduced or transmitted in any form or by any means, including as photocopies or scanned-in or other electronic copies, or utilized by any information storage and retrieval system without written permission from the copyright owner, except for brief quotations embodied in critical articles and reviews. Materials appearing in this book prepared by individuals as part of their official duties as U.S. government employees are not covered by the above-mentioned copyright. To request permission, please contact Wolters Kluwer Health at Two Commerce Square, 2001 Market Street, Philadelphia, PA 19103, via email at permissions@lww.com, or via our website at lww.com (products and services).
9 8 7 6 5 4 3 2 1

Printed in China

Library of Congress Cataloging-in-Publication Data

Chhabra, Avneesh, author, editor.
Musculoskeletal MRI structured evaluation : how to practically fill the reporting checklist/editors, Avneesh Chhabra, Theodoros Soldatos.
p. ; cm.
Includes bibliographical references and index.
ISBN 978-1-4511-8593-5 (hardback : alk. paper)
I. Soldatos, Theodoros, author, editor. II. Title.
[DNLM: 1. Musculoskeletal Diseases–diagnosis. 2. Magnetic Resonance Imaging—methods. WE 141]
RC925.7
616.7′07548—dc23

2014020597

Care has been taken to confirm the accuracy of the information presented and to describe generally accepted practices. However, the authors, editors, and publisher are not responsible for errors or omissions or for any consequences from application of the information in this book and make no warranty, expressed or implied, with respect to the currency, completeness, or accuracy of the contents of the publication. Application of this information in a particular situation remains the professional responsibility of the practitioner; the clinical treatments described and recommended may not be considered absolute and universal recommendations.

The authors, editors, and publisher have exerted every effort to ensure that drug selection and dosage set forth in this text are in accordance with the current recommendations and practice at the time of publication. However, in view of ongoing research, changes in government regulations, and the constant flow of information relating to drug therapy and drug reactions, the reader is urged to check the package insert for each drug for any change in indications and dosage and for added warnings and precautions. This is particularly important when the recommended agent is a new or infrequently employed drug.

Some drugs and medical devices presented in this publication have Food and Drug Administration (FDA) clearance for limited use in restricted research settings. It is the responsibility of the health care provider to ascertain the FDA status of each drug or device planned for use in his or her clinical practice.

LWW.com

To:

Kiran, Ria, and Rohan—my source of academic time during the writing of this book;

my brother, Yogesh, and his family—always inspiring me to accomplish academic endeavors;

my lovely sister, Alka, her family, and, above all, my parents, Krishan and Leela for their unconditional support;

finally, my mentors, John Eng, John A. Carrino, A. K. Chaturvedi, and Neil M. Rofsky, who ignited the lamp of knowledge and inspired me to do the same and spread the light.

—A.C.

To:

My parents, Anastasios and Miranda, and my brother, Panagiotis, for their lifetime love, support, and continuous confidence in me.

My wife, Stavroula, and my sons, Anastasios and Konstantinos, who supported and encouraged me throughout the completion of this book, in spite of all the time that took me away from them.

My professor and friend, Avneesh Chhabra, for believing in me and making all this possible.

Contributors

Shivani Ahlawat, MD
Clinical Instructor
Russell H. Morgan Department of Radiology and Radiological Science
Johns Hopkins University School of Medicine
Baltimore, Maryland

Travis Browning, MD
Assistant Professor
Department of Radiology
Abdominal Imaging
University of Texas Southwestern Medical Center
Director of Radiology Informatics
Medical Informaticist
Parkland Health and Hospital System
Dallas, Texas

John A. Carrino, MD, MPH
Vice Chairman
Department of Radiology and Imaging
Hospital for Special Surgery
New York, NY

Majid Chalian, MD
Resident, Department of Radiology
University Hospitals
Case Western Reserve University
Cleveland, Ohio

Avneesh Chhabra, MD, DNB
Associate Professor Radiology and Orthopaedic Surgery
Division Chief, Musculoskeletal Radiology
University of Texas Southwestern Medical Center
Dallas, Texas
Adjunct Professor

Russell H. Morgan Department of Radiology and Radiological Science
Johns Hopkins University School of Medicine
Baltimore, Maryland

Shadpour Demehri, MD
Assistant Professor Radiology
Musculoskeletal Radiology
Russell H. Morgan Department of Radiology and Radiological Science
Johns Hopkins University School of Medicine
Baltimore, Maryland

Colby S. Engar, MD
Fellow, Musculoskeletal Radiology
Department of Radiology
University of Texas Southwestern Medical Center
Dallas, Texas

Sahar Jalali Farahani, MD, MPH
Research Fellow
Musculoskeletal Radiology Section
Russell H. Morgan Department of Radiology and Radiological Science
Johns Hopkins University School of Medicine
Baltimore, Maryland

David Hitt, MSc
MR Clinical Adoption Specialist
Philips Healthcare

Jared Kasper, MD
Fellow, Musculoskeletal Radiology
University of Texas Southwestern Medical Center
Dallas, Texas

Jonathan Samet, MD
Assistant Professor
Department of Medical Imaging
Lurie Children's Hospital of Chicago
Northwestern University Feinberg School of Medicine
Chicago, Illinois

Theodoros Soldatos, MD, PhD

Consultant Radiologist
Research Unit of Radiology and Medical Imaging
National and Capodestrian University of Athens
Evgenidion Hospital
Athens, Greece

Former Musculoskeletal Radiology Research Fellow
The Russell H. Morgan Department of Radiology and Radiological Science
The Johns Hopkins University School of Medicine
Baltimore, Maryland

Ty K. Subhawong, MD
Assistant Professor
Department of Radiology
University of Miami Miller School of Medicine
Miami, Florida

Kyung Jin Suh, MD, PhD
Professor
Department of Radiology
Chief of Musculoskeletal Section
Dongguk University Gyeongju Hospital
College of Medicine, Dongguk University
Gyung-buk, Korea

Gaurav K. Thawait, MD
Research Fellow
Musculoskeletal Research Section
Russell H. Morgan Department of Radiology and Radiological Science
Johns Hopkins University School of Medicine
Baltimore, Maryland

Vibhor Wadhwa, MBBS
Research Affiliate
Russell H. Morgan Department of Radiology and Radiological Science
Johns Hopkins University School of Medicine
Baltimore, Maryland

Foreword

Musculoskeletal MRI Structured Evaluation: How to Practically Fill the Reporting Checklist is a timely addition to the literature, as the structured reporting trend is gaining momentum, with more and more evidence supporting it as a preferred style by both radiologists and importantly the consumers of the report—referring providers. It has always bewildered me how much emphasis is spent on image acquisition and visualization while so little effort is applied to the reporting task, the key work product of a radiologist. Bringing order to chaos, a well-organized, relevant report can facilitate communication among specialties and provide a means for data mining.

In terms of how to use this book, one perspective is to consider it an example of best practices that can be adopted or adapted for your particular setting based on feedback from and discussion with local referring colleagues.

I believe that you will find this work informative, illustrative, and illuminating.

John A. Carrino, MD, MPH

Preface

Magnetic resonance imaging (MRI) has been established as the most accurate modality and, in some cases, the primary method for imaging evaluation of the musculoskeletal system. During the last decade or so, the growing demand for MRI studies and the higher amount of radiologic information provided by the newer scanners and imaging techniques have challenged the efficiency of modern radiologists. Image readers are frequently asked to combine superior diagnostic accuracy, quality reporting, and speed in their reporting. To achieve this paradigm, an increasing number of institutions have employed structured reporting templates, which (1) mandate a systematic step-by-step approach for evaluating all relevant structures of the examined joint or extremity, so that no important pathology is missed; (2) aid in training of radiology residents and fellows; (3) offer multiple predefined and broadly accepted lexicons to describe the pathology, which results in uniform and accelerated reporting; and (4) facilitate prospective and retrospective research. Structured reports also tend to be easier to navigate for the clinicians, who prefer clear and concise descriptions of the various structures and joint compartments in question, rather than reports with multiple complicated sentences containing radiology jargon and prose. Unfortunately, little information on "how to use structured templates" is available in existing radiology textbooks, creating need for a comprehensive textbook that would help the readers learn, the anatomy and pathology of various gross and fine structures in musculoskeletal system.

Addressed to both in-training and established radiologists and clinicians, *Musculoskeletal MRI Structured Evaluation: How to Practically Fill the Reporting Checklist*, written by experts in musculoskeletal imaging, offers the structured checklists for interpreting and reporting musculoskeletal MRI examinations. It describes the "how to" use these templates and incorporate them into the clinical practice. Each chapter is dedicated to a separate joint or specific group of entities, and includes the reporting template along with a step-by-step description and imaging examples of the entire spectrum of the related pathologies.

Most radiologists are too busy to go through the extensive information available in scientific articles and textbooks when posed with a question. *Musculoskeletal MRI Structured Evaluation* provides relevant text material, cases, and images that could match the ones on their imaging board or monitor. It is a practical guide to interpret musculoskeletal MR imaging studies from day 1 in detail and with incremental accuracy. We aimed to introduce readers to (1) the advantages of using structured templates; (2) the protocols for different musculoskeletal MRI examinations to answer the questions of the referring physician; (3)

the method of filling in the structured template using a checklist approach with suggested terminology for describing normal and abnormal structures and musculoskeletal lesions; and (4) the short path to arrive at the most relevant diagnostic impression. In this endeavor, we have focused our efforts on the most common clinical scenarios encountered in the daily practice. Various related syndromes are summarized at the end of the chapters.

Musculoskeletal MRI Structured Evaluation is remarkably different from available textbooks dedicated to the musculoskeletal system. It contains an unusually large number of images that are characteristic of various pathologies and the text has been kept relevant, short and to the point. It was compiled to provide a virtual musculoskeletal fellowship experience to readers, since different fellowships across the country provide varied experience and skill set to the trainees. Using current knowledge base and scientific evidence, it will help the reader come to an accurate diagnosis, whether the case is simple or complicated.

We hope that you will find this book exciting, educational, and, above all, helpful in enhancing your practice. We have attempted to produce a "see what you can do" rather than a "see what we can do" type of book. We sincerely hope that through *Musculoskeletal MRI Structured Evaluation: How to Practically Fill the Reporting Checklist*, first of its kind, will satisfy the needs of practicing radiologists, musculoskeletal fellows, radiology residents, orthopedic surgeons, internists, plastic surgeons, and physical medicine and rehabilitation physicians in need of a handy reference, as well as technologists performing these musculoskeletal MRI studies.

Avneesh Chhabra, MD, DNB

Theodoros Soldatos, MD, PhD

Acknowledgments

As this book evolved to emerge in this final form, a number of people directly and indirectly contributed in various ways:

- I acknowledge Dr. John A. Carrino for stimulating my interest in structured reporting, when I practiced at Johns Hopkins. Dr. John Eng introduced me to Mr. Jonathan Pine from LWW to help initiate this project. This project would not have been possible or come to completion without the help and encouragement of my co-author and friend, Dr. Theodoros Soldatos.
- I am grateful for the encouragement and support of my family in India, Singapore, and USA, without which a book of this scope could not have been completed.
- I learned a great deal from all my patients and thank them for being a constant source of inspiration. I also wish to thank their caretakers (Orthopedics, Foot and Ankle Surgery, and Plastic Surgery), who provided an insight into the practical challenges of their management.
- I gratefully acknowledge all our teachers for their encouragement, criticism, and motivation. I wish to thank our colleagues, residents, and fellows who have encouraged us in this endeavor.
- My special thanks to all research and clinical fellows, an outstanding group of physicians, who willingly shared new knowledge and insights and provided help with various chapters for our book.
- I acknowledge the inputs from Aaron (Ajay) Schorah, Dwayne Isabell, and Dave Hitts, great MR technologists and scientists, for their help and valuable suggestions regarding the MRI technique improvement over the years.
- The entire team at Lippincott Williams & Wilkins, especially the late Jonathan Pine and Grace Caputo, who approached this assignment with enthusiasm and dealt with suggestions and comments with promptness and proficiency. I thank them cordially for all their efforts.

—A.C.

- I acknowledge my mentors and professors, Dr. John A. Carrino and Dr. Avneesh Chhabra. The former provided me the invaluable opportunity and honor to join a magnificent radiology team in one of the best hospitals in the world, and stimulated my interest in structured reporting. The latter offered me the outstanding opportunity and privilege to

participate as a co-author on this book, which has been the highest step in my academic endeavors. In addition to being my teachers in musculoskeletal radiology, they both made (and still make) a huge impact in my career.

- I wish to thank all my previous teachers for developing my intellectual curiosity and desire to learn, for guiding me throughout my career, and for encouraging me to strive for success.
- My special thanks go to the entire team at Lippincott Williams & Wilkins for their unconditional assistance and support.

—T.S.

Contents

1 The Process of Structured Reporting: Adding Value and Quality
Travis Browning

2 Technical Considerations
Avneesh Chhabra, David Hitt, and Theodoros Soldatos

3 Infection and Inflammation/Arthritis
Avneesh Chhabra and Theodoros Soldatos

4 Bone and Soft Tissue Tumors
Avneesh Chhabra, Kyung Jin Suh, Jonathan Samet, and Theodoros Soldatos

5 Cartilage 131
Avneesh Chhabra, Gaurav K. Thawait, and Theodoros Soldatos

6 The Shoulder
Avneesh Chhabra, Sahar Jalali Farahani, and Theodoros Soldatos

7 The Elbow
Avneesh Chhabra, Majid Chalian, and Theodoros Soldatos

8 The Wrist
Avneesh Chhabra, Shadpour Demehri, and Theodoros Soldatos

9 The Hip
Avneesh Chhabra, Shivani Ahlawat, and Theodoros Soldatos

10 The Knee
Avneesh Chhabra, Vibhor Wadhwa, Ty K. Subhawong, and Theodoros Soldatos

11 The Ankle
Avneesh Chhabra, Jared Kasper, Colby Engar, and Theodoros Soldatos

12 Magnetic Resonance Neurography
Avneesh Chhabra, Theodoros Soldatos, and John A. Carrino

Index

1

The Process of Structured Reporting: Adding Value and Quality ☑

Travis Browning

Structured reporting is a tool, and like any other tool expertise comes with education and practice. The purpose of this tool is to standardize and codify the content of radiologic interpretations to facilitate communication—communication to referring clinicians, communication to future comparing radiologists, and communication for the purposes of quality improvement and research.

The three elements that constitute structured reporting include consistent headings (indication, comparison, findings, etc.), itemized reports with discrete short descriptions, and use of a standard lexicon (1). While there is yet no universal agreement on the construction of these elements, the Radiological Society of North America (RSNA) has championed the process and led the way with first developing RadLex as a standard lexicon and second organizing the first versions of "best practice" radiology report templates in the Radiology Reporting Initiative.

There has been resistance to the use of structured reports. Many users cite the perceived increased length of time of report generation and loss of the "personalized" component of the report. Some feel that the prose style of reporting is more akin to consulting and actually improves communication with the ordering provider. However, it has been shown that the referring clinicians actually prefer the itemized report content over prose (2). It is likely related to clearer, more consistent and objective evaluation and presentation of the imaging findings.

The itemized style can be paralleled to other medical documentation, such as the History & Physical (H&P). The H&P is always structured in similar format with discrete sections in the same order: Details of the presenting complaint, followed by past medical history, then review of symptoms, the vitals and physical examination, and so forth. The physical examination too is ordered in the same way with a general appearance followed by HEENT examination, cardiothoracic, abdominal, and so on. The structured radiology report can be looked at in this same fashion, equating the Impression section condensing the thoughts and recommendations of the radiologist to the clinical physician's assessment and plan.

Even with the first iteration of reports organized by the RSNA, there is much room to

improve. While all individual reports and reporting divisions are structured, there is little agreement across the entire spectrum of published templates on standard headings and element organization. Examples include use of “Clinical Indication” versus “Clinical Information” versus “Clinical History,” the location of the Impression section at the beginning or the end of the report, inclusion of date or time of examination, Observation versus Findings section, and inclusion or not of a Recommendation section. In addition, there is even greater variation in the clinical information content and organization across divisions and across modalities within the same division.

For the next step in evolution, it falls to a single entity or governing body to begin to pull together standardization across the spectrum of reports. One purpose of this manual is to provide such an effort for the entirety of the division of musculoskeletal imaging, to either lead the way for the rest of imaging or facilitate rapid conversion to any future adopted industry standard. Either way, it is strongly encouraged that individual institutions and practices organize their own internal efforts when pursuing structured reporting.

An example of this process is to put together a governance committee, comprising physician leaders for administrative, key clinical service, information technology, and quality assurance/quality improvement components of the practice. Such a group can provide standardization for service branding and billing assurance while maintaining a unified vision for the effort and identifying IT needs and optimization opportunities.

Organized beneath this governance group are the division leaders to champion and drive clinical content of the reports. These leads take the direction back from governance to their respective divisions and then work directly with IT resources to build the structured report content into the locally installed electronic reporting applications. It is important that these leads be direct users of the reports and reporting applications, so that they can identify pressure points of the systems. With this, they can then again work with IT to tweak the report templates to drive continuous gains in efficiency and accuracy within the limits of utilized reporting applications.

End user involvement is the first step to develop generalized buy-in and adoption. The users must have a voice and process to provider user feedback. Disregarding their opinion will not only limit buy-in but could also miss valuable efficiency gains and victories—only the end users can truly know how to best improve the system. Along that same line, it is important to facilitate the close interaction of clinical content experts with IT resources so that technical application knowledge can be leveraged to generate improvements that might not be readily apparent to a clinical end user. After all, each reporting application is different: Some with basic and some with advanced template tools to assist with structured reporting. Toward this, having a radiology or medical informatics position is becoming more and more valuable to physician groups and institutions.

After implementation, rapid cycle change processes should be engaged as often variant uses and short cuts can be developed that the application vendors would never have envisioned. If a template is never changed after implementation, then issues are likely being missed such as punctuation, misspelling, template field optimization, or even simple

nonuse of the templates. Every effort should be made to continuously engage and reengage the users and IT sources of knowledge. In addition, it should be determined whether the reporting application or medical record can be leveraged to track template usage.

By completing these integral organizational components, focus may now be put on the main purpose of this manual—the codification of the clinical content. When reviewing available first-generation templates on the RSNA Radiology Reporting site, two basic organizational forms for findings/observations can be identified—issue centric and anatomy centric.

Issue centric reporting describes the most pertinent issue findings first, then subsequently "everything else." The benefit of this style is that often the content most important to the original ordering provider is listed first whereas items that a referring specialist may not be concerned about come second. The issue centric style tends to presume that the pathology is known to some degree before imaging—which is not always true. The primary issue with this style is that the organization of the report content for the same examination, like an MR of the abdomen, can be strikingly different based on the reason the examination was done. In an age when patients with multiple medical problems may be followed by multiple specialists organized by a primary care physician, tracking findings across multiple reports can become problematic. Imagine a person imaged for abdominal pain found to have a renal mass, a liver mass, and an adrenal mass who then undergoes a renal mass imaging protocol, a liver mass imaging protocol, and an adrenal mass imaging protocol all with reports, although structured, organized differently—it could quickly become confusing trying to track any changes.

In contrast, the anatomy centric style handles this issue in a much more standardized fashion. The liver section is always in the same location. The renal section is always in the same location. And so on. The contents of each section may be more abbreviated or detailed based on the imaging protocol utilized, but the order is the same. Such organization then facilitates tracking findings across multiple reports and is the methodology utilized here.

Standardizing the format and content in this way will encourage the more thorough reading of the Findings sections of imaging reports. With familiarity to the layout, a referring or consulting provider can more rapidly refer to specific sections of their concern, even if not specifically discussed in the Impression section. This then allows the reading radiologist to tailor the Impression section to elements reflective of the reason for examination or urgent incidental discoveries while still facilitating identification of other findings of interest to other consumers of the report who may be referring to it for reasons entirely different than the original indication. Such structure also supports the generation of more complete reports, preventing indication or satisfaction of search from glossing over important elements of information ultimately eliminating the "you didn't say anything about the xyz" phone call.

Implementing this process will create a standardized and codified report, with report details highlighting anatomy and pathology rather than the reporting radiologist preferences and style choices. More complete reports can be created while improving the

ability of the clinical providers to consume the entirety of the report. Specific elements of interest can more readily be tracked through serial reports, even if not part of the original reason for examination. But potentially of greatest impact, this establishes the framework for computerized processing and sorting of report elements. The electronic medical record and imaging create enormous volumes of information; however, with vast components in a format not interpretable by a computer. By facilitating computerized consumption of the report, we set the stage for large-scale (even population based) evaluations pushing the future of medicine from anecdotal to true outcome-based practice.

The following chapters will detail the proposed best practice report templates for musculoskeletal imaging reports. Adhering to the above principles, maximizing reporting application abilities, engaging the reporting and clinical users, and applying the structure and content of these provided templates will advance the specialty of radiology into the next step of standardized structured reporting and toward the future of medicine.

REFERENCES

1. Danton GH. Radiology reporting, changes worth making are never easy. *Appl Radiol.* 2010;39(5):19–23.
2. Naik SS, Hanbidge A, Wilson SR. Radiology reports: Examining radiologist and clinician preferences regarding style and content. *AJR Am J Roentgenol.* 2001;176(3):591–598.

2

Technical Considerations

Avneesh Chhabra, David Hitt, and Theodoros Soldatos

MR imaging is the method of choice for the detection of internal derangements of the various soft tissue structures of joints. Meticulous attention and correct application of various pulse sequences and MR techniques is essential for achieving optimal quality imaging. The latter is important for superior depiction of the bony and soft tissue structures of the joints and related para-articular regions. Ideally, examinations should be directed based on clinical information from the referring clinicians and prescribed by the protocoling radiologist, with active involvement of the performing technologist, as well as engagement of the patient and interpreting radiologist, all participating as a team to obtain the best imaging quality. This chapter presents the MR imaging techniques and available pulse sequences and highlights their advantages and limitations, along with a guide on how to build different musculoskeletal protocols.

HUMAN CONSIDERATIONS

Referring Physician

Close interaction between the referring clinician(s) and the radiologist is important for protocol prescription and correct interpretation of imaging findings. Clinicians should be informed regarding the technical limitations of MR imaging (e.g., larger the anatomy to be covered, the longer the overall examination will take, consequently the resolution could be degraded). The protocols vary depending upon whether the clinical question is injury, pain or other nonspecific symptoms (ortho protocol), infection or inflammation (infection protocol), tumor (mass protocol), labrum, full-thickness rotator cuff tear or loose body (MR arthrogram), slow-flow or high-flow vascular malformation (vascular malformation protocol), cartilage evaluation (cartilage protocol), myositis or myopathy (myositis protocol), metal prosthesis related complications (metal protocol), and peripheral nerve evaluation (MR neurography). The use of gadolinium-based contrast agents is essential in MR arthrograms, as well as in cases of suspected infection, inflammation, vascular malformation, and mass lesion. Image manipulation (postprocessing) becomes important whenever high-end imaging is performed (e.g., with 3D imaging, functional cartilage

imaging, and neurography). Although such high-end imaging may or may not be useful for the radiologist's routine interpretation, the reconstructed longitudinal images, color maps, curved and maximum intensity projections (MIPs) serve as useful preoperative guides for the surgeons. In addition, buy-in of the subspecialist clinicians is also important when one performs such imaging on their patients since high-resolution or 3D imaging demands more imaging time, produces coarser images and lots of thin slices that have the potential to increase the evaluation time. On the other hand, 3D imaging potentially increases the diagnostic confidence of the radiologist since smaller labroligamentous structures and thinner cartilage can be easily evaluated on a series of small sections and at any desired oblique plane. Finally, angular or rotational measurements can be obtained on thicker slab MIPs generated from such scans similar to cross-sectional CT examination (Fig. 1).

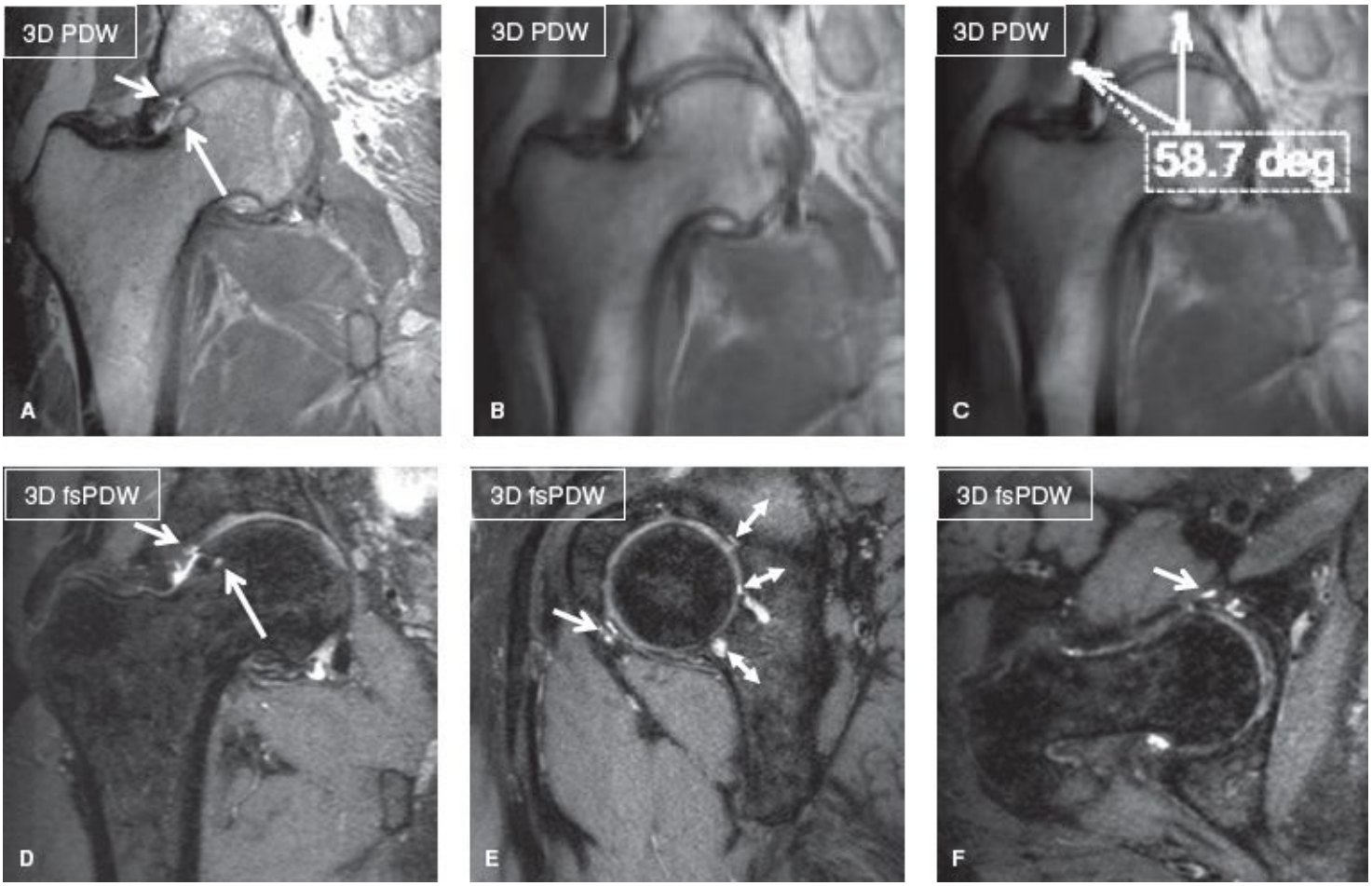

Fig. 1: Three-dimensional hip imaging in femoroacetabular impingement. Coronal non–fat-suppressed 3D **(A),** thick slab **(B, C),** and multiplanar reconstructions from fat-suppressed 3D; **(D–F)** show fibrocystic change of the right femoral head and neck junction (*long arrows*), chondrolabral separations (*short arrows*), and lateral center angle measurement in thick slab MIP **(C).** Notice elegant depiction of multiple cartilage fissures of the posterior acetabulum (*double head arrows* in **E**) in otherwise coarser looking image due to 0.65-mm isotropic resolution.

Patient Coaching

The technologist plays an important role in patient coaching for successful performance of the examination. The patient should fill out a form with most relevant acute or chronic complaints and history of prior regional surgery. Ideally, a marker should be placed at the most symptomatic painful, injured or palpable site, and the patient should be asked to remain still during the image acquisition, as well as to breathe normally. The extremity should be well padded for comfort and the coil tightly wrapped around it to restrict motion during the examination. If there is motion during the study, the technologist should stop the scan, talk to the patient to make him/her comfortable, instruct him/her not to move, and repeat the degraded sequence(s). One could give intravenous glucagon to decrease bowel peristalsis-related artifacts during lumbosacral plexus imaging; however, it is important to remember the contraindications (such as glaucoma) and also instruct the patient of side effects, such as rebound hypoglycemia.

TECHNICAL CONSIDERATIONS

Scanner Selection

Since most musculoskeletal soft tissue structures are relatively small, imaging is best performed on 3T scanners to make use of the higher signal-to-noise ratio (SNR) these machines provide. The 3T SNR can be traded as currency for imaging speed or resolution, or both. Higher SNR translates into higher soft tissue contrast and potentially faster imaging while keeping the slice thickness to a minimum, thereby, enhancing the spatial resolution. One should aim at the smallest in-plane resolution, whether imaging is performed on 1.5T or 3T. Signal averages can be used to further improve the SNR but longer scans risk motion blurring. Reducing signal averages (repeat acquisitions aka number of excitations [NEX]/number of signal averages [NSA]) or prudent use of parallel imaging can achieve faster scanning. In larger joints or larger subjects, it might be necessary to use larger voxels to maintain adequate SNR. One could use enhanced (fast) gradient mode to further improve SNR and reduce blurring effects. Imaging on 3T scanners is advantageous in obtaining 3D imaging with spin echo-type contrast, and this leads to fine evaluation of various small structures, such as menisci, cartilage, ligaments, and nerves in multiple arbitrary planes with isotropic resolution (Figs. 2, 3). Three-dimensional imaging is also relatively devoid of pulsation artifacts and produces better fluid contrast, especially using DRIVE (driven equilibrium) pulse. This pulse not only shortens TR and makes acquisition shorter, but it also increases fluid-cartilage interface conspicuity.

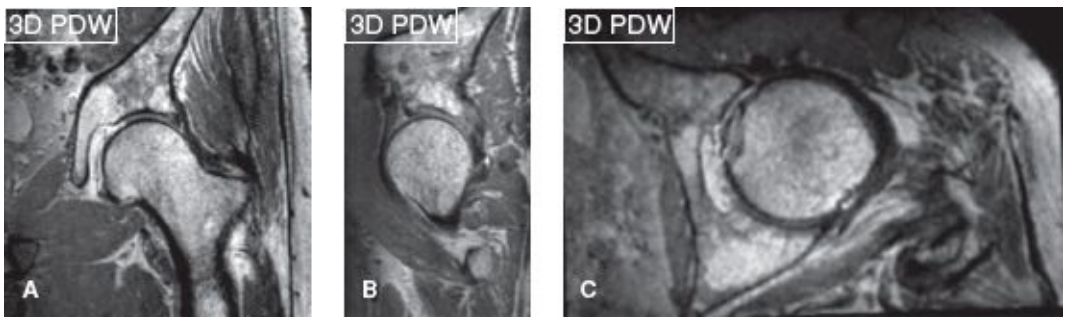

Fig. 2: Three-dimensional hip. Isotropic 0.65-mm coronal acquisition **(A)** and reconstructed sagittal **(B)** and axial **(C)** scans on a 3T scanner (Achieva, Philips Healthcare, Best, Netherlands).

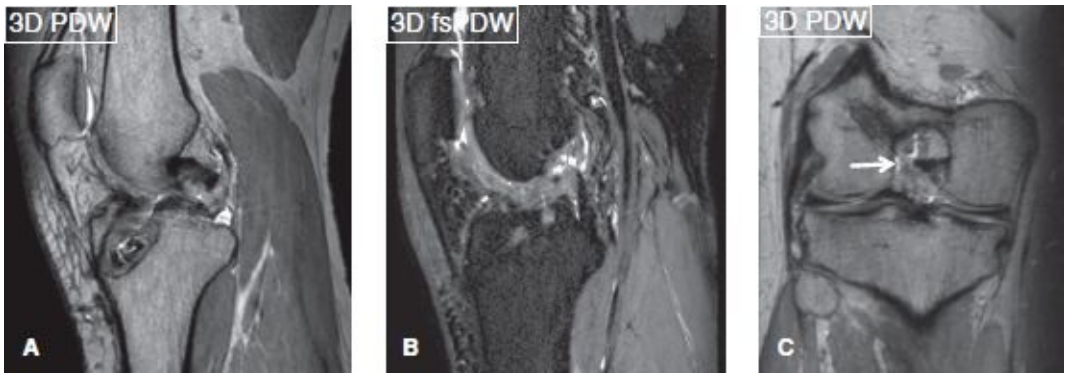

Fig. 3: Three-dimensional knee. Isotropic 0.65-mm sagittal acquisitions **(A, B)** and reconstructed coronal **(C)** scans on a 3T scanner (Achieva, Philips healthcare, Best, Netherlands) showing ACL graft reconstruction with midportion disruption (*arrows*).

Nevertheless, the authors encourage the use of 1.5T as well because the latter scanners perform better in patients with metallic material(s) in the region of imaging, in whom 3T is expected to produce artifacts. Three-dimensional imaging on 1.5T scanners is usually not isotropic due to time limitations. The latter scanners produce finer in-plane images whereas off-plane images are frequently degraded (Fig. 4). Modern 1.5T scanners, however, perform nearly similar to older generation 3T scanners if joint-specific coils are used that possess multiple channels and superior gradient strength. To reduce inhomogeneity in off-center areas, such as shoulder and wrist, one may employ higher second-order shimming (pencil beam [PB]-Volume, Philips) for better field homogeneity, in order to obtain more uniform fat suppression. Higher-field strength, newer coils, faster computer processing and pulse sequences have allowed reduction in the voxel sizes at 3T by a factor of 2 to 5 versus the comparable 1.5T protocols. Similarly, for MR neurography, one should ideally use 3T imaging for multiplanar depiction of peripheral nerves. Two-dimensional imaging is not a problem, but fat-suppressed (fs) 3D imaging is frequently limited on 1.5T scanners (Fig. 5).

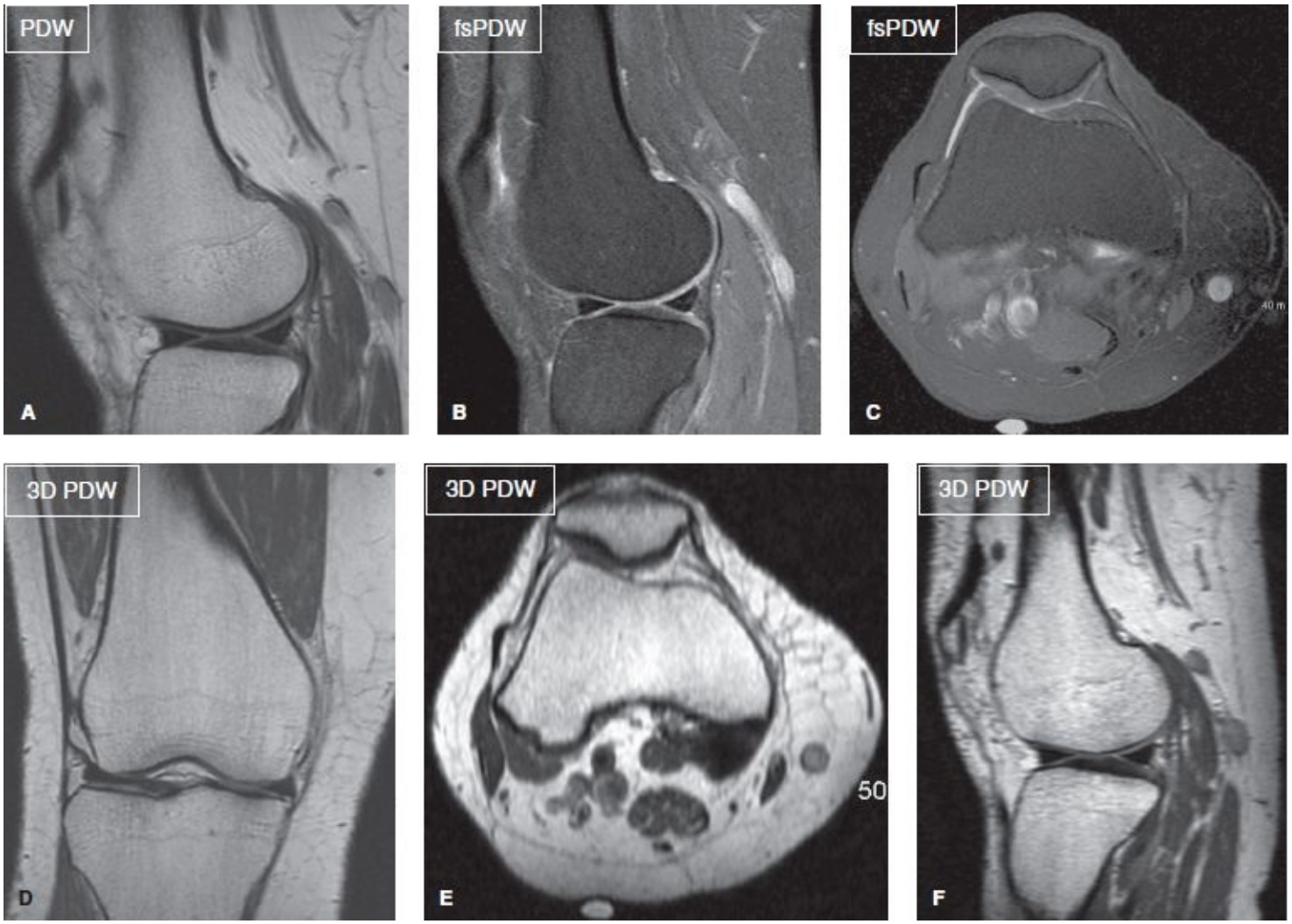

Fig. 4: Two-dimensional versus 3D imaging on 1.5T MR scanner. Sagittal **(A, B)** and axial **(C)** 2D images with high in-plane resolution (0.4 to 0.5 mm). Corresponding nonisotropic coronal acquired 3D image **(D)** shows high (0.65 mm) resolution while the axial and sagittal (off-plane reconstruction) images **(E, F)** are degraded.

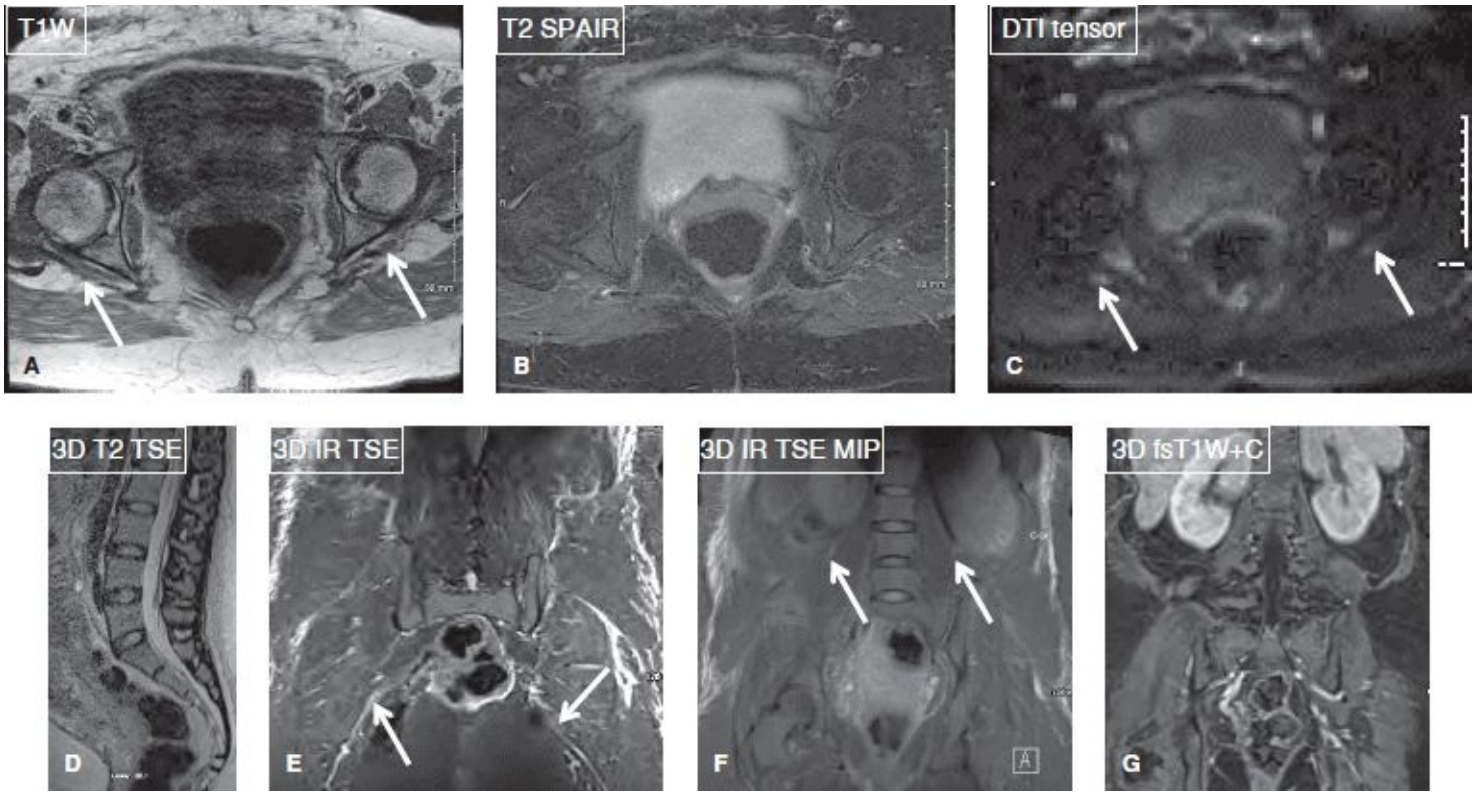

Fig. 5: MR neurography at 1.5T. Axial images **(A–C),** sagittal **(D),** and coronal **(E–G)** images in a case of traction neuropathies of right sciatic and femoral nerves (*arrows*). Notice good axial demonstration, however fat-suppressed 3D long-axis imaging is limited.

Coil Selection

Dedicated multichannel joint coils should be used in the extremities in an attempt to attain the best signal on average-sized patients. For larger-sized patients, large flex coils or torso array coils be more beneficial, especially in off-center areas of the magnet. The technologist should not try to wrap the joint and extremity together and image them both in the same field of view (FOV) because this results in low-quality images with a large blank space around the region of interest (ROI). One should aim at less than 20% blank (air) space around the extremity (Fig. 6). The technologist may have to do phase oversampling to avoid wraparound artifacts and encompass the small FOV imaging. For pelvis, lumbosacral or brachial plexus imaging, spine array coils can be combined with torso array coils on the front of the patient, or if the scanner does not allow that particular combo, a torso coil/cardiovascular coil with front and back coverage may be used to obtain the needed SNR, better signal homogeneity, and uniform fat suppression.

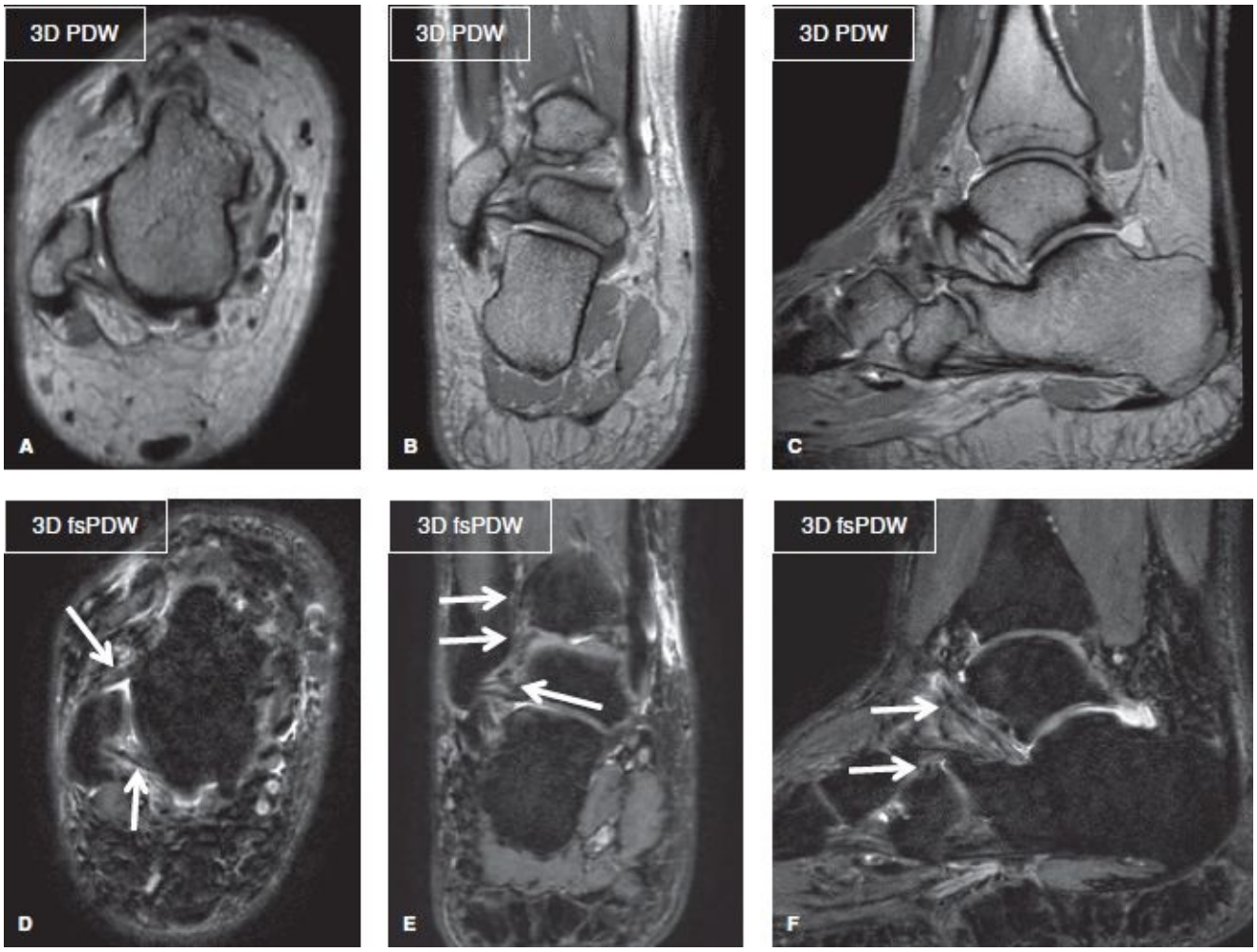

Fig. 6: Three-dimensional isotropic ankle imaging. Multiplanar 3D reformats **(A–F)** from 0.65-mm isotropic ankle images. Notice the tight field of view with less than 20% blank (air) space around this rather larger ankle. Images re coarse-looking but provide fine demonstration of the ankle ligaments (*arrows*).

Controlling Phase Wrap

While it is important to keep the FOV small (less than 10–14 cm for most joint protocols) to obtain good spatial resolution, wrap-around or fold-over artifacts may degrade the imaging. Certain strategies may be used to avoid phase wrap.

1. Use a larger enough FOV, but this may require zooming during image review to focus on the anatomy of interest and may leave excess blank (air) space around the ROI.
2. Use fold-over suppression (Philips) or phase oversampling (Siemens).
3. Employ conventional methods of saturation bands to eliminate signal from adjacent anatomy that is vulnerable to motion (e.g., lungs in arm imaging).
4. Use REST slabs as an alternative to oversampling for reducing the total scan time.
5. Use phase-encoding gradients in the sagittal plane for coronal anatomy (e.g., to avoid arms fold-over in the desired abdominal ROI).

K-space Profiling and Bandwidth

Asymmetric k-space profile ordering is used to reduce scan time by about 30% in proton density-weighted (PDW) and T1-weighted (T1W) images while minimizing blurring as compared to conventional k-space profiling (linear or centric).

- Asymmetric fast spin echo (FSE) scans permit independent specification of echo time (TE), echo spacing (ES), and echo train length (ETL or turbo factor).
- In general, shot length (ETL × ES) should not exceed 4 × TE for PDW images. For T1W images, shot length should be limited to 60 ms for good results.
- ES in most protocols is set at 8 to 9 ms (<8 in metal protocols and diffusion imaging), balancing the shot length against the imaging bandwidth.
- If a different profile order is used (such as linear or centric), reduce the ETL on these protocols by about 30%. Scan times will increase proportionately (Goumas, 2012).

Bandwidth in kHz (Siemens) versus direct specification of water-fat shift (WFS) in pixels (Philips) is an important parameter and measure of potential ringing artifact and impact on SNR independent of field strength, pixel size, and FOV.

- For musculoskeletal imaging, keep WFS between 1 and 2.5 pixels to avoid obscuring pathology (0.5 to 1.5 mm shift), <1.5 pixels for metal protocols (Fig. 7).

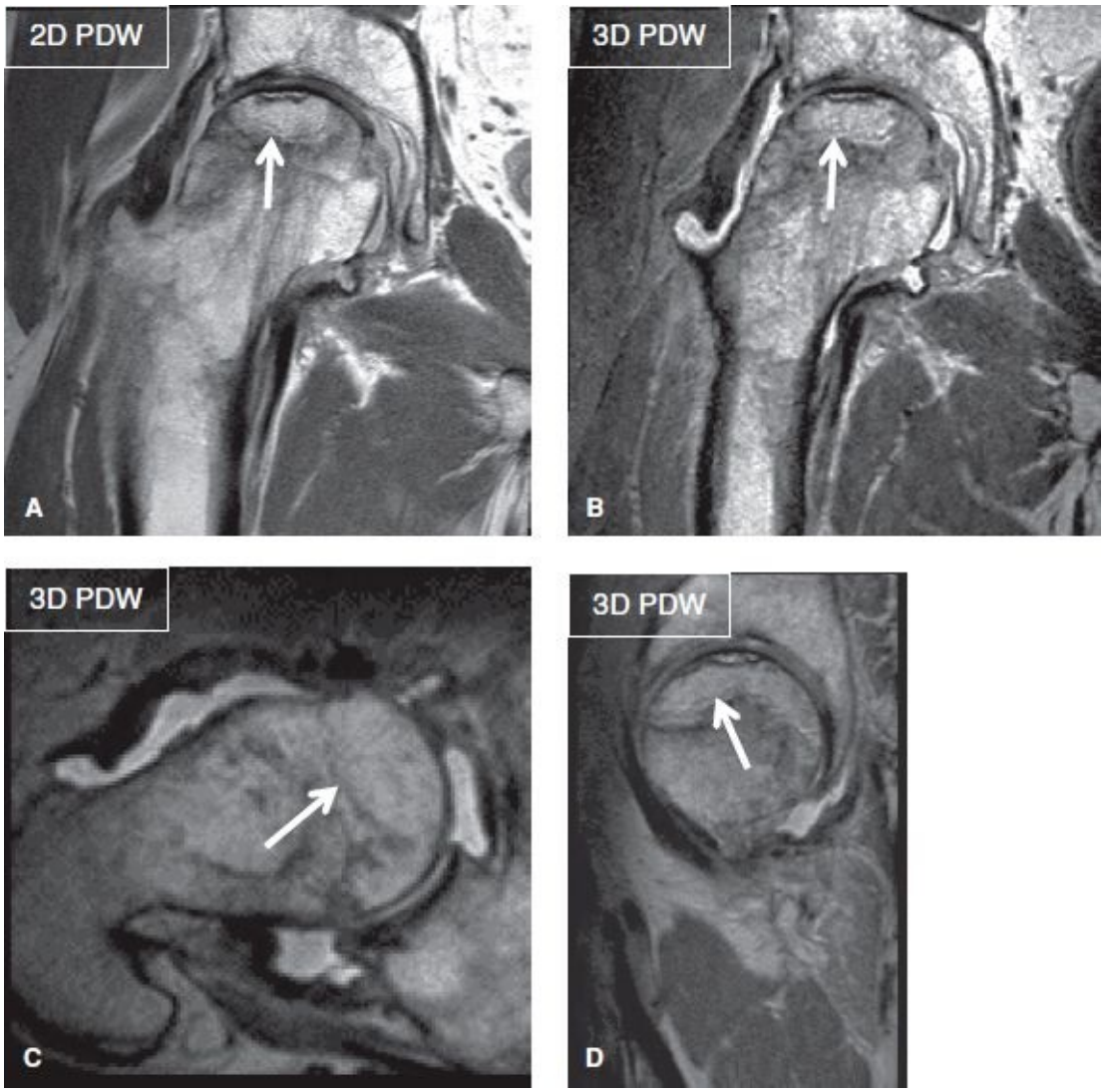

Fig. 7: Tight water-fat shift. Coronal 2D **(A)** and corresponding isotropic 3D **(B–D)** images

(TR/TE—1879/40 milliseconds) show high resolution (acquired 0.4 mm in-plane on 2D and 0.7 mm isotropic on 3D) with tight water-fat shift (1.37 pixel; bandwidth 317 Hz) and echo spacing (5.7). Notice femoral head AVN with subchondral fracture (*arrows*).

- Reducing WFS (increasing BW) reduces ES, which in turn reduces turbo spine echo (TSE) length, as well as image blurring.
- Reducing WFS (increasing BW) also reduces SNR.
- Conversion factors to remember (Goumas, 2012):

3T: BW (kHz) = 0.22 kHz × freq matrix/WFS pixels
1.5T: BW (kHz) = 0.11 kHz × freq matrix/WFS pixels

2D Imaging Pulse Sequences

A variety of 2D imaging pulse sequences are available for high-resolution musculoskeletal imaging resulting in different contrasts.

T1W Imaging

Commonly used sequences include T1W FSE or T1W TSE, T1W fluid-attenuated inversion recovery (T1W FLAIR) and T1W GRE. General advantages of T1W imaging include excellent demonstration of musculoskeletal anatomy with non-suppressed fat contrast, in terms of both bony morphology and alignment. T1W imaging is great for depicting subluxation, malalignment, bony spurs, and osteophytes. Since T2-weighted (T2W) images are very sensitive in identifying pathology (which is usually bright on these images), T1W imaging is very helpful in characterizing them. It characterizes both types of bony lesions that produce substantial T1 darkening in the marrow (fracture, infection, osteonecrosis, tumor infiltration, hemosiderin deposition, subchondral sclerosis, and cysts) and the lesions that produce minimal or no significant darkening in the marrow (red marrow, reactive edema, and disuse osteopenia). T1W images are also helpful in characterizing soft tissue lesions (e.g., most lesions are T1 dark whereas some are bright, such as hemorrhage, fat, melanin, calcification, and minerals).

T1W SE or T1W FLAIR sequences are useful in all musculoskeletal protocols. In routine "ortho" protocols, marrow evaluation is limited if T1W or chemical shift imaging (CSI) is not added (discussed below). T1W GRE is useful for scout imaging (for planning), in- and out-of-phase (for marrow evaluation), MR-guided intervention (MR fluoroscopy), kinematic joint imaging, MR angiography (MRAng), ultra-short TE imaging, arterial spin labeling and T1 mapping techniques used in cartilage imaging. MRAng is best obtained with time (temporally) resolved imaging technique using fast GRE T1W pulse sequence with acquisition of mask images and post-contrast serial 8 to 15 seconds thick slab acquisitions over 2 to 3 minutes. These are variably named as TWIST, TREAT, TRICKS, and 4D TRAK by different vendors. The major disadvantage is decreased spatial resolution, but there are many advantages, including decreased gadolinium dose, no need for test bolus, detection of

directionality of vascular flow, and acquisition of various phases of vascular, lesional and parenchymal enhancement. With subtraction manipulation, these images can be played in a cine loop for demonstration of various phases of vascular contrast enhancement. fsT1W FSE imaging is useful for 2D pre- and postcontrast imaging whereas fsT1W GRE can be applied for obtaining 3D pre- and postcontrast imaging. Three-dimensional GRE T1W is routine in most post-contrast protocols, and they are variably named by different vendors (VIBE, THRIVE, LAVA, mDixon). fsT1W spin echo-type 3D imaging (VISTA, SPACE) is also available for MR arthrogram (Fig. 8). These sequences potentially detect smaller tears that otherwise may be inapparent at 2D imaging. However, blurring on the images may not be pleasing to the reader.

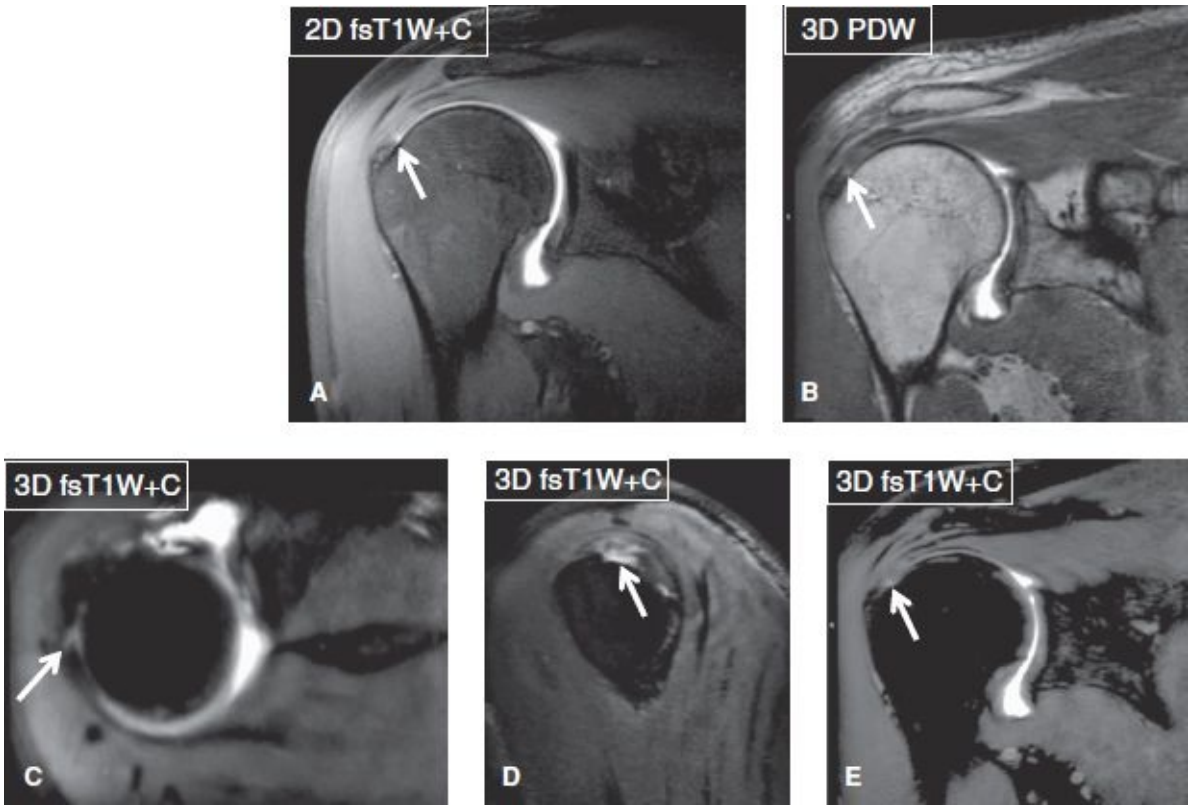

Fig. 8: MR arthrogram: 2D **(A, B)** versus 3D **(C–E)** images. Notice small undersurface tear of the rotator cuff (*arrows*), best seen on multiplanar isotropic 3D images.

PDW Imaging

Commonly used sequences include PDW and fsPDW. General advantages of PDW imaging include highest SNR amongst all available sequences, sharp image resolution, and excellent demonstration of musculoskeletal anatomy and pathology in terms of meniscal, anatomic cartilage, and ligament evaluation (essential for ortho and metal protocols) (Figs. 1–3, 6). Generally, bone marrow evaluation is limited on these ortho protocols if T1W imaging or CSI is not added to the technique (Fig. 9).

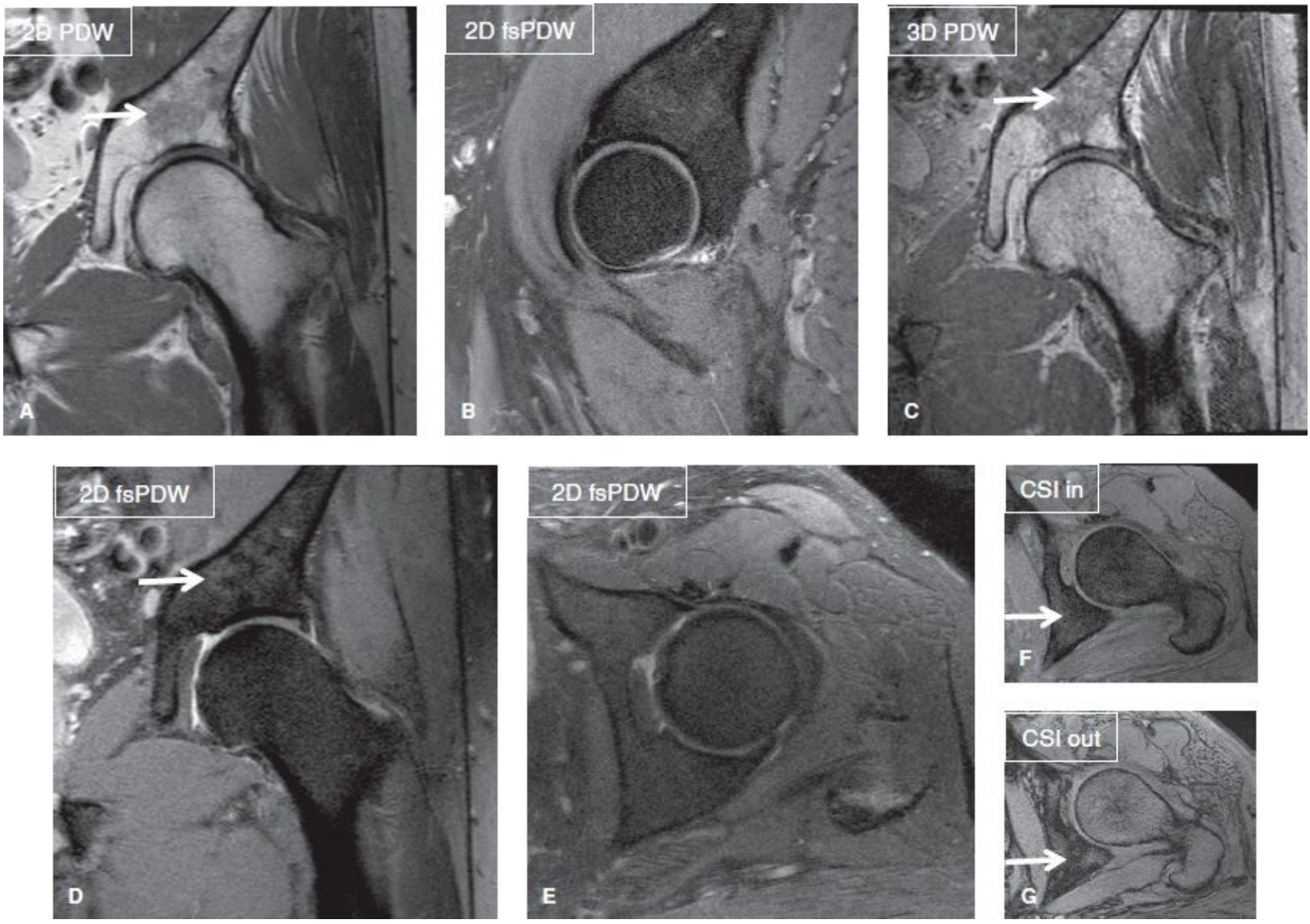

Fig. 9: CSI as part of ortho musculoskeletal (MSK) protocol. Coronal **(A, C, D),** sagittal **(B),** and axial **(E–G)** images show scattered areas of red marrow (*arrows*), which are brighter than muscles on PDW images. One such area is shown to lose signal on the out-of-phase image **(G)** relative to the in-phase image **(E)**.

T2W Imaging

Commonly used sequences include T2W FSE, T2W GRE, steady state, and ultrashort TE (UTE) pulse sequences. T2W imaging is helpful in detecting pathology since most lesions are bright on T2W imaging, e.g., infection, edema, cysts, tumors, and infarcts. Imaging characteristics that aid in lesion differentiation include very bright T2 signal (cyst, myxoma, cartilaginous lesion, slow-flow vascular malformation) or relatively dark T2 signal (hemosiderin in hemorrhage, pigmented villonodular synovitis, rheumatoid arthritis, gouty tophi, amyloid deposits, fibrous lesions, and calcific tendinitis). T2W FSE is also used for T2 cartilage mapping. Due to inherent blurring, less SNR associated with long TE on T2W sequences and longer time required to acquire these sequences, the recent trend is to move away from these sequences in most musculoskeletal “ortho” or “metal” protocols (Fig. 10). fsT2W FSE should be performed in infection, inflammation, and tumor protocols due to its

higher sensitivity for fluid. T2W GRE is used in suspected cases of calcific tendinitis or pigmented villonodular synovitis to demonstrate exaggerated susceptibility artifact (blooming), confirming the presence of above entities. One can easily obtain T2W GRE by employing lower flip angles (less than 30 degrees); and increasing the TE times. T2W GRE is also used for T2 cartilage mapping, which is faster but not superior to T2W FSE, due to inherent poorer SNR and more susceptibility to magnetic field alterations. Two-dimensional steady-state pulse sequences are useful for obtaining fast motion-free predominantly T2W images; however, the technique may be limited by off-resonance (banding) artifacts, suboptimal marrow evaluation, and nonspecific bright signals in all possible structures (fat, fluid, hemorrhage). Therefore, the technique has generally not gained much popularity in musculoskeletal protocols, except in few research papers. UTE (TEs <0.8 ms) is being experimented in musculoskeletal tissues with short T2 characteristics, such as cortical bone, ligaments, tendons, menisci, deep radial and calcified layers of cartilage, that otherwise generate little or no signal on conventional T2W images. With UTE MR imaging, signal from tissues with predominantly short T2 (and T2*) can be detected using TEs that are 20 to 50 times or even 100 to 1,000 times shorter than those used in conventional imaging sequences. The region of the osteochondral junction consisting of the calcified deeper cartilage layer can be evaluated using this sequence. This technique is also useful for delineating early stage of meniscus, ligament, and tendon degeneration; however, it remains experimental at the current stage.

Fig. 10: Thumb imaging. Coronal 3D PDW **(A, B)** and 3D fsT2W **(C)** imaging shows normal accessory collateral ligament at the metacarpophalangeal joint (*arrows* in **A**) and partial tears of the primary collateral ligaments (*arrows* in **B, C**). Note significant blurring on the fat-suppressed image **(C).**

3D Imaging Pulse Sequences

A variety of 3D pulse sequences are available for high-resolution musculoskeletal imaging, resulting in different contrasts. Except for GRE imaging, 3D with optimal SNR and spin echo-type good contrast is best obtained on 3T MR scanners. One can obtain non-fs3D imaging on newer 1.5T scanners; however, the images can be degraded by motion artifacts and nonisotropic reconstructions, and in addition, the sequence requires long imaging times.

T1W Imaging

Commonly used sequences include 3D T1W FSE and 3D T1W GRE. Three-dimensional T1W GRE imaging is mostly used for MR angiograms and contrast-enhanced examinations due to inherent poorer SNR and imaging contrast. Three-dimensional T1W FSE with or without fat suppression is now available and can be used in almost all protocols (Fig. 8).

PDW Imaging and Bone Segmentation

Commonly used sequences include 3D PDW and 3D fsPDW. They are most useful for ortho protocols, as described above (Figs. 1–3, 6). Three-dimensional PDW imaging produces sharp bony margins with superior SNR, and, therefore, it can be used for bone reconstruction and segmentation from MR images (Fig. 11). Currently, surgeons use 3D CT images for preoperative planning to complement the bone morphology information with soft tissue internal derangement findings. Using 3D isotropic sequences, which require an acceptable imaging time of 7 minutes, it is possible to acquire high-resolution 3D segmentations, with appearance similar to 3D CT images. On 3D software, segmentation can be automated, semiautomated or manual. Any of the axial, coronal, or sagittal 3D reconstructed sequences can be used to draw ROIs around the bony cortex. However, it is easiest on axial plane reconstructions. Most available softwares have slice interpolation functionality that allows several slices to be skipped between manual ROIs. The mask should be refined on all projections to ensure that soft tissues/cartilage are not included. Subsequently, all data outside the mask should be excluded and window/level should be adjusted for optimal visualization of the bony cortex. Finally, the color scheme should be adjusted depending on user's preference, and images should be captured and exported to the routine viewing workstation. Although there are many advantages to this approach (including single study for the patient, avoidance of radiation, more comfortable and time saving technique), there are limitations as well. Three-dimensional software is currently more user-friendly for bone segmentation on data derived from the CT examinations. It is a more time-consuming process with MRI (~20 to 30 minutes) since dedicated MRI processing algorithms are not yet available. Bony margins on MRI segmentations are comparable, though not as crisp as CT segmentations at current time.

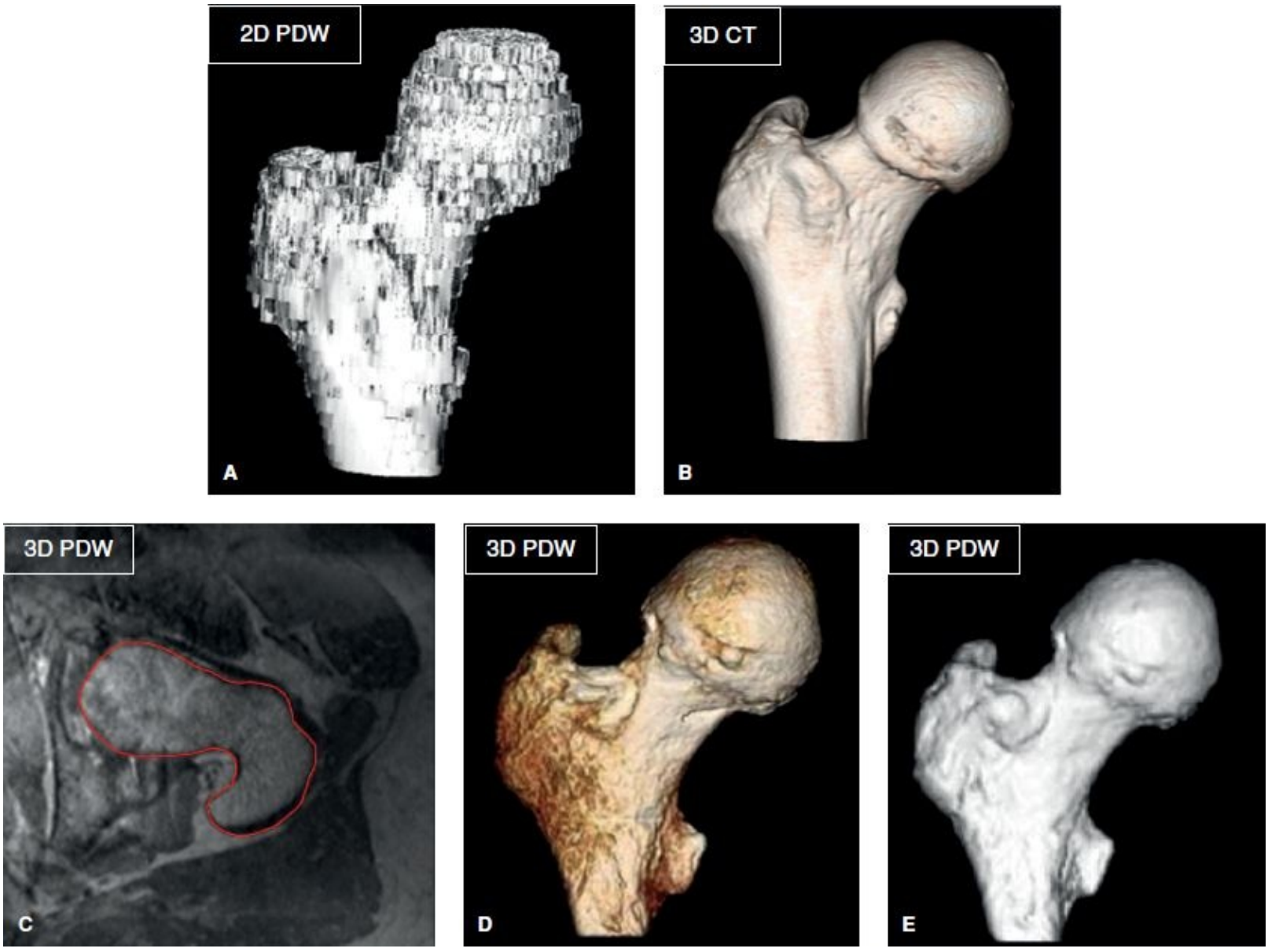

Fig. 11: Three-dimensional bone segmentation using 2D and 3D imaging. Coronal bone segmentation using 2D PDW image **(A)** shows many stair-step artifacts due to intervening gaps. Segmentation using 3D imaging **(C–E)** shows bony margins and morphologic details similar to 3D CT reconstruction **(B)**. Courtesy Shaun Nordeck, RRA.

T2W Imaging

Commonly used sequences include 3D T2W FSE, 3D T2W GRE, 3D steady state, and diffusion-weighted imaging (DWI) pulse sequences. Three-dimensional T2W TSE is used in the evaluation of masses, vascular malformations, as well as in neurography protocols (Fig. 12). Three-dimensional T2W GRE is used in spine imaging to differentiate discs from osteophytes and for detecting cord hemorrhage. Three-dimensional steady-state pulse sequences can be used for neurography (unbalanced 3D DW reversed steady-state free precession for extremity nerves and balanced steady state for intrathecal nerves during plexus evaluation for sharper and selective nerve depiction) (Figs. 12, 13) and cartilage imaging (balanced steady state free precession, SSFP; dual echo steady-state [DESS] imaging). Three-dimensional DESS on 3T scanners shows thicker cartilage with sharper

boundaries and excellent fluid–cartilage contrast as compared to 2D fsPDW (Fig. 14). It allows quantitative assessment of cartilage thickness and volume with good accuracy. In author's experience, some near full-thickness cartilage defects may be occasionally undercalled on DESS imaging if there is not enough fluid–cartilage contrast and the sequence is not optimized (TE should be within T2W range and flip angle approximately 45 to 60 degrees). DESS also has other advantages, such as isotropic 3D imaging, potential for cartilage segmentation, and less susceptibility artifacts compared to 3D GRE. However, DESS suffers from similar disadvantages as 3D GRE, in terms of suboptimal evaluation of subchondral bone marrow signal alterations and inadequate assessment of menisci and ligaments. DWI is obtained using single or multishot echoplanar imaging. Increasing diffusion restriction correlates with increased cellularity (indirectly increased chances of malignancy in indeterminate soft tissue lesions). High signal on DWI with low ADC may also be seen in malignant bone lesions, abscess and, in active inflammation and edema (due to T2 shine through). Hematoma shows mixed signal, with predominant hypointensity, due to combination of T2 shine through and susceptibility artifacts. DWI allows assessment of apparent diffusion coefficient and provides a means for quantitative assessment of pathology. Although demanding on the scanner, diffusion tensor imaging (DTI, employing at least six directions of gradient interrogation) also allows assessment of directionality of diffusion, calculation of fractional anisotropy values and tractography (Fig. 15). DWI and DTI can be used as part of infection, mass, inflammation (myositis), and neurography protocols (Figs. 12, 16). A number of artifacts, such as ghosting, motion, poor fat saturation, and susceptibility may degrade DWI and DTI. Good fat suppression methods, shimming and tighter ES, allow superior diffusion imaging.

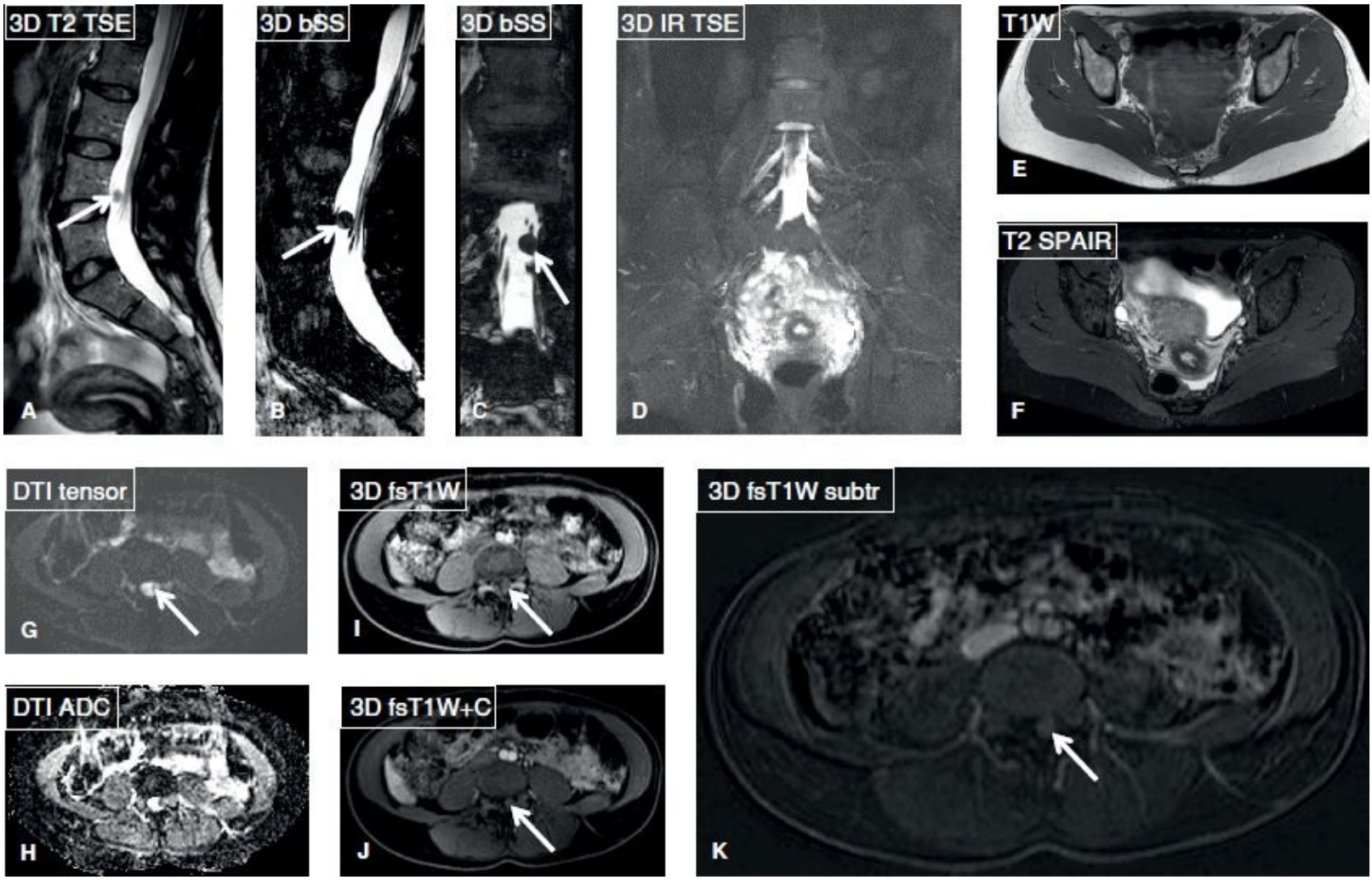

Fig. 12: MR neurography protocol for lumbosacral plexus evaluation. **A–C:** Sagittal spine images. Notice sharper and more distinct demonstration of a small peripheral nerve sheath tumor of the left L4 nerve root (*arrows*) on the balanced steady-state (bSS) sequence as compared to T2W TSE. Coronal **(D)** and axial images **(G–K)** show the bright enhancing mass in different planes (*arrows*).

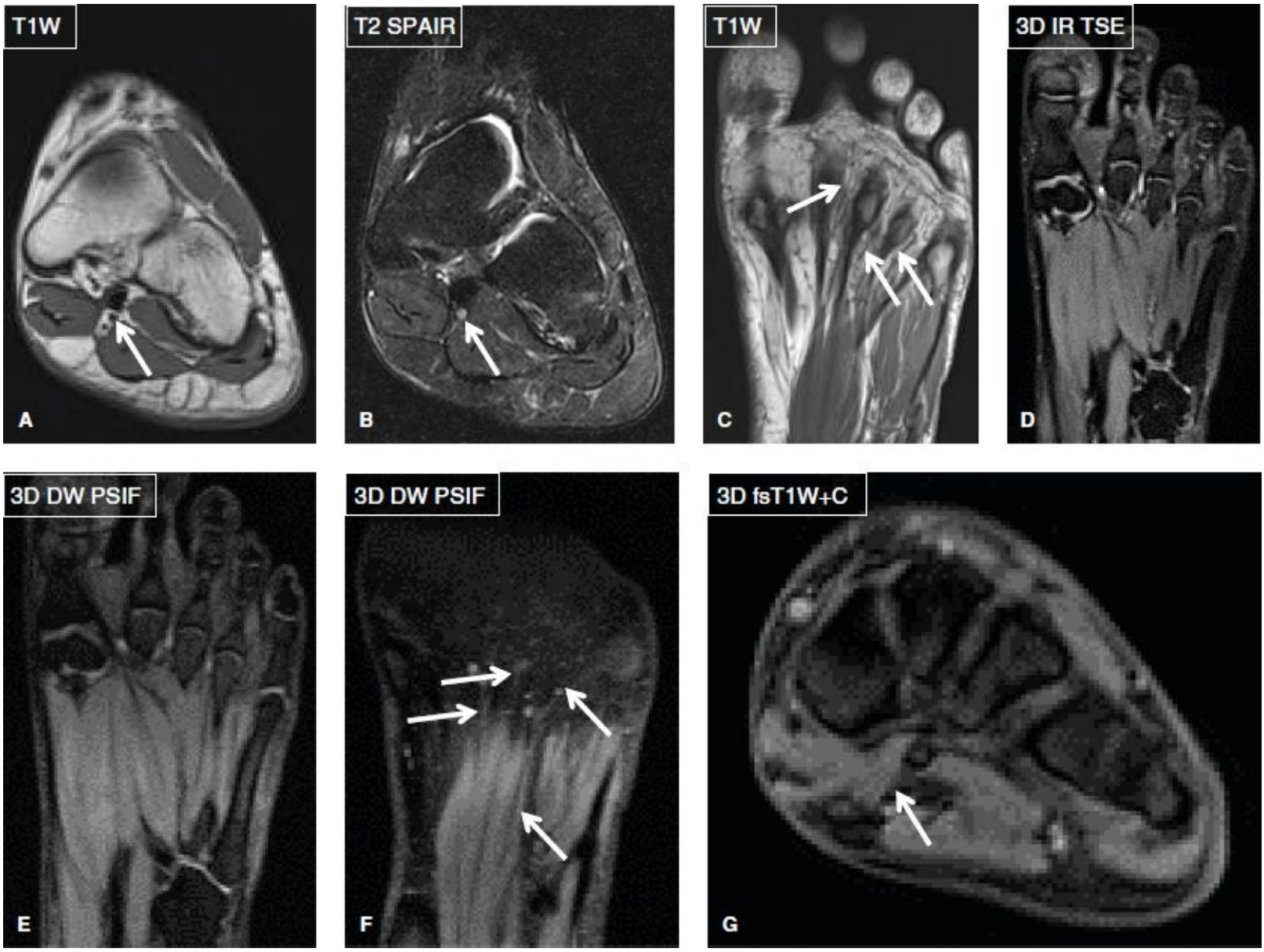

Fig. 13: MR neurography extremity protocol. Short-axis **(A, B),** horizontal long-axis **(C–F),** and postcontrast short-axis **(G)** images of the forefoot and midfoot. Notice normal isointense foot nerves (*arrows*) in all sequences. Medial plantar nerve is bright in **B** due to magic angle phenomenon.

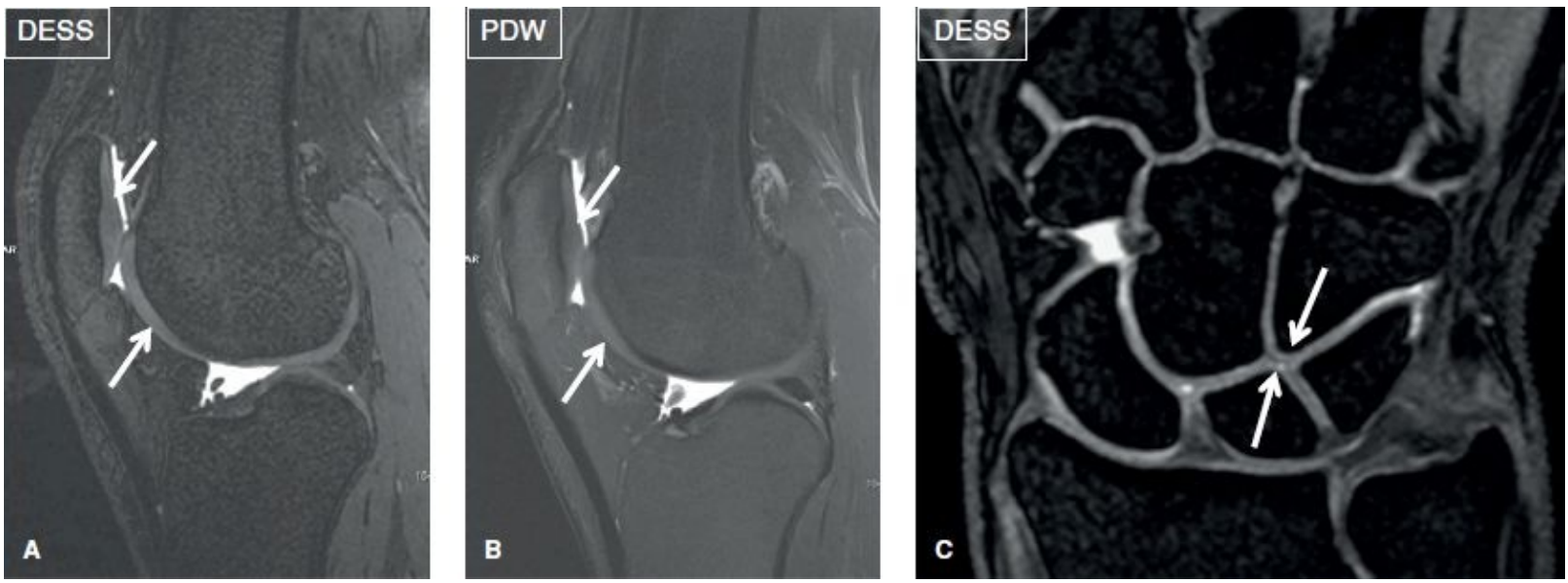

Fig. 14: Three-dimensional DESS and 2D PDW for articular cartilage evaluation. Sagittal **(A, B)** images show excellent fluid–cartilage contrast and sharper cartilage boundary (*arrows*) than 3D DESS **(A)** as compared to 2D PDW imaging **(B)**. Coronal **(C)** image shows type II lunate facet with normal hamatolunate articular cartilage.

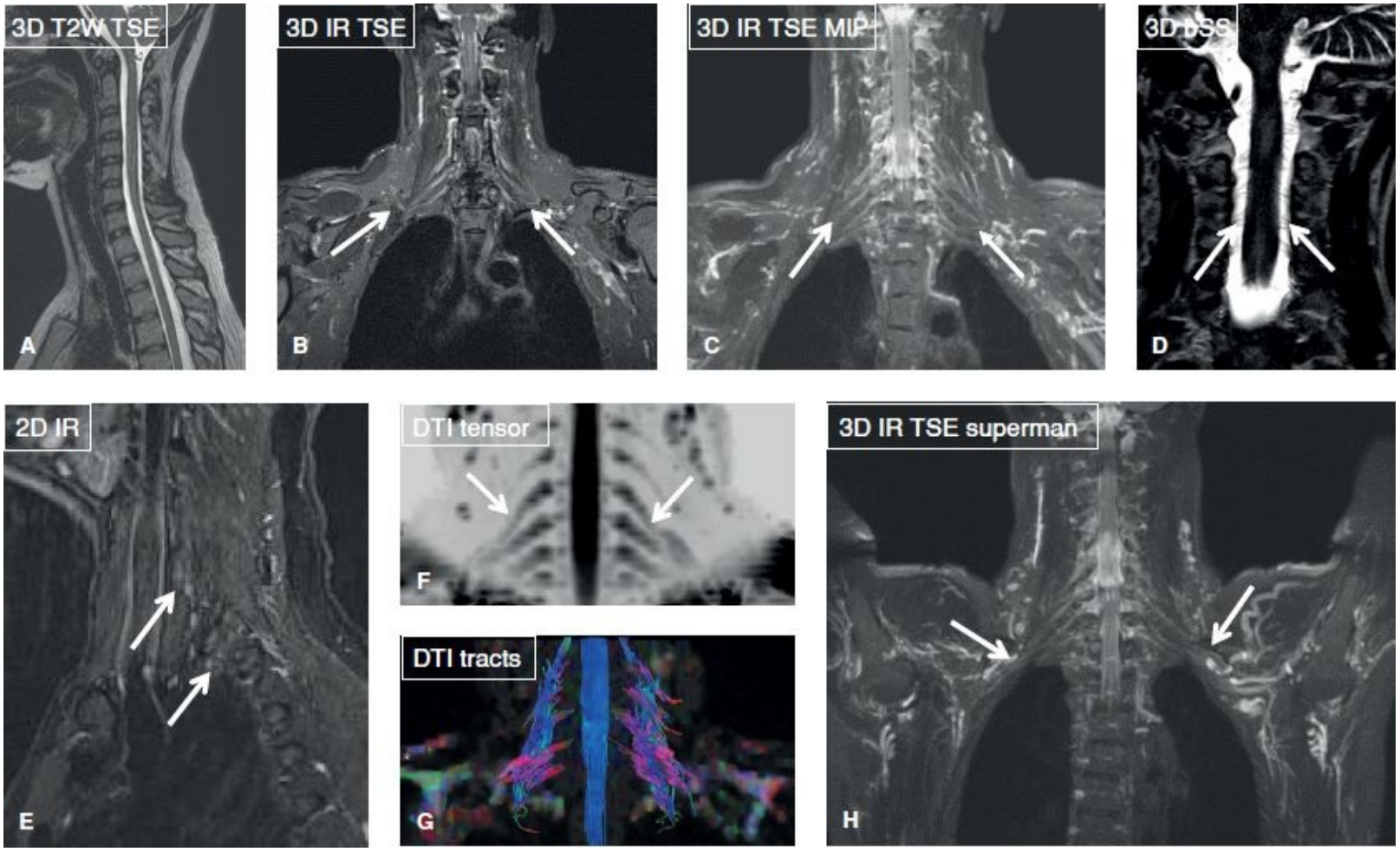

Fig. 15: MR neurography protocol with DTI. Sagittal **(A),** coronal **(B–D),** and sagittal **(E)** images show elegant depiction of normal spine, postganglionic and preganglionic brachial plexuses (*arrows*). Coronal reformatted images and tractography **(F, G)** from axial DTI images show the bilaterally symmetric brachial plexus (*arrows*). Coronal superman position imaging **(H)** shows no abnormal kinking or entrapment of nerve roots (*arrows*).

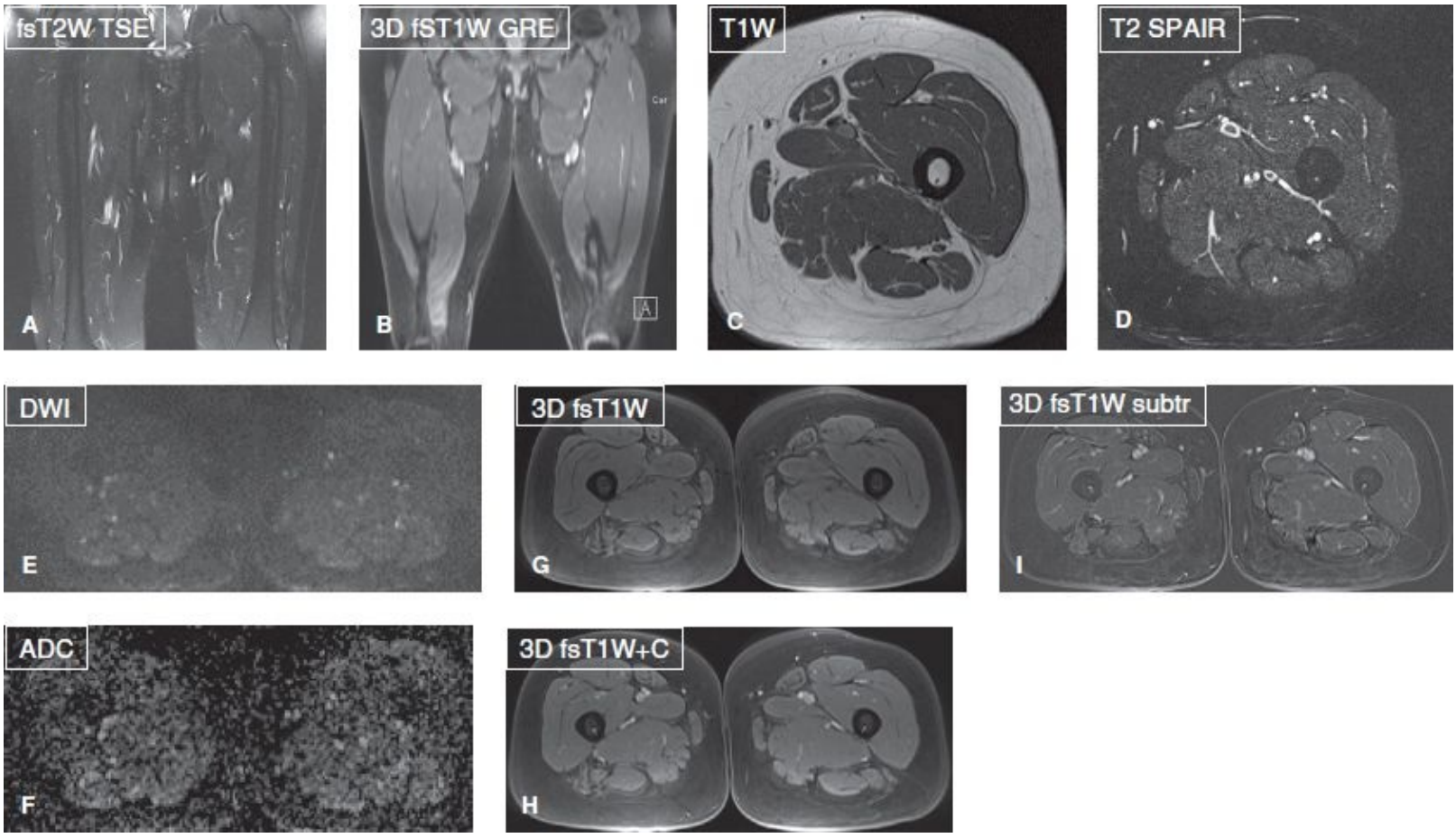

Fig. 16: Myositis protocol. Coronal **(A, B),** axial **(C–I)** images show normal muscles on various sequences in a suspected myositis case.

Fat Suppression Methods

Uniform fat suppression increases contrast-to-noise ratio in MR images. A number of fat suppression methods are available with different advantages and limitations.

Chemical Shift Imaging

CSI is obtained using GRE technique and allows T1W imaging. It is useful for marrow assessment and exclusion of malignancy in focal indeterminate lesions related to red marrow foci and compression fractures by demonstrating more than 20% signal loss on out-of-phase imaging with excellent accuracy (Fig. 9). CSI can be used as an alternative to T1W imaging in ortho, spine, and tumor protocols. It can be obtained in short periods of time and is useful in clinical practice. CSI can also show reverse phenomenon of increased relative signal on out-of-phase images due to hemosiderin deposition (e.g., in hemolytic anemia, PVNS or transfusional siderosis).

Frequency-selective Fat Suppression

This is available for T1W (contrast imaging), PDW (ortho protocol), and T2W imaging (mass protocol). Advantages include high-contrast imaging and superior SNR with little pulsation artifacts (Fig. 17). Disadvantages include loss of fat suppression in off-center

areas, especially on 1.5T imaging and along the curvatures of extremities. Only 2D mode is useful.

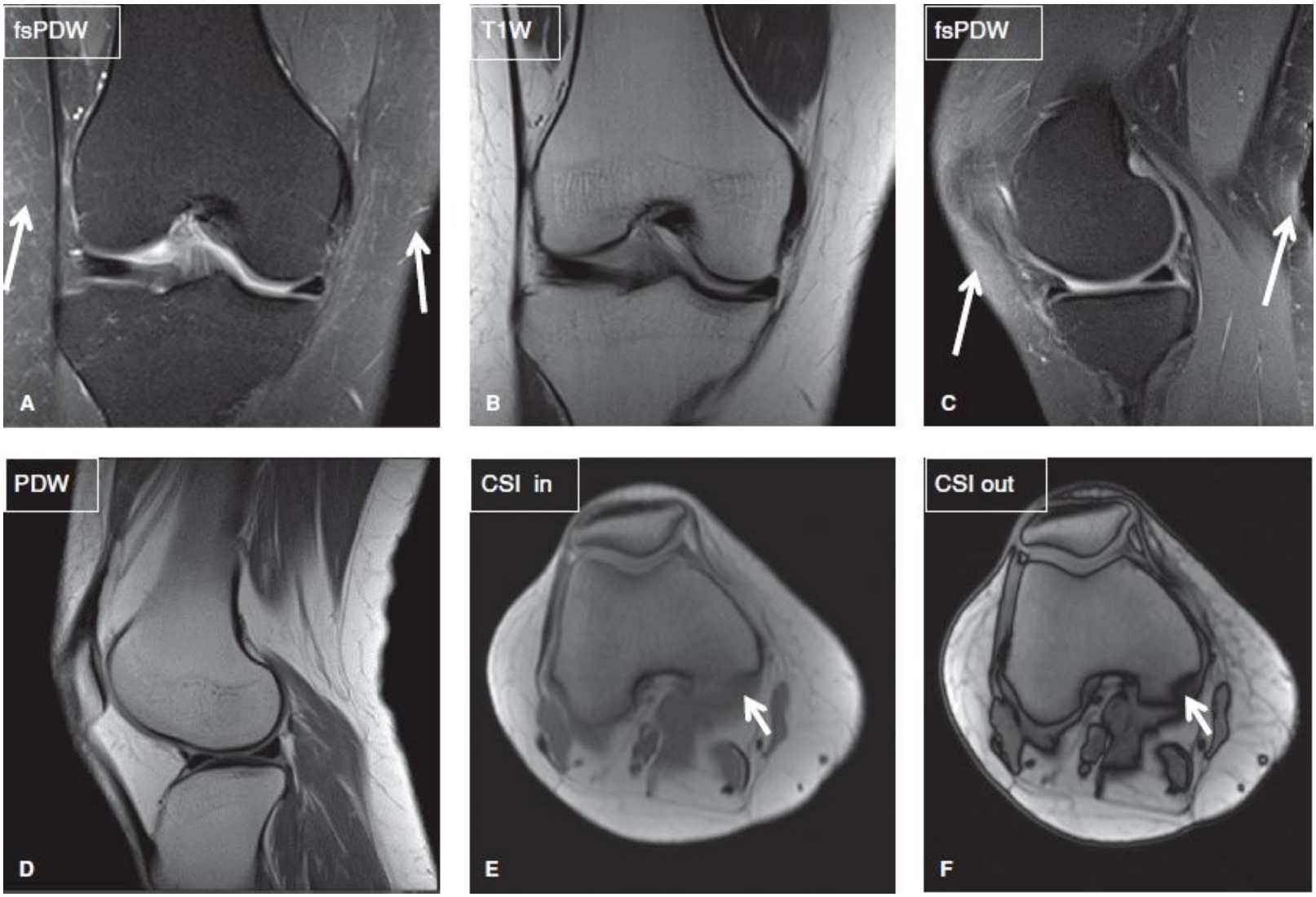

Fig. 17: Knee (ortho) protocol. Coronal **(A, B),** sagittal **(C, D),** and axial **(E, F)** images show inhomogeneous frequency-selective fat suppression at the curvatures of the knee (*long arrows*). Notice loss of signal in benign subcortical avulsive cyst of the far posterior medial femoral condyle (*short arrows*).

Dixon Type or Water Selective (Proset, Philips)

This can be obtained as two-point, three-point, or modified Dixon (mDixon) methods and can be added to any pulse sequence. Advantages include superior fat suppression and generation of multiple images with water only, fat only, and water plus fat contrast images. On some vendors, such as on Philips, Dixon images include water only, fat only, in-phase water plus fat, and out of phase water and fat. This also results in potential scan time savings because of obtaining multiple image types (e.g., Images w/wo FS) in near equal scan times. Lastly, because of the multiple echoes acquired, there is a signal benefit of Dixon that can be traded for time or image quality. Disadvantages in general include, little bit longer imaging times, less soft tissue contrast than frequency selective images, and

infrequent, but possible loss of fat saturation in off-center areas. Until recently, only 2D mode was available with Dixon imaging, but some vendors have incorporated this method with additional 3D imaging. Two-dimensional Dixon produces good results for nerve imaging; however, 3D Dixon also provides vasculature signal nulling, sharper images, and ability for isotropic multiplanar reconstructions (Fig. 18). Three-dimensional mode is also available with water-selective fat saturation technique for GRE (three-dimensional diffusion-weighted reversed fast imaging with steady state precession, 3D DW PSIF). It is a sensitive sequence and requires good shimming, smaller FOVs (limited to 15 cm), and good coils. Three-dimensional PSIF is very useful for extremity neurography for long-axis selective depiction of peripheral nerves (Fig. 13).

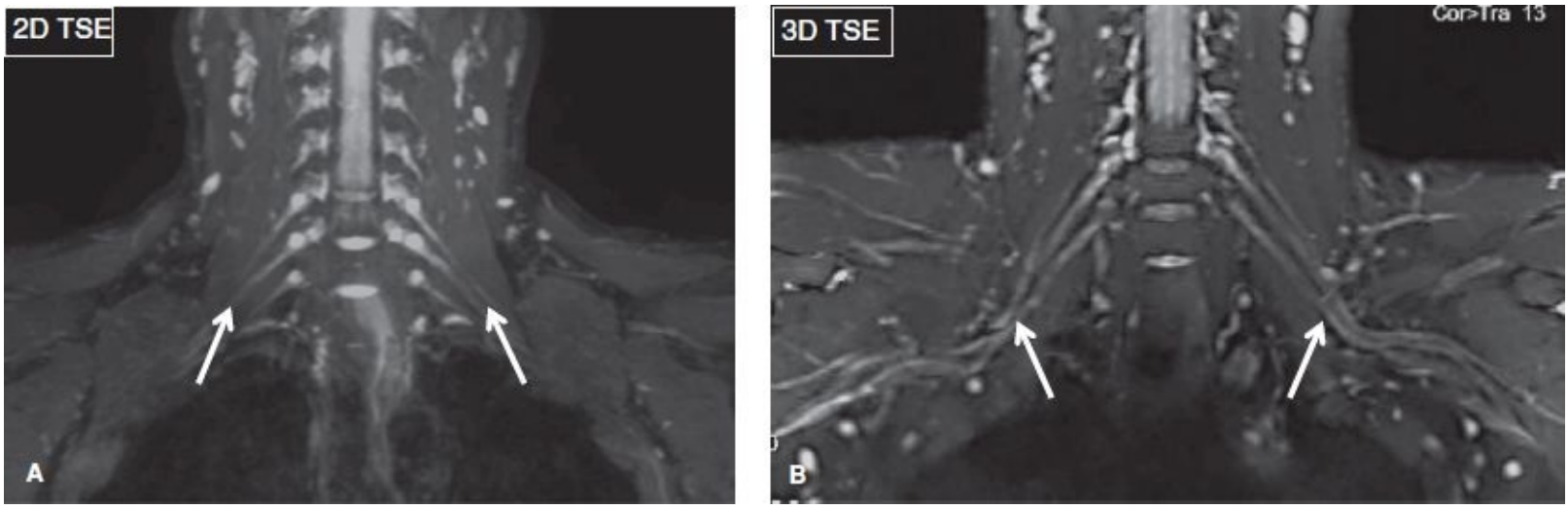

Fig. 18: Two-dimensional Dixon water-only images. Notice high SNR and excellent depiction of bilateral brachial plexuses (*arrows*) on 3D **(B)** image as compared to 2D **(A)** image.

Spectral Adiabatic Inversion Recovery

Spectral adiabatic inversion recovery (SPAIR) is available with T1W, PDW, and T2W imaging. Advantages include superior and more uniform fat suppression in off-center areas with a user adjustable time of inversion and higher SNR than short tau inversion recovery (STIR) imaging, more specific absorption rate (SAR) responsive at 3T and with almost no pulsation artifacts. One can increase the SPAIR inversion time for softer (weak) fat saturation. Disadvantages of SPAIR sequence include slightly less SNR than frequency-selective fsFSE images and loss of fat suppression at the margins of elongated FOVs. However, SPAIR can be set to have more SNR if TI time is selected beyond the null point. It is frequently used in neurography and vascular malformation protocols since both 2D and 3D modes are available and pulsation artifacts are nearly absent in this technique (Figs. 12, 19). On 3T, the tau time for T2 3D SPAIR is approximately 220 to 230 milliseconds, and it is quiet lower for 3D T1W fat suppression (60 to 80 milliseconds). Spectral presaturation inversion recovery (SPIR, Philips) is another technique that uses smaller flip angle for spectral fat inversion than the non-selective STIR. It is more vulnerable to RF inhomogeneity at 3T, but shorter prepulse may be helpful in some applications and scan

times.

Short Tau Inversion Recovery

STIR provides the best fat suppression even at low-field scanners and demonstrates remarkable sensitivity for pathology detection. However, this sequence is not specific, as it can suppress other tissues, such as blood or muscle. Also, STIR is marred by frequent pulsation artifacts and inferior SNR. It is available in both 2D and 3D modes. It is used in 3D neurography of plexuses as well as in myositis, spine, metal, and mass protocols to create longitudinal images for large area coverage due to excellent fat suppression capability (Fig. 15).

PROTOCOLS

With the knowledge of above-described advantages and disadvantages of various available imaging sequences, guides for different musculoskeletal protocols are outlined below.

Ortho Protocol

- Keep TE for PDW (40 to 45 ms), fsPDW (35 to 40 ms), slice for 2D 2.5 to 4 mm depending upon the FOV, in-plane resolution (0.4 to 0.5 mm), voxel for 3D (0.65 to 0.7 mm isotropic) (Figs. 9, 17, 20).
- 3 T: Scout GRE in three planes, 3D PDW TSE and 3D fsPDW TSE, two or more planes 2D PDW TSE or fsPDW TSE (back up for 3D failure, slice 2.5 to 3 mm), CSI GRE (in and out-of-phase T1W). If 3D not available, use protocol similar to 1.5T as below.
- 1.5T: Scout GRE in three planes, 2D PDW TSE and 2D fsPDW TSE in three planes (may reduce 2D PDW TSE in nonessential plane, slice 3 to 4 mm), CSI GRE (in and out-of-phase T1W).

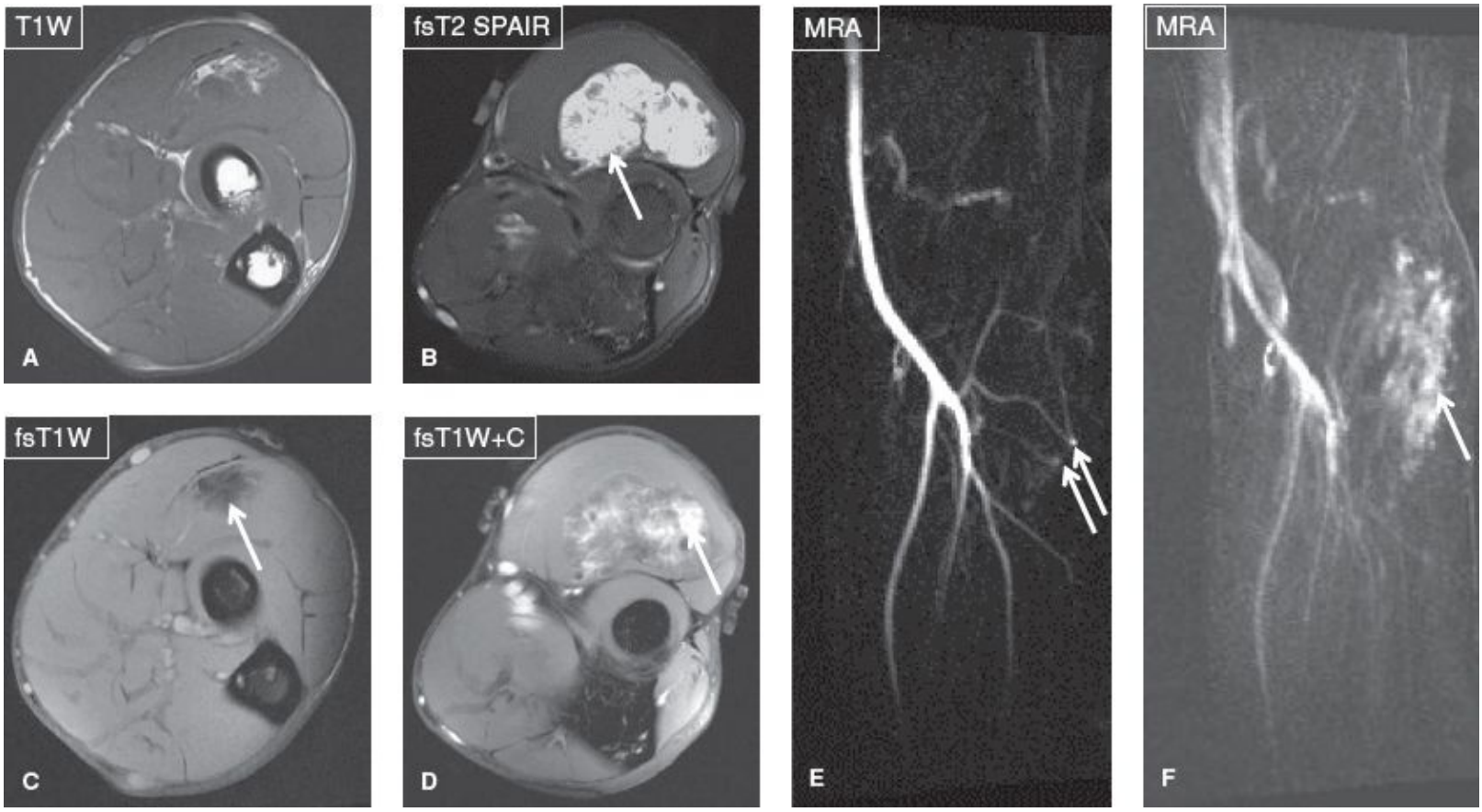

Fig. 19: Vascular malformation protocol. Axial images **(A–D)** show fat-containing intramuscular mass (*arrows* in **A, C**) with internal phleboliths (*arrow* in **B**) and patchy enhancement (*arrow* in **D**) in a hemangioma. Time-resolved MR angiography images early arterial flow (*arrows* in **E**) with persistent dense enhancement (*arrow* in **F**).

2D fsPDW
A
3D PDW
B
3D fsPDW
C
GRE out
D
3D PDW
E
3D PDW
F
3D PDW
G
3D fspDW
H
3D PDW
I
3D PDW
J

Fig. 20: Forefoot–midfoot ortho protocol. Tension-type intratrabecular fracture of the second metatarsal in a young ballerina with small avulsed fragment bone fragment. Short-axis images **(A–C)** and horizontal long-axis out-of-phase GRE **(D)** image shows intact bundles of Lisfranc ligament (*arrows* in **A–C**), best seen on 3D images and fracture (*arrow* in **D**), best seen on GRE image. Corresponding horizontal long-axis images show the different bundles of the Lisfranc ligament, namely dorsal C1M2 (*arrows* in **E, H**), plantar C1M2 (*arrows* in **F, I**), and plantar C1M3 (*arrows* in **G, J**). Notice avulsed fracture fragment is at plantar C1M2 bundle attachment.

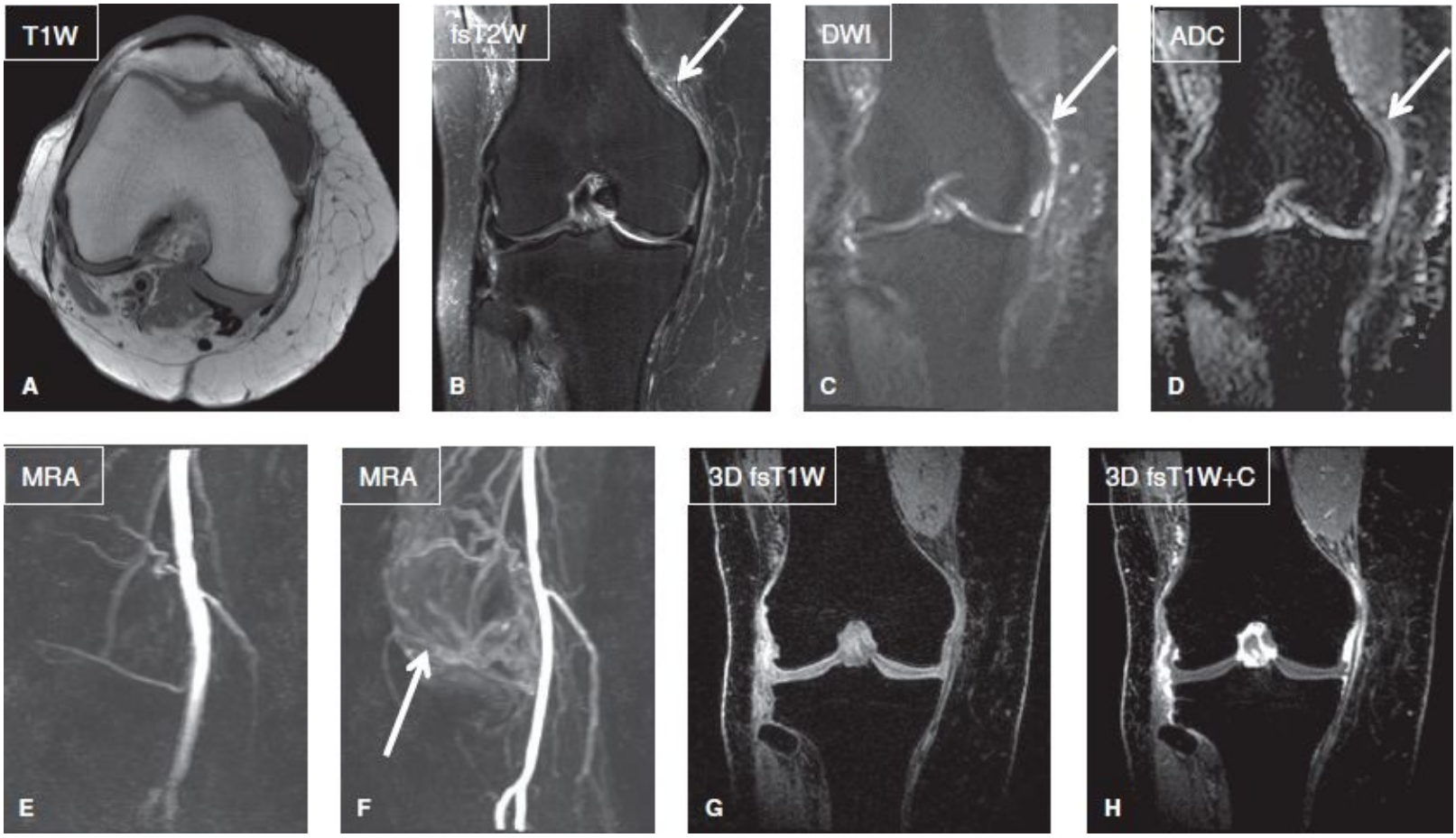

Fig. 21: Infection protocol. Axial **(A)** and coronal **(B–H)** images show posterior soft tissue edema and increased venous phase vascularity in this case of cellulitis (*arrows*).

Infection/Inflammation (Rheumatology) Protocol

- Keep TE for T1W (<8 to 9 ms), STIR (25 to 35 ms), SPAIR (40 to 50 ms), slice for 2D 3 to 4 mm, voxel for 3D (1.5 mm isotropic) (Fig. 21).
- 3 T: Scout GRE in three planes, 3D T1W TSE or axial and coronal 2D T1W, long-axis 3D T2 SPAIR TSE or 2D STIR in two longitudinal planes, axial 2D fsT2 TSE (back up for 3D failure), pre- and postcontrast fs3D T1W TSE (Tau ~60 to 80 ms) or 3D T1W GRE (1.5 mm) with possible subtraction manipulation, if possible.
- 1.5 T: Scout GRE in three planes, axial and coronal 2D T1 W FSE, 2D STIR in two longitudinal planes and axial 2D fsT2W TSE, pre- and postcontrast fsT1W or 3D T1W GRE with possible subtraction manipulation, if possible.

Tumor (Mass) Protocol

- Keep TE for T1W (<8 to 9 ms), STIR (25 to 35 ms), SPAIR (40 to 50 ms), slice for 2D 3 to 4 mm, voxel for 3D (1.5 mm isotropic) (Fig. 22).

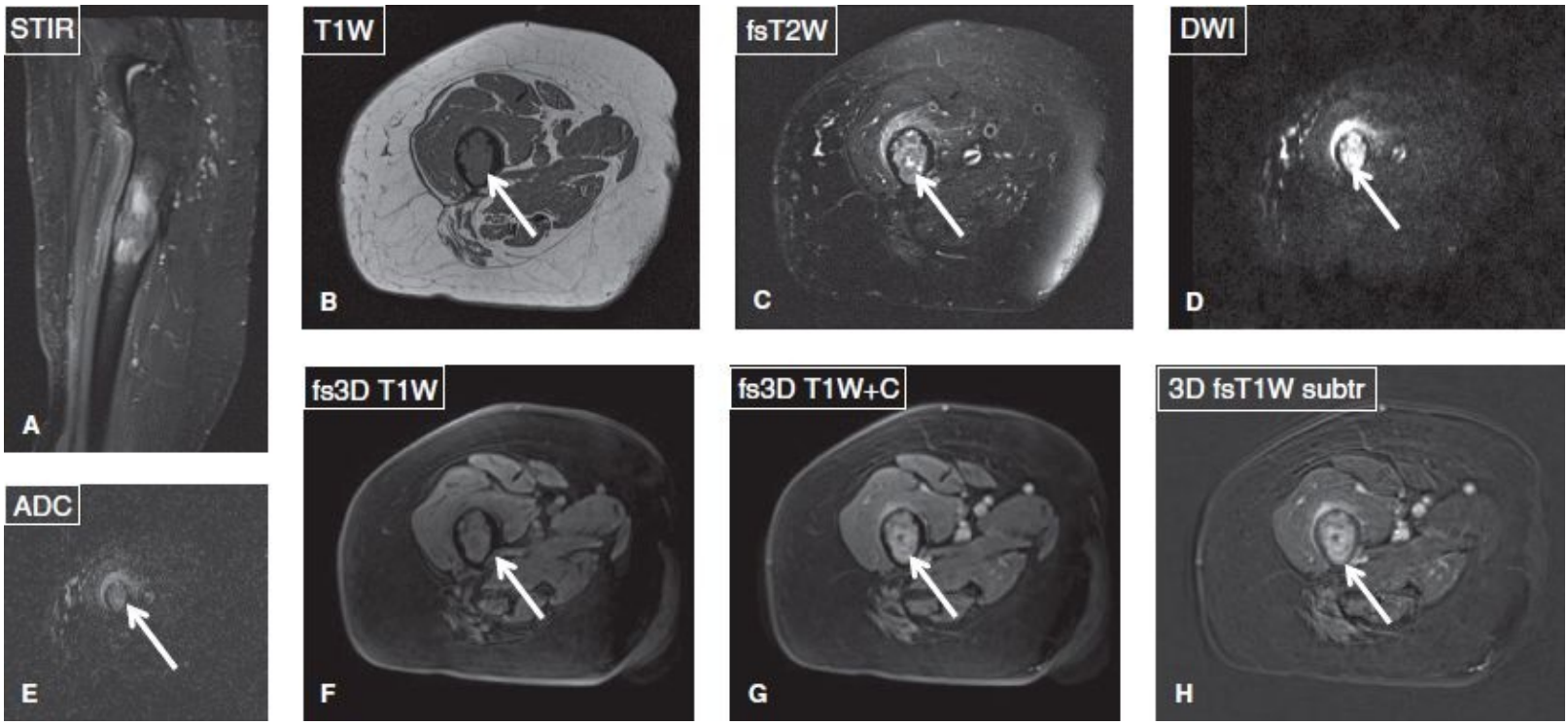

Fig. 22: Tumor protocol. Sagittal **(A)** and axial **(B–H)** pre- and postcontrast images of a metastatic lesion (*arrows*) in the femur.

- 3 T: Scout GRE in three planes, 3D T1W TSE or axial and coronal 2D T1W, long-axis 3D SPAIR FSE or 2D STIR in two longitudinal planes, axial 2D fsT2W TSE (back up for 3D failure), postcontrast MR angiogram using time-resolved technique in coronal plane with subtraction, pre- and postcontrast fs3D T1W (tau ~60 to 80 ms) or 3D GRE with possible subtraction manipulation, if possible and DWI (b values 50, 400, 800 s/mm2).
- 1.5 T: Scout GRE in three planes, axial and coronal 2D T1W TSE, 2D STIR in two longitudinal planes and axial 2D fsT2W TSE, postcontrast MR angiogram using time-resolved technique in coronal plane with subtraction, pre- and postcontrast fsT1W or 3D GRE with possible subtraction manipulation, if possible and DWI (b values 50, 400, 800 s/mm2).

MR Arthrogram Protocol

- Keep TE for fsT1W (<8 to 9 ms), fsPDW (35 to 40 ms), slice for 2D 3 to 4 mm, in-plane resolution (0.4 mm), voxel for 3D (isotropic 0.65 to 0.7 mm), tau for 3D fsT1W (60 to 80 ms) (Fig. 8).
- 3 T: Scout GRE in three planes, coronal 3D fsPDW TSE, 3D fsT1W FSE, two plane 2D fsT1W FSE (for 3D failure), optional coronal 3D PDW TSE, CSI GRE (in and out-of-phase T1W). If 3D not available, use protocol similar to 1.5T.
- 1.5 T: Scout GRE in three planes, coronal 2D fsPDW TSE and three plane 2D fsT1W FSE,

optional 2D coronal PD, CSI GRE (in and out-of-phase T1W).

Vascular Malformation Protocol

- Keep TE for T1W (<8 to 9 ms), SPAIR (40 to 50 ms), slice for 2D 3 to 4 mm, voxel for 3D (1.5 mm isotropic) (Figs. 19, 23).
- 3 T: Scout GRE in three planes, 3D T1W TSE or axial and coronal 2D T1W and long-axis 3D T2 SPAIR or 2D long-axis T2 SPAIR, axial 2D T2 SPAIR (back up for 3D failure), postcontrast MR angiogram using time-resolved technique in coronal plane with subtraction for cine play for various contrast phases, pre- and postcontrast fs3D T1W TSE or 3D GRE with possible subtraction manipulation, if possible.
- 1.5 T: Scout GRE in three planes, axial and coronal 2D T1W TSE, 2D T2 SPAIR in long plane and axial 2D T2 SPAIR, postcontrast MR angiogram using time-resolved technique in coronal plane with subtraction for cine play for various contrast phases, pre- and postcontrast fsT1W TSE or 3D GRE with possible subtraction manipulation, if possible.

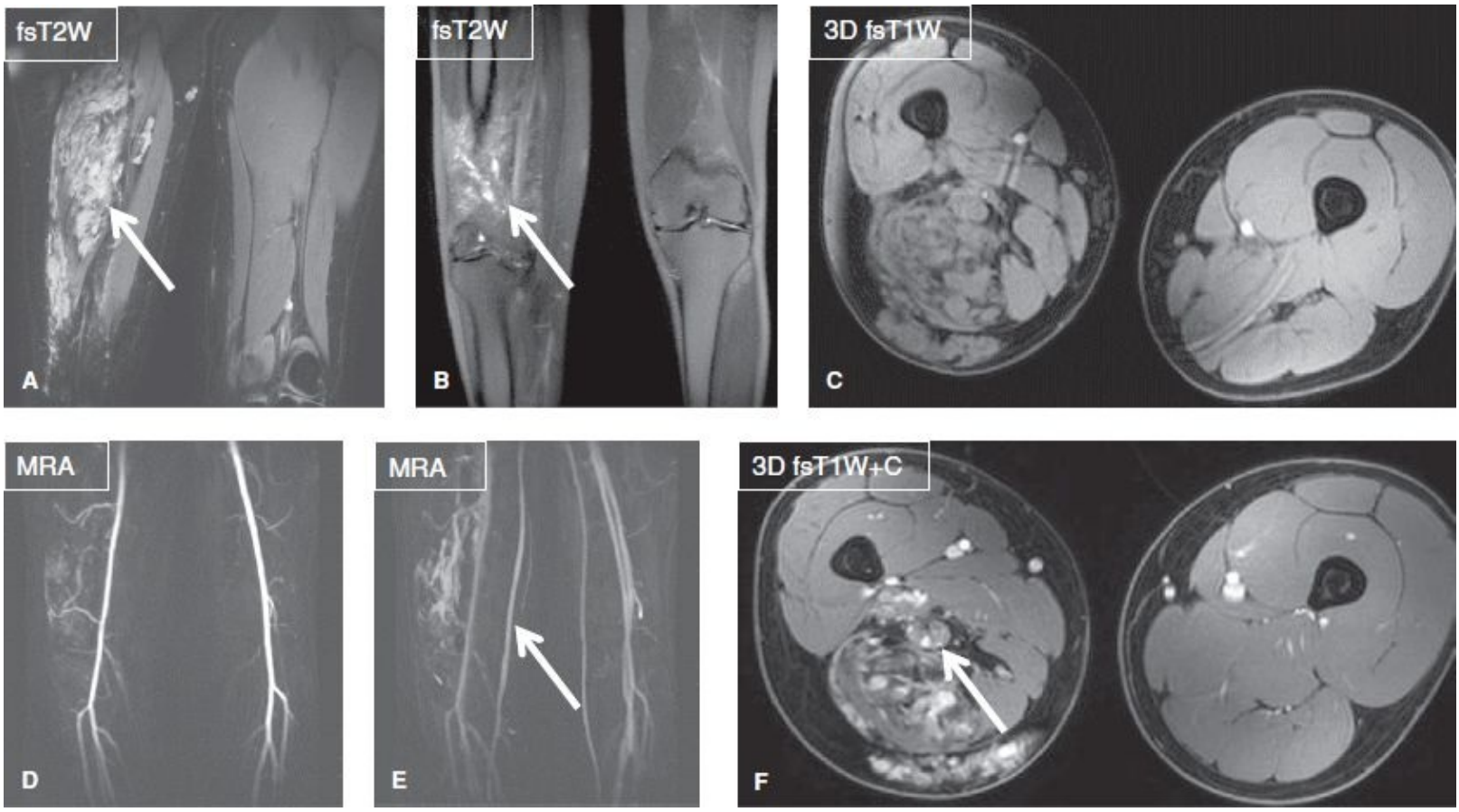

Fig. 23: Vascular malformation protocol. Coronal **(A, B)** images show a slow-flow large infiltrative polylobular vascular malformation (*arrows*) devoid of flow voids. Axial precontrast **(C)** and postcontrast **(F)** images show the vascular enhancement without a soft tissue mass. MRA images in arterial phase **(D)** and venous phase **(E)** show multiple arterial feeders but no venous shunting in the arterial phase. The lesion shows increase in flow via the greater saphenous vein (*arrow* in **E**) and epineurial perisciatic flow (*arrow* in **F**) due to ipsilateral popliteal venous thrombosis. Also note the marked enlargement of the right sciatic nerve.

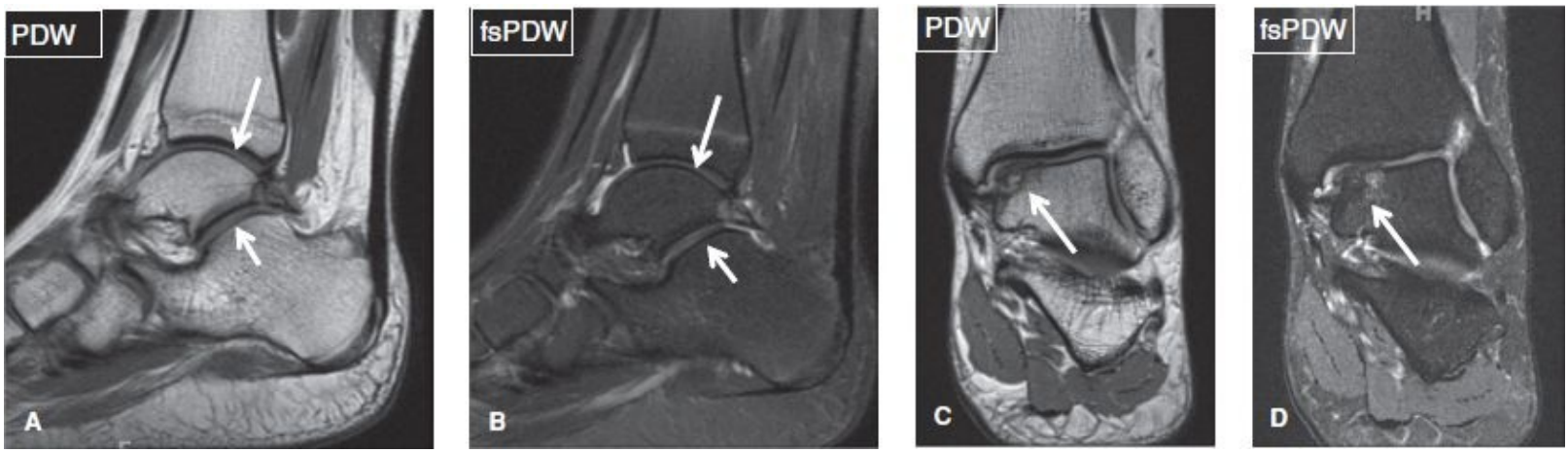

Fig. 24: Routine articular cartilage imaging. Sagittal images **(A, B)** of a normal ankle shows normal tibiotalar (*long arrows*) and posterior subtalar (*short arrows*) cartilage. Coronal images after cartilage repair **(C, D)** show good bony coverage with minimally proud cartilage at the repair site (*arrows*). Notice subjacent bone marrow edema and cysts, expected at early postoperative stage.

Cartilage Protocol

- Keep TE for PDW (40 to 45 ms), fsPDW (30 to 40 ms), slice for 2D 3 to 4 mm, in-plane resolution (0.4 mm), voxel for 3D (0.65 to 0.7 mm isotropic) (Fig. 24).
- 3 T: Scout GRE in three planes, 3D PDW TSE and 3D fsPDW TSE, two or more plane 2D fsPDW TSE (back up for 3D failure), optional 3D DESS sequence. T2 mapping (using GRE or FSE) or T1 mapping (DGEMRIC with gadolinium or T1 rho or gag CEST). Optional DWI. If 3D not available, use 1.5T protocol.
- 1.5 T: Scout GRE in three planes, 2D PDW TSE and 2D fsPDW TSE in three planes (may reduce 2D PDW TSE in nonessential plane). Optional 3D DESS sequence. T2 mapping (using GRE or FSE) or T1 mapping (DGEMRIC with gadolinium or T1 rho or gag CEST). Optional DWI.

Myositis Protocol

- Keep TE for T1W (<8 to 9 ms), STIR (25 to 35 ms), SPAIR (40 to 50 ms), slice for 2D 4 to 5 mm, voxel for 3D (1.5 mm isotropic) (Fig. 16).
- 3 T: Scout GRE in three planes, 3D T1W TSE or axial and coronal 2D T1W and long-axis coronal 3D T2 SPAIR TSE or 2D STIR TSE, axial 2D T2 SPAIR TSE, pre- and postcontrast fsT1W or 3D GRE with possible subtraction manipulation, if possible and DWI (b values 50, 600, 800 s/mm2). If 3D not available, use 1.5T protocol.
- 1.5 T: Scout GRE in three planes, axial and coronal 2D T1W TSE, coronal 2D STIR and axial 2D SPAIR TSE, pre- and postcontrast fsT1W or 3D GRE with possible subtraction manipulation, if possible and DWI (b values 50, 400, 800 s/mm2).

Metal Protocol

- No GRE, no frequency-selective fat suppression, avoid 3T, use only non-fsT1W, PDW and STIR, slice thickness ~4 mm, keep TE low (<20 to 30 milliseconds for PDW), high ETL

(>15), small ES (<9 ms), high band width (or less WFS, <1.5 pixels), frequency encoding direction along the metal, prudent use of available metal reduction software on your machine.

- Scout steady-state sequence in three planes, 2D PDW TSE in three planes, 2D STIR in two planes, contrast if suspecting infection with pre- and postT1 TSE and subtraction manipulation, if possible.

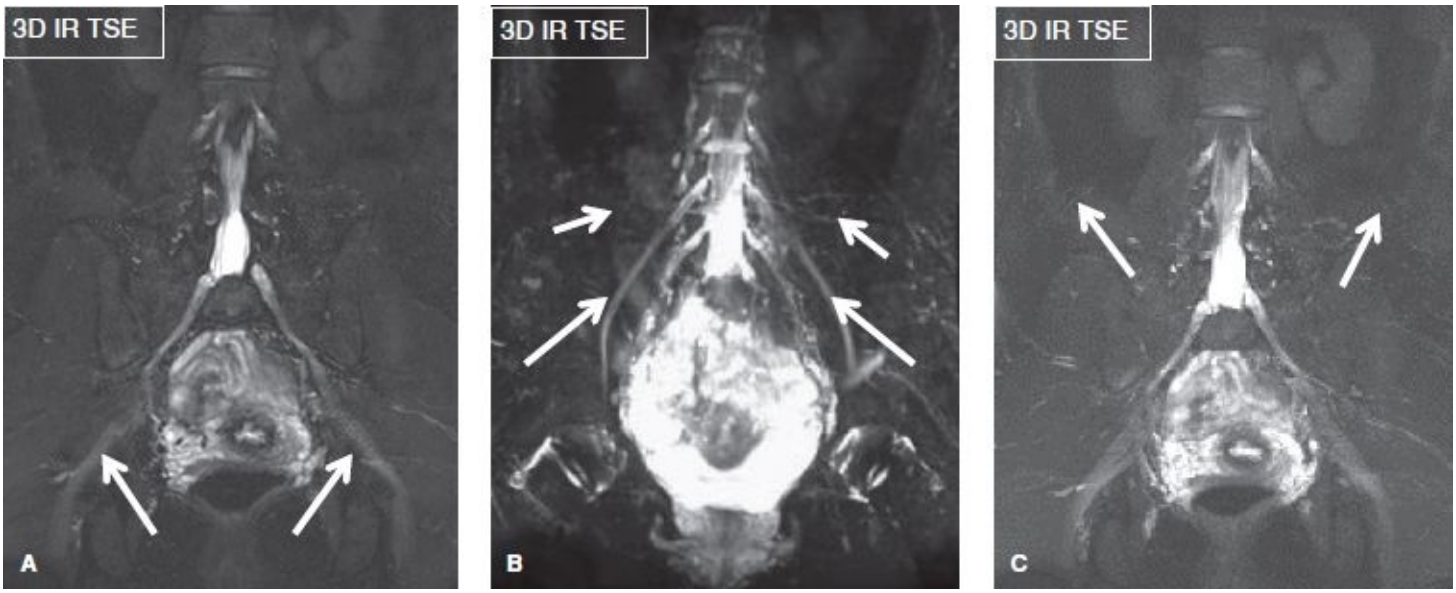

Fig. 25: Lumbosacral plexus MR neurography. Coronal base image **(A)** and MIP images **(B, C)** shows normal symmetrical appearance of bilateral sciatic nerves (*arrows* in **A**), femoral nerves (*long arrows* in **B**), ilioinguinal nerves (*short arrows* in **B**), iliohypogastric nerves (*arrows* in **C**).

Whole Body MRI Protocol

- Keep TE for T1W (<8 to 9 ms), 3D STIR (60 to 80 ms), SPAIR (60 to 80 ms), Voxel for 3D imaging (1.5 mm isotropic).
- 3 T: Scout GRE in three planes, coronal 3D T1W GRE, coronal 3D IR, axial DWI (5 mm slice, no gap, b values 50, 400 s/mm2). Postcontrast 3D T1 W GRE with possible subtraction manipulation, if possible.
- 1.5 T: Scout GRE in three planes with sequences as with 3T. If not possible, replace 3D STIR TSE with 2D STIR. Avoid 1.5T for WBMRI unless metal in FOV.

MR Neurography Protocol

- Keep TE for T1W (<8 to 9 ms), 3D STIR (60 to 80 ms), SPAIR (60 to 80 ms), slice for 2D (2 to 4 mm) depending upon the FOV, voxel for 3D IR or Dixon TSE (1.5 mm isotropic) and for 3D non-fsT2W for spine (0.9 mm isotropic) (Figs. 12, 13, 15, 25).
- 3 T: Scout GRE in three planes, axial 2D T1W and coronal 3D SPAIR TSE (extremities) or coronal 3D STIR TSE (for plexuses) and sagittal 3D T2 TSE (spine), axial 2D SPAIR FSE and coronal 3D DW fsPSIF (b value 60 to 80 s/mm2, water-selective fat suppression, voxel 0.9 mm, extremities) and DTI (3- to 4-mm slice, no gap, b values 50, 800, 1000

s/mm2, 12 to 20 directions of interrogation). Postcontrast imaging is optional with pre- and postcontrast fsT1W or 3D GRE with possible subtraction manipulation, if possible.

- 1.5 T: Scout GRE in three planes with sequences as with 3T. If not possible, replace 3D STIR FSE with 2D STIR. Avoid 1.5T for MR neurography unless metal in FOV.

Whole Body MR Neurography Protocol

- Keep TE for T1W (<8 to 9 ms), 3D STIR (60 to 80 ms), SPAIR (60 to 80 ms), voxel for 3D imaging (1.5 mm isotropic) (Fig. 26).

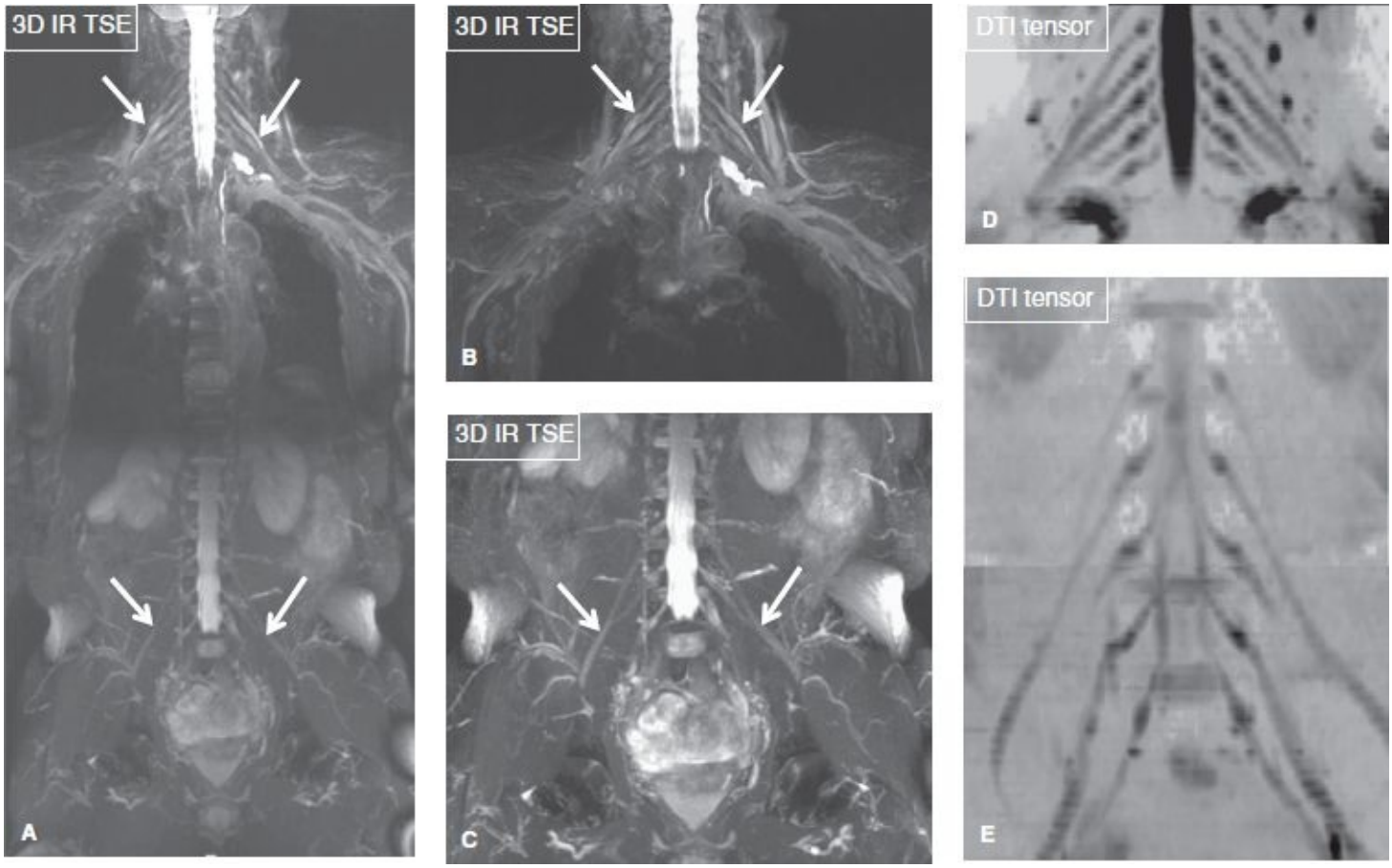

Fig. 26: Whole body MR neurography. Coronal composite image **(A)** and zoomed-up images of the brachial plexus **(B)** and lumbosacral plexus **(C)** show thickened bilateral brachial plexus nerves (*arrows)* and normal-appearing lumbosacral plexus nerves (*arrows*). DTI tensor maps **(D, E)** show the corresponding plexus images with selective depiction of the nerves.

- 3 T: Scout GRE in three planes, coronal 3D T1W GRE, coronal 3D IR or Dixon TSE, axial DTI of brachial and lumbosacral plexuses (4-mm slice, no gap, b values 50, 800, 1000 s/mm2). Postcontrast 3D T1W GRE with possible subtraction manipulation, if possible.
- 1.5 T: Scout GRE in three planes with sequences as with 3T. If not possible, replace 3D STIR TSE with 2D STIR. Avoid 1.5T for WBMRI unless metal in FOV.

MR-guided Intervention Protocol

- Use guidance from prior imaging studies, preferably MR neurography. Use MR

fluoroscopy for real-time needle guidance using fast T1W GRE or steady-state sequence (temporal resolution ~0.5 seconds). Use a five-step approach.

1. Limited planning techniques (axial T1 W ± axial T2 SPAIR imaging) for nerve localization.
2. MR fluoroscopy using fast 2D GRE or steady-state sequence and injection site identification using a syringe tip.
3. Under sterile conditions and percutaneous local anesthetic, MR compatible needle advancement using MR fluoroscopy.
4. Needle adjustments and confirmation of target position using fast axial T1W/PDW imaging (0.5- to 1-minute imaging time).
5. Medication injection and final check imaging using 2D STIR and 3D isotropic IR imaging (Fig. 27).

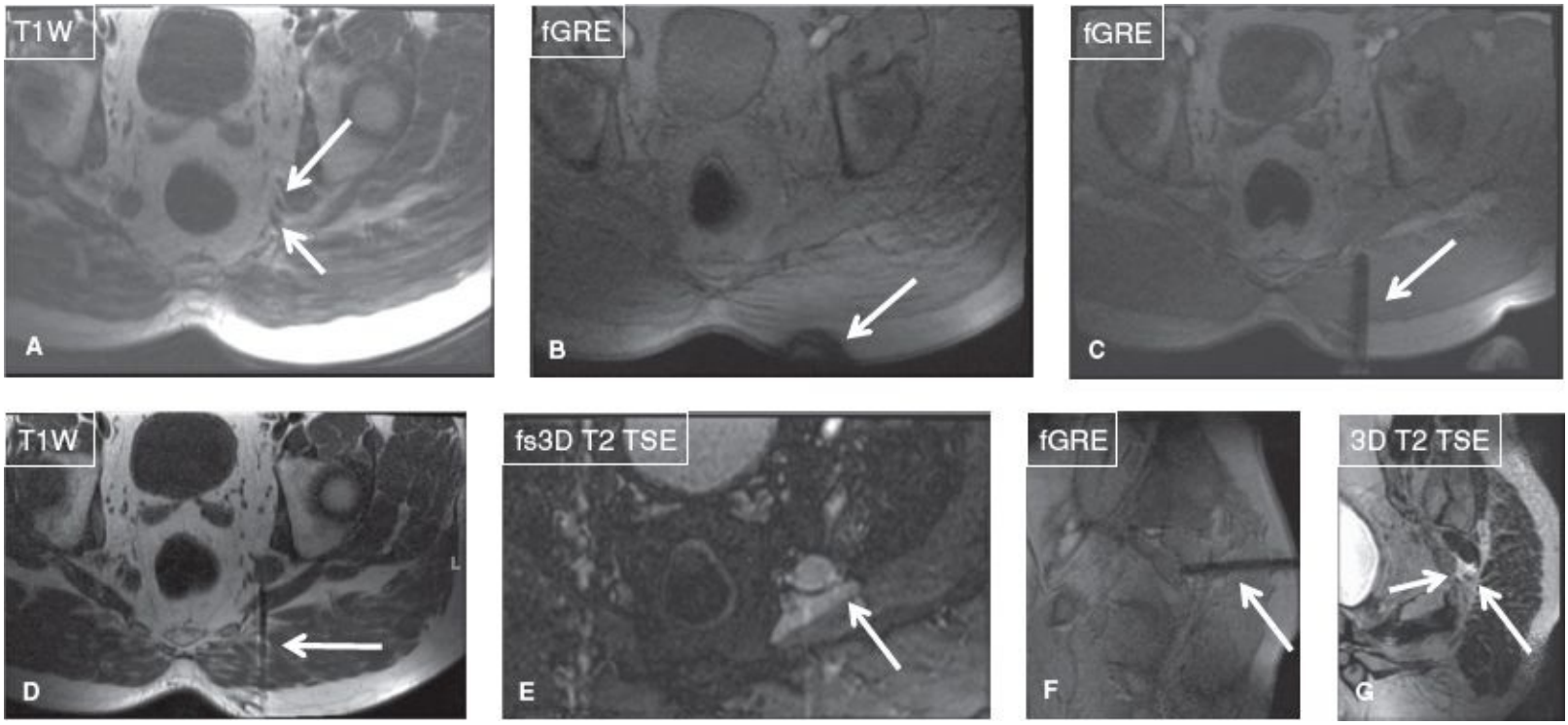

Fig. 27: MR-guided intervention technique and related sequences. A 47-year-old man with MR-guided injection for a schwannoma in the left sciatic notch. **A:** Step 1: Axial T1W planning image shows the lesion (*long arrow*) adjacent to the left sciatic nerve (*short arrow*). **B:** Step 2: MR fluoroscopy using fast gradient echo T1W (6-mm slab) technique during marker placement using a syringe tip (*arrow*). **C:** Step 3: MR compatible needle (*arrow*) placement using MR fluoroscopy. **D:** Step 4: Check axial T1W image showing the final target needle (*arrow*) position before test injection. **E:** Step 5: Axial image showing the perilesional contrast spread (*arrow*). Additional images that can be obtained include GRE image **(F)** along the axis of the needle to identify the needle orientation (*arrow*) in the orthogonal plane and non–fat-suppressed isotropic 3D T2W TSE sequence **(G).** The latter **(G)** shows the lesion (*short arrow*) and perilesional fluid (*long arrow*).

To conclude, a variety of pulse sequences and imaging techniques are currently available,

and one should gain knowledge of their advantages and limitations, in order to optimize their utility in an endeavor toward high-quality imaging.

SUGGESTED READINGS

Chhabra A. Magnetic resonance neurography-simple guide to performance and interpretation. *Semin Roentgenol.* 2013;48(2):111–125.

Chhabra A, Soldatos T, Thawait GK, et al. Current perspectives on the advantages of 3-T MR imaging of the wrist. *Radiographics.* 2012; 32(3):879–896.

Fayad LM, Mugera C, Soldatos T, et al. Technical innovation in dynamic contrast-enhanced magnetic resonance imaging of musculoskeletal tumors: An MR angiographic sequence using a sparse k-space sampling strategy. *Skeletal Radiol.* 2013;42(7):993–1000.

Goumas CG. Protocol panel discussion. Presented at: 21st Magnetic Resonance Imaging in Orthopaedics and Sports Medicine Meeting; 2012; San Francisco, CA.

Kavanagh EC, Read P, Carty F, et al. Three-dimensional magnetic resonance imaging analysis of hip morphology in the assessment of femoral acetabular impingement. *Clin Radiol.* 2011;66(8):742–747.

Kijowski R, Blankenbaker DG, Woods M, et al. Clinical usefulness of adding 3D cartilage imaging sequences to a routine knee MR protocol. *AJR Am J Roentgenol.* 2011;196(1):159–167.

Kijowski R, Davis KW, Woods MA, et al. Knee joint: Comprehensive assessment with 3D isotropic resolution fast spin-echo MR imaging. Diagnostic performance compared with that of conventional MR imaging at 3.0 T. *Radiology.* 2009;252(2):486–495.

Kijowski R, Gold GE. Routine 3D magnetic resonance imaging of joints. *J Magn Reson Imaging.* 2011;33(4):758–771.

Lurie B, Koff MF, Shah P, et al. Three-dimensional magnetic resonance imaging of physeal injury: Reliability and clinical utility. *J Pediatr Orthop.* 2014;34(3):239–245.

Potter HG, Black BR, Chong le R. New techniques in articular cartilage imaging. *Clin Sports Med.* 2009;28(1):77–94.

Thakkar RS, Subhawong T, Carrino JA, et al. Cartilage magnetic resonance imaging techniques at 3 T: Current status and future directions. *Top Magn Reson Imaging.* 2011;22(2):71–81.

Thawait SK, Puttgen K, Carrino JA, et al. MR imaging characteristics of soft tissue vascular anomalies in children. *Eur J Pediatr.* 2013; 172(5):591–600.

3

Infection and Inflammation/Arthritis

Avneesh Chhabra and Theodoros Soldatos

Musculoskeletal infectious and inflammatory processes are discussed together in this chapter, since the clinical presentation is often quiet similar and, in many cases, the clinical picture dictates the final imaging diagnosis. In the domain of inflammatory or infectious arthritis, the role of the radiologist is to confirm or exclude the clinically suspected entity, characterize the severity and extent of the abnormality, and, in some cases, provide an alternative diagnosis. Correlation of MR imaging findings with plain films is quite useful especially in cases where a bony lesion is the predominant finding. The checklist for structured reporting is displayed in Appendices 1 and 2. Conceptual details of related MR physics and imaging protocol are discussed in the chapter of MR imaging protocol optimization.

IMAGE EVALUATION

The below-outlined stepwise interpretation approach is only a practical guide, and all structures should be evaluated in multiple planes for optimal assessment. The following discussion will help reader evaluate infectious and inflammatory processes of the musculoskeletal system with reasonable accuracy.

1. Start with long-axis fluid-sensitive (fat-saturated [fs] T2-weighted [T2W], fs proton density-weighted [PDW], or short-tau inversion recovery [STIR]) images and T1-weighted (T1W) images to detect the lesions, assess their distribution in the regional anatomy, and gauge their extent. Fluid-sensitive sequences are most sensitive for identifying areas of edema, joint effusion, and fluid collection, whereas T1W images are good for anatomic localization, and for further characterization of the lesions, thereby increasing the specificity of the diagnosis.
2. Line up the similar-plane, axial T1W, fluid-sensitive, pre- and postcontrast fsT1W images, and synchronize them for tandem evaluation. If 3D isotropic images have been obtained, the technologist should create reconstructions in prespecified planes, so that reading time can be shortened and similar-plane reconstructions can be synced. Systematic evaluation of this kind allows the reader to outline the anatomy, identify the extent of the pathology

and individual structures involved, and in particular, differentiate reactive bone marrow edema (mostly bright on fluid-sensitive images) from bone marrow infection (bright on fluid-sensitive images but also correspondingly dark on T1W images). On post-contrast images, the enhancing T2 bright areas reflect hyperemic tissue whereas those that lack enhancement, represent devitalized tissue. A rim-enhancing necrotic/cystic lesion in the cloud of edema/hyperemia is highly suspicious for an abscess. Enhanced scans are also useful to evaluate the extent and severity of synovitis, define the extent and distribution of soft tissue infections, identify sinus tracts, and detect foreign bodies. On all sequences, areas of low signal may correspond to fibrous tissue, calcification, sequestrum, air, or foreign bodies.

3. Although not universally obtained, MR angiography, dynamic contrast-enhanced (DCE), and diffusion-weighted (DW) imaging sequences are becoming increasingly popular as parts of musculoskeletal infection and inflammation imaging protocols. MR angiography can be used to evaluate vascular patency in areas of infection, define the proximity of vessels to drainable abscesses, and detect vascular irregularity in underlying vasculitis. DCE imaging offers characterization of enhancement patterns, detection of solid neoplastic tissue, if there is unsuspected underlying tumor, and defines the extent of devitalized tissue. Evaluated in conjunction with other pulse sequences, DW imaging assists in the diagnosis of abscess (which shows restricted diffusion), and in the evaluation of patients who have contraindication to intravenous contrast (including diabetic feet). Dark bone on a DW image usually means no osteomyelitis (OM) (Fig. 1).

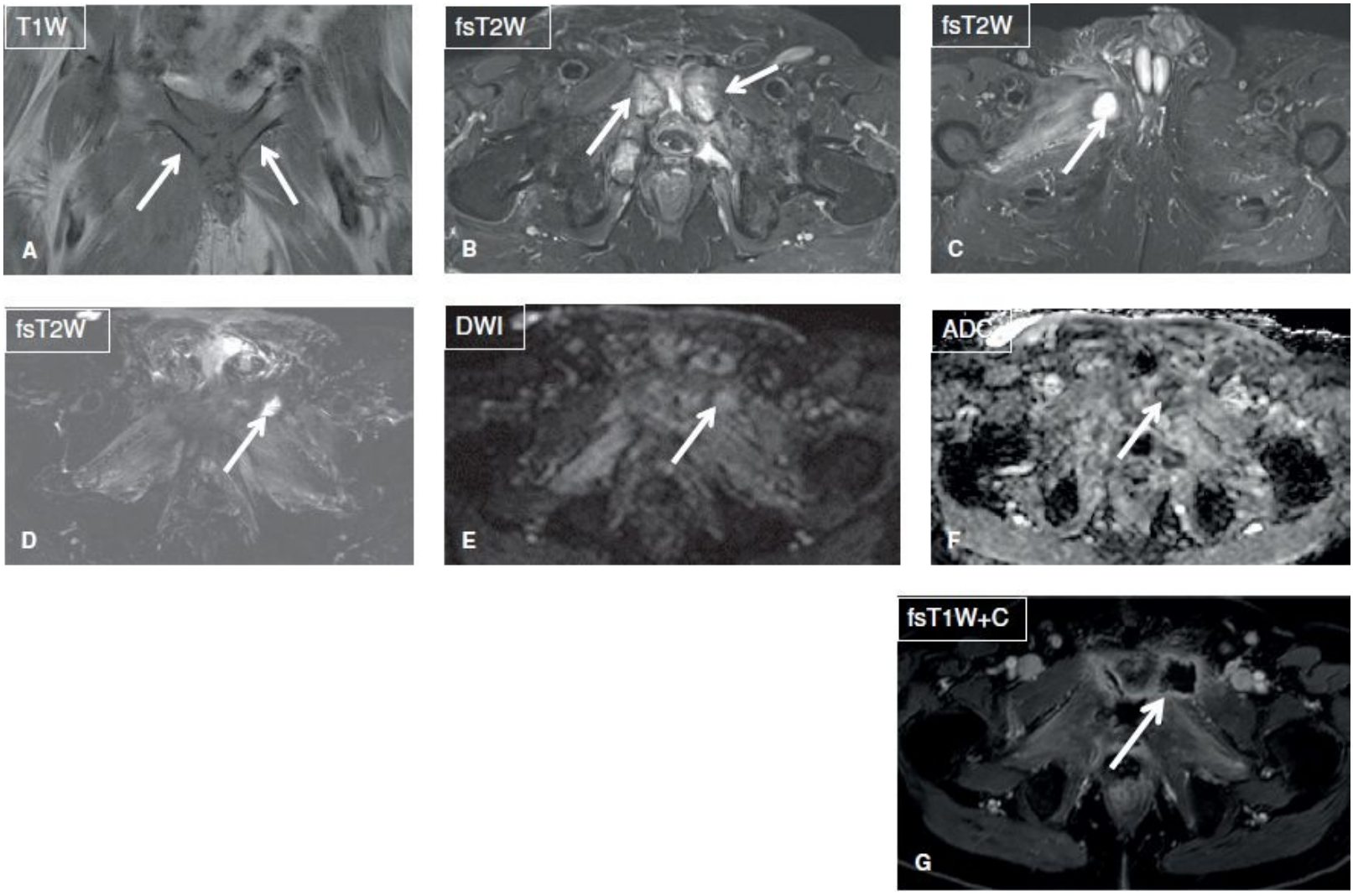

Fig. 1: Osteomyelitis and septic arthritis. **A, B:** Coronal images show confluent T1 hypointensity and T2 hyperintensity in the pubic symphysis with effusion in this patient with pubic osteomyelitis and septic arthritis (*arrows*). Also note surrounding myositis and fasciitis, a hallmark secondary sign of infection. **C:** Axial image shows abscess in the right adductor muscles (*arrow*). **D–G:** After debridement, there is resolution of osteomyelitis (dark on fsT2W and no diffusion restriction) with residual muscle edema. Notice new abscess in the left adductor muscle with mild diffusion restriction (*arrows*).

4. In case, arthritis or a rheumatologic condition is suspected, look for evidence of mono- or polyarthritis findings on the long-axis images. Using long- and short-axis images, check for soft tissue swelling (symmetric or asymmetric), joint effusion, synovial thickening/synovitis, tenosynovitis, bony productive changes (osteophytes, syndesmophytes, enthesophytes), joint space loss/cartilage loss, erosions/cystic changes, bone marrow edema, subluxation/bony malalignment, and ankylosis. Joint effusion should be graded as small, moderate, or large, as described in individual joint chapters in this book whereas synovial thickening/synovitis, bony productive changes, and tenosynovitis should be classified as mild, moderate, or severe. The severity of joint space/cartilage loss, erosions/cystic changes, subluxation, and ankylosis can be graded as involving less or more than the 50% of the articular surfaces. The locations of bone erosions and cystic changes (articular or para-articular surfaces) should be defined. In

carpal involvement, the carpometacarpal ratio should be reported.

5. Finally, report incidental lesions, such as a space-occupying masses and soft tissue ganglion cysts, as well as identifiable internal derangement findings, such as tears of menisci, labrum, triangular fibrocartilage complex, and other ligaments, etc.

BOX 1: The Structured Report: Infection

The checklist for structured reporting of MR imaging of infection. For each field, *Normal* is considered default in the dictation whereas the rest of the elements describe various pathologies that could be encountered during imaging evaluation. See Appendices 1 and 2 at the end of the chapter for a sample completed report.

EXAM: MRI [<EXTREMITY / JOINT>] [<WITH / WITHOUT>] CONTRAST

FINDINGS:

There [<is no> <is> <focal / diffuse>] soft tissue subcutaneous edema.

There [<is no> <is> <focal / diffuse / multifocal>] muscle edema.

There [<is no> <is>] significant superficial or deep fascial fluid.

There [<is no> <is>] large drainable fluid collection.

There [<is no> <is>] focal bone marrow edema.

There [<is no> <is>] large joint effusion.

Incidental Findings: [<_>]

Post-gadolinium Discussion: [<_>]

IMPRESSION:

[<In the order of importance with acute findings first>]

HOW TO FILL THE STRUCTURED REPORT

Reporting Using the Template for Infection

There [<is no> <is> <focal / diffuse>] soft tissue edema.

There [<is no> <is> <focal / diffuse / multifocal>] muscle edema.

There [<is no> <is>] significant superficial or deep fascial fluid.

Musculoskeletal infections are characterized by edema and hyperemia of the involved tissues. Soft tissue edema manifests as area(s) of hyperintensity on fluid-sensitive images, and hypointensity on T1W images, which is usually ill defined and may, less commonly, demonstrate homogeneous soft tissue thickening (due to swelling). Hyperemia or cellulitis manifests as abnormally increased contrast enhancement and edema on T2W images of the involved tissues. Areas of edema-like T2 hyperintensity without abnormally increased contrast enhancement correspond to non-inflammatory edema (e.g., from congestive heart failure, diabetic vascular insufficiency and lymphatic obstruction) (Figs. 1–4). Finally, areas of edema-like T2 hyperintensity with abnormally decreased contrast enhancement reflect devitalized tissue (e.g., in diabetic feet with dry gangrene due to coagulative necrosis, wet gangrene due to liquefactive necrosis, and gas gangrene due to gas forming organisms).

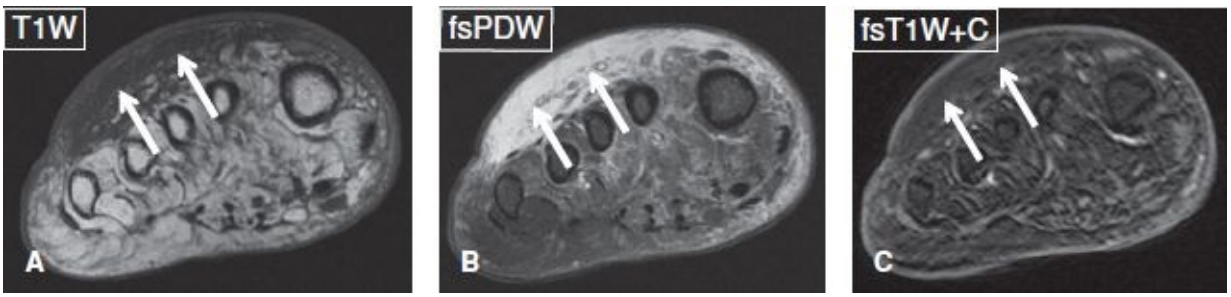

Fig. 2: Subcutaneous edema, without cellulitis in a diabetic subject. Axial images. **A, B:** There is diffuse T1 hypointensity and T2 hyperintensity of the dorsal aspect of the forefoot (*arrows*), in keeping with subcutaneous edema. There is no focal collection. **C:** Absence of contrast enhancement in the above area (*arrows*) indicates absence of hyperemia and excludes cellulitis.

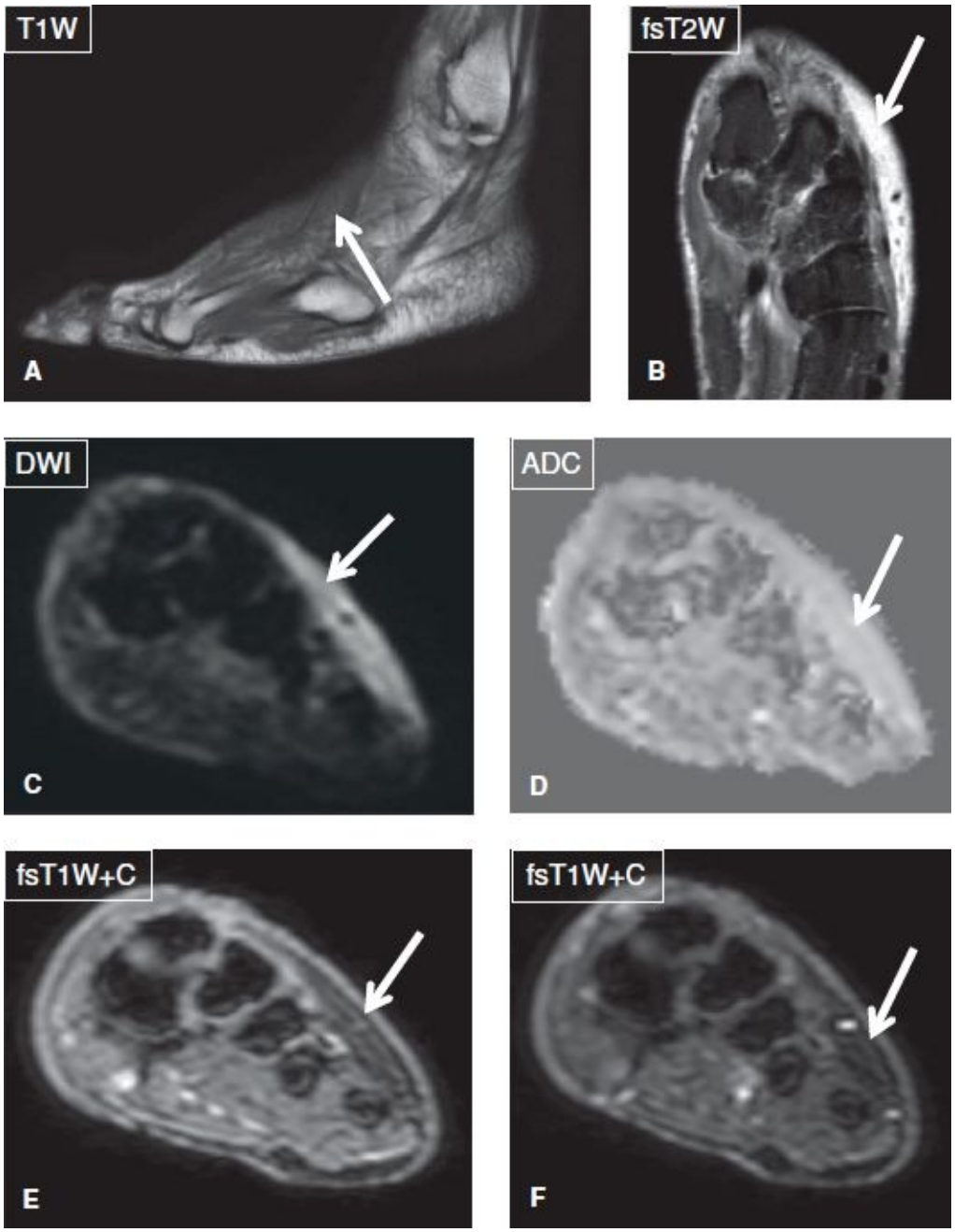

Fig. 3: Soft tissue edema and not cellulitis. Sagittal **(A)** and coronal **(B)** images show dorsal subcutaneous edema (*arrows*). There is no restriction on DWI images (*arrows* in **C, D**) and no significant enhancement on before and after subtraction contrast images (*arrows* in **E, F**).

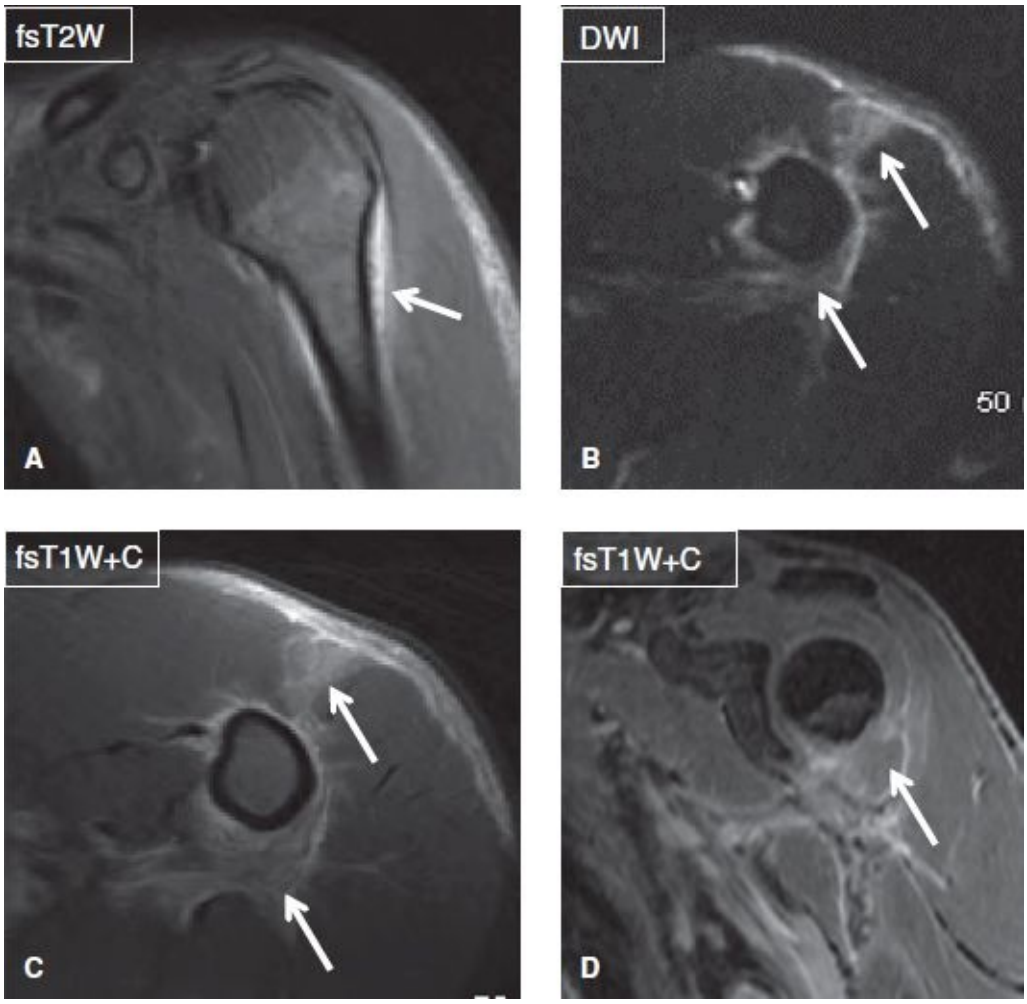

Fig. 4: Cellulitis and myositis. Coronal **(A, D)** and axial **(B, C)** images show edema and enhancement (*arrows*) in the anterior belly of the deltoid muscle and adjacent fascial planes. Notice no collection to suggest superimposed abscess. Also there is no osteomyelitis (dark on DWI and no abnormal enhancement) or evidence of septic arthritis (no effusion or synovitis).

The involvement of the soft tissues may be focal, diffuse, or multifocal. The first pattern usually advocates for a single and contained infectious process, the second pattern indicates an expansile and more aggressive entity, (such as necrotizing fasciitis or Fournier gangrene) whereas the third multifocal pattern likely suggests a systematic infectious process. Musculoskeletal infections can be classified into *superficial lesions,* which include skin ulceration, cellulitis, superficial fasciitis, septic bursitis, and infectious tenosynovitis; and *deep lesions,* which include deep fasciitis, necrotizing fasciitis, pyomyositis, periostitis, osteitis, OM, and septic arthritis. An important role of imaging is to distinguish superficial from deep infections because the latter usually require longer administration of antibiotics and/or surgery to address the primary nidus of deep infectious process or its complications, such as compartment syndrome and tissue necrosis.

Cellulitis is a non-necrotizing infection, restricted to the skin and subcutaneous tissues, without involvement of the underlying fascia or muscles (Figs. 1, 4). The diagnosis is clinical, but MR imaging may be ordered if the disease advances rapidly and/or demonstrates severe systemic manifestations, suggesting an underlying deep extension

and/or abscess formation. Imaging findings include T2 hyperintensity, thickening and moderate contrast enhancement of the involved area.

Septic bursitis is the result of bacterial inoculation of synovial bursa (e.g., from penetrating injury or extension from the joint capsule, e.g., in infected iliopsoas or greater trochanteric bursitis). The most commonly involved sites are the olecranon, greater trochanteric, prepatellar, iliopsoas, and retrocalcaneal bursae. On imaging, the bursa is distended by T1 hypointense and T2 hyperintense homogeneous or heterogeneous fluid collection, and features a thickened and enhancing wall. Internal bursal septations and punctuate signal voids (gas bubbles), as well as edema and enhancement of the overlying skin (associated cellulitis) may also be seen (Fig. 5).

Fig. 5: Septic bursitis. Axial **(A, B)** and coronal **(C, D)** MR images and AP radiograph **(E)** show evidence of chronic pagetoid changes of the right hip (*arrows*). There is superimposed cellulitis, myositis, and greater trochanteric infected bursitis (*arrowheads*). Notice synovitis of the hip joint as well.

Infectious tenosynovitis most often occurs in the hand, wrist, elbow, feet, and ankle. It manifests as thickening and contrast enhancement of the involved tendon sheath, which is distended by complex fluid that shows varying signal alterations, related to pus, gas, blood, and/or debris. The respective infected/inflamed tendon is ill-defined, thickened, and shows intermediate signal. There is typically fascial edema of the surrounding soft tissues, which is a useful pointer in distinguishing it from other causes of inflammatory tenosynovitis. Additional findings suggesting infection include, asymmetrical involvement or isolated

involvement of tendon sheath at the site of prior injury. Because infection evolves rapidly and it may be complicated by skin loss, tendon necrosis, or OM, infectious tenosynovitis is usually considered a surgical case, and early diagnosis and treatment are essential (Figs. 6, 7).

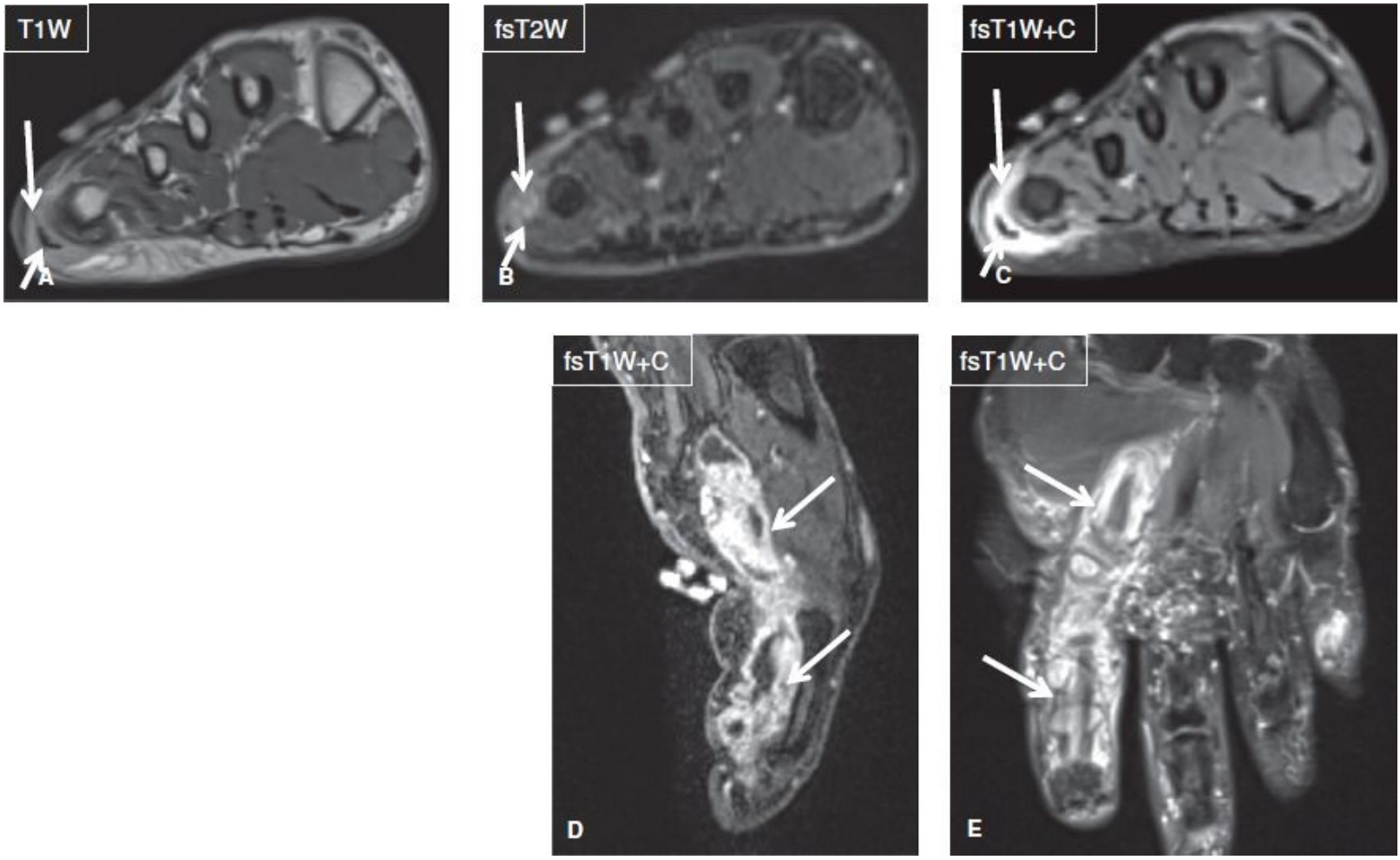

Fig. 6: Infection-related tendinitis. Axial images **(A–C)** demonstrate T2 hyperintensity and enhancement of the lateral aspect of the forefoot (*long arrows*), which reflect edema and enhancement, respectively and are indicative of inflammation. T2 hyperintensity and enhancement of the abductor digiti minimi tendon and muscles (*short arrows*) confirm associated tendinitis. Sagittal **(C)** and coronal **(D)** images in another subject show infectious tendinitis and tenosynovitis (*arrows*) of the flexor tendon of the index finger from atypical mycobacterium.

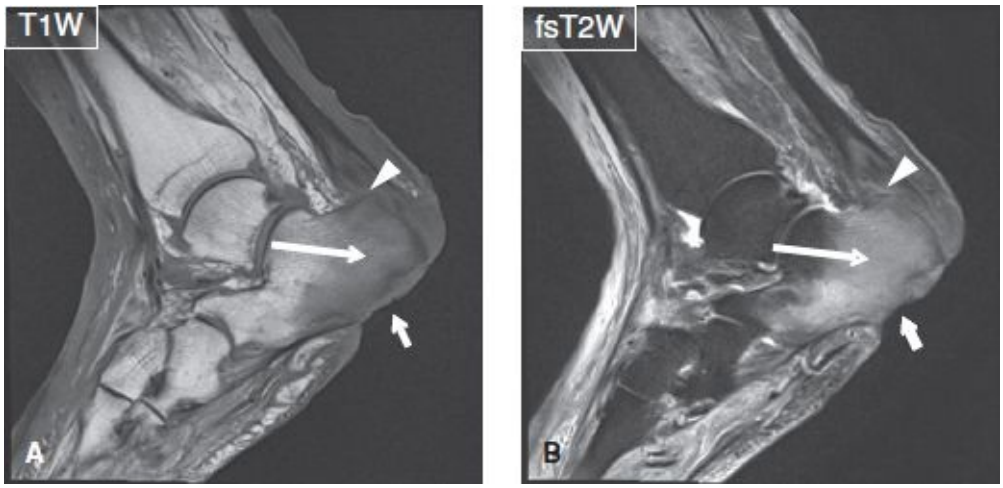

Fig. 7: Osteomyelitis and Achilles tendinitis. Sagittal images **(A, B)** show a T1 hypointense, T2 hyperintense confluent marrow signal alteration (*long arrows*) of the calcaneus corresponding to osteomyelitis. Note the deep ulcer (*short arrows*) of the overlying soft tissues, cortical destruction of plantar aspect of the calcaneus, and insertional Achilles tendinitis and small intratendinous collection (*arrowheads*).

Necrotizing fasciitis is a rapidly progressing infection of the deep fascial layers, which is characterized by widespread fascial necrosis and life-threatening system toxicity. Imaging findings include deep fascial and intermuscular fascial thickening and fluid collections, along with high T2 signal within the muscles, reflecting reactive edema. Contrast enhancement of the deep and intermuscular fascia is present in the early stages of the disease but becomes diminished or absent in the later stages, when the fascial necrosis progresses and the involved tissues become devitalized and avascular. Scattered subcutaneous and fascial foci of low signal are indicative of gas and are considered useful for the diagnosis of the entity. Other causes of emphysema include open wound communication or gas gangrene. The presence of bulging fascia in this setting is suspicious for development of compartment syndrome. The role of imaging is to define the extent of the process and detect fluid collections. It should be noted that the diagnoses of both necrotizing fasciitis and compartment syndrome can be confirmed, but cannot be excluded by imaging.

Pyomyositis (infectious myositis) refers to purulent infection of skeletal muscle. In most patients, a single muscle is affected, but multiple muscles can be involved in up to 30–40% of cases. In the initial stage, the affected muscle is enlarged, edematous and demonstrates architectural distortion along with heterogeneous areas of low T1 and high T2 signal. As the infection evolves, small intramuscular fluid collections develop and subsequently coalesce into larger abscesses (see description on next paragraph) that may demonstrate variable signal characteristics. There is restricted diffusion on DW imaging and peripheral enhancement on post-contrast images (Fig. 8). Delayed onset muscle soreness (DOMS) and rhabdomyolysis are related differentials, which occur following recent heavy exercise or drug abuse. Both entities are considered to be part of the same spectrum of excertional muscle injury. There are usually no clinical signs or laboratory findings of toxemia. The

symptoms and imaging findings are commonly bilateral, and there are associated high serum CPK levels. While DOMS shows multifocal muscle edema-like signal, areas of intramuscular hemorrhage (T1 hyperintensity) are frequently present in rhabdomyolysis (Figs. 9, 10). Myoglobinuria is also more pronounced in rhabdomyolysis. Perimuscular fascial edema can be associated with most benign causes of muscle pathology, including myopathy, muscle strains, pyomyositis, and rhabdomyolysis, while it is characteristically absent in denervation muscle change.

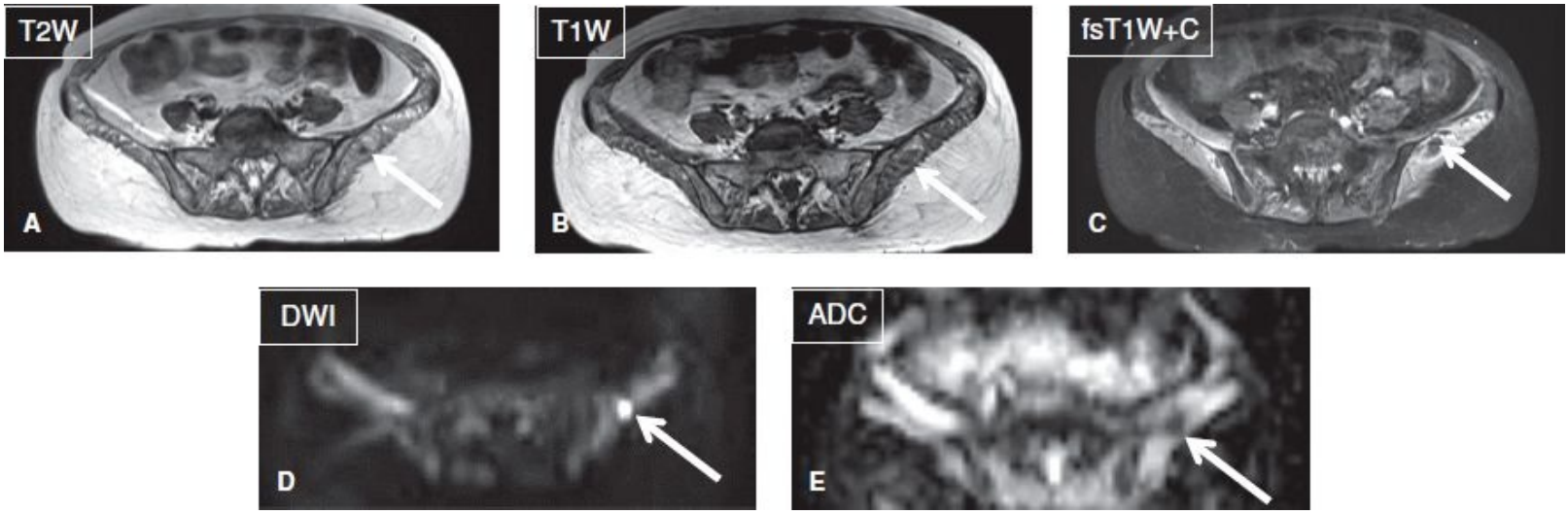

Fig. 8: Intramuscular abscess. Axial images. **A–C:** A relatively well-defined T1 hypointense, T2 hyperintense ring-enhancing lesion (*arrows*) is evident in the left gluteus muscle. Notice diffusely edematous pelvic muscles in this patient with septicemia. **D, E:** The lesion (*arrows*) demonstrates restricted diffusion (ADC = 0.8 × 10 to 3 mm2/s) was found to be a local abscess in otherwise florid case of diffuse myositis.

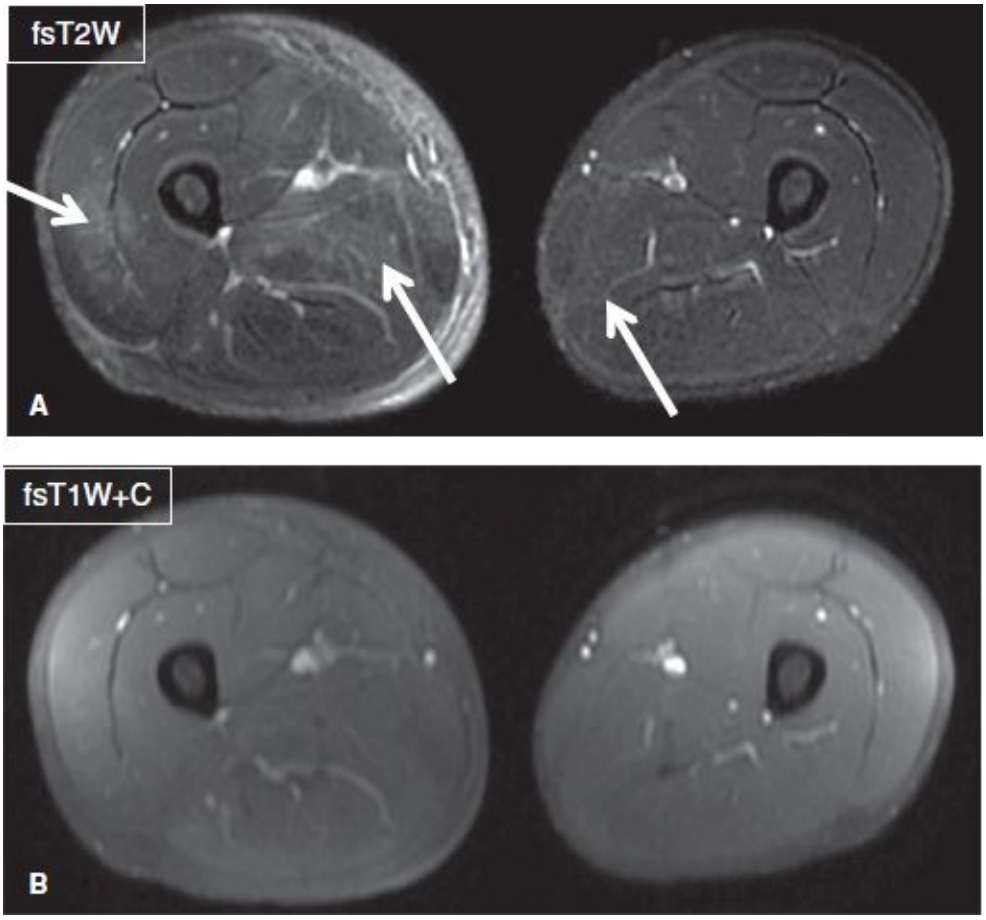

Fig. 9: DOMS. Axial images **(A, B)** show patchy muscle edema and adjacent fascial edema (*arrows*) in multiple compartments of the right leg and minimally in the left leg in this patient who had recently played a soccer match and now complains of leg pain for few days. CPK was elevated and there was no myoglobinuria. Notice no abnormal enhancement on contrast image.

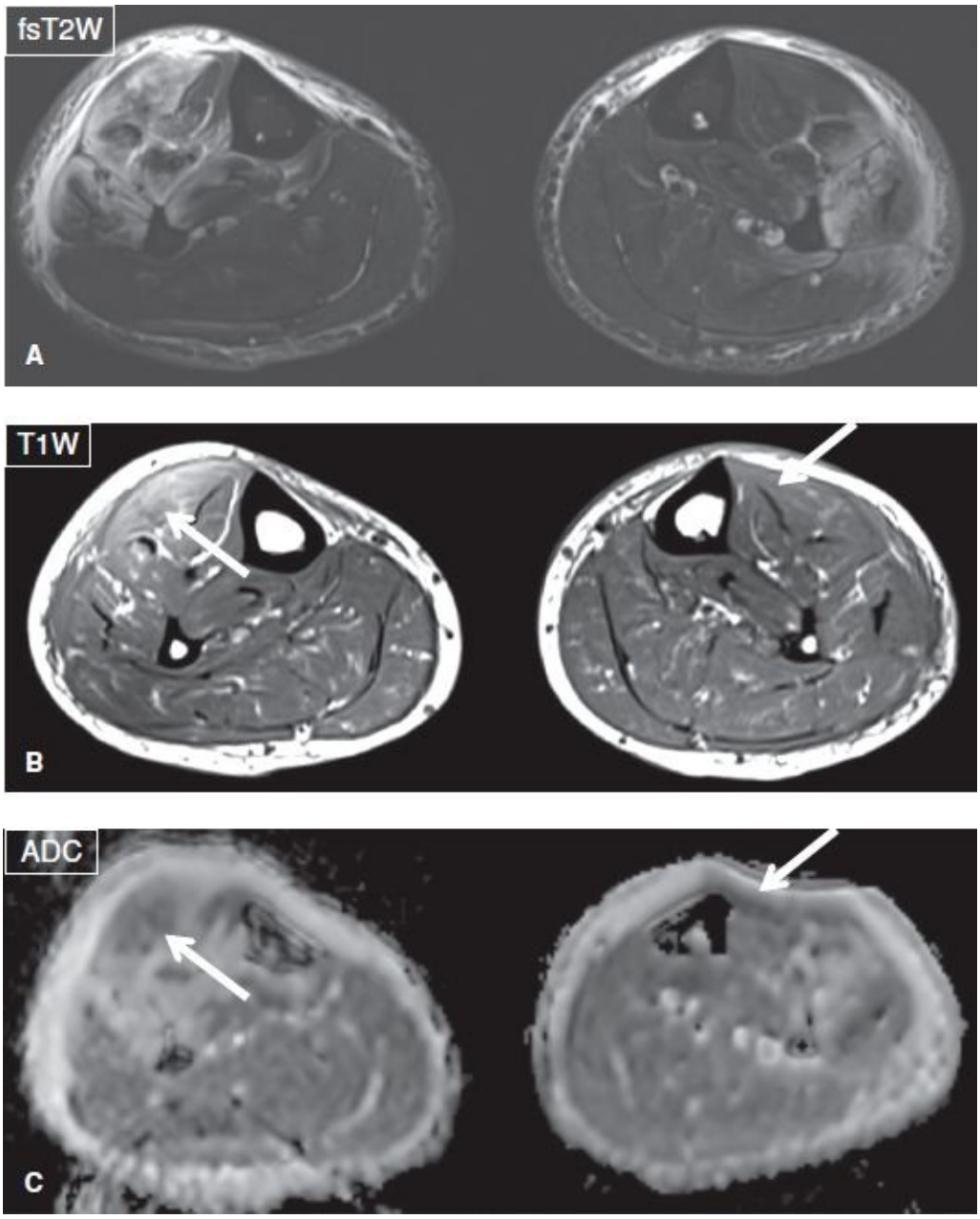

Fig. 10: Rhabdomyolysis. Axial images **(A–C)** show patchy muscle edema, adjacent fascial edema, and bulging fascia in the anterolateral compartments of both legs in this patient who had undergone recent excessive exercise. Notice internal patchy hemorrhage showing up as hyperintensity on T1W images and dark signals on ADC images (*arrows*).

There [<is no> <is>] large drainable fluid collection.

In the setting of infection, any localized fluid collection is considered an abscess, unless proven otherwise. Typical imaging features include a non-enhancing fluid collection of low-to-intermediate T1 signal and high T2 signal, which is demarcated by a hypointense and enhancing thick and irregular wall, and is associated with edema and reticulation of the surrounding tissues. The well-defined borders of the entity differentiate it from phlegmon, which appears as a poorly defined T2 hyperintense enhancing area. If gas develops due to communication with an air-containing hollow organ or open wound, or a gas-forming organism, foci of signal void will appear in the non-dependent portion of the cavity, leading to formation of air–fluid level (s). Abscesses also exhibit restricted diffusion on DW

images, a feature that may assist in case where contrast administration is contraindicated. Another type of infectious (but not walled-off) fluid collection occurs with accumulation of inflammatory fluid within deep fascial layers in necrotizing fasciitis, as described above. This should be differentiated from simple-looking or blood product containing fascial fluid collection that might be observed in trauma-related degloving lesions. The latter lesions are most commonly observed in prepatellar or great trochanteric areas (Fig. 11). Any collection larger than 1–2 cm in the setting of fever should be aspirated, as imaging cannot definitely confirm the sterility of the lesion (Fig. 12).

Fig. 11: Degloving lesion. Left gluteal swelling with history of recent MVA. Notice lobulated fluid collection separating the fascial layers above the gluteal tendon in keeping with a degloving lesion (*arrow*). Also note underlying trochanteric bursitis.

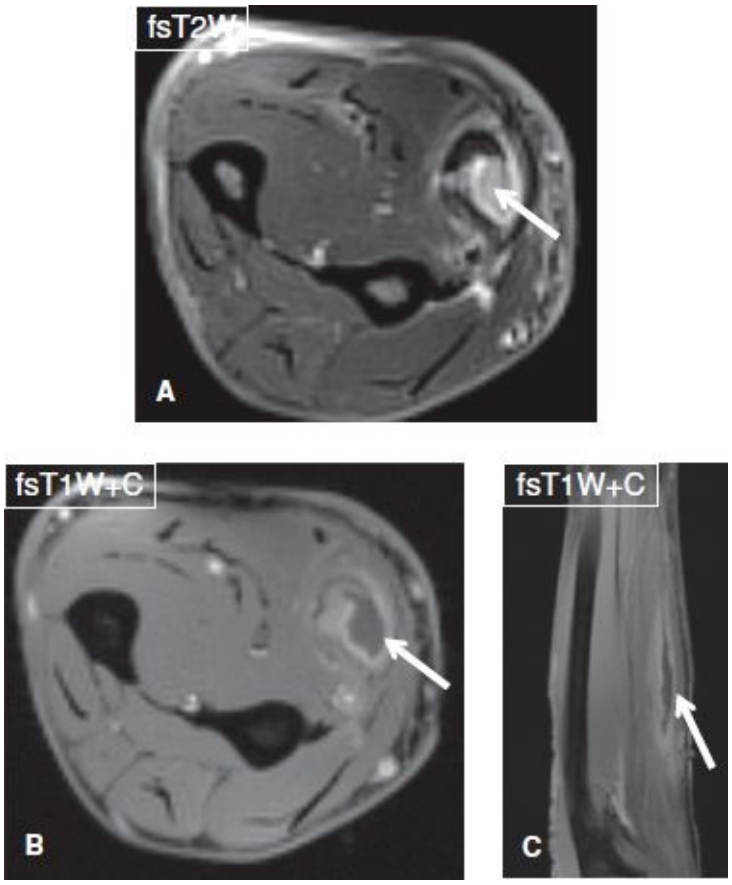

Fig. 12: Drainable intramuscularabscess. Middle-aged female with fever. Axial **(A, B)** and sagittal **(C)** images demonstrate complex rim-enhancing collection in the flexor carpi radialis muscle (*arrows*) with surrounding myositis.

There [<is no> <is>] focal bone marrow edema.

Bone marrow edema manifests as area(s) of hyperintensity on fluid-sensitive images. In the setting of adjacent inflammation/infection, such bone marrow hyperintensity may be attributed to (1) reactive marrow edema, in which the involved marrow space demonstrates either normal or minimal and hazy intermediate T1 signal (mostly in a subchondral location) minimal or no increased signal on DW images at higher b values (400 or above), as well as no or mild contrast enhancement (Fig. 13), or (2) acute-subacute OM, in which the involved marrow exhibits ill-defined and confluent low signal intensity on T1W images, increased signal on DW images, and intense enhancement on post-contrast images. The non-enhancing areas correspond to necrotic tissue or organized intra-osseous abscesses. The latter additonally exhibit rim enhancement, or demonstrate restriction on DW images. Therefore, in the setting of T2 hyperintense bone marrow, T1W images are the key to diagnose OM (Figs. 7, 14, 15), and OM can be excluded, without the use of contrast administration, in case no definite low T1 signal is detected in the involved marrow space. In fact, absence of bone marrow edema on STIR, fsT2W, or DW images virtually excludes OM (Fig. 16). Associated findings of *acute-subacute* OM include adjacent cellulitis, soft tissue phlegmon and/or abscess, subperiosteal abscess, and particularly, overlying ulcer, and/or sinus tract. The latter two findings are very common in adults, to the level that, acute OM is

unlikely, if there is no ulcer or sinus tract. An important, highly specific feature for establishing OM is cortical disruption in the involved area, which is depicted as a focus of cortical discontinuity on T1W images and associated high T2 signal. Cortical involvement or destruction is easily seen as focal cortical enhancement on post-contrast images (Fig. 14). In children, an elongated multilayered necrotic lesion, which reaches but does not cross the growth plate, is also highly suggestive of acute OM (Fig. 17). Presence of fluid collections distinguish OM from neoplastic processes, such as Ewing sarcoma or leukemia, which demonstrate solid-enhancing masses.

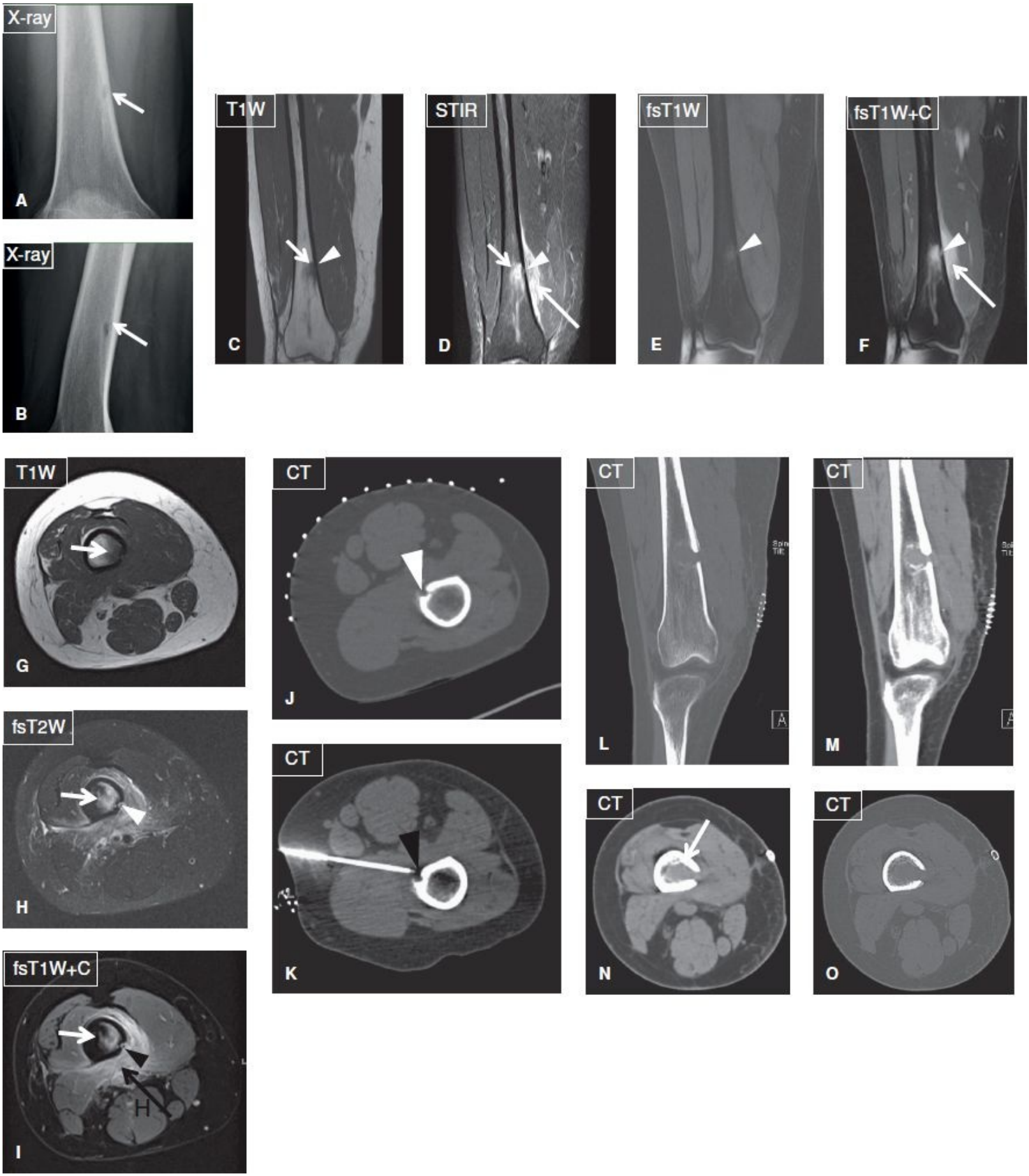

Fig. 14: Focal osteomyelitis in a 31-year-old female with history of furuncles on her thighs, who was treated with oral antibiotics. Anteroposterior **(A)** and lateral **(B)** plain films reveal a radiolucent focus (*arrow*) with relatively ill-defined margins at the distal femoral metadiaphysis. On the corresponding coronal **(C–F)** and axial **(G–I)** MR images, the lesion

(*short arrows*) is T1 hypointense and T2 hyperintense, shows strong contrast enhancement and is associated with edema and enhancement of the adjacent soft tissues (*long arrows*) as well as with an adjacent focus of cortical disruption and enhancement (*arrowheads*). On biopsy under CT guidance **(J, K),** the lesion proved to be a focus of methicillin-resistant *Staphylococcus aureus* osteomyelitis. Again, note the focus of cortical disruption (*arrowheads*). Coronal-reformatted **(L, M)** and axial **(N, O)** CT images demonstrate the postdebridement appearance of the infected area.

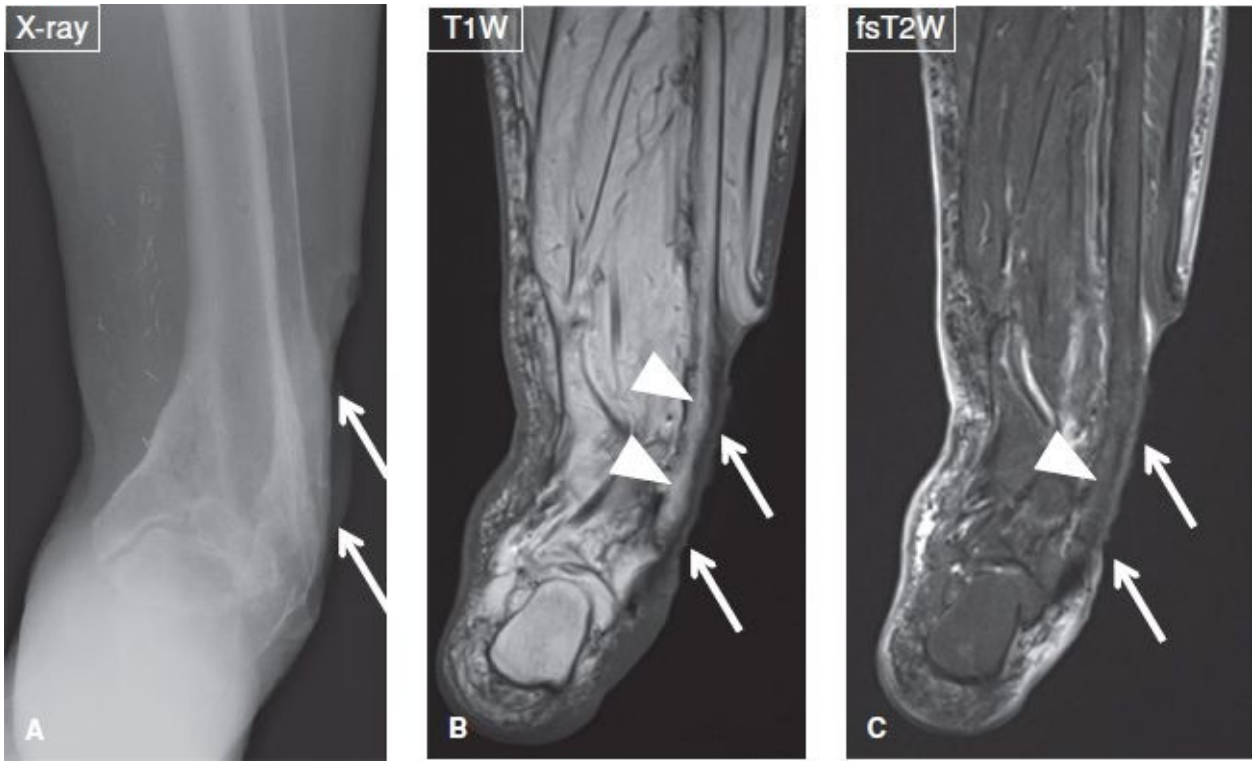

Fig. 13: Reactive bone marrow edema. Case of a 78-year-old female with fever and a deep and extended ulcer of the lateral aspect of the ankle. **A:** Anteroposterior radiograph reveals the ulcer (*arrows*) but shows no cortical destruction in the underlying bone. **B, C:** The respective coronal MR images again exhibit the ulcer (*arrows*), normal marrow on T1W image (*arrowheads* in **B**), and minimal reactive edema on the fs T2W image (*arrowheads* in **C**).

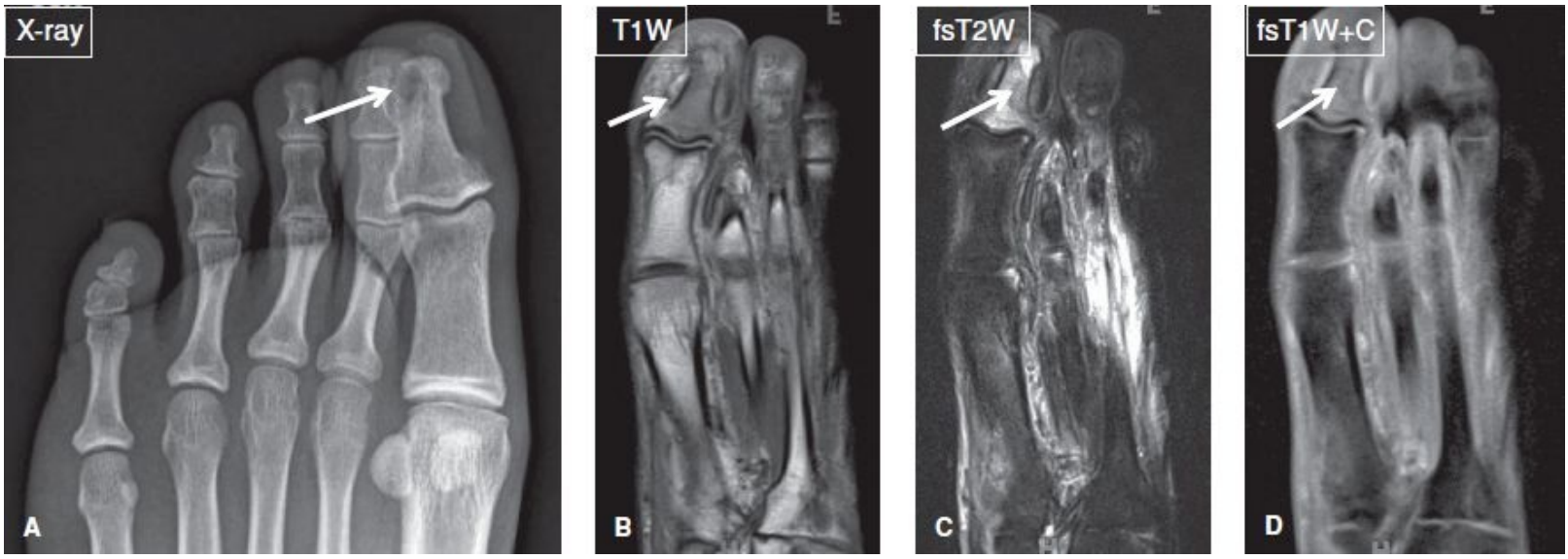

Fig. 15: Patient with diabetes mellitus, and toe swelling due to recent trauma. **A:** Anteroposterior radiograph show a subcortical lytic lesion at the distal phalanx of the great toe (*arrow*). **B–D:** On the corresponding coronal MR images, most of marrow of the phalanx is T1 hypointense/T2 hyperintense and enhances (*arrows*), in keeping with osteomyelitis, later proven on image-guided biopsy. Notice the lytic lesion corresponds to intraosseus abscess.

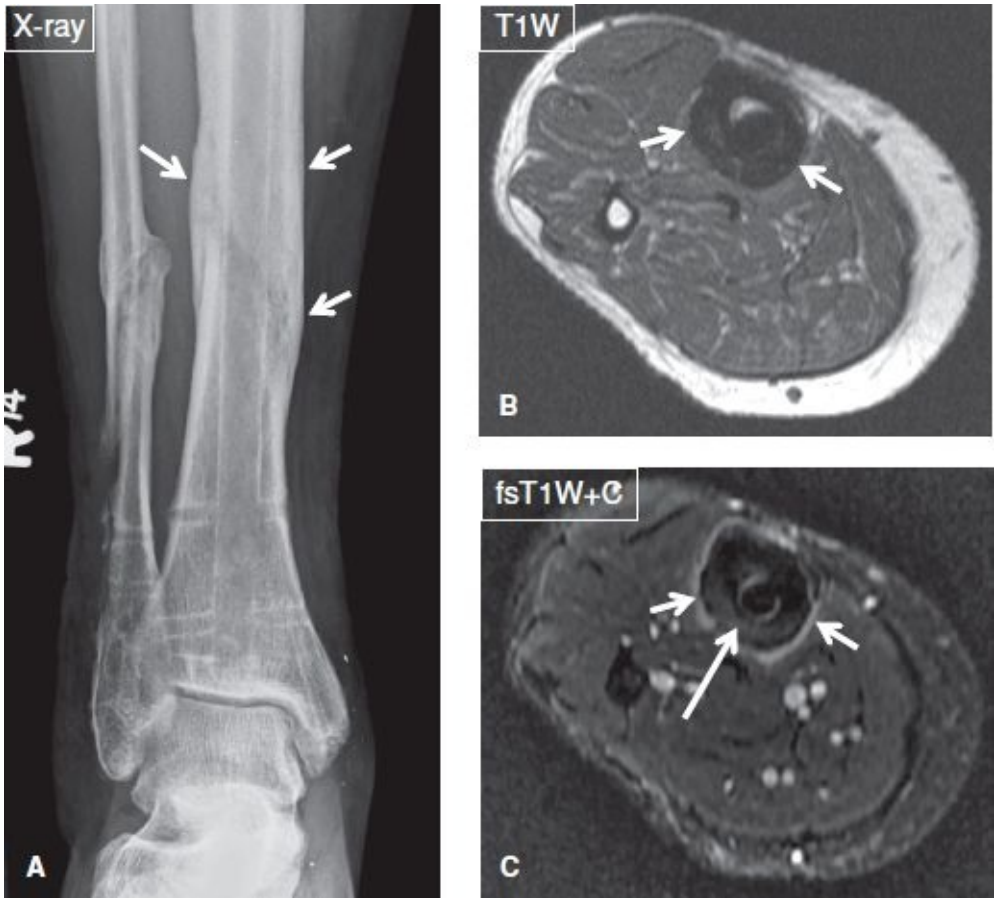

Fig. 16: Osteitis and periostitis but no osteomyelitis in a 47-year-old female who presented with fever and a tibial ulcer. **A:** Anteroposterior radiograph demonstrates chronic postoperative findings of fibular and tibial fractures as well as extensive periosteal thickening (*arrows*) of the tibia. **B, C:** On the respective axial MR images, there is

homogeneous mild thickening and enhancement of the periosteum (*short arrows*), indicating of periostitis, as well as mild enhancement of the cortex (*long arrow*), signifying osteitis. Absence of marrow enhancement excluded osteomyelitis.

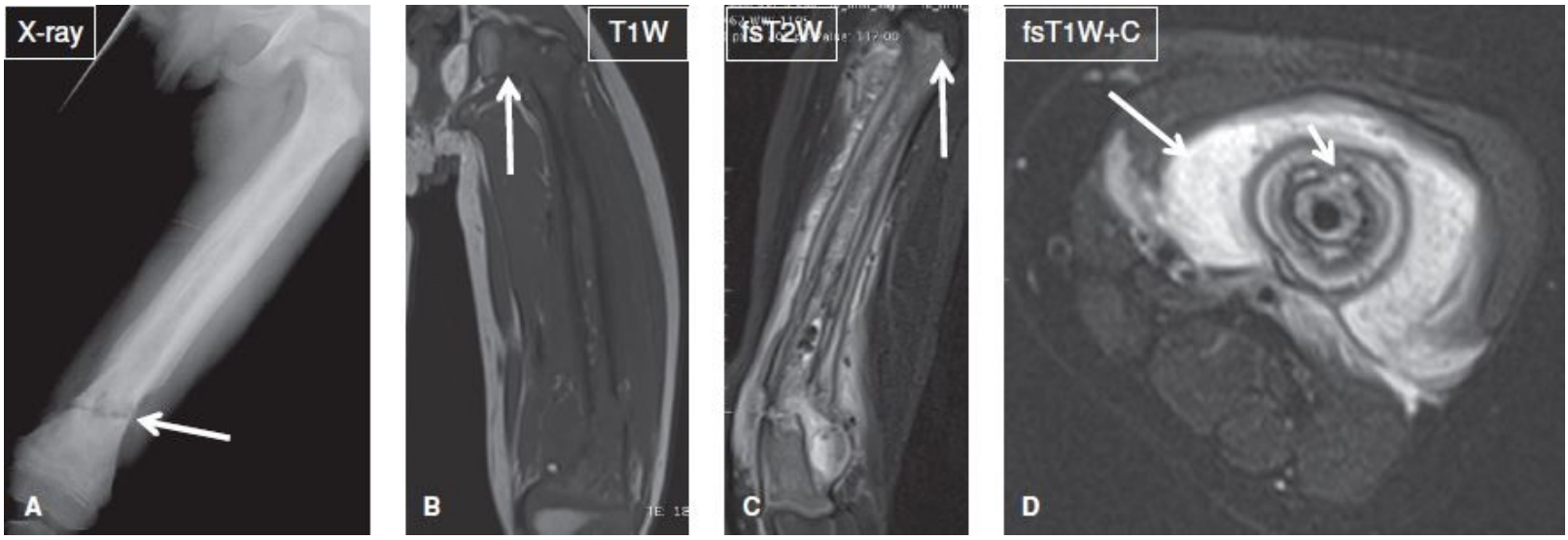

Fig. 17: Osteomyelitis. Young boy with fever and suspected Ewing sarcoma versus osteomyelitis. **A:** AP radiograph shows extensive periostitis, cortical thickening and sclerosis of the femur with a pathologic fracture at the distal metadiaphysis (*arrow*). **B, C:** Coronal MR images show extensive marrow replacement and fascial edema with subperiosteal and perifracture fluid collections. Notice the signal abnormality abruptly stops at the physeal plate (*arrows,* a classic sign of osteomyelitis). **D:** Axial postcontrast image shows extensive intramedullary, periosteal, and soft tissue enhancement (*long arrow*) and cloaca (*short arrow*) in this case of biopsy-proven osteomyelitis.

Subacute OM results from organisms of low virulence, inadequate therapy, abnormal bone, or strong host resistance. The classic form of subacute OM is Brodie abscess, which features a characteristic multizone configuration on T1W images, consisting of an innermost necrotic area of low signal, a relatively high signal intensity T1 rim, representing mineralized tissue; an outer low-to-intermediate signal rim of granulation tissue; and an outermost ill-defined zone of relatively low signal, which corresponds to marrow edema or hyperemia. Brodie abscesses usually develop in the metaphysis and may demonstrate finger-like extensions, which occasionally extend into the adjoining physeal plate and usually fail to cross it. This phenomenon is known as “tunneling,” and is pathognomonic of the condition (Figs. 18, 19).

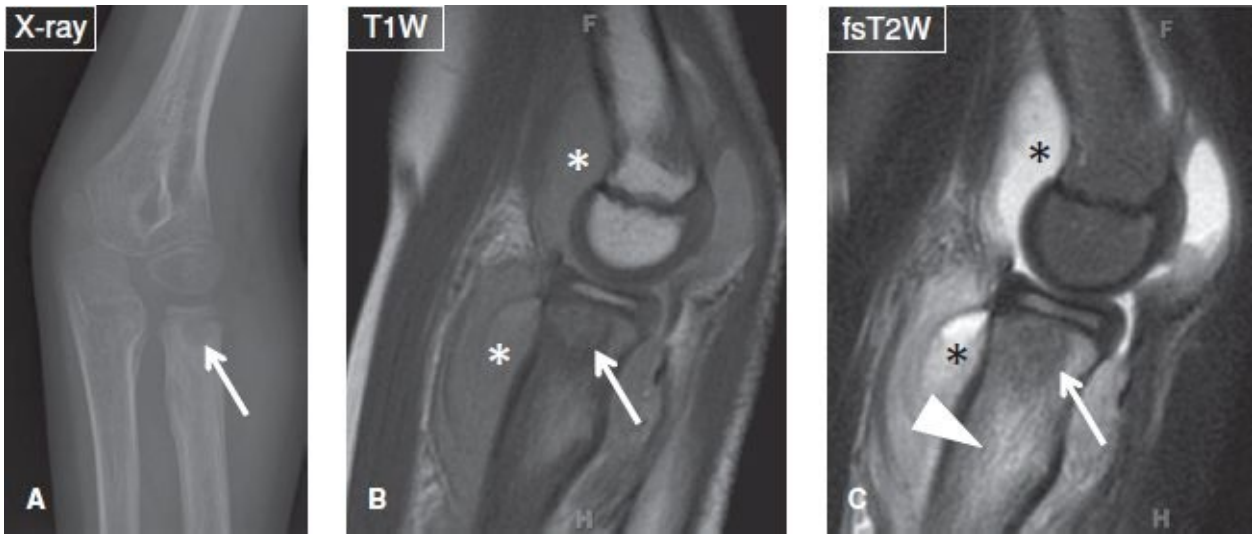

Fig. 18: Brodie abscess. **A:** Anteroposterior radiograph of the elbow demonstrates a well-defined radiolucent lesion (*arrow*) with surrounding sclerosis at the proximal radial metaphysis. Notice the sclerosis fades into the surrounding marrow (a sign indicative of Brodie abscess), unlike the sharp border of sclerosis frequently seen in neoplastic lesions. **B, C:** The corresponding sagittal MR images, the lesion (*arrows*) is hypointense, feature a multizone configuration and is surrounded by extensive marrow edema (*arrowhead*). Also note reactive joint effusion (*asterisks*) and surrounding fascial edema.

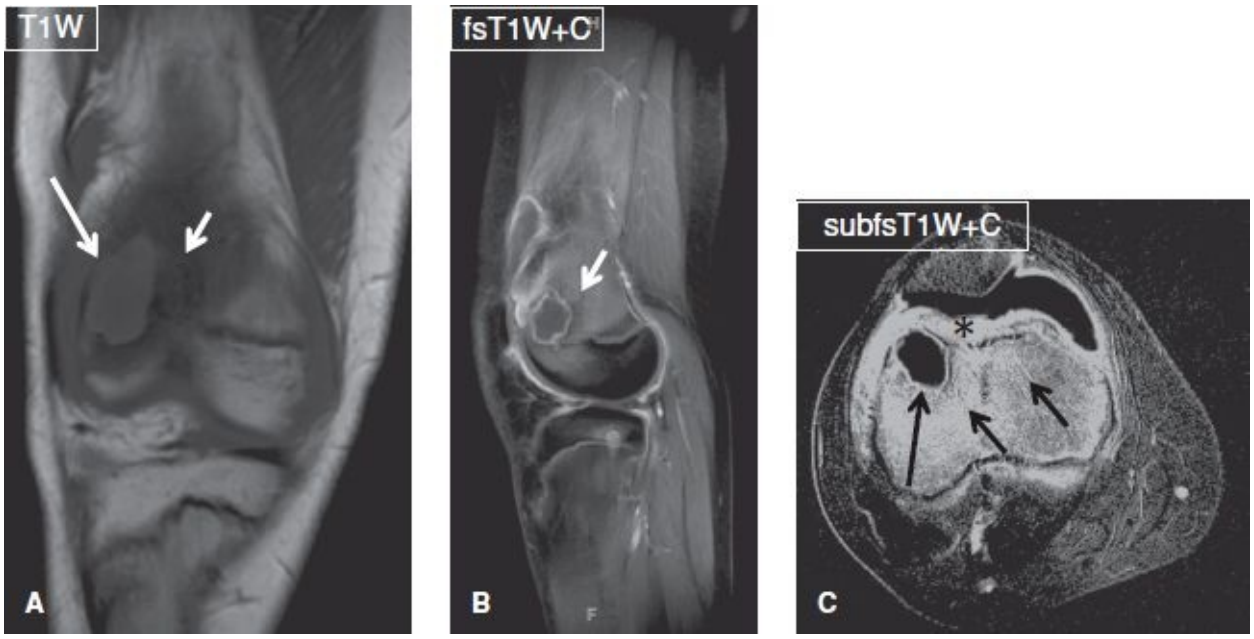

Fig. 19: Brodie abscess. Coronal **(A),** sagittal **(B),** and axial **(C)** images exhibit a well-defined ring-enhancing T1 hypointense lesion (*long arrows*) at the femoral metaphysis, which is surrounded by edematous and hyperemic marrow (*short arrows*) and feature a multizone periphery. Notice the intense enhancement of the prefemoral fat pad (*asterisk*) and synovium, in keeping with associated septic arthritis.

Inadequately treated infection leads to chronic OM, which is defined as persistent infection for more than 1 to 3 months. It is characterized by bone necrosis and sequestrum formation. On MR imaging, there is cortical thickening, bone expansion, and remodeling.

As opposed to acute OM, in chronic OM, the tissue planes are better defined, and there is a sharp interface between normal marrow and the infectious area, which exhibits low signal on T1W images, mixed signal on T2W images, and enhances minimally to moderately after gadolinium administration. The sequestrum appears as a central area of low signal on all sequences and lacks contrast enhancement, which, in turn, confirms devitalized bone. It might extrude out of the bony opening (cloaca), and the reactive bone around that hole is called the involucrum (Fig. 17). The latter features low signal on all sequences and is separated by the underlying cortical bone by a linear zone of intermediate-to-high signal on fluid-sensitive images. As the infection becomes controlled, the dead cortical bone is incorporated with the involucrum, forming a focus of thickened cortex. The involucrum is more commonly found in infants and children. The cloaca also permits drainage of pus and granulation tissue from the medullary space into the adjacent soft tissues to the skin. This channel of cloaca appears hyperintense on fluid-sensitive fat suppressed images.

Fungal OM is uncommon and generally presents in an indolent fashion. It is usually the result of a fungal (commonly respiratory or urinary) infection, with the organism hematogenously settling in the bone marrow. Whereas any fungus may be responsible, the most common pathogens are *Coccidioides immitis* (coccidioidomycosis), *Blastomyces dermatitidis* (blastomycosis), and *Sporotrichum schenckii* (sporotrichosis). On MR imaging, findings are non-specific, except for a few features, such as multifocal lesions, no or minimal fluid collection, not so pronounced fascial edema, intralesional T1 hyperintensity due to minerals and lesser degree of contrast enhancement of the involved marrow. Recent travel or residence of the patient in the endemic areas, along with imaging evidence of infectious foci elsewhere in the body (mainly in the lungs) suggests the diagnosis (Fig. 20). The final diagnosis is usually established on bone biopsy.

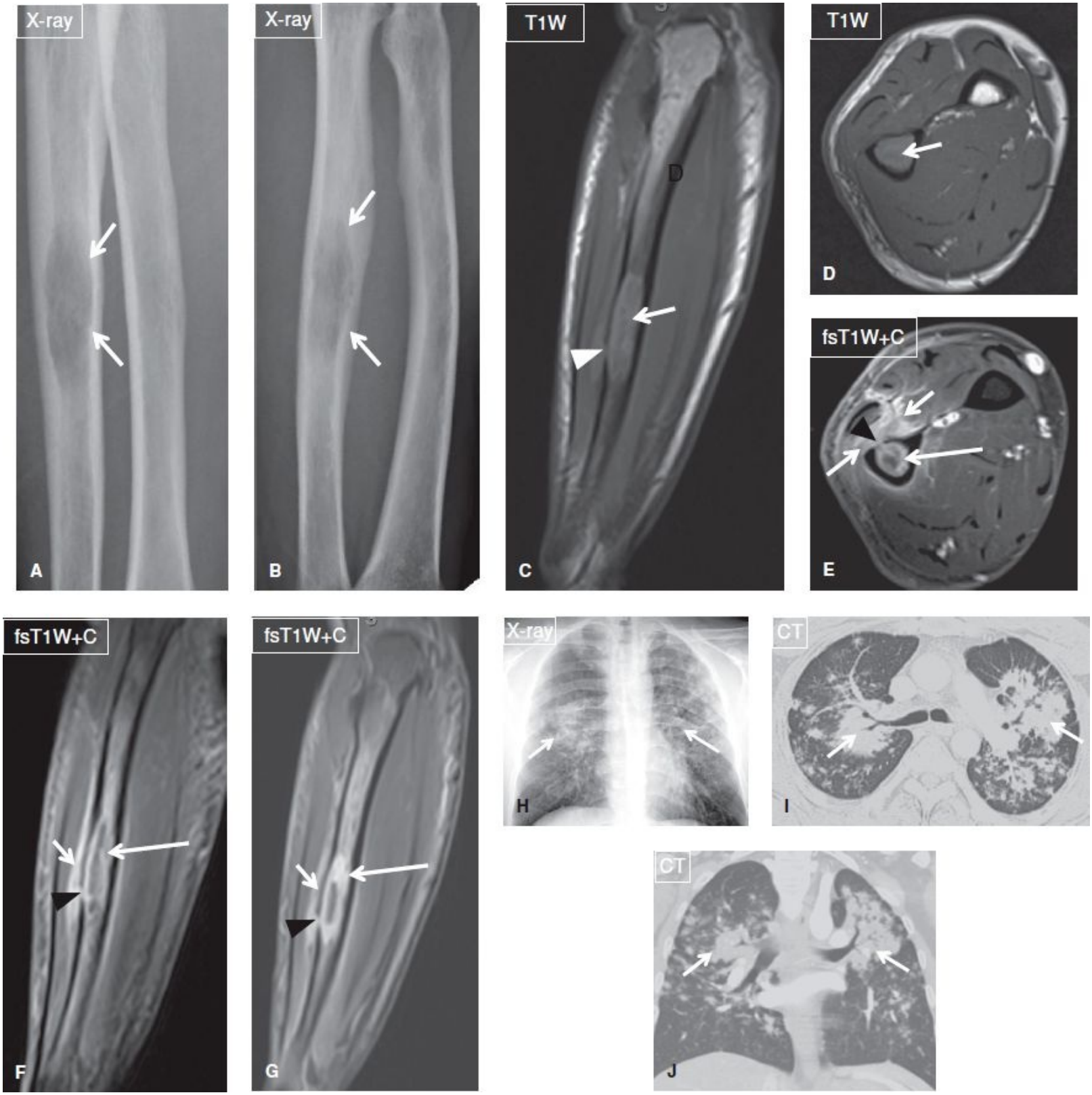

Fig. 20: Fungal (coccidioidomycosis) osteomyelitis. Anteroposterior **(A)** and oblique **(B)** radiographs of the forearm reveal an ill-defined radiolucent lesion (*arrows*) at the ulnar diaphysis. On the respective nonenhanced sagittal **(C)** and axial **(D)** MR images, the lesion (*arrows*) shows intermediate-to-high T1 signal, and is associated with focal cortical disruption (*arrowhead* in **C**). **E, F:** After contrast administration **(E–G),** the lesion (*long arrows*) exhibits thick peripheral enhancement, confirming the diagnosis of a necrotic lesion. Through the cortical disruption (*arrowheads*), infectious/inflammatory material has escaped to the adjacent soft tissues (*short arrows*), which demonstrate strong enhancement, reflecting hyperemia. Anteroposterior chest radiograph **(H),** and axial **(I)** and coronal-reformatted **(J)**

CT images demonstrate bilateral alveolar infiltrates (*arrows*), mostly in a perihilar and peribrochovascular distribution. Sputum culture and bone biopsy reveal *Coccidioides immitis,* establishing the diagnosis of coccidioidomycosis pulmonary infection and fungal osteomyelitis.

Chronic recurrent multifocal osteomyelitis (CRMO) refers to an autoinflammatory disorder of children and young adults, which is characterized by non-bacterial OM. Patients typically present with multifocal bone pain secondary to sterile osseous inflammation, and the disease exhibits a relapsing and remitting course. CRMO is a diagnosis of exclusion based on the following criteria: Lack of causative organism; no abscess formation, fistula, or sequestra; atypical location compared with infectious OM, frequent involvement of the clavicle, and multifocality. MR imaging, and recently whole-body MR imaging, enable evaluation of the true extent of the disease because the latter often shows greater marrow involvement than suspected on radiographs. On MR images, there is marrow edema and heterogeneous contrast enhancement, often with periosteal new bone formation. Abscess formation is very unusual (Figs. 21, 22).

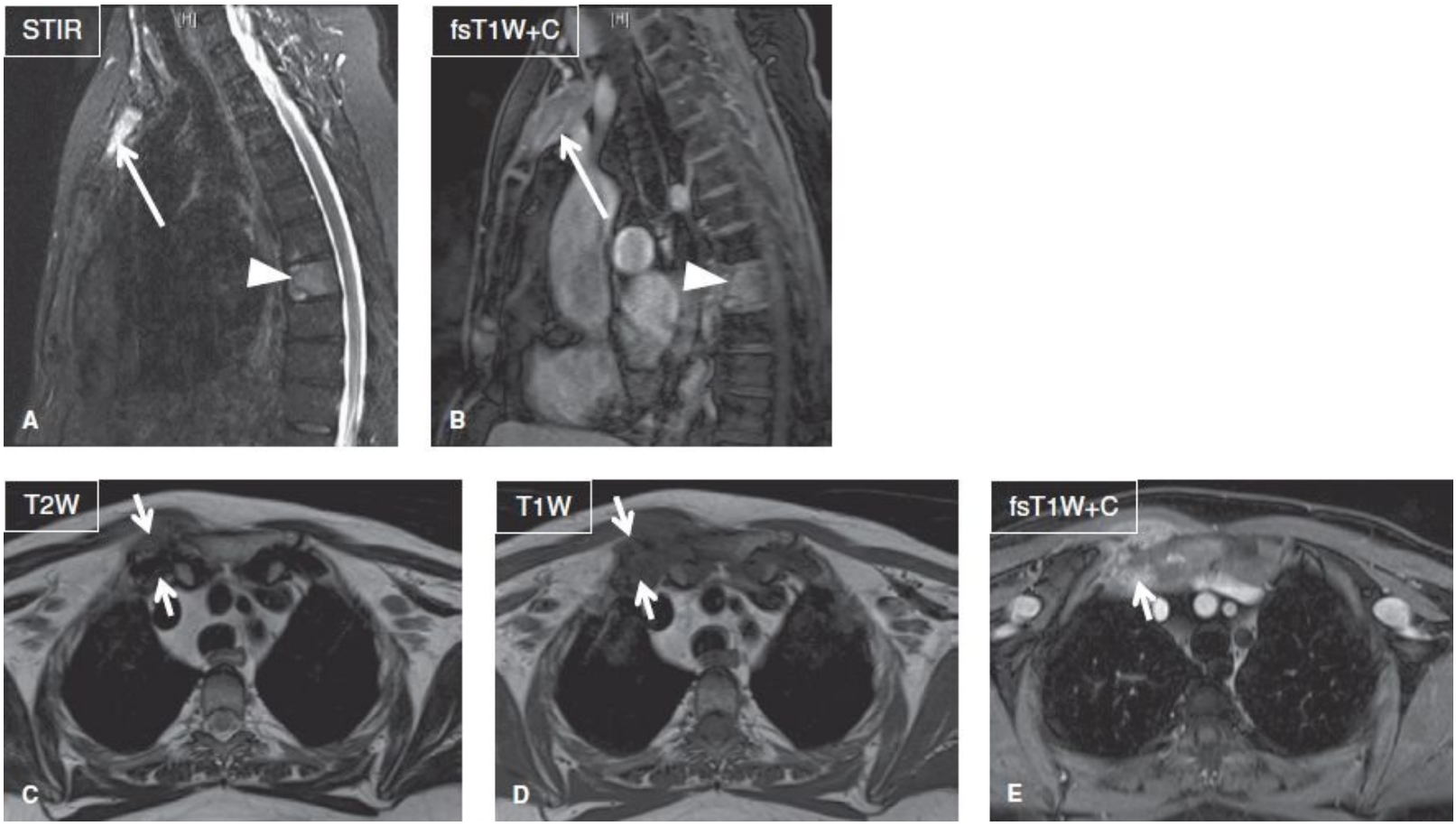

Fig. 21: Chronic recurrent multifocal osteomyelitis with SAPHO syndrome. Sagittal **(A, B)** and axial **(C–E)** images demonstrate marrow edema and contrast enhancement of the T8 vertebral body (*arrowheads*) and manubrium of the sternum (*long arrows*) indicative of osteomyelitis. Also note severe inflammatory arthropathy of the right sternoclavicular joint (*short arrows*).

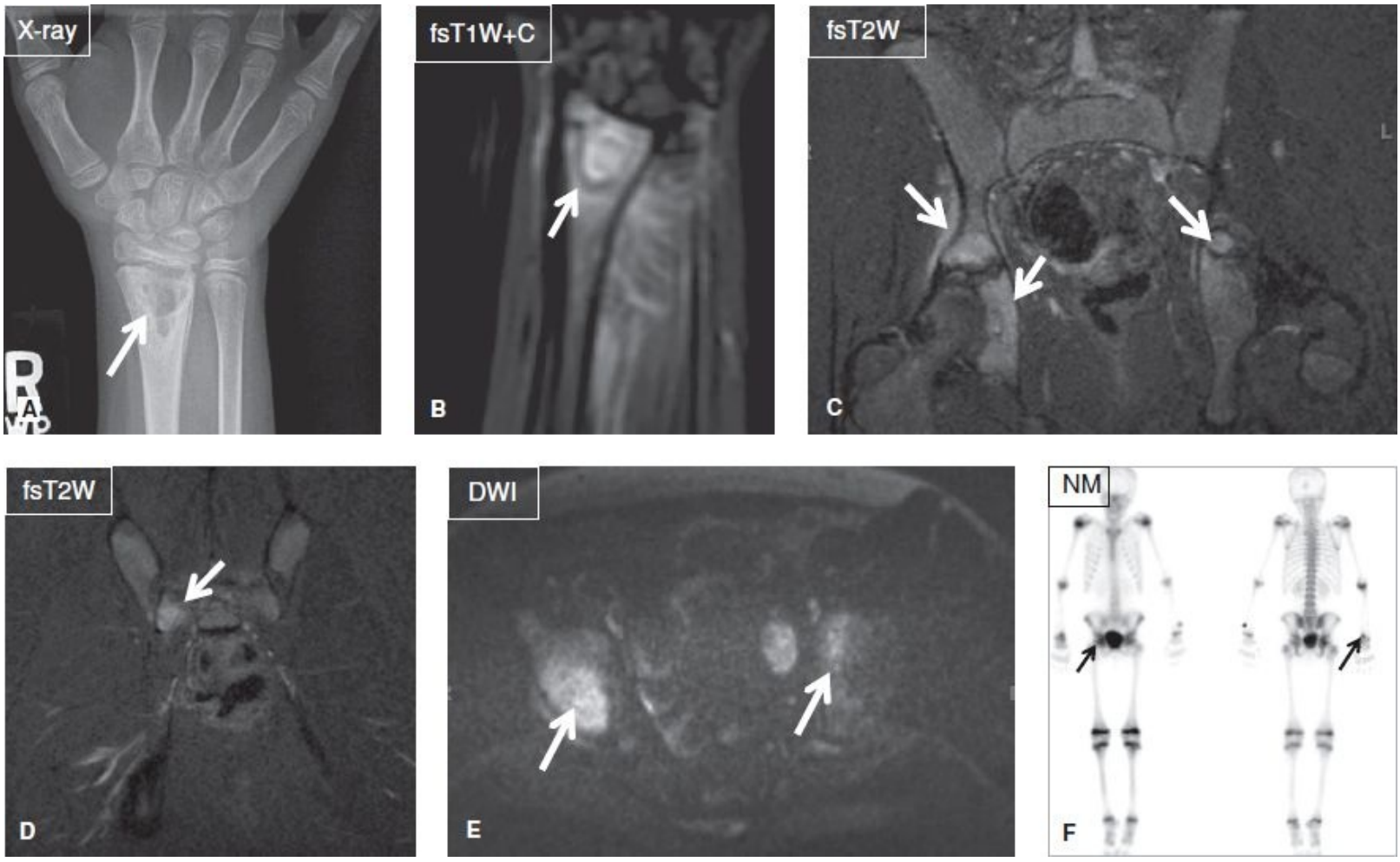

Fig. 22: Chronic recurrent multifocal osteomyelitis. **A:** Anteroposterior radiograph shows a well-defined multilocular lytic lesion (*arrow*) at the radial metaphysis. **B:** On the respective MR image, the lesion (*arrow*) and adjacent marrow enhance intensely, reflecting hyperemia. **C–E:** Coronal images of the pelvis exhibit multiple areas (*arrows*) of marrow edema and enhancement, reflecting infectious foci. **F:** On the bone scintigraphy Tc99 m MDP scan, the above foci (*arrows*) all demonstrate increased radionuclide update.

Since the body's own immunologic response is less effective in areas of impaired vascularity, patients with sickle cell disease show increased incidence of bone infarction and OM. In these individuals, bone infarcts tend to occur in the epiphyses, frequently in the femoral and humeral heads, and these lesions are more often bilateral compared to avascular necrosis in other diseases. The most typical cause of OM in sickle cell disease is Salmonella. Differentiation between the two entities is important for treatment purposes and is based on fsT2W and post-contrast T1W images. Whereas both entities present with reactive marrow edema and surrounding hyperemia, acute infarcts demonstrate thin, linear rim contrast enhancement, in contrast to acute OM, which shows more geographic and irregular marrow enhancement. In addition, acute OM may be associated with subperiosteal or intraosseous fluid collection, a feature, which is not evident in acute infarcts (Fig. 23). Finally, bone pain in sickle cell disease is much more common in acute infarct as compared to acute OM. The final diagnosis is, however, established on blood culture or bone aspiration/biopsy.

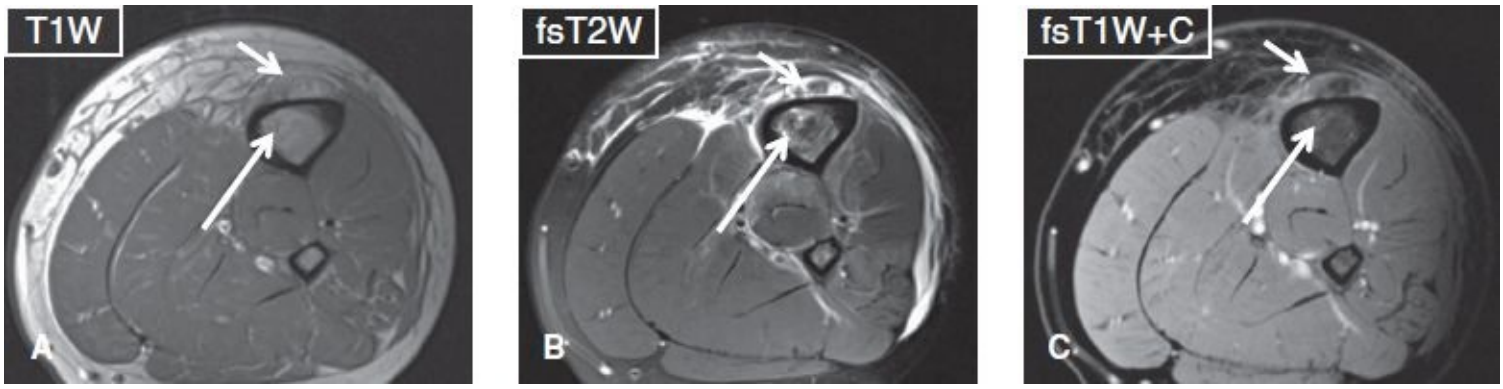

Fig. 23: Subperiosteal abscess. Axial images **(A–C)** show periosteal elevation along with an underlying ring-enhancing fluid collection (*short arrows*), in keeping with subperiosteal abscess. Also note tiny enhancing T1 hypointense, T2 hyperintense foci (*long arrows*) in the marrow, which correspond to osteomyelitis.

The differential diagnosis for acute OM related bone marrow edema pattern includes bone contusions and fractures, non-infectious inflammatory and metabolic bone lesions, histiocytosis, osteoid osteoma, Ewing's sarcoma, bone infarct, leukemia, and metastases (Fig. 24). Therefore, clinical history and findings frequently assist in establishing the correct diagnosis. Subacute OM, in particular, can mimic a neoplasm (most often Ewing's sarcoma), in both clinical manifestations and imaging findings. Helpful discriminators of infection versus neoplasm include the rim sign, which refers to a well-defined rim of low signal intensity surrounding the active disease on all sequences, and the penumbra sign, which appears on T1W images as a discrete and relatively hyperintense zone of transition between the intermediate-to-low signal intensity abscess cavity and the adjacent edematous or sclerotic bone marrow.

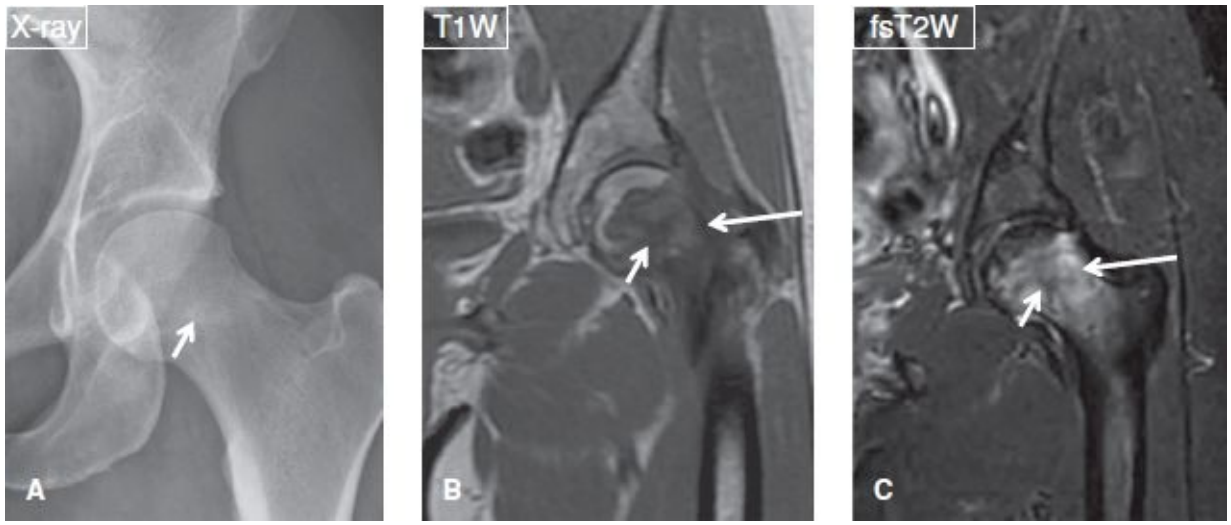

Fig. 24: Anteroposterior radiograph **(A)** and corresponding coronal MR images **(B, C)** show an intratrabecular fracture (*short arrows*) with a background of marrow infiltration caused by leukemia (*long arrows*). Notice absence of lesion conspicuity on the radiograph, not uncommon with round cell or other marrow infiltrative lesions.

In diabetic patients, the infectious lesions occur at the site of bony protrusion or

ulceration. For evaluation of toe OM, one should obtain sagittal images, otherwise the deformities (hammer toe/claw toe) related to diabetic neuropathy and vasculopathy make the assessment of marrow infiltration quiet challenging (Fig. 25). In addition, neuropathic arthropathy (NpA) of the foot may be challenging to differentiate from OM. The imaging features that assist in differentiating the two entities include the following:

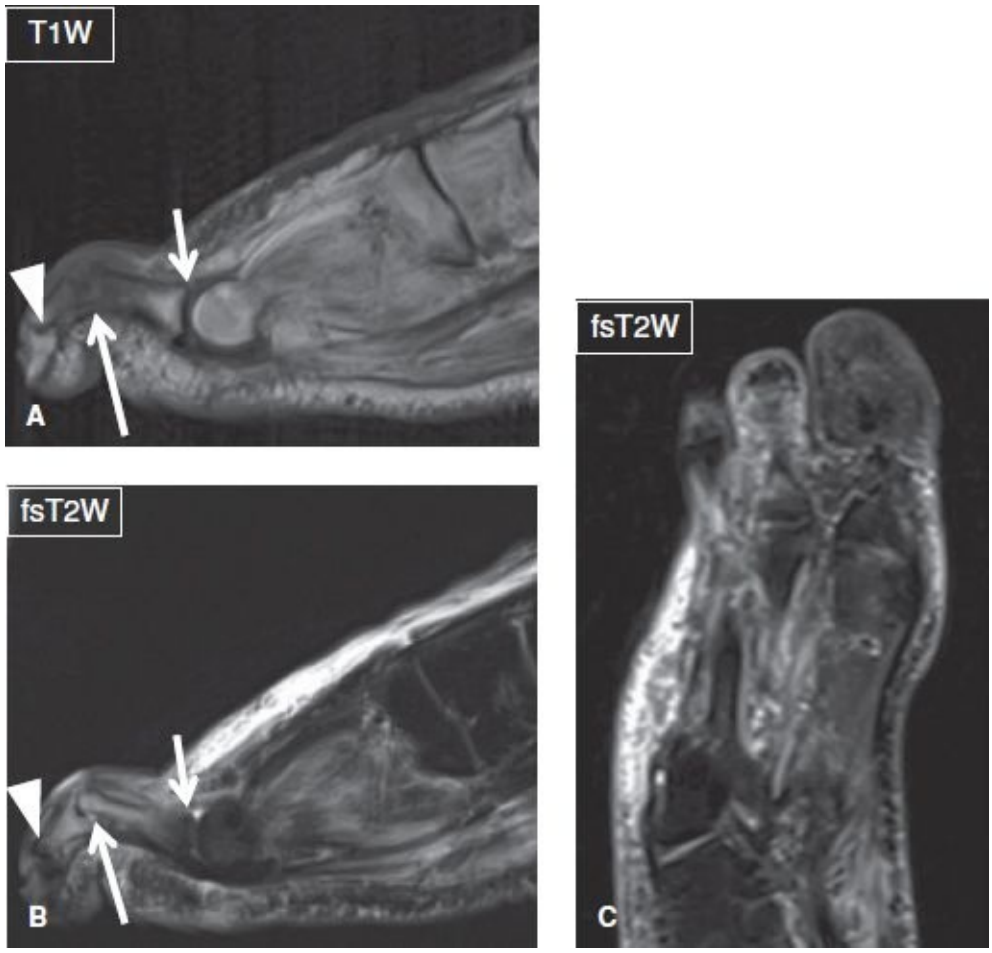

Fig. 25: Osteomyelitis with hammertoe deformity in a patient with diabetes mellitus. **A, B:** Sagittal images show flexion deformity of the third proximal interphalangeal joint (*long arrows*), with hyperextension of the respective metatarsophalangeal (*short arrows*) and distal interphalangeal (*arrowheads*) joints. Notice osteomyelitis with septic arthritis at the PIP joint and overlying cellulitis. **C:** The corresponding coronal (*long axis*) image detects the abnormal configuration of the forefoot but is unable to characterize the lesion.

- Soft tissue changes, with the overlying skin being edematous but intact in NpA; but commonly featuring an ulcer, abscess, and/or sinus tract in OM (Fig. 26)

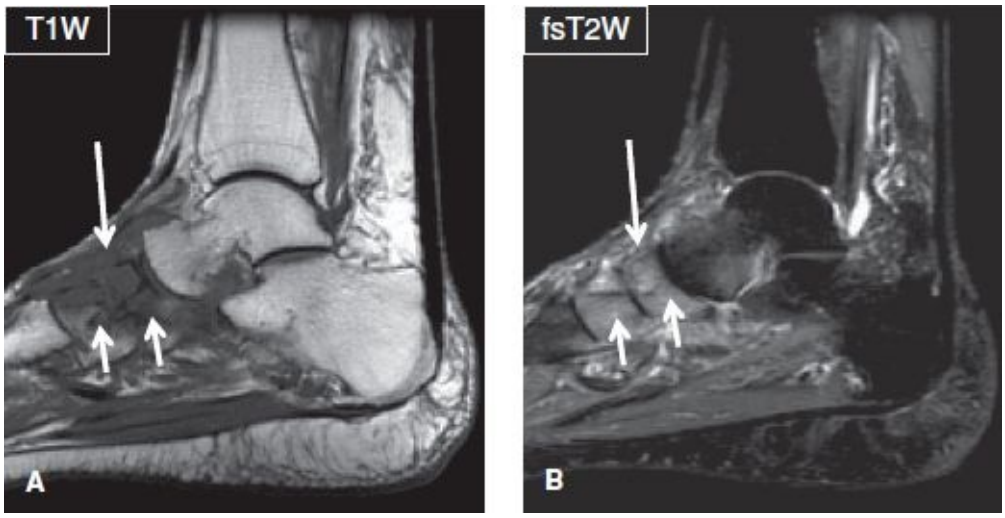

Fig. 26: Neuropathic arthropathy. Sagittal images **(A, B)** demonstrate architectural distortion of the midfoot joints, bony fragmentation, and marrow edema of the articulating tarsal bones (*short arrows*), as well as edema of the surrounding soft tissues (*long arrows*). There is no skin ulceration, collection, or sinus tract to suggest superimposed infection.

- The pattern of bone marrow edema, which tends to be diffuse in OM and, predominantly subchondral in NpA. Associated fascial edema or subperiosteal fluid is seen in infections as compared to NpA.
- The bone distribution, with OM usually involving one or two bones in a weight-bearing region (e.g., toes, metatarsal heads, calcaneus, dorsal aspect of phalanges in hammer toes) and NpA commonly involving multiple bones, usually in midtarsal joints of midfoot and often occurs bilaterally
- Typical presence of bone and joint deformity in NpA, a feature uncommon in OM unless there is underlying NpA
- Extensive cystic changes of the bones (common in NpA, cysts usually become inconspicuous with superimposed infection and reappear with resolution of infection)
- Finally, diffuse dark bones on all imaging sequences are only noted with NpA

There [<is no> <is>] large joint effusion.

A large joint effusion at or adjacent to a site of infection is highly suspicious for septic arthritis. In most instances, it is impossible to define the cause of infectious synovitis (Fig. 27). In the latter case, the effusion is often complex, features intermediate T1 and T2 signal, and is commonly associated with features of synovitis (synovial thickening and intense contrast enhancement), perisynovial edema, and capsular outpouchings (Fig. 28). If present, intra-articular gas bubbles appear as foci of signal void. Subacute and chronic cases may additionally feature joint erosions and rim-enhancing abscesses. It is important to know that absence of joint effusion does not exclude septic arthritis, and definite diagnosis should be based on joint aspiration. If dry joint tap is received, it is prudent to instill saline into the joint and aspirate back to send for Gram stain and culture sensitivity. One will see excessive white cell count with predominance of polymorphs, and leukocyte esterase test

can be performed to augment the diagnostic accuracy. Septic arthritis is considered an orthopedic emergency because delayed diagnosis and treatment may result in disabling joint destruction.

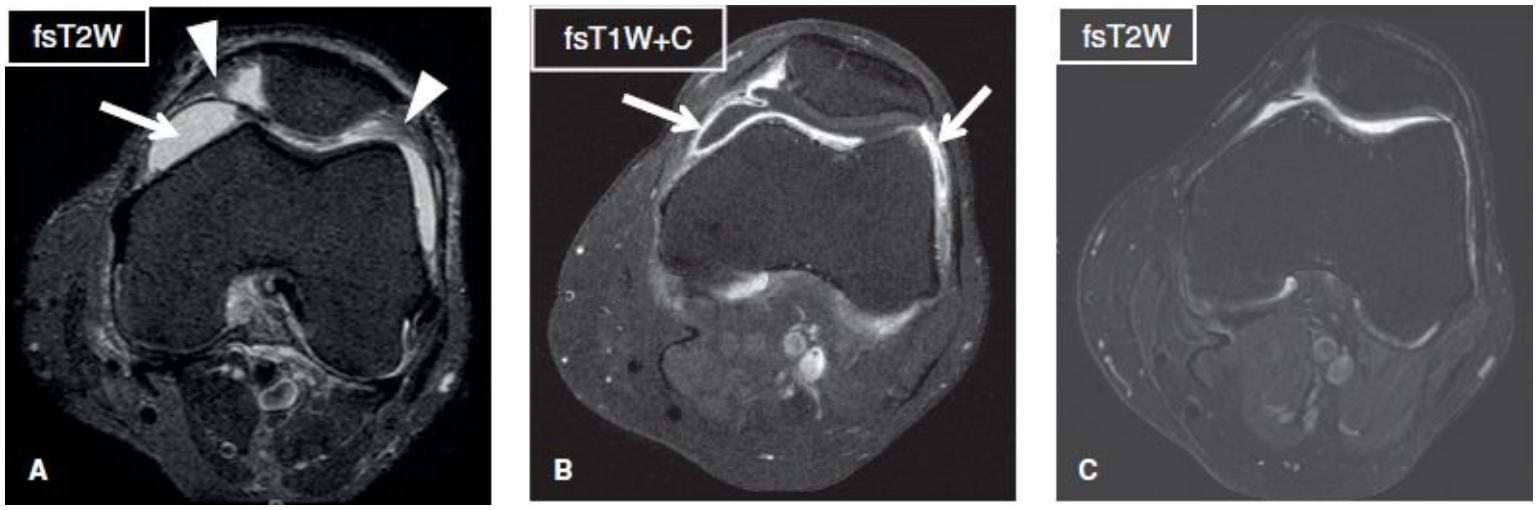

Fig. 27: Lyme synovitis. Axial images. **A:** There is moderate joint effusion (*arrow*) with synovial proliferation (*arrowheads*) of the knee joint. **B:** The synovial membrane shows homogeneous thickening and strong enhancement (*arrows*), suggestive of hyperemia/inflammation. **C:** Follow-up image while on treatment reveals resolution of effusion and synovial thickening.

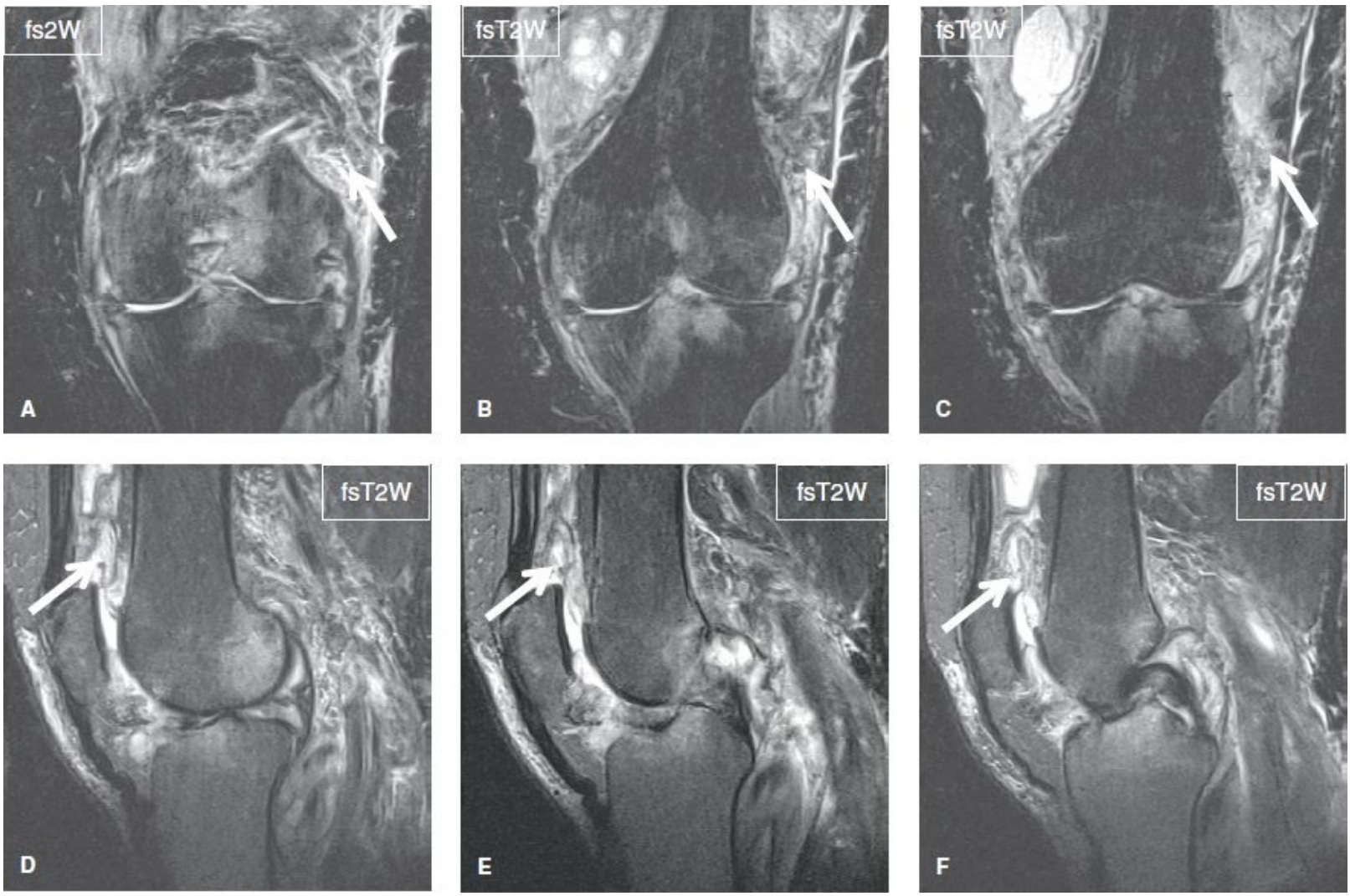

Fig. 28: Septic arthritis. Sequential coronal **(A–C)** and sagittal **(D–F)** images show heterogeneous moderate joint effusion (*arrows*) along with extensive diffuse edema of the surrounding soft tissues and areas of reactive bone marrow edema.

Incidental Findings

Foreign bodies are typically located within the inflammatory area, and these demonstrate variable features depending on their substance (signal void, susceptibility artifacts, etc.). Occasionally, a sinus tract is identified adjacent to the foreign body, demarcating the route of entrance within the soft tissues. The sinus tract and foreign body are particularly well seen on intravenous contrast examination. Correlation with radiographs is useful to distinguish soft tissue gas from a foreign body or calcification.

Post-Gadolinium Discussion

Studies that are entirely normal based on unenhanced sequences should not be complemented with intravenous gadolinium. Gadolinium administration, however, improves the conspicuity and defines the extent of the inflammatory process already visible on fluid-sensitive images. Post-contrast images also assist in upgrading the severity of the inflammation and in detecting additional marrow and soft tissue abscesses, as well as cortical destruction. Contrast-enhanced images are also useful in distinguishing abscesses from surrounding cellulitis/myositis. In OM, the role of contrast administration is not only to establish the diagnosis, but also to delineate the extent of the infection, assess for devitalized (nonenhancing) tissues, cortical involvement, and detect potential sequestrum. It is important to remember that lack of contrast enhancement rules out infection with a high degree of certainty. However, gadolinium administration cannot be used to reliably distinguish infectious from non-infectious inflammatory conditions.

Spinal Infections

Spondylodiskitis and vertebral OM are the most common types of spinal infections. In spondylodiskitis, there is obliteration of the intranuclear cleft and reduction of the disk height whereas both the disk and the adjacent endplates demonstrate low and high signal intensity on T1W and T2W images, respectively (reflecting edema) and enhance after gadolinium administration (reflecting hyperemia). Concomitant irregularity, erosions or bony sclerosis of the endplates, and long areas of edema and enhancement along the longitudinal ligaments assist in differentiating the condition from Modic type I changes, which can assume similar signal intensity changes. Epidural or paravertebral abscesses may coexist (Fig. 29).

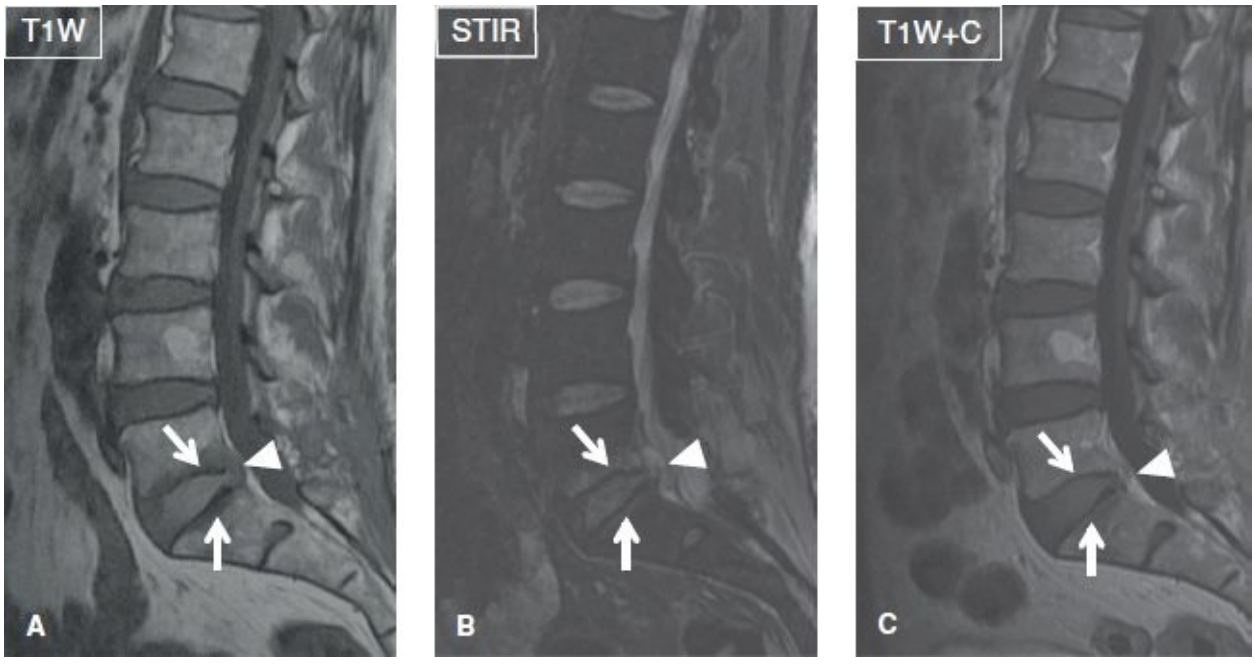

Fig. 29: Spondylodiskitis with epidural abscess. Sagittal images **(A–C)** demonstrate marrow edema and contrast enhancement of the opposing endplates (*arrows*) at the L5–S1 level, along with a small, peripherally enhancing fluid collection (*arrowheads*) in the epidural space.

BOX 2: The Structured Report: Inflammation/Arthritis

The checklist for structured reporting of MR imaging of inflammation/arthritis. For each field, *Normal* is considered default in the dictation whereas the rest of the elements describe various pathologies that could be encountered during imaging evaluation. See Appendices 3 and 4 at the end of the chapter for a sample completed report.

EXAM: MRI [<EXTREMITY / JOINT>] [<WITH / WITHOUT>] CONTRAST

FINDINGS:

There [<is no> <is> <focal / diffuse>] soft tissue subcutaneous edema.

There [<is no> <is> <focal / diffuse / multifocal>] muscle edema.

JOINT INVOLVED: [<_>]

Alignment: [<Normal> <Less than 50% subluxation / More than 50% subluxation>]

Fluid: [<Normal> <Small / Moderate / Large effusion>]

Synovial thickening/synovitis: [<Absent> <Mild / Moderate / Severe>]

Bony productive changes: [<Absent> <Mild / Moderate / Severe> <Osteophytes / Syndesmophytes / Enthesophytes>]

Tenosynovitis: [<Absent> <Mild / Moderate / Severe>]

Joint space/cartilage: [<Normal> <Less than 50% loss / More than 50% loss>]

Erosion/cystic change: [<Absent> <Less than 50% / More than 50% of joint surface> <Articular / Para-articular>]

Bone marrow edema: [<Absent> <Present>]

Ankylosis: [<Absent> <Less than 50% / More than 50%>]

Incidental Findings: [<_>]

Post-gadolinium Discussion: [<_>]

IMPRESSION:

[<In the order of importance with acute findings first>]

In isolated vertebral OM, the aforementioned signal changes are restricted to the bone marrow whereas the disk may appear normal. The latter finding, as well as non-contiguous multilevel involvement are not uncommon in spinal tuberculosis. Generally, the tuberculous infections occur in immigrants or immunocompromised subjects in the inner city areas. Imaging features include feature intermediate T1 and intermediate-to-high T2 marrow signal psoas or other cold abscesses, calcification of the lesions in subacute phases, isolated vertebral body involvement with disc sparing, kyphotic or gibbus deformity, isolated posterior vertebral element involvement, and finally, lung involvement in about 50% of cases (Fig. 30). Both tubercular and fungal infections are usually insidious, lack substantial hyperintensity of the intervertebral disc, are not associated with gas within the lesions, and contrast enhancement is less pronounced in extent and intensity as compared to pyogenic infections.

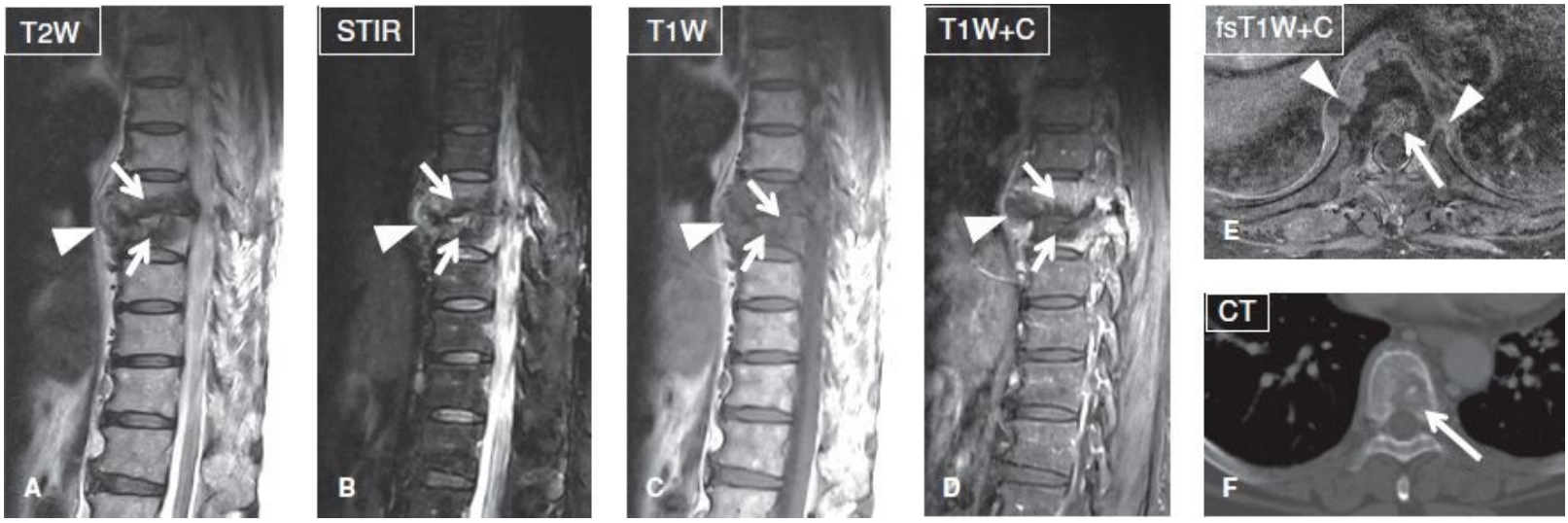

Fig. 30: Tuberculous spondylodiskitis in a middle-aged female with a 6-month history of back pain. **A–D:** Sagittal images display partial collapse, marrow edema, contrast enhancement, and irregular opposing endplates of the T8 and T9 vertebra (*arrows*), along with an abscess (*arrowheads*) beneath the anterior longitudinal ligament and in paravertebral location. The paraspinal collections (*arrowheads*) are confirmed on the respective axial MR **(E)** and CT **(F)** images. Also evident are the vertebra body erosions (*arrows*).

Reporting Using the Template for Inflammation/Arthritis

Compared to radiography, MR imaging not only offers earlier identification and expanded extent of bony erosions but is additionally able to detect bone marrow edema and soft tissue changes, which often are not detectable on plain films, and constitute the hallmarks of early or treatable inflammatory arthritis. This information can be used to improve diagnostic accuracy, decide on early treatment, predict prognosis, and monitor therapy. There are various radiographic scoring systems available for staging and monitoring progression of the inflammatory disease. However, most of these have been developed for rheumatoid arthritis (RA) and osteoarthritis (OA), and they cannot be completely extrapolated to MR imaging because of the heterogeneity of imaging protocols among institutes (fields of view, pulse sequences, field strength, etc.), and the different accuracy and reliability of the two modalities. In addition, most scoring systems also include clinical findings, and often more than one joints (those not in the imaging field of view) may have to be evaluated to define the final score.

There [<is no>] soft tissue subcutaneous edema.

There [<is no>] muscle edema.

In the setting of active musculoskeletal inflammation/arthritis, there may be edema and hyperemia of the involved soft tissues (subcutaneous layer, fascia or skeletal muscles), which demonstrate signal alterations and enhancement characteristics as previously

described for musculoskeletal infections. The lesions can demonstrate symmetric soft tissue edema and enhancement, for example, in RA (metacarpophalangeal and proximal interphalangeal joints) (Fig. 31) and psoriasis (proximal and distal interphalangeal joints); or they may occur at enthesis (e.g., in seronegative arthropathies). Other soft tissue findings include asymmetric soft tissue nodules (in conditions such as atypical RA, gout, amyloid, sarcoid, and reticulohistiocytosis) and finally, as cloud of edema around the hypointense deposits at the tendon or ligament attachments (calcium hydroxyapatite deposition) (Figs. 32–34).

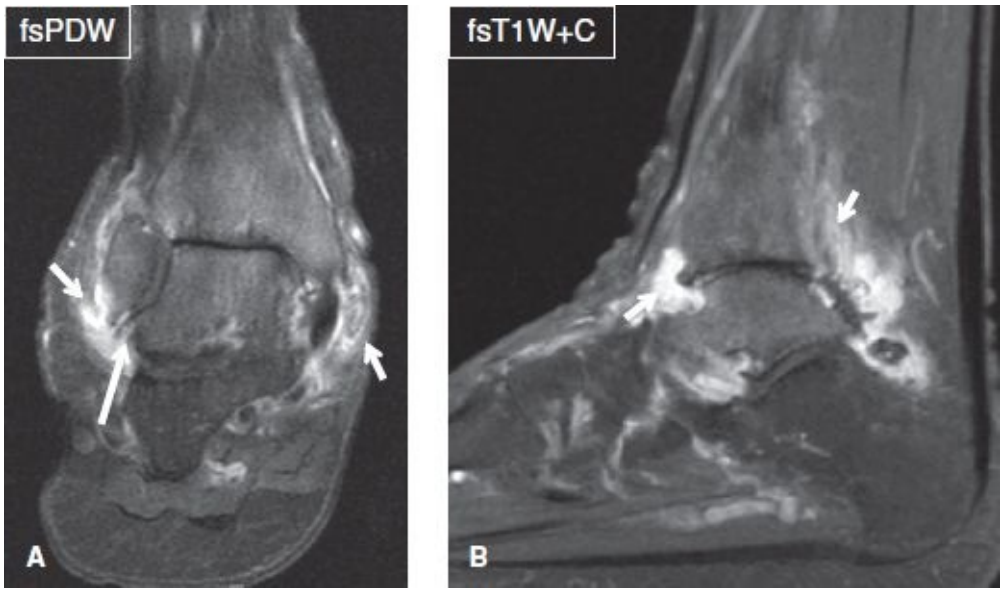

Fig. 31: Rheumatoid arthritis involving the ankle. Coronal **(A)** and sagittal **(B)** images demonstrate moderate effusion (*long arrows*), synovial enhancement and symmetrical joint loss with soft tissue enhancement (*short arrows*).

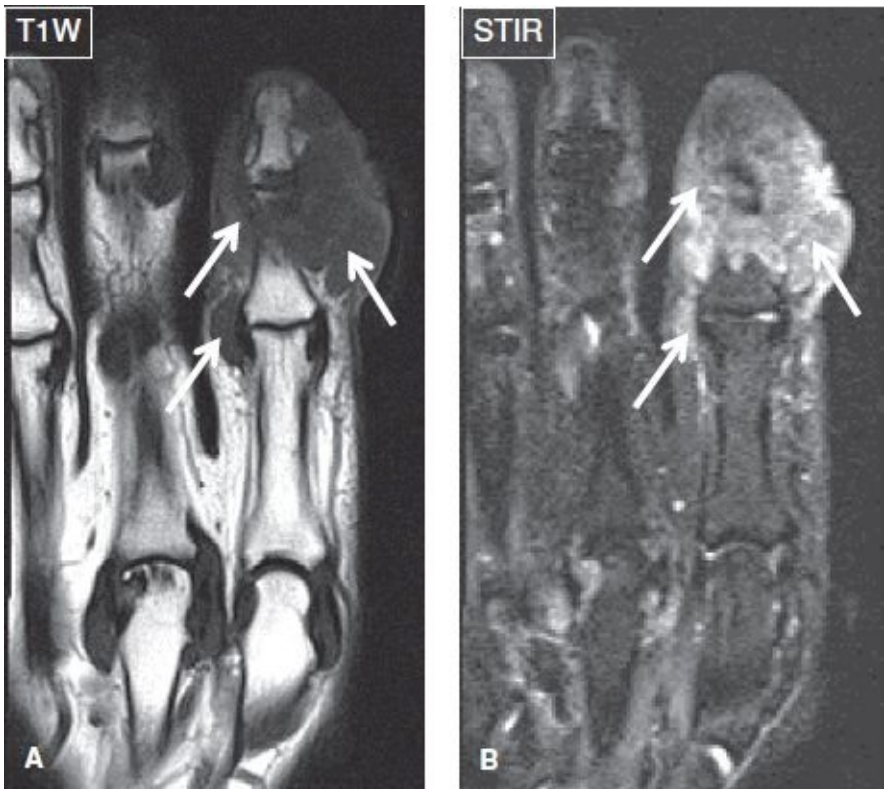

Fig. 32: Gout. Coronal images **(A, B)** demonstrate relatively homogeneous para-articular soft tissue nodules (*arrows*) of intermediate T1 and high T2 signal alterations, some of them causing eccentric bone erosions at the proximal and distal interphalangeal joints of the index finger and MCP joints of index and middle fingers.

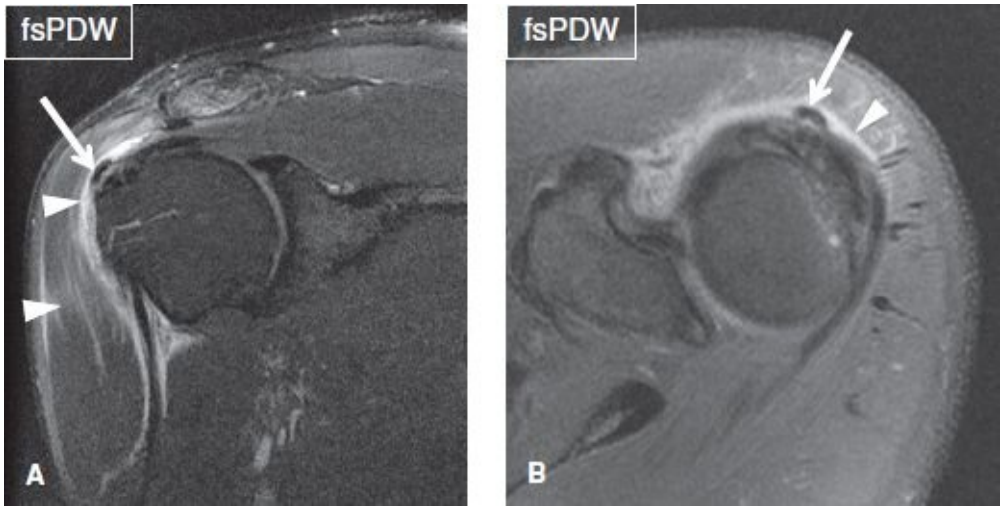

Fig. 33: Calcium hydroxyapatite crystal deposition disease. Coronal **(A)** and axial **(B)** images show a focus of low signal (*arrows*) at the supraspinatus tendon insertion, corresponding to calcific tendinitis. Also note subacromial/subdeltoid bursitis and adjacent myofascial edema (*arrowheads*).

Fig. 34: Multicentric reticulohistiocytosis. **A, B:** Anteroposterior radiographs of the left and right feet demonstrate joint space narrowing of PIP and DIP joints and relatively well-circumscribed marginal erosions (*arrows*) at the distal interphalangeal tufts of third to fifth digits. Also note soft tissue swelling around the respective distal phalanges. **C, D:** The respective coronal MR images of the right foot exhibit subchondral marrow edema at the distal fourth and fifth phalanges as well as soft tissue nodularity (*arrows*) abutting the distal phalanges. **E:** Anteroposterior radiograph of the hand from the same patient reveal bony resorption (*arrow*) of the fourth distal phalanx in this known case of multicentric reticulohistiocytosis.

Seronegative spondyloarthropathies (SpAs) are a heterogeneous group of diseases, which include psoriatic arthritis (PsA), reactive arthritis (Reiter syndrome), ankylosing spondylitis (AS), and inflammatory bowel disease. The hallmark of soft tissue manifestations in SpAs is enthesopathy, which refers to inflammation at sites where tendons, ligaments, or joint capsules attach to bones. Acute enthesopathy (enthesitis) manifests as florid inflammatory changes (T2 hyperintensity and contrast enhancement) of the soft tissues surrounding the enthesis, along with reactive bone marrow edema (osteitis) subjacent to that site. In the spine, the above changes are located at the anterosuperior corners of vertebrae (aka Romanus lesions in AS), at the vertebral end plates, spinous processes, and the facet joints (Figs. 35–37).

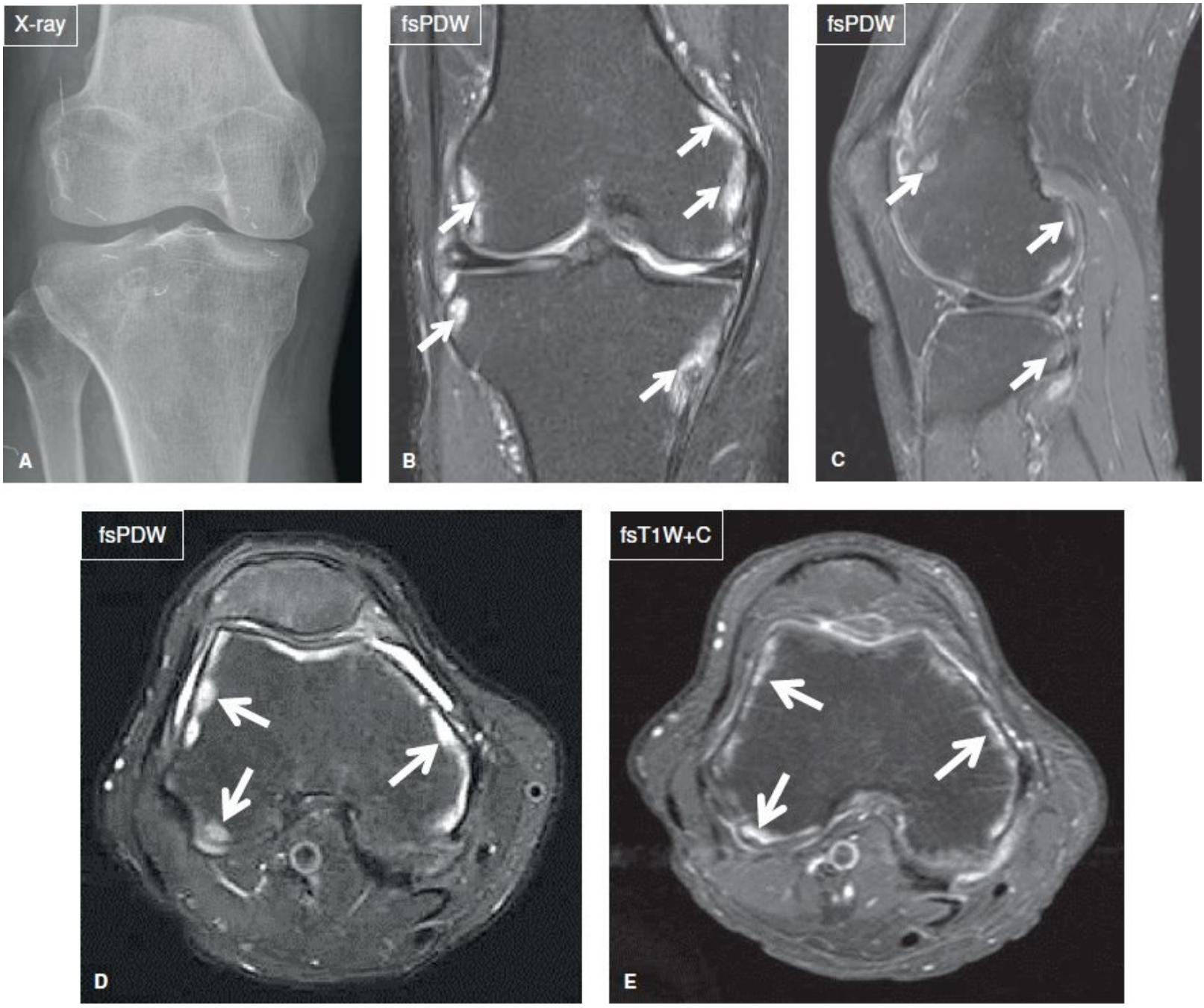

Fig. 35: Enthesitis in seronegative arthropathy in a middle-aged female with bilateral knee pain. Anteroposterior radiograph **(A)** reveals no erosive abnormality around the knee joint. Coronal **(B),** sagittal **(C),** and axial **(D, E)** MR images demonstrate multiple subcortical foci of marrow edema and contrast enhancement (*arrows*), some of which correspond to enthesitis at the attachment of retinaculae, collateral ligaments, and gastrocnemius tendon attachments.

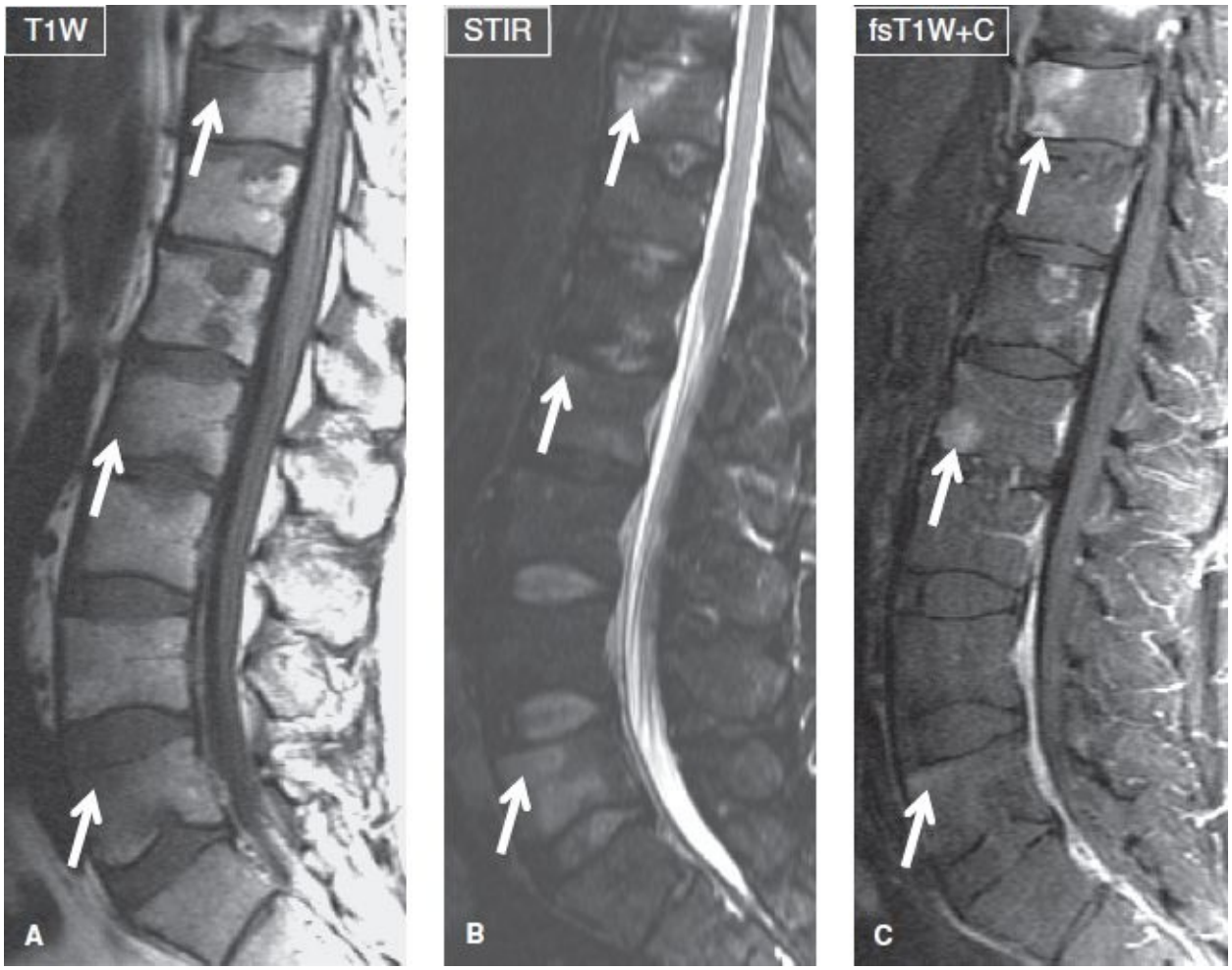

Fig. 36: Ankylosing spondylitis. Sagittal images **(A–C)** demonstrate "squaring" of the vertebral bodies, some of which exhibit edema and contrast enhancement at their endplates, reflecting enthesitis. Notice, many of these lesions are seen at the anterior-superior aspect of the vertebral bodies (*arrows*), corresponding to ligamentous attachment sites, also known as Romanus lesions.

Fig. 37: Ankylosing spondylitis. Sagittal images **(A, B)** show areas of marrow edema (*arrows*) adjacent to sites of ligamentous and tendinous attachments.

The soft tissue involvement in gout appears as nodular masses of monosodium urate crystals, which are known as tophi, and these can develop in almost any periarticular location. Gouty tophi may erode bones and result in eccentric cystic changes. In the latter

case, they are typically metaphyseal and periosteal in location, and the joint space or cartilage is preserved until the late stage. Tophi typically feature low signal on T1W images and variable signal on T2W images depending on their calcium concentration, with the majority of lesions being heterogeneously hypointense on T2W images and variably bright on fluid-sensitive images (Fig. 32). They usually demonstrate fairly homogeneous contrast enhancement, but may show peripheral enhancement in more chronic stages.

Amyloid arthropathy is most commonly seen in patients undergoing chronic hemodialysis or with history of multiple myeloma. It is characterized by extensive deposition of fibrinous protein (amyloid), which covers the synovial membrane, fills subchondral cystic defects, and extends to periarticular soft tissues. The intra- and periarticular lesions typically show low signal on T1W and T2W images, as well as moderate enhancement after contrast administration (Fig. 38). The intra-articular deposits frequently communicate with subchondral bone lesions, as described later in the chapter.

Fig. 38: Metabolic shoulder arthropathy in a patient with renal failure. Sagittal **(A)** and coronal **(B, C)** images exhibit subacromial–subdeltoid bursitis (*long arrows* in **B, C**), complete cartilage loss (*short arrows* in **B, C**), as well as multiple hypointense intra-articular lesions (*arrows* in **A**), which correspond to amyloid deposits.

Bursitis is a common finding in patients with early RA. Most commonly, it involves the gastrocnemius-semimembranosus bursa (Baker's cyst), intermetatarsal, retrocalcaneal, olecranon, and subacromial bursae, and typically appears as a well-defined lesion of fluid signal, which in active stage, shows significant wall enhancement following contrast administration, reflecting inflammation (Fig. 39). Associated synovial thickening or rice bodies can be seen in these bursae. Intermetatarsal bursitis is more frequent in the second and third web spaces. Other soft tissue manifestations of RA include rheumatoid nodules (25% of patients), which usually develop in the subcutaneous tissues at pressure points, and adjacent to bony protuberances. They feature low signal on T1W images, low (when solid) or high (when cystic) signal on T2W images, and demonstrate variable (intense or faint, solid or ring-like) contrast enhancement. Complications of rheumatoid nodules include ulceration, superinfection, sinus tract formation, and sepsis. In advanced stages of RA, there is resorption of the soft tissue and bony structures in and around the joint, with scar

formation, fibrosis, and joint and/or extremity contractures.

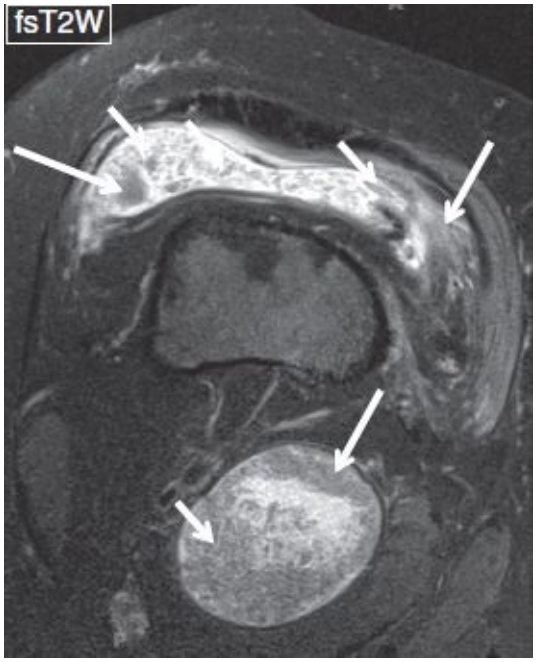

Fig. 39: Rheumatoid arthritis. Axial image demonstrates joint effusion and Baker cyst, along with synovial thickening (*long arrows*), indicating synovitis. Intermediate-signal rice bodies (*short arrows*) fill both the suprapatellar bursa and Baker cyst.

Calcium pyrophosphate deposition disease (CPPD; also known as pseudogout) is characterized by deposition of crystals in and around joints, and particularly in articular cartilage and fibrocartilage. These crystals demonstrate low signal on T1W images with punctate signal void. On T2W images, the signal varies, depending on the crystal concentration and the amount of associated granulation tissue and fibrosis. Rim enhancement is rarely noted. Crystals are detected in the hyaline cartilage and fibrocartilage of the knees, the triangular fibrocartilage of the wrist, the fibrocartilage of the symphysis pubis, and the acetabular labrum of the hips. In the acute stage, there is diffuse inflammation of the periarticular soft tissues, which manifests as T2 hyperintensity and contrast enhancement. Extensive cystic changes may be seen in the carpal bones (Fig. 40) similar to other depositional arthropathies, such as sarcoid, amyloid, gout, or infectious/inflammatory arthropathies (e.g., tuberculosis, RA).

Fig. 40: CPPD arthropathy. Coronal image shows extensive cystic changes (*arrows*) of the carpus with joint effusion in this known case of CPPD arthropathy.

In multicentric reticulohistiocytosis, there are multiple cutaneous nodules, which are distributed rather diffusely throughout the body as compared to the periarticular tissues. These nodules never undergo calcification. The disease can manifest in the hands or less commonly in the feet, as erosions of distal phalanges or erosive OA-like appearance of the middle and distal interphalangeal joints (Fig. 34). In hydroxyapatite deposition disease (HADD), calcium hydroxyapatite crystals deposit in tendons, peritendinous tissues, bursae, and ligaments. On imaging, these crystals manifest as rounded areas of low signal on all sequences, which are particularly conspicuous on gradient-echo images, and vary in size from a few millimeters to several centimeters. In the acute symptomatic phase of HADD, the inflammatory process has an aggressive appearance with soft tissue and bone marrow edema and the calcification on the plain radiograph appears amorphous, the findings, may mimic infection, trauma, or neoplasm (Fig. 41). Correlation with radiographs is essential. In advanced stages, the joints may be markedly destroyed (Milwaukee shoulder) similar to NpA.

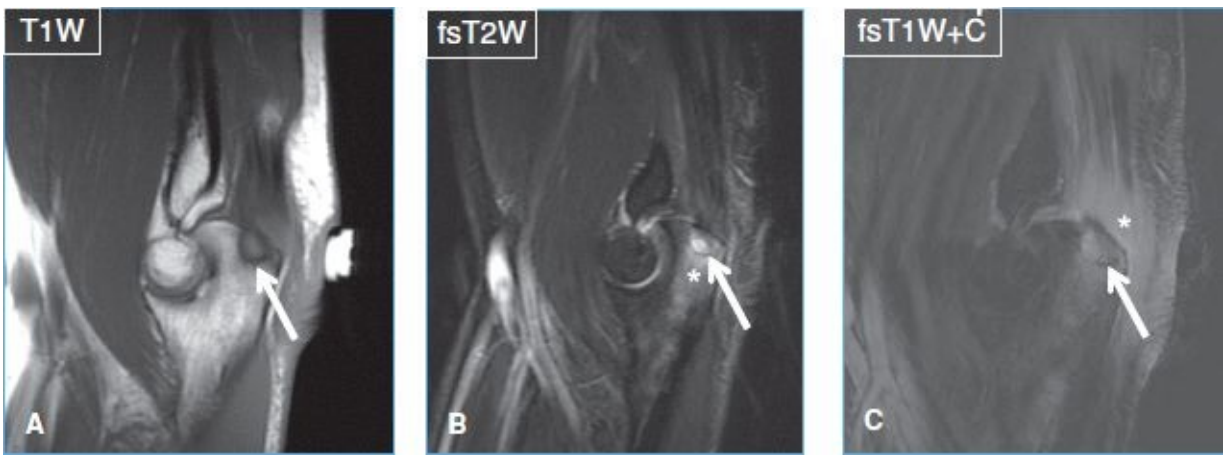

Fig. 41: Calcium hydroxyapatite crystal deposition disease. Sagittal images of the elbow **(A–**

C) exhibit a well-defined bone erosion (*arrows*) at the triceps attachment. Also note reactive edema and enhancement of the adjacent bone marrow (*asterisk* in **B**) and soft tissues (*asterisk* in **C**) in keeping with active disease.

In NpA, the periarticular soft tissues and overlying skin demonstrate diffuse T2 hyperintensity and contrast enhancement, reflecting reactive edema and hyperemia, as described above. However, no fluid collection, ulcer, or sinus tract are present, as noted in infections (Fig. 42).

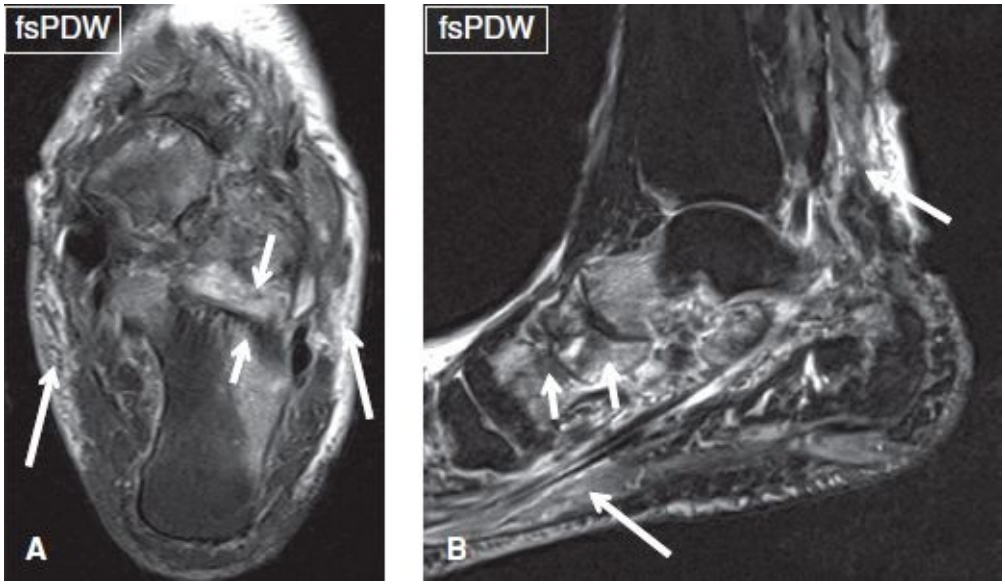

Fig. 42: Neuropathic arthropathy. Same patient as in Fig. 26. Axial **(A)** and sagittal **(B)** images of the contralateral foot similarly exhibit architectural distortion of the mid- and hindfoot joints, subchondral cysts, and marrow edema of the articulating bones (*short arrows*). Notice diffuse edema of the surrounding soft tissues (*long arrows*) but no ulcer, sinus tract, or fluid collection.

There [<is no> <is> <one, multiple>] joint abnormalities.

Involvement of one or multiple joints is referred to as monoarthropathy and polyarthropathy, respectively. It should be noted that monoarthropathy on imaging, however, does not mean that clinically that would be the only site of affliction. Identification of polyarthropathy diagnosis can substantially change the clinical differential.

The hallmark of RA is bilateral symmetric arthritis of more than three joints. In early stages, the entity most commonly involves the second and third metacarpophalangeal and the third proximal interphalangeal joints. Other common sites include radiocarpal, intercarpal, carpometacarpal, metacarpophalangeal, and proximal interphalangeal joints (Figs. 43, 44). Bilateral and symmetric involvement of foot joints is another typical manifestation of RA, predominating in the metatarsophalangeal and interphalangeal joints. The disease can be asymmetric in certain conditions of overuse (more advanced in the right

hand of right-handed persons) or underuse (less advanced in the paralyzed hand). In advanced stages or juvenile RA, large extremity joints and joints of the vertebral spine (particularly the facet joints of the cervical spine and the atlantoaxial joint) may be affected.

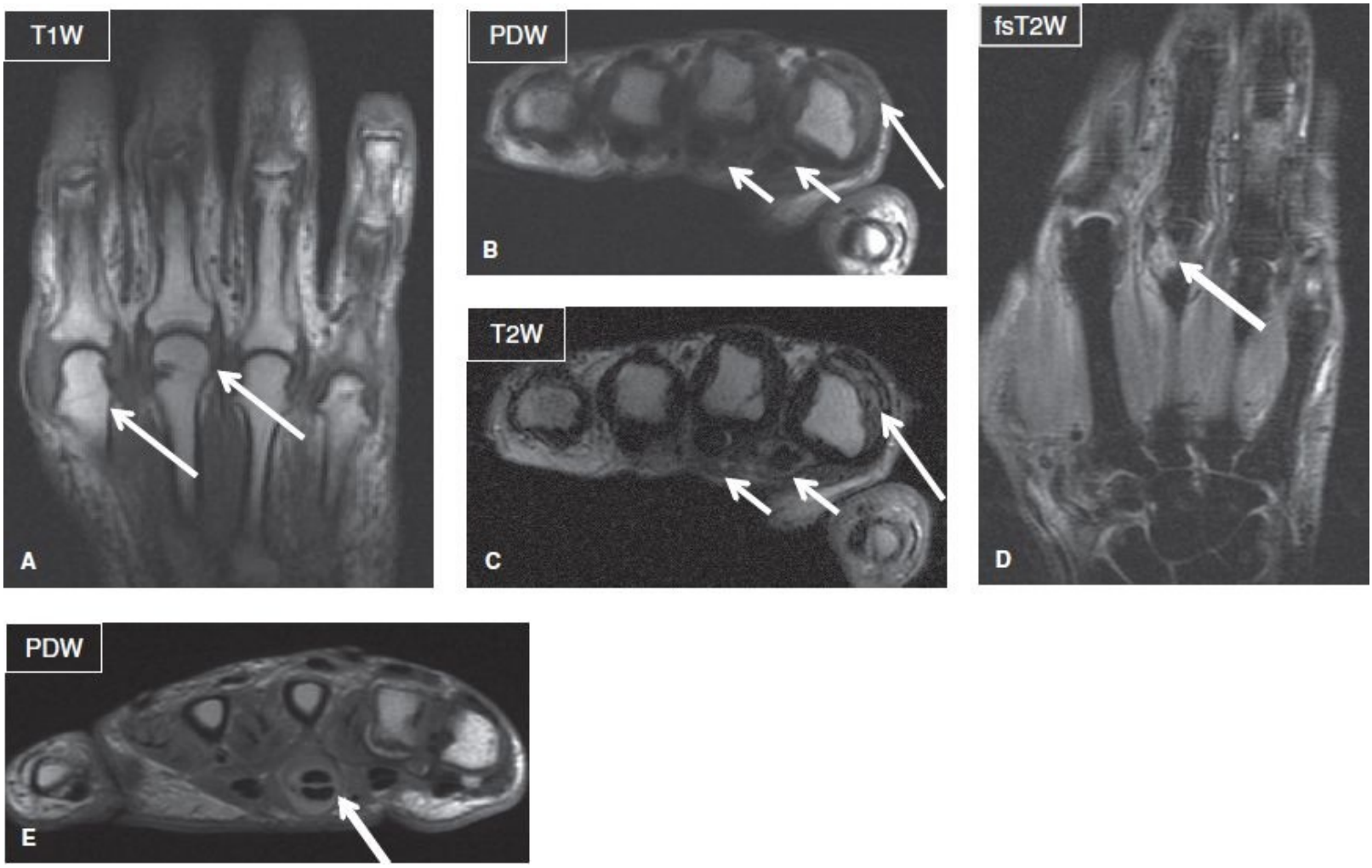

Fig. 43: Bilateral involvement in rheumatoid arthritis. Middle-aged female with bilateral hand pain, right > left. Left hand coronal **(A)** and axial **(B, C)** images show synovial thickening of the first and second MCP joints (*long arrows*) and tenosynovitis of the index and middle fingers (*short arrows*). Note erosion of the 2nd MC head. Coronal **(D)** and axial **(E)** images show erosion of the 3rd MC head (*arrow* in **D**) and long finger tenosynovitis (*arrow* in **E**).

Fig. 44: Enhancing pannus in rheumatoid arthritis. Coronal image exhibits enhancing pannus (*arrows*) at the first and second metacarpophalangeal joints, which show mild contrast enhancement, indicating activity (hyperemia/inflammation) in this known case of RA.

SpAs can involve joints of both the axial and the peripheral skeleton. The involvement of the sacroiliac joints is bilateral and symmetric in AS and inflammatory bowel disease, and unilateral and asymmetric in PsA and reactive arthritis (Reiter syndrome) (Figs. 45, 46). Unlike RA, which has a polyarticular presentation, early PsA can occur in any of the distal small hand joints, mostly as monoarthritis or oligoarthritis. Reactive arthritis most commonly involves the feet. Two types of involvement of the hand and foot suggest PsA: (1) The row pattern, primarily, which affects the distal interphalangeal joints, and (2) the ray pattern, which manifests as (mostly flexor and less commonly extensor) tenosynovitis, which can involve several fingers simultaneously or one finger (sausage digit). The ray pattern lesions can be associated with additional synovitis or soft tissue edema.

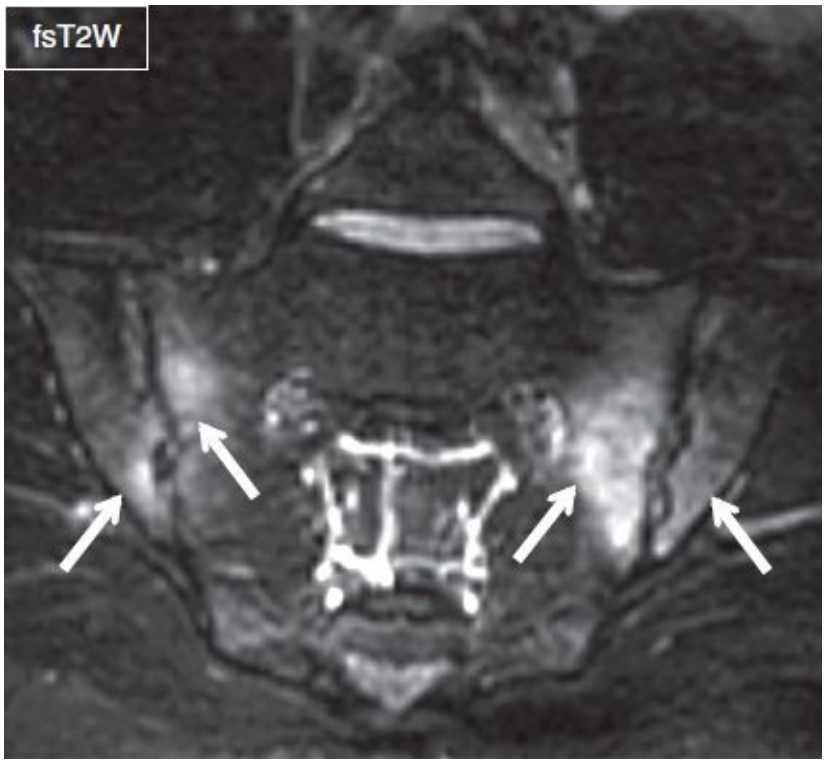

Fig. 45: Ankylosing spondylitis. Coronal image through the sacroiliac joints shows bilateral and nearly symmetric subarticular marrow edema (*arrows*), a classic finding of ankylosing spondylitis. Other differentials of this symmetric pattern of SI joint involvement include inflammatory bowel disease, rheumatoid arthritis, and hyperparathyroidism.

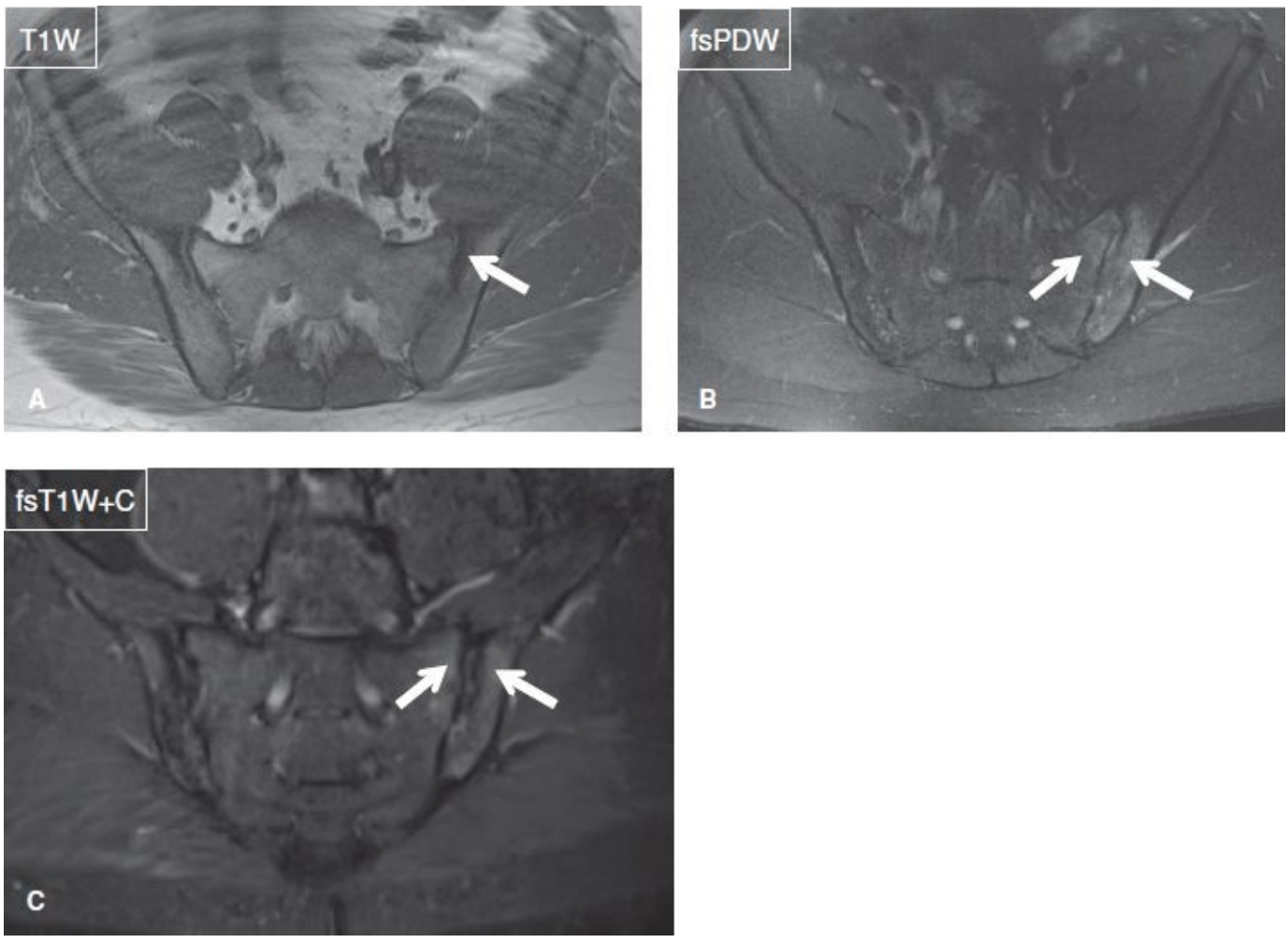

Fig. 46: Psoriatic arthritis. Axial images **(A–C)** demonstrate asymmetric involvement of the left sacroiliac joint (*arrows*), which features subarticular marrow edema and contrast enhancement, indicating inflammation. The contralateral sacroiliac joint shows minimal degenerative changes. Other differential of this asymmetric pattern includes osteoarthritis, reactive arthritis, and infection.

Amyloid arthropathy may involve the axial skeleton (especially the cervical) or the peripheral skeleton. The involvement is usually bilateral, and common sites include the large joints, such as the hips, wrists, shoulders, knees, and spine (Fig. 47). Gout is an asymmetrical polyarticular disease, most often affecting the foot, and showing a predilection for the first metatarsophalangeal joint. The next most common areas of involvement are the hands (Fig. 32) and wrist, with the elbow and knee affected less commonly (Fig. 48).

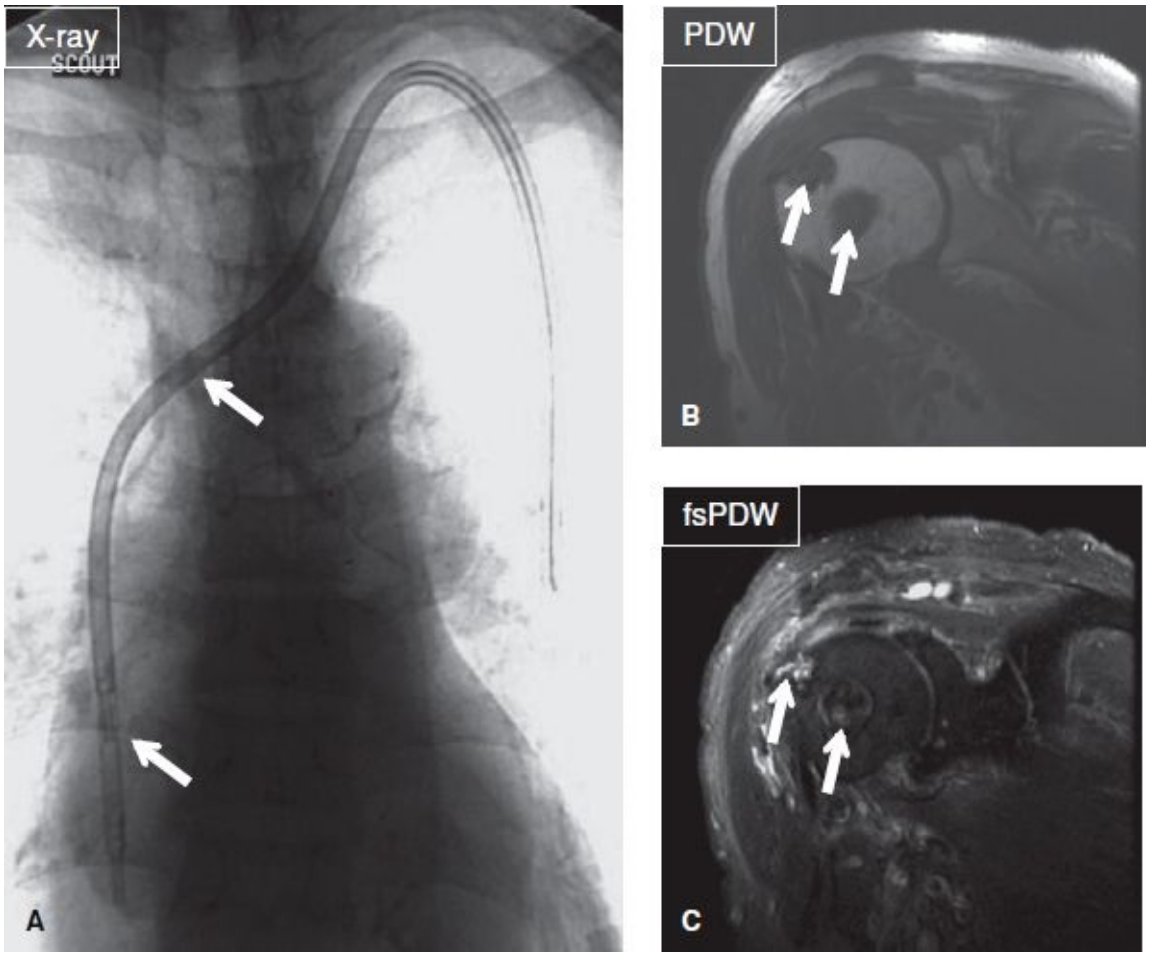

Fig. 47: Amyloidosis in renal failure. **A:** Anteroposterior chest radiograph shows a jugular vein dialysis catheter (*arrows*). **B, C:** Coronal images of the shoulder in the same patient reveal hypointense hemosiderin deposits (*arrows*) eroding the humeral head.

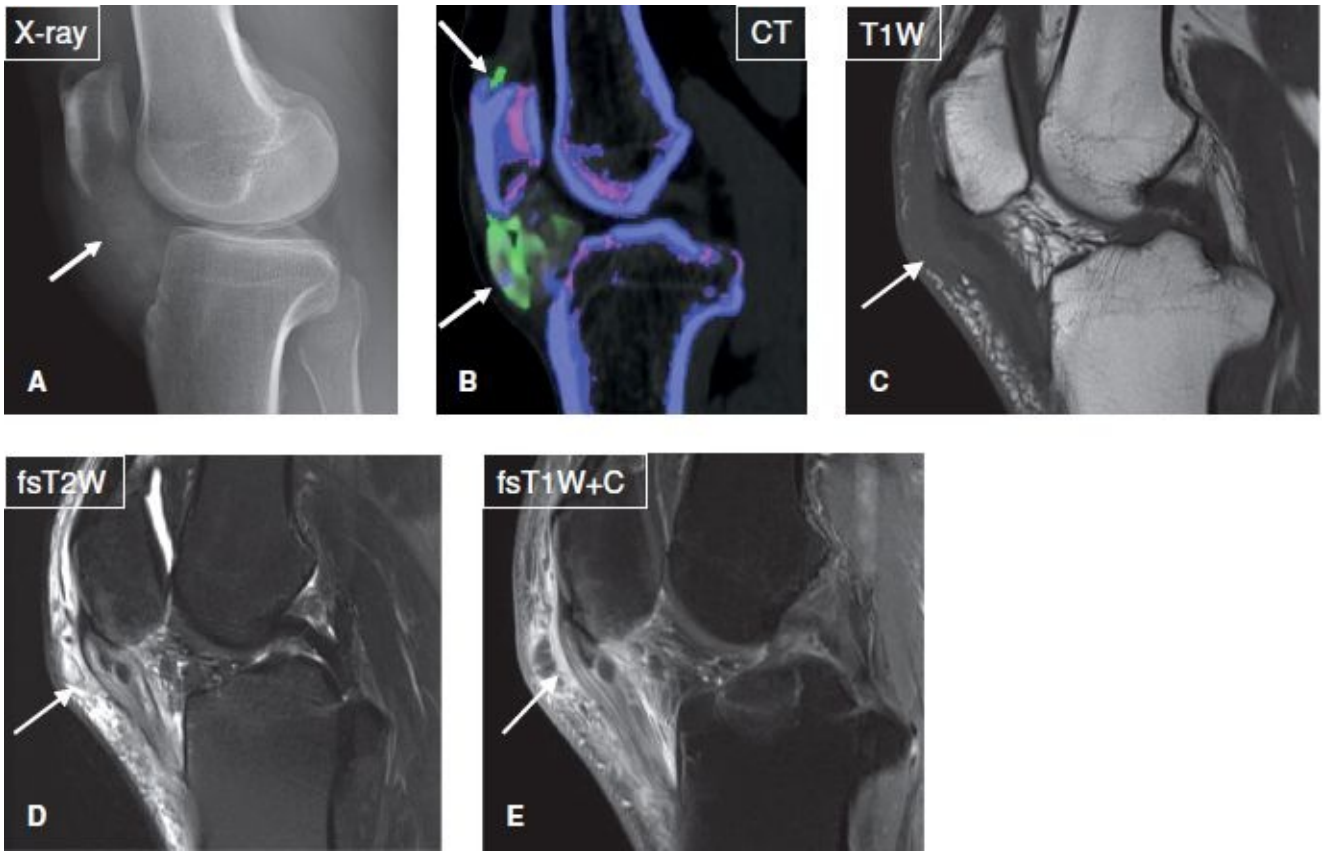

Fig. 48: Adult males with anterior knee pain and known gout. Patient 1 **(A, B)** shows calcified tophi in the patellar tendon and Hoffa fat pad (*arrows*) on lateral knee radiograph **(A)** and dual source sagittal CT image **(B)**. Patient 2 **(C, D, E)** shows similar findings on MRI sagittal images (Case courtesy Tae Yong Moon, MD).

Pseudogout may involve almost any joint although the knees, wrists, and hips are most often affected. This condition is the most usual cause of secondary metabolic OA. The most common form of juvenile RA is the *pauciarticular* subtype, which usually involves large peripheral joints such as the knee, ankle, elbow, and wrist. The less common *polyarticular* subtype mostly affects the hands, wrists, knees, ankles, and feet bilaterally. In most cases, the diagnosis is suggested on the radiographs since chondrocalcinosis is difficult to detect on MRI.

The typical presentation of lupus arthritis is symmetric polyarthritis that preferentially involves the small over the large joints. The entity most commonly involves the metacarpophalangeal, proximal interphalangeal, and distal interphalangeal joints, as well as the knees, and less commonly the shoulders, ankles, and elbows. Typical findings include joint subluxations, and soft tissue swelling due to tenosynovitis, with relative lack of joint erosions. Bilateral tenosynovitis may be seen in the hands or wrists (see Chapter 8).

Approximately 50% of the patients with multicentric reticulohistiocytosis develop bilateral polyarthropathy (Fig. 34). The disease may affect any of the peripheral joints but mainly involves the interphalangeal joints of the fingers, and sometimes, the knees, shoulders, wrists, hips, ankles, feet, elbows, temporomandibular joint, and spine. In the latter, the disease may lead to atlantoaxial joint involvement and erosion of the odontoid process leading to subluxation.

Typically, OA affects specific joints at a particular patient age although the pattern of involvement may vary across individuals depending on their body habitus, overload from different daily activities, and prior traumatic insults. The earlier sites of involvement include the acromioclavicular, first carpometacarpal, distal interphalangeal joints. The knees and hips are usually involved after the fourth to fifth decades of life. OA classically affects the weight-bearing and stress locations sites of joints. In multi-compartmental joints, OA initially involves one compartment, and then may continue to another. When multiple joints are involved, changes are asymmetrically distributed in the body. In the wrist, there is initial involvement of the radioscaphoid joint, followed by the lunocapitate joint and, finally, the radiolunate joint (Fig. 49). Bone marrow edema in OA is related to stress reactions in most instances, due to loss of cartilage and bony overload (Fig. 50). Erosive OA, however, has a significant inflammatory component when affecting the distal and proximal interphalangeal joints. Secondary OA occurs at an early age and affects atypical joints. Other features include symmetric joint involvement, multi-compartmental changes, and/or unusual radiographic appearance. In secondary OA cases, one should try to identify causes predisposing to cartilage destruction, such as trauma, underlying meniscal or labral tear, crystal deposition, NpA, RA, and hemophilia (Fig. 51).

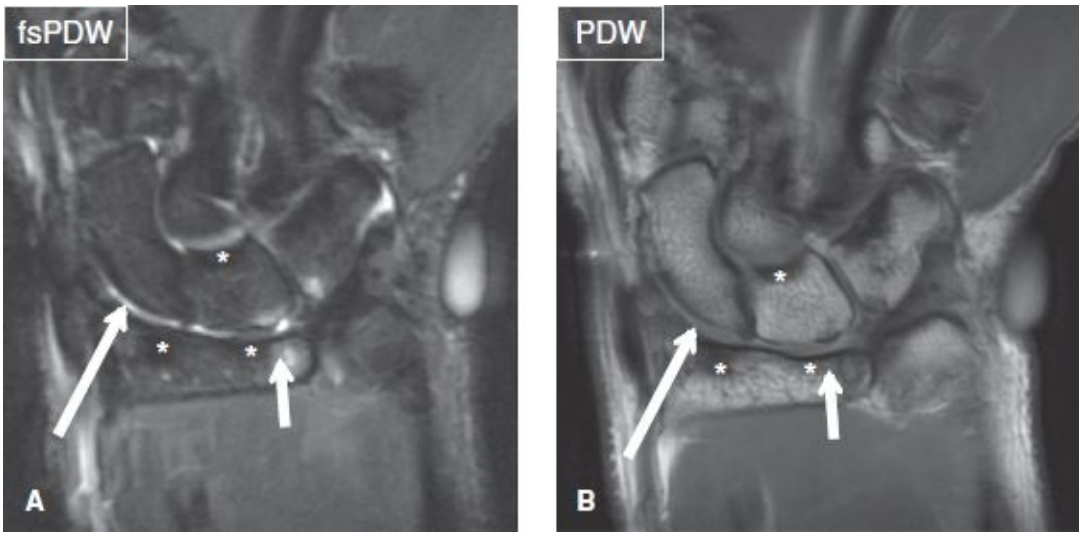

Fig. 49: Osteoarthritis of the wrist. Coronal images **(A, B)** show full-thickness cartilage defects at the radioscaphoid (*long arrows*) and radiolunate (*short arrows*) joints. Also note the associated foci of subchondral sclerosis (*asterisks*).

Fig. 50: Severe osteoarthritis. Coronal image show complete cartilage loss at the right hip joint, resulting in bone abutment and extensive marrow edema (*short arrows*) of the opposing bones. Also note geodes in the acetabulum (*arrowheads*) and moderate joint effusion (*long arrow*). Note the classic asymmetry of joint involvement even in this advanced stage, and also differential involvement from the other side.

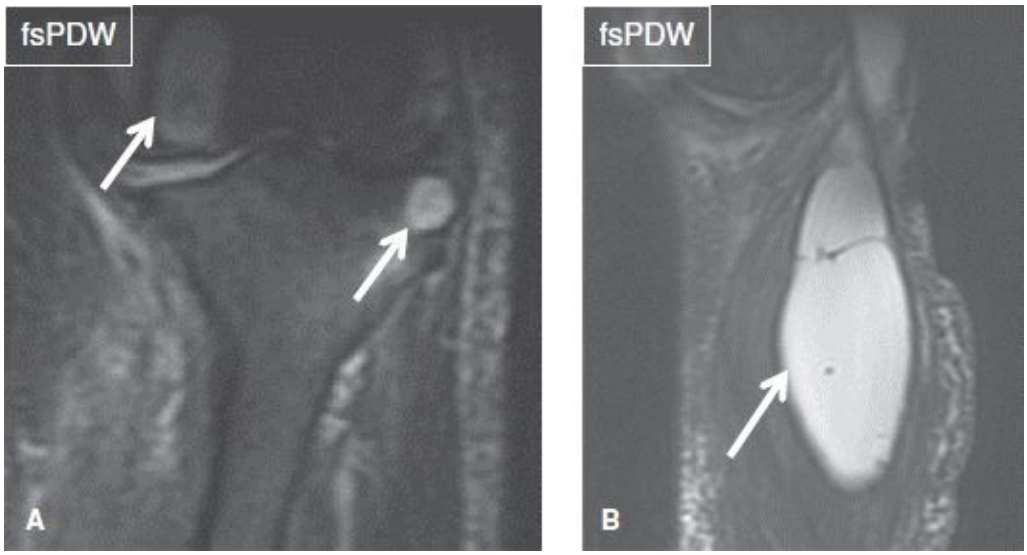

Fig. 51: Secondary osteoarthritis due to long-standing rheumatoid arthritis of the knee. **A:** Coronal image shows complete cartilage loss with geodes (*arrows*) and bone-on-bone contact of the medial and lateral compartments. Notice remodeled, partially resorbed medial condyle of tibia. **B:** A large Baker cyst is evident in the proximal calf (*arrow*).

NpA (or Charcot joint) is a progressive degenerative/destructive joint disorder involving patients with abnormal pain sensation and proprioception. It may present in both mono- and polyarticular fashion and commonly involves the feet, knees, shoulders, elbows, and wrists (Figs. 26, 42).

Primary synovial osteochondromatosis (SOC) and HADD typically present in a monoarticular fashion. In order of frequency, SOC most commonly involves the knee (50% to 65% of cases), hip, elbow, shoulder, and ankle whereas HADD most commonly involves the shoulder, hip, elbow, wrist, and hand (Figs. 33, 41, 52).

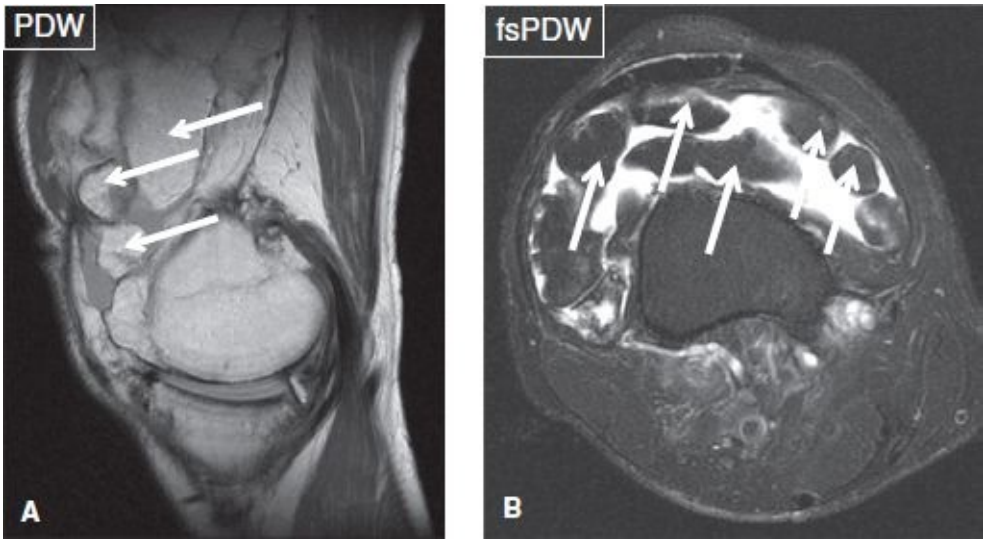

Fig. 52: Primary synovial osteochondromatosis. Sagittal **(A)** and axial **(B)** images display multiple similar-sized osseous bodies (*arrows*) within the suprapatellar bursa. The patient had accelerated knee osteoarthrosis with complete cartilage loss in the medial compartment.

Hemophilic arthropathy is the result of repeated hemorrhages within synovial joints and subsequent degenerative changes in patients with bleeding disorders. In descending order, the knee, ankle, elbow, and shoulder are the most commonly affected joints. Bilateral involvement is common although a single joint is usually involved in each episode of bleeding. Hemosiderin staining is classically present on MR imaging (Fig. 53).

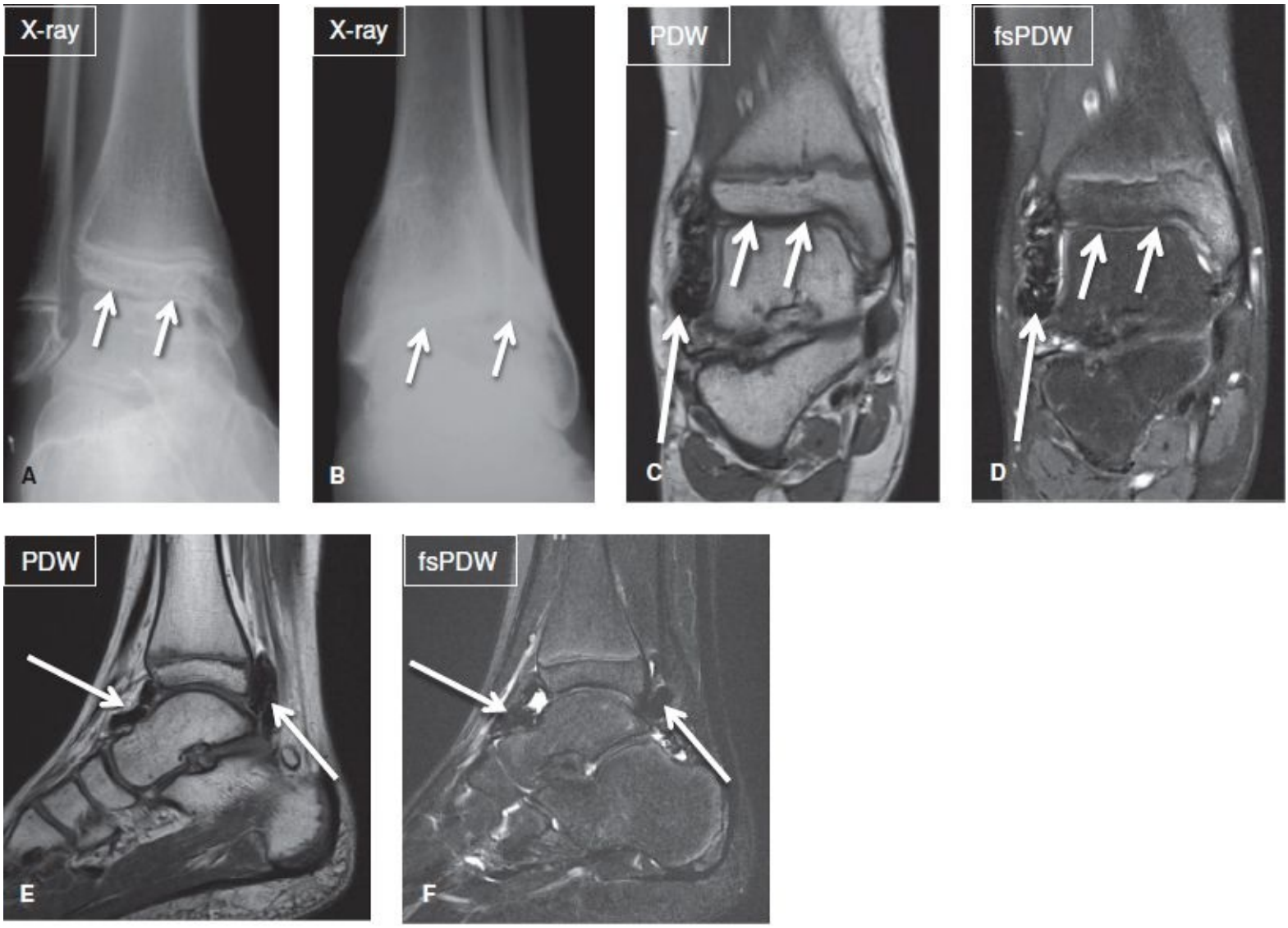

Fig. 53: Hemophilic arthropathy. Anteroposterior **(A)** and oblique **(B)** radiographs reveal epiphyseal enlargement of the tibia, which is typically most prominent on the medial side (tibiotalar slants), and leads to overpronated foot. Note the diffuse narrowing of the tibiotalar joint spaces due to secondary OA (*arrows*). On the respective coronal **(C, D)** and sagittal **(E, F)** MR images, there is diffuse thinning of the tibiotalar cartilage (*short arrows*), along with thickening and hypointensity of the tibiotalar joint synovium (*long arrows*), reflecting hemosiderin deposition.

ALIGNMENT: [<Normal> <Less than 50% subluxation / More than 50% subluxation>]

Advanced stages of arthritis, especially RA, is characterized by subluxation or dislocation, caused by laxity of the capsule and ligaments due to inflammatory destruction, capsular shrinkage due to fibrosis, and inflammatory or degenerative pathologic changes of tendons and tendon sheaths. Best depicted on plain films, these deformities predominate in the hand joints. At fairly early stages, there is ulnar deviation of the second to fifth metacarpophalangeal joints (windswept deformity) whereas deformities of more advanced stages include *mallet finger* (caused by laxity/disruption at the insertion of the extensor tendon on the distal phalanx, resulting in distal phalanx drop), *swan-neck deformity* (caused

by hyperextension of the proximal interphalangeal joint and flexion of the distal interphalangeal joint), *boutonnière deformity* (caused by flexion of the proximal interphalangeal joint and hyperextension of the distal interphalangeal joint), and *hitchhiker deformity* (caused by flexion of the proximal metacarpophalangeal joint and hyperextension of the distal interphalangeal joint). Genu valgum is a common feature in untreated RA. There might be valgus deformity in one knee in association with compensatory varus deformity in the other knee, resulting in proximity of the two joints. In the wrist, erosive changes, synovitis, chronic degeneration, and laxity of the supporting ligaments may result in carpal translocation to the ulnar, radial, dorsal, or volar directions. Ulnar more common than radial carpal translocation is prevalent, and is identified by more than 50% shift of the lunate off the lunate fossa. In the hip, axial (medial) migration and development of protrusio acetabuli are more common compared to the superolateral migration seen in OA. In the spine, RA typically affects the sacroiliac joints and the cervical spine, with predisposition to dens erosion, atlantoaxial subluxation, and other cervical level subluxations. In juvenile RA, hyperemia may lead to overgrowth of the distal tibial epiphysis, and result in tibiotalar slant, similar to hemophilic arthropathy.

NpA is characterized by subluxations, dislocations, joint deformities, periarticular debris, and bone fragmentation leading to midfoot disorganization. Correlation of MR imaging findings with plain films is useful.

FLUID: [<Normal> <Small/Moderate/Large effusion>]

Joint effusion is a common feature of inflammatory arthritis, usually indicating acute inflammation or exacerbation. In small joints, identification of small effusions may be assisted by comparing neighboring joints, but in general, effusion is diagnosed when the joint is filled with fluid that causes bulging of the capsule. In large joints, quantitative measurements or filling of certain non-dependent recesses may be used to diagnose effusion, as described in the joint-specific chapters. In the setting of synovitis, reliable discrimination of joint effusion from thickened synovium may require contrast-enhanced fsT1W, heavy fsT2W, and/or DW images (described in next section) (Fig. 54). Joint effusions should be graded as small, moderate, or large.

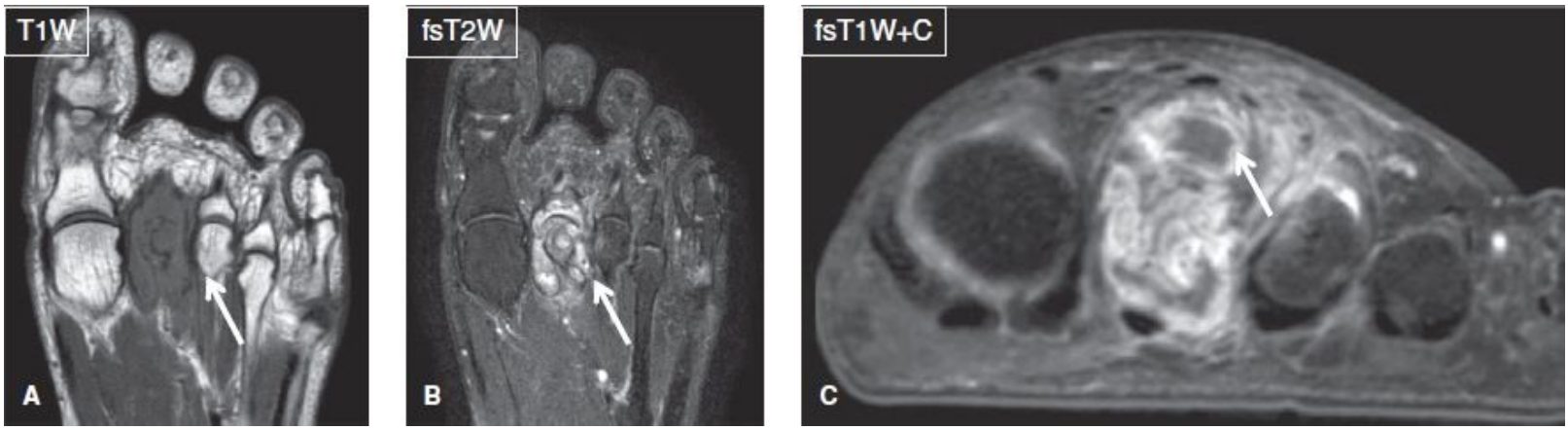

Fig. 54: Rheumatoid arthritis: Joint effusion versus pannus. Coronal **(A, B)** images show

bone erosive pannus and complex effusion (*arrows*), the relative amounts are difficult to quantify without contrast. Contrast-enhanced axial image **(C)** shows a very small effusion (*arrow*), and most of the lesion is in fact enhancing active pannus.

Joint effusion is non-specific and is seen in OA and other types of arthritis, such as RA (early in the course of the disease), gout, pigmented villonodular synovitis (PVNS), lupus arthritis or mixed connective tissue disorder, NpA, amyloid arthropathy, and hemophilic arthropathy (hemarthrosis). In late stages of RA, intra-articular uniformly sized loose bodies of synovial origin, known as rice bodies, might be identified within the effusion. They are typically multiple and, although they mimic SOC, they are significantly smaller and remain hypointense on T2W images, featuring no central marrow signal (Figs. 55, 56).

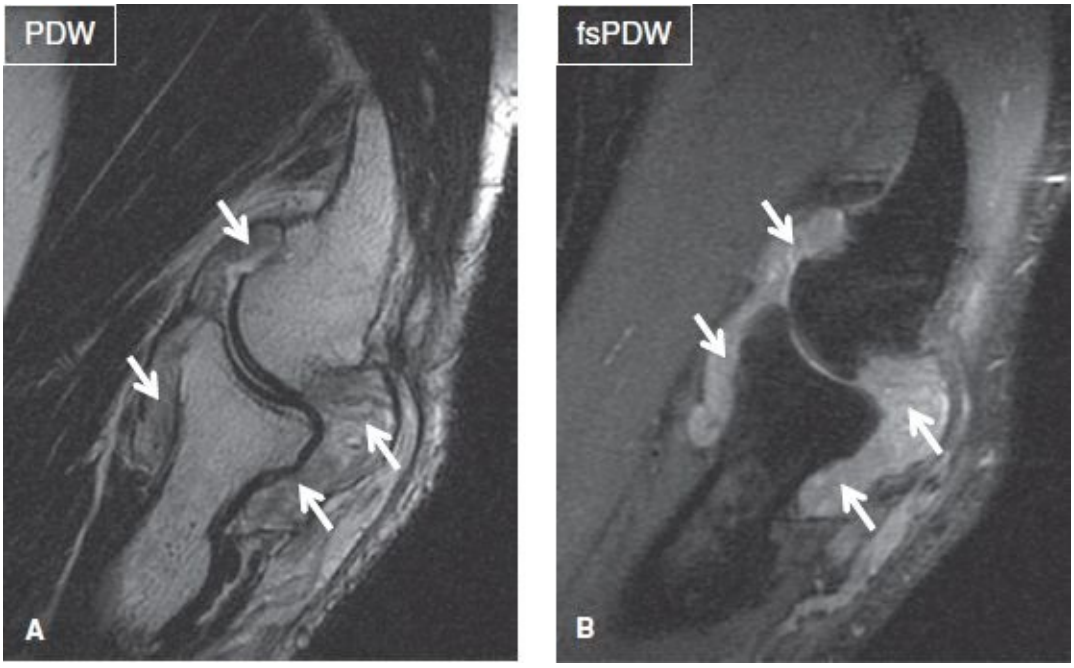

Fig. 55: Rheumatoid arthritis. Sagittal images **(A, B)** exhibit marked elbow joint effusion, which is filled by large amount of amorphous pannus tissue (*arrows*) of intermediate signal. Notice diffuse loss of joint space and cartilage thinning.

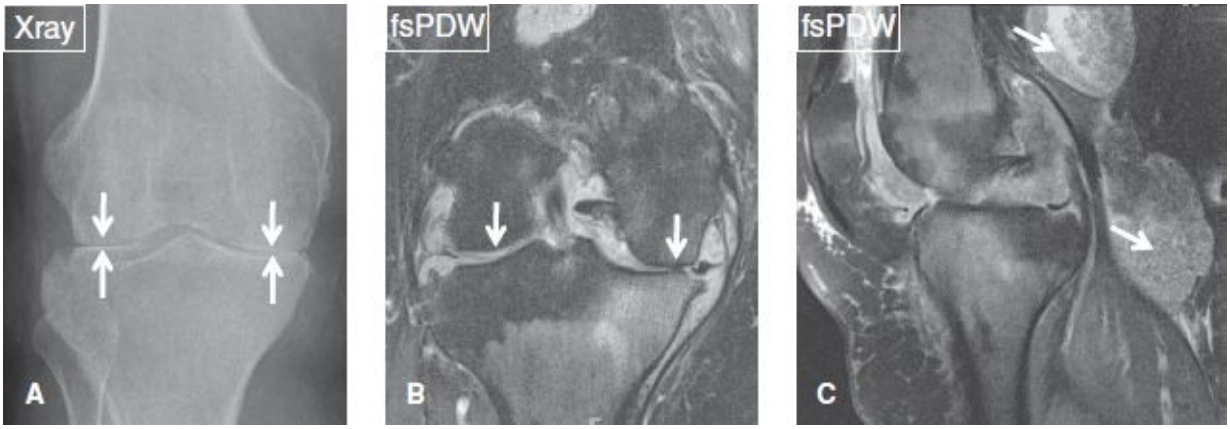

Fig. 56: Rheumatoid arthritis involving the knee. Anteroposterior radiograph **(A)** shows areas of diffuse severe joint space loss and osteopenia (*arrows*) in keeping with secondary OA appearance. The respective coronal **(B)** and sagittal **(C)** MR images display severe

cartilage loss (*arrows* in **B**) along with moderate joint effusion, which contains foci of intermediate signal, compatible with rice bodies. Notice similar bodies in the Baker cyst (*arrows* in **C**).

Primary SOC is characterized by the development of multiple intra-articular chondral bodies of similar size (ranging from few millimeters to several centimeters), which form as a result of chondroid metaplasia of the synovium, and undergo progressive mineralization during the course of the disease. There is no identifiable cause. Depending on the stage of the disease and the mineralization of the loose bodies, the latter may manifest as (1) lobulated lesions of homogeneous signal, which are isointense or slightly hyperintense to muscle on T1W images and hyperintense on T2W images (early stages with unmineralized chondral bodies, not evident on radiographs); (2) lesions similar to those just described, but with additional foci of signal void on all imaging sequences, which correspond to calcifications and are more conspicuous on gradient-echo images (midstage with bodies evident on radiographs-most commonly encountered pattern) (Fig. 57); or (3) lesions similar to those just described, but with additional foci of peripheral low signal, which surround central areas with signal characteristic of fat (late stage-osteochondral bodies bone-like configuration, also visible in radiographs) (Fig. 52). In some joints, the lesions may erode eccentrically into the adjacent bones and extend to adjacent communicating bursae and tendon sheaths. This finding is particularly prevalent in the hip, and in 40–71% of cases, there is extension into the iliopsoas and obturator externus bursae (Fig. 58). The latter findings are important to report to ensure complete surgical excision.

Fig. 57: Primary synovial osteochondromatosis involving a synovial bursa. Axial **(A)** and sagittal **(B, C)** images exhibit multiple foci (*arrows*) of low signal and similar size within the bicipitoradial bursa with surrounding synovial enhancement.

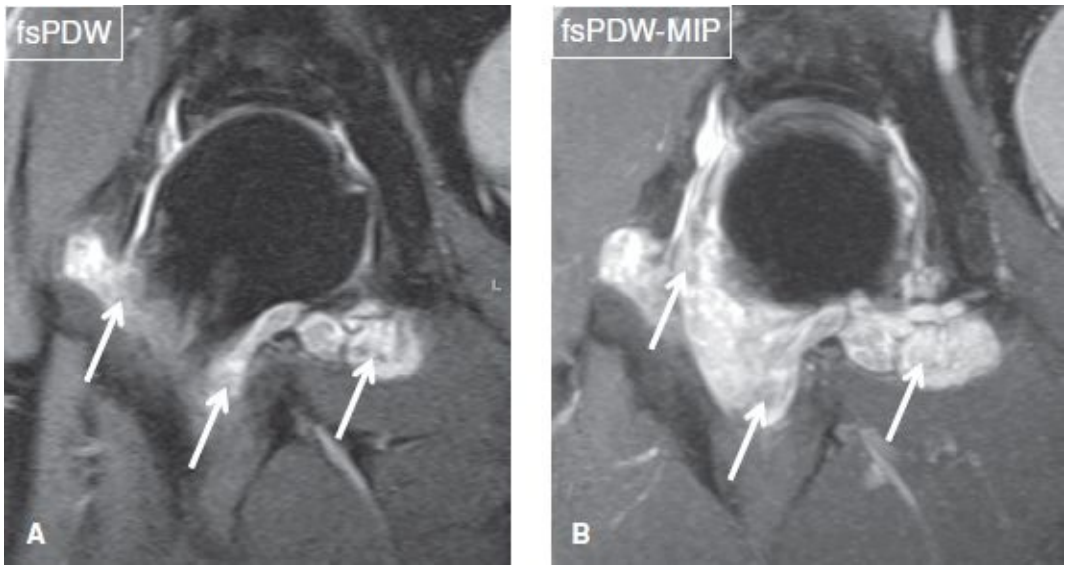

Fig. 58: Primary synovial chondromatosis. Coronal images of the right hip **(A, B)** demonstrate moderate effusion and numerous intra-articular bodies (*arrows*) of similar size distending the hip joint and its various recesses. No labrocartilage abnormality is evident or other internal derangement is evident. Notice minimal bony erosion and edema of the lateral aspect of the femoral neck.

Secondary SOC is the result of chronic arthritic or mechanical disorders. Differentiation from primary SOC may be challenging because long-standing primary SOC predisposes to degenerative joint disease, and conversely secondary SOC is caused by degenerate change. A useful differentiating feature is that in the primary form the mineralized bodies are usually numerous (normally over five) and similar-sized, whereas in the secondary form there are fewer bodies and they are of variable sizes (Fig. 59).

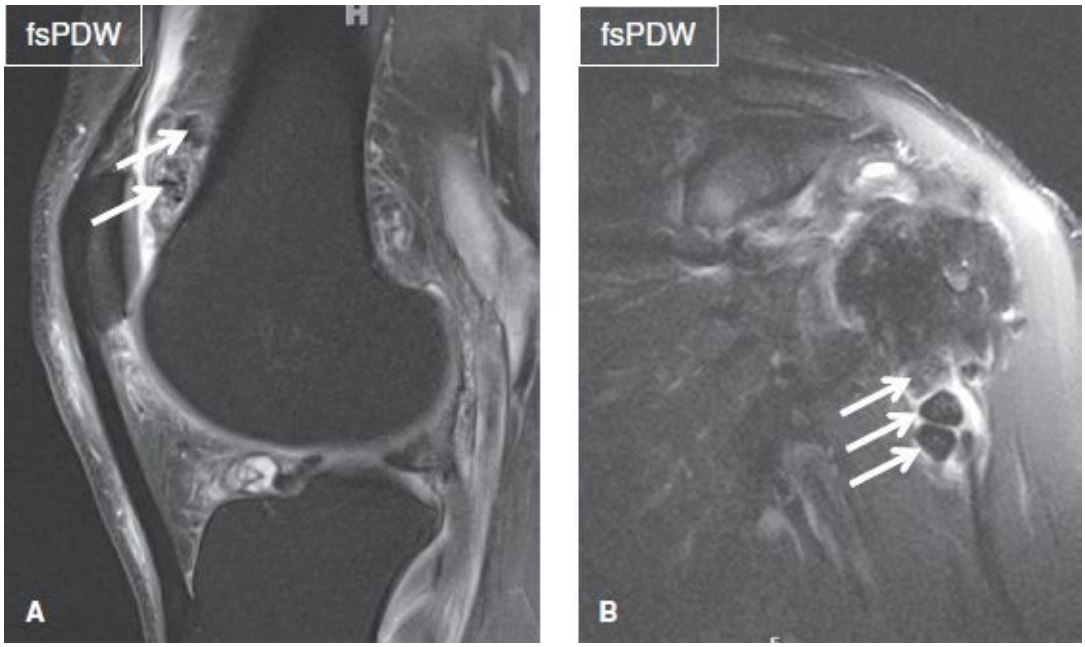

Fig. 59: Secondary synovial osteochondromatosis. Sagittal **(A)** and coronal **(B)** images from different cases demonstrate osteochondral bodies (*arrows*) of low-to-intermediate signal lodged within the prefemoral fat pad and biceps tendon sheath, respectively.

SYNOVIAL THICKENING/SYNOVITIS: [<Absent> <Mild/Moderate/Severe>]

The thin synovial tissue that lines normal joint cavities, bursae, and tendon sheaths is pencil thin on MR images, similar to pleural or peritoneal linings. Synovial thickening is most commonly seen as a manifestation of internal derangement or degenerative disease. It also increases over time with worsening disease. In OA, the thickened synovium can become fibrofatty over time, therefore lipoma arborescence should not be overdiagnosed in middle-aged or elderly patients (Fig. 60). Some enhancement may be noted during acute episodes of joint inflammation; however, identification of bilateral synovitis, marked synovial thickening, nodular thickening, or intense enhancement should indicate underlying inflammatory disorder, such as RA, PVNS, etc.

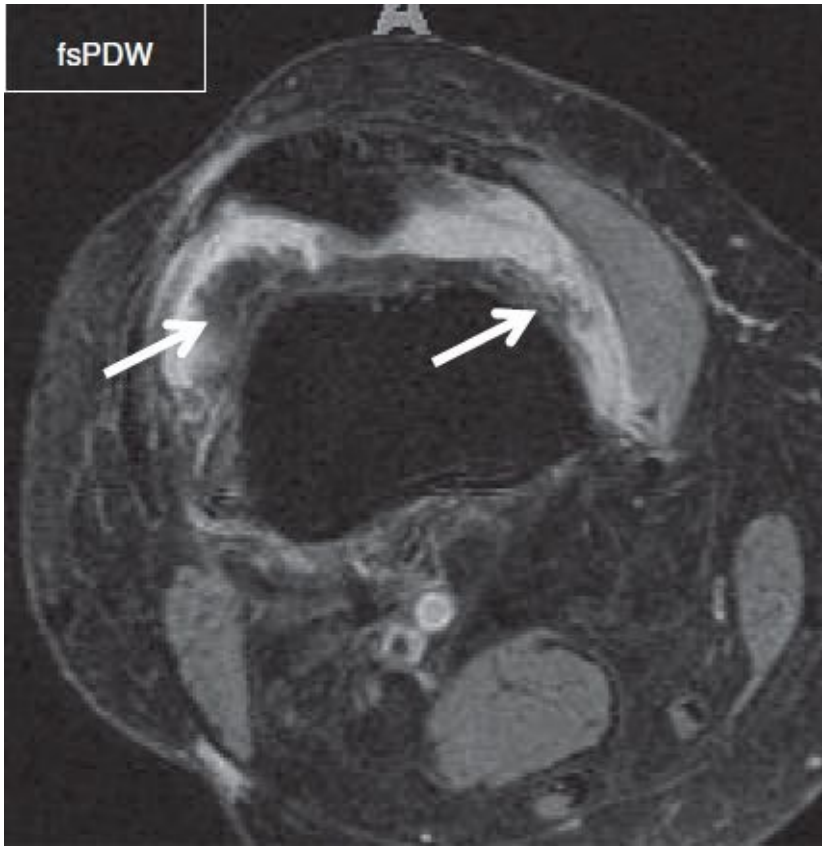

Fig. 60: Synovial proliferation in OA. Axial image shows moderate synovial proliferation with fibrofatty components (*arrows*) in the suprapatellar pouch, not an uncommon finding in chronically deranged knees in middle-aged and elderly patients.

Synovitis is the earliest pathologic abnormality in RA and is usually, but not exclusively, bilateral. It manifests as thickening and T2 hyperintensity (indicating inflammatory edema of the pannus), as well as increased contrast enhancement (reflecting hyperemia) of the synovium. In the setting of joint effusion, synovitis is hard to discriminate from synovial fluid, and the diagnosis may be alternatively established based on (1) post-contrast fsT1W images obtained within 5 minutes of gadolinium administration, which adequately depict the thickened and intensely enhancing synovium (Fig. 54); (2) heavy T2W images, on which the synovium demonstrates lower signal compared to the effusion; or (3) DW images,

in which synovitis (but not synovial fluid) demonstrates restricted diffusion. Detection of persistent synovitis in the setting of clinical remission implies ongoing inflammation and may represent subclinical disease progression.

Although synovitis is a major feature of RA, it is not a predominant finding in most SpAs. In PVNS, images typically show mass-like synovial proliferation, which features lobulated margins. Synovial proliferation may be extensive (diffuse form) or limited to a well-defined single nodule (localized form) (Figs. 61, 62). The synovium demonstrates low signal on T1W and T2W images (reflecting hemosiderin deposition, more evident on gradient-echo images and accentuated at high-field strength). The contrast enhancement is variable although marked enhancement is more common in diffuse disease due to the hypervascular nature of the disease. Thickened synovium with areas of low signal is also a feature of hemophilic arthropathy (Fig. 63), RA, and multicentric reticulohistiocytosis-associated arthropathy. The differentiation between these entities may be difficult on imaging if they manifest as monoarticular diseases (uncommon for multicentric reticulohistiocytosis and RA). Synovitis is also present in gout and pseudogout in the early stages of the disease, as well as in amyloid arthropathy, juvenile RA, lupus arthritis, primary Sjögren syndrome, and occasionally in primary SOC (Figs. 64–66). In all cases, synovitis should be graded as mild, moderate, or severe (marked).

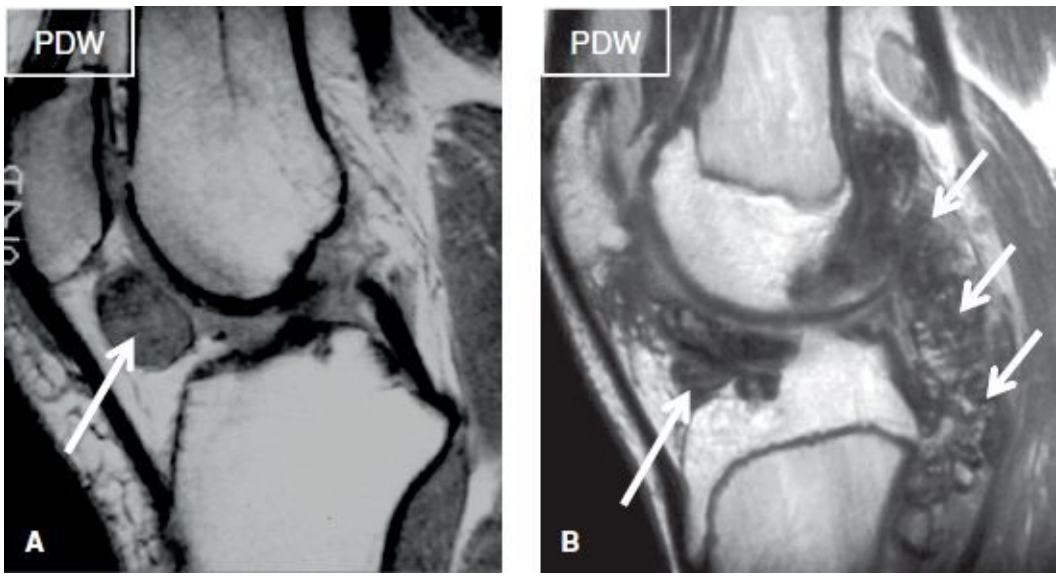

Fig. 61: Pigmented villonodular synovitis. Sagittal images from different patients show single (*arrow* in **A**) and multiple (*arrows* in **B**) intra-articular mass-like lesions of low signal that correspond to hemosiderin synovial deposits, in keeping with focal **(A)** and diffuse **(B)** intra-articular forms of the disease.

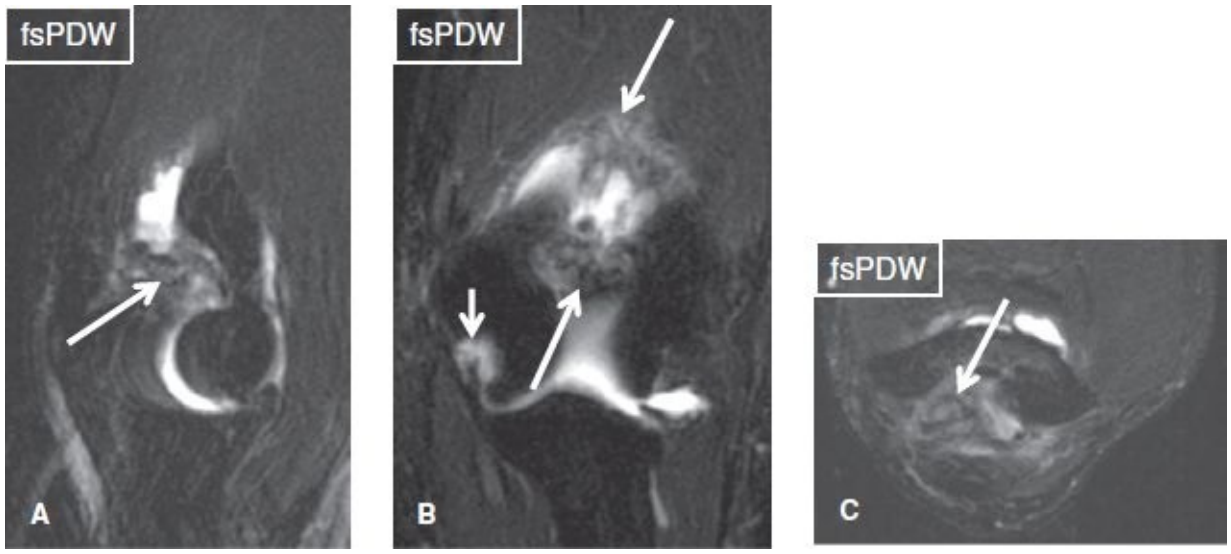

Fig. 62: Pigmented villonodular synovitis. Sagittal **(A),** coronal **(B),** and axial **(C)** images display moderate amount of mass-like synovium (*long arrows*) within the elbow joint, which is homogeneously hypointense due to hemosiderin deposition. Also note small-to-moderate joint effusion and cystic bone erosion (*short arrow*).

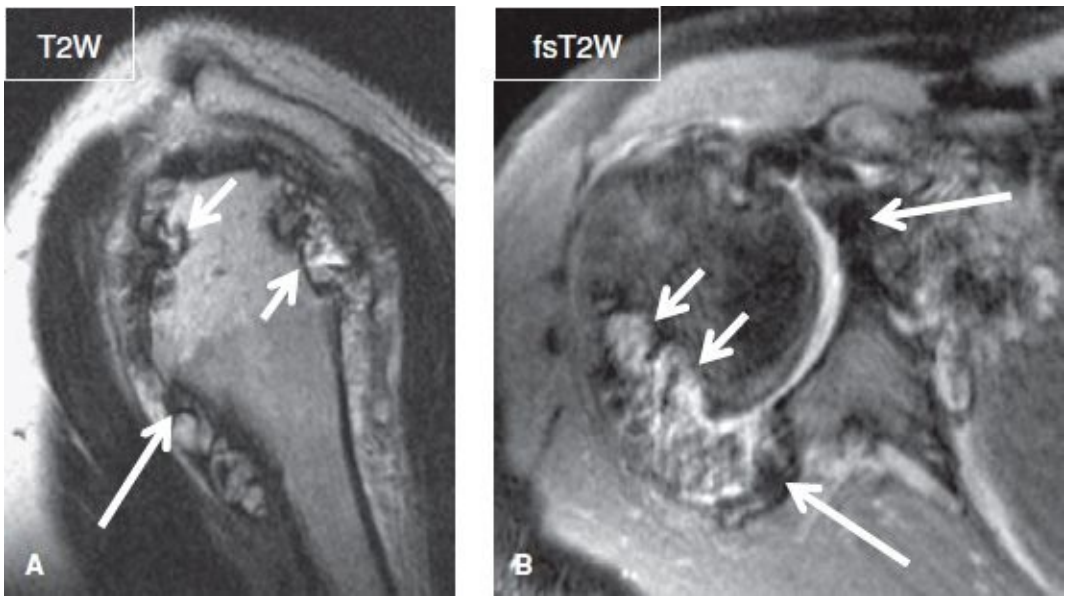

Fig. 63: Hemophilic arthropathy. Sagittal **(A)** and axial **(B)** images show hypointense intra-articular marked hemosiderin deposits (*long arrows*) along with small effusion and erosions (*short arrows*) of the humeral head.

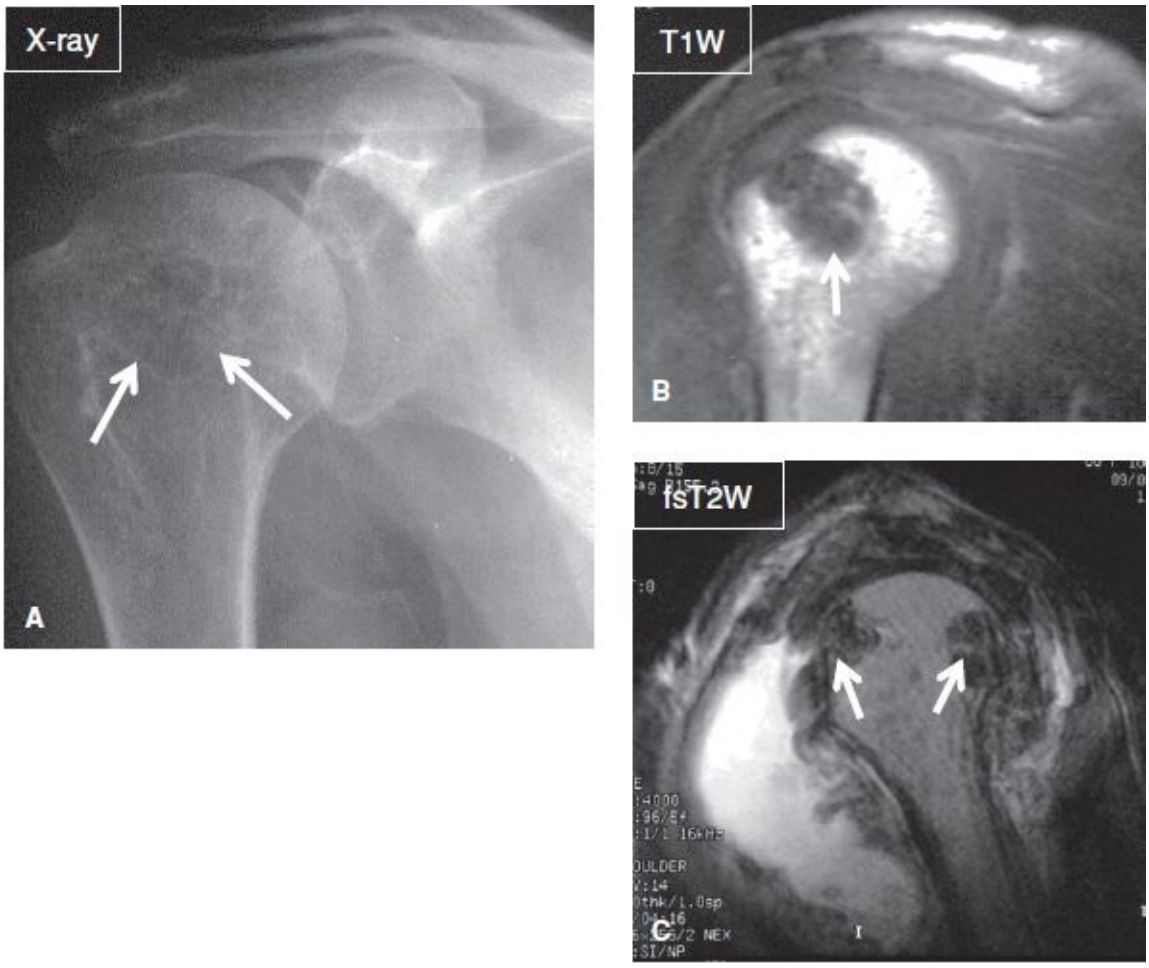

Fig. 64: Amyloid arthropathy. Anteroposterior radiograph **(A)** shows a faint lytic lesion in the centre of the humeral head with sclerotic margin. The respective coronal **(B)** and sagittal **(C)** MR images reveal hypointense marked amyloid tissue (*arrows*) eroding the humeral head.

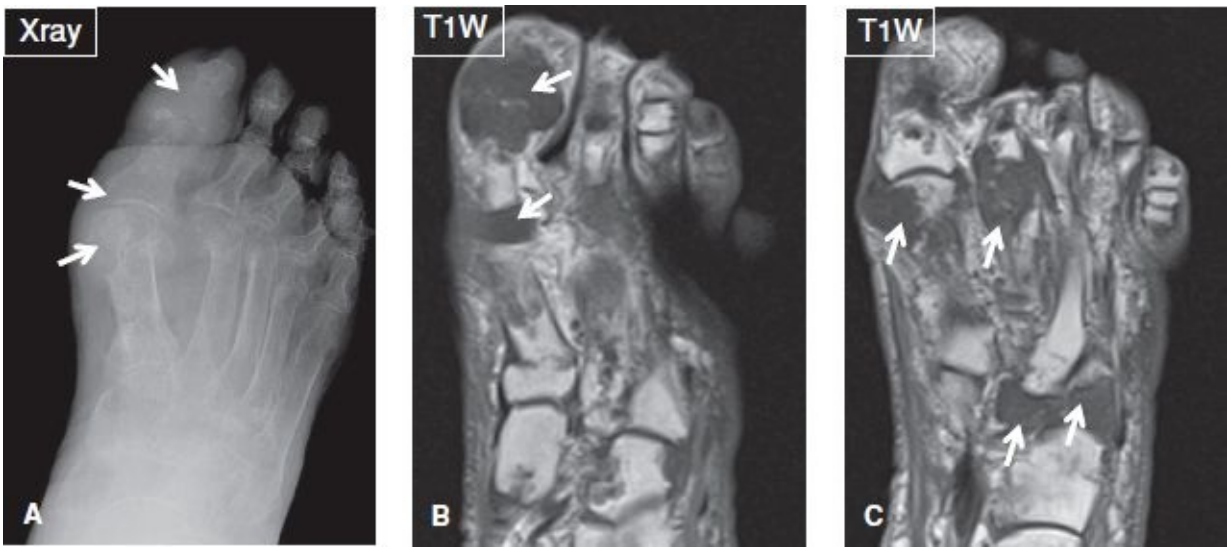

Fig. 65: Gout. **A:** Anteroposterior radiograph show multifocal eccentric erosive changes of the foot, predominantly in the great toe (*arrows*). **B, C:** The respective sequential axial MR images reveal that the bone lesions have been caused by para-articular soft tissue masses (*arrows*) of homogeneous intermediate signal, reflecting gouty tophi.

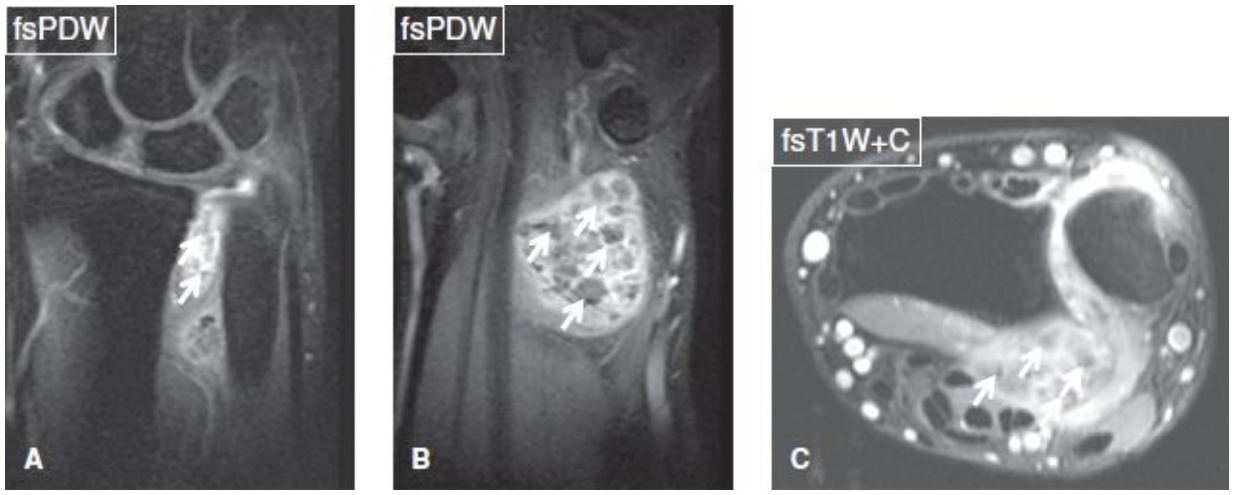

Fig. 66: Primary synovial osteochondromatosis. Coronal **(A, B)** and axial **(C)** images exhibit multiple bodies (*arrows*) of intermediate signal and variable size within the distal radioulnar joint, which appears widened. Also note thickened and enhancing synovium reflecting severe reactive synovial proliferation.

BONY PRODUCTIVE CHANGES: [<Absent> <Mild/Moderate/Severe> <Osteophytes/Syndesmophytes/Enthesophytes>]

Osteophytes are characteristic features of OA, and are depicted as sharp bony projections at the margins of the joint, which develop originally as outgrowths of cartilage and subsequently undergo endochondral ossification. They are thought to buttress an osteoarthritic joint in an attempt to prevent structural disorganization. Their size is usually related to the degree of joint malalignment. Osteophytes show low-signal cortical margins, which are continuous with the adjacent bone cortex, and central area that follows the signal of marrow fat on all sequences. Initially, osteophytes run horizontally, but when they enlarge during later stages, they tend to extend vertically and may eventually bridge with corresponding osteophytes of the opposing articular surface, finally resulting in ankylosis.

There are two types of OA, primary and secondary. The former type is significantly more common and is considered a “wear and tear” OA, resulting from aging (mostly appearing around the age of 55 to 60 years). The secondary variety strikes at an earlier age and has a specific cause, such as an injury, meniscal or labral tear, obesity, genetic alterations, inactivity, or other underlying inflammatory diseases (e.g., RA, pseudogout, NpA, and hemophilia). In secondary OA, bony hypertrophy is usually less pronounced, and there are more diffuse chances of cartilage loss, uniform joint space loss, subchondral collapse, and ankylosis (Figs. 51, 52, 56).

Syndesmophytes are vertically orientated trabecular bone with slender outgrowths, which are hiistologically similar to osteophytes. They are a feature of SpAs and are considered a result of repeated episodes of inflammation and repair. In AS and inflammatory bowel disease, syndesmophytes are symmetric and marginal (developing at the discovertebral junction), whereas in PsA and reactive arthropathies, they are asymmetric and non-marginal (developing at the lateral surface of the vertebral body, at a variable distance

from the discovertebral junction), and are also termed parasyndesmophytes. Syndesmophytes of the anterior and lateral spine are the hallmark of AS, which is considered as less erosive and more ossifying arthropathy. As they enlarge, syndesmophytes eventually bridge the intervertebral disk, forming a "bamboo spine." Although the aforementioned changes of AS are better delineated on plain films and computed tomography, MR imaging maintains its role in the following scenarios:

- Early diagnosis of sacroilitis (depicted as T2 hyperintensity, diffusion restriction and contrast enhancement of the subchondral bone, with or without joint effusion)
- Early detection of cartilage loss, bone erosions, and subchondral bone changes in the discovertebral junctions
- In established spondylosis cases for the detection of pseudoarthrosis, spinal canal stenosis, and arachnoid diverticula
- For evaluation of cauda equina syndrome
- Detection of spine fracture through the disc in a bamboo spine and evaluation of associated ligament injury or epidural hematoma (Fig. 67)

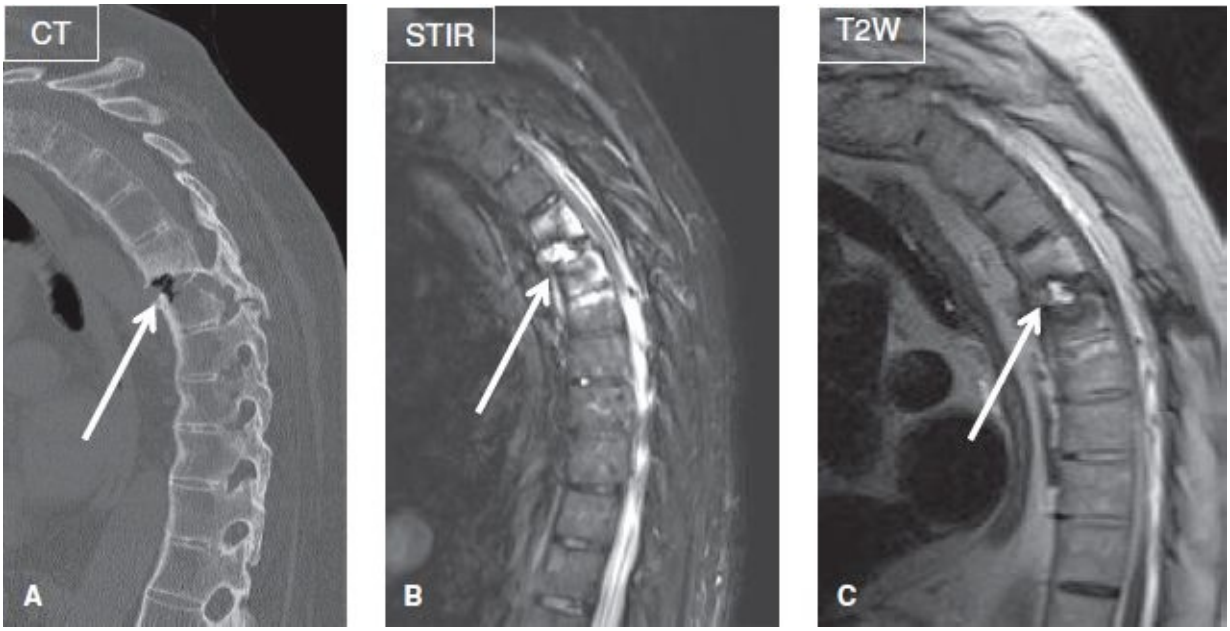

Fig. 67: Ankylosing spondylitis. Sagittal-reformatted CT image **(A)** and respective sagittal MR images **(B, C)** reveal the typical bamboo spine, typical of ankylosing spondylitis, and a banana stick-like discovertebral fracture (*arrows*) through the upper thoracic spine.

The absence of bony proliferative changes (unless associated with secondary OA) assists in differentiating RA from SpAs.

Diffuse idiopathic skeletal hyperostosis (DISH) is an enthesopathy, which mostly involves males aged 50 to 75 years of age, and is characterized by bone proliferation at sites of tendinous and ligamentous attachments. The entity typically involves the anterior (and less commonly also the posterior) longitudinal ligament at the level of the lower thoracic spine although the lumbar and cervical spine are also commonly affected. The entity manifests with (1) flowing calcifications and ossifications (low signal on all MR pulse sequences)

along the anterolateral (and less commonly the posterior) aspect of at least four contiguous vertebral bodies, with or without associated osteophyte formation; (2) preservation of vertebral marrow signal and disk height in the involved areas, as well as absence of excessive disk disease; (3) absence of bony ankylosis of the facet joints; or (4) absence of sacroiliac erosion, sclerosis, or bony fusion (although narrowing and sclerosis of facet joints are acceptable). The diagnosis is established on plain films or computed tomography. MR imaging is required in rare cases with neurologic symptoms, to exclude ossification of the posterior longitudinal ligament with potential spinal cord compression and edema as well as disc fractures similar to AS (Figs. 68, 69).

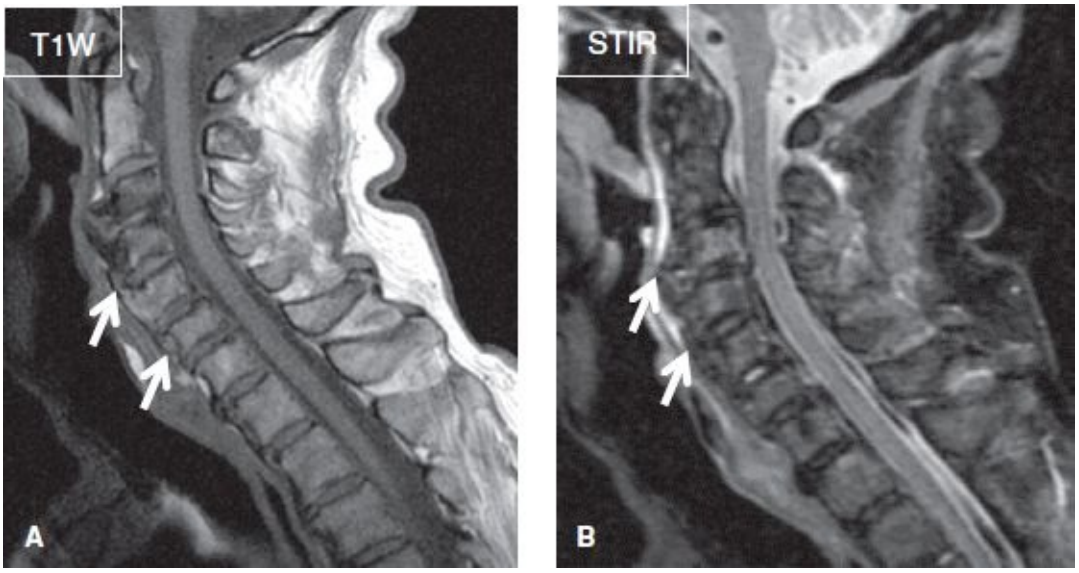

Fig. 68: Diffuse idiopathic skeletal hyperostosis. Sagittal images **(A, B)** demonstrate flowing ossification of the anterior longitudinal ligament (*arrows*) in the cervical spine from C2 to C5 levels.

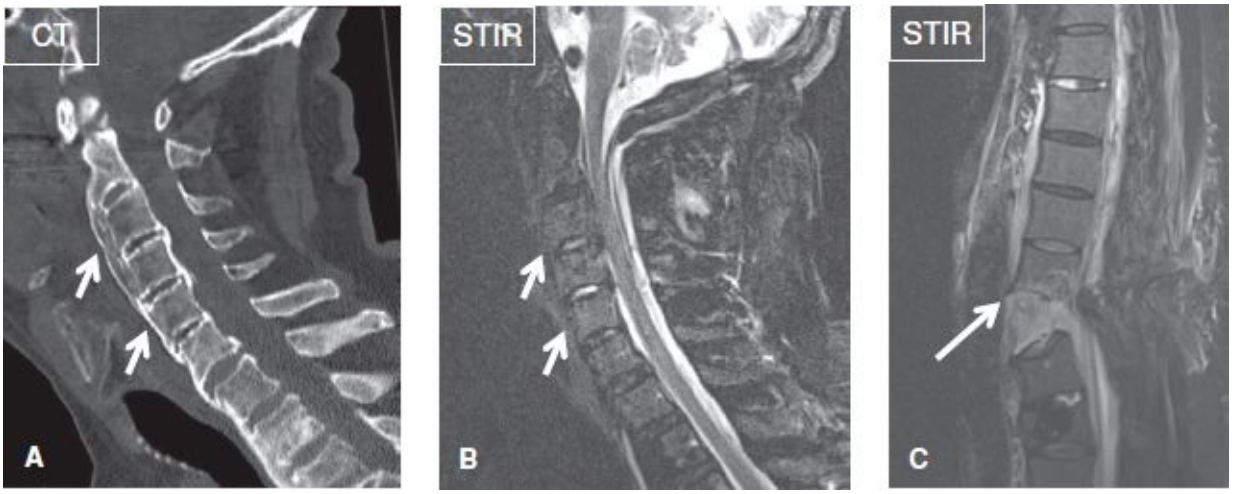

Fig. 69: Diffuse idiopathic skeletal hyperostosis with discovertebral fracture from recent injury. Sagittal-reformatted CT **(A)** and sagittal MR **(B)** images through the cervical spine demonstrate diffuse ossification of the anterior longitudinal ligament (*arrows*), better seen on CT image. Sagittal image through the thoracic spine **(C)** reveals a banana stick-like fracture involving the vertebra and adjacent upper disc space with loss of normal kyphotic

curvature (*arrow*).

TENOSYNOVITIS: [<Absent> <Mild/Moderate/Severe>]

In the setting of arthritis, the detection of adjacent tenosynovitis is a non-specific finding, which can result from mechanical derangement inflammation, or infection. In most cases, involvement of a single tendon indicates derangement; involvement of multiple tendons or marked tenosynovitis is suggestive of RA or other inflammations (Fig. 70); whereas tenosynovitis with associated fascial edema or fluid collection and/or intense enhancement raises the suspicion of an infectious process.

Fig. 70: Rheumatoid arthritis-associated tenosynovitis. Axial **(A)** and sagittal **(B)** images show longitudinal split tear (*long arrows*) of the peroneal brevis tendon along with severe peroneal tenosynovitis (*short arrows*).

Tenosynovitis is commonly seen in early RA of the wrists and hands and appears as increased fluid within the tendon sheath, increased thickness or contrast enhancement of the tendon sheath synovium, or a combination thereof. The synovial fluid is considered abnormally increased when it completely surrounds the tendon and/or features diameter greater than the diameter of the corresponding tendon. In early RA, tenosynovitis is important to report because (1) joint synovitis and tenosynovitis represent activity, and in some patients, tenosynovitis predominates over joint synovitis; therefore, both conditions should be considered together when evaluating the degree of inflammation (2) extensor and less commonly flexor tenosynovitis of the wrist can be associated with tendon rupture. Tenosynovitis and associated tendonitis or spontaneous tendon rupture may also be seen with lupus arthritis, gout, amyloid, and mixed connective tissue disorders (Fig. 71).

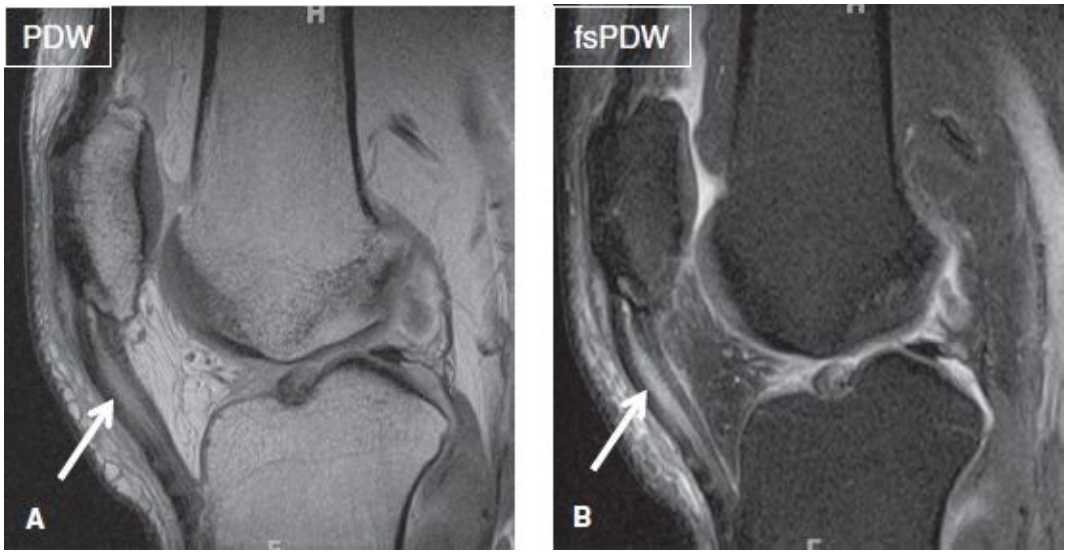

Fig. 71: Gout with spontaneous tendon delamination. Sagittal images **(A, B)** demonstrate spontaneous delamination of the distal patellar tendon (*arrows*).

JOINT SPACE/CARTILAGE: [<Normal> <Less than 50%loss/More than 50% loss>]

The joint space is best evaluated on plain films and the respective articular cartilage on MR images. The articular cartilage should be assessed with regards of tissue size and structural integrity. The report should include the location and depth of fissures and focal areas of cartilage loss (defects). Based on the depth, cartilage lesions are classified as *low-grade,* when involving less than 50% of cartilage thickness, *high-grade,* when involving greater 50% but less than full-thickness, and *full-thickness,* when the underlying bone has been exposed. In case of diffuse cartilage thinning, the report should include the degree of cartilage thinning (low-grade, high-grade, full-thickness) as well as whether it involves more or less than 50% of the total articular cartilage of the joint.

Joint space narrowing in advanced RA is predominantly concentric in contrast to OA, in which, the narrowing is predominantly eccentric. In radiographic scoring methods, joint space narrowing and bone erosions are considered the most suitable measures of RA severity and progression. Similar to radiographs, the carpo-metacarpal ratio can be used in RA as quantitative measure of disease progression. The ratio reflects joint space reduction (rather than erosive damage) in the wrist, and diminishes as carpal involvement progresses. It is calculated by dividing the longitudinal length of the carpus (from the volar–ulnar margin of the distal radius to the base of the third metacarpal bone at its cortical midpoint) by the length of the third metacarpal bone. Normal values exceed 0.60, and ratio alterations are reported during serial evaluation.

In gout and amyloid arthropathy, the joint space is preserved until the late stages of the disease. The joint space is generally preserved in PVNS whereas it is uncommonly widened in primary SOC, due to distention by accumulation of loose bodies (Figs. 61, 62, 66).

Degeneration of the articular cartilage is a structural hallmark of OA and predominates in the weight-bearing aspects of the articulate surfaces. Based on severity, cartilage lesions include *early degeneration or chondromalacia,* which is mostly identified on high spatial

resolution spin-echo images as inhomogeneous signal intensity; *low-grade lesions,* depicted as cartilage defects involving less than half of the cartilage thickness (0% to 50%); *high-grade lesions,* shown as cartilage defects involving more than half of the cartilage but less than full-thickness (51% to 99%); and *full-thickness lesions* (100%), demonstrated as cartilage defects with bone exposure (denuding) (see Chapter 5 for more details).

Crystal deposition in the articular cartilage is a major feature of pseudogout. These crystals, which appear as calcifications on plain films and computed tomography scans, manifest on spin-echo images as prominent linear or punctuate areas of low signal, occasionally surrounded by a hyperintense halo, probably due to susceptibility artifact. They are best detected on gradient-echo images. The most common joints involved by CPDD are knee (where crystal deposition also occurs in the menisci), wrist (also involving the triangular fibrocartilage), hip, and symphysis pubis. In late stages, the disease leads to joint destruction. Destruction of an upper extremity joint is rarely a result of OA and should raise the suspicion for underlying pseudogout. The latter is also associated with joint space narrowing.

In NpA, there is diffuse or multifocal cartilage degeneration and subsequently total cartilage loss. The joint space is widened in the initial stages and narrowed in the later stages of the disease. In hemophilic hemarthrosis, there is homogeneous loss of the joint cartilage with dark hemosiderin deposition in the synovium or cartilage, and subsequent joint space narrowing (involving all compartments in the knee or ankle), which may finally lead to exposure of the underlying bone (Fig. 73).

Fig. 72: Early gout mimicking septic arthritis in a patient with fever, ankle pain and high white cell count. **A:** Lateral radiograph shows small effusion (*arrow*) with no narrowing of the ankle joint space. Also note plantar calcaneal spur. **B, C:** The respective sagittal MR images exhibit small tibiotalar and posterior subtalar joint effusions (*arrows* in **B**), along with synovitis, resembling inflammatory/infectious process. Aspiration revealed gouty crystals.

Fig. 73: Secondary osteoarthrosis due to recurrent hemarthrosis in a 45-year-old male with history of hemosiderosis. Anteroposterior radiograph **(A)** shows subchondral erosion (*short arrow*), a hook-like osteophyte (*long arrow*) at the head of the first metacarpal bone, as well as a smaller osteophyte (*open arrow*) at the base of the proximal phalanx. There are additional degenerative changes of the long finger PIP joint. Coronal **(B)** and axial **(C)** images of the right shoulder show severe cartilage loss at the glenohumeral joint (*arrows* in **B**) and diffuse hypointensity of the synovium (*arrows* in **C**).

EROSION/CYSTIC CHANGE: [<Absent> <Less than 50%/More than 50% joint surface> <Articular / Para-articular>]

Erosions may be articular or para-articular in location. The former commonly result from inflammation, pannus formation, and associated cartilage loss, and the latter from inflammation and/or traction changes from tendons or ligaments (enthesis). Articular erosions are a definite feature of RA. They initially occur at the “bare area,” which exists between the cartilage and immediate adjacent intra-articular bone and manifest as bone lesions, which are visible in two planes (important to identify in multiple planes to avoid overestimation of the lesions), with a cortical break seen in at least one plane. These lesions appear hyperintense on fluid-sensitive images and enhance. On T1W images, they feature focal loss of the normal low signal of the cortex and normal high signal of the underlying marrow. The contrast enhancement of erosions reflects inflamed synovium within the defect, differentiating them from fluid-filled erosions, which lack enhancement. In the hand, erosions most commonly involve the capitate, triquetrum, and lunate, the radial aspect of the second and third metacarpal bones, the lateral aspect of the fifth metatarsal bone, the base of the styloid process of the ulna and the pisotriquetral joint (Figs. 43, 54, 74). The

bony erosive cystic changes of RA are occasionally present in lupus arthritis and primary Sjögren syndrome, and differentiation of the latter entities from (particularly early) RA may be difficult by MR imaging. Erosions initiate as focal subchondral edema (bright on fluid-sensitive images and normal or minimally dark on PDW or T1W images) and evolve into cysts (bright on fluid-sensitive images and dark on T1W images), and finally metamorphose into fat (bright on all images except fat-suppressed images) or sclerosis (dark on all sequences). Mixture of signal alterations may be seen due to varying stages of evolution of the disease process at the time of imaging.

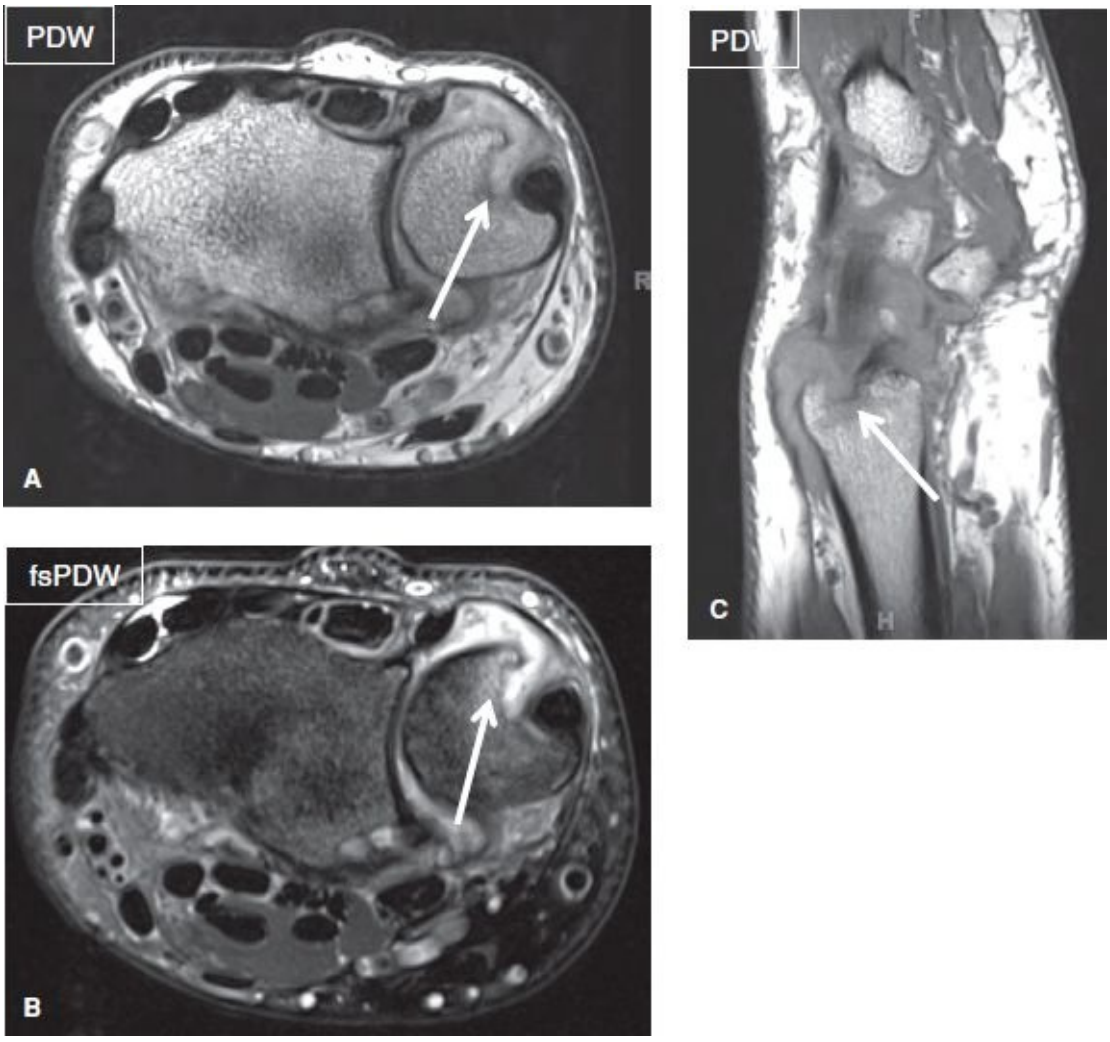

Fig. 74: Early rheumatoid arthritis. Axial **(A, B)** and sagittal **(C)** images show focal erosion of the base of the ulnar styloid process (*arrows*) with associated synovitis.

Para-articular erosions are seen in gout, PVNS, SOC, and hemophilic arthropathy. The hallmark of gout is "punched-out" erosions with sclerotic margins and overhanging edges (Figs. 32, 65). The overhanging cortex, which is present in approximately 40% of cases, reflects bone resorption due to pressure from an enlarging tophus (Fig. 75). In PVNS, erosions develop on one or both sides of the joint, arising from cartilaginous defects created by the pressure from underlying synovial mass. These erosions may be filed with synovial fluid or PVNS tissue and display corresponding signal alterations (Fig. 76). In SOC, pressure effects from the intra-articular bodies may cause periarticular erosions in up to 30% of

cases, particularly in joints with tight capsule or potential for excessive load of loose bodies, such as the hip, wrist, and small joints of the hand and foot. Erosions are less common in joints with large capsules or recesses, such as the knee and shoulder (Figs. 52, 58). On imaging, erosions demonstrate fluid-like signal and range from well-defined cortical defects to circumferential lesions, which result in an "apple-core" appearance of the affected bone. In hemophilic arthropathy, the signal intensity of the para-articular defects (erosions and/or cystic changes) varies and may indicate the presence of fluid (high signal on T2W images), soft tissue (intermediate signal), or commonly, synovial tissue with hemosiderin (low signal) (Fig. 63).

Fig. 75: Gouty erosion. Anteroposterior radiograph **(A)** and coronal images **(B–D)** show focal eccentric erosion of the fibular aspect of the third metatarsal head with bone marrow edema, cystic changes, and peripheral enhancement (*arrows*) in a known case of gout.

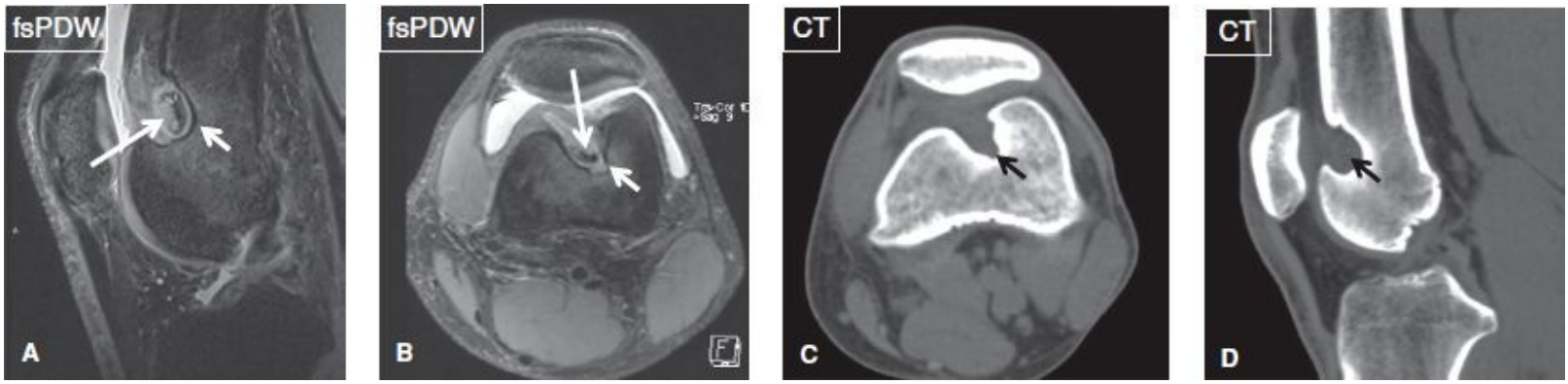

Fig. 76: Pigmented villonodular synovitis. Sagittal **(A)** and axial **(B)** images demonstrate an ovoid lesion (*long arrows*) of low signal, lodged within a well-defined erosion of the femoral metaphysis (*short arrows*). The erosion (*arrows*) is well depicted in the corresponding axial **(C)** and sagittal-reformatted **(D)** CT images as showing a sclerotic base indicating subacute chronic pressure erosion.

Amyloid arthropathy is characterized by subchondral bone lesions, which show low signal on T1W images. On T2W images, the signal can range from low to high, depending on the combination of amyloid deposits and fluid collection within the subchondral lesions. In the

appropriate clinical setting (dialysis patient or multiple myeloma), however, detection of an intraosseous lesion with relatively low signal intensity on all images strongly supports the diagnosis (Figs. 47, 64). The lesions frequently communicate with intra-articular deposits and exhibit mild to moderate enhancement after contrast administration. Well-defined bone erosions occasionally appear in HADD and are usually, though not invariably, associated with surrounding marrow edema (Figs. 41, 77).

Geodes are common space occupying lesions seen in a variety of disorders including OA, RA, pseudogout, and avascular necrosis. They are typically well-defined and subchondral in location and can occur as single or multiple lesions, usually ranging from 2 to 20 mm in size. Geodes may be cavitary or non-cavitary. Cavitary geodes, also known as subchondral cysts, are filled with synovial or proteinaceous fluid and form when synovial fluid is forced into the subchondral bone, causing a cystic collection of joint fluid, or following a bone contusion, in which the contused bone forms a cyst. Non-cavitary geodes include various combinations of myxoid, fibrous, and adipose contents. Most large geodes on MR imaging show interspersed marrow fat and appear flame-shaped or elongated. These features, along with communication of the lesion with the articular surface and underlying arthritic changes, aid in distinguishing these lesions from other sinister neoplastic lesions of the bone (Figs. 50, 51, 78). In OA or RA, subchondral cysts or geodes are often (but not always) detected in conjunction with neighboring cartilage damage, and are strongly associated with bone marrow edema-like lesions in the same subregion. Depending on their content, after contrast administration they can demonstrate no enhancement (when they include joint fluid, which has entered via fissured or ulcerated cartilage), partial enhancement (due to surrounding fibrous connective tissue), or complete enhancement (due to intrusion of synovial tissue). Complete enhancement is only seen in lesions less than 1 to 2 cm. Subchondral cystic erosions in OA occur at syndesmoses, such as the pubis symphysis, sacroiliac, temporomandibular, and acromioclavicular joints due to excessive stresses (i.e., posttraumatic osteolysis). In radiographic scoring methods, bone erosions together with joint space narrowing are considered the most suitable measures of RA severity and progression. Large subchondral cysts also develop in pseudogout and are commonly associated with extensive subchondral sclerosis. In multicentric reticulohistiocytosis, there are symmetric marginal bone erosions, which tend to be well-circumscribed and are located around the distal interphalangeal joints, unlike those in RA (Fig. 34).

BONE MARROW EDEMA: [<Absent> <Present>]

Bone marrow edema is important to report as it correlates with clinical symptoms and can either disappear with treatment or convert to cystic, fat, or sclerotic changes similar to Modic changes in spinal end plates. It is also a precursor to the development of frank joint erosions. As described above, it manifests as an ill-defined focal area within trabecular bone, which shows high signal on fluid-sensitive images and minimal subchondral signal hypointensity or no signal change on T1W images. In RA, marrow edema usually occurs adjacent to cartilage in the subchondral bone (Fig. 43). In SpAs, marrow edema is much less

extensive and is observed in the diaphysis of the phalanges at a considerable distance from the subchondral bone and the capsular enthises (Figs. 35–37). In lupus arthritis and primary Sjögren syndrome, marrow edema presents in a similar fashion as mentioned for RA. In PsA, bone marrow edema begins at the corner of the phalanx at the insertion of the capsule and spreads to involve the entire bone as the disease progresses. It is usually ill-defined with intact overlying cortex. Associated periostitis may be present in both PsA and RA.

In OA, bone marrow edema-like lesions are often detected in conjunction with neighboring cartilage damage. These reflect stress-related changes of edema, bone marrow necrosis, fibrosis, and trabecular abnormalities seen in OA. In middle or advanced stages of OA, lesions are frequently associated with subchondral bone attrition, which is caused by altered mechanical loading and resulting remodeling and appear as depression or flattening of the subchondral surface, along with associated cortical thickening, sclerosis and loss of bone stock (Figs. 49–51).

Bone marrow edema also appears in the acute symptomatic phase of HADD and is usually, though not invariably, associated with cortical erosions, fascial, or peritendinous/periligamentous edema (Fig. 77). In NpA, marrow edema is typically subchondral and is associated with sclerosis (from eburnation) and cystic changes of the subchondral bone (Fig. 42).

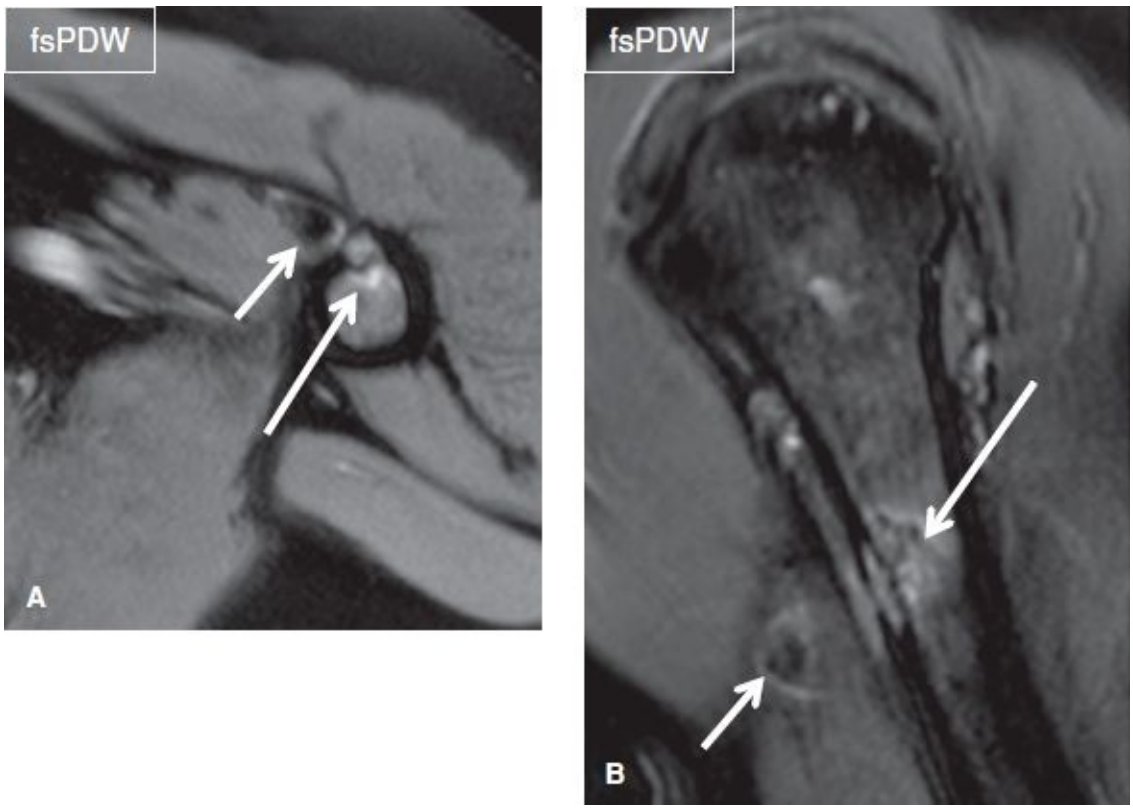

Fig. 77: Calcium hydroxyapatite crystal deposition disease. Axial **(A)** and sagittal **(B)** images demonstrate a focus of low signal (*short arrows*) in the pectoralis major tendon, compatible with calcification. Notice adjacent fascial edema as well as bony erosion at the insertion site on the humerus (*long arrows*).

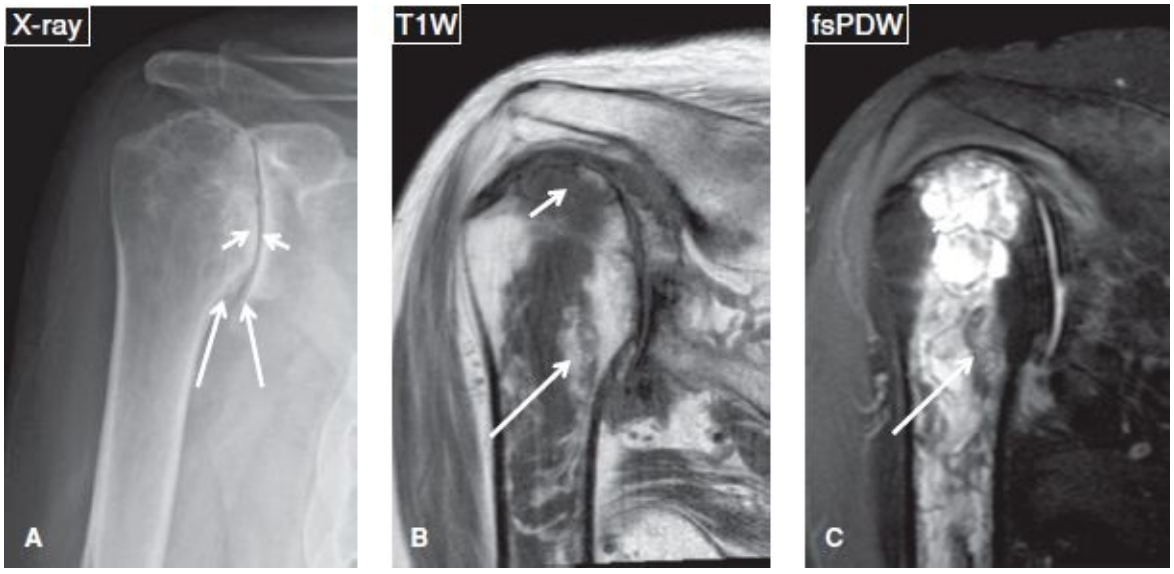

Fig. 78: Cyst- and fat-containing geode. **A:** Anteroposterior radiograph shows subchondral sclerosis (*short arrows*), osteophytes (*long arrows*), and significant loss of joint space at the glenohumeral joint, in keeping with severe osteoarthritis. Notice underlying osteopenia. **B, C:** The respective coronal MR images reveal fluid-containing (*short arrows*) and fat-containing (*long arrows*) subchondral lesions, compatible with geode.

ANKYLOSIS: [<Absent> <Less than 50%/More than 50%>]

Ankylosis may occur in the late stages of RA, PsA, AS, and juvenile RA or idiopathic arthritis; long-standing OA; chronic cases of septic arthritis and reactive arthritis; severe gout; fluorosis or ochronosis. Facet fusion is common in juvenile RA and AS. Imaging features include partial or complete joint fusion with complete joint space loss and bony (osteophytes or syndesmophytes), trabecular, or fibrous bridges running across the articulation. Ankylosing should be graded as involving more or less than 50% of the total joint space.

Incidental Findings

Epiphyseal overgrowth due to hyperemia is a characteristic, though invariably present, feature of hemophilic arthropathy. It may be associated with skeletal changes in certain joints, such as the knee (widened intercondylar notch, squared inferior margin of the patella, bulbous femoral condyles, flattened condylar surfaces), elbow (enlarged radial head, widened trochlear notch), and ankle (overgrowth of medial malleolus and/or undergrowth of the lateral side of the tibial epiphysis, leading to pronated foot and talar tilt, aka tibiotalar slant) (Fig. 53). Epiphyseal overgrowth may also be seen in tubercular arthritis and juvenile RA.

A common presentation of PsA affecting the appendicular joints is dactylitis (or “sausage digit”), which refers to diffuse fusiform swelling of a digit due to soft tissue inflammation (mainly tenosynovitis and polyenthesitis) (Fig. 79). Except from PsA, other causes include OM, sickle cell anemia, sarcoidosis and tuberculous dactylitis (spina ventosa), or syphilitic

dactylitis (spina lutea). Another characteristic feature of PsA is irregular or smooth cortical thickening alongside the diaphysis of the phalanges. This reflects cortical bone proliferation due to periostitis, which represents a part of the spectrum of enthesitis, and is depicted as focally increased contrast enhancement. Periostitis in digits can also be seen in RA due to hyperemia.

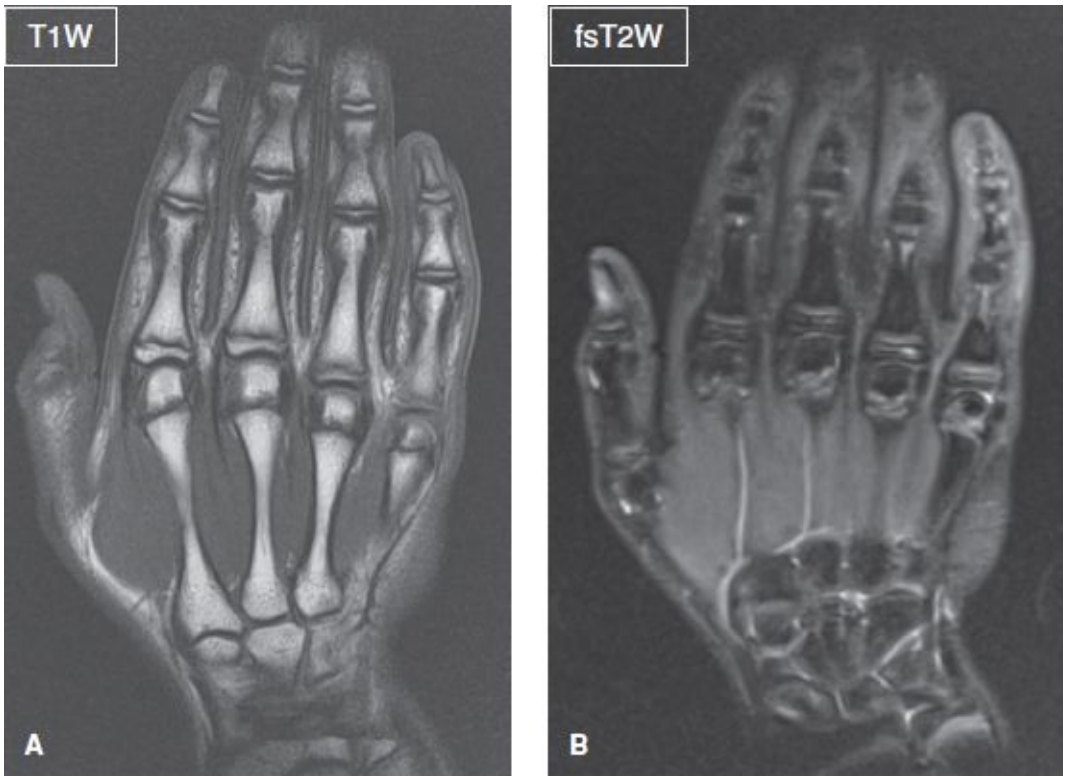

Fig. 79: Sausage digits in psoriasis. Coronal images show diffuse swelling of ring and little fingers, centered around the PIP and DIP joints in this newly diagnosed case of psoriasis. The patient had mild nail pitting in these digits.

Soft tissue ganglion and Baker cysts are common findings in degenerative and inflammatory arthritis (particularly in RA and PVNS) (Figs. 51, 56), and if large and/or heterogeneous, they can mimic tumors or extend within adjacent peripheral nerve sheaths and cause compressive peripheral neuropathy (e.g., foot drop/shoulder weakness). If there is any doubt to their characterization, contrast administration will confirm their benignity by showing peripheral enhancement.

POST-GADOLINIUM DISCUSSION: [<Synovitis or other findings>]

Contrast administration is important in inflammatory arthritis, as it nicely shows areas of increased enhancement reflective of hyperemia and ongoing inflammation. It is not that critical for bony lesions as most hyperemic areas in the bones appear as bright on fat-suppressed fluid-sensitive sequences, but it is very important for soft tissue lesions, such as for establishing active synovitis, the diagnosis of which is otherwise difficult on the basis of unenhanced images alone (Fig. 54). Using dynamic contrast MR imaging, quantitative parameters characterizing contrast uptake dynamics (e.g., initial rate of enhancement,

maximal enhancement, etc.) can be used to quantify the inflammatory process in RA, to better investigate the treatment response. In cases of contraindication to contrast, one might look at the DW images for diffusion restriction, which can also confirm the sites of active inflammation.

To conclude, clinical findings supplemented by MR imaging play an essential role in the diagnosis of infectious and inflammatory arthropathies and related soft tissue lesions. A systematic approach to their detection, evaluation, and reporting is essential for correct diagnosis, proper management, and follow-up strategies.

SUGGESTED READINGS

Amrami KK. Imaging of the seronegative spondyloarthropathies. *Radiol Clin North Am.* 2012;50:841–854.

Anandarajah A. Imaging in psoriatic arthritis. *Clin Rev Allergy Immunol.* 2013;44:157–165.

Baraliakos X, Hermann KG, Braun J. Imaging in axial spondyloarthritis: Diagnostic problems and pitfalls. *Rheum Dis Clin North Am.* 2012;38:513–522.

Dalbeth N, Doyle AJ. Imaging of gout: An overview. *Best Pract Res Clin Rheumatol.* 2012;26:823–838.

Damasio MB, de Horatio LT, Boavida P, et al. Imaging in juvenile idiopathic arthritis (JIA): An update with particular emphasis on MRI. *Acta Radiol.* 2013;54:1015–1023.

Demertzis JL, Rubin DA. MR imaging assessment of inflammatory, crystalline-induced, and infectious arthritides. *Magn Reson Imaging Clin N Am.* 2011;19:339–363.

Feydy A, Pluot E, Guerini H, et al. Role of imaging in spine, hand, and wrist osteoarthritis. *Rheum Dis Clin North Am.* 2009;35:605–649.

Forney MC, Winalski CS, Schils JP. Magnetic resonance imaging of inflammatory arthropathies of peripheral joints. *Top Magn Reson Imaging.* 2011;22:45–59.

Grainger AJ, Rowbotham EL. Rheumatoid arthritis. *Semin Musculoskelet Radiol.* 2013;17:69–73.

Guermazi A, Hayashi D, Eckstein F, et al. Imaging of osteoarthritis. *Rheum Dis Clin North Am.* 2013;39:67–105.

Jaramillo D. Infection: Musculoskeletal. *Pediatr Radiol.* 2011;41(suppl 1):S127–S134.

Lalam RK, Cassar-Pullicino VN, Tins BJ. Magnetic resonance imaging of appendicular musculoskeletal infection. *Top Magn Reson Imaging.* 2007;18:177–191.

Loeuille D, Chary-Valckenaere I. MRI in OA: From cartilage to bone marrow lesion. *Osteoporos Int.* 2012;23(suppl 8):S867–S869.

Machado PM, Koevoets R, Bombardier C, et al. The value of magnetic resonance imaging and ultrasound in undifferentiated arthritis: A systematic review. *J Rheumatol Suppl.* 2011;87:31–37.

Mattar M, Salonen D, Inman RD. Imaging of spondyloarthropathies. *Rheum Dis Clin North Am.* 2013;39:645–667.

McQueen FM. Imaging in early rheumatoid arthritis. *Best Pract Res Clin Rheumatol.* 2013;27:499–522.

Pattamapaspong N, Sivasomboon C, Settakorn J, et al. Pitfalls in imaging of musculoskeletal infections. *Semin Musculoskelet Radiol.* 2014; 18:86–100.
Pedersen SJ, Weber U, Ostergaard M. The diagnostic utility of MRI in spondyloarthritis. *Best Pract Res Clin Rheumatol.* 2012;26:751–766.
American College of Rheumatology Rheumatoid Arthritis Clinical Trials Task Force Imaging Group and Outcome Measures in Rheumatology Magnetic Resonance Imaging Inflammatory Arthritis Working Group. Review: The utility of magnetic resonance imaging for assessing structural damage in randomized controlled trials in rheumatoid arthritis. *Arthritis Rheum.* 2013;65:2513–2523.
Roemer FW, Crema MD, Trattnig S, et al. Advances in imaging of osteoarthritis and cartilage. *Radiology.* 2011;260:332–354.
Soldatos T, Durand DJ, Subhawong TK, et al. Magnetic resonance imaging of musculoskeletal infections: Systematic diagnostic assessment and key points. *Acad Radiol.* 2012;19:1434–1443.
Spira D, Kotter I, Henes J, et al. MRI findings in psoriatic arthritis of the hands. *AJR Am J Roentgenol.* 2010;195:1187–1193.
Tins BJ, Cassar-Pullicino VN, Lalam RK. Magnetic resonance imaging of spinal infection. *Top Magn Reson Imaging.* 2007;18:213–222.
Turecki MB, Taljanovic MS, Stubbs AY, et al. Imaging of musculoskeletal soft tissue infections. *Skeletal Radiol.* 2010;39:957–971.
Yu JS, Habib P. MR imaging of urgent inflammatory and infectious conditions affecting the soft tissues of the musculoskeletal system. *Emerg Radiol.* 2009;16:267–276.

APPENDIX 1: Sample Completed Structured Report: Infection: NORMAL

EXAM: MRI [<EXTREMITY/JOINT>] [<WITH / WITHOUT>] CONTRAST

FINDINGS:

There [<is no>] subcutaneous edema.

There [<is no>] muscle edema.

There [<is no>] significant superficial or deep fascial fluid.

There [<is no>] large drainable fluid collection.

There [<is no>] focal bone marrow edema.

There [<is no>] large joint effusion.

JOINT INVOLVED: [<_>]

Alignment: [<Normal>]

Fluid: [<Normal>]

Synovial thickening/synovitis: [<Absent>]

Bony productive changes: [<Absent>]

Tenosynovitis: [<Absent>]

Joint space/cartilage: [<Normal>]

Erosion/cystic change: [<Absent]

Bone marrow edema: [<Absent>]

Ankylosis: [<Absent>]

INCIDENTAL FINDINGS: [<_>]

Post-gadolinium Discussion: [<Synovitis or other findings>]

IMPRESSION:

[<In the order of importance with acute findings first>]

APPENDIX 2: Sample Completed Structured Report: Infection: ABNORMAL

EXAM: MRI [<RIGHT ANKLE>] [<WITH AND WITHOUT>] CONTRAST

FINDINGS:

There is diffuse soft tissue subcutaneous edema, anterior more than posterior.

There is patchy muscle edema of the extensor digitorum brevis.

There is no significant superficial or deep fascial fluid.

JOINT INVOLVED: [<Ankle>]

Alignment: [<Normal>]

Fluid: [<Moderate effusion>]

Synovial thickening/synovitis: [<Mild diffuse thickening>]

Bony productive changes: [<Absent>]

Tenosynovitis: [<Mild tenosynovitis of all long flexor tendons>]

Joint space/cartilage: [<Mild cartilage fissuring anterior medial talar dome>]

Erosion/cystic change: [<Focal cortical erosion anterior medial talar dome>]

Bone marrow edema: [<Present anterior medial talar dome>]

Ankylosis: [<Absent>]

INCIDENTAL FINDINGS: [<Mild fatty infiltration of abductor digit minimi>]

Post-gadolinium Discussion: [<Intense synovial enhancement of the ankle joint. Diffuse anterior soft tissue and extensor digitorum brevis muscle enhancement. Focal enhancement in the anterior medial talar dome.>]

IMPRESSION:

1. Findings suggest septic arthritis of ankle joint with focal osteomyelitis of the anterior medial talar dome. Joint aspiration advised for confirmation.

2. Mild long flexor tenosynovitis, cellulitis, and extensor digitorum brevis myositis.

APPENDIX 3: Sample Completed Structured Report: Inflammation/Arthritis: NORMAL

EXAM: MRI [<EXTREMITY/JOINT>] [<WITH / WITHOUT>] CONTRAST

FINDINGS:

There [<is no>] soft tissue subcutaneous edema.

There [<is no>] muscle edema.

There [<is no>] significant superficial or deep fascial fluid.

There [<is no>] joint abnormalities.

JOINT INVOLVED: [<_>]

Alignment: [<Normal>]

Fluid: [<Normal>]

Synovial thickening/synovitis: [<Absent>]

Bony productive changes: [<Absent>]

Tenosynovitis: [<Absent>]

Joint space/cartilage: [<Normal>]

Erosion/cystic change: [<Absent>]

Bone marrow edema: [<Absent>]

Ankylosis: [<Absent>]

INCIDENTAL FINDINGS: [<_>]

Post-gadolinium Discussion: [<Synovitis or other findings>]

IMPRESSION:

[<In the order of importance with acute findings first>]

APPENDIX 4: Sample Completed Structured Report: Inflammation/Arthritis: ABNORMAL

EXAM: MRI [<RIGHT HAND>] [<WITH AND WITHOUT>] CONTRAST

FINDINGS:

There is no soft tissue subcutaneous edema.

There is no muscle edema.

JOINT INVOLVED: [<2nd and 3rd metacarpophalangeal joints>]

Alignment: [<Normal at the 2nd metacarpophalangeal joint. Less than 50% ulnar subluxation at the 3rd metacarpophalangeal joint.>]

Fluid: [<Small effusion at the 2nd metacarpophalangeal joint>]

Synovial thickening/synovitis: [<Present, mild>]

Bony productive changes: [<Mild osteophytosis at the 1st carpometacarpal joint and triscaphe joint>]

Tenosynovitis: [<Mild long flexor tenosynovitis at the long finger>]

Joint space/cartilage: [<Less than 50% loss at the 2nd and 3rd metacarpophalangeal joints>]

Erosion/cystic change: [<Present, articular, less than 50% involvement of the articular surface at the 2nd and 3rd metacarpophalangeal joints>]

Bone marrow edema: [<Present at the 3rd metacarpophalangeal joint>]

Ankylosis: [<Absent>]

INCIDENTAL FINDINGS: [<Small, 1 cm lipoma of the thenar musculature>]

Post-gadolinium Discussion: [<Asymmetric synovial enhancement at the 3rd more than 2nd metacarpophalangeal joints>]

IMPRESSION:

1. Findings suggesting inflammatory arthritis of 3rd more than 2nd metacarpophalangeal joints and long flexor tenosynovitis of the long finger. Consider rheumatoid arthritis clinically.

2. Small incidental thenar muscle lipoma.

4

Bone and Soft Tissue Tumors

Avneesh Chhabra, Kyung Jin Suh, Jonathan Samet, and Theodoros Soldatos

The musculoskeletal system is affected by a variety of (benign and malignant) tumors and tumor-like conditions that involve bones, joints, muscles, soft tissues, and peripheral nerves. Tumor-like conditions may be related to traumatic, infectious, arthritic, or developmental etiologies that lead to the development of soft tissue or bony mass-like lesions, which mimic neoplasia. Systematic assessment of the above lesions, correlation with plain films, and description in a structured reporting format are very useful to arrive at a definitive diagnosis (or the most relevant differential diagnosis), and to decide upon further management, including biopsy, surgery, and follow-up strategies. For appropriate imaging analysis and structured reporting, the lesions can be separately described using different templates for bone tumors and soft tissue tumors, depending upon the predominant respective tissue involvement and epicenter of the lesions. The checklist for structured reporting is outlined in Appendices 1–4 with samples of normal templates and abnormal (positive) reports. Conceptual details of related MR physics and imaging protocol are discussed in the chapter on MR protocol optimization.

IMAGE EVALUATION

The below-outlined stepwise interpretation approach is only a practical guide, and all bone and soft tissue structures should be evaluated in multiple planes for their optimal assessment. The following discussion will help reader perceive which lesion characteristics are best depicted/evaluated in which particular plane.

1. The traditional tumor MR imaging protocols include one or two long-axis T1-weighted (T1W) images and three plane fluid-sensitive fat-suppressed T2-weighted (fsT2W) or short-tau inversion recovery (STIR) images. Most examinations include pre- and post-contrast evaluation in multiple planes or isotropic three-dimensional (3D) T1-weighted (T1W) gradient-echo images, which can be reconstructed in multiple planes. Recently, many tertiary care centers have incorporated diffusion-weighted (DW) and chemical shift (CS) imaging to evaluate the amount of diffusion restriction (e.g., cellularity by measuring apparent diffusion coefficient [ADC] value) and the presence of microscopic

intralesional fat (benignity suggested by >20% relative loss of signal in bony lesions on out-of-phase imaging), respectively. MR angiography can be added in the protocol to assess the vascularity (vascular involvement, enhancement pattern) of neoplasms. The modality is particularly used in the preoperative imaging of sarcomas.

2. If available, plain film, US and/or CT findings should be correlated with MR features (Fig.1). The former modalities can be used for detecting presence of fat, calcification, bony cortex integrity, and periosteal reaction. MR imaging is beneficial for characterization of the bone marrow; however, the MR features of osseous lesions may sometimes confuse the reader, and clearly benign or indolent lesions on radiographs may occasionally appear aggressive on MR images. The diagnosis of bone lesions should be preferably based on radiographs and/or CT whereas MR imaging can be employed for further characterization, and definition of their extent.

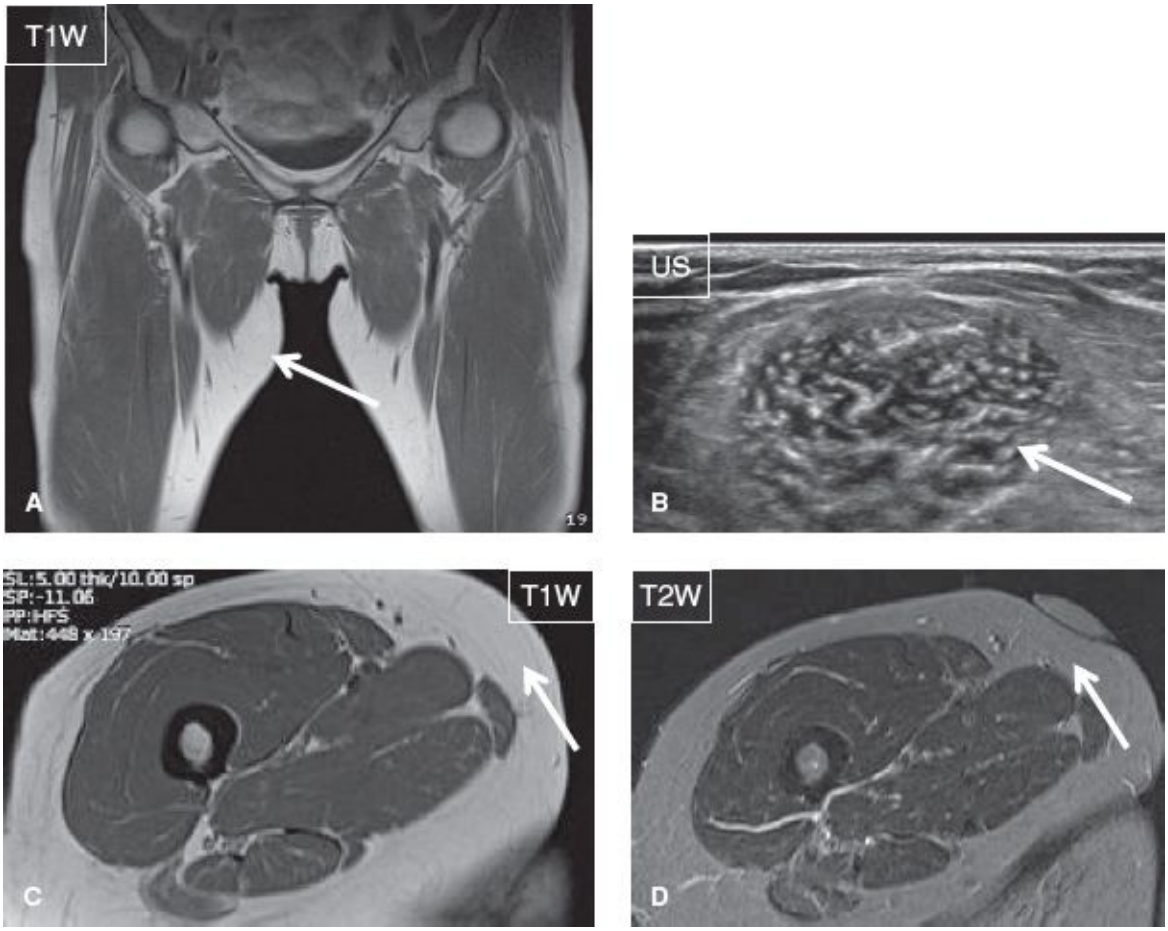

Fig. 1: Simple lipoma. Medial thigh palpable mass. Coronal **(A)** and axial **(C, D)** MR images and corresponding focused ultrasound image **(B)** show a purely fat-containing lesion (*arrows*) with a thin capsule in the medial proximal thigh at the site of the marker, consistent with a lipoma.

3. On MR imaging, the initial evaluation is performed on long-axis images to grossly assess the presence/absence of the lesion, its size, regional major soft tissue involvement, joint involvement, and presence or absence of skip lesions. Typically, lesions with elongated shape, and associated marked fascial and soft tissue edema, fascial or subperiosteal fluid,

and/or sinus tract are infectious in etiology. The neoplasms do not produce much fascial edematous or fluid-like changes unless they are markedly aggressive with extra-compartmental extension. The appearance of the lesion is further characterized on T1W and T2W images to identify the predominant tissue composition, such as fat (T1 and T2 bright), fibrous (T1 and T2 dark), fluid or myxoid (T1 dark and T2 bright), cartilage (T1 intermediate and T2 bright), hemorrhage (T1 bright and T2 mixed), or calcification/osseous component (predominantly T1 and T2 dark ± internal fatty marrow elements).

4. Line up the axial T1W, T2W, pre- and post-contrast T1W (and subtraction, if available) images and synchronize them for tandem evaluation. If 3D (isotropic) T1W or T2W sequences have been obtained, the technologists should create reconstructions in prespecified axial, coronal, and sagittal planes to save reading time. Axial planes are ideal for the following purposes:
   - Evaluating the internal characteristics of lesions, such as the predominant type of tissue, internal hemorrhage, calcification, fibrosis, necrosis, fluid–fluid levels, myxoid or cystic changes, etc.
   - Determining the amount of cortical erosion or endosteal scalloping.
   - Defining the intra- or extracompartmental location and potential intra-articular extension of the lesions.
   - Assessing the involvement of neurovascular bundles.
5. If CS imaging is available, check for either relative ($>20\%$) signal loss in the bone lesion on out-of-phase images, which would indicate presence of microscopic fat and likely benignity of a marrow lesion; or for relative signal loss on in-phase images in the soft tissue lesions, which signifies presence of hemorrhage, such as in pigmented villonodular synovitis (PVNS). If DW imaging is available, check the ADC values as well as the presence and amount of diffusion restriction. Low ADC values ($<1.1\times 10^{-3}$ mm^2/s) are seen with highly cellular, potentially malignant lesions, whereas high ADC values are seen with lower cellularity, probable benign or low-grade lesions. Evaluate CS and DW images in conjunction with the conventional images, e.g., fatty metamorphosis or fibrosis of lesion following successful treatment will also restrict diffusion. Finally, if time-resolved MR angiography has been performed, evaluate the degree increased or decreased regional vascularity, and perfusion of the lesion apart from patency of regional vessels for preoperative mapping. Fast and early uptake and/or wash out of contrast from the lesion indicate an aggressive vascularized lesion, and the potential responsiveness of the latter to radiation treatment. Post-treatment evaluation for residual or recurrent lesion is also better performed using time-resolved MR angiography and pre- as well as post-contrast delayed imaging, as part of the tumor imaging protocol. One would see early blush of nodular contrast enhancement with residual/recurrent disease, while gradual mild diffuse fill-in of contrast would be observed in post-radiation granulation tissue and scar tissue.
6. After filling the structured report, compile the imaging (MR, CT, plain film) findings

together to indicate whether the lesion is benign (e.g., ganglion, lipoma, vascular malformation, nonossifying fibroma (NOF), cortical avulsive deformity, and unicameral bone cyst; Figs. 1–6); indeterminate (e.g., solid or centrally enhancing soft tissue lesion, bony lesion with ill-defined margins and/or periostitis; Fig. 7); or clearly malignant, unless proven otherwise (e.g., infiltrative soft tissue mass extending into different compartments, large heterogeneous necrotic mass, and bony lesion with cortical erosion and soft tissue mass; Fig. 8). Table 1 provides useful guides for differentiating between malignant and benign musculoskeletal lesions whereas Table 2 illustrates the differential diagnosis of various benign entities based on their specific tissue characteristics and locations in soft tissues.

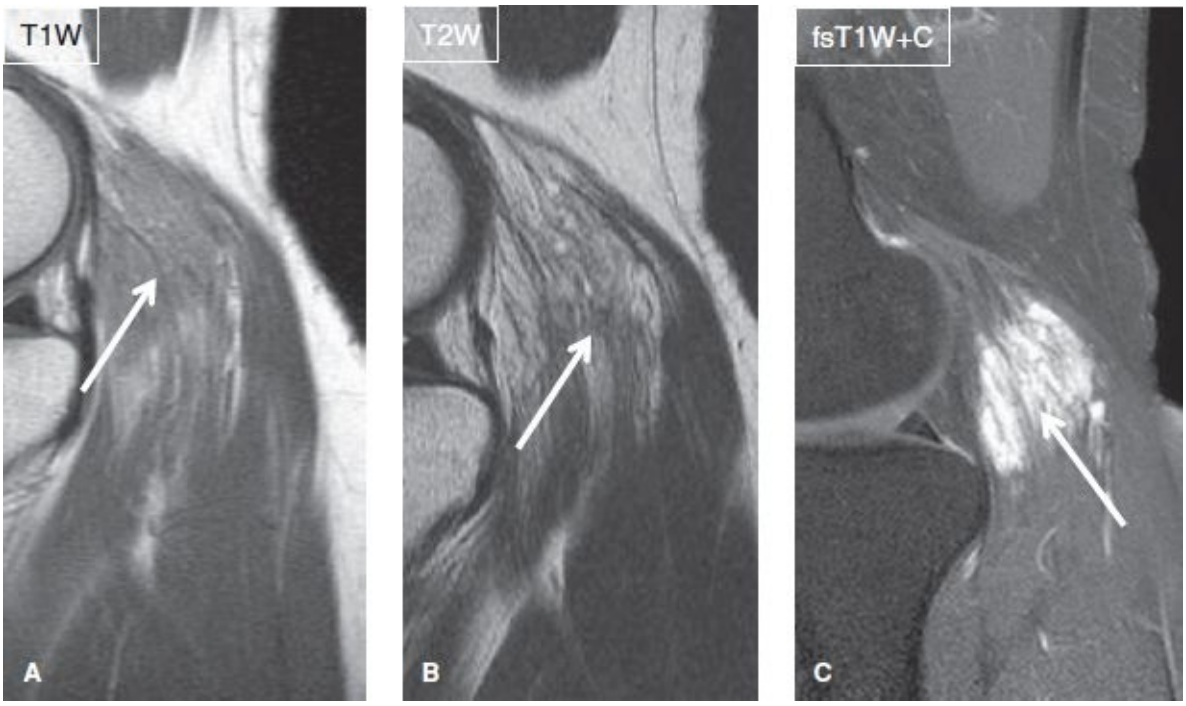

Fig. 2: Intramuscular hemangioma in a 27-year-old woman, who presented with a tender mass in the popliteal region. Sagittal images. **A, B:** The noncontrast images demonstrate multiple linear strandy areas of fat signal (*arrows*) within the gastrocnemius muscle with bubbly hyperintensities, without associated architectural distortion or other aggressive features. **C:** The postcontrast image reveals an intensely enhancing lesion (*arrow*), compatible with intramuscular hemangioma. (Courtesy of Dr. Okwha Kim, South Korea.)

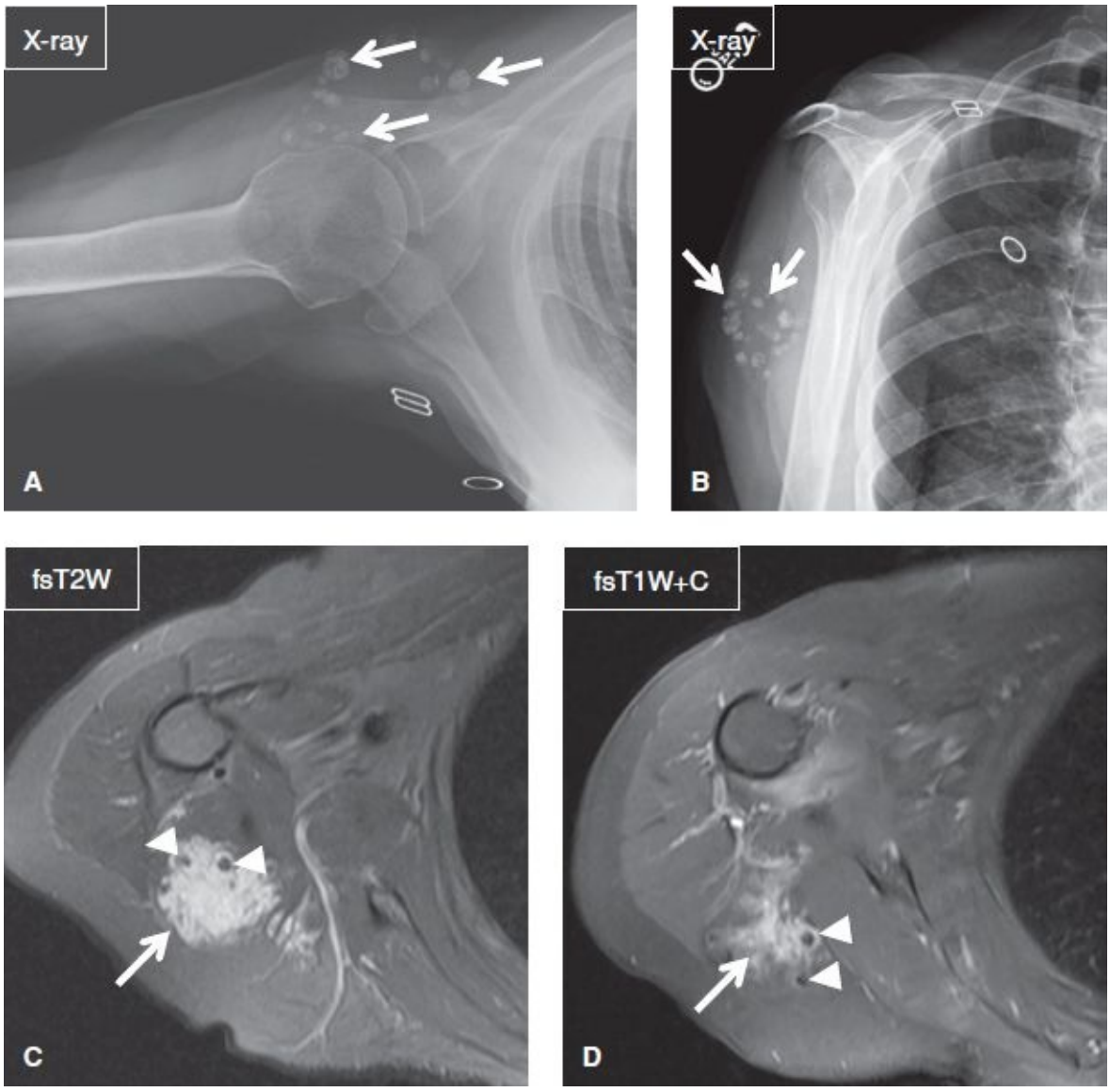

Fig. 3: Venous malformation in a 65-year-old woman. Axial view **(A)** and scapular Y view **(B)** radiographs of the right shoulder reveal multiple ovoid and punctuate calcifications (*arrows*) within the soft tissues of the posterior aspect of the shoulder. On the corresponding axial MR images **(C, D),** the lesion (*arrows*) appears well-defined, partially intramuscular and consists of multiple T2 hyperintense lobules including flow voids (*arrowheads*), and demonstrates serpiginous contrast enhancement.

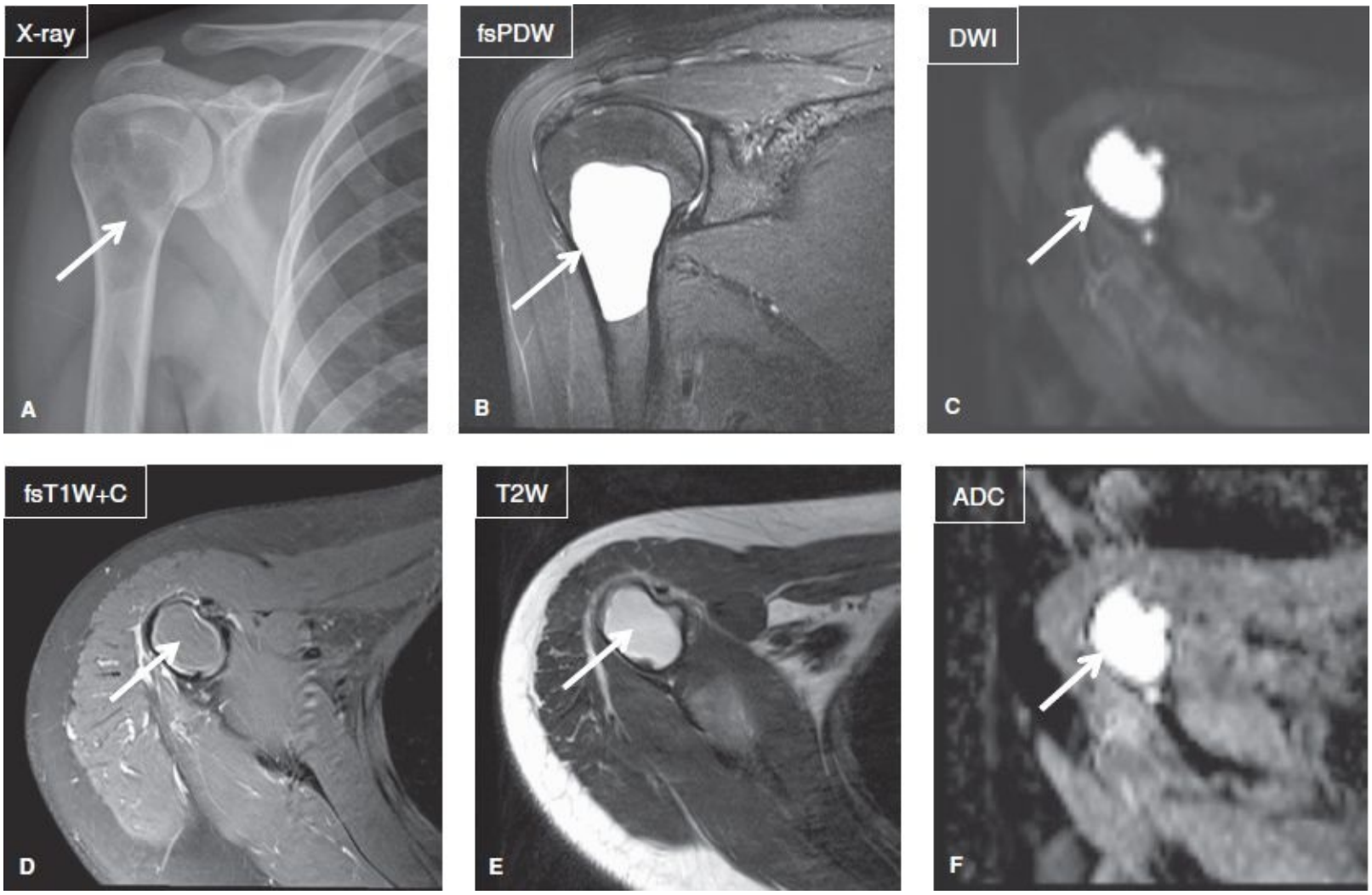

Fig. 4: Unicameral (simple) bone cyst in a 26-year-old woman. Anteroposterior radiograph **(A)** demonstrates a radiolucent lesion (*arrow*) with narrow zone of transition in the proximal humerus. On the corresponding coronal **(B)** and axial **(D, E)** MR images, the lesion (*arrows*) appears well defined, cystic, and nonenhancing. On quantitative imaging **(C, F),** the lesion (*arrows*) shows high ADC—2.5 $\times$ 10^{-3} mm^2/s and increased signal on DWI due to T2 shine through, features, which indicate benignity.

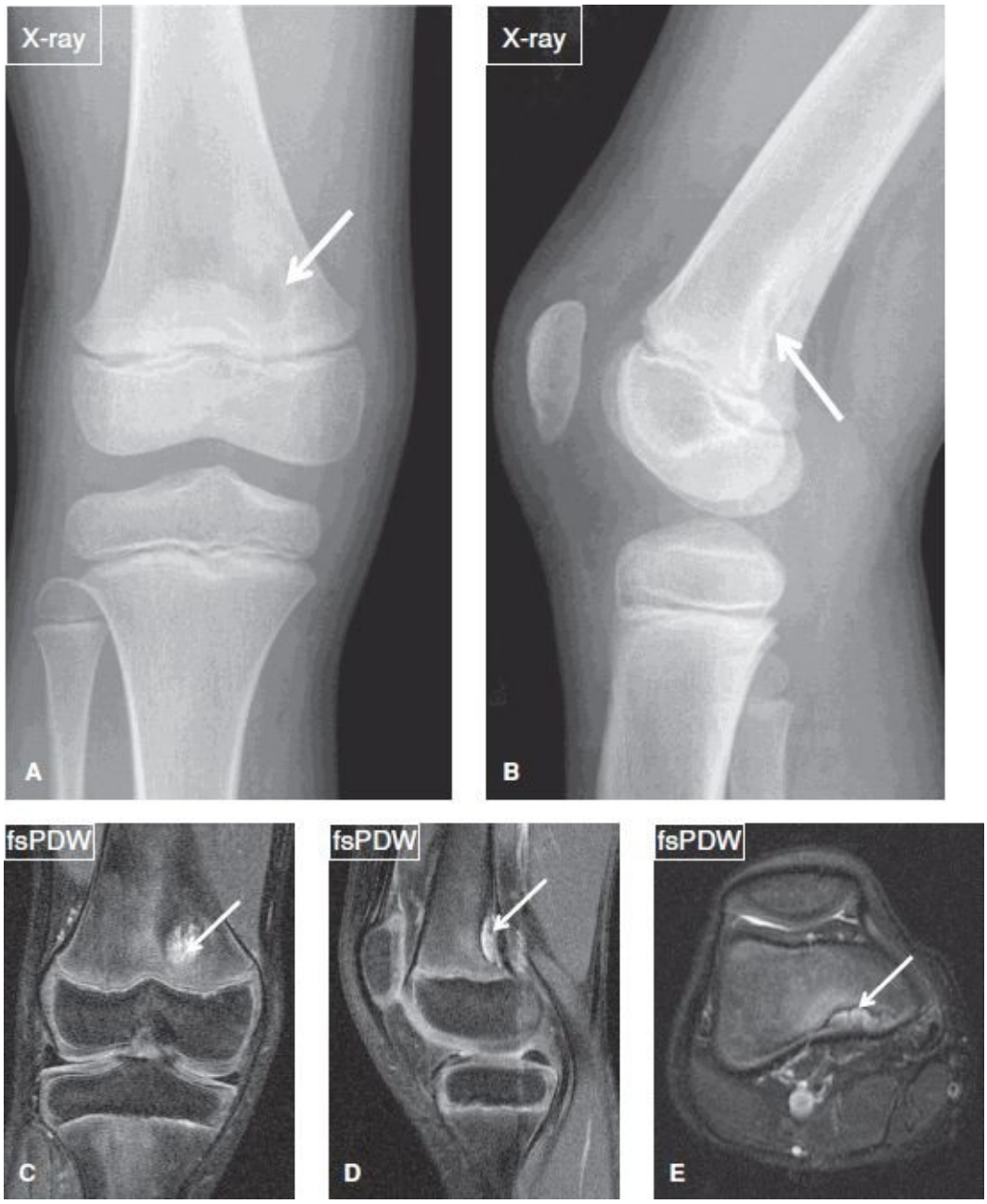

Fig. 5: Avulsive cortical irregularity (cortical desmoid). Anteroposterior **(A)** and lateral **(B)** radiographs of the knee reveal a saucer-shaped radiolucent cortical irregularity (*arrows*) involving the posteromedial aspect of the distal femoral metaphysis. On the respective coronal **(C),** sagittal **(D),** and axial **(E)** MR images, the area of irregularity (*arrows*) is T2 hyperintense and corresponds to the attachment of the adductor magnus tendon. Cortical desmoid belongs to the skeletal “don’t touch” lesions.

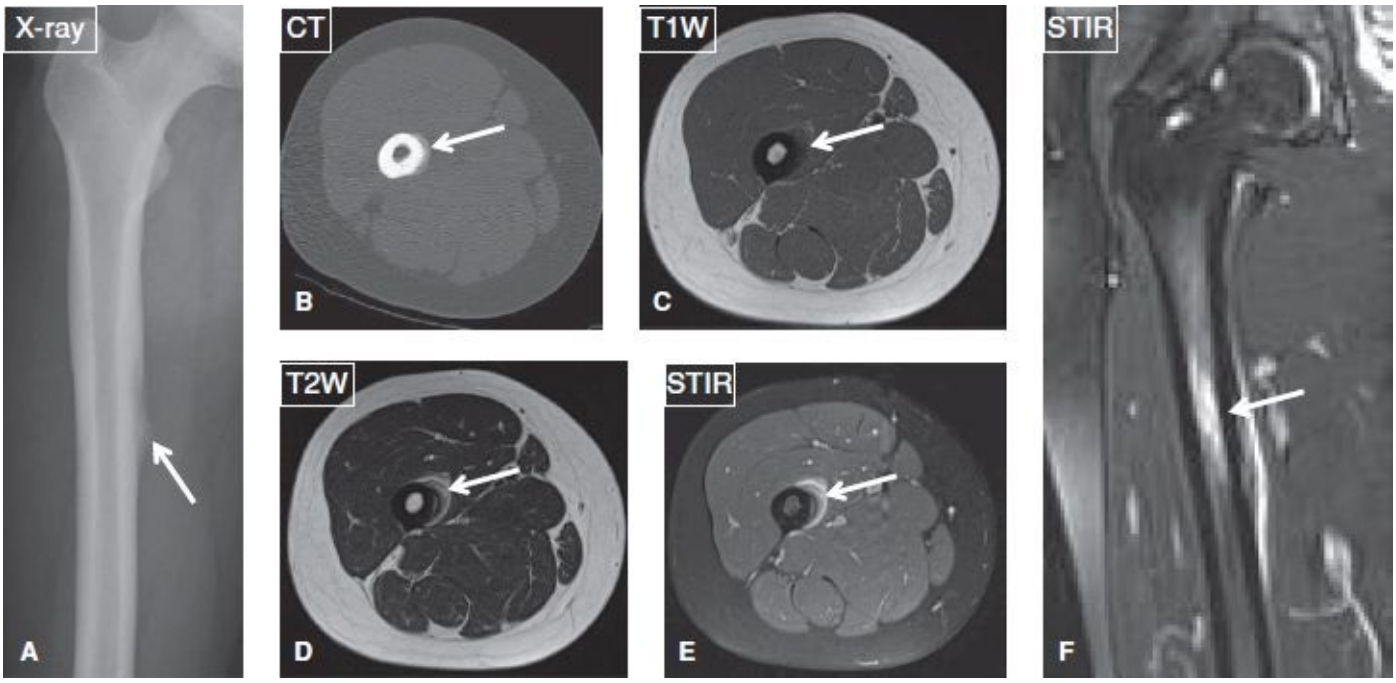

Fig. 6: Adductor insertion avulsion syndrome (thigh splint) in a 19-year-old woman ballet dancer, who presented with right thigh pain since 1 month. **A:** Anteroposterior radiograph shows focal periosteal reaction at the medial femoral shaft near the insertion of the adductor tendons (*arrow*). **B:** The periosteal reaction (*arrow*) is better delineated on the axial CT image. The respective axial **(C–E)** and coronal **(F)** MR images show linear hyperintensity and contrast enhancement (*arrows*), indicative of edema and hyperemia, respectively, along the medial aspect of the femoral shaft.

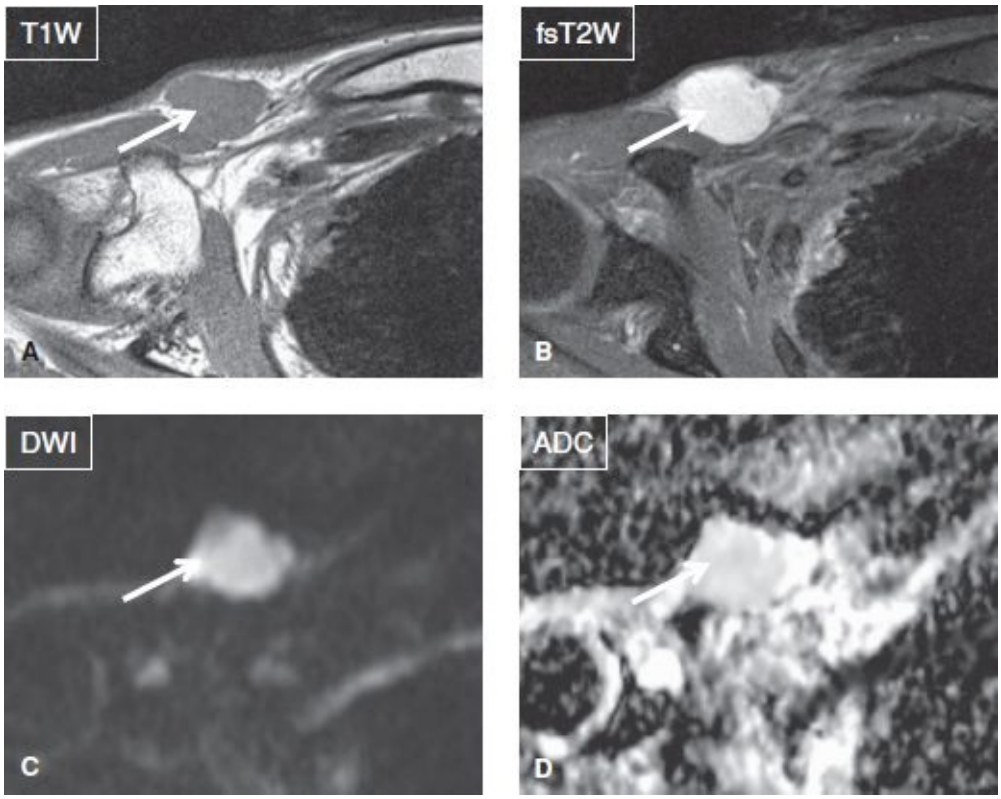

Fig. 7: Indeterminate lesion. Solid palpable mass in a 49-year-old female. Axial images demonstrate a well-defined mass (*arrows*) of homogeneous T1 isointense and homogeneous T2 hyperintense signal. Notice hyperintensity on DWI with high ADC value (1.8×10^{-3}

mm2/s). Final biopsy diagnosis was well-differentiated myxoid liposarcoma.

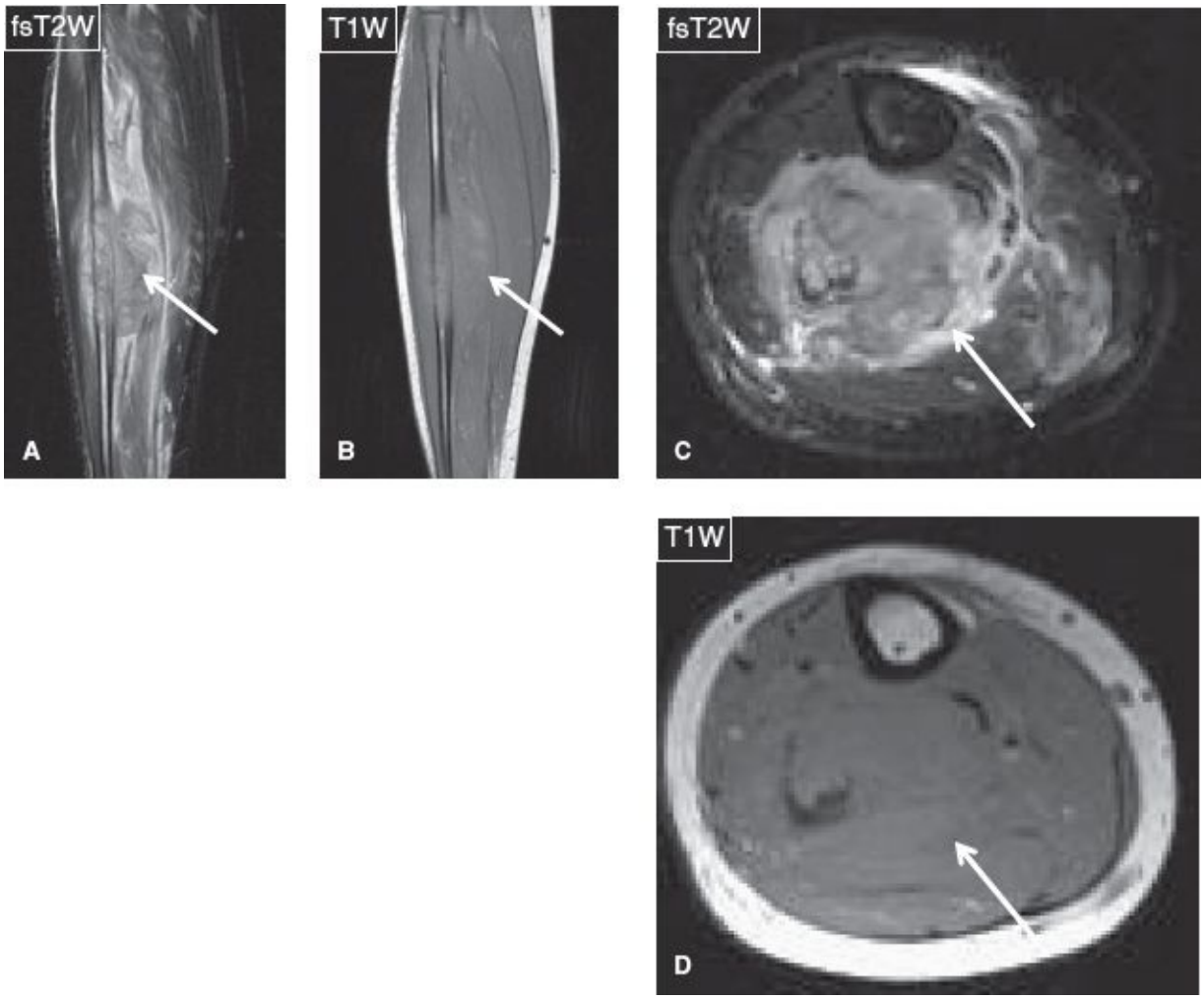

Fig. 8: Osteosarcoma. Coronal **(A, B)** and axial **(C, D)** images of the calf demonstrate an ill-defined mass (*arrows*) of marked heterogeneous signal and contrast enhancement, which emanates from the fibula and infiltrates the adjacent soft tissues.

HOW TO FILL THE STRUCTURED REPORT

Markers have been [<placed> <not placed>] at the site of concern.

It is important that the technologist places markers on the painful and/or palpable bony or soft tissue findings. Thereby, if a large area is imaged, it becomes easier for the reader to identify the lesion, even if the latter is subtle or relatively obscure. This is particularly helpful if the lesion merely represents a palpable unencapsulated fat lobule or skin lesion.

TABLE 1: The MR imaging features, which assist in differentiating between malignant and benign musculoskeletal lesions*a*

Features Indicating Indeterminate or Malignant Entity	Features Indicating a Benign Entity
Heterogeneous signal alterations	Homogeneous signal alterations
Large size (>4–5 cm)	Small size (<2–3 cm)
Periosteal mass and relative lack of fascial edema	Linear periosteal reaction and marked fascial edema or fluid collection
Involvement of multiple compartments	Involvement of a single compartment
Soft tissue mass (in bone lesions)	Intralesional fluid and/or fluid–fluid levels
Solid, thick peripheral nodular or central enhancement	None or thin peripheral enhancement
Unilateral patchy bone marrow infiltration with iso- or hypointense T1 signal alteration relative to skeletal muscle	Bilateral/symmetric bone marrow infiltration with high T1 signal or dark signal on both T1 and fsT2W images
Low ADC value: $<1.5 \times 10^{-3}$ mm^2/s $<1.1 \times 10^{-3}$ mm^2/s is highly suggestive of malignancy	High ADC value: $>1.5 \times 10^{-3}$ mm^2/s
Fast and early uptake and/or wash out of contrast	Slow and gradual contrast uptake and/or persistent enhancement

[a]Imaging findings given in table are a guide and not the rule.

TABLE 2: Differential diagnosis of benign soft tissue lesion based on tissue and specific location characteristics[a]

Points to Consider Regarding the Lesion in Question	Entities to Consider
Could it be a normal structure?	Accessory, supernumerary, or anomalous muscle; muscle strain; muscle hernia; and unencapsulated fat tissue
Does it have fluid?	Hematoma, seroma, ganglion cyst or myxoma, intramuscular cyst, geyser phenomenon, Morel-Lavallée lesion, and abscess
Does it have fat?	Lipoma, hemangioma, angiolipoma, elastofibroma, heterotopic ossification, neural fibrolipomatous hypertrophy, lipoma arborescence, lipoblastoma in children
Does it have prominent areas of T2 hypointensity?	Fibroma, fibromatosis, soft tissue callus, and calcium hydroxyapatite deposition disease
Is it located within or adjacent to a joint?	Synovial chondromatosis, pigmented villonodular synovitis, ganglion cyst or geyser phenomenon, loose body, synovial hemangioma, lipoma arborescens, and particle disease
Is it related to a tendon or ligament?	Giant cell tumor, hydroxyapatite deposition disease, amyloid, gout, and xanthoma
Is it a predominantly vascular abnormality?	Venous malformation, arteriovenous malformation, hemangioma, and lymphatic malformation
Is it a nerve-related abnormality?	Peripheral nerve sheath tumor, fibrolipomatous hamartoma, and perineurioma

[a]These entities should be considered and excluded, before reporting the soft tissue lesion as indeterminate or potentially malignant.

Size: [<>] × [<>] × [<>] cm

Generally, the larger the size of the lesion, the more are the chances that it is ominous or malignant (Fig. 9). A few exceptions to this rule include clear fat-containing lipoma, fibrolipomatous hypertrophy of the nerve, fluid-containing lesions, vascular malformations and fascial fibrous lesions, such as fibromatosis or desmoid (Figs. 10–12). Some benign lesions are associated with elongated bizarre-shaped lesions with or without cortical deformity and thickening, such as in fibrous dysplasia, neurofibromatosis, and Paget disease (Figs. 13–15). The above lesions have other characteristics that aid in the diagnosis such as young age, relative epiphyseal sparing unless associated with McCune Albright syndrome, cortical thickening and remodeling and mixed marrow signal changes and cystic changes with regions of T2 darkening in fibrous dysplasia; cutaneous stigmata, genetic markers, bony pseudoarthrosis, target and tail signs within the tumors and multiple NOFs in neurofibromatosis; predominant cortical/subcortical involvement and thickening with fibrofatty marrow changes, bone expansion and trabecular thickening, and predisposition among elderly Caucasian males in Paget disease.

Fig. 9: Large mass: Synovial sarcoma. Coronal **(A, B)** and axial **(C, D)** images show a markedly enhancing T2 heterogeneous lesion (*arrows*) infiltrating the soft tissues of the medial aspect of the hindfoot and midfoot, including the tarsal tunnel.

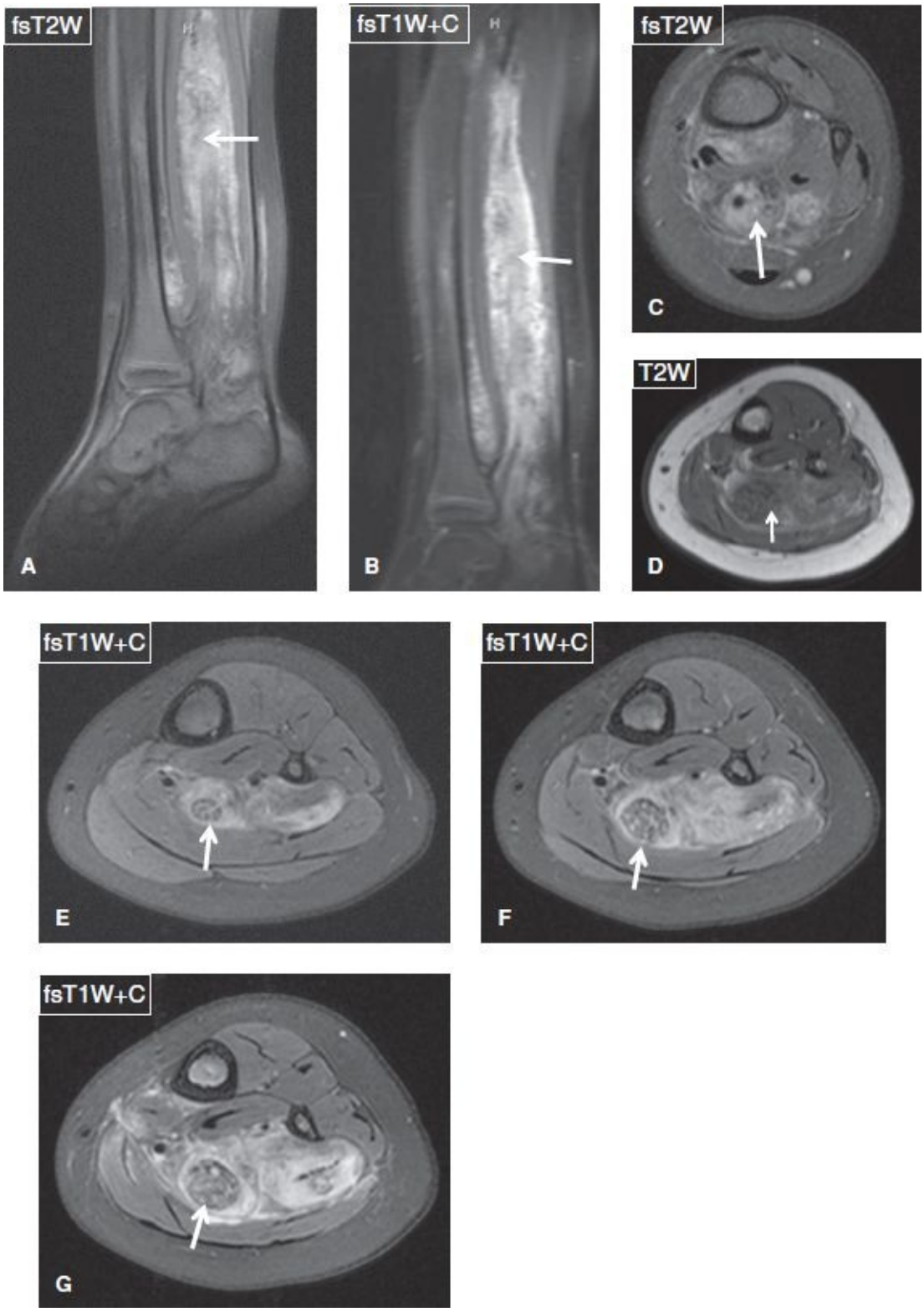

Fig. 10: Fibrolipomatous hamartoma (new name: lipomatosis of nerve, WHO 2013 classification): Noncontrast sagittal **(A)** and axial **(C, D),** and postcontrast sagittal **(B)** and axial **(E–G)** images show extensive fibrofatty hypertrophy of the tibial nerve (*arrows*) along with a vascular malformation in this otherwise benign developmental entity of fibrolipomatous hypertrophy. Notice coaxial cable appearance of the tibial nerve on the axial postcontrast images, classic for this entity.

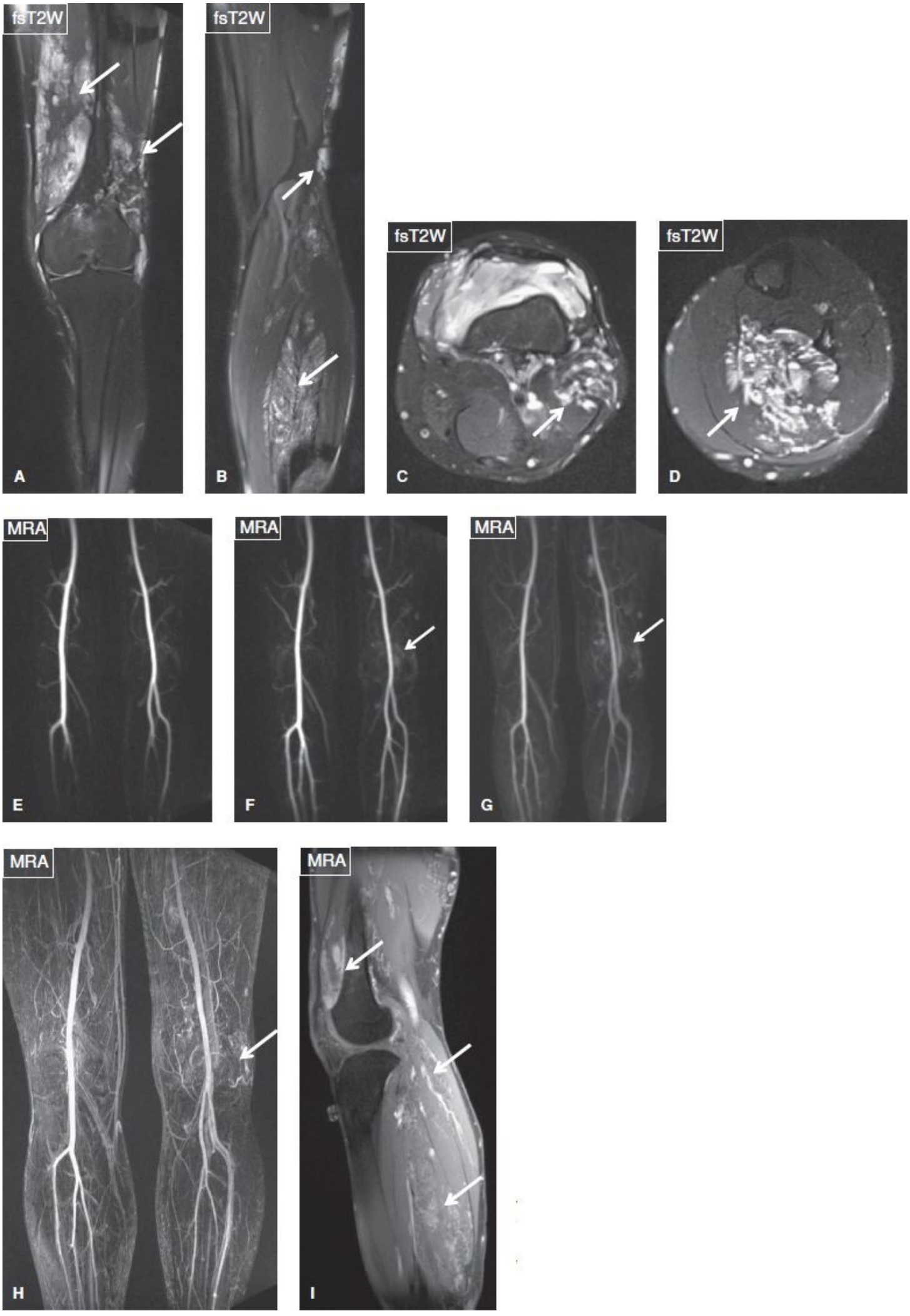
fsT2W
fsT2W
fsT2W
fsT2W
A
B
C
D
MRA
MRA
MRA
E
F
G
MRA
MRA
H
I

Fig. 11: Whole-leg venous malformation in a 25-year-old man. Coronal **(A, B)** and axial **(C, D)** images show numerous dilated vessels (*arrows*) within the muscles and subcutaneous tissues of the lower extremity. **E–G:** Coronal images from time-resolved MR angiography using Ablavar show delayed filling of the dilated vessels in the venous phase (*arrows*) with no arterovenous shunting. **H–I:** The malformation (*arrows*) is depicted on delayed MR angiography images.

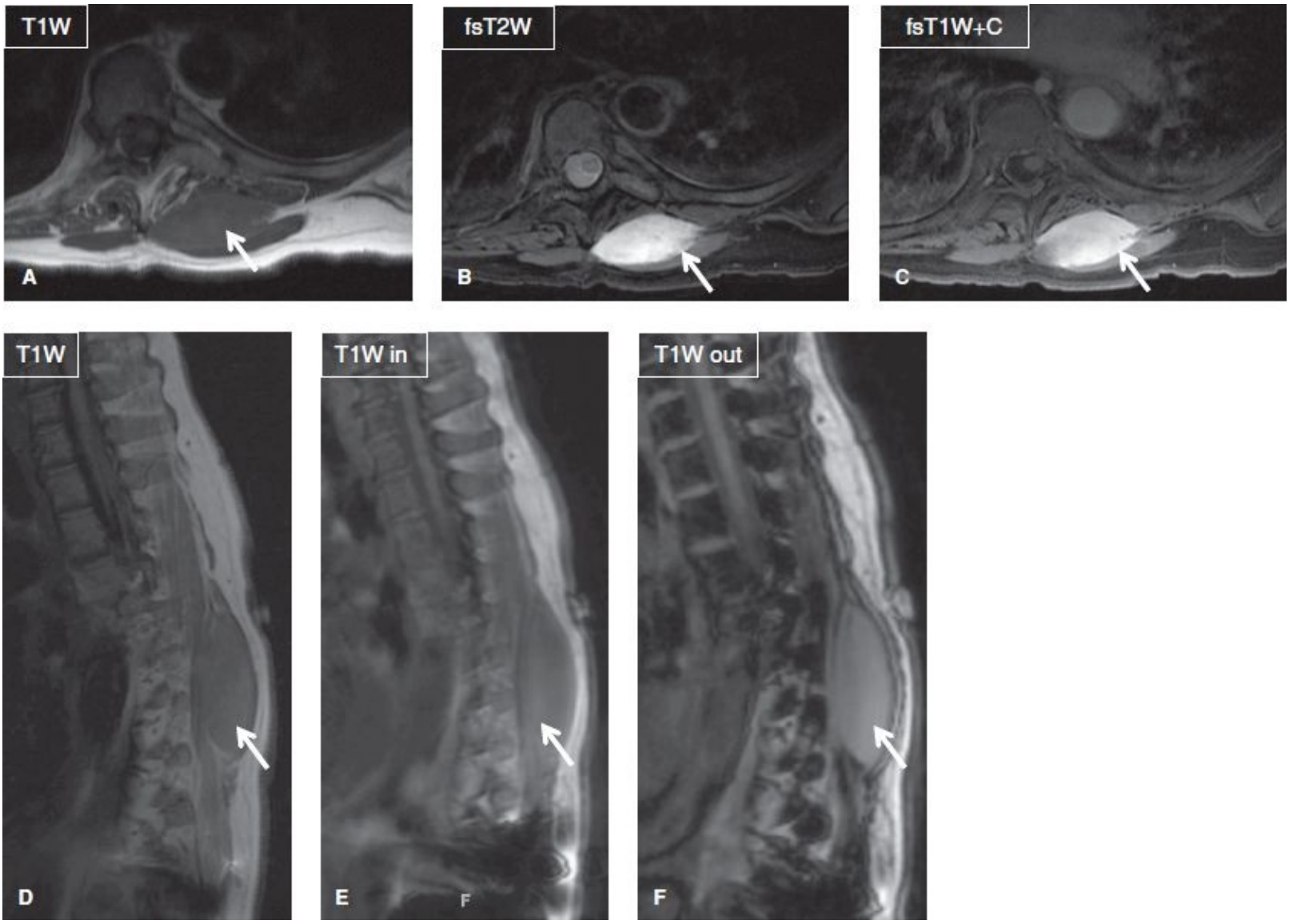

Fig. 12: Desmoid tumor in a 65-year-old woman. Axial **(A–C)** and sagittal **(D–F)** images exhibit a well-defined enhancing mass (*arrows*) of homogeneous intermediate T1 and high T2 signal within the paraspinal musculature. No loss of signal is seen within the lesion on out-of-phase images.

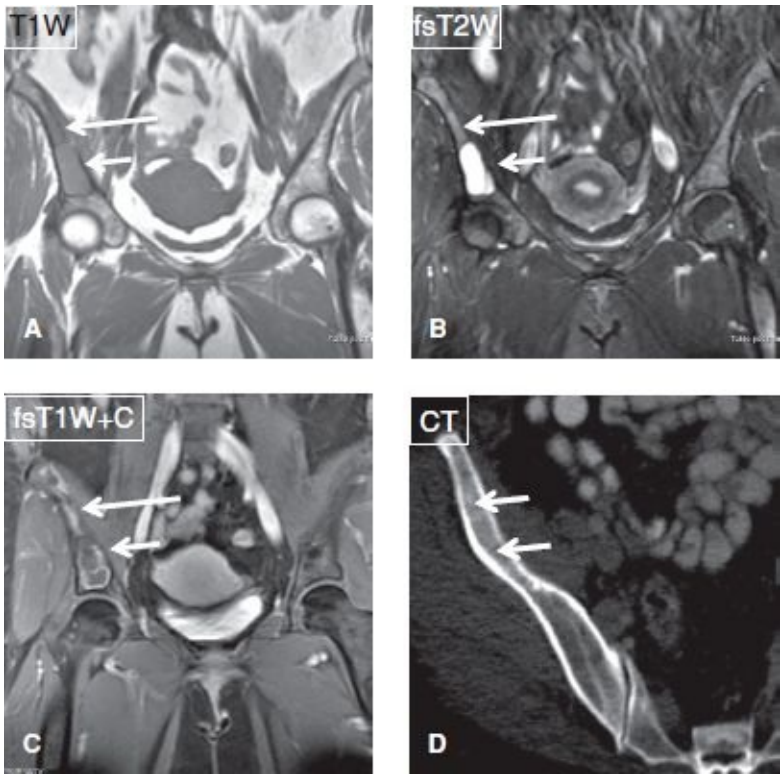

Fig. 13: Fibrous dysplasia in a 47-year-old woman. **A–C:** Coronal MR images show a lesion (*long arrows*) of intermediate T1 signal, mixed T2 signal, and peripheral enhancement involving the right iliac bone. A portion of the lesion (*short arrows*) is cystic. **D:** On axial CT scan, the lesion (*arrows*) features the typical ground-glass appearance of this entity.

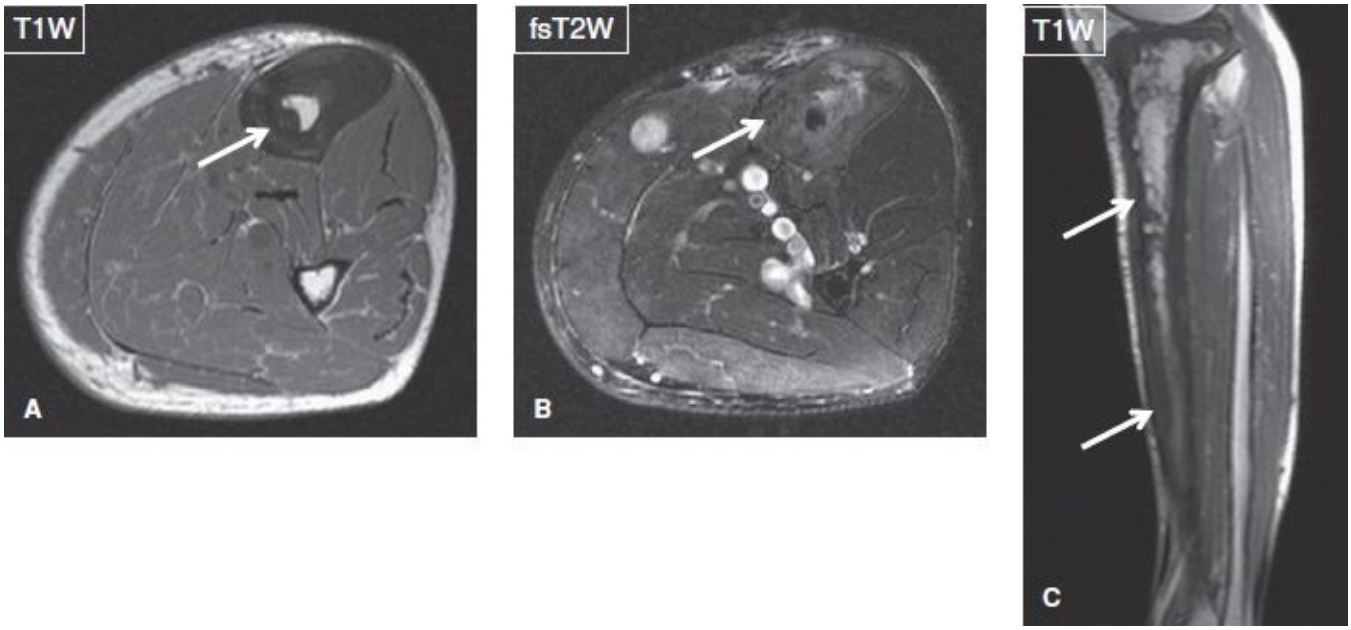

Fig. 14: Paget disease. Axial **(A, B)** and sagittal **(C)** images exhibit diffuse cortical thickening (*arrows*) and enlargement of the tibia with internal fibrofatty proliferation.

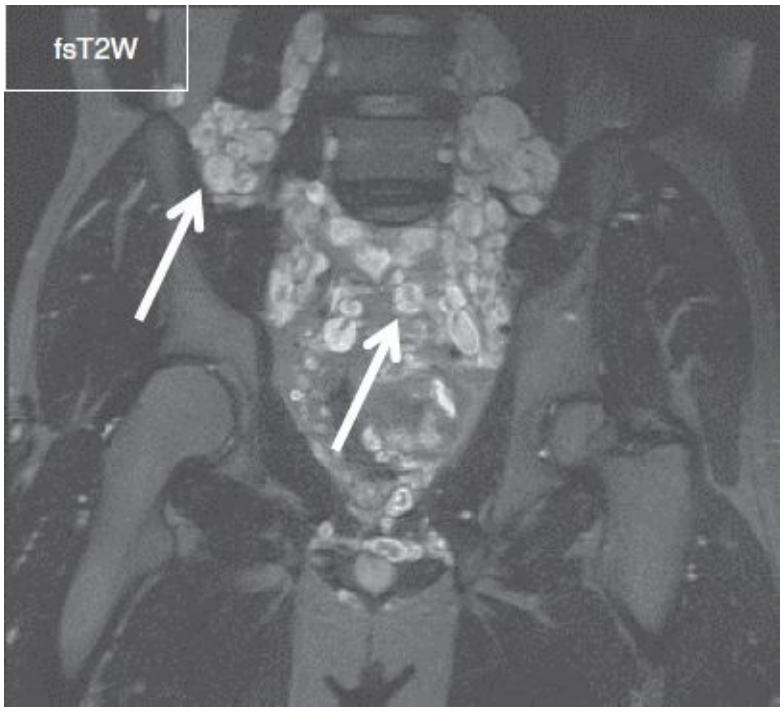

Fig. 15: Neurofibromatosis type I. Coronal image at the level of the pelvis demonstrates numerous ovoid T2 hyperintense lesions with target signs (*arrows*), which correspond to neurofibromas in this patient with extensive neurofibromatosis ("bag-of-worms" sign).

Location: [< >]

Location is very important for both bone and soft tissue lesions (e.g., malignancy almost never occurs within the joints with rare exceptions (Fig. 16), and in nearly all circumstances mass-like intra-articular lesions represent benign synovial processes) (Fig. 17).

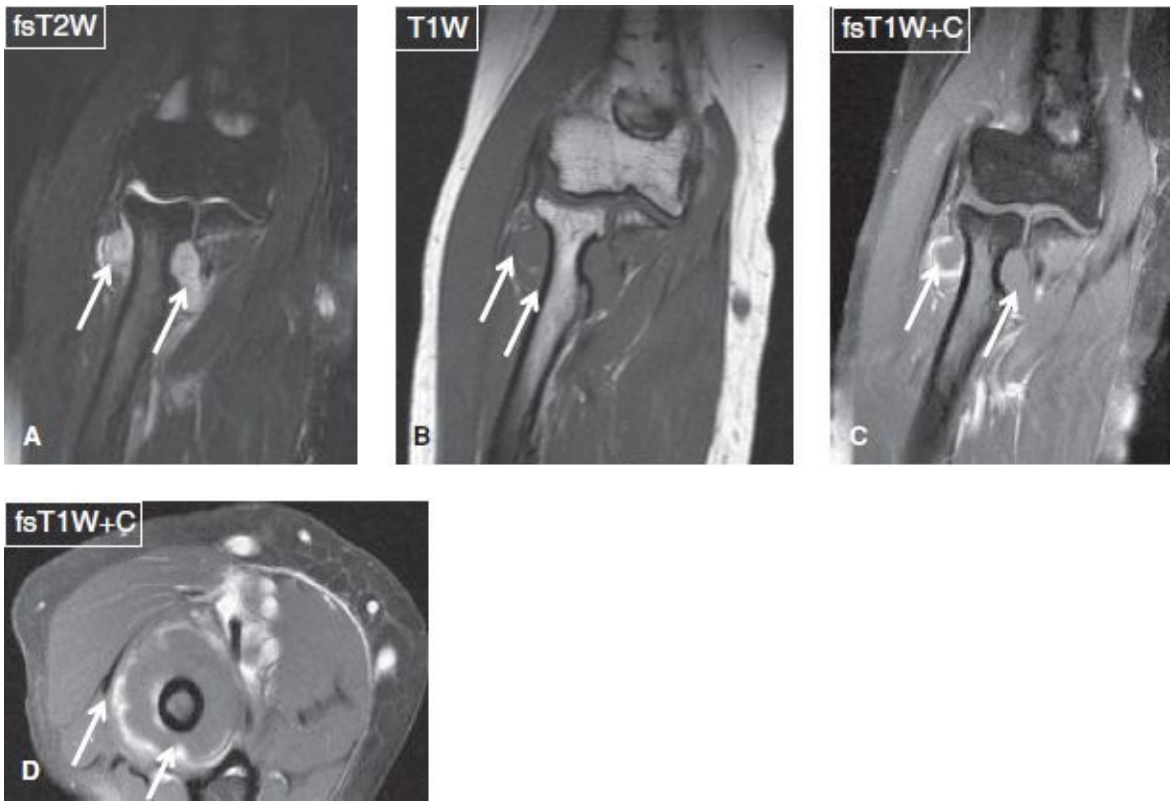

Fig. 16: Synovial chondrosarcoma in a middle-aged woman with a recent history of

palpable mass around the right elbow. Coronal **(A–C)** and axial **(D)** images show lobulated mass (*arrows*) in the proximal radioulnar joint causing eccentric bony erosions and encircling the radius neck with peripheral nodular enhancement.

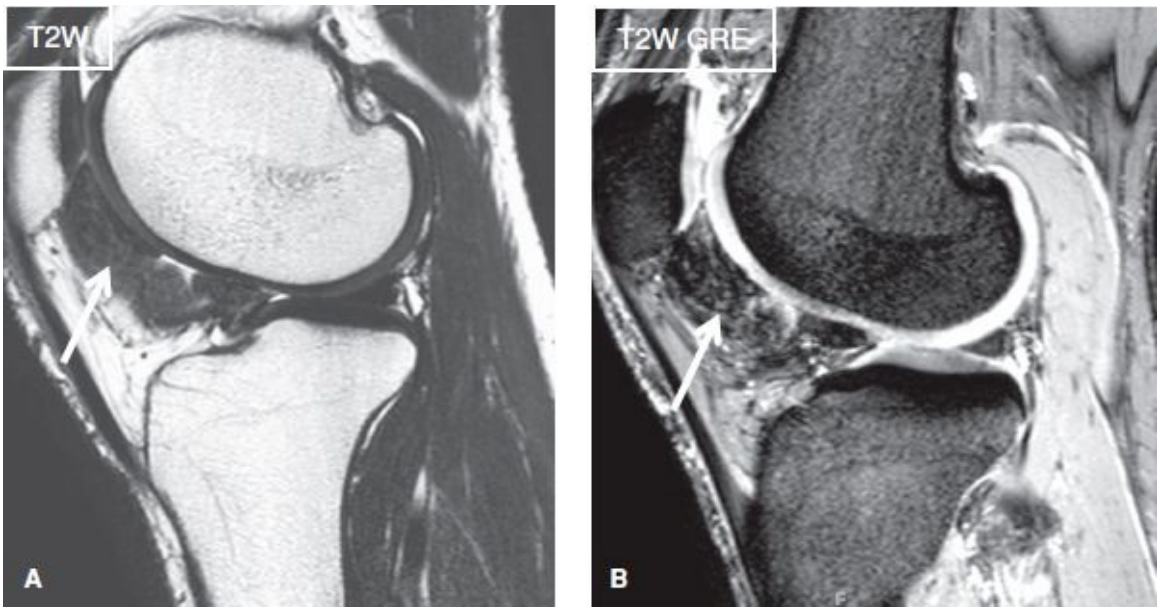

Fig. 17: Pigmented villonodular synovitis in a 45-year-old female. Sagittal images **(A, B)** show a hypointense amorphous lesion (*arrows*) at the posterior aspect of Hoffa fat pad, which corresponds to hemosiderin laden synovial mass. The signal is particularly evident on the gradient-echo image. Findings consistent with PVNS (new name: Tenosynovial giant cell tumor diffuse type, WHO 2013 classification).

Let's discuss bony lesions first. Since metaphysis is the portion with the richest vascularity in long bones, most tumors start or eventually lodge in this location. Therefore, what could help the reader in the differential diagnosis would be the lesion epicenter preference in other areas. In children, lesions involving the epiphyses (or apophyses) include eosinophilic granuloma, subchondral cyst, and chondroblastoma. In adults, lesions involving the epiphyses include giant cell tumor (GCT, extending from the metaphysis after physeal fusion), clear cell chondrosarcoma, myeloma, metastasis, subchondral cyst (geode), and lipoma (Figs. 18–22). Lesions involving the diaphyses include osteoid osteoma, fibrous dysplasia, enchondroma, Ewing sarcoma, metastasis, myeloma, adamantinoma (in the tibia), lymphoma, and eosinophilic granuloma (mnemonic: O FEMALE) (Figs. 23, 24).

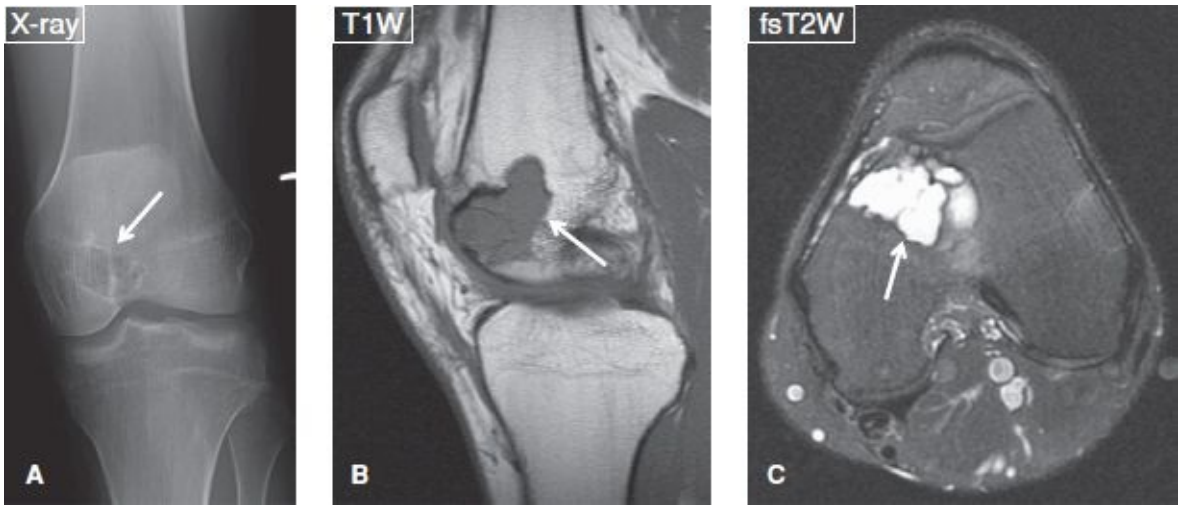

Fig. 18: Chondroblastoma. Anteroposterior radiograph **(A)** reveals a well-defined lytic lesion (*arrow*) with thin sclerotic margins at the femoral epiphysis. On the corresponding sagittal **(B)** and axial **(C)** MR images, the lesion (*arrows*) demonstrates lobulated margins and homogeneous fluid-like signal. Notice associated bone marrow edema, quiet common with chondroblastoma.

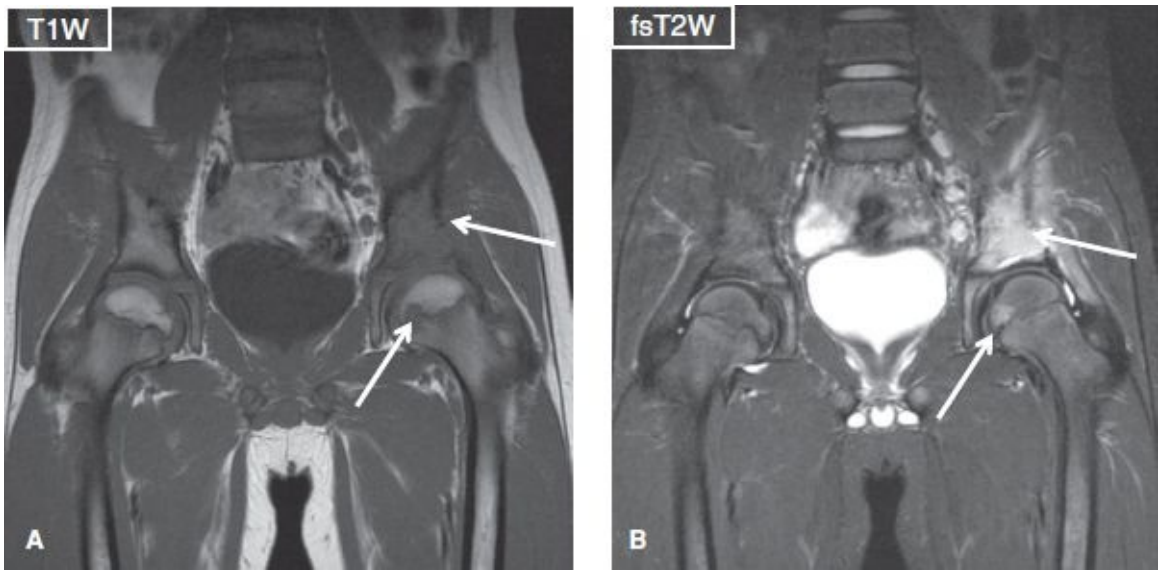

Fig. 19: Eosinophilic granuloma. Coronal images exhibit homogeneous T1 isointense/T2 hyperintense lesion (*arrows*) involving a large area of the left acetabular roof and an additional focus of the ipsilateral femoral head. Notice fascial edema in active stage of the disease, not an uncommon finding, and it can mimic infection.

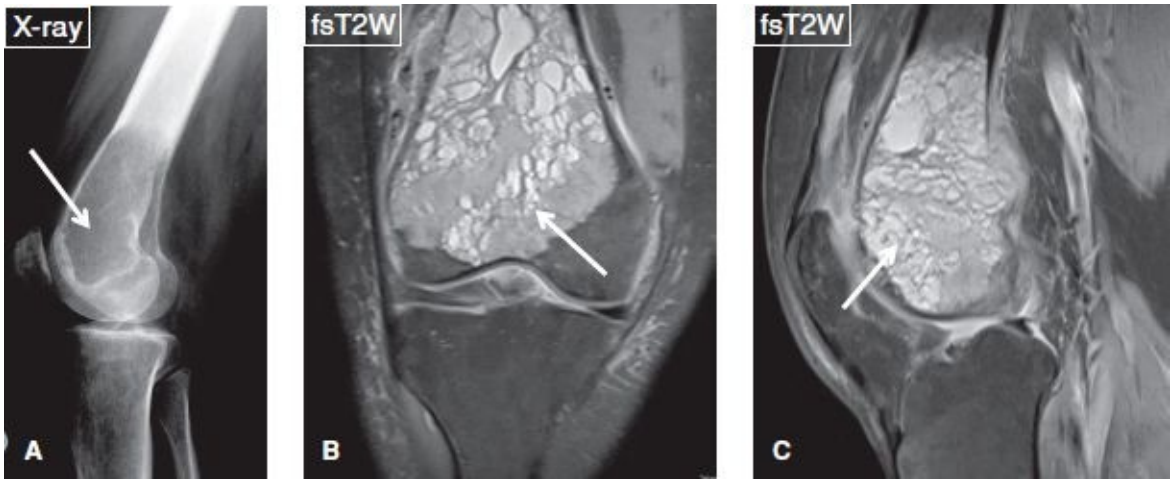

Fig. 20: Giant cell tumor in a 35-year-old woman. Lateral radiograph **(A)** of the knee displays a well-defined lytic lesion (*arrow*) without sclerotic margins at the distal femoral metaphysis extending into the epiphysis. The corresponding coronal **(B)** and sagittal **(C)** MR images reveal that the lesion (*arrows*) abuts the articular surface and appears heterogeneously T2 hyperintense to hypointense. Notice associated cortical permeation, not uncommon with this lesion.

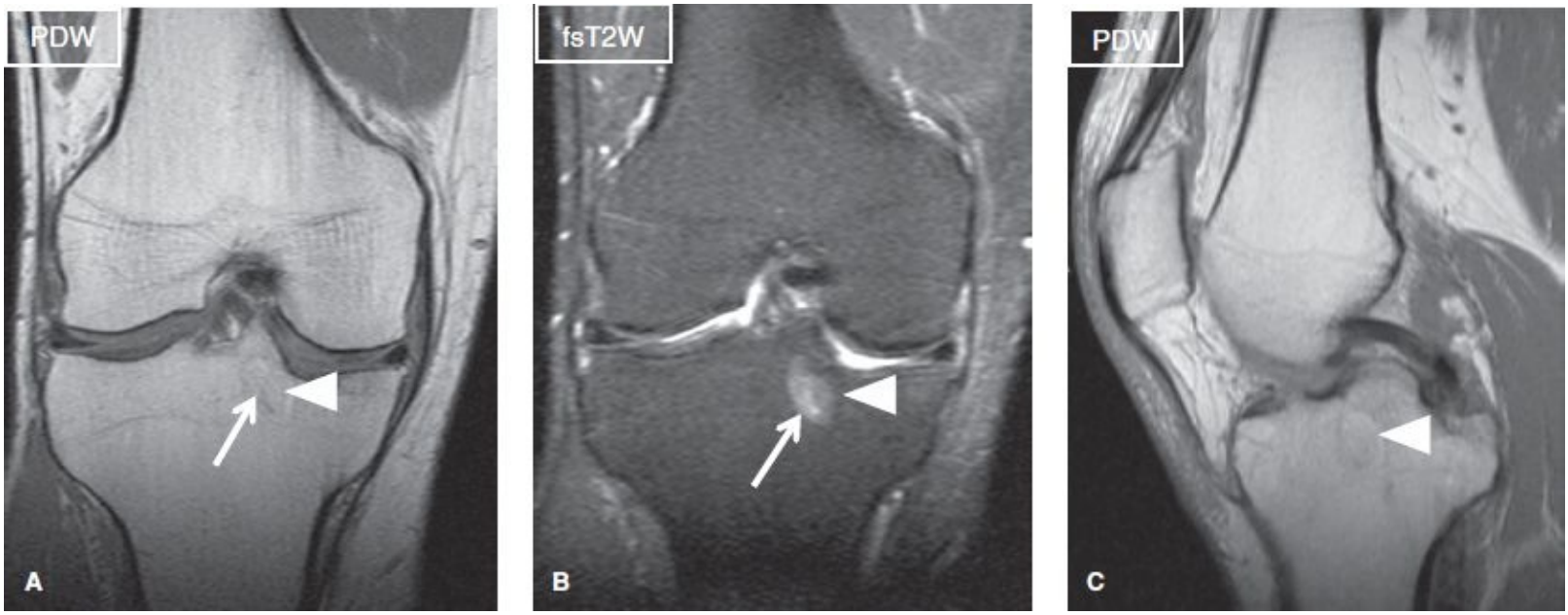

Fig. 21: Lipoma with cystic degeneration. Coronal **(A, B)** and sagittal **(C)** images demonstrate a well-defined lesion at the tibial epiphysis, which features partially fluid (*arrows*) and partially fat (*arrowheads*) signal.

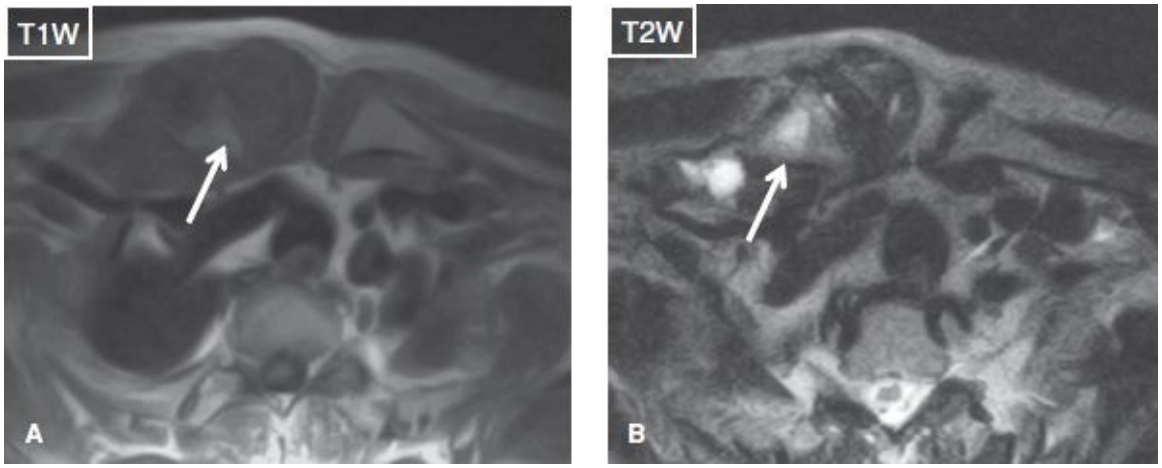

Fig. 22: Severe sternoclavicular joint osteoarthritis. Middle-aged patient presenting with palpable mass over the right sternoclavicular joint. Axial images exhibit significant capsular hypertrophy of the right sternoclavicular joint in the setting of severe osteoarthritis. Notice subchondral cysts in the right distal clavicle (*arrows*).

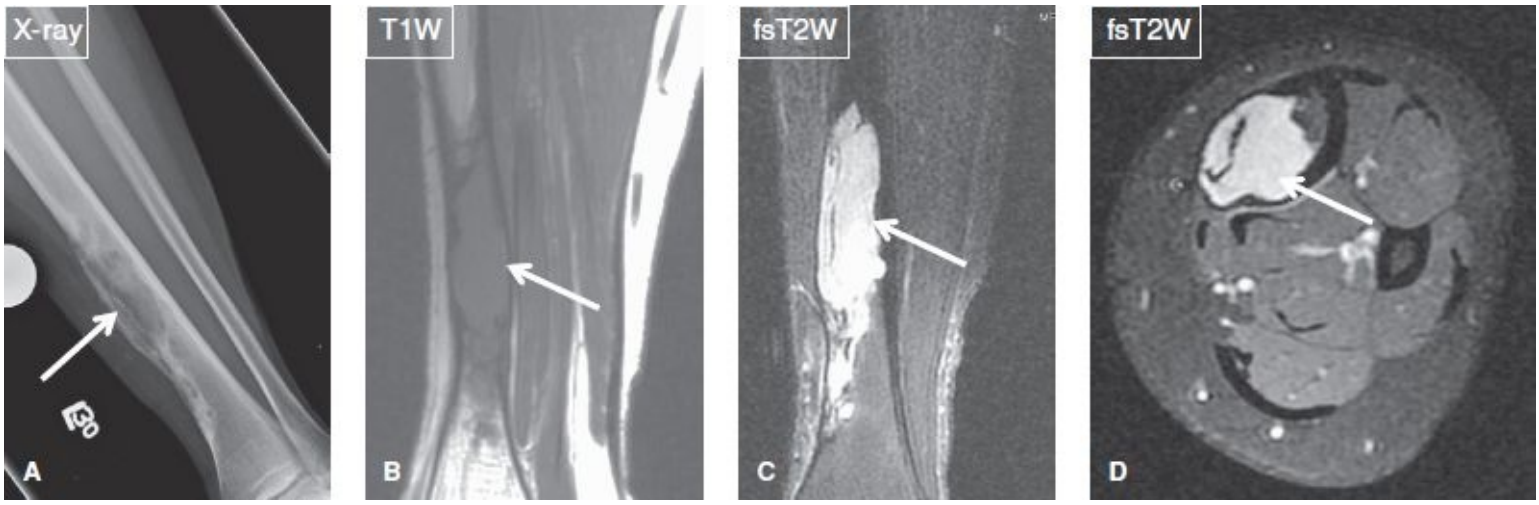

Fig. 23: Adamantinoma in a young woman. Anteroposterior radiograph **(A)** of the lower extremity demonstrates an aggressive lytic lesion (*arrow*) involving the distal tibial diaphysis. The corresponding coronal **(B, C)** and axial **(D)** MR images confirm the locally aggressive nature of the lesion (*arrows*), which appears solid, infiltrates the marrow and causes cortical erosion and bone enlargement.

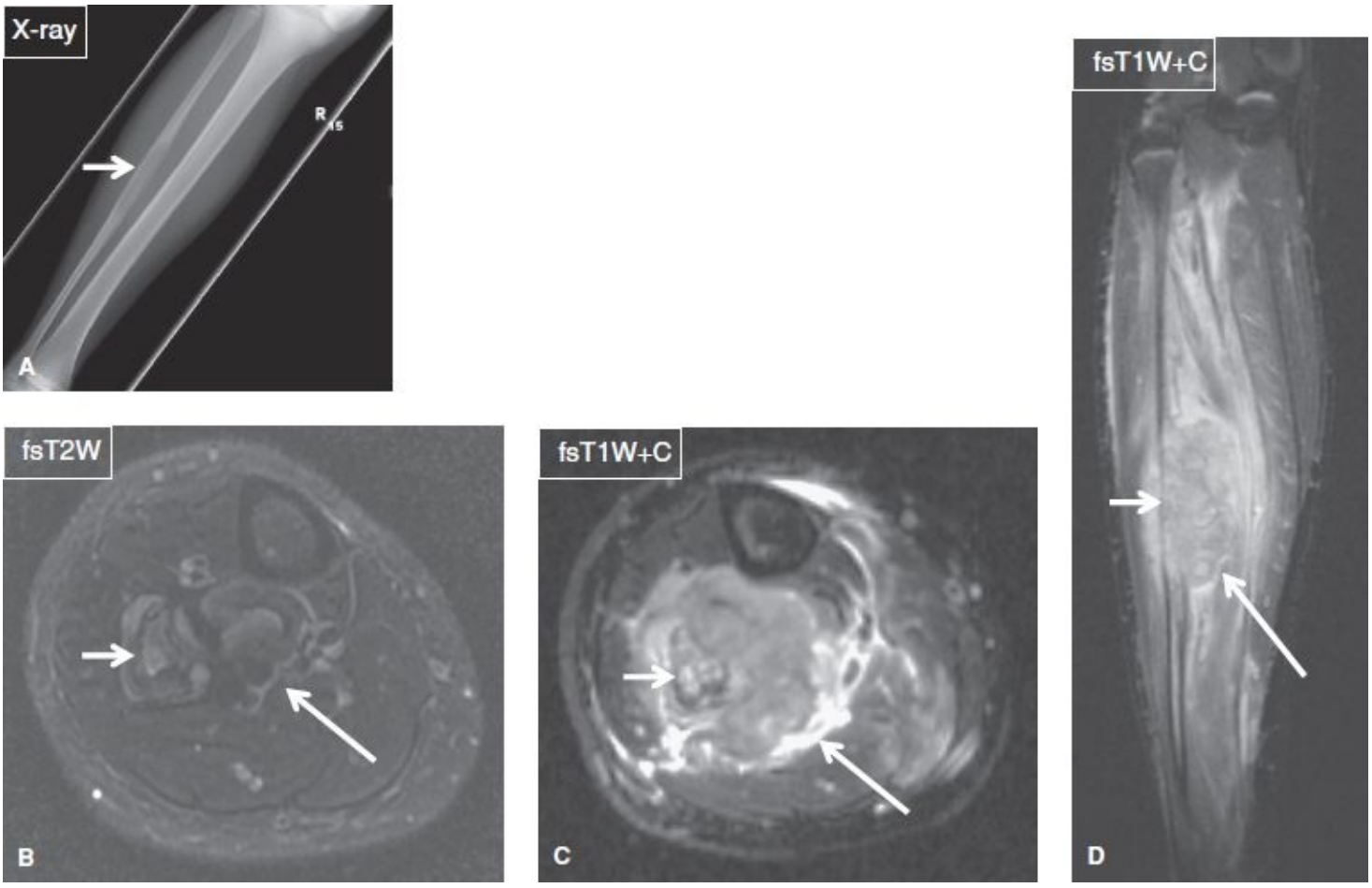

Fig. 24: Ewing sarcoma in a 12-year-old female. Anteroposterior radiograph **(A)** shows a lytic lesion (*arrow*) with wide zone of transition of the fibular diaphysis. Axial **(B, C)** and sagittal **(D)** MR images show a soft tissue mass (*long arrows*) of heterogeneous signal and contrast enhancement, which emanates from the (infiltrated) fibula (*short arrows*) and shows extracompartmental extension with encasement of the posterior tibial neurovascular bundle.

Lesions that classically and preferentially occur in the toes or fingers include Nora's lesion, glomus tumor, epidermoid cyst, enchondroma, brown tumor, metastasis from lung cancer (Figs. 25–30). In the spine, most lesions occur in predictable locations: GCT, plasmacytoma, benign notochordal tumor, chordoma and clear cell chondrosarcoma mostly involve the vertebral bodies; chordoma in the lower sacrum or the C2 vertebra; osteoid osteoma, osteoblastoma, and metastases in the pedicles; aneurysmal bone cyst (ABC) and chondrosarcoma in the posterior elements; and peripheral nerve sheath tumors and perineural cysts in and around the neural foramina (Figs. 31–41). Multiple posterior element involvement may be seen with chondrosarcoma, ABC, and tuberculosis (Fig. 42). A limited number of lesions can cross the joint capsule, include GCT, ABC, chondrosarcoma, and plasmacytoma. Finally, synovial sarcoma rarely arises in the joint, but it commonly occurs in para-articular locations.

Fig. 25: Nora lesion (bizarre periosteal osteochondromatous proliferation, BPOP) of finger. **A:** Lateral radiograph of the index finger shows aberrant periosteal and cortical thickening (*arrow*) of the distal phalanx as well as swelling of the surrounding soft tissues (*asterisk*). **B, C:** The respective sagittal MR images exhibit intensely enhancing T2 hyperintense subcutaneous tissues (*arrows*) at the distal phalanx, associated with marrow edema and enhancement.

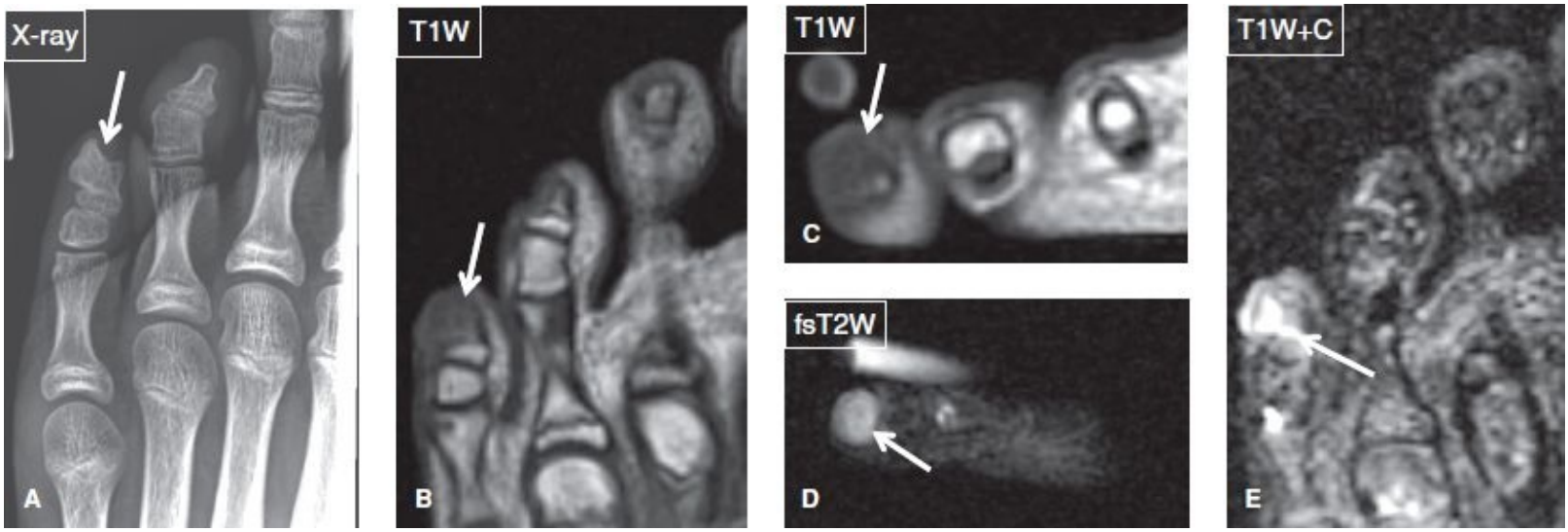

Fig. 26: Nora lesion (bizarre parosteal osteochondromatous proliferation) of little toe. Anteroposterior radiograph **(A)** of the forefoot shows a well-defined osseous proliferation (*arrow*) at the tip of the distal phalanx of the fifth toe. On the respective coronal **(B),** axial noncontrast **(C, D),** and coronal **(E)** postcontrast MR images, the lesion (*arrows*) shows intermediate T1 and high T2 signal with soft tissue and bone marrow edema and enhancement.

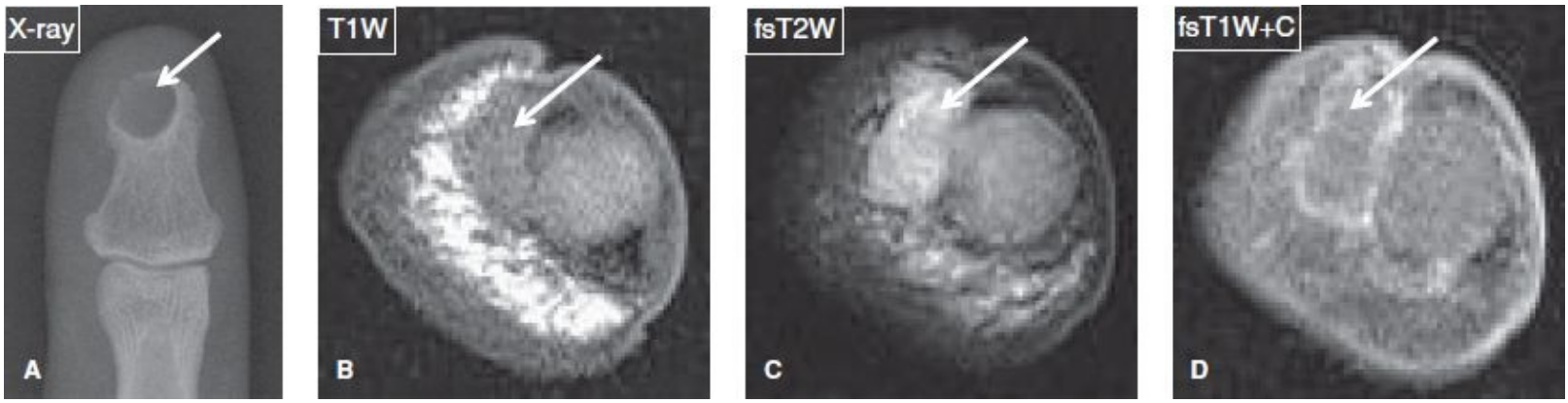

Fig. 27: Epidermoid cyst. **A:** Anteroposterior radiograph of the thumb demonstrates a well-defined lytic lesion (*arrow*) with narrow zone of transition at the tip of the distal phalanx. **B–D:** On the corresponding axial MR images, the lesion (*arrows*) shows fluid-like signal and thin peripheral enhancement.

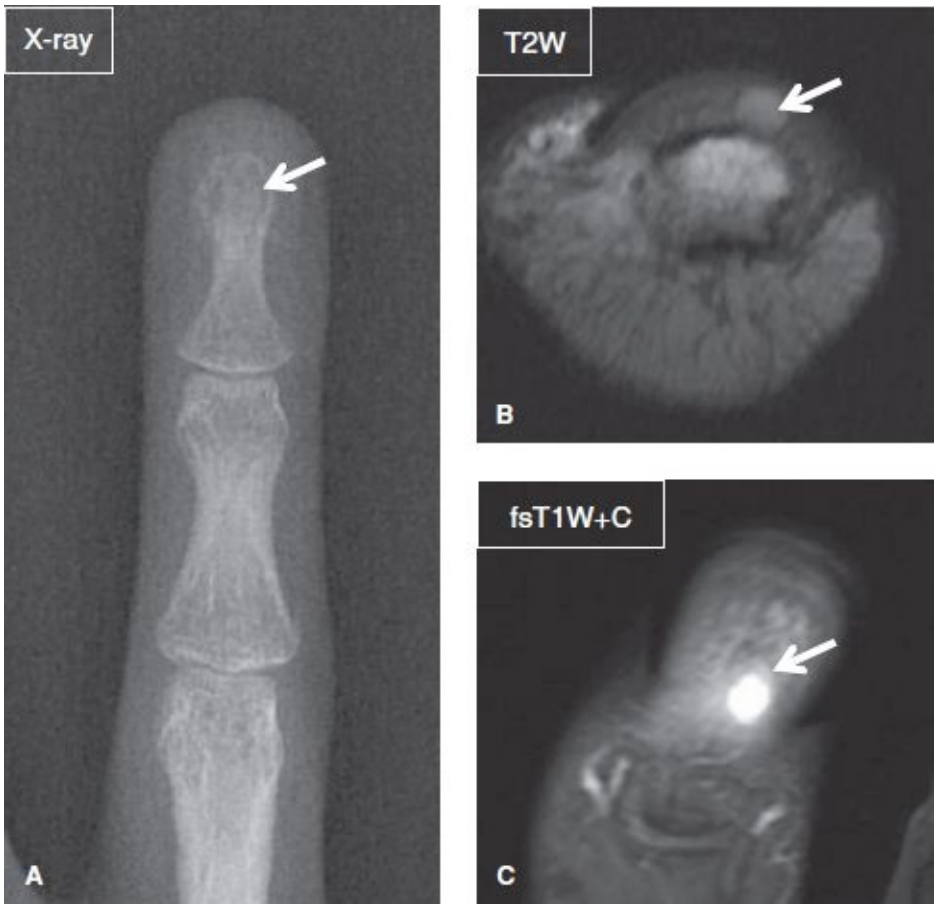

Fig. 28: Glomus tumor. Anteroposterior radiograph **(A)** demonstrates mild focal erosion (*arrow*) of the distal phalanx of the finger with soft tissue swelling. The respective axial **(B)** and coronal **(C)** MR images reveal a small ovoid intensely enhancing lesion (*arrows*) of high T2 signal, located between the nail and the distal phalanx.

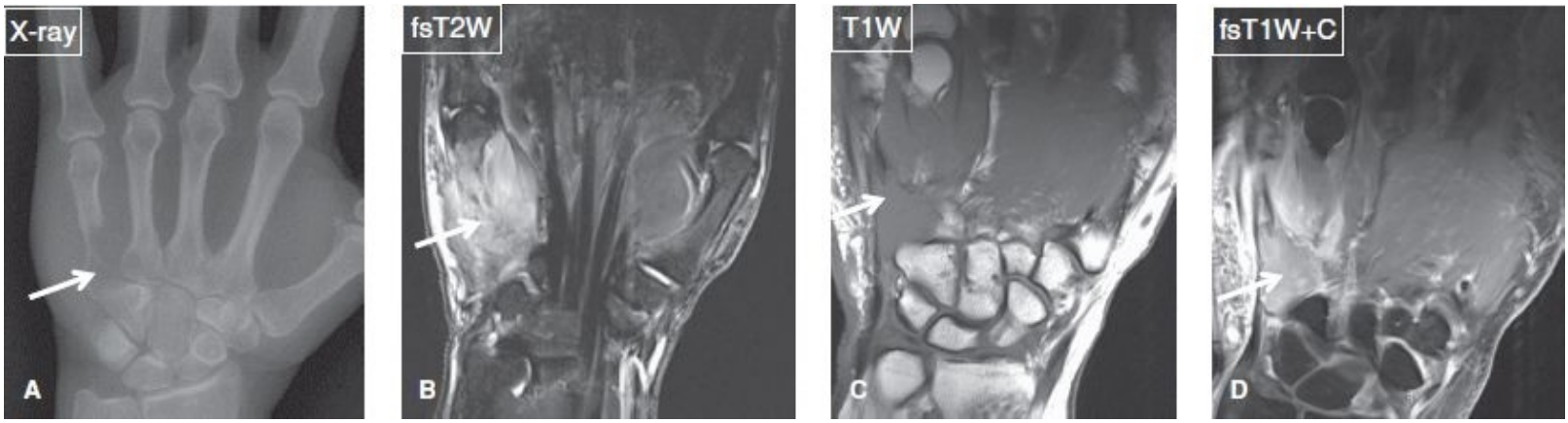

Fig. 29: Metastasis to the hand from lung cancer. **A:** Anteroposterior radiograph of the hand reveals extensive osteolysis (*arrow*) at the proximal half of the fifth metacarpal bone. **B–D:** The corresponding coronal MR images show an intensely enhancing ill-defined soft tissue mass (*arrows*) arising from metastasis to the fifth metacarpal bone.

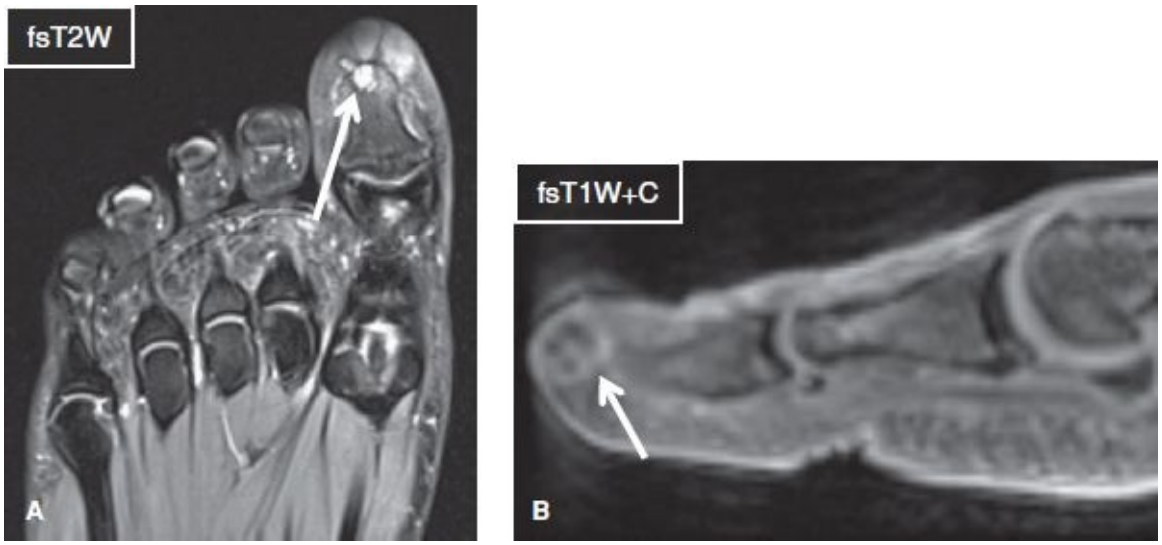

Fig. 30: Bone metastasis in a 30-year-old woman with history of malignancy. Axial **(A)** and sagittal **(B)** images of the forefoot exhibit a well-defined T2 hyperintense lesion (*arrows*) at the tip of the distal phalanx of the first toe, which demonstrate mild, mostly peripheral contrast enhancement. Biopsy proved metastatic tumor from lung carcinoma.

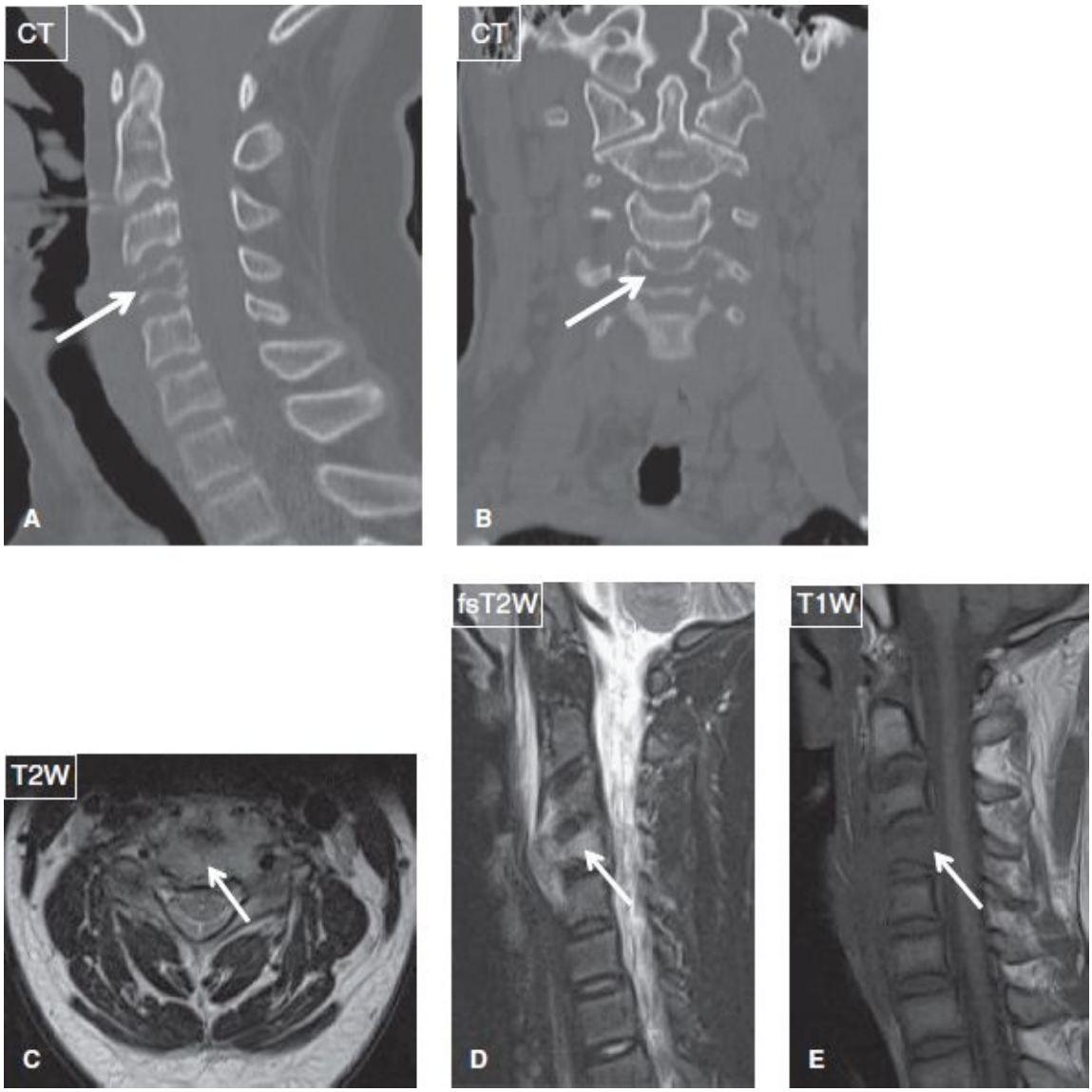

Fig. 31: Eosinophilic granuloma (Langerhans cell histiocytosis). Sagittal **(A)** and coronal **(B)** reformatted CT images demonstrate osteolytic lesion and compression fracture of the C4 vertebral body (*arrows*). On the respective axial **(C)** and sagittal **(D, E)** MR images, T2 hyperintense and T1 isointense mass (*arrows*) erodes the C4 vertebral body and spreads to the prevertebral space.

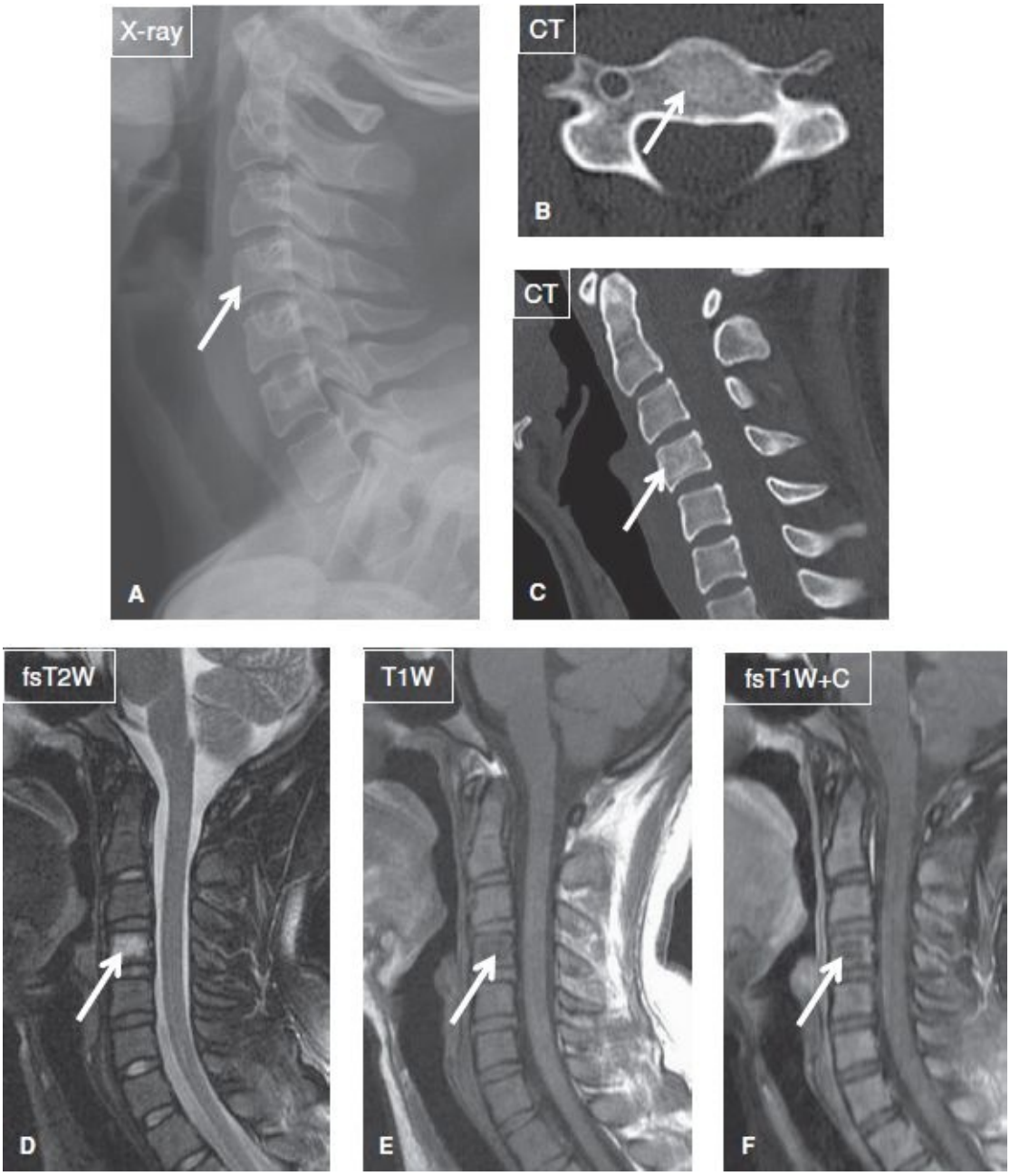

Fig. 32: Benign notochordal cell tumor in a young woman. **A:** An indistinct ovoid lesion (*arrow*) with thin sclerotic margins is seen in the C4 vertebral body on lateral radiograph of the cervical spine. Axial **(B)** and sagittal **(C)** reformats from a CT study reveal an ill-defined lesion with internal sclerosis (*arrows*). **D–F:** On the corresponding sagittal MR images, the lesion (*arrows*) shows relatively low T1/high T2 signal and no appreciable contrast enhancement.

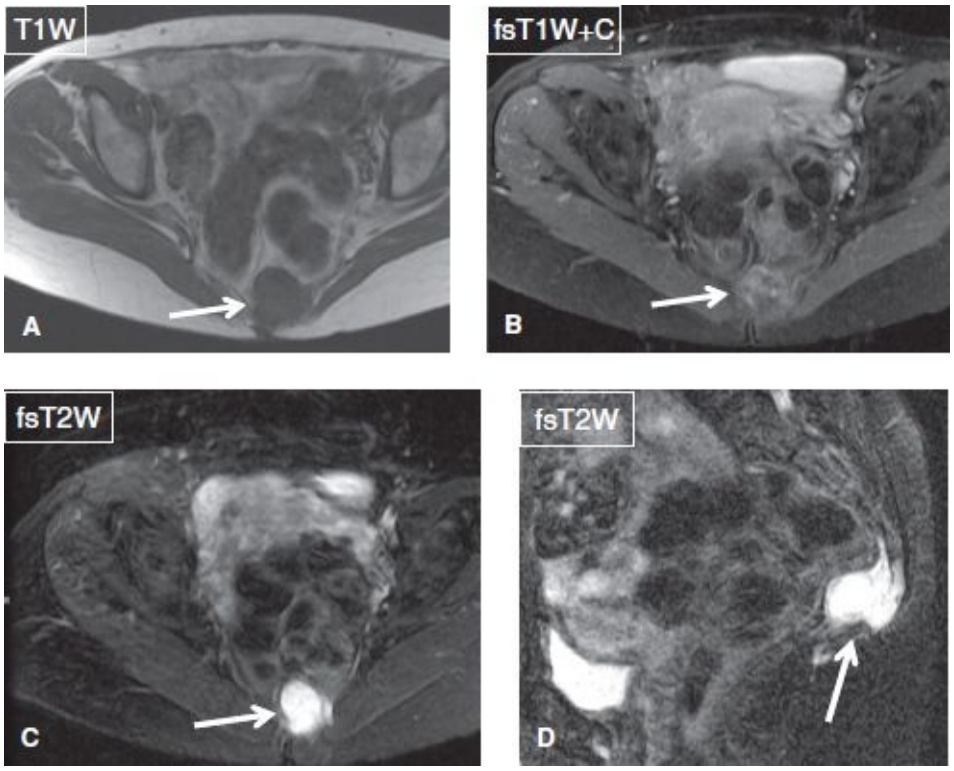

Fig. 33: Small chordoma in an old woman. Axial **(A–C)** and sagittal **(D)** images demonstrate a T1 isointense, T2 hyperintense, and heterogeneously enhancing mass (*arrows*) eroding the lower sacrum and coccyx.

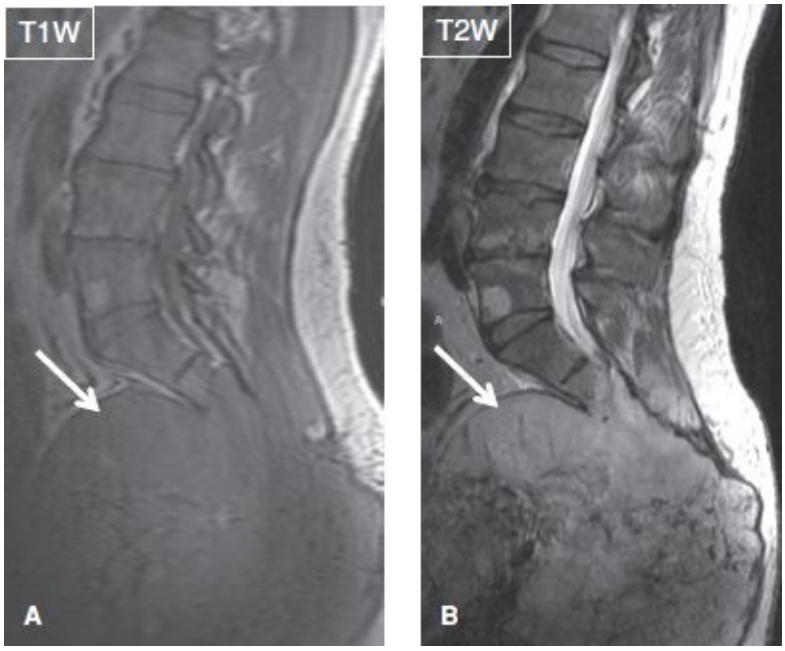

Fig. 34: Large chordoma in a middle-aged man. Sagittal images of the lumbosacral region exhibit a large and heterogeneous mass (*arrows*) emanating from the sacrum and coccyx. Notice incidental hemangioma in L5 vertebra.

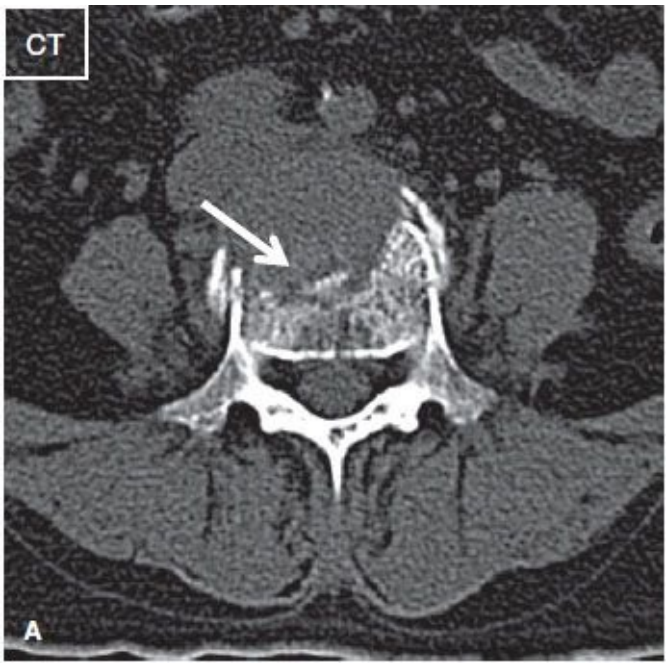

Fig. 35: Multiple myeloma in a middle-aged woman with several month history of low back pain. **A:** Axial CT image shows erosion (*arrows*) of the anterior aspect of the L4 vertebral body with a soft tissue mass. No sclerosis or internal mineralization seen.

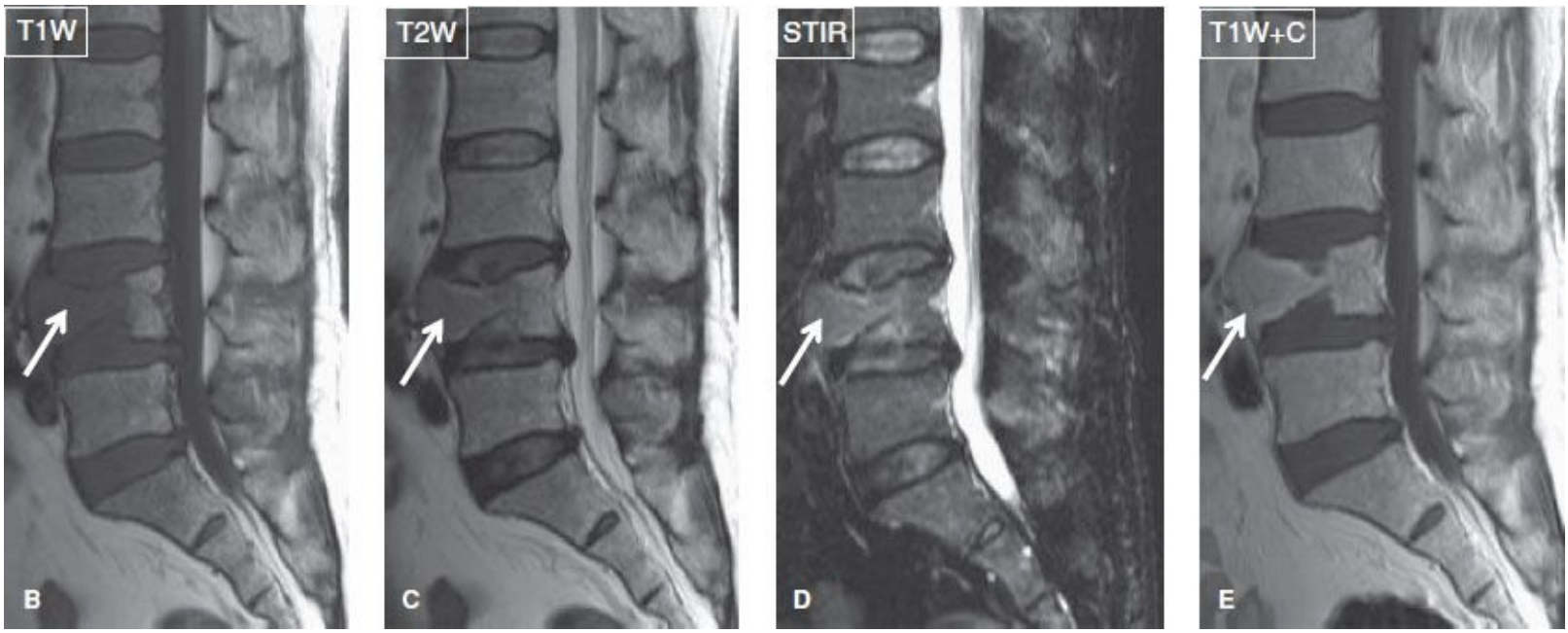

Fig. 35: **B–E:** On the corresponding sagittal MR images, there is a compression fracture of the L4 vertebral body, the anterior aspect of which is infiltrated by homogeneous tissue (*arrows*) of intermediate T1/relatively high T2 signal and moderate contrast enhancement.

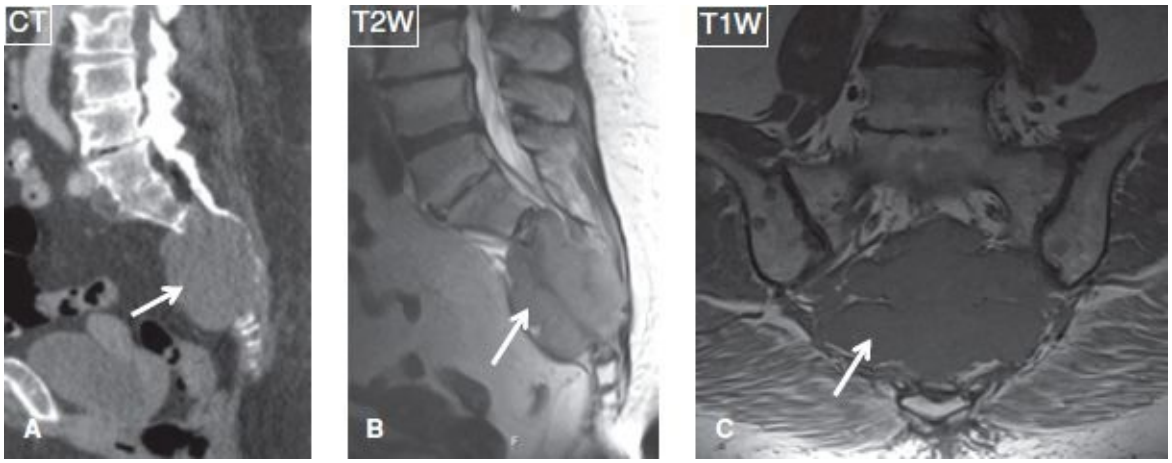

Fig. 36: Plasmacytoma. **A:** Sagittal reformat from a CT study demonstrate an isodense mass (*arrows*) eroding the sacrum with epicenter in the sacral body. **B, C:** The lesion (*arrows*) features intermediate T1 and minimally increased T2 signal intensity.

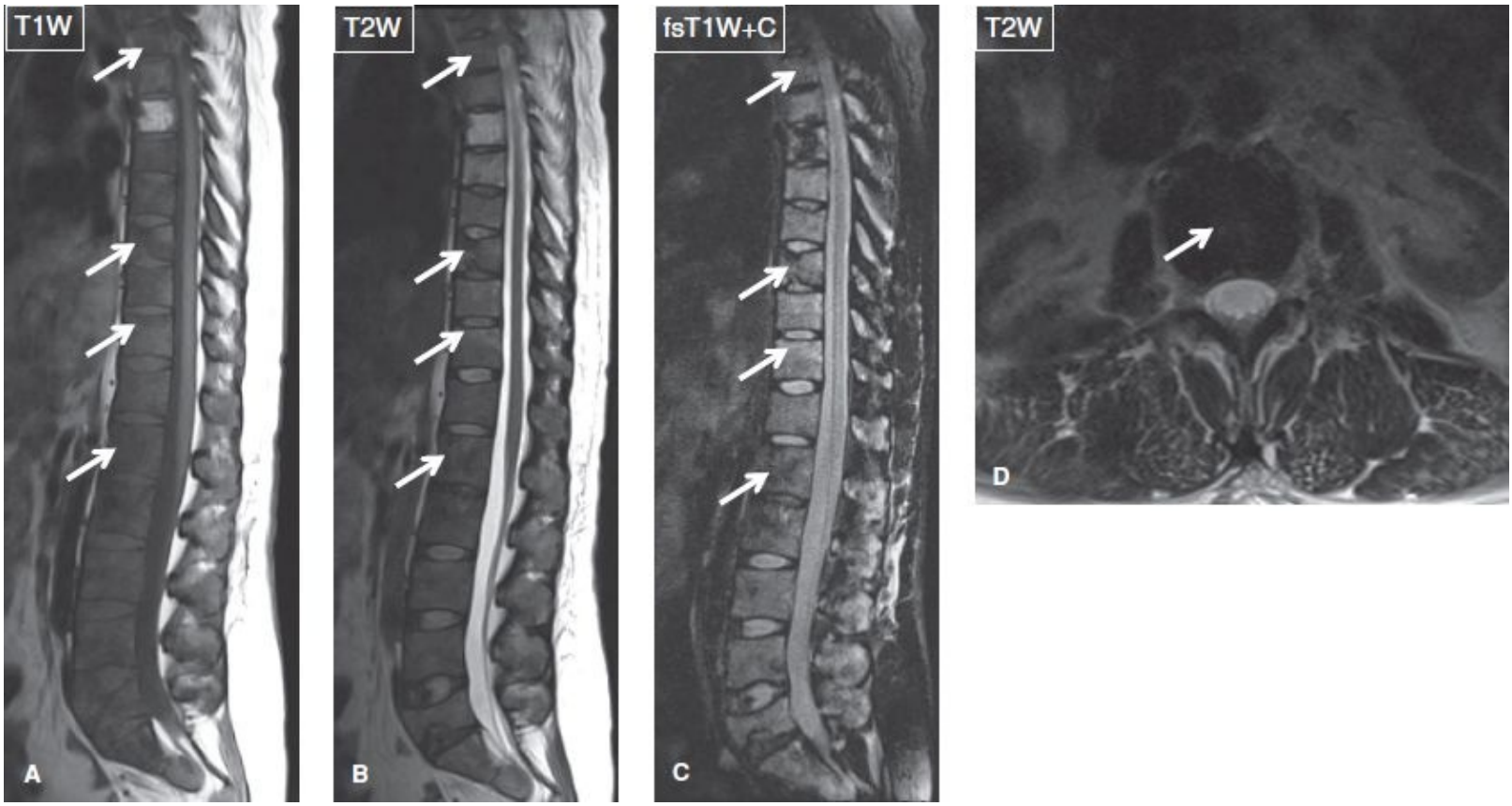

Fig. 37: Breast metastases. Sagittal **(A–C)** and axial **(D)** images of the thoracic and lumbar spine demonstrate numerous hypointense, enhancing lesions (*arrows*) diffusely infiltrating the vertebrae, which correspond to sclerotic metastatic foci. Notice L5 vertebral collapse with diffuse marrow infiltration and pot belly anterior margin in keeping with a pathologic compression fracture.

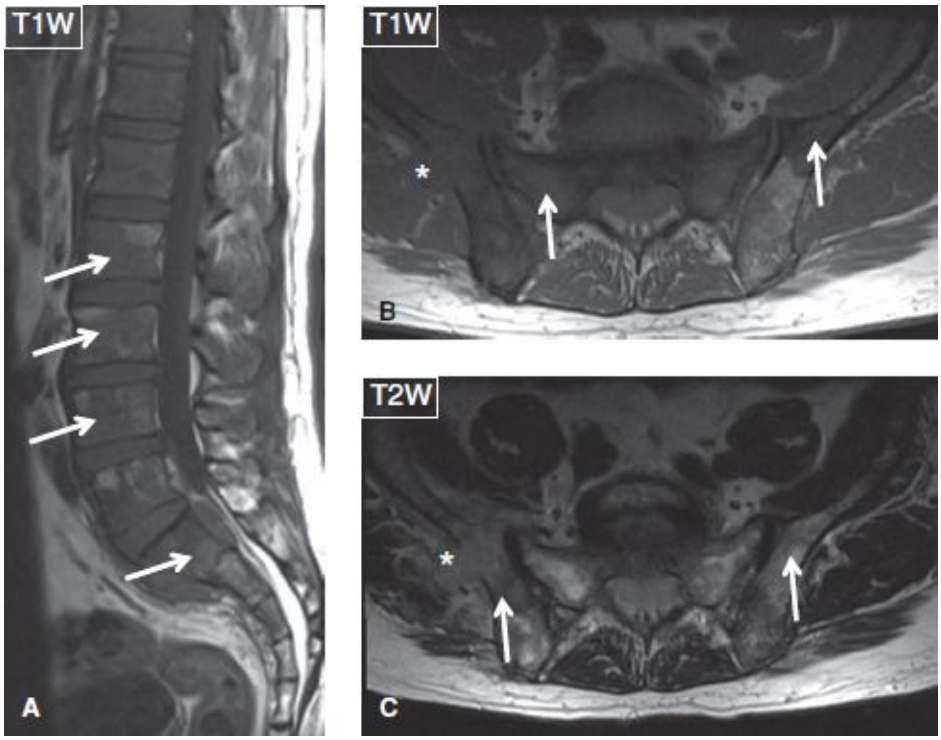

Fig. 38: Lymphoma. Sagittal **(A)** and axial **(B, C)** images exhibit multiple T1 hypointense/T2 hyperintense lesions (*arrows*) at the spine, sacrum, and iliac bones, one of which (*asterisk*) features extraosseous extension.

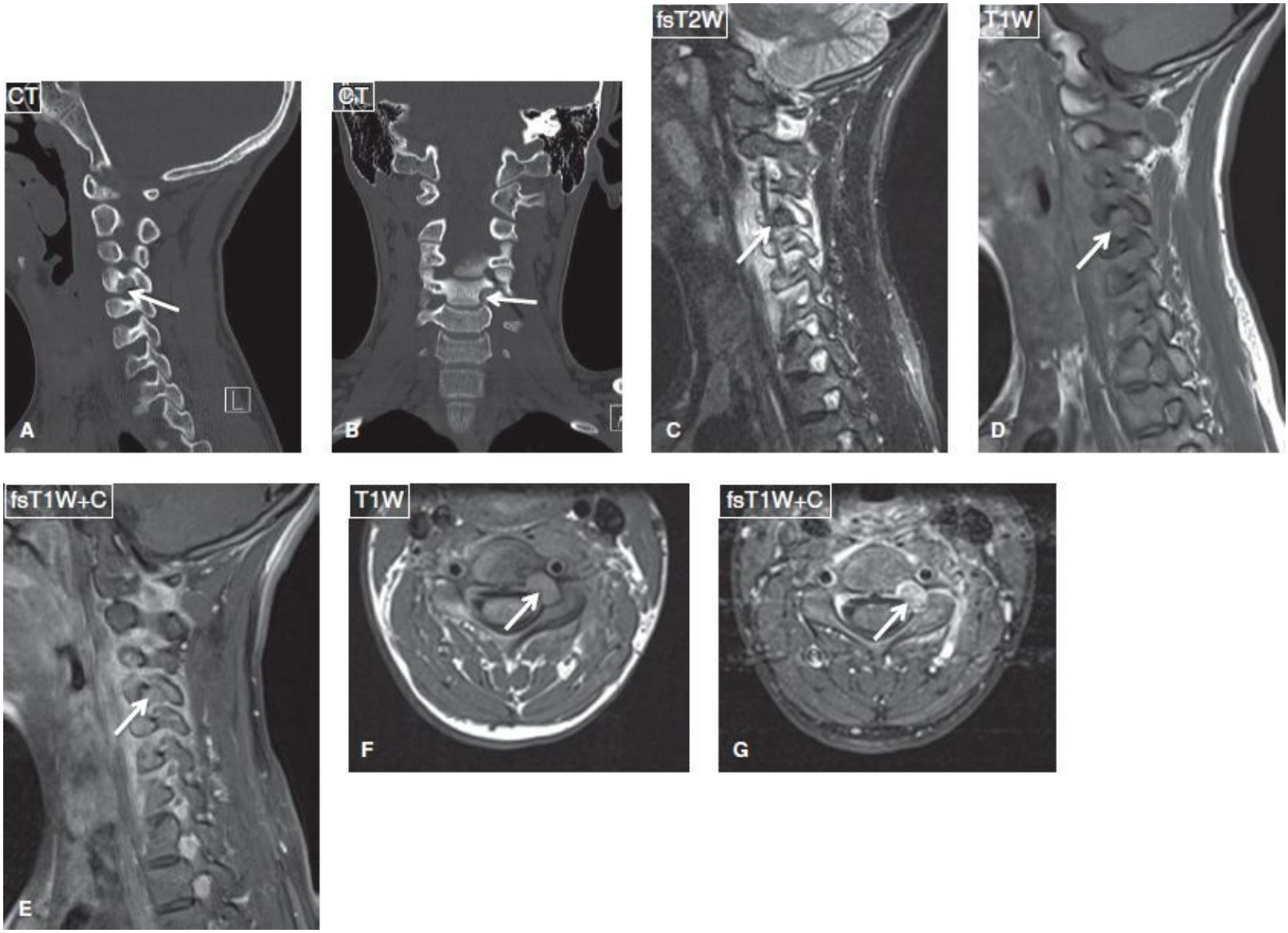

Fig. 39: Osteoid osteoma. Sagittal **(A)** and coronal **(B)** reformatted CT images demonstrate focal lytic lesion with internal mineralization and peripheral sclerosis of the left C4 pedicle (*arrows*). On the respective sagittal **(C–E)** and axial **(F, G)** MR images, the lesion (*arrows*) features intermediate T1/T2 signal and intense contrast enhancement and is associated with edema of the adjacent bone marrow and soft tissues.

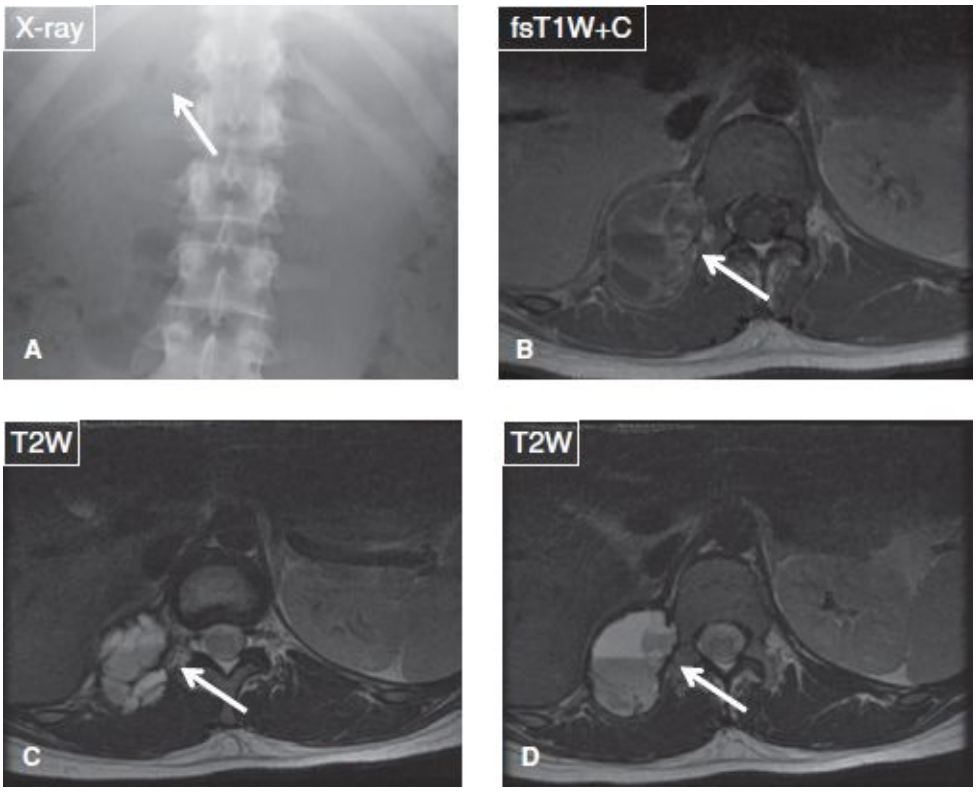

Fig. 40: Aneurysmal bone cyst. **A:** Anteroposterior radiograph shows osteolysis of the right twelfth rib and erosion of the adjacent posterior elements of T12 vertebra (*arrow*). **B–D:** The corresponding axial MR images demonstrate a well-defined multiloculated lesion (*arrows*), featuring fluid signal and fluid–fluid levels. The lesion shows peripheral and internal septal enhancement, typical of ABC.

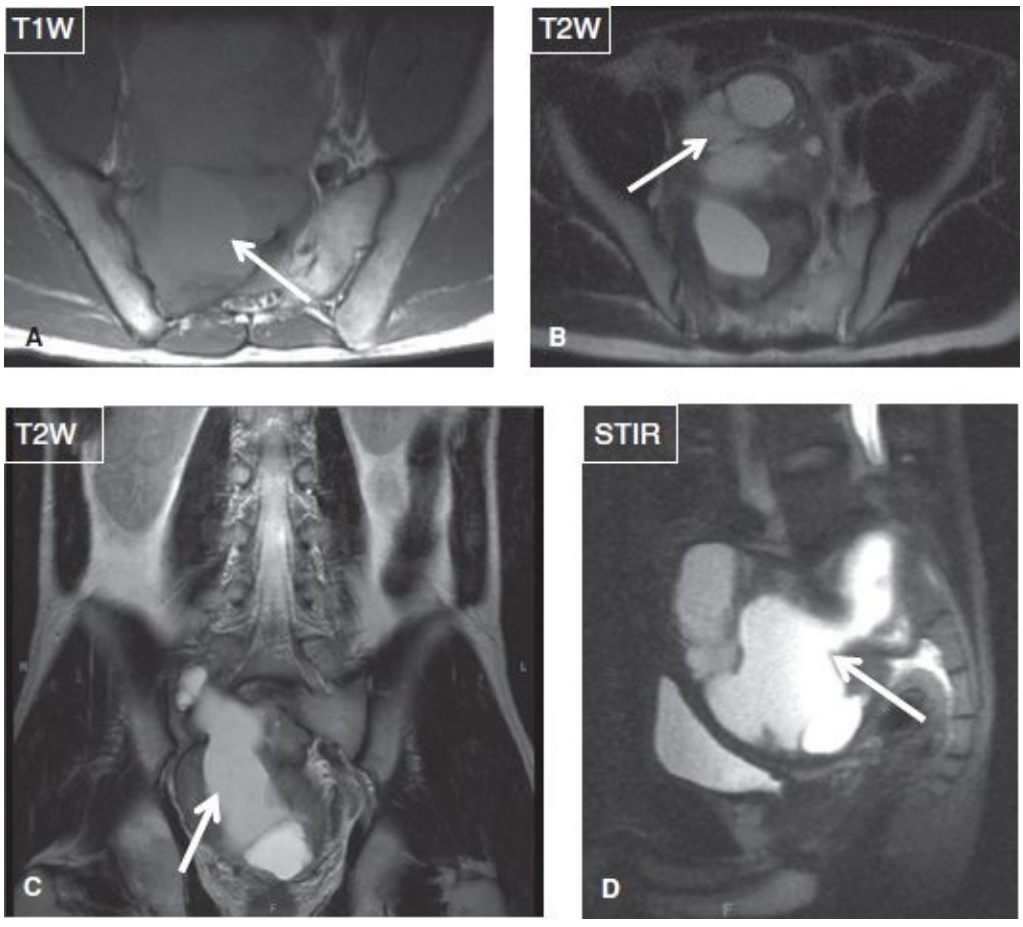

Fig. 41: Cystic schwannoma in a young man. Axial **(A, B),** coronal **(C),** and sagittal **(D)** images show a large mass (*arrows*), which emanates from the right sacral neural foramina, projects in the pelvic cavity, and features cystic and hemorrhagic components.

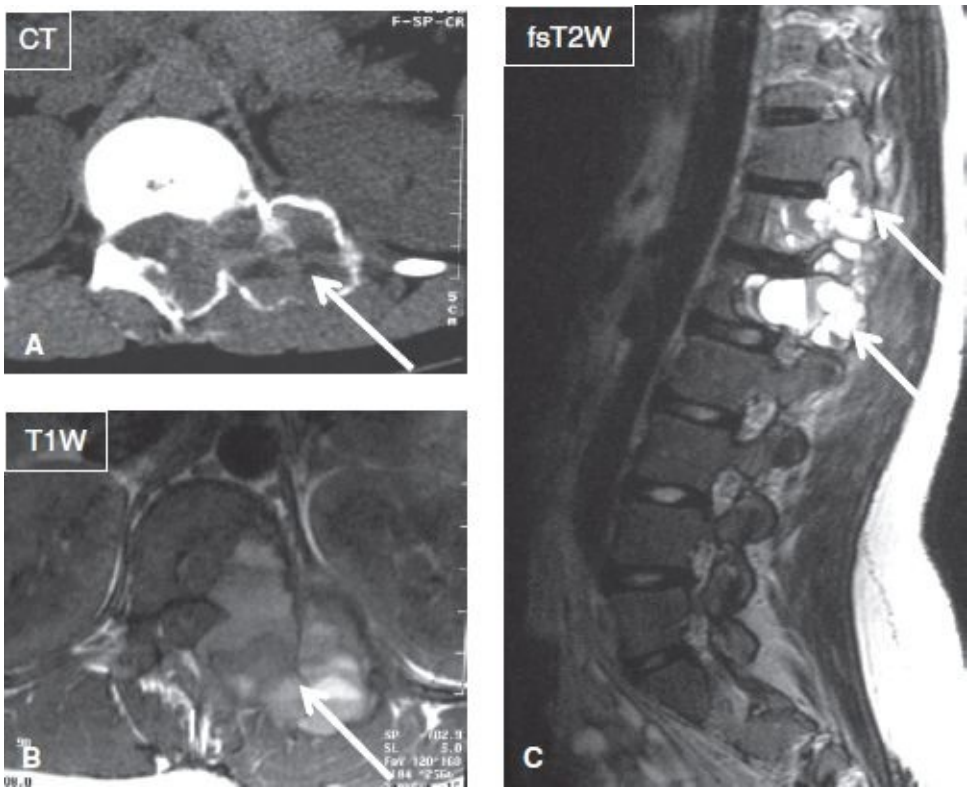

Fig. 42: ABC. Axial CT image **(A)** along with axial **(B)** and sagittal **(C)** MR images shows an expansile osteolytic lesion with fluid–fluid levels (*arrows*) involving the T12 and L1 vertebrae in continuity.

Among soft tissue tumors, location is also very important from diagnostic perspective apart from internal characteristics. Soft tissue lesions can be accurately diagnosed merely based on location. Intra-articular bodies or cysts are encountered in or near a joint and include ganglion, parameniscal, paralabral, pericruciate, geyser phenomenon, various bursal lesions around the knee, postoperative or injury-related seroma, and Morel-Lavallée (i.e., degloving lesion from injury) (Figs. 43–48). Lesions developing within skeletal muscles include intramuscular cyst, parasitic infestation, myxoma, lipoma, elastofibroma dorsi, venous malformation, endometriosis, and myositis ossificans/heterotopic ossification (Figs. 49–53). Lesions developing in tendons, fasciae, and ligaments include calcium hydroxyapatite disease, gout, GCT of tendon sheath, amyloidosis, xanthoma, fibroma in relation to plantar fascia, juvenile aponeurotic fibroma, nodular fasciitis, myositis ossificans, fibromatosis, desmoid tumor, and dermatofibrosarcoma protuberance in the skin and subcutis. Elastofibroma dorsi typically develops in the periscapular and gluteal areas (Fig. 50). The most common soft tissue lesions arising in the foot include intermetatarsal bursitis (along the dorsum of the toes), Morton neuroma and foreign body granuloma (along the plantar aspect of the toes), adventitial bursitis (at pressure points), and tophi or granulomatous nodules from rheumatoid arthritis and sarcoidosis (Figs. 54–61). Finally,

lesions developing along the transverse axis of long bones may be characterized as follows.

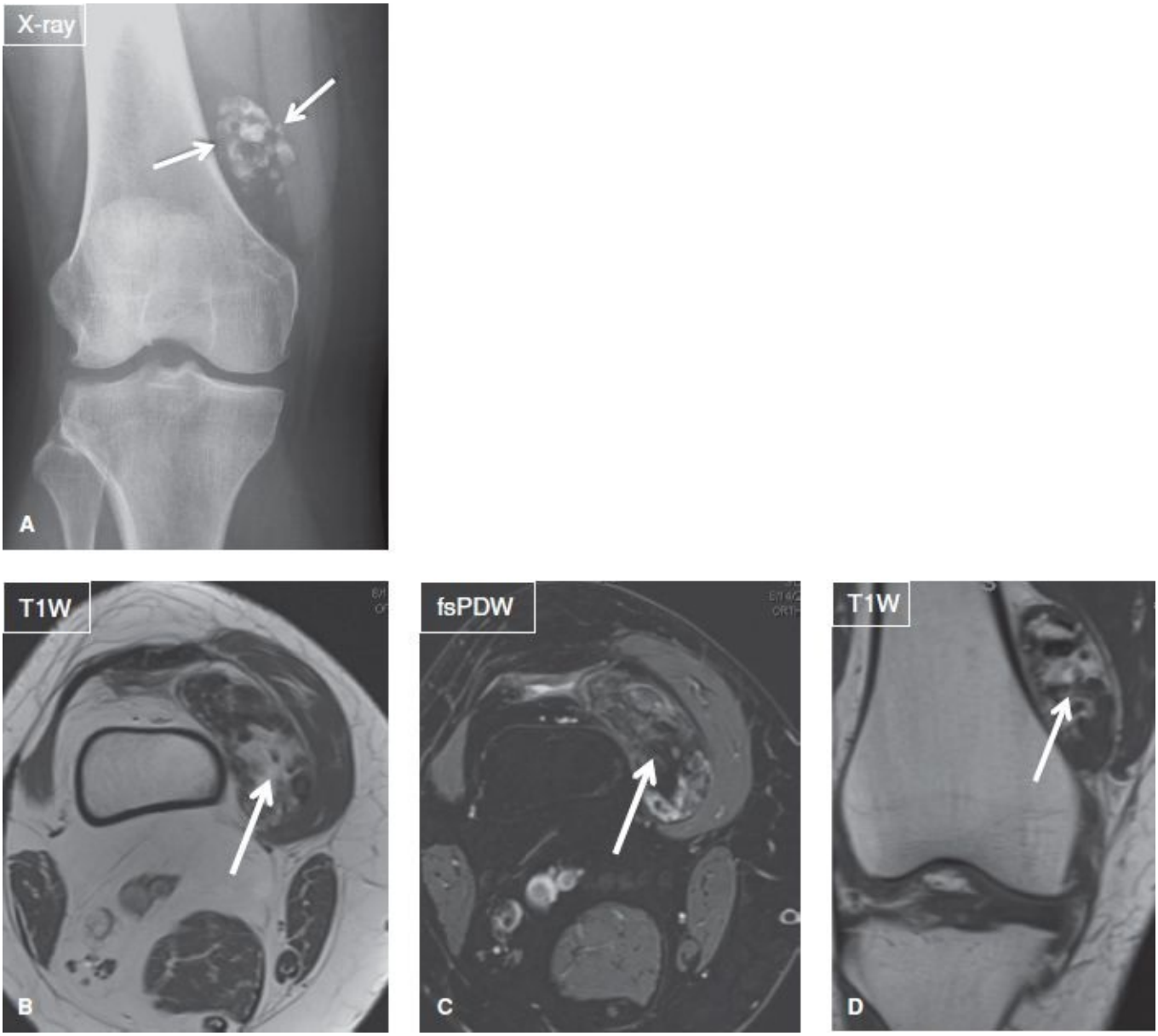

Fig. 43: Intra-articular body in a middle-aged woman who presented with knee pain. Anteroposterior **(A)** radiograph reveals a cluster of coarse calcifications (*arrows*) in the region of suprapatellar pouch. Notice underlying moderate degenerative changes. The respective axial **(B, C)** and coronal **(D)** MR images show a heterogeneous mass-like lesion within the suprapatellar bursa, a large osteochondral body.

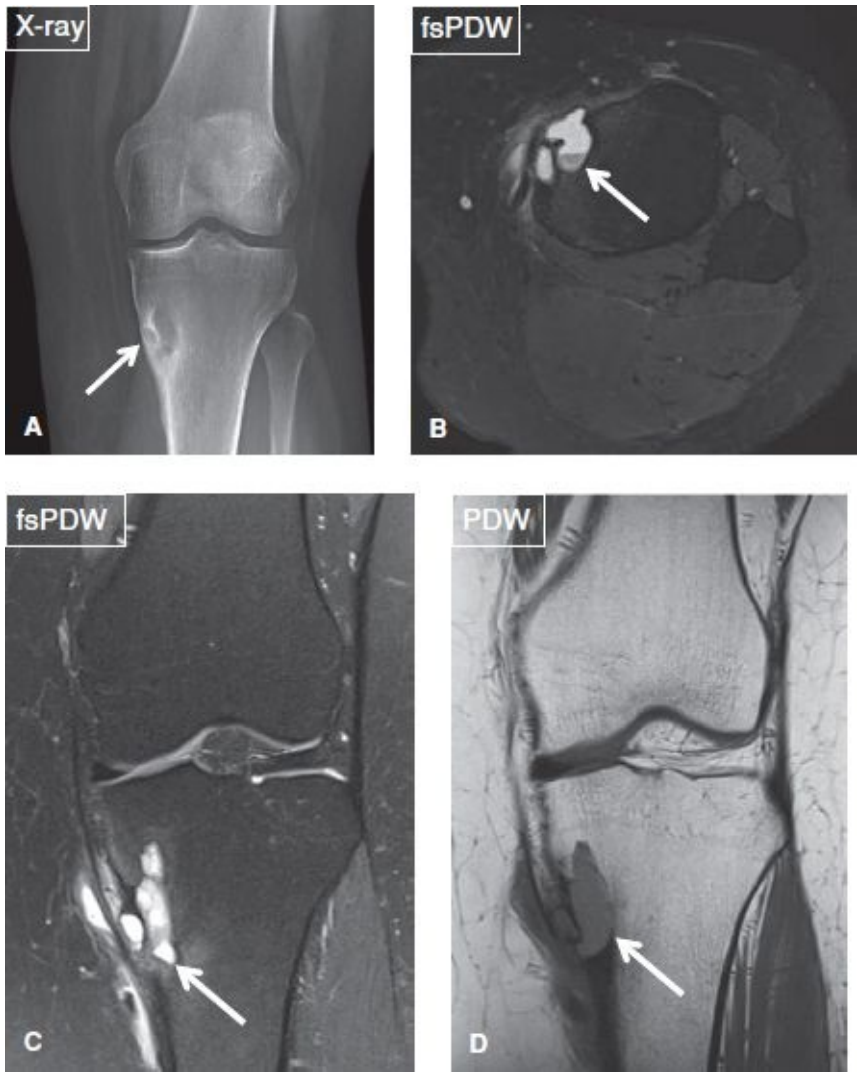

Fig. 44: Cortical avulsion cystic change. Anteroposterior radiograph **(A)** of the knee shows an radiolucent lesion at the tibial metaphysis with sclerotic margin. On the respective axial **(B)** and coronal **(C, D)** MR images, the lesion (*arrows*) appears cystic with fluid level, is located at the pes anserinus insertion, and is associated with overlying cortical discontinuity. Findings are consistent with avulsive cystic change.

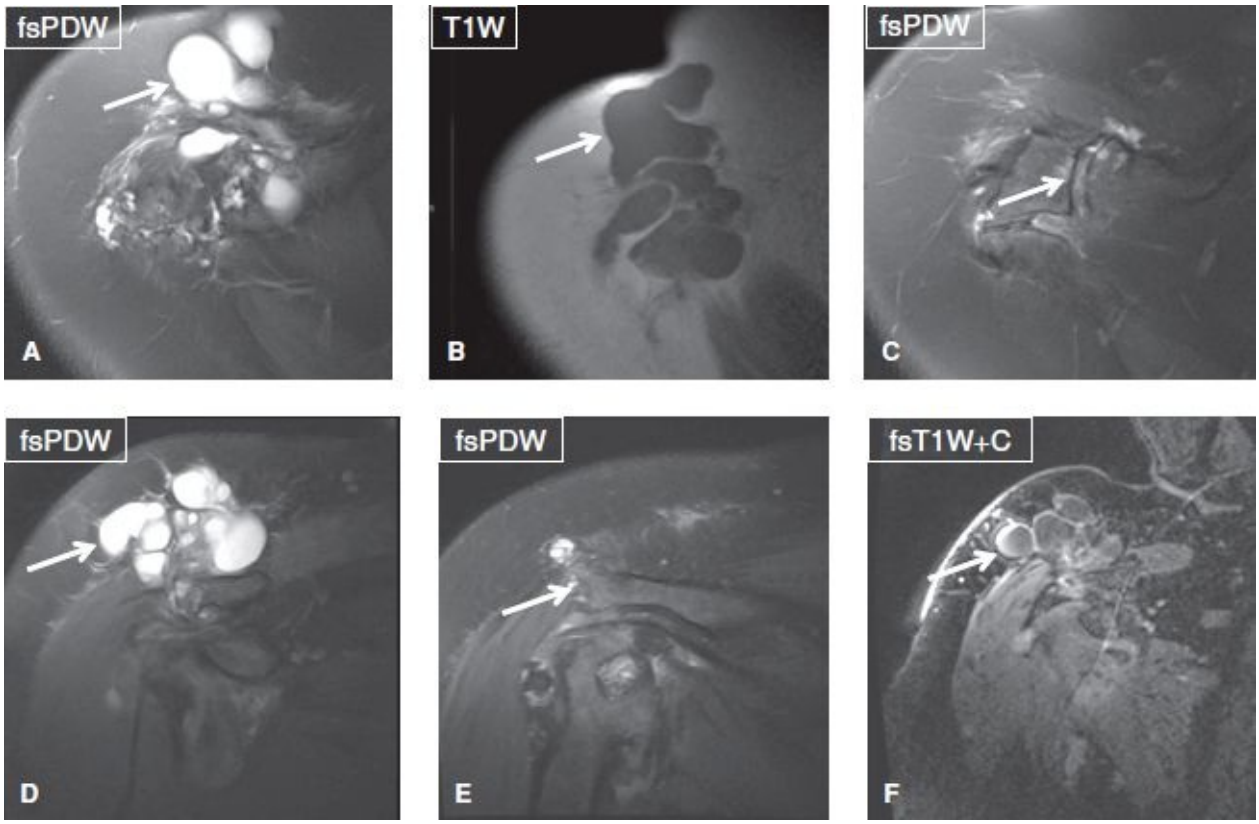

Fig. 45: Geyser phenomenon in a 59-year-old woman who presented with focal swelling at the level of the acromioclavicular joint. Axial **(A–C)** and coronal **(D–F)** images of the right shoulder exhibit a multiloculated cystic lesion (*arrows* in **A, B, D, F**) superior to and abutting the acromioclavicular joint and os acromiale synchondrosis, which show degenerative changes (*arrows* in **C, E**). There was peripheral enhancement on postcontrast images. Underlying rotator cuff was deficient. Findings consistent with geyser phenomenon, a ganglion that communicates with the shoulder joint and develops along the path of least resistance, usually from AC joint. In this case, it also extended from the os acromiale synchondrosis (*arrow* in **E**).

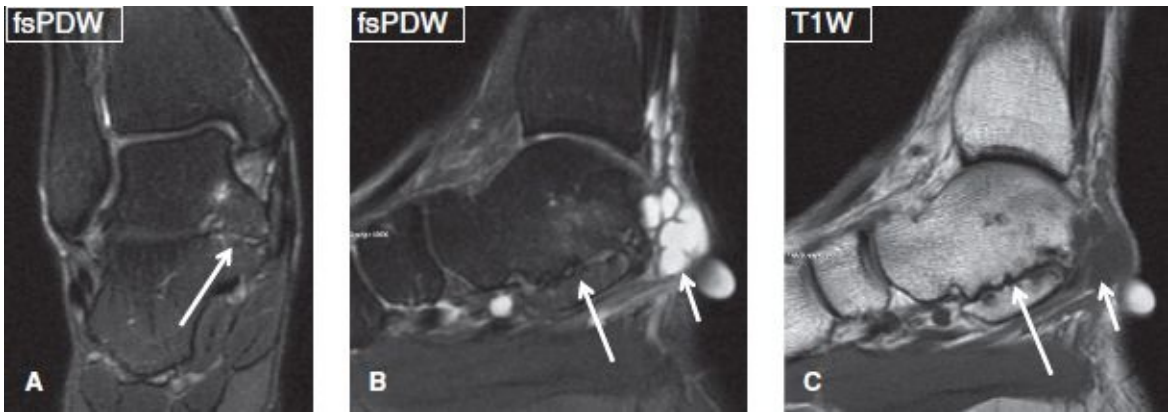

Fig. 46: Ganglion cyst from coalition pseudoarthrosis. Coronal **(A)** and sagittal **(B, C)** MR images show middle and posterior facet talocalcaneal fibrous coalition at the ankle (*long arrows*). Notice the ganglion cyst (*short arrows*) arising from the posterior aspect of the coalition, presenting as a palpable mass.

Fig. 47: Morel-Lavallée lesion in a 18-year-old man. Axial **(A)** and sagittal **(B, C)** images of the left knee exhibit a heterogeneous hematoma, developed between the subcutaneous fat and the superficial fascia, as a result of traumatic separation of the fascial layers.

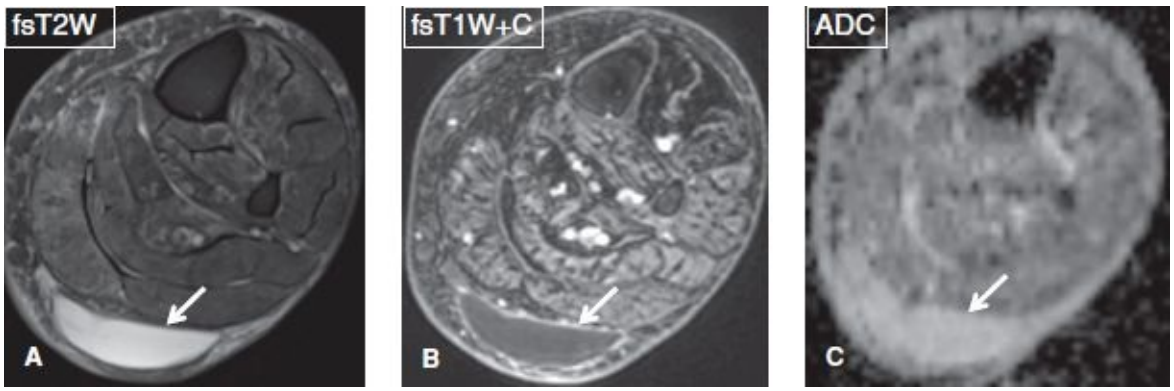

Fig. 48: Seroma. Axial images. **A, B:** A smoothly marginated lesion (*arrows*) is evident between the muscles and the subcutaneous tissues of the posterior superficial compartment, which features homogeneous high T2 signal and thin peripheral enhancement, in keeping with a postoperative seroma. **C:** The high ADC value (2.4×10^{-3} mm^2/s) of the cystic lesion (*arrow*) confirms its cystic nature.

Fig. 49: Myxoma. Axial images through the pelvis demonstrate a well-defined multiloculated cystic lesion (*arrows*) in the gluteal muscles with cystic appearance and mild patchy internal enhancement on the postcontrast subtraction image **(C),** a classic site and imaging appearance of intramuscular myxoma.

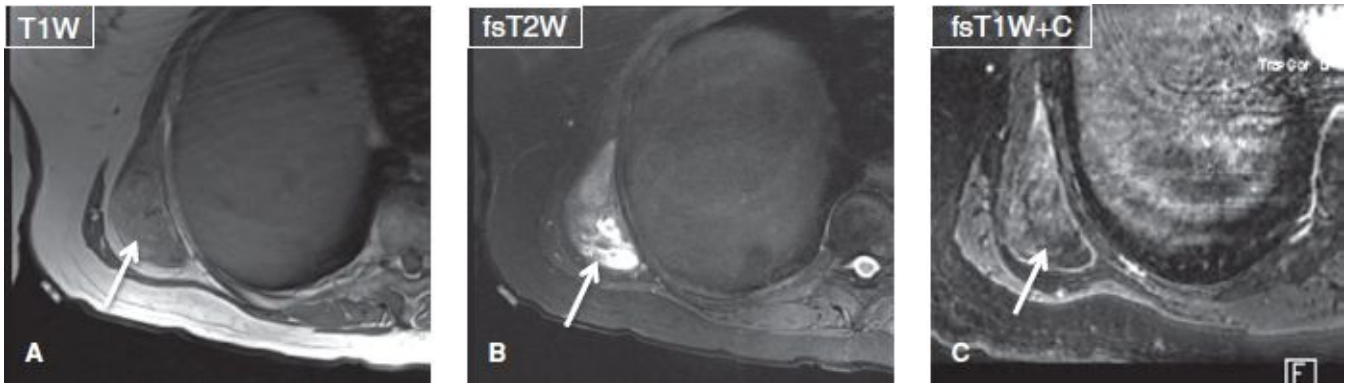

Fig. 50: Elastofibroma dorsi. Axial images display a well-defined heterogeneous fat-containing mass (*arrows*) in the right upper posterior abdominal wall, which features patchy and serpiginous contrast enhancement. A lesion, which is common at the friction sites, for example, periscapular area, gluteal region, and abdominal wall and contains internal fat/fibrous tissue and prominent vessels.

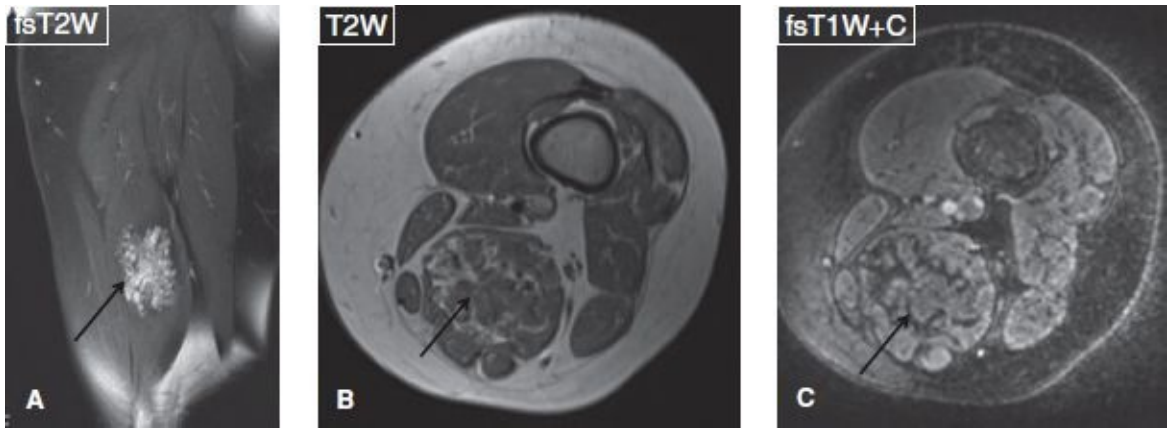

Fig. 51: Intramuscular venous malformation. Sagittal **(A)** and axial **(B, C)** images exhibit a T2 hyperintense bubbly and serpiginous lesion (*arrows*) with internal fatty components within the semimembranosus muscle. Minimal delayed venous phase enhancement is seen with no fascial edema, a typical appearance of a low-flow venous malformation. Phleboliths, if present within the lesion, further confirm the diagnosis.

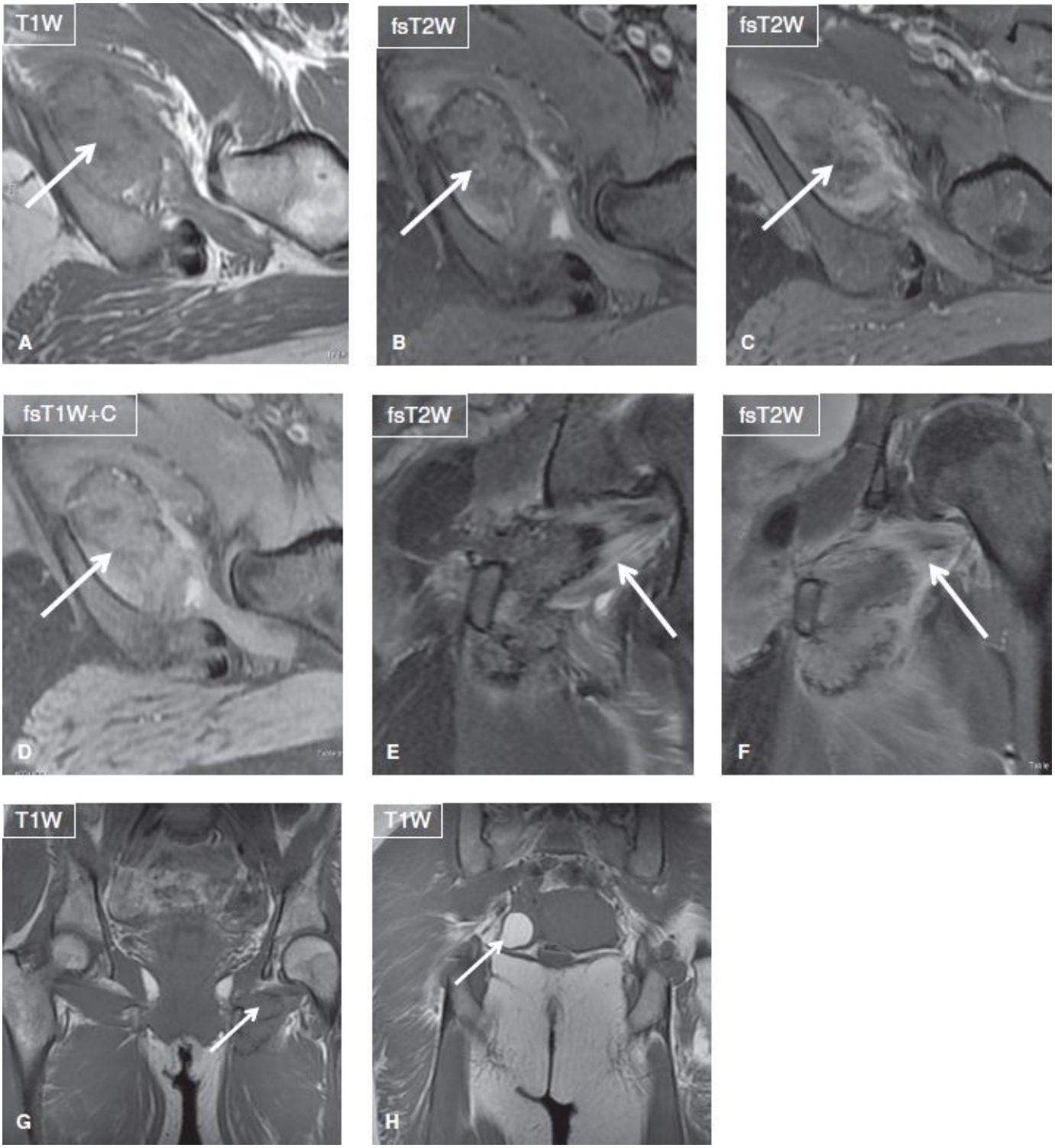

Fig. 52: Extra- and intra-abdominal endometriosis in a 45-year-old woman. Axial **(A–D)** and coronal **(E–G)** images show an ill-defined and mildly heterogeneous T1 hyperintense/hemorrhagic lesion (*arrows*) in the left obturator and adductor muscles, which demonstrates moderate contrast enhancement. Biopsy revealed extra-abdominal endometriosis. Another coronal image **(H)** shows an chocolate cyst (*arrows*) of the right ovary, commonly associated with extra-abdominal endometriosis.

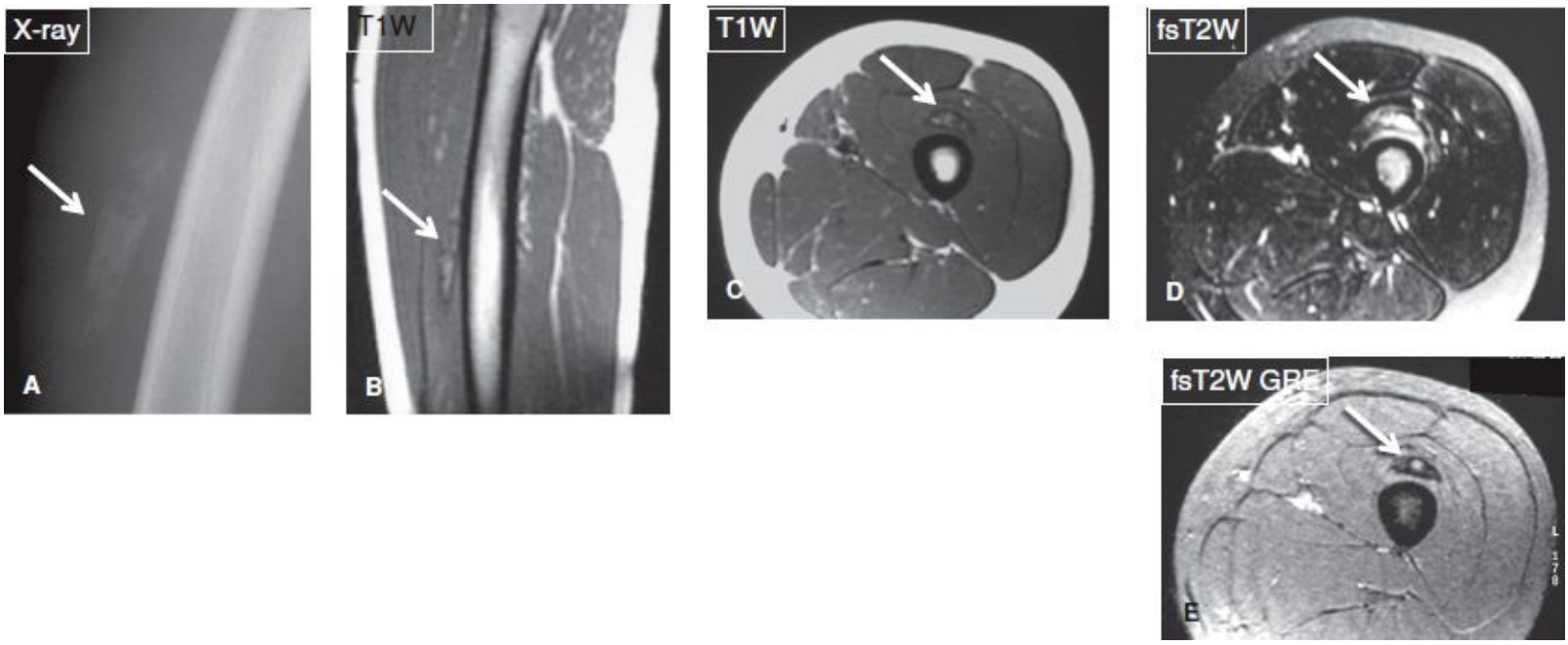

Fig. 53: Myositis ossificans/heterotopic ossification. Lateral radiograph **(A)** of the thigh shows a large amorphous calcification (*arrow*) in the anterior compartment, linear in shape with peripheral more mature calcification. On the respective sagittal **(B)** and axial **(C–E)** MR images, the lesion is located within the vastus intermedius, and features periphery of low T1/T2 signal, which corresponds to lamellar bone, and center of intermediate T1/high T2 signal, which corresponds to maturing bone marrow (zonal phenomenon). Because of its calcified nature, the lesion is particularly evident on the gradient-echo image **(E).** There is no associated soft tissue mass.

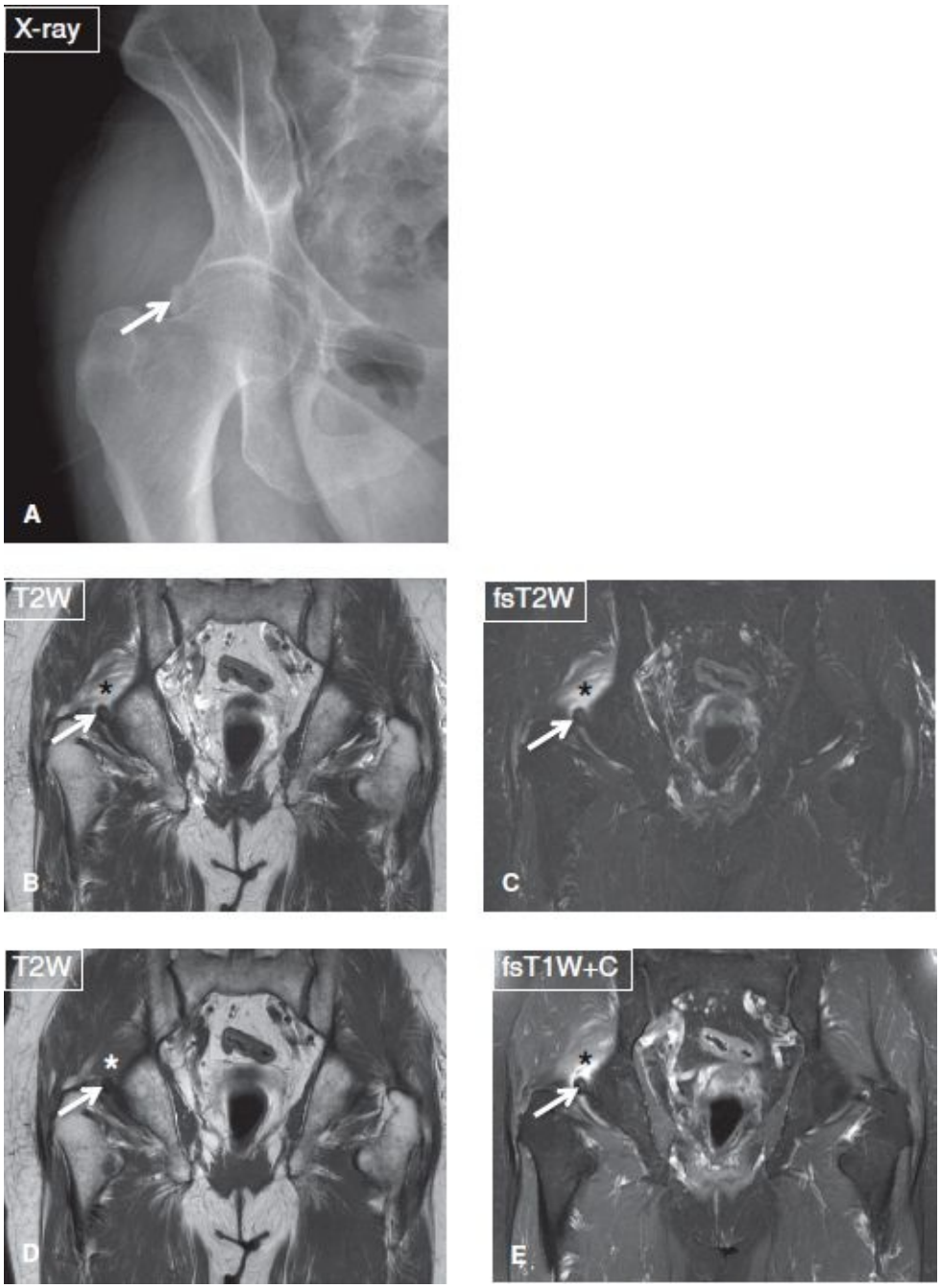

Fig. 54: Calcific tendinosis of superior gemellus muscle in a 71-year-old woman who presented with right hip pain. **A:** Oblique radiograph of right hip reveals a linear calcification (*arrow*) lateral to the acetabulum. **B–E:** The calcification appears as a signal void (*arrows*) on the respective coronal MR images and corresponds to the location of the superior gemellus tendon. Adjacent to the lesion, the latter muscle (*asterisk*) shows T2 hyperintensity and contrast enhancement, indicating edema and hyperemia, respectively. (Courtesy Dr Sunjung Kim, MD.)

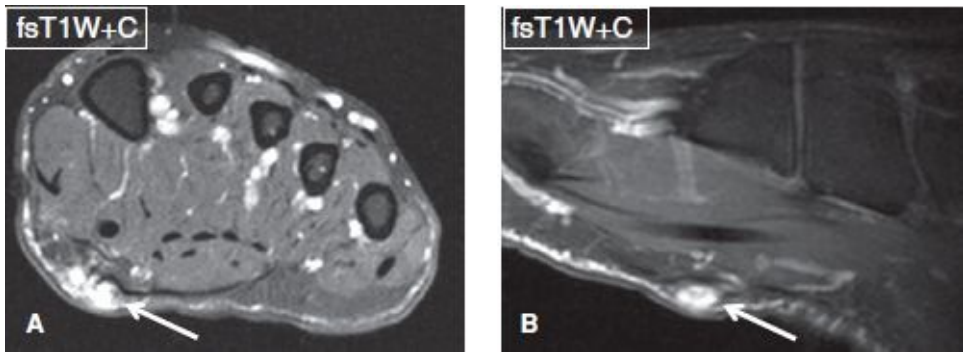

Fig. 57: Plantar fibroma. Axial **(A)** and sagittal **(B)** images of the left midfoot exhibit a T2 hyperintense and intensely enhancing pea-shaped mass (*arrows*) at the medial aspect of the central third of the plantar fascia, a classic site and appearance of plantar fibroma. The lesions are typically dark on T2W images.

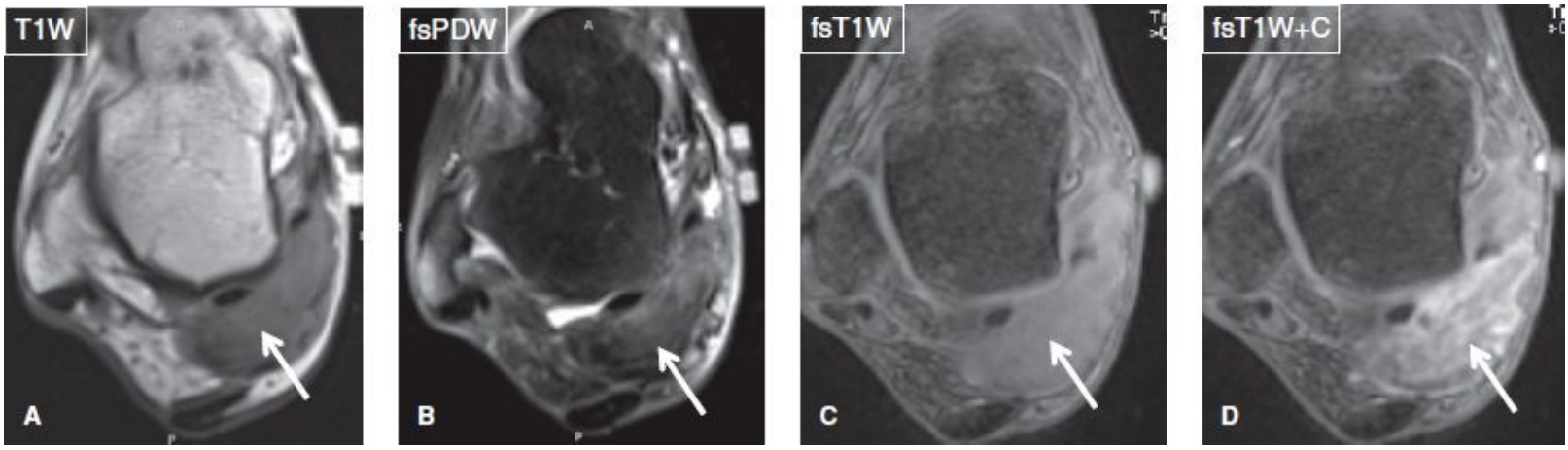

Fig. 55: Focal extra-articular pigmented villonodular synovitis (giant cell tumor of the tendon sheath). Axial images demonstrate tissue (*arrows*) of intermediate T1/low T2 signal intensity and moderate heterogeneous contrast enhancement filling and expanding the flexor hallucis longus tendon sheath.

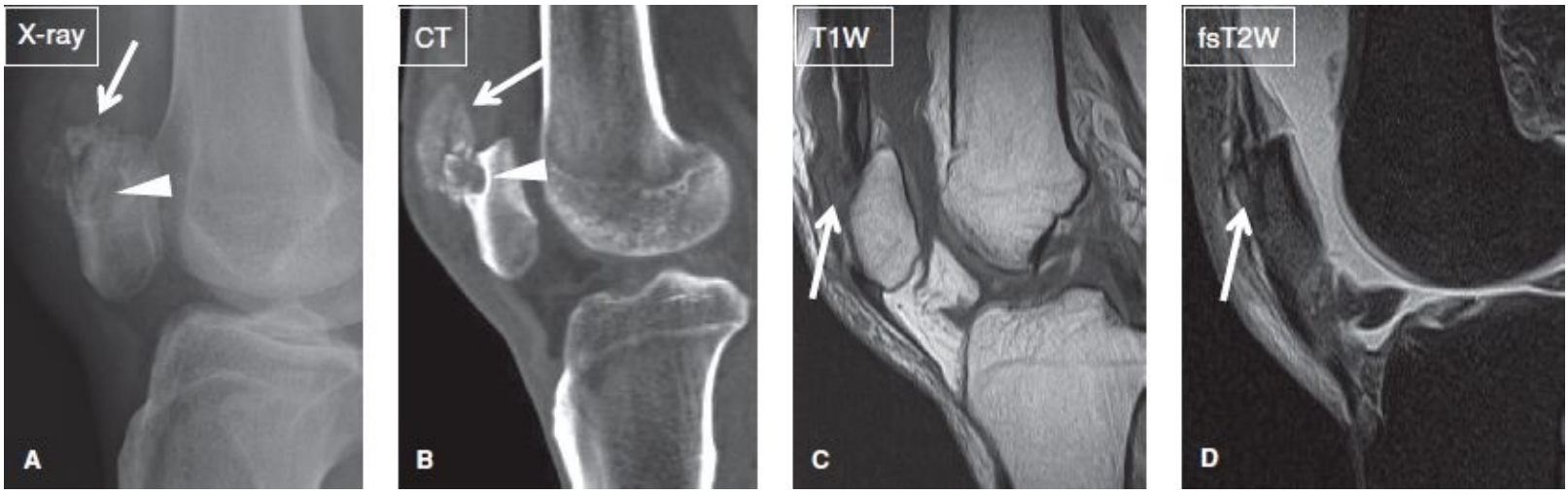

Fig. 56: Gout in a 47-year-old man. **A:** Lateral radiograph of the right knee shows calcifications (*arrows*) at the anatomic location of the quadriceps tendon with erosions showing sclerotic margin of the superior pole of the right patella (*arrowhead*). **B:** Sagittal CT reconstruction of the right knee reveals the true extent of the punched out erosion

(*arrowhead*) and calcified tophus (*arrow*). **C, D:** Sagittal MR images confirm the involvement of the distal quadriceps tendon (*arrows*), which has suffered a partial tear. Notice the tophus shows T1/T2 dark signals, which is common; however, it is not the rule.

Fig. 58: Fibromatosis in a 27-year-old woman. Axial **(A),** coronal **(B),** and sagittal **(C)** images show a heterogeneous, predominantly T2 hyperintense mass (*arrows*) infiltrating the right axillary region. The lesion shows T2 dark signals with maturity and decreased cellular content with aging and on treatment with mitotic inhibitors. The location in fascial layers of the friction sites, such as periscapular area, gluteal area, hands, feet, and abdominal wall is classic.

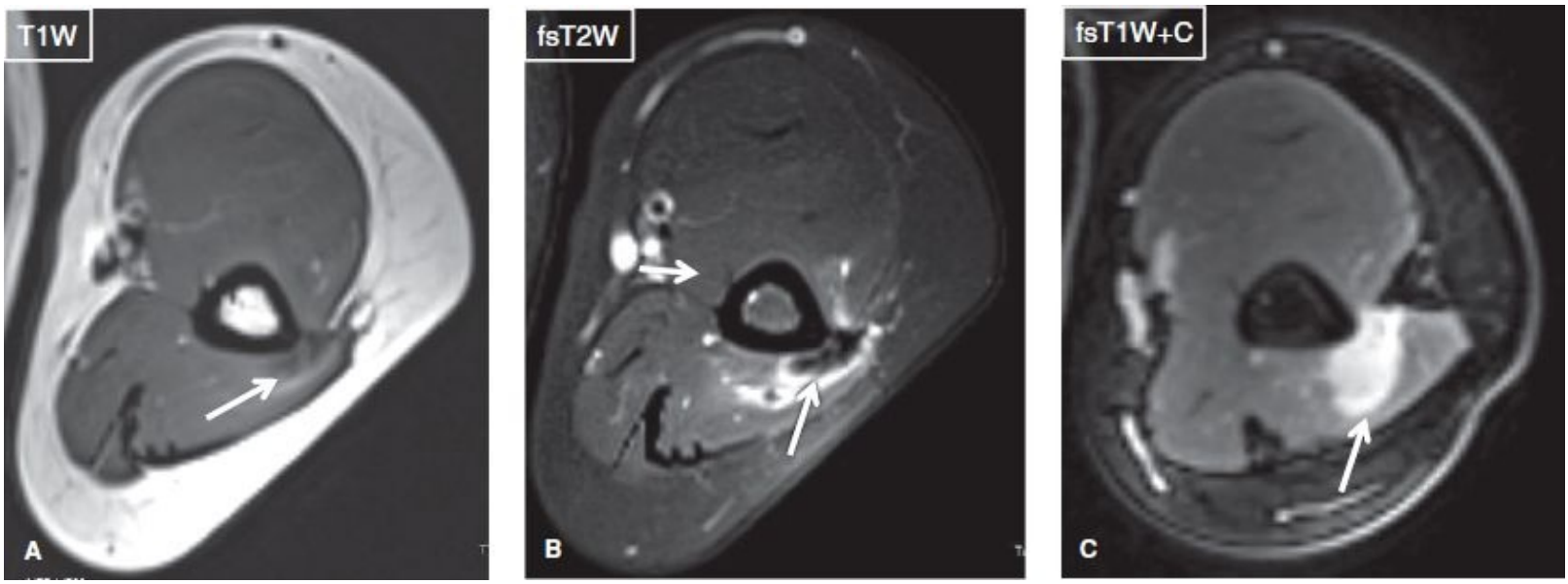

Fig. 59: Desmoid tumor in a 44-year-old woman. Axial images exhibit a T1/T2 hypointense lesion (*arrows*) in the triceps muscle, which is associated with edema of the adjacent soft tissues and intense enhancement.

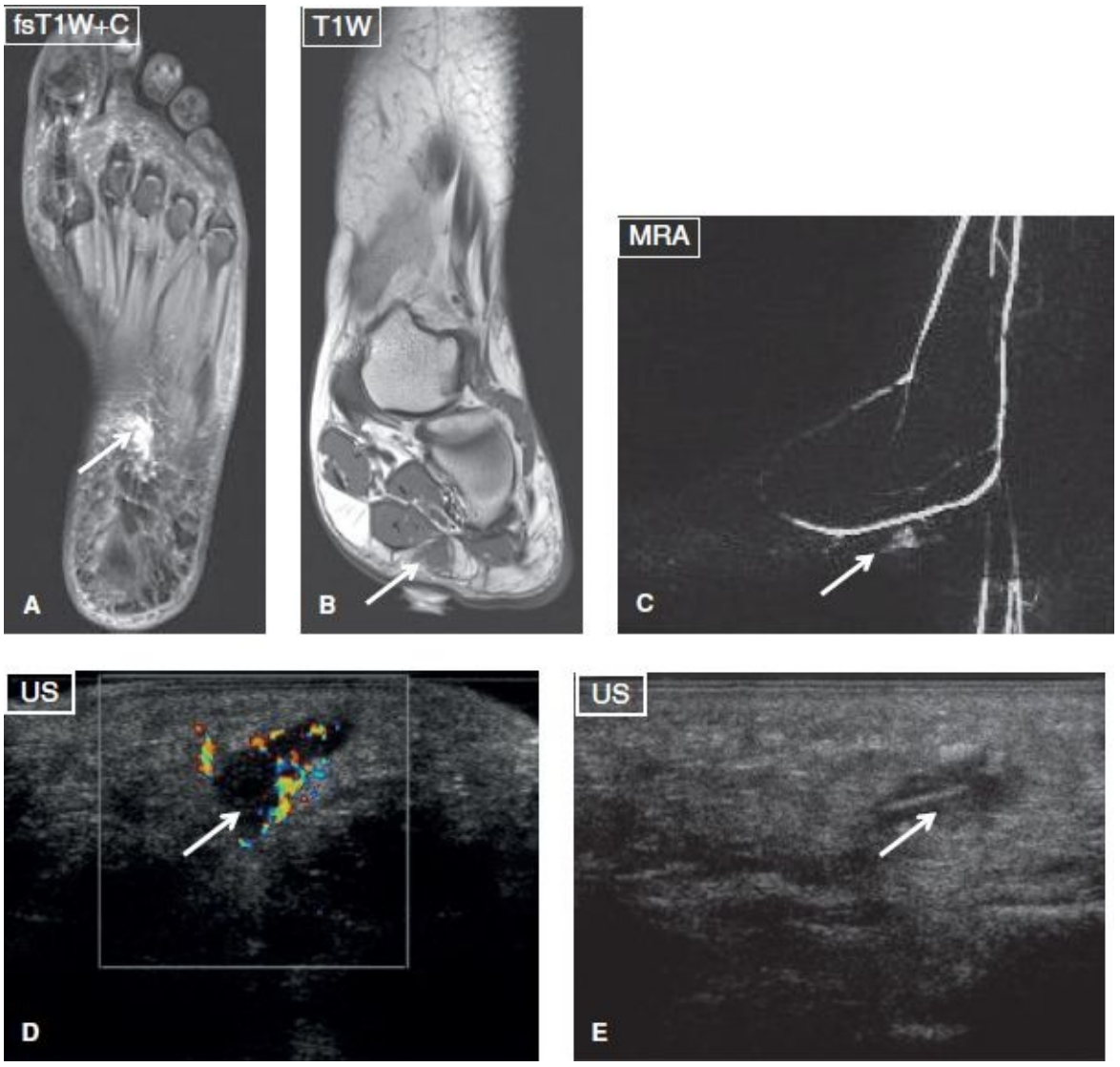

Fig. 60: Foreign body granuloma with fasciitis. Axial **(A)** and coronal **(B)** images demonstrate a intermediate T1 and enhancing subcutaneous lesion (*arrows*) at the hindfoot. On dynamic MR angiography **(C),** the lesion (*arrow*) shows early arterial enhancement. Ultrasound sections show peripheral Doppler flow around the hypoechoic area (*arrow* in **D**) containing the linear hyperechoic foreign body (*arrow* in **E**).

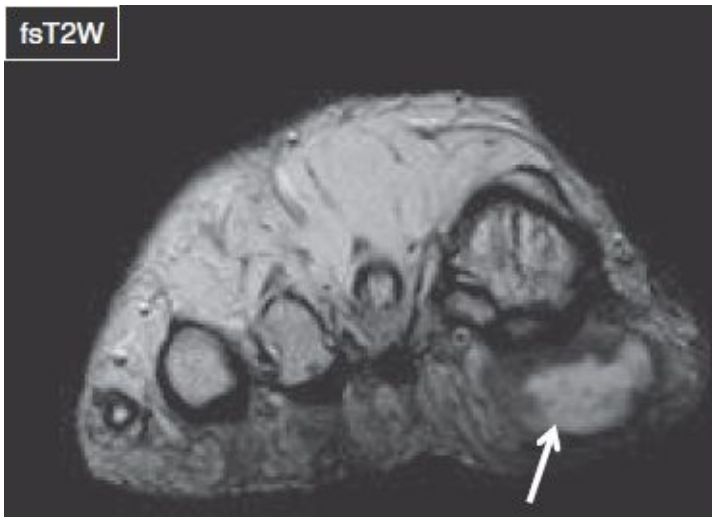

Fig. 61: Adventitial bursitis. Classic location at the base of the first metatarsal head (*arrow*). Notice diffuse dorsal soft tissue edema in this diabetic subject.

- Predominantly cortical/subcortical—osteochondroma, infection, osteoid osteoma, NOF, tug lesion, adamantinoma or cortical avulsive deformity at muscle or tendon attachments (e.g., gastrocnemius, pes anserinus origins, or patellar tendon), cortical metastases, and Paget disease (Figs. 62–67).

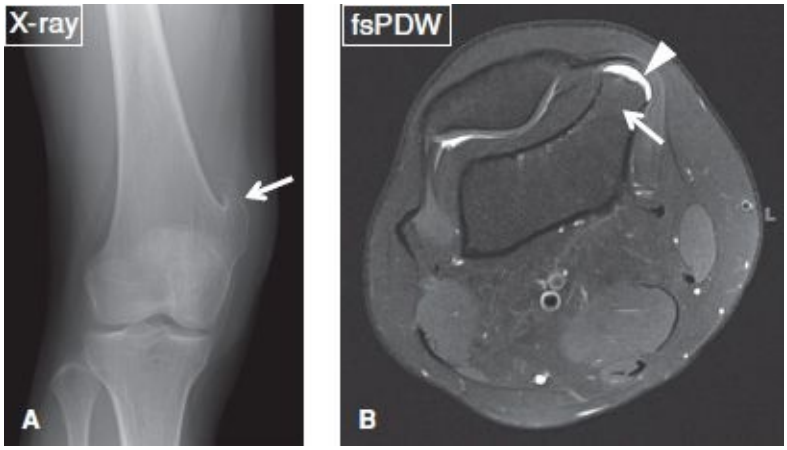

Fig. 62: Osteochondroma in a young woman, who presented with knee pain. **A:** Anteroposterior radiograph displays a well-defined pedunculated bony protuberance (*arrow*), which emanates from the metaphyseal region and projects away from the epiphysis. **B:** On the respective axial MR image, the lesion (*arrow*) is continuous with the bone, shows similar marrow signal. A thin T2 hyperintense cap (*arrowhead*) corresponds to cartilage.

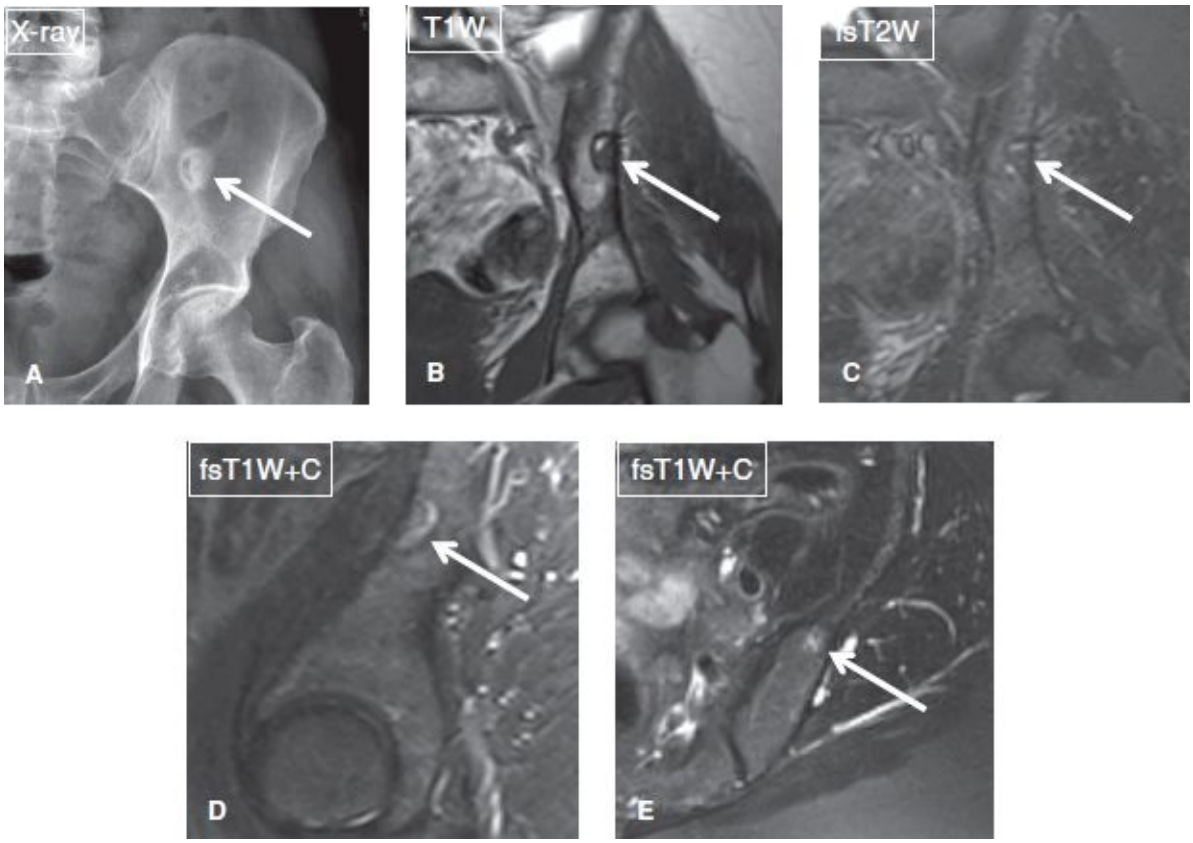

Fig. 63: Fibrous dysplasia in a 56-year-old woman. A sclerotic lesion (*arrow* in **A**) in the left iliac bone was incidentally detected on plain film. The corresponding coronal **(B, C),** sagittal **(D),** and axial **(E)** MR images demonstrate a well-defined, predominantly T1

hypointense heterogeneous lesion (*arrows*) in cortical–subcortical location with mild central and peripheral enhancement and lack of surrounding marrow edema.

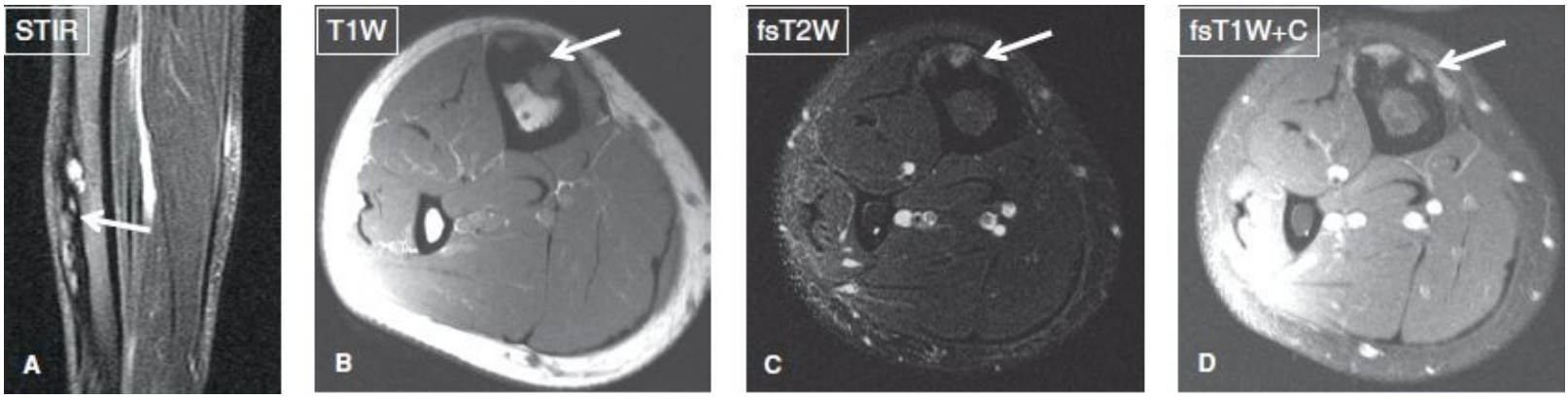

Fig. 64: Adamantinoma.Sagittal **(A)** and axial **(B–D)** MR images of the tibia demonstrate multiple enhancing foci of intermediate T1 and high T2 signal (*arrows*), which are interspersed within an area of cortical sclerosis and thickening. Note cortical permeation in **(C)** and **(D)** (*arrows*).

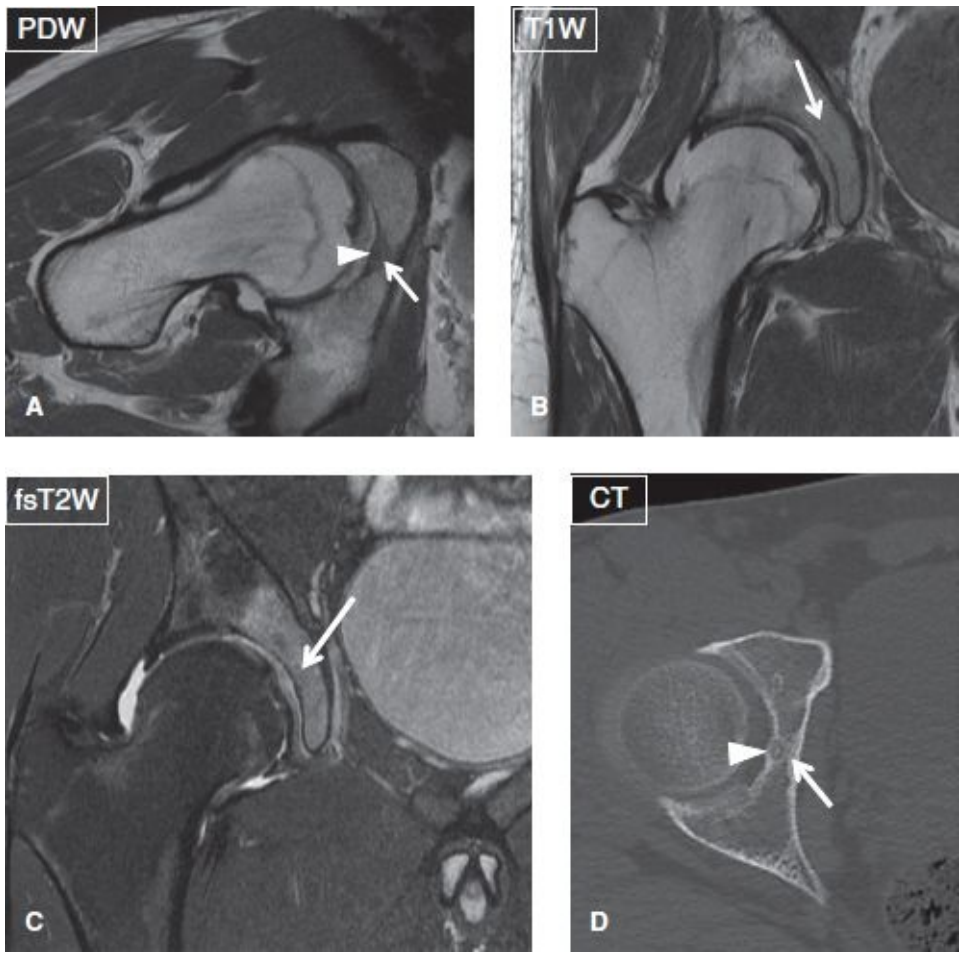

Fig. 65: Osteoid osteoma. Axial **(A)** and coronal **(B, C)** MR images demonstrate a well-circumscribed cortically based lesion (*arrow* in **A**) of intermediate signal at the acetabulum, which includes a hypointense central focus (*arrowhead* in **A**), corresponding to the nidus. Marrow edema (*arrows* in **B, C**) surrounds the lesion. **D:** The lesion (*arrow*) and the radiolucent nidus (*arrowhead*), which include a central sclerotic focus, are better delineated

in the corresponding axial CT image.

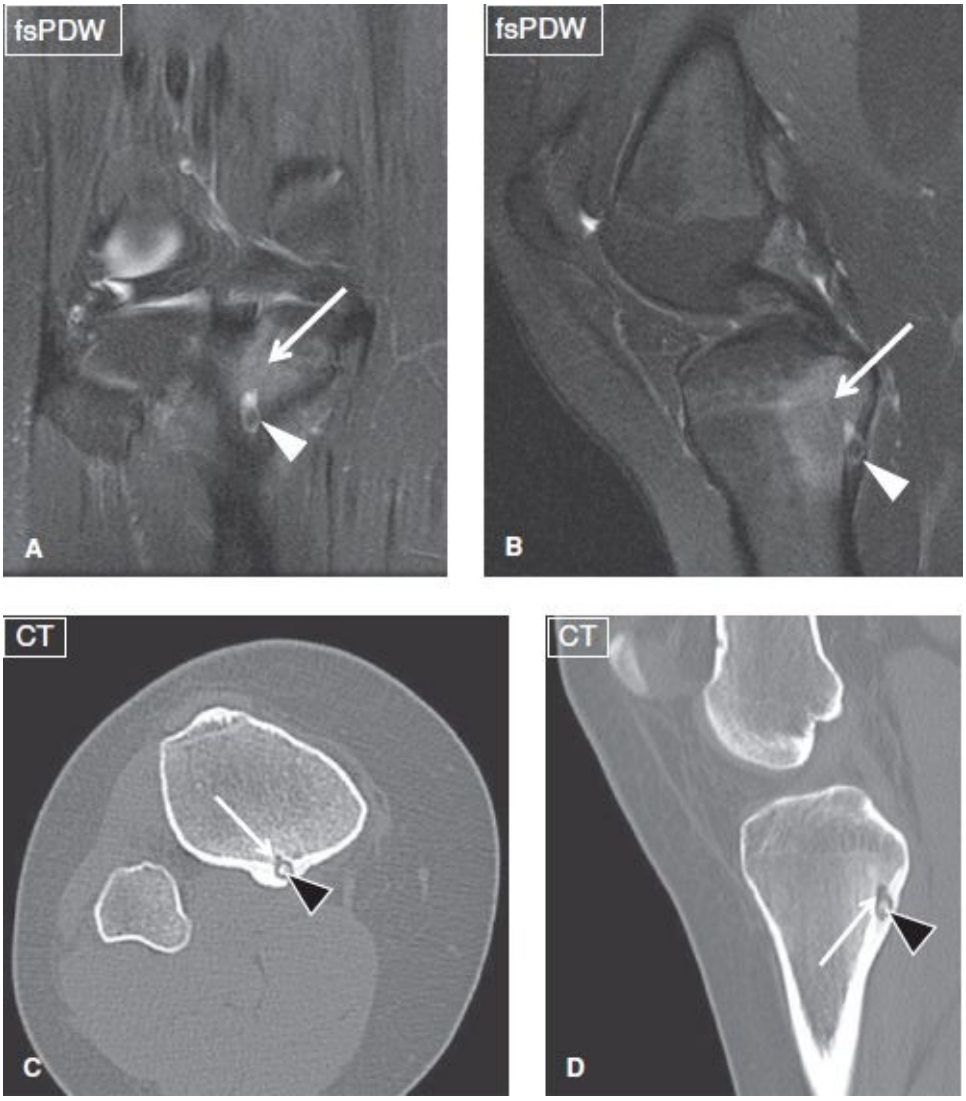

Fig. 66: Osteoid osteoma. Coronal **(A)** and sagittal **(B)** images exhibit a T2 hyperintense cortically based T2 hyperintense lesion (*arrowheads*) at the posterior medial tibial condyle, which features a hypointense center, and is associated with surrounding marrow edema (*arrows*). Axial **(C)** and sagittal reformatted **(D)** CT images delineate the lesion (*arrows*) along with the radiolucent nidus (*arrowheads*), which includes a central hyperdense focus.

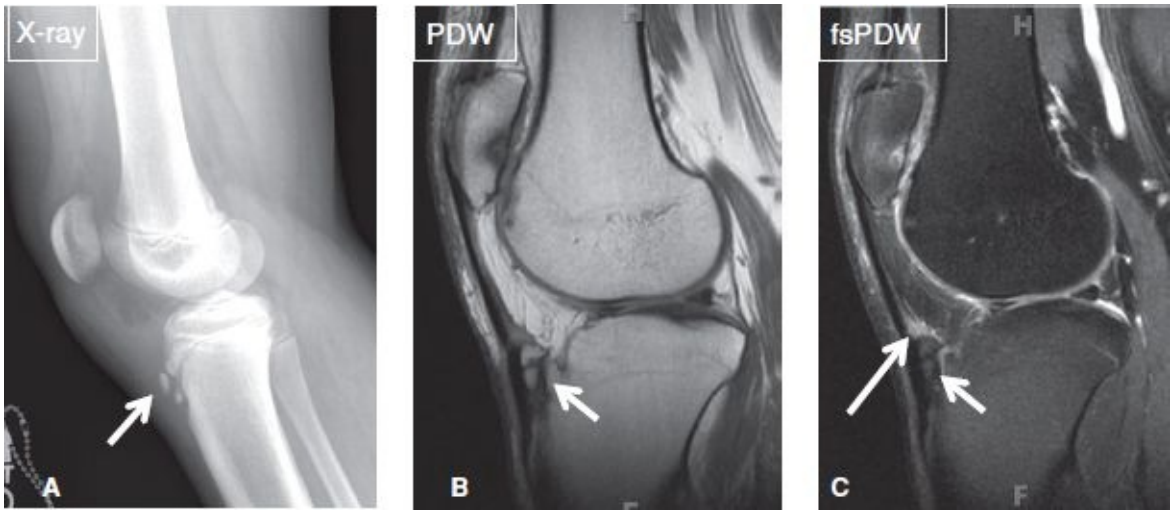

Fig. 67: Cortical avulsive change aka Osgood–Schlatter disease. **A:** Lateral radiograph shows fragmentation and chronic avulsions (*arrow*) of the tibial tuberosity with adjacent soft tissue swelling in the Hoffa fat pad. **B, C:** The corresponding sagittal MR images confirm the plain film finding (*short arrows*), and additionally demonstrate focal adjacent distention (*long arrow*) of the deep infrapatellar bursa.

- Predominantly periosteal/subperiosteal—subperiosteal hematoma, lipoma, abscess, periosteal osteosarcoma, and periosteal chondrosarcoma (Fig. 68).

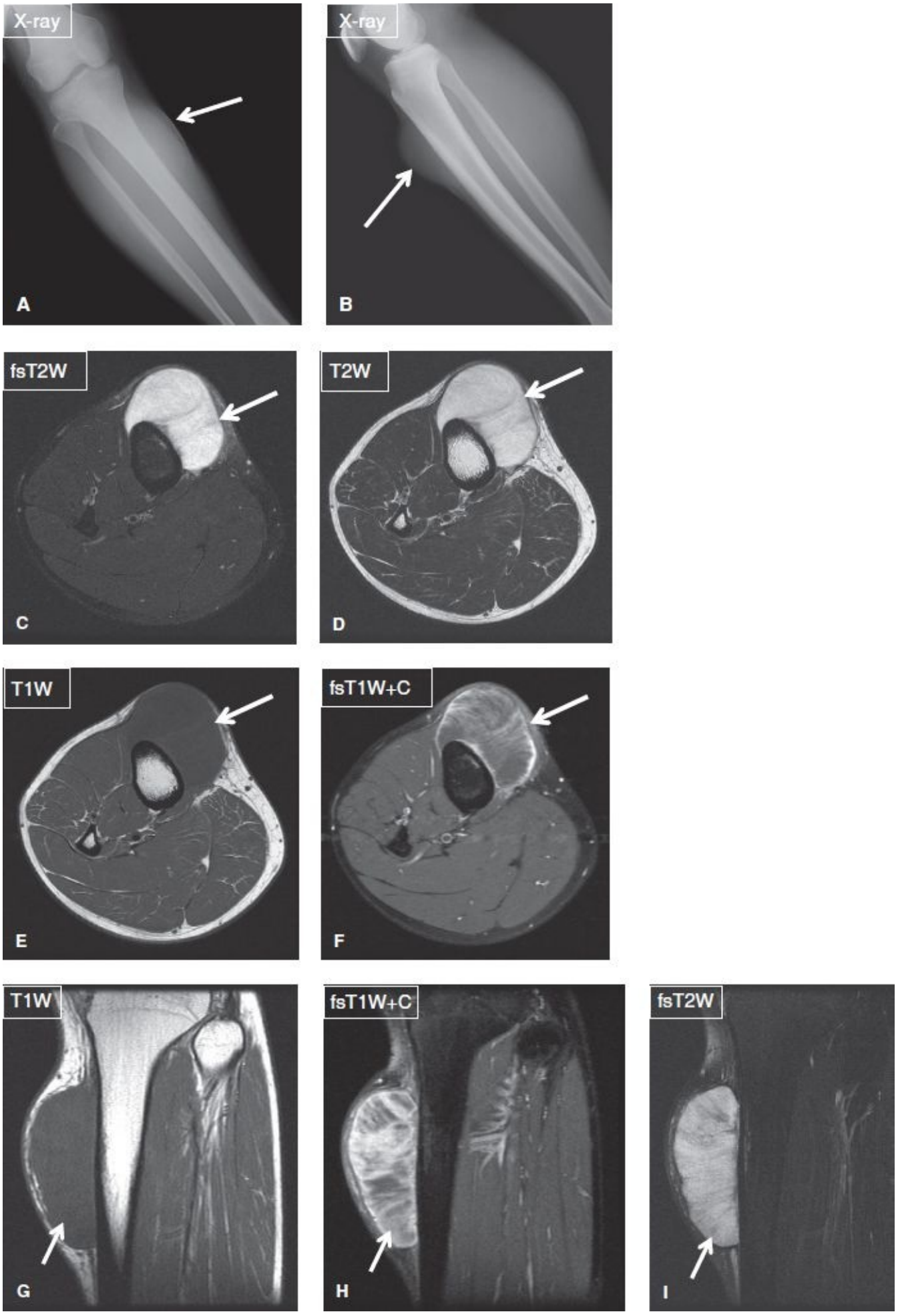

Fig. 68: Periosteal chondrosarcoma in a young boy, who presented with a 6-month history of progressively enlarging painful mass in the right proximal tibia. Anteroposterior **(A)** and

lateral **(B)** radiographs of the lower extremity show focal soft tissue swelling (*arrows*) anterior to the proximal tibial metadiaphysis. On the corresponding axial **(C–F)** and sagittal **(G–I)** MR images, the subperiosteal lesion with cartilaginous matrix is well seen with significant striated enhancement (*arrows*). There is minimal subcortical bone marrow edema and enhancement.

Characteristics

Matrix: [<T1 and T2 signal characteristics>]

Uniformity: [<Heterogeneous> <Homogeneous>]

Fluid–fluid levels: [<No>]

Transition zone: [<Narrow-edema absent>]

Periosteal reaction: [<None>]

MR imaging enables characterization of the predominant tissue of musculoskeletal lesions, as well as adequate evaluation of their matrix. If the lesion is fat-containing, the differential diagnosis includes the following.

- Lipoma: Simple fat-containing encapsulated lesion, similar in signal intensity and approximately the same architecture as the adjacent subcutaneous fat, with/without thin (<2 mm) fibrovascular septations (Fig. 1)
- Atypical lipomatous lesion: New WHO terminology encompassing atypical lipoma and well-differentiated liposarcoma due to their similar growth behaviors; it is seen as an encapsulated lesion with minimally thicker septations or dirty fat appearance (Fig. 69)

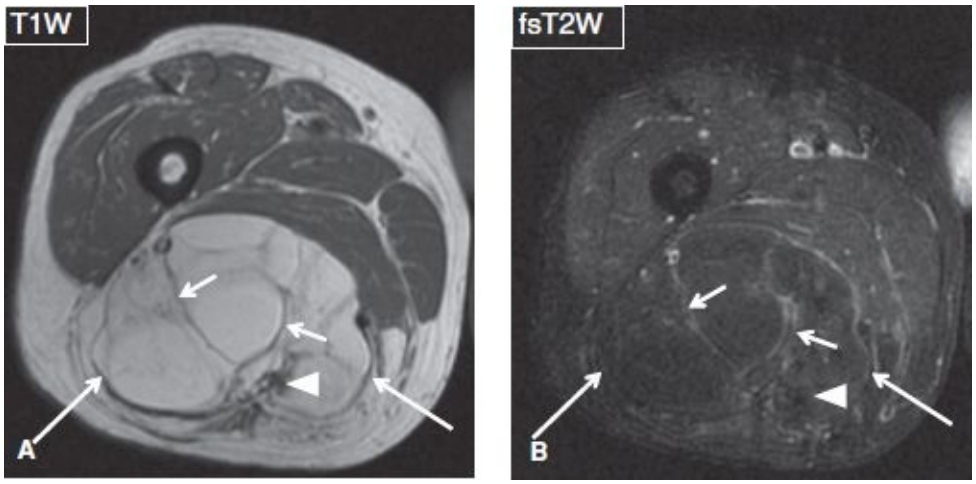

Fig. 69: Atypical lipomatous tumor in an 82-year-old man. Axial images demonstrate a mass (*long arrows*) in the posterior femoral compartment, which features predominantly fat signal, but also includes relatively thicker septae (*short arrows*) and areas of fat necrosis (*arrowheads*), giving a dirtier appearance as compared to the subcutaneous fat.

- Liposarcoma: Ill-defined lesion with small amounts of fat or no appreciable fat, and nodular enhancing areas interspersed with thicker septations and/or capsular breach with surrounding soft tissue infiltration or metastasis (Figs. 7, 70, 71)

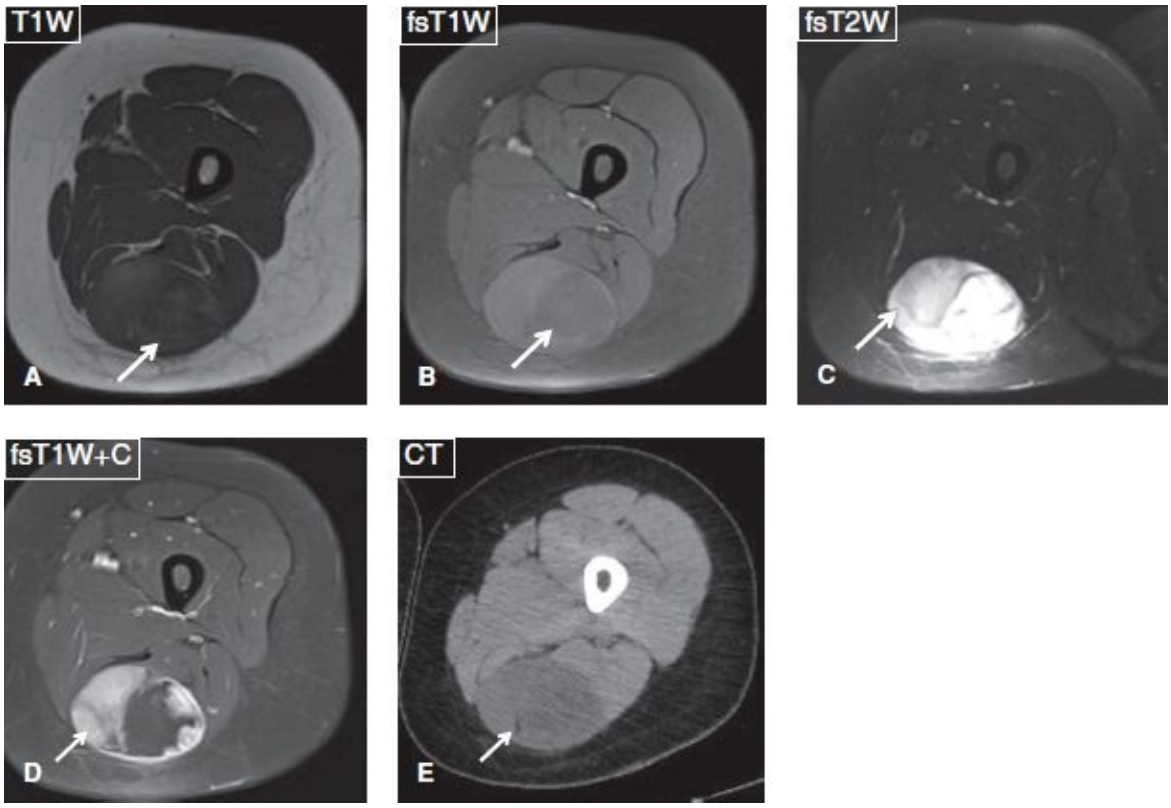

Fig. 70: Liposarcoma—intracompartmental disease. **A–D:** Axial MR images exhibit a well-defined mass (*arrows*) in the posterior compartment of the thigh, which features cystic- and solid-enhancing components. **E:** On the respective axial CT image, the lesion (*arrow*) is mildly hypodense with respect to the skeletal muscles and shows minimal fat. Minimal fat streaks in a soft tissue mass could be the only imaging sign of a high grade liposarcoma.

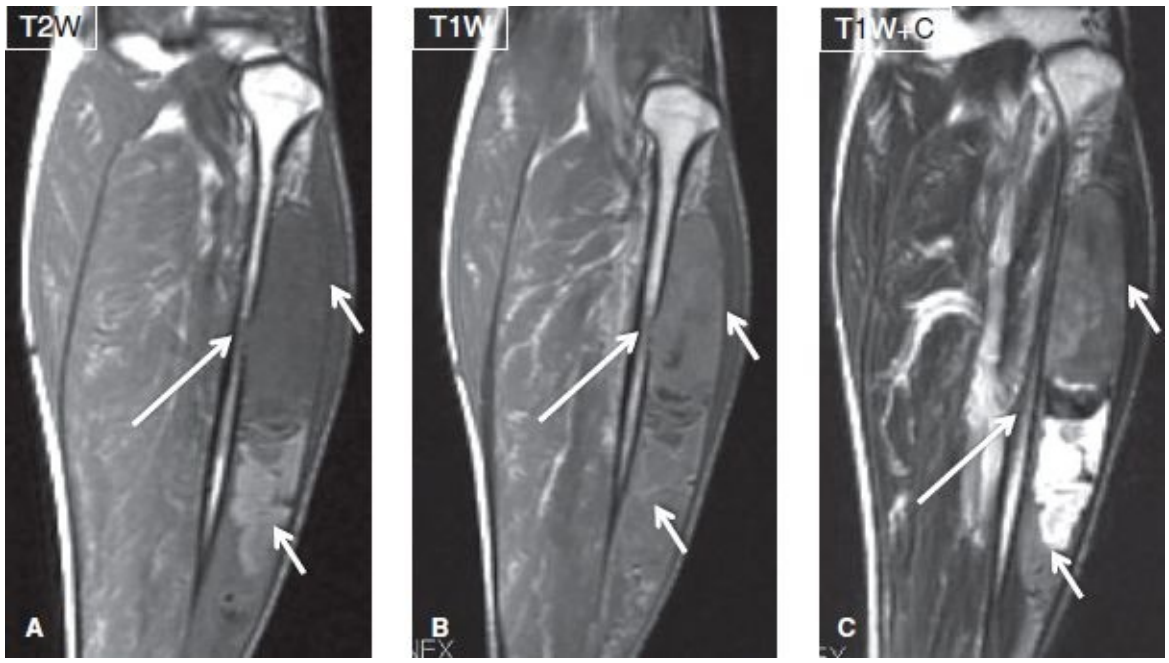

Fig. 71: Liposarcoma—extracompartmental disease. Coronal images show an elongated

heterogeneous mass (*short arrows*) in the lateral aspect of the calf with areas of T1 hyperintensity and nodular enhancement. Notice eccentric cortical permeation in the fibula (*long arrows*).

- Angiolipoma: With flow voids and enhancing vessels (Fig. 72)

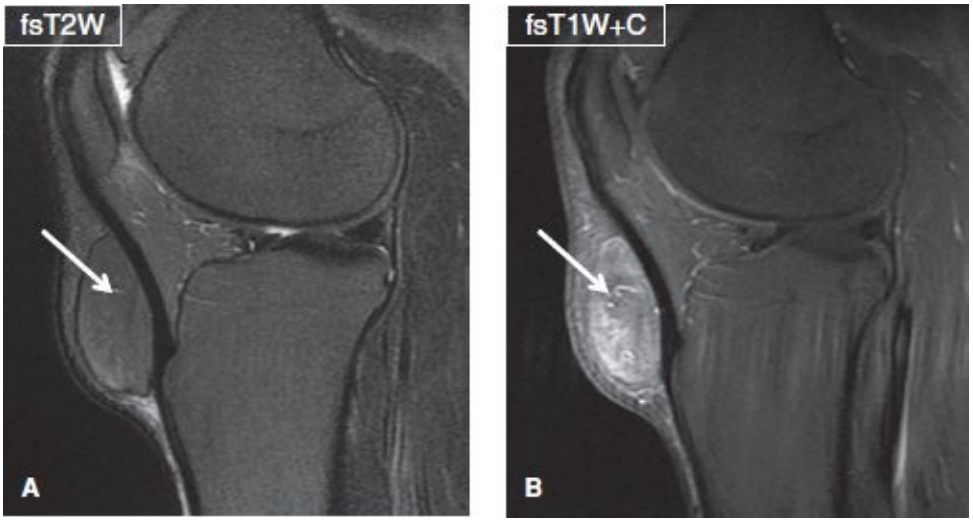

Fig. 72: Angiolipoma. Sagittal images exhibit a well-defined subcutaneous mass (*arrows*) of intermediate signal abutting the patellar tendon. The lesion shows intense contrast enhancement and internal vascularity, reflecting its vascular nature.

- Hemangioma: With phleboliths, rich vascularity, soft tissue components, and internal fat deposition related to steal phenomenon (Fig. 73)

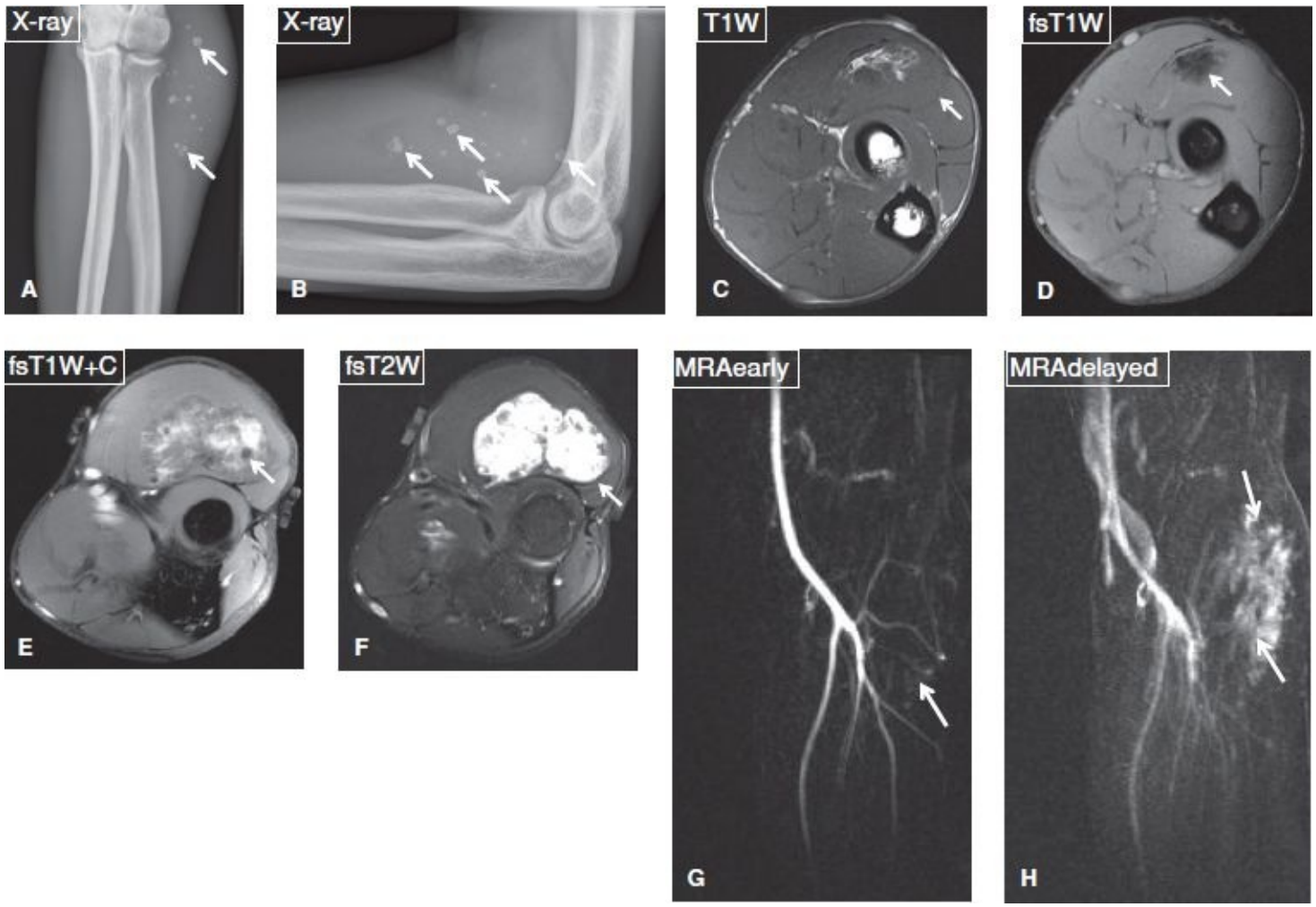

Fig. 73: Hemangioma. Noninvoluting congenital hemangioma (NICH). Anteroposterior **(A)** and lateral **(B)** radiographs of the upper extremity demonstrate enlargement of the soft tissues of the ulnar side of the proximal forehand, in which numerous ovoid calcifications (phleboliths; *arrows*) are evident with some surrounding lucency. **C–F:** The corresponding axial MR images exhibit a well-defined soft tissue mass (*arrows*) of heterogeneous signal, internal fat, and intense contrast enhancement within the extensor carpi radialis muscle. **G–H:** Coronal images from dynamic MR angiography examination reveal predominant delayed persistent enhancement of the lesion (*arrows*), which includes numerous moderately enlarged vessels. No arteriovenous shunting is seen to suggest high-flow vascular malformation.

- Heterotopic ossification: Peripheral mature calcification with or without internal marrow fat (Fig. 53)
- Elastofibroma dorsi: In the periscapular or gluteal area with internal vascularity (Fig. 50)
- Hibernoma: Similar to angiolipoma, with areas of fat and flow voids, and histologically contains vestigial brown fat (Fig. 74)

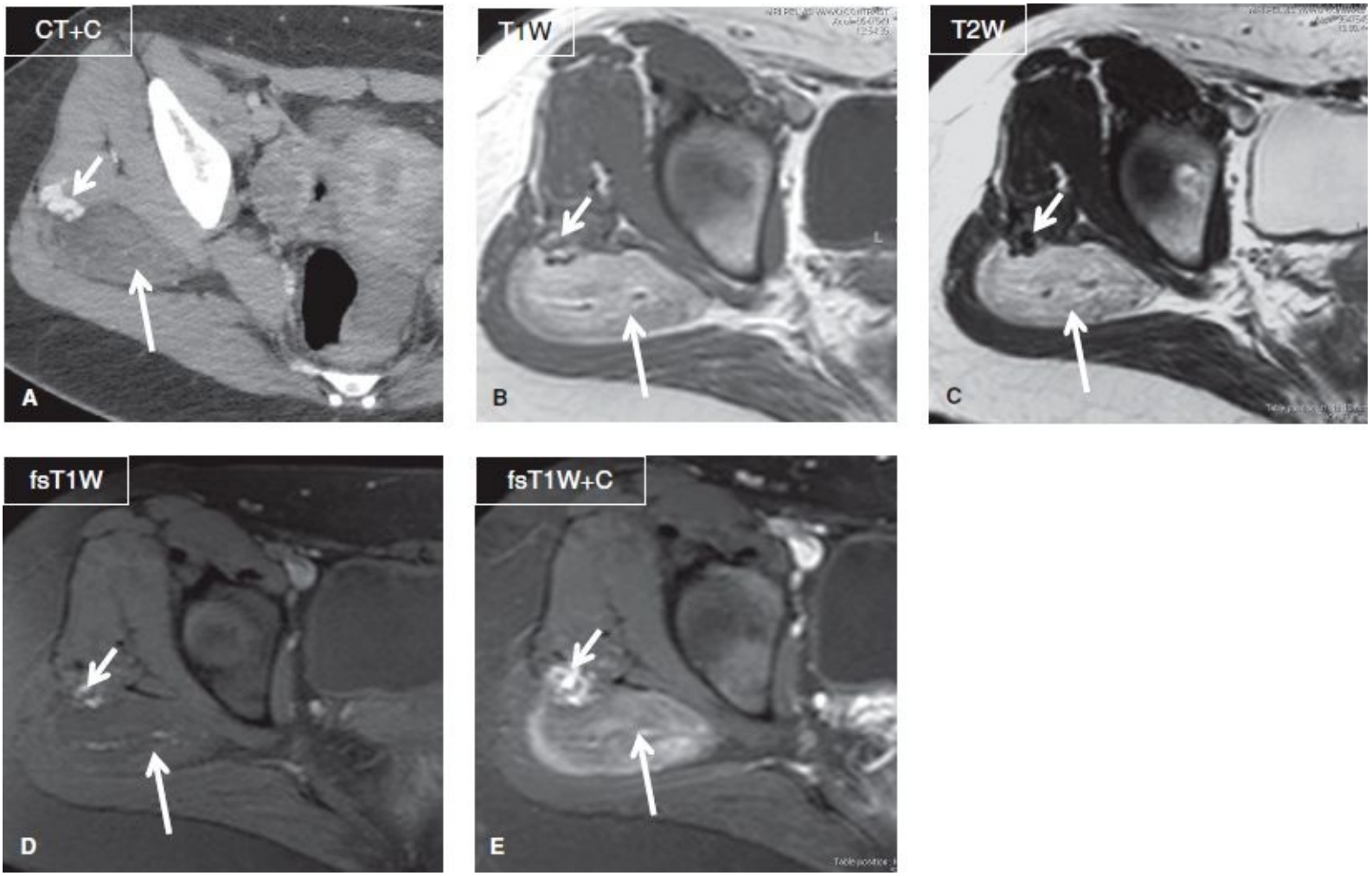

Fig. 74: Hibernoma in a 23-year-old woman. Axial CT **(A)** and MR **(B–E)** images at the level of the pelvis reveal a well-defined lesion (*long arrows*) situated between the right gluteus maximus and medius muscle, which shows density and signal between that of fat and skeletal muscle. The lesion shows moderate enhancement, and features eccentric enlarged vessels (*short arrows*).

- Neural fibrolipoma: Thickened nerve with fibrofatty proliferation, favored distribution includes, median, tibial nerve, and plantar nerves (Fig. 10)
- Lipoma arborescence: Fibrofatty synovial proliferation in the large joints (Fig. 75)

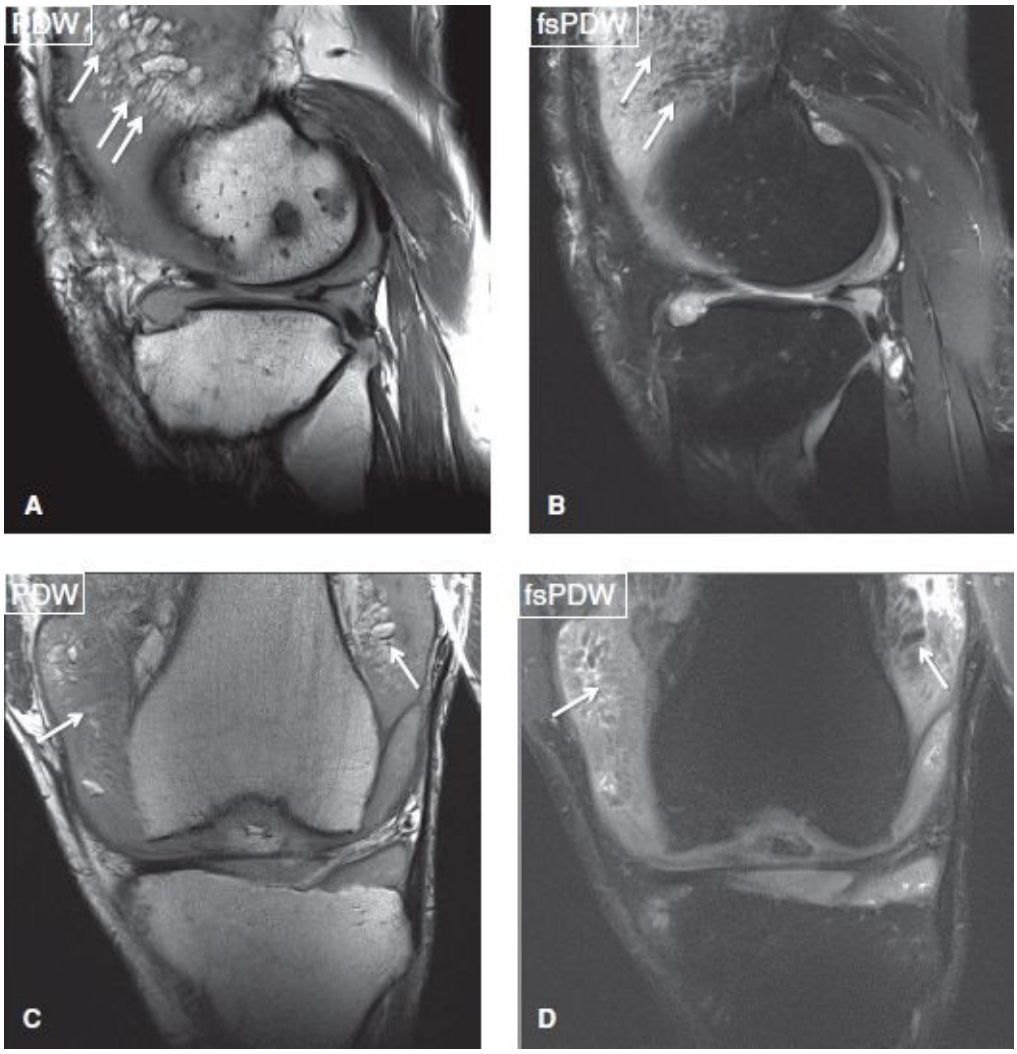

Fig. 75: Lipoma arborescens in a patient with long-standing rheumatoid arthritis. Sagittal **(A, B)** and coronal **(C, D)** images show large knee joint effusion with numerous "frond like" synovial projections (*arrows*) within the suprapatellar bursa, which follow the signal of fat on all pulse sequences.

When fat is encountered in a bone lesion, the differential diagnosis should be limited to subchondral geode, lipoma, liposclerosing myxofibrous tumor (in the femoral neck), Paget marrow, bone infarct, osteochondroma, and (uncommonly) enchondroma or fibrous dysplasia (Figs. 21, 62, 76–80).

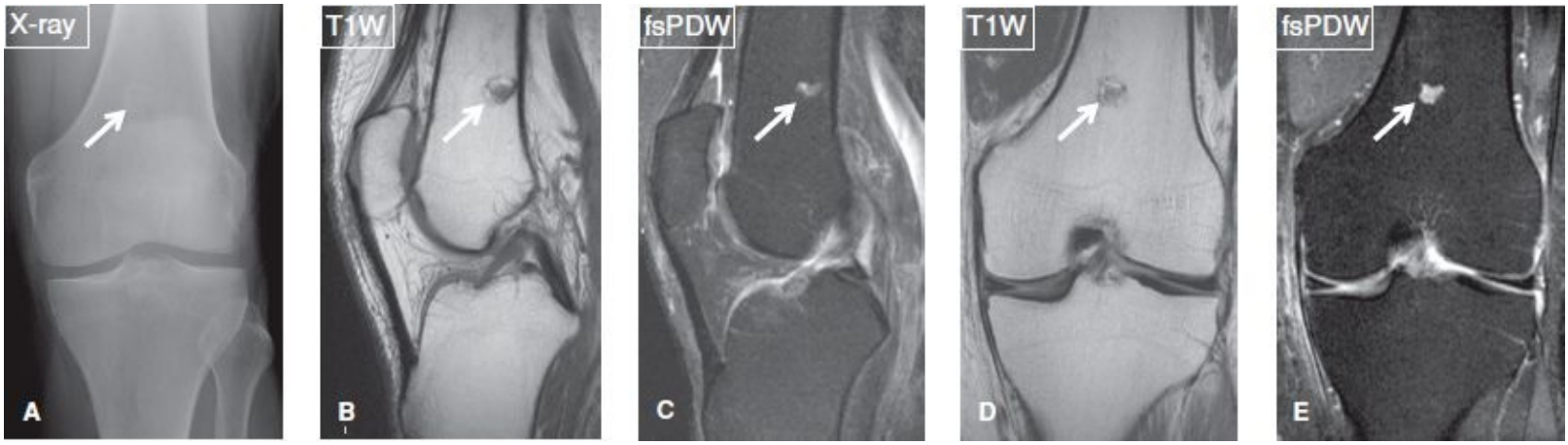

Fig. 76: Lipoma with cystic degeneration. Anteroposterior radiograph **(A)** shows a faint

lesion (*arrow*) with sclerotic margins at the femoral metaphysis. On the corresponding sagittal **(B, C)** and coronal **(D, E)** MR images, the lesion (*arrows*) features fat signal in the periphery and fluid signal in the center.

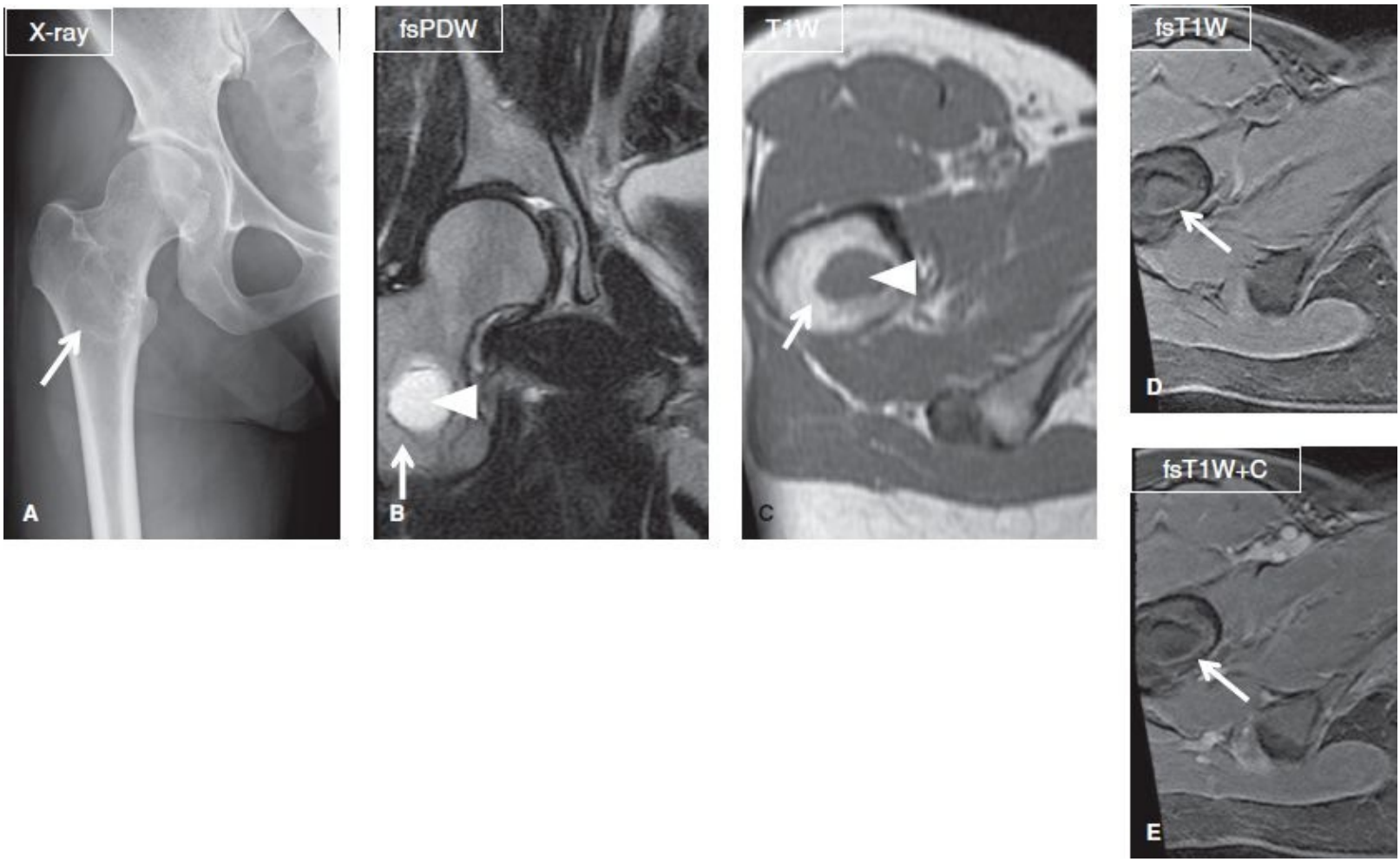

Fig. 77: Lipoma with cystic degeneration. Anteroposterior radiograph **(A)** shows a lytic lesion (*arrow*) with thin sclerotic margin at the intertrochanteric area. On the respective coronal **(B)** and axial **(C–E)** MR images, the lesion features fat signal in the periphery (*arrows* in **B, C**) and fluid signal in the center (*arrowheads* in **B, C**) and also lacks contrast enhancement (*arrows* in **D, E**).

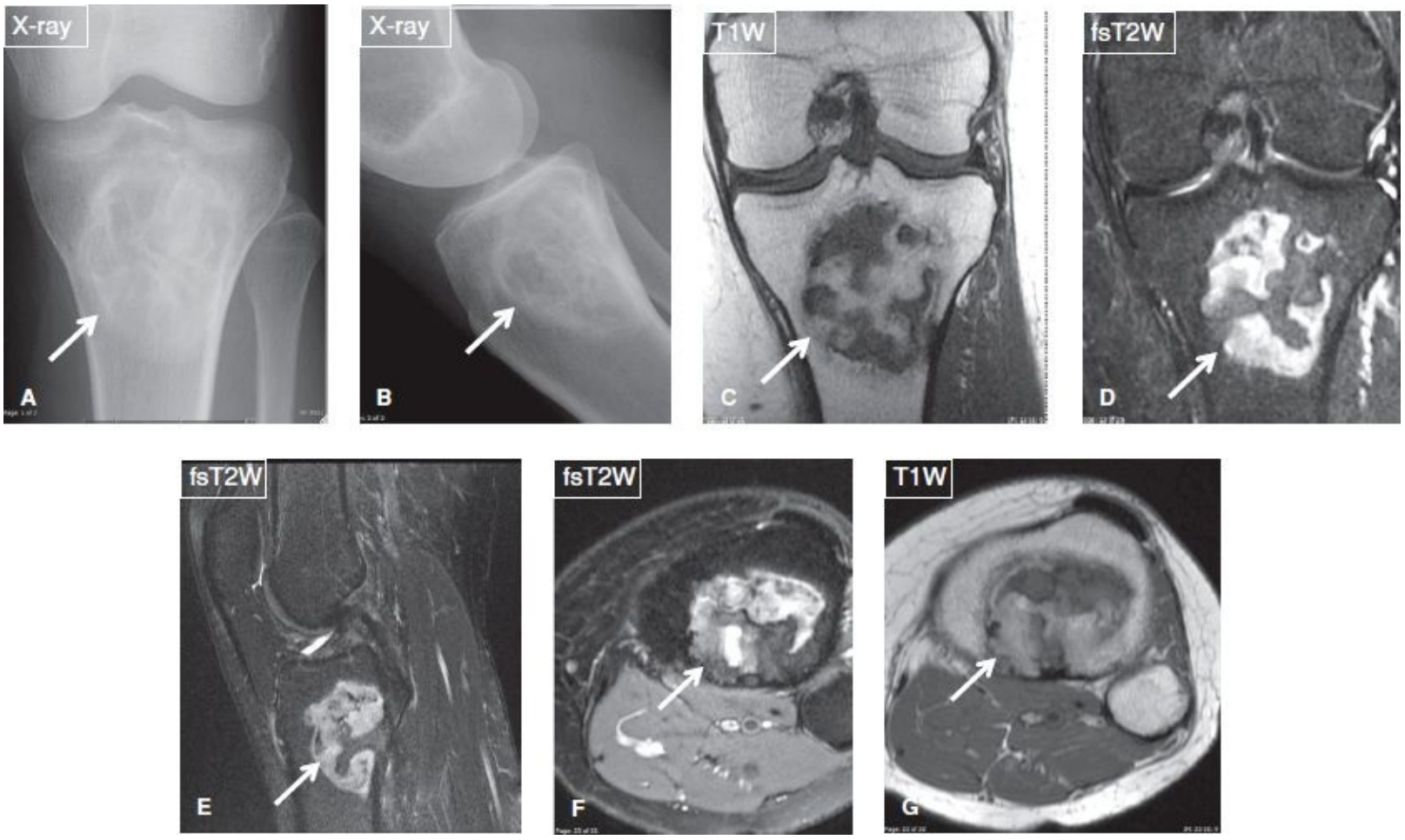

Fig. 78: Bone infarct. Anteroposterior **(A)** and lateral **(B)** radiographs of the left knee demonstrate a relatively well-defined sclerotic lesion (*arrows*) in the proximal tibia with internal lucencies (*arrows*). On the respective coronal **(C, D),** sagittal **(E),** and axial **(F, G)** MR images, the lesion shows cystic and fatty changes, a classic appearance for a chronic bone infarct.

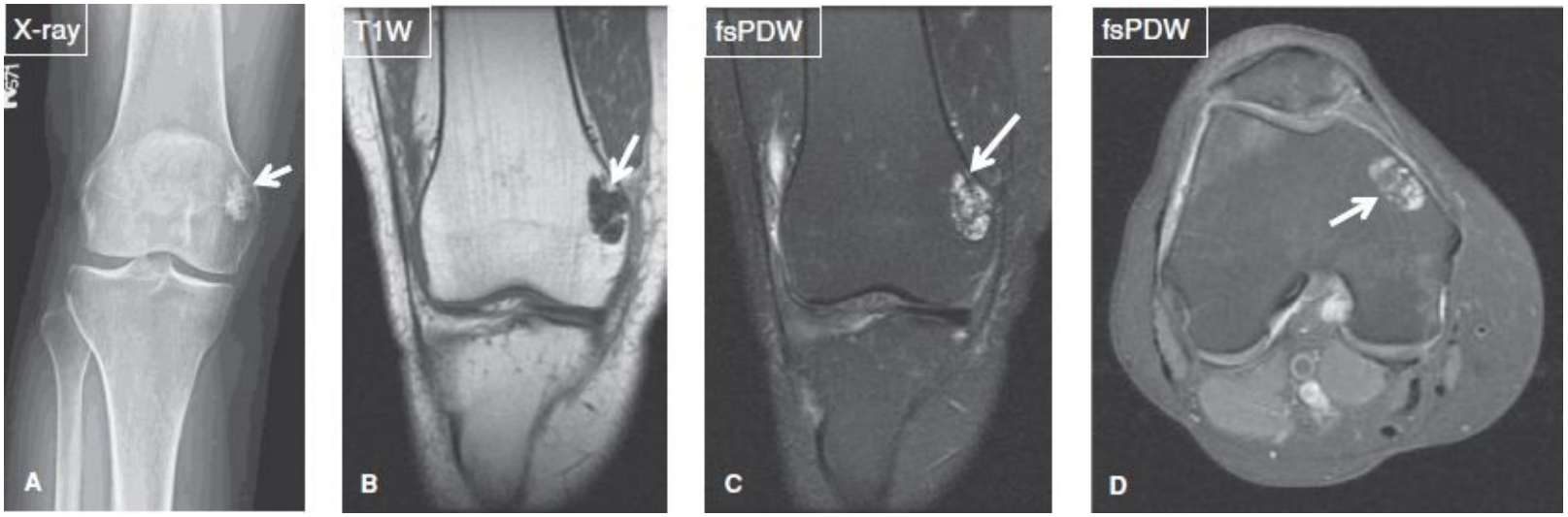

Fig. 79: Enchondroma. **A:** Anteroposterior radiograph demonstrates a cluster of rings and arcs calcifications (*arrow*) at the femoral metaphysis, typical of enchondroma. **B:** On the corresponding coronal **(B, C)** and axial **(D)** MR images, the lesion (*arrow*) is well defined, lacks surrounding edema, and features numerous tiny T2 hyperintense locules, that appear to coalesce with one another, reflecting the high fluid content of hyaline cartilage. Notice

internal hypointensities of mineralization and minimal fat peripherally (*arrows* in **B, C**).

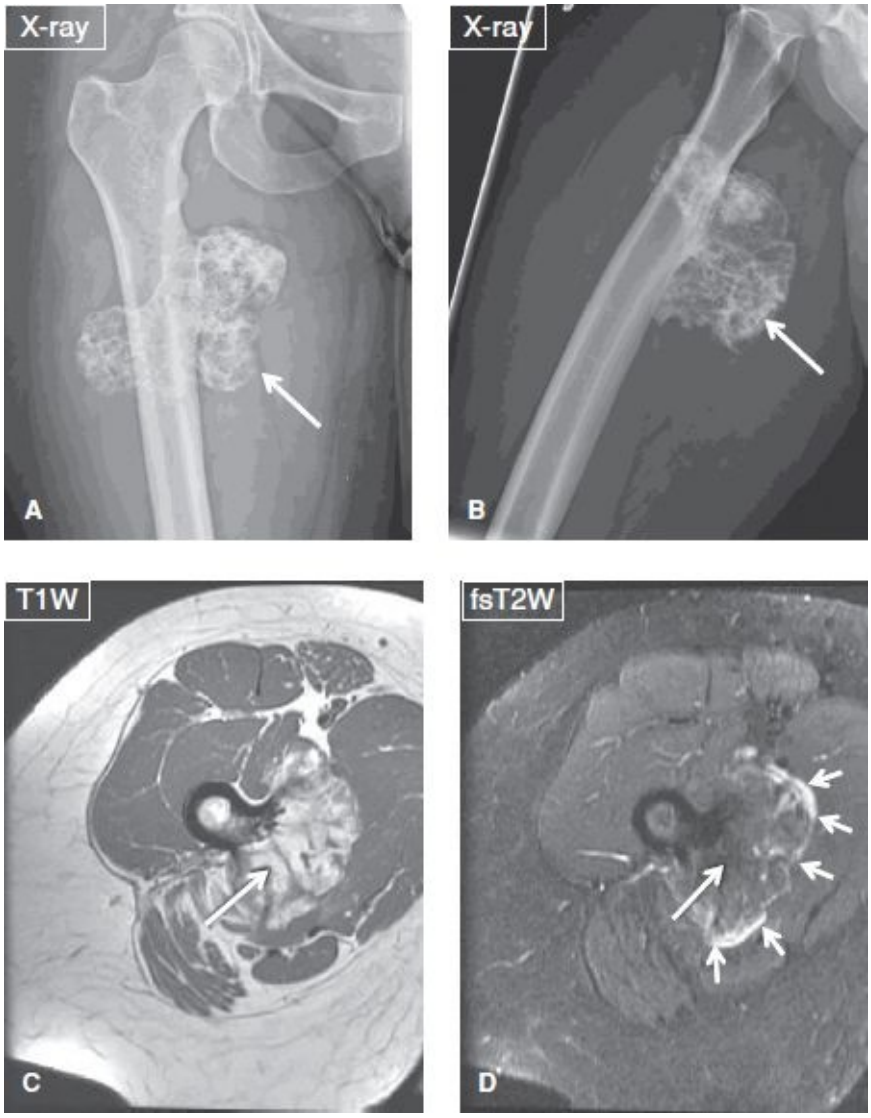

Fig. 80: Osteochondroma. Anteroposterior **(A)** and lateral **(B)** radiographs of the right femur show a calcified lesion (*arrows*) at the posterolateral aspect of the thigh. **C, D:** On the respective axial MR images, the lesion is continuous with the femur, displaces the adjacent muscles without signs of infiltration, and features extensive internal fat signal (*long arrows*), which corresponds to fatty marrow, as well as a thin T2 hyperintense cap (*short arrows*), which corresponds to hyaline cartilage.

Most tumors are T2 bright. If the lesion is predominantly T2 dark, it may indicate one of the following (Figs. 81–87).

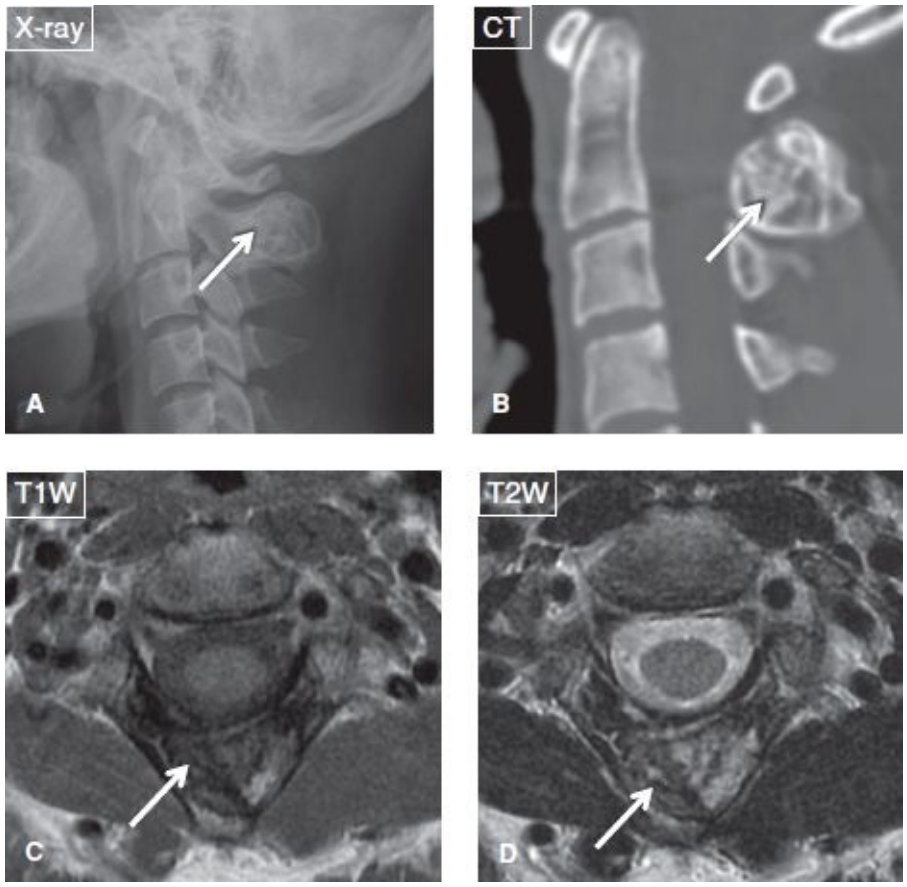

Fig. 81: Fibrous dysplasia of the spine as an incidental finding in a young man. Lateral radiograph **(A)** and sagittal reformation CT image **(B)** of the cervical spine reveal posterior element enlargement of the C2 vertebra (*arrows*), which features a ground glass and partially calcified internal appearance. On the corresponding axial MR images **(C, D),** the lesion (*arrows*) shows heterogeneous, mixed, predominantly intermediate-to-low T1/T2 signal.

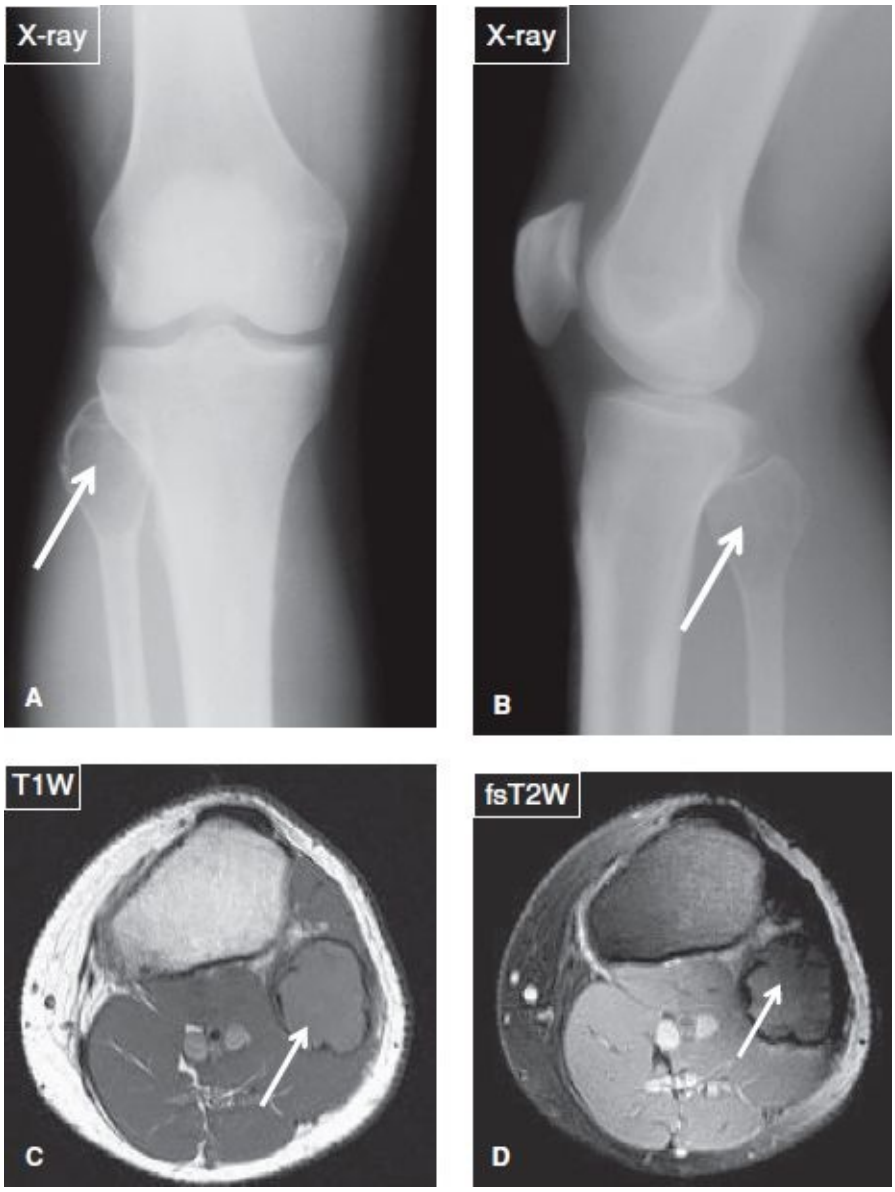

Fig. 82: Giant cell tumor. Anteroposterior **(A)** and lateral **(B)** radiographs of the knee demonstrate a relatively well-defined lytic lesion (*arrows*) involving the proximal fibular metaphysis with immediate subcortical extension. **C, D:** The respective axial MR images show a homogeneous lesion (*arrows*) of intermediate T1 signal and dark T2 signal abutting the proximal fibular articular surface.

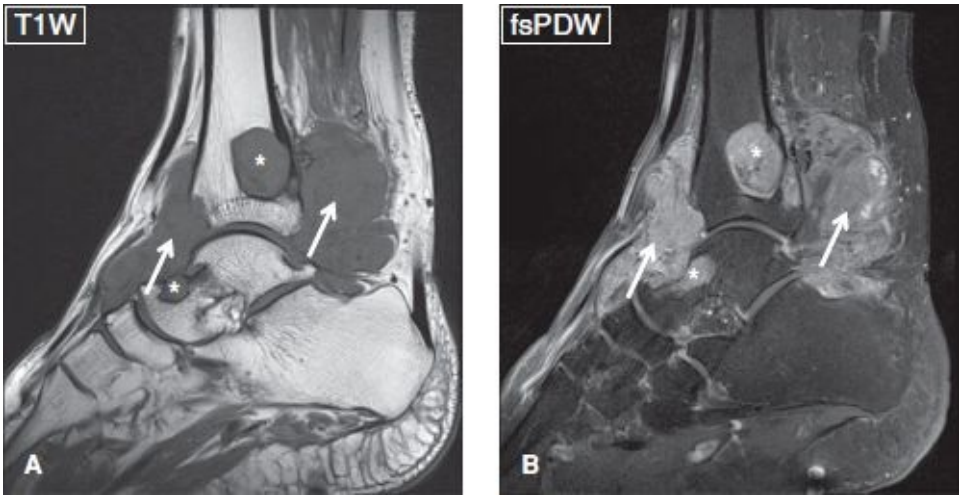

Fig. 83: Diffuse pigmented villonodular synovitis. Sagittal images demonstrate a large

amount of heterogeneous tissue (*arrows*) of intermediate T1/mixed, predominantly low T2 signal within the ankle joint, which causes bone erosions (*asterisks*).

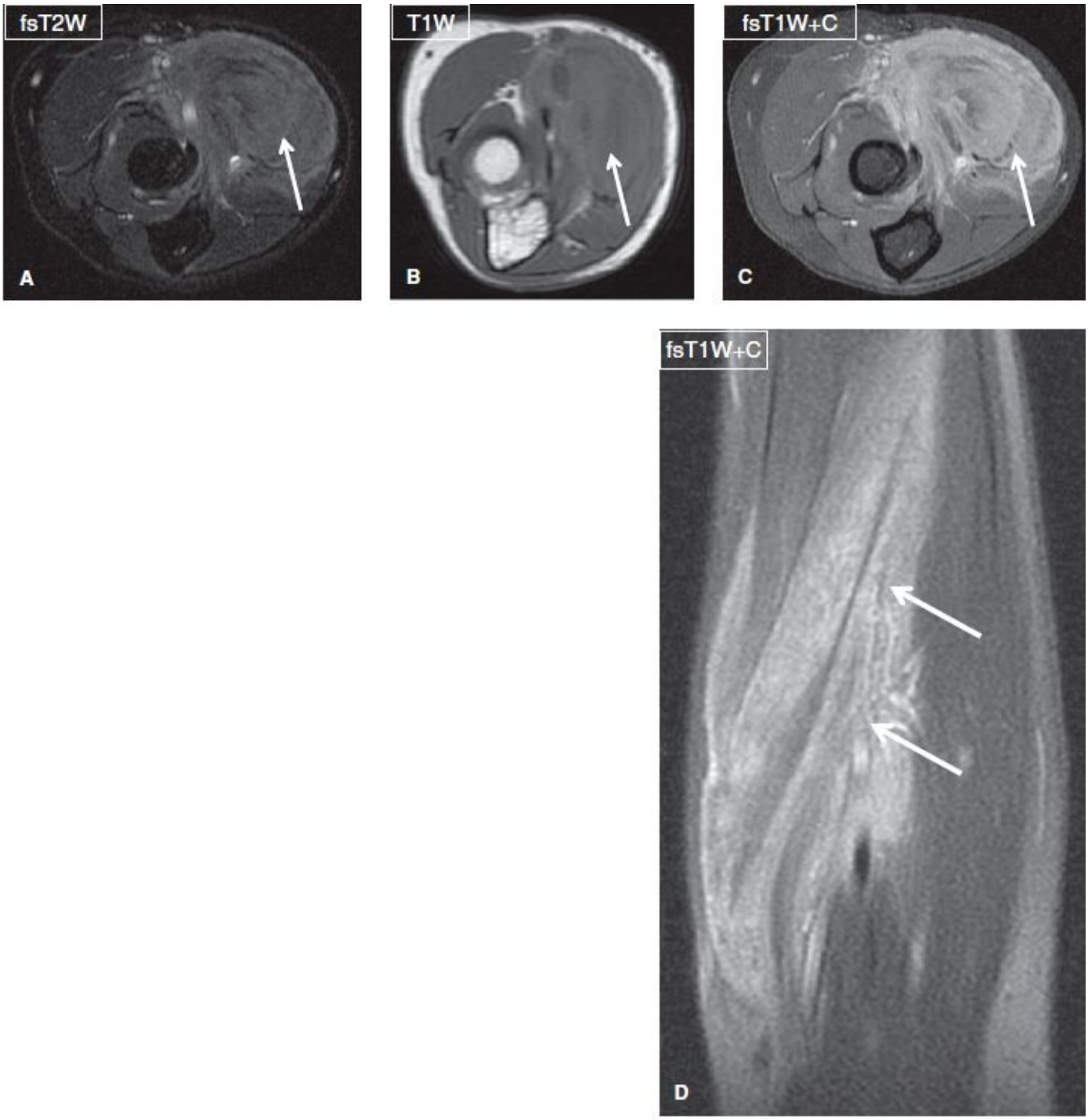

Fig. 84: Sarcoid. Axial **(A–C)** and sagittal **(D)** images of the upper extremity demonstrate diffuse enlargement and heterogeneous, predominantly hypointense T2 signal alteration and moderate diffuse contrast enhancement of the muscles (*arrows*) of the anterior compartment of the forearm, biopsy-proven sarcoid.

Fig. 85: Bone infarcts. Oblique **(A)** and anteroposterior **(B)** radiographs of the ankle show a medullary lesion (*arrows*) at the distal tibia, which features sheet-like central lucency and is surrounded by shell-like sclerosis with serpiginous border. Similar changes are also seen in the talus and calcaneus with talar dome articular surface irregularity. On the corresponding coronal **(C)** and sagittal **(D)** MR images, the lesion (*arrows*) demonstrates internal fat signal, T2 dark signals, and is surrounded by a thin serpiginous T2 hyperintense border. Additional similar lesions are evident in the calcaneus (*double asterisk*) and the talus (*single asterisk*), the latter also exhibiting superior articular surface collapse.

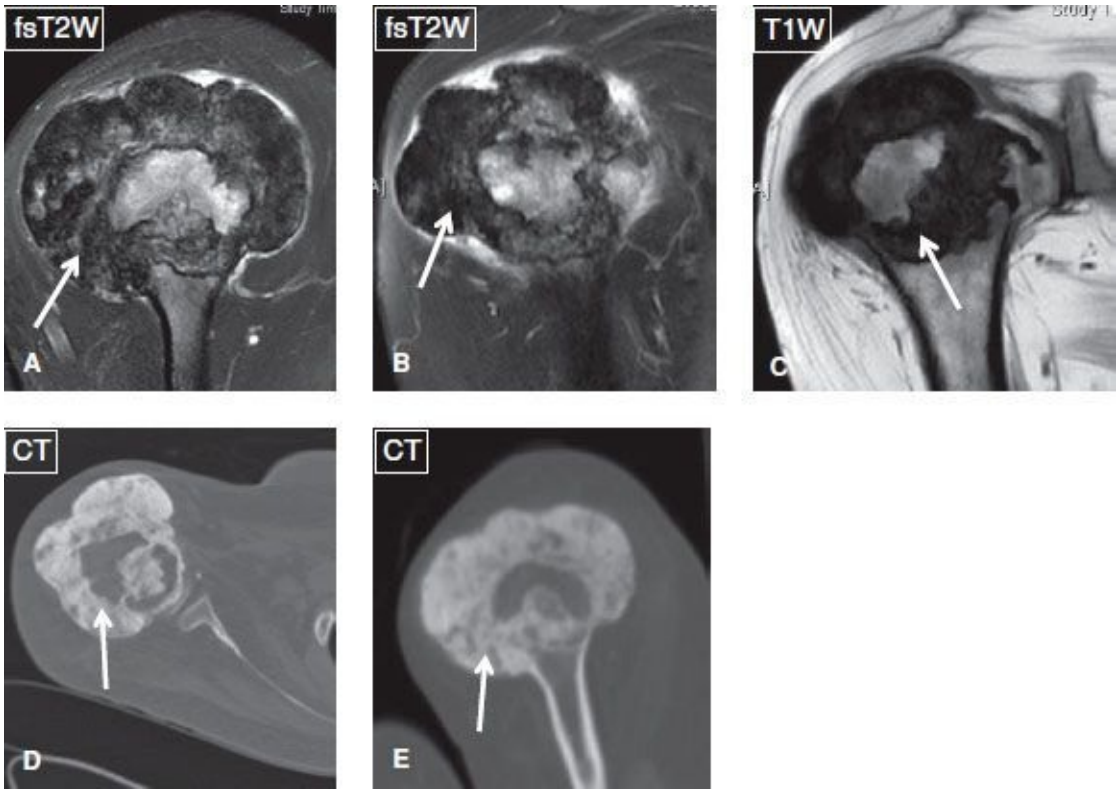

Fig. 86: Heterotopic ossification. Sagittal **(A)** and coronal **(B, C)** MR images show an expansile heterogeneous hypointense mass (*arrows*) at the humeral head with surrounding muscle atrophy. Axial **(D)** and sagittal reformatted **(E)** images from the respective CT scan reveal the ossified nature of the lesion (*arrows*).

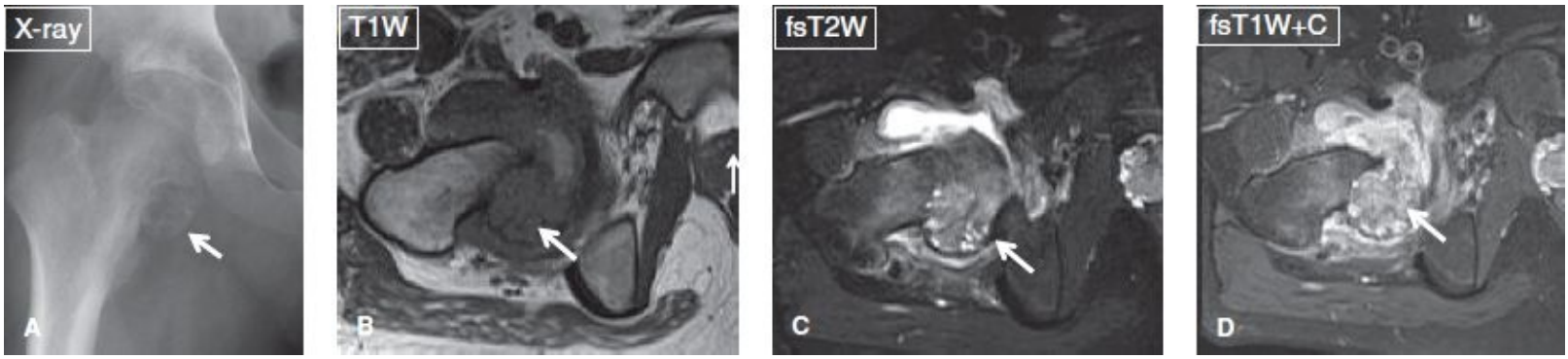

Fig. 87: Osteoblastoma. Anteroposterior radiograph **(A)** of the right hip shows a mineralized mass of the femoral neck (*arrow*). Corresponding axial MR images **(B–D)** show locally destructive lesion (*arrows*) with intermediate T1/T2 signal alterations, associated fascial edema, enhancement and right hip effusion, biopsy-proven osteoblastoma. (Courtesy of Dr. In Sook Lee, MD.)

- Fibrous tissue composition, such as in fibroma, fibromatosis, fibrous dysplasia, nodular fasciitis, soft tissue callous, NOF, fibromyxoid sarcoma, and undifferentiated pleomorphic sarcoma (aka MFH)
- High cellularity, such as in lymphoma
- Calcification(s), such as in synovial osteochondromatosis, juvenile aponeurotic fibroma, calcium hydroxyapatite deposition, gouty tophi, and bone infarcts

- Hemorrhage, such as in PVNS, hemophilic pseudotumor and endometriosis
- Granulation tissue, such as in rheumatoid nodules, sarcoidosis, or tuberculosis
- Osseous tissue, such as in osteosarcoma (aggressive features, Codman triangle, sunray or hair-on-end periostitis, soft tissue mass, skip lesions, and metastases), heterotopic ossification, osteoid osteoma (size <1.5 cm, extensive cortical and periosteal thickening, bone marrow and soft tissue edema, enhancing nidus and night pains relieved by nonsteroidal anti-inflammatory drugs), osteoblastoma (size >1.5 cm, involving posterior elements of the spine, causing painful scoliosis, potentially malignant, may harbor secondary ABC), GCT (young to middle-aged individuals, subarticular extension, expansion, no sclerosis on plain film, soft tissue extension or calcifying metastasis may be seen uncommonly, secondary ABC can develop), and desmoplastic fibroma (young age, metaphyseal with thick trabeculations)

Soft tissue sarcomas that most commonly show calcifications on the correlative radiographs include synovial sarcoma, undifferentiated pleomorphic sarcoma, and liposarcoma (Fig. 88).

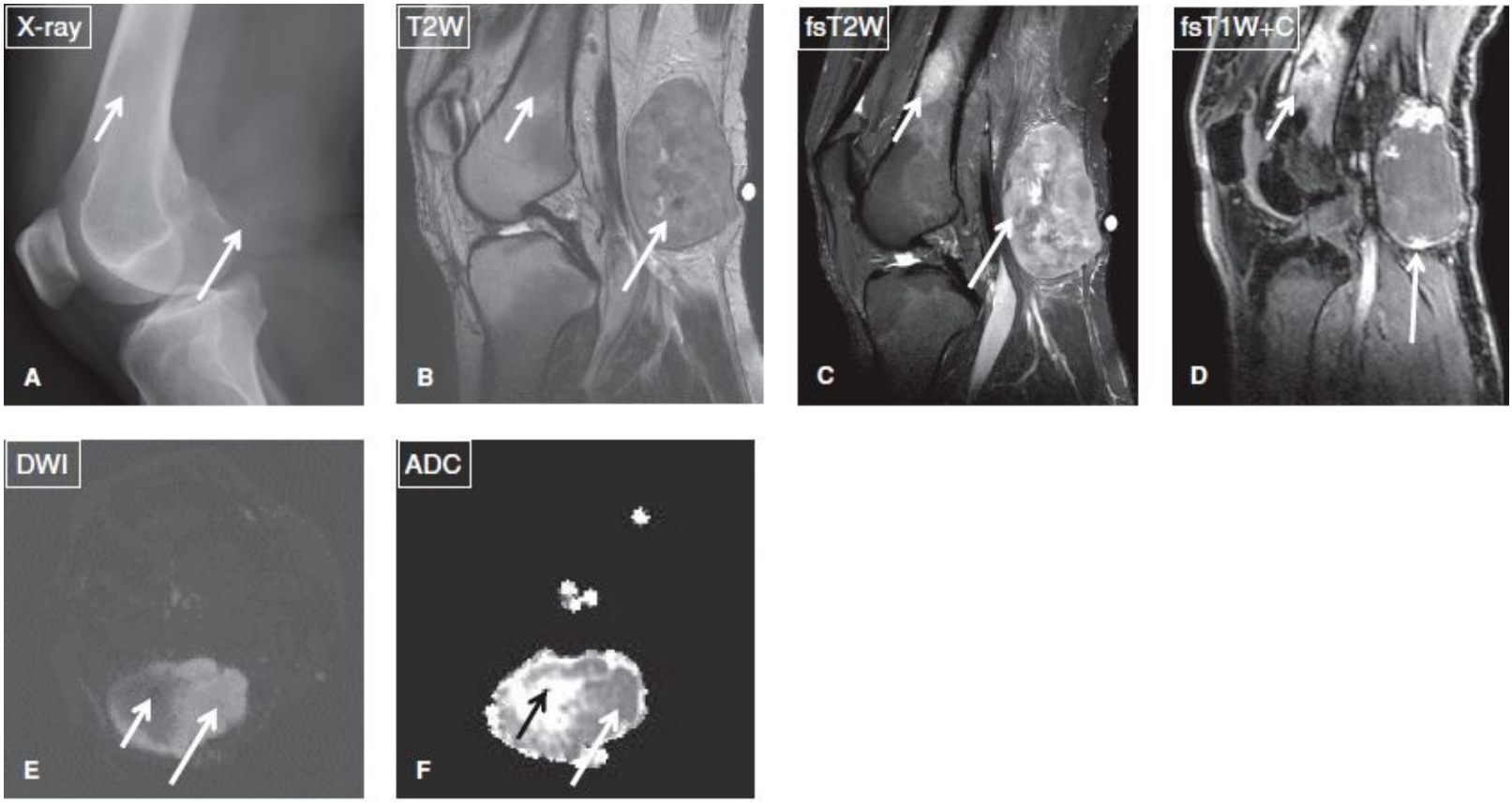

Fig. 88: Pleomorphic undifferentiated sarcoma. **A:** Lateral radiograph of the knee shows a soft tissue mass with internal mineralization in the popliteal fossa (*long arrow*). Also note lucent lesion in the femoral metaphysis (*short arrow*). **B–D:** Corresponding sagittal MR images **(B–D)** show a heterogeneously enhancing mass in the femoral necrosis and (*short arrows*) and a lobulated popliteal soft tissue mass with peripheral nodular enhancement (*long arrows*). **E, F:** Axial DWI images show internal mineral (*short arrows*) with peripheral solid component and restricted diffusion (ADC value: 0.8×10^{-3} mm2/s).

If the lesion is fluid-containing, it may represent ganglion cyst (in close proximity to synovial lining or ligaments, multilocular, peripheral or no enhancement), bursitis (at known bursal locations or adventitial bursitis at pressure points of extremities or on top of osteochondroma due to constant friction), abscess (multiple mural layers due to organization, surrounding facial edema and fluid, sinus tract, and history of toxemia or skin induration), hematoma, degloving lesion or seroma (blood products, organized multilayered lesion, lesion-spreading fascial layers, history of anticoagulation or trauma), geyser phenomenon (cystic lesion communicating with the acromioclavicular joint or os acromiale synchondrosis), intramuscular cyst (with parasitic infestation or delaminating tear of the tendon), and lymphatic malformation (fluid–fluid levels, hemorrhage, slow flow, none or peripheral septal enhancement, can be associated with cavernous components, aka cavernolymphatic malformation) (Fig. 89). It is important to obtain precontrast fsT1W images for accurate comparison with postcontrast fsT1W images since fat suppression alters the image contrast, rendering hemorrhagic or proteinaceous lesions bright, which might lead to false impression of nodular enhancement (Fig. 90).

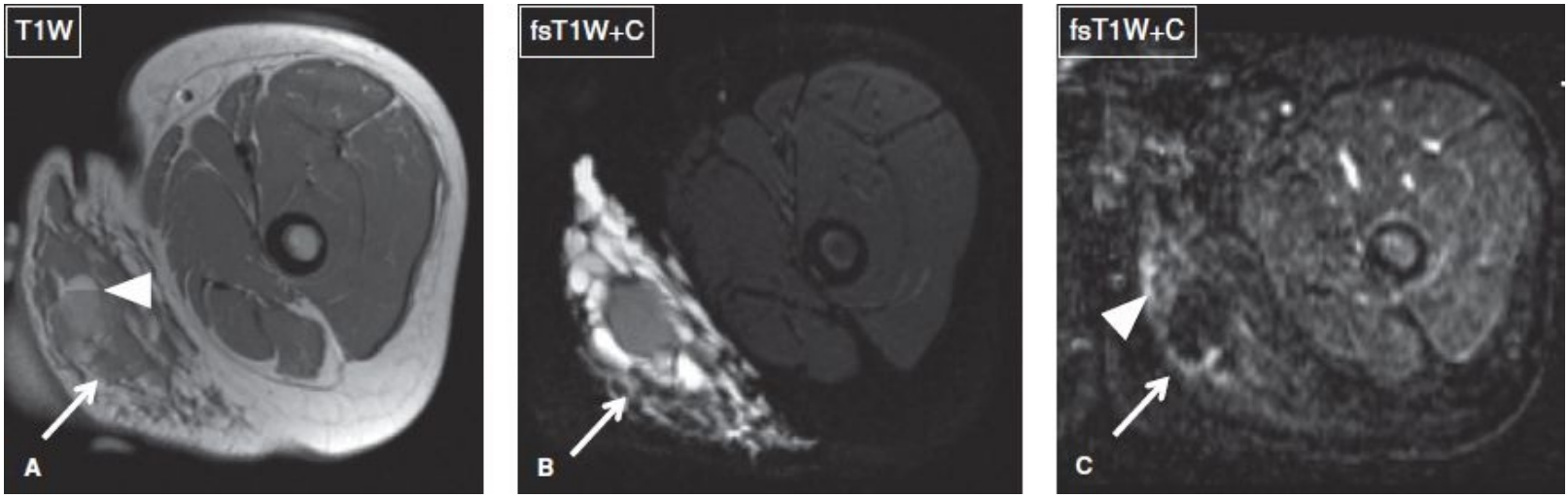

Fig. 89: Lymphatic malformation in a 2-year-old boy. Axial images show a multilocular cystic-appearing mass (*arrows*) with minimal peripheral enhancement (*arrowhead* in **C,** postcontrast subtraction image) and a fluid–hemorrhage level (*arrowhead* in **A**).

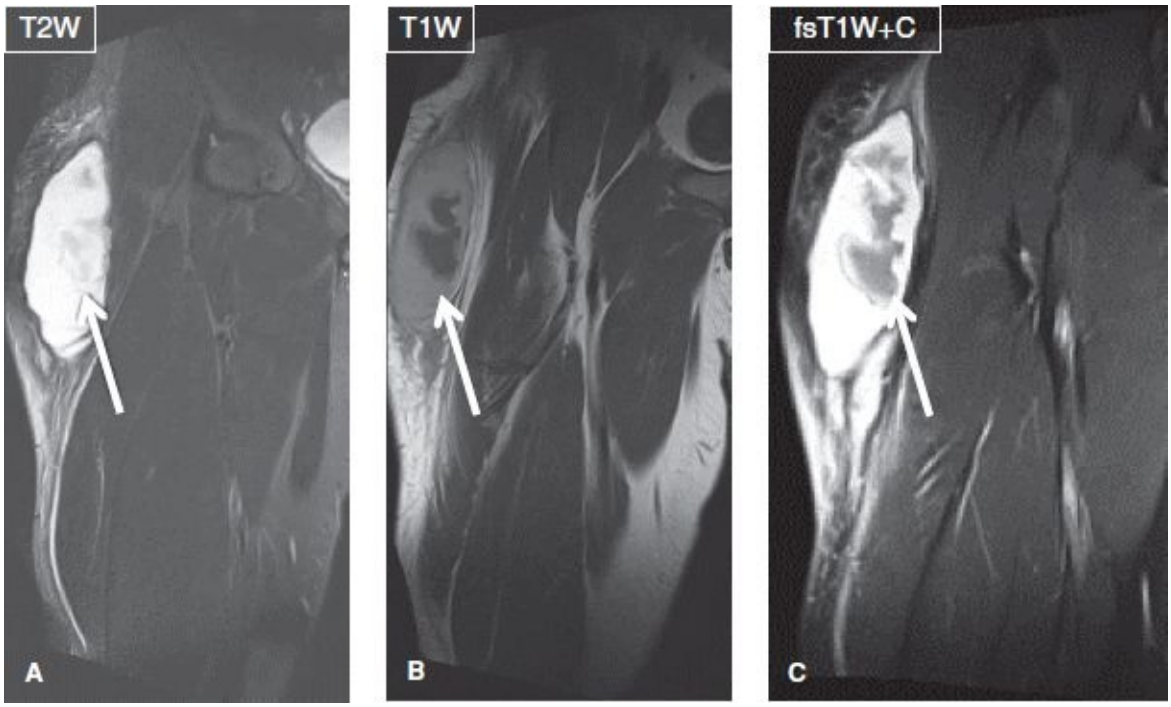

Fig. 90: Morel-Lavallée lesion in a young man with history of recent thigh trauma. Coronal MR images show a well-defined T1 hyperintense (hemorrhagic) fluid collection (*arrows*) between the subcutaneous fat and the superficial fascia, as a result of traumatic separation of the latter structures. Notice nodular enhancing appearance on the fat-suppressed postcontrast images mimicking a neoplastic lesion.

If the lesion contains cartilage (T1 intermediate and T2 bright with bubbly appearance, internal mineralization in rings-and-arcs configuration, as well as peripheral and septal enhancement), it may suggest one of the following:

- Enchondroma: Size <4 cm, $<50\%$ or no endosteal scalloping, no bone marrow edema or periostitis, minimal enhancement, usually asymptomatic (Fig. 79)
- Osteochondroma: Cartilage cap <1.5 cm thick, mature calcification of the cap, minimal or no growth after skeletal maturity, no cortical destruction, no periostitis, no soft tissue mass, no bone marrow edema unless there is recent injury, and minimal to no enhancement (Fig. 80)
- Chondrosarcoma: Size >4 cm, $>50\%$ to 75% endosteal scalloping of the cortex or frank cortical destruction, bone marrow edema, periostitis or soft tissue mass, growing mass, heterogeneous enhancement, new or increasing pain symptoms (Fig. 68)
- Synovial osteochondromatosis: Young age for primary type and older age for secondary type, bags of nodular masses with or without calcification adjacent to the facet joints of the spine, or in joints, such as the knee, hip, and temporomandibular joint with or without eccentric bony erosions and minimal peripheral or no enhancement
- Chondroblastoma: Young age, located in the epiphysis or apophysis, 50% showing internal mineralization, bone marrow edema, periosteal reaction, joint effusion (Fig. 91)

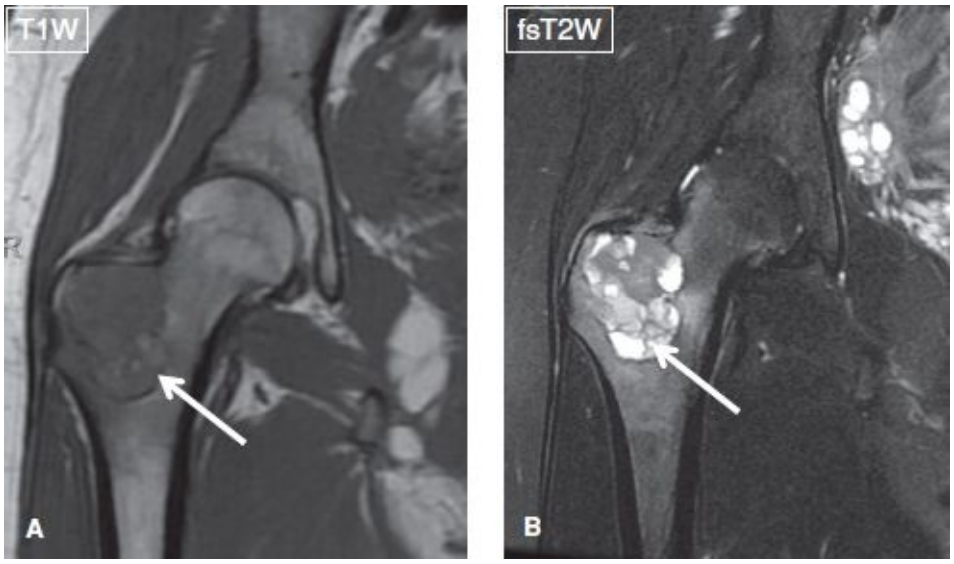

Fig. 91: Chondroblastoma with associated aneurysmal bone cyst. Coronal images demonstrate a well-defined expansile lesion (*arrows*) at the greater trochanter, which features intermediate T1 and heterogeneous high T2 signal, and is associated with surrounding marrow edema.

- Chondromyxoid fibroma—eccentric location, rarely mineralizes on plain films (Figs. 92, 93)

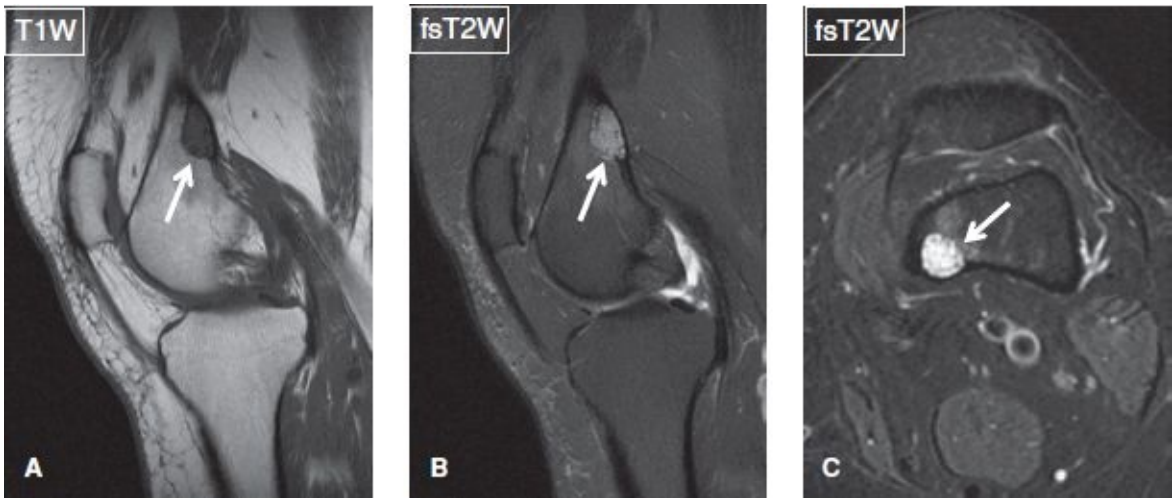

Fig. 92: Chondromyxoid fibroma. Sagittal **(A, B)** and axial **(C)** images demonstrate a eccentric well-defined T1 hypointense/T2 hyperintense ovoid lesion (*arrows*) at the femoral metaphysis, with long axis paralleling the long axis of the femur.

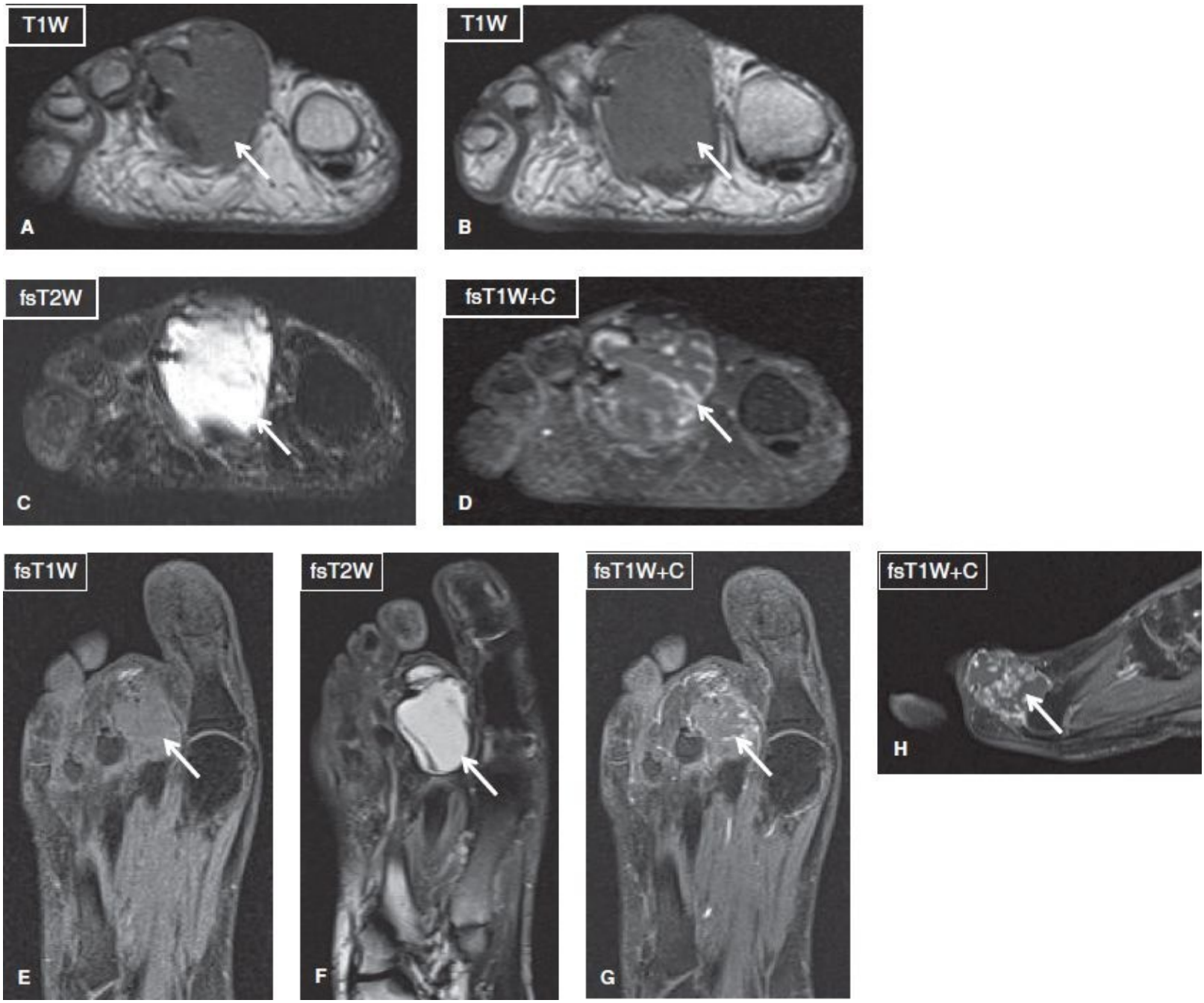

Fig. 93: Chondromyxoid fibroma. Axial **(A–D),** coronal **(E–G),** and sagittal **(H)** images exhibit a well-defined cartilaginous mass (*arrows*) at the forefoot arising from the proximal phalanx with typical ring and septal enhancement, a biopsy-proven chondromyxoid fibroma.

- Extraskeletal chondroma or chondrosarcoma: Cartilaginous matrix, T2 bright, peripheral septal or nodular enhancement, imaging cannot reliably differentiate benign from malignant lesion unless there is presence of infiltration of extracompartmental tissues or metastases (Fig. 94)

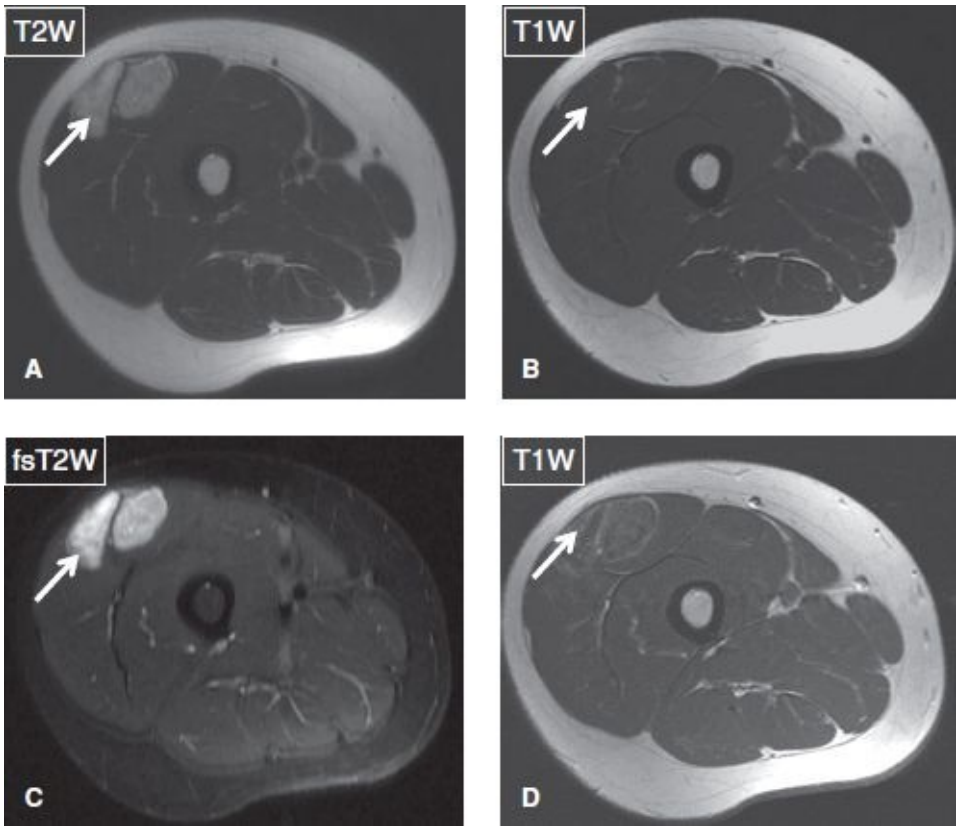

Fig. 94: Extraskeletal chondroma in a young boy, who presented with a painless palpable thigh mass. Axial MR images show a well-defined multilobulated mass (*arrows*) of intermediate T1/high T2 signal and mild contrast enhancement within the vastus lateralis muscle. Imaging cannot differentiate among intramuscular myxoma from chondroma or chondrosarcoma, as all of these entities will give similar MRI appearances.

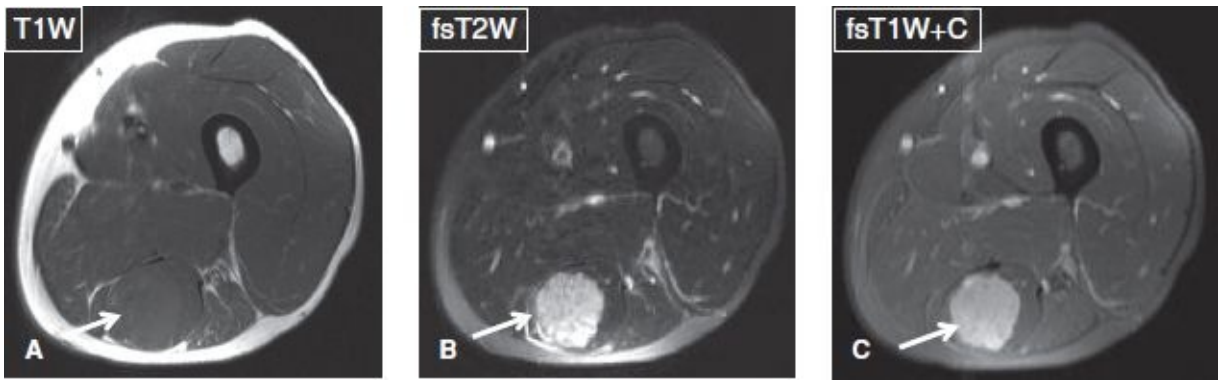

Fig. 95: Intramuscular metastasis in an old man with history of lung adenocarcinoma. Axial MR images demonstrate a well-defined solid homogeneous and intensely enhancing mass (*arrows*) in the semitendinosus muscle, a biopsy-proven metastasis.

Homogeneity on MR imaging is not a very useful criterion to differentiate benign from malignant lesions. Although heterogeneity is more commonly seen in malignant lesions and homogeneity in benign lesions; some types of soft tissue sarcomas, hemangioendothelioma, and bone metastasis may appear quite homogeneous (Fig. 95). One should administer contrast or check DW images to further evaluate such a lesion unless the latter corresponds to a clear-cut ganglion or bursitis (Fig. 96). Typical struts of bony trabeculations may be

seen with plasmacytoma in the vertebral body (mini-brain appearance). It should be remembered that any lesion, which shows solid, thick, peripheral, nodular, or central enhancement, it should be referred to as an indeterminate or malignant lesion. Further management strategy depends upon the confidence of the radiologist whether to do a short-term follow-up in 6 weeks to 3 months or refer for percutaneous biopsy or surgical sampling. It should be noted that the above radiologic approach and grading are different from how WHO dictates the classification of bone lesions based on pathologic examination. According to the latest WHO classification, benign lesions are cured by curettage or local excision, have limited capacity for local recurrence, and if they do recur, they reappear in a local nondestructive fashion. Intermediate lesions are of two types, locally aggressive and rarely metastasizing. The former feature infiltrative and locally destructive growth pattern, with no potential for metastasis, and these typically require wide excision with local adjuvant therapy (e.g., grade I chondrosarcoma or osteoblastoma). The rarely metastasizing group show a low risk for metastasis (<2%, e.g., chondroblastoma or GCT). Finally, malignant lesions have greater than 2% risk for metastasis, and often, it is in the range of 20% to 100% (e.g., osteosarcoma and high-grade chondrosarcoma).

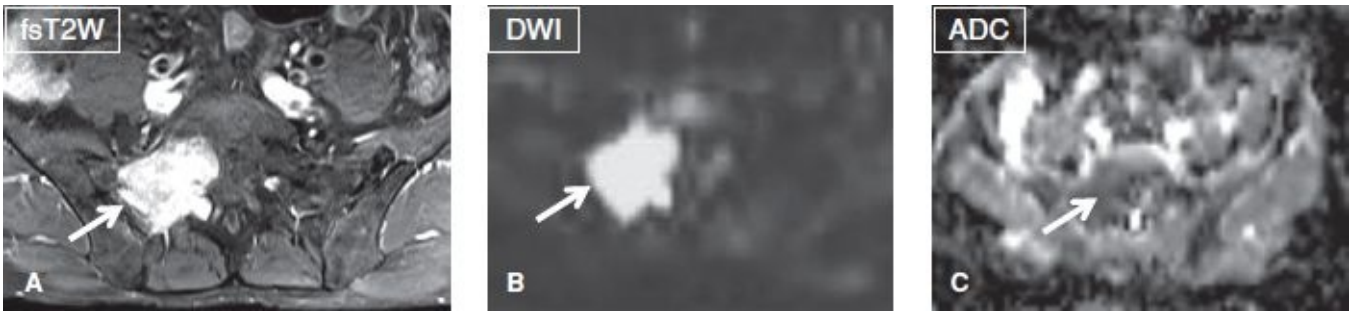

Fig. 96: Multiple myeloma in an older man with right leg pain. Axial images demonstrate a homogenous mass (*arrows*) with restricted diffusion (ADC value: 0.8 × 10^{-3} mm2/s) involving the sacrum, a biopsy-proven myeloma lesion.

Fluid–fluid levels are mostly seen in benign lesions, such as ABC (two-third of cases, occurring before skeletal maturity), simple bone cyst, hemangioma, secondary ABC (one-third of cases, complicating underlying GCT, osteoblastoma, fibrous dysplasia, and chondroblastoma), abscess, lymphatic malformation, and soft tissue hematoma (Figs. 97, 98). Rarely, telangiectatic osteosarcoma may show this feature; however, additional aggressive features of soft tissue–enhancing mass, periostitis, and bone marrow edema are also as differentiating features.

Fig. 97: Aneurysmal bone cyst in a young woman who presented with ankle pain. Coronal images from a study performed to rule out ligamentous injury reveal a well-circumscribed multiloculated cystic lesion (*arrows*) with minimal fluid levels and no aggressive features in the tibial metaphysis.

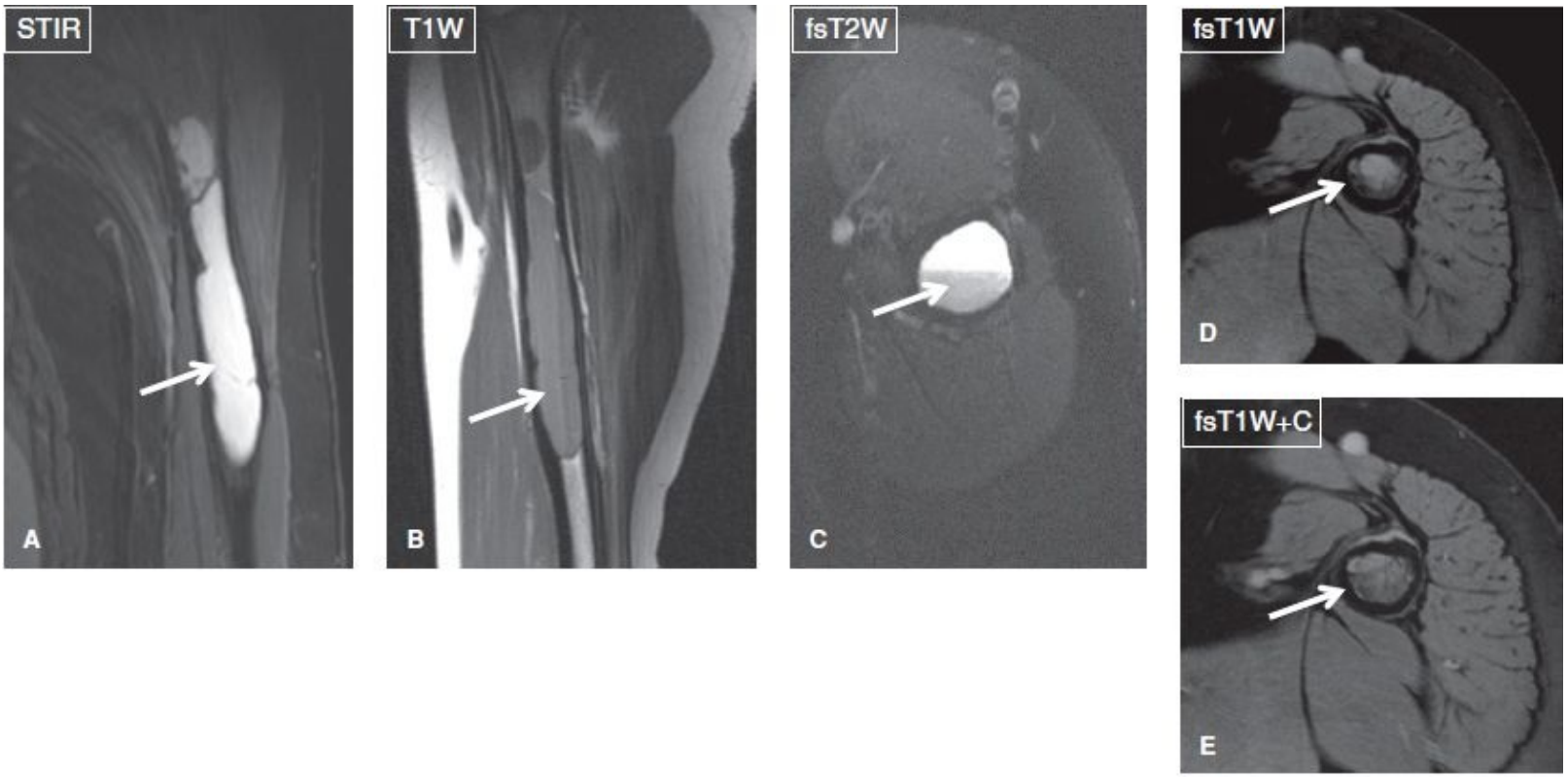

Fig. 98: Simple bone cyst. Coronal **(A),** sagittal **(B),** and axial **(C–E)** images demonstrate a well-defined nonenhancing cyst (*arrows*) with fluid–fluid level in the humeral metadiaphysis.

The transition zone, which is imperative factor in distinguishing benign from malignant lesions on radiographs, is not considered equally important on MR imaging. Malignant primary and secondary bone or soft tissue neoplasms frequently show narrow zone of transition, whereas benign lesions, such as GCT, ABC, chondroblastoma, eosinophilic

granuloma, abscess, and degloving lesions, may show wide zone of transition (Figs. 7, 18–20, 47, 70, 91, 94, 95).

Periosteal reaction is often suggestive of aggressive pathology, such as bone or soft tissue sarcoma, especially if associated with a soft tissue mass. However, many benign lesions can demonstrate periostitis and/or associated soft tissue mass, such as osteoid osteoma, chondroblastoma, GCT, eosinophilic granuloma, traumatic periosteal avulsion, and infection (Figs. 99–102). Usually, periostitis associated with benign lesions is linear and without a soft tissue mass. The underlying bone either lacks T1 hypointensity or shows minimal T1 hypointensity, which is disproportionate to the extensive marrow edema present on T2W images.

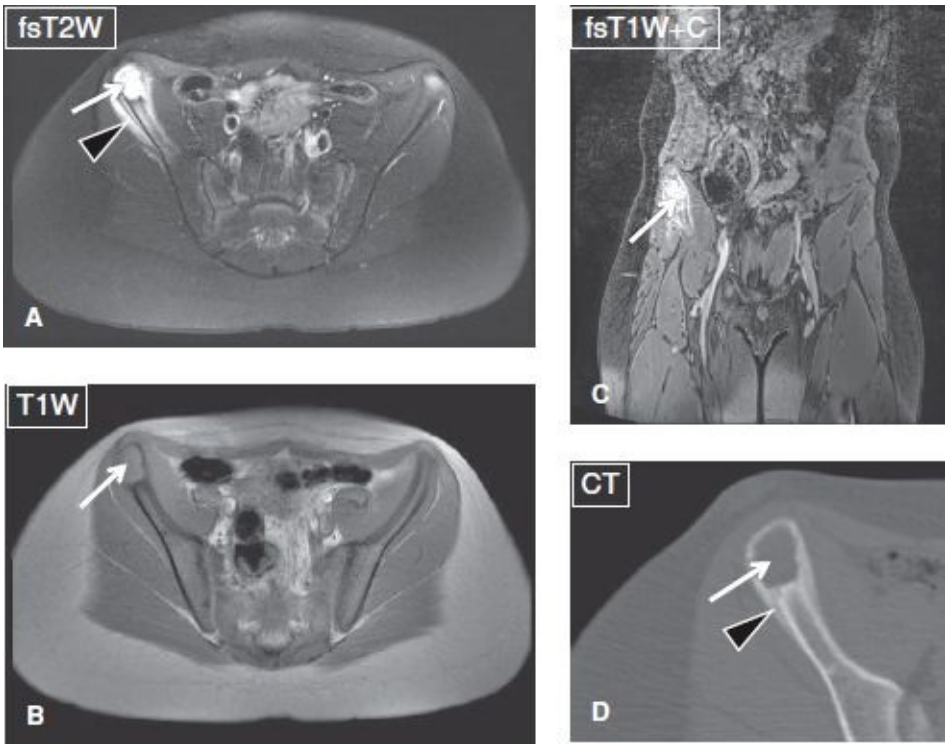

Fig. 99: Eosinophilic granuloma. Axial **(A, B)** and coronal **(C)** MR images exhibit a T2 hyperintense expansile enhancing lesion (*arrows*) at the right iliac crest, which is associated with periosteal reaction (*arrowhead*), as well as with edema of the adjacent marrow and soft tissues. The respective axial CT image **(D)** confirms the periosteal reaction (*arrowhead*), and shows the lesion (*arrow*) is lytic.

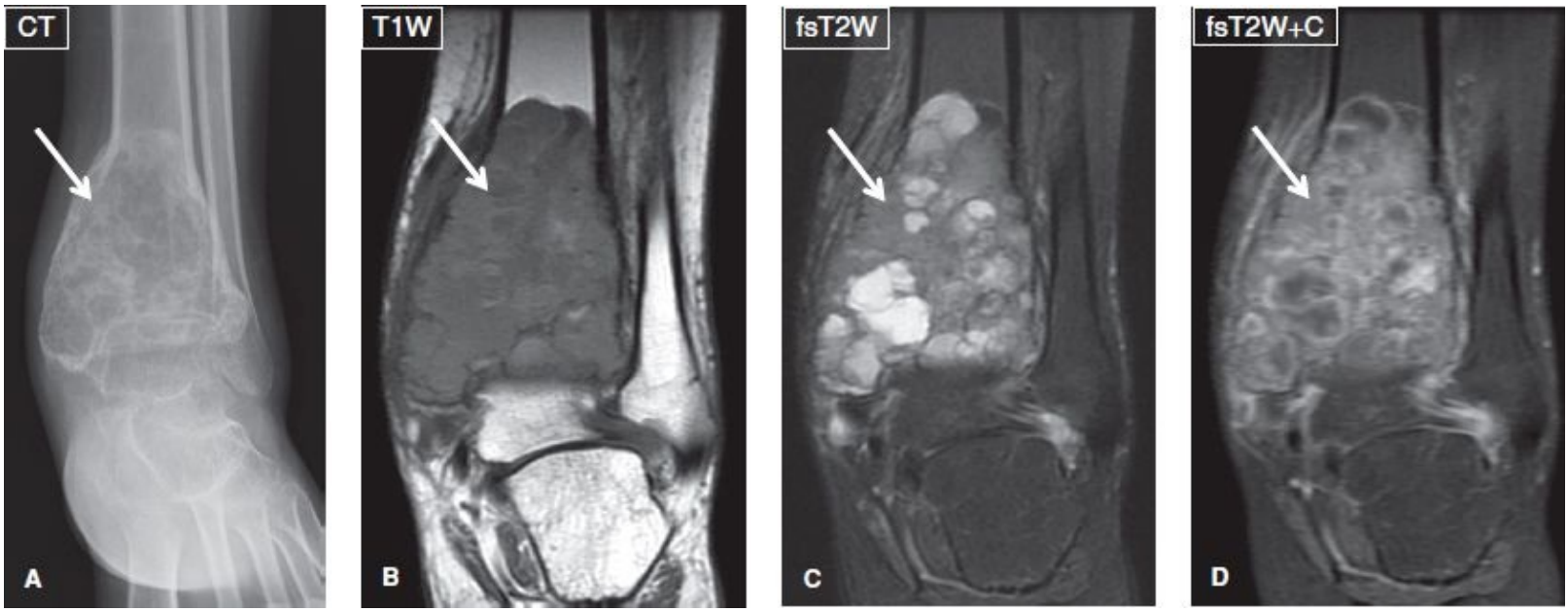

Fig. 100: Chondroblastoma. **A:** Anteroposterior radiograph exhibits an expansile-mixed (lytic/sclerotic) lesion (*arrow*) involving the distal tibia with periostitis. **B–D:** On the corresponding coronal MR images, the lesion (*arrows*) shows cystic areas and periostitis along with markedly heterogeneous signal and contrast enhancement.

Fig. 101: Giant cell tumor. Coronal MR images exhibit an aggressive lesion (*arrows*) arising from the left iliac bone and sacrum with extension into the adjacent soft tissues.

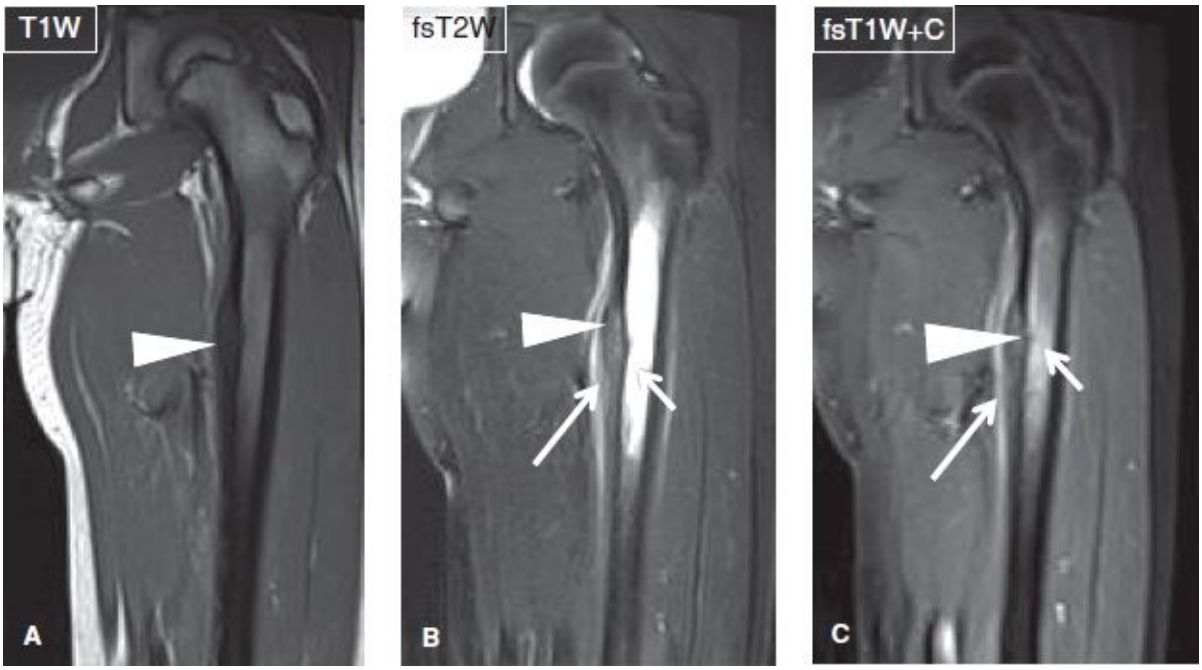

Fig. 102: Periostitis related to adductor avulsion in a young soccer player. Coronal MR images show the periosteal reaction (*arrowheads*), and additionally demonstrate marrow edema (*short arrows*), as well as linear hyperintensity and contrast enhancement (*long arrows*), indicative of edema and hyperemia, respectively, along the medial aspect of the femoral shaft.

Extent:

Compartment: [<Intracompartmental> <Extracompartmental> <Indeterminate>]

Bone involvement: [<No>]

Intra-articular involvement: [<No>]

Neurovascular involvement: [<No>]

Nodal involvement: [<No>]

The Enneking system (Table 3) is widely used by musculoskeletal tumor societies for the surgical staging of bone and soft tissue tumors. This system is based on grade (G), site (T), and metastasis (M), employs histologic, imaging and clinical criteria and should be reserved for staging mesenchymal lesions (rather than non-mesenchymal ones, such as lymphoma and leukemia). By imaging alone, obviously one cannot determine the grade, but the reader should be aware of the compartmental anatomy of the extremities and axial skeleton to describe the extent of the lesion. Lesions crossing multiple compartments are usually malignant (Fig. 71); however, some local aggressive benign lesions may behave similarly, such as fibromatosis, GCT, and grade I chondrosarcoma (Figs. 58, 101). Occasionally, fascial edema extends across compartments, rendering determination of the extracompartmental extension of the lesion difficult. In such cases, the indeterminate category of compartment

description should be used.

Bone involvement by a soft tissue mass is much more uncommon than soft tissue involvement by a bony lesion. Therefore, if there is concomitant bony and soft tissue lesion, one should first consider bone as the primary origin of the mass lesion. In indeterminate cases, one should check whether the epicenter of the lesion lies primarily in the soft tissues or in the bone. Other findings that may help include erosion or endosteal scalloping (suggestive of bony lesions) versus cortical scalloping (indicative of a slow-growing soft tissue lesion). In either case, bone to soft tissue or soft tissue to bone involvement indicates extracompartmental disease extension, and one should first think of malignant lesions, such as Ewing sarcoma, osteosarcoma, and multiple myeloma, rather than benign lesions, such as GCT, intraosseous or soft tissue ganglion, and enchondroma protuberance (Fig. 103).

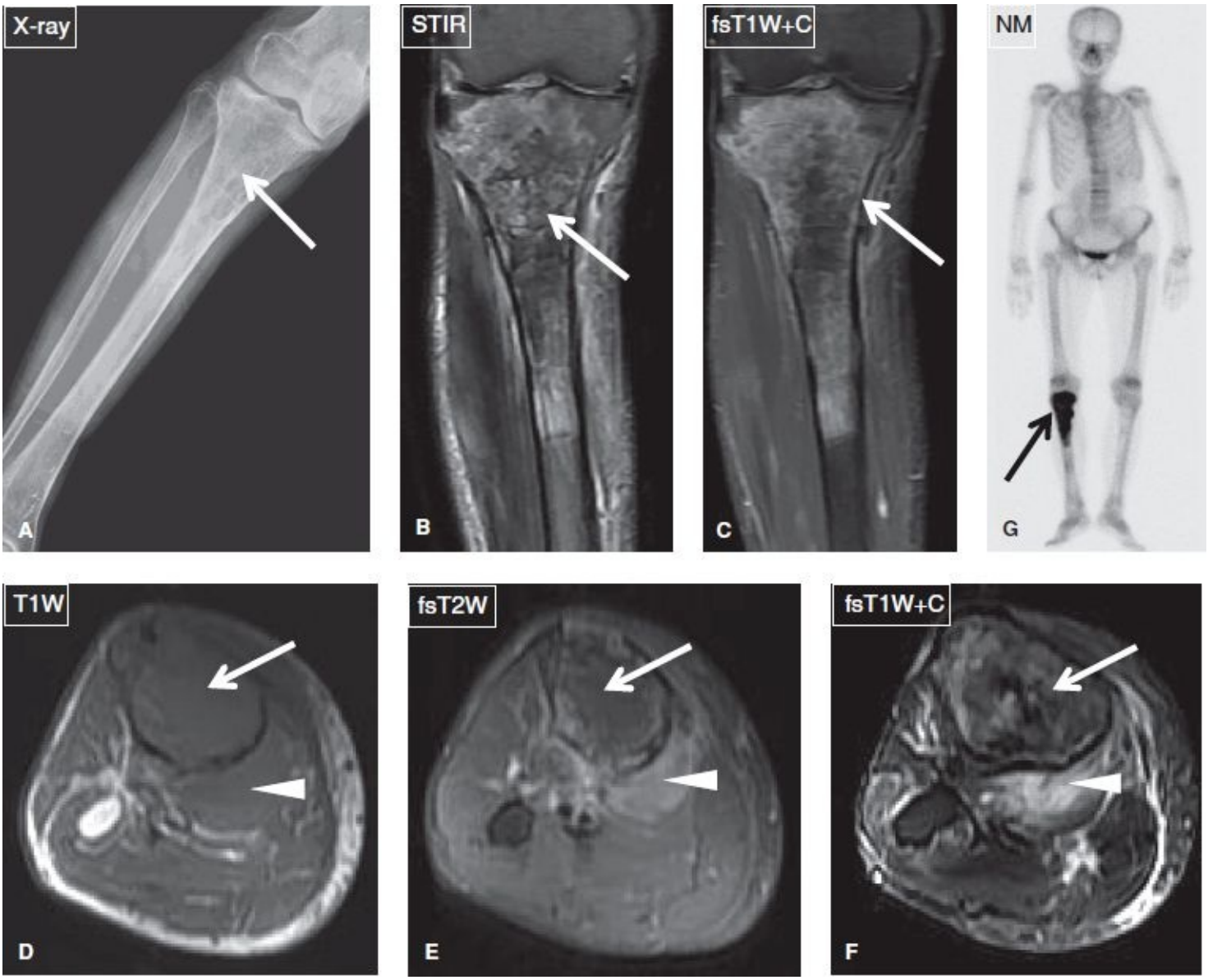

Fig. 103: Osteosarcoma in an old man. Anteroposterior radiograph **(A)** shows an ill-defined mixed (lytic/sclerotic) lesion in the proximal tibia. The corresponding coronal **(B, C)** and axial **(D–F)** MR images display the true extent of the lesion (*arrows*), which features markedly heterogeneous signal and contrast enhancement and is associated with an extraosseous soft tissue component (*arrowheads*). There is partial encasement of the

neurovascular bundle. **G:** On the Tc99m MDP bone scintigraphy scan, the lesion (*arrows*) shows increased radionuclide agent uptake.

Bone marrow infiltration or replacement by neoplastic processes should be distinguished from benign red marrow reconversion. The red marrow reconversion focus (1) is brighter than muscle on T1W images; (2) demonstrates greater than 20% signal drop on CS imaging, less than 35% to 40% enhancement on postcontrast imaging and lacks significant diffusion restriction, with ADC values above 1.5×10^{-3} mm2/s except in fatty or fibrosed marrow; (3) spares the epiphyses/apophyses and pedicles; and (4) shows no soft tissue mass, cortical destruction, periosteal reaction, or marrow edema (Fig. 104). However, some benign storage disorders, such as Gaucher disease, mastocytosis, histiocytosis, and Erdheim–Chester disease may mimic malignancy, and the above rules described for benign red marrow reconversion may or may not apply. In the latter cases, the clinical setting and bilateral bone involvement is usually helpful in suggesting the diagnosis (Fig. 105). Otherwise, the lesion is labeled as indeterminate, and biopsy may be performed for confirmation. In serous atrophy of the bone marrow, typical imaging features include cystic/bubbly marrow lesions, and there may be inability to suppress the subcutaneous or marrow fat, even on inversion recovery images. This finding is usually encountered in the setting of extreme emaciation, following chemotherapy, or with underlying immunodeficiency, etc. Finally, treated lesions, such as leukemia, lymphoma, and myeloma, may metamorphose to fatty deposits or fibrosis, resulting in heterogeneous marrow appearance. However, lack of nodular bright foci on STIR imaging or significant enhancement confirms that the disease is in remission. In general, marrow involvement of greater than 60% or cortical involvement of greater than 50% predisposes the bone to pathologic fracture. Benign versus pathologic acute vertebral compression fractures can be differentiated using the criteria illustrated in Table 4 (Figs. 37, 106).

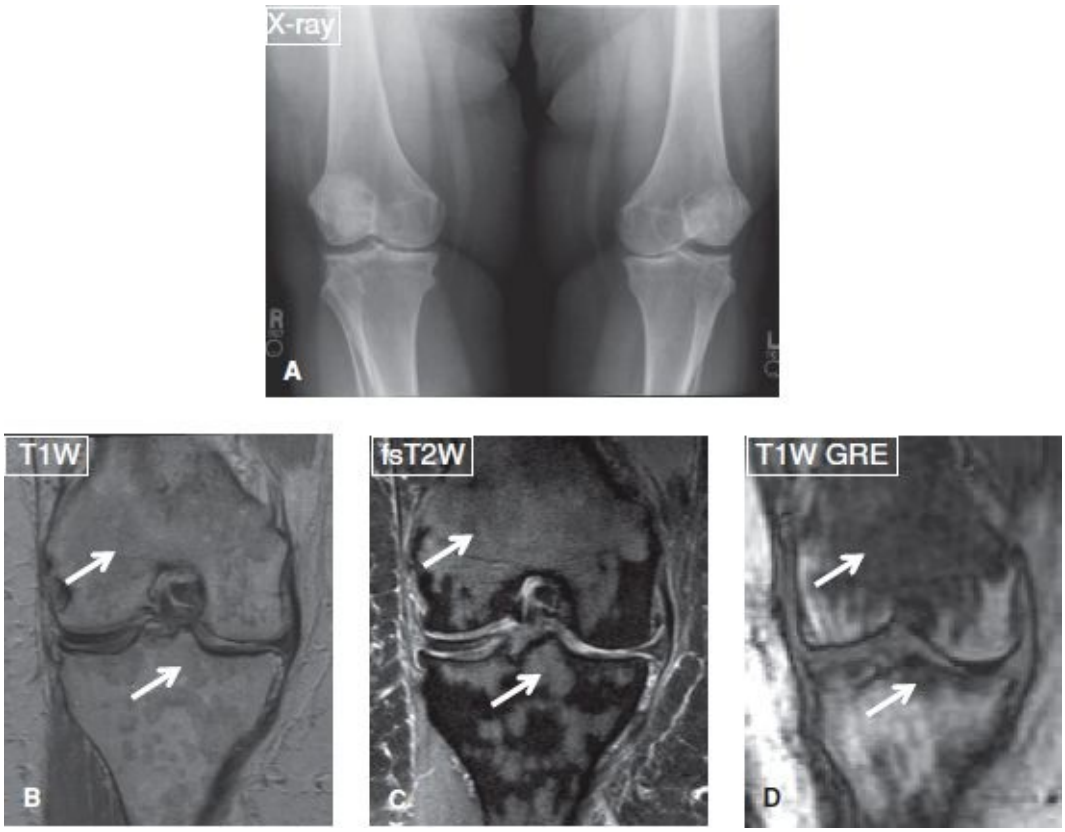

Fig. 104: Benign red marrow reconversion. **A:** Anteroposterior radiograph of the knees shows degenerative changes of both knees with no lytic or sclerotic lesion. **B–D:** On the respective coronal MR images, there are multifocal areas (*arrows*) of red marrow reconversion in the femur and tibia, which show hyperintense signal as compared to normal skeletal muscle on T1W images and signal dropout on out-of-phase GRE image.

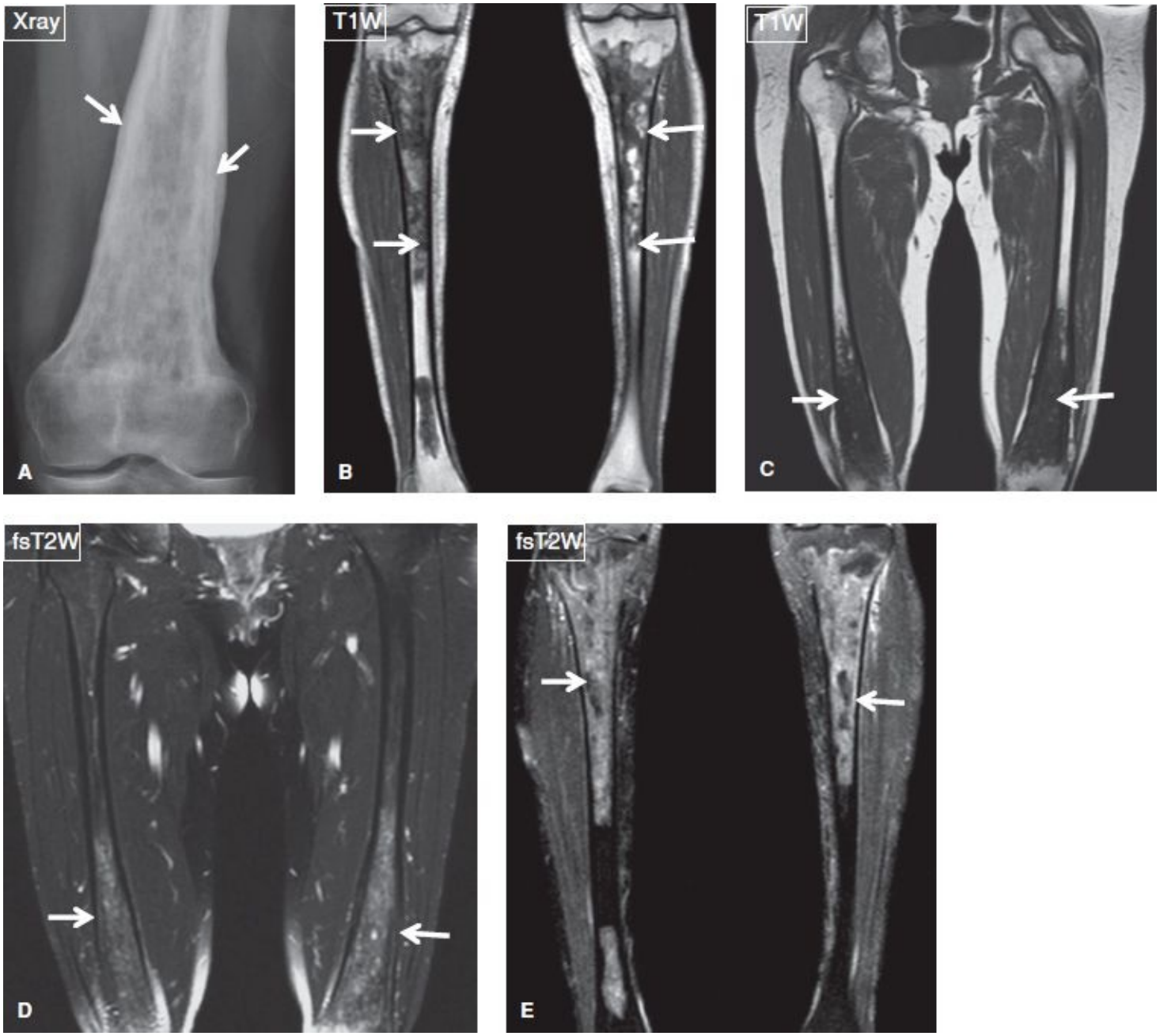

Fig. 105: Erdheim–Chester disease involving an old woman with diabetes insipidus. **A:** Anteroposterior radiograph shows cortical thickening (*arrows*) and diffuse metaphyseal and diaphyseal sclerosis and trabecular coarsening of the distal femur. **B–E:** The respective coronal MR images demonstrate bilateral diffuse infiltration of the marrow of the femur and tibia by heterogeneous T1 hypointense/T2 hyperintense tissue (*arrows*), a biopsy-proven case of Erdheim–Chester disease.

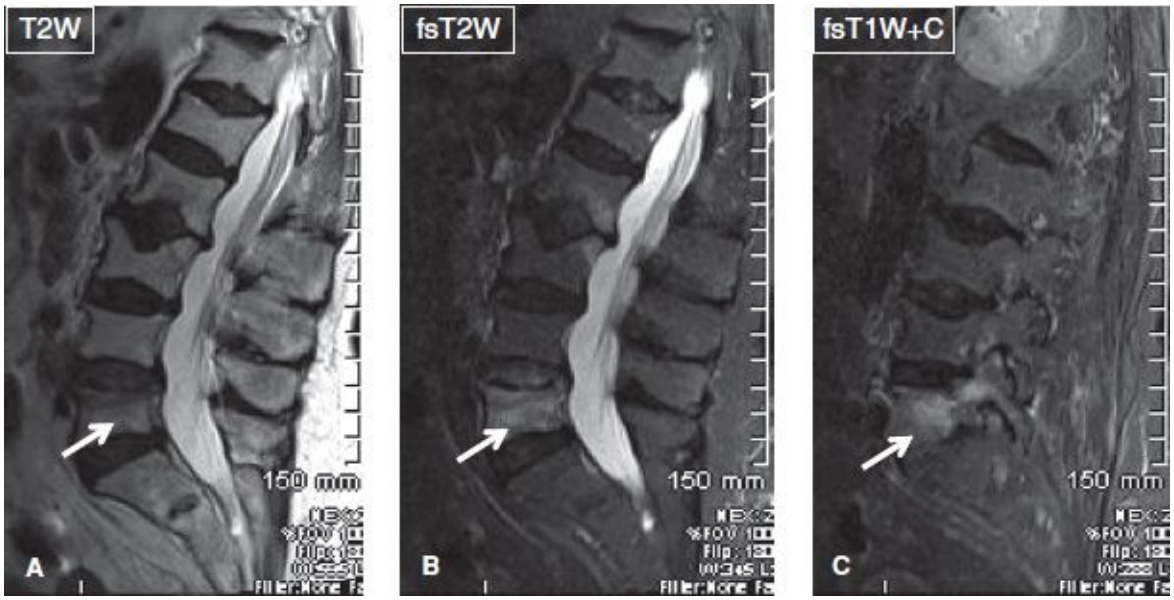

Fig. 106: Benign fracture. Sagittal images show mild diffuse T2 hyperintensity and fracture line of the superior end plate of the L5 vertebra. There is also contrast enhancement (*arrows*) of the L5 vertebral body and pedicles. No pot belly vertebral margin, cortical destruction, or soft tissue mass is seen. The findings resolved in few weeks of conservative treatment.

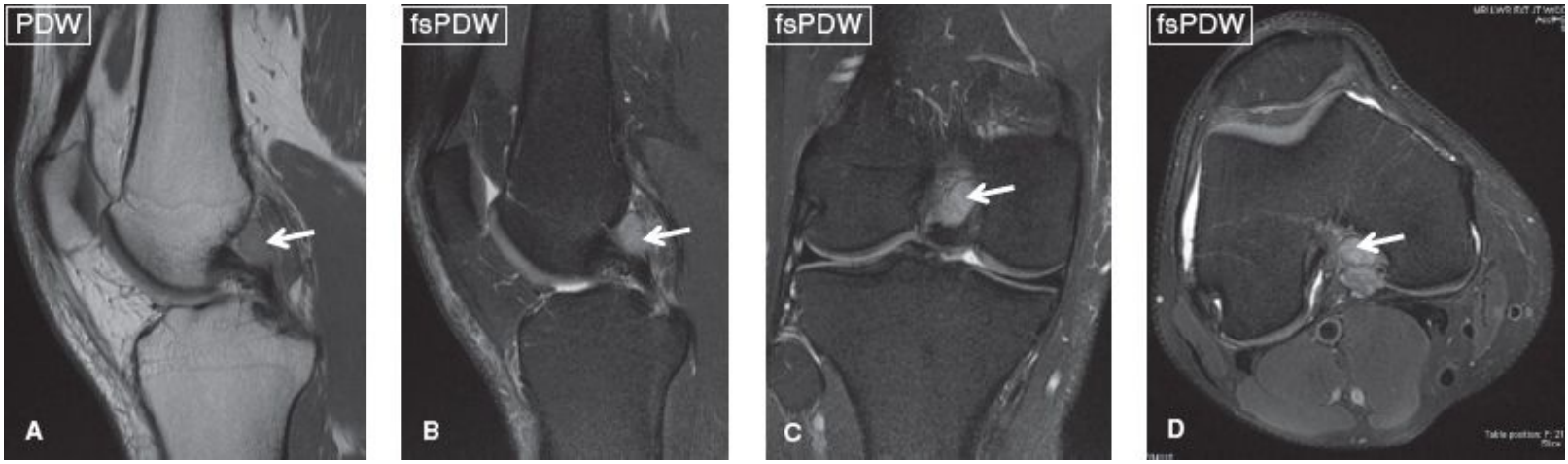

Fig. 107: Pigmented villonodular synovitis in a 27-year-old man. Sagittal **(A, B),** coronal **(C),** and axial images of the left knee reveal a well-defined ovoid lesion (*arrows*) of mild T2 hyperintensity abutting the posterior cruciate ligament.

TABLE 3: The Enneking system for the surgical staging of bone and soft tissue tumors*a*

Stage	Grade	Site	Metastasis
IA	G1	T1	M0
IB	G1	T2	M0
IIA	G2	T1	M0
IIB	G2	T2	M0
IIIA	G1–G2	T1	M1
IIIB	G1–G2	T2	M1

[a]Grade is based on histology with aid of radiographic findings and clinical correlation (G1: Low-grade, uniform cell type without atypia, few mitoses; G2: High-grade, atypical nuclei, mitoses pronounced). Site refers to whether the lesion is confined within the limits of periosteum (intracompartmental, T1) or spreads beyond its anatomic compartment of origin (extracompartmental, T2). Metastasis refers to whether there is no identifiable skip lesions or distant metastases (M0), or there are skip lesions, regional lymph nodes, and/or distant metastases (M1).

Intra-articular involvement is important as it may necessitate disarticulation rather than below joint amputation. Generally, absence of joint extension or joint effusion on MR imaging is sufficient to confirm non-involvement. In the presence of joint effusion with the tumor in close proximity, one cannot definitely exclude microscopic involvement. However, malignancy very rarely arises in joints, with only scant case reports in the literature. Of the thousands of sarcomas the authors have seen, only one case was seen arising from the suprapatellar pouch of the knee. In joints, one should think of nodular synovitis (common in Hoffa or prefemoral fat pad from friction), PVNS (T2 dark, hemosiderin staining, and nodular or diffuse varieties), synovial osteochondromatosis or loose bodies (partially calcified nodular or faceted bodies), synovial hemangioma (enhancing mass in Hoffa fat pad), lipoma arborescence (fibrofatty synovial proliferation), and chondroma (cartilaginous matrix) (Figs. 83, 107).

Neurovascular involvement or neurovascular origin of a lesion should be described as it aids in the diagnosis and management. Neurovascular involvement makes the lesion extracompartmental and if encased, may render it unresectable (Fig. 108). Primary neural lesions include benign and malignant peripheral nerve sheath tumors (tail sign, split-fat sign, target sign, fascicular sign, bag-of-worms sign in plexiform lesions) (Fig. 15). Schwannomas and neurofibromas are indistinguishable by imaging. Clues more suggestive of schwannomas (which are more prevalent) include eccentric location in the nerve, one or two fascicular continuity between nerve and lesion, cystic changes or calcifications, and underlying schwannomatosis. Features indicative of neurofibromas include central location in the nerve, greater number of involved fascicles, target sign (more common), and underlying neurofibromatosis (Figs. 109–111). Perineurioma is another peripheral nerve sheath tumor, which usually involves young individuals, and presents with predominant motor symptoms, classically in the lower limbs in the sciatic or femoral nerve distribution.

The tumor shows up as a fusiform-elongated mass with uniform honeycomb appearance on cross-sectional imaging and homogeneous strong enhancement. The mass can show low ADC values of 1.0 to 1.1 × 10−3 mm2/s; however, other clinical and imaging features aid in its straightforward diagnosis (Fig. 112). Malignant degeneration of these lesions is indicated by new onset or worsening pain or new motor–sensory deficits, large (>4 to 5 cm) size, heterogeneous necrotic appearance, internal calcifications, peritumor edema, ADC values of less than 1.1 × 10−3 mm2/s, F18-FDG PET uptake with SUV greater than 3 to 4 and increased delayed uptake, local invasion and metastasis (Fig. 113). Since ancient or degenerated schwannomas can be large and may show low ADC value due to internal hemorrhages, it is probably more useful to use the incremental value of diffusion restriction in small masses rather than large masses (i.e., a small mass with low ADC value would be probably more cellular and malignant in etiology). Finally, any diffusely thickened nerve may assume a mass-like appearance, such as in fibrolipomatous hypertrophy (as described above) or hereditary or acquired demyelinating-type neuropathy (Fig. 114).

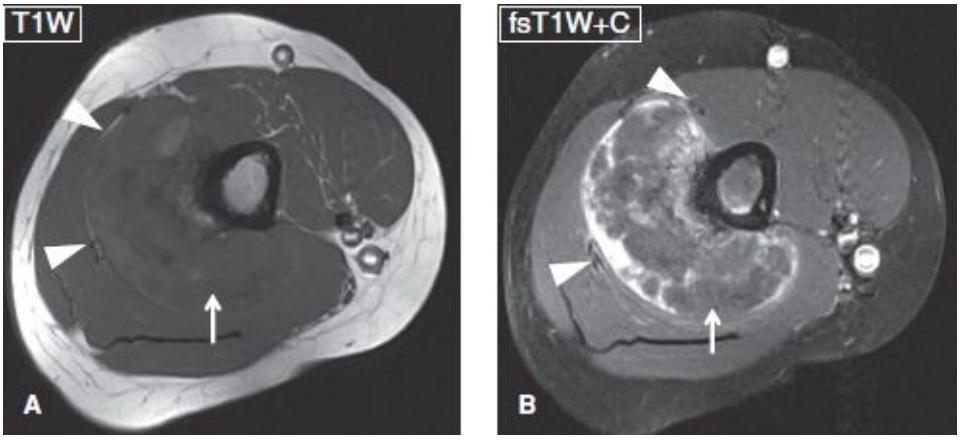

Fig. 108: Parosteal osteosarcoma. Axial MR images exhibit a large soft tissue mass (*arrows*) of marked heterogeneity in signal and contrast enhancement. A thick stripe of fat (*arrowheads*) at the periphery of the lesion signifies the latter displaces, rather than infiltrates, the adjacent neurovascular bundles.

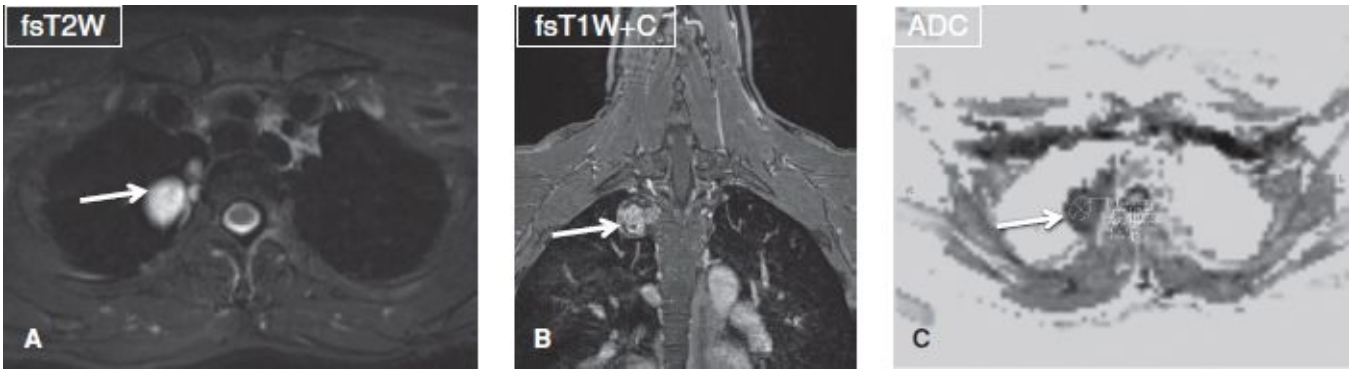

Fig. 109: Schwannoma. Axial **(A, C)** and coronal **(B)** MR images exhibit a well-defined soft tissue mass (*arrows*) with heterogeneous enhancement at the right T1–2 neural foraminal level. The ADC measures 2.1 × 10−3 mm2/s.

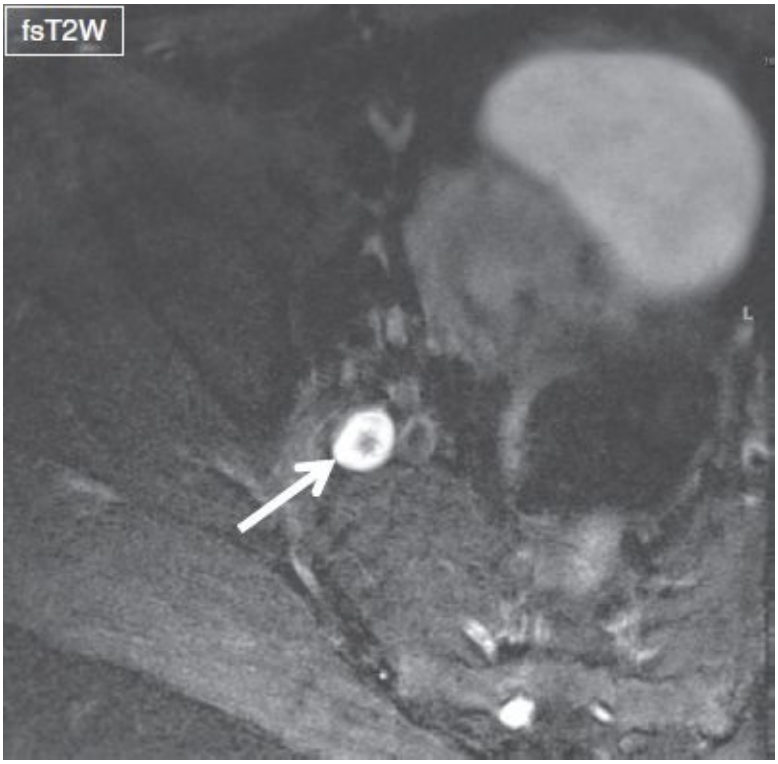

Fig. 110: Neurofibroma of the sciatic nerve in a young woman. Axial image of the pelvis shows an ovoid T2 hyperintense lesion (*arrow*) proximal to the sciatic foramen, which has a hypointense center, forming a "target" sign due to central dense collagenous tissue and peripheral myxomatous tissue.

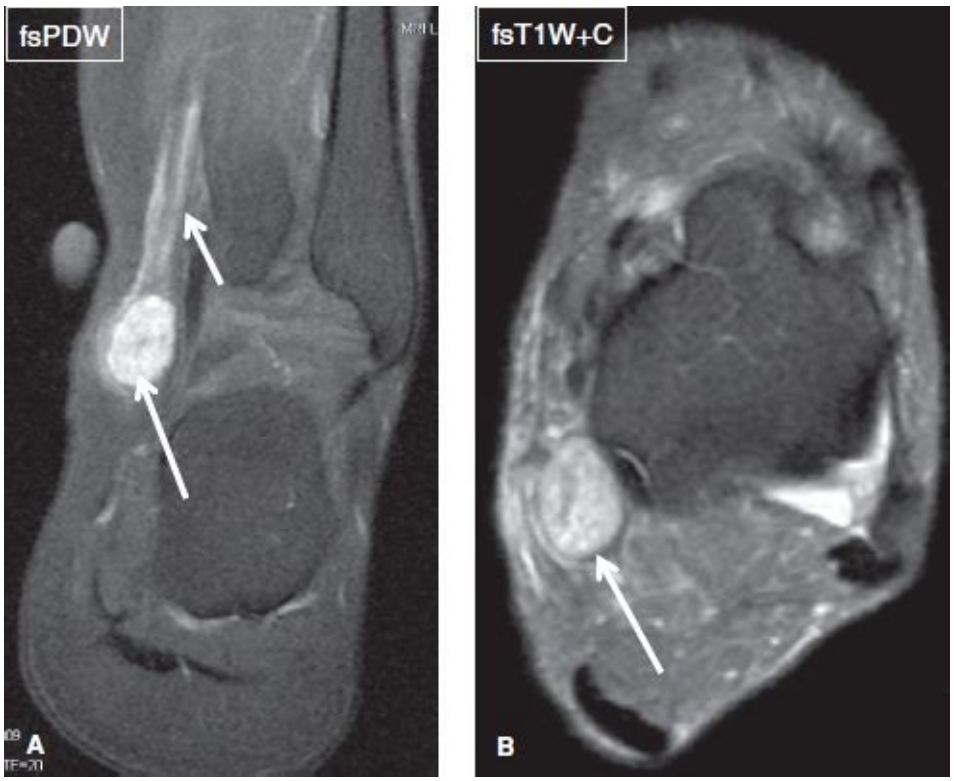

Fig. 111: Neurofibroma in a 55-year-old woman with known NF type I. Coronal **(A)** and axial **(B)** images show a well-defined T2 hyperintense mass (*long arrows*), featuring central target sign, as well as intense enhancement with fascicular sign, which is indicated as *tiny dots* within the lesion in **(B).** Note associated multifascicular enlargement of the tibial nerve (*short arrow*) proximal to the lesion.

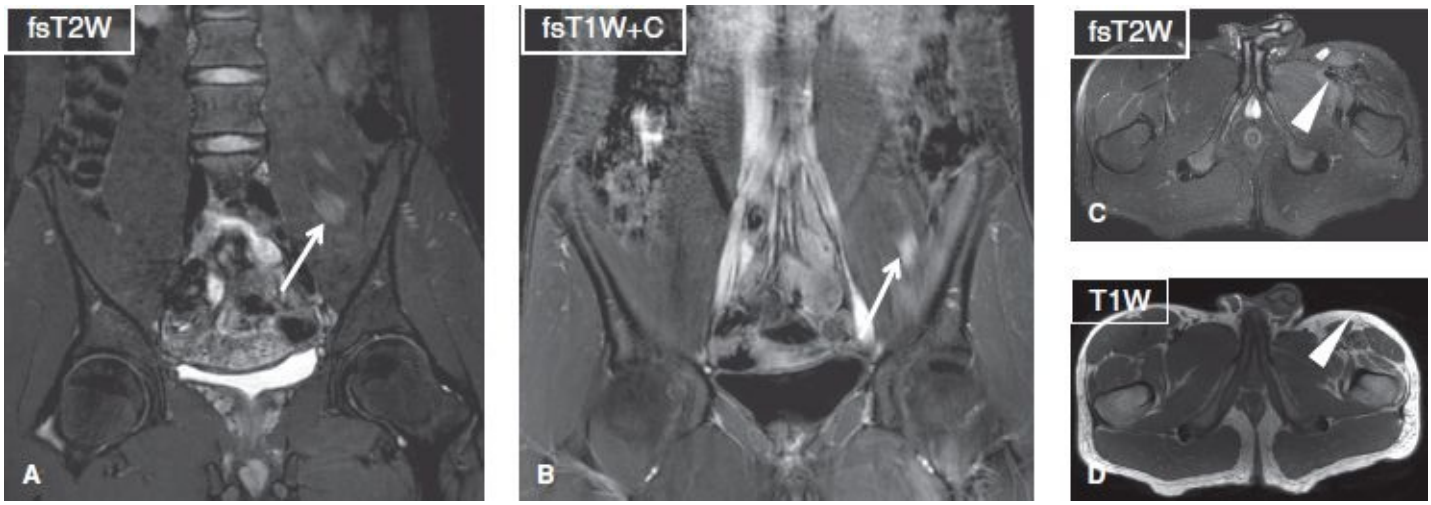

Fig. 112: Perineurioma of the femoral nerve. Coronal **(A, B)** and axial **(C, D)** images exhibit diffuse enlargement, prominent fascicular morphology, marked T2 hyperintensity, and contrast enhancement of the left femoral nerve (*arrows*). Also note edema like T2 signal alteration and fatty atrophy of the anterior compartment muscles (*arrowheads*) of the ipsilateral thigh, reflecting denervation change.

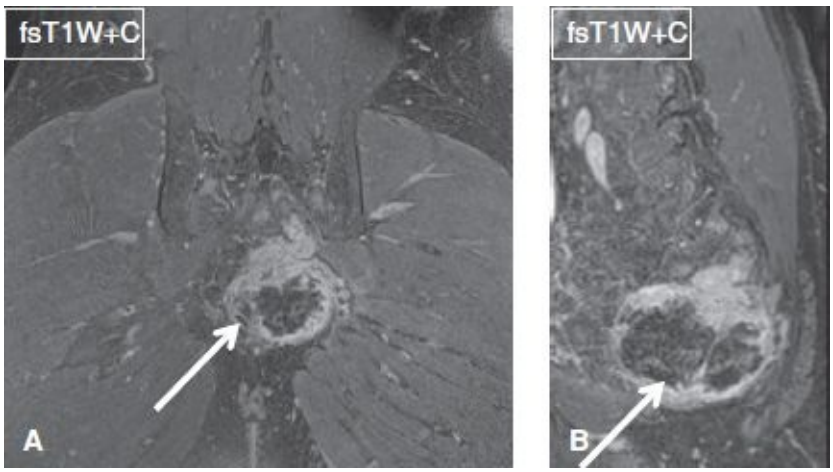

Fig. 113: Malignant peripheral nerve sheath tumor in a patient with neurofibromatosis type I. Coronal **(A)** and sagittal **(B)** postcontrast images at the level of the pelvis demonstrate a large mass (*arrows*) with peripheral nodular enhancement and central necrosis, a biopsy-proven malignant peripheral nerve sheath tumor.

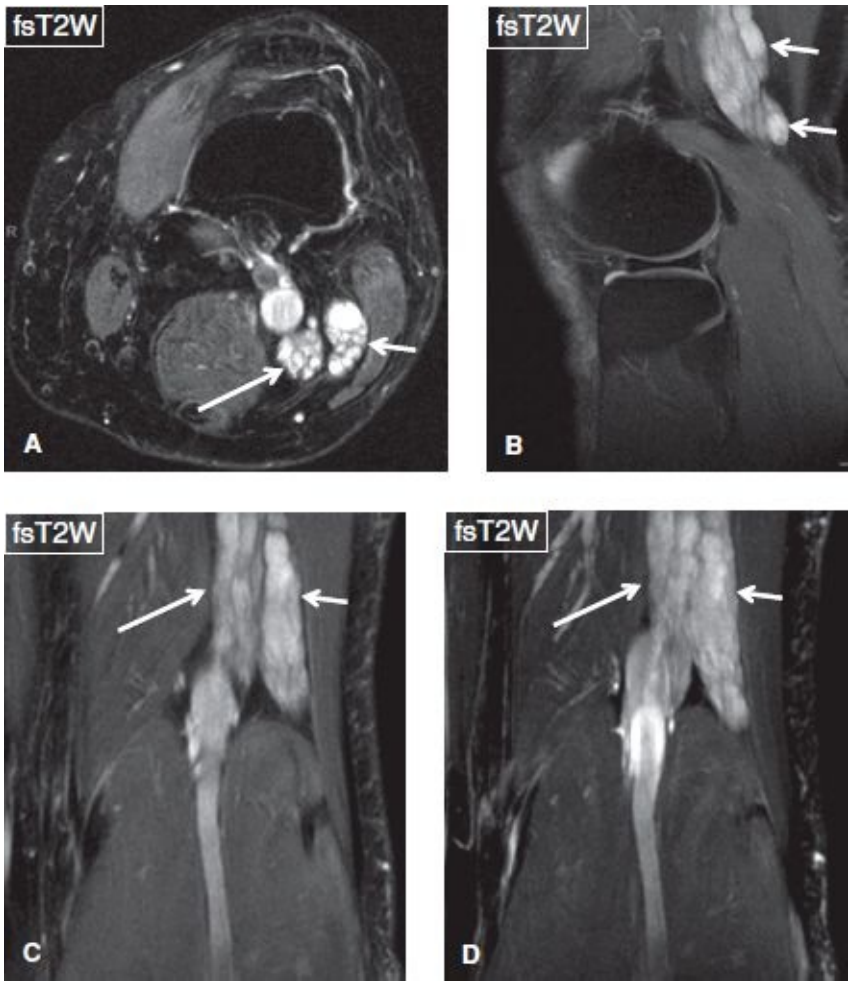

Fig. 114: Charcot–Marie–Tooth disease (hereditary neuropathy). Axial **(A),** sagittal **(B),** and coronal **(C, D)** images exhibit diffuse enlargement and hyperintensity of the tibial (*long arrows*) and common peroneal (*short arrows*) nerves.

TABLE 4: Imaging criteria that assist in differentiating between benign and malignant vertebral compression fractures

Imaging Feature	Benign	Malignant
Involvement of posterior elements	Less common	More common
Overall vertebral body mass	Diminished	Increased
Epidural and/or paraspinal mass	Absent, except hematoma or edema	Common
Convexity of posterior body cortex	Uncommon	Common (frequently asymmetric & extending to the pedicle, pot belly margin)
Marrow on T1W images	Some sparing of fatty marrow in the vertebra	Entire vertebra usually affected by T1 fatty marrow replacement
Band-like area or linear striation of low T1 signal bordering the fractured end plate	Can be present	Rarely
Retropulsion of a posterior fragment	Can be present (most commonly in a posterosuperior location in a angulated fashion)	Rarely (in an irregular & asymmetric aspect)
Focal, linear, or triangular areas of fluid signal adjacent to the end plate on STIR images	Can be present	Rarely
Signal void within the body (intravertebral vacuum cleft)	Can be present	Rarely
Contrast enhancement	Usually homogeneous	Usually heterogeneous
Apparent diffusion coefficient (ADC)	No significant restriction. ADC $>1.5 \times 10^{-3}$ mm^2/s	Significant restriction. ADC $<1.1 \times 10^{-3}$ mm^2/s
CSI	More than 20% loss of SI	Less than 20% loss of SI

Primary vascular lesions include vascular masses and malformations. Vascular masses have a soft tissue enhancing nodular mass-like component and are pathologically classified as hemangioma (benign), epithelioid hemangioma (intermediate), and epitheliod hemangioendothelioma and angiosarcoma (malignant) (Table 5). Bone hemangiomas are common in the spine and can form a part of the syndrome, aka hemangiomatosis. These lesions show some T1 shortening and loss of signal on CS imaging. Often, trabecular or reticular appearance may be seen on MR imaging confirming their etiology (Figs. 115, 116). Atypical hemangiomas are predominantly T1 dark, and these may show associated soft tissue epidural or paravertebral component. Finally, hemangiomas should be distinguished from the more commonly encountered focal fatty marrow lesions. Hemangiomas may contain some fat and not total fat. Therefore, they are visible on fs images, while focal fatty marrow islands, although contributing to heterogeneous appearance to the marrow, usually suppress completely on fs images. Most soft tissue hemangiomas disappear in the first decade of life (rapidly involuting congenital

hemangioma, RICH due to auto-infarction and not apoptosis) while some may persist (noninvoluting congenital hemangioma, NICH and partially involuting congenital hemangioma, PICH) (Fig. 73). Most enhancing vascular lesions in adults are not hemangiomas, but they are venous malformations, that is, no soft tissue enhancing mass is seen with the latter lesions (Fig. 51). In general, hemangiomas and vascular malformations show close proximity to vessels. They are well-defined masses, homogeneously bright on T2W images, with no surrounding tissue reaction unless there happens to be superimposed hemorrhage or regional trauma and, sometimes feature intralesional fat due to steal phenomenon. Epitheliod hemangioendothelioma may show multiple small-to-moderate–sized reticulated T2 bright enhancing lesions in the extremity bones or multiple spinal vertebrae. These lesions grow slowly over time. Angiosarcoma appears as a vascular mass, similar to any other soft tissue sarcoma. Vascular malformations do not have a soft tissue mass and are classified as, high-flow and low-flow malformations. High-flow malformations include arteriovenous malformation (AVM) and arteriovenous fistulas (AVFs) and show intralesional flow voids due to fast flow, as well as venous shunting in the arterial phase. Both AVM and AVF can occur in sporadic fashion, in association with hereditary hemorrhagic telangectasia or capillary malformations. AVMs can be simple (one artery, nidus, and multiple veins), complex or glomus (multiple arteries and multiple veins), whereas AVFs only have one feeding artery and one draining vein. Low-flow malformations do not show venous shunting in the arterial phase, and these can be venous (most prevalent, flow voids due to slow flow, phleboliths, homogeneous delayed enhancement, and these can occur isolated, with familial predisposition or can be associated with lymphatic malformation, capillary malformation, and AVM in various combinations, aka combined vascular malformation. Blue rubber bleb nevus syndrome and glomulovenous syndrome includes venous malformations), lymphatic (peripheral septal or no enhancement, microcystic, macrocystic or mixed forms, blood–fluid levels, in children or with Klippel–Trenaunay–Weber syndrome and Turner syndromes), and mixed cavernolymphatic (mixed delayed enhancement patterns) (Figs. 89, 117). Table 6 depicts different syndromes associated with vascular malformations. Lymphangiomatosis or cystic angiomatosis may produce punched out myeloma-like lesions on plain films, although these occur in young age group. These lesions may widely infiltrate the marrow and destroy bony cortices as well as cross the joints (Vanishing bone disease or Gorham disease) (Fig. 118). The description of a vascular malformation should include whether it is discrete or multilobular; is there involvement of joints, muscles, bones, or nerves; and are there flow voids indicative of high flow? In addition the report should describe the condition of underlying veins (dysplastic or thrombosed) and arteries (tortuous, dysplastic, aneurysm, or thrombosis).

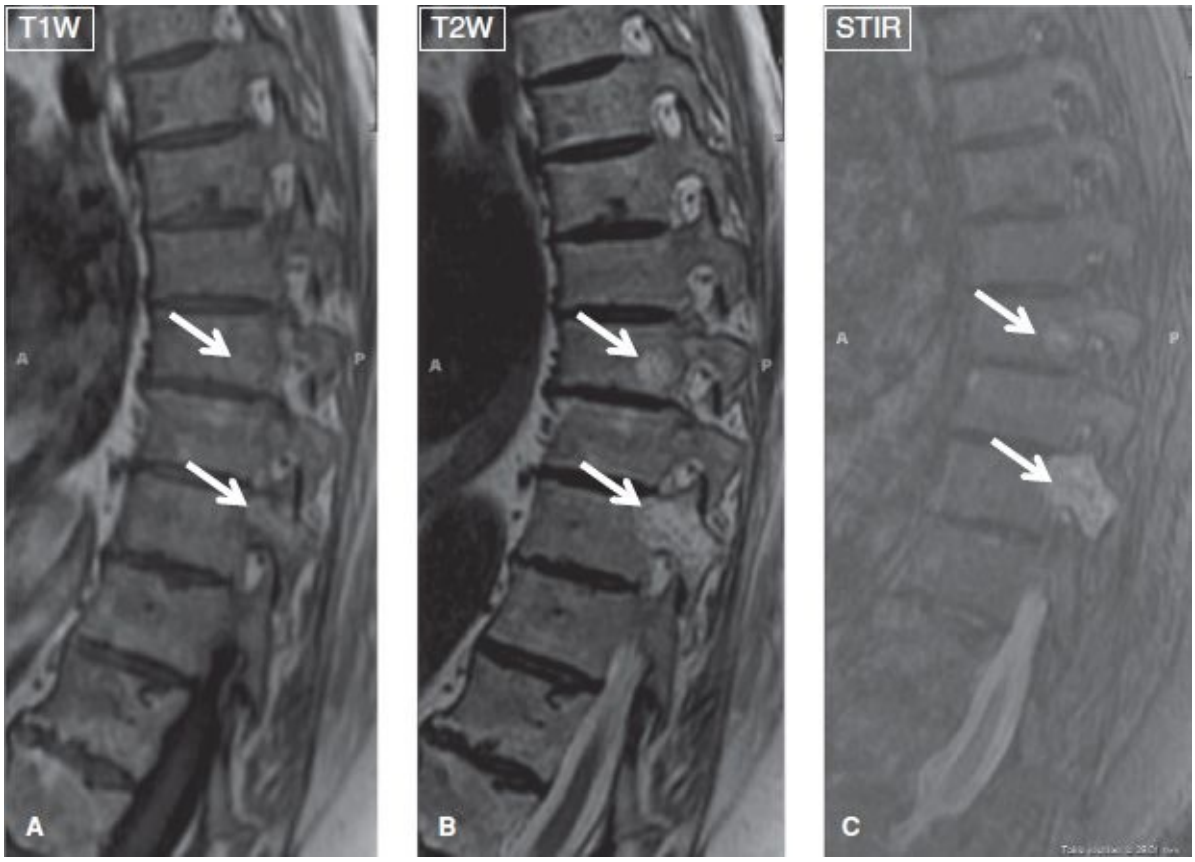

Fig. 115: Hemangiomatosis in a 78-year-old woman. Sagittal images show multiple hyperintense vertebral lesions (*arrows*) on all sequences in keeping with hemangiomas. Notice the internal trabeculated appearance.

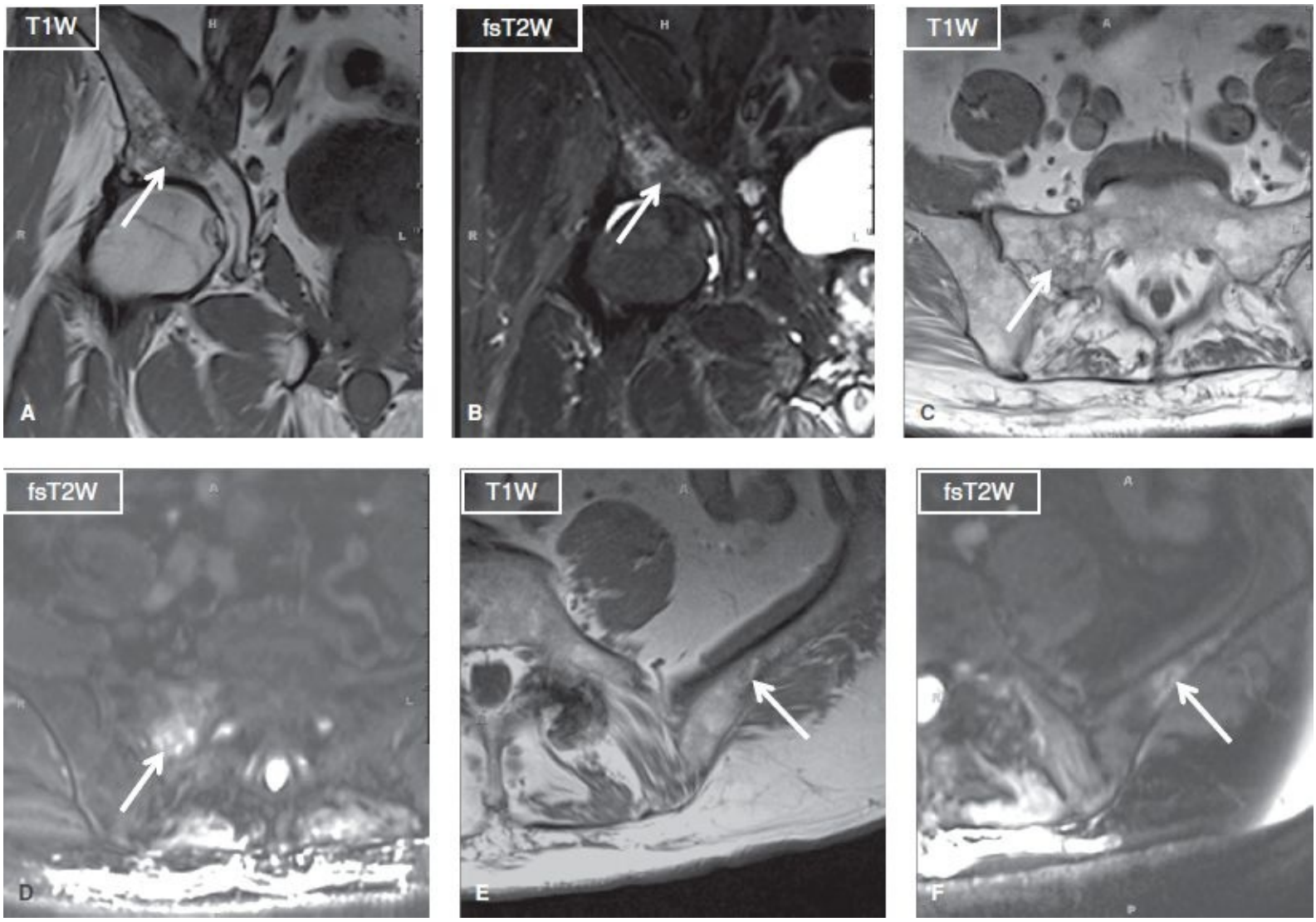

Fig. 116: Hemangiomatosis in a middle-aged man. Coronal **(A, B)** and axial **(C–F)** images at the level of the pelvis demonstrate trabeculated fat-containing lesions (*arrows*) of high T2 signal and intermediate/high T1 signal at the sacrum and iliac bones.

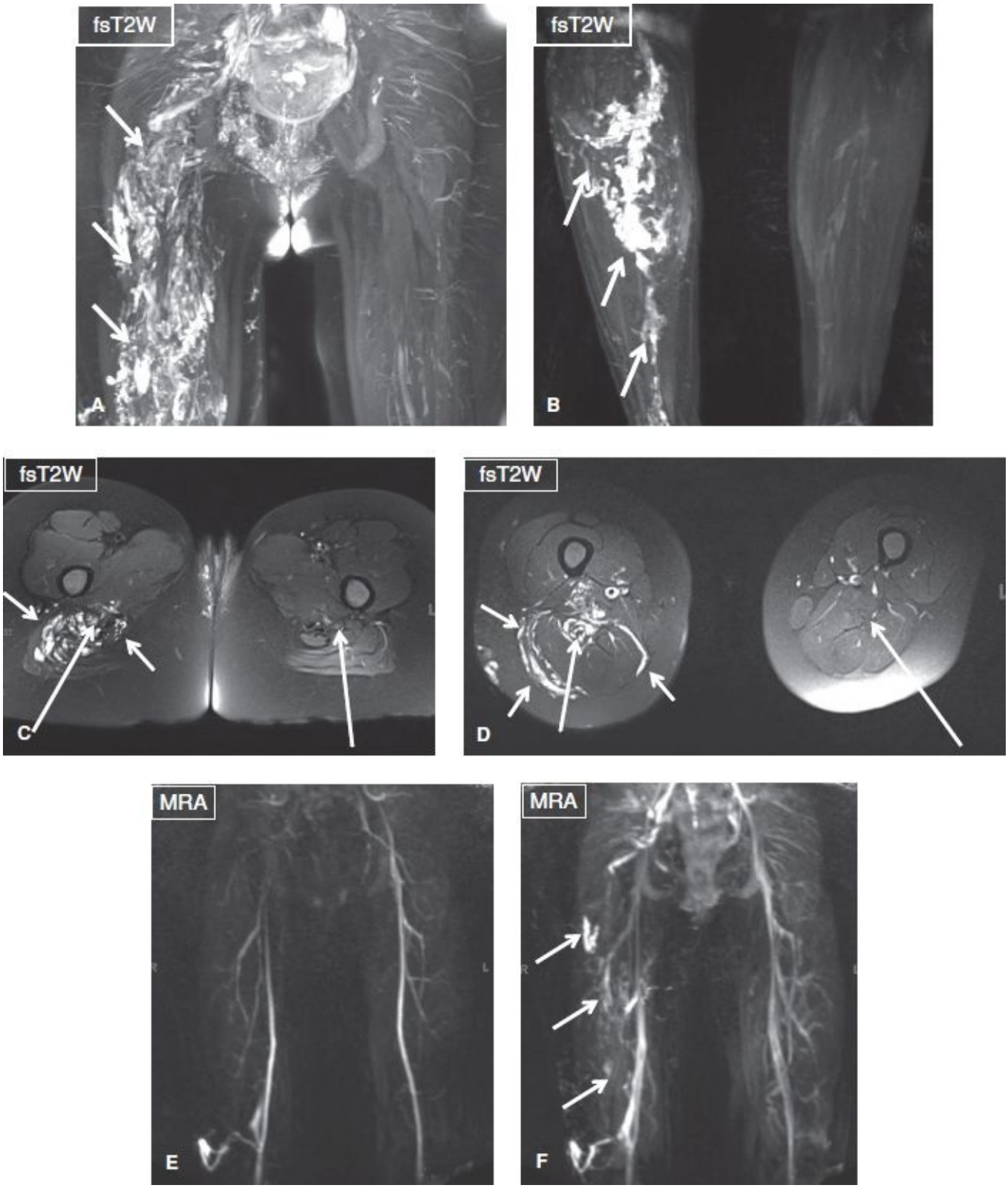

Fig. 117: Klippel–Trenaunay–Weber (KTW) syndrome in a young woman. Coronal **(A, B)** and axial **(C, D)** images demonstrate numerous dilated vessels (*short arrows*) within muscles and subcutaneous tissues of the entire right lower extremity without evidence of flow voids. The malformation involves the right sciatic (*right long arrow* in **C, D**), as opposed to the left sciatic nerve (*left long arrows* in **C, D**), which appears normal. Coronal images **(E, F)** from time-resolved MR angiography using Ablavar shows delayed filling of the dilated vessels (*arrows*), confirming their venous nature.

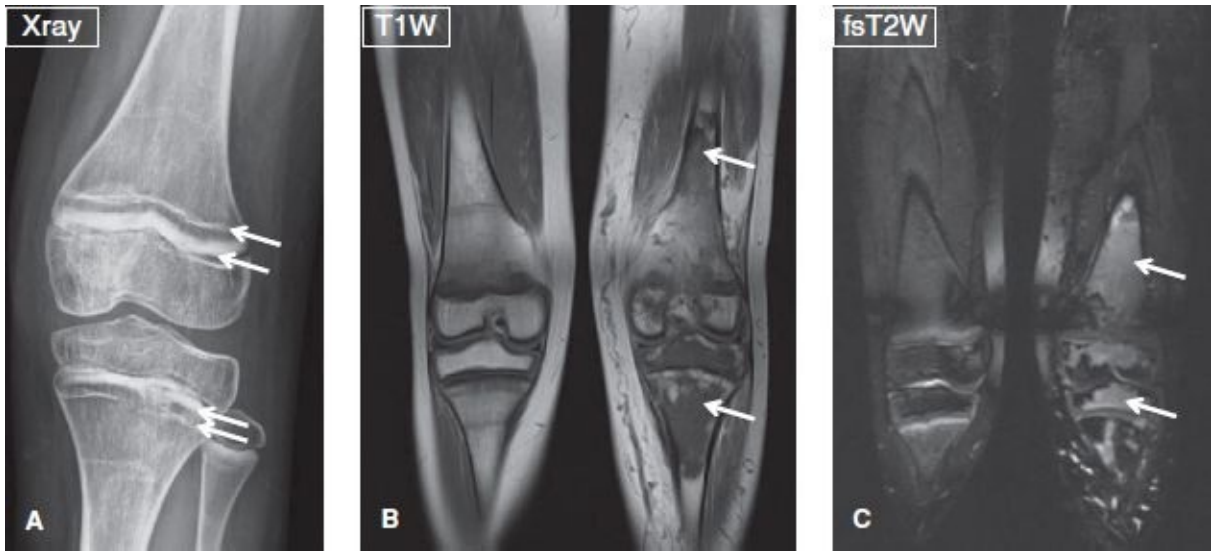

Fig. 118: Cystic angiomatosis in a young girl. **A:** Anteroposterior radiograph of the left knee shows faint radiodensities and radiolucencies at the femoral and tibial metaphyses with osteopenia (*arrows*). **B, C:** The corresponding coronal MR images demonstrate marrow-replacing multifocal lesions (*arrows*) of hyperintense signal, a biopsy-proven case of cystic angiomatosis.

Post-Gadolinium Discussion

None or thin peripheral enhancement virtually excludes malignancy, except in the rare cases of soft tissue melanoma or soft tissue Ewing sarcoma. Solid, central, or peripheral thick enhancement renders the lesion indeterminate or potentially malignant. Such lesions demand further follow-up (suspected heterotopic ossification, granulomatous infection, fibromatosis, desmoid, nodular fasciitis, myxoma, GCT of tendon sheath, PVNS, nodular synovitis), or can be referred for percutaneous biopsy or surgical sampling to exclude sarcoma, depending upon the readers' comfort and experience with neoplastic lesions and related pseudomasses. The lesions can be treated by intralesional excision (GCT, FD); marginal excision (includes pseudocapsule, e.g., in locally aggressive lesions); wide excision (includes resection of the normal tissue around the lesion, e.g., in low grade tumors); and finally, radical excision (entire compartment is excised, e.g., in high grade tumors). Limb salvage with radical excision has a similar risk of local recurrence (~10%) as with amputation (~8%), with similar overall survival. The bone tumors excision is followed by endoprosthesis or allograft reconstruction. Of note, skip metastasis have worse prognosis than distant metastasis in osteosarcoma cases. For treated lesions following radiotherapy or chemotherapy, one should look at the residual nodular enhancement. Of note, more than 95% necrosis is required for good prognosis in osteosarcoma cases following chemo-radiation. Nodular early enhancement with rapid washout indicates residual or recurrent disease whereas diffuse slow enhancement and/or washout indicates posttreatment changes. Of note, tumor size in sarcoma may increase on chemo-radiation and Recist criteria are not very useful.

If contrast examination is not available or cannot be performed due to renal insufficiency

or other reasons, one can look at DW images, as a supplemental tool to assess cellularity by virtue of ADC restriction and making further decisions. Typically, increasing ADC values indicate good response and potential necrosis in the lesion. DW images should not be evaluated in isolation, to avoid false diagnoses (e.g., T2 shine through artifact, diffusion restriction in benign lesions, such as hematoma or abscess, and some benign cellular tumors, such as granular cell tumor or perineurioma of peripheral nerves). Many times, treated myeloma or leukemia/lymphoma lesions result in fibrosis or fatty metamorphosis, which can be confirmed on fat suppressed or CS imaging. These post-treatment changes lead to heterogeneous marrow on T1W and T2W images. Fat-suppressed, and particularly inversion recovery images are often useful to detect any residual/recurrent lesions by showing T2 prolongation and brightness among the lesions (Figs. 119, 120).

Fig. 119: Posttreatment myeloma lesion of the right humerus in a 72-year-old woman. Coronal images show a heterogeneous T2 lesion (*arrows*) at the humeral metaphysis, which shows foci of T1 signal drop (*arrowheads*) on the out-of-phase sequence that correspond to intracellular fat of fatty marrow, signifying treatment response.

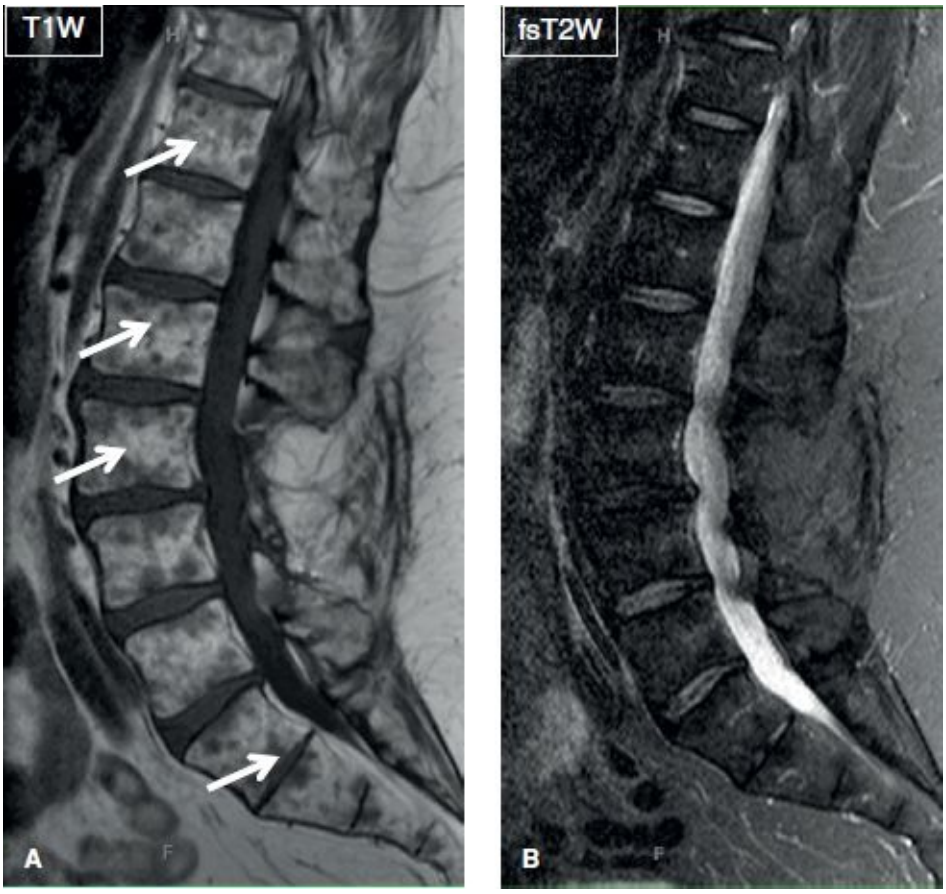

Fig. 120: Treated leukemia. Sagittal images show numerous T1 and T2 hypointense foci (*arrows*) in the vertebrae and sacrum, which lack high T2 signal on the fat-suppressed image.

Finally, combining all the imaging criteria in perspective, the reader should decide whether the lesion is benign (no further follow-up and leave alone), suggestive of malignancy (percutaneous biopsy or surgical sampling), or indeterminate. A heterogeneous mass located at a site where benign lesions usually develop (e.g., the prepatellar bursa) should also be considered indeterminate (Fig. 121). Indeterminate lesions, which are decided to be monitored, should be followed up to 2 years, doubling the follow-up intervals at each time, except in cases when they become smaller or resolve. The important regional extensions and involvements of these lesions should be described in the impression. The definitive diagnosis can be given for benign entities but should be avoided in indeterminate lesions or suspected soft tissue sarcomas, except the obvious fat-containing liposarcoma since even pathologists apply many tumor markers before arriving at a definitive diagnosis at current times.

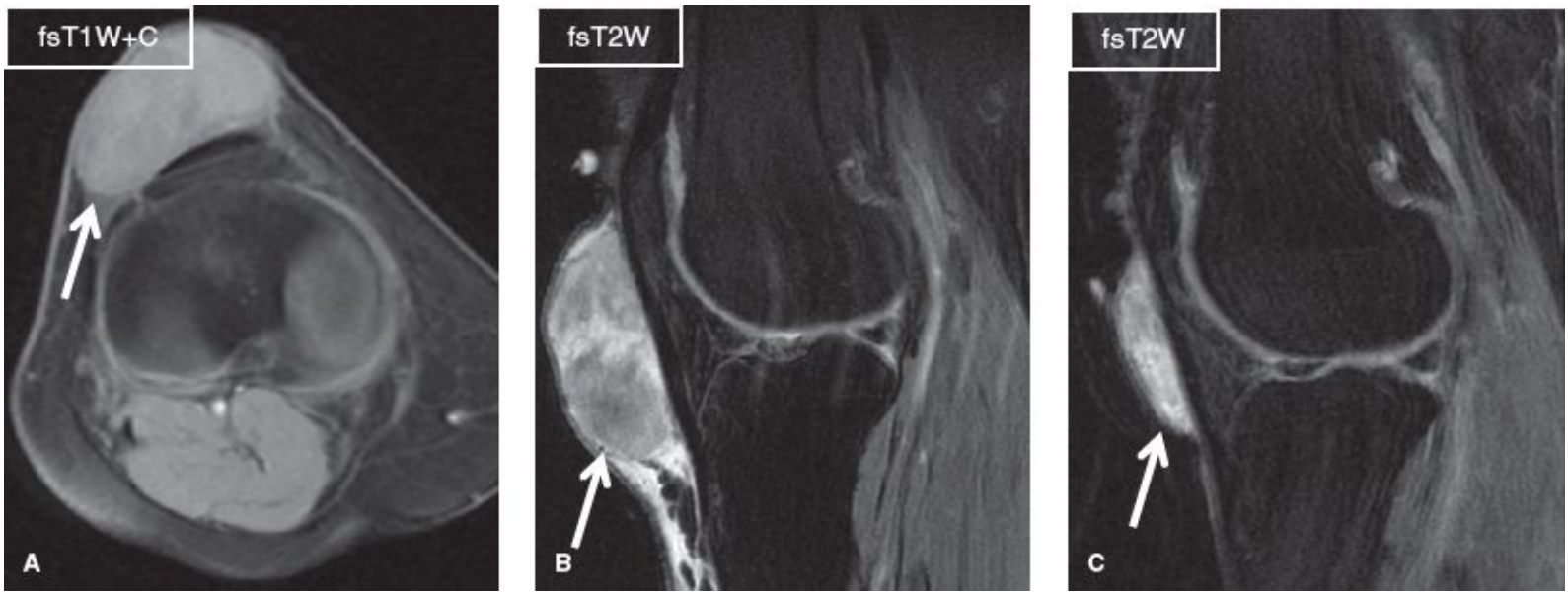

Fig. 121: Indeterminate lesion in an old woman due to age and heterogeneous appearance. It turned out to be soft tissue sarcoma. Axial **(A)** and sagittal **(B, C)** images show a well-defined heterogeneous T2 hyperintense mass (*arrows*) at the prepatellar bursa location with solid enhancement.

SUGGESTED READINGS

Adams ME, Saifuddin A. Characterisation of intra-articular soft tissue tumours and tumour-like lesions. *Eur Radiol.* 2007;17(4):950–958.

Arkun R, Argin M. Pitfalls in MR imaging of musculoskeletal tumors. *Semin Musculoskelet Radiol.* 2014;18(1):63–78.

Beaman FD, Jelinek JS, Priebat DA. Current imaging and therapy of malignant soft tissue tumors and tumor-like lesions. *Semin Musculoskelet Radiol.* 2013;17(2):168–176.

Boruban S, Sancak T, Yildiz Y, et al. Embolization of benign and malignant bone and soft tissue tumors of the extremities. *Diagn Interv Radiol.* 2007;13(3):164–171.

Chan WP. Magnetic resonance imaging of soft-tissue tumors of the extremities: A practical approach. *World J Radiol.* 2013;5(12):455–459.

Chhabra A, Soldatos T. Soft-tissue lesions: When can we exclude sarcoma? *AJR Am J Roentgenol.* 2012;199(6):1345–1357.

Chung WJ, Chung HW, Shin MJ, et al. MRI to differentiate benign from malignant soft-tissue tumours of the extremities: A simplified systematic imaging approach using depth, size and heterogeneity of signal intensity. *Br J Radiol.* 2012;85(1018):e831–e836.

Costa FM, Canella C, Gasparetto E. Advanced magnetic resonance imaging techniques in the evaluation of musculoskeletal tumors. *Radiol Clin North Am.* 2011;49(6):1325–1358, vii–viii.

Drape JL. Advances in magnetic resonance imaging of musculoskeletal tumours. *Orthop Traumatol Surg Res.* 2013;99(1 Suppl):S115–S123.

Ergun T, Lakadamyali H, Derincek A, et al. Magnetic resonance imaging in the visualization of benign tumors and tumor-like lesions of hand and wrist. *Curr Probl Diagn*

Radiol. 2010;39(1):1–16.
Goodwin RW, O'Donnell P, Saifuddin A. MRI appearances of common benign soft-tissue tumours. *Clin Radiol.* 2007;62(9):843–853.
Harish S, Lee JC, Ahmad M, et al. Soft tissue masses with "cyst-like" appearance on MR imaging: Distinction of benign and malignant lesions. *Eur Radiol.* 2006;16(12):2652–2660.
Heck RK, O'Malley AM, Kellum EL, et al. Errors in the MRI evaluation of musculoskeletal tumors and tumorlike lesions. *Clin Orthop Relat Res.* 2007;459:28–33.
Hermann G, Abdelwahab IF, Miller TT, et al. Tumour and tumour-like conditions of the soft tissue: Magnetic resonance imaging features differentiating benign from malignant masses. *Br J Radiol.* 1992;65(769):14–20.
Howe BM, Johnson GB, Wenger DE. Current concepts in MRI of focal and diffuse malignancy of bone marrow. *Semin Musculoskelet Radiol.* 2013;17(2):137–144.
Ma LD, Frassica FJ, Scott WW Jr, et al. Differentiation of benign and malignant musculoskeletal tumors: Potential pitfalls with MR imaging. *Radiographics.* 1995;15(2):349–366.
Manaster BJ. Soft-tissue masses: Optimal imaging protocol and reporting. *AJR Am J Roentgenol.* 2013;201(3):505–514.
Morris CD, Parsons TW 3rd, Schwab JH, et al. Imaging interpretation of oncologic musculoskeletal conditions. *Instr Course Lect.* 2012;61:541–551.
Moulton JS, Blebea JS, Dunco DM, et al. MR imaging of soft-tissue masses: Diagnostic efficacy and value of distinguishing between benign and malignant lesions. *AJR Am J Roentgenol.* 1995;164(5):1191–1199.
Murphey MD, Carroll JF, Flemming DJ, et al. From the archives of the AFIP: Benign musculoskeletal lipomatous lesions. *Radiographics.* 2004;24(5):1433–1466.
Stacy GS, Dixon LB. Pitfalls in MR image interpretation prompting referrals to an orthopedic oncology clinic. *Radiographics.* 2007;27(3):805–826; discussion 27–28.
Stacy GS, Kapur A. Mimics of bone and soft tissue neoplasms. *Radiol Clin North Am.* 2011;49(6):1261–1286, vii.
Ulaner G, Hwang S, Landa J, et al. Musculoskeletal tumours and tumour-like conditions: Common and avoidable pitfalls at imaging in patients with known or suspected cancer: Part B: Malignant mimics of benign tumours. *Int Orthop.* 2013;37(5):877–882.
Ulaner G, Hwang S, Lefkowitz RA, et al. Musculoskeletal tumors and tumor-like conditions: Common and avoidable pitfalls at imaging in patients with known or suspected cancer: Part A: Benign conditions that may mimic malignancy. *Int Orthop.* 2013;37(5):871–876.
Weatherall PT. Benign and malignant masses. MR imaging differentiation. *Magn Reson Imaging Clin N Am.* 1995;3(4):669–694.

APPENDIX 1: Sample Completed Structured Report: Soft Tissue Tumor:

NORMAL

EXAM: MRI SOFT TISSUE TUMOR <WITH OR WITHOUT> CONTRAST

FINDINGS:

Markers have been [<placed> <not placed>] at the site of concern.

Size: [< >] × [< >] × [< >] cm

Location: [< >]

Characteristics:

Matrix: [<T1 and T2 signal characteristics>]

Uniformity: [<Heterogeneous> <Homogeneous>]

Fluid–fluid levels: [<No>]

Transition zone: [<Narrow-edema absent>]

Periosteal reaction: [<None>]

Extent:

Compartment: [<Intracompartmental> <Extracompartmental> <Indeterminate>]

Bone involvement: [<No>]

Intra-articular involvement: [<No>]

Neurovascular involvement: [<No>]

Nodal involvement: [<No>]

POST-GADOLINIUM DISCUSSION:

IMPRESSION:

1. Findings suggestive of [<Benign> <Indeterminate> <Malignant>]

2. Diagnosis is suggestive of [< >]

3. Suggested recommendation: [<Follow-up> <Biopsy or surgical sampling>]

☑ APPENDIX 2: Sample Completed Structured Report: Soft Tissue Tumor: ABNORMAL

EXAM: MRI [<SOFT TISSUE TUMOR>] [<WITH AND WITHOUT>] CONTRAST

FINDINGS:

Markers have been [<placed>] at the site of concern in the right thigh.

Size: [<3 × 5.2 × 6>] cm

Location: [<Right anterior thigh in the anterior compartment soft tissues>]

Characteristics:

Matrix: [<Predominantly hyperintense on T1W and T2W images>]

Uniformity: [<Heterogeneous>]

Fluid–fluid levels: [<No>]

Transition zone: [<Narrow>]

Periosteal reaction: [<Absent>]

Extent:

Compartment: [<Intracompartmental>]

Bone involvement: [<No>]

Intra-articular involvement: [<No>]

Neurovascular involvement: [<No>]

Nodal involvement: [<No>]

POST-GADOLINIUM DISCUSSION: [<Heterogeneous nodular enhancement>]

IMPRESSION:

1. Findings suggest malignant lesion.

2. Diagnosis is suggestive of liposarcoma.

3. Suggested recommendation: Biopsy or surgical sampling.

APPENDIX 3: Sample Completed Structured Report: Bone Tumor: NORMAL

EXAM: MRI BONE TUMOR [<WITH OR WITHOUT>] CONTRAST

FINDINGS:

Markers have been [<placed> <not placed>] at the site of concern.

Size: [< >] × [< >] × [< >] cm

Location: [< >]

Characteristics:

Matrix: [<T1 and T2 signal characteristics>]

Uniformity: [<Heterogeneous> <Homogeneous>]

Fluid–fluid levels: [<No>]

Transition zone: [<Narrow-edema absent>]

Periosteal reaction: [<None>]

Extent:

Soft tissue mass: [<No>]

Intra-articular involvement: [<No>]

Neurovascular involvement: [<No>]

Nodal involvement: [<No>]

POST-GADOLINIUM DISCUSSION:

IMPRESSION:

1. [<Benign> <Indeterminate> <Malignant>]

2. Diagnosis is suggestive of [< >]

3. Suggested recommendation: [<Follow-up> <Biopsy or surgical sampling>]

APPENDIX 4: Sample Completed Structured Report: Bone Tumor: ABNORMAL

EXAM: MRI [<BONE TUMOR>] [<WITH OR WITHOUT>] CONTRAST

FINDINGS:

Markers have [<not been placed>] at the site of concern.

Size: [<12 × 3 × 4.2>] cm

Location: [<Right humerus proximal metadiaphysis>]

Characteristics:

Matrix: [<Predominantly hypointense on T1W and mixed signal on T2W images>]

Uniformity: [<Heterogeneous>]

Fluid–fluid levels: [<Present>]

Transition zone: [<Wide with adjacent bone marrow edema>]

Periosteal reaction: [<Present with associated Codman triangle>]

Extent:

Soft tissue mass: [<Yes, involving the biceps muscle>]

Intra-articular involvement: [<No>]

Neurovascular involvement: [<Yes, musculocutaneous nerve encasement>]

Nodal involvement: [<No>]

POST-GADOLINIUM DISCUSSION: [<Heterogeneous enhancement present in the bone lesion and in the associated soft tissue mass>]

IMPRESSION:

1. Findings suggest malignant lesion.

2. Diagnosis is suggestive of osteosarcoma, telangectatic variety.

3. Suggested recommendation: Biopsy or surgical sampling.

5

Cartilage

Avneesh Chhabra, Gaurav K. Thawait, and Theodoros Soldatos

The articular surfaces of synovial joints are covered by hyaline cartilage, which protects the underlying subchondral bones by distributing loads and absorbing shock, maintains low-contact stresses, reduces friction and enables smooth motion of the articulating osseous structures. Damage to the hyaline cartilage usually results from everyday weight-bearing forces or sport activities and might be worsened with additional destabilizing pathology, such as tears (and, thus, subsequent loss of the supportive function) of menisci or labrum.

MR imaging is the method of choice to identify articular cartilage injuries and evaluate the post-operative reconstitution of cartilage repair tissue. Although various experimental techniques, such as T2 mapping, post-contrast T1 mapping, T1 rho imaging, glycosaminoglycan chemical exchange saturation transfer imaging (GAG CEST), and sodium MR imaging, are becoming feasible for the assessment of cartilage tissue architecture, conventional morphologic MR imaging remains the mainstay for the pre- and post-operative evaluation of the articular cartilage (Fig. 1). This chapter describes the structural anatomy of the articular cartilage, along with the respective normal and abnormal imaging appearances and delineates various grading systems and guidelines used in clinical practice for the imaging definitions of cartilage injury (chondrosis). In addition, surgical techniques for cartilage reconstitution are briefly discussed, and instructions are provided for filling in the structured template for the MR imaging description of repaired cartilage.

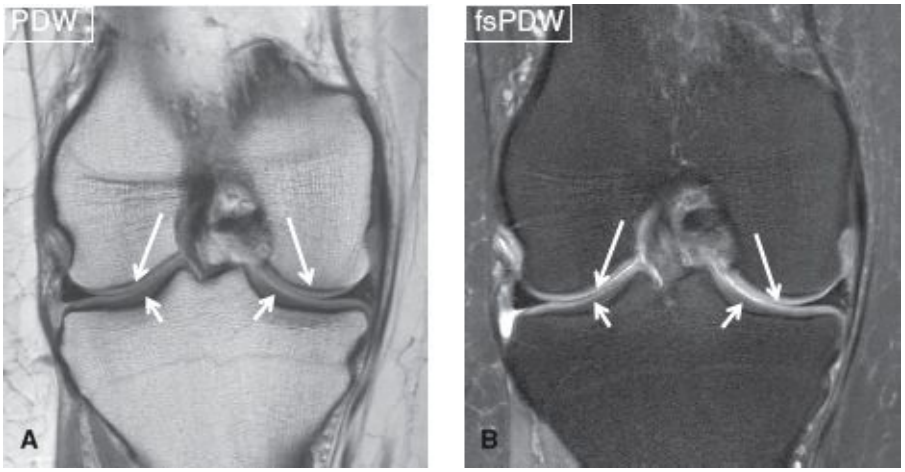

Fig. 1: Normal articular cartilage. Coronal images **(A, B)** of the knee demonstrate normal

articular cartilage of the femoral condyles (*long arrows*) and tibial plateau (*short arrows*), featuring homogeneous thickness and a gradual increase in signal from the bone surface to the articular surface.

ANATOMICAL ARCHITECTURE AND PATHOPHYSIOLOGY

The hyaline cartilage is a thin layer of soft tissue, wrapped around complex intra-articular anatomical structures. It is composed of 70% water, 20% collagen, and 5–10% proteoglycans and is very hypocellular since it is only composed of about 4% chondrocytes by wet weight. From superficial (near the joint fluid) to deep (near the subchondral bone), the cartilage is composed of (1) the lamina splendens, which is a thin hypointense protective layer; (2) a superficial layer of horizontal collagen fibers, which provide resistance against shear stress; (3) an intermediate/transitional layer of oblique fibers, which provide resistance against shear and compression stress; (4) a deep layer of radial fibers, which provide resistance against compression stress; and (5) a calcifying/tidemark zone, which tightly bonds the cartilage to the underlying bone.

The cartilage is subject to repetitive forces throughout life, and a normal adult loses 1% to 3% of articular cartilage thickness per year after 30 years of age, a process, which further worsens with the onset of osteoarthrosis or secondary insults from acute trauma, infection, or joint instability from meniscoligamentous injuries or inflammatory arthropathies. In general, arthritis-related cartilage defects show irregular and obtuse margins due to repetitive wear and tear whereas acute trauma-related defects are usually focal, isolated and demonstrate well-defined shouldered margins.

Cartilage damage progresses from chondromalacia (softening) to chondrosis (fissures, defects, flaps, delamination, and denudation on one side of the joint) and osteoarthrosis (cartilage defects or loss on both sides of the joint). Cartilage injuries are usually repaired by chondrocytes, which usually form fibrocartilage. The latter, however, is not very resilient in dealing with stresses as compared to the native hyaline cartilage. Full-thickness cartilage loss commonly results in stress changes in the underlying bone, causing pain and decreased range of motion in the affected joint.

On MR imaging, the normal five-layered configuration of hyaline cartilage is rarely visible, except in areas where it is thickest, for example, in patella. It is also only possible if high-resolution techniques combined with joint-specific coils and high-field strength ($\geq$3 T) scanners are employed. On conventional (proton density-weighted [PDW] and fat-suppressed PDW [fsPDW]) imaging, the articular cartilage usually features a trilaminar configuration, composed of a low-signal deep layer (tidemark and radial zone), a thicker intermediate to hyperintense middle layer (oblique and horizontal fibers), and a thin low-signal surface layer (lamina splendens). In general, there is a gradual increase in signal from the bone surface to the articular surface. Additionally, the thickness of different layers of the cartilage vary for different surfaces of the articular bony margins (e.g., the radial layer is thicker in the weight-bearing central aspect of the tibia, and the transitional layer is

thicker in the peripheral aspect) (Fig. 1).

IMAGING OF ARTICULAR CARTILAGE PATHOLOGY

Cartilage injury is often a part of osteochondral lesions (OCLs). OCLs refer to one or two lesions on either joint surface, which have resulted from trauma, osteochondritis dissecans (OCD), or insufficiency fracture. More than two to three lesions are generally clubbed together as part of osteoarthrosis. MR imaging is the method of choice for the evaluation of both OCLs and intrasubstance lesions. A number of terms have been used for describing cartilage lesions on MR imaging, and multiple grading schemes have been proposed. Some of these include the Outerbridge Classification (1961), the Osteoarthritis Cartilage Histopathology Grading and Staging (OARSI, 2006), the International Cartilage Repair Society (ICRS) Classification (Table 1), and the Whole Organ MR Imaging Score (WORMS). Remembering and incorporating these ever-changing grading systems is a challenging task for both radiologists and referring physicians. In addition, on MR imaging, a number of lesions of varying severity may be identified, the interobserver variability tends to increase with complicated scoring systems, and a particular scoring system may not be efficient in classifying all such lesions. It is, therefore, better to describe the lesions in each compartment of a joint using accurate terminology rather than trying to fit all lesions into a particular scoring system. The terminology used in common clinical practice for describing cartilage lesions is illustrated in the following paragraphs.

TABLE 1: The International Cartilage Repair Society (ICRS) classification

Grade	Cartilage Key Feature
1	Normal
2	Surface fibrillation and/or superficial laceration
3	Partial-thickness defect <50% of thickness
4	Partial-thickness defect >50% of thickness

Signal Heterogeneity

On MR imaging, signal heterogeneity may be caused by chondromalacia, fibrocartilage formation, cartilage degeneration, or mineralization. In most circumstances, chondromalacia (blistering or softening) is the earliest stage of cartilage injury; although it may be present in the cartilage either focally or diffusely in combination with higher grades of injury. The lesion usually involves the deeper layers of the cartilage and is likely related to fluid imbibition from a not-so-well seen surface fissure. The name derives from soft "malacic" feeling on arthroscopic probing. MR imaging may show focal area(s) of increased fluid-like T2 signal intensity in the deeper layers of the cartilage, with or without associated

focal cartilage swelling. It can be differentiated from fissure and defect from the fact that the overlying lamina splendens hypointensity remains preserved. More commonly, the chondromalacic cartilage features diffusely increased signal with loss of the normally observed gradual deep to superficial signal alteration as described above (Figs. 2, 3).

Fig. 2: Patellar chondromalacia. Axial images from different cases show diffuse hyperintensity (*long arrows*) of the lateral patellar facet cartilage (faint in **A,** prominent in **B**), which is indicative of chondromalacia. In **(B),** an additional full-thickness shouldered cartilage defect (*short arrow*) can be seen at the median patellar ridge.

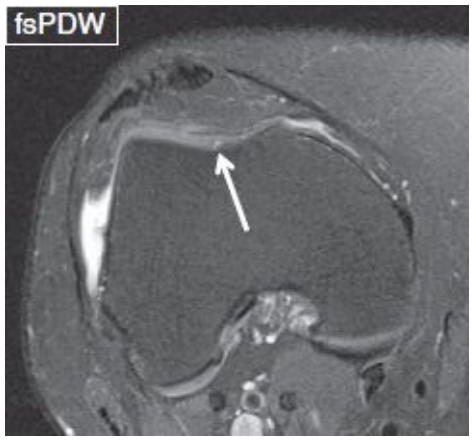

Fig. 3: Trochlear chondromalacia. Axial image reveals a tiny blister-like increased signal (*arrow*) at the central aspect of the trochlear cartilage.

Fibrocartilage formation, cartilage degeneration, and/or chondrocalcinosis are the result of subacute/chronic cartilage injury, as the cartilaginous tissue attempts to self-heal by fibrosis or mineralization. MR imaging shows focal or diffuse areas of low signal intensity within the articular cartilage (Figs. 4, 5). It is often difficult to differentiate fibrocartilage from chondrocalcinosis although the latter tends to be more focal and punctate and may additionally show blooming artifact on gradient echo images (Fig. 6). Correlation with plain films may assist in identifying the calcifications, although the lesions are often not visible, due to the low sensitivity and poor soft tissue contrast of conventional radiographs. Large areas of chondrocalcinosis may mimic incomplete discoid meniscus or vacuum in the joint (Fig. 7).

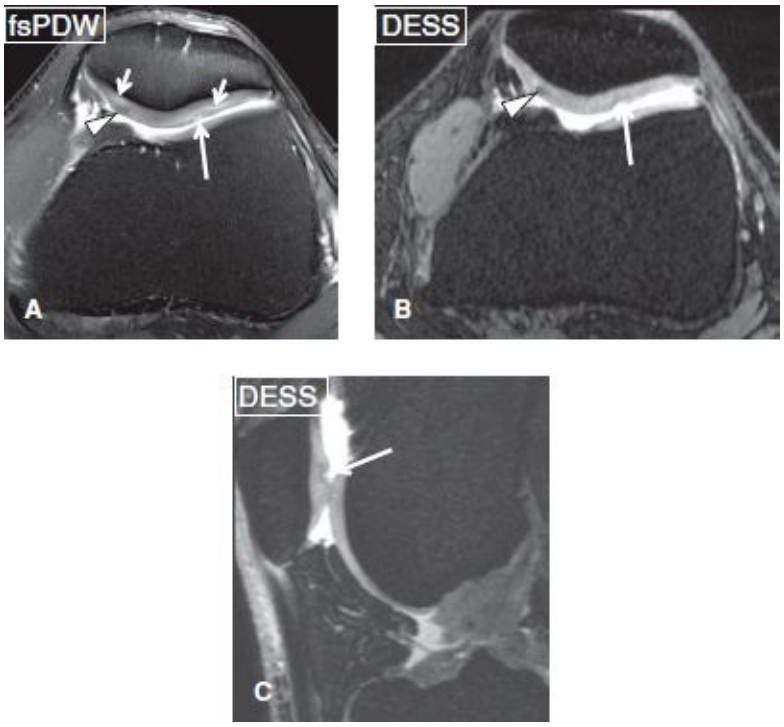

Fig. 4: Multiple patellar cartilage abnormalities. Axial image **(A)** exhibits linear areas of hyperintensity (*short arrows*) at the cartilage of both facets, which are indicative of chondromalacia, a hypointense focus (*arrowhead*) in the medial facet cartilage, which corresponds to fibrocartilage, as well as low-grade cartilage defects (*long arrows*) at the lateral facet. Axial **(B)** and coronal **(C)** reformations from a three-dimensional dual echo steady state sequence render the fibrocartilage focus (*arrowheads*) and cartilage defect (*arrows*) more prominent. Chondromalacia is less well seen on these 3D images.

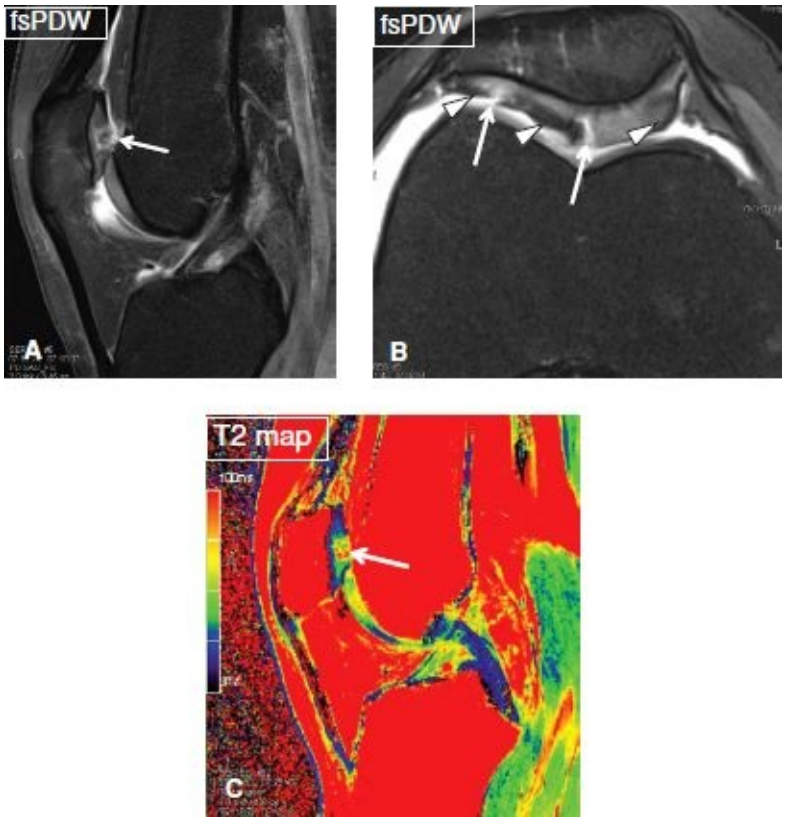

Fig. 5: Multifocal patellar chondrosis and signal alterations: Sagittal **(A),** axial **(B),** and corresponding sagittal color-coded T2 map **(C)** show multifocal high-grade patellar cartilage

defects (*arrows*) with background areas of chondromalacia and fibrocartilage formation (*arrowheads*), not an uncommon finding in patellar malalignment cases.

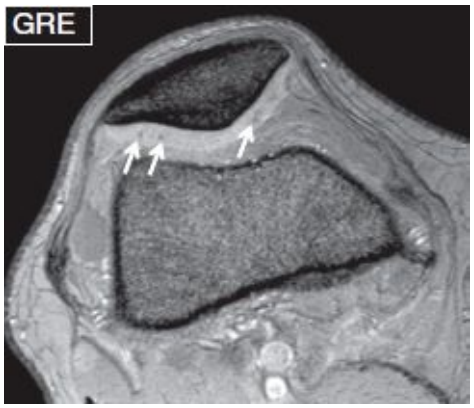

Fig. 6: Chondrocalcinosis. Axial gradient echo image exhibits punctuate foci (*arrows*) of low signal within the patellar cartilage, which correspond to calcifications.

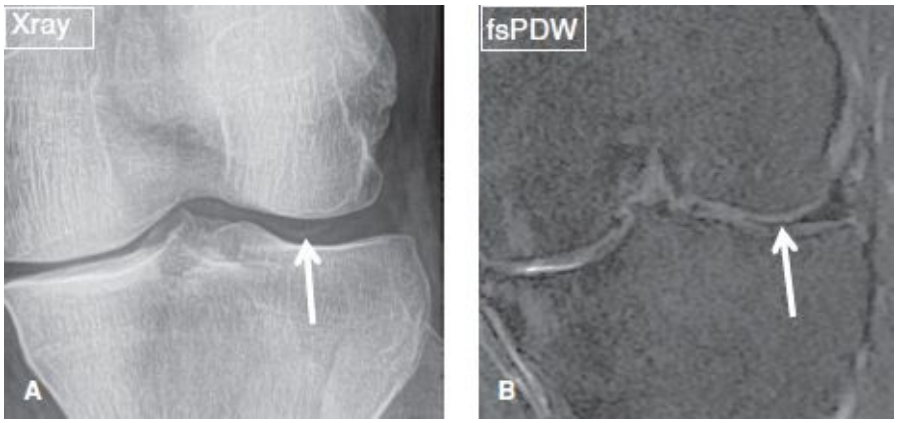

Fig. 7: Chondrocalcinosis. **A:** Anteroposterior plain film exhibits reveal linear opacity (*arrow*) in the lateral joint space, in keeping with chondrocalcinosis. **B:** On the corresponding coronal MR image, this chondrocalcinosis mimics incomplete discoid meniscus (*arrow*).

Partial-thickness Lesions

Partial-thickness defects qualify under chondrosis, and the term chondromalacia should not be used to describe them. These lesions can show a variety of morphologic appearances such as surface fibrillation, fissures, flaps, defects, or simply thinning. Apart from using these terms, one should describe whether the lesion is less than or more than 50% in thickness, namely low grade or high grade, respectively. If uncertain, one can use the term intermediate grade instead. Surface fibrillation represents an early stage of cartilage loss. On MR images, the cartilage shows minimal surface irregularity (fraying) and loss of the dark layer of the lamina splendens (Fig. 8). Cartilage fissure or flap results from further surface damage. Fissures are identified as tiny linear T2 bright gaps of less than 2 mm in transverse width, which assume a nearly perpendicular orientation to the articular surface (Fig. 9). A flap is formed by an obliquely oriented fissure, which causes elevation of the

superficial (<50%) or deep (>50%) semi-separated layers of the articular cartilage (Figs. 10, 11). Cartilage defects are larger gaps with transverse width of greater than 2 mm. Based on the involved thickness, they can also be classified as low- and high grade, similar to fissures and flaps (Figs. 4, 5). In general, acute–subacute trauma related defects are well defined with shouldered margins, show acute angles and are fewer in number and are limited to the trauma sites. The osteoarthritis (OA)-related defects show obtuse margins, are ill-defined and occur at all sites, especially worse in the weight-bearing areas. Cartilage thinning appears as diffuse decrease of the cartilage thickness, with or without focal defects. In an individual joint, comparison with the cartilage thickness of the normal-appearing compartment assists in identifying the abnormality. Sometimes the cartilage may show low-intermediate grade thinning; however, presence of bony changes of sclerosis, cysts, and edema may indicate underlying full-thickness fissuring (Figs. 12–14). Patellofemoral pain syndrome patients will classically show patellofemoral cartilage abnormalities at the opposing surfaces with associated underlying friction-related Hoffa's fat pad edema (Fig. 15). In addition, these subjects might show excessive or isolated cartilage loss of the far posterior medial or lateral femoral condyles in the tibiofemoral compartments (Fig. 16).

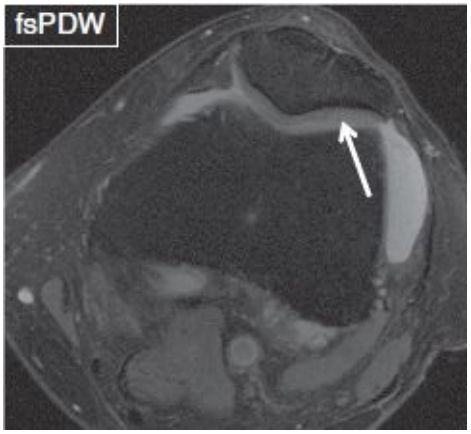

Fig. 8: Cartilage surface fibrillation. Axial image demonstrates minimal surface irregularity, thinning and loss of the dark layer of the lamina splendens (*arrow*) at the cartilage of the lateral patellar facet. Notice underlying chondromalacia of the lateral facet. This is already at the stage of chondrosis.

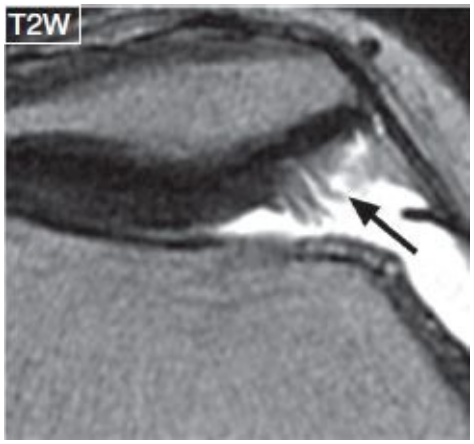

Fig. 9: Cartilage fissures. Magnified axial image demonstrates multiple high-grade cartilage

fissures (*arrow*) at the medial patellar facet.

Fig. 10: Cartilage flap. Axial image shows an obliquely oriented fissure (*arrow*), which causes elevation of the superficial layers of the patellar cartilage.

Fig. 11: Cartilage injury caused by transient patellar dislocation. Sagittal **(A)** and axial **(B)** images exhibit contusion and a high-grade flap (*arrows*) at the medial patellar facet cartilage with subchondral bony defect.

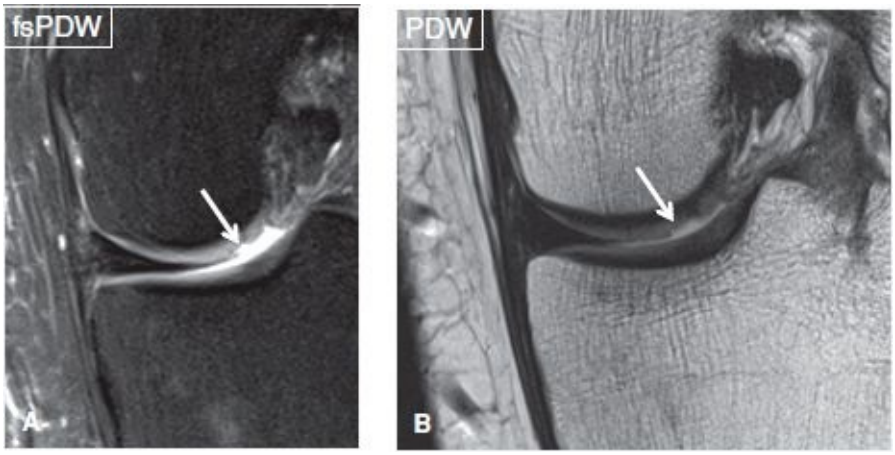

Fig. 12: Trauma-related shouldered cartilage defect. Coronal images **(A, B)** reveal a well-defined shouldered defect at the lateral aspect of the medial femoral condyle (*arrows*).

Fig. 13: Osteoarthritis-related cartilage loss. Coronal **(A)** and sagittal **(B)** reformatted images from a three-dimensional sequence show low- to intermediate-grade cartilage defects (*short arrows*) at the anterior aspect of the talar dome and the opposing surface of the tibia, as a result of chronic injury and resulting OA. Underlying subchondral cysts (*long arrows*) are presumably caused by thin, nonvisible fissures. Also note the foci of fibrocartilage (*arrowheads*) formation of the tibial articular cartilage.

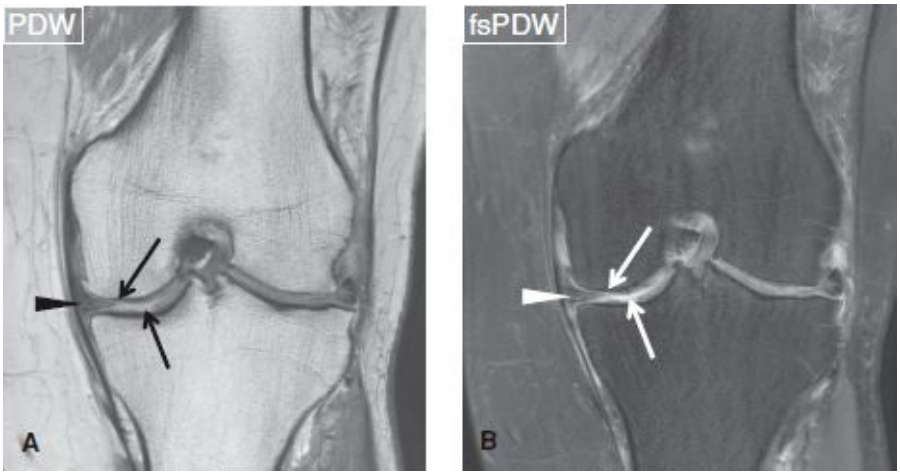

Fig. 14: Osteoarthritis-related cartilage lesions. Coronal images **(A, B)** exhibit areas of high-grade cartilage thinning (*arrows*) at the medial compartment. Also note medial meniscus degeneration (*arrowhead*).

Fig. 15: Patellofemoral friction syndrome. High-grade cartilage lesions in a patient with

patellofemoral pain. Sagittal image shows superolateral Hoffa's fat pad edema (*short arrow*), which is indicative of the entity, along with high-grade cartilage thinning (*long arrows*) at the trochlea and patella, due to chronic friction.

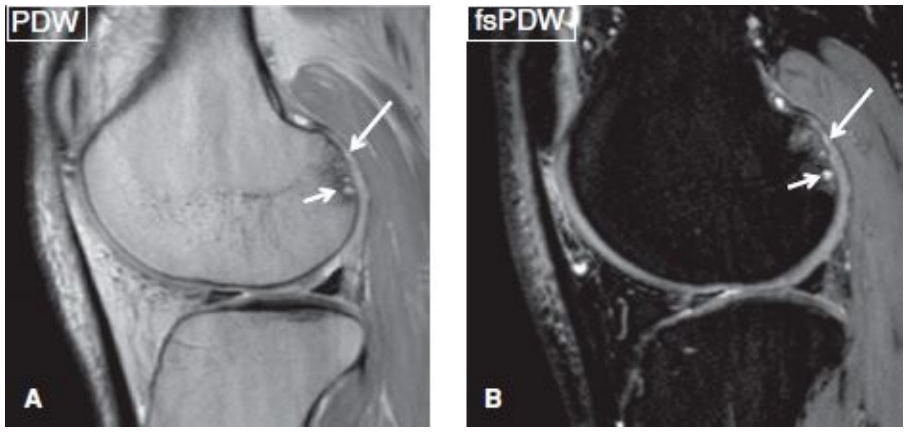

Fig. 16: High-grade cartilage lesions in a patient with patellofemoral pain. Sagittal reformatted three-dimensional images **(A, B)** demonstrate subchondral cysts (*short arrows*) at the far posterior aspect of the lateral femoral condyle, which are associated with high-grade thinning of the overlying cartilage (*long arrows*) and presumably cartilage fissures. This finding is not common in young persons with patellofemoral malalignment and maltracking syndromes.

Full-thickness Lesions

Full-thickness cartilage fissures or defects are the most severe abnormalities, which rapidly evolve over time and lead to loss of stress shielding of the underlying bone leading to subchondral edema, cysts, and/or sclerosis (Figs. 5, 13, 16–21). The latter manifestations are evident on PDW and fsPDW images: edema is disproportionately apparent on fsPDW images; cysts are proportionately apparent on PDW and fsPDW images as dark/bright lesions on PDW and bright lesions on fsPDW images; sclerosis is proportionately dark on both PDW and fsPDW images. Other reactive bony changes include subchondral insufficiency fracture, articular surface collapse, and chondral or marginal osteophyte formation. Among these lesions exist, cartilage delamination and denudation. Delamination refers to debonding of the articular cartilage from the subchondral bone at the tidemark zone and is regarded as one of the most severe cartilage lesions. MR imaging shows fluid-like signal interposed between the cartilage and the bone, with or without buckling of the delaminated cartilage (Figs. 22, 23). Denudation ranges from broad areas of full-thickness cartilage defects to complete loss of the cartilage from the weight-bearing areas of the bone (Fig. 24). In worst case scenarios, both opposing surfaces of the bone might be completely denuded, leading to bone-on-bone articulation and osteoarthrosis.

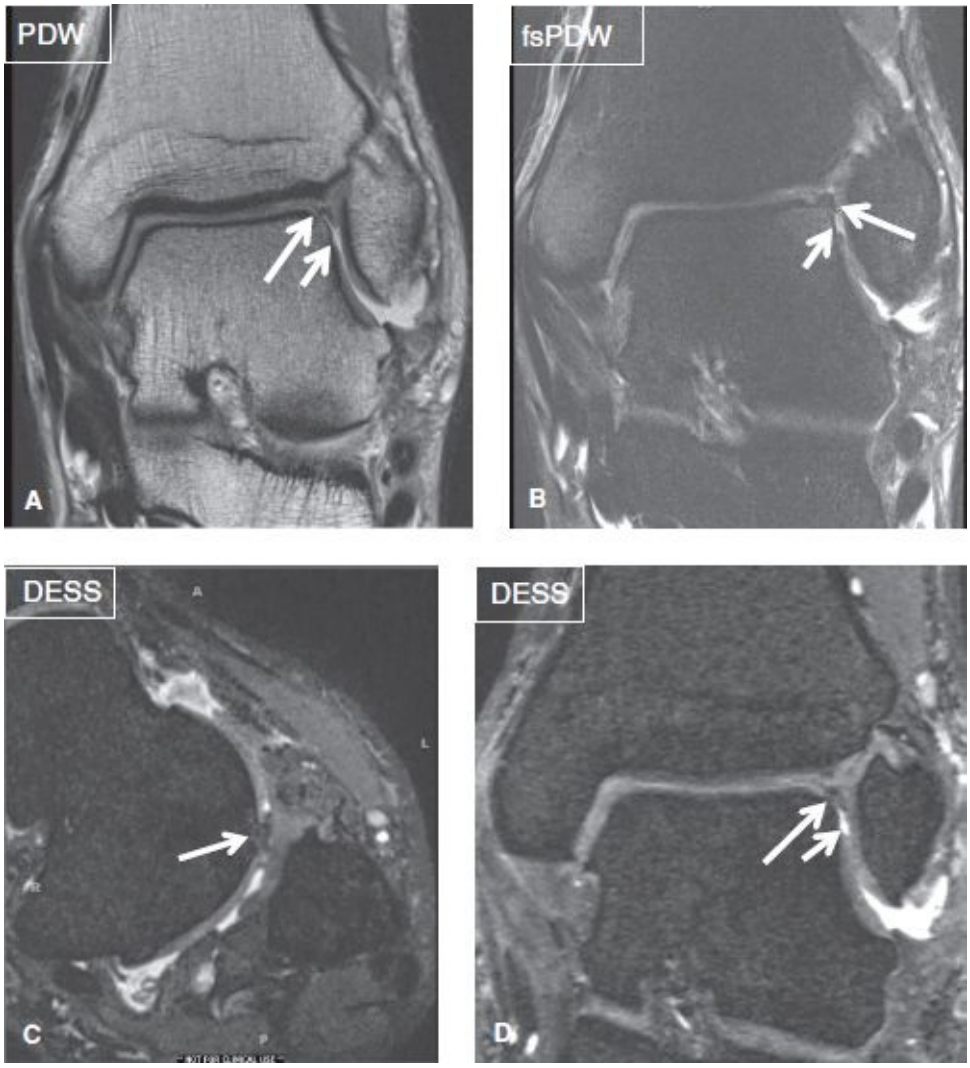

Fig. 17: Full-thickness cartilage defect. Coronal images **(A, B)** reveal full-thickness cartilage defect (*short arrows*) of the lateral talar dome, along with hypointense focus (*long arrows*) in the adjacent cartilage, signifying degeneration. Findings are similarly appreciated on reconstructions in the oblique **(C)** and coronal **(D)** planes from a three-dimensional sequence.

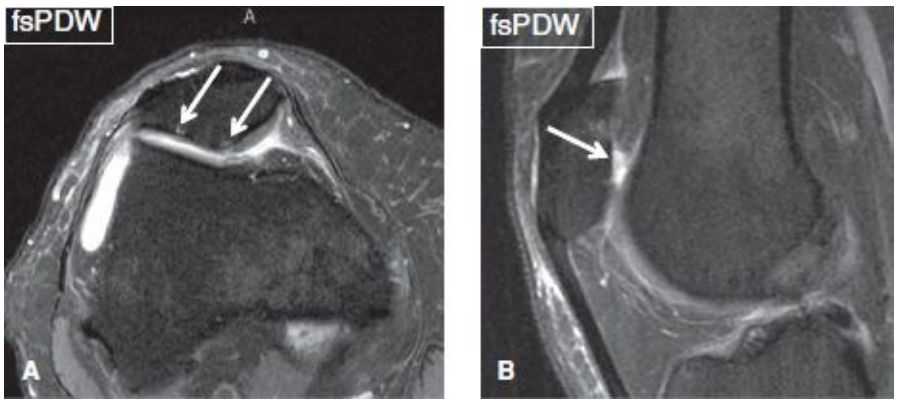

Fig. 18: Osteoarthritis-related patellofemoral cartilage lesions. **A:** Axial image demonstrates homogeneous high-grade thinning of the lateral facet cartilage, lateral facet trochlea, and full-thickness defect of the median ridge with scattered subchondral cysts (*arrows*). **B:** Sagittal image from a different case show a full-thickness cartilage defect (*arrow*).

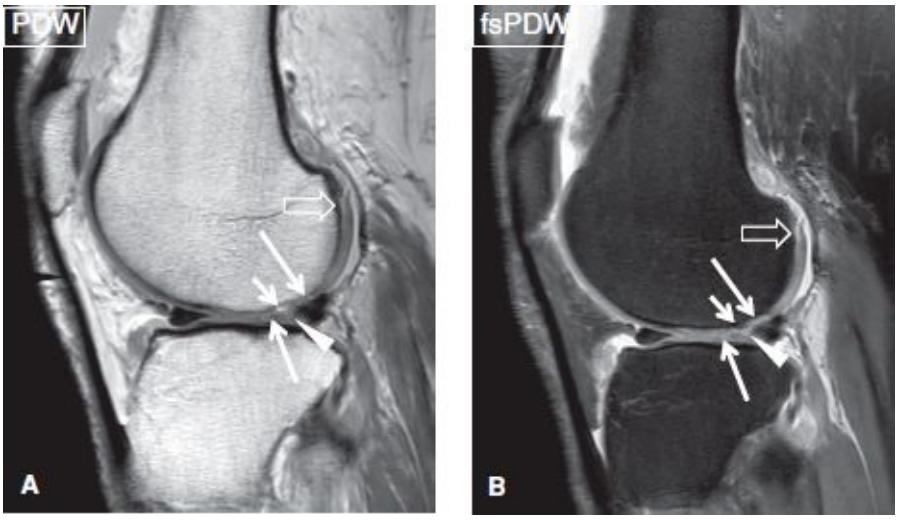

Fig. 19: Osteoarthritis-related cartilage lesions. Sagittal images **(A, B)** reveal high-grade and full-thickness cartilage defects (*long arrows*) at both articular surfaces of the lateral knee compartment. Also note associated chondral osteophyte formation (*short arrows*), a high-grade cartilage flap (*open arrows*) at the far posterior condyle, as well as posterior horn truncation (*arrowheads*) of the ipsilateral meniscus.

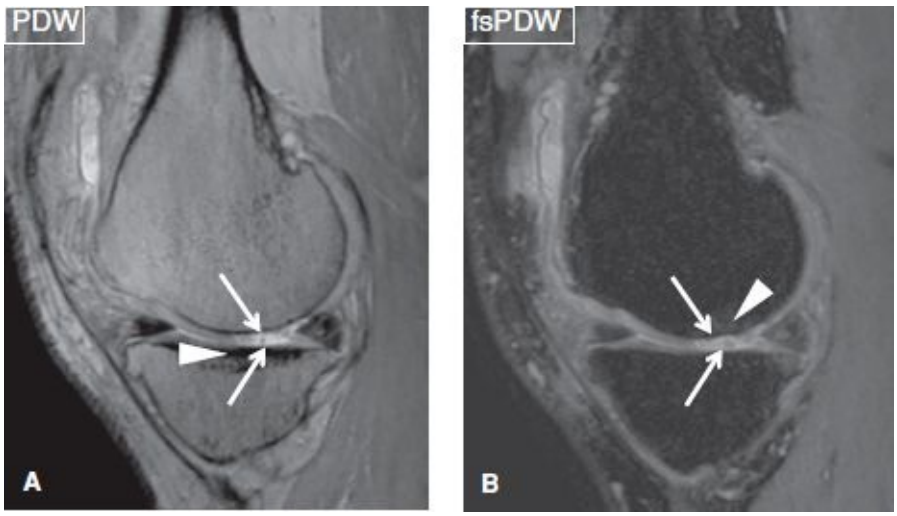

Fig. 20: Osteoarthritis-related cartilage lesions. Sagittal reformations from a three-dimensional sequence reveal broad areas of full-thickness cartilage defects (*arrows*) at both sides of the medial knee compartment. Also note subchondral sclerosis (*arrowhead* in **A**) of the medial plateau and faint edema (*arrowhead* in **B**) at the ipsilateral femoral condyle, signifying recurrent bone abutment.

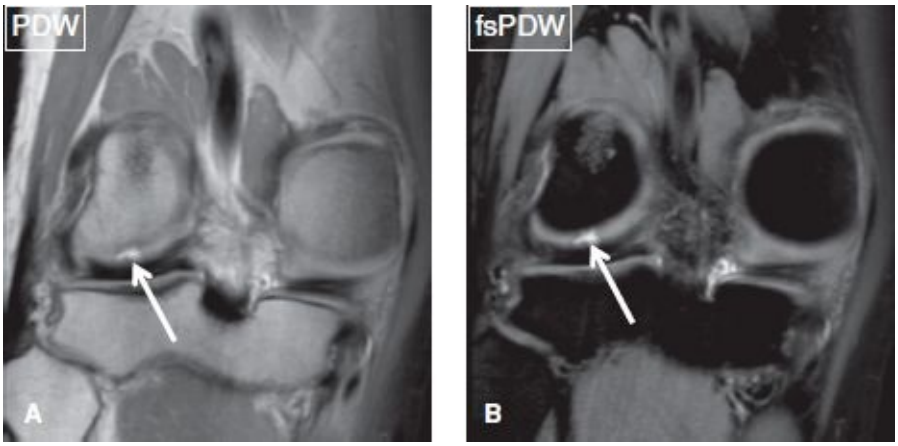

Fig. 21: Trauma-related shouldered cartilage defect. Coronal conventional image **(A)** and coronal reformatted three-dimensional image **(B)** demonstrate a shouldered full-thickness cartilage defect (*arrows*) at the lateral femoral condyle.

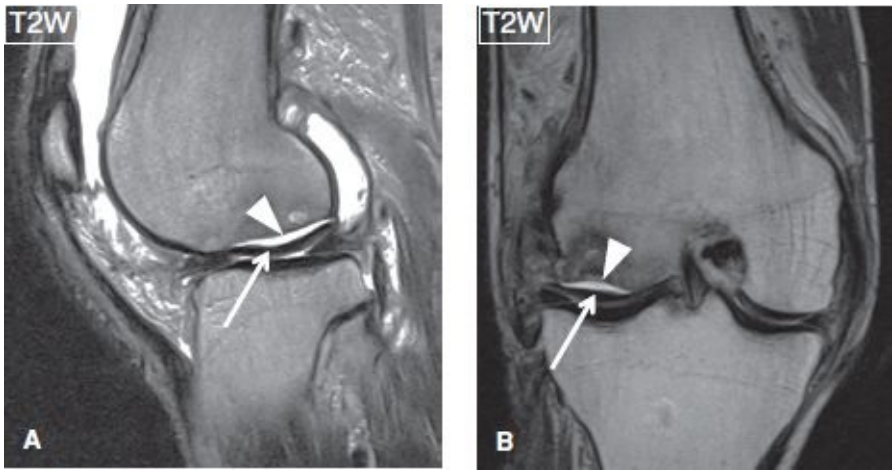

Fig. 22: Cartilage delamination. Sagittal **(A)** and coronal **(B)** images exhibit debonding of the central and posterior aspect of the medial femoral condyle cartilage from the subchondral bone at the tidemark zone from recent trauma. Fluid-like signal (*arrowheads*) is interposed between the cartilage and the bone. Notice underlying subchondral cysts and sclerosis indicative of subjacent chronic osteochondral lesion.

Osteochondral Lesions

The term OCLs refers to one or two lesions of the articular cartilage, which are associated with reactive changes of the underlying subchondral bone. OCLs may be related to meniscal or labral tears a.k.a subchondral insufficiency fractures or stress injuries; acute trauma a.k.a osteochondral fracture; or overactivities of adolescence a.k.a OCD. Osteochondral fractures manifest as one or a combination of findings such as bone marrow edema, partial- or full-thickness shouldered cartilage lesions, as detailed above, and impaction injury or fracture of the subchondral bone. In the acute stage, there is associated perilesional fascial edema or joint effusion. In the subacute and chronic stages, the edema evolves into subchondral cysts, fat, and/or sclerosis, with or without articular surface depression and/or loose body formation (Figs. 25, 26). Therefore, to identify these lesions, it is important to evaluate fs

and non-fs similar-plane images in tandem. Currently, OCDs are considered disorders of the secondary physis and these are associated with history of prior trauma in about half of the cases. OCDs appear as crescentic lesions, which are usually located in a non–weight-bearing aspect of the bone surface and these may be associated with the secondary bony changes described above for the trauma-related OCLs (Figs. 27–30). Some locations are characteristic for this lesion, including the medial aspect of the lateral femoral condyle, the talar dome, and the capitellum. The overlying articular cartilage may be flush with the remaining cartilage, or it could be proud, or may show cartilage fissuring or flaps.

Fig. 23: Cartilage delamination. Axial image demonstrates debonding of the trochlear cartilage (*arrow*) from the subchondral bone at the tidemark zone.

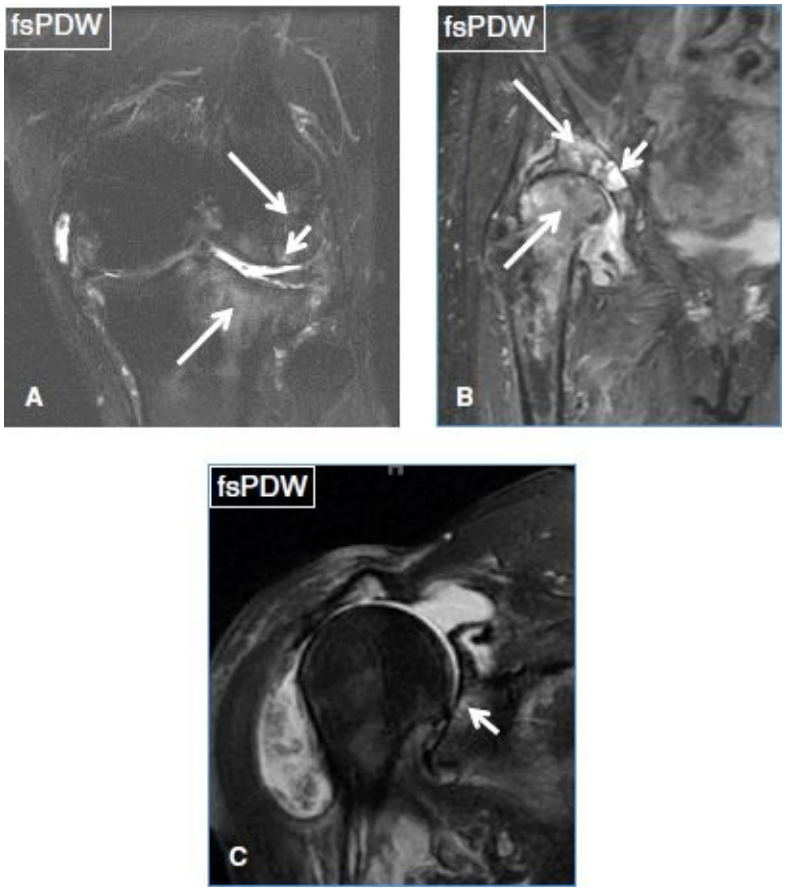

Fig. 24: Osteoarthritis-related bone-on-bone abutment. Coronal images of the knee **(A),** hip **(B),** and shoulder **(C)** reveal complete cartilage denuding at both sides of the joints, with associated subchondral edema (*long arrows*) and subchondral cystic changes (*short arrows*).

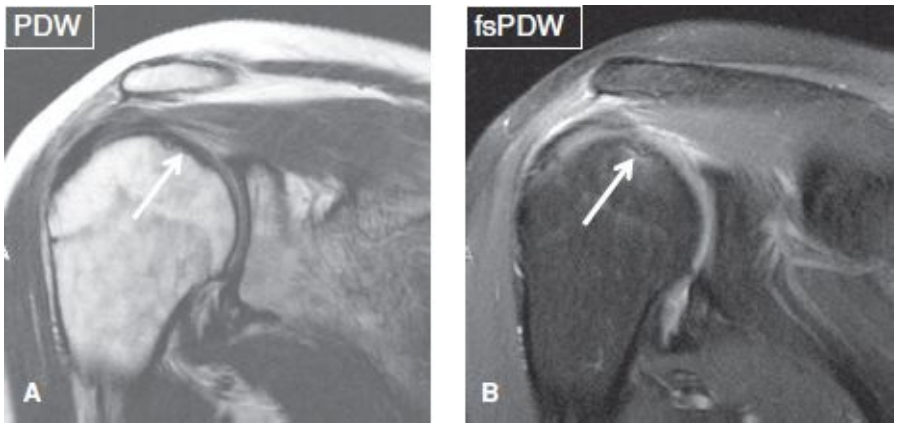

Fig. 25: Osteochondral fracture caused by crutch injury. Coronal images **(A, B)** show an osteochondral fracture (*arrows*) at the superior aspect of the humeral head.

Fig. 26: Osteochondral fracture of the tibia. Sagittal images. **A:** A displaced transverse fracture (*arrow*) is evident at the anterior aspect of the radial head from recent elbow dislocation. **B:** Hypointense intra-articular osteochondral bodies (*arrows*) float within the anterior joint effusion.

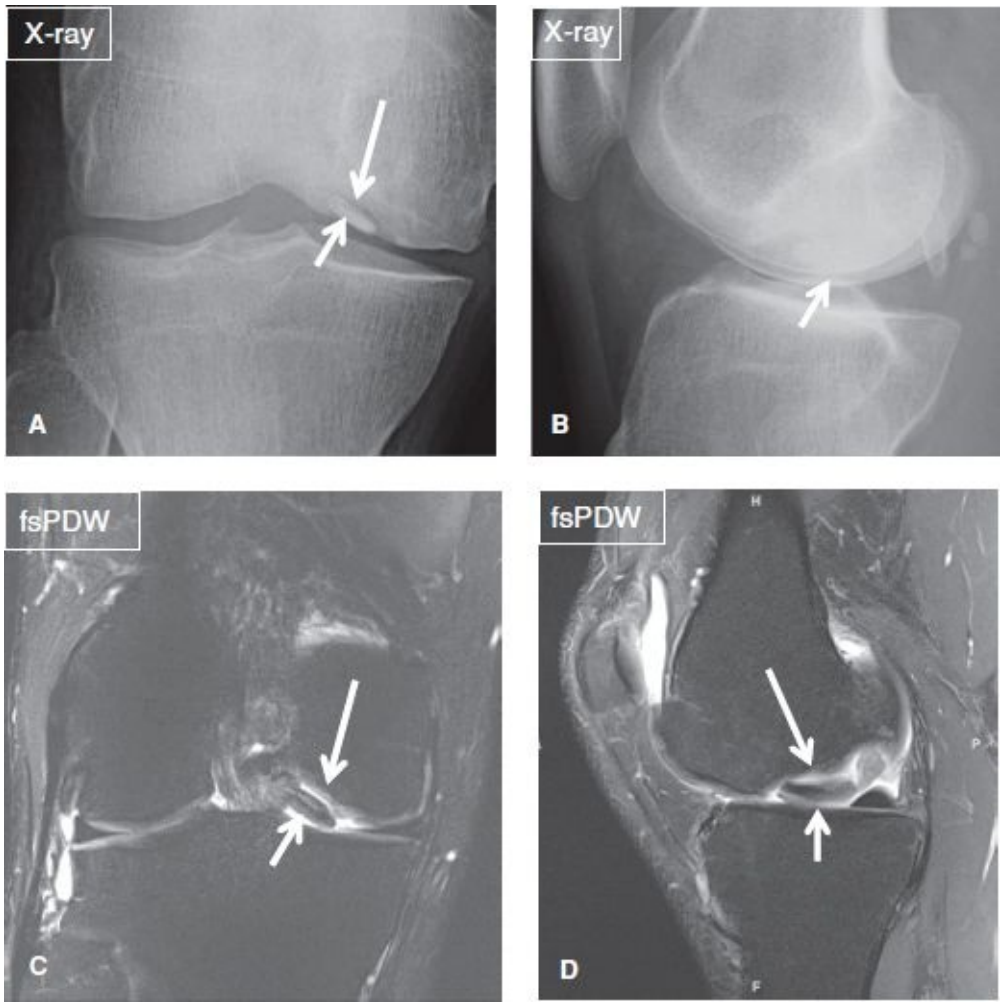

Fig. 27: Osteochondritis dissecans with in situ body. Anteroposterior **(A)** and lateral **(B)** radiographs reveal an osteochondral defect (*long arrows*) at the medial femoral condyle, with in situ osseous bodies (*short arrows*). The lesions are better appreciated on the respective coronal **(C)** and sagittal **(D)** MR images depicting the unstable lesion with overlying cartilage loss.

Fig. 28: Osteochondritis dissecans of the capitellum. Coronal images **(A, B)** demonstrate a crescentic subchondral lesion (*arrows*) in the capitellum, which is surrounded by marrow edema.

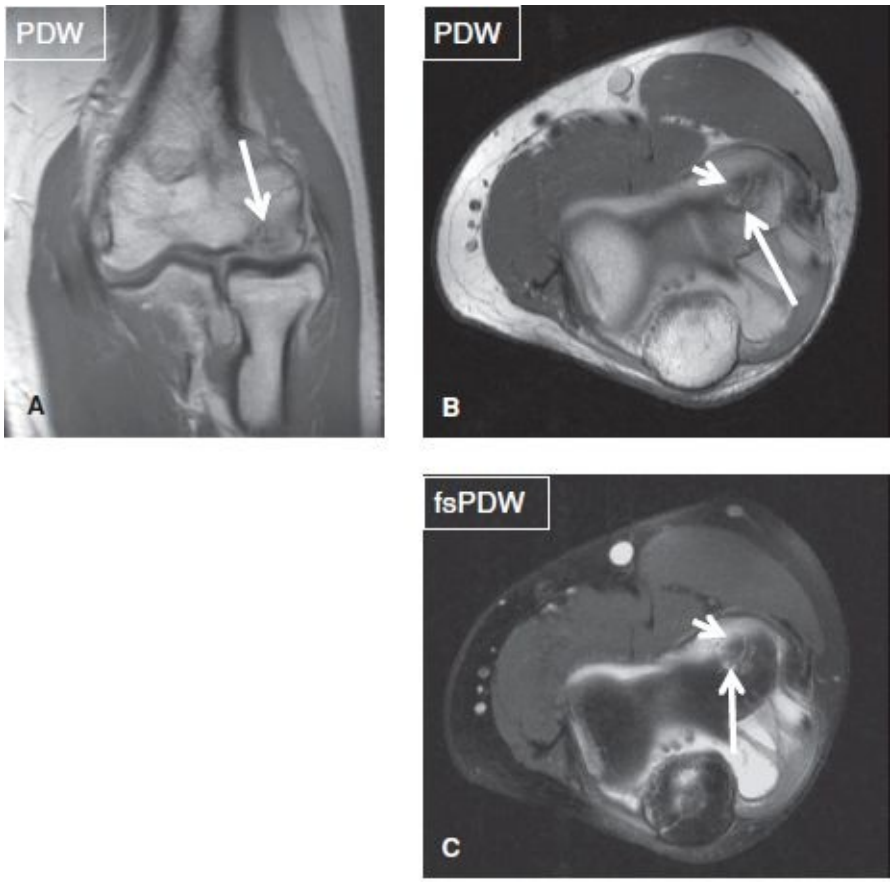

Fig. 29: Osteochondritis dissecans of the capitellum with in situ body. Coronal image **(A)** shows a crescentic subchondral lesion (*arrow*) in the capitellum. On the respective axial images **(B, C),** there is an osteochondral defect in the capitellum (*long arrows*), which is filled with an in situ osteochondral body (*short arrows*). The latter is surrounded by fluid, indicating an unstable lesion.

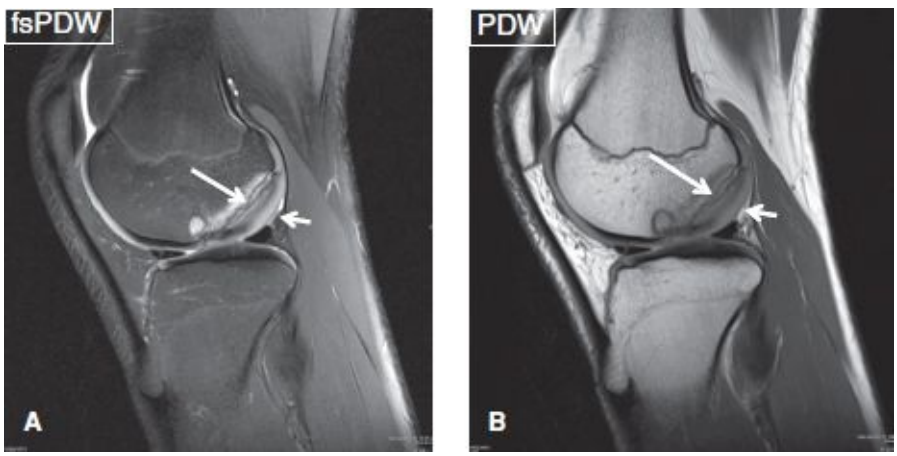

Fig. 30: Osteochondritis dissecans of the knee. Sagittal images **(A, B)** reveal thickened secondary physis (*long arrows*) with subchondral cysts at the posterior aspect of the lateral femoral condyle. The overlying cartilage (*short arrows*) is proud and chondromalacic.

PITFALLS IN CARTILAGE INTERPRETATION

Except in OCLs and OCDs, bone marrow edema and subchondral cysts may appear in various other entities such as trauma (contusions and fractures can evolve into cysts),

avulsive changes (in tendon or meniscal root attachments, usually associated with underlying enthesophyte formation), infection (intraosseous abscesses can mimic cysts), and neoplasms. Features assisting in differentiating cartilage-related cystic changes from the above entities include a bubbly or multiloculated appearance, communication with the articular surface or presence of a neck reaching the articular surface, epicenter located close to the articular surface, irregularity of overlying cartilage or bony endplate, and internal fat, which may be seen in larger cysts, and which reflects seepage of joint fluid around the normal marrow fat. In uncertain cases, contrast administration will reveal enhancement in the periphery of large cysts, mimicking synovial enhancement.

SURGICAL REPAIR TECHNIQUES FOR TREATMENT OF INJURED CARTILAGE

Given the limited primary self-healing ability of the articular cartilage, surgical procedures have been developed to repair cartilage defects. These can be prudently classified into repair, reconstruction, and regeneration techniques.

Repair techniques include debridement (smoothening the eroded surface), abrasion arthroplasty (erosion of few millimeters of subchondral bone, causing local bleeding and subsequent development of fibrocartilage-like cover on the defect), and microfracture (multiple perforations to the subchondral bone stimulating the migration of hematopoietic and mesenchymal stem cells to form the new tissue). Microfractures are effective in small injuries and small (<1–2 cm2) cartilage defects, which feature intact subchondral plate (Fig. 31). However, the result is fibrocartilage formation, which is not as strong as the hyaline cartilage in terms of shock-absorbing properties.

Reconstruction techniques include autologous osteochondral graft osteochondral autograft transfer system (OATS) procedure (graft received from a non–weight-bearing area of the intra-articular bone and transplanted into the cartilage injury defect) (Figs. 32–34), mosaicoplasty (multiple osteochondral autografts bundled like a coaxial cable or cigarette butt to cover a larger area), and synthetic grafts/osteochondral plugs (bioabsorbable devices to press fit into the gap). Regenerative techniques include one-step technique, juvenile (*de novo*) cartilage implantation (drilling a smooth crater at the OCL site and filling with juvenile cartilage cells covered with glue or periosteal patch on the top) (Figs. 35, 36) and two-step technique, autologous chondrocyte implant (ACL) (harvesting the host articular cartilage from a non–weight-bearing area of the knee, culturing chondrocytes in vitro, and reimplantation at the cartilage defect site, with coverage using periosteal patch or synthetic patch). These techniques can be used for lesions between 1 to 2 and 10 cm2. These techniques are being ever evolving and multiple clinical trials are being conducted to test their efficiency. From Asia, there have been case reports of uniform microfracturing of entire femoral condyles or other large areas with stem cell infusion treatments in the joint, that have shown promising early results (Figs. 37, 38).

Postoperative follow-up imaging of the repair cartilage is essential to determine the

extent of defect filling, the degree of peripheral integration with the host tissue, the morphologic structure and signal of the repair tissue, and the integrity of the host cartilage. Recommended at 3 to 6 months, the initial follow-up examination provides assessment of the volume and the integration of the repair tissue. Subsequent imaging in the first postoperative year enables evaluation of the maturation of the graft and identification of any complications. Initially proposed by Marlovits et al., who employed two-dimensional MR sequences, the Magnetic Observation of Cartilage Repair Tissue (MOCART) scoring system is the most widely used technique for monitoring the cartilage repair over serial intervals. The system is based on the analysis of the following nine variables: degree of repair filling, integration of the cartilage repair tissue to the border zone, structure of the surface, structure of the whole repair tissue, signal intensity of the repair tissue, constitution to the subchondral lamina, status of the subchondral bone, possible adhesions, and possible joint effusion. With the increasing clinical utility of high-field scanners and three-dimensional sequences, a modified MOCART score was proposed by Welsch et al. that includes 11 variables (Appendices 1 and 2). In general, bone marrow edema, and cartilage hyperintensity at the repair site should resolve by the first 12 months. Surface irregularity is commonly observed as a normal finding, and the margins of the repair site may normally remain visible for prolonged periods of time. Persistent bone marrow edema beyond 12 to 18 months post-repair, chondral osteophyte or extensive cyst formation, and cartilage delamination are poor prognostic indicators and suggest repair failure. Additional complications include arthrofibrosis and graft hypertrophy. The latter can lead to joint locking and may require debridement.

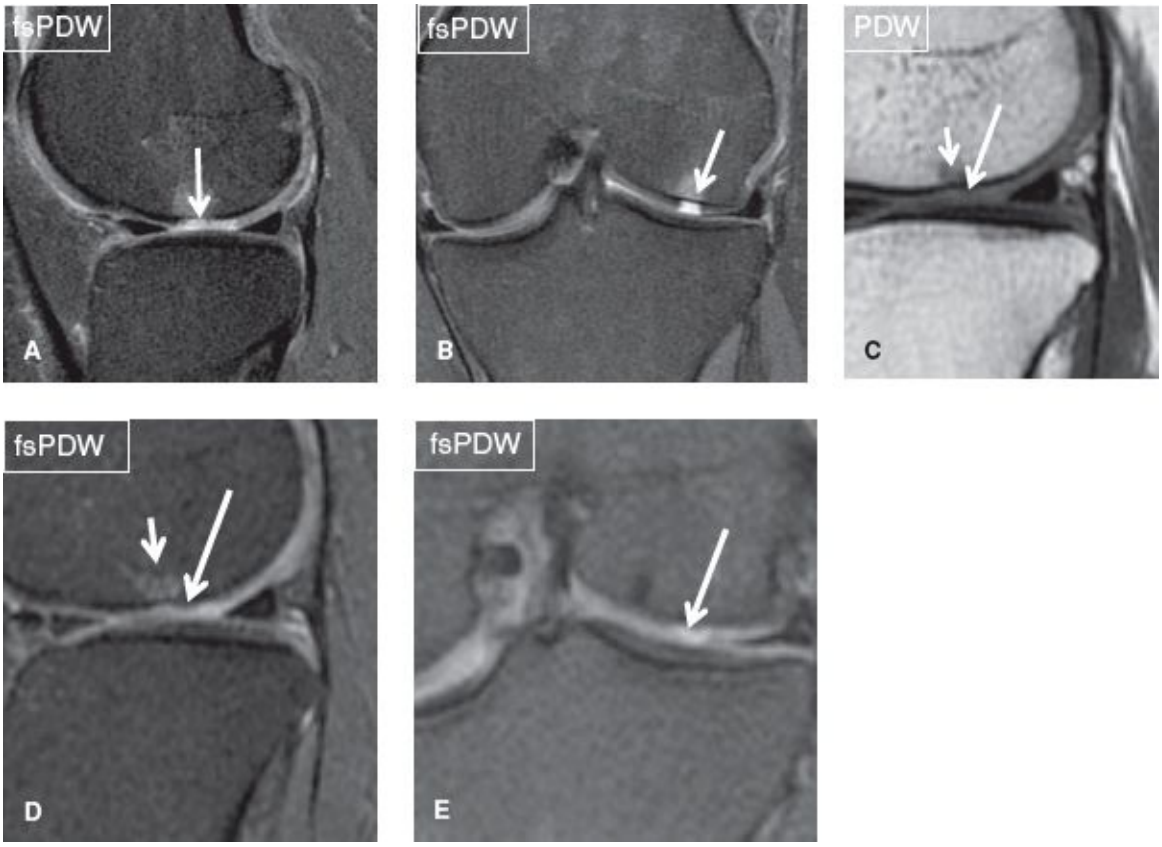

Fig. 31: Microfracture technique. Sagittal **(A)** and coronal **(B)** images reveal a large full-

thickness shouldered cartilage defect at the lateral femoral condyle. Sagittal **(C, D)** and coronal **(E)** images exhibit the postoperative result. Based on the MOCART scoring system, there is underfilling of the defect (*long arrows*), complete coverage of cartilage and bone interfaces, surface irregularity, and homogeneous hyperintensity of the repair tissue. The subchondral lamina is intact with the formation of small subchondral cyst (*short arrows*), and no evidence of joint effusion or chondral osteophyte formation.

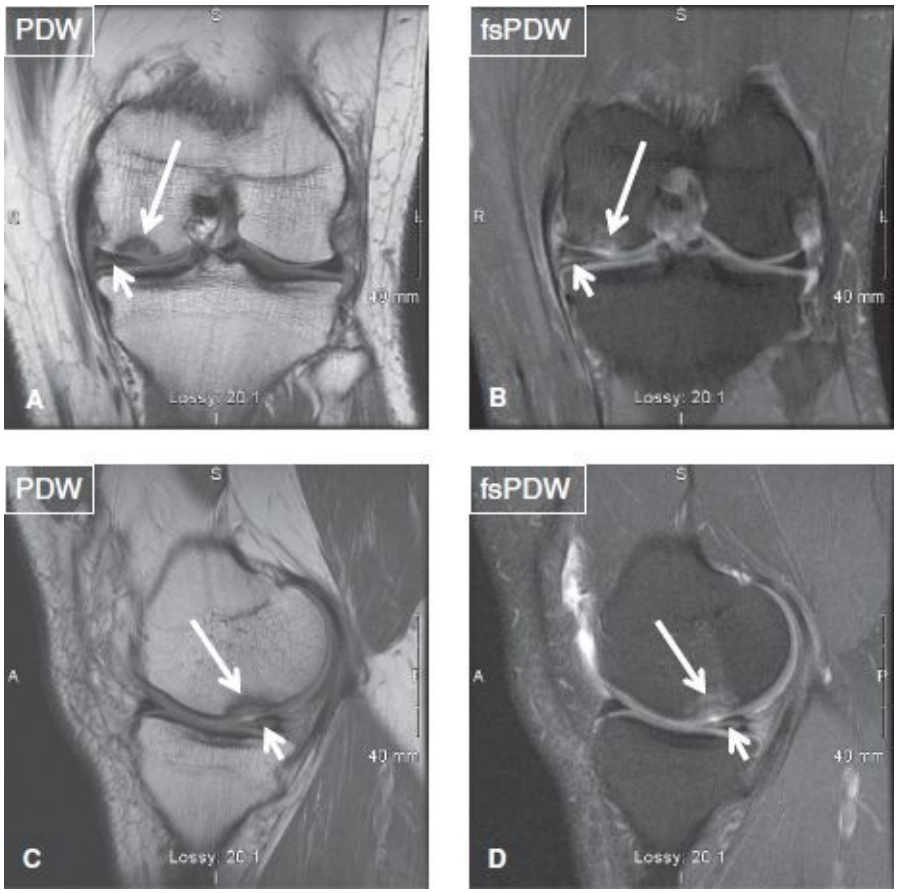

Fig. 32: Autologous osteochondral graft procedure. Coronal **(A, B)** and sagittal **(C, D)** images show a subchondral fracture (*long arrows*) of the medial femoral condyle, with minimal surrounding marrow edema and early cyst formation. Also note a horizontal tear (*short arrows*) of the medial meniscus. The patient underwent autologous osteochondral graft procedure. (Continued in Fig. 33.)

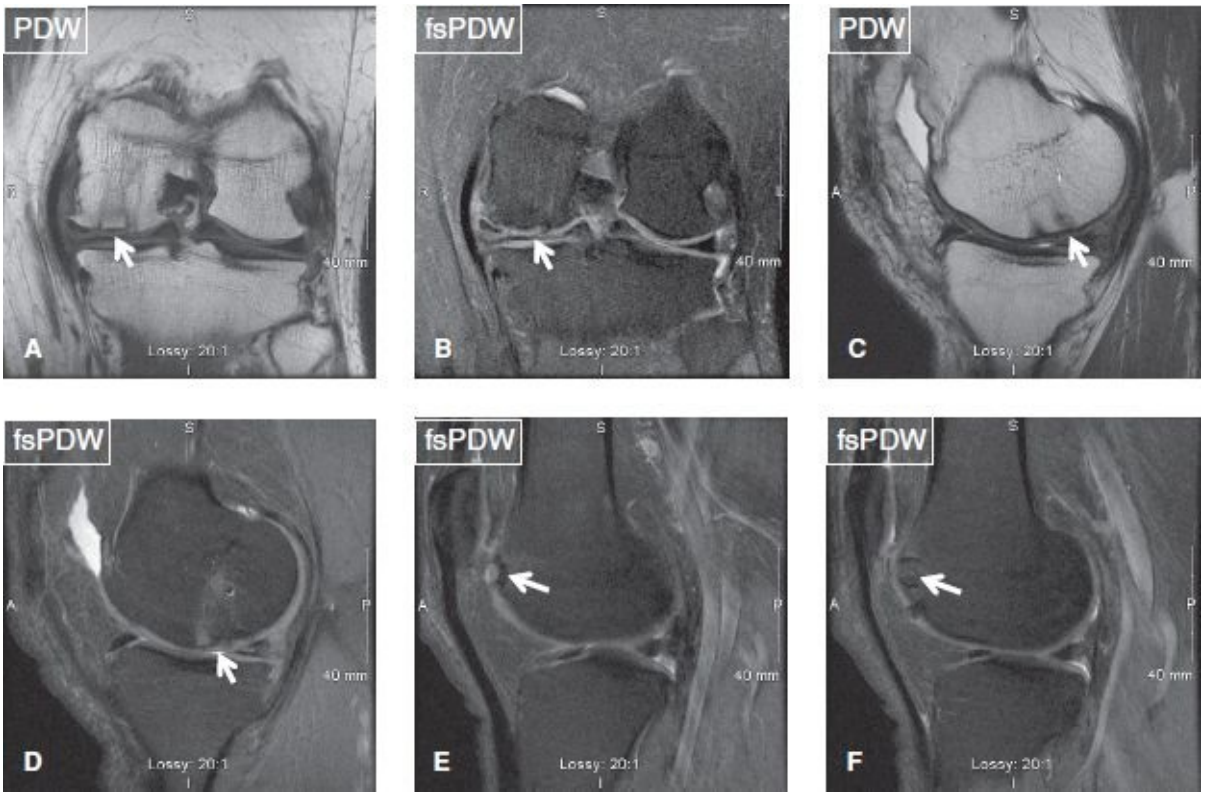

Fig. 33: Postoperative MR examination of the patient in Fig. 32 2 months after the procedure. On coronal **(A, B)** and sagittal **(C, D)** images, there is minimal underfilling (>50%) of the osteochondral defect, with the repair tissue (*arrows*) showing complete coverage of the bone interface, complete cartilage interface in the sagittal plane and incomplete (defect <50%) in the coronal plane, intact surface, and homogeneously normal signal. The subchondral lamina is intact, and there is minimal subchondral edema. Sagittal images **(E, F)** show the graft harvest site (*arrows*) at the trochlea. (Continued in Fig. 34.)

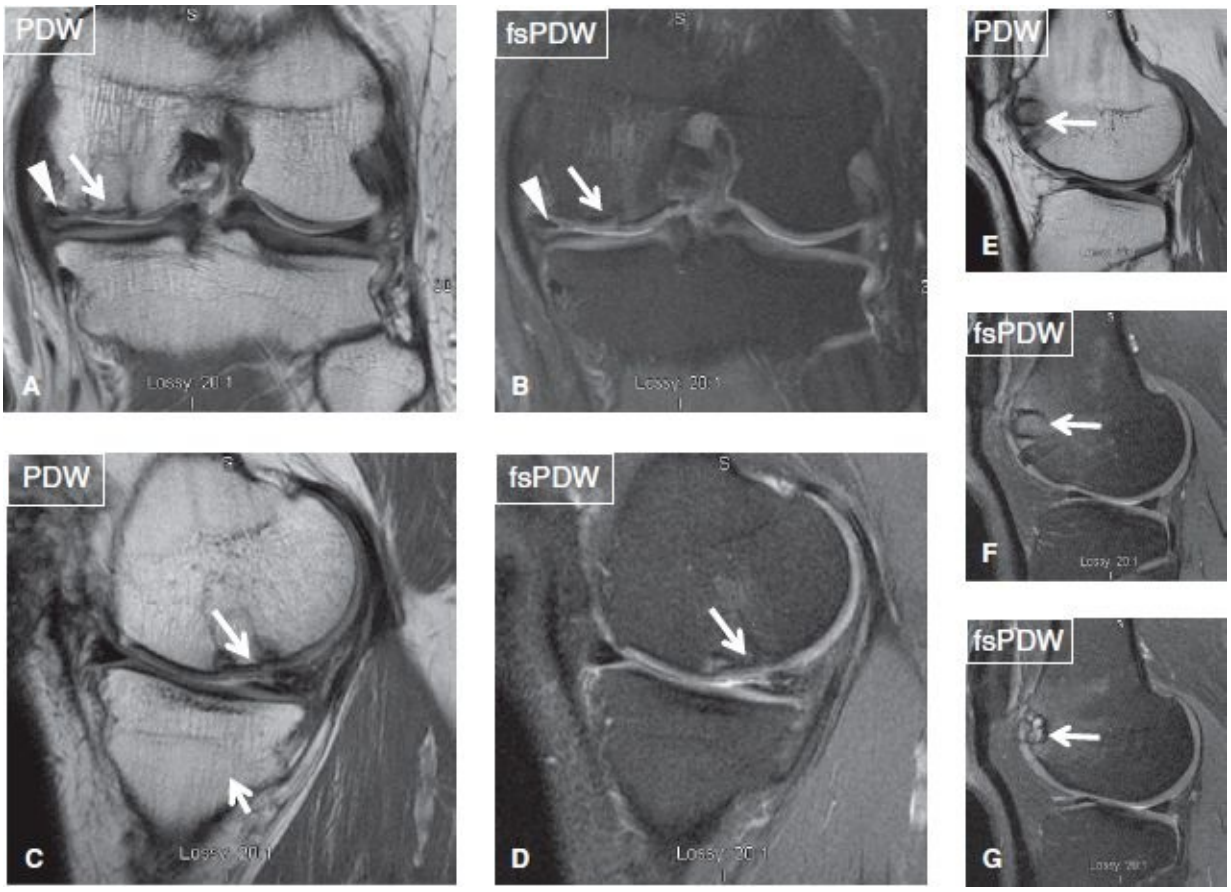

Fig. 34: Postoperative examination of the patient in Figs. 32 and 33 1 year after the procedure. Compared with the 2-month postoperative images, coronal **(A, B)** and sagittal **(C, D)** images now show repaired tissue that is flush with the adjacent cartilage and even less incomplete cartilage interface in the coronal, indicating maturation of the graft (*arrows*). Also note the postoperative configuration of the medial meniscus (*arrowheads*). **E–G:** Sagittal images demonstrate the graft harvest site (*arrows*), which underwent reconstitution by a combination of hyaline and fibrous cartilage. The formation of cystic changes and increasing edema (depicted in **G**) suggest deterioration due to stress changes from underlying uncorrected patellar malalignment.

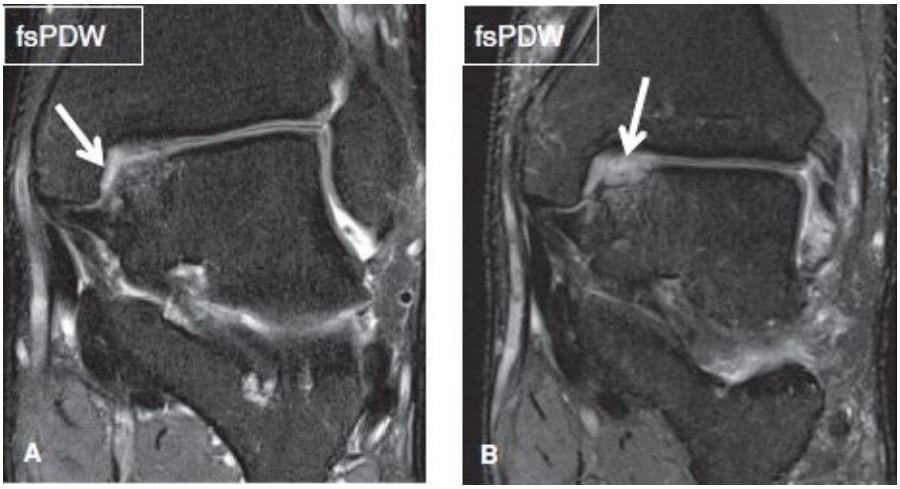

Fig. 35: Surgical repair of a talar cartilage lesion with *de novo* juvenile cartilage cell technique. Coronal images. **A:** A high-grade cartilage defect (*arrow*) is evident at the medial aspect of the talar dome with subjacent cysts and edema. **B:** Postoperative image after *de*

novo cartilage filling of the defect shows mild hypertrophy of the repair tissue, nearly flush with the native cartilage (*arrow*), which features complete bone and cartilage interfaces, intact surface and internal structure, as well as relatively homogeneous signal. The subchondral lamina is intact. A small area of marrow edema persists.

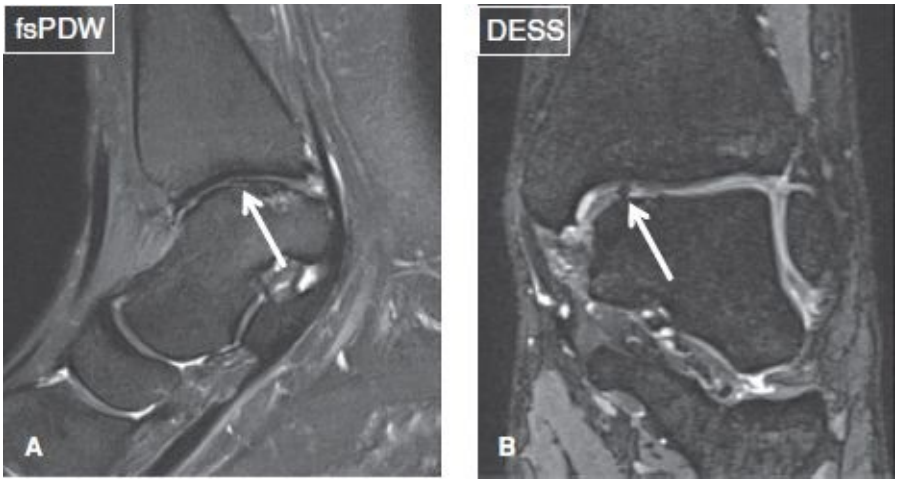

Fig. 36: Surgical repair of a talar cartilage lesion using juvenile cartilage cells. Postoperative sagittal **(A)** and coronal **(B)** 3D images show mild hypertrophy (<50%) of the repair tissue, which features incomplete bone and incomplete cartilage interfaces with a flap at the anterior and medial aspect of the lesion on the talar dome (*arrows*), irregular surface and heterogeneous internal structure, as well as relatively homogeneous signal. The subchondral lamina is intact. There is no marrow edema, joint effusion, or chondral osteophyte formation. Minimal residual subchondral cysts are seen at the posterior aspect of the lesion.

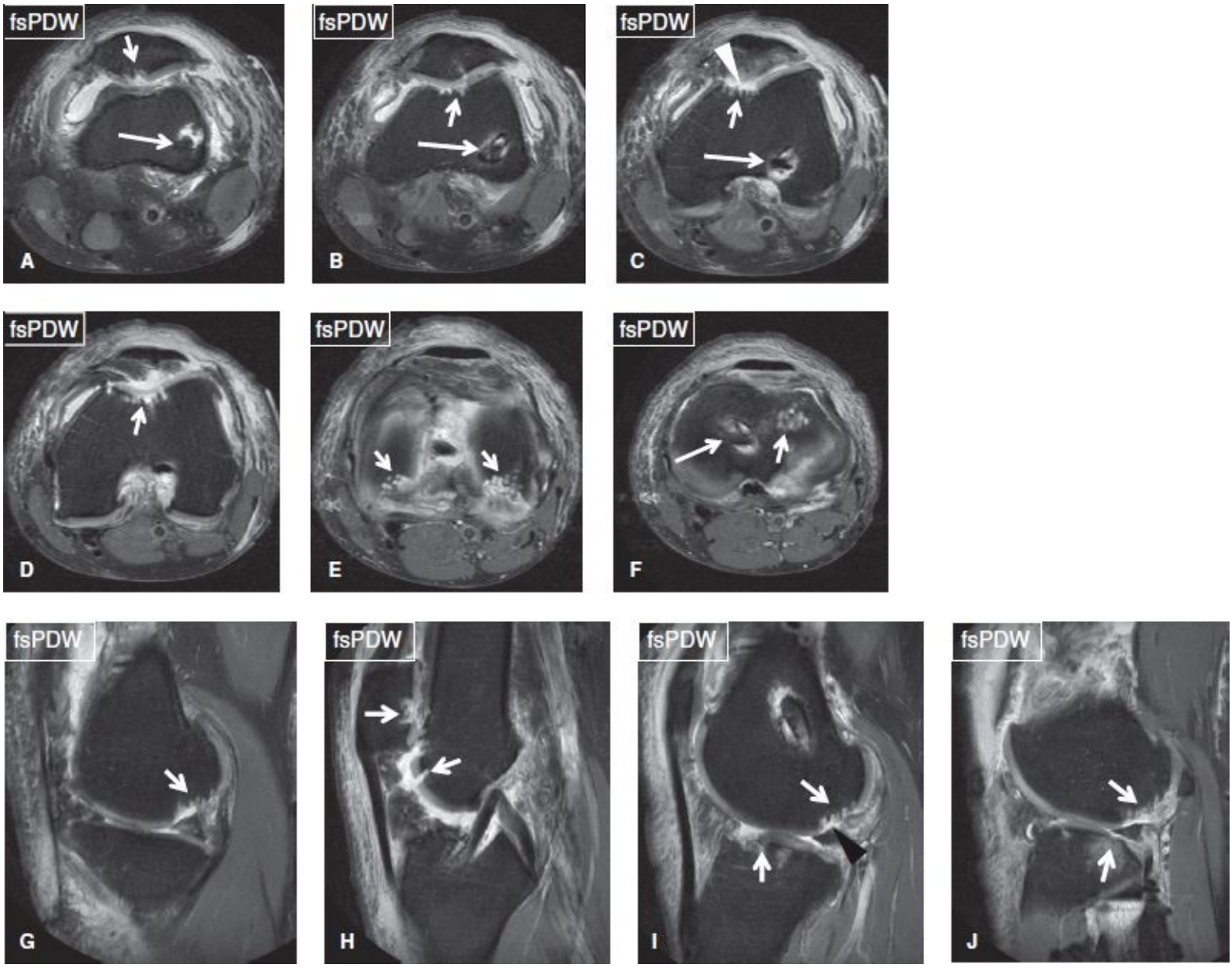

Fig. 37: Multisite drilling large area technique for cartilage repair. Sequential axial **(A–F)** and sagittal **(G–J)** images demonstrate multiple uniformly placed microfractures (*short arrows*) drilled in the subchondral bone at the patella, trochlea, femoral condyles, and lateral tibial plateau for the repair of overlying cartilage lesions (*arrowhead*). The surgery also included anterior cruciate ligament reconstruction (*long arrows*). Subsequently, peripheral stem cell harvest and weekly intra-articular injections of stem cells and Hyalgan followed for 6 weeks, along with physiotherapy and continuous passive motion on a daily basis. The results are shown in Fig. 38. (Case courtesy of Dr. Shahrin Merican, MD.)

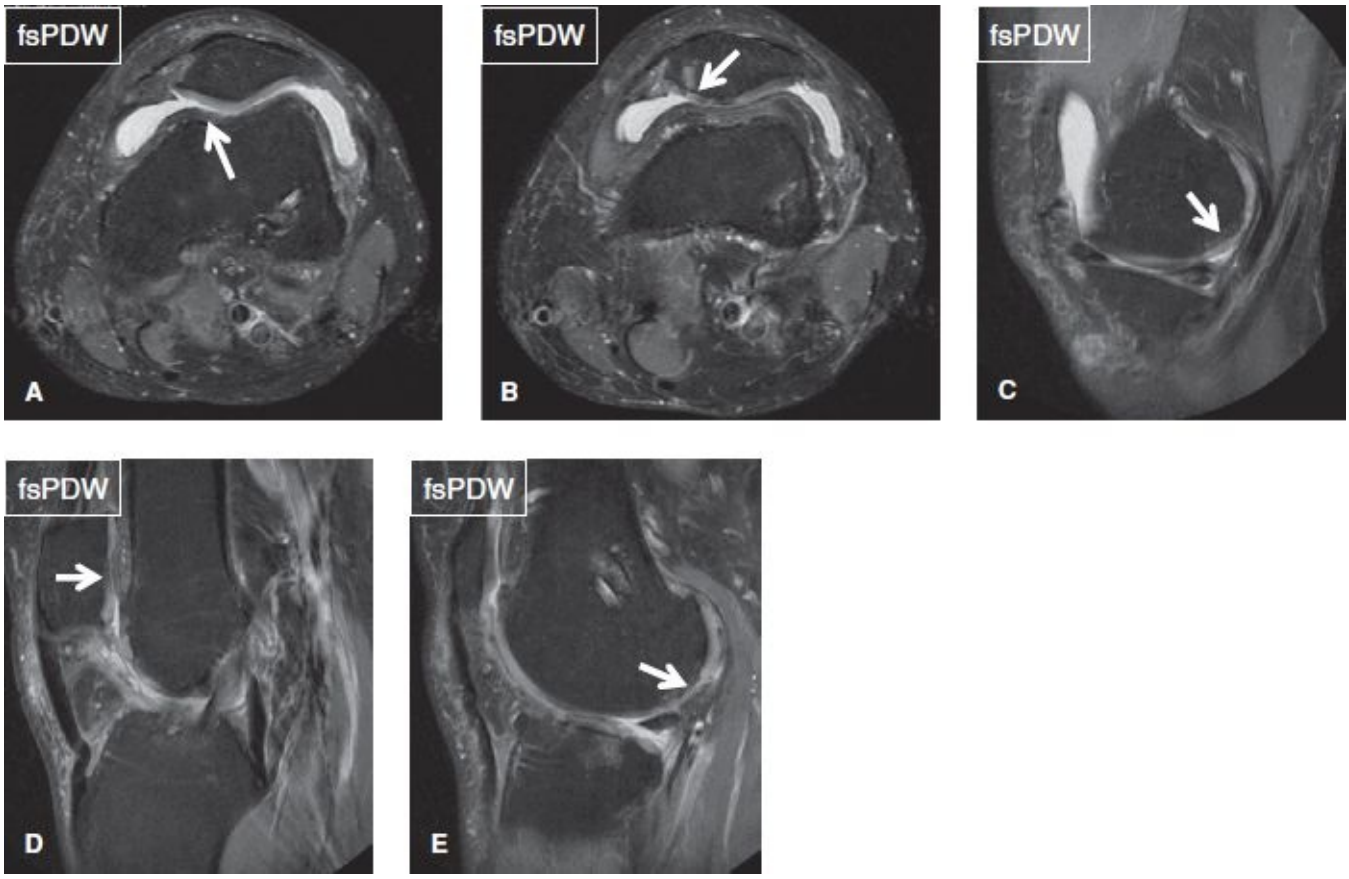

Fig. 38: Postoperative evaluation of the patient in Fig. 37 9 months after the surgery. *Arrows* in axial **(A, B)** and sagittal **(C–E)** images indicate the drilling sites. In all sites there is mild underfilling of the defects with cartilage, which features complete bone and cartilage interfaces, heterogeneous signal, and mild surface irregularity. The subchondral lamina is intact with small joint effusion and minimal marrow edema in the medial facet of the patella.

To conclude, descriptive terminology should be used in cartilage description. One should distinguish trauma-related shouldered defects from OA-related obtuse marginated lesions since the treatments are different. Finally, structured reporting, especially MOCART scoring system, should be used for postoperative cartilage repair tissue.

SUGGESTED READINGS

Alparslan L, Winalski CS, Boutin RD, et al. Postoperative magnetic resonance imaging of articular cartilage repair. *Semin Musculoskelet Radiol.* 2001;5(4):345–363.

Black BR, Chong le R, Potter HG. Cartilage imaging in sports medicine. *Sports Med Arthrosc.* 2009;17(1):68–80.

Choi JA, Gold GE. MR imaging of articular cartilage physiology. *Magn Reson Imaging Clin N Am.* 2011;19(2):249–282.

Choi YS, Potter HG, Chun TJ. MR imaging of cartilage repair in the knee and ankle. *Radiographics.* 2008;28(4):1043–1059.

Forney M, Subhas N, Donley B, et al. MR imaging of the articular cartilage of the knee and ankle. *Magn Reson Imaging Clin N Am.* 2011; 19(2):379–405.

Goodwin DW. MR imaging of the articular cartilage of the knee. *Semin Musculoskelet Radiol.* 2009;13(4):326–339.
Guermazi A, Hayashi D, Eckstein F, et al. Imaging of osteoarthritis. *Rheum Dis Clin North Am.* 2013;39(1):67–105.
Hayter C, Potter H. Magnetic resonance imaging of cartilage repair techniques. *J Knee Surg.* 2011; 24(4):225–240.
Ho-Fung VM, Jaramillo D. Cartilage imaging in children: Current indications, magnetic resonance imaging techniques, and imaging findings. *Radiol Clin North Am.* 2013;51(4):689–702.
Jazrawi LM, Alaia MJ, Chang G, et al. Advances in magnetic resonance imaging of articular cartilage. *J Am Acad Orthop Surg.* 2011;19(7):420–429.
Moktassi A, Popkin CA, White LM, et al. Imaging of osteochondritis dissecans. *Orthop Clin North Am.* 2012;43(2):201–211, v–vi.
Potter HG, Chong le R, Sneag DB. Magnetic resonance imaging of cartilage repair. *Sports Med Arthrosc.* 2008;16(4):236–245.
Potter HG, Foo LF. Magnetic resonance imaging of articular cartilage: Trauma, degeneration, and repair. *Am J Sports Med.* 2006;34(4):661–677.
Roemer FW, Crema MD, Trattnig S, et al. Advances in imaging of osteoarthritis and cartilage. *Radiology.* 2011;260(2):332–354.
Vasiliadis HS, Danielson B, Ljungberg M, et al. Autologous chondrocyte implantation in cartilage lesions of the knee: Long-term evaluation with magnetic resonance imaging and delayed gadolinium-enhanced magnetic resonance imaging technique. *Am J Sports Med.* 2010;38(5):943–949.

APPENDIX 1: The Structured Report: Modified MOCART

SITE: [<Femoral condyle> <Tibial plateau> <Patella>]

1. **DEFECT FILL (degree of defect repair and filling of the defect in relation to the adjacent cartilage):** [<Flush with the adjacent cartilage)> <Hypertrophy (proud as compared to the adjacent cartilage)> <Underfilling (below the level of the adjacent cartilage)>] Additional qualifier: [<Thickness less than 50% of the adjacent cartilage> <Thickness more than 50% of the adjacent cartilage>]

2. **CARTILAGE INTERFACE (integration with adjacent cartilage to border zone in two planes)**

• Sagittal (femur, patella, trochlea, tibia): [<Demarcating split-like border visible> <Complete> <Defect less than 50%> <Defect more than 50%>]

• Coronal (femur, tibia); axial (patella, trochlea): [<Demarcating split-like border visible> <Complete> <Defect less than 50%> <Defect more than 50%>]

Additional qualifier: Whole area of cartilage repair: [<Integration less than 50%> <Integration more than 50%>]

3. **BONE INTERFACE (integration of the transplant to the subchondral bone; integration of a possible periosteal flap):** [<Complete> <Partial delamination> <Complete delamination>]

Additional qualifier: Whole area of cartilage repair: [<Delamination less than 50%> <Delamination more than 50%>]

4. **SURFACE (constitution of the surface of the repair tissue):** [<Intact> <Less than 50% depth damage> <More than 50% depth damage> <Adhesions>]

Additional qualifier: Whole area of cartilage repair: [<Less than 50%> <More than 50%>]

5. **STRUCTURE (constitution of the repair tissue):** [<Homogeneous> <Inhomogeneous / Cleft formation>]

Additional qualifier: Whole area of cartilage repair: [<Less than 50%> <More than 50%>]

6. **SIGNAL INTENSITY (intensity of MR signal of the repair tissue in comparison to the adjacent cartilage: normal = identical to adjacent cartilage; nearly normal = slight areas of signal alterations; abnormal = large areas of signal alteration):** [<Nearly normal> <Normal> <Abnormal>]

7. **SUBCHONDRAL LAMINA (constitution of the subchondral lamina):** [<Intact> <Not intact>]

Additional qualifier: Whole area of cartilage repair: [<Less than 50%> <More than 50%>]

8. **CHONDRAL OSTEOPHYTES (osteophytes within the cartilage repair area):** [<Absent> <Osteophytes less than 50% of repair tissue> <Osteophytes more than 50% of repair tissue>]

9. **BONE MARROW EDEMA (maximum size and localization in relation to the cartilage repair tissue and other alterations assessed in the 3D MOCART score: small = less than 1 cm, medium = less than 2 cm, large = less than 4 cm):** [<Absent> <Small > <Medium > <Large > <Diffuse>]

10. **SUBCHONRAL BONE (constitution of the subchondral bone):** [<Intact> <Granulation tissue> <Cyst formation>]

Additional qualifier: Whole area of cartilage repair: [<Less than 50%> <More than 50%>]

11. **EFFUSION (approximate size of joint effusion visualized in all planes):** [<Absent> <Small> <Medium> <Large>]

Impression:

1. [< >]

APPENDIX 2: Sample Completed Structured Report: Modified MOCART: ABNORMAL/POSITIVE

SITE: Lateral femoral condyle—central weight-bearing portion

1. **DEFECT FILL (degree of defect repair and filling of the defect in relation to the adjacent cartilage):** [<Underfilling>]

Additional qualifier: [<Thickness more than 50% of the adjacent cartilage>]

2. **CARTILAGE INTERFACE (integration with adjacent cartilage to border zone in two planes)**

• Sagittal: [<Demarcating split-like border visible and the defect is less than 50%>]

• Coronal: [<Complete>]

Additional qualifier: Whole area of cartilage repair: [<Integration more than 50%>]

3. **BONE INTERFACE (integration of the transplant to the subchondral bone; integration of a possible periosteal flap):** [<Complete>]

4. **SURFACE (constitution of the surface of the repair tissue):** [<Intact>]

5. **STRUCTURE (constitution of the repair tissue):** [<Homogeneous>]

6. **SIGNAL INTENSITY (intensity of MR signal of the repair tissue in comparison to the adjacent cartilage:** [<Nearly normal = slight areas of signal alterations>]

7. **SUBCHONDRAL LAMINA (constitution of the subchondral lamina):** [<Intact>]

8. **CHONDRAL OSTEOPHYTES (osteophytes within the cartilage repair area):** [<Absent>]

9. **BONE MARROW EDEMA (maximum size and localization in relation to the cartilage repair tissue and other alterations assessed in the 3D MOCART score: small = less than 1 cm, medium = less than 2 cm, large = less than 4 cm):** [<Small>]

10. **SUBCHONRAL BONE (constitution of the subchondral bone):** [<Intact>]

11. **EFFUSION (approximate size of joint effusion visualized in all planes):** [<Small>]

Impression:

1. Status post OATS procedure lateral femoral condyle, satisfactory result with mild underfilling. No subchondral exposure or delamination.

2. Small joint effusion.

6

The Shoulder

Avneesh Chhabra, Sahar Jalali Farahani, and Theodoros Soldatos

The shoulder is a complex ball-and-socket articulation, which involves synchronized motion among four joints, the glenohumeral (GH) joint, acromioclavicular (AC) joint, sternoclavicular joint, and the scapulothoracic joint. Abnormalities of one joint may secondarily affect the other joints. The structured reporting includes the GH and AC joints, since the other two joints are only partially included within the imaging field of view.

The humerus is formed from three ossification centers, which are located at the head, lesser, and greater tuberosities. These ossifications centers appear before the age of 5 years and fuse by the age of 18 to 19 years. The glenoid articular surface is concave, and its overlying cartilage is relatively thinner in the center and thicker in the periphery. The average glenoid version is 1 to 2 degrees anteversion. The hemispheric humeral head is covered by cartilage, which is thicker in the middle and thinner at the periphery and superior aspect of the humeral head. The humerus neck-shaft angle is approximately 131 degrees (120–140 degrees). Since the glenoid cup is much smaller than the humeral head, joint stability is maintained (a) by the labroligamentous complex, which acts as passive restraint and increases the glenoid surface (b) the rotator cuff (RC), which acts as a dynamic restraint.

This chapter discusses the imaging evaluation approach and describes how to fill in the structured checklist in Box 1. Conceptual details of related MR physics and imaging protocol are discussed in the chapter on MR protocol optimization.

IMAGE EVALUATION

The stepwise interpretation approach outlined below is only a practical guide, and all shoulder structures should be evaluated in multiple planes for optimal assessment. This will also help readers perceive which structures are best depicted/evaluated on which particular plane.

1. Line up the similar plane non–fat-saturated and fat-saturated images and synchronize them for tandem evaluation.
2. Start with the coronal images in order to evaluate the AC joint and

subacromial/subdeltoid (SASD) bursa abnormalities, superior humeral subluxation, low-set acromion (AC subluxation), or lateral downsloping of the acromion. From posterior to anterior, check the teres minor muscle, infraspinatus tendon (coursing obliquely upward inserting on the middle facet), junctional area of the infraspinatus and supraspinatus tendons (straightening up), and supraspinatus tendon (running horizontally inserting on the superior facet) for tendinosis, tears, and retraction. Subsequently, look at the long head of the biceps tendon (LHBT), biceps–labral anchor, and superior and inferior labrum. Next, evaluate the (anterior and posterior bands of the) inferior glenohumeral ligament (IGL), GH cartilage, and especially the superior humeral head and the subchondral bone for edema, cystic changes, and osteophytes. Coronal images are also suitable for discriminating and assessing the (conoid and trapezoid) bands of the coracoclavicular (CC) ligament in suspected AC joint sprains. Finally, look at the RC muscles for fatty replacement, edema-like signal, and atrophy.

3. On sagittal images, assess the acromion curvature and potential anterior downsloping. Correlate the tendon abnormalities on coronal images with sagittal images to estimate the anteroposterior extent (width) of tendon tears and distinguish among the involved tendons by using cross-referencing localizers. Note that about 15 mm proximal to the insertion on the greater tuberosity, the supraspinatus and infraspinatus tendons overlap, merge, and become inseparable. Sagittal images also provide adequate evaluation of the subscapularis tendon and the horizontal (intra-articular) portion of LHBT for tendinosis and integrity. Correlation of labral abnormalities with other planes is also possible although sagittal images are not considered primary for labral evaluation. The RC muscles can also be evaluated, along with occupancy ratios in the supraspinatus and infraspinatus fossae, though it should be remembered that in cases of full-thickness tendon tears with retraction, the latter fossae will appear empty, despite the muscle bulk being normal. Therefore, it is imperative to evaluate the RC muscles on the coronal view. Finally, this plane is ideal for the assessment of the subcoracoid fat, rotator interval, and coracohumeral ligament (CHL).
4. Axial (short axis) images are essential for the evaluation of the subscapularis tendon, LHBT, superior glenohumeral ligament (SGL), middle glenohumeral ligament (MGL), anterior and posterior labrum, and the detection of (anterior or posterior) humeral decentring/subluxation. They are also useful for the detection of os acromiale and tears of the anterior-most supraspinatus tendon. The axial plane is the most useful for the evaluation of central shoulder cartilage, glenoid retroversion, glenoid bone stock for potential shoulder replacement cases, glenoid remodeling in overhead throwers (posterosuperior and superior), and glenoid dysplasia (posteroinferior and posterior portions). Other incidental abnormalities which may also be detected include lung lesions, axillary lymph nodes, and scapulothoracic bursitis.

BOX 1: The Structured Report: Shoulder

The checklist for structured reporting of MR imaging of the shoulder. For each field, *Normal* is considered default in the dictation, whereas the rest of the elements describe various pathologies that could be encountered during imaging evaluation. See Appendices 1 and 2 at the end of the chapter for sample completed reports for normal and abnormal exam results.

EXAM: **MRI OF SHOULDER**

FINDINGS:

Alignment: [<Normal> <Anterior / Posterior / Superior glenohumeral subluxation>]

Fluid:

Subacromial/subdeltoid bursa: [<Normal> <Mild bursitis> <Moderate or large bursitis> <Partial bursal rupture>]

Glenohumeral: [<Normal> <Small effusion> <Moderate effusion> <Large effusion> <Cartilaginous or osteochondral bodies> <Synovial hypertrophy>]

Long head of biceps brachii tendon: [<Normal> <Small fluid> <Tenosynovitis> <Cartilaginous or osteochondral bodies>]

Acromial arch:

Shape: [<Flat / Curved / Hooked / Convex> <Low-set acromion>]

Subacromial spur: [<Absent / Present> <Keel / Heel / Traction / Bird beak spur>]

Lateral / anterior downsloping: [<Absent / Present>]

Acromioclavicular joint: [<Normal> <Osteoarthrosis> <Sprain>]

Rotator cuff:

Supraspinatus: [<Normal> <Mild / Moderate / Severe tendinosis> <Bursal / Articular-sided fraying> <Tear> <Retraction> <Muscle atrophy>]

Infraspinatus: [<Normal> <Mild / Moderate / Severe tendinosis> <Bursal /

Articular-sided fraying> <Tear> <Retraction> <Muscle atrophy>]

Subscapularis: [<Normal> <Mild / Moderate / Severe tendinosis> <Tear> <Retraction> <Muscle atrophy>]

Rotator interval and long head of biceps brachii tendon:

Rotator interval: [<Normal> <Synovial thickening> <Acute sprain>]

Biceps–labral anchor: [<Intact> <Tear>]

Horizontal portion: [<Normal> <Mild / Moderate / Severe tendinosis> <Tear>]

Vertical portion: [<Normal> <tendinosis> <Tear>]

Genu: [<Normal> <Mild / Moderate / Severe tendinosis> <Tear> <Subluxed>]

Glenohumeral joint:

Labrum: [<Normal> <Degenerative fraying> <Tear> <Paralabral cyst>]

Glenohumeral ligaments: [<Normal> <Thickening / Acute sprain of ligament>]

Glenohumeral cartilage: [<Normal>]

Bones: [<Normal> <Greater tuberosity / Lesser tuberosity cysts> <Enthesopathy>]

Muscles: [<Otherwise normal>]

Vessels: [<Normal>]

Nerves: [<Normal>]

Other:

IMPRESSION:

[<In the order of importance with acute findings first>]

HOW TO FILL THE STRUCTURED REPORT

ALIGNMENT: [<Normal> <Anterior / Posterior / Superior glenohumeral subluxation>]

The evaluation of bony alignment is best performed on non–fat-suppressed images. Normal alignment means bony articulation congruency at the AC and GH joints, as well as an

acromiohumeral distance of greater than 9 mm. In RC pathology (tendinosis/tears), there is often posterior, superior, or posterosuperior decentering (aka ascent or subluxation) of the humerus with narrowing (<8 mm) of the acromiohumeral distance (Fig. 1). Less commonly, there is anterior or inferior humeral subluxation. Instability is clinically tested using anterior or posterior apprehension tests for anterior and posterior instability, respectively. Constituted by the acromion posteriorly, and the coracoid process and coracoacromial ligament anteriorly, the coracoacromial arch contains the SASD bursa, supraspinatus muscle and tendon, and LHBT. It is best evaluated on coronal and sagittal images. The coracoacromial ligament has two bundles (anterolateral and posteromedial) and prevents anterosuperior translation of the humeral head in the setting of rotator interval and/or RC injuries. At the AC joint, a low-set (inferiorly subluxed) acromion may be present, indicating prior injuries to the AC capsule, inferior, and/or superior AC ligaments (Fig. 2). Thickening, attenuation, or deficiency of one or both of these ligaments should be reported. A common pattern observed in weight lifters and overhead throwers includes low-set acromion, deficient or attenuated inferior AC ligament and thickened superior AC ligament.

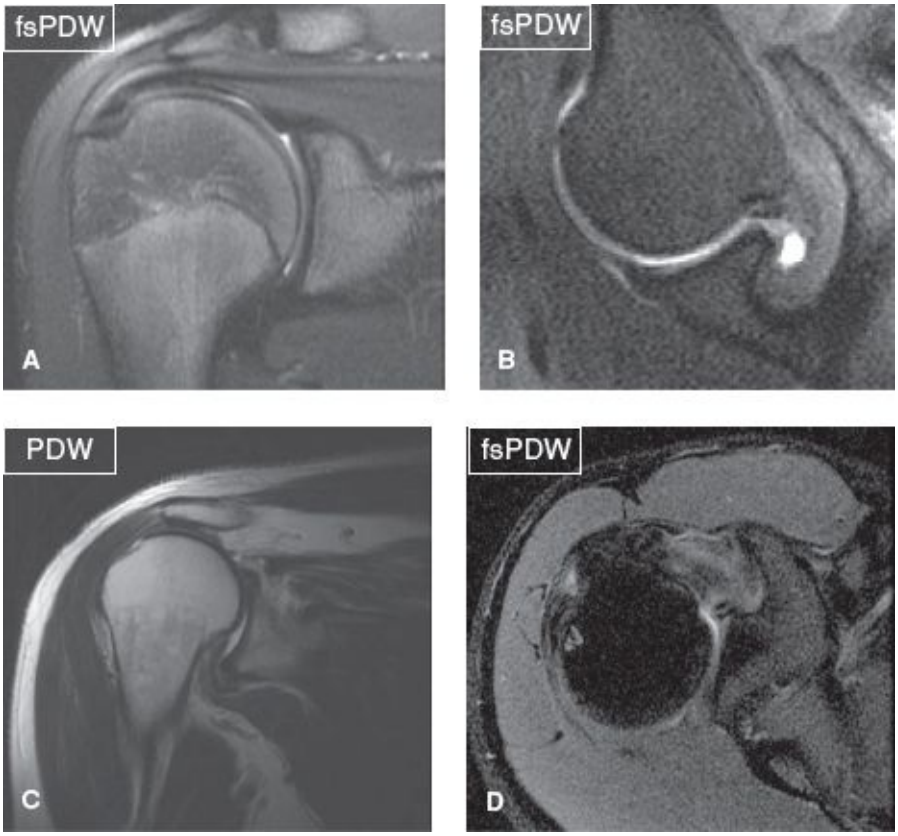

Fig. 1: Normal and abnormal alignment. Coronal image **(A)** and axial image in abduction and external rotation (ABER) **(B)** demonstrate normal anatomic relationship between the humeral head and the glenoid. Coronal **(C)** and axial **(D)** images show superior and posterior humeral subluxation, respectively.

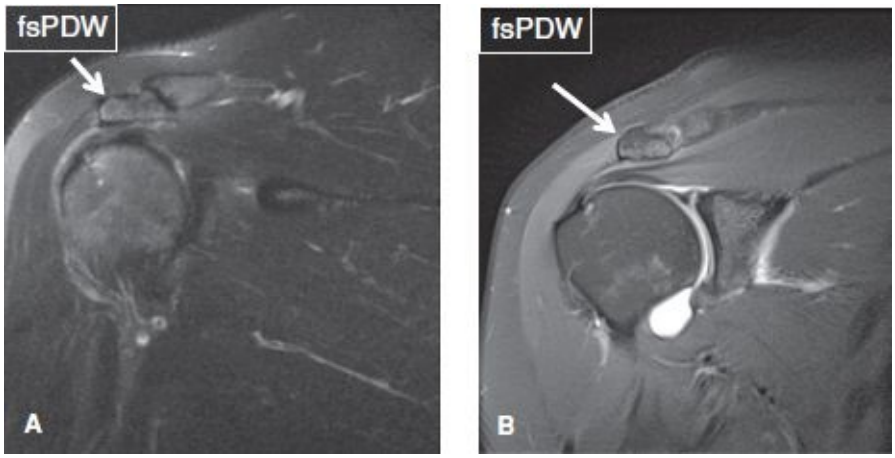

Fig. 2: Low-set acromion. On coronal images **(A, B)**, the acromion (*arrows*) is parallel to but lower in position with respect to the clavicle. Notice the thickened superior AC ligament in **(B)** and attenuated inferior AC ligament in both images.

FLUID:

Subacromial/subdeltoid bursa: [<Normal> <Mild bursitis> <Moderate or Large bursitis> <Partial bursal rupture>]

Glenohumeral joint: [<Normal> <Small effusion> <Moderate effusion> <Large effusion> <Cartilaginous or osteochondral bodies> <Synovial hypertrophy>]

Long head of biceps brachii tendon: [<Normal> <Small fluid> <Tenosynovitis> <Cartilaginous or osteochondral bodies>]

The normal SASD bursa lies under the acromion and deltoid muscle, extends up to the level of the humeral metaphysis level, is normally less than 2 mm thick, and shows minimal T2 hyperintense signal. Any fluid layer equal or greater than 2 mm in thickness indicates mild bursal distention, which could be related to full-thickness RC tear, partial bursal-sided tear, injury, or inflammatory/infectious bursitis. Although there are no defined rules, mild bursitis refers to fluid reaching laterally to the level of the acromion, mild to moderate bursitis refers to fluid underneath the acromion and deltoid muscle belly, whereas moderate refers to significant distention of the bursa at both places (Fig. 3). Severe bursal distention is uncommon and is usually due to long-standing inflammatory conditions, such as rheumatoid arthritis or chronic massive RC tears. In addition, one should look for internal synovial thickening (indicating chronic bursitis); adjacent fascial, muscle, or bone marrow edema (may indicate infection); calcific hypointense debris (calcium hydroxyapatite deposition); rice bodies (rheumatoid arthritis); and synovial chondromatosis (uniform in size and shape, numerous rounded bodies) (Figs. 4, 5). Finally, fascial fluid extending below the humeral metaphysis and medially under the acromion or around the RC muscles indicates recent partial bursal rupture and, in most cases, is related to recent trauma (fall) (Fig. 6). In subacute/chronic stages, these leaks can seal and form a synovial diverticulum (presenting as a unilocular fluid collection with a neck) or a ganglion cyst (presenting as a

multilocular fluid collection with/without a definite neck).

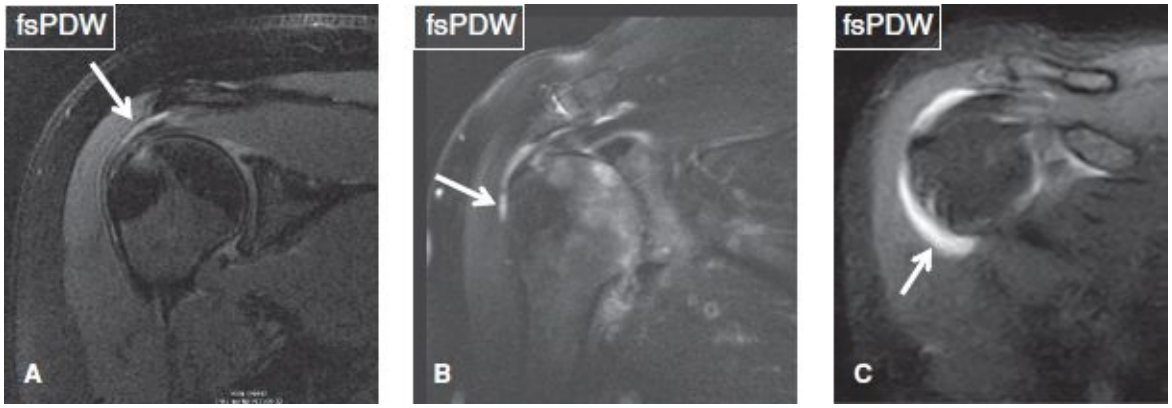

Fig. 3: Fluid within the subacromial/subdeltoid bursa (*arrows*). Coronal images. **A:** Small amount of fluid is evident within the bursa, in keeping with mild bursitis. **B:** The bursa contains fluid, which extends underneath the deltoid muscle, in keeping with mild to moderate bursitis. **C:** There is substantial fluid distention of the bursa, with fluid tracking underneath the deltoid muscle. This case is compatible with moderate bursitis.

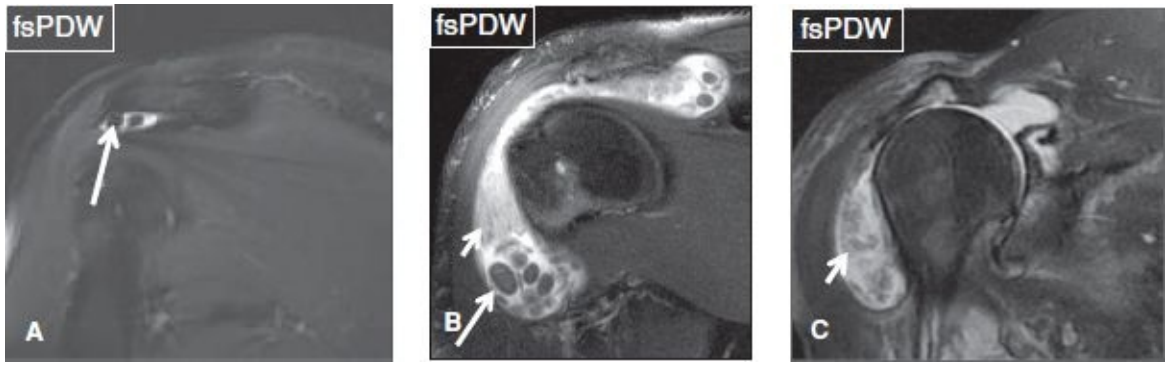

Fig. 4: Coronal images **(A–C)** demonstrate multiple bodies (*long arrows*) within the subacromial/subdeltoid bursa. In **(B)** and **(C),** large fluid distention and synovial thickening (*short arrows*) indicate a chronic inflammatory process.

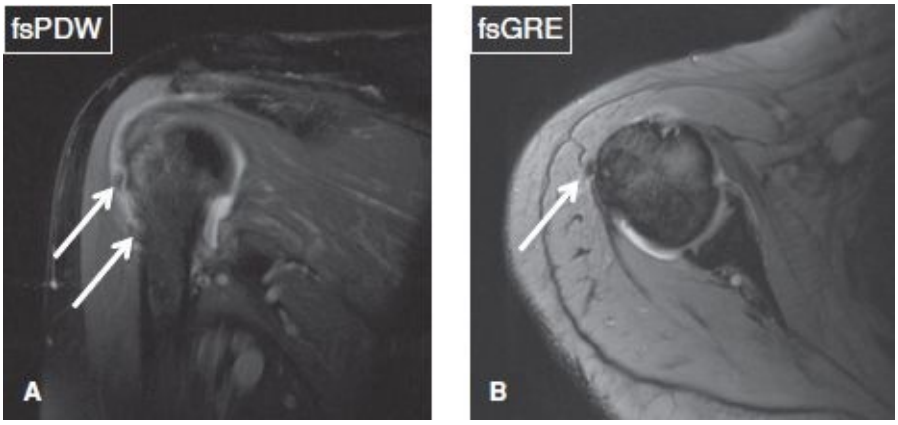

Fig. 5: Calcific subacromial/subdeltoid bursitis. Coronal **(A)** and axial **(B)** images demonstrate hypointense ovoid bodies (*arrows*) within the subacromial/subdeltoid bursa, which correspond to calcium hydroxyapatite deposition.

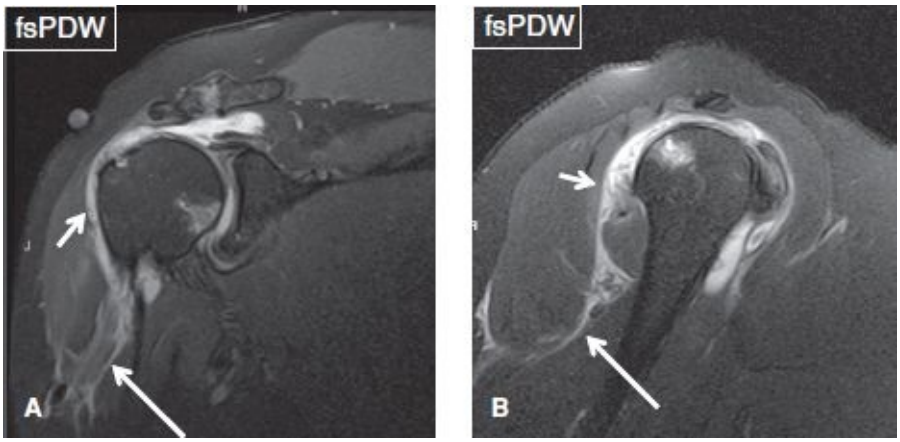

Fig. 6: Coronal **(A)** and sagittal **(B)** images demonstrate moderate fluid collection in the subacromial/subdeltoid bursa (*short arrows*), as well as an adjacent ill-defined fluid tracking below the humeral metaphysis (*long arrows*) and around the subscapularis muscle, indicating bursal rupture.

The GH joint normally contains minimal fluid, which does not significantly distend the capsule. It includes an anterosuperior subscapularis recess, an inferior (axillary) recess, and a posterior recess. Synovial thickening and loose bodies commonly develop and lodge in these recesses, respectively. The joint capsule communicates with the LHBT sheath and occasionally features a superior plica (Fig. 7). In cases of adhesive capsulitis (joint contraction), fluid normally and preferentially collects in the subscapularis recess and the LHBT sheath. Therefore, one should not overdiagnose biceps tenosynovitis in such cases. In small effusion, there is mild distention of the joint, predominantly involving the inferior dependent recess, whereas in moderate effusion there is distention of all recesses (Fig. 8). Similar to the SASD bursa, large distention occurs in inflammatory conditions such as rheumatoid arthritis, pigmented villonodular synovitis (PVNS), synovial osteochondromatosis, septic arthritis, or significant trauma. One should look for and report synovial thickening (indicating long-standing internal derangement), loose bodies, and/or blood clots (Figs. 8, 9). Hemarthrosis, depicted as T1 hyperintense joint effusion, may be related to recent trauma (look for associated local bony or soft tissue injury), hemophilia (look for associated enlargement of the humeral head and fluid–fluid levels), or vascular malformation. Finally, capsular injuries with fascial fluid (from trauma, humeral subluxation, or dislocation), synovial diverticulae, and ganglion may also be identified. Synovial diverticulae are particularly common following prior arthroscopy or surgical procedures, probably formed from pseudo-encapsulation of capsular leaks caused by fluid distention, which is required during these procedures. Best depicted on sagittal images, the subcoracoid bursa is a separate bursa, which is located anterior to the subscapularis muscle, and extends along the entire superoinferior extent of the latter, as opposed to the subscapularis recess, which occupies only the upper third of the subscapularis. The subcoracoid recess communicates with the SASD bursa; therefore, its distention can be used as indirect sign of full-thickness RC tear (Figs. 10–12).

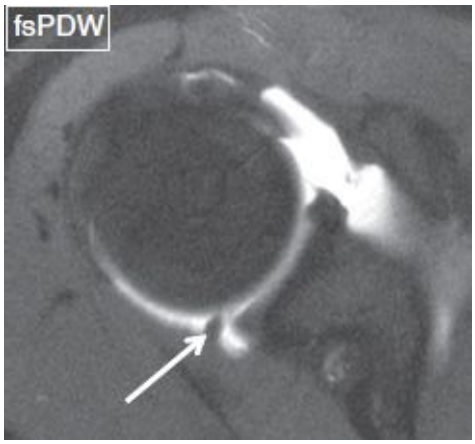

Fig. 7: Superior plica. Axial image reveals a thick plica (*arrow*) in the posterosuperior portion of the joint.

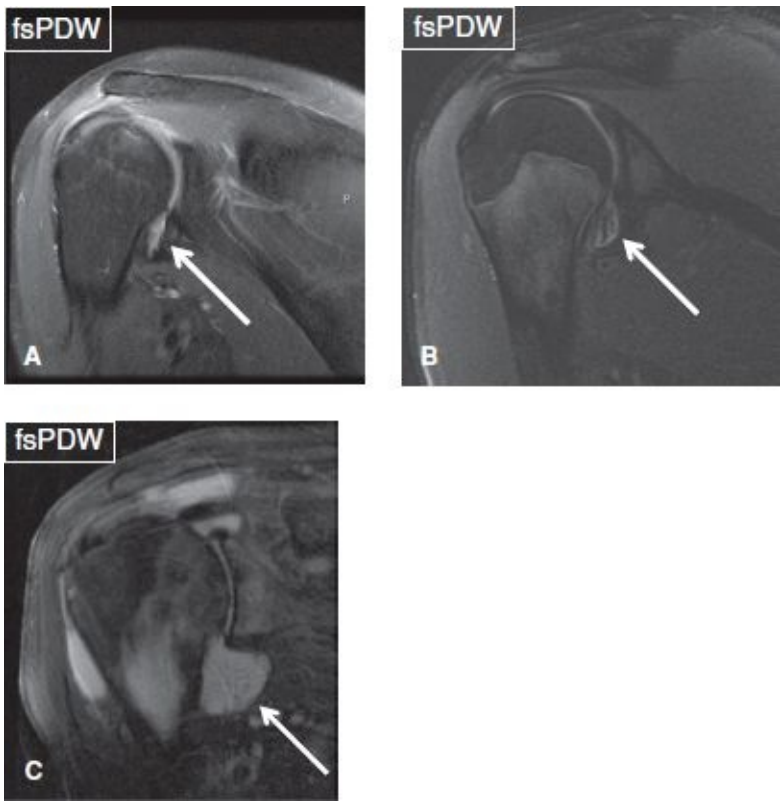

Fig. 8: Glenohumeral joint effusion. Coronal images show small **(A, B)** and moderate **(C)** glenohumeral joint effusions (*arrows*). In **(B)**, loose bodies are evident within the joint space.

Fig. 9: Synovial osteochondromatosis of the glenohumeral joint. Coronal images **(A–C)**

displaysevere osteoarthritis of the glenohumeral joint. In **(B)** and **(C),** ossified intra-articular loose bodies (*arrows*) reflect secondary osteochondromatosis.

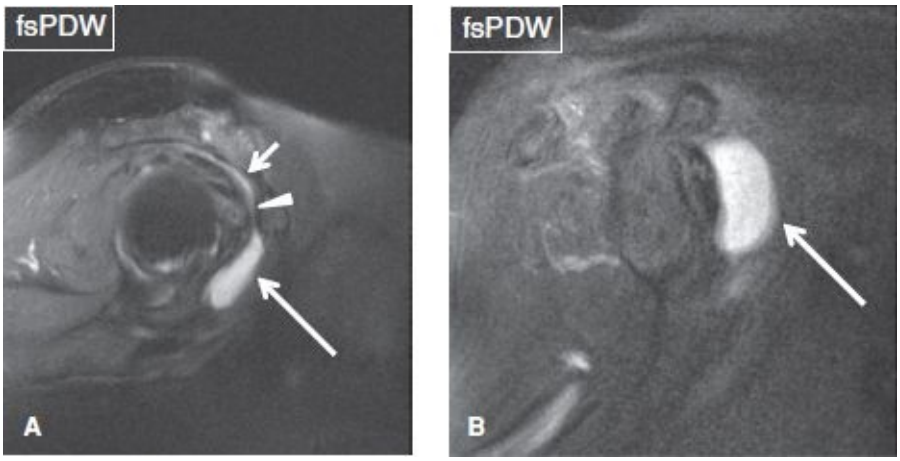

Fig. 10: **A:** Sagittal image exhibits mild subacromial/subdeltoid bursitis (*short arrow*) and concomitant moderate subcoracoid bursitis (*long arrow*). *Arrowhead* shows the communication between the two bursae. **B:** Sagittal image from another subject with moderate subcoracoid bursitis (*arrow*). Both subjects had full-thickness cuff tears (not shown).

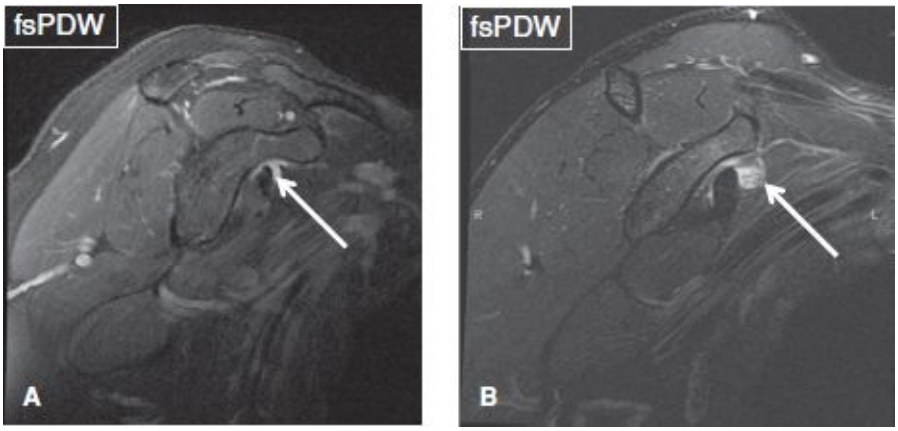

Fig. 11: Coronal images **(A, B)** demonstrate small fluid collection within the subscapularis recess (*arrows*). In **(B),** heterogeneous fluid content is due to synovial chondromatosis.

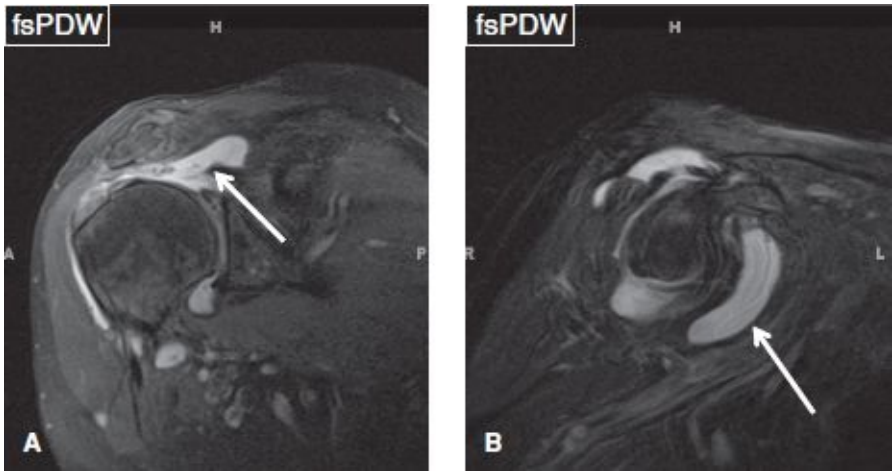

Fig. 12: Subcoracoid bursa distention in the setting of full-thickness rotator cuff tear. **A:**

Coronal image demonstrates full-thickness tears of the supraspinatus tendon, with proximal retraction (*arrow*). **B:** Corresponding sagittal image exhibits fluid distention of the subcoracoid bursa (*arrow*).

Because of its normal communication with the shoulder joint, the LHBT sheath normally contains trace amount of fluid. Tenosynovitis is established only if the fluid is circumferential around the tendon and if it is disproportionate with respect to the shoulder joint fluid. Circumferential fluid around the LHBT may also be seen in the setting of significant GH joint effusion (due to the aforementioned communication) or adhesive capsulitis (due to preferential pooling of fluid, related to thickened and contracted capsule). In the latter cases, coexisting tenosynovitis cannot be excluded, but the possibilities become higher if there is LHBT sheath synovial thickening, LHBT tear, or tendinosis. Similar to other synovial spaces, synovial leaks can occur with acute trauma (usually weight lifting injuries), whereas in subacute/chronic stages, diverticula and ganglion can arise from the tendon sheath (Figs. 13–15). It is important not to confuse in-plane flow phenomenon in the circumflex humeral vein (branching structure) with synovial diverticulum of the biceps tendon sheath.

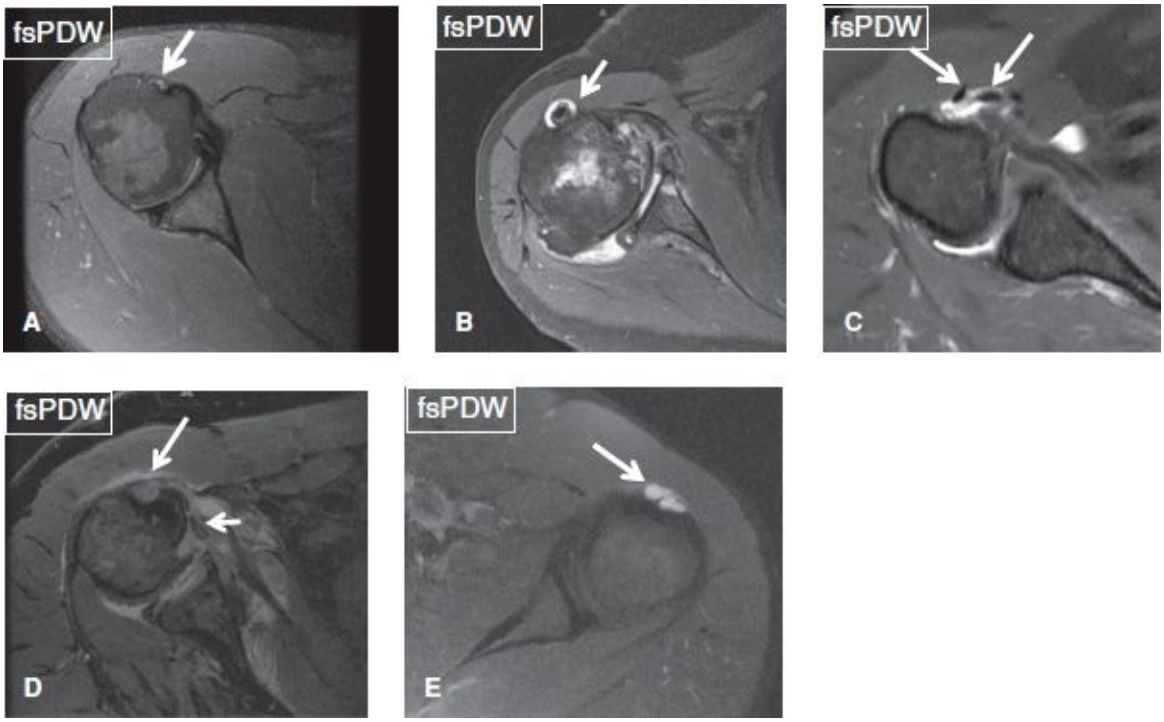

Fig. 13: Normal and abnormal long head of the biceps brachii tendon. Axial images. **A:** Normal long head of the biceps brachii tendon (*arrow*), located within the bicipital sulcus and surrounded by trace amount of fluid. **B:** Small amount of fluid (*arrow*) surrounds the tendon with synovial thickening, in the setting of shoulder effusion. **C:** Moderate amount of fluid surrounds the tendon, which is congenitally bifid (*arrows*). **D:** Rupture of the tendon sheath with fluid extravasation (*long arrow*) and medial tendon dislocation (*short arrow*). **E:** Synovial diverticulum of the tendon sheath (*arrow*).

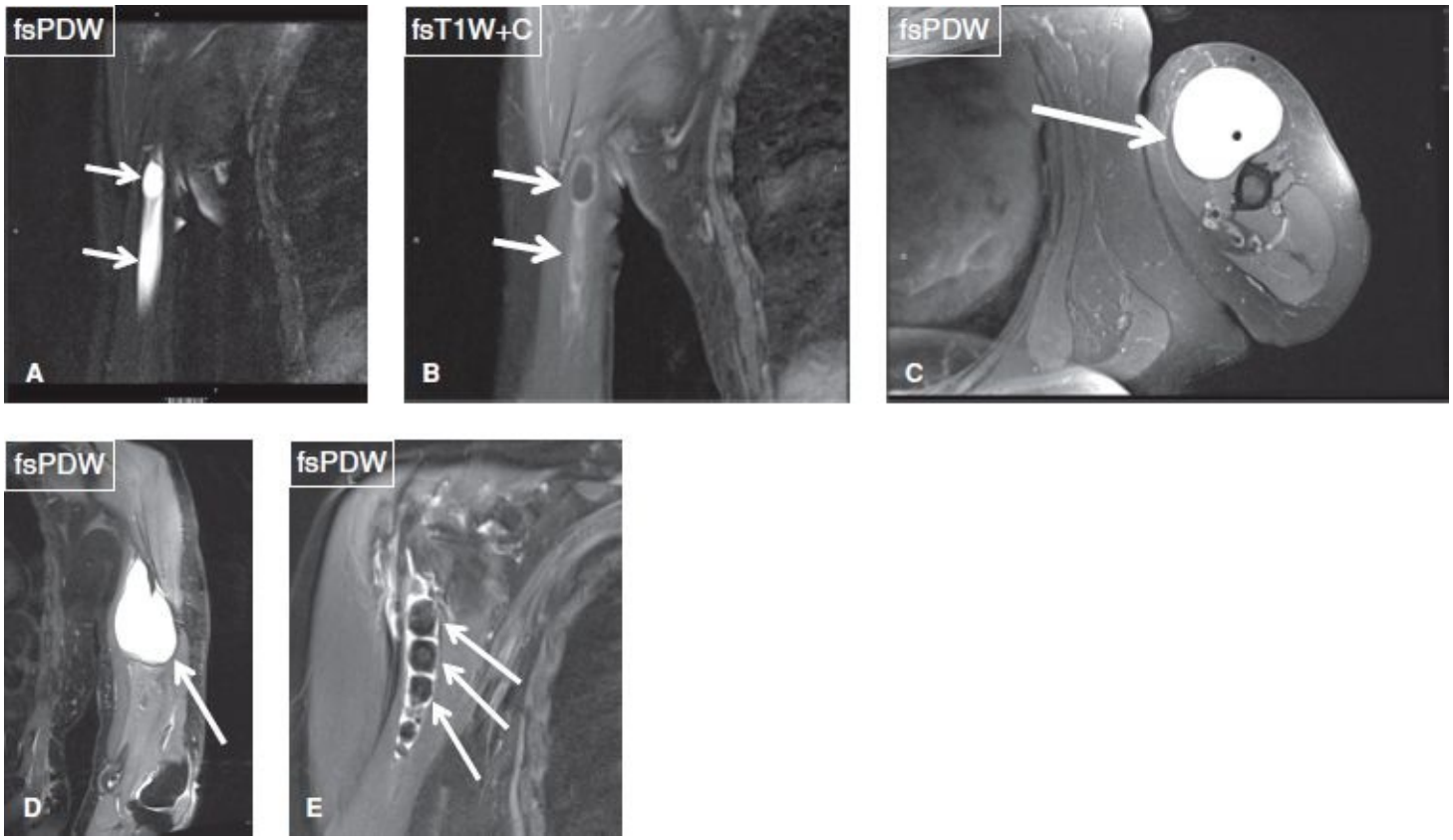

Fig. 14: Abnormalities of the long head of the biceps brachii tendon sheath. **A, B:** Coronal images exhibit ganglion from the biceps tendon sheath (*arrows*). Notice peripheral enhancement on contrast in **(B),** which excludes the possibility of tumor. **C, D:** Axial **(C)** and coronal **(D)** images show a ganglion cyst (*arrows*) of the biceps tendon sheath. **E:** Multiple hypointense loose bodies (*arrows*) are evident within the biceps tendon sheath, in this case of synovial chondromatosis of the long head of the biceps tendon sheath.

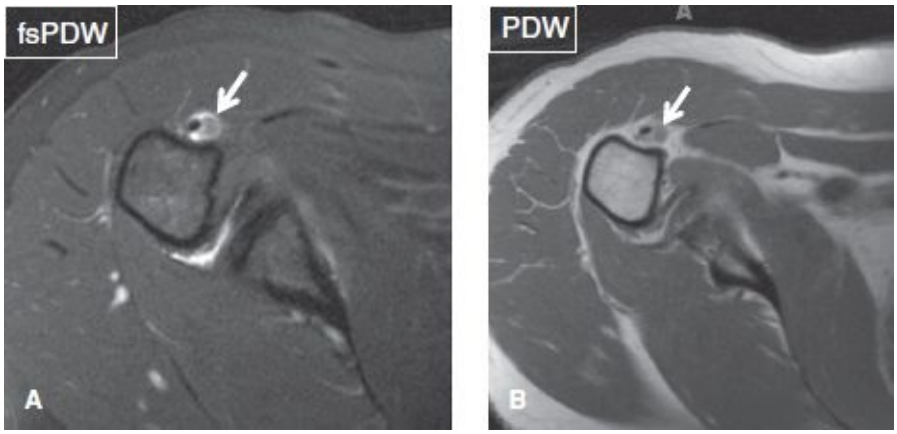

Fig. 15: Clot within the biceps tendon sheath. Axial images **(A, B)** show an isointense ill-defined lesion within the biceps tendon sheath, corresponding to a blood clot (*arrows*).

ACROMIAL ARCH:

Shape: [<Flat / Curved / Hooked / Convex> <Low-set acromion>]

Subacromial spur: [<Absent / Present> <Keel / Heel / Traction / Bird beak spur>]

Lateral / Anterior downsloping: <Absent / Present>]

Acromioclavicular joint: [<Normal> <Osteoarthrosis> <Sprain>]

The AC joint is formed by the distal end of the clavicle and the acromion and normally contains trace amount of synovial fluid and a hypointense articular disc. Thickenings of the joint capsule form the superior, posterior, and inferior AC ligaments, which provide anteroposterior static joint stability. Superoinferior static joint stability is provided by the CC ligament, which has two bands, the (triangular-shaped) posteromedial conoid band and the (quadrilateral-shaped) anterolateral trapezoid band. Functionally, the conoid band is the more important. The deltoid and trapezius muscles provide further dynamic reinforcement to the AC capsule and ligaments.

The acromial shape is best assessed on sagittal images, midway between the AC joint and the outer border of the acromion. If evaluated too close to the joint, a curved acromion may look like hooked. The most common acromial shape is flat (type I) or concave (type II), whereas convex or hooked (type III) acromion shapes are rare (Fig. 16). The acromion normally parallels the curvature of the humeral head. Lateral and anterior downsloping is detected on coronal and sagittal non–fat-suppressed proton density-weighted (PD) images, respectively, indicated by lack of parallel orientation between the acromion and the humeral head (Fig. 17).

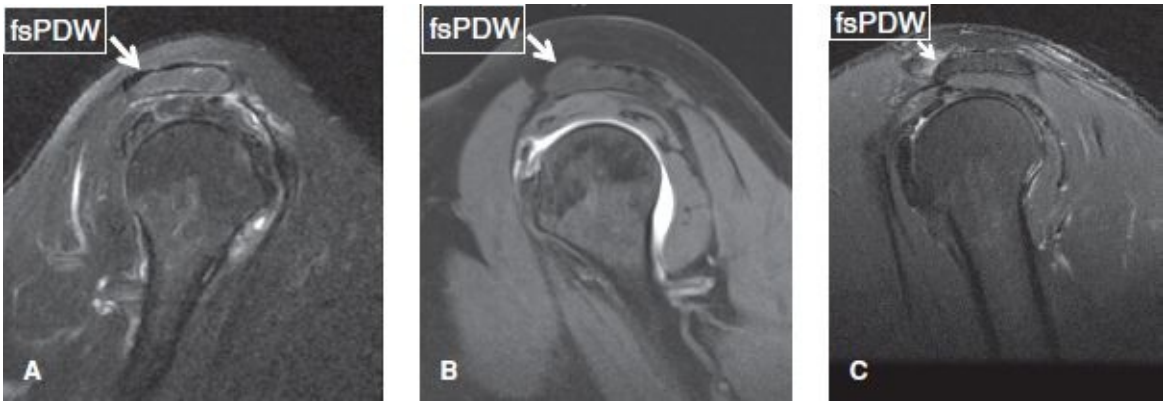

Fig. 16: Sagittal images demonstrate flat **(A),** concave **(B),** and hooked **(C)** acromion (*arrows*).

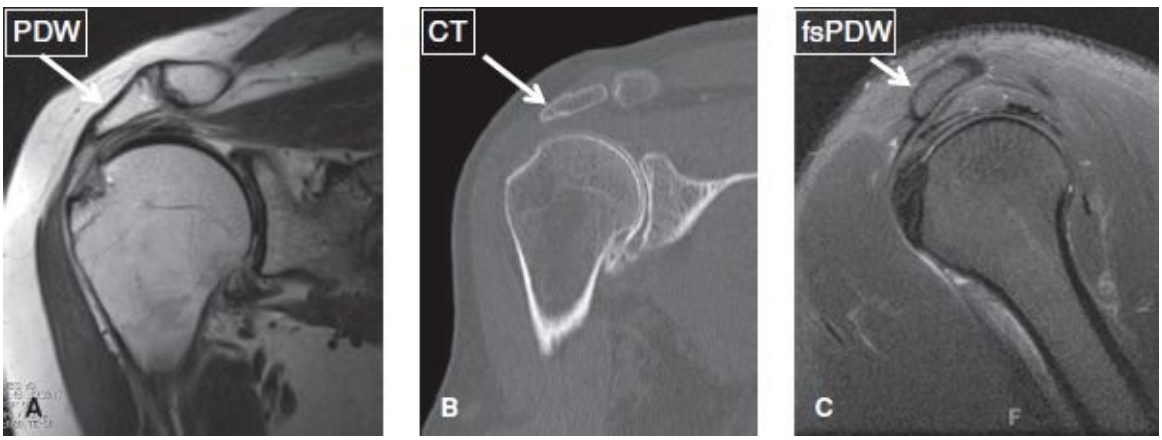

Fig. 17: Acromial downsloping. MR **(A)** and CT **(B)** images in the coronal plane show a laterally downsloping acromion (*arrows*). **C:** Sagittal MR image displays an anteriorly downsloping acromion (*arrow*).

Painful compression of the supraspinatus tendon and subacromial bursa between the coracoacromial arch and the humeral head is referred to as subacromial impingement (anterosuperior or extrinsic impingement). However, impingement is a clinical diagnosis, and one can only comment on whether anatomy associated with impingement is present (primary extrinsic impingement) or absent (secondary extrinsic impingement and internal impingement). Secondary extrinsic impingement may be related to myotendinous fatigue or capsular laxity, the latter, particularly resulting in multidirectional instability. Internal impingement is related to capsular stiffening posteriorly and inferiorly with laxity anteriorly, commonly seen in overhead throwers, as detailed below.

It should be noted that the more important findings related to subacromial impingement (primary extrinsic impingement) are the presence or absence of a subacromial spur and downsloping acromion rather than the acromion shape itself. Subacromial spurs are best seen on coronal non–fat-suppressed PD images, since hypointense coracoacromial ligament thickening or deltoid muscle origin from the acromion can mimic a spur on fat-suppressed PD images. There are five types of spurs that include traction spurs (enthesophytes at the deltoid attachment), bird beak spurs (traction spurs plus remodeled concave undersurface acromion due to superiorly riding humerus), keel spurs (enthesophytes at the coracoacromial ligament attachment), heel spurs (combination of traction, undersurface remodeling, and keel components), and medial spurs (part of AC osteoarthritis [OA]) (Figs. 18, 19). Traction spurs are usually associated with RC tendinosis/partial tears. Bird beak and keel spurs are commonly associated with partial RC tears, whereas heel spurs are usually associated with full-thickness RC tears. Impingement is clinically tested by using the Neer test (arm in full flexion) or the Hawkin test (arm in 90 degrees forward flexion and internal rotation). The Neer test is performed by placing the arm in forced flexion and full pronation. The scapula should be stabilized during the maneuver to prevent scapulothoracic motion. Hawkin test is particularly directed to supraspinatus evaluation and is considered to be more sensitive than the positive Neer sign. Notice that RC pathology manifests with weakness more than pain versus other pathologies, such as SASD bursitis and AC joint arthritis, which manifest with pain more than weakness.

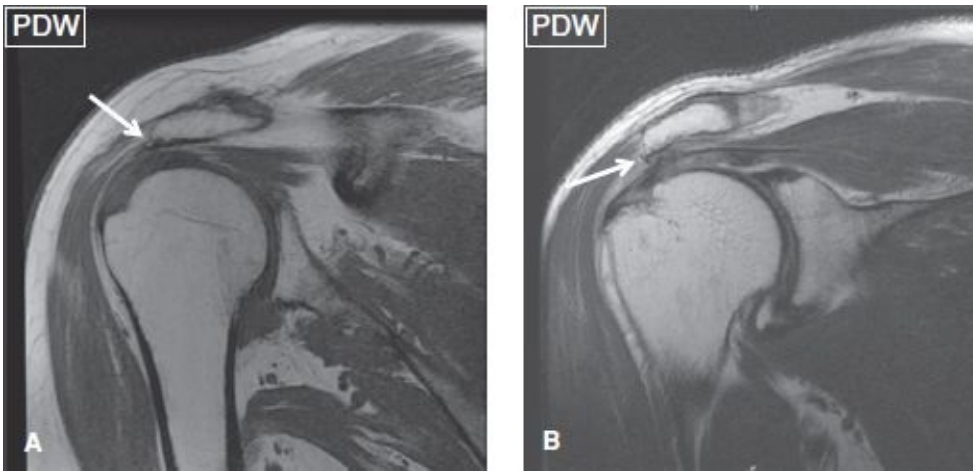

Fig. 18: Acromial spurs. Coronal images show traction (*arrow* in **A**) and bird-beak (*arrow* in **B**) acromial spurs.

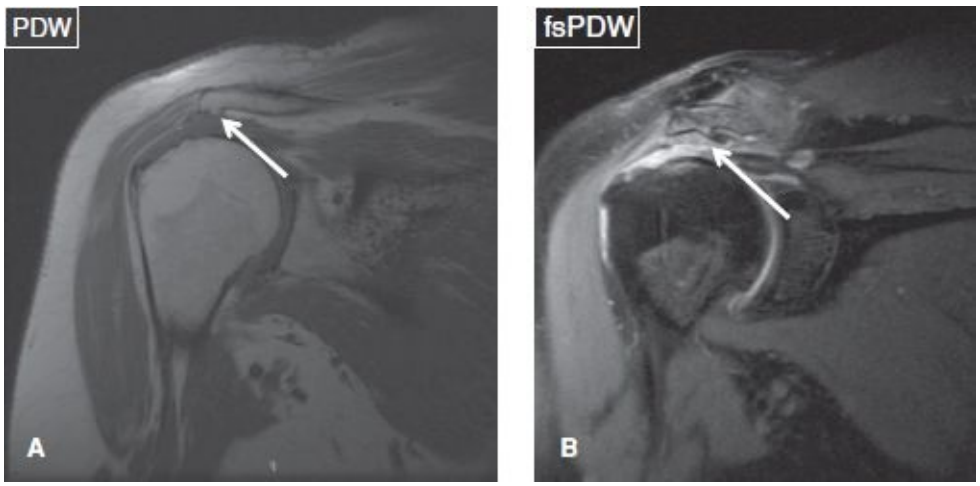

Fig. 19: Acromial spurs. Coronal images show keel (*arrow* in **A**) and heel (*arrow* in **B**) acromial spurs. Notice full-thickness rotator cuff tear in **(B).**

One should look for os acromiale (~3.5% prevalence in the general population), which can be bilateral in about 60% of cases. It predisposes to RC pathology, as the deltoid muscle inserts on the accessory ossicle rather than the acromion itself, and it can contribute to instability. Since the accessory ossification center for the acromion generally fuses around the age of 25 years, the diagnosis of os acromiale should be avoided in subjects younger than this age. However, the unfused ossification center can develop stress-related bone marrow edema, cystic changes, or disruption of the synchondrosis (depicted as widening of the joint space along with fluid signal), particularly in overactive athletes, such as gymnasts, earlier than the fusion age of 25 years. These findings should be reported as they can be symptomatic and predispose to frank disruption of the synchondrosis. There are four common types of os acromiale (pre-acromion—a small ossicle at the coracoacromial ligament attachment, meso-acromion—a equilateral triangular shaped larger ossicle, meta-acromion—further larger triangular ossicle, and basiacromion—adjacent to the base of the acromion process, with the mesoacromion being the most common). Os acromiale is best identified on axial images, whereas the above-described pathologic stress related imaging

findings are equally well seen on axial and coronal images (Fig. 20). Similar to AC joint pathology although less commonly, one may encounter fluid distention of the os acromiale synchondrosis, stress-related bone marrow edema across the synchondrosis, synovial diverticula(e), or even geyser phenomenon (fluid outpouching in the subcutaneous tissues from completely/partially disrupted synchondrosis) (Figs. 21–23).

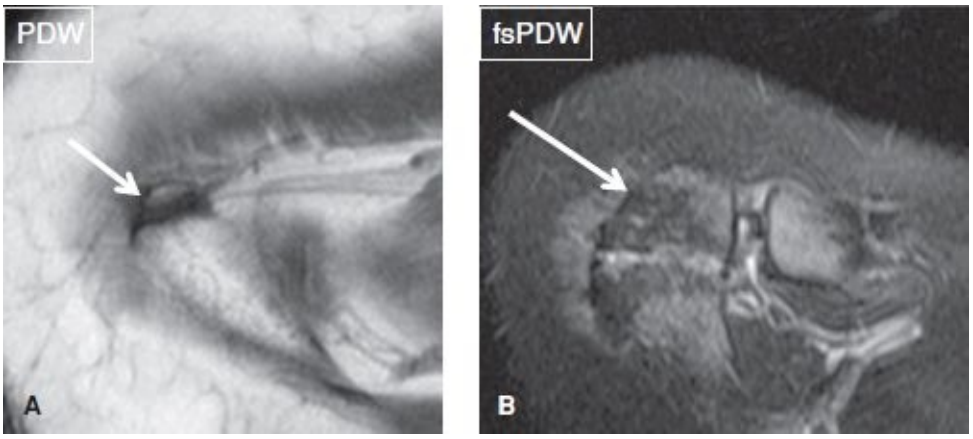

Fig. 20: Types of os acromiale. Axial images exhibit a preacromion (*arrow* in **A**) and a mesoacromion (*arrow* in **B**).

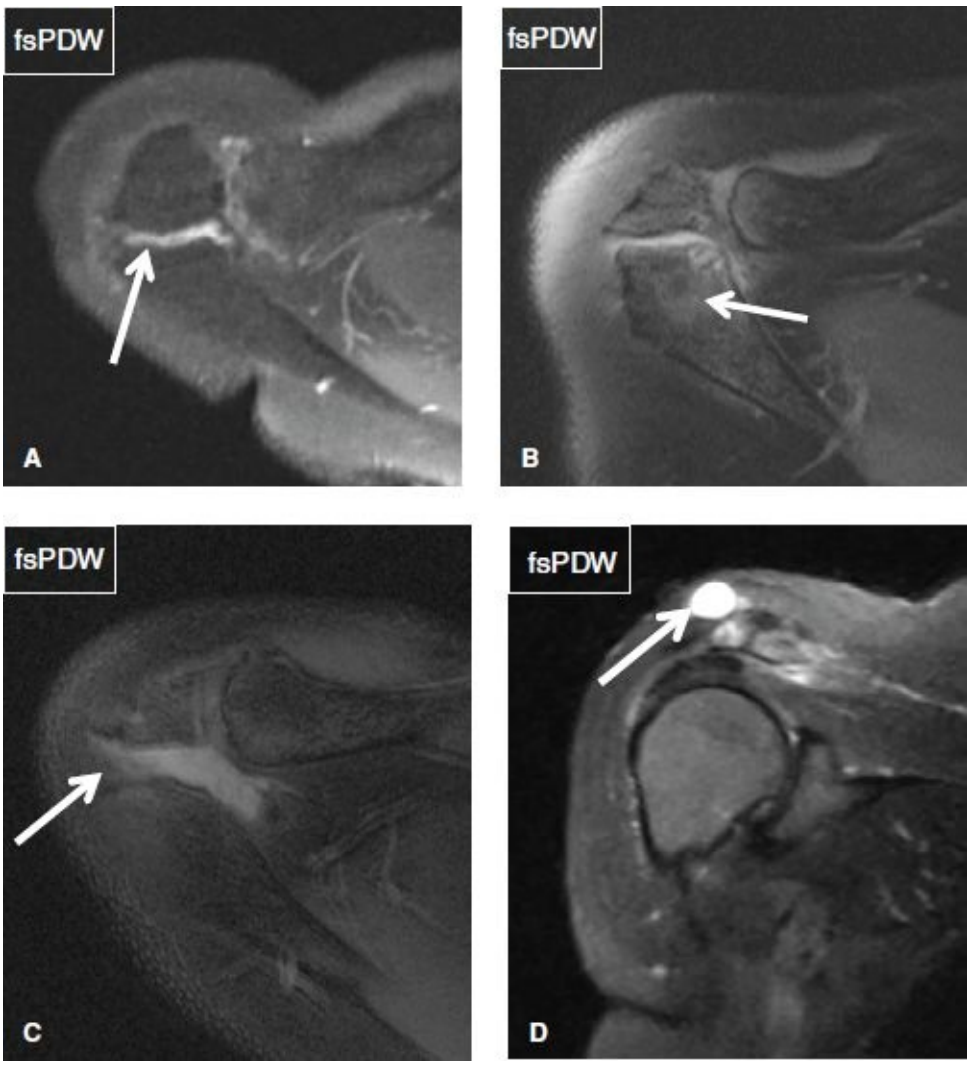

Fig. 21: Os acromiale abnormalities. **A:** Axial image shows trace fluid collection (*arrow*) within the os acromiale synchondrosis. **B:** Axial image demonstrates stress-induced bone

marrow edema (*arrow*) across the os acromiale synchondrosis, along with subarticular cystic changes. **C:** Axial image exhibits disruption and moderate fluid distention (*arrow*) of the os acromiale synchondrosis. **D:** Coronal image shows a well-defined fluid collection (*arrow*) superior to a partially disrupted os acromiale synchondrosis, corresponding to geyser phenomenon.

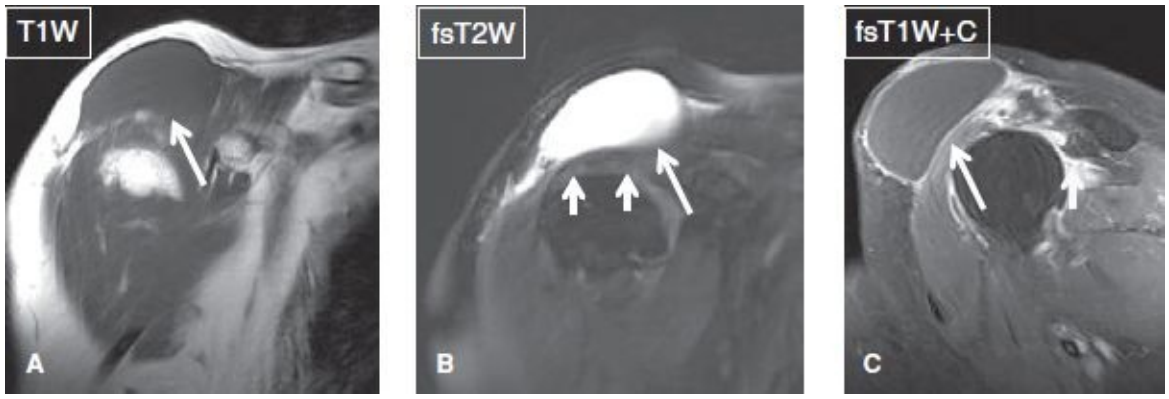

Fig. 22: Geyser phenomenon. Coronal conventional **(A, B)** and sagittal contrast-enhanced **(C)** images show a well-defined fluid collection (*long arrows*) adjacent to the acromioclavicular joint. The cyst is believed to result from leakage of synovial fluid through the joint due to a massive rotator cuff tear (*short arrows* in **B**). Note associated proximal retraction of the supraspinatus tendon (*short arrow* in **C**).

Fig. 23: Geyser phenomenon mimicking sarcoma. Axial **(A)** and coronal **(B)** unenhanced images and coronal contrast-enhanced image **(C)** show a subcutaneous multiloculated and lobulated fluid collection projecting superior to the shoulder joint. Without image **(C),** which confirms the absence of solid components, the possibility of a soft tissue sarcoma cannot be entirely excluded.

AC joint OA should be classified as mild, moderate, or severe. Associated findings, such as capsular thickening, bony hypertrophy, subchondral edema, sclerosis, and cystic changes should be reported. OA grading is similar to other joints, with capsular thickening/small osteophytes suggesting mild OA, mild–moderate cartilage loss with subchondral cysts/sclerosis/significant edema with moderate OA, and large osteophytes, bony

deformities and greater than 50% cartilage loss with severe OA (Fig. 24). AC joint pathology is clinically tested using the "cross arm test," in which the arm is put into forward elevation to 90 degrees with active adduction. AC joint OA should be differentiated from AC joint sprains, which usually affect younger individuals and those involved in bench pressing. AC joint sprains are associated with capsular thickening, superior and inferior AC ligament thickening/attenuation/tears, and feature the key finding of periarticular fascial edema. However, underlying OA may also be present, especially in older individuals. Other associated findings may include AC joint widening with or without post-traumatic osteolysis (erosions/edema of the joint surfaces), CC ligament sprain, and deltoid or trapezius muscle strains apart from history of recent trauma. AC joint injuries can be graded according to the Rockwood classification (Table 1) (Figs. 25–27) Types I to III are typically treated conservatively, whereas types IV to VI usually require surgery. There is increased risk of infection in type IV injury. One should also look for related differential diagnoses or associated injuries, such as distal clavicle fracture (isolated clavicle-sided bone marrow and fascial edema, along with a hypointense subchondral fracture line) or posttraumatic osteolysis (ill-defined cortical margin/erosions, commonly associated with muscular body habitus) (Figs. 28, 29).

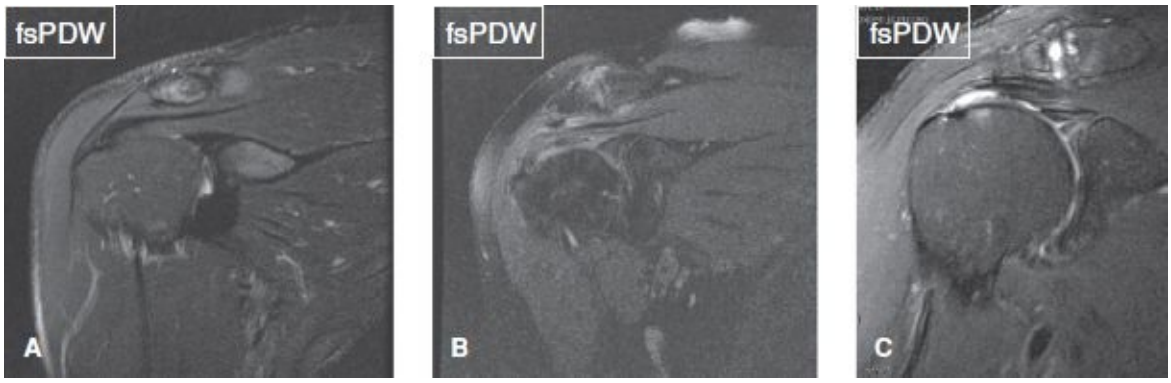

Fig. 24: Acromioclavicular joint osteoarthritis. Coronal images demonstrate a normal joint **(A),** and cases of mild **(B),** and moderate to severe **(C)** osteoarthritis.

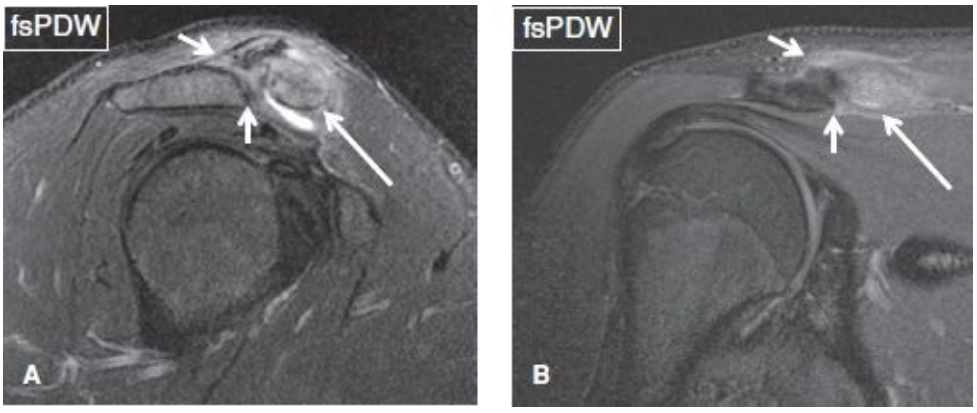

Fig. 25: Acromioclavicular joint type I sprain in the setting of clavicular fracture. On sagittal **(A)** and coronal **(B)** images, there are high-grade partial tears of acromioclavicular ligaments (*short arrows*) without joint space widening. Marrow edema of the distal clavicle (*long arrows*) is due to subchondral fracture. Notice associated fascial edema, common

finding in AC sprains, unlike simple OA.

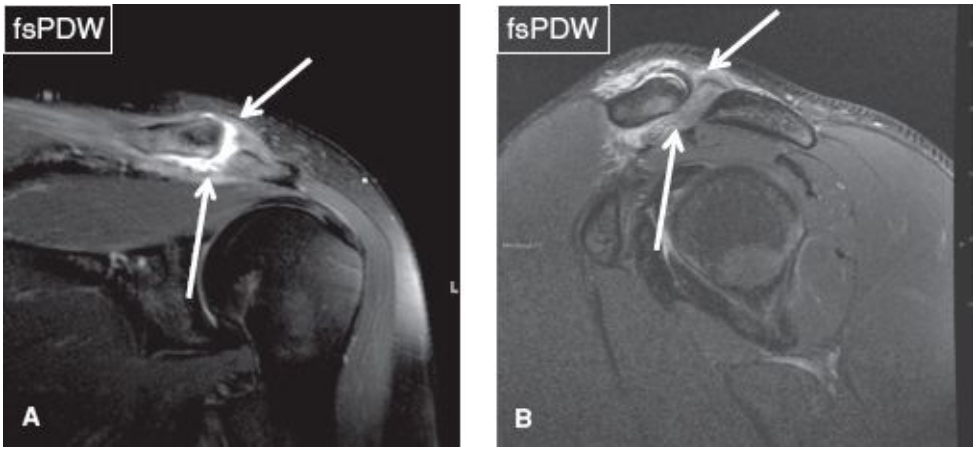

Fig. 26: Acromioclavicular joint type II sprain. Coronal **(A)** and sagittal **(B)** images demonstrate complete rupture of the superior and inferior acromioclavicular ligaments (*arrows*).

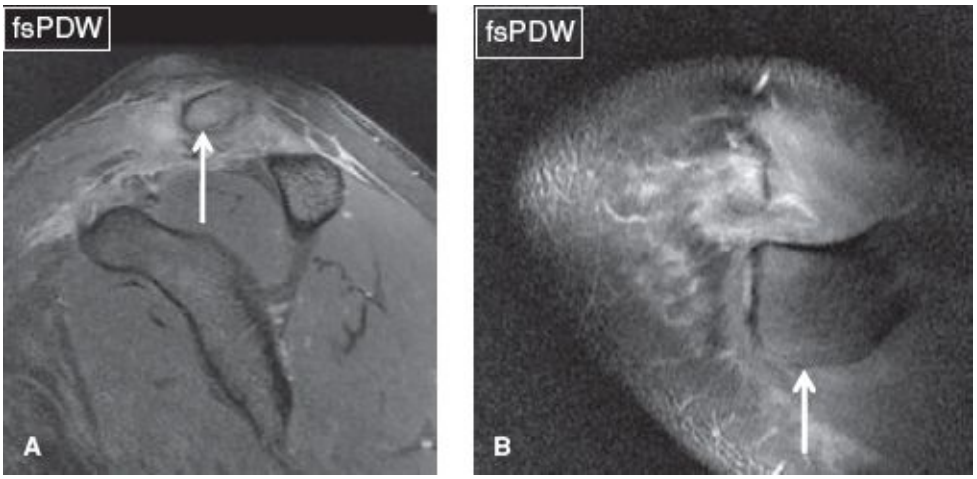

Fig. 27: Acromioclavicular joint type IV sprain. Sagittal **(A)** and axial **(B)** images demonstrate acromioclavicular joint separation along with posterior clavicular subluxation (*arrows*).

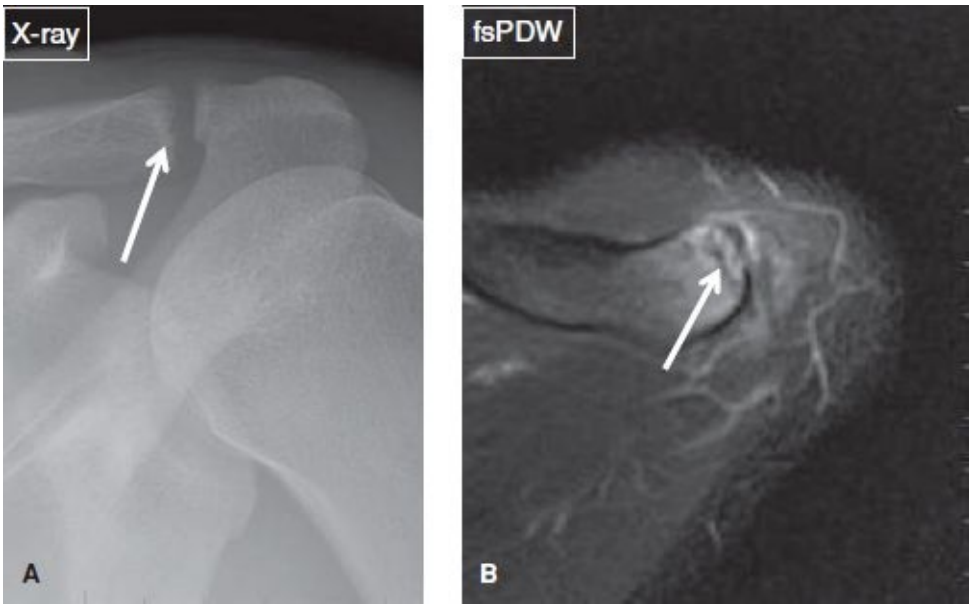

Fig. 28: Subchondral clavicular fracture. **A:** Radiograph displays ill-defined distal clavicular cortex (*arrow*). **B:** The corresponding axial MR image shows a subarticular hypointense fracture line (*arrow*) in the distal clavicle with associated bone marrow edema.

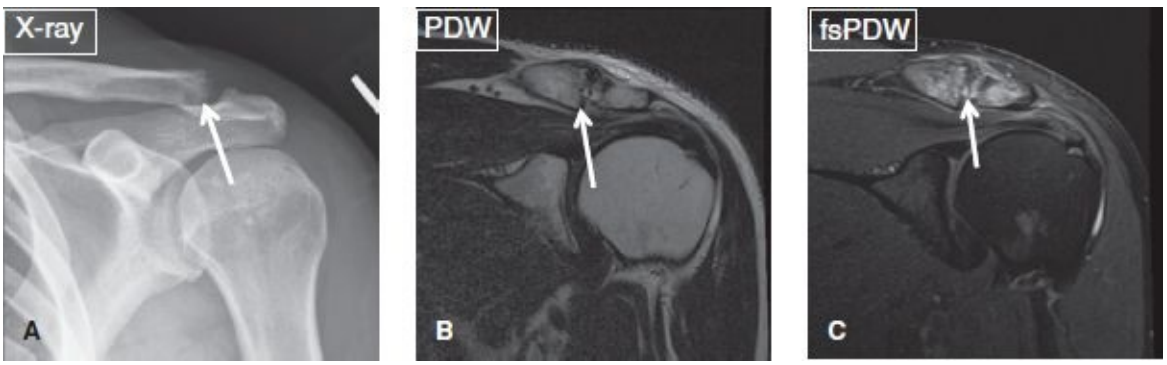

Fig. 29: Posttraumatic clavicular osteolysis. *Anteroposterior* radiograph **(A)** and coronal MR images **(B, C)** demonstrate cortical erosions of the distal clavicle (*arrows*). In **(C),** bone marrow edema and fascial edema are evident across the joint line.

TABLE 1: The Rockwood classification for grading acromioclavicular joint injury

Injury Type	Imaging Features[a]
I	Partial tear (sprain) of the AC or CC ligaments Joint normal on radiographs
II	Complete tear of the AC ligaments Partial tear (sprain) of the CC ligament AC joint space widening (>6 mm)
III	Complete tear of the AC and CC ligaments Superior clavicle displacement AC joint space widening Increased (>13 mm) CC distance
IV	Posterior subluxation of the clavicle in the trapezius muscle
V	Marked superior clavicle displacement (CC distance > ×2 or ×3 of normal) Torn deltoid and trapezius muscles Clavicle displaced in subcutaneous position
VI	Inferior clavicle displacement

AC, acromioclavicular; CC, coracoclavicular.

[a]Normal values for acromioclavicular joint space width are less than 5 mm (or less than 2 to 3 mm difference between right and left side). Normal values for coracoclavicular distance are 11 to 13 mm (or less than 50% difference or less than 5 mm difference between right and left side).

(Adapted from Rockwood CA, Williams GR, Young DC. Acromioclavicular injuries. In: Rockwood CA, Green DP, Bucholz RW, Heckman JD, eds. *Fractures in Adults*. Vol 1. 4th ed. Philadelphia, PA: Lippincott-Raven; 1996:1341–1413.)

ROTATOR CUFF:

Supraspinatus: [<Normal> <Mild / Moderate / Severe tendinosis> <Bursal / Articular-

sided fraying> <Tear> <Retraction> <Muscle atrophy>]

Infraspinatus: [<Normal> <Mild / Moderate / Severe tendinosis> <Bursal / Articular-sided fraying> <Tear> <Retraction> <Muscle atrophy>]

Subscapularis: [<Normal> <Mild / Moderate / Severe tendinosis> <Tear> <Retraction> <Muscle atrophy>]

To understand RC tears, it is important to learn the anatomic architecture in three planes. In the coronal plane, horizontally from lateral to medial, the cuff is divided into the following:

- The attachment site (leading edge/extra-articular portion, about 1 cm in width)
- The critical zone (extending 1 cm proximal to greater/lesser tuberosity and about 1 cm in width, also known as avascular zone although a misnomer, since it can be hypervascular instead)
- The myotendinous junction (about 1 to 2 cm in width, usually located between 11 and 1 o'clock location)
- The muscle fibers

In the sagittal plane, the cuff is composed of the following (Figs. 30–33):

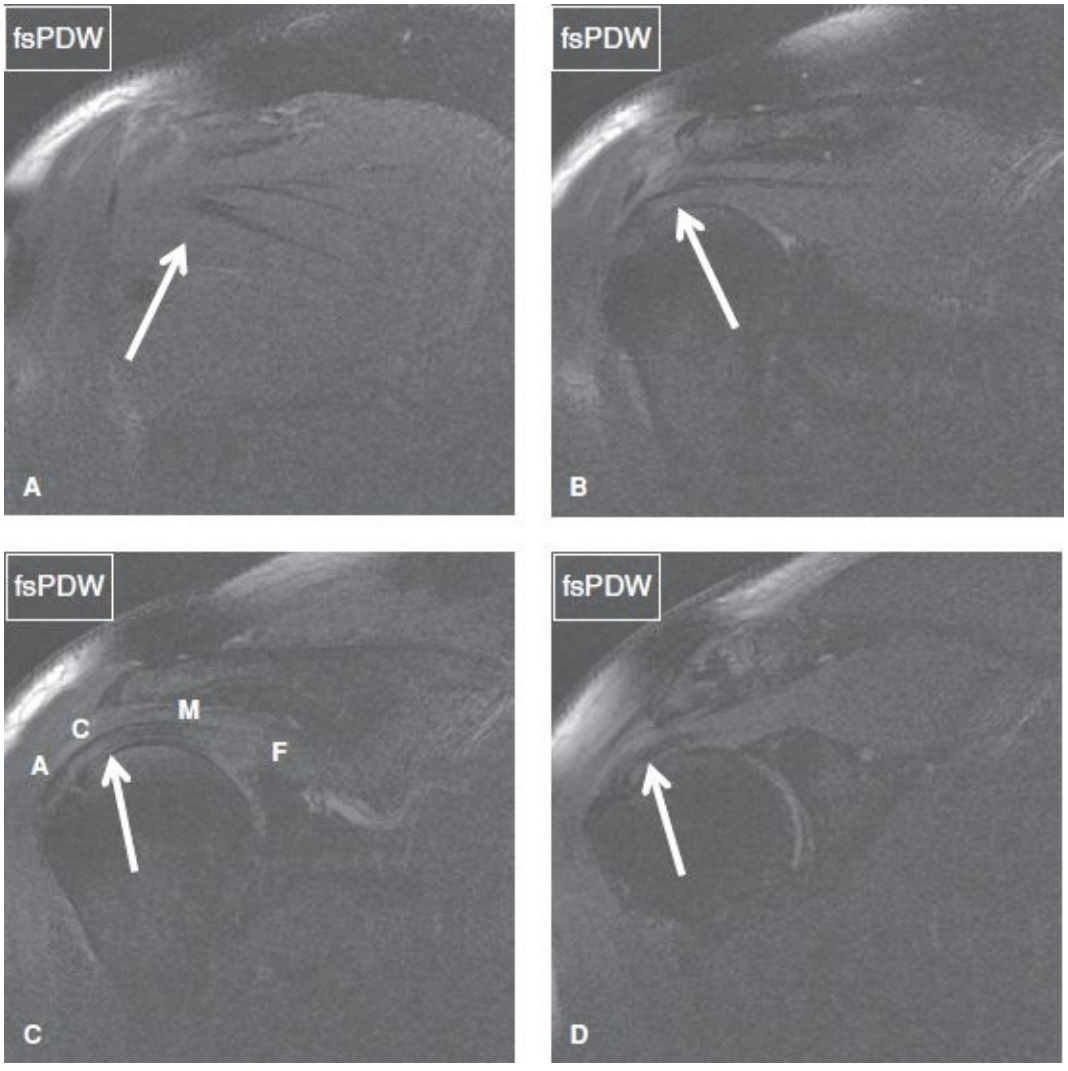

Fig. 30: The rotator cuff muscle/tendons. In posterior to anterior **(A–D)** coronal images, *arrows* denote infraspinatus **(A),** anterior infraspinatus and posterior supraspinatus **(B),** posterior supraspinatus **(C),** and anterior supraspinatus **(D).** In **(C),** (*A*) corresponds to the attachment site, (*C*) to the critical zone, (*M*) to the myotendinous junction, and (*F*) to the muscle fibers.

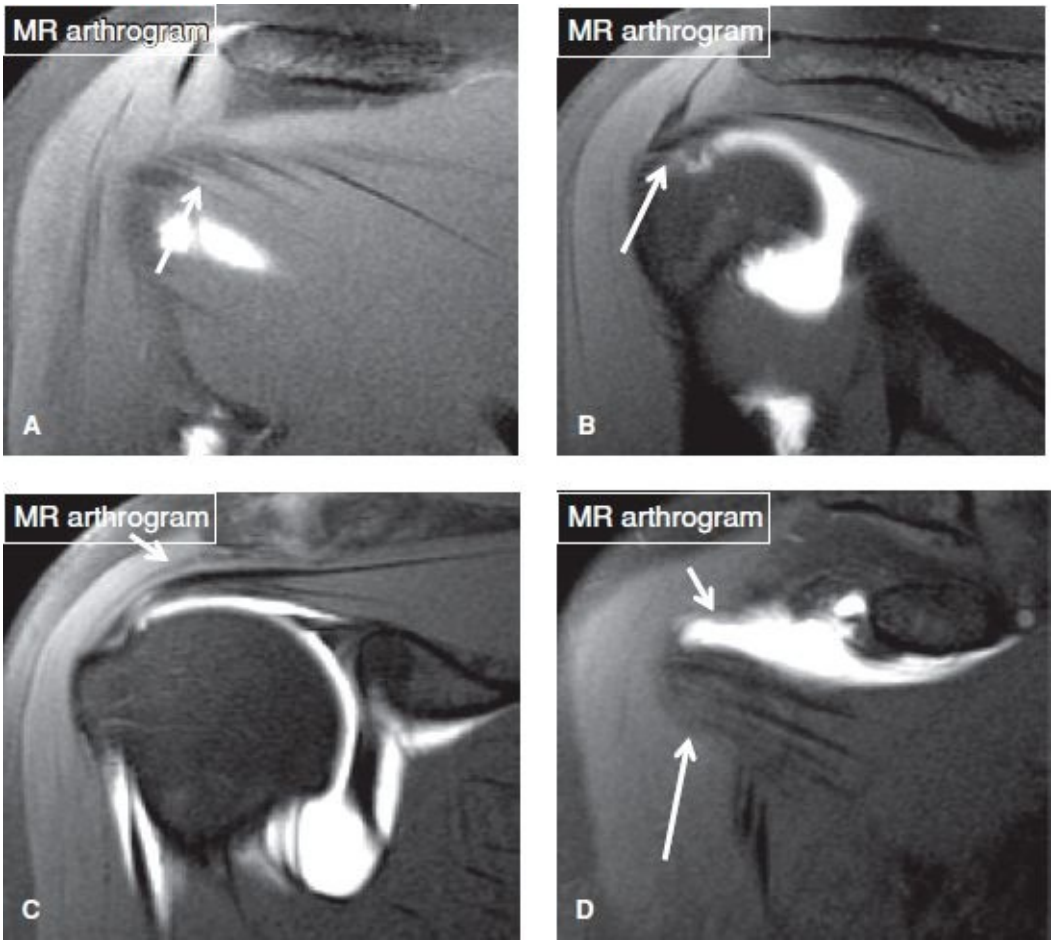

Fig. 31: The rotator cuff muscle/tendons. *Long arrows* in posterior to anterior (**A–D**) coronal MR arthrography images indicate the infraspinatus **(A, B),** the supraspinatus **(C),** and the subscapularis **(D).** Notice the normal gap of the rotator interval (*short arrow* in **D**).

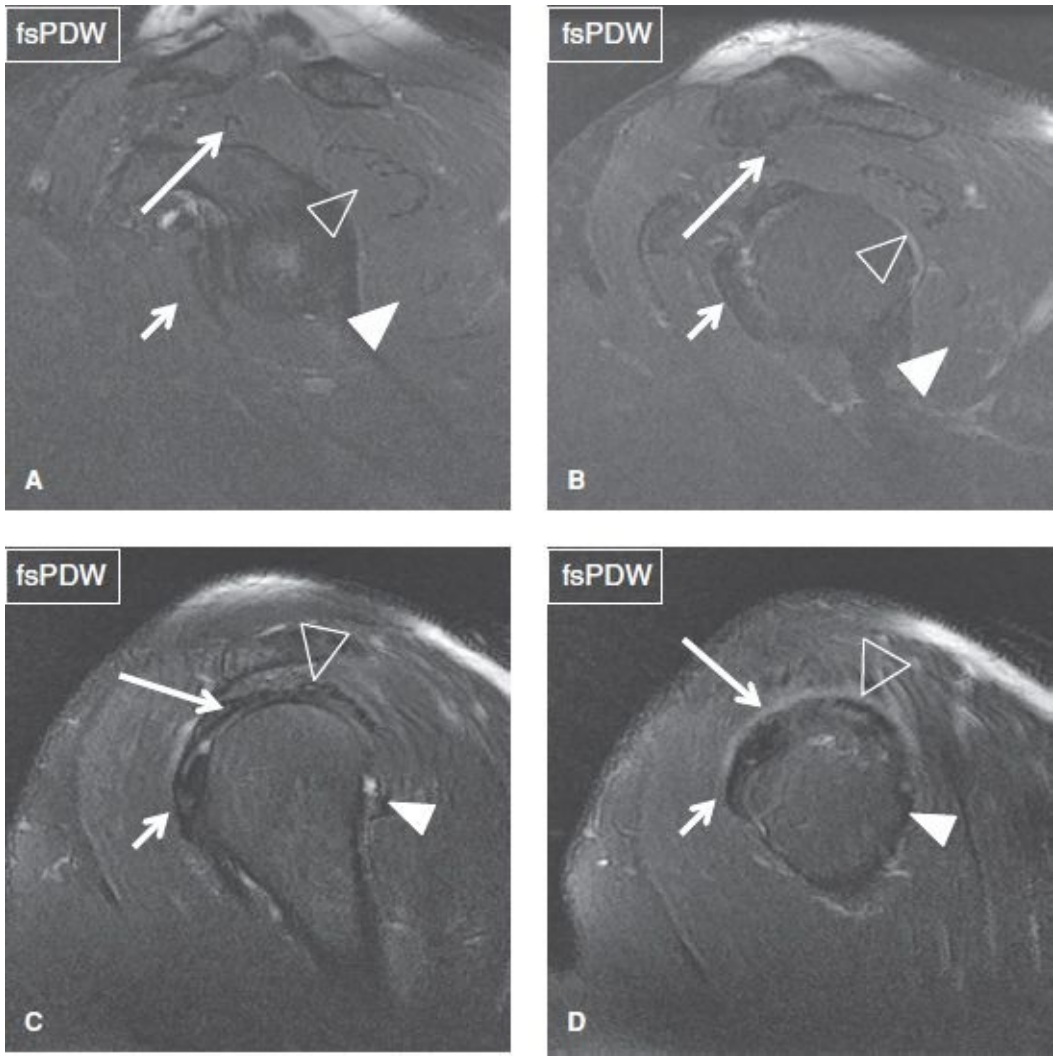

Fig. 32: The rotator cuff muscle/tendons. *Arrows* in medial to lateral **(A–D)** sagittal images indicate the subscapularis (*short arrows*), supraspinatus (*long arrows*), infraspinatus (*open arrowheads*), and teres major (*solid arrowheads*).

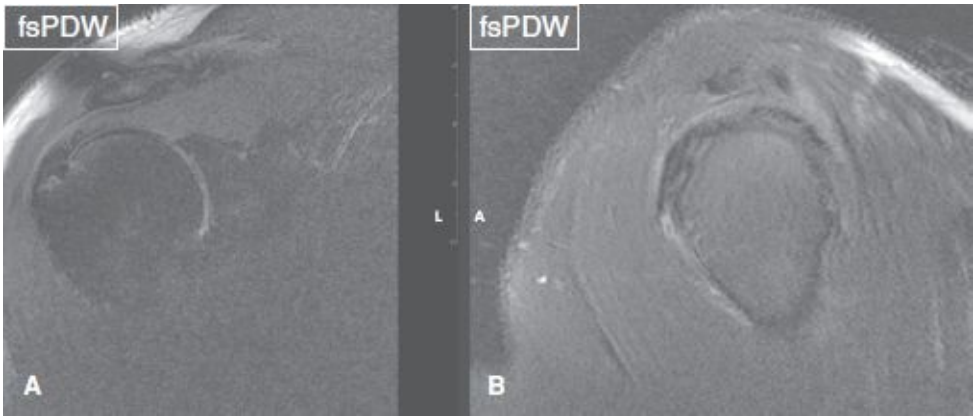

Fig. 33: The supraspinatus–infraspinatus tendon junction. Coronal image **(A)** corresponds to the vertical plane of sagittal image **(B)** and designates the junction between the supraspinatus and infraspinatus tendons, which unite into a single tendon close to the rotator cuff attachment site.

- The subscapularis anteriorly (1.8 to 2 cm in craniocaudal diameter)
- The supraspinatus anterosuperiorly (2 to 2.5 cm in anteroposterior width)

- The infraspinatus posterosuperiorly (1.8 to 2 cm in anteroposterior width)
- The teres minor posteriorly (a few millimeters to 1 cm in width)

In the coronal plane, the RC measures 6 to 7 mm in (craniocaudal) thickness, especially in the cable area (described below). It has five layers, which are formed from superior to inferior by the CC ligament, compact tendon fibers, loosely organized tendon fibers, CHL with connective tissue fibers, and the joint capsule. Neurovascular supply to the RC derives mostly from the bursal rather than the articular side of the tendons.

Scuffing and fraying is the terminology popular among orthopods for minor cuff alterations. Scuffing refers to capsular abrasions (only seen arthroscopically), whereas fraying refers to tears of the enveloping CHL and fibrillations of the tendon fibers (can be easily seen with current high-field MR imaging techniques). RC degenerative fraying and tears should be further described as articular-sided or bursal-sided. The authors uncommonly use the term "intrasubstance tears in isolation," since pure intrasubstance tears are less common. These lesions can be seen in the (bipennate) infraspinatus tendon more commonly compared to the (multipennate) supraspinatus and subscapularis tendon, which have intertwined myotendinous fibers. Intrasubstance extension of articular- or bursal-sided tears is much more common leading to intermediate- or high-grade tears. Such tears are frequently associated with intrasubstance fluid dissection, resulting in delaminating lesions and intramuscular cyst formation (Figs. 34, 35). Because of the laminar architecture of the tendons, fluid tends to dissect between tight and loose tendon layers. Since the teres minor tendon is seldom injured at the attachment site, the evaluation of the RC is usually limited in clinical practice to the assessment of the supraspinatus, infraspinatus, and subscapularis tendons.

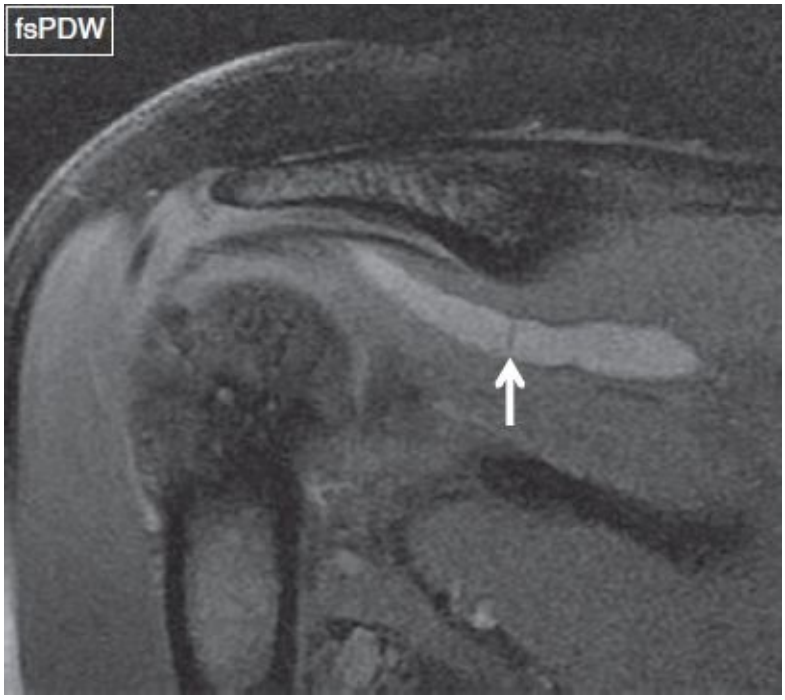

Fig. 34: Intramuscular cyst. Coronal image shows a cystic lesion (*arrow*) within the supraspinatus tendon, which has resulted due to seepage of fluid through the delaminating tendon tear extending from the attachment (not shown) to the myotendinous junction

(*arrow*).

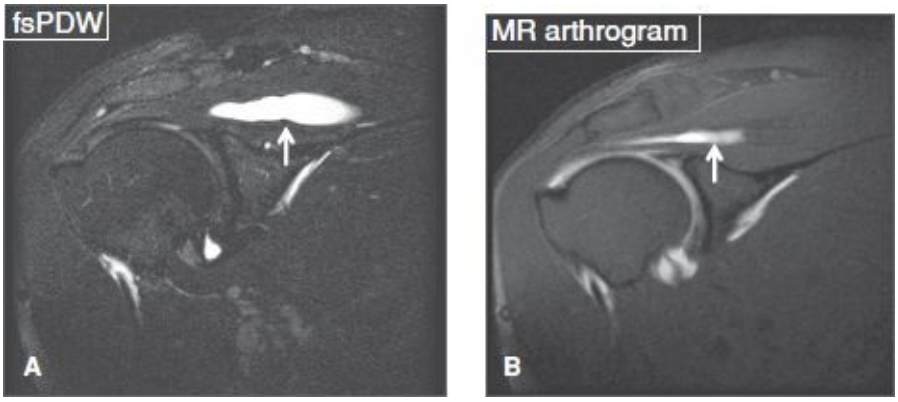

Fig. 35: Intramuscular cyst. Coronal conventional fsT2 W **(A)** and arthrography fsT1 W **(B)** images show a cystic lesion (*arrows*) within the supraspinatus tendon. On the latter image, the cyst partially fills with contrast.

Tendinosis and tears should both be described. However, it is important to first understand the mechanisms of RC tendinosis and tears. The initial theory of subacromial impingement, described by Neer et al., suggested that acromial hook, downsloping acromion, os acromiale, AC joint OA, thick coracoacromial ligament, and subacromial spurs are the factors which, in isolation or combination, contribute to RC impingement and/or tears. However, that theory was unable to explain why articular-sided (undersurface) RC tears occur more frequently as compared to the bursal-sided tears, if impingement was the only predisposing factor. The "fatigue failure" theory, explains the rotator cuff pathology in a more intuitive way. As a result of repetitive trauma and microinjuries caused by everyday activities or excessive stress on shoulder, recurrent RC microtears occur, particularly at its myotendinous junction. In children and relatively younger adults, the healing capacity is much more than the tearing predisposition. With increasing age, the healing capacity lags, leading to the development of RC tendinosis and focal partial tears. Tendinosis and partial tears are common in young and middle-aged individuals, whereas high-grade partial tears and tears that progress to full-thickness tears are common in the older population. This phenomenon may be further complicated by factors such as increasing stresses from recurrent overhead activities, such as in high-performance athletes; superimposed blunt or penetrating trauma; and presence of underlying comorbidities that could contribute to poorer healing, such as gout, collagen vascular disease, steroid intake, renal failure, etc. In the latter case with underlying chronic comorbidities, tendinosis can be much more pronounced, and tears may develop spontaneously due to poorer healing. To summarize, both theories of impingement and fatigue failure may play roles in rotator cuff pathology, and are not exclusive mechanisms. The "impingement" could be primary (abnormal subacromial anatomy) or secondary (due to abnormal GH motion), whereas "fatigue failure" likely plays an important role in the initiation or progression of RC tears, which can be further impacted by worsening impingement anatomy, as the tears progress. Patients with RC pathology usually present with weakness, night pain, and lateral shoulder

and arm pain. In suspected RC injury or failure, the commonly used clinical tests include the above described impingement (Neer and Hawkins) tests; “Apley Scratch Test,” in which the person tries to touch the superior and inferior surfaces of the opposite scapula to assess the loss of range of motion; and the “Drop Arm Test,” in which the elevated arm is slowly lowered to the waist.

A common imaging finding in young weight lifters and overhead throwers is the so-called “rim-rent” tear. The term “rim-rent” *tear* (widely used by radiologists, although not so prevalent in the orthopedic community) refers to a partial articular-sided tear of the leading edge of the supraspinatus or infraspinatus tendons. The mechanism of such tears is explained below. With repeated or excessive overhead activities and underlying or developmental impingement anatomy, as the RC tendons slides under the hypertrophied AC joint, thickened coracoacromial ligament, low-set acromion, and/or subacromial spurs, there is repeated rubbing of the cuff with this altered subacromial impingement morphology leading to bursal surface scuffing and/or fraying. The latter is uncomfortable and/or painful and leads to further, uncoordinated (jerky) movements during shoulder abduction and external rotation. The subacromial impingement anatomy indents the myotendinous junction of the RC creating a pulley effect, which predisposes the RC tendon fibers to tear and avulse from the undersurface attachment at the greater tuberosity, leading to “attachment tear” a.k.a “rim-rent tear.” This mechanism also explains the well-known Burkhart’s concept of RC “cable and crescent” model. The crescent refers to peripheral attachment fibers of the RC on the greater tuberosity extending approximately 14 mm in transverse width. The cable is the thickened layer of the RC with a fibrous band that courses along the undersurface of the supraspinatus and infraspinatus tendons and blends with the CHL, at around 12 mm medial to the crescent and immediately lateral to the myotendinous junction. It was previously hypothesized that, in younger patients, the crescent plays the primary biomechanical role in RC function, but with age, and as the crescent weakens, the cable undergoes hypertrophy and assumes an important role in shielding the crescent from stress. Similar to a suspension bridge, the crescent tears first, and since few fibers (wires) avulse at a time, there is a nonuniform extension of the tear from anterior to posterior width of the rotator cuff. The crescent tears basically reflect “rim-rent” type of tears. Although partial-thickness tears may partially fill with fibrous tissue to some extent, more commonly, with advancing age, healing capacity lags and these tears progress. Therefore, partial tear, if left untreated, progresses to full-thickness tear, (best seen on coronal and axial images); and also increase in anteroposterior extent, progressing from incomplete to complete width, (best identified on the sagittal images). The normal cable should not be mistaken for partial articular-sided tear. On the other hand, a prominent cable appearance (abrupt contour change of supraspinatus articular surface) indicates the presence of a partial articular-sided tear.

RC tendinosis should be classified as mild, moderate, and severe to provide the clinician a sense of the degree of normalcy or quality of tendon fibers, in case repair is attempted. Again, there are no set rules; however, mild tendinosis is identified as intermediate signal

(not fluid-bright) with maintained fiber continuity. This should not be overdiagnosed or mistaken for artifactual increased signal in the critical zone of the supraspinatus tendon due to magic angle phenomenon. Moderate tendinosis is identified as intermediate signal and mild thickening (>6 mm) of the tendon. Severe tendinosis refers to near fluid-bright and moderately thickened tendon, where differentiation from coexistent tears becomes difficult due to diffuse increased signal (Fig. 36). The term "focal tendinosis" should be avoided, since any focal area of signal hyperintensity, even if not fluid-bright, most likely represents a tear filled in with granulation tissue or fibrosis. Additional findings which might help in identifying focal partial tears include, missing tendon fibers (laminar retraction due to tear at the attachment), missing tight or loose tendon surfaces (surface tears), prominent cable, and presence of subcortical cysts in the greater or lesser tuberosity with focally increased, near-fluid signal in the tendon fibers adjacent to the cysts. The cysts may reflect cartilage rests (displaced cartilage from the physeal scar), or commonly, the RC tear can be traced to the individual cysts. The mechanism involves fibers getting avulsed from the bony attachment site, leading to tear of the enveloping synovium, which then results in filling of the cyst(s) by synovial fluid (or injected contrast). The various causes of RC tears include primary extrinsic impingement, secondary extrinsic impingement, internal impingement, regional bony derangements and tendinopathy related to systemic causes, apart from local direct or indirect trauma.

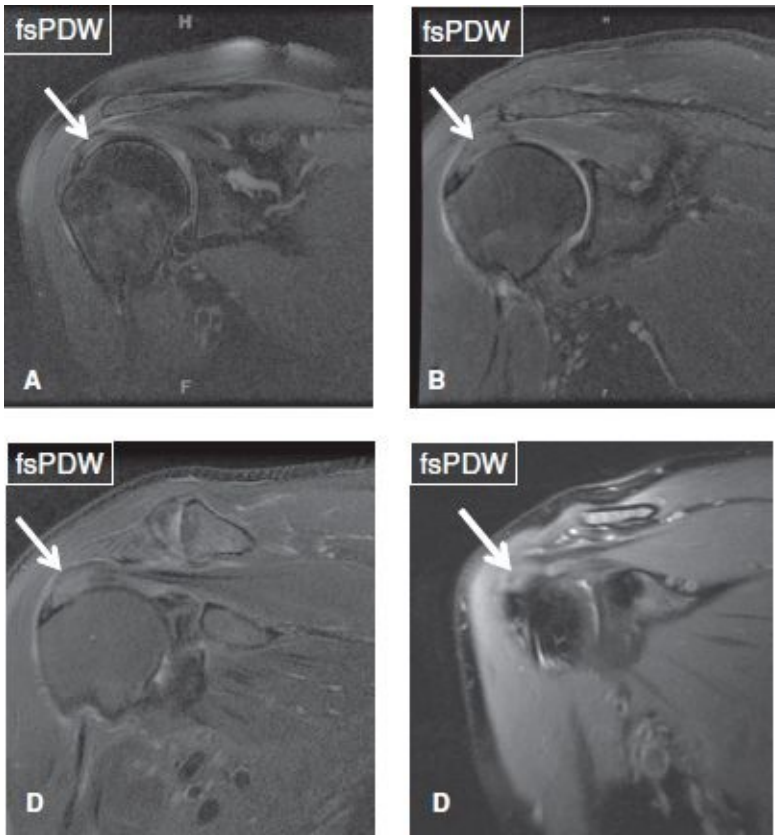

Fig. 36: Rotator cuff tendinosis. *Arrows* indicate mild **(A),** mild to moderate **(B),** moderate **(C),** and severe **(D)** rotator cuff tendinosis.

Calcific tendinitis is a self-limited painful disorder resulting from deposition of calcium

hydroxyapatite crystals on the surface or within the substance of the RC tendons, most commonly of the supraspinatus tendon. Evident on radiographs as calcifications varying from a few millimeters to several centimeters in size, these crystals appear on MR images as rounded lesions of low signal on all pulse sequences, and are particularly conspicuous on gradient echo images. These are commonly located within 1 cm from the tuberosities. The natural history of calcific tendinitis usually follows the below described phases:

1. The silent phase, in which patients experience minimal or no symptoms, and radiographs demonstrate well-defined calcified deposits (Fig. 37).

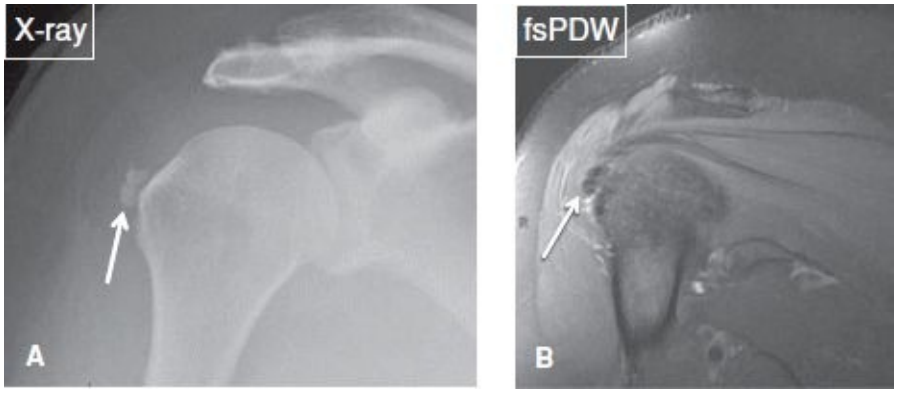

Fig. 37: Silent phase of calcific tendinitis. **A:** Anteroposterior radiograph demonstrates two rounded calcifications adjacent to the greater tuberosity (*arrow*). **B:** On the corresponding coronal MR image, the calcified bodies are depicted as hypointense lesions (*arrow*).

2. The active phase, in which patients experience impingement-like symptoms. The calcified deposits disperse into the adjacent bursa or peribursal soft tissues, and either disappear or become ill-defined on radiographs, whereas bursitis and/or inflammation of peribursal soft tissues are evident on MR images (Figs. 38–42).

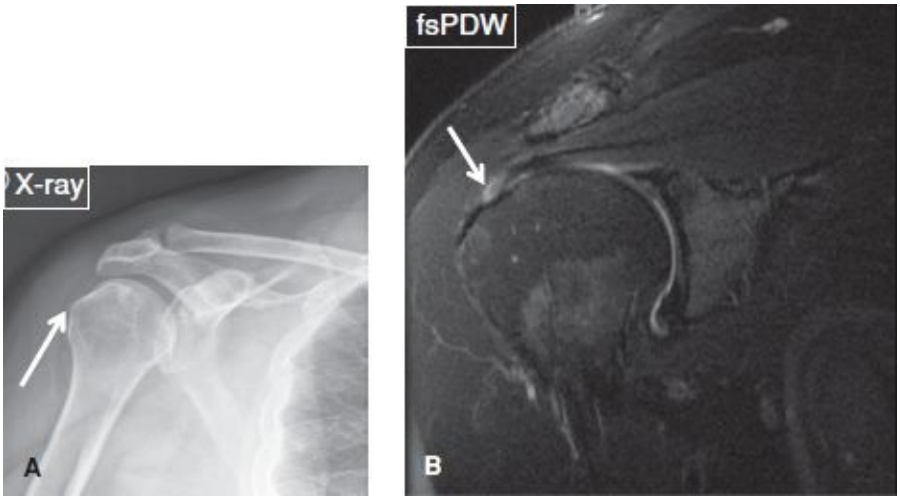

Fig. 38: Calcific tendinitis. **A:** Anteroposterior radiograph shows a calcification (*arrow*) adjacent to the greater tuberosity, corresponding to calcific tendinitis. **B:** The respective coronal MR image exhibits a high-grade bursal-sided partial tear (*arrow*) in the distal supraspinatus tendon.

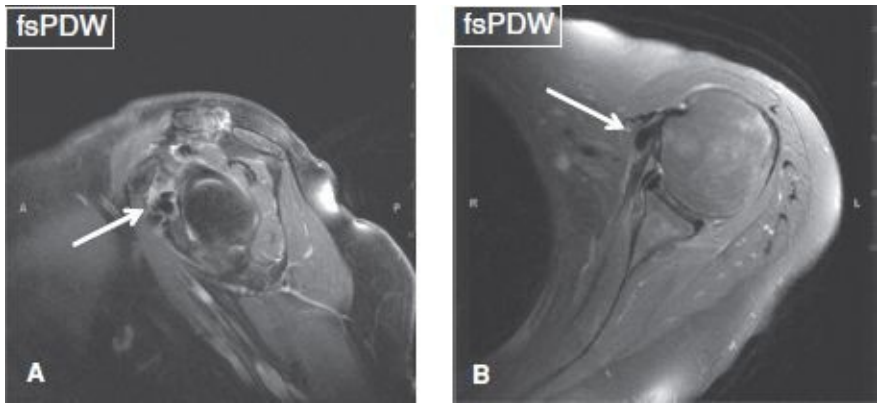

Fig. 39: Calcific tendinitis of the subscapularis muscle. Silent phase. Sagittal **(A)** and axial **(B)** images show hypointense lesions corresponding to calcific deposits (*arrows*) in the distal subscapularis tendon.

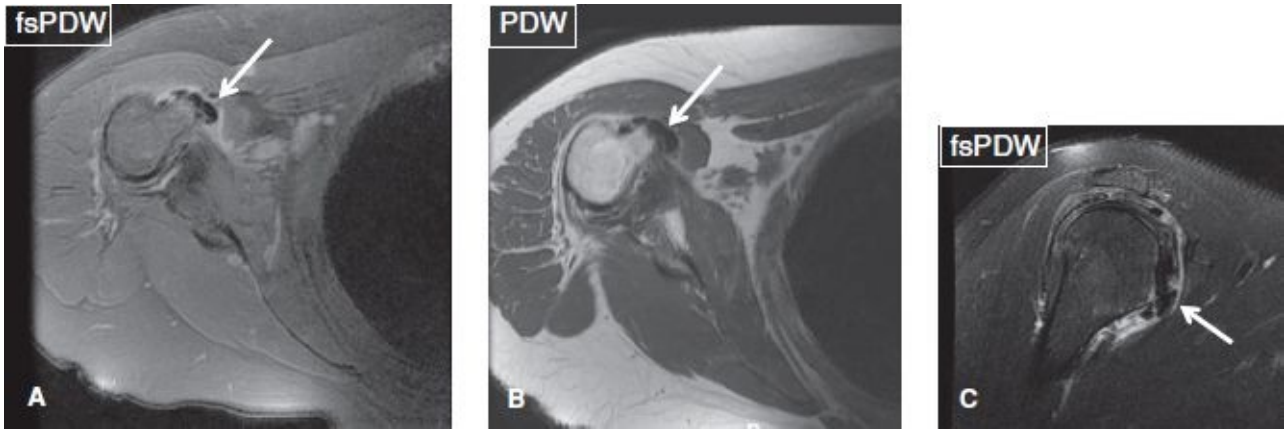

Fig. 40: Calcific tendinitis of the subscapularis muscle. Axial **(A, B)** and sagittal **(C)** images show hypointense lesions, corresponding to calcific deposits (*arrows*), in the distal subscapularis tendon. Notice associated subcoracoid bursitis.

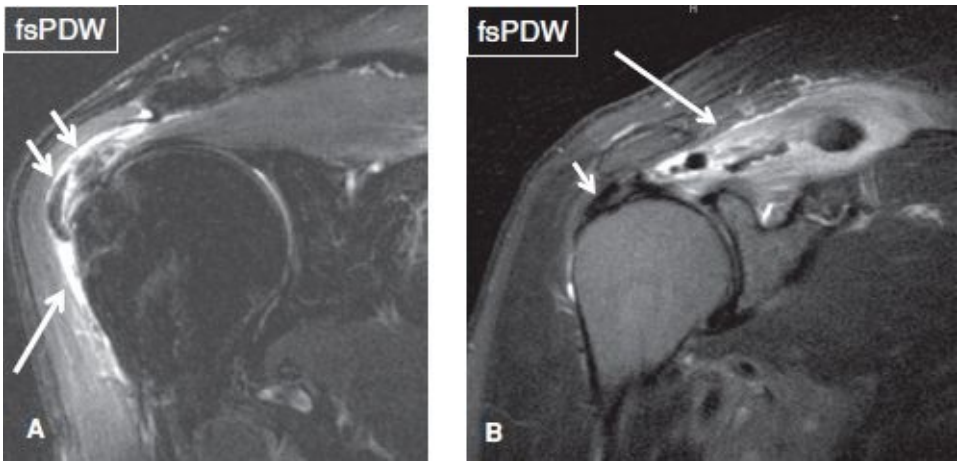

Fig. 41: Active phase of calcific tendinitis. Coronal images of different cases. **A:** Note moderate subacromial/subdeltoid bursitis (*long arrow*), as well as hypointense lesions (*short arrows*) adjacent to the greater tuberosity, corresponding to calcified deposits. **B:** Hypointense lesion (*short arrow*) adjacent to the greater tuberosity corresponds to calcified tendinous deposits. Edema of the supraspinatus tendon (*long arrow*) reflects calcific myositis.

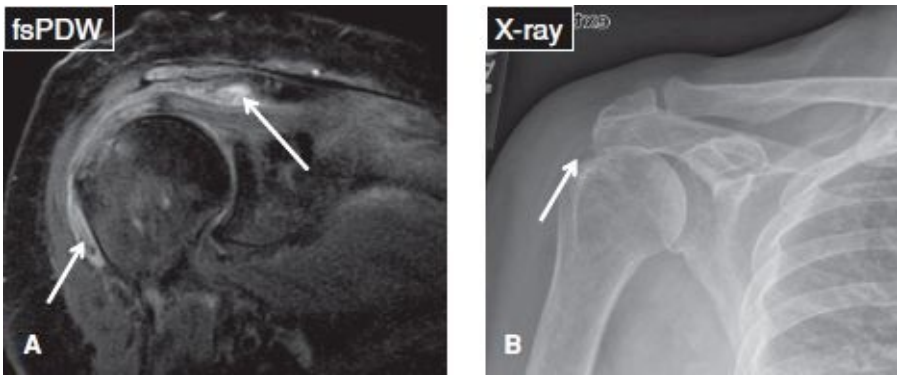

Fig. 42: Active phase of calcific tendinitis. **A:** Coronal image demonstrates moderate subacromial/subdeltoid bursitis with calcific debris (*arrows*). **B:** There is faint amorphous calcification on the anteroposterior radiograph (*arrow*).

3. The adhesive periarthritis phase, which is characterized clinically by debility, pain, and limited range of motion. Imaging modalities exhibit SASD bursitis changes, synovial thickening and calcified deposits within the RC and occasionally within the adjacent bone (Fig. 43).

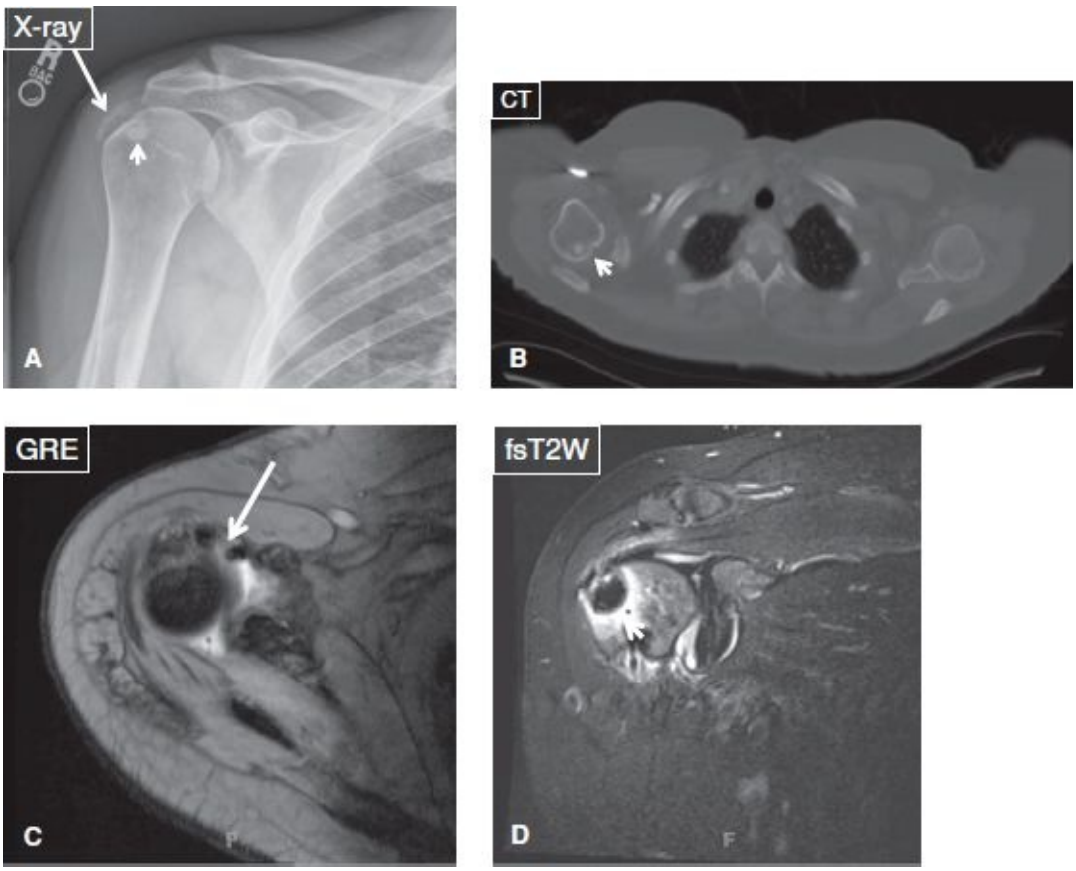

Fig. 43: Calcific tendinitis mimicking tumor. Anteroposterior radiograph **(A),** axial CT scan **(B),** and axial **(C)** and coronal **(D)** MR images demonstrate a relatively large calcified subarticular deposit (*short arrows*) within the humeral head, which can mimic a neoplasm. The adjacent calcified deposits (*long arrows*) within the rotator cuff confirm the case is calcific tendinitis.

RC tendon contusions from direct injury may mimic RC tears but can be differentiated

from the latter by the absence of focal tendon contour changes, the normal position of the myotendinous junction, as well as by associated signs of trauma, such as bursal rupture, muscle strain, bony contusion, or fracture.

Partial RC tendon tears can be graded according to either the *Ellman classification,* which classifies tears based on their thickness and depth, into low grade (thickness <3 mm, involving <25% of RC thickness), intermediate grade (thickness 3 to 6 mm, involving 25% to 50% of RC thickness), and high grade (thickness >6 mm, involving >50% of RC thickness); or the *Cofield classification,* which classifies tears based on their anteroposterior width, into small (<1 cm), medium (1 to 3 cm), large (3 to 5 cm), and massive (>5 cm). Some orthopods use simple terminology, whether one tendon is torn or, two or more tendons are torn to decide their treatment approach. Snyder and Stetson developed a comprehensive classification that describes the tear location, size of the tear, and tendon quality for each RC tendon separately. In each RC tendon (supraspinatus, infraspinatus, subscapularis), the status of the articular (A) and bursal (B) sides is graded using a 5-scale scoring system (0 = normal, I = scuffing, II = fraying, III = partial-thickness tear, IV = near full-thickness tear). Full-thickness tears (C) are graded using a 4-scale scoring system (I = small full-thickness pinhole tear or <1 cm tear, II = 1 to 3 cm full thickness tear, III = 3 to 5 cm full-thickness tear, IV = >5 cm, complex/delaminating tear) (Figs. 44–57).

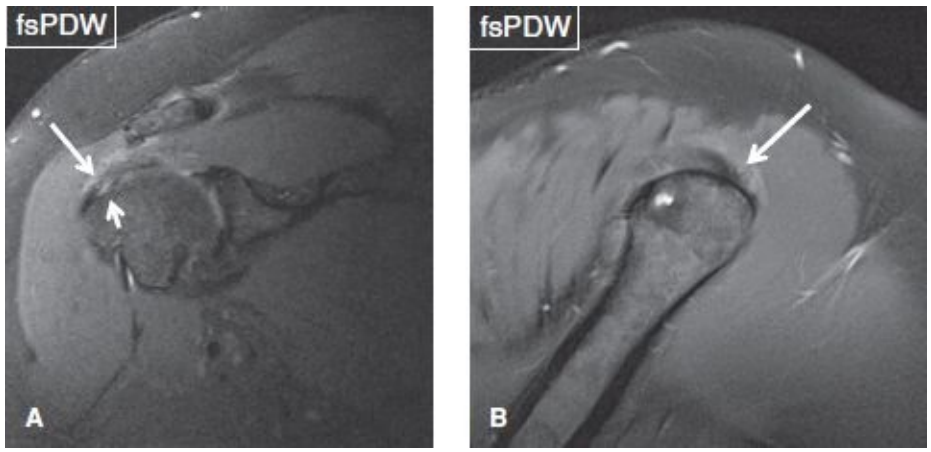

Fig. 44: Coronal **(A)** and sagittal **(B)** images demonstrate fraying of the bursal surface of the supraspinatus tendon (*long arrows*). *Short arrow* in **(A)** indicates a coexistent articular-sided, low-grade partial tear of the tendon attachment.

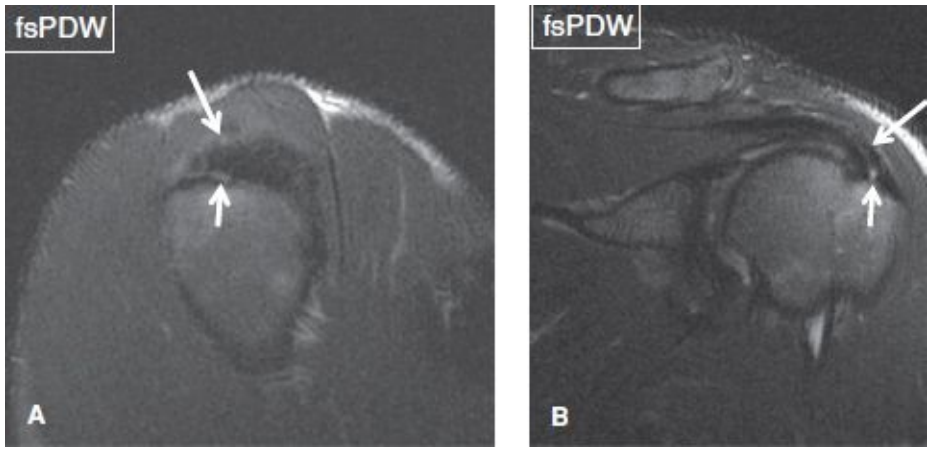

Fig. 45: Sagittal **(A)** and coronal **(B)** images demonstrate fraying of the bursal surface (*long arrows*) and a partially fibrosed low-grade articular-sided partial tear (*short arrows*) of the supraspinatus tendon.

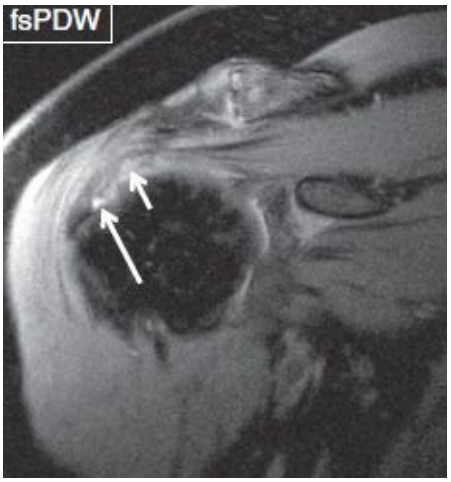

Fig. 46: Coronal image exhibits diffuse fraying of the articular surface of the supraspinatus tendon, as well as an intermediate-grade articular-sided partial tears at the attachment site (*long arrow*) and the critical zone (*short arrow*).

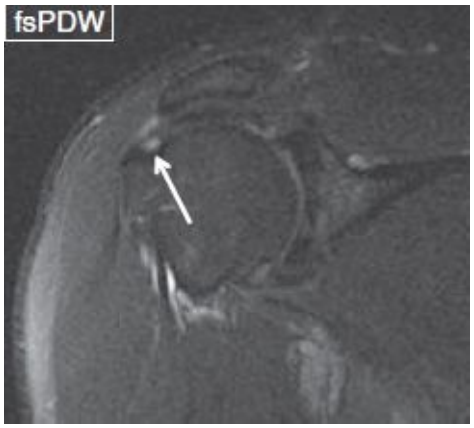

Fig. 47: Coronal image shows a high-grade articular-sided partial tear (*arrow*) of the supraspinatus tendon.

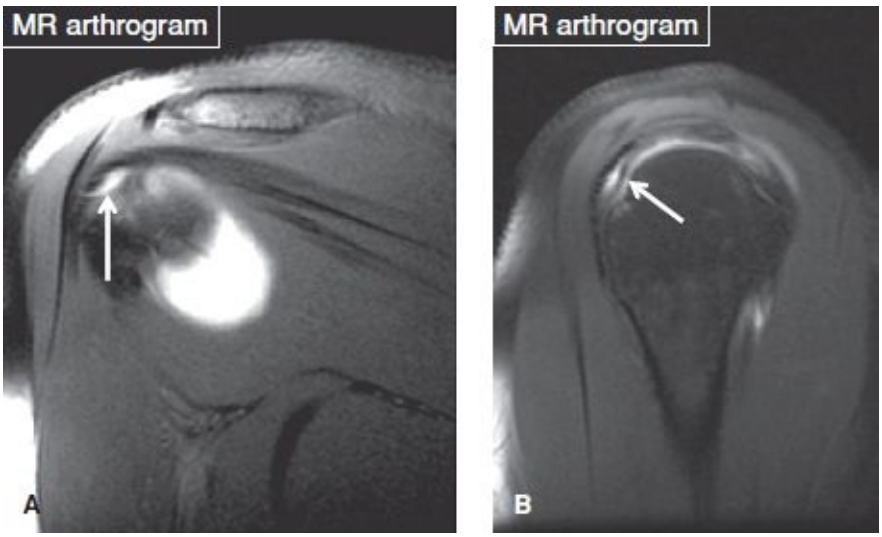

Fig. 48: Coronal **(A)** and sagittal **(B)** MR arthrography images exhibit an intermediate-grade articular-sided tear of the infraspinatus tendon (*arrows*).

Fig. 49: Coronal image shows a near full-thickness tear of the supraspinatus tendon (*arrow*).

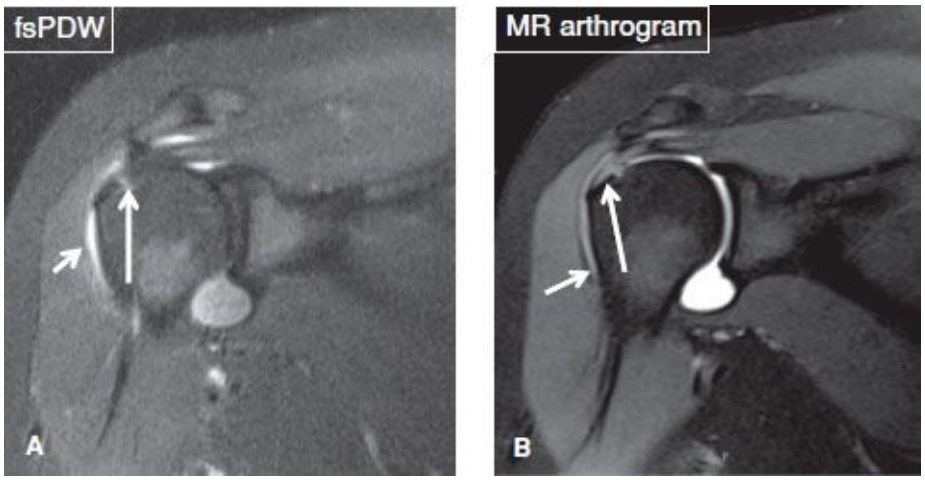

Fig. 50: Pinhole full-thickness tear of the supraspinatus tendon. **A:** Coronal image show a near full-thickness tear of the supraspinatus tendon (*long arrow*). Concomitant fluid collection within the subacromial/subdeltoid bursa raises suspicion that the tear might be of full thickness. **B:** The corresponding coronal MR arthrography image demonstrates extravasation of contrast within the subacromial/subdeltoid bursa (*short arrow*), establishing the diagnosis of a pinhole full-thickness rotator cuff tear. More intrasubstance extension of the tear is also evident (*long arrow*).

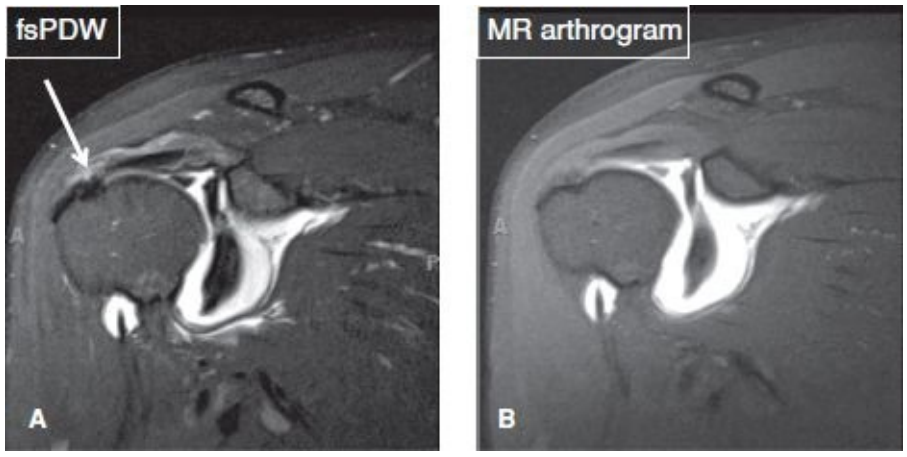

Fig. 51: Bursal-sided rotator cuff tear. **A:** Coronal image show a bursal-sided intermediate-grade tear of the supraspinatus tendon (*arrow*). **B:** In the corresponding MR arthrography image, the tear is not evident since the contrast medium cannot reach the bursal surface of the tendon. Therefore, it is important to do T2 W or PDW image as part of MR arthrography imaging.

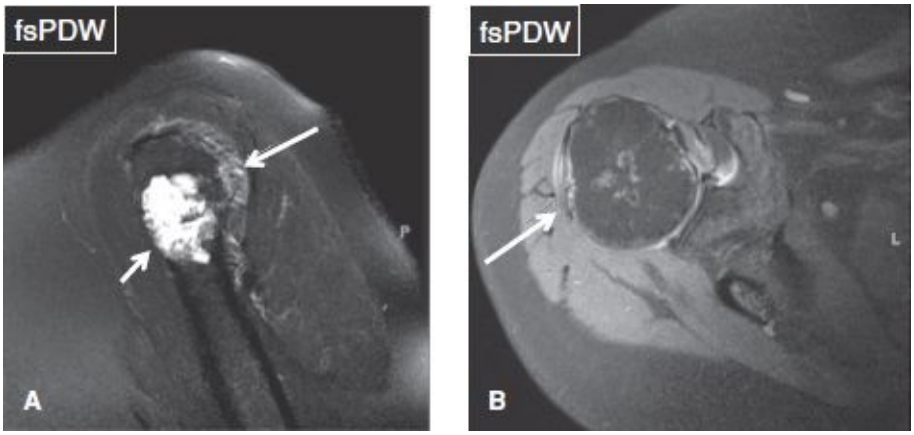

Fig. 52: Teres minor tendon tear. Sagittal **(A)** and axial **(B)** images show an intermediate-grade partial tear of the distal teres minor tendon (*long arrows*). Note incidental enchondroma of the humeral head (*short arrow* in **A**).

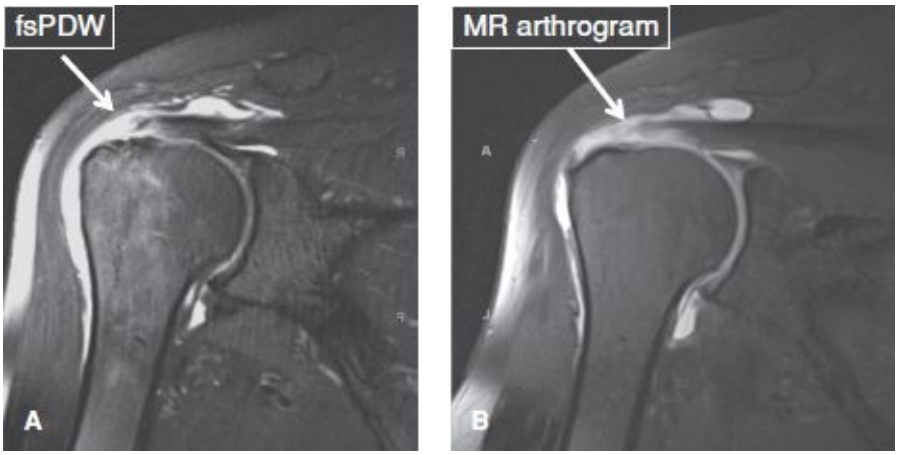

Fig. 53: Full-thickness rotator cuff tear. Conventional **(A)** and arthrography **(B)** coronal images demonstrate full-thickness tear of the supraspinatus tendon with proximal retraction (*arrows*). Notice more retraction of the articular-sided fibers, common finding in associated

delaminations.

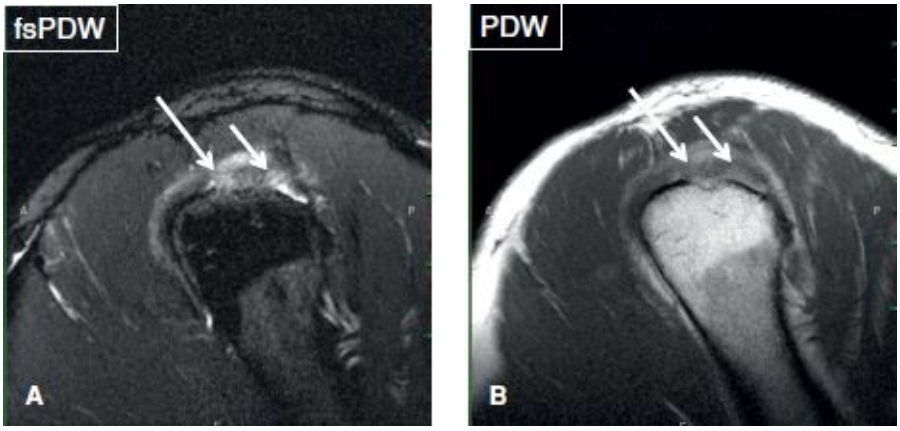

Fig. 54: Near full-thickness and high-grade rotator cuff tears. Sagittal images demonstrate near full-thickness (*long arrows*) and high-grade (*short arrows*) tears of the infraspinatus tendon at the attachment site.

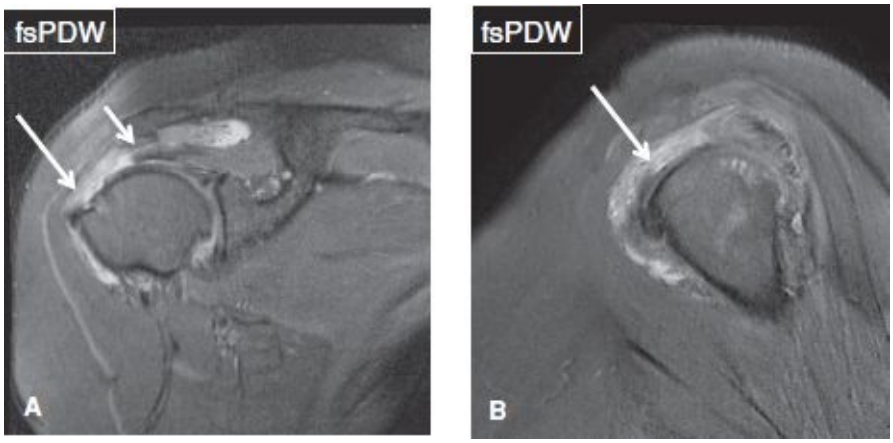

Fig. 55: Full-thickness and full-width supraspinatus tendon tear. Coronal **(A)** and sagittal **(B)** images demonstrate complete (full-width) tear of the supraspinatus tendon at the attachment site (*long arrows*). The torn tendon is moderately retracted (*short arrow* in **A**).

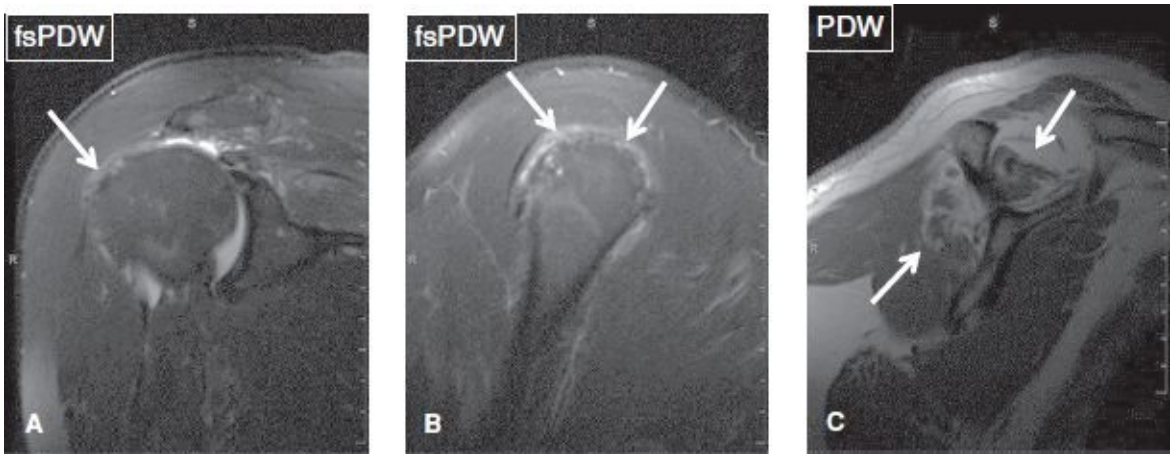

Fig. 56: Full-thickness and full-width masssive rotator cuff tear. Coronal **(A)** and sagittal **(B)** images demonstrate complete (full-width, full-thickness) tears of the supraspinatus and infraspinatus tendons (*arrows*). The torn tendons are severely retracted to the level of the

glenoid. Sagittal image **(C)** severe muscle atrophy (*arrows*).

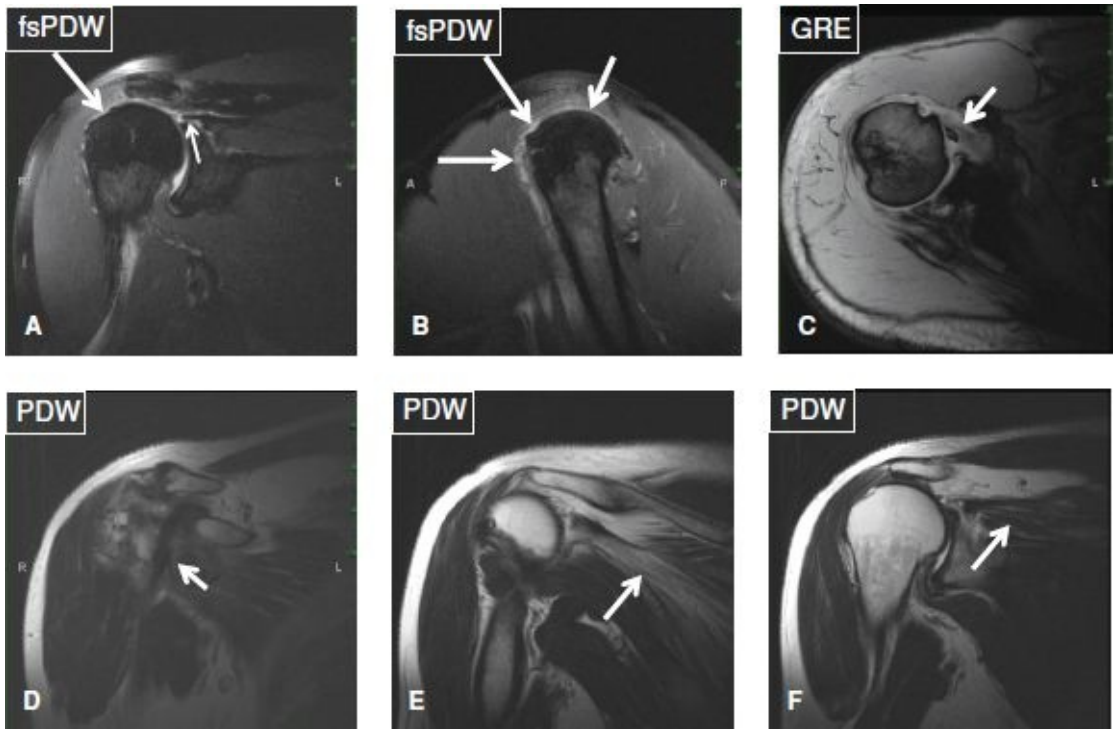

Fig. 57: Massive rotator cuff tear. Coronal **(A)** and sagittal **(B)** images demonstrate complete (full–thickness, full-width) tears of the supraspinatus, infraspinatus, and subscapularis tendons (*long arrows*). The supraspinatus tendon is severely retracted (*short arrow* in **A**). Axial **(C)** and coronal **(D)** images show medial subluxation of the biceps tendon (*arrows*), whereas the humeral head is posteriorly subluxed. The respective coronal images **(E)** exhibit severe (grade 4) fatty infiltration of the infraspinatus (*arrow* in **E**) and mild (grade 1) fatty infiltration of the supraspinatus (*arrow* in **F**) muscle.

With the above knowledge, we are now ready to fill out the checklist. First, describe tendinosis as mild, moderate, or severe based on the degree of diffuse signal alterations and/or thickening on the coronal and sagittal images. If tendon is completely torn and retracted, it may be difficult to assess the tendon quality, and it is a moot point at that juncture anyway. Describe any articular or bursal fraying to suggest tendon quality. Then, describe the superimposed partial tear, as articular- or bursal-sided for the supraspinatus and infraspinatus tendons and indicate its location (attachment site, critical zone, or myotendinous junction). Measure the craniocaudal size of the tear in the coronal plane and grade it as low-grade, intermediate-grade, or high-grade/near full-thickness. Measure the anteroposterior size of the tear in the sagittal plane or describe how much portion of the supraspinatus and/or infraspinatus tendons is involved (such as anterior half, anterior two-thirds, or central one-third fibers, etc.). Find any full-thickness components, separately measure and report. Sometimes, there may be a puddle of fluid in the SASD bursa adjacent to the high-grade/near full-thickness tear, and then add a disclaimer; full-thickness pinhole perforation cannot be not entirely excluded. Such perforations can be confirmed by MR/CT arthrogram, which shows leakage of contrast into the SASD bursa. If there are multiple

articular-sided/bursal-sided tears, one can broadly mention multifocal tears, and measure the one/two larger ones on each surface.

One should distinguish isolated myotendinous muscle strains/tears from attachment tears. They can occur in both the supraspinatus and the infraspinatus (Figs. 58–60). Musculotendinous tears of the infraspinatus have been referred to as "novel lesions." They are important to correctly characterize and describe, as most of the involved individuals will develop fatty replacement and atrophy of the infraspinatus over time. These patients are treated with physiotherapy and surgical results have not been encouraging. It has recently been suggested that early diagnosis and tendon repair may restore muscle tension and prevent complete functional muscle loss.

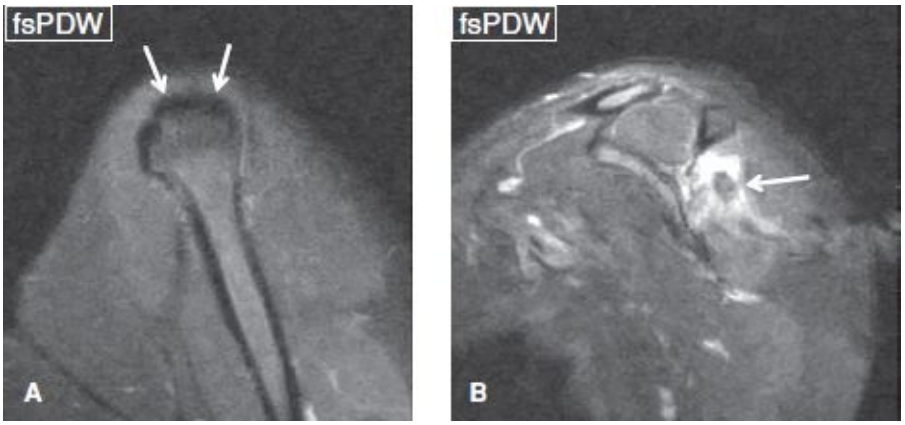

Fig. 58: Myotendinous junction rotator cuff tear. Sagittal images. The rotator cuff tendons are normal at their attachment site (*arrows* in **A**). At the level of the scapula, there is a high-grade myotendinous junction tear of the infraspinatus muscle (*arrow* in **B**), a critical diagnosis to establish, since the entity is considered inoperable and is best treated by physiotherapy and rehabilitation.

Fig. 59: Myotendinous junction rotator cuff partial tear. Coronal image shows fluid-like signal in the myotendinous junction of the supraspinatus muscle (*arrow*), along with surrounding perimuscular edema.

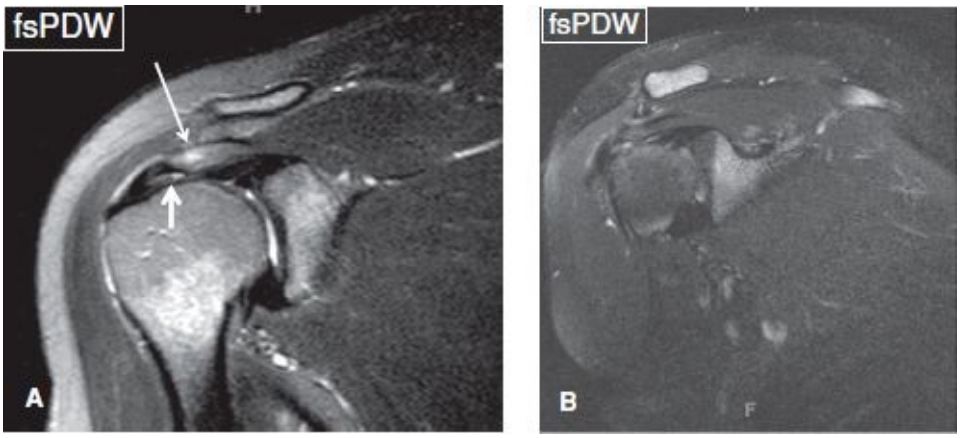

Fig. 60: Myotendinous tear of the supraspinatus tendon. **A:** Coronal image shows a tear of the myotendinous junction (*long arrow*) as well as an articular-sided tear of the critical zone of the supraspinatus muscle (*short arrow*). **B:** Coronal image from a 5-month follow-up examination some fill-in of the fibrous tissue in the myotendinous tear and persistence of the critical zone tear.

In the subscapularis tendon, intrasubstance (interstitial or delaminating) tears are common. The subscapularis tears can also be measured in two dimensions on the axial and sagittal images, and described as partial or full-thickness tears. Alternatively, one can define involvement of the superior or inferior fibers on the sagittal images, and attachment, mid-portion and myotendinous junction involvement on the axial images. The tears are more commonly interstitial and often appear longer on axial images as compared to the sagittal images. Most subscapularis tendon tears involve the superior third of the tendon, and most often, these occur near the attachment (Figs. 61–65). They may be associated with lesser tuberosity cysts and enthesopathy. Subscapularis tendon tears present with anterior shoulder pain and tenderness, and decreased internal rotation. The commonly used clinical test includes the lift-off test, in which the patient rests the dorsum of the hand on the back in the lumbar area. Inability to move the hand off the back by further internal rotation of the arm suggests injury to the subscapularis muscle or tendon; however, this test may have limited utility if there is limited range of motion due to pain. Underlying subcoracoid impingement (anterior pain with internal rotation) may be present, and that could also be primary or secondary. Most often, it is secondary related to supraspinatus/infraspinatus tears and RC muscle dyskinesia that leads to narrowing of the subcoracoid space to less than 8 to 9 mm (normal >11 mm). Coracoid index and other measurements have been described that correlate with impingement. It is again a clinical diagnosis similar to other impingements, however, one should look for both bony and soft tissue findings that can raise the suspicion of impingement, such as, subscapularis tendon lesions (tendinosis and/or tears), LHBT lesions (tendinosis, tenosynovitis, subluxation, or tears), and changes in the lesser tuberosity and/or the coracoid process (bony hypertrophy, enthesopathy, cystic changes, and/or edema) (Fig. 66). Primary (anterior) subcoracoid impingement is less common and is defined as narrowing of the subcoracoid space less than 5.5 mm, associated with one or a combination of the above described soft tissue and bony lesions (Figs. 67, 68).

Primary impingement may require coracoplasty and subacromial decompression.

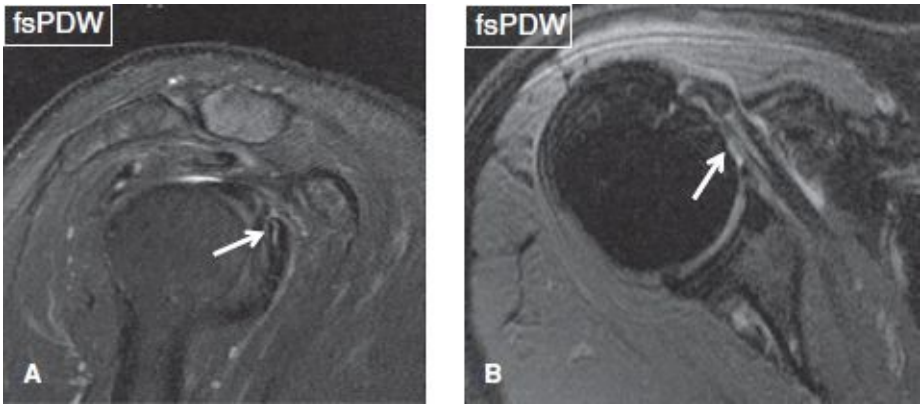

Fig. 61: Low-grade tear of the subscapularis tendon. Sagittal **(A)** and axial **(B)** images exhibit fluid-like linear signal (*arrows*) within the superior third of the subscapularis tendon.

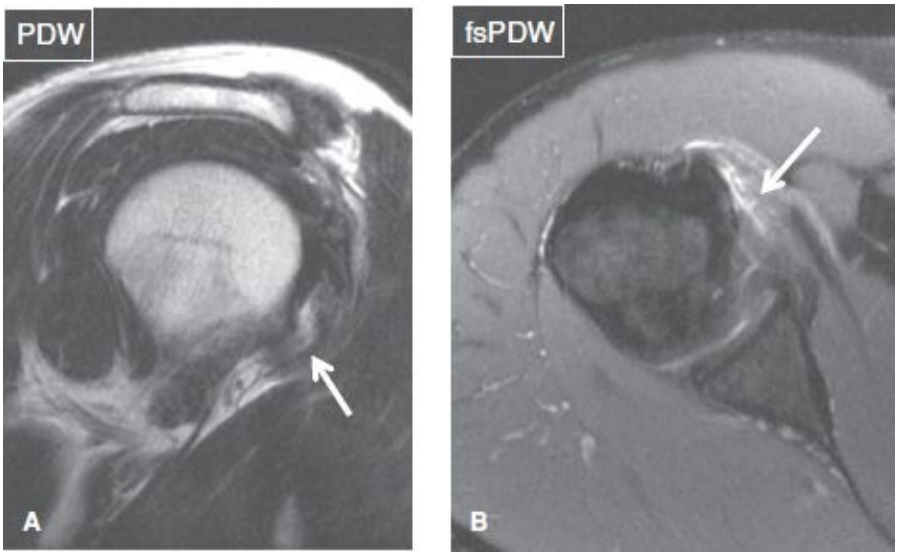

Fig. 62: High-grade tear of the subscapularis tendon. On sagittal **(A)** and axial **(B)** images, there is high-grade tear of the fibers of the inferior half of the subscapularis tendon (*arrows*).

Fig. 63: Full-thickness tear of the subscapularis tendon. Sagittal image demonstrates fluid-

like signal and complete absence of attachment of fibers of the subscapularis tendon (*arrow*).

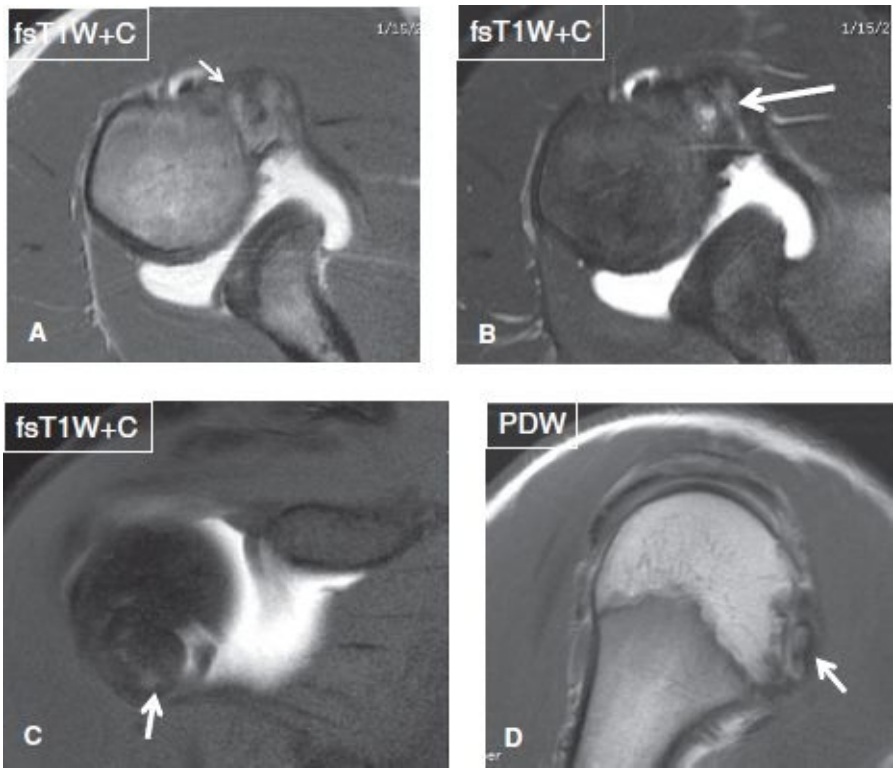

Fig. 64: Subscapularis tear with avulsion of the lesser tuberosity. Axial **(A, B),** coronal **(C),** and sagittal **(D)** images demonstrate acute on chronic avulsion of the lesser tuberosity (*short arrows*) along with a tear of the subscapularis tendon at the attachment site (*long arrow* in **B**).

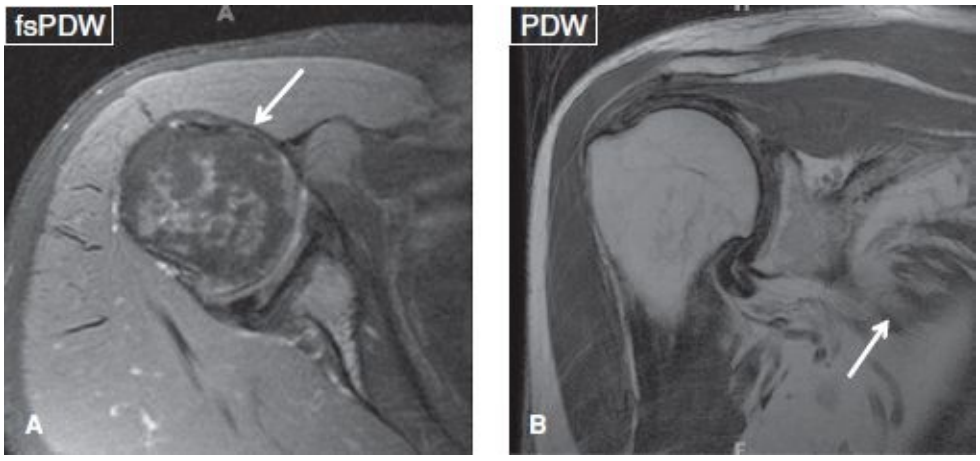

Fig. 65: Chronic subscapularis tear. **A:** On the axial image, the subscapularis tendon is not visualized at its expected location, and the lesser tuberosity (*arrow*) is covered with a thin fibrous band. **B:** The respective coronal image demonstrates grade 3 fatty infiltration of the subscapularis muscle (*arrow*) due to chronic disuse.

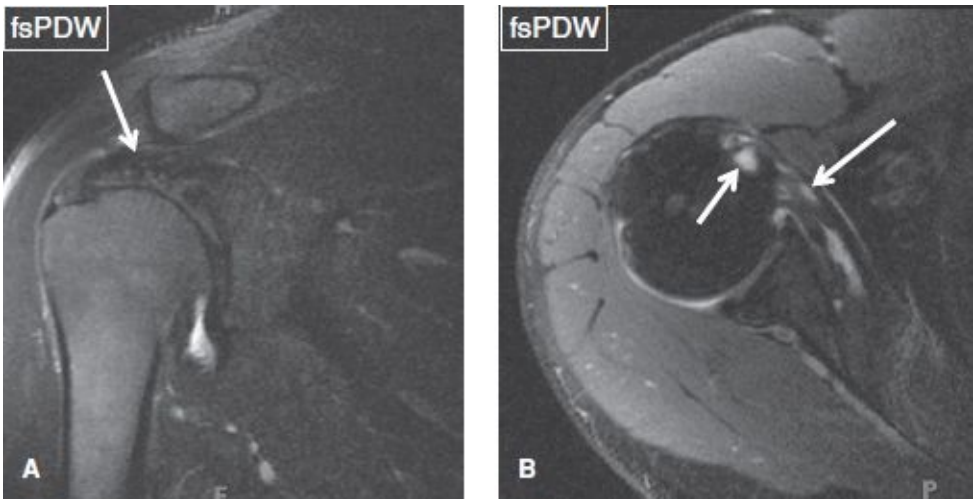

Fig. 66: Secondary subcoracoid impingement findings. **A:** Coronal image demonstrates moderate tendinosis of the supraspinatus tendon with multifocal low-grade undersurface tears (*arrow*). **B:** The respective axial image exhibits interstitial tears of the subscapularis tendon (*long arrow*) and subcortical cystic changes at the lesser tuberosity (*short arrow*).

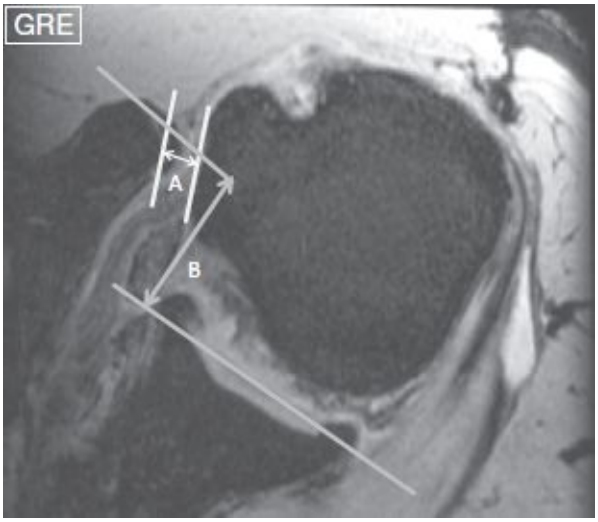

Fig. 67: Primary subcoracoid impingement. Axial image shows narrow subcoracoid space measuring 5 mm (normal >11 mm) **(A)** and high coracoid index **(B)** measuring 19 mm (normal >8 to 10 mm). Coracoid index is measured as the distance from the tip of the coracoid process to the tangential plane of the glenoid articular surface.

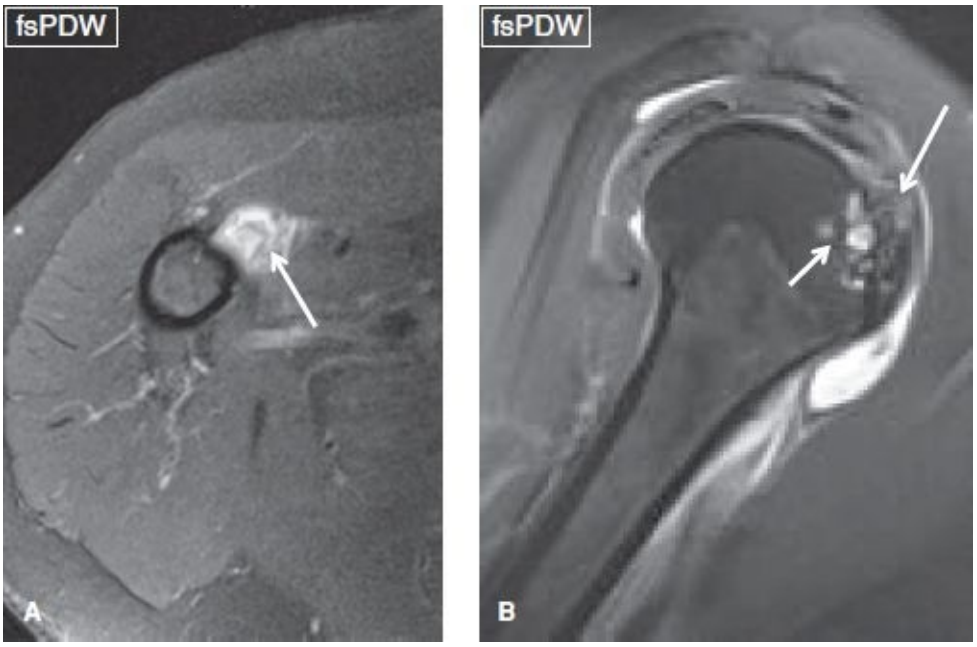

Fig. 68: Primary subcoracoid impingement. **A:** Axial image shows tenosynovitis of the biceps sheath with absent (torn) biceps tendon (*arrow*). **B:** The respective sagittal image exhibits low-grade tears of the superior subscapularis muscle, moderate tendinosis (*long arrow*) along with underlying subcortical cystic changes (*short arrow*).

In full-thickness tears, measure the tendon retraction in the coronal plane. Mild, moderate, and severe retraction refer to displacement of torn tendon adjacent to the attachment site, at the level of midhumeral head, and to the level of the glenoid, respectively. In delaminating tears, there is variable retraction of articular and bursal tendon fibers, and both retractions should be reported separately (Figs. 69–73). The surgeon may have to resect both retracted tendons, refashion the edges to bring them to similar level, and reattach them to the greater tuberosity. Isolated bursal tears are less common and are associated with one of the three common causes, such as moderate to severe subacromial impingement (especially in older patient), hydroxyapatite deposition disease, or recent fall with direct impact injury. Falls are commonly associated with partial SASD bursal rupture, which should direct the attention of the reader to evaluate bursal side of the RC tendonss.

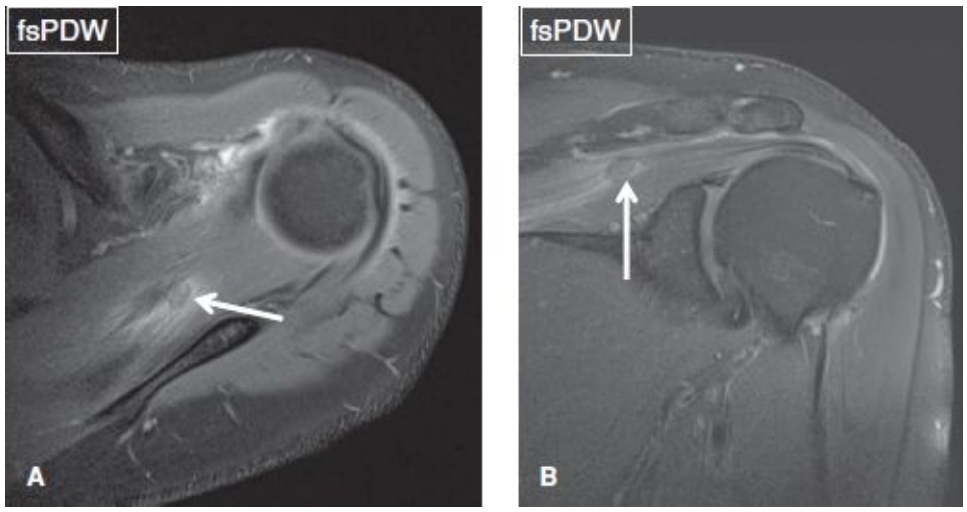

Fig. 69: Delaminating rotator cuff tear. On axial **(A)** and coronal **(B)** images, a portion of the supraspinatus tendon has retracted proximally within the muscle and has assumed a rounded configuration (*arrows*).

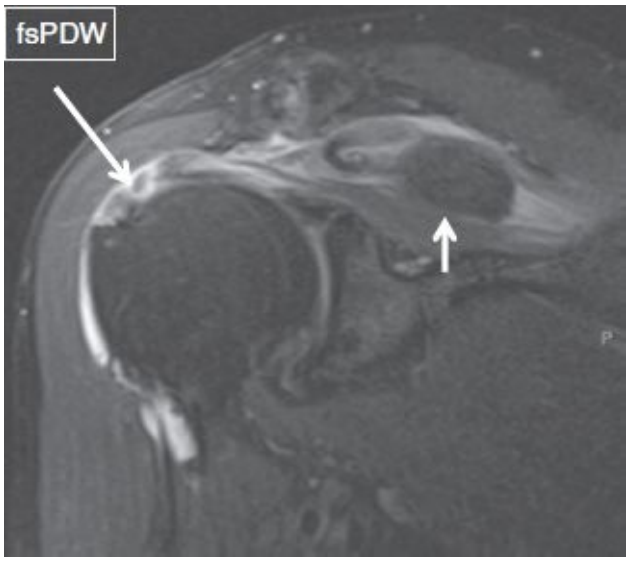

Fig. 70: Delaminating rotator cuff tear. Coronal image shows a full-thickness tear of the supraspinatus tendon (*long arrow*). The torn fibers have retracted proximally and have assumed a rounded configuration (*short arrow*).

Fig. 71: Delaminating rotator cuff tear. Coronal image shows a near full-thickness tear of the supraspinatus tendon (*long arrow*) with proximal retraction of the torn fibers (*short arrow*).

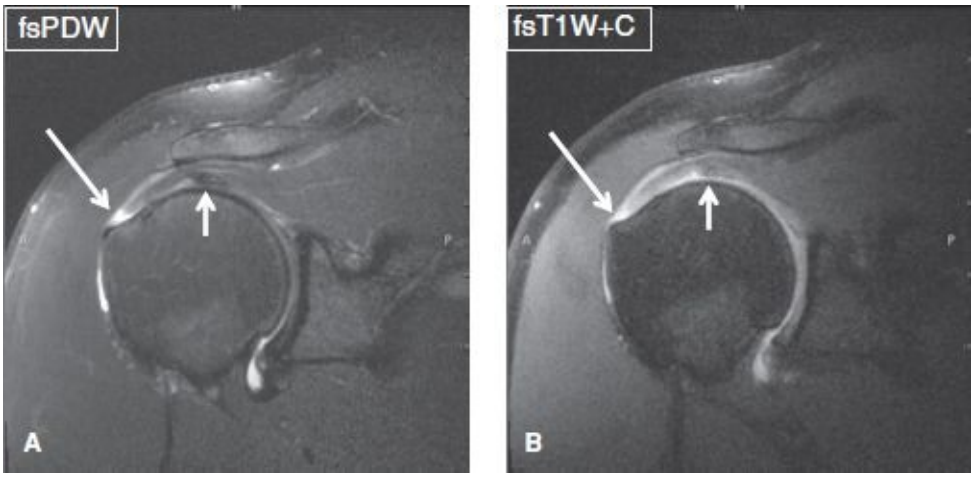

Fig. 72: Delaminating rotator cuff tear. Coronal conventional **(A)** and arthrography **(B)** images demonstrate a full-thickness tear of the supraspinatus tendon with moderate proximal retraction of the torn articular fibers (*short arrows*) and mild retraction of the bursal fibers (*long arrows*).

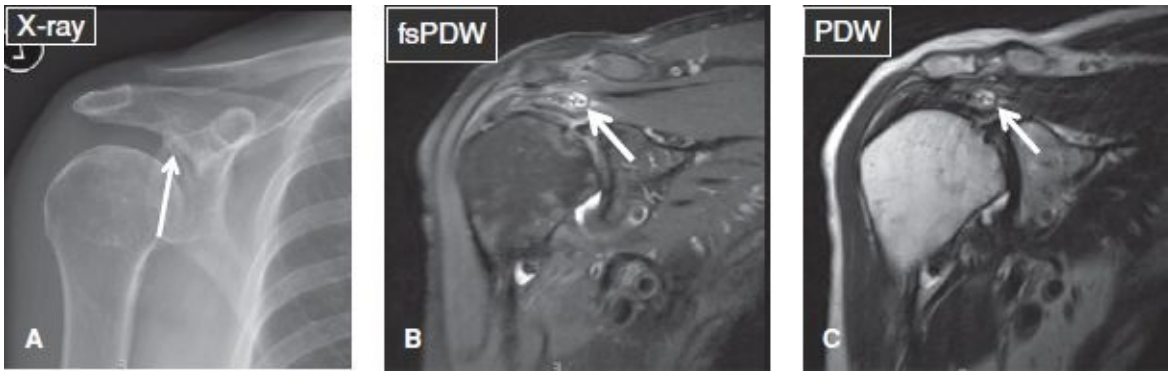

Fig. 73: Delaminating rotator cuff tear. Anteroposterior radiograph **(A)** and coronal **(B, C)** images demonstrate rotator cuff cyst containing bodies (*arrows*) between the layers of the supraspinatus muscle, formed as a result of a delaminating tear.

RC tears are associated with disuse atrophy of muscles over time. Fatty replacement and atrophy of RC muscles can be separately described, as these can be disproportionately present. Supraspinatus atrophy can be described based on occupation ratio of the suprascapular fossa (Thomazeau classification), as normal/mild atrophy (>0.6 to 1), moderate atrophy (0.4 to 0.6), and severe atrophy (<0.4). Fatty degeneration of RC muscles is described based on the four stages of Goutalliers classification (in which *grade 0* refers to normal muscle with no fatty atrophy, *grade I* to some fatty streaks, *grade II* to <50% fatty replacement/atrophy, *grade III* to 50% fatty replacement/atrophy, and *grade IV* to >50% fatty replacement/atrophy) (Fig. 57). Authors prefer to assess atrophy and fatty replacement on coronal non–fat-suppressed PD images rather than on the sagittal ones (Fig. 74). This is particularly useful in cases of full-thickness RC tear and severe tendon retraction, in which the muscle bulk may be normal, but the suprascapular fossa may appear empty on sagittal images, giving the false impression of muscle atrophy.

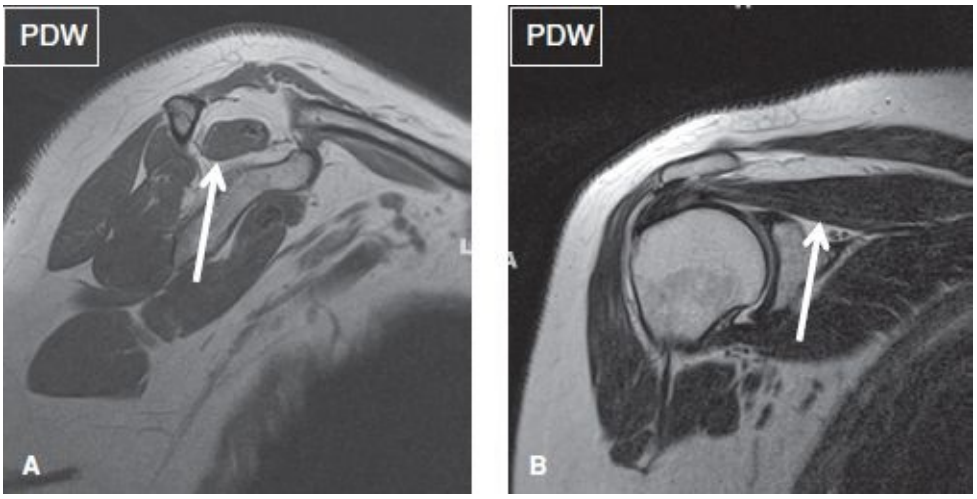

Fig. 74: False impression of supraspinatus muscle atrophy. **A:** On the sagittal image, increased fat around the supraspinatus muscle creates the impression that the muscle is lower in size with respect to the other rotator cuff muscles, indicating moderate atrophy. **B:** In the corresponding coronal image; however, the muscle is normal in size.

ROTATOR INTERVAL AND LONG HEAD BICEPS BRACHII TENDON:

Rotator interval: [<Normal> <Synovial thickening> <Acute sprain>]

Biceps–labral anchor: [<Intact> <Tear>]

Horizontal portion: [<Normal> <Mild / Moderate / Severe tendinosis> <Tear>]

Vertical portion: [<Normal> <tendinosis> <Tear>]

Genu: [<Normal> <Mild / Moderate / Severe tendinosis> <Tear> <Subluxed>]

The rotator interval is a normal triangular-shaped space located between the anterior inferior border of the supraspinatus and the superior border of the subscapularis tendons, with the coracoid process forming the base, and the intertrabecular groove forming the apex. It is filled with fat, contains the CHL, LHBT, and SGL, and is best evaluated on coronal and sagittal images. The rotator interval prevents inferior translation of the humerus (especially in abducted and externally rotated positions), as well as excessive flexion and external rotation. The CHL extends from the coracoid process to the humeral tuberosities and has a medial bundle which attaches to the subscapularis tendon, and a lateral bundle, which attaches to the supraspinatus tendon. These bundles are best seen on sagittal images (Fig. 75). The CHL forms the roof of the LHBT and reinforces the transverse ligament covering the biceps groove. The long head of the biceps muscle can originate from the supraglenoid tubercle, the superior or posterosuperior glenoid labrum or both, whereas the short head arises from the coracoid process, along with the coracobrachialis and pectoralis minor muscles. The LHBT functions as a humeral head depressor and is a secondary restraint to anterior instability, particularly in the abducted and internally

rotated position. The biceps pulley is formed by investing fibers from the SGL, CHL, and the adjacent subscapularis and supraspinatus tendons. From lateral to medial, best seen on sagittal images, the long head of biceps tendon is enveloped by CHL on top and SGL at bottom; at the mid joint level, SGL forms a T-shaped structure with CHL; and finally, near the biceps attachment to labrum, both CHL and SGL cover the biceps lying on the top of the tendon.

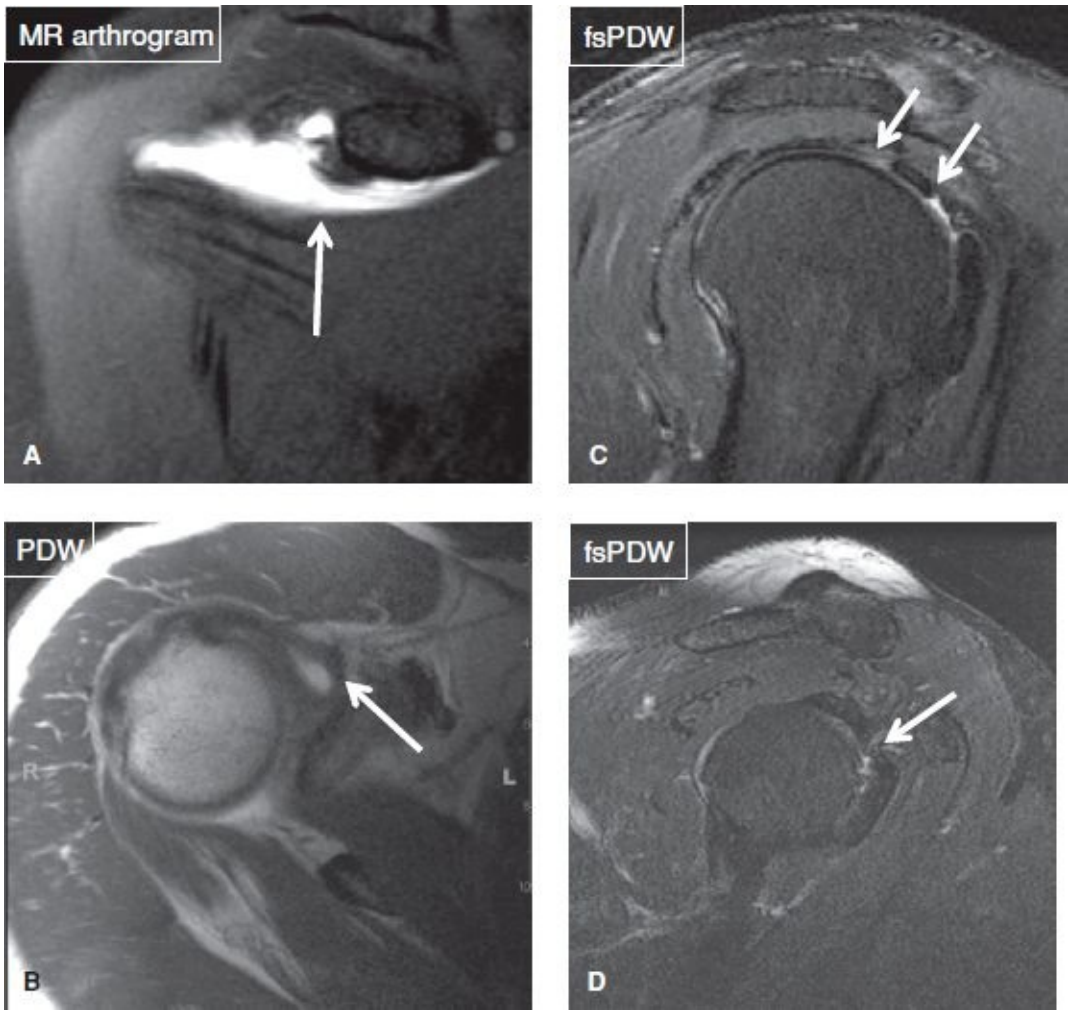

Fig. 75: Normal rotator interval anatomy. **A:** Coronal arthrography image demonstrates the rotator interval filled with contrast (*arrow*). **B:** *Arrow* in axial image indicates the superior glenohumeral ligament paralleling the coracoid process. **(C, D).** Sagittal images show the lateral (*arrows* in **C**) and medial (*arrow* in **D**) bundles of the coracohumeral ligament.

Acute rotator interval injuries are mostly seen in young subjects, and clinically manifest as anterior shoulder pain and instability feeling, especially in 90-degree abducted and externally rotated positions. On MR images, one can see ligamentous and periligamentous edema, as well as fascial fluid within and superior to the interval (Figs. 76, 77). The injury is also referred to as the "hidden lesion" as it is often hidden at arthroscopy. Larger lesions may be associated with injury to the biceps pulley, supraspinatus or infraspinatus tendons. On MR arthrogram, contrast may be seen tracking at the base of the coracoid process or superior to the rotator interval. In subacute and chronic injuries (mostly seen in elderly individuals), one may encounter synovial diverticulum from the interval,

thickened/attenuated CHL or SGL, anteriorly and/or medially subluxed LHBT, or synovial thickening and fibrosis of the rotator interval (Figs. 78–81). Failure to repair the injured structure(s) may result in pain and chronic inferior instability, even after RC surgery.

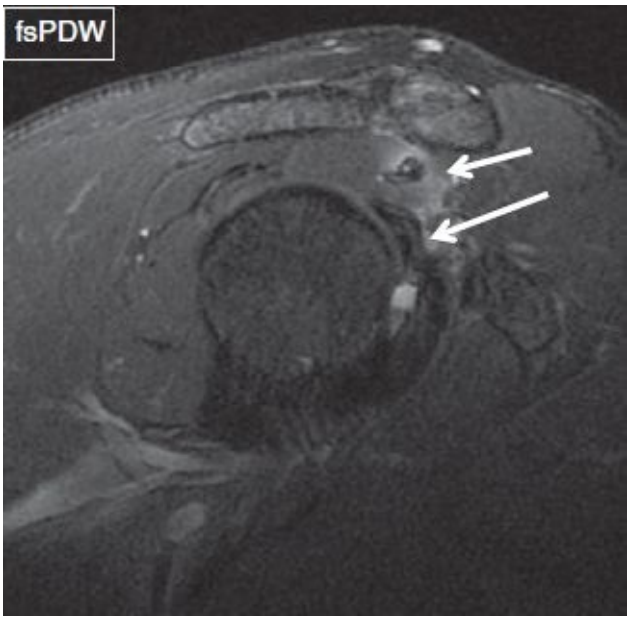

Fig. 76: Acute rotator interval injury. Sagittal image demonstrates mild edema within the rotator interval (*short arrow*). Also note myotendinous junction strain of the supraspinatus muscle. The lateral bundle of CHL is still intact with evidence of periligamentous edema (*long arrow*).

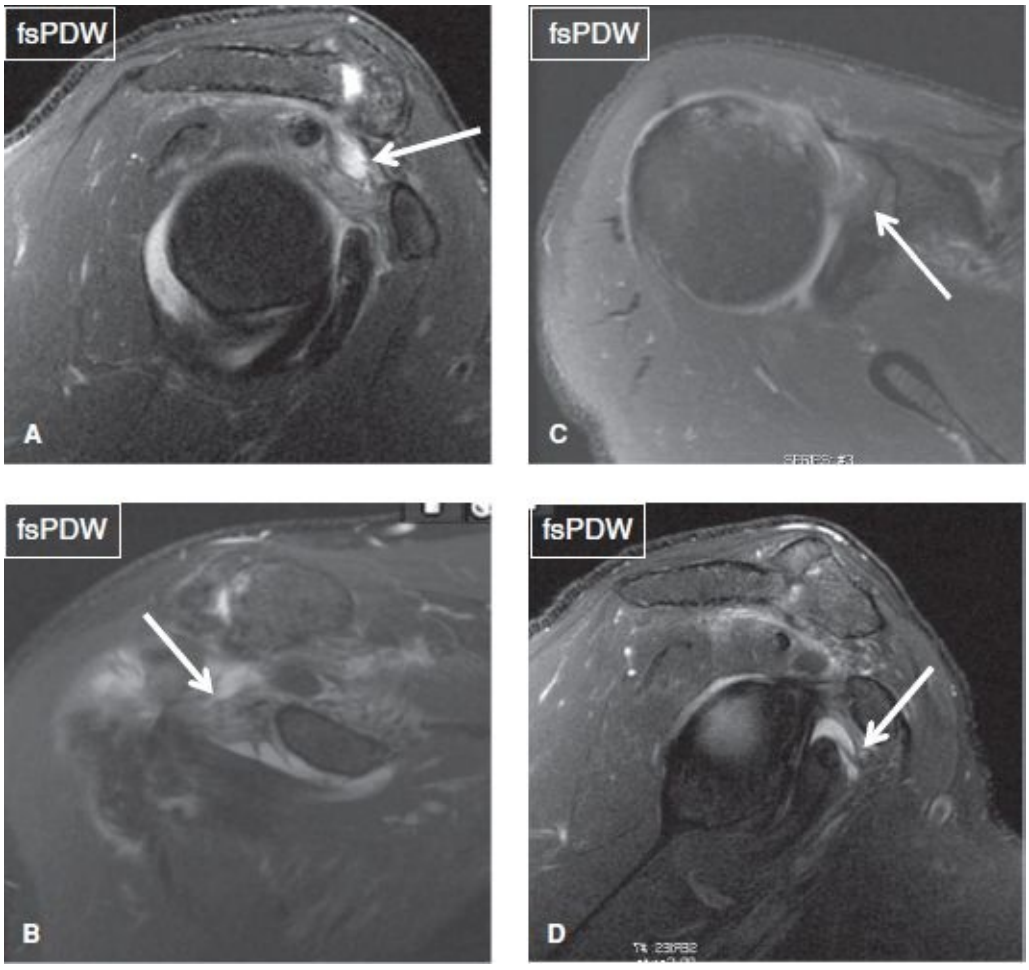

Fig. 77: Rotator interval injury. **A:** Sagittal image shows edema of the rotator interval with thickened partially torn lateral bundle of CHL and ganglion formation (*arrow*), in keeping with subacute injury. **B:** Coronal image exhibits thickening and heterogeneity of the coracohumeral ligament (*arrow*), corresponding to grade II sprain. **C:** Axial image displays a heterogeneous, thickened, and ill-defined superior glenohumeral ligament (*arrow*), also compatible with grade II sprain. **D:** Sagittal image shows intact medial bundle of CHL (*arrow*).

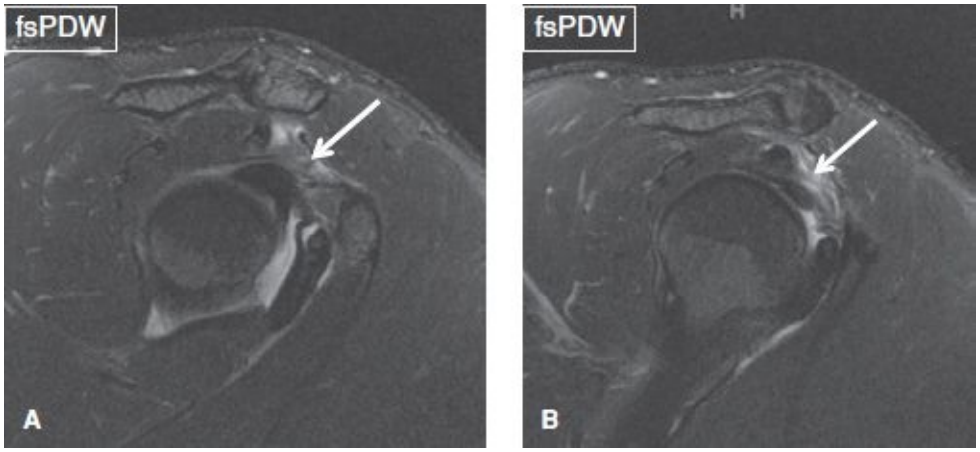

Fig. 78: Subacute grade II sprain of the coracohumeral ligament. Sagittal images show ill-definition of the lateral bundle of the coracohumeral ligament (*arrows*) along with edema and early ganglion formation in the surrounding soft tissues.

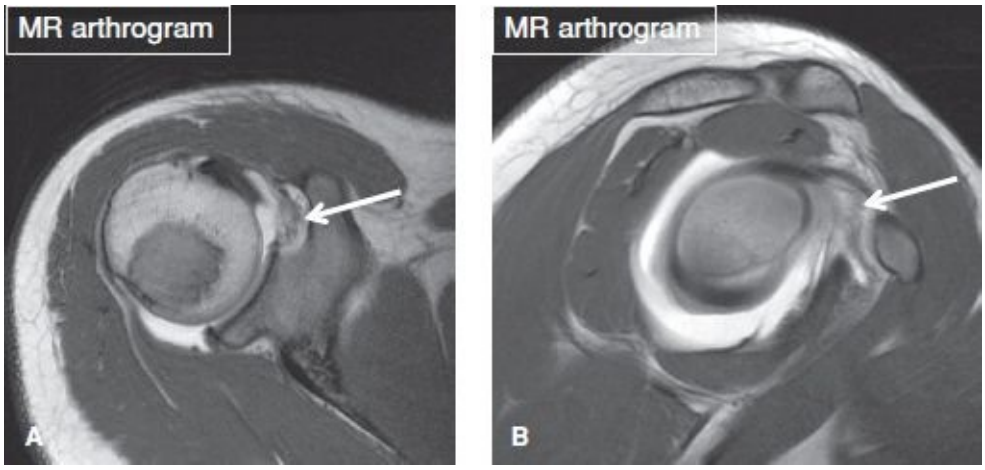

Fig. 79: Subacute grade II sprain of the superior glenohumeral ligament. Axial **(A)** and sagittal **(B)** images exhibit ill-definition of the superior glenohumeral ligament (*arrows*). Notice intact CHL.

Fig. 80: Rotator interval injury. Sagittal **(A),** axial **(B),** and coronal **(C)** images demonstrate tear of the medial bundle of the coracohumeral ligament (*long arrows* in **A** and **C**). Notice intact lateral bundle of CHL (*short arrow* in **A**). The SGL is thickened (*short arrow* in **B**), and a synovial diverticulum (*long arrow* in **B**) has formed.

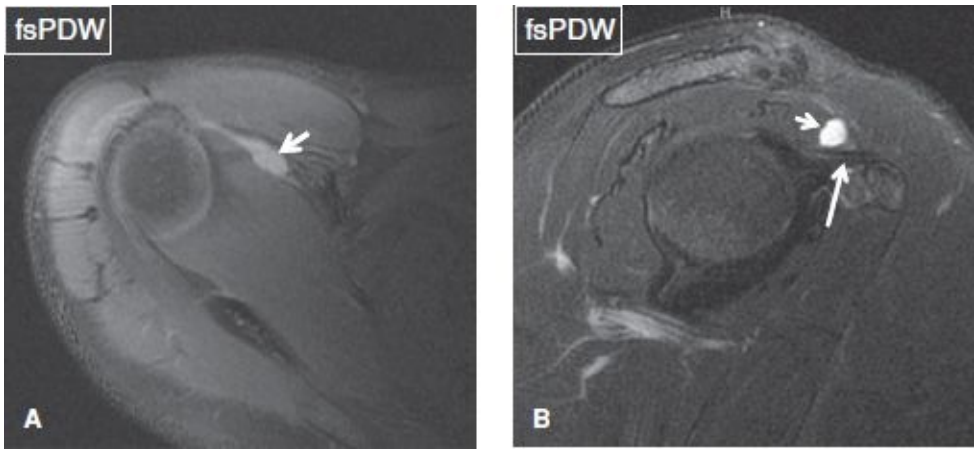

Fig. 81: Indirect indicator of mild prior rotator interval injury. Axial **(A)** and coronal **(B)** images show formation of a synovial diverticulum (*short arrows*) in relation to the roof of the rotator interval. The underlying coracohumeral ligament (*long arrow* in **B**) ligament appears intact.

The LHBT traverses horizontally through the shoulder joint and the rotator interval and is supported by the SGL. The vertical portion is supported by the transverse ligament, which is formed by the subscapularis tendon and the investing layer of the CHL. Within the concave bicipital notch, it is encompassed within a synovial sheath, which normally contains trace amount of fluid, as well as one or two residual synovial strands called the mesotenons. The horizontal and vertical portions of the LHBT normally form a 90-degree angle. Common pathologies include tenosynovitis with or without synovial thickening/loose bodies and tendinosis (depicted as diffuse increased signal and thickening >4 to 5 mm, or attenuation of the tendon) (Figs. 82, 83). Longitudinal split tears are also not uncommon and may involve the vertical or horizontal portions of the tendon (Fig. 84). These lesions are particularly common at the junctional portion (genu of the tendon) due to the increased stress from other associated RC tears. In clinical practice, the most commonly encountered imaging abnormality is diffusely increased signal and thickening of the genu and intra-articular portion of the tendon, with or without superior labral tear/degeneration (Figs. 83,

84). Generally, in elderly and middle-aged subjects, the biceps tendon is most commonly torn from the anchor, while in younger subjects, it tears from the bicipital tuberosity of the radius (Figs. 85, 86). A congenitally bifid LHBT (which demonstrates a diffusely smooth bifid configuration up to the level of the myotendinous junction with possible distinct muscle bellies) should be differentiated from a split tendon (which shows one or more focal split areas with associated tendinosis and/or tenosynovitis) (Figs. 87, 88).

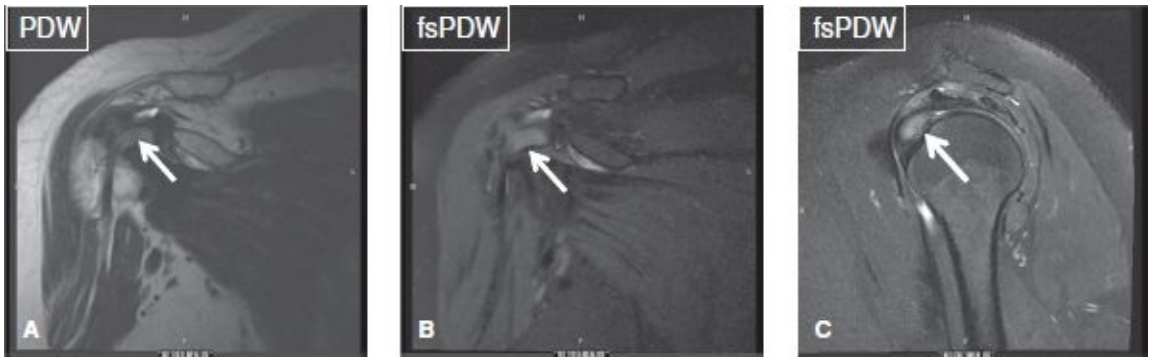

Fig. 82: Biceps tendinosis. Coronal **(A, B)** and sagittal **(C)** images demonstrate moderate enlargement and T2 hyperintensity of the genu and the horizontal portion of the biceps tendon (*arrows*), in keeping with moderate tendinosis.

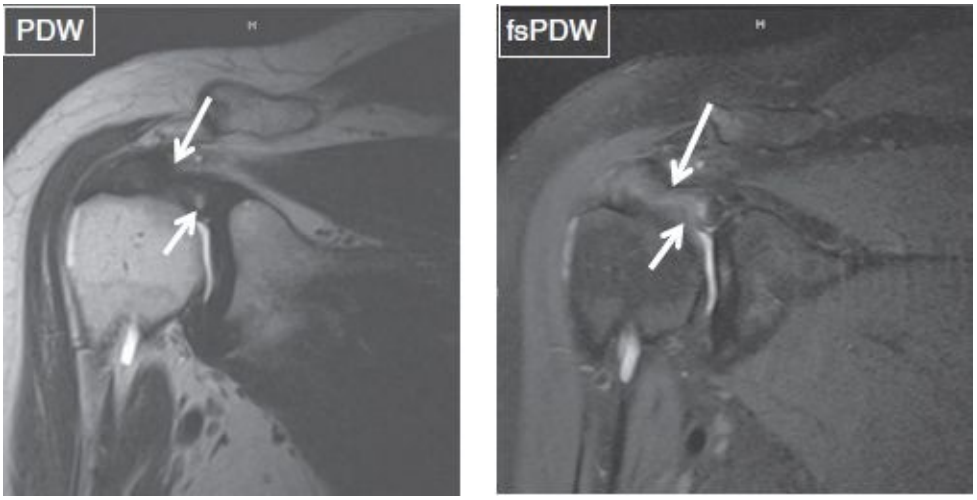

Fig. 83: Biceps tendinosis. Coronal **(A, B)** images exhibit marked enlargement and T2 hyperintensity of the horizontal portion of the biceps tendon and anchor (*long arrows*), in keeping with severe tendinosis. Also note partial tear of the biceps anchor (*short arrows*).

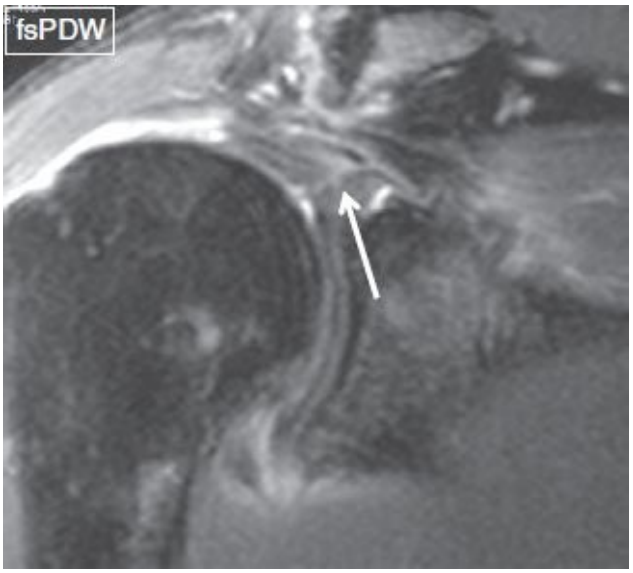

Fig. 84: Partial tear of the biceps anchor. Coronal image exhibits irregular cleft (*arrow*) partly traversing the biceps anchor in keeping with partial tear.

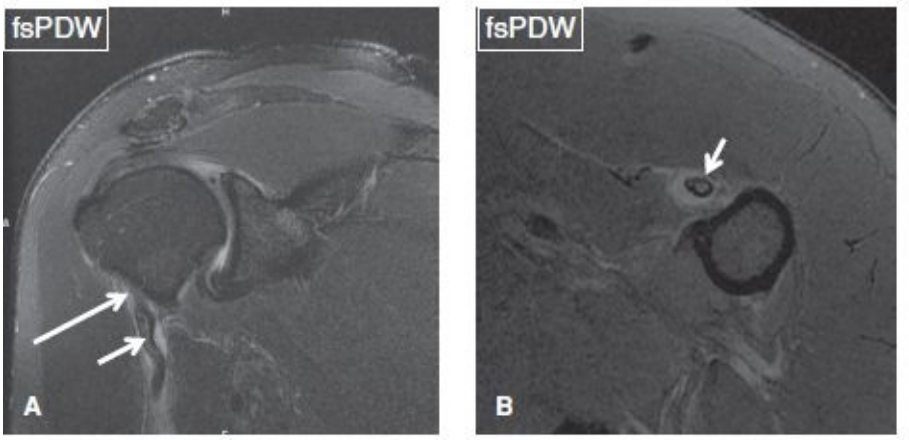

Fig. 85: Biceps tendon tear. Coronal **(A)** and axial **(B)** images demonstrate complete tear and distal retraction of the biceps tendon (*long arrow* in **A**). A longitudinal split tear is also evident in the retracted tendon (*short arrows*).

Fig. 86: Biceps tendon tear at the level of the anchor. Axial **(A),** coronal **(B),** and sagittal **(C)** images exhibit retraction of the linear-shaped torn tendon (*long arrows*) and bulbous-

shaped anchor (*short arrow* in **C**) at the level of the midhumerus.

Fig. 87: Subluxation of bifid biceps tendon. Coronal **(A)** and axial **(B, C)** images show the two subtendons (*short arrows*) of a congenitally bifid biceps tendon. The medial subtendon is subluxed within a partial interstitial tear of the subscapularis tendon (*long arrow* in **B**).

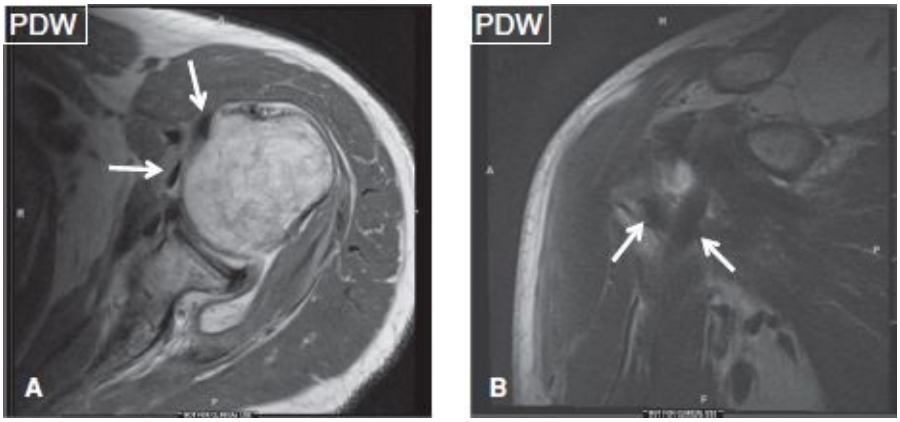

Fig. 88: Subluxation of bifid biceps tendon. Axial **(A)** and coronal **(B)** images show subluxation of both subtendons (*arrows*) of a congenitally bifid biceps tendon in the setting of complete subscapularis tear.

LHBT subluxation is associated with pulley injuries as follows.

- Type I pulley injury (anterior LHBT subluxation) is related to transverse ligament tear (± CHL and/or SGL injury). Underlying shallow bicipital groove may be present.
- Type II pulley injury (anteromedial LHBT subluxation) involves supraspinatus tendon tear and injury to the lateral bundle of the CHL (Fig. 89).

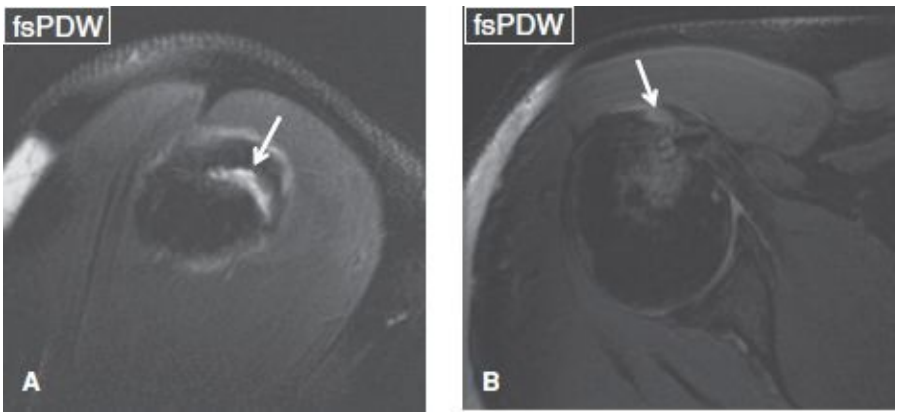

Fig. 89: Type II biceps pulley injury. Sagittal **(A)** and axial **(B)** images show a partial articular-sided tear of the supraspinatus tendon, extending into the transverse ligament (*arrows*) and the lateral bundle of CHL (not shown).

- Type III pulley injury (medial LHBT subluxation into the subscapularis substance) is associated with delaminating/interstitial tear of the subscapularis tendon and injury to the medial bundle tear of the CHL (Figs. 90, 91).

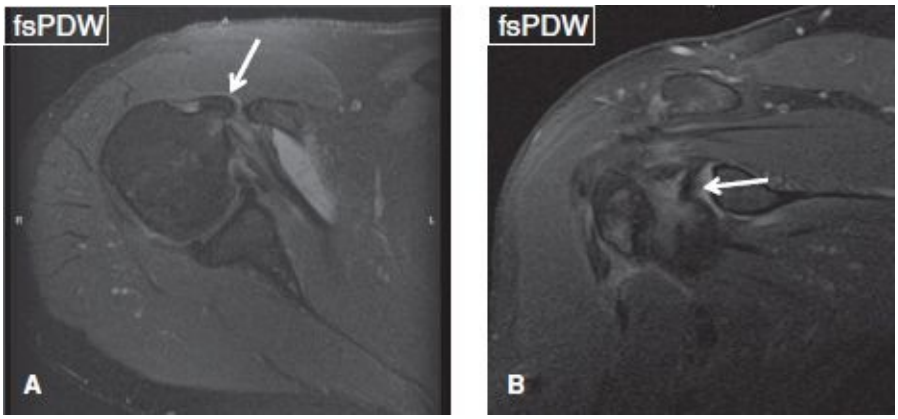

Fig. 90: Type III pulley injury. Axial **(A)** and coronal **(B)** images show medial subluxation of the biceps tendon (*arrows*), which is perched over the lesser tuberosity and minimally extends into a delaminating tear of the subscapularis tendon.

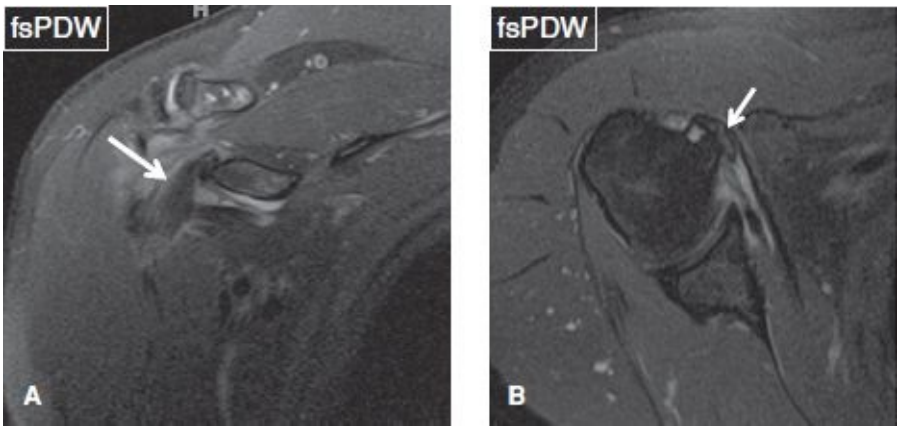

Fig. 91: Type III biceps pulley injury. Coronal **(A)** and axial **(B)** images exhibit subluxation of the biceps tendon (*arrows*) within an interstitial tear of the subscapularis tendon.

- Type IV pulley injury involves complete tear of subscapularis tendon with often associated tears of the supraspinatus tendon and CHL, leading to intra-articular dislocation of the LHBT (Fig. 92).

Fig. 92: Type IV pulley injury. Axial image exhibits complete tear of subscapularis tendon (*long arrow*) along with intra-articular dislocation of the biceps tendon (*short arrow*).

GLENOHUMERAL JOINT:

Labrum: [<Normal> <Degenerative fraying> <Tear> <Paralabral cyst>]

Glenohumeral ligaments: [<Normal> <Thickening / Acute sprain of ligament>]

Glenohumeral cartilage: [<Normal>]

The glenoid labrum increases the surface area of the relatively small glenoid, thus, providing static stability to the shoulder joint. The healthy labrum has a triangular shape, and features sharp margins and homogeneous low signal in all pulse sequences (Fig. 93). The anterior and posterior portions of the labrum are best seen on axial images, whereas the anterosuperior, superior, posterosuperior, and inferior portions are best evaluated on coronal images. The labrum is intimately associated with the GH ligaments, and often exhibits anatomic variations, mostly at its anterosuperior portion, including the sublabral foramen (located anterosuperiorly at the 12 o'clock to 3 o'clock position), sublabral sulcus or recess (located superiorly at the 11 o'clock to 1 o'clock position) (Fig. 94), and Buford complex (referring to absent anterosuperior labrum and thickened MGL). Many of these variations are actually a consequence of high insertion of anterior band of IGL on glenoid. Generally, no labral variations exist below the level of the coracoid process or posterior to the biceps tendon origin. The labrum also changes shape on internal/external rotation and may be developmentally hypertrophied, or even dysplastic or hypoplastic.

Fig. 93: Normal glenoid labrum. Coronal image shows a normal glenoid labrum (*long arrow*), which is tightly attached to an undercutting glenoid cartilage (*short arrow*).

Fig. 94: Normal sublabral sulcus (recess). Coronal image shows normal contrast fluid (*arrow*) between the superior labrum and the underlying glenoid cartilage.

Labral tears present clinically with deep posterior shoulder pain exacerbated by arm abduction and external rotation (ABER). The symptoms particularly manifest when there are flares of peritear inflammations. Other symptoms include clicking and/or popping sensation. The O'Brien test is positive on physical examination. Imaging criteria for diagnosing labral tear include one or a combination of imaging findings, such as abnormal labral morphology with irregular/truncated surface, missing labral fragment, fluid-like signal within the substance of the labrum extending to the surface (with or without focal intralabral widening of the signal), fluid imbibed into the substance of the labrum, fluid undercutting the chondrolabral junction, intra- or paralabral cyst with or without undelying

bony involvement, and labral detachment or avulsion (Figs. 95, 96). Secondary signs include periosteal stripping and tearing, bone injuries such as Hill–Sachs and osseous Bankart lesions, and hyaline cartilage injuries such as the GLAD lesion (see below). A potential pitfall in labral evaluation is misinterpreting the normal anterosuperior recess (or foramen) for a labral tear. The recess is identified as a 1- to 3-mm thick, smooth, unilocular fluid-like signal undercutting the labrum and following the glenoid contour, without hyperintense signal traversing into the substance of the labrum. The recess also does not go extending beyond the biceps–labral anchor.

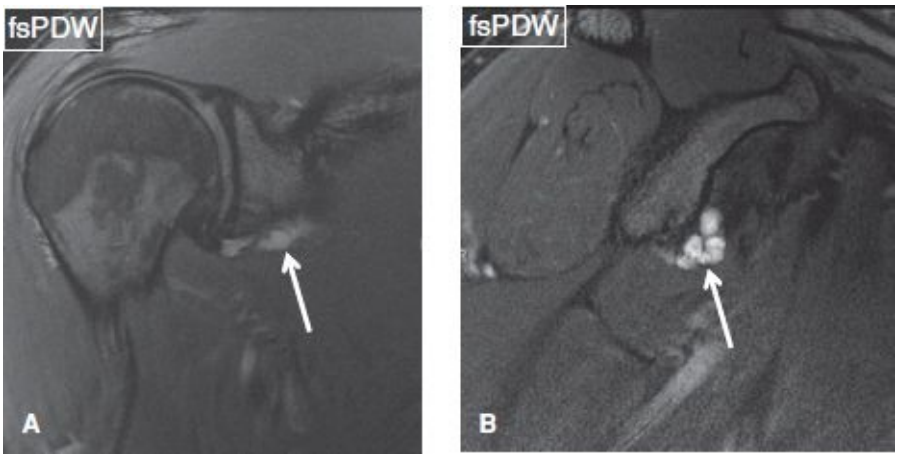

Fig. 95: Paralabral cyst. Coronal **(A)** and sagittal **(B)** images show a multilocular cystic lesion (*arrows*) adjacent to the inferior glenoid.

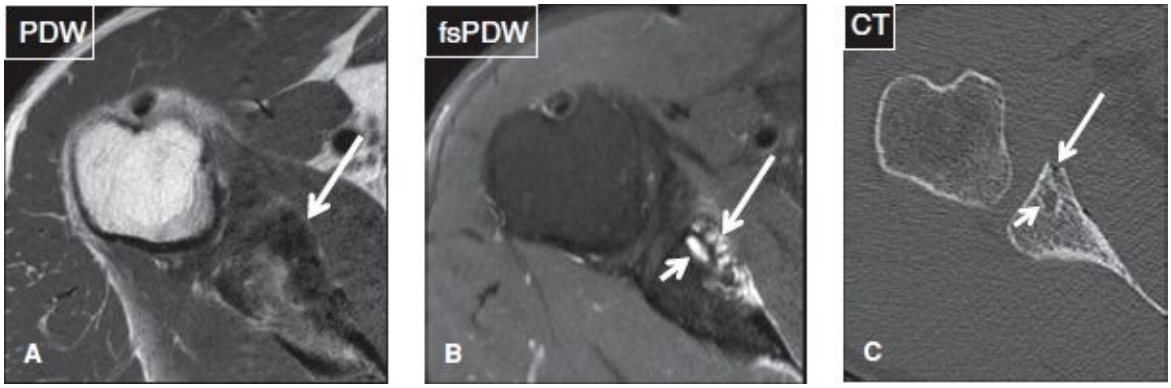

Fig. 96: Paralabral cyst. Axial CT **(A)** and MR **(B, C)** images show a multilocular cystic lesion (*long arrows* in **A** and **B**), which has a bony component (*short arrows* in **B** and **C**), as well as intracystic air (*long arrow* in **C**).

Labral tears can be conveniently described in relation to o'clock position or as three distinct categories: Bankart and Bankart variants, superior labrum anterior to posterior (SLAP) lesions, and posterior labral tears.

Bankart lesions can be soft tissue–only lesions (anteroinferior labral and periosteal tear) or mixed soft tissue and bony lesion. These result as a consequence of anteroinferior shoulder subluxation/dislocation or multidirectional instability (Figs. 97–99). Seventy-five percent of shoulder dislocations result in Bankart lesions. The latter are associated with Hill–Sachs fracture of the posterosuperior or posterolateral humeral head, which may vary

from bony contusions to depressed impaction fractures (the latter demonstrating an average 4-mm cortical depression). Both humeral and glenoid abnormalities (best seen on axial images), and the labral surface (partial) tear versus detachment (complete tear) should be documented. Small labral tears can be debrided, whereas larger ones require surgical repair and reattachment. Symptoms of recurrent instability usually are related to both Bankart lesion and coexistent laxity of the IGL, rather than from an isolated Bankart lesion. Cases with greater than 25% bony deficiency in the anteroinferior glenoid likely require bone grafting or coracoid transfer during labral repair/reconstruction (Bristow or Latarjet procedure). To estimate the bony deficiency of glenoid, one can draw a best fit circle on the glenoid on the sagittal image and measure the percentage of bone missing along the diameter of the circle. Latarjet procedure is most popular due to low recurrence rate of subluxations as it results in triple protective effect—restoration of the glenoid contact area, support by conjoint tendon to subscapularis and anteroinferior capsule, and finally, reinforcement by the repaired shoulder capsule. Larger (a.k.a engaging) Hill–Sachs lesions can lead to shoulder instability with painful popping and catching, as the humeral head depression perches over and engages with the glenoid defect. Two distinct Bankart variants may be seen, both characterized by an intact glenoid periosteum. These include the Perthes lesion (nondisplaced torn labrum) and ALPSA (medialized displaced Bankart lesion aka anterior labrocapsular periosteal sleeve avulsion [ALPSA]) (Figs. 100, 101). In ALPSA lesions, the labrum requires either resection or reattachment to the glenoid, whereas in Perthes lesions, the labrum can be in situ repaired. Occasionally, Perthes lesions resynovialize and become difficult to identify. In suspected Perthes cases, imaging in ABER position assists in the diagnosis as it helps fluid imbibe at the site of tear while the IGL pulls on the labrum. ABER positioning might also define the true extent of the tear or displacement of the lesion (Fig. 102). Glenoid labrum articular cartilage defect (GLAD) is another type of stable anteroinferior labral tear that involves an adjacent focal articular cartilage defect (Fig. 103). However, with high-field imaging, articular cartilage abnormalities are commonly evident as part of various labral injuries and vary from contusions to fissures and larger defects. Of note, GLAD lesion is a stable lesion related to local impaction injury and is not caused by or predispose to instability.

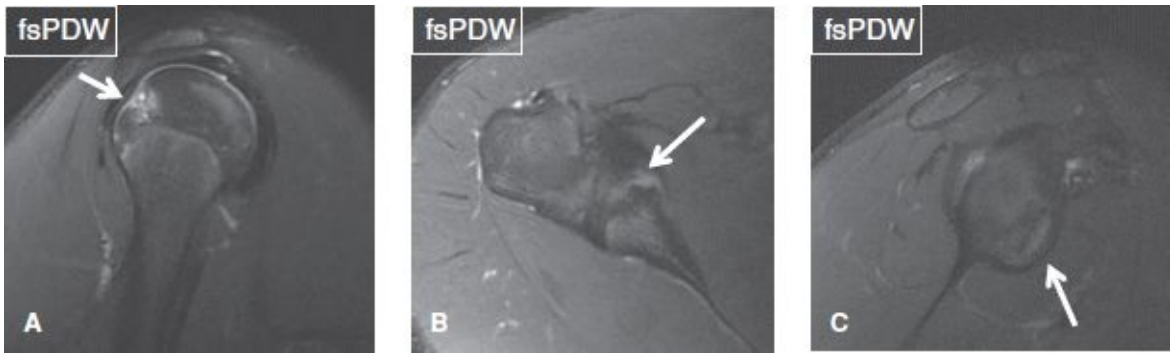

Fig. 97: Hill–Sachs fracture and Bankart lesion. **A:** Sagittal image demonstrates cortical depression of the posterosuperior humeral head, in keeping with Hill–Sachs lesion. On axial **(B)** and sagittal **(C)** images from the same patient, there is a fracture of the anteroinferior

glenoid (*arrows*) and torn and anteriorly displaced overlying labrum, in keeping with a bony and soft tissue Bankart lesion.

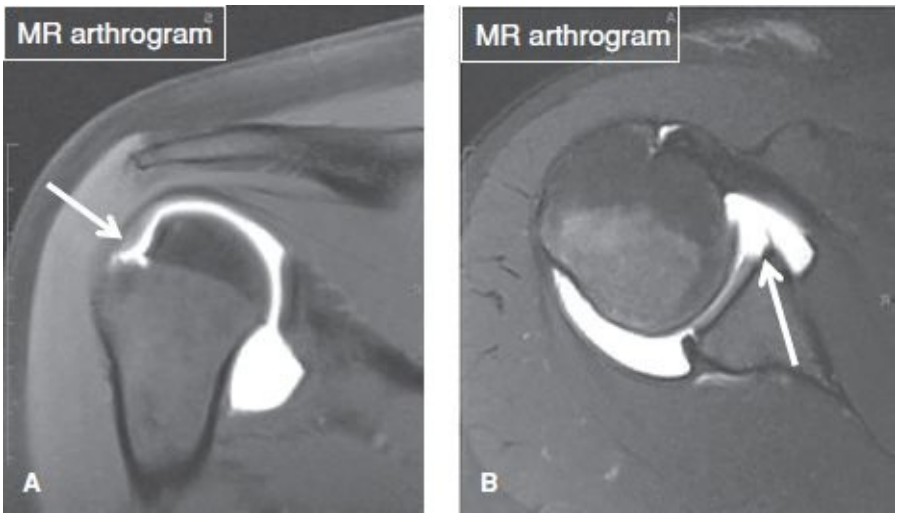

Fig. 98: Hill–Sachs fracture and Bankart lesion. Coronal **(A)** and axial **(B)** arthrography images exhibit a compression fracture of the posterosuperior humeral head (*arrow* in **A**) along with a tear of the anteroinferior labrum and adjacent cartilage (*arrow* in **B**).

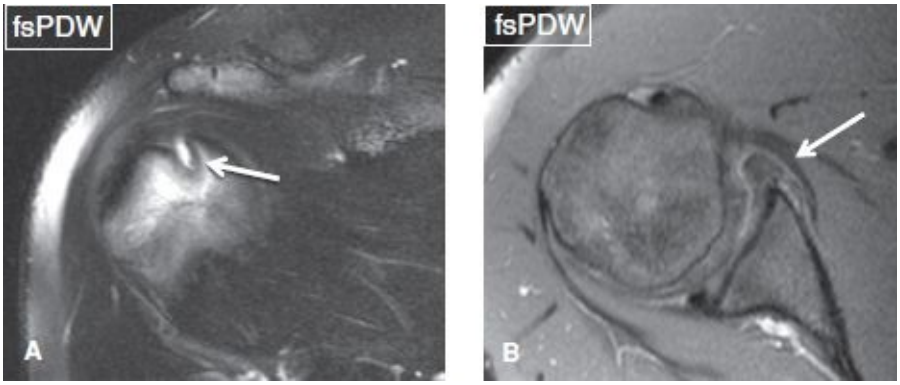

Fig. 99: Hill–Sachs facture and Bankart lesion. **A:** Coronal image shows a cortical depression fracture of the posterosuperior humeral head (*arrow*), in keeping with a Hill–Sachs lesion. **B:** The corresponding axial image demonstrates a torn, nondisplaced anterior labrum (*arrow*) with discontinuity of the periosteum, in keeping with a Bankart lesion.

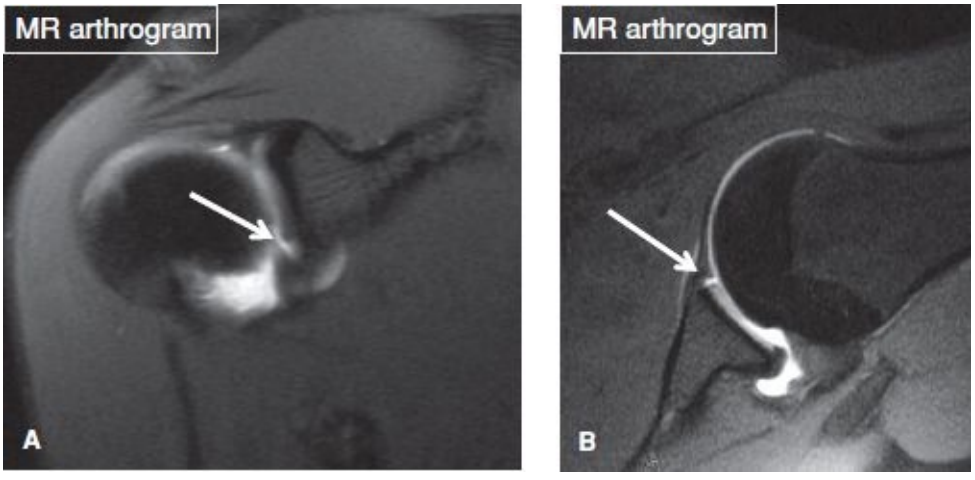

Fig. 100: Perthes lesion. Coronal **(A)** and axial **(B)** arthrography images (**B** in ABER position) show a nondisplaced torn anteroinferior labrum with intact periosteum (*arrows*).

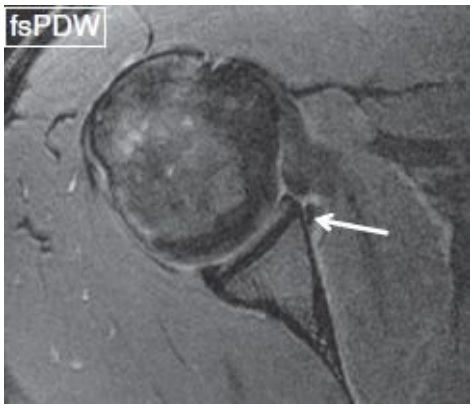

Fig. 101: ALPSA lesion. Axial image exhibits anterior labroligamentous periosteal sleeve avulsion with medially displaced labrum (*arrow*).

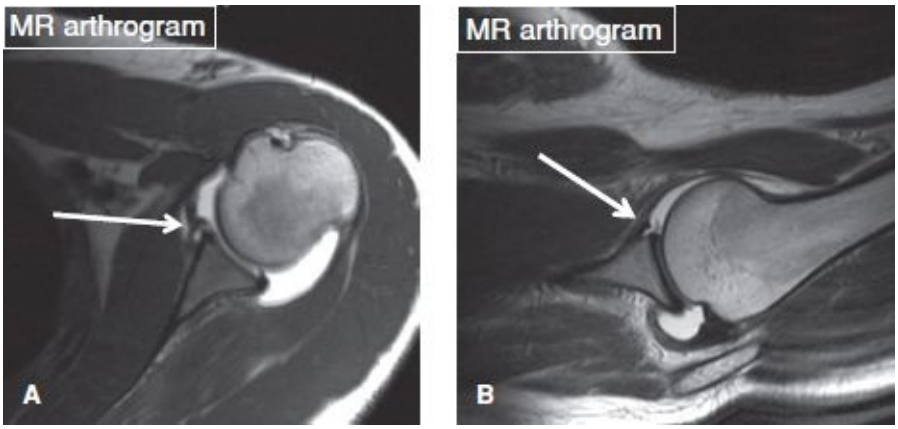

Fig. 102: ALPSA lesion. **A:** Axial arthrography image. A nondisplaced or minimally displaced inferior labral tear is evident (*arrow*), suggesting a Perthes lesion. **B:** Same patient's scan in **A**BER position reveals medial displacement (*arrow*), indicating the lesion should be defined as ALPSA instead.

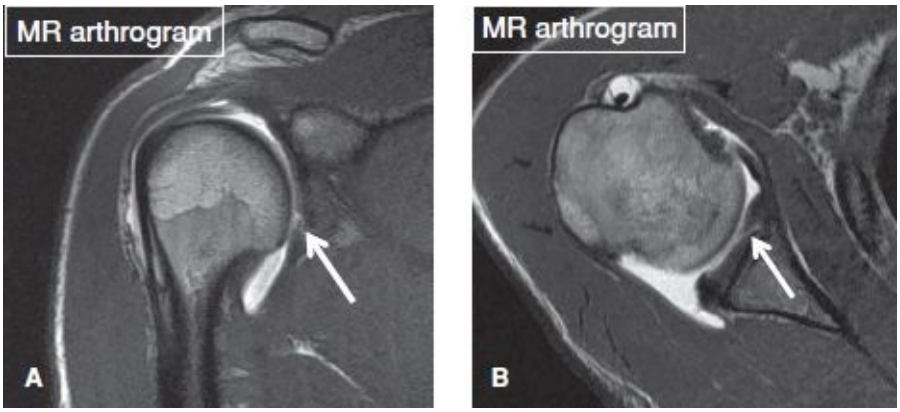

Fig. 103: GLAD lesion. Coronal **(A)** and axial **(B)** arthrography images show a linear disruption/defect (*arrows*) of the anteroinferior portion of the glenoid cartilage.

There are several different types of SLAP lesions (I to X). These lesions may be caused by

humeral impaction (fall on outstretched hand) or from biceps tendon traction and are best depicted on the coronal and axial images. Of note, not many practices follow the classification of SLAP types and it is also difficult for Orthopods to remember the SLAP types. For the readers, who like attention to detail, the different SLAP types are described below and relevant illustrations are shown.

- Type I lesion refers to labral degeneration (internal increased, but not as high as fluid, and signal not contacting labral surface), surface fraying, or attenuation (Fig. 104). It is commonly encountered as asymptomatic finding, especially involving the posterosuperior labrum, in overhead throwers and adults older than 50 years of age. It usually does not need treatment.

Fig. 104: Type I SLAP lesion. Coronal image demonstrates increased (though not fluid-like) signal and surface fraying of the superior labrum (*arrow*), in keeping with degeneration.

- Type II lesion is a classic SLAP tear resulting from biceps tendon traction and is further subdivided into IIa (anterosuperior), IIb (posterosuperior), and IIc (anterosuperior to posterosuperior) subtypes (Figs. 105–109). It may be seen as one or a combination of findings, such as fluid signal undercutting the chondrolabral junction, hyperintense signal within the labrum contacting its surface, labral truncation with or without associated paralabral cyst, or frank labral detachment/displacement. Secondary findings of type IIa lesions include loss of cartilage underneath the labral tear, and paralabral cyst extending into the rotator interval. Type IIb or IIc lesions may show frequently show paralabral cysts that extend into the spinoglenoid notch. Type II lesions are treated by debridement.

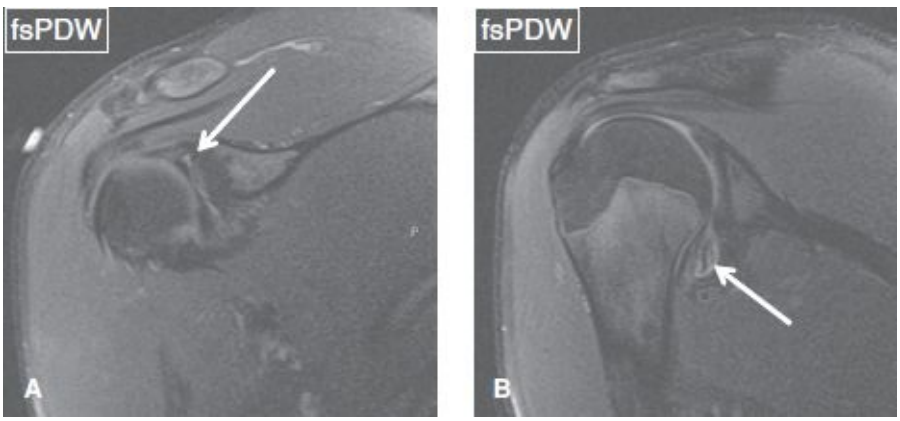

Fig. 105: Type IIa SLAP lesion. Coronal images show a tear of the anterosuperior labrum (*arrow* in **A**), along with a labral fragment in the axillary pouch (*arrow* in **B**).

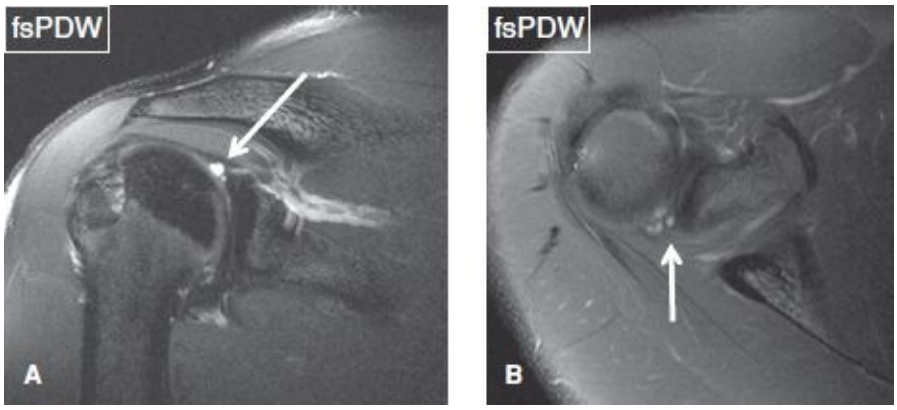

Fig. 106: Type IIb SLAP lesion. Coronal **(A)** and axial **(B)** images exhibit fluid-like signal within a truncated posterosuperior labrum with associated paralabral cyst (*arrows*).

Fig. 107: Type IIc SLAP lesion. Coronal **(A)** and axial **(B)** images exhibit a labral tear extending from the anterosuperior labrum to superior labrum (*arrow* in **A**) and to the posterosuperior labrum (*arrow* in **B**).

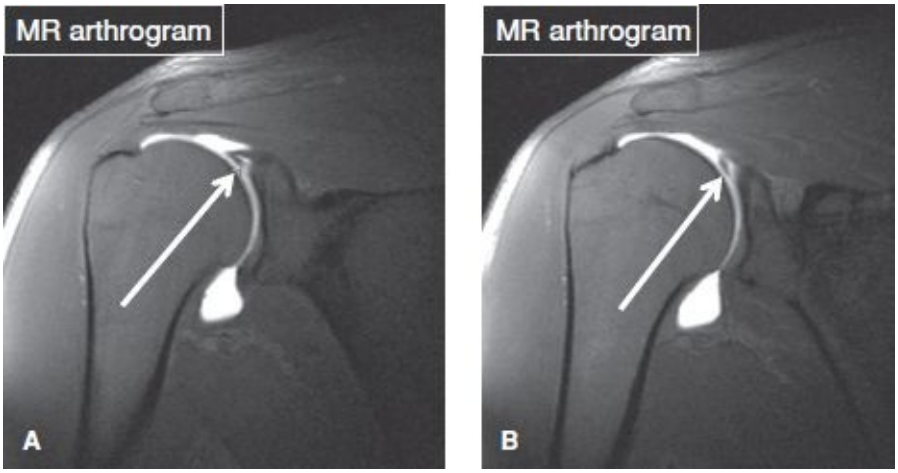

Fig. 108: Type IIc SLAP lesion. Coronal arthrography images **(A, B)** show contrast imbibing the superior anterior to the posterosuperior labrum (*arrows*), in keeping with a tear.

Fig. 109: Type IIc SLAP lesion. Axial image shows tears of the superior labrum, which extend from the anterosuperior to the posterosuperior labrum (*long arrows*), with associated with paralabral cysts. The larger cyst posteriorly encroaches into the spinoglenoid notch (*short arrow*).

- Type III lesion is a bucket-handle tear, which extends from anterior to posterior and features a reverse "V" shape labrum on the coronal images (Fig. 110). This lesion commonly requires a resection of the displaced fragment.

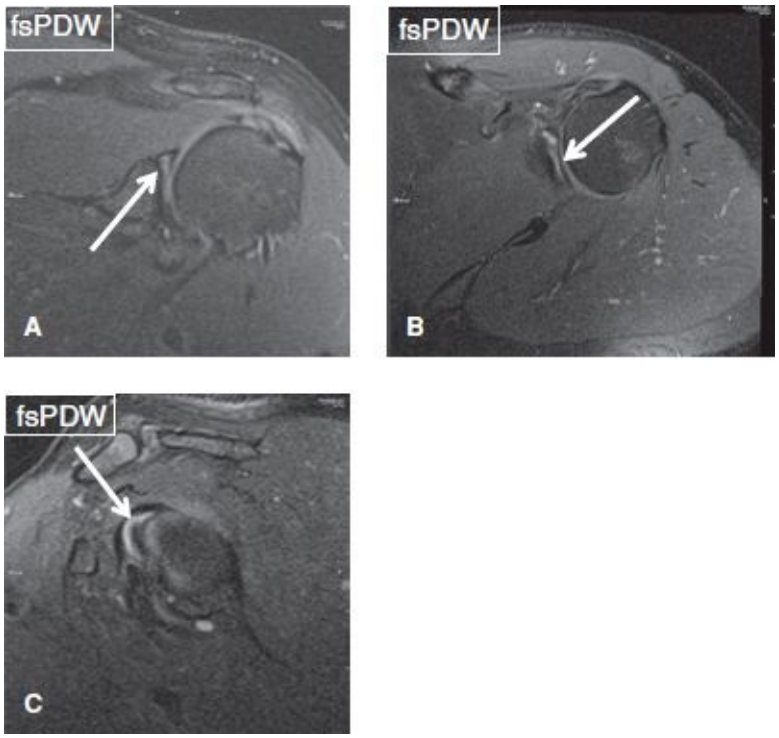

Fig. 110: Type III SLAP lesion. Coronal **(A),** axial **(B),** and sagittal **(C)** images show a bucket-handle lesion (*arrows*) of the superior labrum. Notice the reverse V shape of the labrum in image A.

- Type IV lesion is a SLAP tear that extends into the biceps anchor and/or tendon and is best observed on sagittal and coronal images (Fig. 111). Type IV lesion requires a repair of the labrum and/or biceps tendon.

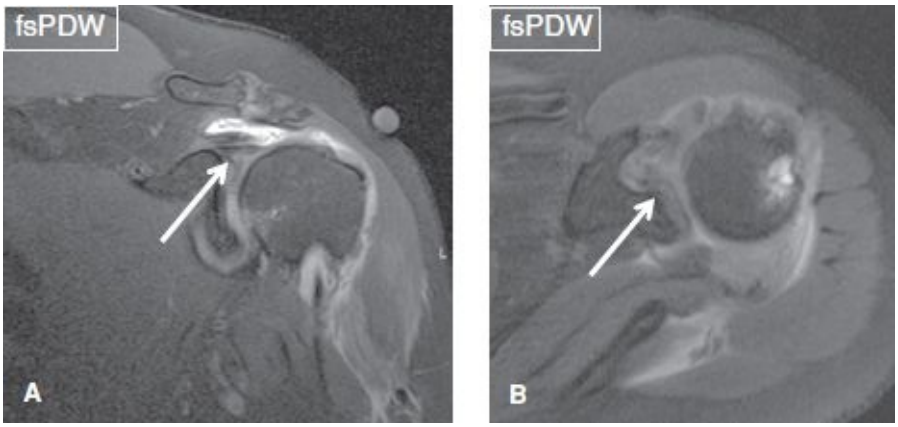

Fig. 111: Type IV SLAP lesion. Coronal **(A)** and axial **(B)** images exhibit a superior labral tear (*arrows*), which extends into the biceps anchor.

- Type V lesion refers to anteroinferior labral tear below the equator of the glenoid plus a SLAP lesion (Fig. 112). In practice, most of these injuries represent superior extension of a Bankart lesion, involving the anterosuperior/superior glenoid labrum above the equator of glenoid.

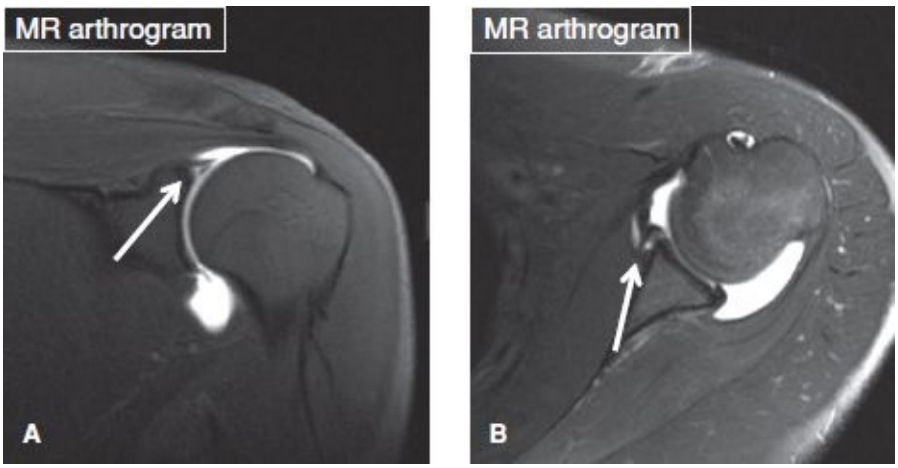

Fig. 112: Type V SLAP lesion. Coronal **(A)** and axial **(B)** arthrography images exhibit a superior labral tear (*arrows*), which extends anteroinferiorly below the equator of glenoid.

- Type VI is a focal flap or flip tear of the superior labrum (unlike the bucket-handle tear that extends from anterosuperior to posterosuperior) (Fig. 113). It is best seen on coronal and sagittal images.

Fig. 113: Type VI SLAP lesion. Coronal arthrography image shows a focal flip (flap) tear of the superior labrum (*arrow*).

- Type VII lesions involve the MGL and are difficult to interpret, since MGL can have normal variations, and it can be normally bifid or absent. Nevertheless, abnormal morphology of the MGL with fascial edema and superior/anterior labral lesion is an important clue to this lesion (Fig. 114).

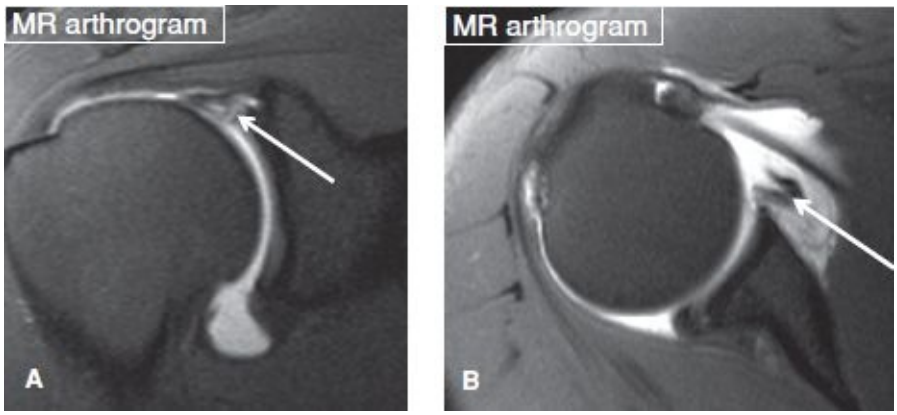

Fig. 114: Type VII SLAP lesion. Coronal **(A)** and axial **(B)** arthrography images show a superior labral tear (*arrow* in **A**) that extends to the middle glenohumeral ligament (*arrow* in **B**).

- Type VIII lesions involve the posterior labrum below the equator of the glenoid (Fig. 115).

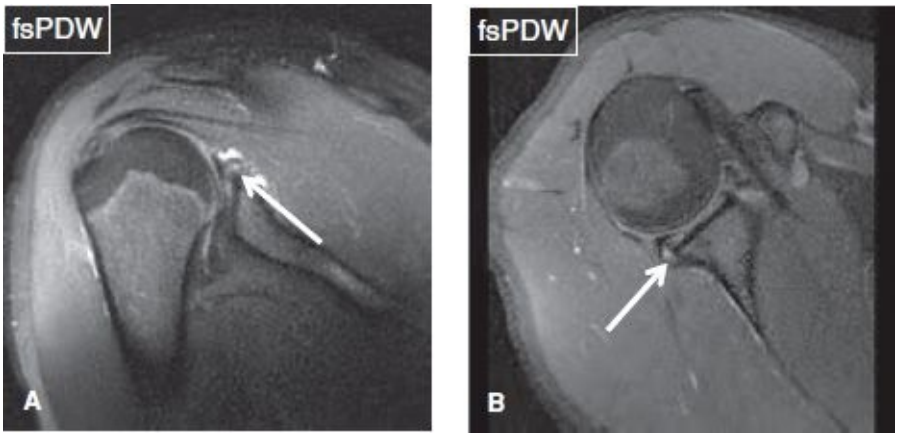

Fig. 115: Type VIII SLAP lesion. Coronal **(A)** and axial **(B)** images demonstrate a superior labral tear (*arrows*), which extends to the posterior labrum, below the equator with associated paralabral cysts.

- Type IX lesions involve the whole labrum circumference as multifocal tears (Fig. 116).

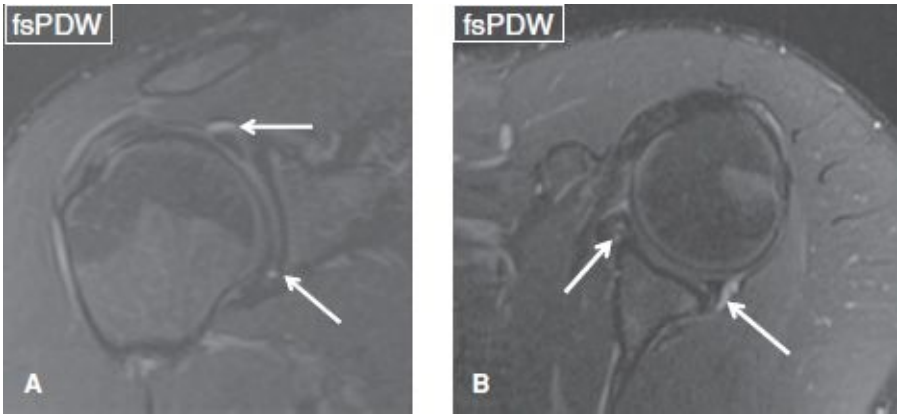

Fig. 116: Type IX SLAP lesion. Coronal **(A)** and axial **(B)** images exhibit multifocal labral tears and paralabral cysts (*arrows*).

- Type X lesions involve the SGL/rotator interval and are best seen on axial and sagittal images (Figs. 117, 118). Finally, presence of a subchondral contusion or fracture of the superior humeral head or focal cartilage loss in that area can be commonly associated with a superior labral tear (aka SLAP fracture) (Fig. 119).

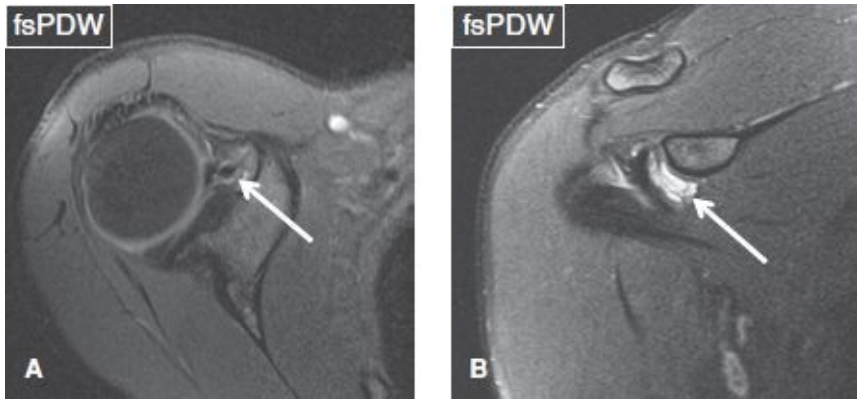

Fig. 117: Type X SLAP lesion. Axial **(A)** and coronal **(B)** images show anterior superior labral tear extending into the SGL (*arrow* in **A**) with a paralabral cyst (*arrow* in **B**) that extrudes into the rotator interval.

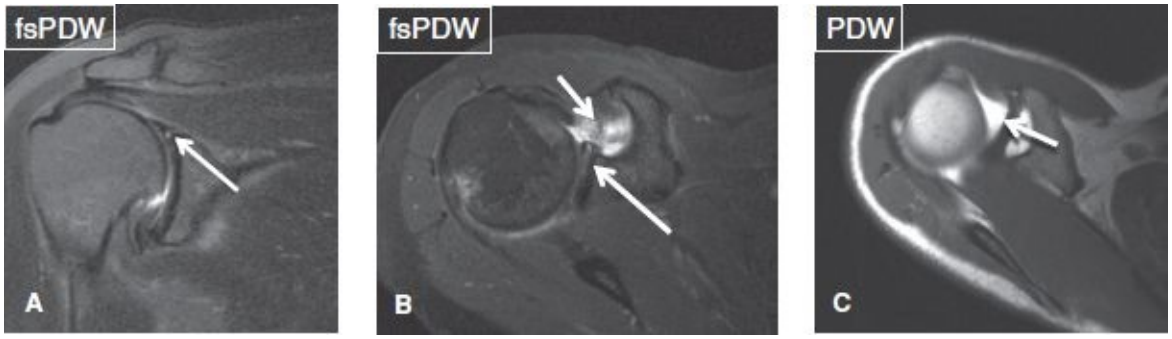

Fig. 118: Type X SLAP lesion. Coronal **(A)** and axial **(B and C)** images demonstrate a superior labral tear (*arrow* in **A**), which also involves the anterosuperior labrum and SGL (*arrows* in **B**). For comparison, notice normal SGL in a different patient (*arrow* in **C**).

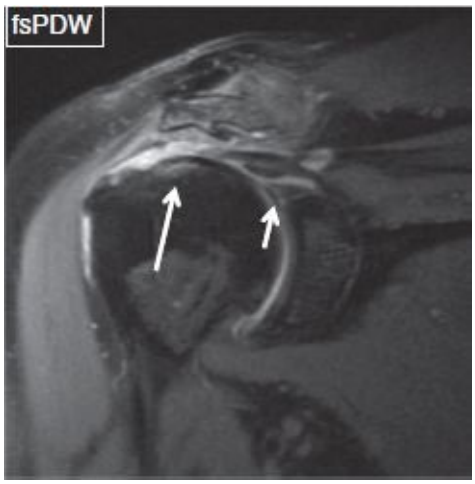

Fig. 119: SLAP fracture. Coronal image shows a subchondral marrow edema of the superior humeral head (*long arrow*). Notice superior labral tear (*short arrow*) and full-thickness rotator cuff tear.

Posterior labral tears are associated with posterior peel-back lesion, prior or recent episodes of posterior subluxation/dislocation, underlying glenoid dysplasia/retroversion, and as a consequence of multidirectional instability. Posterior peel-back lesions (aka internal impingements) typically affect overhead throwers. In these individuals, it is hypothesized that due to repeated microtrauma from overhead throwing activities in the late cocking and early acceleration phases, the posterior/posteroinferior capsule undergoes thickening from stretching/remodeling, and/or calcification (Bennett lesion), whereas the anterior capsule becomes stretched and lax. There is associated scapular dyskinesia and dysfunction of the periscapular muscles, which ultimately leads to glenoid internal rotation deficit (GIRD) and posterior shoulder pain, especially on abduction and external rotation. The consequence for the athlete is markedly decreased throw velocity (aka dead arm). The thickened posterior capsule results in posterosuperior ascent of the humerus, which ultimately leads to buckling of the posterior supraspinatus tendon between the greater tuberosity and the posterosuperior glenoid. The resultant soft tissue lesions include posterosuperior labral degeneration or tear, and undersurface tendinosis and/or RC tear at the junction of the posterior supraspinatus and anterior infraspinatus tendons while the bony lesions include subcortical edema or subcortical cyst formation of the posterosuperior humerus head (Figs. 120–122). These subjects almost universally show posterosuperior glenoid contour rounding and/or sclerosis on imaging. Glenoid remodeling can be differentiated from glenoid dysplasia, since the latter commonly involves the posteroinferior and posterior portions, and it might be associated with overlying compensatory labral and cartilage hypertrophy. Sclerosis of the posterosuperior glenoid is part of bony adaptation in throwing athletes. When sclerosis extends into the central

glenoid, it likely reflects more widespread arthrosis in the shoulder. Glenoid dysplasia can also be associated with multidirectional or posterior instability. Other common bony findings include posterosuperior subluxation of the humeral head and exaggerated glenoid retroversion (Fig. 122). In some athletes, a thick and lax IGL may be seen protruding into the anterior joint as a normal finding. Any fluid undercutting the posterior labrum/chondral junction is abnormal. If present, paralabral cysts confirm the labral tear (Figs. 123, 124) but require careful evaluation since they can be mimicked by synovial diverticulae at the posterior capsule-labral junction, which result from prior capsular injuries. Posterior subluxation/dislocation may occur from recent direct blunt trauma to shoulder, such as in wrestling injuries, line blocker, swimming, or seizures, and is associated with posterosuperior/posterior labral tear and the trough sign (anteromedial head contusion/impaction fracture) (Fig. 125). Another posterior lesion similar to ALPSA, termed POLPSA (posterior labrocapsular periosteal sleeve avulsion), can result from posterior GH subluxation/dislocation (Figs. 126, 127). Other injuries in throwing athletes include scaphoid stress fractures, abdominal wall muscle injuries, osteochondral impaction injuries of the glenoid, and the entity of "batter's shoulder," which causes posterior subluxation, posterior glenohumeral instability, and tear of the posteroinferior labroligamentous complex. Finally, a recently recognized entity associated with posterior instability is referred to as the Kim's lesion. It appears as incomplete avulsion of the posteroinferior labrum, which is concealed by apparently intact superficial portion. The clinical significance of this lesion is the need for surgeons to convert this concealed incomplete lesion to a complete tear and repair it with the posterior band of the IGL. A failure to address this lesion may result in persistent posterior instability. On arthroscopy, one would observe a superficial fissure at the posteroinferior chondrolabral junction. However, probing of the lesion will show detachment of the deep portion of the posteroinferior labrum, which is truncated, small in height, and has associated retroversion of the chondrolabral glenoid. Labroplasty is usually required to restore the labral height along with capsular shift with or without rotator interval closure for good functional results and prevention of recurrent instability.

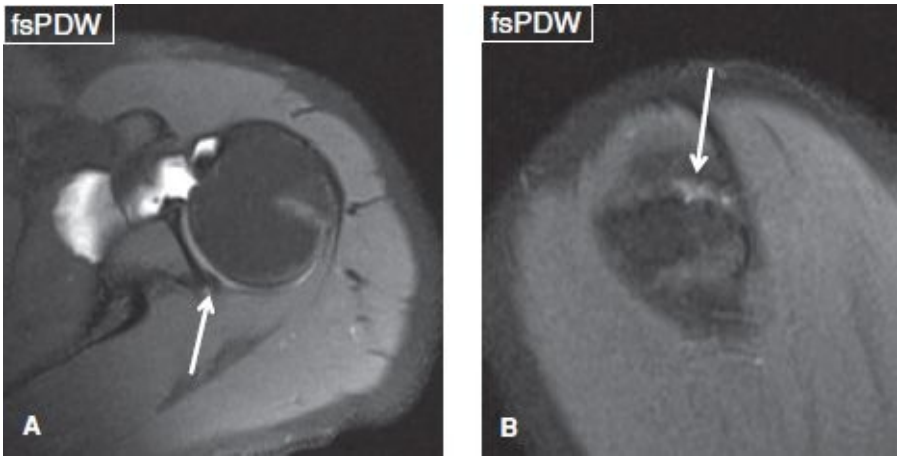

Fig. 120: Posterior peel-back lesion. Axial **(A)** and sagittal **(B)** images demonstrate degeneration of the posterior labrum with intralabral cyst (*arrow* in **A**) along with a rotator

cuff tear (*arrow* in **B**) at the junction of the posterior supraspinatus and anterior infraspinatus tendons. Note mild posterior subluxation of the humeral head.

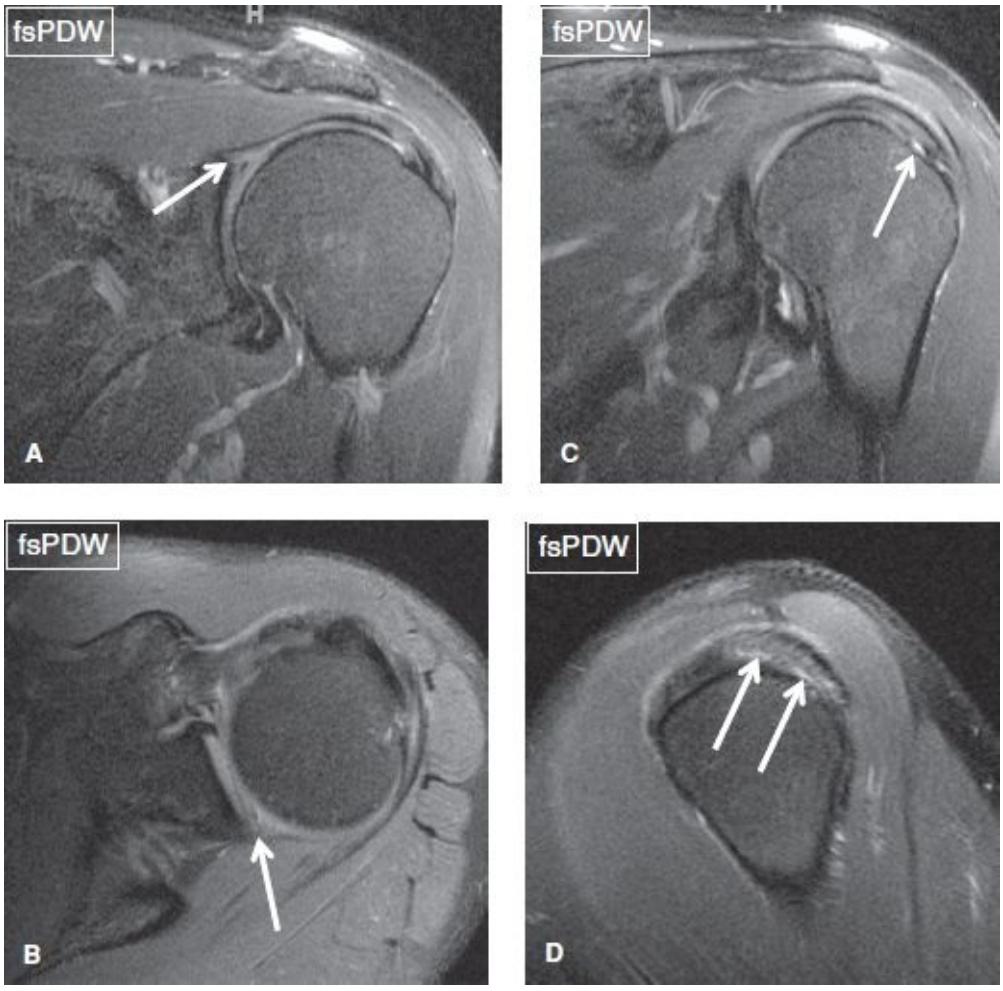

Fig. 121: Posterior peel-back lesion. Coronal **(A)** and axial **(B)** images show a type IIb SLAP lesion (*arrows*) and mild posterior subluxation of the humeral head with subcortical cysts. Corresponding coronal **(C)** and sagittal **(D)** images reveal a rotator cuff tear (*arrows*) of the a posterior supraspinatus and anterior infraspinatus tendons.

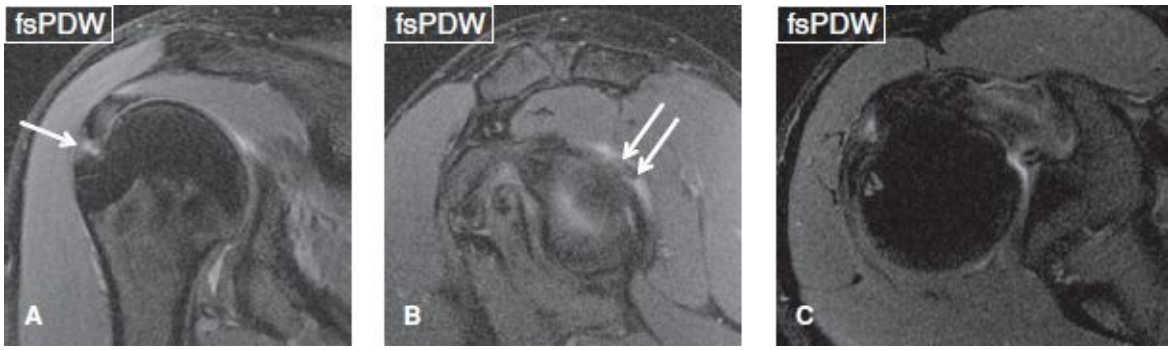

Fig. 122: Posterior peel-back lesion. **A:** Coronal image shows a tear at the attachment site (*arrow*) of the posterior supraspinatus/anterior infraspinatus tendons. **B:** Sagittal image demonstrates a flap tear of the posterior labrum (*arrows*). **C:** Axial image exhibits posterior subluxation of the humeral head, subcortical cysts, and degeneration of the posterosuperior labrum. Notice underlying posterosuperior glenoid rounding/remodeling as well as exaggerated glenoid retroversion.

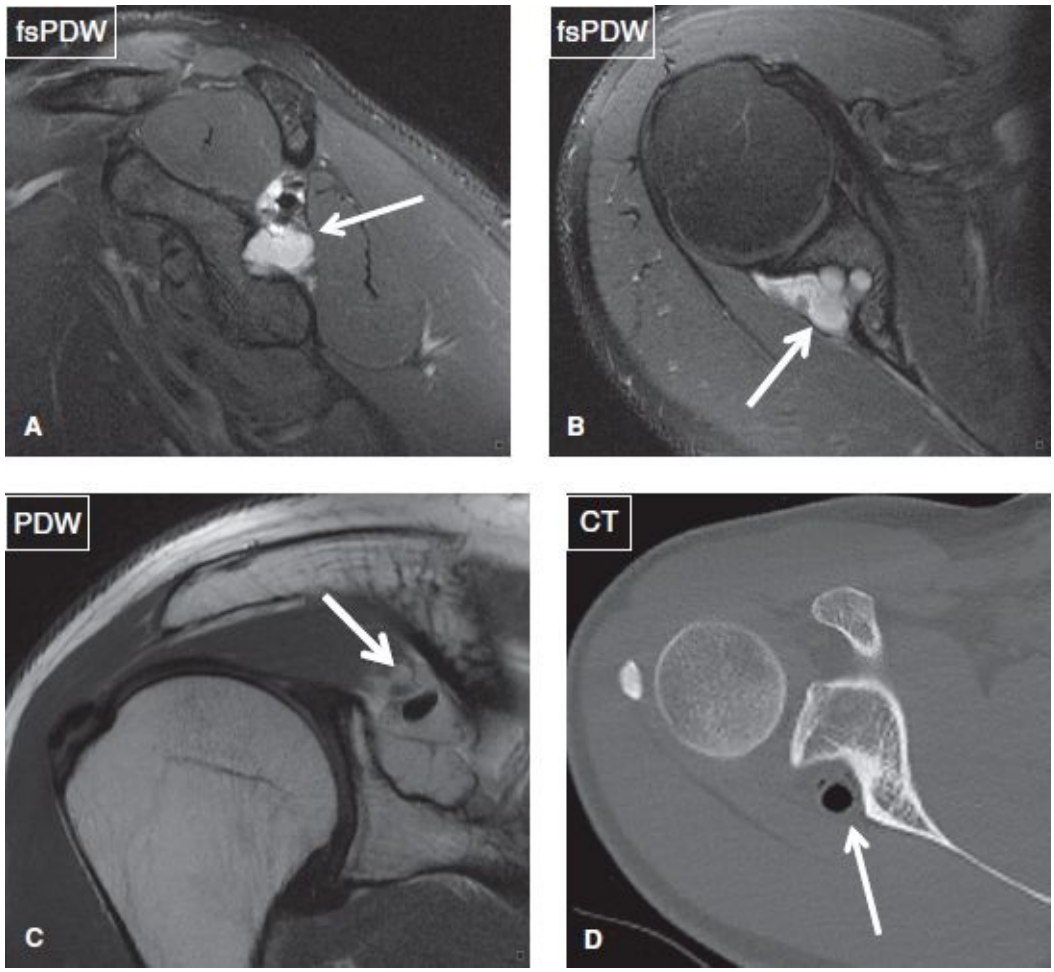

Fig. 123: Paralabral cyst. Sagittal **(A),** axial **(B),** and coronal **(C)** MR images as well as axial CT image **(D)** show a multiloculated paralabral cyst (*arrows*), extending into the spinoglenoid notch and contains air and debris. The cyst intrudes into the bone mimicking a tumor. Notice lack of muscle denervation change despite the large size, which can happen in cysts, which extend into the bone, preventing much mass effect on the suprascapular nerve.

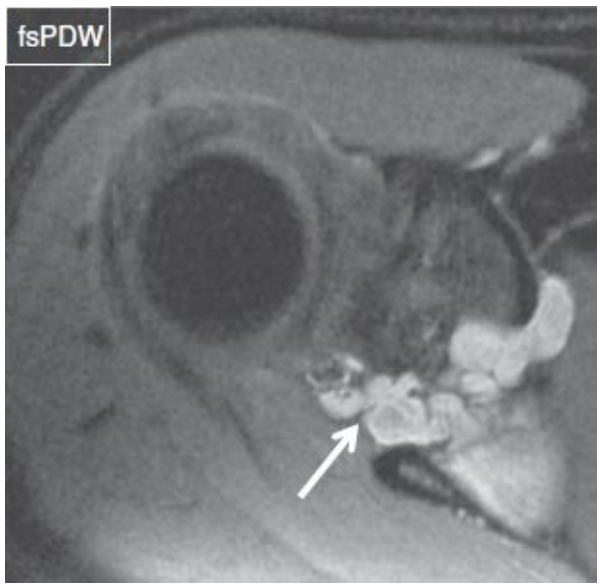

Fig. 124: Large paralabral cyst. Axial image shows a large paralabral cyst (*arrow*) spanning both suprascapular and spinoglenoid notches.

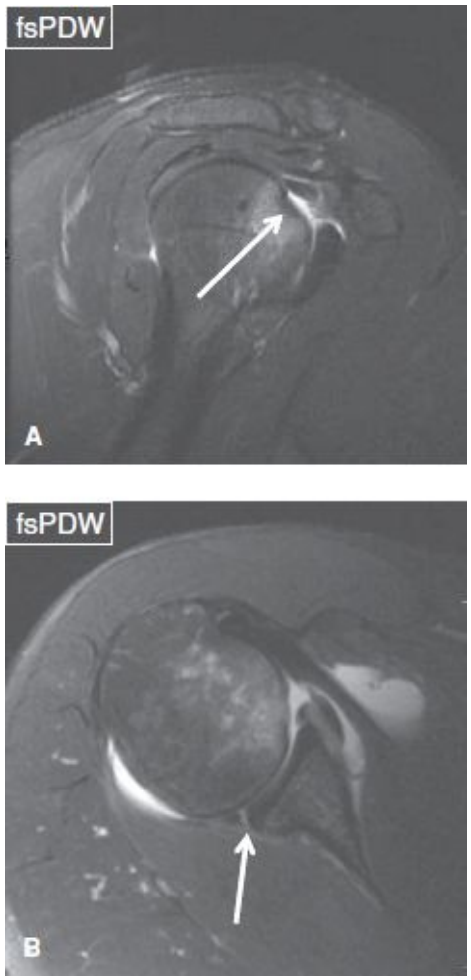

Fig. 125: Posterior labral tear. Sagittal **(A)** and axial **(B)** images from a recent posterior humeral subluxation exhibit an impaction fracture of the anterosuperior humeral head (trough sign) (*arrow* in **A**) along with a tear of the posterior labrum (*arrow* in **B**).

Fig. 126: POLPSA lesion. Axial image shows a posteroinferior labral tear along with labrocapsular periosteal sleeve avulsion (*arrow*).

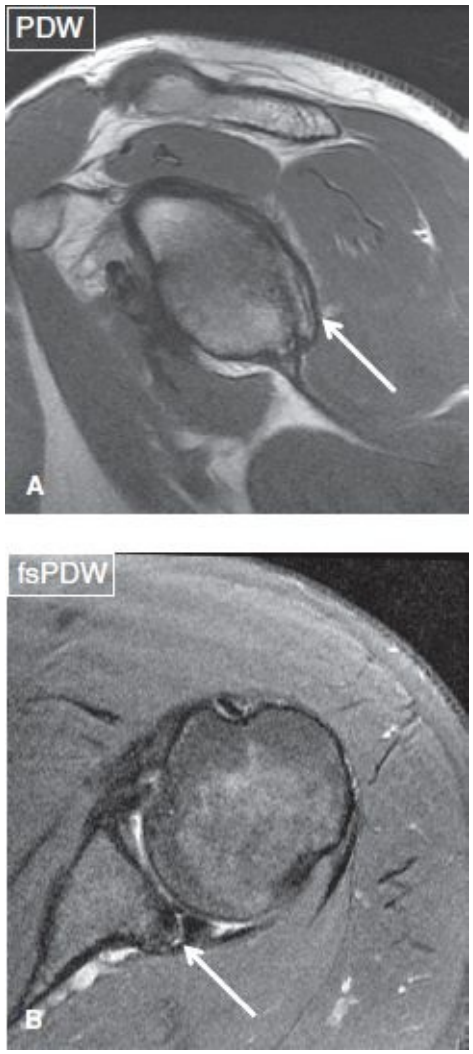

Fig. 127: Bennett and POLSPA lesions. **A:** Sagittal image demonstrates mineralization of the posterior band of the inferior glenohumeral ligament (*arrow*). **B:** The corresponding axial image shows posterior inferior labrocapsular periosteal sleeve avulsion (*arrow*).

The glenohumeral ligaments represent capsular thickenings similar to other joints (Fig. 128). The SGL originates from the labrum, just anterior to the LHBT origin and inserts on the lesser tuberosity. It is not only the primary restraint to inferior humeral subluxation, but also limits anterior translation and external rotation when the arm is in adduction. Along with the CHL, the SGL prevents posterior humeral translation when the arm is in flexion, adduction, and internal rotation. The SGL is 2 to 3 mm thick and best seen on axial images, paralleling the coracoid process. It can be injured in rotator interval sprains, biceps pulley injuries, and SLAP type X lesions (Figs. 117, 118). One should remember that it can artifactually appear thickened due to surrounding suppressed fat on fat-saturated axial images. However, periligamentous edema and fluid is best seen on these images.

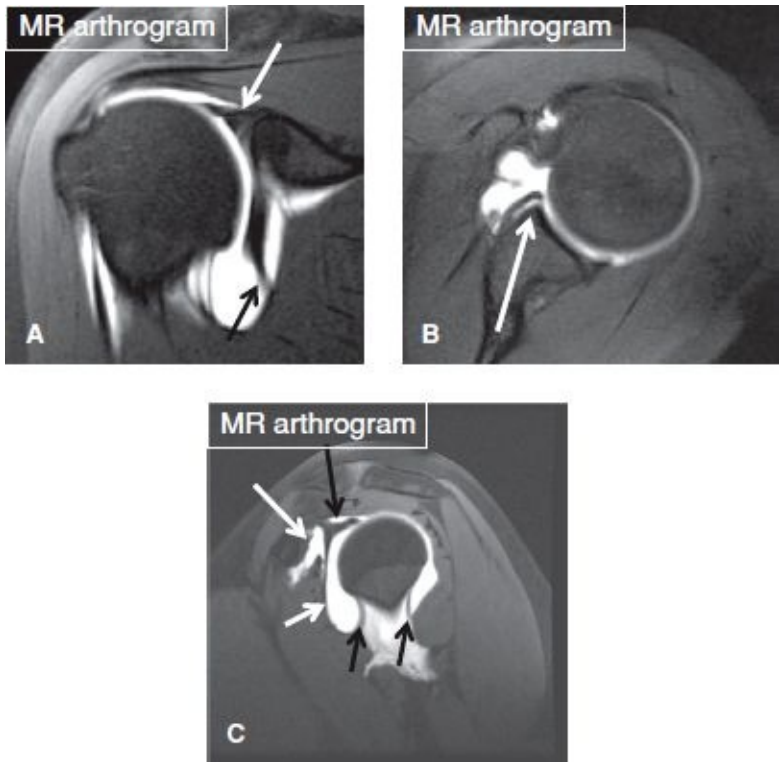

Fig. 128: Normal MR arthrography of the shoulder. **A:** Coronal image demonstrates the superior labrum (*white arrow*) and the inferior glenohumeral ligament (*black arrow*). **B:** Axial image exhibits contrast within the thin, smooth sublabral foramen (*arrow*), which may be normally located at anterosuperior (12 to 3 o'clock) portion of the glenoid. **C:** Sagittal image shows contrast within the subscapularis recess (*long white arrow*). There is clear delineation of the superior (*long black arrow*) and middle (*short white arrow*) glenohumeral ligaments, as well as of the two bands of the inferior glenohumeral ligament (*short black arrows*).

The MGL arises from the labrum immediately below the SGL origin and also inserts on the humerus, medial to the lesser tuberosity. It provides static stability against anterior humeral translation and external rotation in 0 to 45 degrees of abduction. It also limits inferior humeral translation when the arm is in adduction. It is 2 to 3 mm thick and is best seen on axial images, located beneath the subscapularis myotendinous junction. It has a number of variations and can be bifid, absent, or thickened (Buford complex associated with absent anterosuperior labrum). The MGL may be injured alone or as part of SLAP type VII lesions (Fig. 129) (Fig. 114).

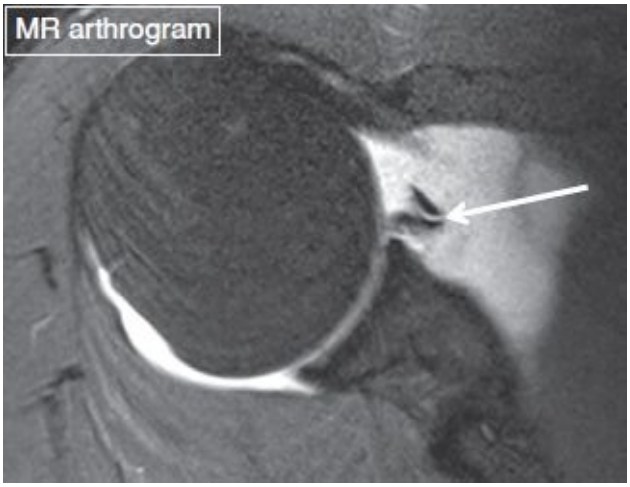

Fig. 129: Middle glenohumeral ligament tear. Axial MR arthrography image shows a tear (*arrow*) of the middle glenohumeral ligament

The IGL has two bands, the thick (3 to 4 mm) and stronger anterior band, and the relatively thin (2 to 3 mm) and weaker posterior band. These bands, along with shoulder joint capsule, form the axillary pouch. The IGL connects the inferior half (3 to 9 o'clock) of the glenoid labrum to expand the surface area for the humeral head, just below its articular surface. The anterior band restrains against anterior translation and the posterior band against posterior translation of the humerus in greater degrees of abduction. The IGL is also a secondary restraint against inferior humeral translation in abduction. They IGL may undergo injury in GH subluxation/dislocation.

The three glenohumeral ligaments (SGL, MGL, and IGL) roughly form a Z or reverse Z configuration in left/right shoulder coronal images, respectively, with the MGL forming the vertical component of Z, and the SGL and IGL oriented in a more horizontal fashion, extending from the glenoid to the humeral neck (Fig. 128).

On the axial images, an overlapping MGL and anterosuperior labrum with sublabral recess can mimic a labral tear, a pitfall, which can be avoided with clear knowledge of anatomy. The fixed arrangement of structures from anterior to posterior includes the subscapularis tendon, the MGL, and the anterior labrum. On sequential superior to inferior axial images, the labrum and MGL can be distinguished, since the glenoid labrum courses posteriorly and unites with the anterior or anteroinferior labrum after the recess finishes, whereas the MGL courses anteriorly toward the subscapularis tendon and inserts on the humerus. High insertion of the IGL, which is associated with absent anterosuperior labrum or Buford complex, can also cause confusion, but careful evaluation of the course of various structures can prevent erroneous diagnosis of labral tears.

It is important not to overcall IGL injury if one sees fascial edema from the capsular injury from recent trauma or shoulder subluxation, since the diagnosis of IGL rupture might necessitate an open instead of an otherwise arthroscopic procedure. Similar to other ligaments, IGL injuries are categorized as grade I, II, or III sprains. Various types of IGL tears include tear in the midportion (IGL tear), glenoid site avulsion (GAGL), humeral site avulsion of the anterior band with or without bony component (HAGL/BHAGL,

respectively), and humeral site avulsion of the posterior band (PHAGL) (Figs. 130–133).

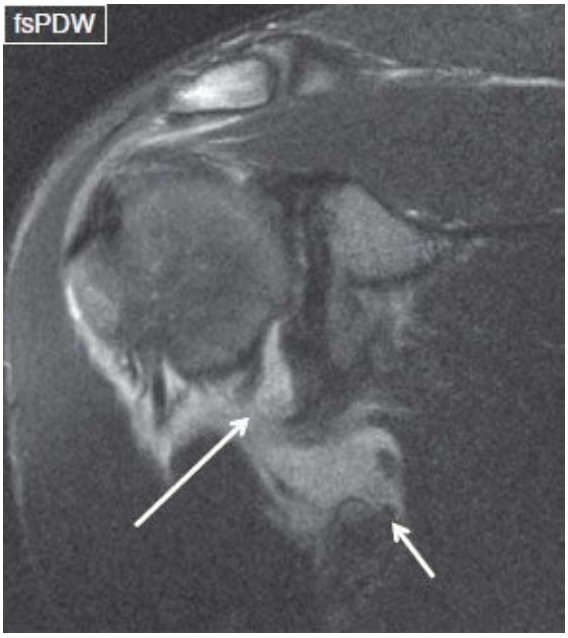

Fig. 130: Inferior glenohumeral ligament tear. Coronal image shows focal discontinuity of the inferior glenohumeral ligament (*long arrow*) along with leakage of synovial fluid (*short arrow*) into the adjacent extra-articular soft tissues.

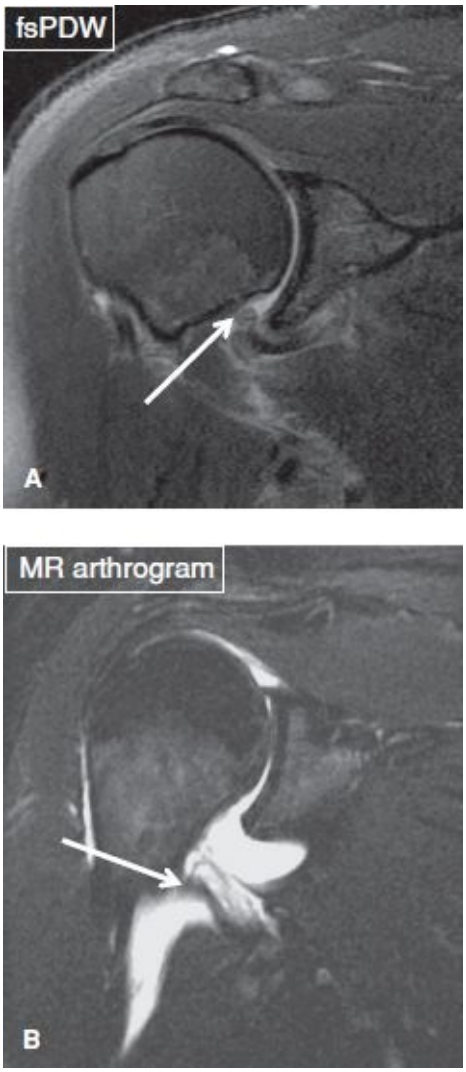

Fig. 131: HAGL lesion. Coronal conventional **(A)** and arthrography **(B)** images from

different patients reveal avulsion of the anterior band of the inferior glenohumeral ligament (*arrows*) from the humerus a.k.a J sign.

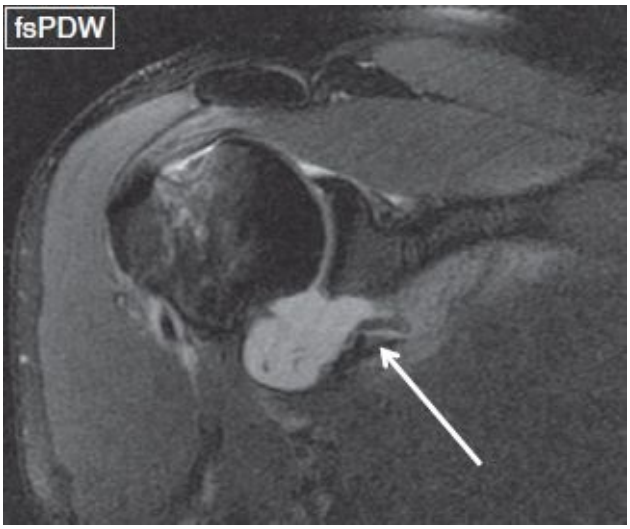

Fig. 132: GAGL lesion. Coronal image demonstrates avulsion of the inferior glenohumeral ligament at the glenoid attachment site (*arrow*).

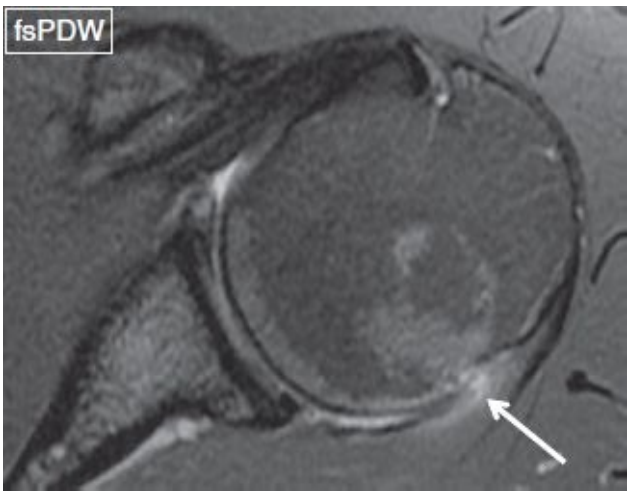

Fig. 133: Reverse HAGL or PHAGL lesion. Axial image shows avulsion of the posterior band of IGL from the humeral attachment (*arrow*).

IGL thickening (>4 mm) and ligamentous/periligamentous edema is commonly seen in the setting of adhesive capsulitis (frozen shoulder). The latter entity presents clinically with decreased range of motion and occasionally pain. If joint distention is absent, the IGL may artifactually appear thickened. Adhesive capsulitis may be primary (absence of preceding trauma) or secondary (related to antecedent injury, low-level repetitive trauma, surgery, or rheumatologic conditions). It involves a combination of inflammatory hypervascular synovitis and progressive fibroblastic response in the capsular and pericapsular tissues leading to capsular contracture and eventually decreased joint capacity. On imaging, the diagnosis should be suggested upon the presence of one or more of findings: inferior glenohumeral ligamentous/periligamentous edema and/or contrast enhancement, synovial thickening (increased signal on sagittal fat-suppressed PDW/T2 W images) and/or fibrosis

(hypointense signal on sagittal T1 W/PDW images) in the rotator interval, partial or complete effacement of the subcoracoid fat planes (usually progressing from the capsule toward the coracoid process), thickened (>4 mm) CHL, and disproportionate pooling of the fluid into the subscapularis recess and biceps tendon sheath (Fig. 134).

Fig. 134: Adhesive capsulitis. Coronal **(A, B)** images show diffuse thickening of the inferior glenohumeral ligament (*arrows*). **C:** Sagittal fsPDW image shows synovial thickening of the rotator interval (*arrow*).

The articular cartilage of the GH joint is harder to evaluate compared to the knee joint cartilage unless high-resolution small field of view imaging is obtained. The evaluation is further complicated by the fact that the dome of the humeral head has relatively thinner cartilage. As a normal variant, a bare area showing absent or very thin cartilage may be present in the central glenoid, and it should not be misdiagnosed as full-thickness cartilage defect (Fig. 135). If a major repair or surgery is contemplated, it is important to assess the status of the cartilage in multiple imaging planes, and particularly report any high-grade or full-thickness defects, as well as associated subchondral bone changes (sclerosis/osteophytes on non–fat-suppressed PD images and marrow edema/cystic changes on fat-suppressed PD images) (Fig. 136). GH joint OA is graded as mild/moderate/severe using similar rules as described above for the AC joint (Figs. 137–140). Usually, the shoulder joint space narrowing and cartilage loss is predictable, e.g., axial narrowing with rheumatoid arthritis associated with diffuse cartilage loss, superior migration of humerus with RC tears and superior cartilage loss, anterosuperior cartilage loss with AVN, and posterior cartilage loss with OA. Rapid chondrolysis may sometimes result following arthroscopy, potentially related to thermal injury or response to injected medications, or it might be predisposed by subchondral fractures associated with labral tears.

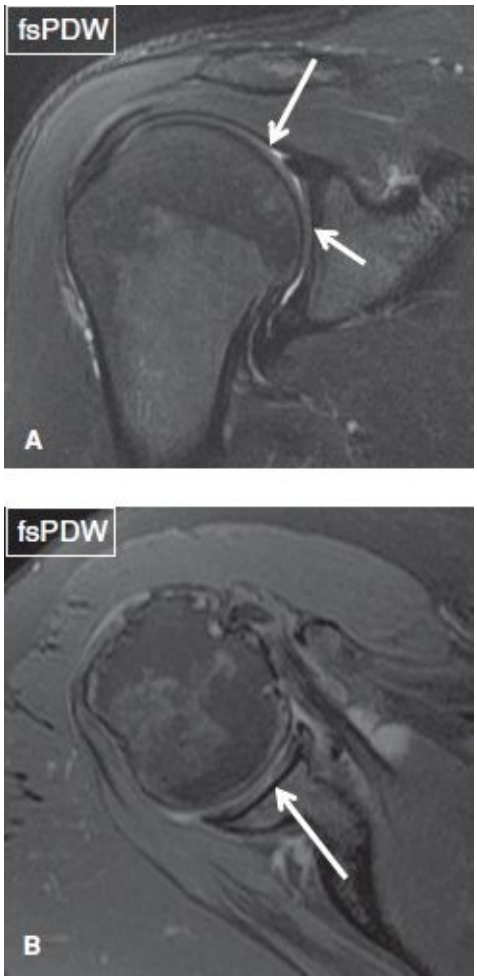

Fig. 135: Normal glenohumeral joint cartilage. **A:** Coronal image shows normal articular cartilage of the humeral head (*long arrow*) and glenoid (*short arrow*). **B:** Axial image from another subject exhibits the centrally located bare area of the glenoid (*arrow*), in which the cartilage is absent.

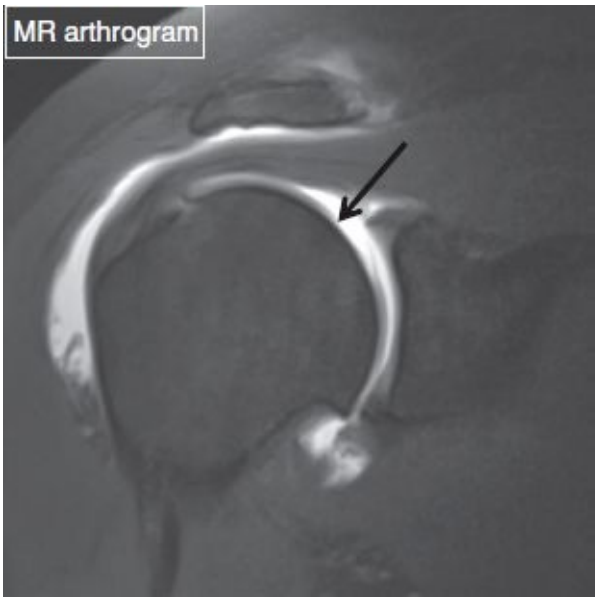

Fig. 136: Articular cartilage thinning. Coronal MR arthrogram image shows an area of high-grade cartilage thinning of the humeral head (*arrow*).

Fig. 137: Severe glenohumeral joint osteoarthritis. Coronal images exhibit osteophytes and high-grade thinning and areas of full-thickness cartilage loss of the glenohumeral joint (*long arrows*), in keeping with severe osteoarthritis. A T1 hypointense, T2 hyperintense fat-containing lesion of the humeral metaphysis (*short arrows*) corresponds to a large geode.

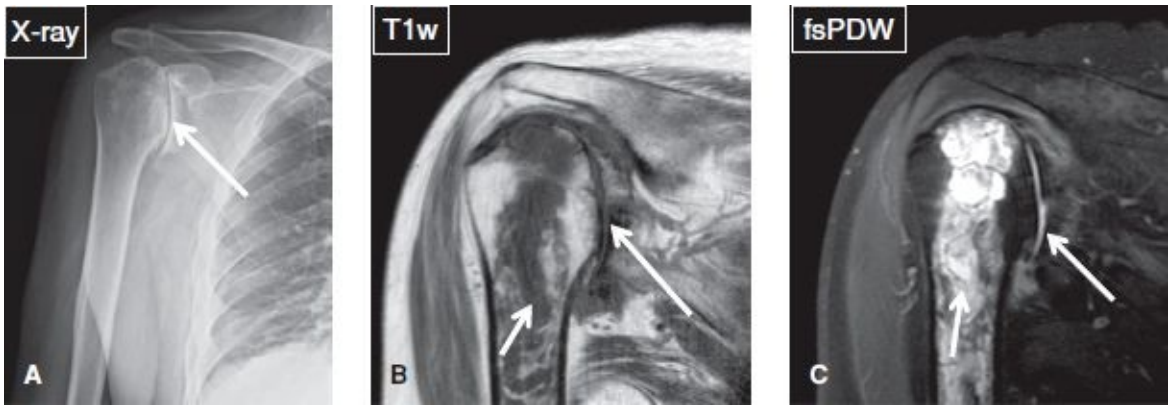

Fig. 138: Severe glenohumeral joint osteoarthritis. *Long arrows* in anteroposterior radiograph **(A)** and coronal MR images **(B, C)** indicate cartilage denudement and bone-on-bone configuration of the humeral head and glenoid in the setting of severe osteoarthritis. **B, C:** Short arrows indicate a T1 hypointense, T2 hyperintense lesion with internal fatty components, which runs along the length of the humerus and corresponds to a large geode.

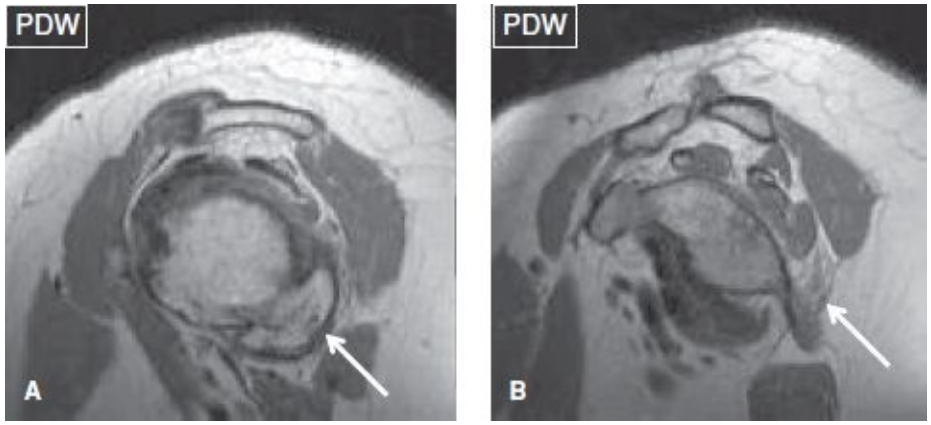

Fig. 139: Quadrilateral space syndrome as a consequence of severe glenohumeral osteoarthritis. Sagittal images. **A:** A large osteophyte (*arrow*) of the inferior glenoid projects into the quadrilateral space. **B:** Arrow indicates the teres minor muscle, which has undergone atrophy and fatty degeneration, presumably due to denervation from

compression of the axillary nerve by the large osteophytes.

Fig. 140: Articular cartilage denuding in the setting of severe osteoarthritis. Coronal image shows partial ankylosis of the glenohumeral joint (*arrow*), along with completely denuded articular cartilage.

The most common types of arthritis include OA (manifested as asymmetrical cartilage loss, joint space narrowing, osteophytes, subchondral sclerosis and cysts, effusion, synovial thickening, and loose bodies), rheumatoid arthritis (bilateral symmetric involvement, juxta-articular osteoporosis, symmetrical joint space narrowing, erosions, effusions, rice bodies, large fat-containing geodes, pannus formation), gout (well-corticated eccentric erosions, also known as rat bites, eccentric soft tissue masses, preferential involvement of the AC joint), hydroxyapatite deposition disease (calcific tendinitis or bursitis, Milwaukee shoulder in advanced stages with rapid RC and shoulder cartilage destruction mimicking neuropathic joint), septic arthritis (clinical evidence of toxemia, effusion, synovial thickening, surrounding bursitis, fascial edema, or myositis, reactive marrow edema or osteomyelitis with bone destruction and avid contrast enhancement), PVNS (affects young individuals with unilateral or one joint involvement, effusion and heterogeneous nodular mass and hemosiderin staining), and neuropathic joint (involving patients with neuropathy or diabetes, and depicted as joint destruction, disorganization, debris, dislocation, hypointense signal intensity on all sequences) (Figs. 141–144).

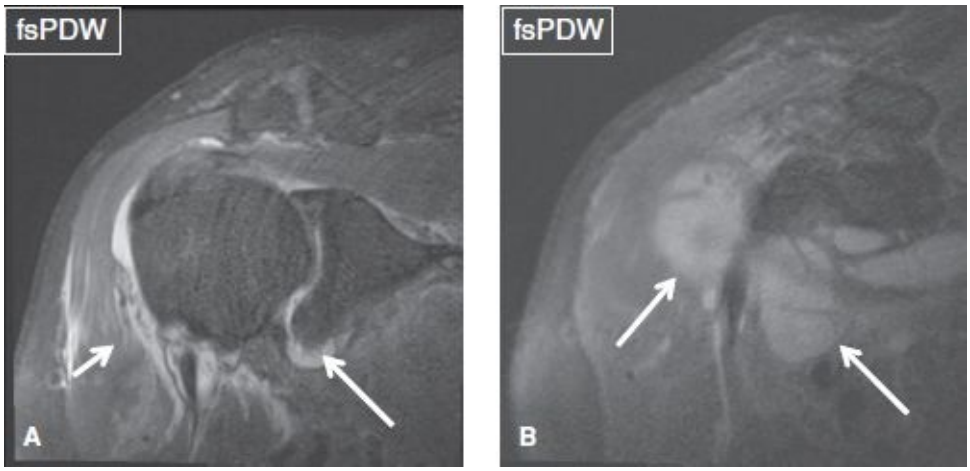

Fig. 141: Septic arthritis and myositis. Coronal images. **A:** There is muscle edema (*short arrow*), complex fluid within the glenohumeral joint, along with edema of the surrounding soft tissues (*long arrow*). **B:** Rounded, septated fluid collections anteriorly correspond to abscesses (*arrows*).

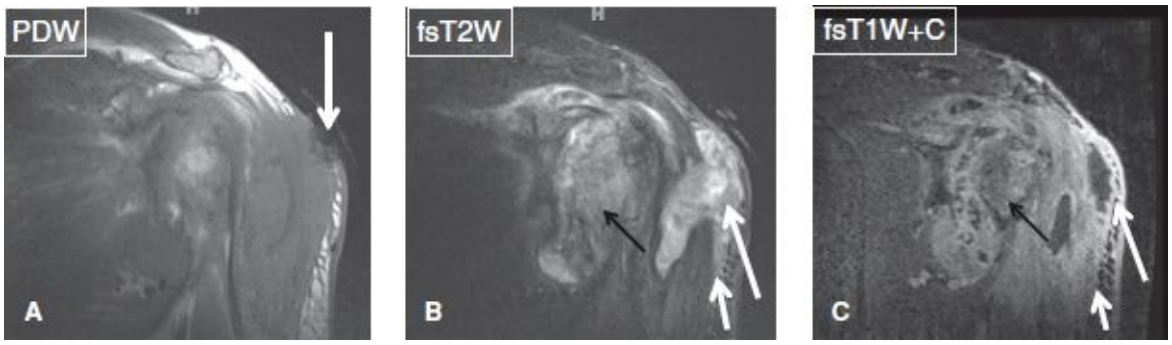

Fig. 142: Septic shoulder. Coronal conventional **(A, B)** and contrast-enhanced **(C)** images show extensive skin ulcerations, osteomyelitis (*short black arrows* in **B** and **C**), peripherally enhancing abscesses (*long arrows* in **B** and **C**), and complex joint fluid. Notice associated cellulitis and myositis, a common indicator of infection (*short white arrows* in **B** and **C**).

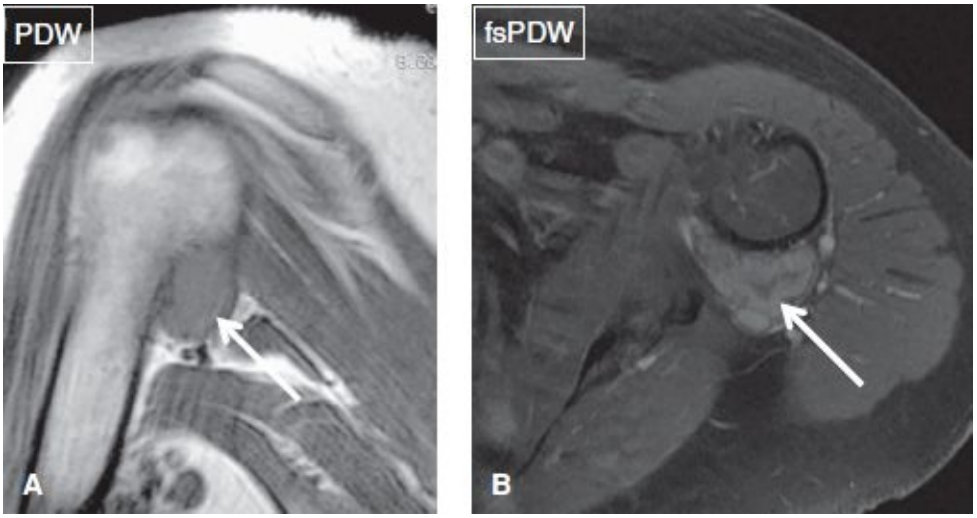

Fig. 143: Pigmented villonodular synovitis. Coronal **(A)** and axial **(B)** images demonstrate filling of the axillary pouch by T1 isointense and heterogeneous T2 hyperintense lesion, a biopsy proven PVNS (*arrows*).

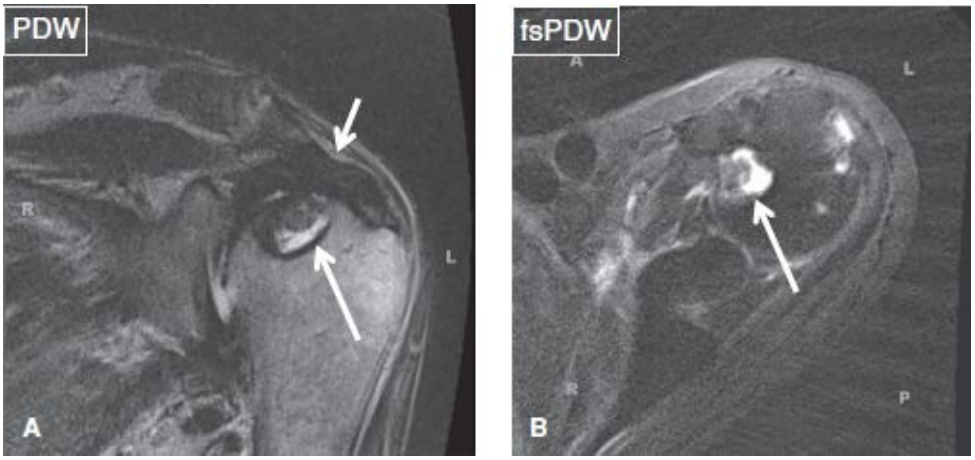

Fig. 144: Amyloid arthropathy in the setting of chronic renal insufficiency. Coronal **(A)** and axial **(B)** images show hypointense thickening of the joint capsule underneath the rotator cuff due to deposition of hypointense soft tissue (*short arrow* in **A**), along with hypointense material containing erosive, cystic lesions of the humeral head (*long arrows*).

BONES: [<Otherwise normal> <Greater tuberosity / Lesser tuberosity cysts> <Enthesopathy>]

In avascular necrosis (AVN) of the humeral head, the osteonecrotic area is usually half-moon shaped, demonstrates heterogeneous signal, does not enhance after contrast administration, and is demarcated by a hypointense band, which is sometimes paralleled by a T2 hyperintense band (double line sign) (Figs. 145, 146). Later stages are characterized by subchondral fracture, collapse, and secondary OA. One should look for the underlying cause such as trauma, alcoholism, steroid intake, sickle cell anemia, Gaucher disease, etc.

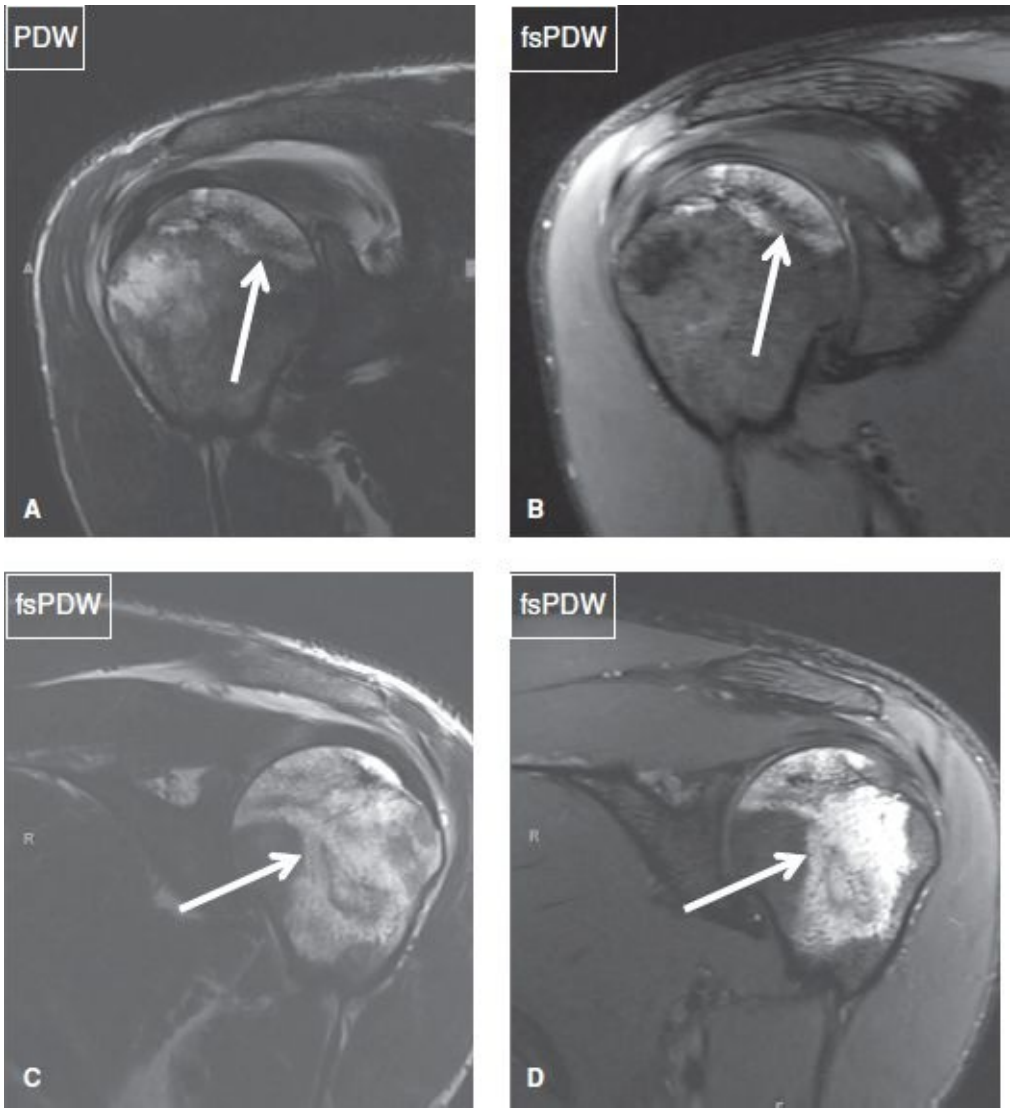

Fig. 145: Bone infarcts in the setting of sickle cell disease. Coronal images (**A–D**) of both shoulders demonstrate geographic hyperintense marrow areas in bilateral humeral heads (*arrows*) corresponding to bone infarcts. Notice underlying red marrow reconversion.

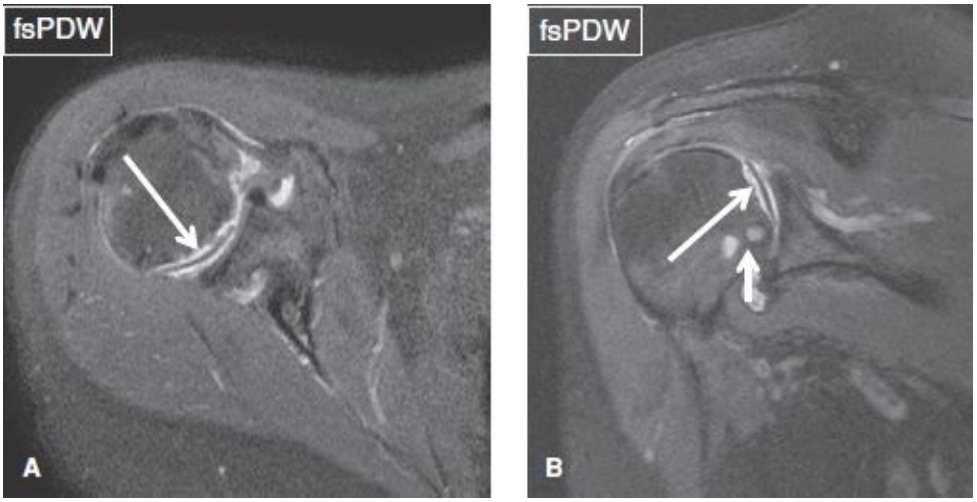

Fig. 146: Chronic avascular necrosis. Axial **(A)** and coronal **(B)** images show a thin crescentic T2 hyperintense subchondral area (*long arrows*), which represents an unstable fragment of the humeral head subchondral surface. Notice underlying subchondral cysts of chronic AVN (*short arrow*).

Little Leaguer's shoulder refers to acute or subacute Salter I fracture of the proximal humeral epiphysis. The entity mostly involves 12- to 16-year-old pitchers and is identified as widening and hyperintensity of the humeral physis on fat-suppressed PDW/T2W images, more pronounced along its lateral aspect. In the subacute and chronic stages, there is development of periphyseal cysts and sclerosis.

Other bony findings that may be detected include, greater/lesser tuberosity and humeral neck fractures, subchondral superior humeral head fracture (from crutches), greater/lesser tuberosity cysts, and enthesopathy (Figs. 147–149). Cystic lesions on the greater tuberosity may occur due to avulsions of the RC fibers (associated with articular sided tendon tears), subacromial impingement (at the undersurface of the acromion and anterior or central greater tuberosity), or posterior peel-back lesion (posterior aspect of the greater tuberosity under the junction of posterior SS and anterior IS tendons), cartilage rests (<1 cm, unrelated to RC tears and closer to the physeal scar), or enchondroma (multilabulated bubbly lsion, more than 1 cm and may show mineralization). Lesser tuberosity cysts are generally related to avulsion cystic changes of subscapularis attachment or subcoracoid impingement (in the latter case, cysts may occur on coracoid process as well). Marrow changes mimicking mass lesions can result from red marrow reconversion or Paget disease. Common incidental mass lesions include enchondroma, unicameral bone cyst, osteosarcoma (in children), and multiple myeloma, lymphoma, or metastatic deposits (in adults) (Figs. 150–154). The marrow may undergo serous atrophy due to radiation treatment, chemotherapy, immunodeficiency state and malnutrition. It appears as cystic marrow lesions or diffuse marrow hyperintensity of the skin and subcutaneous tissues with inability to suppress marrow fat on fat-suppressed fluid sensitive images (Fig. 155).

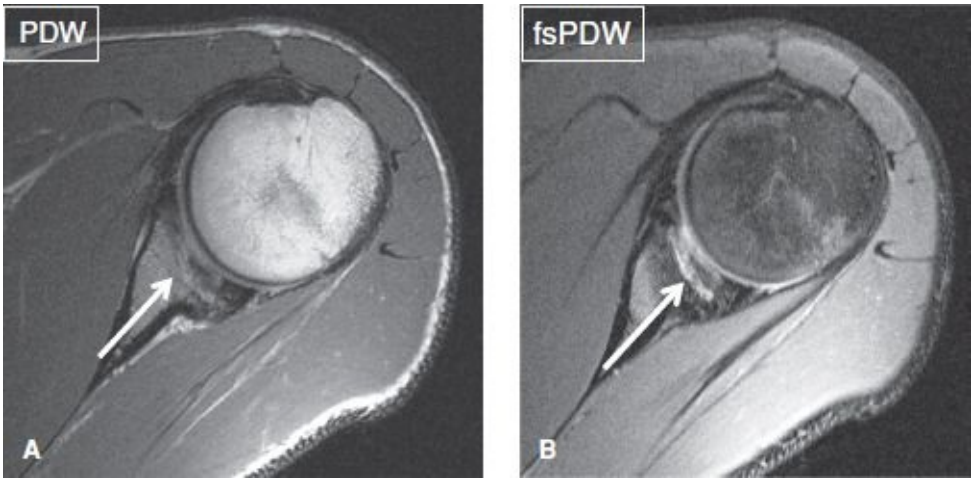

Fig. 147: Osteochondral fracture of the glenoid. Axial images (**A, B**) show an impaction fracture of the articular surface of the glenoid (*arrows*), involving both bony and cartilaginous elements.

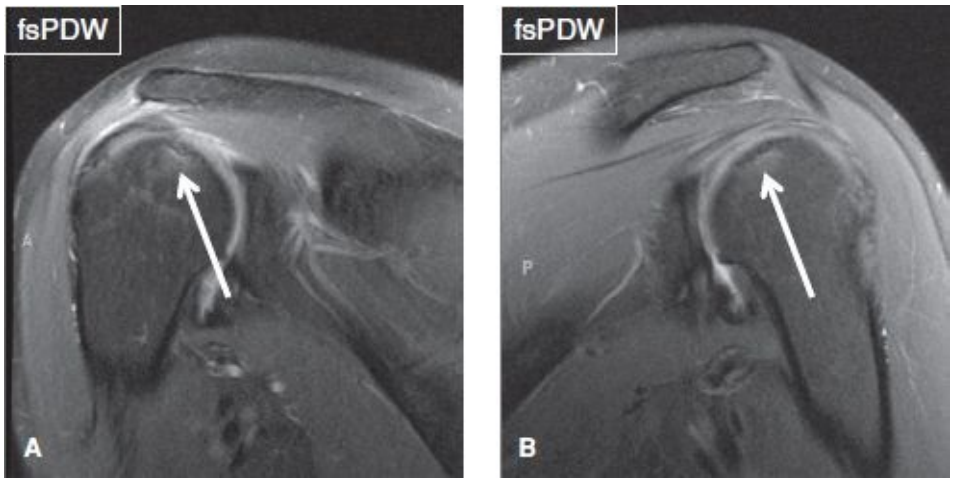

Fig. 148: Osteochondral humeral head fractures. Coronal images (**A, B**) from different cases show osteochondral fractures of the superior portion of the humeral heads (*arrows*), a common pattern seen in patients on crutches.

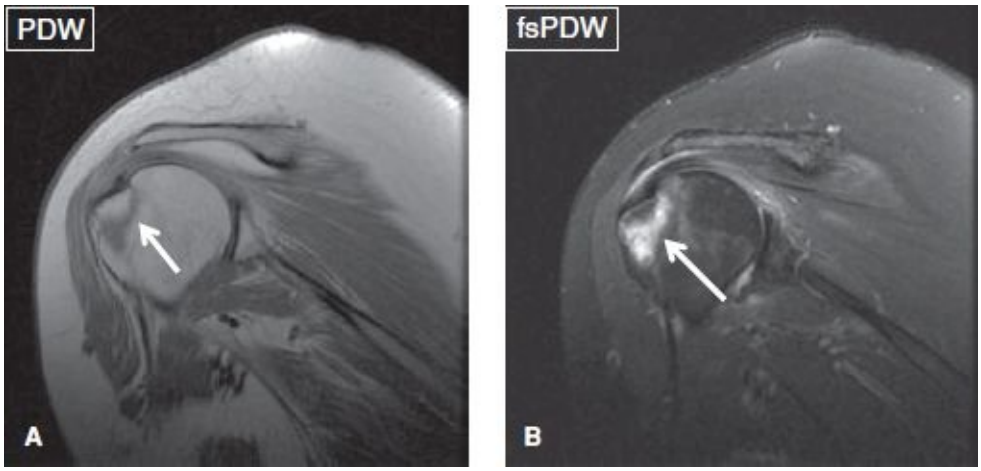

Fig. 149: Greater tuberosity fracture. Coronal images (**A, B**) show a impaction fracture of the greater tuberosity.

Fig. 150: Bone marrow reconversion in the setting of extramedullary hematopoiesis. Sagittal **(A)** and coronal **(B)** images show hyperintensity of the humeral epiphysis, corresponding to hematopoietic marrow. Notice mass lesion on the top of the acromion, a biopsy proven

extramedullary hematopoiesis.

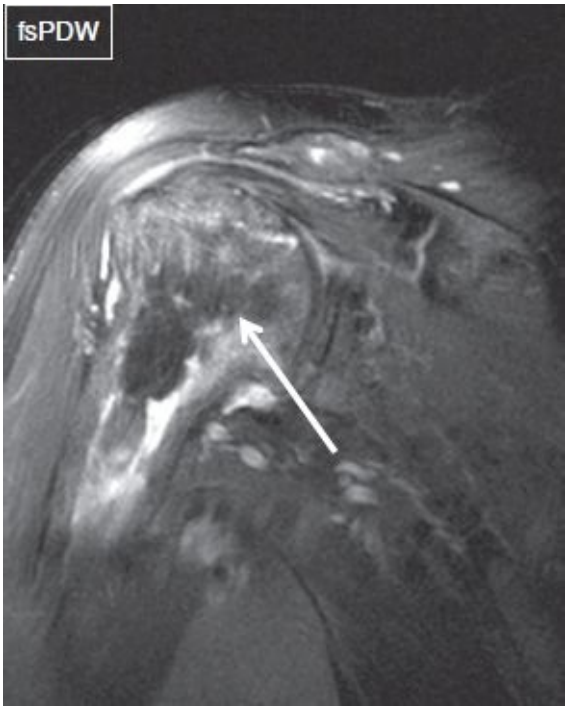

Fig. 151: Paget disease. Coronal image shows a heterogeneous lesion (*arrow*) involving the superior third of the humerus. Notice cortical thickening and endosteal hyperintensity typical of mixed phase of this lesion. One might also see fibro-fatty marrow proliferation in more chronic stage of the disease.

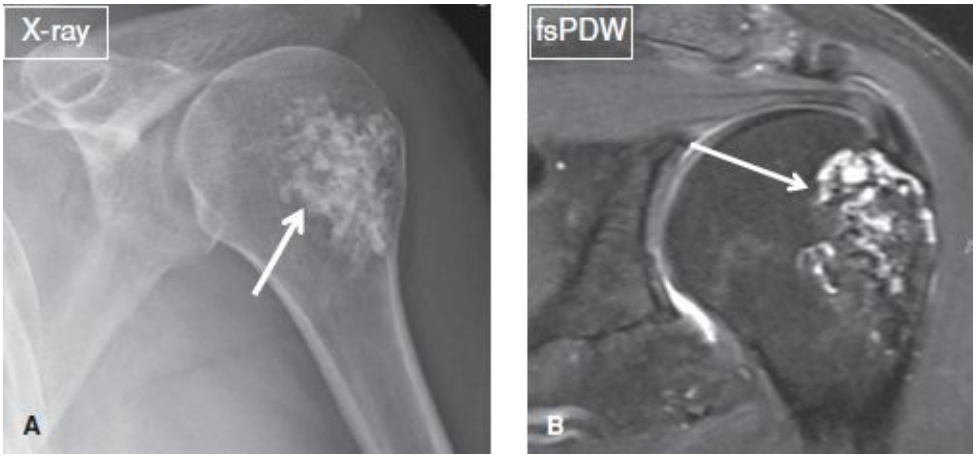

Fig. 152: Humeral head enchondroma. **A:** Anteroposterior radiograph shows multiple chondroid-type (rings and arcs) calcifications (*arrow*) in the humeral head. **B:** The respective coronal MR image shows a nonaggressive intramedullary lesion (*arrow*) with sharp irregular (popcorn-like) contours, and internal chondral (T2 hyperintense) components and dark mineralization.

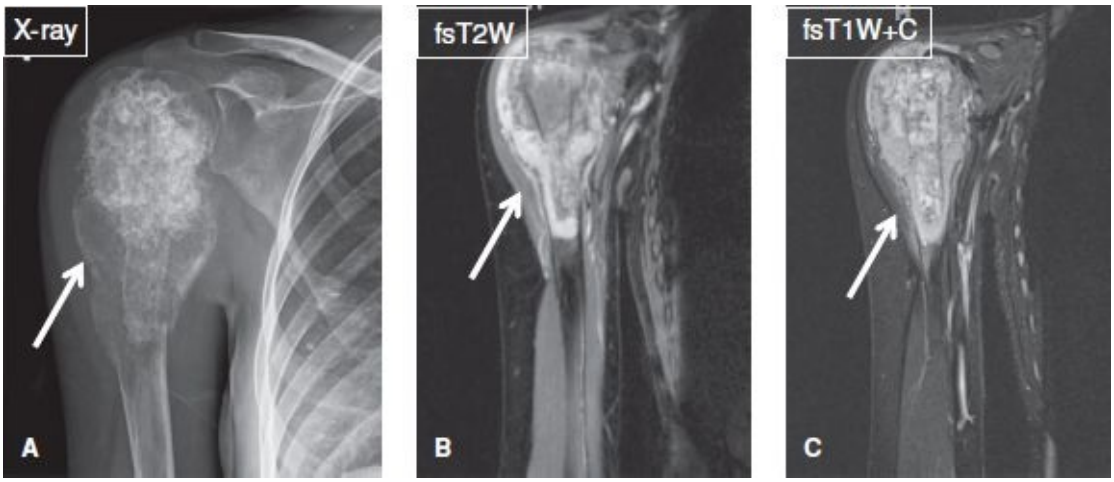

Fig. 153: Osteosacroma of the humerus. Coronal conventional **(A, B)** and contrast-enhanced **(C)** images demonstrate an aggressive lytic and bone-productive lesion (*arrows*), which has extensive soft tissue components and shows intense contrast enhancement. MRI confirms the epiphyseal involvement.

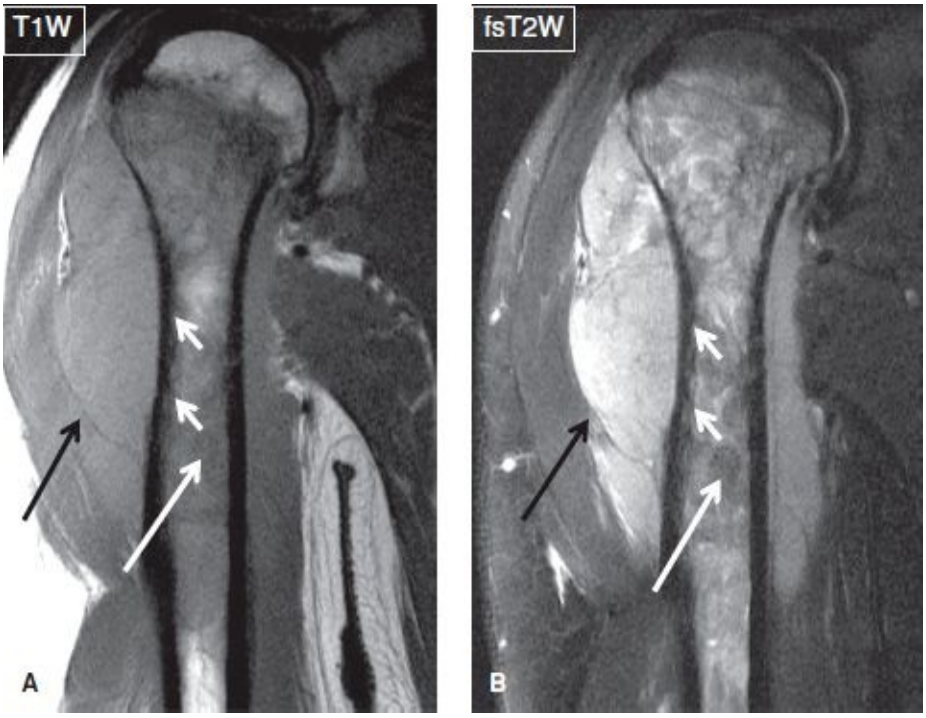

Fig. 154: Bone lymphoma. Coronal images show a heterogeneous intramedullary lesion (*long white arrows*), which causes permeative changes in the cortex (*short white arrows*) and is associated with an extramedullary soft tissue mass (*black arrows*).

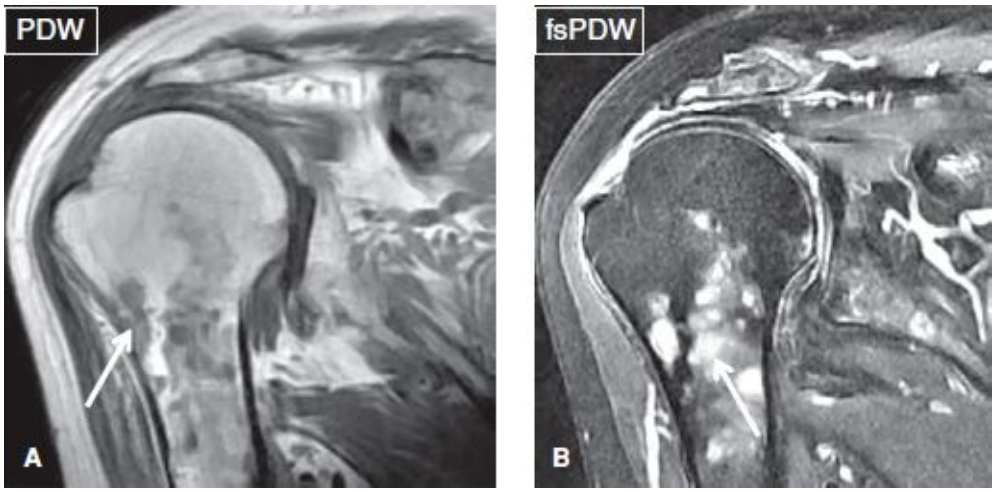

Fig. 155: Serous atrophy of bone marrow. Coronal images demonstrate multiple cystic appearing lesions in the humeral metaphysis and epiphysis, corresponding to foci of serous marrow atrophy (*arrows*).

MUSCLES: [<Otherwise normal>]

Various muscle abnormalities may be encountered around the shoulder joint, including RC muscle atrophy and fatty replacement (usually resulting from RC tears, and demonstrating diffuse involvement in the distribution of the involved tendons), muscle strains (from trauma), infectious/inflammatory myopathy (patchy edema-like signal in the muscle and fascia on fat-suppressed PDW images, T1 hyperintensity or hemorrhage with rhabdomyolysis), Parsonage–Turner syndrome (also known as acute brachial plexopathy, depicted as diffuse muscle denervation changes in the distribution of the involved nerves, commonly with more than two to three muscles affected, lack of fascial edema, hyperintense/enlarged suprascapular/axillary nerves, and/or brachial plexus), and denervation changes from suprascapular nerve impingement (identify paralabral cysts or varicosities in the suprascapular notch, spinoglenoid notch, or quadrilateral space) (Figs. 156–159).

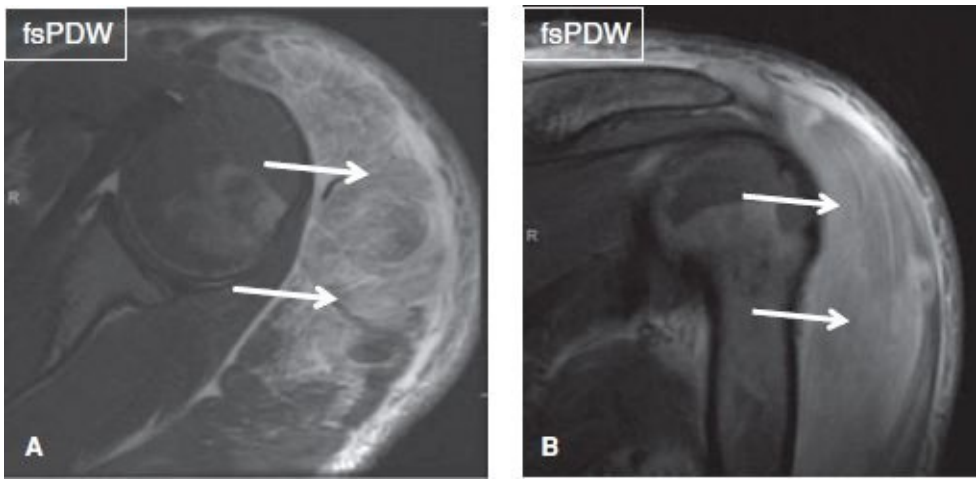

Fig. 156: Rhabdomyolysis. Axial **(A)** and coronal **(B)** images demonstrate diffuse edema and enlargement of the deltoid muscle with perimuscular fascial edema (*arrows*).

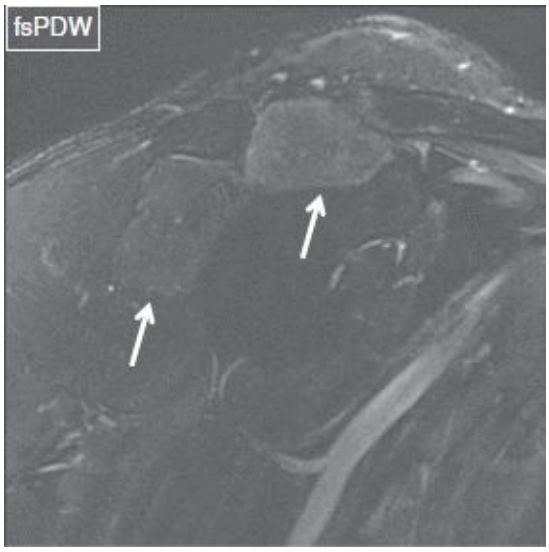

Fig. 157: Parsonage–Turner syndrome. Sagittal image demonstrates diffuse edema of the supraspinatus and infraspinatus muscles (*arrows*). Notice lack of fascial edema, typical of denervation change.

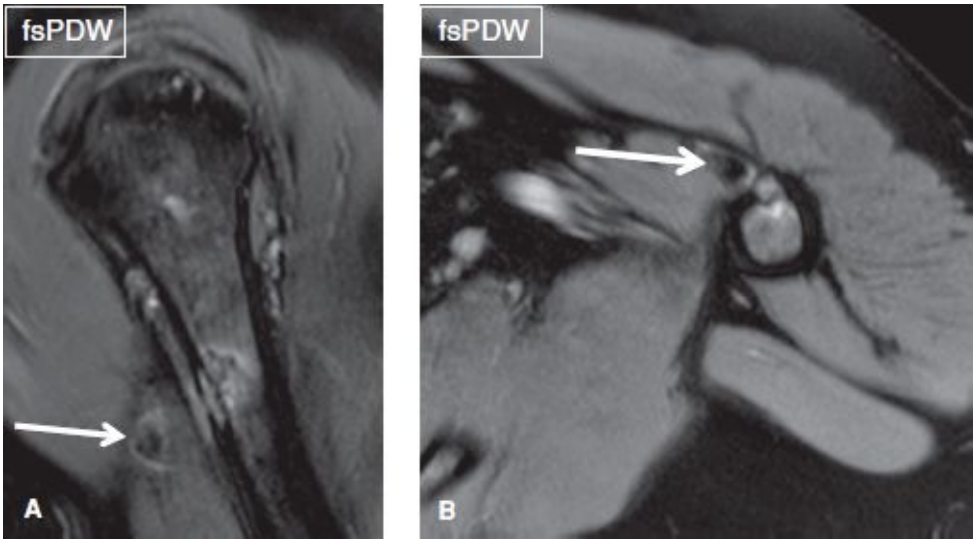

Fig. 158: Calcium hydroxyapatite deposition disease. Sagittal **(A)** and axial **(B)** images exhibit a hypointense lesion (*arrows*), corresponding to calcification, within the pectoralis major muscle. Minimal perilesional edema is seen due to inflammation.

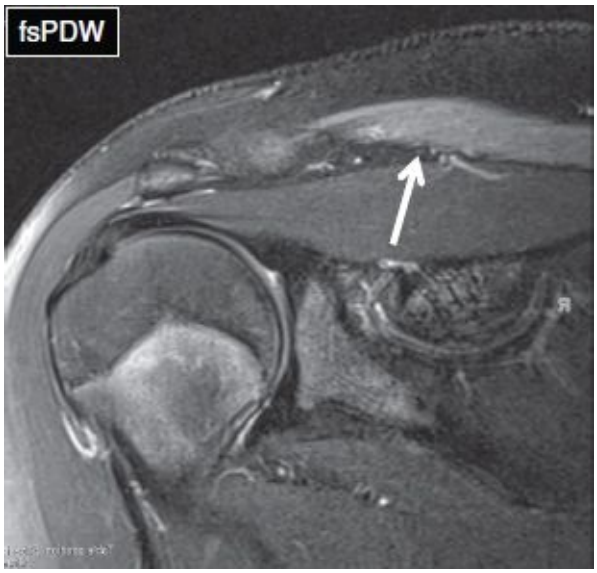

Fig. 159: Denervation of the trapezius muscle. Coronal image exhibits diffuse edema-like signal of the trapezius muscle (*arrow*) without fascial edema.

Finally, teres minor muscle edema, fatty replacement, and/or atrophy are commonly encountered as isolated findings and are thought to result from muscle disuse or from injury to the supplying branch of axillary nerve (Fig. 160). The nerve may sustain local trauma or traction injury, may be entrapped by paralabral cyst or large osteophyte, or more commonly, become involved with inflammation around the IGL in cases of adhesive capsulitis.

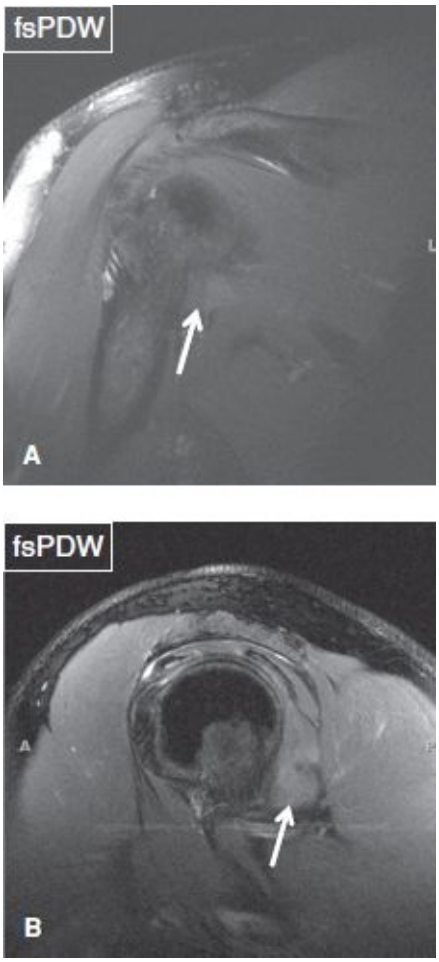

Fig. 160: Teres minor muscle edema. Coronal **(A)** and sagittal **(B)** images exhibit mild edema-like signal of the teres minor muscle (*arrows*), a common incidental finding.

VESSELS: [<Normal>]

Look for prominent varicosities in the suprascapular/spinoglenoid notches or other vascular malformations. High flow vascular malformations show flow voids, while slow-flow vascular malformations feature phleboliths or fluid–fluid levels (Fig. 161). Further details about imaging characteristics of vascular malformations are available in Chapter 4.

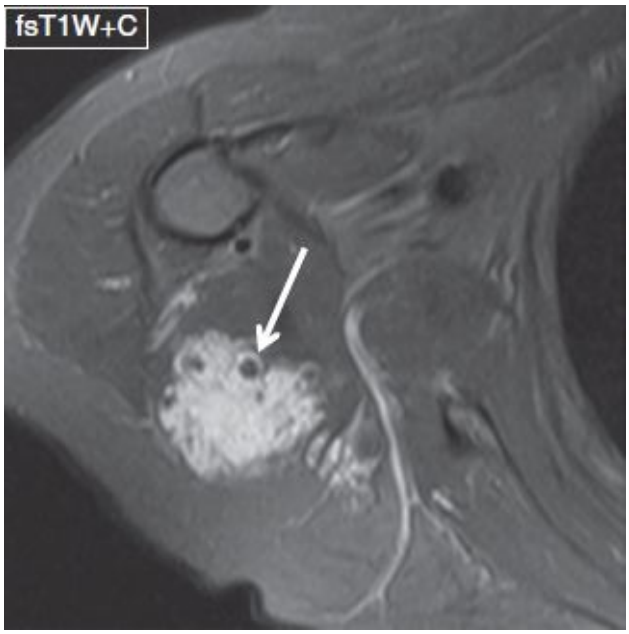

Fig. 161: Venous malformation. Axial image shows an intramuscular lobulated lesion with phleboliths (*arrow*) and intense contrast enhancement.

NERVES: [<Normal>]

Look for findings suggesting nerve entrapment. Paralabral cysts compress the suprascapular nerve and cause denervation of the supraspinatus and infraspinatus muscles (when occupying the suprascapular notch, which is located anterosuperior to the scapular spine) (Fig. 124), or infraspinatus muscle (when projecting into the spinoglenoid notch, which is located posteroinferior to the scapular spine) (Fig. 123). Paralabral cysts, fibrous bands, large osteophytes, or other mass lesions can project into the quadrilateral space (formed by the teres minor muscle superiorly, the teres major muscle inferiorly, the humerus laterally, and the long head of the triceps muscle medially) and impinge on the axillary nerve, causing denervation of the deltoid and teres minor muscles (Fig. 139). Finally, Parsonage–Turner syndrome can involve multiple shoulder muscles, most commonly the supraspinatus, infraspinatus, and teres minor (Fig. 157). MR neurography of the brachial plexus may be performed to confirm the clinical suspicion. Among the upper extremity nerves, the ulnar nerve is the least likely affected by this syndrome.

Postoperative Findings

Reconstructed tendons and ligaments should follow their normal course, feature anatomic continuity, and not demonstrate fluid-like signal. Mild signal alteration or thickening is a common postoperative finding, and should gradually regress over many months following the surgery as the tendons/ligaments heal, remodel, and mature. The following paragraphs describe the most common surgical procedures performed in the shoulder joint along with their imaging findings.

RC repair may be performed via arthroscopy, bursoscopy, or open procedure. The entry portal is usually via the deltoid muscle. A torn RC tendon can be reattached with tendon anchors if there is an anterior leading edge high-grade or full-thickness tear, or debrided if there is bursal-sided fraying or flap tear. Surgery is only opted in cases of intermediate- to high-grade articular-sided tears due to low vascularity and poorer healing capacity. While even low- to intermediate-grade bursal-sided tears are amenable to be tackled with surgery, as they are more likely to be symptomatic and respond to debridement or repair due to the good vascularity on the bursal side. It is debatable whether single row or double row suture repair produces better results. One will see two or more anchors with double row repair. If the tendon tear is large, the humeral head may be recontoured, the subscapularis tendon may be shortened, and the RC is reattached more medially at the footprint. More proximal tears are sutured together. Underlying humeral head cartilage defects may be treated with abrasion chondroplasty during the same surgery for expected fibrocartilage filling. Massive tears may be treated with patch graft or by reverse shoulder arthroplasty in older subjects, especially in the setting of moderate–severe muscle atrophy.

Normal postoperative MR appearances include a reattached, continuous RC with susceptibility artifacts from the tendon anchors, but no fluid cleft through the tendon (mild T2 heterogeneity or thickening is normal) (Fig. 162). A small amount of fluid is normal in the SASD bursa postoperatively. On MR arthrography, contrast medium may leak into the SASD bursa via the arthroscopy portal site and through the rotator interval. Signs indicating a retear include a fluid cleft through the tendon or discontinuous tendon, exposed tendon anchors that are uncovered by the retorn RC tendon(s), loose or dislocated anchors, and moderate bursal distention with tenosynovitis. Factors predisposing to retear include a previous large RC tear, old age, underlying systemic comorbidities, and history of recent fall/trauma (Figs. 163–166). Other complications include rapid chondrolysis (see above) and deltoid muscle atrophy or tears at or adjacent to the site of the portal placement.

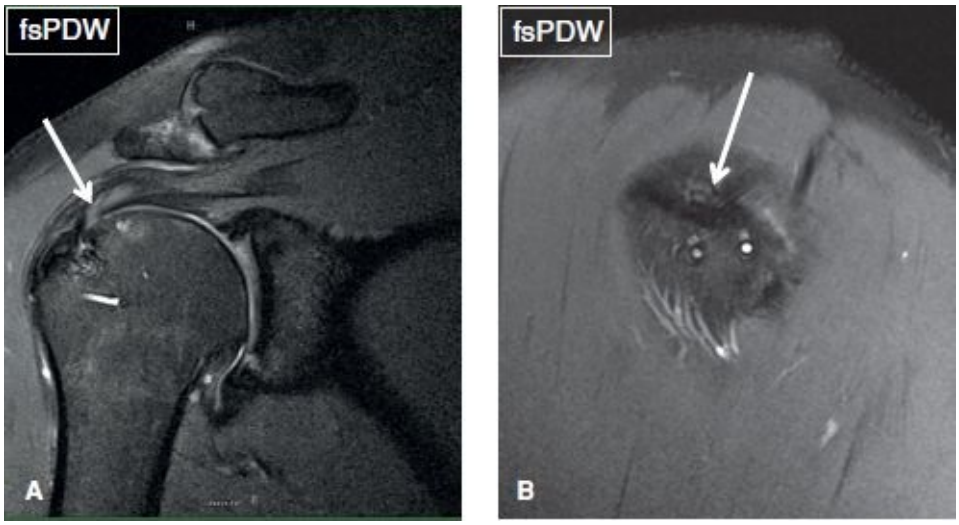

Fig. 162: Normal postoperative rotator cuff. Coronal **(A)** and sagittal **(B)** images show absence of fluid signal within the reattached rotator cuff tendons (*arrows*).

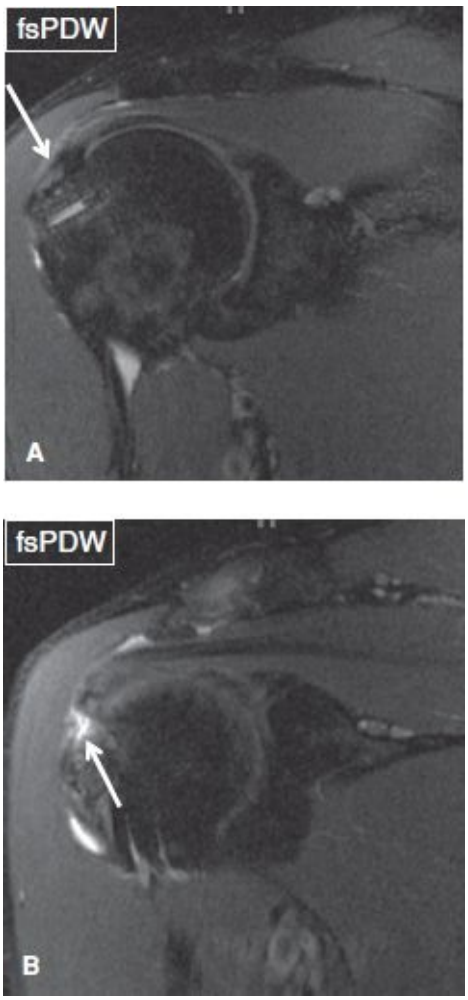

Fig. 163: Rotator cuff retear. **A:** Coronal image shows intact reattached tendon with a single row repair (*arrow*). **B:** Following a recent fall, repeat coronal image shows a full-thickness retear (*arrow*) with mild distention of the subacromial/subdeltoid bursa.

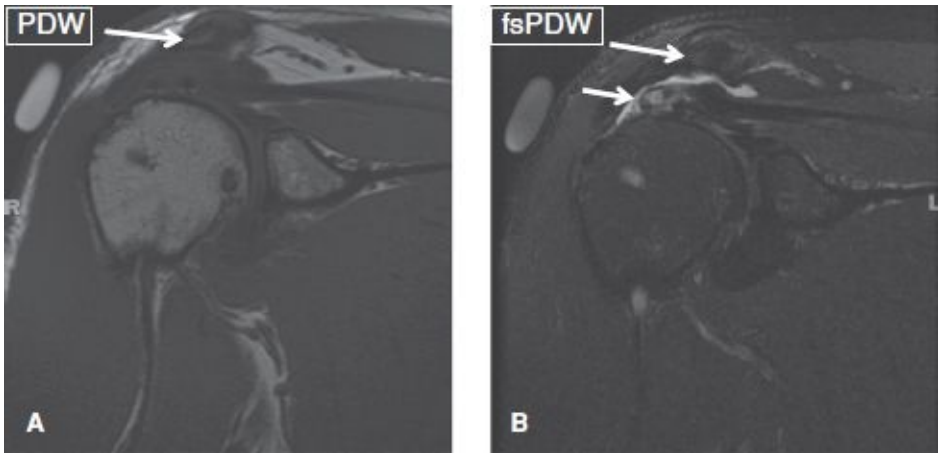

Fig. 164: Retear of the rotator cuff with retraction. Coronal images **(A, B)** exhibit acromioplasty changes (*long arrows*) as well as full-thickness tear of the rotator cuff, which is proximally retracted (*short arrow* in **B**) to the level of the humeral head.

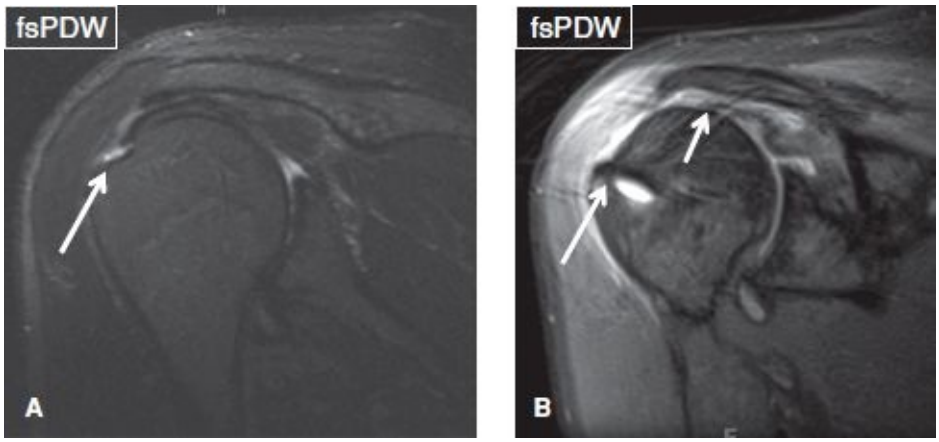

Fig. 165: Full-thickness rotator cuff retear due to recent fall. Coronal images. **A:** There is a full-thickness tear (*arrow*) of the rotator cuff at the attachment site. **B:** Postoperative changes (*long arrow*) are evident in the greater tuberosity along with acromioplasty from rotator cuff surgical repair. Notice full-thickness retear (*short arrow*) following a recent fall.

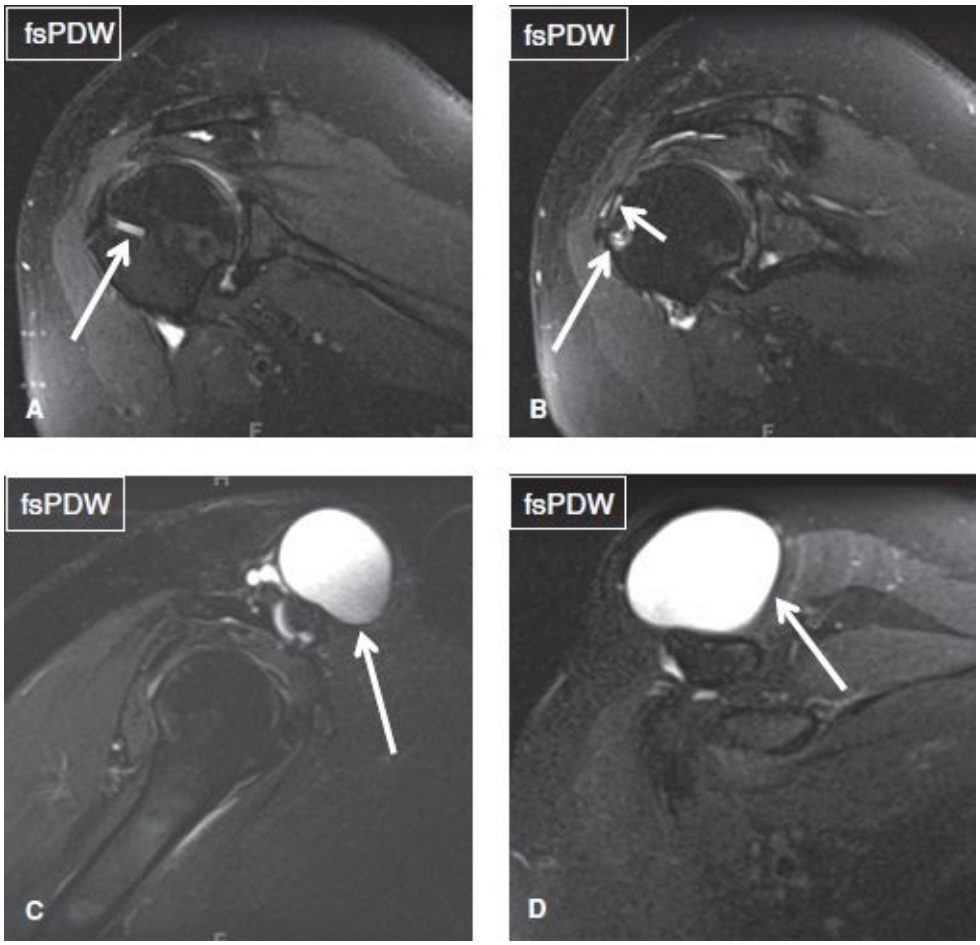

Fig. 166: Retear of the rotator cuff with geyser phenomenon. Coronal images **(A, B)** demonstrate postoperative changes with tendon anchors of the rotator cuff (*long arrows*) and a partial tear (*short arrow* in **B**) at the attachment site. The corresponding sagittal **(C)** and coronal **(D)** images exhibit a well-defined cystic lesion (*arrows*) superior to the acromioclavicular joint, in keeping with geyser phenomenon.

Low-grade tears of the LHBT can be treated with debridement, whereas high-grade and full-thickness tears are treated with tenodesis (in which an anchor is used to tether the tendon at the bicipital groove), or less commonly, tenotomy (complete cutting of tendon, allowing it to retract distally).

For hypertrophic changes of the AC joint, the Mumford procedure is commonly performed, which involves resection of the distal (up to 1 cm) clavicle. Postoperatively, the AC joint space will appear normally widened. Care is required during the surgery not to inadvertently resect the CC ligament. Acromioplasty involves resection of the subacromial spur and smoothening of acromion undersurface. In the postoperative setting, the acromion features a concave undersurface with or without subcortical cystic changes (Fig. 167) (Figs. 164, 165). AC joint undersurface partial resection might also be performed along with acromioplasty.

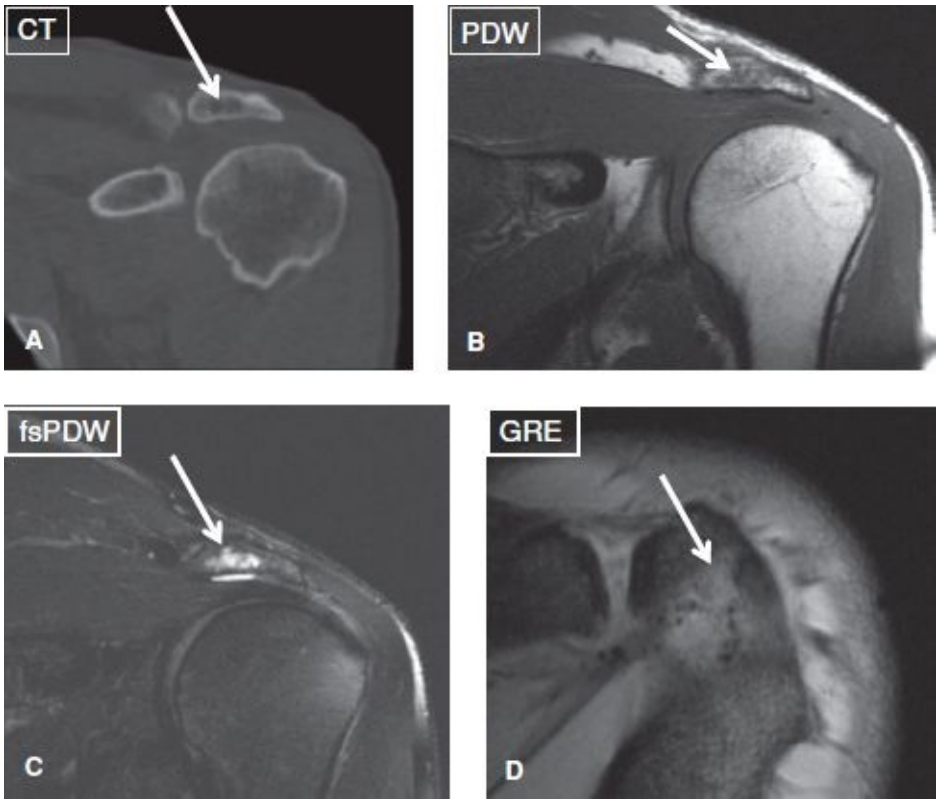

Fig. 167: Acromioplasty-related changes. Coronal CT image **(A)** and coronal **(B, C)** and axial **(D)** MR images demonstrate small cysts (*arrows*) at the distal acromion with susceptibility artifacts attributed to postoperative changes.

Small labral tears are treated with debridement, whereas larger, detached, or bucket-handle tears are repaired using labral tacks or anchors. Many surgeons these days fix the labral tear around 12 o'clock position superiorly. Therefore, one might see residual tear anterosuperiorly and posterosuperiorly, which can make the interpretation regarding retear challenging on the subsequent examination. A lax joint capsule could be reefed up with plication, laser, or thermal treatment, which would limit the external rotation. In posterior peelback lesions, the lax anterior capsule is tightened with inferior capsular shift. The idea is to move the center of rotation more distal and medial. Torn ligaments are reattached if possible. The Latarjet–Bristow procedure is used for bony Bankart lesions to beef up the defect using the coracoid process. More than 25% glenoid bone loss demonstrated qualitatively as 'reverse pear' shaped glenoid on the sagittal image, is an indication to perform this surgery in order to prevent recurrent instability. To measure the amount of glenoid bone loss, on sagittal image, draw a best fit circle on the glenoid and draw a perpendicular line from the one circumference to the other anteroposteriorly. The percentage of missing bone is calculated along that line. Larger glenoid defects (greater than 40% of the area) can be repaired using bone allografts or by transferring the infraspinatus tendon and the adjacent greater tuberosity into the defect (Connolly procedure). Large Hill-Sachs lesions may require bone grafting or remplissage procedure with IS tendon and posterior capsule interposition in the bony defect to prevent recurrent instability. This procedure has been shown to be useful in engaging Hill-Sachs lesions, prone to recurrent instability. On imaging, the repaired labrum appears mildly truncated and

amorphous compared to the native labrum. However, there should be no fluid clefts through the labrum or detachment. Retears are indicated by fluid (or gadolinium, if MR arthrogram is obtained) undercutting the repaired labrum and loose anchors/tacks (Figs. 168–170). Small surface lesions, or fraying/retears may also occur over time due to degeneration. If there is no clear cut sublabral cleft or tear, err on the side of calling it as normal postoperative change.

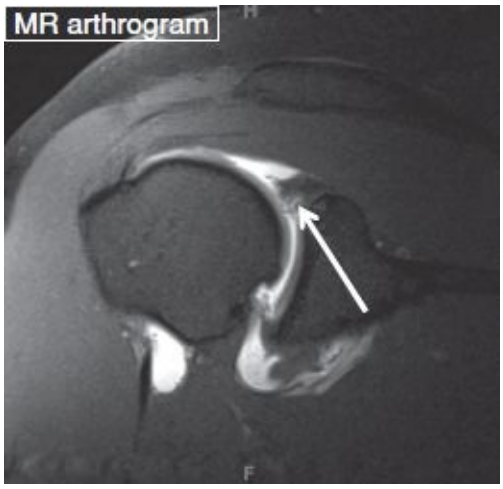

Fig. 168: Retear of a surgically repaired labrum. Coronal arthrography image demonstrates retear of a previously repaired superior labrum (*arrow*).

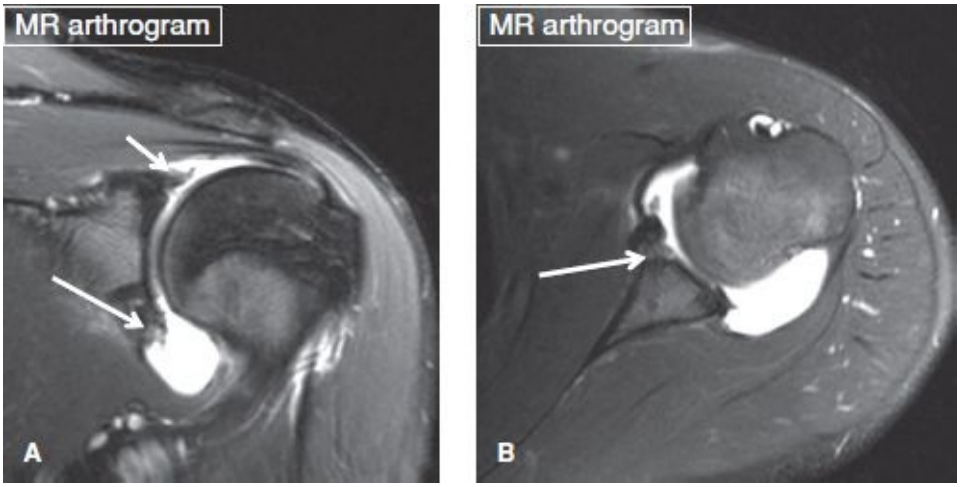

Fig. 169: Retear of a surgically repaired labrum. Coronal **(A)** and axial **(B)** arthrography images show surface retear of a surgically repaired inferior labrum (*long arrows*). Also note normal postoperative minimal truncation of the superior labrum (*short arrow* in **A**).

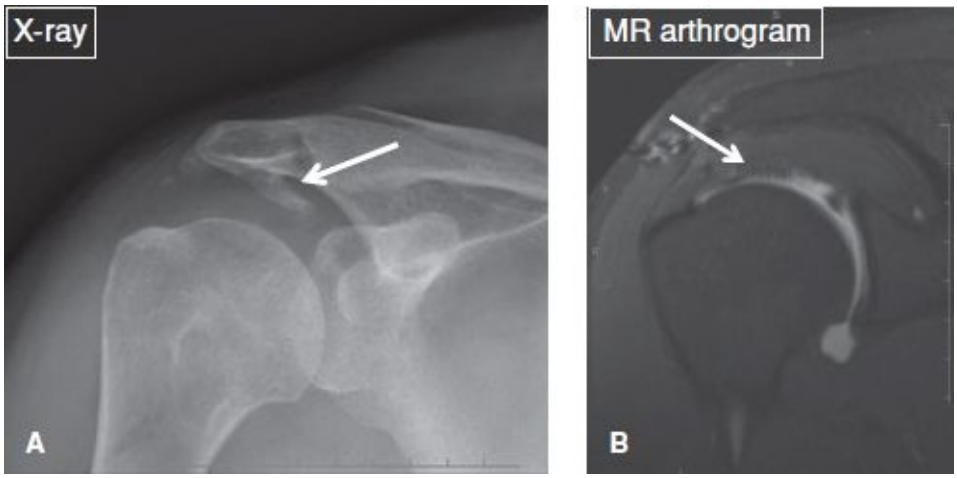

Fig. 170: Displaced screw. In an anteroposterior radiograph **(A)** and coronal MR image **(B),** a displaced surgical screw (*arrow*) is faintly seen lying within the joint along the undersurface of the tendon.

Other

Elastofibroma dorsi is a benign soft tissue tumor, which is composed of fibrous tissue with internal fatty streaks and is typically located in the infrascapular region, deep to the serratus anterior and latissimus dorsi musculature. Although well defined, the lesion shows no capsule, appears isointense to muscle on T1W and T2W images and enhances heterogeneously (Fig. 171). These may contain flow voids and can be quite vascular. Other mass lesions include fibromatosis or desmoid in the periscapular area. These lesions show predominantly T2 hypointense although variable signal characteristics (Fig. 172). Intense enhancement is seen with contrast examination. Other incidental findings include lung lesions, axillary lymph nodes, lipoma, and scapulothoracic bursitis (Figs. 173–175). Scapulothoracic bursitis can occur along inferior medial border of scapula, superomedial border, or under the serratus anticus muscle. It may be idiopathic or may occur in association with an osteochondroma. Finally, pseudoarticulations between the clavicle and coracoid process or first rib might be identified and these may present as soft tissue swelling or pain (Figs. 176, 177).

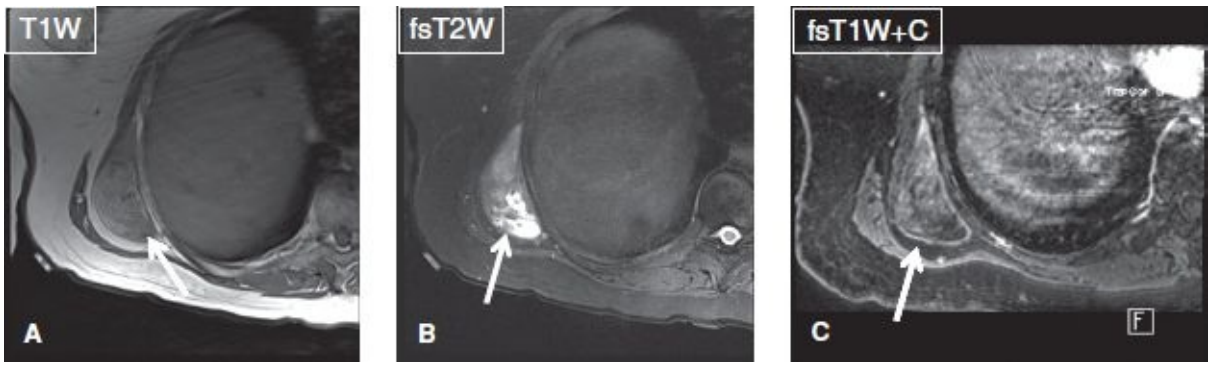

Fig. 171: Elastofibroma dorsi. Axial conventional **(A, B)** and contrast-enhanced **(C)** images demonstrate a heterogeneous well-defined fat containing mass (*arrows*) in the infrascapular fossa, classic for elastofibroma dorsi.

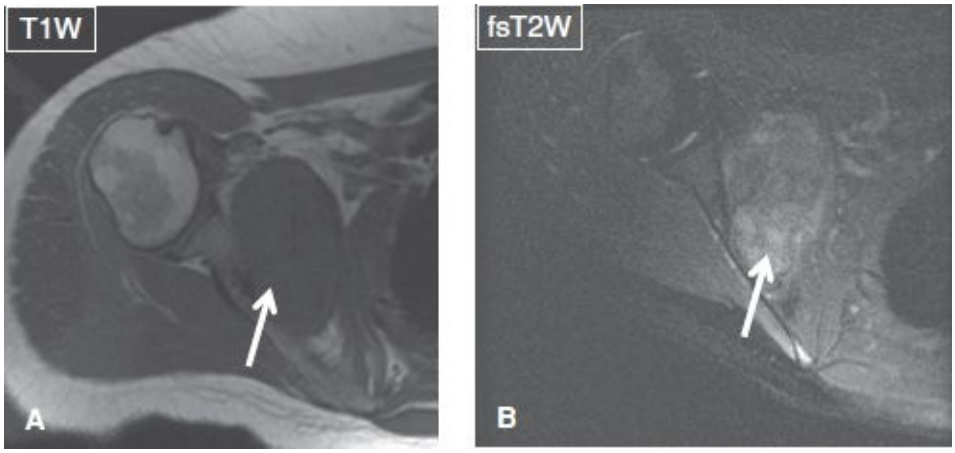

Fig. 172: Desmoid tumor. Axial images **(A, B)** exhibit a well-defined T2 heterogeneously hypointense mass lesion (*arrows*) in the scapulothoracic fossa, a biopsy-proven desmoid tumor.

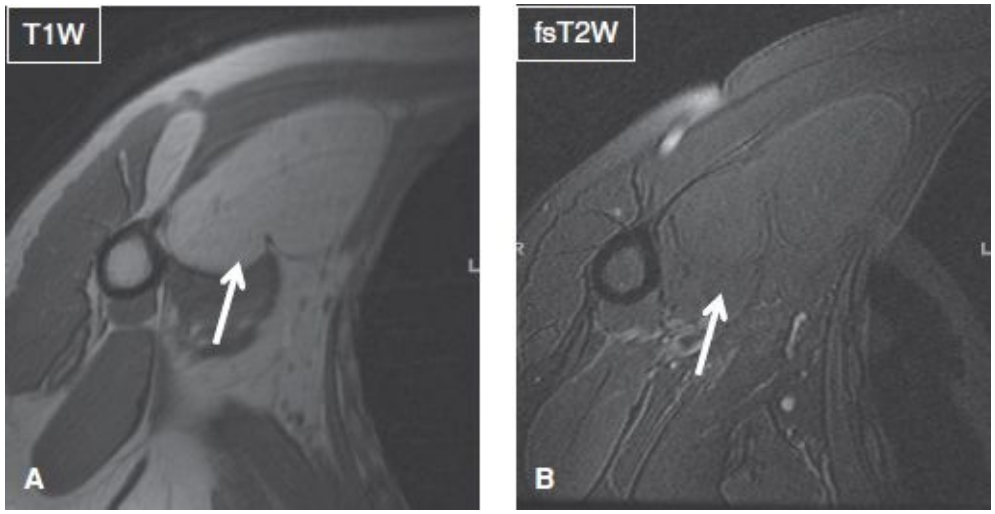

Fig. 173: Intra- and perimuscular simple lipoma. Axial T1 W **(A)** and fsT2 W **(B)** images show an intra- and perimuscular lipoma underneath the pectoral muscles and enveloping the anterior belly of the deltoid muscle (*arrows*). No complex features are noted.

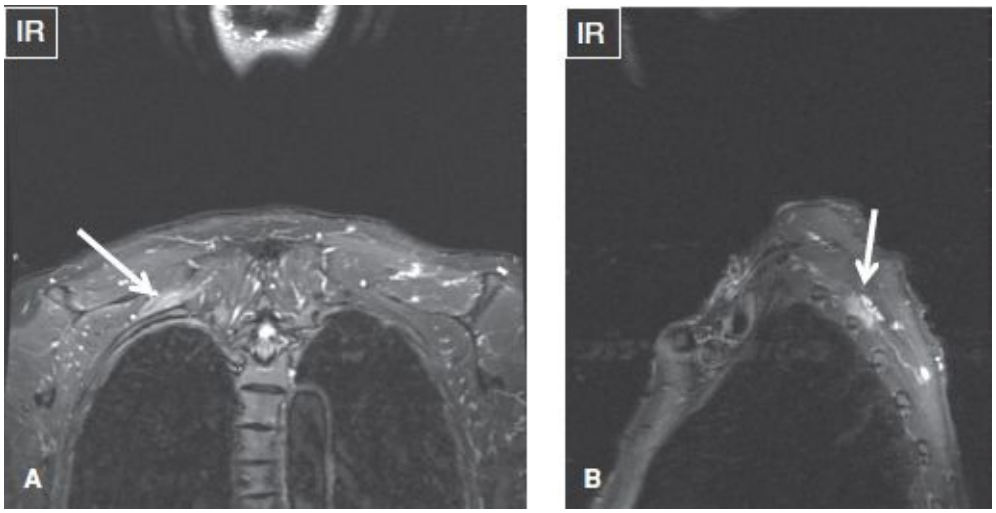

Fig. 174: Idiopathic scapulothoracic bursitis. Coronal **(A)** and sagittal **(B)** images demonstrate small fluid collection within the scapulothoracic bursa along the superomedial border of the scapula (*arrows*) in keeping with bursitis.

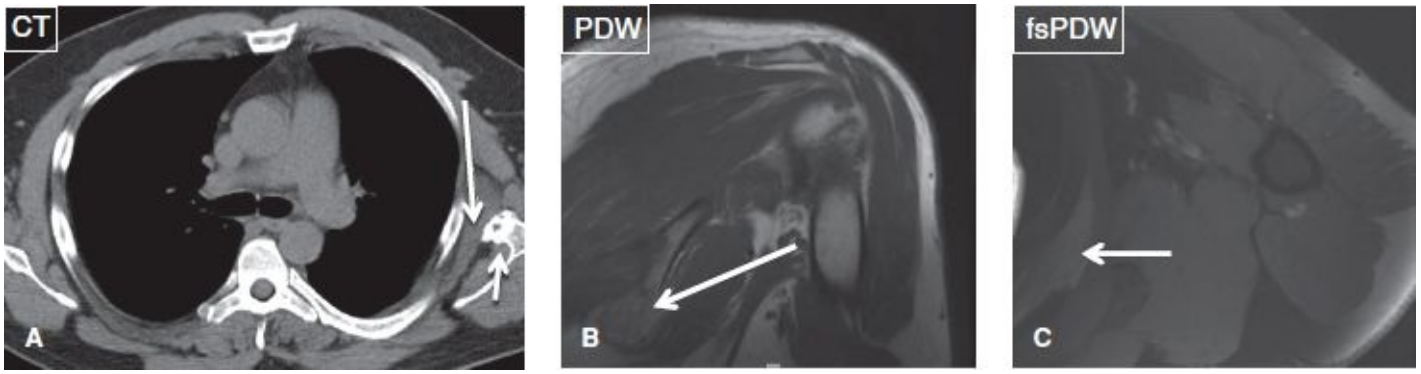

Fig. 175: Scapulothoracic bursitis. Axial CT **(A)** image exhibits fluid collection within the left scapulothoracic bursa (*long arrow*), associated with an adjacent osteochondroma of the scapula (*short arrow*). Coronal **(B)** and axial **(C)** MR images confirm the osteochondroma (*arrow* in **B**) and left scapulothoracic bursitis (*arrow* in **C**).

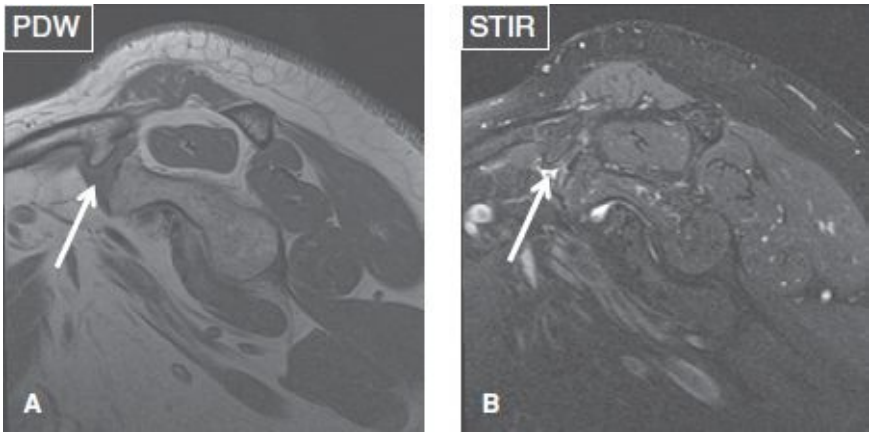

Fig. 176: Sagittal images **(A, B)** show coracoid bony hypertrophy and pseudoarticulation with the clavicle. Notice mild edema (*arrows*) reflecting acute or chronic sprain.

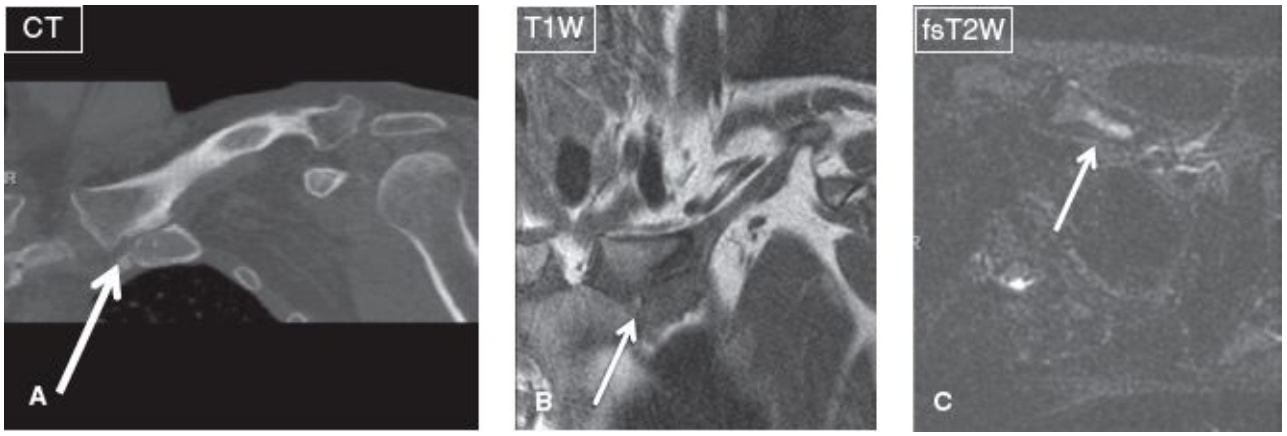

Fig. 177: Coronal CT **(A)** and coronal **(B)** and axial **(C)** MR images show left clavicle and first rib pseudoarthrosis (*arrows* in **A and B**) with bone marrow edema and cyst formation of the left clavicle (*arrow* in **C**), reflecting acute on chronic stress at the pseudoarticulation.

SUGGESTED READINGS

Anderson MW, Brennan C, Mittal A. Imaging evaluation of the rotator cuff. *Clin Sports Med.* 2012;31(4):605–631.

Bancroft LW, Wasyliw C, Pettis C, et al. Postoperative shoulder magnetic resonance imaging. *Magn Reson Imaging Clin North Am.* 2012;20(2):313–325.
Chalian M, Faridian-Aragh N, Soldatos T, et al. High-resolution 3 T MR neurography of suprascapular neuropathy. *Acad Radiol.* 2011; 18(8):1049–1059.
Chang D, Mohana-Borges A, Borso M, et al. SLAP lesions: Anatomy, clinical presentation, MR imaging diagnosis and characterization. *Eur J Radiol.* 2008;68(1):72–87.
Chhabra A, Subhawong TK, Carrino JA. MR imaging of deltoid ligament pathologic findings and associated impingement syndromes. *Radiographics.* 2010;30(3):751–761.
Cook TS, Stein JM, Simonson S, et al. Normaland variant anatomy of the shoulder on MRI. *Magn Reson Imaging Clin North Am.* 2011; 19(3):581–594.
Dunham KS, Bencardino JT, Rokito AS. Anatomic variants and pitfalls of the labrum, glenoid cartilage, and glenohumeral ligaments. *Magn Reson Imaging Clin North Am.* 2012; 20(2):213–228.
Fitzpatrick D, Walz DM. Shoulder MR imaging normal variants and imaging artifacts. *Magn Reson Imaging Clin North Am.* 2010; 18(4):615–632.
Gazzola S, Bleakney RR. Current imaging of the rotator cuff. *Sports Med Arthrosc.* 2011;19(3): 300–309.
Goh CK, Peh WC. Pictorial essay: Pitfalls in magnetic resonance imaging of the shoulder. *Can Assoc Radiol J.* 2012;63(4):247–259.
Gruson KI, Kwon YW. Atraumatic osteonecrosis of the humeral head. *Bull NYU Hosp Jt Dis.* 2009;67(1):6–14.
Huang BK, Hughes TH. Imaging of the rotator cuff. *Sports Med Arthrosc.* 2011;19(3):279–299.
La Rocca Vieira R, Rybak LD, Recht M. Technical update on magnetic resonance imaging of the shoulder. *Magn Reson Imaging Clin North Am.* 2012;20(2):149–161, ix.
Lee JC, Guy S, Connell D, et al. MRI of the rotator interval of the shoulder. *Clin Radiol.* 2007;62(5):416–423.
McMenamin D, Koulouris G, Morrison WB. Imaging of the shoulder after surgery. *Eur J Radiol.* 2008;68(1):106–119.
Murray PJ, Shaffer BS. Clinical update: MR imaging of the shoulder. *Sports Med Arthrosc.* 2009;17(1):40–48.
Nakata W, Katou S, Fujita A, et al. Biceps pulley: Normal anatomy and associated lesions at MR arthrography. *Radiographics.* 2011;31(3):791–810.
Opsha O, Malik A, Baltazar R, et al. MRI of the rotator cuff and internal derangement. *Eur J Radiol.* 2008;68(1):36–56.
Parker BJ, Zlatkin MB, Newman JS, et al. Imaging of shoulder injuries in sports medicine: Current protocols and concepts. *Clin Sports Med.* 2008;27(4):579–606.
Petchprapa CN, Beltran LS, Jazrawi LM, et al. The rotator interval: A review of anatomy, function, and normal and abnormal MRI appearance. *AJR Am J Roentgenol.* 2010;195(3):567–576.
Polster JM, Schickendantz MS. Shoulder MRI: What do we miss? *AJR Am J Roentgenol.* 2010;

195(3):577–584.
Reijnierse M. MR arthrography of the shoulder: Glenohumeral ligaments. *JBR-BTR.* 2009; 92(1):48–53.
Robinson G, Ho Y, Finlay K, et al. Normal anatomy and common labral lesions at MR arthrography of the shoulder. Clin Radiol. 2006; 61(10):805–821.
Rudez J, Zanetti M. Normal anatomy, variants and pitfalls on shoulder MRI. Eur J Radiol. 2008; 68(1):25–35.
Sanders TG, Zlatkin M, Montgomery J. Imaging of glenohumeral instability. Semin Roentgenol. 2010;45(3):160–179.
Simoni P, Scarciolla L, Kreutz J, et al. Imaging of superior labral anterior to posterior (SLAP) tears of the shoulder. J Sports Med Phys Fitness. 2012;52(6):622–630.
Vazquez J, Kassarjian A. MRI of shoulder trauma. Semin Musculoskelet Radiol. 2006;10(4):268–283.
Vinson EN, Wittstein J, Garrigues GE, et al. MRI of selected abnormalities at the anterior superior aspect of the shoulder: Potential pitfalls and subtle diagnoses. AJR Am J Roentgenol. 2012;199(3):534–545.
Zhao W, Zheng X, Liu Y, et al. An MRI study of symptomatic adhesive capsulitis. PLoS One. 2012;7(10):e47277.
Zlatkin MB, Sanders TG. Magnetic resonance imaging of the glenoid labrum. *Radiol Clin North Am.* 2013;51(2):279–297.

APPENDIX 1: Sample Completed Structured Report: Shoulder: NORMAL

EXAM: MR SHOULDER [<WITH> OR <WITHOUT>] CONTRAST

HISTORY: [] year-old <Patient Sex> with <Order Reason for Study>

TECHNIQUE: Imaging was performed [<without IV contrast> <before and after IV / after intra-articular contrast>]. Multiplanar, multisequence MR images of the [<right / left>] shoulder were obtained on a [1.5 or 3.0] Tesla magnet.

COMPARISON: [<None>]

FINDINGS:

Alignment: [<Normal>]

Fluid:

Subacromial/subdeltoid bursa: [<Normal>

Glenohumeral joint: [<Normal>]

Long head of biceps brachii tendon: [<Normal>]

Acromial arch:

Shape: [<Curved>]

Subacromial spur: [<Absent>]

Lateral / Anterior downsloping: [<Absent>]

Acromioclavicular joint: [<Normal>]

Rotator cuff:

Supraspinatus: [<Normal>]

Infraspinatus: [<Normal>]

Subscapularis: [<Normal>]

Rotator interval and long head of biceps brachii tendon:

Rotator Interval: [<Normal>]

Biceps–labral anchor: [<Intact>]

Horizontal portion: [<Normal>]

Vertical portion: [<Normal>]

Genu: [<Normal>]

Glenohumeral joint:

Labrum: [<Intact>]

Glenohumeral ligaments: [<Normal>]

Glenohumeral cartilage: [<Normal>]

Bones: [<Normal>]

Muscles: [<Normal>]

Vessels: [<Normal>]

Nerves: [<Normal>]

Other:

IMPRESSION:

1. [< >]

APPENDIX 2: Sample Completed Structured Report: Shoulder: ABNORMAL

EXAM: MR SHOULDER WITHOUT CONTRAST

HISTORY: [<45-year-old woman with shoulder pain and restricted range of motion>]

TECHNIQUE: Imaging was performed [<without>] IV contrast. Multiplanar, multisequence MR images of the [<right>] shoulder were obtained on a [<3.0>] Tesla magnet.

COMPARISON: [<Radiographs from 7/5/14>]

FINDINGS:

Alignment: [<Mild posterior decentering>]

Fluid:

Subacromial/subdeltoid bursa: [<Small amount of fluid>]

Glenohumeral joint: [<Normal>]

Long head of biceps brachii tendon: [<Small amount of fluid>]

Acromial arch:

Shape: [<Curved>]

Subacromial spur: [<Bird beak spur present>]

Lateral / Anterior downsloping: [<Mild lateral downsloping present>]

Acromioclavicular joint: [<Moderate osteoarthritis with bony and capsularhypertrophy, marrow edema and subchondral cystic changes>]

Rotator cuff:

Supraspinatus: [<Moderate tendinosis. High-grade articular-sided tear at theattachment measuring 6 × 9 mm>]

Infraspinatus: [<Mild tendinosis. Low-grade articular sided tear at the attachmentmeasuring 4 × 7 mm>]

Subscapularis: [<Mild tendinosis. Low-grade interstitial tear 4 × 12 mm superiorfibers>]

Rotator interval and long head of biceps brachii tendon:

Rotator interval: [<Normal>]

Biceps–labral anchor: [<Intact>]

Horizontal portion: [<Moderate tendinosis>]

Vertical portion: [<Normal>]

Genu: [<Moderate tendinosis>]

Glenohumeral joint:

Labrum: [<Superior labral tear from anterior superior to posterior superior. It extends below the equator of the glenoid to involve posterior inferior labrum. Small posterosuperior paralabral cyst>]

Glenohumeral ligaments: [<Thickened IGL with intra- and periligamentous edema>]

Glenohumeral cartilage: [<Diffuse low grade thinning. Small subchondral cystic change posterior glenoid>]

Bones: [<Greater and lesser tuberosity cysts and enthesopathy>]

Muscles: [<Grade I fatty replacement supra- and infraspinatus muscles. Mild atrophy infraspinatus muscle. Grade 3 fatty replacement teres minor muscle>]

Vessels: [<Normal>]

Nerves: [<Normal>]

Other: [<Small reactive appearing axillary lymph nodes>]

IMPRESSION:

1. Multifocal partial rotator cuff tears with anatomy associated with subacromial impingement.

2. SLAP type VIII lesion.

3. Moderate glenohumeral and mild acromioclavicular joint osteoarthritis.

4. Imaging findings that can be seen with adhesive capsulitis.

5. Denervation change teres minor muscle.

7

The Elbow

Avneesh Chhabra, Majid Chalian, and Theodoros Soldatos

The elbow is a highly congruent hinge joint that is stabilized by its bony configuration, as well as ligamentous and capsular structures. It is composed of three distinct articulations, which are enveloped by a common synovial-lined capsule. These include the following:

- The ulnohumeral joint, a near-uniaxial hinge articulation, which is constituted by the trochlea of the humerus and the trochlear notch of the ulna, and bears ~40% of the forces.
- The radiohumeral joint, which is formed by the radial head and the capitellum of the humerus, and bears ~60% of the forces.
- The proximal radioulnar joint, a pivot-type articulation, which is composed of the radial head the radial notch of the ulna.

Supplemented by a limited number of strong ligaments, the above anatomy provides excellent static stabilization, whereas more than 20 associated muscles provide dynamic stabilization. The above complex configuration allows forearm flexion and extension, as well as pronation and supination, thereby enabling the hand to perform various skilled and precise motions.

The hyaline cartilage covers (1) the circumference of the radial head, being relatively thin at its anterolateral aspect (which is thought to predispose to radial fractures in this location in elbow subluxations/dislocations); (2) the trochlea over an arc of approximately 330 degrees, except at the longitudinally coursing anteriorly located trochlear ridge and sulcus; and (3) the capitellum, except at its posterior aspect, referred to as the bare area or pseudodefect. The fibrous capsule ensheaths the articulating surfaces of the elbow and creates (1) an anterior recess, which extends from the anterior surface of the trochlea and capitellum to the radial and coronoid fossae; (2) a posterior (olecranon) recess, which is more capacious, and extends from the distal humerus to the radius and ulna around the olecranon process; and (3) an annular recess, which surrounds the radial neck, and represents the most distal extension of the synovial cavity.

The elbow is susceptible to a variety of injuries because of the excessive forces that are generated and transferred to this joint during heavy (particularly arm weight-bearing) activities, especially in athletes involved in overhead throwing (particularly in racket

sports). Compared to other joints, elbow is the second most frequently affected joint by overuse injuries. A systematic image analysis and structured reporting is essential for optimal diagnostic assessment of the elbow structures. This chapter discusses the imaging evaluation approach and describes how to fill in the structured checklist (Box 1). Conceptual details of related MR physics and imaging protocol are discussed in the chapter on MR protocol optimization.

IMAGE EVALUATION

The below-outlined stepwise interpretation approach is only a practical guide, and all structures of the elbow should be evaluated in multiple planes for optimal assessment. This will also help readers perceive which structures are best depicted/evaluated on which particular plane.

1. Line up the similar-plane fat-saturated (fs) and non-fs images and synchronize them for tandem evaluation.
2. Start with the sagittal images to look for possible effusion in the elbow joint by interrogating the recesses described above. Subsequently, check for cartilaginous or osteochondral bodies and assess the bony alignment. Then, evaluate the triceps and biceps tendons for continuity, pathology, or abnormality of their attachment sites (e.g., olecranon bursitis, enthesopathy, avulsive cystic changes). Finally, check the cartilage and bone marrow for osteochondral lesions (OCLs) or ulnohumeral osteoarthritis. Far-lateral images are particularly suitable for assessing the lateral ulnar collateral ligament (LUCL).
3. In the coronal plane, check for asymmetric widening of posterolateral joint space, which may indicate underlying posterolateral instability. Moving from anterior to posterior images, interrogate the radial collateral ligament (RCL), the three bundles of the ulnar collateral ligament (UCL), and then evaluate the medial epicondyle, the overlying common flexor tendon (CFT) and the adjacent muscles. Moving to the lateral side, check for OCLs of the capitellum and trochlea, and then interrogate the lateral ligamentous and musculotendinous structures.
4. The axial plane is best for evaluating the peripheral nerves and assessing lesions of the biceps, brachialis, and triceps tendons. Axial images are also useful for evaluating the annular ligament, the posterior bundle of the UCL, the biceps tuberosity, and the bicipital radial bursa. The cubital tunnel, elbow vessels, and masses are also optimally evaluated in the axial plane.

BOX 1: The Structured Report: Elbow

The checklist for structured reporting of MR imaging of the elbow. For each field,

Normal, None, or *Intact* is considered default in the dictation, whereas the rest of the elements describe various pathologies that could be encountered during imaging evaluation. See Appendices 1 and 2 at the end of the chapter for a sample completed reports for normal and abnormal (positive) examination results.

MRI of Elbow

FINDINGS:

Alignment: [<Normal> / <Posterior subluxation> / <Dislocation>]

Joint fluid: [<None> <Small effusion> <Moderate effusion> <Large effusion>]

Intra-articular bodies: [<None> <Cartilaginous or Osteochondral bodies>]

Medial structures:

Ulnar collateral ligament: [<Intact> <Thickened> <Attenuated> <Acute sprain>]

Common flexor tendon: [<Normal> <Tendinosis> <Partial tear (low/high grade)> <Complete tear>]

Medial epicondyle: [<Normal> <Enthesopathy> <Bone marrow edema>]

Lateral structures:

Radial collateral ligament: [<Intact> <Thickened> <Attenuated> <Acute sprain>]

Lateral ulnar collateral ligament: [<Intact> <Thickened> <Attenuated> <Acute sprain>]

Annular ligament: [<Intact> <Thickened> <Acute Sprain>]

Common extensor tendon: [<Normal> <Tendinosis> <Partial tear (low/high grade)> <Complete tear>]

Lateral epicondyle: [<Normal> <Enthesopathy> <Bone marrow edema>]

Posterior structures:

Triceps: [<Normal> <Tendinosis> <Enthesopathy> <Partial tear> <Complete tear>]

Olecranon bursa: [<Normal> <Distended>]

Olecranon: [<Normal> <Enthesopathy> <Bone marrow edema>]

Anterior structures:

Biceps: [<Normal> <Tendinosis> <Tenosynovitis> <Partial tear> <Complete tear>]

Brachialis: [<Normal> <Tendinosis> <Tenosynovitis> <Partial tear> <Complete tear>]

Bicipitoradial bursa: [<Normal> <Distended>]

Articular:

Radiocapitellar joint: [<Normal> <Osteochondral lesion> <Osteoarthritis>]

Ulnohumeral joint: [<Normal> <Osteoarthritis>]

Proximal radioulnar joint: [<Normal> <Osteoarthritis>]

Bones: [<Normal>]

Muscles: [<Normal>]

Vessels: [<Normal>]

Nerves: [<Cubital tunnel normal> <Retinaculum deficient> <Hyperintense ulnar nerve>]

Other: [<None>]

Impression:

[<In the order of importance with acute findings first>]

HOW TO FILL THE STRUCTURED REPORT

Alignment: [<Normal> <Posterior subluxation> <Dislocation>]

The evaluation of bony structures and bone alignment is best performed on non-fs images, since the latter provide clear depiction of the fatty marrow, bone cortex, and osteophytes. Normal alignment means bony articulation congruency at the ulnohumeral and proximal radioulnar joints. Generally, the central axis of the capitellum should continue distally as the axis of radial head and shaft in all positions and planes (radiocapitellar line), whereas

the anterior humeral cortical line should cross the capitellum at the intersection of its anterior and middle thirds (anterior humeral line). Sagittal images are best for detecting subluxation or dislocation of the radiocapitellar joint and/or the ulnohumeral joint (perched trochlea) since in most cases the elbow misaligns posteriorly or posterolaterally (posterolateral rotary instability). The other malalignments may be related to anterior subluxation (rare and is usually associated with olecranon fracture), valgus instability (acute with UCL rupture with or without radial head fracture) or chronic overload (valgus extension overload syndrome due to attenuated anterior bundle of UCL, especially in throwing athletes), and varus instability (associated with rupture of RCL). Sagittal images are also suitable for evaluating associated entrapped osteochondral fracture fragments and assessing respective donor sites (medial epicondyle, radial head, coronoid process, and posterior capitellum). Anterior or medial elbow subluxation or dislocation is uncommon, seen in less than 10% cases.

Proximal radioulnar subluxation (or dislocation) is a relatively common injury in children and is caused a sudden pull on the extended pronated arm (nursemaid's elbow). Imaging shows increased radiocapitellar distance with anterior displacement (subluxation) of the radial head out of the sigmoid notch of the ulna, along with tear and interposition of the annular ligament in the radiocapitellar space. In adults, the injury is additionally associated with complex lateral ligamentous injury and/or fracture.

Other useful anatomic relationships to evaluate clinically or on imaging include the *carrying angle* (normal range: 154–178 degrees in men, 158–178 degrees in women), which is formed by the axes of the arm and the forearm with the elbow in full extension, and the *humeral angle* (normal range: 77–95 degrees in men, 72–91 degrees in women), which is formed by the intersection of the long axis of the humerus and the transverse line drawn tangentially across the most distal points of the articular surfaces of the trochlea and capitellum.

JOINT FLUID:

Effusion: [<None> <Small effusion> <Moderate effusion> <Large effusion>]

Intra-articular body: [<None> <Cartilaginous> <Osteochondral body>]

The elbow and proximal radioulnar joints have thin synovial lining and small amount of fluid for nutrition and lubrication, which does not normally distend (produce convex margins) the capsule. Joint effusion is established when there is capsular distention, a finding, which is usually more prominent at the anterior (non-dependent) portion of the capsule if imaging is performed in the "superman" position. When present, the joint effusion should be graded as small, moderate, or large (Fig. 1). Irregularity, attenuation, and/or thickening of the joint capsule are usually indicative of recent or remote injury. Associated findings that may indicate underlying internal derangement(s) include synovial thickening, debris, intra-articular cartilaginous (intermediate signal) or osteochondral

bodies (dark ring with/without internal fatty marrow signal), synovial diverticula(e), and ganglion cysts (Fig. 2).

Fig. 1: Normal and abnormal amount of joint fluid. Sagittal images demonstrate normal amount of joint fluid **(A),** as well as mild **(B),** moderate **(C),** and large joint effusion **(D)** in the elbow.

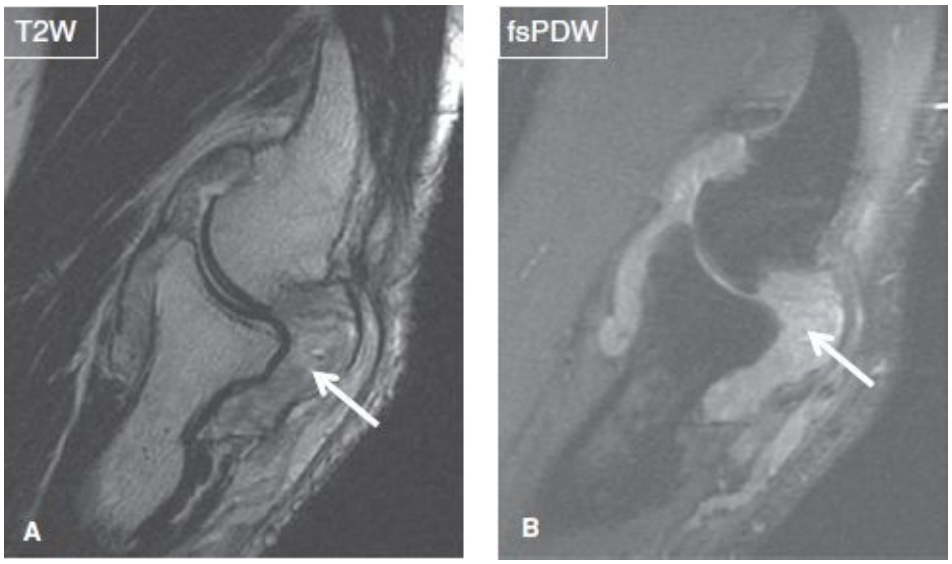

Fig. 2: Rheumatoid arthritis involving the elbow. Sagittal images **(A, B)** demonstrate large joint effusion with diffuse synovial thickening (*arrows*).

Loose bodies typically lodge in the olecranon or the coronoid recesses. Potential diagnostic pitfalls include (1) a synovial fringe (meniscus), which is commonly present in the radiocapitellar joint space (Fig. 3); (2) an os supratrochlear dorsale, which is an accessory ossicle adjacent to the olecranon, representing an unfused secondary ossification center; and (3) detached enthesophytes adjacent to the epicondyles, resulting from chronic epicondylitis. Synovial osteochondromatosis is a benign metaplastic proliferative disorder of the synovium, which manifests as numerous osteochondral loose bodies of similar size (primary form) or less number of bodies of variable (secondary form) size. The secondary form is typically seen in older individuals and is associated with prior trauma or arthritis

(Fig. 4).

Fig. 3: Normal MR anatomy of the elbow. Coronal images show the posterior band of the ulnar collateral ligament (*arrows*), the lateral ulnar collateral ligament (*arrowheads* in **B**), and a normal synovial fringe (*asterisk* in **A**).

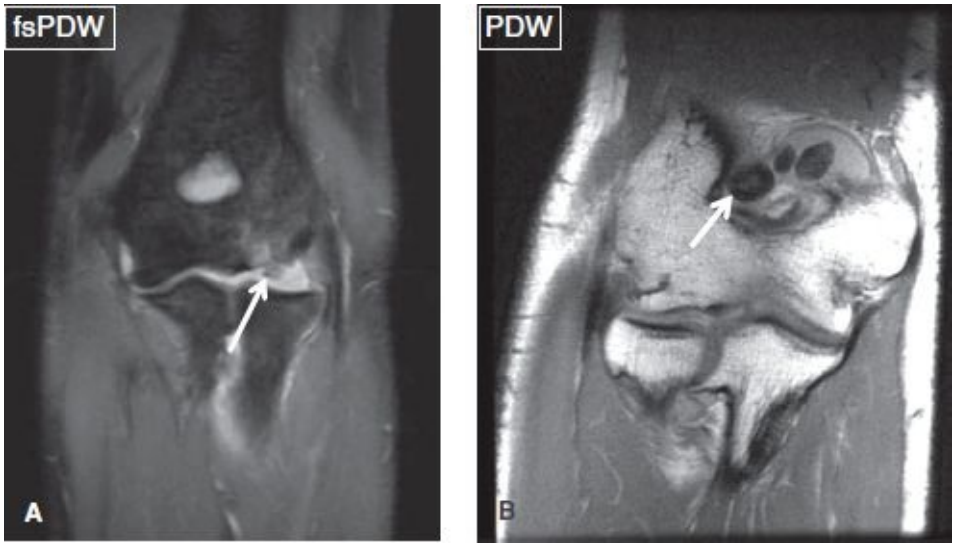

Fig. 4: Loose intra-articular bodies. Coronal images in two different subjects display a loose cartilage body (*arrow* in **A**) adjacent to the capitellum with posttraumatic marrow. Notice in a different patient, olecranon recess distended with multiple loose osteochondral bodies of variable size (*arrow* in **B**), in this case of secondary osteochondromatosis.

Fatty synovial fronds may be seen with synovial hypertrophy, an entity that is referred to as lipoma arborescens and is defined as partial or complete, depending upon the degree of joint involvement. In most cases, it a response to chronic internal joint derangement, and less commonly a primary process (usually in children), which may require arthroscopic resection.

MEDIAL STRUCTURES:

Ulnar collateral ligament: [<Intact> <Thickened> <Attenuated> <Acute sprain>]

Common flexor tendon: [<Normal> <Tendinosis> <Partial tear (low/high grade)> <Complete tear>]

Epicondyle: [<Normal> <Enthesopathy> <Bone marrow edema>]

The UCL is a thickening of the medial capsule, which provides the primary static restraint to valgus stress. It extends from the medial epicondyle to the medial coronoid process, lies immediately under the common flexor tendons and consists of three bundles. The anterior bundle, which is the strongest and most important restraint against valgus instability extends from the inferior aspect of the medial epicondyle to the sublime tubercle of the ulna, and less commonly, up to 3 mm distal to ulnar articular surface. The transverse bundle (Cooper ligament) extends from the medial olecranon to the inferomedial coronoid process and partly forms the floor of the cubital tunnel. The fan-shaped posterior bundle originates from the medial epicondyle, slightly posterior to its most inferior portion and inserts broadly onto the olecranon. It forms the majority of the floor of the cubital tunnel and provides secondary stability when the elbow is flexed beyond 90 degrees. Structurally, the anterior bundle of the UCL is composed of two separate bands, anterior and posterior.

The UCL is primary evaluated in the coronal plane (where it is usually visible on two or three consecutive slices) and secondarily in the axial plane. It appears as a thin band, which extends along the medial surface of the joint, and features homogeneous low signal on all pulse sequences. Small amounts of interspersed hyperintense fat or invaginated synovium may normally exist near the humeral attachment of the anterior bundle, which should not be mistaken for partial tear (Figs. 5, 6). Chronic UCL degeneration appears as ligamentous thickening or attenuation, with or without intrinsic abnormal signal, and is often accompanied by foci of calcification or ossification and enthesopathy. Partial tears (grade I/II sprains) of the UCL can involve the humeral or the ulnar attachment (sublime tubercle). Proximal tears typically involve the deep layer of the humeral attachment (with preservation of the overlying superficial layer) and may be difficult to detect unless joint effusion is present (Figs. 7, 8). Distal tears may be associated with bony fleck avulsion or may feature a T-sign configuration, in which joint fluid extends in a linear fashion along the medial margin of the coronoid process, through the disrupted deep UCL fibers (Fig. 9). MR arthrography is recommended in uncertain cases when conventional images are unrevealing due to scarring. It should be noted that the T-sign can be a normal finding in children, and in some adults. Presence of adjacent fascial edema is a confirmatory finding of partial tear. Complete tears (grade III sprains) of the UCL can involve the midsubstance of the ligament, in which case there is full-thickness ligament discontinuity and irregularity with laxity of torn fragments, or these lesions might be observed as full-thickness avulsion of the ulnar or humeral attachments (Figs. 10–12). The adjacent soft tissues are usually T2 hyperintense, reflecting hemorrhage and edema. Associated injuries include CFT tear, elbow subluxation or dislocation, osteochondral injury, medial epicondyle avulsion, and ulnar

nerve (UN) injury.

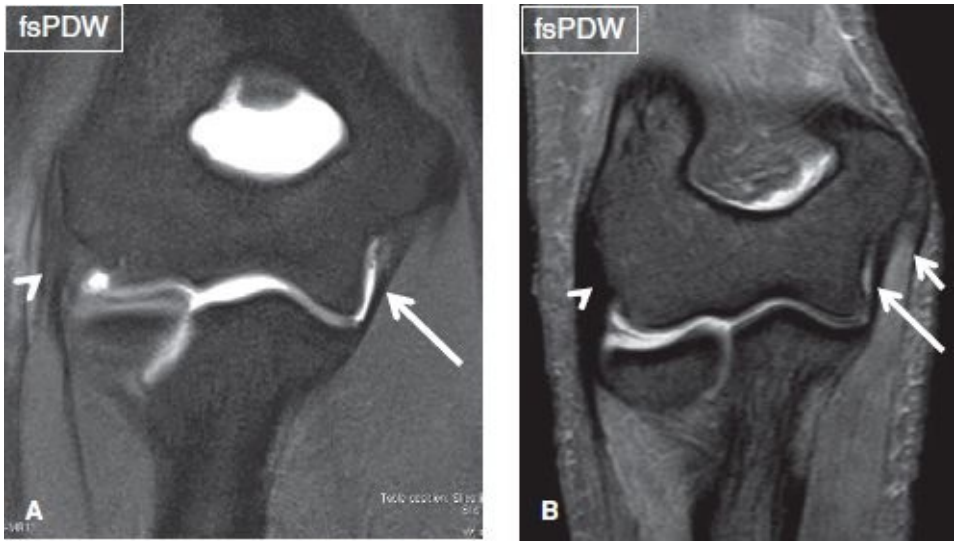

Fig. 5: Normal MR anatomy of the elbow. Consecutive coronal images demonstrate the anterior (*arrow* in **A**) and the transverse (*long arrow* in **B**) bands of the ulnar collateral ligament, the common extensor tendon (*arrowhead* in **A, B**), and the common flexor tendon (*short arrow* in **B**).

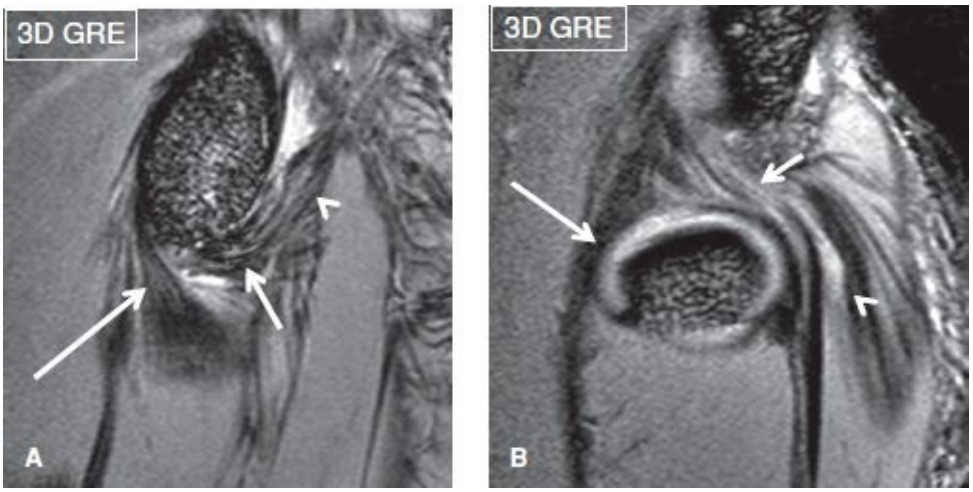

Fig. 6: Normal ulnar collateral ligament. **A:** Far medial image demonstrates the anterior (*long arrow*), transverse (*short arrow*), and posterior (*arrowhead*) bundles of the ulnar collateral ligament. **B:** Far lateral image shows the radial collateral ligament (*long arrow*), the lateral ulnar collateral ligament (*short arrow*), and the common extensor tendon (*arrowhead*).

Fig. 7: Sprains of the ulnar collateral ligament. Coronal images. **A, B:** Sequential images demonstrate mild hyperintensity and thickening of the ulnar collateral ligament (*arrows*), corresponding to grade I/II sprain. Note the associated marrow edema (*arrowheads*) of the proximal ulna and distal humerus. **C:** A partial tear is evident at the posterior band of the ulnar collateral ligament (*long arrow*), corresponding to grade II sprain. Note the normal RCL (*short arrow*).

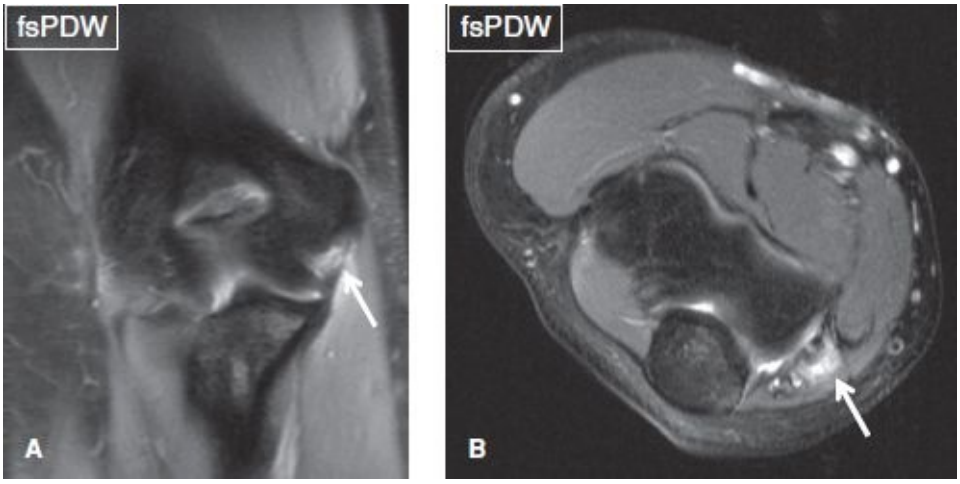

Fig. 8: Grade II sprain of the ulnar collateral ligament. **A:** Coronal image shows partial discontinuity of the ulnar collateral ligament (*arrow*), corresponding to grade II sprain. **B:** In the respective axial image, the lesion involves all the three bundles of ligament (*arrow*).

Fig. 9: Partial tear (grade II sprain) of the ulnar collateral ligament. Coronal images. **A:** Image shows stripping of the distal attachment of the ulnar collateral ligament from the

sublime tubercle, creating a "T-sign" (*arrow*). **B:** Image demonstrates hyperintensity of the proximal portion of the ulnar collateral ligament (*arrow*), indicating a partial tear. **C:** Images exhibit a normal synovial recess, which exists on the lateral aspect of the joint (*arrow*), and should not be perceived for lateral collateral ligament tear.

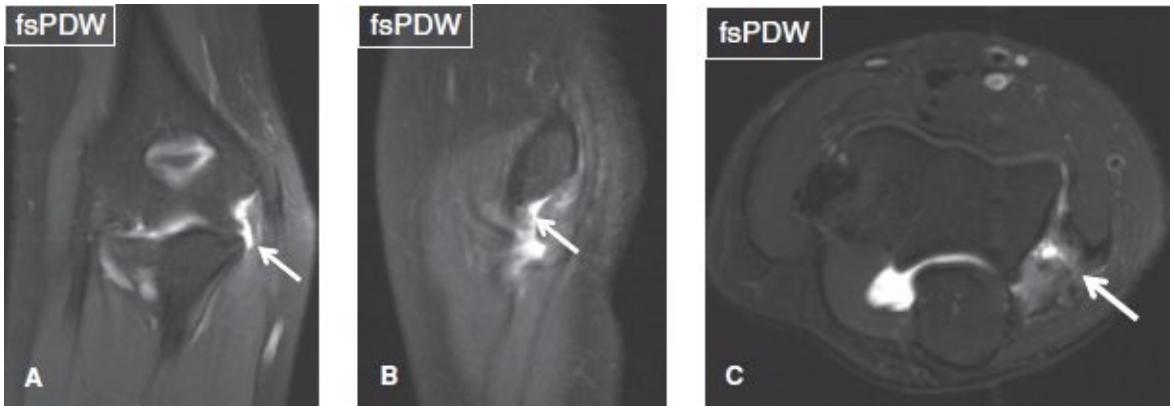

Fig. 10: Grade III sprain of the ulnar collateral ligament. Coronal **(A),** sagittal **(B),** and axial **(C)** images exhibit complete deficiency of all three bundles of the ulnar collateral ligament (*arrows*).

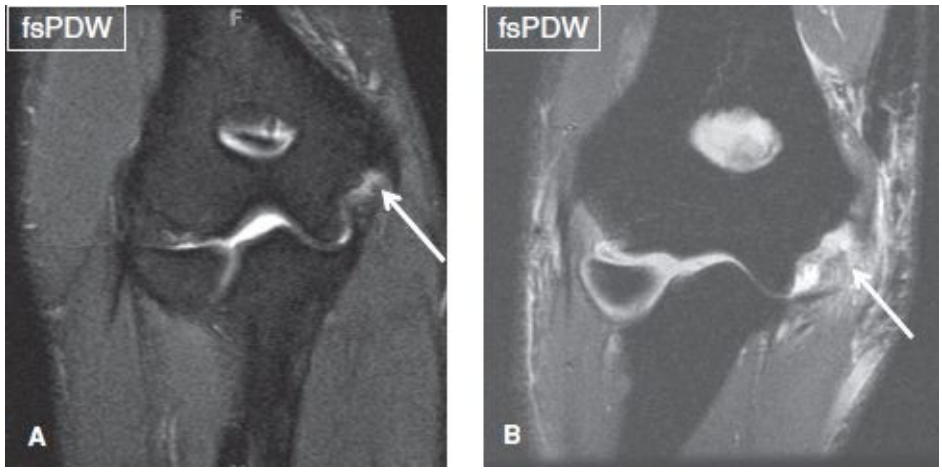

Fig. 11: Grade III sprain of the ulnar collateral ligament. Coronal images. **A:** Complete discontinuity of the posterior bundle of the ulnar collateral ligament (*arrow*) is evident at its proximal attachment. **B:** Complete tear and proximal retraction of all of the three bundles of the ulnar collateral ligament (*arrow*) at its humeral attachment.

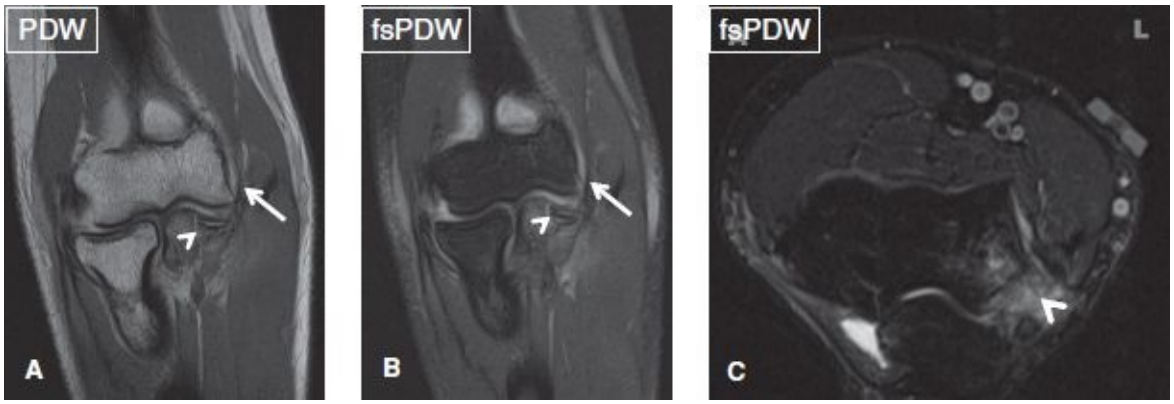

Fig. 12: Grade III sprain of the ulnar collateral ligament. Coronal (**A, B**) and axial **(C)** images demonstrate avulsion of the humeral attachment of ulnar collateral ligament (*arrows*), along with an associated fracture of the coronoid process (*arrowheads*).

The CFT origin includes the tendons of pronator teres, flexor carpi radialis, palmaris longus, flexor carpi ulnaris, and flexor digitorum superficialis muscles. The CFT arises from the medial epicondyle and overlies the UCL, providing dynamic support to the latter in resisting valgus stress. The CFT is best evaluated on coronal and axial images and normally demonstrates homogeneous low signal on all sequences (Fig. 5). Repetitive stress or overuse of the flexor and pronator musculature may result in common flexor tendinosis and/or partial tear, which may finally progress to complete tear. The condition is known as medial epicondylitis (golfer's or pitcher's elbow). Tendinosis is graded similar to the rotator cuff, as mild (intermediate intrasubstance signal), moderate (thickening and diffuse intermediate increased signal), and severe (diffusely near-fluid-bright intrasubstance signal, difficult to differentiate from tears). The subjacent epicondyle may show bone marrow edema (avulsive), enthesopathy, and/or subcortical avulsive cystic changes, reflecting chronic stress changes. Partial CFT tears manifest as focal increased fluid-like signal or fiber discontinuity on fs proton density–weighted (PDW) or fs T2–weighted (T2W) images, often with underlying tendinosis (Figs. 13, 14). The tears should be graded as low-grade (involving less than 50% of tendon thickness), high-grade (involving 50% to 99% of tendon thickness), or full-thickness (tendon discontinuity and avulsion). In both partial and full-thickness tears, the adjacent soft tissues may be edematous in acute/subacute cases.

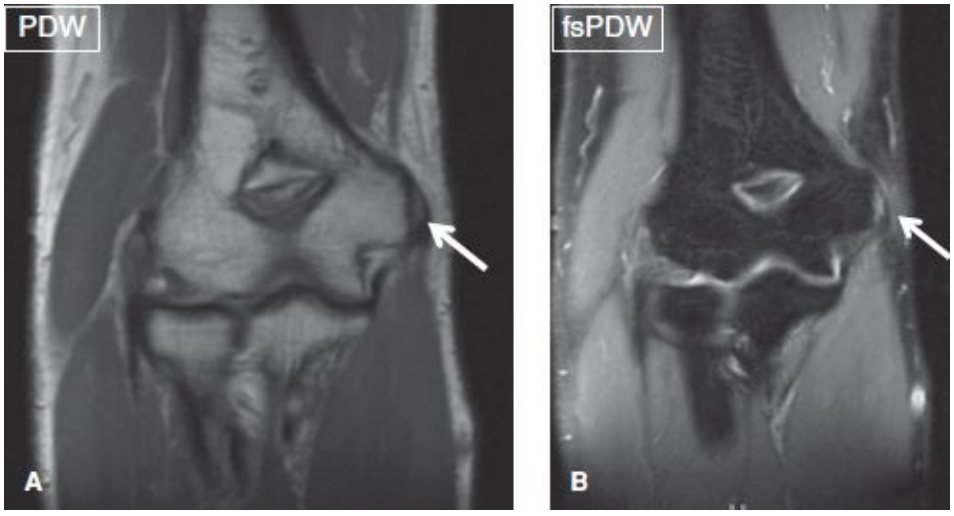

Fig. 13: Grade II sprain of the common flexor tendon. Coronal images show a partial, low-grade tear of the common flexor tendon (*arrows*).

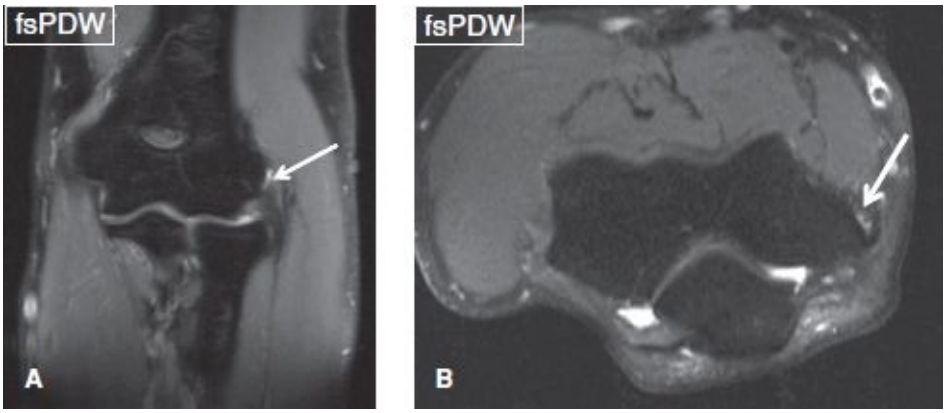

Fig. 14: Grade II sprain of the common flexor tendon. Coronal **(A)** and axial **(B)** images show a partial, low-grade tear of the common flexor tendon (*arrows*).

In adolescents involved in sports with throwing activities, repetitive valgus overload upon the elbow may cause injury to the immature medial epicondyle apophysis. The entity is known as "little leaguer's elbow," and it manifests as marrow edema of the apophysis (reflecting stress reaction) in mild cases, frank separation of the apophysis (Salter I injury) in moderate cases, or fragmentation of the apophysis (fracture) in severe cases, in which the degree of displacement is important to report, as apophyseal avulsions larger than 3 or 4 mm necessitate surgical intervention (Figs. 15, 16). Associated findings may include complete tears or avulsions of the UCL, flexor and/or pronator muscle strains, and proximal ulna stress fractures, whereas some cases may be associated with osteochondritis dissecans (OCD) of the capitellum.

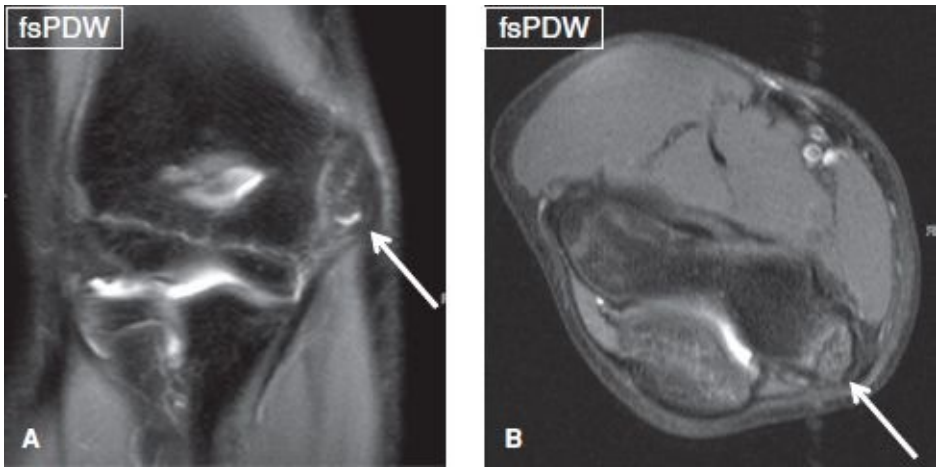

Fig. 15: Little leaguer's elbow. Coronal **(A)** and axial **(B)** images demonstrate osseous fragmentation of the medial epicondyle (*arrows*) in the case of a 12-year-old baseball player.

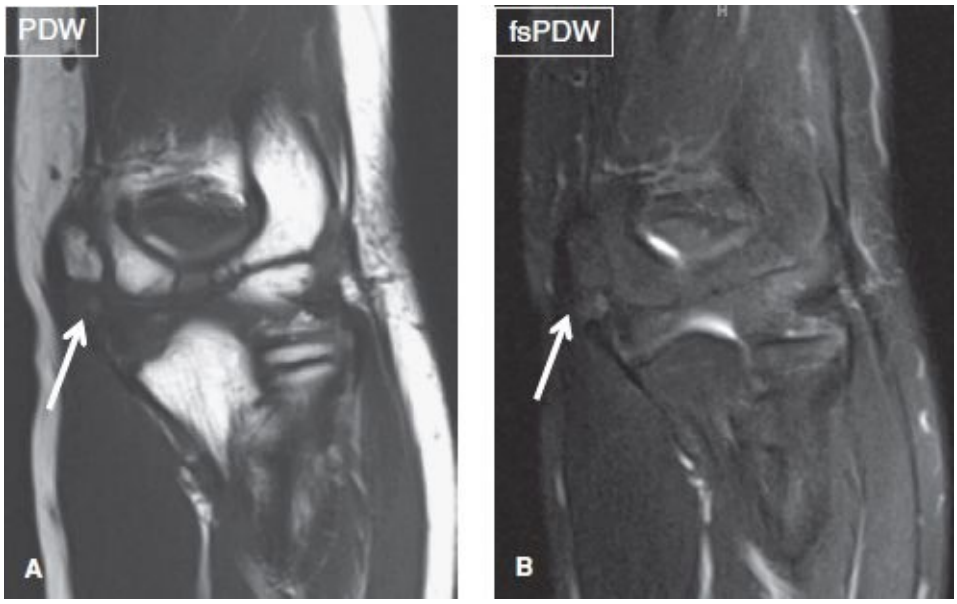

Fig. 16: Chronic avulsion of the medial epicondyle. Coronal images **(A, B)** exhibit partially united mildly edematous avulsed fragment of the medial epicondyle (*arrows*).

LATERAL STRUCTURES:

Radial collateral ligament: [<Intact> <Thickened> <Attenuated> <Acute sprain>]

Lateral ulnar collateral ligament: [<Intact> <Thickened> <Attenuated> <Acute sprain>]

Annular ligament: [<Intact> < Thickened> <Acute sprain>]

Common extensor tendon: [<Normal> <Tendinosis> <Partial tear (low/high grade)> <Complete tear>]

Lateral epicondyle: [<Normal> <Enthesopathy> <Bone marrow edema>]

The lateral collateral ligamentous structures include the RCL, which is the main restraint to varus stress, and the LUCL that provides posterolateral static stability. The RCL extends from the anterior aspect of the lateral epicondyle to the annular ligament and fascia of the supinator muscle. The LUCL originates from the lateral epicondyle, blends with RCL fibers at its origin, courses posterior to the radius, and inserts on the supinator crest of the ulna. It is absent in up to 10% of anatomic specimens. The RCL is relatively straight and lies anterior to the LUCL, which is obliquely oriented. The RCL and LUCL are best visualized on sequential coronal images from anterior to posterior, respectively. The annular ligament attaches to the anterior and posterior margins of the ulnar sigmoid notch, encircling the radial head like a sling. It serves as the primary stabilizer of the proximal radioulnar joint and is optimally visualized on axial images (Figs. 17, 18). The inconstantly present accessory annular ligament extends from the annular ligament to the supinator crest of the ulna.

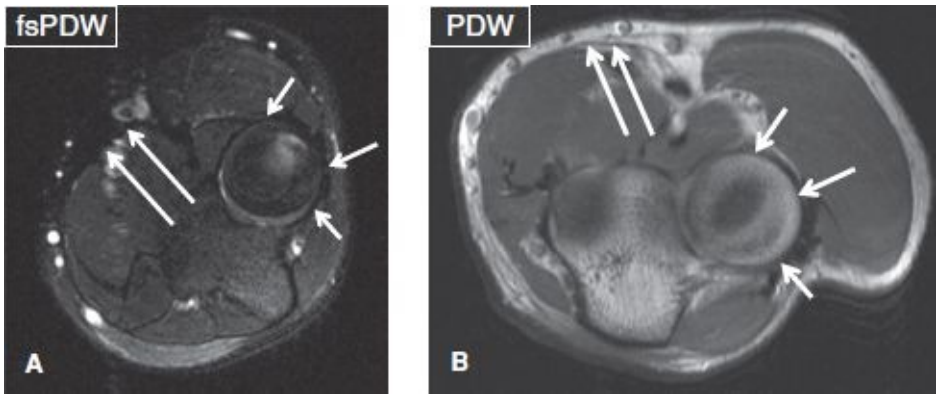

Fig. 17: Normal annular ligament and bicipital aponeurosis (lacertus fibrosus). Axial images **(A, B)** show the annular ligament (*short arrows*) and the bicipital aponeurosis (*long arrows*).

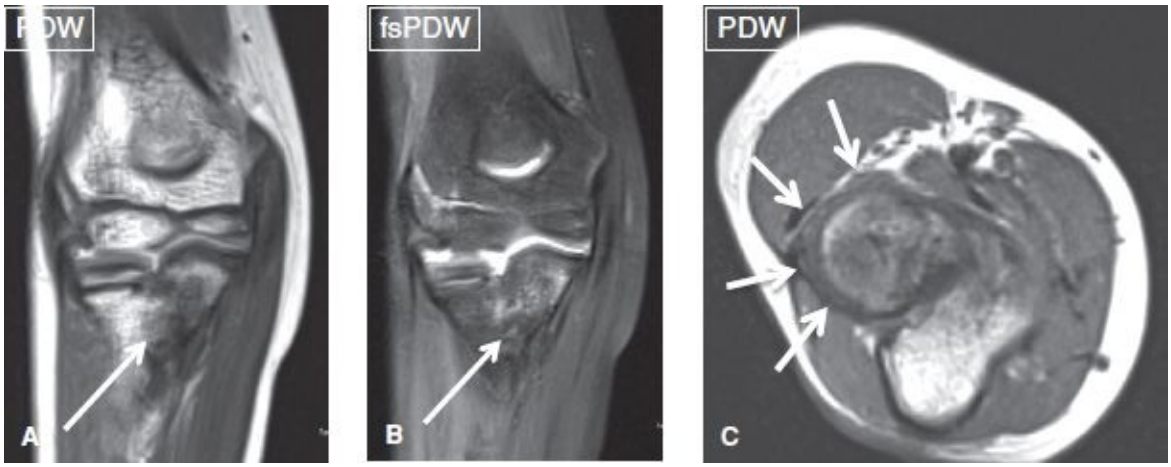

Fig. 18: Thick annular ligament in the setting of congenital proximal radioulnar synostosis. Coronal **(A, B)** images demonstrate proximal radioulnar synostosis (*arrows*) in this young individual (note the unfused epiphyses). **C:** The corresponding axial image shows diffuse thickening of the annular ligament (*arrows*), as a result of the developmental and remodeling abnormality.

The lateral collateral ligaments normally exhibit uniform thickness and homogeneous low-signal intensity on all sequences (Figs. 7, 19). They can be injured by acute varus stress injury or elbow dislocation, which may result in posterolateral rotary instability, especially with injury to the LUCL. Posterolateral instability is tested by pivot-shift test clinically using axial and valgus load in supination position. Ligament sprains are graded similar to other ligaments of the body, with grade III sprains indicating complete disruption, which most often involve the humeral attachments (Figs. 20–23). Avulsions from bony attachments may be associated with marrow edema and/or underlying enthesopathy. RCL injury is commonly associated with common extensor tendon (CET) tear in lateral epicondylitis (described in the next paragraph). Disruption of the LUCL results in pivot-shift phenomenon and posterolateral rotary instability of the joint, which is best seen on coronal images as asymmetric posterolateral joint space widening. Disruption of the annular ligament results in subluxation of the radial head, which is best depicted on sagittal images with a secondary sign of radiocapitellar line disruption. Table 1 presents the classification system for staging

elbow instability.

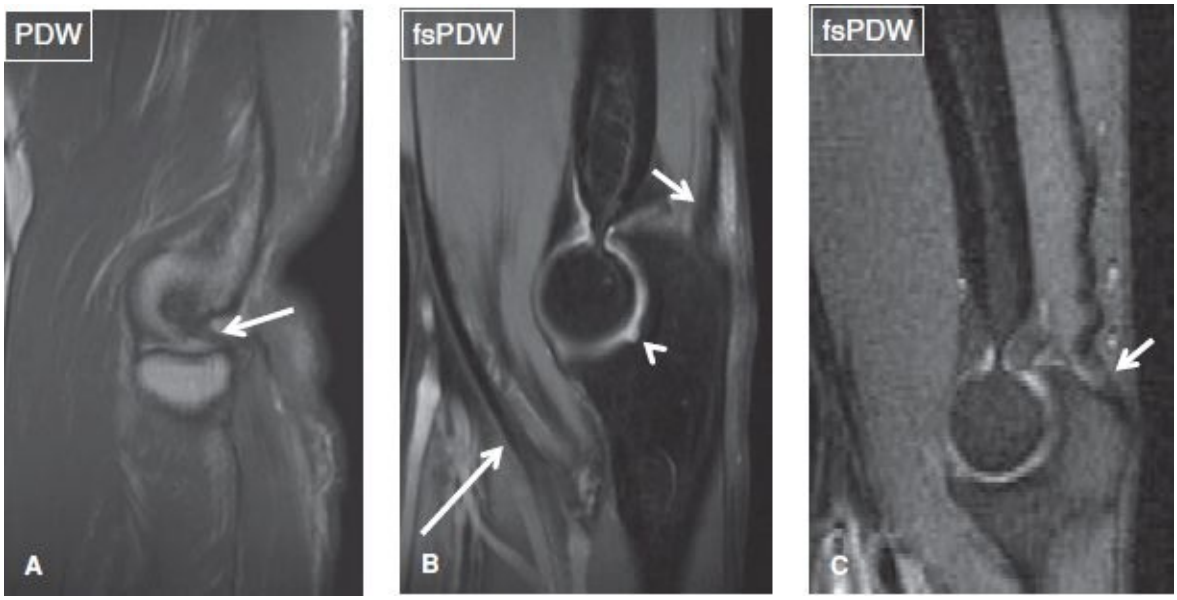

Fig. 19: Normal MR anatomy of the elbow. Sagittal images exhibit the lateral ulnar collateral ligament (*arrow* in **A**), the biceps tendon (*long arrow* in **B**), a redundant triceps tendon (*short arrows* in **B, C**), and the bare area of the trochlear notch (*arrowhead* in **B**).

Fig. 20: Grade III sprain of the radial collateral ligament. Coronal images **(A, B)** show complete discontinuity of the radial collateral ligament (*arrows*).

Fig. 21: Grade III sprain of the radial collateral ligament. Coronal image displays complete discontinuity of the radial collateral ligament (*arrow*).

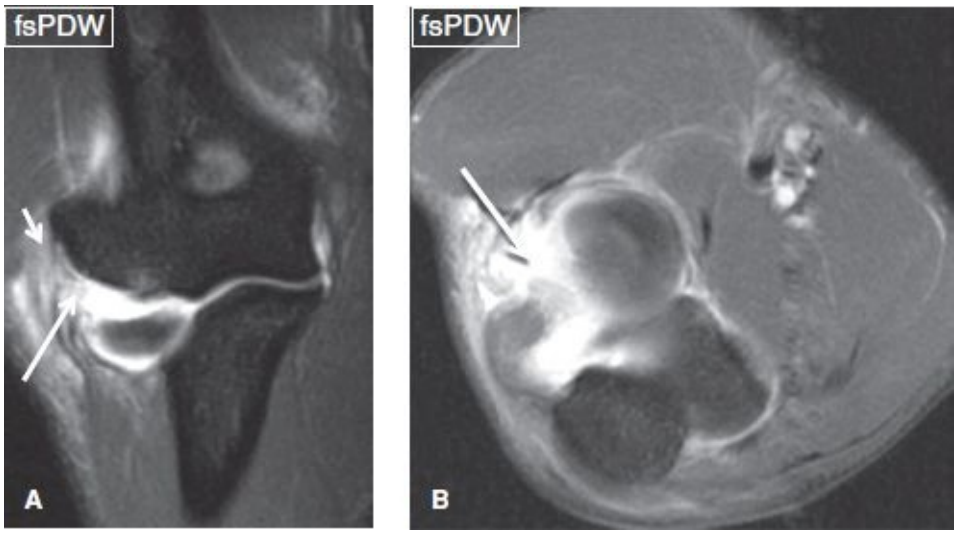

Fig. 22: Grade III sprain of the lateral ulnar collateral ligament. Coronal **(A)** and axial **(B)** images demonstrate complete discontinuity of the lateral ulnar collateral ligament (*arrows*). Also note the high-grade partial tear of the common extensor tendon origin (*short arrow*), fascial edema, and posterolateral joint space widening that would be seen in the setting of posterolateral instability.

Fig. 23: Sprains of the collateral ligaments in the setting of elbow fracture-dislocation. Coronal **(A–C)** and sagittal **(D–F)** images show tears of the RCL (*arrow* in **B**), UCL (*long arrow* in **C**) and LUCL (*short arrows* in **C, D**), fracture of the radial head (*long arrow* in **D**), and large joint effusion (*arrow* in **E**) with a loose body (*arrow* in **F**).

The CET origin includes the extensor carpi radialis brevis and longus, extensor digitorum, extensor digiti minimi, and extensor carpi ulnaris muscles. The CET originates from the anterior aspect of the lateral epicondyle and supracondylar ridge and normally exhibits uniform thickness and homogeneous low signal on all sequences. The tendon may undergo degeneration (tendinosis), or partial or complete tears, particularly in individuals engaged in occupations or sports that involve repetitive varus stress to the lateral aspect of the elbow (Figs. 24–28). The entity is known as lateral epicondylitis or “tennis elbow,” and is much more common compared to its medial counterpart. Tendinosis and tears are graded similar to CFT as described above. Additional findings, which may be present in tennis elbow include marrow edema of the lateral epicondyle, enthesopathy, avulsive cystic changes, and RCL injury.

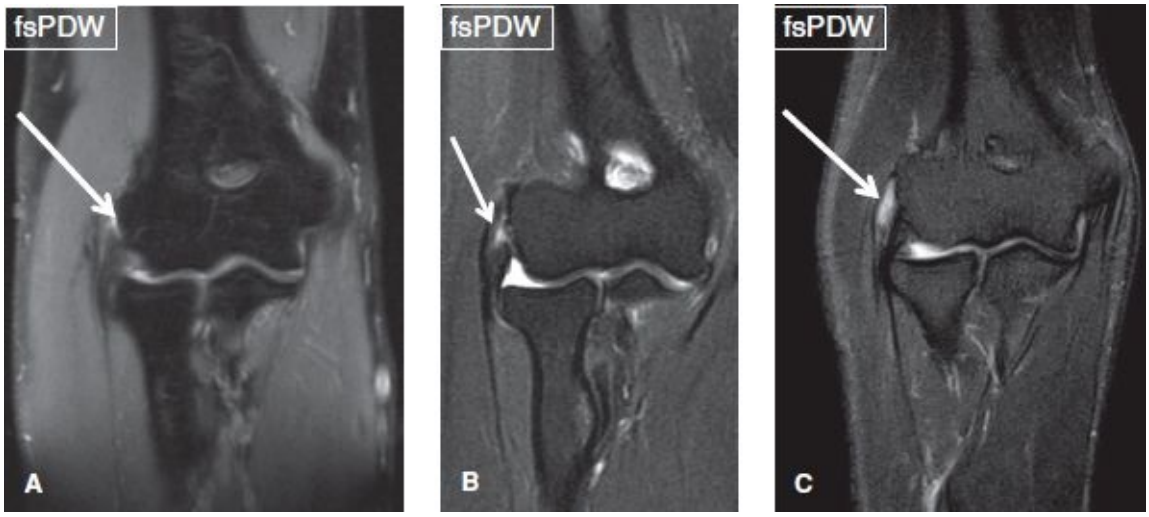

Fig. 24: Grade II sprain of the common extensor tendon. Coronal images **(A, B, C)** display three different cases of partial tears of the common extensor tendon (*arrows*), low-, intermediate-, and high-grade tears, respectively.

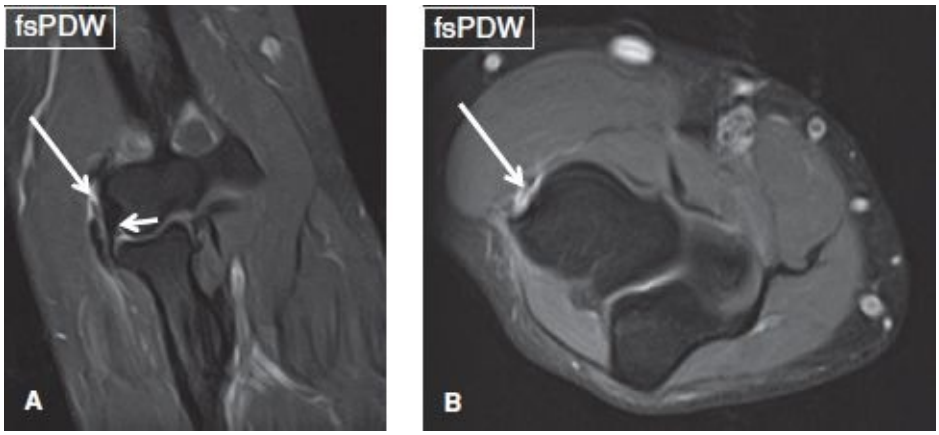

Fig. 25: Grade III sprain of the common extensor tendon. Coronal **(A)** and axial **(B)** images exhibit complete tear and distal retraction of the common extensor tendon at its humeral attachment (*long arrows*). Note the underlying mildly thickened radial collateral ligament (*short arrow* in **A**).

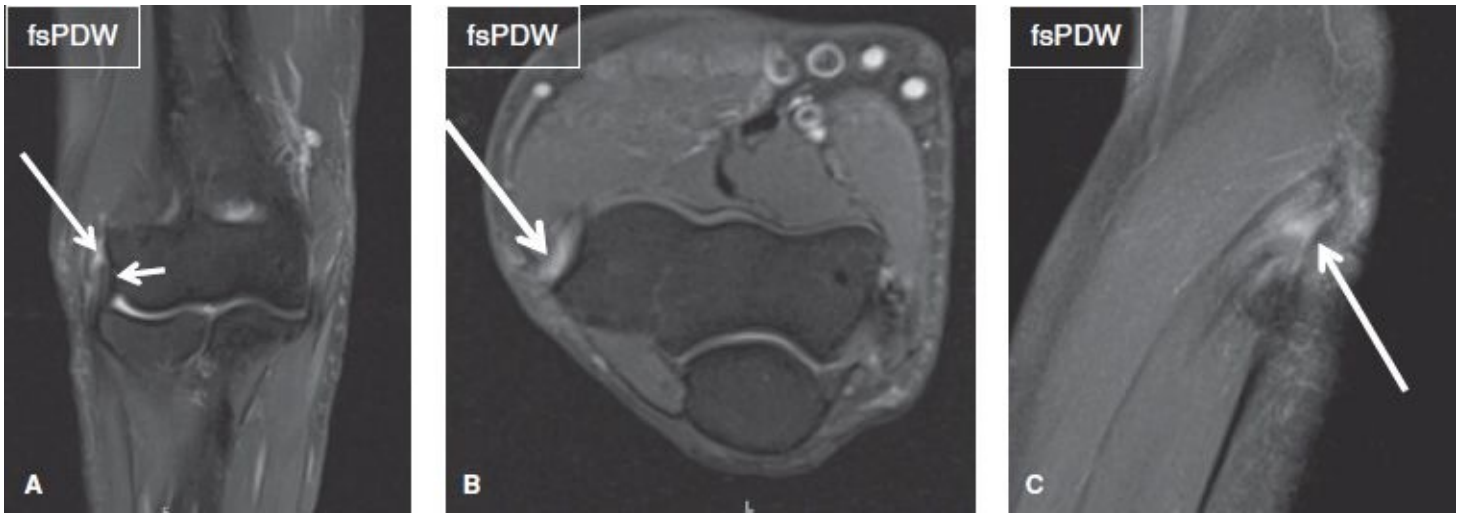

Fig. 26: Near-full-thickness tear of the common extensor tendon. Coronal **(A),** axial **(B),** and sagittal **(C)** images show near-full-thickness discontinuity of the common extensor tendon

(*long arrows*). Note the mildly thickened underlying radial collateral ligament (*short arrow* in **A**).

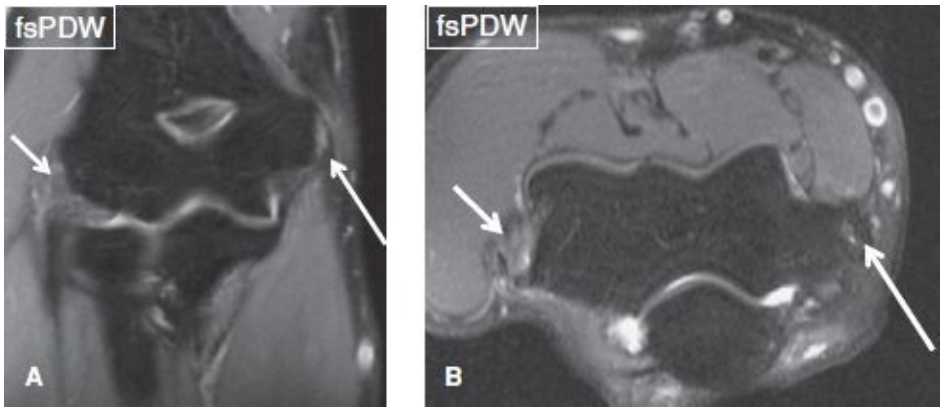

Fig. 27: Simultaneous grade II sprains of the common flexor and extensor tendons. Coronal **(A)** and axial **(B)** images exhibit partial, low-grade tears of the common flexor (*long arrow*) and extensor (*short arrows*) tendons with underlying moderate to severe common extensor tendinosis.

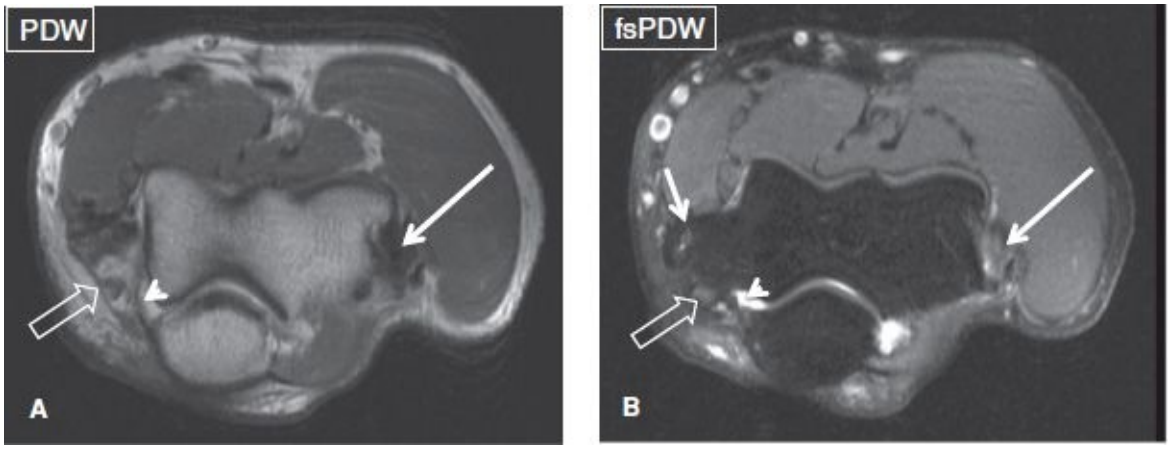

Fig. 28: Simultaneous grade II sprains of the common flexor and extensor tendons. Axial images **(A, B)** exhibit low-grade partial tears and underlying mild tendinosis of the common flexor (*short arrow* in **B**) and moderate tendinosis of extensor (*long arrows*) tendons. Note the normal posterior bundle of the ulnar collateral ligament (*arrowheads*), adjacent to the ulnar nerve (*open arrows*) forming the floor of the cubital tunnel.

TABLE 1: The O'Driscoll classification system for staging posterolateral elbow instability

Stage	Soft Tissue Injury	Anatomic Result
1	LUCL disruption	Posterolateral elbow subluxation (positive lateral pivot-shift test)
2	Disruption of anterior and posterior capsules	Incomplete elbow dislocation, coronoid perched under the trochlea
3		Full elbow dislocation, coronoid rests behind the humerus
3A	All soft tissue structures ruptured except anterior band of UCL	Elbow stable to valgus stress after reduction
3B	All soft tissue structures ruptured	Elbow unstable to valgus stress
3C	Entire distal humerus stripped of soft tissues	Elbow grossly unstable at 0–90° and stable when flexed to >90°

LUCL, lateral ulnar collateral ligament; UCL, ulnar collateral ligament.

From O'Driscoll SW. Classification and evaluation of recurrent instability of the elbow. *Clin Orthop Relat Res.* 2000;(370):34–43.

POSTERIOR STRUCTURES:

Triceps: [<Normal> <Tendinosis> <Enthesopathy> <Partial tear> <Complete tear>]

Olecranon bursa: [<Normal> <Distended>]

Olecranon: [<Normal> <Enthesopathy> <Bone marrow edema>]

The triceps muscle extends the elbow joint and is the direct antagonist of the biceps and brachialis muscles. It is located along the posterior aspect of the humerus and is composed of three heads, which converge into a long musculotendinous junction that culminates in a broad tendon, that mainly inserts on the posterior aspect of the olecranon, whereas a few fibers run distally and superficial to the anconeus muscles blending with the deep fascia of the forearm. The triceps tendon is best depicted on sagittal and axial images, and normally demonstrates uniform thickness and homogeneous low-signal intensity on all pulse sequences although distinct striations caused by interdigitation of fibrofatty tissue may be normally present near the insertion.

In triceps tendinosis, the tendon demonstrates diffuse intermediate signal and features areas of thickening, contour irregularity, or calcifications related to calcific tendinitis (Figs. 29, 30). Triceps tendinosis is graded similar to rotator cuff or common flexor/extensor tendinosis, as described above. In low- or high-grade partial tears, intrasubstance areas of focal high-signal intensity or tendon discontinuity are evident on fsPDW or fsT2W images (Fig. 31). Complete tears are characterized by proximal retraction of tendon fibers (Figs. 32, 33). The transverse and anteroposterior extent of the tear is best assessed on axial images, whereas the retraction of the tendon is accurately measured on sagittal images. Pitfalls may occur in cases of partial tears involving the posterior portion of the tendon, which may be retracted into a high position, and remain undetected on sagittal images, as the intact anterior portion may simulate a normal tendon. Secondary signs, which assist in

establishing the correct diagnosis, include hemorrhage and edema of the adjacent soft tissues, and exposure of the footprint on the olecranon. In decreasing order of frequency, complete disruption of the triceps occurs at the attachment site, myotendinous junction, or in the midsubstance. In complete tears at the attachment site, there is typically a large fluid-filled gap between the olecranon process and the distal tendon exhibits variable retraction, reporting of which is important for presurgical planning. Avulsive edema or cystic change of the olecranon may be present in insertional tears, and intramuscular hemorrhage is observed in tears at myotendinous junction. Triceps tears associated with trivial injury are seen in the setting of underlying systemic disorder, such as renal failure, connective tissue disorder, gout, etc., or with anabolic steroid intake since these systemic conditions predispose to poor tendon healing response and exaggerated background tendinosis.

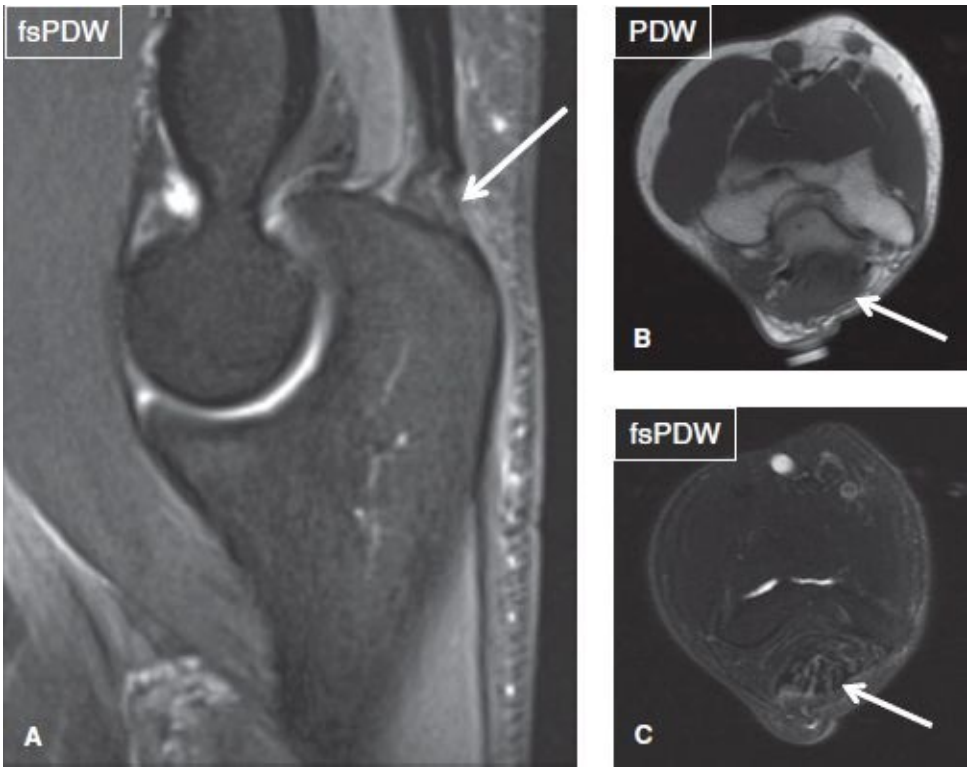

Fig. 29: Triceps tendinosis. **A:** Sagittal image shows focal hyperintensity of the distal triceps tendon (*arrow*), corresponding to mild tendinosis. **B, C:** Axial images show diffuse thickening and moderate hyperintensity of the triceps tendon (*arrows*), in keeping with moderate tendinosis. Small interstitial tears are also evident in **(C).**

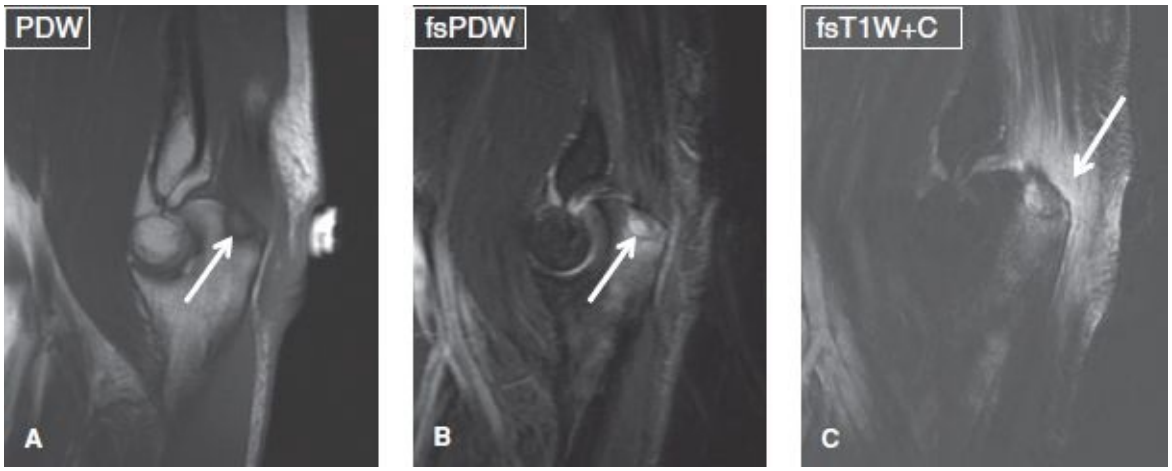

Fig. 30: Calcific triceps tendinitis. Sagittal images show avulsive cystic change (*arrows* in **A, B**) and edema of the triceps attachment with insertional tendinosis related to calcific tendinitis. Note the exuberant enhancement (*arrow* in **C**) in active stage of the disease.

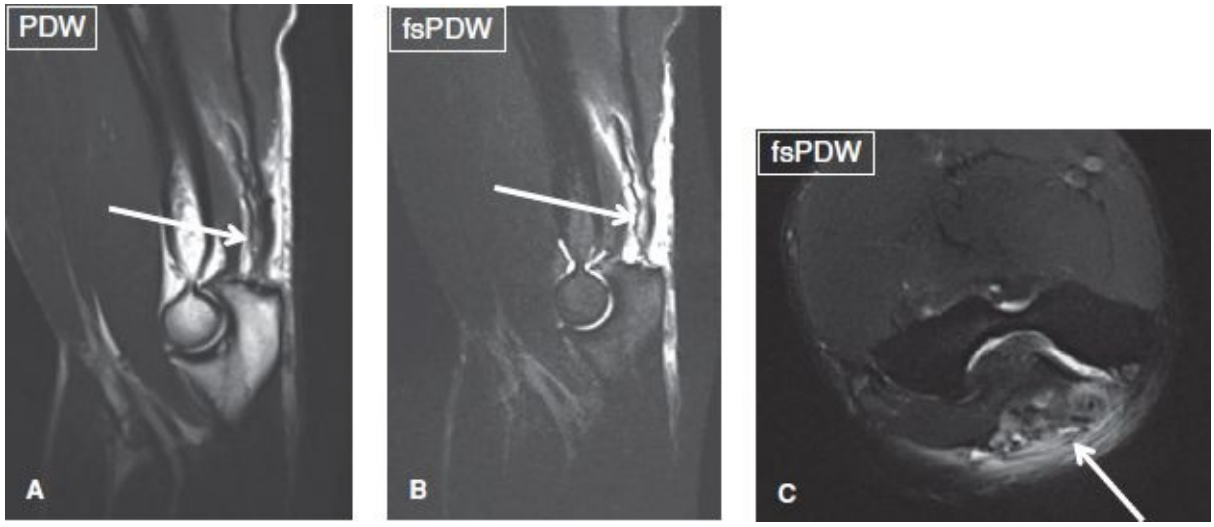

Fig. 31: Grade II sprain of the triceps tendon. Sagittal **(A, B)** and axial **(C)** images exhibit near-fluid-bright T2 signal within the distal portion of the triceps tendon (*arrows*), in keeping with a partial tear.

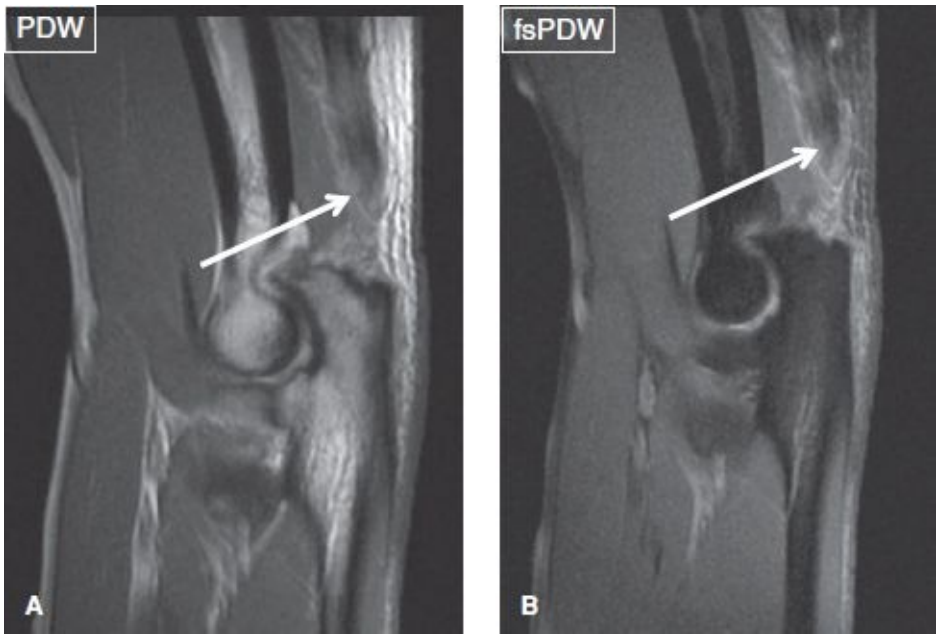

Fig. 32: Grade III sprain of the triceps tendon. Sagittal images **(A, B)** demonstrate complete discontinuity and proximal retraction of the triceps tendon (*arrow*), in keeping with a grade III sprain.

Fig. 33: Grade III sprain of the triceps tendon. Sagittal image exhibits complete discontinuity and retraction of the triceps tendon (*arrow*), in keeping with a grade III sprain.

Accounting for about 20% of adult elbow fractures, olecranon fractures are typically caused by high-energy trauma and are often associated with other upper extremity injuries, particularly fractures of the coronoid process. When caused by minor injury, olecranon fractures should raise the suspicion for underlying metabolic bone abnormality, that may lead to tendinosis or bone weakening, such as hyperparathyroidism. The fractures appear as hypointense lines, which traverse the olecranon and are commonly associated with underlying diffuse T2 hyperintensity, reflecting stress or contusion-related marrow edema. Detached enthesophytes from the olecranon should not be mistaken for loose bodies and, similar to quadriceps detached enthesophytes, one should suspect underlying full-thickness triceps tendon tears (Fig. 34). Erroneous diagnosis of fractures may happen in adolescents with fusion failure of the olecranon ossification center that normally occurs at ages of 16 to 18 years. Persistent epiphyseal plates can also be seen in adults. Presence of marrow edema and fluid cleft at the fracture site confirm the presence of trabecular discontinuity and fracture.

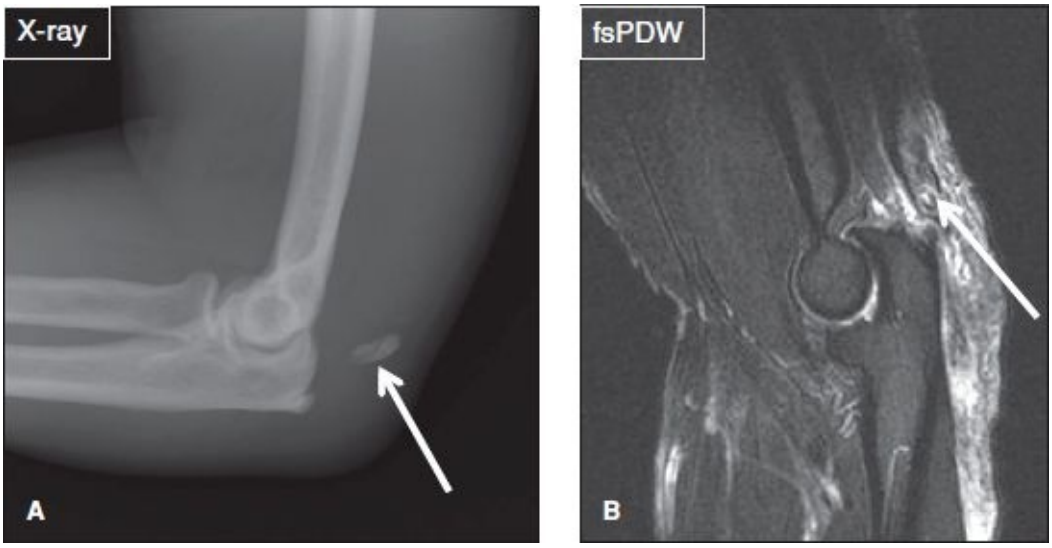

Fig. 34: Olecranon avulsion fracture. Lateral radiograph **(A)** and sagittal MR image **(B)** demonstrate avulsion of an enthesophytic bony fragment (*arrows*) from the olecranon process. Note the complete tear and retraction of the triceps tendon attached to the bony fragment on the MR image.

The olecranon bursa is located between the olecranon and the overlying skin. It features a superficial and a subtendinous layer, which are situated dorsal and deep to triceps tendon, respectively. It is a variably-sized synovium-filled sac that provides smooth and almost frictionless tendon motion between the skin, subcutaneous tissues and olecranon. Due to its superficial location, it is a common site for injury, inflammation, and infection. Most direct elbow infections initiate in this bursa. A severe single episode of injury or repeated work-related trauma to the elbow may result in olecranon bursitis ("student's elbow"), which demonstrates as well-circumscribed fluid collection superficial to the olecranon (Fig. 35). Olecranon bursitis may also be secondary to rheumatoid arthritis. Although considerable overlap exists between septic and non-septic olecranon bursitis, absence of bursal and adjacent soft tissue/fascial enhancement strongly suggests lack of infection. Olecranon bursitis is typically a clinical diagnosis, and imaging is requested to evaluate for complicating osteomyelitis or extent of infection and abscess.

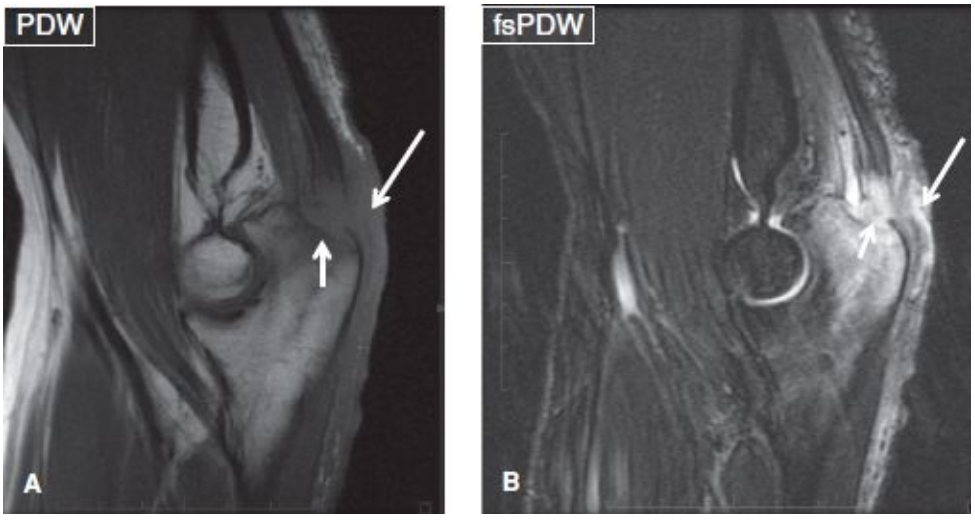

Fig. 35: Olecranon bursitis. Sagittal images (**A, B**) show heterogeneous fluid filling the

olecranon bursa (*long arrows*) in this case of olecranon osteomyelitis. Note the cortical erosions of the olecranon and triceps tendinitis (*short arrows*).

ANTERIOR STRUCTURES:

Biceps: [<Normal> <Tendinosis> <Tenosynovitis> <Partial tear> <Complete tear>]

Brachialis: [<Normal> < Tendinosis> <Tenosynovitis> <Partial tear> <Complete tear>]

Bicipitoradial bursa: [<Normal> <Distended>]

The biceps brachii muscle flexes the elbow and supinates the forearm. The two heads of the muscle arise from the scapula and nearly fuse or stay in close apposition approximately 3 cm above the elbow joint to form a common belly. The common belly continues in the forearm as a long and strong tendon that crosses the elbow joint and inserts into the radial tuberosity. Some fibers attach to the bicipital aponeurosis (lacertus fibrosus) that radiates toward the ulnar part of the antebrachial fascia, and assists the biceps tendon remain in proper position (Fig. 17). The biceps tendon is not covered by a tendon sheath but is instead separated from the radial tuberosity by the bicipitoradial bursa (described in the following paragraph). The tendon is best evaluated on axial and sagittal images and normally exhibits uniform thickness and low-signal intensity on all sequences (Fig. 36). It is obliquely oriented in the sagittal plane and the imaging field of view should extend at least 5 cm below the level of the elbow joint to encompass the insertional portion.

Fig. 36: Normal biceps and brachialis tendons. Axial image distal to the elbow joint line demonstrates the biceps (*long arrow*) and the brachialis (*short arrow*) tendons at their insertion sites.

Biceps tendon tears account for 3% to 10% of elbow injuries, with the vast majority being complete ruptures. In the latter injuries, the tendon is not identified at its insertion site but

is instead wavy, heterogeneous, and retracted at a variable distance from the radial tuberosity, which may itself demonstrate avulsive marrow edema and/or enthesopathy (Figs. 37–39). However, retraction is inhibited and the tendon remains close to normal insertion site despite complete rupture if the bicipital aponeurosis remains intact (Fig. 37). The extent of partial tears or variable involvement of the two heads of the biceps tendon is best assessed on axial images (Fig. 40). Soft tissue edema, or less commonly, a mass-like area of fluid-signal intensity, is evident in the antecubital fossa, which may compress or irritate the adjacent median nerve (MN). Similar to the triceps tendon, the degree of retraction and the location of the torn tendon margin are important to report for surgical treatment purposes.

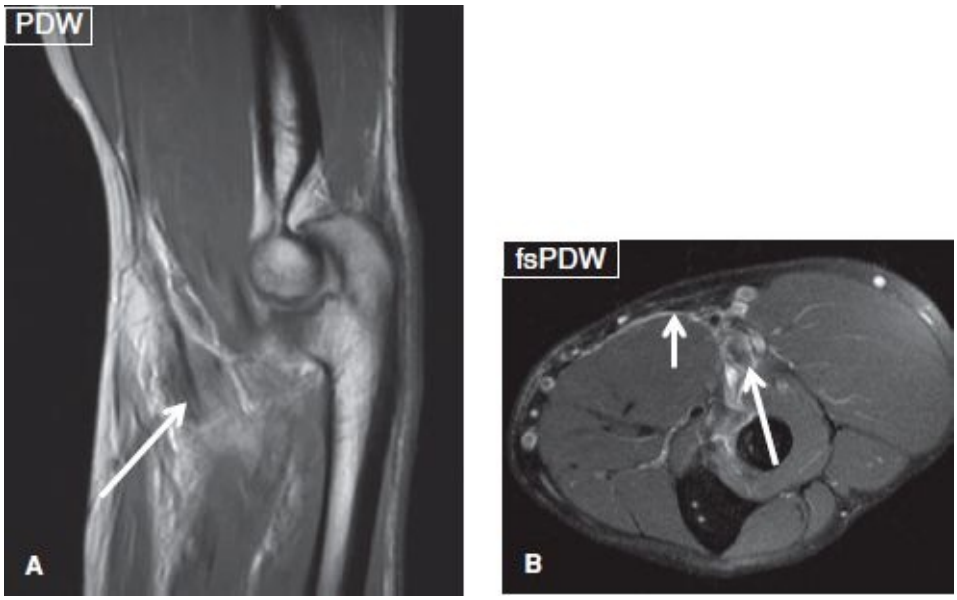

Fig. 37: Grade III sprain of the biceps tendon. **A:** Sagittal image demonstrates complete tear and mild retraction of the biceps tendon (*arrow*). **B:** On the corresponding axial image, the bicipital aponeurosis is intact (*short arrow*) and has prevented significant retraction of the biceps tendon (*long arrow*).

Fig. 38: Grade III sprain of the biceps tendon. **A:** Sagittal image demonstrates complete tear

and significant retraction of the biceps tendon and muscle (*arrow*). **B:** On the corresponding axial image proximal to the elbow joint level, hemorrhage and edema surround the retracted tendon (*arrow*).

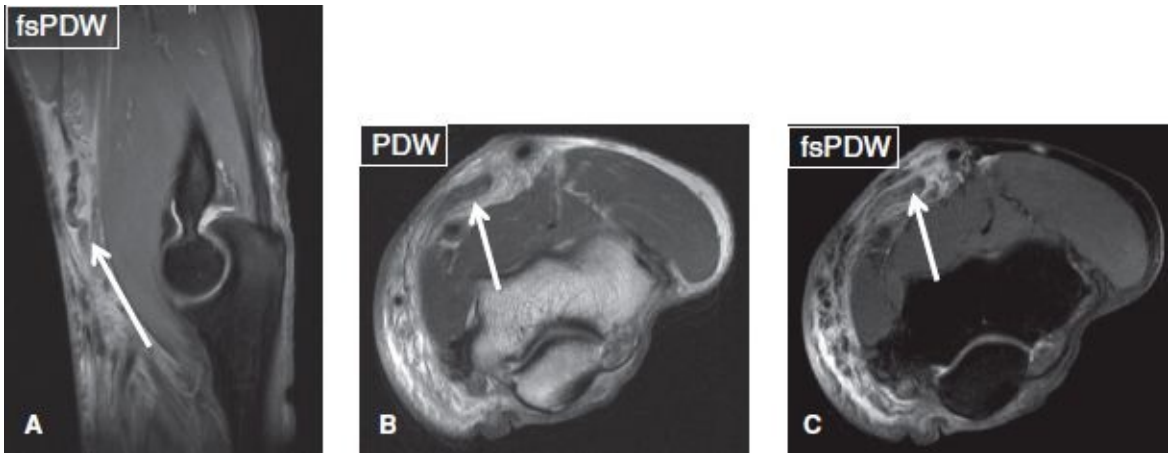

Fig. 39: Grade III sprain of the biceps tendon. **A:** Sagittal image demonstrates complete tear and significant retraction of the biceps tendon (*arrow*). **B, C:** On the corresponding axial images, the bicipital aponeurosis is torn (*arrows*).

Biceps tendinopathy appears as intermediate intrasubstance signal of the tendon on all sequences, with or without tendon thickening (Fig. 41). Partial tears can be differentiated from tendinopathy by their focal nature and fluid-bright T2 signal. Secondary findings include marrow edema of the radial tuberosity, fascial edema and fluid distention of the bicipitoradial bursa.

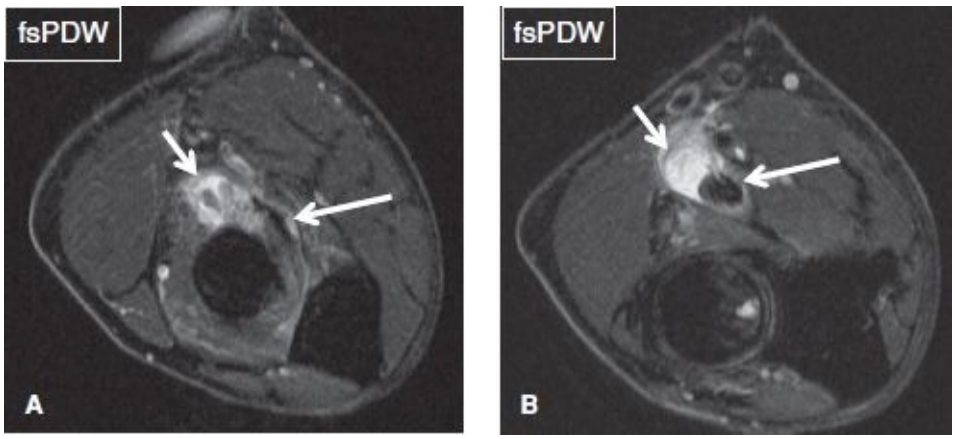

Fig. 40: Grade II sprain of the biceps tendon. Axial images **(A, B)** exhibit a low-grade partial tear of the biceps tendon (*long arrows*), along with bicipital bursitis (*short arrows*).

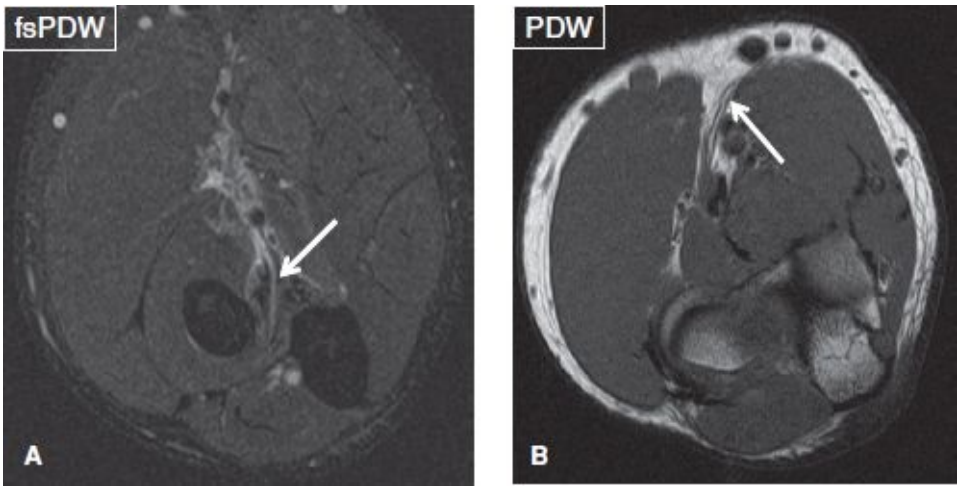

Fig. 41: Biceps tendinopathy. Axial images show intermediate signal of the distal biceps tendon with a low grade partial tear (*arrow* in **A**), in keeping with insertional tendinosis, as well as intact bicipital aponeurosis (*arrow* in **B**).

The brachialis muscle is the most powerful elbow flexor. It originates from the anteroinferior humerus, crosses the elbow joint, and inserts just below the coronoid process of the ulna. It has a long myotendinous junction and features a tendon, that is well protected by the surrounding muscle and much shorter compared to the biceps tendon. Similar to the latter tendon, however, the brachialis tendon is best evaluated on the axial and sagittal planes and normally features uniform thickness and homogeneous low signal on all sequences (Fig. 36). Tendinosis appears as intermediate signal within the tendon, with or without tendon thickening. In partial or complete tears, a fluid-filled gap is evident between the torn fragments, along with adjacent soft tissue edema and hemorrhage (Fig. 42). Strains of the brachialis muscle or of its myotendinous junction (climber's elbow) result from repetitive movement, such as climbing, pull-ups, or from direct blow to the tendon.

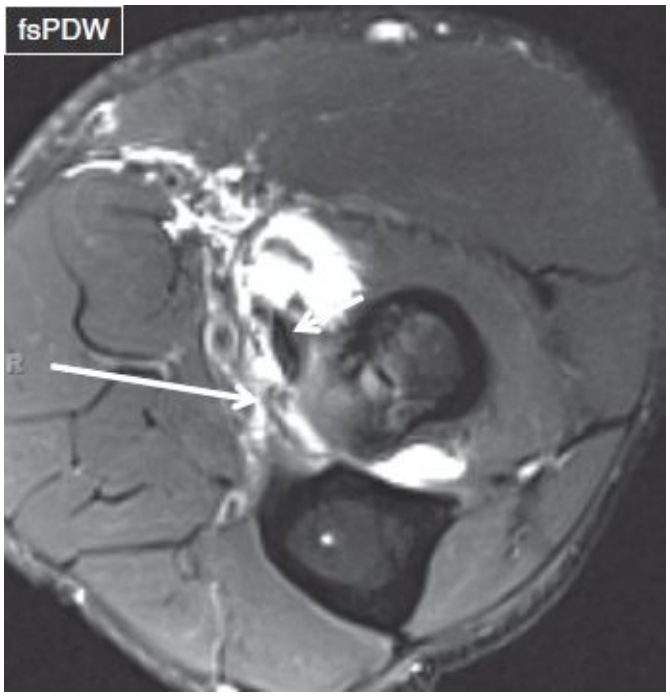

Fig. 42: Grade III sprain of the brachialis and biceps tendons. Torn and partially retracted

brachialis (*long arrow*) and biceps (*short arrow*) tendons. Note the associated effusions in the proximal radioulnar joint and bicipital bursa.

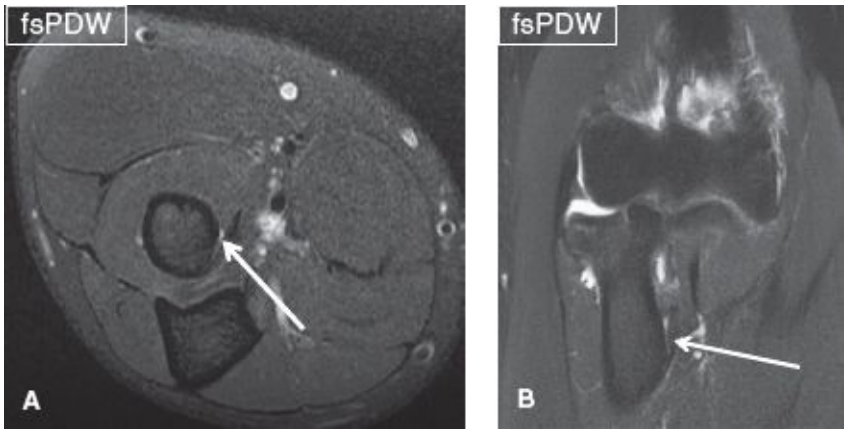

Fig. 43: Normal bicipitoradial bursa. Axial **(A)** and coronal **(B)** images show the bicipitoradial bursa (*arrows*), which contains normal, minimal amount of synovial fluid.

The bicipitoradial bursa wraps partially or completely around the biceps tendon and ensures frictionless motion between the biceps tendon and the radial tuberosity during pronation and supination of the forearm. It normally may have trace fluid (Fig. 43). Accumulation of fluid suggests biceps tendon injury or inflammation (bursitis), and it may less commonly occur as an isolated finding (Figs. 40, 42, 44). If large, the bursal effusion may cause mass effect on the cubital fossa and compress adjacent nerves, most commonly the superficial or the deep branch of the radial nerve (RN). Rheumatoid arthritis (synovial thickening, rice bodies, adjacent bony erosions), synovial osteochondromatosis (nodular uniform bodies), and infection (adjacent fascial edema, muscle edema, and intense enhancement) may also affect the bicipitoradial bursa and cause heterogeneous or complex bursal effusions.

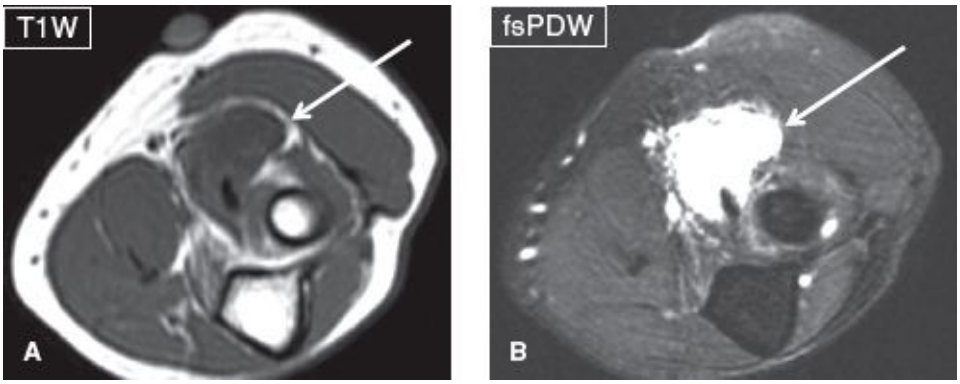

Fig. 44: Isolated bicipital bursitis. Axial images **(A, B)** show moderate to large fluid distention of the bicipital radial bursa (*arrows*), without an associated visible etiology.

ARTICULAR:

Radiocapitellar joint: [<Normal> <Osteochondral lesion> <Osteoarthritis>]

Ulnohumeral joint: [<Normal> <Osteoarthritis>]

Proximal radioulnar joint: [<Normal> <Osteoarthritis>]

Osteochondrosis of the capitellum (Panner disease) is a self-limited entity that affects young (<10 to 11 years old) athletes. It manifests as low-signal intensity on T1W/PDW and mixed signal intensity on fsPDW/fsT2W images throughout the entire capitellar ossification center and is occasionally associated with fragmentation of the capitellum. The lesion resolves over time with no residual deformity, instability or loose body. This is contrary to OCL due to osteochondral fracture or injury and OCD as these entities are usually focal and may progress and lead to formation of unstable fragments or loose bodies. OCDs typically involve immature athletes (12 to 16 years old), whereas OCL is an umbrella term, which is used for any such focal lesion in adults. OCL may be post-traumatic or may result from chronic lateral impaction related to exaggerated valgus stress. Most commonly, injuries to the elbow involve valgus lateral impaction and medial distraction mechanisms, which lead to contusions or fractures of the lateral side of the joint and osteophyte formation in the medial side. OCLs most often occur in the anterior aspect of the capitellum, and less commonly in the trochlea, radial head, and olecranon (Figs. 45–49). Important features to report for treatment planning and prediction of outcome include the location and the size of the osteochondral fragment, the potential instability of the fragment (Table 2), and the viability of a non-displaced osteochondral fragment, which could be determined using intravenous contrast administration.

Fig. 45: Stable osteochondral lesion of the capitellum. Sagittal **(A)** and coronal **(B)** images show a small osteochondral lesion in the anterior aspect of the capitellum (*long arrows*), which lacks signs suspicious for instability. Note the normal pseudodefect at the posterior aspect of the capitellum (*short arrow* in **A**).

Fig. 46: Potentially unstable osteochondral lesion of the capitellum in a child. Coronal images **(A, B)** demonstrate an osteochondral lesion in the anterior aspect of the capitellum (*arrows*), which is greater than 1 cm in size and shows cystic changes as well as edema at the base of the lesion.

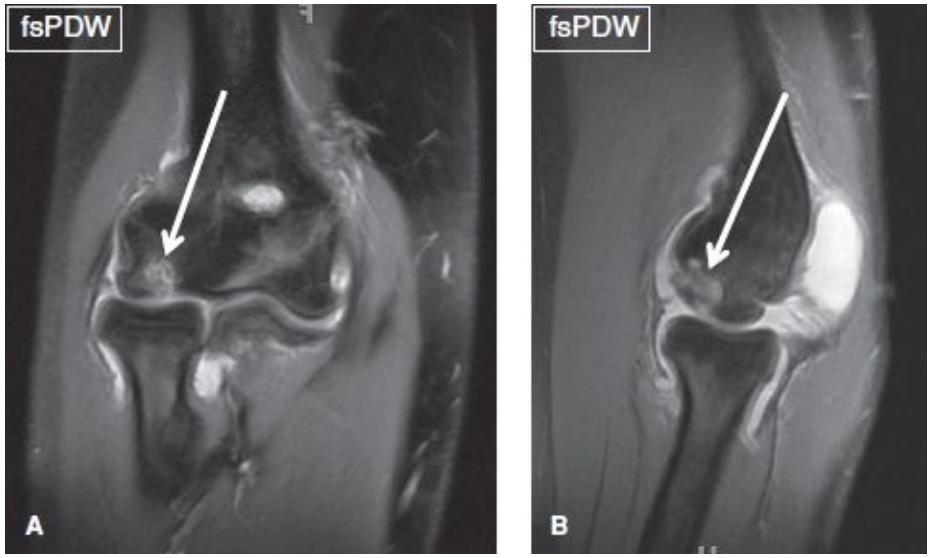

Fig. 47: Potentially unstable osteochondral lesion of the capitellum. Coronal **(A)** and sagittal **(B)** images exhibit an osteochondral lesion in the anterior aspect of the capitellum (*arrows*), which is greater than 1 cm in size and features cystic changes and edema at the base of the lesion with overlying cartilage defect.

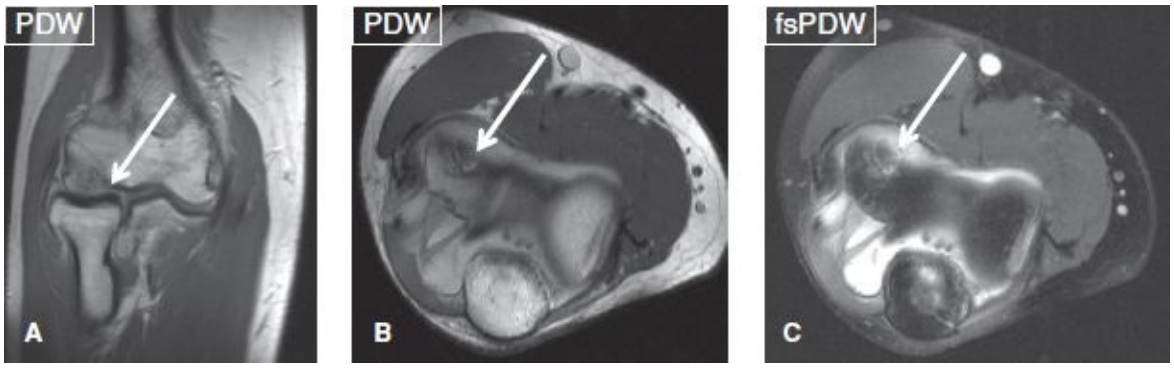

Fig. 48: Potentially unstable osteochondral lesion of the capitellum. Coronal **(A)** and axial (**B, C**) images show an osteochondral lesion in the anterior aspect of the capitellum (*arrows*), which is greater than 1 cm in size and features cystic changes and overlying cartilage flaps.

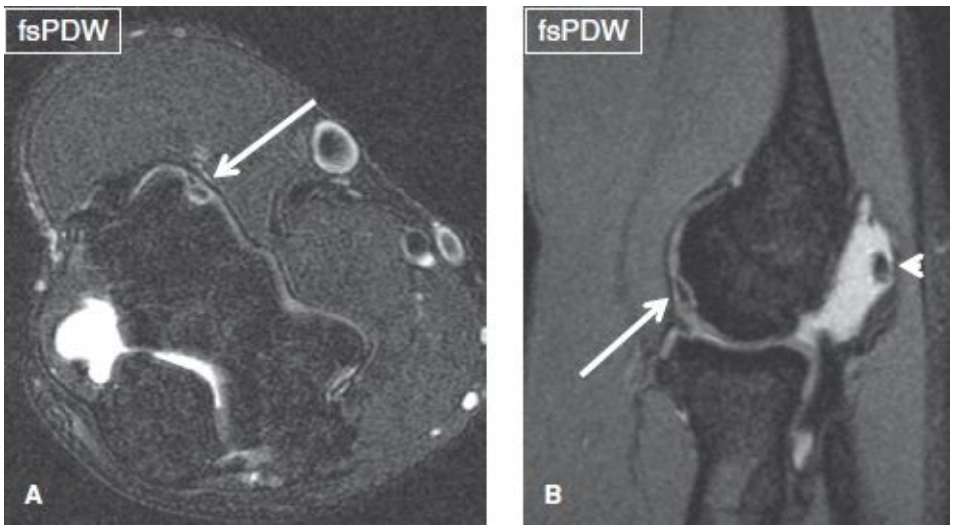

Fig. 49: Unstable osteochondral lesion of the capitellum. Axial **(A)** and sagittal **(B)** images demonstrate an in situ body adjacent to a defect of the anterior capitellum (*arrows*), in keeping with unstable osteochondral lesion. Note the associated loose body within the joint effusion (*arrowhead* in **B**).

Osborne–Cotterill lesion refers to an osseous or osteochondral fracture of the posterolateral margin of the capitellum at the attachment of the LUCL, which is usually the result of recurrent elbow dislocation and has been associated with posterolateral rotatory instability (Fig. 50). Imaging findings include an osseous defect and/or detachment of a bone fragment in the posterolateral aspect of the capitellum, and occasionally a crater or a shovel-like defect in the radial head. The pseudodefect of the capitellum is a focal irregularity of the posterior capitellum, produced by the abrupt transition between the smooth articular surface of the posterior-inferior aspect of the capitellum and the rough non-articular surface of the adjacent lateral epicondyle (Fig. 45). The transition is accentuated with a trough-like undermining with the lateral capitellar margin overhang. This area may get impaction contusions during elbow subluxation or dislocation. In general, however, the pseudodefect of the capitellum can be differentiated from an OCL or OCD by its posterior location and lack of features, which are typical for the latter entities, such as

marrow edema, flattening of the capitellar articular surface, cortical discontinuity and linear, cystic, or arc-like marrow signal changes of the subchondral bone. A similar pseudodefect exists as a notch on the medial and lateral sides of the trochlear groove, located at the junction of the olecranon and coronoid processes. It mimics a fracture on parasagittal images through the ulna, and is absent on the midline sagittal images. A normal transverse ridge runs through this bare area, is devoid of cartilage, and should not be mistaken for an OCL.

Fig. 50: Posterolateral elbow instability. Coronal fsPDW images **(A, B)** show posterolateral subluxation of the radial head, with associated osteochondral fracture of the posterolateral capitellum.

TABLE 2: The MR imaging classification of osteochondral lesions

Stage	Imaging Features	Injury Status
I	Isolated bone marrow edema or sclerosis	Stable
II	Articular cartilage breached, low-signal rim or high-signal rim (but less than fluid-bright) surrounding the OCL (indicating fibrous or granulation tissue, respectively), minimal cystic changes	Stable
III	OCL greater than 1 cm in size, extensive cystic changes, or overlying large cartilage flap	Potentially unstable
IV	Pockets of fluid (or gadolinium) surrounding the OCL, or in situ body or displaced osteochondral fragment	Unstable

OCL, osteochondral lesion.

After the shoulder, elbow is the second most common joint to undergo dislocation. Most

dislocations are posterior or posterolateral and, these may be associated with fracture or contusion of the anterior coronoid process; radial head or posterior aspect of the capitellum; rupture of the RCL, LUCL, and UCL; injury to the CET and CFT; and brachialis muscle strain (Fig. 51). Medial, divergent, and anterior dislocations are uncommon (<10% cases). Most elbow dislocations are treated by conservative means; however, in significant fractures, one should note that at least 50% of the coronoid process of ulna and 50% of the olecranon fossa are required for stability. In radial head fractures associated with elbow dislocations, the indications for surgery include, more than 2 mm cortical step-off, more than 30% radial head involvement or associated radial head dislocation. If it happens to be a good quality bone, younger patient and less than or equal to 3 pieces of fractured bone, one could repair the radial head with pinning. Otherwise, prosthetic replacement is required. Coronoid process fracture is divided into 3 types (1,2,3) based on increasing size of the fracture fragment anteriorly.

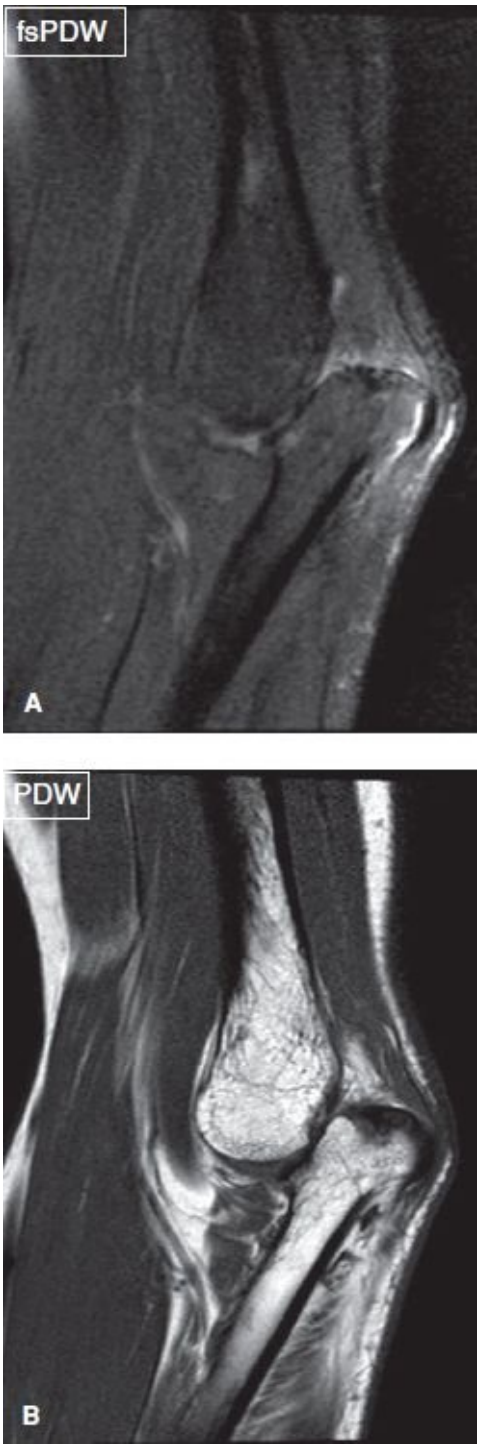

Fig. 51: Posterior elbow dislocation. Sagittal images **(A, B)** demonstrate posterior dislocation at the elbow joint.

The elbow has synovial folds (plicae) that are remnants of the embryologic formation of the joint. Of the several synovial plicae described, the posterolateral plica (aka synovial fringe or meniscus), which is located between the radial head and the capitellum, and the posterior plica, which is situated at the superior margin of the lateral olecranon process, are the most frequently identified. The synovial fringe is a small triangular shaped hypointense structure (Fig. 3) and normal posterior plica is a thin linear hypointense structure. Inflammatory arthropathy or local repetitive microtrauma may cause thickening of the plica and potentially lead to symptoms of locking, mimicking the clinical presentation of intra-articular bodies (Fig. 52). It is, therefore, recommended that thick fringes ($\geq$3–4 mm

thickness) or plicae (≥ 2 mm thickness) should be reported.

Fig. 52: Enlarged synovial fringe. Coronal image demonstrates a thickened synovial fringe (*arrow*) at the posterolateral aspect of the joint.

Bones: [<Normal>]

Normal large red marrow islands located in the distal humeral metaphysis and the radial neck occasionally appear bright on fat-suppressed fluid-sensitive images, and can simulate pathology, such as reactive marrow edema, bone stress injury, or occult fracture. However, these islands are usually brighter than muscles on T1W/PDW sequences. The differential diagnosis is based on history, clinical findings, and evaluation of surrounding structures for signal changes. Marked hyperintensity on fsPDW/fsT2W with or without associated hypointensity on T1W/PDW sequences and/or subchondral or subcortical predominance of the marrow signal, as well as associated fascial edema/fluid favor pathology over red marrow reconversion. Relative hypointensity of the marrow signal on T1W and PDW images as compared to muscle is useful to differentiate infection, subchondral cysts, infarcts, and fractures from reactive bone marrow edema. The latter is more evident on fsPDW and fsT2W images with relative lack of T1/PD W hypointensity. Most infections in the elbow are traumatic in origin and develop through the olecranon bursa. In adults, if there is no ulcer, there is little chance of pyogenic osteomyelitis. Helpful and commonly associated findings of osteomyelitis include sinus tract reaching the bone, loss of cortical

hypointensity, cellulitis, myositis, and soft tissue abscess (Figs. 53, 54).

Fig. 53: Isolated intramuscular abscess. Sagittal image of the forearm shows a well-defined fluid collection with peripheral enhancement (*arrow*) in the flexor carpi radialis muscle, in keeping with intramuscular abscess.

Fig. 54: Brodie abscess and septic arthritis. Coronal **(A, B)**, sagittal **(C),** and axial **(D)** images demonstrate a well-defined isointense lesion (*long arrows*) in the radial metaphysis abutting the physeal scar with multilayered appearance, which shows pronounced rim enhancement and is surrounded by reactive marrow edema. Note the associated joint

effusion, cellulitis, and synovitis (*short arrows*).

Osteoarthritic changes (osteophytes, cysts, sclerosis), enthesopathic changes (ligament, tendon, and/or muscle attachment bony productive changes), as well as neuropathic changes (extensive cystic or destructive) may be evident in the elbow (Figs. 55, 56) and can be seen in combination or in isolated fashion. The procedural options for prosthesis include, radial head replacement (unipolar, bipolar, press-fit, cemented), capitellar resurfacing and total elbow replacement. Upper limb neuropathic arthropathy is relatively uncommon and is usually associated with syringomyelia.

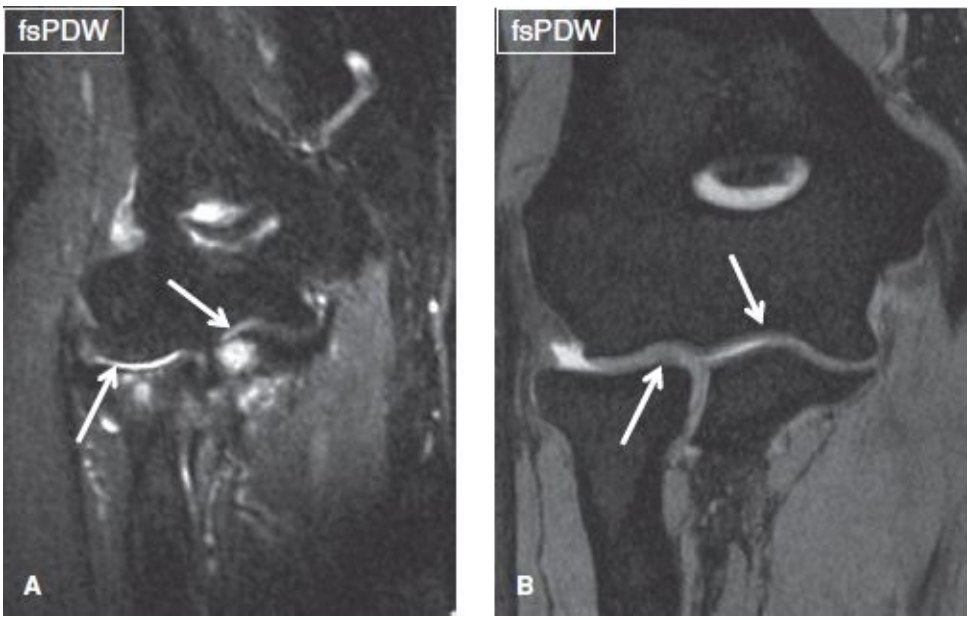

Fig. 55: Severe osteoarthritis. **A:** Coronal image shows large osteophytes, subchondral cysts, as well as complete absence of hyaline cartilage in the radiocapitellar joint and high-grade cartilage defects in the ulnohumeral joint (*arrows*), in this case of severe elbow osteoarthritis. **B:** In a similar image of a normal elbow, smooth cartilage of uniform thickness (*arrows*) covers the articular surfaces of the joint.

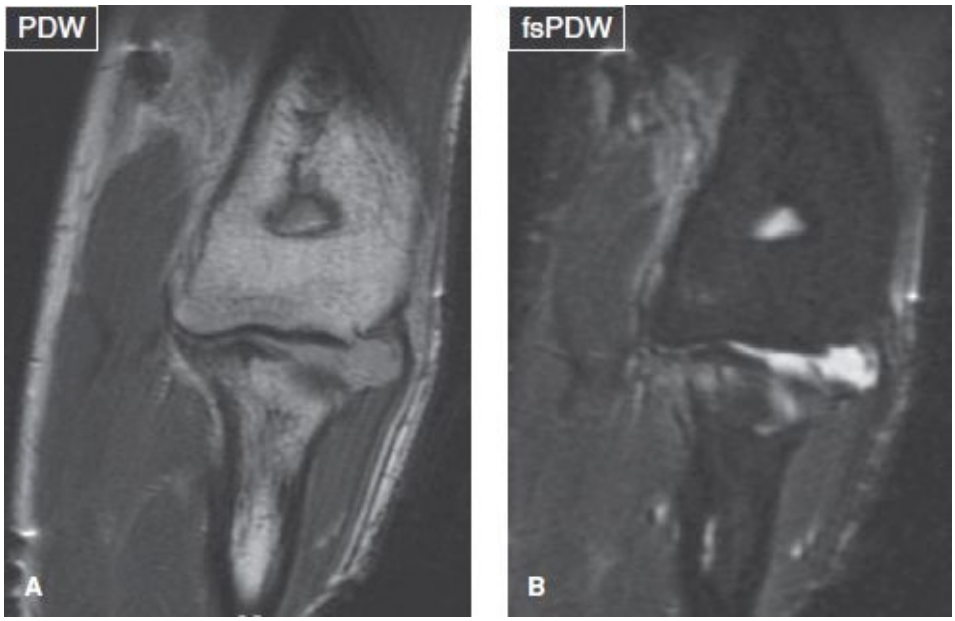

Fig. 56: Osteoarthritis in the setting of congenital absence of the radius. Coronal images **(A, B)** show severe osteoarthritis of the elbow (ulnohumeral) joint, associated with underlying congenital absence of radius.

Similar to the humeral head, osteonecrotic foci manifest as geographic or serpiginous marrow areas, which demonstrate heterogeneous signal, and are demarcated by a hypointense band, which is sometimes paralleled by a hyperintense band on T2W images (double-line sign), and show lack of or only peripheral enhancement after contrast administration (Fig. 57). Chronic stages are characterized by subchondral fractures, articular surface collapse, and secondary osteoarthritis. One should look for underlying causes such as trauma, alcoholism, steroid intake, sickle cell anemia, Gaucher disease, etc. Various benign and malignant tumors including aneurysmal bone cyst, osteoid osteoma, giant cell tumor, osteosarcoma, Ewing sarcoma, multiple myeloma, lymphoma, and metastasis may arise in the vicinity of elbow, and these show similar characteristics as elsewhere in the body.

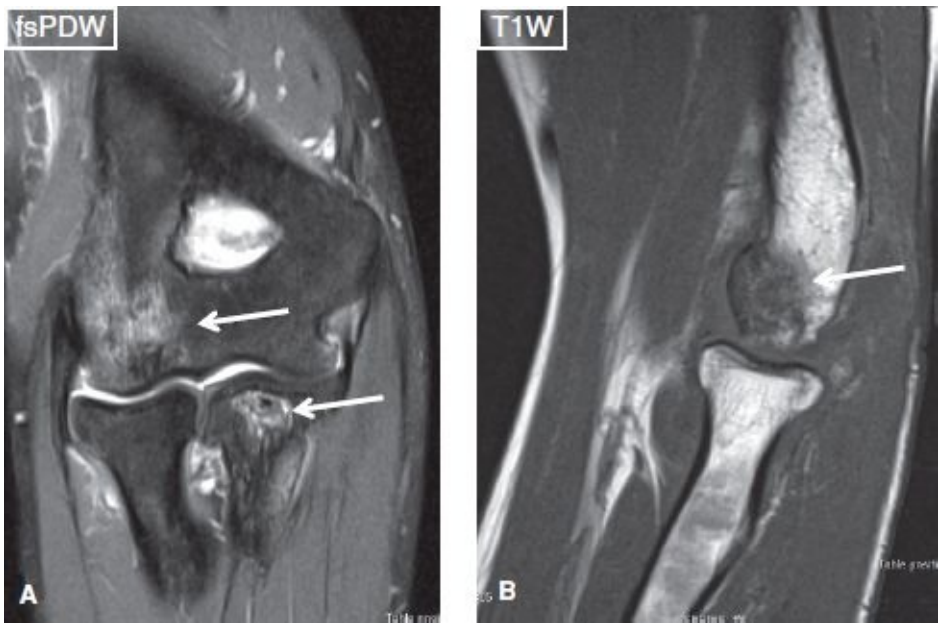

Fig. 57: Bone infarcts. Coronal **(A)** and sagittal **(B)** images show relatively well-demarcated T1 hypointense/T2 hyperintense marrow areas with geographic margins in the capitellum and proximal ulna (*arrows*) in a patient with underlying sickle cell disease, compatible with osteonecrosis.

The supracondylar process is a horn-shaped bony protuberance/exostosis present in 0.2% to 3% of the population. It arises from the anteromedial aspect of the distal humeral shaft, approximately 5 to 7 cm above the medial epicondyle, projects toward the elbow, and is often connected to the latter by a fibrous band (ligament of Struthers). This anatomic variation should not be misinterpreted for osteochondroma, as the latter develops in different locations, points away from the joint, and may feature a cartilage cap. Rarely, the ligament of Struthers may cause symptomatic compression of the MN, brachial artery, or

the UN. A spectrum of congenital elbow, forearm and hand bony deficiencies may be encountered. These can be conveniently divided into: (1) Radial longitudinal axis deficiency [>2 mm radial shortening, absence of carpus or coalitions in carpus, loss of 2nd metacarpal base flare due to absent carpus, association with syndromes, such as Halt Oram, THAR, Fanconi anemia]; (2) Ulnar longitudinal axis deficiency [varies from ulnar deficiency to radial deficiency in the worsening stages, associated elbow and foot anomalies]; (3) Central axis deficiency [central cleft, strong hereditary component and bilaterality, association with acrosyndactily and acropolydactily]; (4) Transverse axis deficiency; (5) Amniotic band syndrome; (6) Oliver syndrome (skin and scalp abnormalities associated); and (7) Symbrachidactyly (all fingers are short).

Muscles: [<Normal>]

Normal muscles feature homogeneous intermediate signal on PDW and fsPDW images. Fatty infiltration and atrophy are best depicted on T1W and PDW images, and edema-like signal on the fluid sensitive fat suppressed (fsPDW, fsT2W, STIR) images. In cases of muscle strain, myopathy, or myositis, the changes are usually focal, involve one or more muscles that are not in a nerve distribution, and there is often associated fascial edema. In muscle denervation, the changes involve muscles of a particular nerve distribution and are usually diffuse and located distal to the neuropathy site, without associated fascial edema. Muscle denervation changes are the key for detection of regional neuropathies. Radial neuropathy affects the brachioradialis, inferolateral portion of brachialis, triceps, anconeus, supinator, and extensor compartment muscles (posterior interosseous nerve [PIN]). If the triceps is spared, the lesion is distal to the spiral groove. Musculocutaneous neuropathy affects the biceps and brachialis muscles. Median neuropathy involves the pronator teres and flexor compartment muscles, whereas anterior interosseous neuropathy selectively affects the flexor pollicis longus, pronator quadratus, and the lateral half of the flexor digitorum profundus muscles. Finally, ulnar neuropathy involves the flexor carpi ulnaris and the medial half of the flexor digitorum profundus muscle, as well as the intrinsic muscles of the hand.

As elsewhere in the body, early myositis ossificans manifests as an ill-defined mass that is isointense and hyperintense to the muscles on T1W and T2W images, respectively, and occasionally features contrast enhancement and/or fluid–fluid levels. The above appearance can be misleading since the peripheral calcification may not be well seen on MR imaging, and T2 hyperintensity (edema) of the soft tissues may extend beyond the apparent calcific rim. In later stages, the lesion mimics bone, demonstrating thin hypointense (calcified) periphery, and central portion, which features marrow-like signal on all sequences. These mature lesions lack central or substantial contrast enhancement (Fig. 58). Vascular malformations, neoplasms, and tumor-like disorders of the muscles around the elbow joint exhibit typical imaging features, similar to elsewhere in the body (Figs. 59–62).

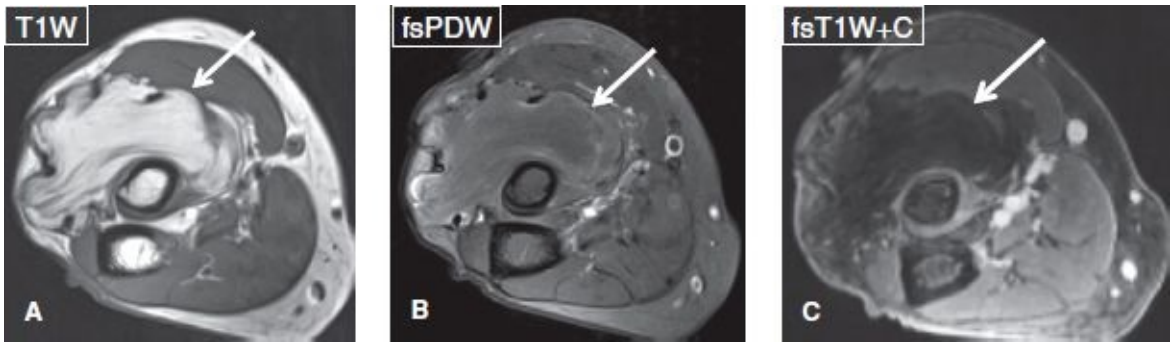

Fig. 58: Myositis ossificans. Axial images **(A–C)** exhibit a well-defined nonenhancing space-occupying mass (*arrows*), which crosses the fascial planes, and features thin hypointense periphery, as well as marrow-like internal signal.

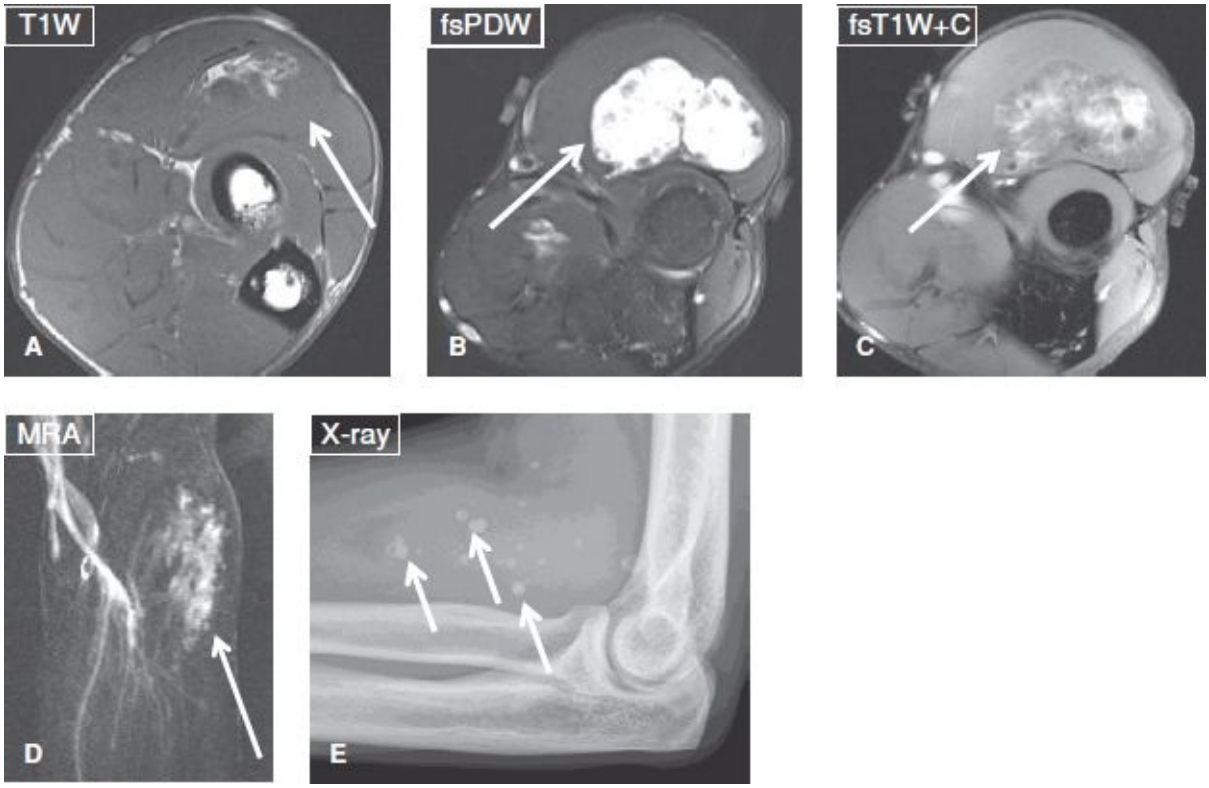

Fig. 59: Hemangioma of the forearm musculature. **A–C:** Axial images demonstrate a well-defined heterogeneously enhancing space-occupying mass containing internal fat within the lateral compartment muscle (*arrows*). **D:** On dynamic MR angiography, there is patchy enhancement (*arrow*) in capillary and venous phase with no venous shunting. **E:** On a lateral radiograph, the lesion exhibits multiple phleboliths (*arrows*).

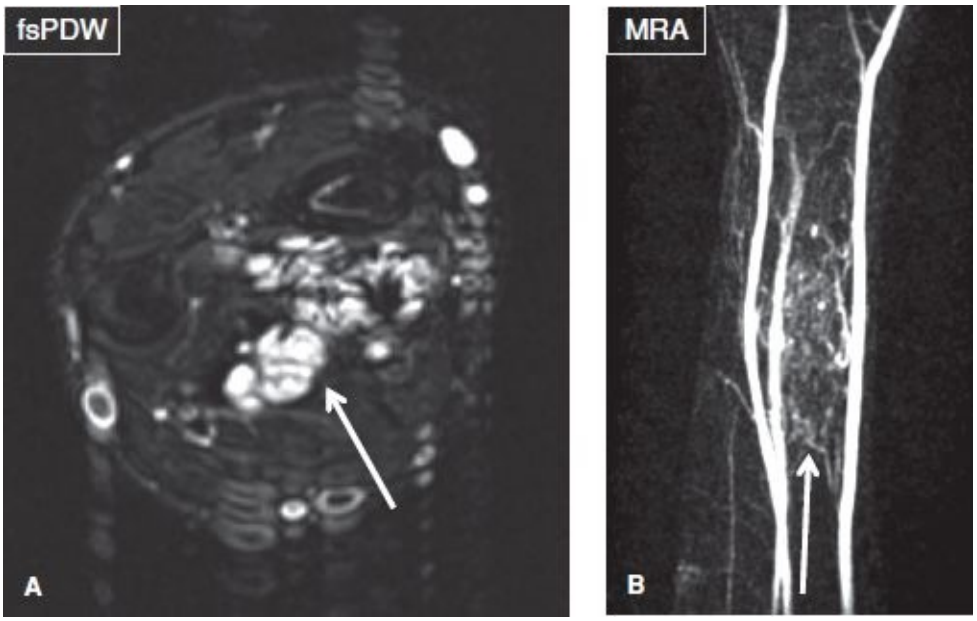

Fig. 60: Venous malformation of the forearm. Axial **(A)** and dynamic MR angiography **(B)** images show a tangle of dilated vessels (*arrows*) in the anterior compartment of the forearm. Note the pulsation artifacts in **(A)**. No arteriovenous (AV) shunting is noted on MR angiogram (MRA).

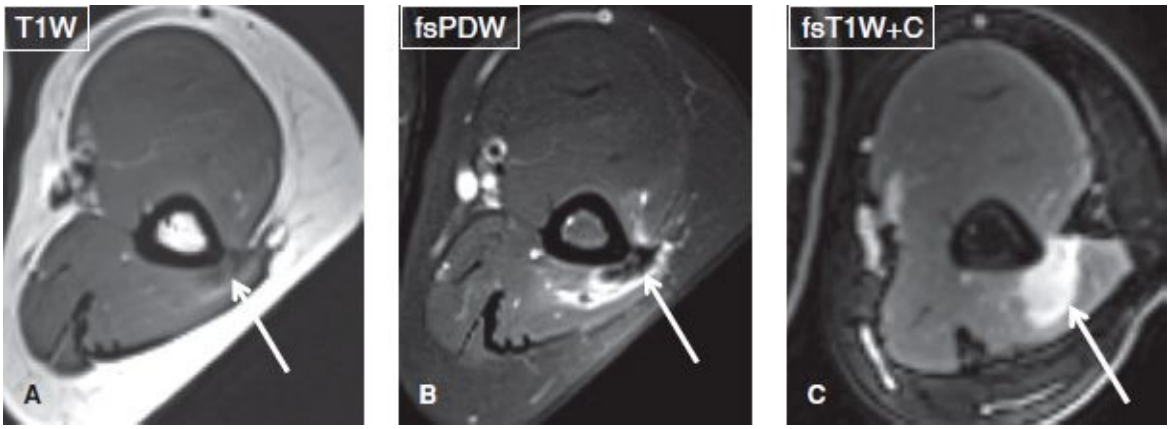

Fig. 61: Desmoid tumor of the upper extremity. Axial images **(A–C)** show a relatively ill-defined hypointense lesion (*arrows*) adjacent to the humerus with surrounding edema and avid enhancement.

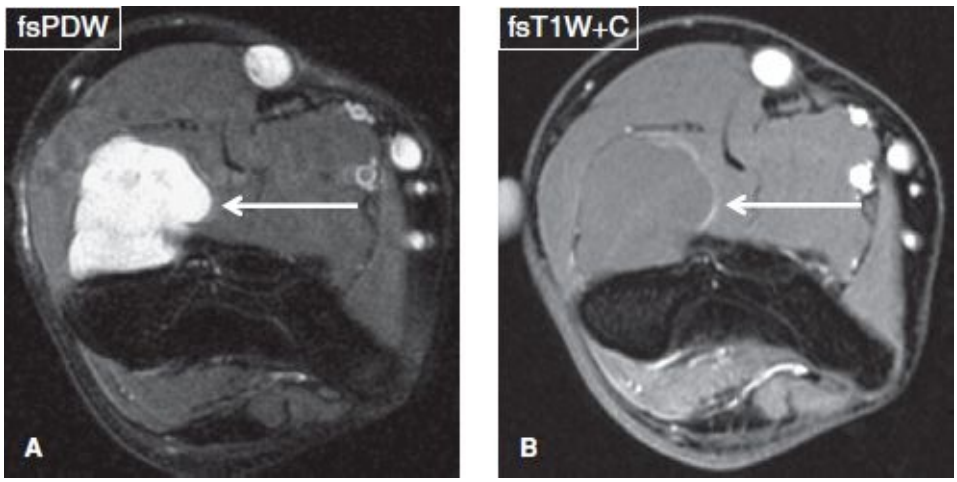

Fig. 62: Synovial sarcoma of the upper extremity. Axial images **(A, B)** exhibit a well-defined

lobulated space-occupying lesion (*arrows*), within the muscles of the anterior aspect of the elbow and shows mild peripheral and central enhancement.

Vessels: [<Normal> <Abnormal>]

The continuations of the axillary artery, the brachial artery, and its branches at the radial neck (ulnar and radial arteries) should normally exhibit flow voids, especially on fsPDW or T2W images. If present, prominent venous varicosities and vascular malformations should be reported. The cephalic and basilic veins run along the lateral and the medial aspect of the biceps muscle in a subcutaneous location, respectively, and are sometimes involved in superficial venous thrombosis.

Nerves: [<Cubital tunnel normal> <Retinaculum deficient> <Hyperintense ulnar nerve>]

At the level of the elbow, the MN runs medial and parallel to the brachial artery through the antecubital fossa, deep to the biceps aponeurosis, and anterior to the brachialis muscle. It then courses between the humeral and ulnar heads of the pronator teres muscle and enters the anterior compartment of the forearm, passing beneath the fibrous arch of the heads of the flexor digitorum superficialis muscle. The MN is depicted on axial images as a round to oval structure, which is isointense to muscles on all sequences, and features uniform fascicular appearance. Mild short-segment T2 hyperintensity is common, as it follows an oblique course under the pronator teres, which normalizes distally. Also, mild flattening is common as a normal variant at the level of the flexor digitorum superficialis fascial sheath.

Apart from space-occupying lesions, the MN may be compressed (1) between the humeral and ulnar heads of the pronator teres muscle (pronator teres syndrome); (2) by the ligament of Struthers, a fibrous band-like vestigial remnant, present in up to 2.7% of the population, as it extends from the anteromedial aspect of the distal humerus to the medial epicondyle; (3) by the bicipital aponeurosis; or (4) by the fibrous arch (sublimis bridge) of the flexor digitorum superficialis muscle, which is a fibrotendinous arcade joining the humeral and ulnar heads of the latter muscle. In pronator teres syndrome, denervation changes (edema, fatty degeneration, and/or atrophy) are evident in the pronator teres, flexor carpi radialis, palmaris longus, and flexor digitorum superficialis muscles.

At the level of the elbow, the UN courses within the cubital tunnel, which is a fibro-osseous channel formed by the olecranon process laterally, the posterior cortex of the medial epicondyle medially, the elbow joint capsule and posterior bundle of the UCL anteriorly, and the cubital retinaculum (ligament of Osborne) posteriorly. Within the cubital tunnel, the UN is best depicted on axial images as a round or oval structure normally surrounded by fat, maintaining a constant cross-sectional area along the elbow, and is typically isointense to muscle to all sequences. Mild T2 hyperintensity of the UN within the cubital tunnel can be commonly seen in asymptomatic subjects, especially on short tau inversion recovery (STIR) images.

The cubital tunnel is the most common site of UN injury or compression. The resulting neuropathy, known as cubital tunnel syndrome, may be caused by trauma or processes that limit the space or distort the anatomy of the tunnel, including progressive cubitus valgus deformity, osteoarthritis, rheumatoid arthritis, prolonged bed rest, anconeus epitrochlearis accessory muscle (prevalence rate of 3% to 28%), thickened cubital retinaculum, malunion or nonunion of a condylar fracture, soft tissue masses, ganglion cyst, and trochlear hypoplasia. The imaging findings include moderate or severe T2 hyperintensity, increased longitudinal extent of signal abnormality, and enlargement or flattening of the UN at the level of the cubital tunnel, which may be associated with abnormal fascicular morphology and secondary denervation changes (edema, fatty degeneration, and/or atrophy) in the flexor carpi ulnaris and the ulnar half of the flexor digitorum profundus muscles (Figs. 63–68). The UN may undergo subluxation or dislocation over the tip of the medial epicondyle, usually during flexion, and rarely during extension, of the elbow. The entity is best depicted on axial images, although may be asymptomatic (in up to 15% population), and can be associated with a hypoplastic groove.

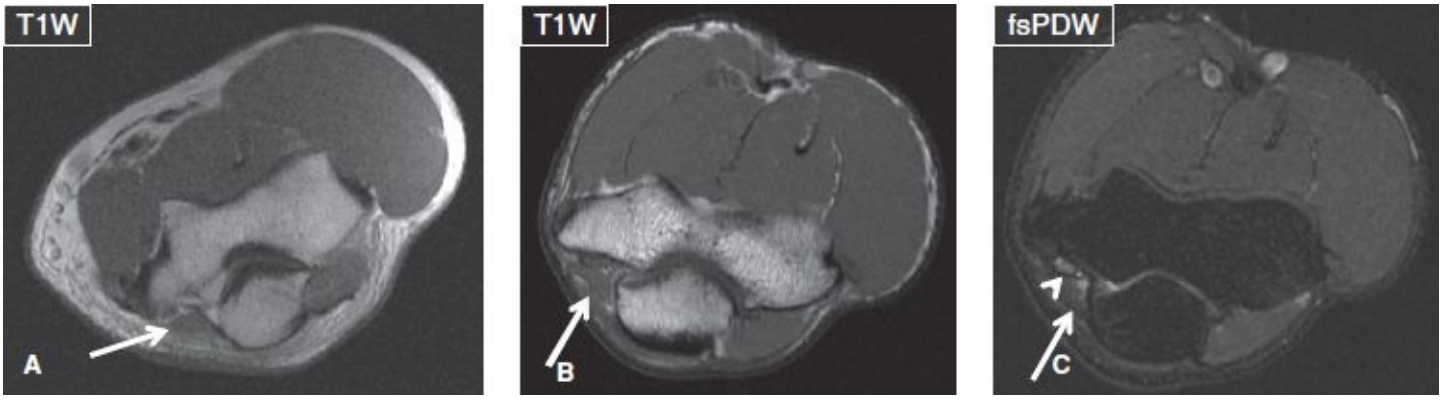

Fig. 63: Anconeus epitrochlearis muscle. **A:** Axial image shows the accessory muscle within the cubital tunnel (*arrow*). **B, C:** Axial images from another case again demonstrate the accessory anconeus muscle (*long arrows*) with mildly hyperintense and flattened ulnar nerve (*arrowhead* in **C**), in keeping with compressive neuropathy.

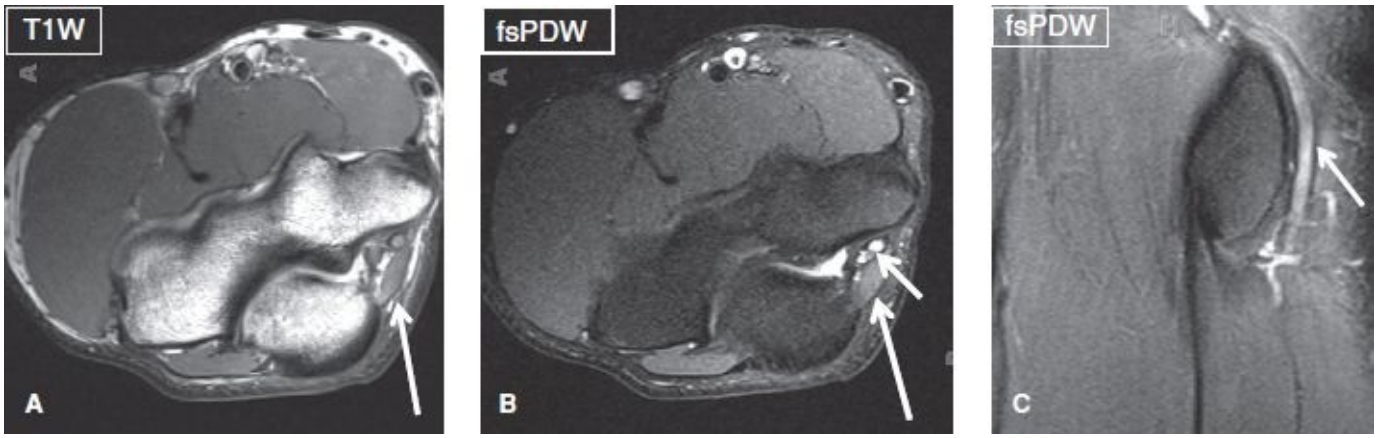

Fig. 64: Ulnar neuropathy secondary to compression by anconeus epitrochlearis muscle. **A, B:** Axial images show the accessory muscle within the cubital tunnel (*long arrows*). The ulnar nerve (*short arrow* in **B**) is flattened and T2 hyperintense with prominent fascicles, in

keeping with neuropathy. **C:** The extent of hyperintensity (*arrow*) is nicely seen on the respective sagittal image.

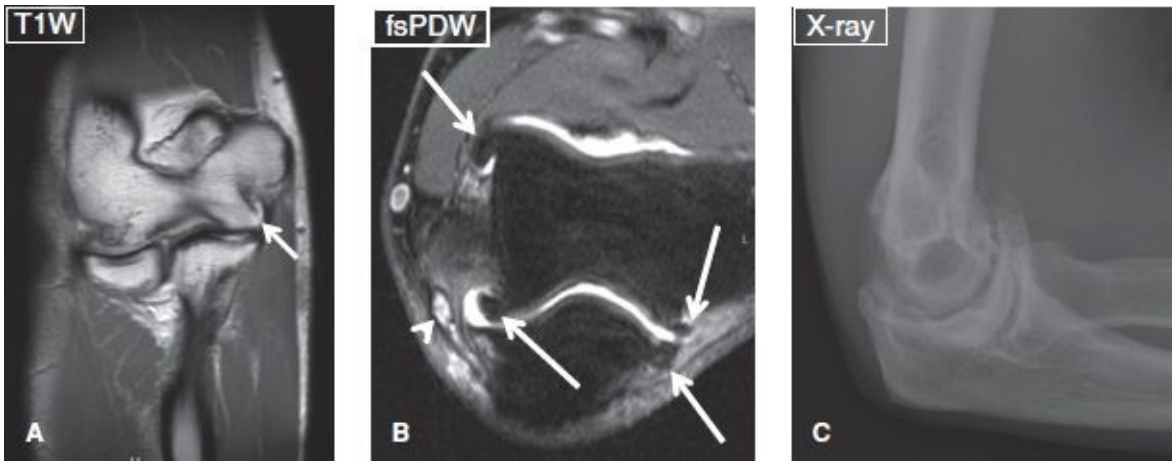

Fig. 65: Ulnar neuropathy secondary to severe elbow osteoarthritis. Coronal **(A)** and axial **(B)** images show large osteophytes (*arrows*) in the radiocapitellar and ulnohumeral joints. Some of the osteophytes and synovium protrude into the cubital tunnel, causing compressive ulnar neuropathy, depicted as flattening and T2 hyperintensity of the ulnar nerve (*arrowhead* in **B**). **C:** Note the osteoarthritic changes in the corresponding lateral radiograph.

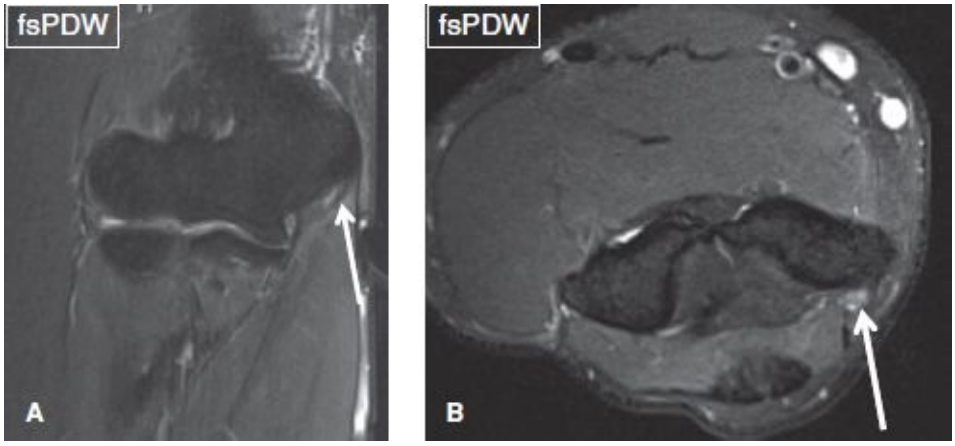

Fig. 66: Ulnar neuropathy with associated sprain of the ulnar collateral ligament. Coronal **(A)** and axial **(B)** images demonstrate partial tear of the ulnar collateral ligament (*arrow* in **A**), and T2 hyperintensity of the ulnar nerve (*arrow* in **B**) within the cubital tunnel, in keeping with neuropathy.

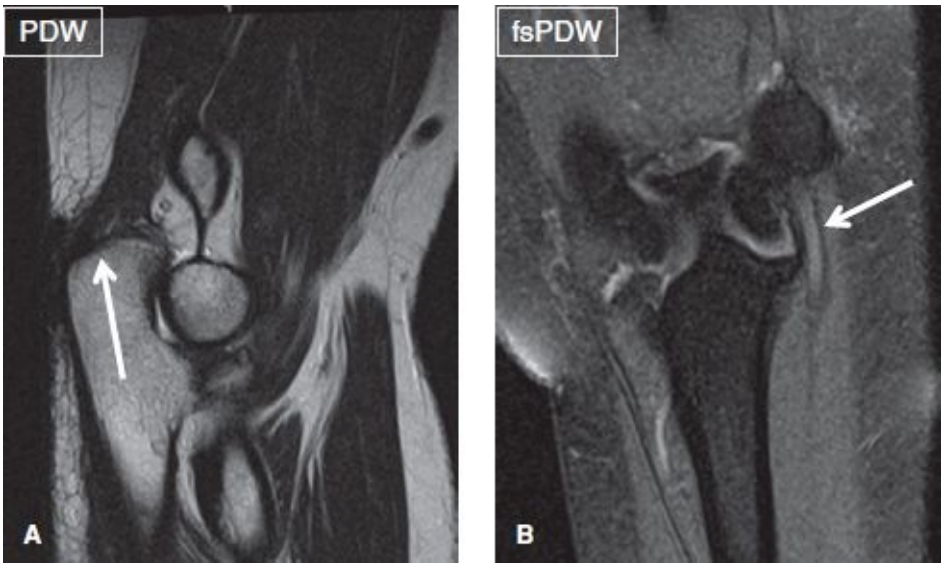

Fig. 67: Broad muscular insertion of the triceps causing ulnar neuropathy. **A:** Sagittal image shows a broad insertion of the medial head of the triceps muscle at the olecranon, a variation which may cause compression and/or displacement of the ulnar nerve (snapping triceps syndrome). **B:** In the corresponding coronal image, the ulnar nerve is minimally hyperintense (*arrow*).

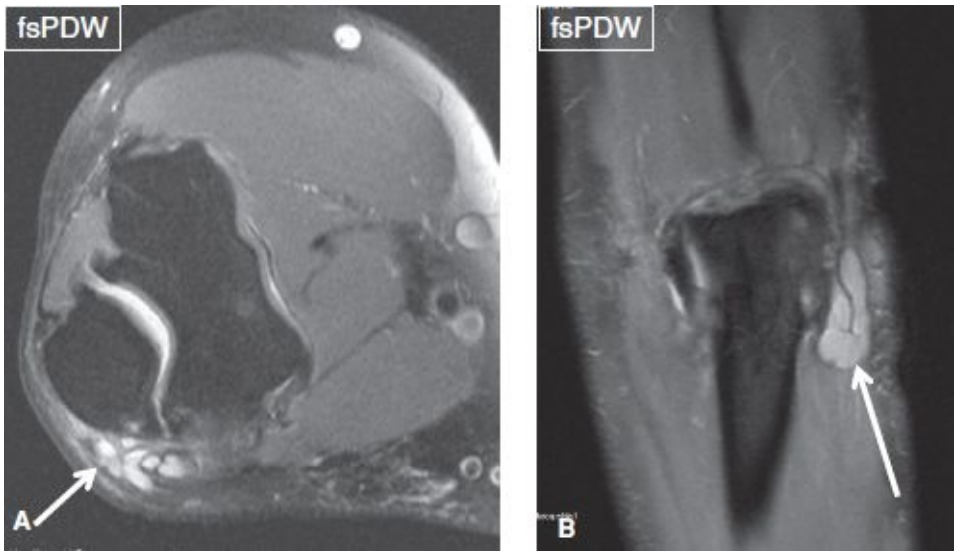

Fig. 68: Intraepineurial ganglion of the ulnar nerve. Axial **(A)** and coronal **(B)** images exhibit a multiloculated tubular hyperintense structure (*arrows*) within and around the ulnar nerve at the level of the cubital tunnel. The entity causes compression of the ulnar nerve and associated neuropathy.

At the level of the elbow, the RN courses along the volar aspect of the joint through the lateral intermuscular septum. Just anterior to the lateral epicondyle, the RN divides into a deep motor branch and a superficial sensory branch. The former branch crosses between the superficial and deep heads of the supinator muscle and through the fibrous arcade of Frohse (a congenital fibrous adhesion between the brachialis and brachioradialis muscles, present in 30% to 50% of the population) to exit into the posterior compartment of the forearm. After exiting the supinator muscle, the deep motor branch is referred to as the PIN. The RN

is depicted on axial images as a round structure, which is located between the brachialis and brachioradialis muscles, and is normally isointense to muscles on all sequences. The PIN can be identified more distally and posteriorly, where it penetrates the supinator muscle.

Variations in anatomic structures at the elbow level may cause compression of the RN or PIN. The resulting neuropathies are known as radial tunnel syndrome and PIN syndrome, respectively. In PIN syndrome, the respective nerve may demonstrate abnormal T2 hyperintensity, whereas the most common compression site is at the arcade of Frohse, which is occasionally identified as a low-signal band at the proximal edge of the supinator muscle. In most cases, imaging fails to identify the causative compressive agent although the modality can indirectly establish the diagnosis by depicting the characteristic distribution of muscle denervation changes.

Syndromes and Others

The MR reader should be aware of the medial epitrochlear lymph node, which may show high signal on fsPDW or fsT2W images, and, although a normal structure, it should be considered suspicious for pathology when enlarged, such as in cases of cat scratch disease, tuberculosis, lymphoproliferative disorders, and rarely in myeloma or metastatic involvement (Fig. 69). Generally, an enlarged medial epitrochlear lymph node, which maintains its oval shape, enhances heterogeneously, and is associated with stranding and soft tissue edema or conglomeration with other lymph nodes, raises suspicion for an inflammatory/infectious process (Fig. 70).

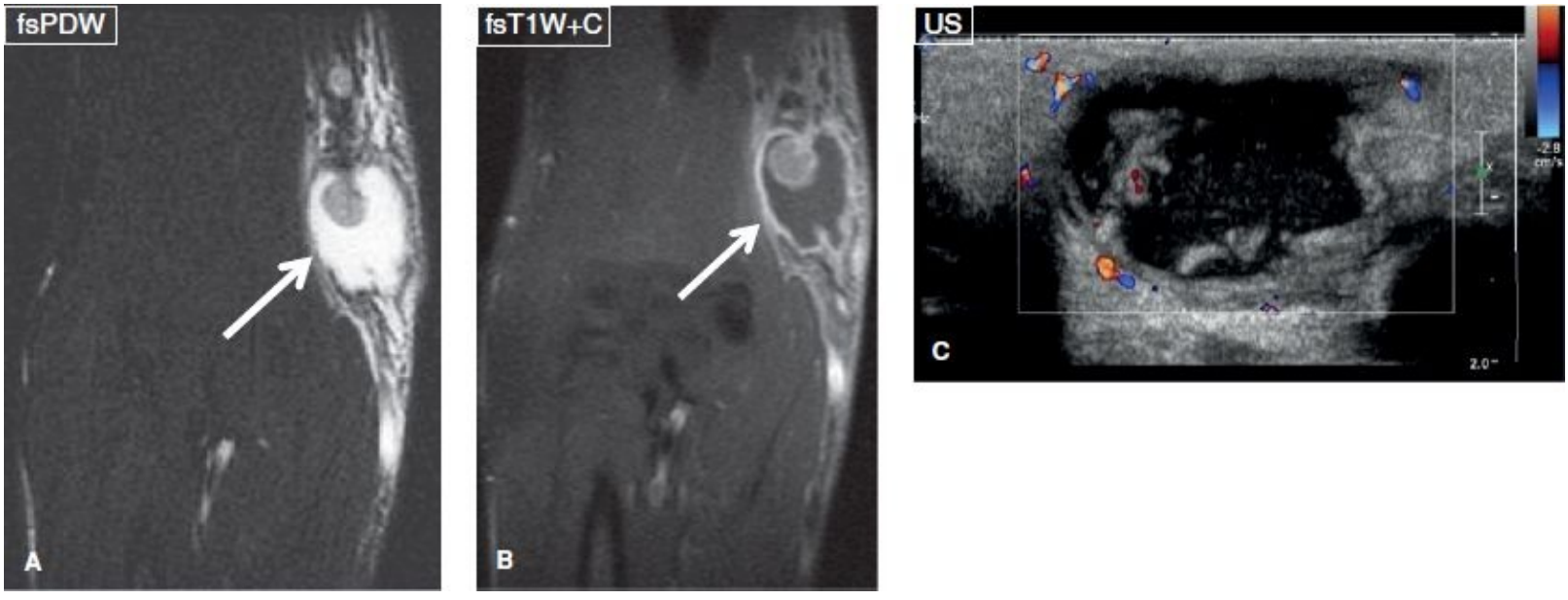

Fig. 69: Cat scratch disease. **A, B:** Coronal images show an enlarged medial epitrochlear lymph node with central necrosis (*arrow*). **C:** The internal morphology of the necrotizing lymphadenitis is shown in detail in the respective color Doppler ultrasound image.

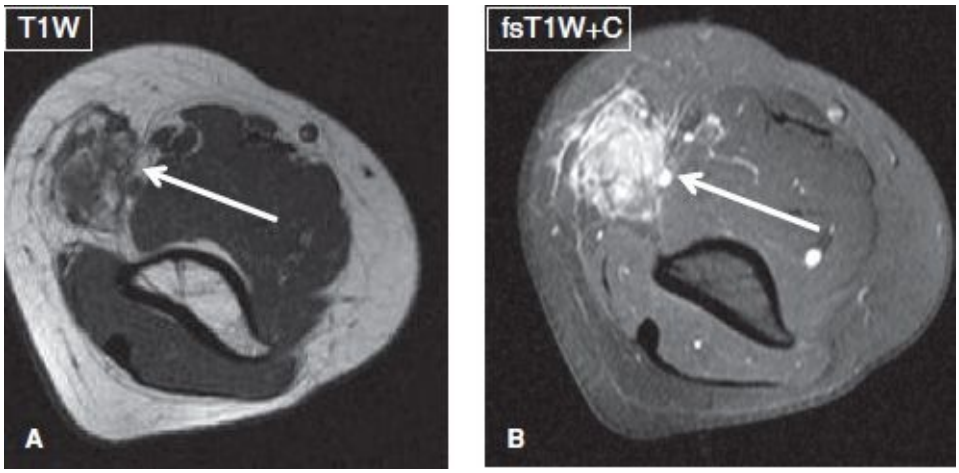

Fig. 70: Kimura disease. A case of this rare chronic inflammatory disorder of unknown etiology is shown on axial images **(A, B)** through the distal humerus, which demonstrate an ill-defined subcutaneous T2 hyperintense lymph node lesion (*arrows*), representing vascular proliferation and fibrosis. (Courtesy of Dr. Kyung Jin Suh.)

Valgus extension overload syndrome, an entity associated with elbow derangement, results from chronic UCL insufficiency (mainly of the anterior bundle, which might be attenuated or deficient) and predisposes to repeated radiocapitellar impaction during valgus stress. It is clinically evaluated using valgus extension overload test and on imaging, manifests with bone marrow edema, sclerosis, development of OCLs, ulnohumeral osteophyte formation, loose body, and rarely, olecranon stress fracture. Chronic cases may result in posteromedial elbow impingement, which causes painful mechanical abutment of bone and soft tissues in the olecranon fossa. Imaging findings include osteophyte formation in the medial aspect of the olecranon fossa, chondral defects, scarring, and secondary ulnar neuropathy (Fig. 71). Posterolateral impingement is another recognized entity, which may result from synovial thickening (plica thickening of more than 2–3 mm or synovial fringe thickening more than 3–4 mm) in the posterolateral joint recess, with bone marrow edema and OCLs. These patients present with posterolateral pain and tenderness, unrelated to lateral epicondylitis.

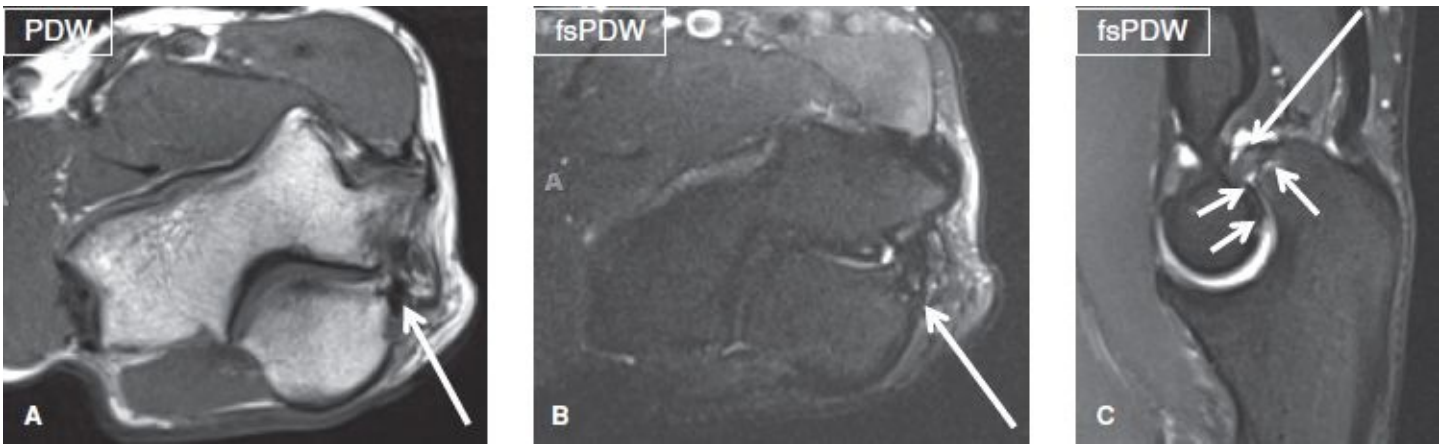

Fig. 71: Chronic posteromedial impingement. Axial (**A, B**) and sagittal **(C)** images demonstrate scarring of the posteromedial aspect of the elbow joint (*arrows*). Note the posteromedial ulnohumeral osteophytes and cartilage defect–related subchondral cysts.

Post-operative Findings

One should be aware of the common surgical procedures performed in different areas of the elbow for various structures and their normal and abnormal imaging appearances. In general, reconstructed tendons and ligaments should follow their normal course, feature anatomic continuity, and lack fluid-like signal. Following US guided needling with or without plasma-rich protein infusion, the tendon should heal and mature to darker signal over time. Mild signal alteration or thickening is a common normal postoperative finding and should gradually resolve over many months following the surgery, as the tendon/ligament heals and matures. In some settings, however, such as in the case of the common flexor or extensor tendon, the structure may remain thickened for prolonged periods, simulating chronic tendinosis, even after normal signal has been regained. The procedures are performed for recalcitrant medial or lateral epicondylitis to prevent loss of the forearm extensor strength, relieve the pain, and recover the grip strength. The triceps and biceps tendons can be surgically repaired or reconstructed using autografts (from the ipsilateral palmaris longus tendon) or allografts (Fig. 72). Medial epicondylitis is treated by conservative means. In case of avulsed medial epicondyle fragment, surgery is indicated if there is displaced or entrapped fragment, or with recurrent valgus instability.

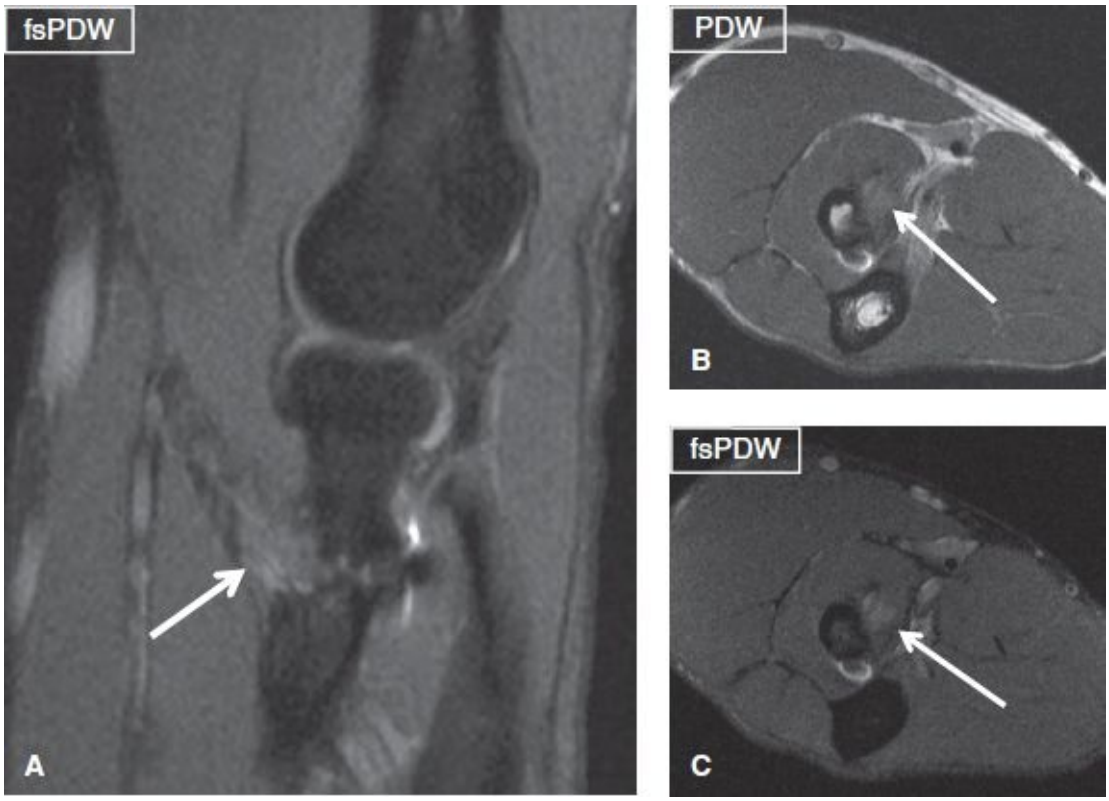

Fig. 72: Retear of a surgically repaired biceps tendon. Sagittal **(A)** and axial **(B, C)** images demonstrate a partial tear (grade II sprain) of the surgically repaired biceps tendon (*arrows*). Note the susceptibility artifacts from screw placed for repair at the bicipital tuberosity.

OCLs can be treated by microabrasion, osteochondral implant (OCI) placement, or

autologous cartilage implantation (ACI). Generally, treatment is recommended for potentially unstable or symptomatic lesions. Similar to the knee, the postoperative imaging evaluation of OCDs is based on the magnetic observation of cartilage repair tissue (MOCART) scoring scale. In terms of analysis, the most important features to evaluate are as follows.

- The quality of the regenerated cartilage (hyaline/fibrocartilage, atrophic, hypertrophic, or flush with the native cartilage)
- The binding of the regenerated cartilage at the border zone with the native cartilage
- The binding of the regenerated cartilage with the subchondral plate (any exposure of the subchondral surface)
- The presence of subchondral bony reaction (edema, cysts, or chondral osteophyte)
- The presence of joint effusion and/or synovitis

In *UCL reconstruction,* the normal intact graft appears thickened, particularly at its humeral attachment, demonstrates distinct fibers, and low to intermediate signal intensity on all pulse sequences (Figs. 73, 74). The graft should be taut; otherwise it could be torn or might not be providing adequate stability, particularly in flexion. UN may be transposed anteriorly in some cases as a preventive measure. In case of effusion, joint fluid may normally extend between the distal graft and the sublime tubercle and create a T-sign, which is due to the different distal attachment of the graft compared with the native ligament, and this sign in isolation should not reflect retear. In graft degeneration, there is significant thickening of the graft and inability to discern its fibers, along with diffuse increased signal on T1W images and mild hyperintensity on T2W images. In large graft tears, there is frank disruption of graft fibers and/or fluid signal within the graft on T2W images (Fig. 75). Small tears may be difficult to detect unless arthrography is employed.

Fig. 73: Ulnar collateral ligament surgical repair. Coronal images **(A, B)** show a thickened but intact surgically repaired ulnar collateral ligament (*arrows*).

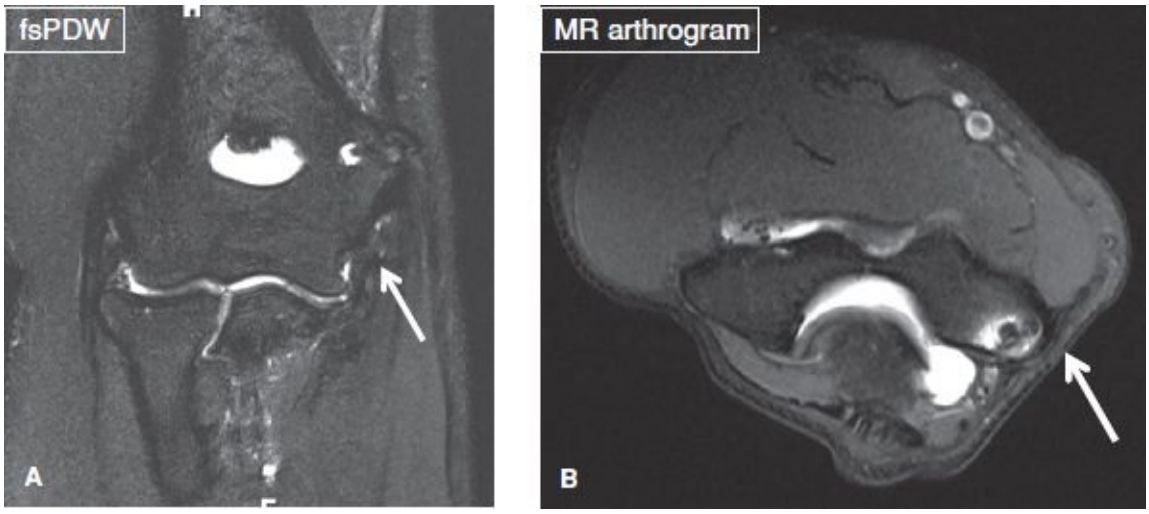

Fig. 74: Ulnar collateral ligament surgical repair. Coronal **(A)** and axial **(B)** images show an intact surgically repaired ulnar collateral ligament (*arrows*).

In cubital tunnel syndrome, *surgical decompression of the UN* involves in situ release and neurolysis, which may be supplemented by anterior subcutaneous or submuscular transposition. Radial tunnel syndrome or pronator syndrome is similarly treated by neurolysis, with or without resection of superficial head of supinator and pronator muscles, respectively. Approximately 4 to 6 weeks following surgery, the size, signal, and fascicular morphology of the neurolyzed nerve should decrease and in some cases, return to near-normal. Persistent or increasing nerve T2 hyperintensity with enlarged, disrupted or effaced fascicles, and/or T1 hypointense fibrotic tissue abutting or surrounding the nerve indicate re-entrapment neuropathy. Secondary regional muscle denervation changes may still be evident. Additional features to report include possible nerve angulation or deviation from the smooth expect course and intervention-related neuroma formation.

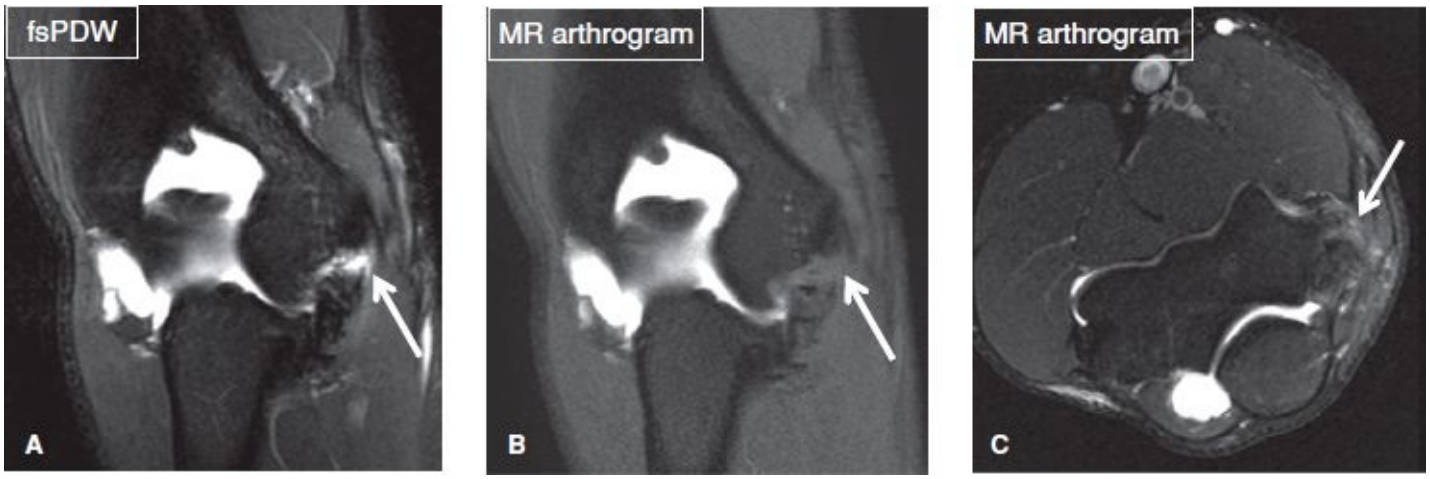

Fig. 75: Retear of a surgically repaired ulnar collateral ligament. Coronal conventional **(A)** and coronal **(B)** and axial **(C)** postcontrast images show a high-grade, near-complete external surface partial tear of the ulnar collateral ligament (*arrows*). No contrast extravasation is seen.

SUGGESTED READINGS

Andreisek G, Crook DW, Burg D, et al. Peripheral neuropathies of the median, radial, and ulnar nerves: MR imaging features. *Radiographics*. 2006;26(5):1267–1287.
Frick MA, Murthy NS. Imaging of the elbow: Muscle and tendon injuries. *Semin Musculoskelet Radiol*. 2010;14(4):430–437.
Hayter CL, Giuffre BM. Overuse and traumatic injuries of the elbow. *Magn Reson Imaging Clin N Am*. 2009;17(4):617–638.
Jeon IH, Micic ID, Yamamoto N, et al. Osborne-Cotterill lesion: An osseous defect of the capitellum associated with instability of the elbow. *AJR Am J Roentgenol*. 2008;191(3):727–729.
Kaplan LJ, Potter HG. MR imaging of ligament injuries to the elbow. *Radiol Clin North Am*. 2006;44(4):583–594.
Levine WN, Prickett WD, Prymka M, et al. Treatment of the athlete with multidirectional shoulder instability. *Orthop Clin North Am*. 2001;32(3):475–484.
Miller TT, Reinus WR. Nerve entrapment syndromes of the elbow, forearm, and wrist. *AJR Am J Roentgenol*. 2010;195(3):585–594.
Miller TT, Shapiro MA, Schultz E, et al. Comparison of sonography and MRI for diagnosing epicondylitis. *J Clin Ultrasound*. 2002; 30(4):193–202.
O'Driscoll SW. Classification and evaluation of recurrent instability of the elbow. *Clin Orthop Relat Res*. 2000;(370):34–43.
Pasternack I, Tuovinen EM, Lohman M, et al. MR findings in humeral epicondylitis. A systematic review. *Acta Radiol*. 2001;42(5):434–440.
Rosenberg ZS, Beltran J, Cheung YY. Pseudodefect of the capitellum: Potential MR imaging pitfall. *Radiology*. 1994;191(3):821–823.
Sampaio ML, Schweitzer ME. Elbow magnetic resonance imaging variants and pitfalls. *Magn Reson Imaging Clin N Am*. 2010;18(4):633–642.
Simonson S, Lott K, Major NM. Magnetic resonance imaging of the elbow. *Semin Roentgenol*. 2010;45(3):180–193.
Singh RK, Pooley J. Complete rupture of the triceps brachii muscle. *Br J Sports Med*. 2002; 36(6):467–469.
Stein JM, Cook TS, Simonson S, et al. Normal and variant anatomy of the elbow on magnetic resonance imaging. *Magn Reson Imaging Clin N Am*. 2011;19(3):609–619.
Stevens KJ. Magnetic resonance imaging of the elbow. *J Magn Reson Imaging*. 2010;31(5):1036–1053.
Stroyan M, Wilk KE. The functional anatomy of the elbow complex. *J Orthop Sports Phys Ther*. 1993;17(6):279–288.
Thornton R, Riley GM, Steinbach LS. Magnetic resonance imaging of sports injuries of the elbow. *Top Magn Reson Imaging*. 2003;14(1):69–86.
Walz DM, Newman JS, Konin GP, et al. Epicondylitis: Pathogenesis, imaging, and treatment. *Radiographics*. 2010;30(1):167–184.
Waseem M, Nuhmani S, Ram CS, et al. Lateral epicondylitis: A review of the literature. *J Back Musculoskelet Rehabil*. 2012;25(2):131–142.

APPENDIX 1: Sample Completed Structured Report: Elbow: NORMAL

EXAM: MR ELBOW [<WITH> OR <WITHOUT>] CONTRAST

HISTORY: [] year-old [<Patient Sex>] with [<Order Reason for Study>]

TECHNIQUE: Imaging was performed [<without IV contrast/before and after IV/after intra-articular contrast>]. Multiplanar, multisequence MR images of the [<right/left>] elbow were obtained on a [1.5 or 3.0] Tesla magnet.

Comparison: [<NONE>]

FINDINGS:

Alignment: [<Normal>]

Joint fluid: [<None>]

Intra-articular bodies: [<None>]

Medial structures:

Ulnar collateral ligament: [<Intact>]

Common flexor tendon: [<Normal>]

Medial epicondyle: [<Normal>]

Lateral structures:

Radial collateral ligament: [<Intact>]

Lateral ulnar collateral ligament: [<Intact>]

Annular ligament: [<Intact>]

Common extensor tendon: [<Normal>]

Lateral epicondyle: [<Normal>]

Posterior structures:

Triceps: [<Normal>]

Olecranon bursa: [<Normal>]

Olecranon: [<Normal>]

Anterior structures:

Biceps: [<Normal>]

Brachialis: [<Normal>]

Bicipitoradial bursitis: [<None>]

Articular:

Radiocapitellar joint: [<Normal>]

Ulnohumeral joint: [<Normal>]

Proximal radioulnar joint: [<Normal>]

Bones: [<Normal>]

Muscles: [<Normal>]

Vessels: [<Normal>]

Nerves: [<Normal>]

Other: [<None.>]

Impression:

1. [<>]

APPENDIX 2: Sample Completed Structured Report: Elbow: ABNORMAL

EXAM: MR ELBOW WITHOUT CONTRAST

HISTORY: [<30-year-old man with lateral elbow pain and instability>]

TECHNIQUE: Imaging was performed [<without>] IV contrast. Multiplanar, multisequence MR images of the [<right>] elbow were obtained on a [<3.0>] Tesla magnet.

COMPARISON: [<Radiographs dated 11/11/2014>]

FINDINGS:

Alignment: [<Asymmetrical opening of the posterolateral joint space>]

Joint fluid: [<Small effusion with mild synovial thickening>]

Intra-articular bodies: [<None>]

Medial structures:

Ulnar collateral ligament: [<Intact>]

Common flexor tendon: [<Mild tendinosis>]

Medial epicondyle: [<Mild enthesophyte formation>]

Lateral structures:

Radial collateral ligament: [<Grade III sprain>]

Lateral ulnar collateral ligament: [<Grade III sprain>]

Annular ligament: [<Intact>]

Common extensor tendon: [<High-grade partial tear>]

Lateral epicondyle: [<Moderate enthesophyte formation with subjacent bone marrow edema>]

Posterior structures:

Triceps: [<Mild tendinosis with enthesophyte formation>]

Olecranon bursa: [<Normal>]

Olecranon: [<Normal>]

Anterior structures:

Biceps: [<Normal>]

Brachialis: [<Normal>]

Bicipitoradial bursitis: [<Normal>]

Articular:

Radiocapitellar joint: [<Mild diffuse cartilage thinning. Small subchondral cyst of the capitellum>]

Ulnohumeral joint: [<Mild posterior ulnohumeral osteophytes>]

Proximal radioulnar joint: [<Normal>]

Bones: [<Otherwise normal>]

Muscles: [<Grade I strain ECRB>]

Vessels: [<Normal>]

Nerves: [<Mild nonspecific hyperintensity of the ulnar nerve in the cubital tunnel>]

Other: [<Posterolateral fascial edema and fluid from capsular injury>]

Impression:

1. Findings of acute on chronic lateral epicondylitis with posterolateral instability as detailed above.

2. Degenerative changes of the radiocapitellar joint and other findings as described above.

3. Mild nonspecific hyperintensity of the ulnar nerve, to be correlated clinically.

8

The Wrist

Avneesh Chhabra, Shadpour Demehri, and Theodoros Soldatos

The wrist is a complex arrangement of multiple bones, ligaments, and cartilage, which bridges the hand with the forearm, and allows for a significant degree of physiologic motion. Being central to the majority of daily living activities, wrist is one of the most commonly injured sites of the musculoskeletal system. The wrist is composed of the following.

- The carpus, comprising eight bones, which are arranged in two rows and articulate among themselves in a manner of three-dimensional cohesion, forming the midcarpal and intercarpal joints
- The radiocarpal and ulnocarpal joints
- The distal radioulnar joint (DRUJ) compartment, in which the distal radius articulates with the adjacent ulna
- The five carpometacarpal (CMC) joints, in which the carpus articulates with the metacarpal bones

Whereas the CMC joints can communicate with the midcarpal and intercarpal joints, the radiocarpal joint and DRUJ are tight isolated compartments.

The inherently unstable structure of the wrist is balanced by multiple intrinsic (intercarpal) and extrinsic (connecting forearm to wrist bones) ligaments. These ligaments can be involved by various pathologies, potentially leading to carpal imbalance, distortion in force transmission, and progression to permanently altered biomechanics, chondral wear, and degenerative changes. A systematic imaging analysis and structured reporting is essential for optimal diagnostic assessment of the wrist structures. This chapter discusses the imaging evaluation approach and describes how to fill in the structured checklist in Box 1. Conceptual details of related MR physics and imaging protocol are discussed in the chapter on MR protocol optimization.

IMAGE EVALUATION

The below-outlined stepwise interpretation approach is only a practical guide, and all wrist structures should be evaluated in multiple planes for optimal assessment. This will also help

the readers perceive which structures are best depicted/evaluated on which particular plane.

1. Line up the similar plane fat-saturated (fs) and non-fs images and synchronize them for tandem evaluation.
2. Start with the coronal images to check for carpal and DRUJ effusions. On proton density-weighted (PDW) images, check the scapholunate (SL) and lunotriquetral (LT) intervals, ulnar variance, Gilula's three arcs, intercarpal spaces (for possible carpal coalition, type II lunate facet hamatolunate chondromalacia), scaphotrapeziotrapezoid (STT) joint, radiocarpal, CMC and metacarpophalangeal (MCP) joints. On fsPDW images, look for bone marrow edema and bone or soft tissue cysts and evaluate the membranous portions of the SL and LT ligaments, triangular fibrocartilage complex (TFCC), radial and ulnar collateral ligaments (UCLs) while correlating with non-fsPDW images.
3. On sagittal images, check the radiolunate and lunocapitate alignment. In case of SL ligament tear, the SL angle should be measured by superimposing sagittal images depicting the scaphoid and lunate axes since these bones are not in the same plane. This is also a good plane to evaluate the dorsal (dorsal intercarpal [DIC] ligament and radiocarpal ligament) and volar extrinsic (radioscaphocapitate, radiolunotriquetral, or long radiolunate) ligaments, the short radiolunate ligament, TFCC disc, and the ulnolunate and ulnotriquetral ligament attachments of the TFCC. It serves as the secondary plane to evaluate the extent of flexor/extensor tenosynovitis, tendon tears or retraction, and ganglion cysts.
4. The evaluation continues on axial images, where the flexor and extensor tendons should be assessed for tendinosis, tear, and tenosynovitis. The axial plane is also optimal for assessing the volar and dorsal bands of the SL and LT ligaments (findings can be secondarily correlated with coronal images), the neurovascular bundles, carpal tunnel, Guyon canal, as well as the thenar, hypothenar, and interosseous muscles. Subsequently, evaluate the pisotriquetral (PT) joint and DRUJ, the volar and dorsal radioulnar ligaments, and finally, check for mass lesions and other incidental findings, such as os styloideum, lunula, etc.

BOX 1: The Structured Report: Wrist

The checklist for structured reporting of MR imaging of the wrist. For each field, *Normal* is considered default in the dictation whereas the rest of the elements describe various pathologies that could be encountered during imaging evaluation. See Appendices 1 and 2 at the end of the chapter for sample completed reports of normal and abnormal examination results.

Exam: **MRI of Wrist**

FINDINGS:

Alignment: [<Normal / Abnormal>]

Ulnar variance: [<Neutral / Negative / Positive>]

Distal radioulnar joint: [<Congruent / Subluxation>]

Scapholunate dissociation: [<Absent / Present> <DISI / VISI / Midcarpal instability>]

Fluid:

Carpus joint effusion: [<None> <Small / Moderate / Large>]

Distal radioulnar joint effusion: [<None> <Small / Moderate / Large>]

Intrinsic ligaments:

Scapholunate ligament: [<Intact> <Thickened> <Acute sprain (<Dorsal / Membranous / Volar band>)>]

Lunotriquetral ligament: [<Intact> <Thickened> <Acute sprain (<Dorsal / Membranous / Volar band>)>]

Ulnar side:

Triangular fibrocartilage: [<Intact> <Degeneration> <Acute sprain (<Central / Peripheral>)>]

Lunate facet: [<Present / Absent>]

Hamate–lunate joint: [<Normal / Chondrosis / Osteoarthritis>]

Ulnocarpal impaction: [<None / Ulnolunate / Ulnotriquetral>]

Extensor compartment:

I: [<Normal> <Tenosynovitis / Tendinosis / Tear>]

II: [<Normal> <Tenosynovitis / Tendinosis / Tear>]

III: [<Normal> <Tenosynovitis / Tendinosis / Tear>]

IV: [<Normal> <Tenosynovitis / Tendinosis / Tear>]

V: [<Normal> <Tenosynovitis / Tendinosis / Tear>]

VI: [<Normal> <Tenosynovitis / Tendinosis / Tear>]

Flexor compartment:

Flexor retinaculum: [<Normal> <Thickened / Bowed / Discontinuous>]

Flexor tendons: [<Normal / Tenosynovitis / Tendinosis / Tear>]

Carpal tunnel: [<Normal> <Effaced deep fat pad>]

Median nerve: [<Normal> <Hyperintense> <Proximal enlargement with distal flattening>]

Guyon canal: [<Normal> <Hyperintense ulnar nerve>]

Articular:

Thumb–carpometacarpal/Metacarpophalangeal joints: [<Normal> <Osteoarthritis>]

Scaphotrapeziotrapezoidal joint: [<Normal> <Osteoarthritis>]

Pisiform–triquetral joint: [<Normal> <Effusion> <Ganglion>]

Extrinsic ligaments:

Radial collateral ligament/Ulnar collateral ligament: [<Normal> <Attenuated> <Acute Sprain>]

Dorsal intercarpal ligament/Volar extrinsic ligaments: [<Normal> <Acute Sprain>]

Bones: [<Normal / Otherwise normal>]

Muscles: [<Normal>]

Vessels: [<Normal>]

Other: [<None>]

Impression:

[<In the order of importance with acute findings first>.]

HOW TO FILL THE STRUCTURED REPORT

ALIGNMENT: [<Normal / Abnormal>]

Ulnar variance: [<Neutral / Negative / Positive>]

Distal radioulnar joint: [<Congruent / Subluxation>]

Scapholunate dissociation: [<Absent / Present> <DISI / VISI / Midcarpal instability>]

The wrist bones and their alignment are best evaluated on non-fs images. Normal alignment refers to articular surface congruency (convexity of an articular surface matching with the concavity of the opposite articular surface) at the DRUJ, radiocarpal, and intercarpal joints (Figs. 1–3). On the coronal images, similar to the plain radiographs, Gilula A, B, and C lines (following the proximal aspect of proximal carpal row, distal aspect of the proximal carpal row, and proximal aspect of the capitate–hamate articulations, respectively) should be smooth curves with no abrupt step-off(s); and on the axial image, the scaphoid should not protrude beyond the line connecting dorsal aspects of scaphoid and lunate (Fig. 4). Most patients with instability present with one or more symptoms, such as pain, swelling, clicking during physical examination or feeling of wrist clunk. The lesions could involve one bone in isolation, such as in pisiform subluxation or, more commonly, multiple carpal bones. The resulting dynamic instability and maltracking of bones can be detected earlier and more confidently with kinematic evaluation under fluoroscopy, kinematic MRI or 4D CT, whereas conventional MRI depicts anatomic abnormalities in more advanced cases with static carpal malalignments.

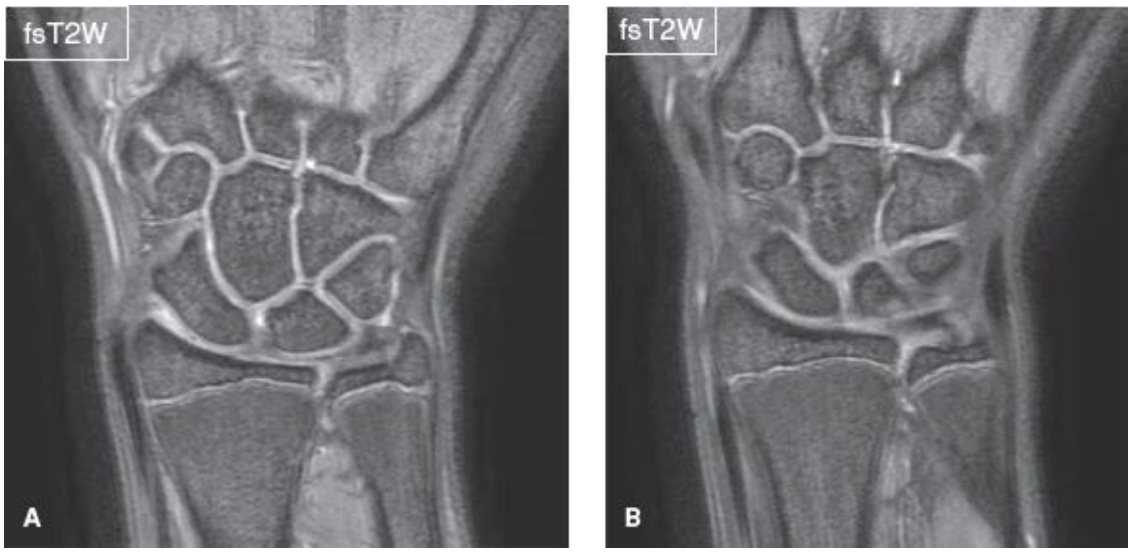

Fig. 1: Normal wrist anatomy. Sequential coronal gradient-echo images **(A, B)** show articular surface congruency at the distal radioulnar, radiocarpal, and intercarpal joints.

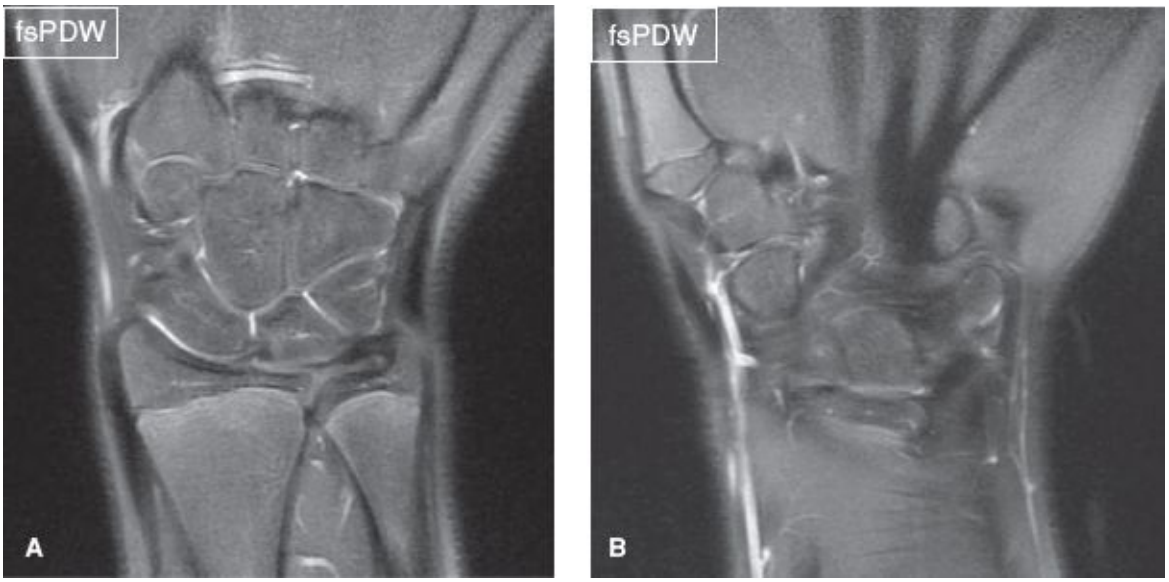

Fig. 2: Normal wrist anatomy. Sequential coronal spin-echo images **(A, B)** show articular surface congruency at the distal radioulnar, radiocarpal, and intercarpal joints.

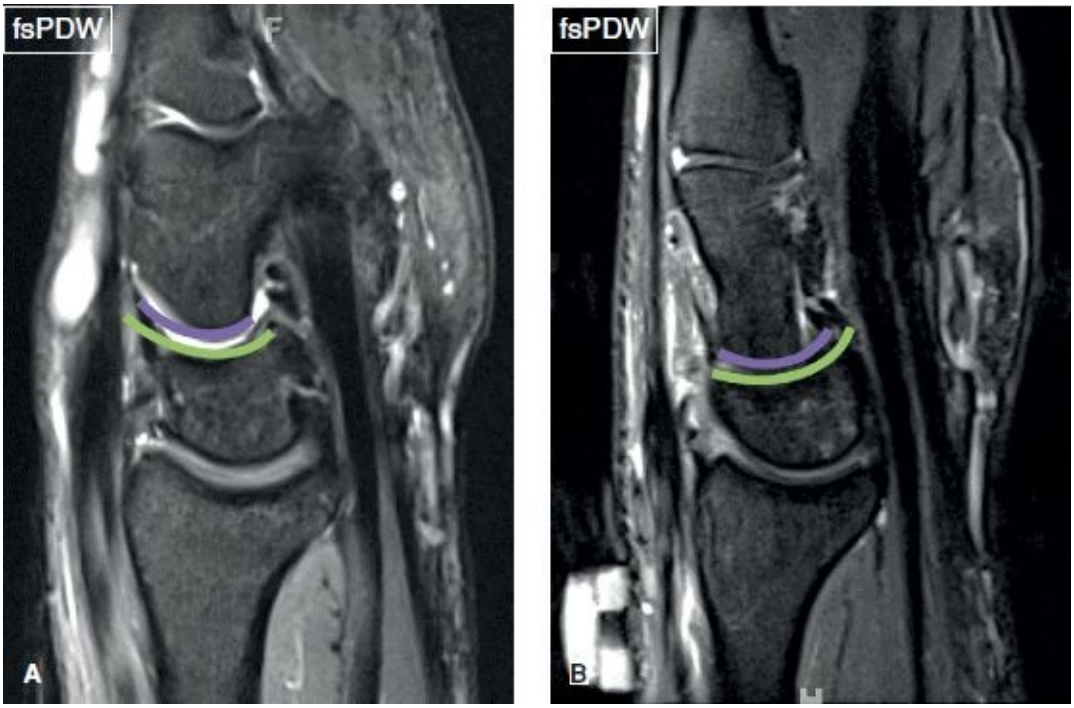

Fig. 3: Normal carpal alignment. **A:** Sagittal image in neutral position shows the concavity of the lunate matches with the convexity of the capitate (green and purple lines, respectively). **B:** Notice similar congruity in the extended position.

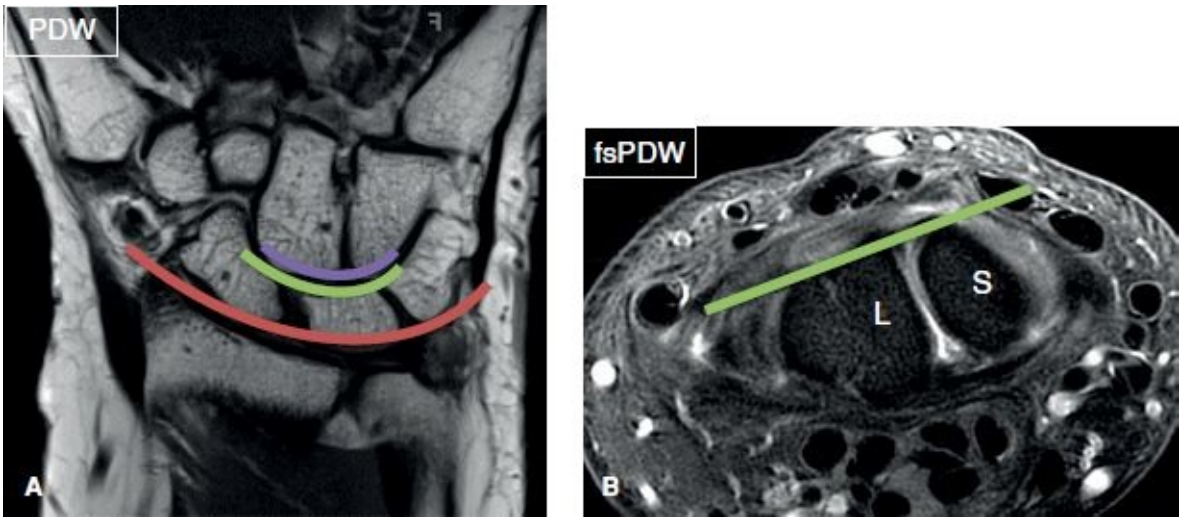

Fig. 4: Gilula lines. **A:** Coronal image shows the three parallel Gilula lines (A is red, B is green, C is purple). **B:** Axial image shows articular surface congruency at the scapholunate (SL) space with no dorsal protrusion of the scaphoid (S).

Ulnar variance refers to the relative lengths of the distal articular surfaces of the radius and ulna. It is defined as neutral, positive, or negative based on whether the distal articular surface of the ulna is aligned with the distal articular surface of the radius, or lies >2 mm distal, or >2 mm proximal to the latter, respectively (Figs. 5, 6). Negative ulnar variance is believed to be associated with osteonecrosis of the lunate (Kienböck's disease), and positive ulnar variance with ulnocarpal abutment and TFCC tears. However, one should note that ulnocarpal abutment can also be seen in the setting of neutral or negative ulnar variance. Of the several measurement methods available to evaluate the congruity of the DRUJ, the easiest and reproducible are (1) the congruency method, which looks for simple congruency between the arc of the sigmoid notch and the convexity of dome of ulnar head, and (2) Mino's method, in which two lines are drawn through the dorsal and volar aspects of the distal radius at the level of sigmoid notch, excluding the Lister tubercle. The distal ulna should normally be located between these lines or within 10% to 20% of these confines, otherwise dorsal or volar subluxation exists (Fig. 7). Detection of chronic insufficiency or acute tears of volar and distal radioulnar ligaments can assist in the clinical diagnosis of dorsal and volar DRUJ instability, respectively. If available, comparison with the contralateral wrist is also useful. At the level of the DRUJ, the location of the ulnar styloid process in the axial plane reveals the position of the wrist: The styloid process is located volarly, dorsally, and medially when the wrist is in pronation, supination, and in neutral position, respectively. Other etiologies that may be implicated in DRUJ instability include sigmoid rim fracture, sigmoid notch hypoplasia, complex radial fractures, ulnar styloid fracture (especially involving its base), and ulnar head abnormality from prior injury or partial resection. On the coronal images, other imaging findings that may indicate DRUJ subluxation, include radial shortening, widening of DRUJ space, and negative ulnar variance of greater than 5 mm.

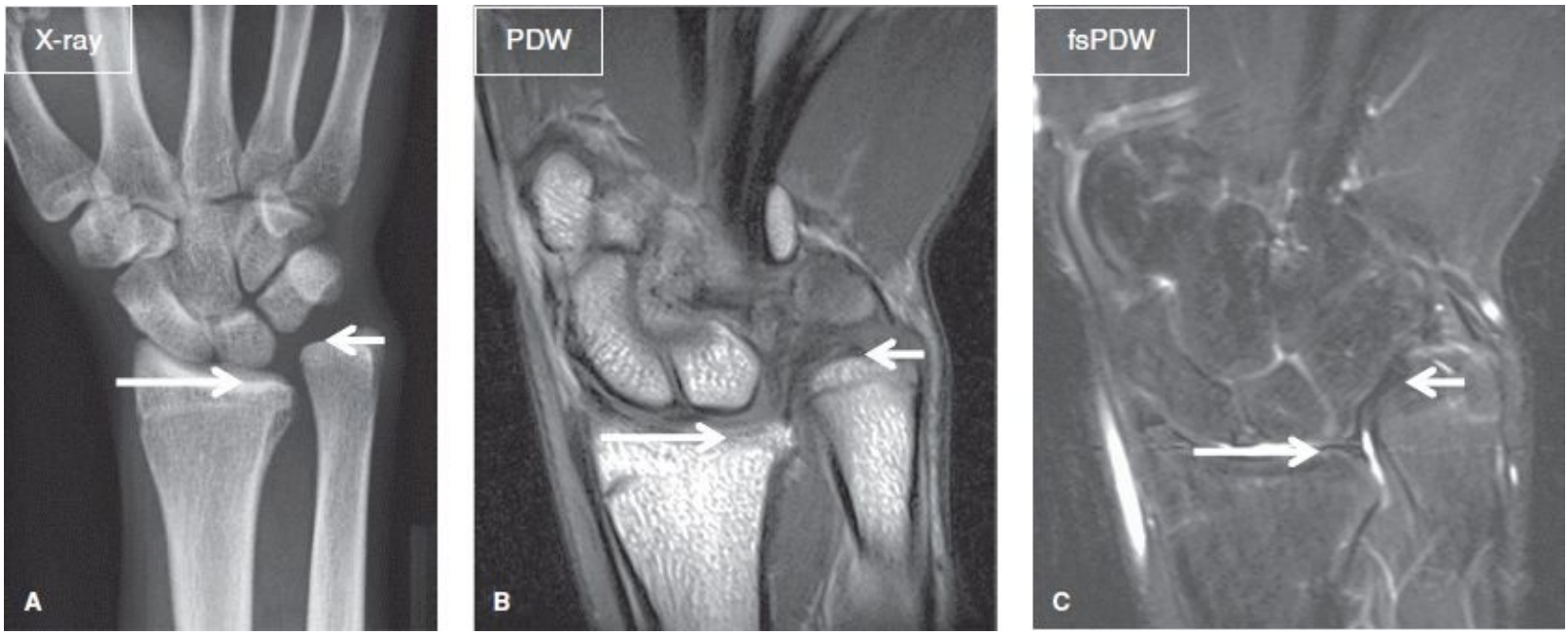

Fig. 5: Positive ulnar variance. On anteroposterior radiograph **(A)** and respective coronal MR images **(B, C),** the distal articular surface of the ulna (*short arrows*) lies more than 2 mm distal to the distal articular surface of the radius (*long arrows*).

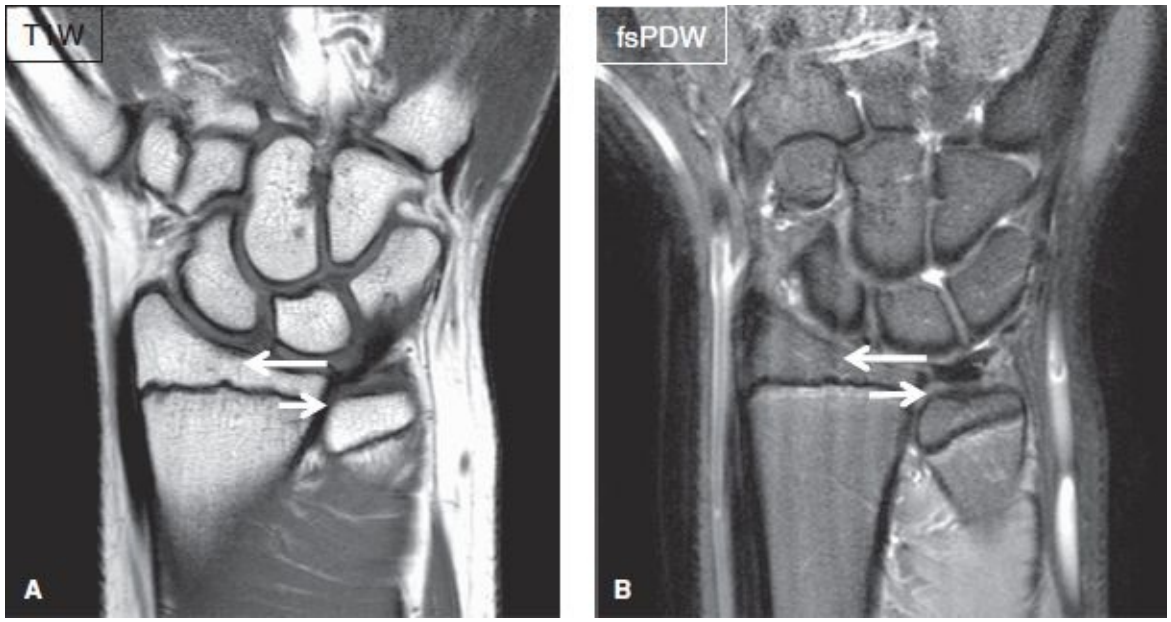

Fig. 6: Negative ulnar variance. On coronal MR images **(A, B)**, the distal articular surface of the ulna (*short arrows*) lies more than 2 mm distal to the distal articular surface of the radius (*long arrows*).

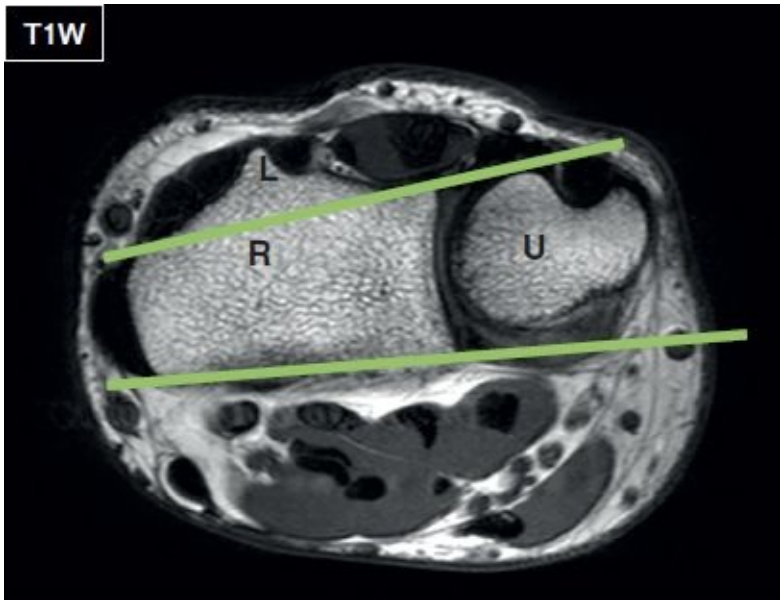

Fig. 7: Normal DRUJ alignment. Two lines are drawn through the dorsal and volar aspects of the distal radius **(R)** at the level of sigmoid notch, excluding the Lister tubercle **(L)**. The distal ulna **(U)** should normally be located between these lines or within 10% to 20% of these confines, otherwise dorsal or volar subluxation exists.

The bones of the proximal carpal row (scaphoid, lunate, triquetrum) move as an intercalated segment, which is stabilized by multiple ligaments. The segment has no muscular attachments, and its motion follows the movements of the distal carpal row and forearm bones. Therefore, *intercalated instability* refers to incongruent movement between the proximal and distal carpal rows. Instability can also be defined as dissociative, nondissociative, or adaptive. *Dissociate instability* refers to instability related to incongruent carpal bones in the same row (implying intrinsic ligament injury) whereas *nondissociate instability* indicates instability involving incongruent intercalated segments (implying extrinsic ligament injury). *Adaptive instability* is related to prior trauma, such as radius fracture.

The integrity of the intercalated segment may be disrupted in cases of SL or LT dissociation. On coronal images, the SL interval is normally less than 3 mm and on sagittal images, the SL angle ranges between 30 and 60 degrees, with values between 60 and 80 degrees considered borderline normal. In SL dissociation, there is diastasis ($\geq$3 mm) of the SL space (Fig. 8), the scaphoid undergoes volarflexion (rotatory subluxation) and dorsal displacement with narrowing of the radioscaphoid space whereas the triquetrum pulls the lunate into dorsiflexion. The resulting deformity is termed as dorsal intercalated segmental instability (DISI) and is characterized by increased ($>$80 degrees) SL angle, increased ($>$30 degrees) lunocapitate angle, increased radiolunate ($>$15–20 degrees) angle, and radiodorsal shift of the lunate with loss of lunocapitate interspace congruency. Clinically, Watson test is performed to evaluate SL instability. The examiner places a thumb over the patient's scaphoid tubercle, applying dorsal pressure. The wrist is then moved from ulnar to radial deviation. A painful "clunk" reflects positive test for SL instability. If radiographs are available, comparison to the other side is quiet useful. Secondary radiographic findings

include, lunate overlap on capitate on the PA view and more vertical position of the scaphoid. DISI usually involves SL ligament tear with injury to the extrinsic ligaments (commonly radioscaphocapitate ligament). The entity may also develop in cases of unstable scaphoid waist fractures, which allow the distal scaphoid pole to translate proximal and volar while the proximal pole remains attached and tilts dorsally with the lunate. Other radiographic signs include, foreshortening of the scaphoid (ring sign) and a triangular-shaped lunate (due to rotation). In advanced stages of SL instability, the capitate migrates proximally between the scaphoid and lunate, forcing the two bones further apart, in a configuration known as SL advanced collapse (SLAC) (Fig. 8). The condition is most commonly caused by trauma (associated with other imaging evidence of trauma findings) or calcium pyrophosphate arthropathy (associated with chondrocalcinosis and cystic degenerative changes of carpus). Another related entity is scaphoid nonunion advanced collapse (SNAC), which also shows proximal capitate migration similar to SLAC, however, it occurs in the setting of nonunited scaphoid fracture.

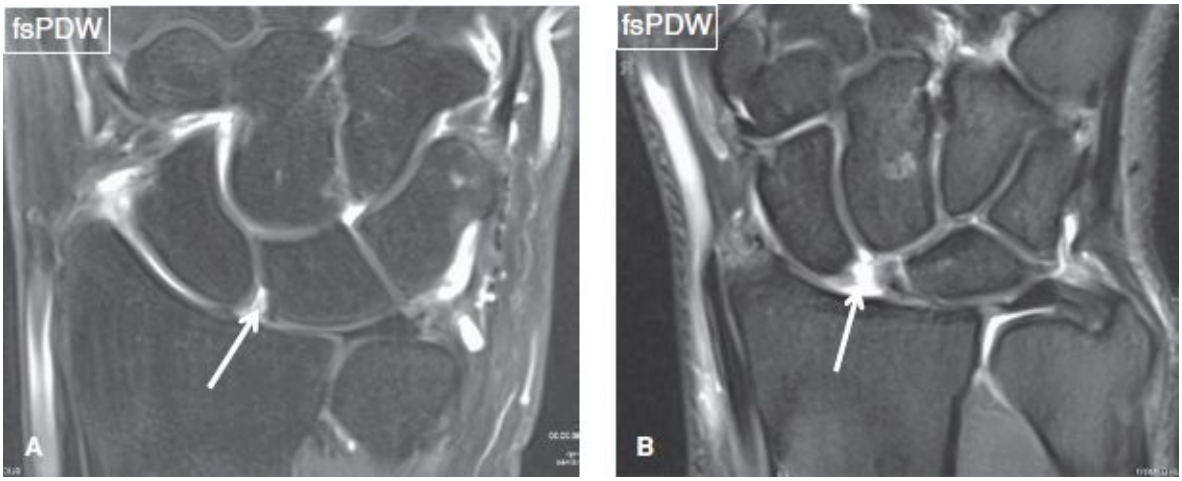

Fig. 8: Scapholunate dissociation and SLAC. Coronal images from different patients demonstrate complete tears (*arrows*) of the scapholunate ligament. In **(A),** there is widening of the scapholunate space in keeping with SL dissociation while in **(B)** there is proximal capitate migration in keeping with a SLAC wrist.

In LT dissociation, the lunate and scaphoid tilt volarly and the capitate dorsally, in a deformity known as volar intercalated segmental instability (VISI), which is depicted as decreased (<30 degrees) SL angle and increased (>30 degrees) lunocapitate angle (Fig. 9). VISI involves disruption of the LT & volar radiolunotriquetral ligaments, as well as attenuation or rupture of the dorsal radiotriquetral (DIC ligament) attachments. The entity may result from trauma, and has been associated with rheumatoid arthritis and Kienböck's disease (Fig. 10). Lunottriquetral instability is evaluated clinically using Ballottement test or compression test. The Ballottement test is performed by securing the pisotriquetral unit with the thumb and index finger of one hand and the lunate with the other hand. Volar and dorsal stresses are placed on the LT joint. The criteria for a positive test are increased excursion of the triquetrum and accompanying painful crepitus. The compression test

involves painful displacement of the triquetrum ulnarly during radioulnar deviation. In VISI lesions, one should check for DRUJ or TFCC injury, since the latter associations are common. Bilateral VISI deformity should raise the suspicion of Marfan syndrome.

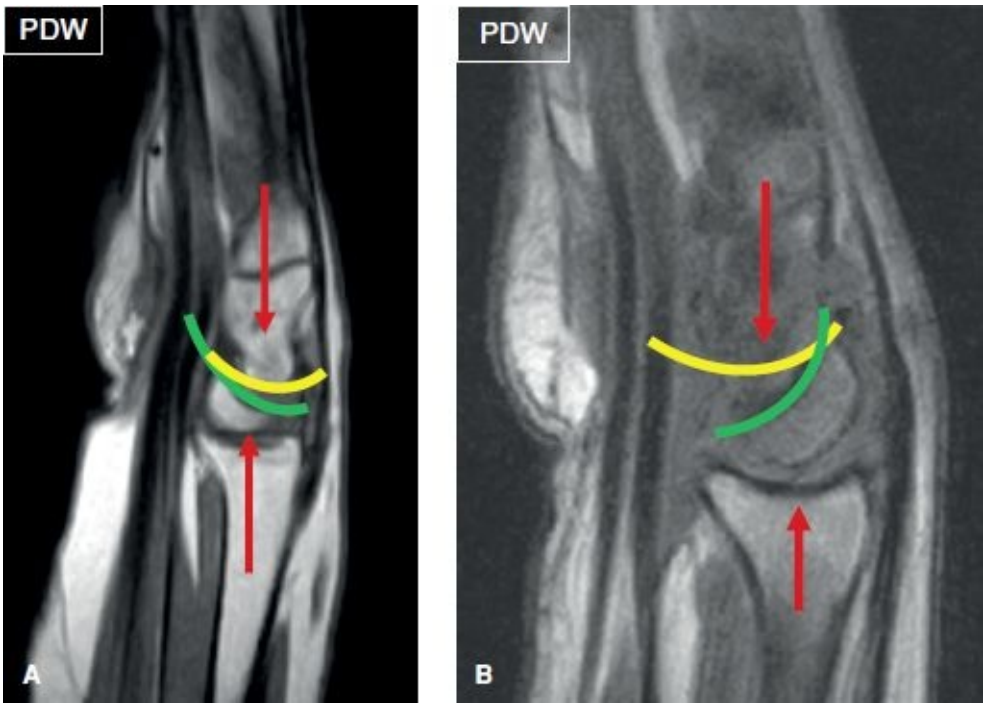

Fig. 9: DISI vs VISI. **A:** Dorsal intercalated segmental instability. Sagittal image shows loss of colinearity between the lunate and capitate (yellow and green lines) with normal alignment of radius and capitate (*red arrows*). The lunocapitate angle is increased and scapholunate angle measured 88 degrees. **B:** Volar intercalated segmental instability complicating a case of rheumatoid arthritis. Sagittal image shows loss of colinearity between the capitate and lunate (yellow and green lines) with volar tilt of lunate. Note maintained colinearity between radius and capitate (*red arrows*). The scapholunate and lunocapitate angles were measured 10 degrees and 50 degrees, respectively.

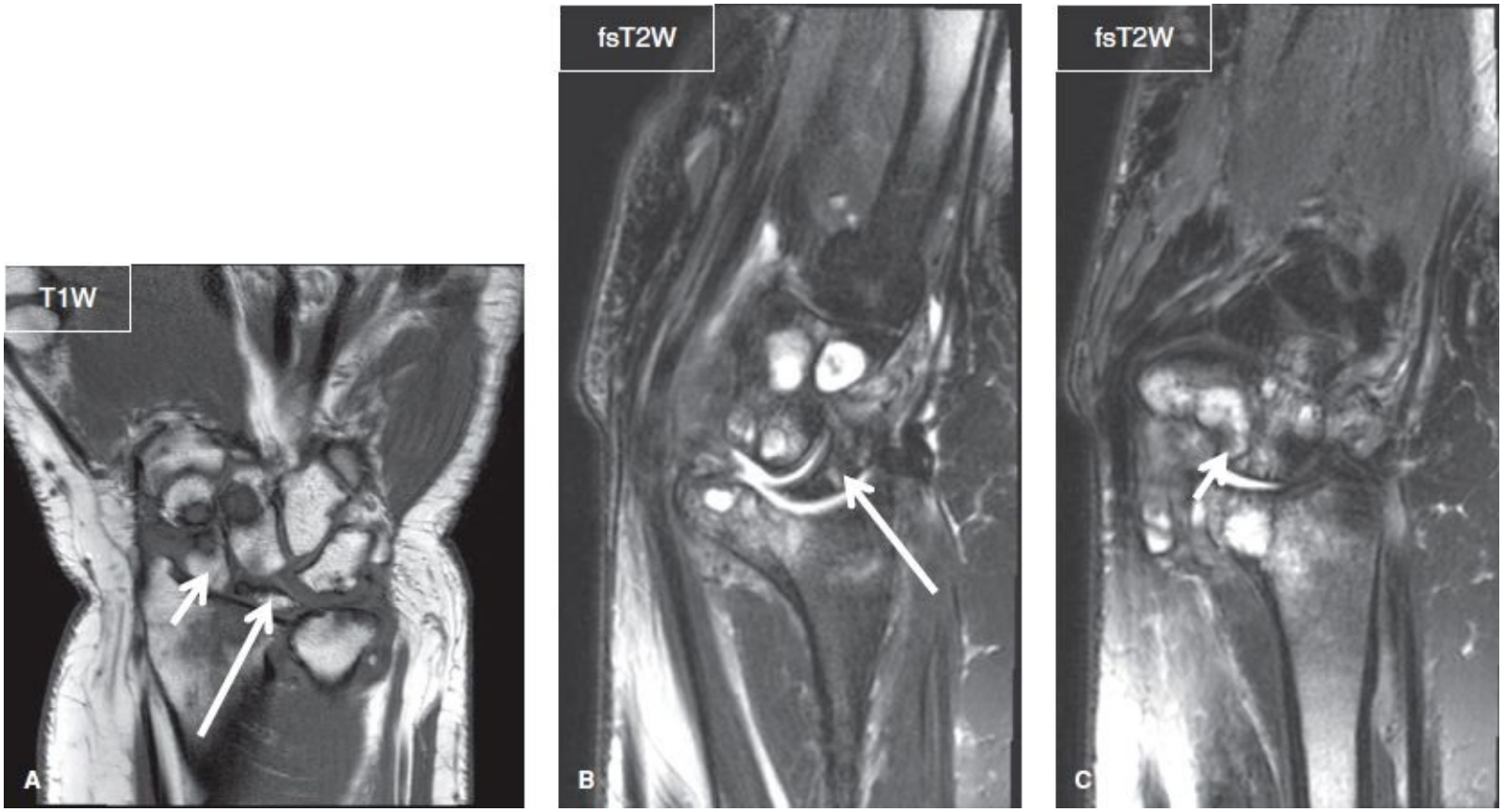

Fig. 10: Volar intercalated segmental instability complicating a case of rheumatoid arthritis. Coronal **(A)** and sagittal **(B, C)** images show scattered cystic–erosive changes of the wrist bones. Notice SLAC wrist **(A),** volar tilt of the scaphoid (*short arrows*), and lunate (*long arrows*) **(B, C).** The scapholunate and lunocapitate angles were measured 9 degrees and 76 degrees, respectively.

Instability may propagate around the lunate with maintenance of colinearity between radius and lunate. This perilunate instability progresses from the SL and capitolunate joints to the LT joint. About 25% of perilunate instabilities are missed at initial presentation and can present as carpal tunnel syndrome. Based on severity, it can be classified as follows.

- Stage I—is characterized by SL and volar radioscaphocapitate ligament injury, along with scaphoid instability
- Stage II—in which there is dorsal subluxation of the capitate relative to the lunate along with opening of the space of Poirier (V-shaped area of weakness in the palmar wrist formed by the volar carpal ligaments)
- Stage III—established with radiotriquetral (long and short radiolunate) ligament failure and triquetral dislocation
- Stage IV—in which the lunate dislocates from the radiolunate fossa following failure of the radiocarpal (radiocapitate, radiotriquetral), and DIC ligaments.

Midcarpal instability refers to incongruity at the midcarpal spaces and abrupt step-offs in Gilula B and C lines. The entity may manifest as excessive dorsal tilt of the lunate and dorsal subluxation of the capitate at the lunocapitate joint, due to insufficiency of the deltoid (arcuate or midcarpal) ligament and occasionally of the volar extrinsic

radioscaphocapitate ligament. Therefore, there is loss of radiocapitate alignment. Another variant is triquetrohamate incongruency, due to insufficiency of the deltoid ligament and occasionally of the long radiolunate ligament. In general, SL instability is more common than midcarpal instability, which is also more common than LT instability.

Carpal translocation can occur in any direction but is more common in the ulnar direction. In the latter case, the lunate shifts out toward the ulnar aspect of the radiocarpal joint, and exhibits greater than 50% subluxation from the lunate fossa of the radius. The condition is most commonly seen with rheumatoid arthritis (entire carpus may translocate) and trauma (scaphoid may remain in place or entire carpus may translocate), but authors have also seen it occurring in an idiopathic fashion and involving both wrists simultaneously.

FLUID:

Carpus joint effusion: [<None> <Small / Moderate / Large>]

Distal radioulnar joint effusion: [<None> <Small / Moderate / Large>]

Coronal images are most useful to assess for radiocarpal joint and DRUJ effusions, and axial images for PT joint effusion. These joints have thin synovial linings and normally contain a small amount of fluid for nutrition and lubrication. Joint effusion is noted when excessive fluid causes distention of the joint capsule (Fig. 11). Findings such as synovial thickening, intra-articular debris, loose bodies, synovial diverticula(e), and ganglion cysts should also be reported, as they may be associated with underlying internal derangement and/or injury (Figs. 12, 13). Capsular injuries may occur from recent or prior trauma and manifest as irregularity, attenuation, and/or thickening of the joint capsule. Synovial diverticulae (unilocular with wide communication with the joint space) commonly arise from the PT recess of the joint and the volar aspect of the radioscaphoid joint. Ganglion cysts (uni- or multilocular cysts with narrow or obliterated neck) reflect chronic processes and these lesions can be painful, even if they are small. The neck of the ganglion should be identified as it can lead the reader to the site of its origin and help identify underlying synovial or ligament injury (Fig. 14). Common locations and associated injuries include DIC ligament, volar band SL, and peripheral TFCC tears.

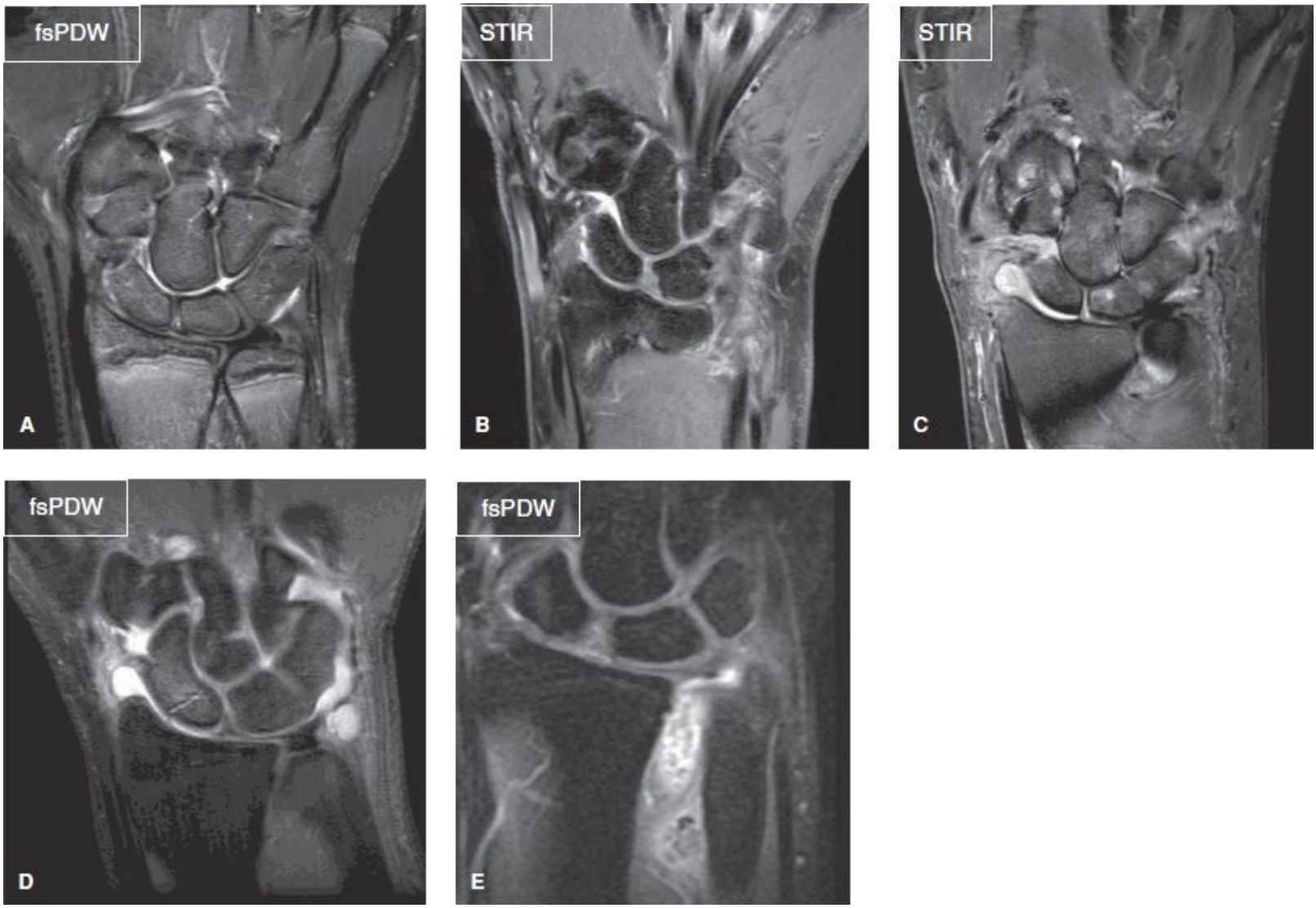

Fig. 11: Normal and abnormal joint fluid. Coronal images from different cases demonstrate normal joint fluid **(A)**, small **(B)**, moderate **(C)**, and large **(D)** effusions in the wrist joints. In **(E)**, there is large effusion isolated to the distal radioulnar joint with synovial chondromatosis.

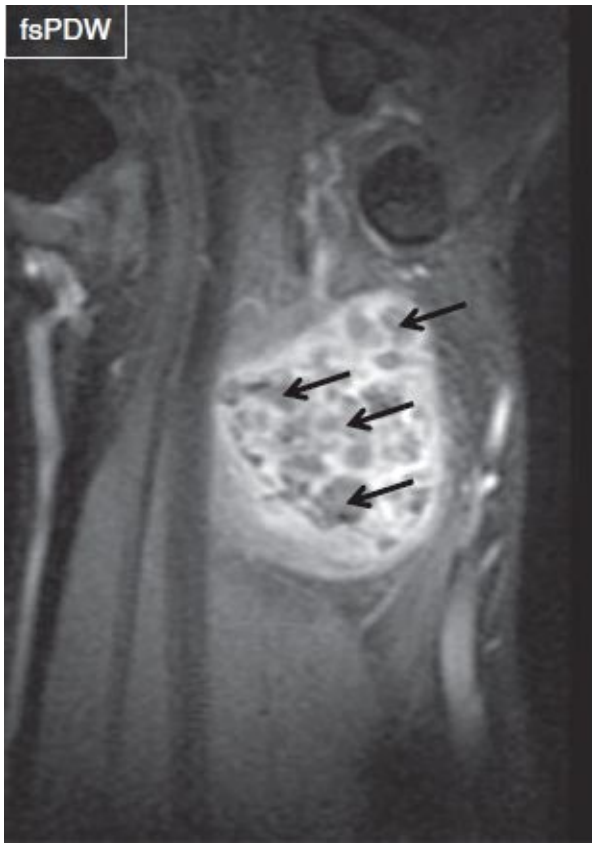

Fig. 12: Primary osteochondromatosis. Coronal image shows large effusion in the distal radioulnar joint containing numerous nodular lesions (*arrows*) of intermediate signal.

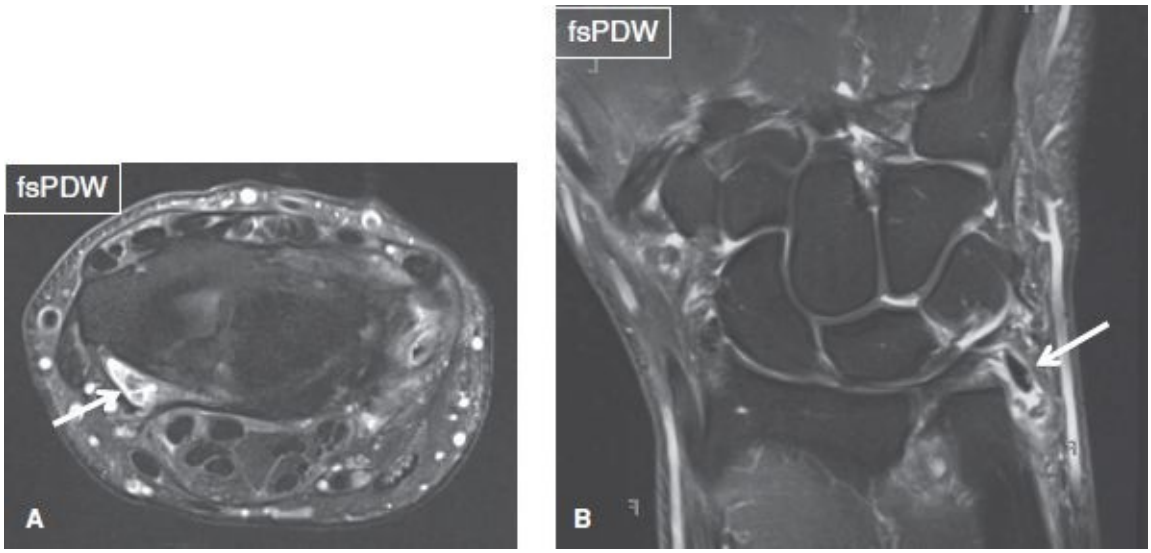

Fig. 13: Intra-articular loose bodies. Axial **(A)** and coronal **(B)** images from different patients exhibit loose bodies (*arrows*) within the radiocarpal and ulnocarpal joints, respectively.

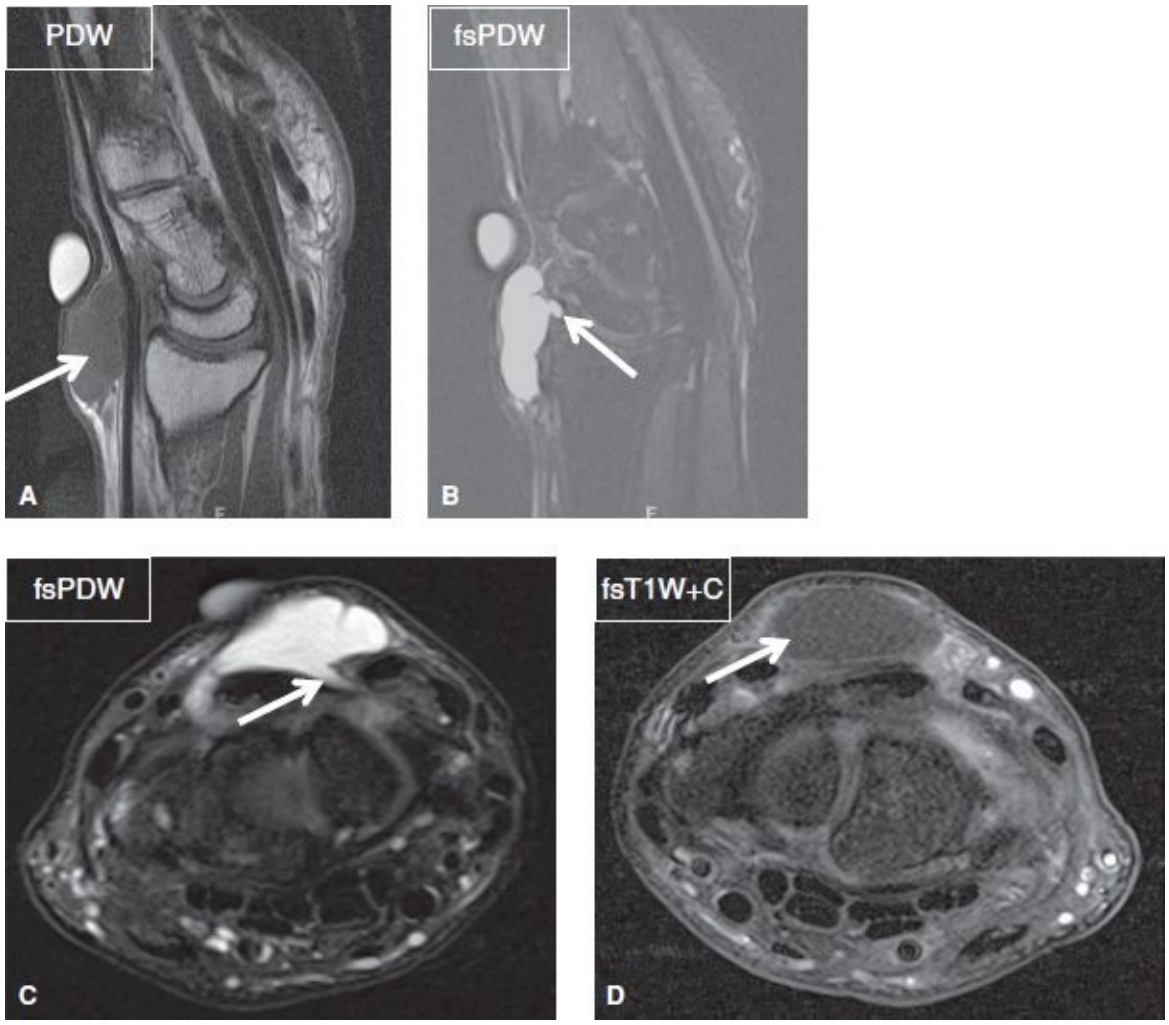

Fig. 14: Ganglion cyst. Sagittal **(A, B)** and axial **(C, D)** images show a ganglion cyst (*arrow* in **A**) with the neck extending beneath the dorsal intercarpal ligament (*arrows* in **B, C**). Notice minimal peripheral enhancement (*arrow* in **D**), confirming the cystic nature of the mass lesion.

INTRINSIC LIGAMENTS:

Scapholunate ligament: [<Intact> <Thickened> <Acute sprain (<Dorsal / Membranous / Volar band>)>]

Lunotriquetral ligament: [<Intact> <Thickened> <Acute sprain (<Dorsal / Membranous / Volar band>)>]

The SL and LT ligaments are clinically and biomechanically important wrist stabilizers, which link the bones of the proximal carpal row. They both feature dorsal band, volar band, and a thin central membranous (proximal) portion, which in combination create a water-tight seal between the radiocarpal and midcarpal spaces.

The SL ligament stabilizes the palmar rotation force of the scaphoid against the dorsal rotation force of the lunate. It is approximately 18 mm long and 2–3 mm thick. The volar band is composed of thin oblique fibers and is the weakest and most vulnerable to tear, particularly at its scaphoid attachment. The dorsal band is the thickest, strongest, and

functionally the most important part of the ligament. The volar and dorsal bands are best evaluated on axial images, where they appear as band-like structures, with the former featuring homogeneous signal intensity and the latter showing minimally heterogeneous striate morphology. The membranous portion is best depicted on coronal image, where it features heterogeneous signal and appears band-like at its dorsal aspect, triangular at its central aspect, and trapezoidal at its volar aspect (Figs. 15, 16).

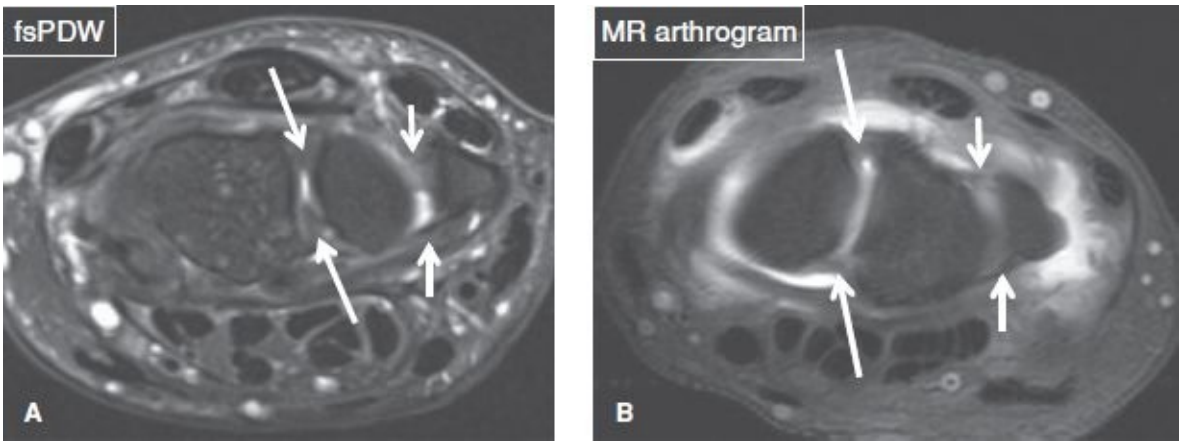

Fig. 15: Normal intrinsic ligaments. Axial conventional **(A)** and arthrography **(B)** images demonstrate the normal dorsal and volar bands of the scapholunate (*long arrows*) and lunotriquetral (*short arrows*) ligaments.

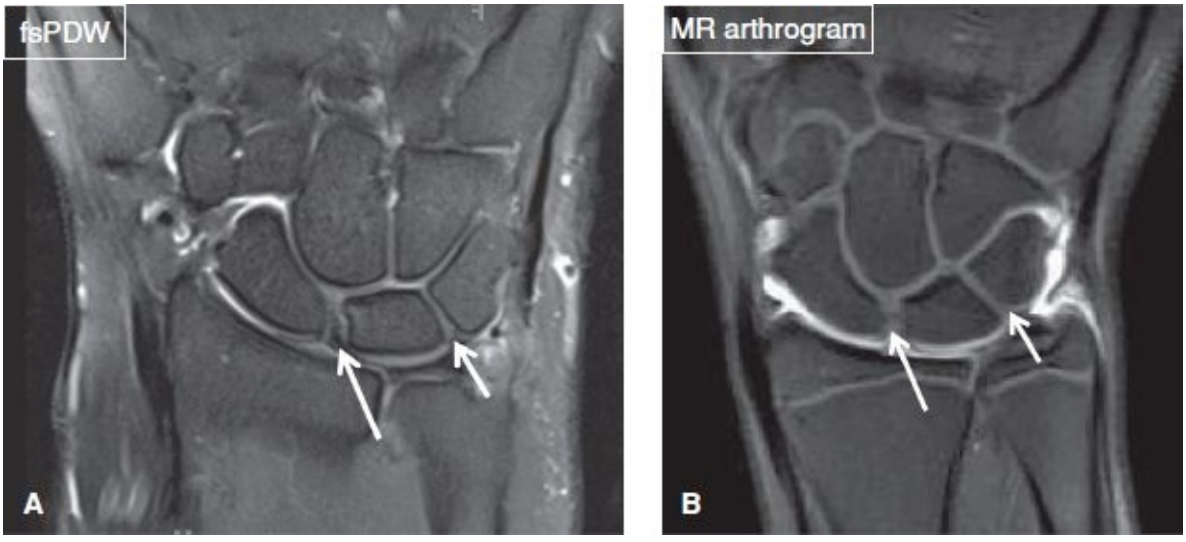

Fig. 16: Normal intrinsic ligaments. Coronal conventional **(A)** and arthrography **(B)** images demonstrate the normal membranous bands of the scapholunate (*long arrows*) and lunotriquetral (*short arrows*) ligaments.

The LT ligament preserves the relationship of the lunate to the triquetrum, allowing the latter to move from a proximal to a distal position during ulnar deviation. In contrast to the SL ligament, the dorsal band of the LT ligament is relatively thinner whereas the volar component is thicker, stronger, functionally more important and interdigitates with longitudinally oriented fibers of the lunocapitate ligament. Similar to the SL ligament, the dorsal and volar bands of the LT ligament are best seen on axial images and the

membranous portion is well seen on coronal images. The ligament appears triangular or, less commonly, linear or bar-like in shape and normally demonstrates uniform low signal intensity. Normal variant includes a thin line of increased signal intensity inside the body of the ligament but not completely traversing through its entire thickness.

SL and LT ligament tears may be categorized as complete or incomplete, on the basis of whether there is involvement of all or only some components of the ligament, and as full-thickness or partial-thickness, based on whether they extend through the entire thickness of the ligament band or leave a portion intact. Acuity of tear is suggested by adjacent fascial edema, fluid, or signs of recent trauma. Primary signs of SL ligament injury (sprain) include fluid-like signal or discontinuity of the ligament on fsPDW or fs T2-weighted (T2W) images, distorted morphology with fraying, irregularity, thickening, and/or thinning and complete absence of the ligament (Figs. 8, 17–20). Secondary signs, which may help in identifying the ligament injury include traction-related avulsive cystic/enthesopathy changes at the osseous attachment, SL dissociation (SL interval >3 mm), soft tissue ganglia from associated capsular injuries or ligament degeneration, and carpal arch (Gilula arc) disruption. Differentiation between types of tears is clinically important because partial-thickness tears may self-resolve without ever causing carpal instability whereas full-thickness tears and complete ligament disruptions often lead to carpal instability. Complete disruption of the dorsal or volar bands is suggestive of trauma or may be associated with rheumatoid arthritis whereas isolated perforations of the membranous portion are commonly degenerative in nature and asymptomatic. Concomitant injury to adjacent volar extrinsic (radioscaphocapitate) ligament results in static instability (rotary subluxation or DISI).

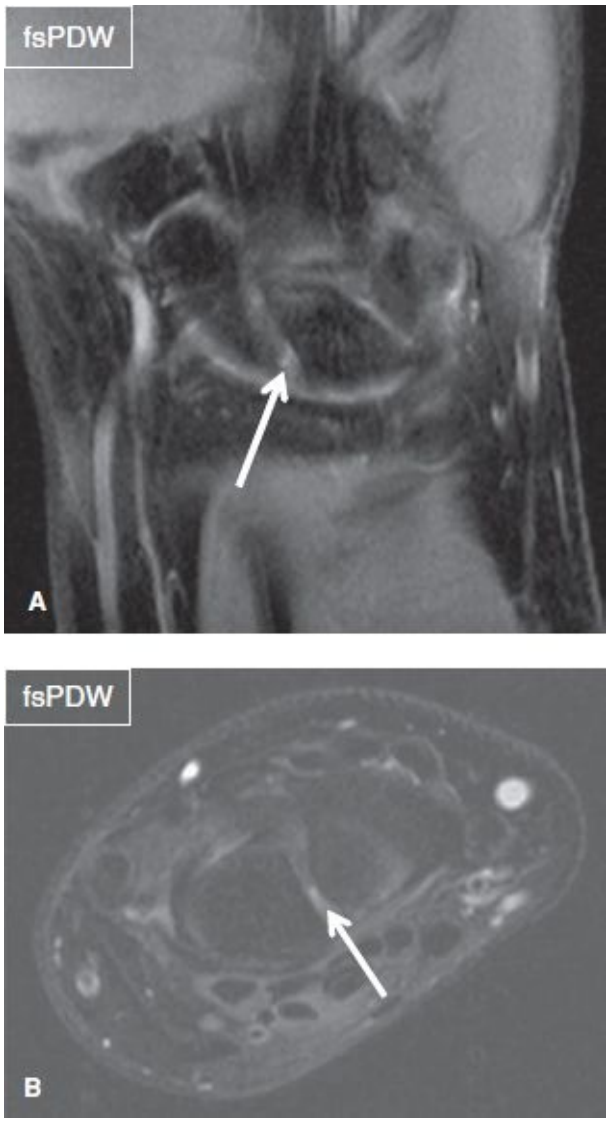

Fig. 17: Scapholunate ligament incomplete injury. Coronal **(A)** and axial **(B)** images show full-thickness tear (*arrows*) of the volar band of the scapholunate ligament.

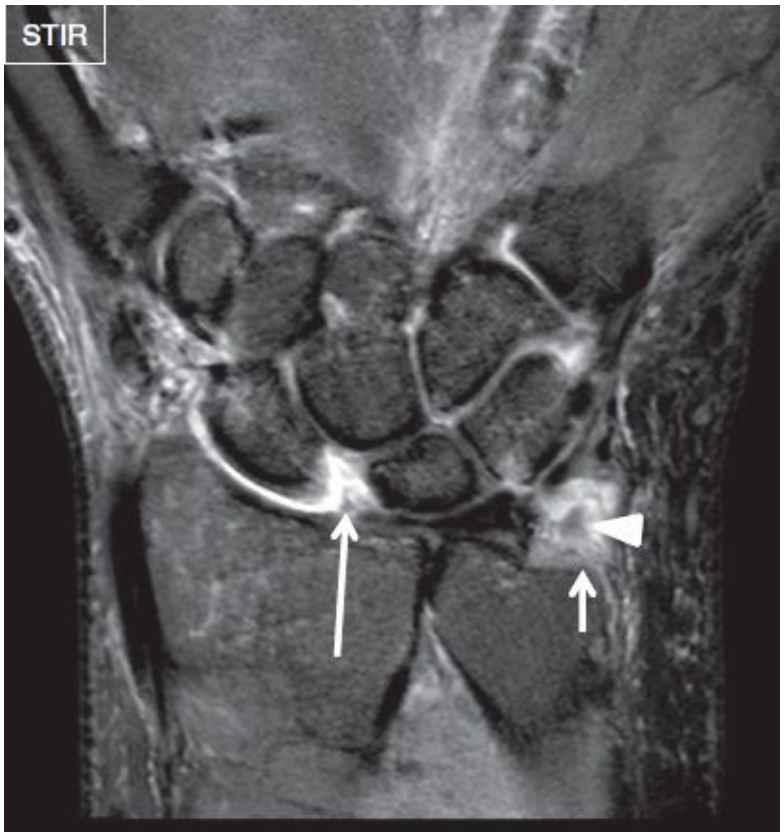

Fig. 18: Complete scapholunate ligament injury. Coronal image exhibits complete tear (*long arrow*) of the scapholunate ligament with scapholunate dissociation. Also note tears of the styloid (*arrowhead*) and foveal (*short arrow*) attachments of the triangular fibrocartilage.

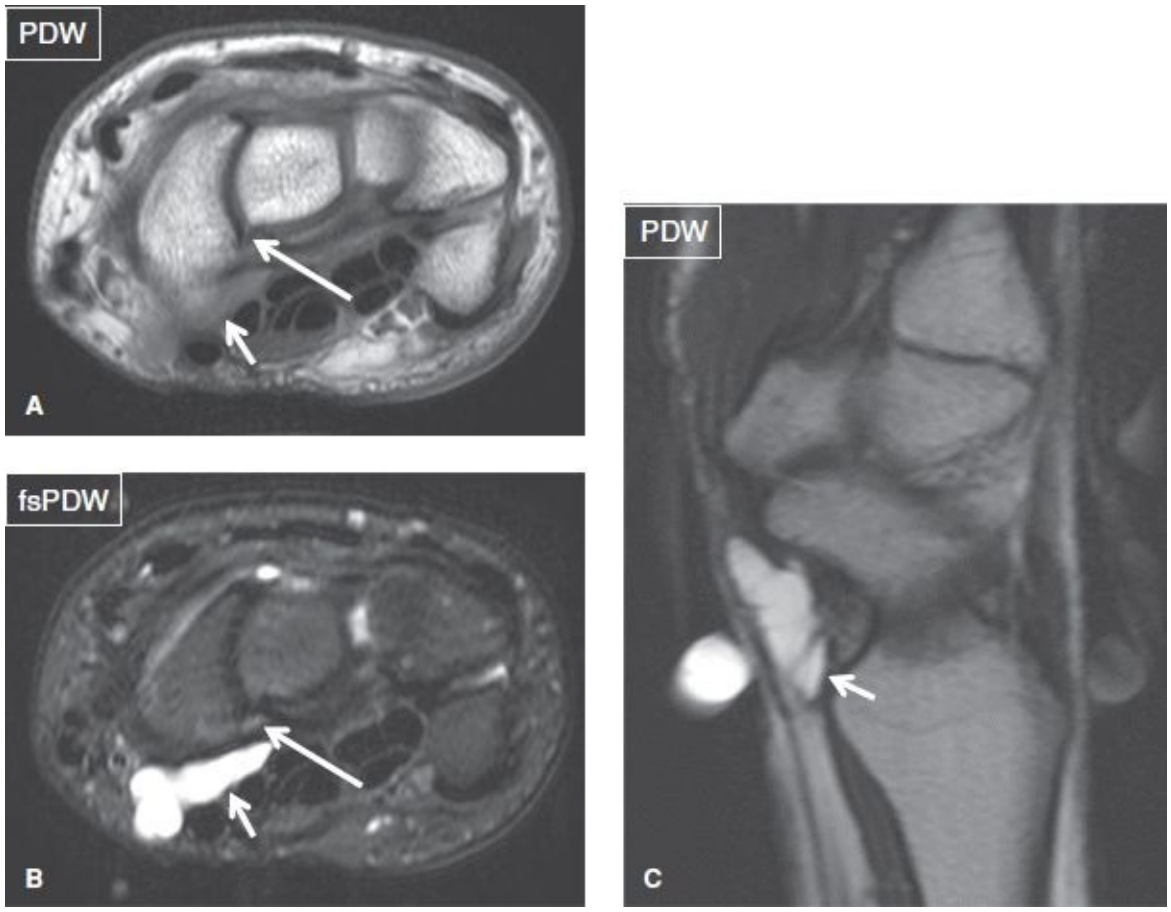

Fig. 19: Scapholunate ligament injury with ganglion formation. Axial **(A, B)** and sagittal **(C)** images show partial tear of the volar band of the scapholunate ligament (*long arrows*) with

an associated ganglion (*short arrows*).

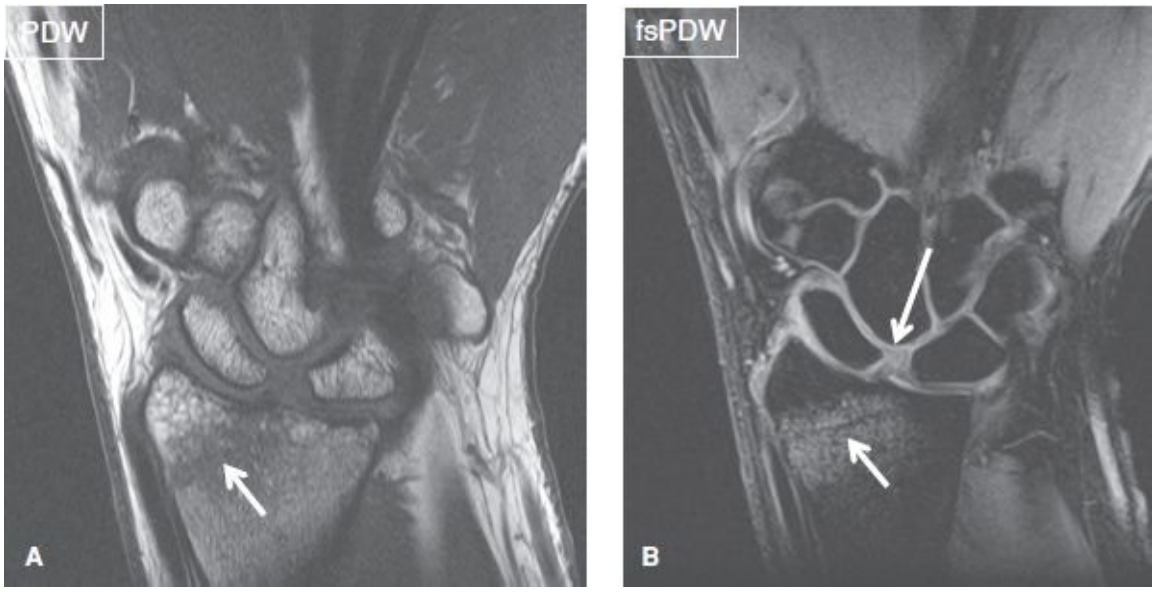

Fig. 20: Acute complete scapholunate ligament injury. Coronal images **(A, B)** exhibit widening of the scapholunate space due to complete tear (*long arrow*) of the scapholunate ligament. Also note an acute fracture of the distal radial epiphysis (*short arrows*).

Tears of the LT ligament are much less common than SL ligament tears, occurring only about one-sixth as often. Degenerative perforations are usually asymptomatic and often associated with ulnocarpal abutment (see below). They typically involve the membranous portion of the ligament, leaving the volar and dorsal portions intact. Again, one should search for secondary signs, such as traction-related avulsive cystic changes or enthesopathy at the osseous attachments, LT curve step-off, and soft tissue ganglion from associated capsular injury or ligament degeneration (Figs. 21, 22). Associated widening of the LT interval is usually evident. A complete LT ligament tear is usually not sufficient for development of static carpal collapse or VISI. There is often associated capsular and extrinsic ligament damage (DIC ligament). Based on severity, ulnar-sided perilunate instability can be classified as follows.

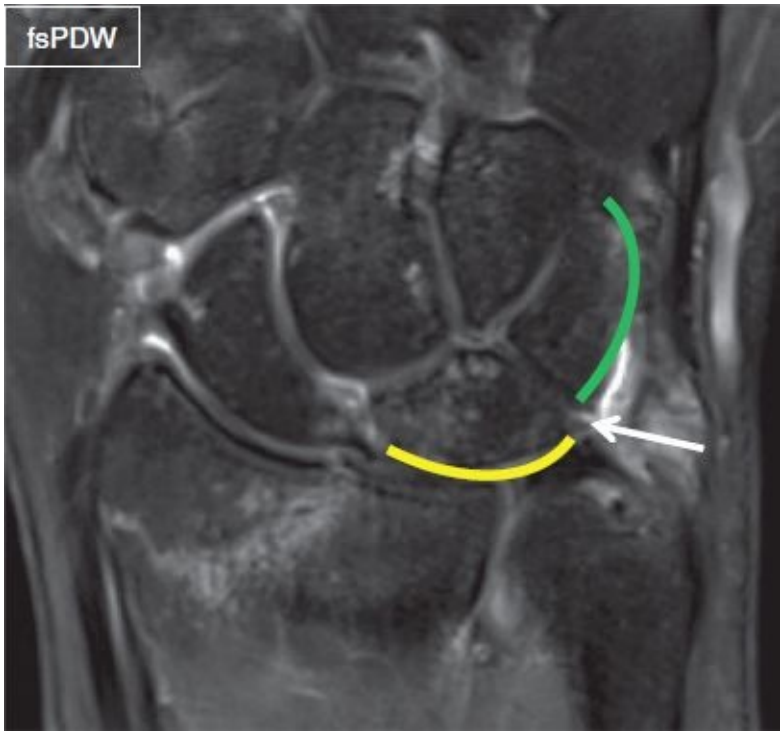

Fig. 21: Lunotriquetral ligament injury. Coronal image exhibits perforation of the membranous portion (*arrow*) of the lunotriquetral ligament. There is step-off at the Gilula A line (yellow and green lines). Also note nondisplaced fracture of the distal radius.

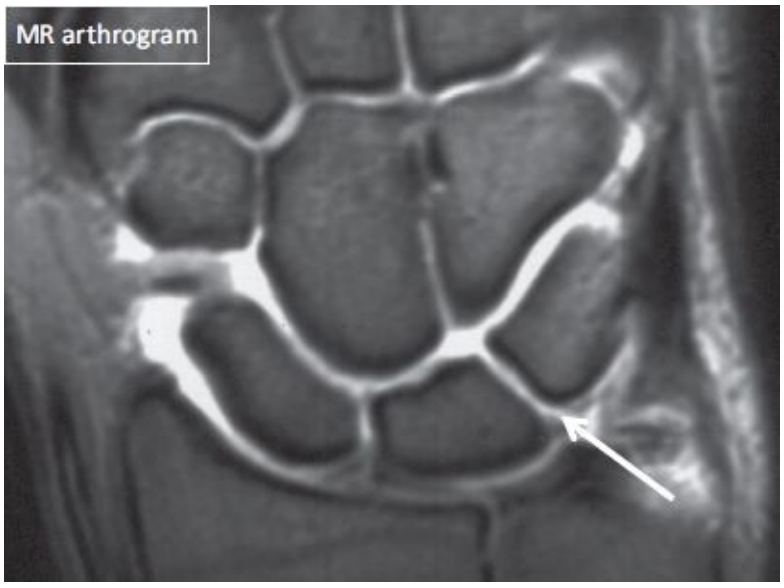

Fig. 22: Lunotriquetral ligament injury. Coronal image exhibits perforation of the membranous portion (*arrow*) of the lunotriquetral ligament with contrast extension from radiocarpal joint into the midcarpal space. Notice step-off at the Gilula A line on this arthrography image.

- Stage I—characterized by partial or complete tear of LT ligament (no VISI)
- Stage II—defined as complete LT ligament tear along with disruption of the palmar LT ligaments (dynamic VISI)
- Stage III—characterized by complete LT ligament tear, disruption of the palmar LT, and dorsal radiocarpal ligaments (static VISI)

Finally, multi-ligament degeneration or tears are not uncommon in the setting of advanced inflammatory arthropathy, such as rheumatoid arthritis (Fig. 23).

Fig. 23: Scapholunate and lunotriquetral ligament injury. Coronal image exhibits complete tear of the scapholunate ligament (*short arrow*) and perforation of the membranous portion of the lunotriquetral ligament (*long arrow*). Notice step-off at the Gilula A line on this arthrography image in a patient with rheumatoid arthritis.

ULNAR SIDE:

Triangular fibrocartilage ligament: [<Intact> <Degeneration> <Acute sprain (<Central / Peripheral>)>]

Lunate facet: [<Present / Absent>]

Hamate–lunate joint: [<Normal / Chondrosis / Osteoarthritis>]

Ulnocarpal impaction: [<None / Ulnolunate / Ulnotriquetral>]

The TFCC is composed of fibrocartilaginous and ligamentous structures situated in the ulnocarpal space. It allows force transmission from the carpus to the ulna, cushions the ulnar fovea and lunate during ulnar deviation of the wrist, and provides DRUJ and ulnocarpal stability. It consists of various components, including the triangular fibrocartilage disc, UCL, meniscus homolog, ulnocarpal (ulnolunate and ulnotriquetral) ligaments, extensor carpi ulnaris (ECU) tendon sheath, volar and dorsal radioulnar ligaments, and DRUJ capsule (Fig. 24).

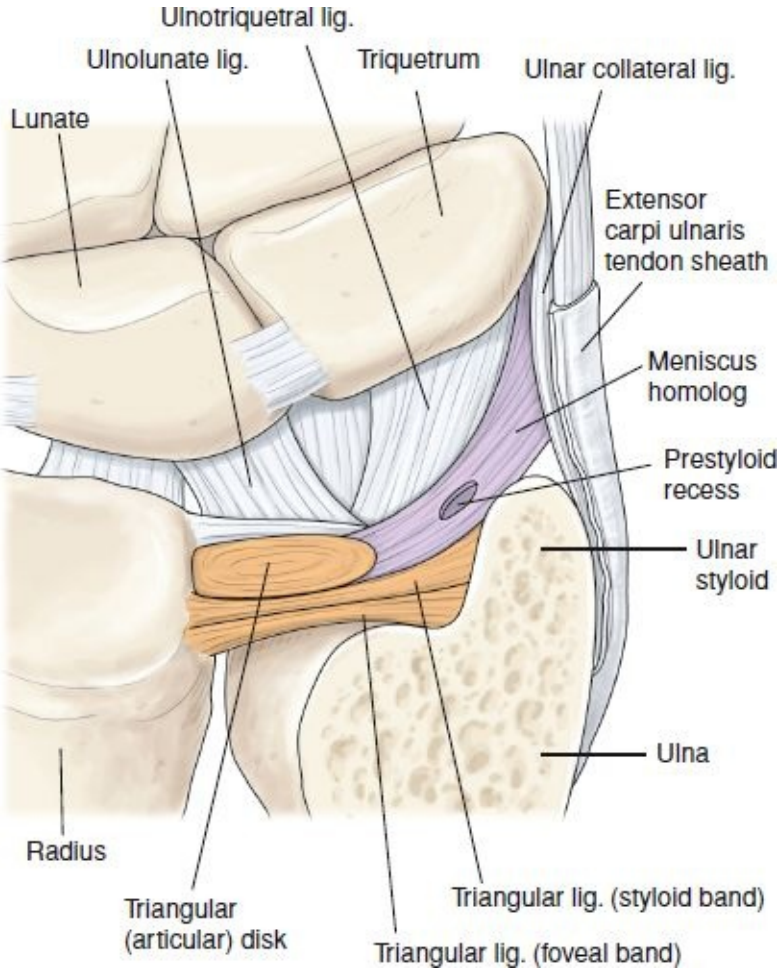

Fig. 24: TFCC complex showing various components of the complex.

The bowtie-shaped articular disc is anchored to the ulnar side of the distal radius and attaches as two distinct bands onto the ulnar styloid process and ulnar fovea, and more distally onto the hamate, triquetrum, and base of the fifth metacarpal bone. The disc is best depicted on coronal images and normally features homogeneous low signal intensity on all pulse sequences but occasionally appears slightly brighter on the gradient-echo images (Fig. 25). The two ulnar insertions are composed of fibrofatty and vascularized connective tissue, and, thus, normally feature a striated configuration, which is particularly evident on 1.5T and 3T MR images. The space between the two insertions is filled by vascularized connective tissue, which is known as the ligamentum subcruentum. The latter normally features intermediate signal intensity, which should not be misinterpreted as a tear. The hyaline cartilage, which is located underneath the lateral portion of the TFCC attachment to the radius, normally exhibits intermediate signal intensity and should not be misinterpreted for radial-sided tear (Fig. 26). The thickness of the disc is inversely proportional to the degree of ulnar variance. In case of a neutral variant, it is approximately 5 mm thick at the ulnar side and 2 mm at the radial side but becomes thicker in subjects with negative ulnar variance and thinner (and thus weaker) in individuals with positive ulnar variance, possibly explaining the increased vulnerability of the latter population to TFCC degenerative tears and maceration. The ulnolunate and ulnotriquetral ligaments are evaluated on coronal and sagittal images (Fig. 27). The dorsal and volar radioulnar ligaments attach bone to bone

versus TFCC connects ulna to the radial cartilage. These ligaments are best seen on axial and coronal images.

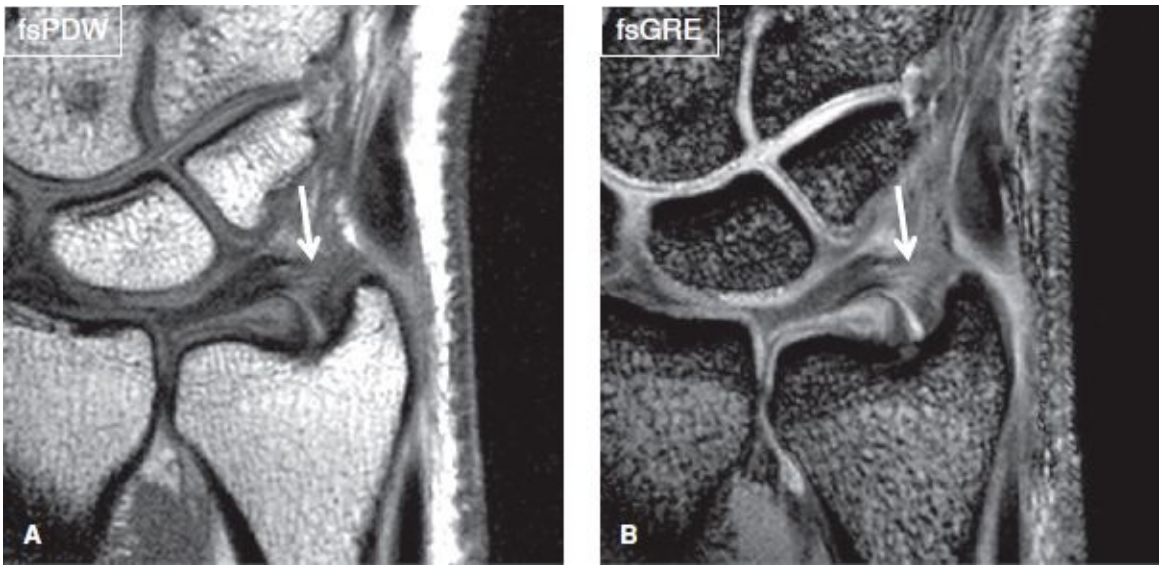

Fig. 25: TFCC appearance on different coronal **(A, B)** sequences. Notice mild brightness on GRE sequence (*arrows*) as compared to the conventional spin-echo sequence, a normal variant.

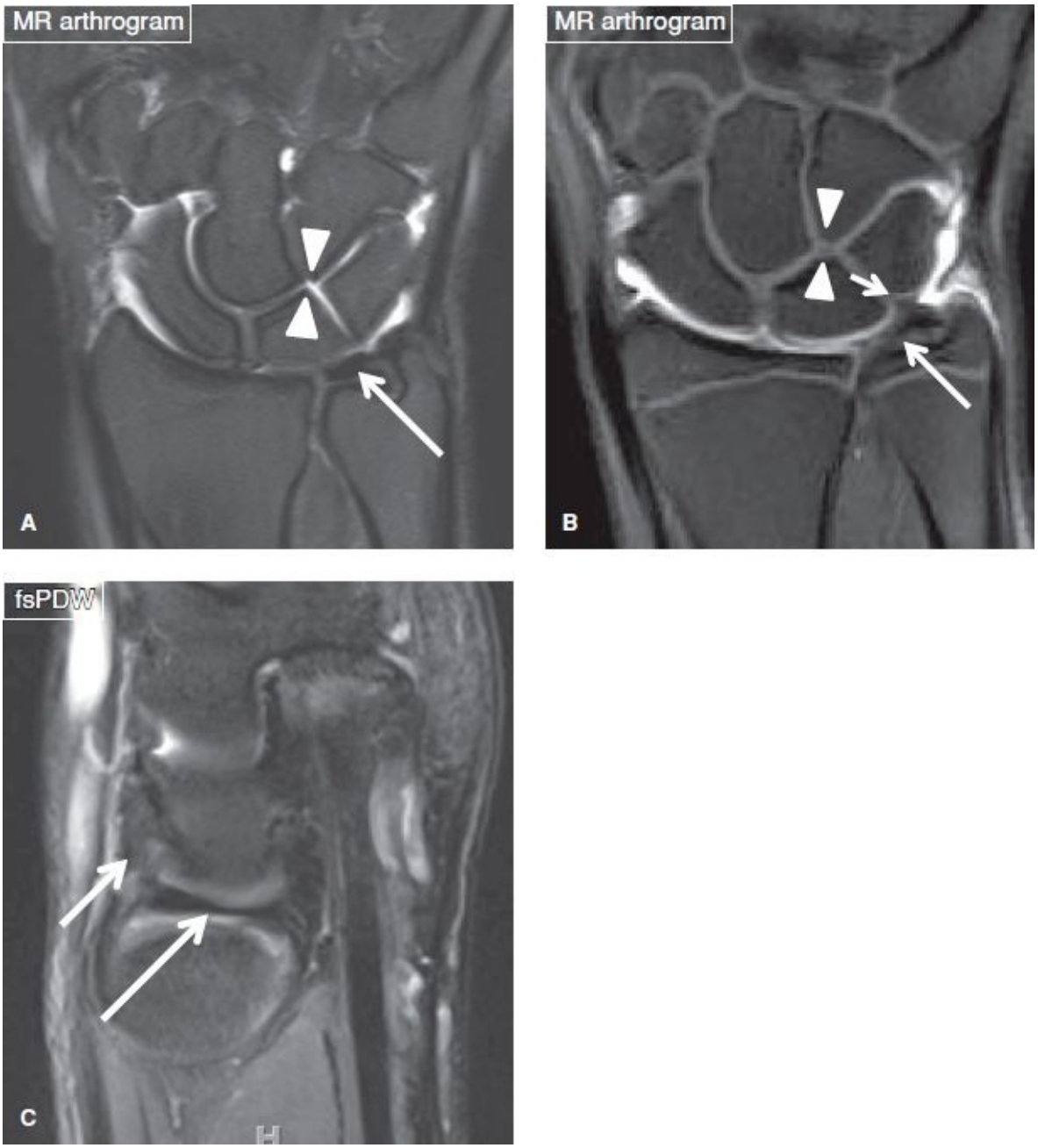

Fig. 26: Normal TFCC. **A, B:** Coronal arthrography images exhibit normal triangular fibrocartilage disc (*long arrows*) and ulnolunate ligament (*short arrow*). Also note type I (*arrowheads* in **A**) and type II (*arrowheads* in **B**) lunate facets. Notice normal cartilage undercutting the lateral TFCC attachment to the radius. **C:** Sagittal image shows normal ulnolunate ligament (*short arrow*) attaching the disc to the lunate dorsal surface.

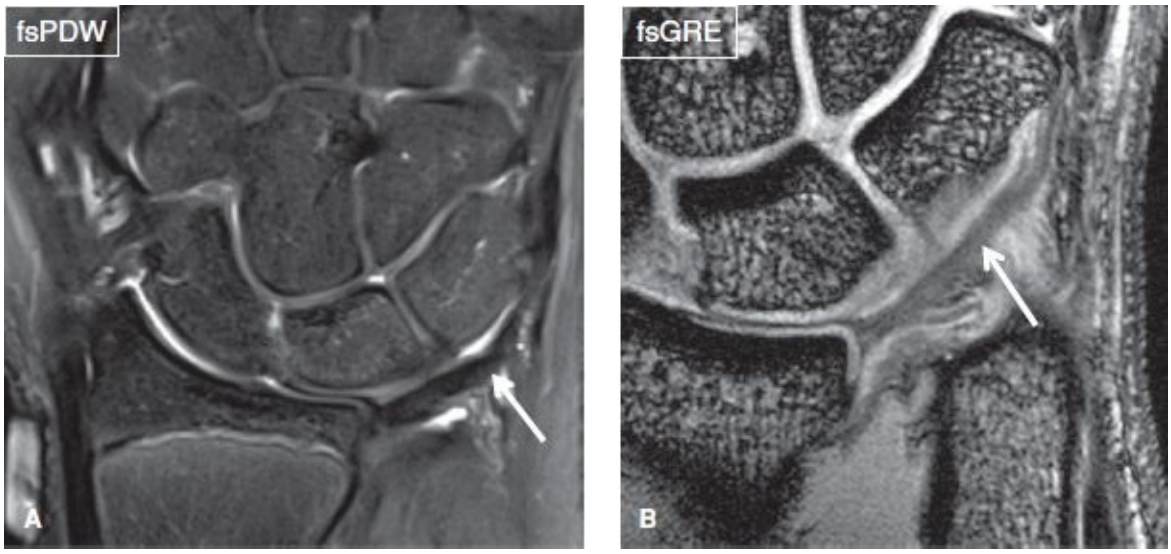

Fig. 27: TFCC complex. Coronal images **(A, B)** show the ulnotriquetral ligament (*arrows*).

Degeneration of the TFCC disc is commonly seen as asymptomatic finding that appears as intrasubstance intermediate signal on T1-weighted (T1W) and PDW images, which does not increase to fluid-like signal on fsPDW/fsT2W images. The signal alteration may be associated with disc thickening, thinning, or fraying of the edges. The signal may be more pronounced in patients with positive ulnar variance and could reflect ulnocarpal abutment-related derangement.

TFCC disc tears can be asymptomatic or symptomatic and these lesions appear either as detachment of the radial or ulnar disc attachments, or as fluid-like signal/gaps in the disc margins, which disrupt one or both articular surfaces (surface tears) (Figs. 28–36). TFCC tears can occur toward the foveal aspect or toward the carpus, and depending on the location of the lesion, the surgical approach may vary from arthroscopy to open approach. Tears are traditionally classified as peripheral (when located at the foveal or styloid attachments), central (when located in the middle of the disc, usually encountered more toward the radial side), or radial-sided (when the radial attachment of the disc is avulsed). Associated findings of TFCC tear include abnormal morphology, attenuation and/or discontinuity of the disc, avulsive bone marrow cystic changes and edema at the ulnar styloid or foveal attachments, and extension of fluid and/or edema along the medial aspect of the distal ulna, proximal to the base of the styloid process. TFCC disc tears may also be associated with stripping of the UCL from the ulna, abnormal morphology of the normally triangular-shaped meniscus homolog, sprains of the ulnocarpal (ulnolunate and ulnotriquetral) ligaments, avulsion of the tip or base of the styloid process (best seen on PDW images), tendinosis, tear, tenosynovitis, or subluxation of the ECU tendon (with extensor retinaculum or subsheath injury, best seen on axial images), and soft tissue or intraosseous ganglion formation. TFCC disc perforations are identified based on a common finding of fluid distention of the DRUJ, but this latter finding is nonspecific, as it can also be present in isolated arthritis or inflammation of the joint. Reporting the transverse location of TFCC tears is important for patient management. The TFCC has good vascularity toward its ulnar side; therefore, peripheral tears are expected to heal if the torn

edges are held in close contact, or are surgically repaired. The indications for repair include, large tears, unstable tears, or symptomatic tears. If symptomatic, central perforations are treated with débridement. Treatment of radial-sided tears depends upon the coexistence of DRUJ ligament tears or instability. Traumatic and degenerative tears of the TFCC are graded according to the Palmer classification (Table 1), in which simultaneous pathology of the LT ligament upgrades the stage of the TFCC injury and alters the treatment options.

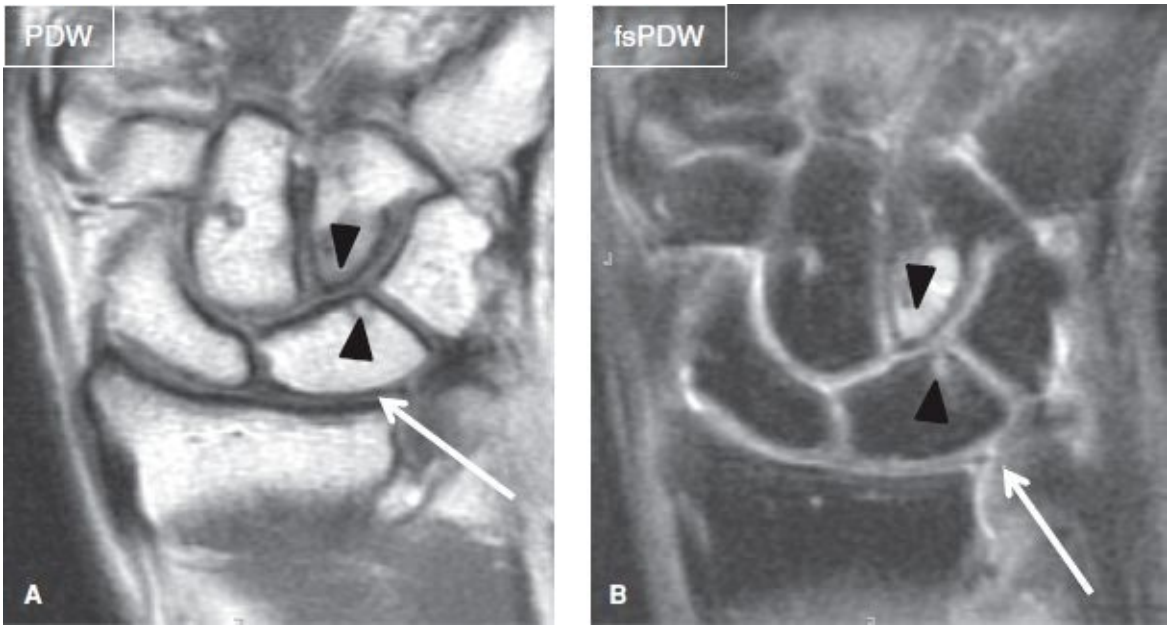

Fig. 28: Triangular fibrocartilage disc perforation. Coronal images **(A, B)** show central perforation (*arrows*) of the triangular fibrocartilage disc. Also note type II lunate with associated hamatolunate osteoarthrosis (*arrowheads*).

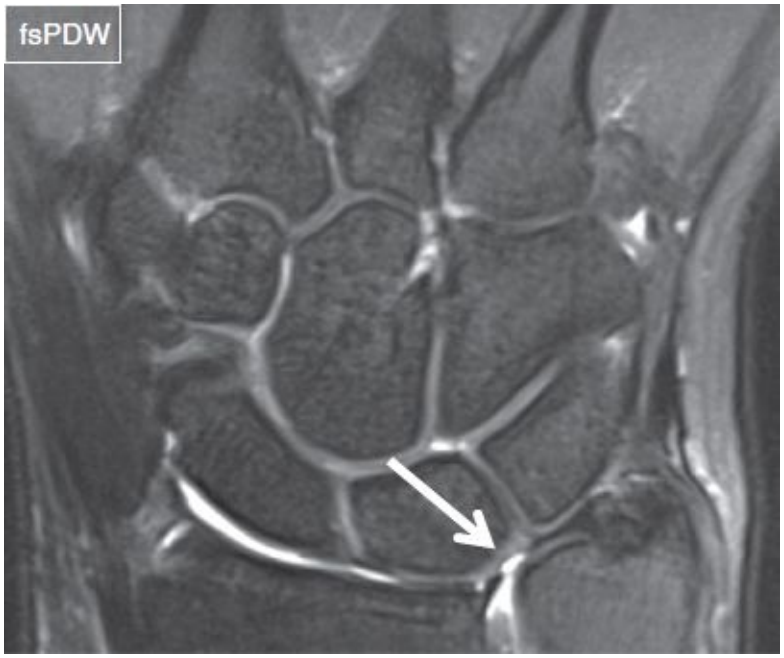

Fig. 29: Triangular fibrocartilage disc injury. Coronal image shows central perforation (*arrow*) of the triangular fibrocartilage disc. Notice type II lunate facet with hamatolunate chondrosis.

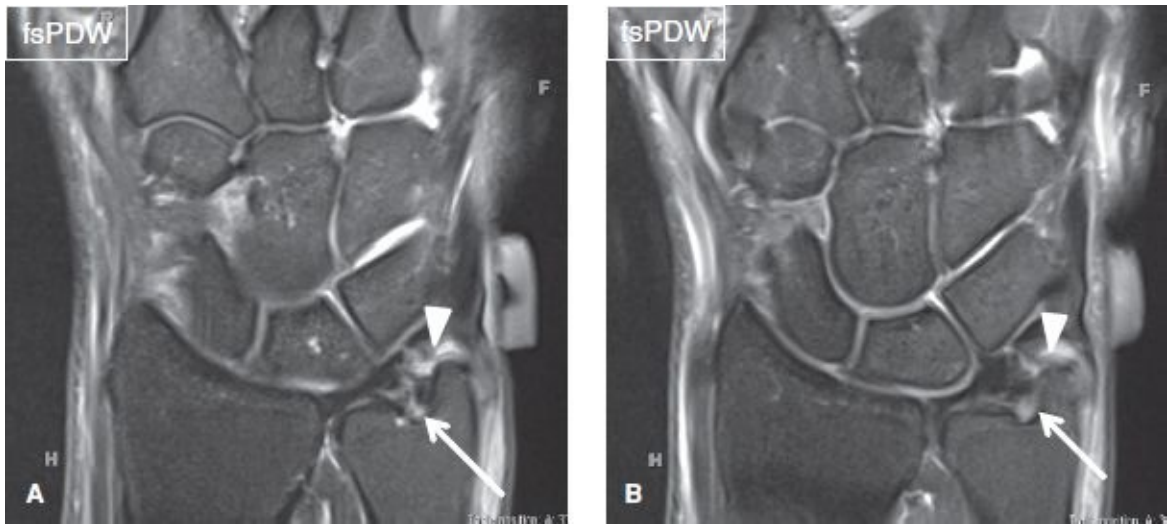

Fig. 30: Grade II sprain of the triangular fibrocartilage disc. Sequential coronal images **(A, B)** show partial tear of the foveal (*arrows*) and styloid (*arrowheads*) attachments of the triangular fibrocartilage disc. Notice subcortical cyst at the foveal attachment of the disc.

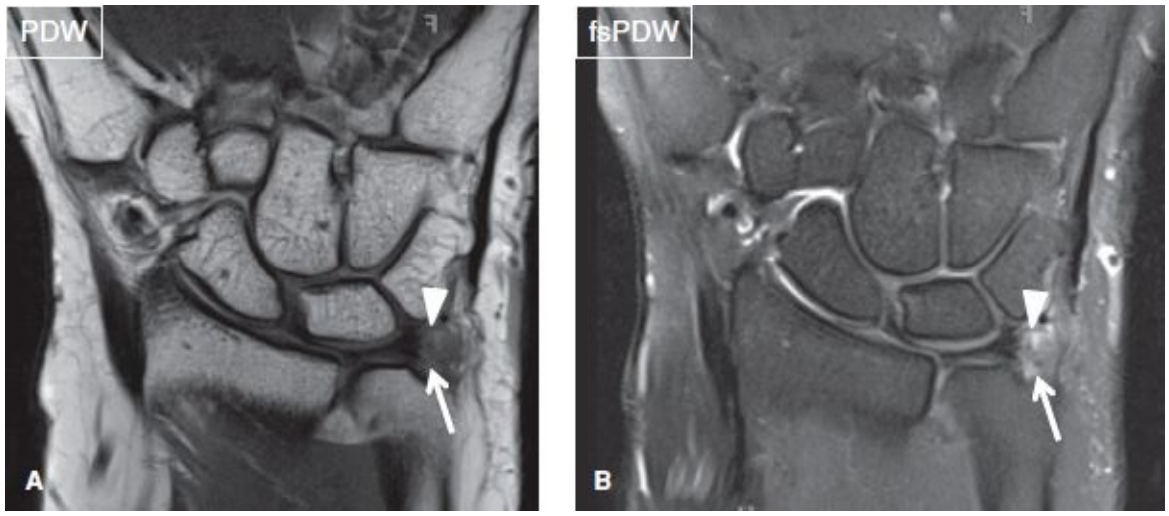

Fig. 31: Triangular fibrocartilage disc injury. Coronal images **(A, B)** exhibit near-complete tears of the foveal (*arrows*) and styloid (*arrowheads*) attachments of the triangular fibrocartilage disc.

Fig. 32: TFCC injury. Coronal image exhibits complete tears of the foveal (*long arrow*) and styloid (*arrowhead*) attachments of the triangular fibrocartilage disc. Also note tear (*short arrow*) of the ulnar collateral ligament and thickening of the ulnotriquetral ligament (*arrowhead*).

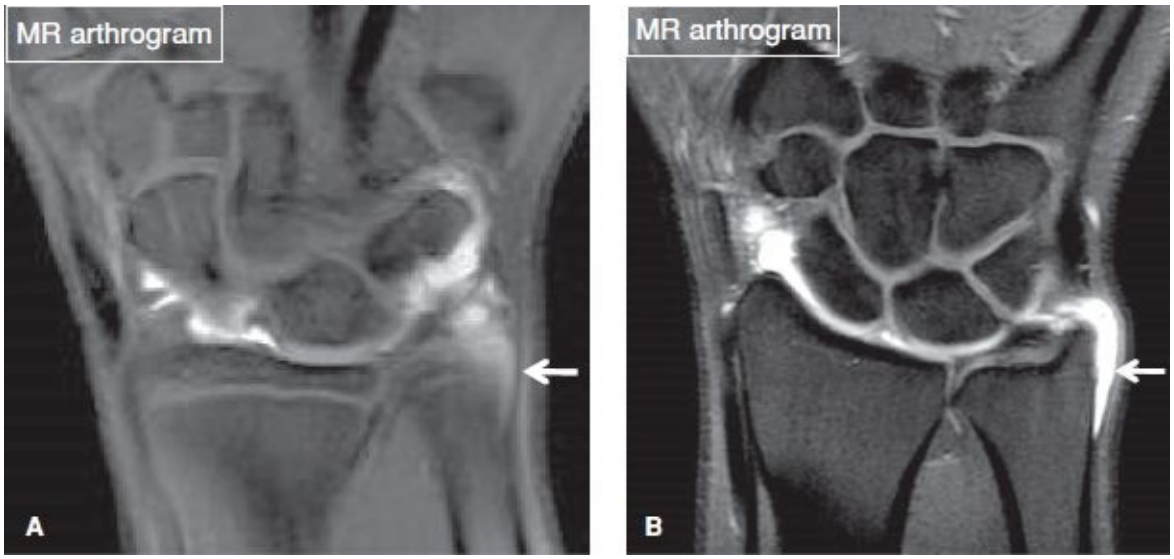

Fig. 33: TFCC peripheral tear. Coronal arthrography **(A, B)** images in two different cases show contrast extension medial to the ulna (*arrows*), proximal to the base of the styloid process, confirming the peripheral TFCC tears.

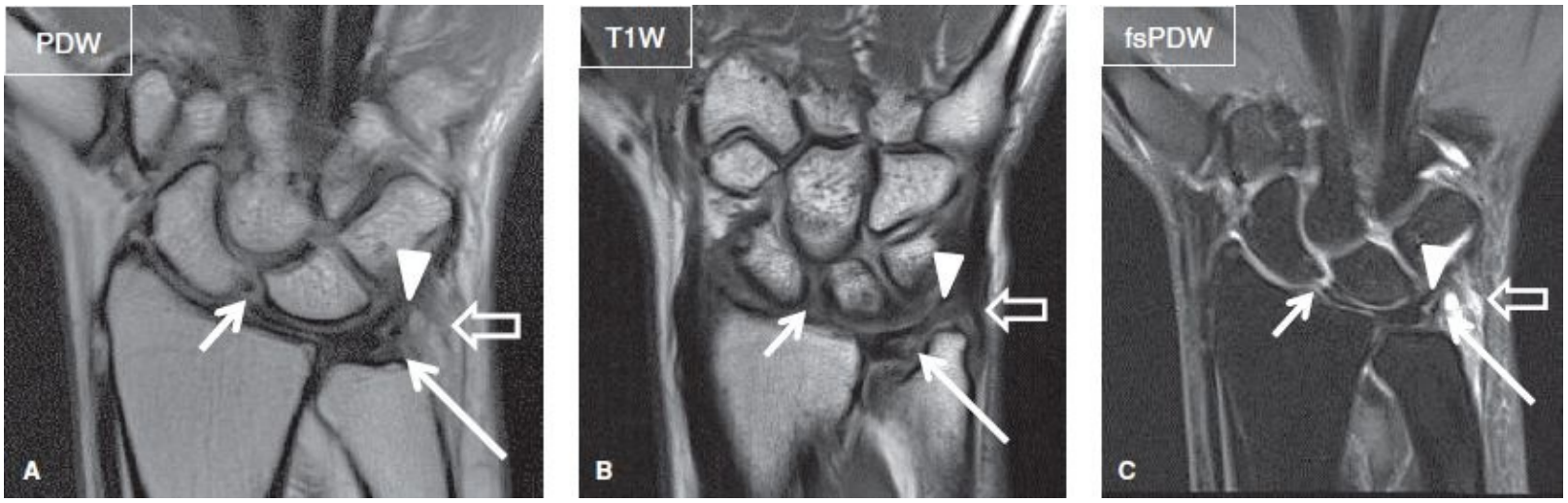

Fig. 34: TFCC and SL ligament injury. Coronal images **(A–C)** exhibit complete tear of the foveal (*long arrows*) and styloid (*arrowheads*) attachments of the triangular fibrocartilage disc, as well as ulnar-sided stripping of the ulnar collateral ligament (*open arrows*). There is also full-thickness tear of the volar band of the scapholunate ligament (*short arrows*). Notice mild cartilage thinning in the radioscaphoid space.

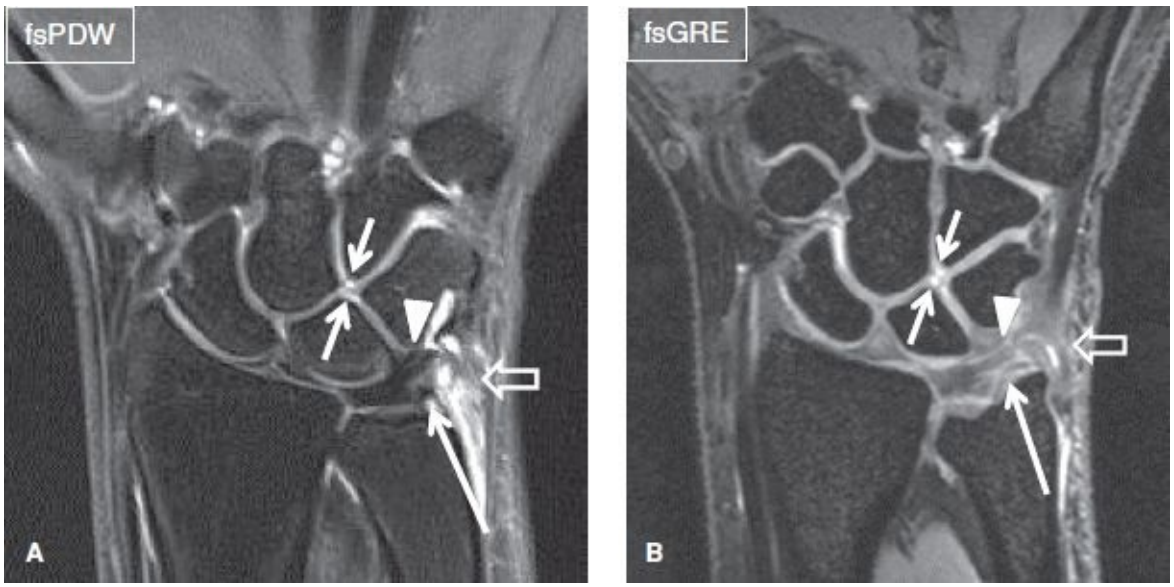

Fig. 35: Multiple carpal ligamentous injury. Coronal spin-echo **(A)** and gradient-echo **(B)** images display near-complete tears of the foveal (*long arrows*) and styloid (*arrowheads*) attachments of the triangular fibrocartilage disc, as well as near–full-thickness tear of the ulnar collateral ligament with ulnar-sided stripping (*open arrows*). Also note type II lunate, with associated chondrosis (*short arrows*) of the articular surfaces.

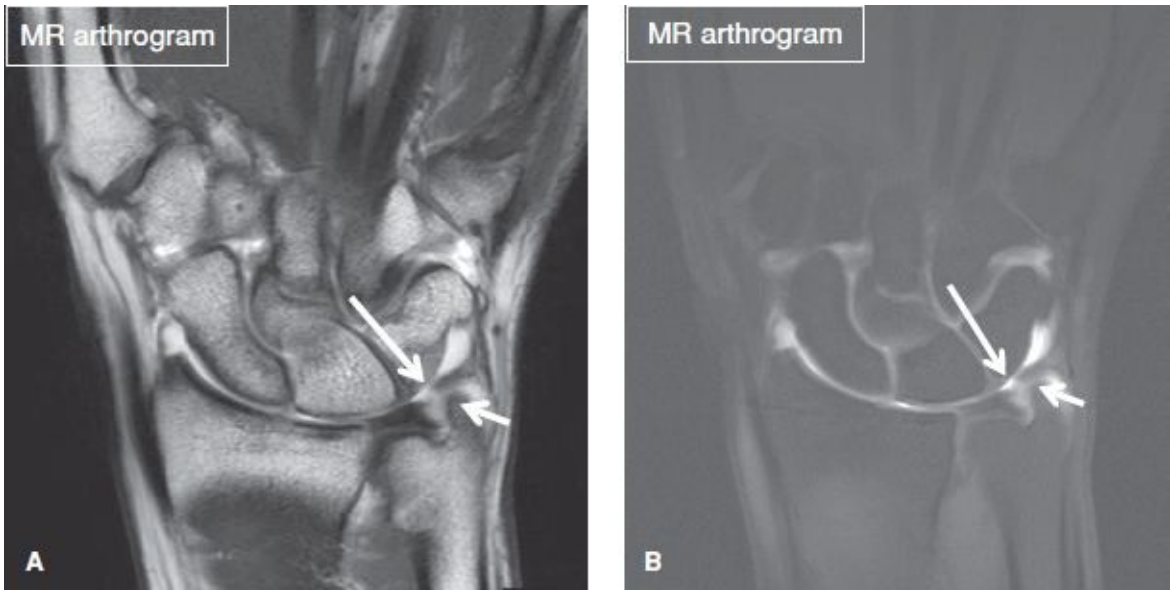

Fig. 36: Triangular fibrocartilage complex injury. Coronal arthrography images **(A, B)** show tears of the styloid attachment of the triangular fibrocartilage (*short arrows*) and ulnotriquetral ligament (*long arrows*).

The meniscus (ulnomeniscal) homolog is an inconsistently present fibrocartilaginous structure. It arises from the dorsoulnar part of the TFCC, is joined by fibers of the UCL, and it inserts on the lunate, triquetrum, hamate, base of fifth metacarpal, and LT ligament. It provides weight-bearing cushion for the ulna and also serves as a stabilizer of the PT joint. It is best depicted on coronal images and features a triangular shape with intermediate signal intensity on all pulse sequences (Fig. 37). Fluid-like signal partially or fully disrupting the meniscal homolog indicates a tear and may be associated with ulnar-sided wrist pain. More commonly, one will see attenuated or macerated homolog in the setting of chronic TFCC tears.

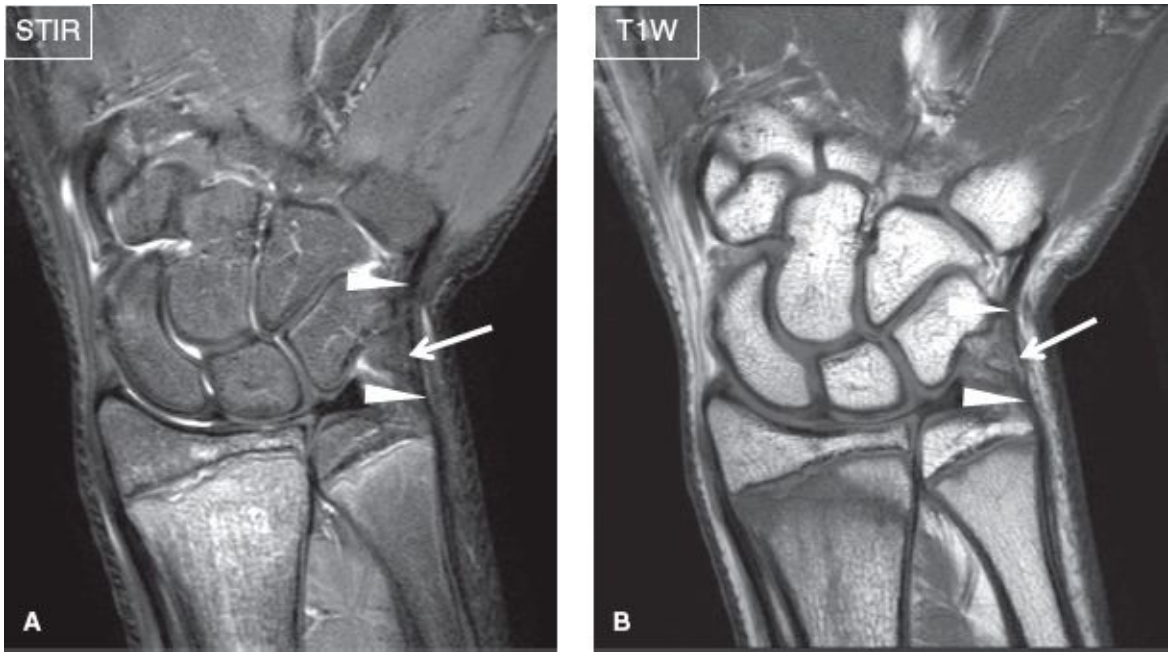

Fig. 37: Normal meniscus homolog and ulnar collateral ligament. Coronal images **(A, B)** exhibit a normal intermediate-signal triangular-shaped meniscus homolog (*arrows*), and

superficial to it, the ulnar collateral ligament (*arrowheads*).

The ulnocarpal ligaments are intimately attached to the TFCC, and serve as stabilizers of the lunate and LT joint while keeping the TFCC under tension. This group includes (1) the ulnolunate ligament, which arises from the palmar border of the articular disc, courses parallel to the short radiolunate ligament and inserts on the lunate; and (2) the ulnotriquetral ligament, which arises medial to the ulnolunate ligament and inserts on the triquetrum, assuming a different obliquity, nearly parallel to the triquetrum (Fig. 27). Both ligaments are best depicted on coronal and sagittal images and show great variability in size. Signs of injury include increased signal intensity and/or discontinuity, as well as avulsion, which can be seen in severe traumatic injuries of the TFCC leading to ulnocarpal instability and/or palmar translocation of the lunate or triquetrum (Fig. 36).

TABLE 1: The Palmer classification for TFCC abnormalities

Class 1: Traumatic
A. Central perforation
B. Ulnar avulsion with or without distal ulnar fracture
C. Distal avulsion (ulnocarpal ligaments)
D. Radial avulsion with or without sigmoid notch fracture
Class 2: Degenerative (ulnocarpal abutment syndrome) stage
A. TFCC wear
B. TFCC wear with lunate and/or ulnar chondromalacia
C. TFCC perforation with lunate and/or ulnar chondromalacia
D. TFCC perforation with lunate and/or ulnar chondromalacia and LT ligament perforation
E. TFCC perforation with lunate and/or ulnar chondromalacia, LT ligament perforation, and ulnocarpal arthritis

The prestyloid recess is a synovium-lined pouch bordered by the meniscal homolog distally, TFCC attachments to the ulnar styloid process proximally, and the central TFCC disk radially. It is best depicted on coronal images, where it features saccular, tubular, or conical shape and normally contains a small amount of fluid, which should not be misinterpreted as peripheral TFCC tear (Fig. 38). In peripheral TFCC tears, one may see fluid leaking from this recess along the side of the ulnar metaphysis. Whereas mild enhancement of the recess is normal after contrast administration, marked enhancement and synovial villi protruding within the space are indicative of synovitis. The prestyloid recess serves as a cushion for TFCC during forearm rotations.

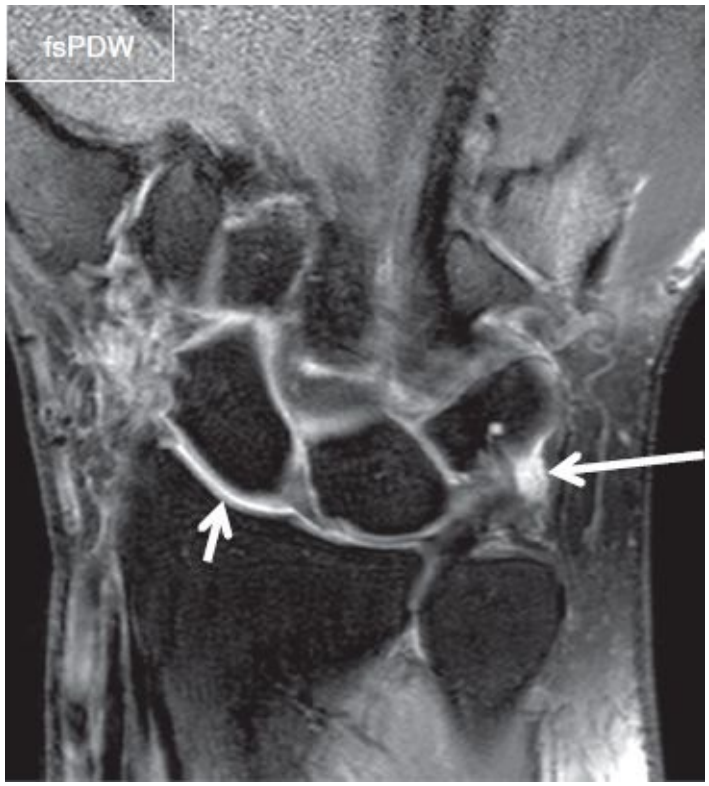

Fig. 38: Prestyloid recess. Coronal image shows the prestyloid recess (*long arrow*), which is located deep to the ulnar collateral ligament. Notice mild thinning of the radioscaphoid joint space cartilage (*short arrow*).

Finally, one should look for an extra facet of the lunate for the hamate (type II lunate), which is a common (44% to 73%) anatomical variant and is associated with hamatolunate chondrosis or osteoarthrosis (cartilage loss, bone marrow edema, or cystic changes) (Figs. 26, 28, 29, 35). It could be a cause of ulnar-sided wrist pain and this facet can be resected if this is the only finding in case of ulnar-sided wrist pain. Of note, type II facet confers stability in cases of SL ligament tear.

Ulnocarpal abutment (also known as ulnar impaction syndrome) refers to chronic repetitive impaction of the ulnar head against the lunate and triquetrum causing degenerative cartilage and subchondral bone changes in the impacting bones (Figs. 39–41). The entity has been associated with positive ulnar variance, malunion of a distal radial fracture, previous radial head resection, and daily activities causing excessive loading of the ulnar carpus. One should note that ulnocarpal abutment can also develop with neutral or negative ulnar variance. MR imaging study demonstrates the spectrum of class 2 lesions as described in the Palmar classification (Table 1). In early stages (where plain films could be unrevealing), MR imaging shows bone marrow edema, chondromalacia and cystic changes. In later stages with increasing chondrosis, subchondral sclerosis develops, which is depicted as subchondral areas of low signal intensity on all sequences. For treatment purposes, it is important to differentiate whether LT ligament tear is traumatic or is part of ulnocarpal abutment since the former is treated with LT joint stabilization and the latter by ulnar shortening. A long ulnar styloid process or a nonunited styloid process fracture deformity may also impact on the proximal triquetrum and result in chondromalacia and subchondral

cystic changes in the impacting bones, and potentially in LT joint instability (ulnar styloid impaction syndrome). Finally, a (congenitally or iatrogenically) short ulna may impinge on the distal radius, proximal to the sigmoid notch and form a painful pseudoarthrosis, which is aggravated by pronation and supination. The entity is known as ulnar impingement syndrome. MR imaging may assist in early diagnosis by demonstrating marrow edema and cystic changes, before degenerative sclerosis and hypertrophic bony productive changes are apparent (Fig. 42).

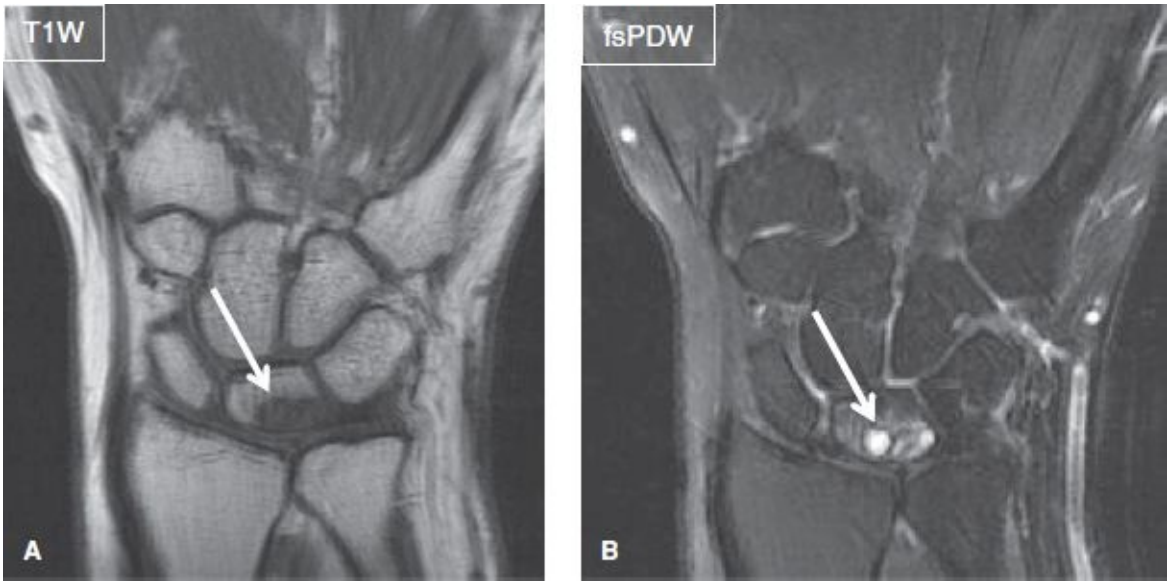

Fig. 39: Ulnocarpal abutment. Coronal images **(A, B)** show subchondral cysts and bone marrow edema (*arrows*) of the lunate, opposite to the ulnar articular surface. Notice mild positive ulnar variance.

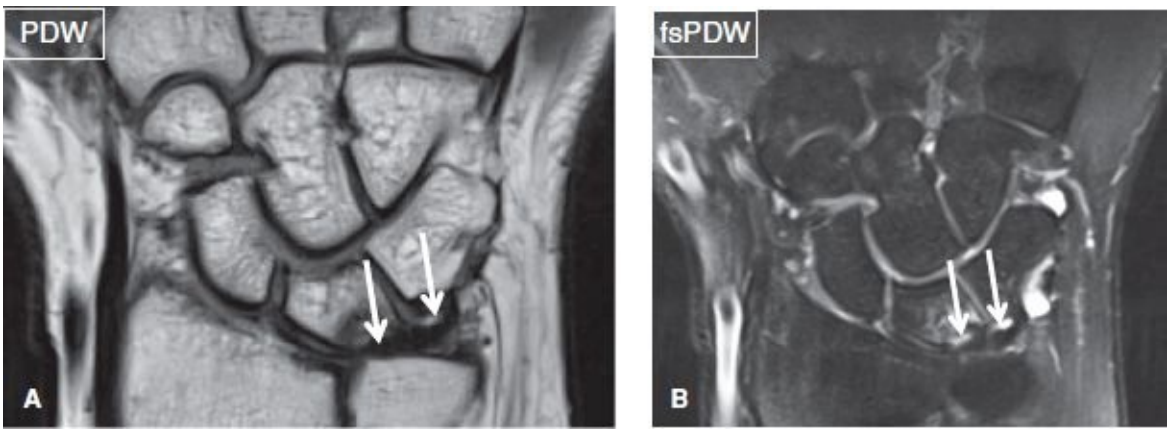

Fig. 40: Ulnocarpal abutment. Coronal images **(A, B)** exhibit subchondral cysts and mild marrow edema (*arrows*) at the lunate and triquetrum opposite the ulnar articular surface. Notice mild positive ulnar variance.

Fig. 41: Ulnocarpal abutment. Anteroposterior radiograph **(A)** and coronal MR images **(B, C)** demonstrate subchondral cystic changes with marrow edema and cystic changes at the lunate, triquetrum (*short arrows*), and ulna (*large arrows*). There is also an old fracture of the ulnar styloid process.

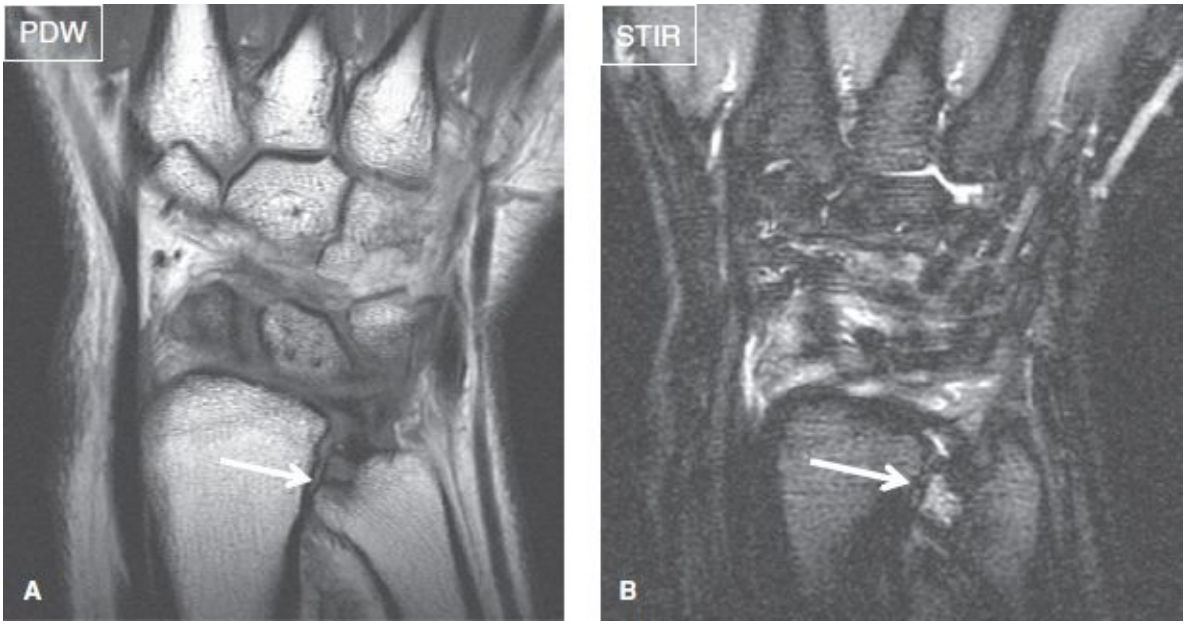

Fig. 42: Ulnar impingement syndrome. Coronal images **(A, B)** show chronic ulnar impingement changes with short ulna and subcortical foveal cystic changes (*arrows*).

EXTENSOR COMPARTMENT:

I: [<Normal> <Tenosynovitis / Tendinosis / Tear>]

II: [<Normal> <Tenosynovitis / Tendinosis / Tear>]

III: [<Normal> <Tenosynovitis / Tendinosis / Tear>]

IV: [<Normal> <Tenosynovitis / Tendinosis / Tear>]

V: [<Normal> <Tenosynovitis / Tendinosis / Tear>]

VI: [<Normal> <Tenosynovitis / Tendinosis / Tear>]

The extensor retinaculum attaches to ulnar styloid process, medial margin of pisiform and triquetrum, and to the lateral radius margin. From the radial to the ulnar side, the extensor tendons are arranged under the extensor retinaculum into six extensor compartments (Fig. 43).

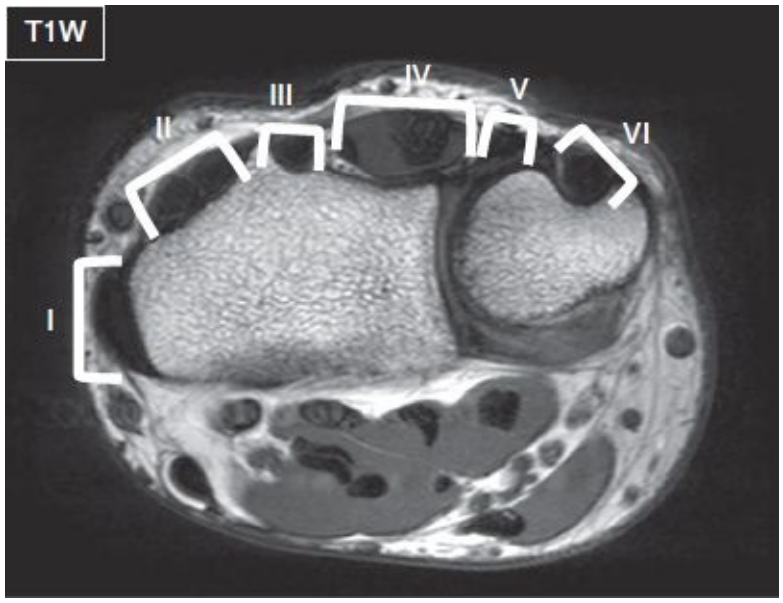

Fig. 43: Normal extensor tendons. Axial image displays the extensor tendons, grouped in numbered compartments.

- Compartment I—the abductor pollicis longus (APL) and extensor pollicis brevis (EPB) tendons
- Compartment II—the extensor carpi radialis longus and brevis tendons
- Compartment III—the extensor pollicis longus (EPL) tendon
- Compartment IV—the extensor digitorum and indices tendons
- Compartment V—the extensor digiti minimi tendon
- Compartment VI—the ECU tendon

The APL originates from the dorsal ulna and radius and inserts on the first metacarpal base and trapezium. The EPB arises from the dorsal midradius and inserts on the base of proximal phalanx of the thumb. The EPL originates from dorsal ulna and inserts onto base of the distal phalanx of the thumb. The extensor indicis arises from the dorsal ulna and interosseous membrane and inserts onto the extensor hood of the index finger. The extensor carpi radialis longus and brevis originate from the lateral epicondyle and inserts onto the dorsal radial aspects of the second and third metacarpals, respectively. The extensor digitorum arises from the lateral epicondyle and inserts onto the middle and distal phalanges of index, middle, ring, and little fingers. The extensor digiti minimi originates from the lateral epicondyle and inserts onto the extensor hood of little finger proximal

phalanx. The ECU originates from the lateral epicondyle and inserts onto the dorsal aspect of the base of the fifth metacarpal base. The above muscles are innervated by the radial nerve and its posterior interosseous branch.

Extensor tendinosis is depicted as intermediate intratendinous signal, with or without associated tendon thickening. The entity most commonly affects compartment VI. Sources of potential error include (1) multiple intrasubstance slips within extensor tendons or intracompartmental intertendinous septations on high-resolution axial images, which are both normal findings and should not be mistaken for longitudinal split tears, and (2) increased signal due to magic angle artifact in the ECU tendon at the level of the ulnar groove and in the EPL tendon as the level of Lister tubercle. The artifact is minimized on long-echo time images (fsPDW/fsT2W). Longitudinal split tears and full-thickness tendon tears (empty tendon sheath) are best seen on axial images whereas longitudinal sagittal and coronal images can be used to demarcate the tendon gap and define tendon retraction.

Trace-dependent fluid in the tendon sheaths is a normal finding, but circumferential fluid around the tendon indicates tenosynovitis (Figs. 44–50). The entity is usually symptomatic if there is moderate or large distention of the sheath, associated synovial thickening with septations, and fluid loculations (stenosing tenosynovitis), or if it is associated with fascial edema, tendon tear, or subtendinous bone marrow edema. Tenosynovitis most often involves compartments VI and I.

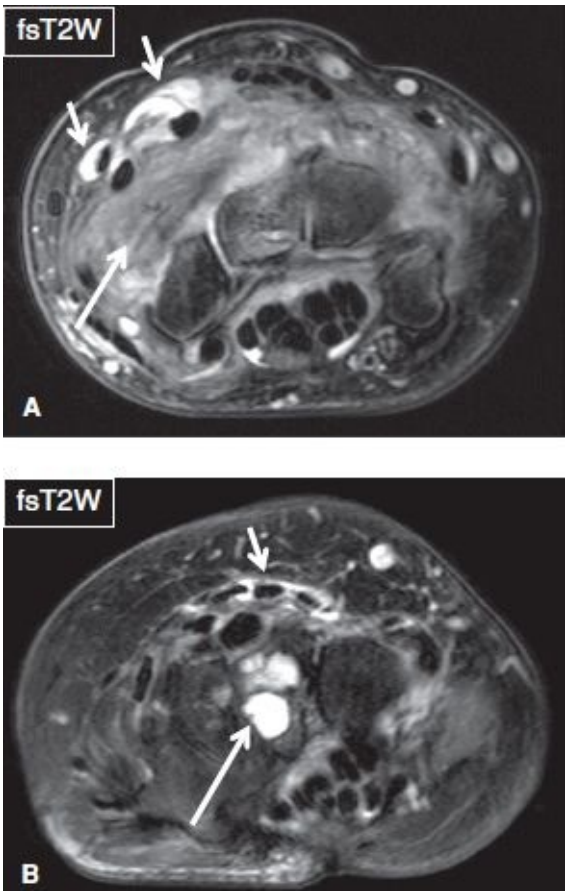

Fig. 44: Extensor tenosynovitis. Axial images demonstrate increased fluid within the tendon sheaths of extensor compartments II and III (*short arrows* in **A**) and extensor compartment IV (*short arrow* in **B**). Notice extensive pannus formation under the dorsal intercarpal

ligament (*long arrow* in **A**) and interosseus cystic changes (*long arrow* in **B**) in this case of rheumatoid arthritis.

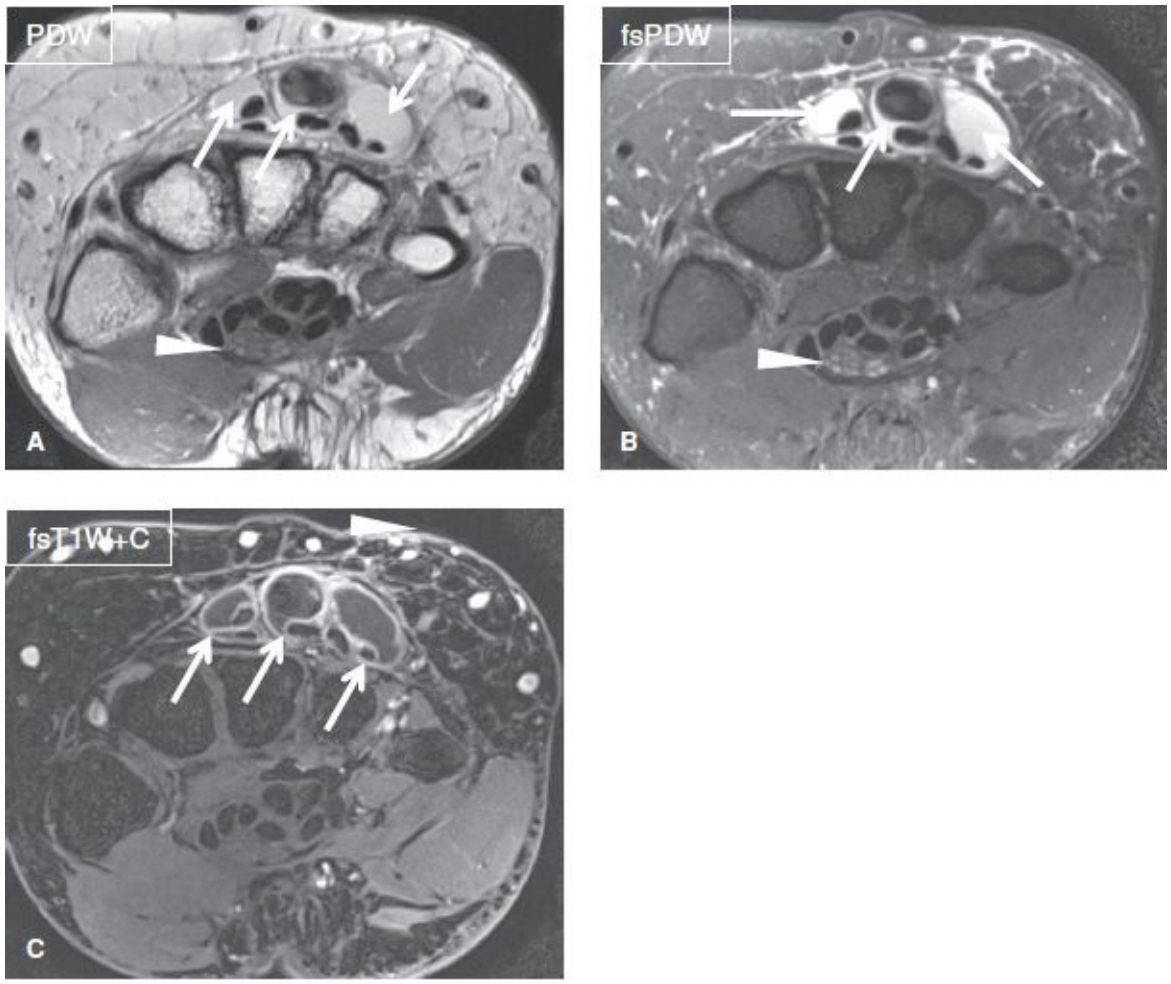

Fig. 45: Mechanical tenosynovitis. Axial images. **A, B:** Moderate synovial fluid distends the tendinous sheaths of extensor compartment IV (*arrows*), in keeping with tenosynovitis. **C:** Increased contrast enhancement of the tendinous sheaths (*arrows*) is indicative of hyperemia and inflammation. The fluid distention gradually increased over many years. Notice prominent medial nerve and its fascicles (*arrowheads*), incidental carpal tunnel syndrome findings.

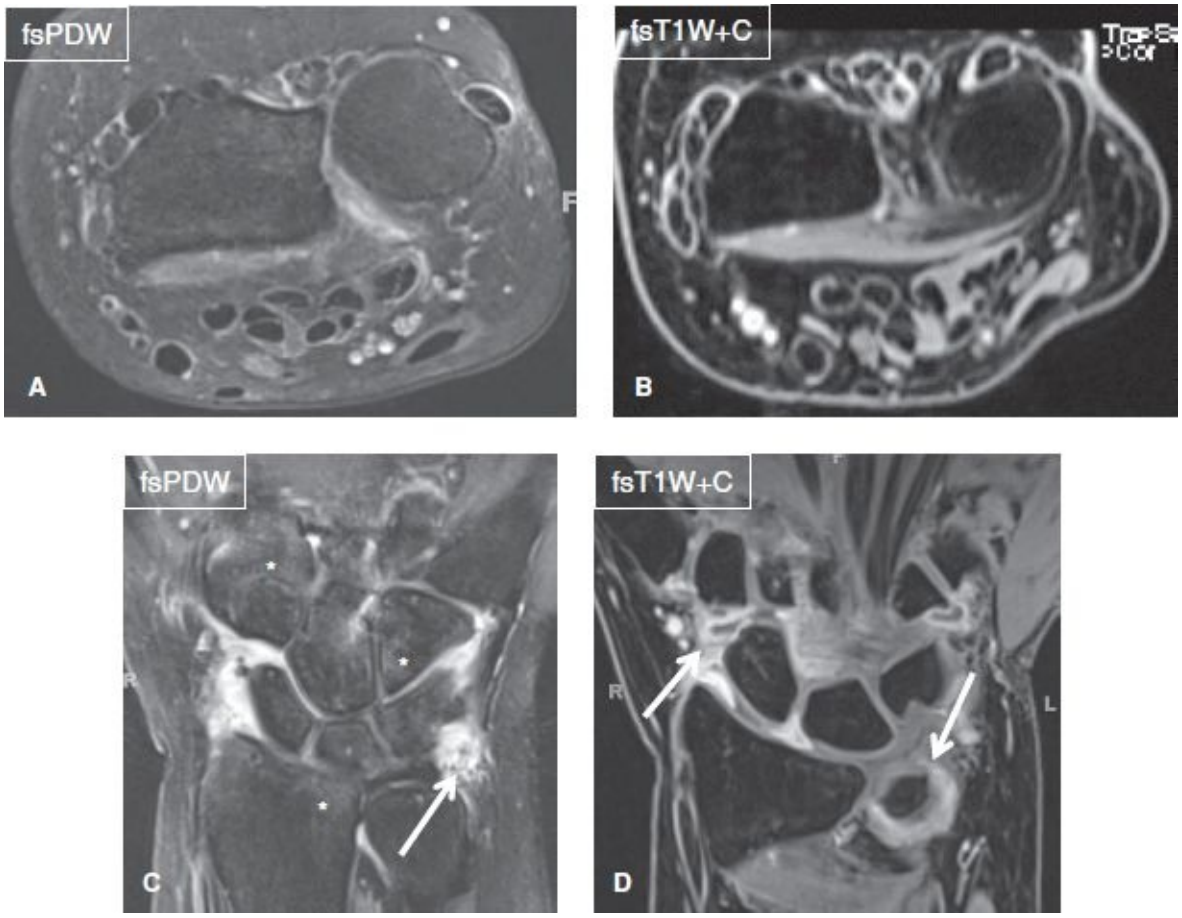

Fig. 46: Systemic lupus erythematous-related tenosynovitis. **A, B:** Axial images show minimal circumferential fluid and increased contrast enhancement, reflecting hyperemia of tendon sheaths all extensor compartments in this case of lupus tenosynovitis. **C, D:** The respective coronal images show synovitis (*arrows*), as well as scattered foci of mild bone marrow edema (*asterisks*).

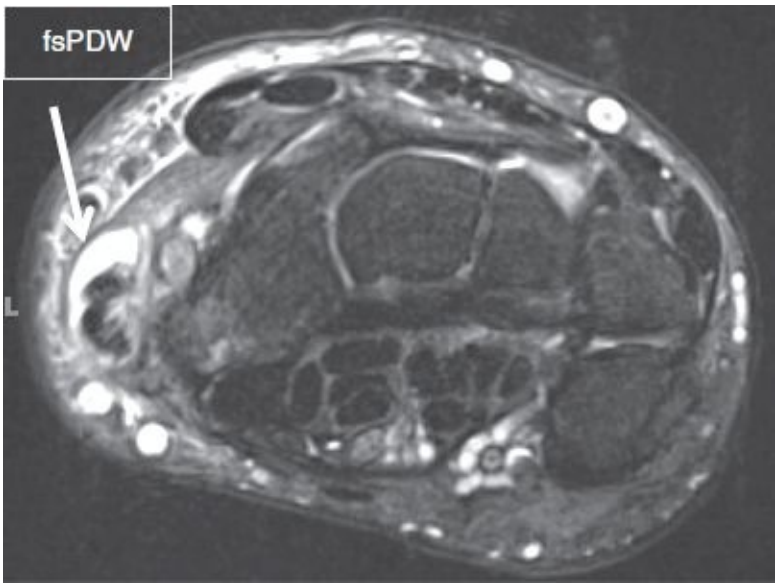

Fig. 47: De Quervain tenosynovitis. Axial image demonstrates abnormal amount fluid (*arrow*) within the tendon sheath of extensor compartment I.

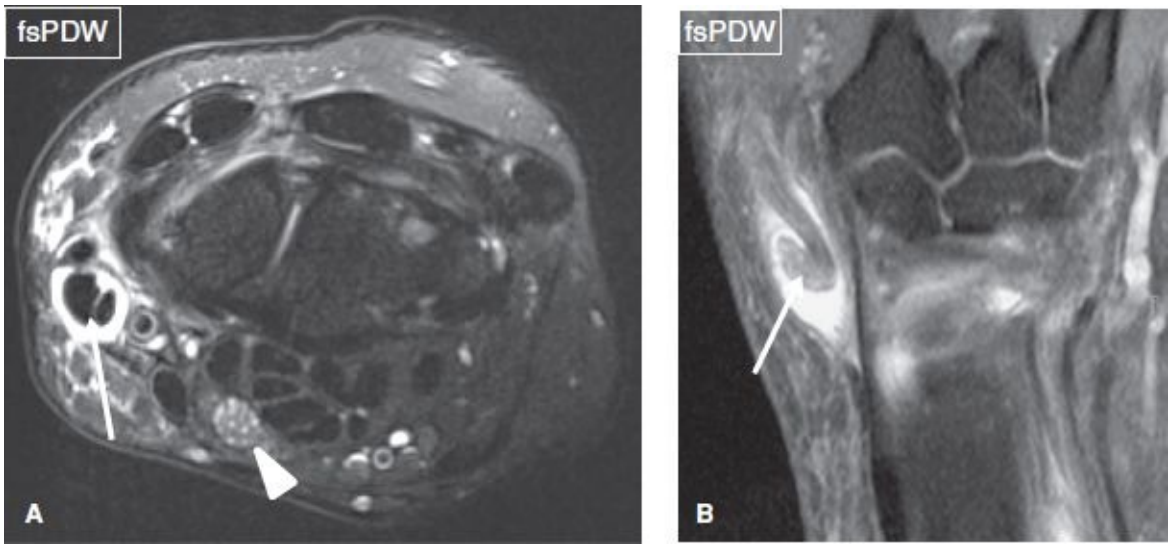

Fig. 48: Extensor tenosynovitis with tendon tears. **A:** Axial image exhibits abnormal amount of fluid within the tendon sheath of extensor compartment I with split tear of APL (*arrow*). Also note abnormally hyperintense median nerve (*arrowhead*) featuring enlarged fascicles. **B:** Coronal image shows full-thickness EPL tear with tenosynovitis and tendon retraction (*arrow*).

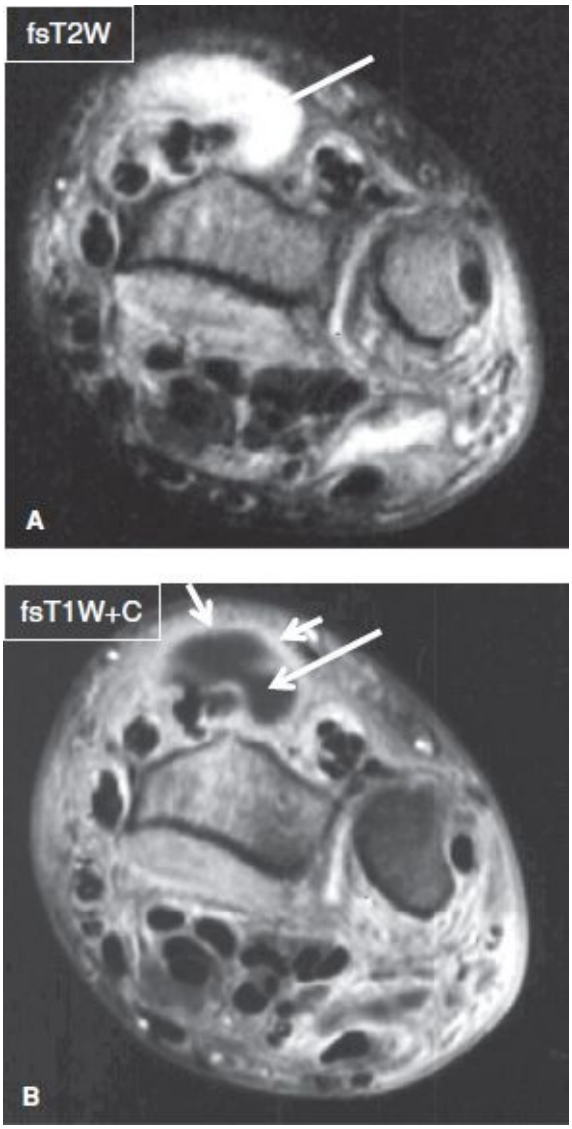

Fig. 49: Infectious (staphylococcal) extensor tenosynovitis. Axial images **(A, B)** exhibit large

amount of fluid (*long arrows*) within the synovial sheath of extensor compartment II, along with thickening and contrast enhancement of the sheath (*short arrows*). Notice surrounding fascial edema and cellulitis as well as additional mild I and IV compartment tenosynovitis suggesting the presence of the infection.

In chronic fibrosing tenosynovitis, imaging findings are more prominent on PDW and T1W images as compared to the fluid-sensitive fsPD or fsT2W images. When involving compartment I, the entity is also known as de Quervain tenosynovitis (or syndrome), and usually results from chronic repetitive motion (Figs. 47, 48). Infectious tenosynovitis manifests as thickening and contrast enhancement of the involved tendon sheath, which is distended with complex fluid and shows varying signal, related to pus, gas, blood, and/or debris. The respective tendon is ill-defined, thickened, and shows intermediate signal. There is typically edema and enhancement of the surrounding soft tissues (Fig. 49). In most cases, the cause of tenosynovitis cannot be accurately established solely based on imaging features, as long-standing mechanical tenosynovitis can also feature synovial thickening and appear similar to inflammatory tenosynovitis (Fig. 45). The clinical findings of infection and associated soft tissue edema, fascial fluid and edema, and/or abscess formation suggest an infectious cause. Bilateral tenosynovitis generally favors a (seropositive or seronegative) inflammatory origin, especially when associated with cystic or erosive bone marrow changes, and synovial thickening or enhancement (Fig. 46). Unilateral tenosynovitis can be mechanical or tuberculous (typical or atypical). Other characteristic tenosynovitis syndromes include (1) the intersection syndrome, which refers to focal tendon tears, tendinosis, or tenosynovitis at the crossing of the first and second extensor compartment tendons, located in the distal forearm, approximately 4 to 8 cm proximal to Lister tubercle (most often in individuals with prominent dorsal radial ridge), and (2) the distal intersection or decussation syndrome, which shows similar findings but is more common and it involves the second and third extensor compartment tendons at the level of wrist (Figs. 50, 51). Because of the constricted anatomy of the above areas, minimal synovial fluid is commonly encountered as an incidental and normal finding, similar to Henry's knot in the foot. One should look for associated fascial or soft tissue edema, substantial fluid loculation, and tendon abnormalities, findings that would likely better correlate with the clinical symptoms.

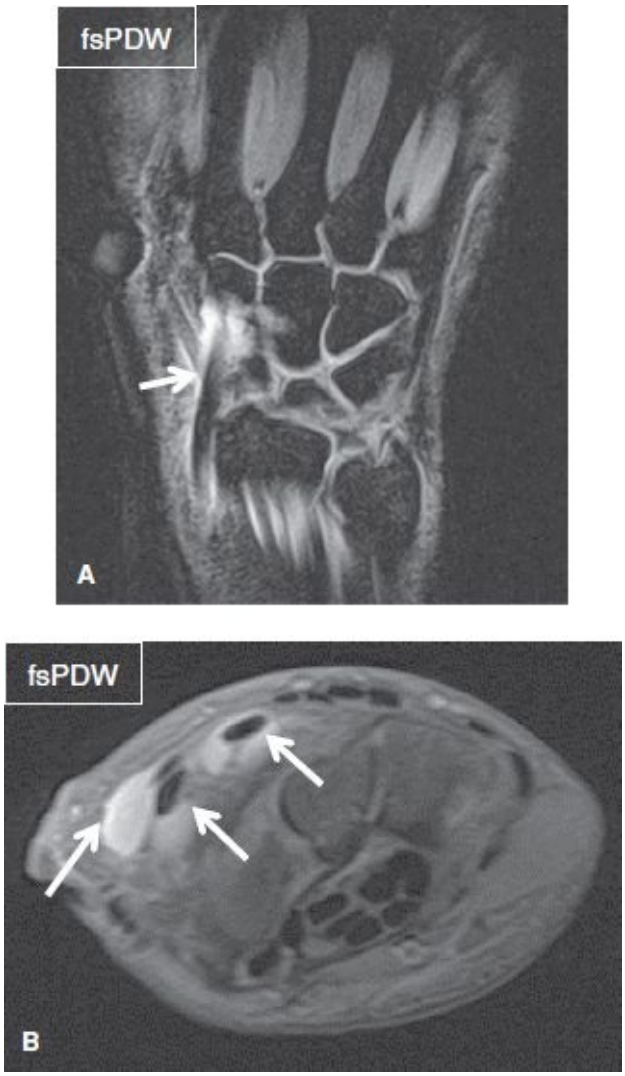

Fig. 50: Distal intersection (decussation) syndrome. Coronal **(A)** and axial **(B)** images reveal tenosynovitis of the extensor compartment II and III (*arrows*) at the level where they cross each other.

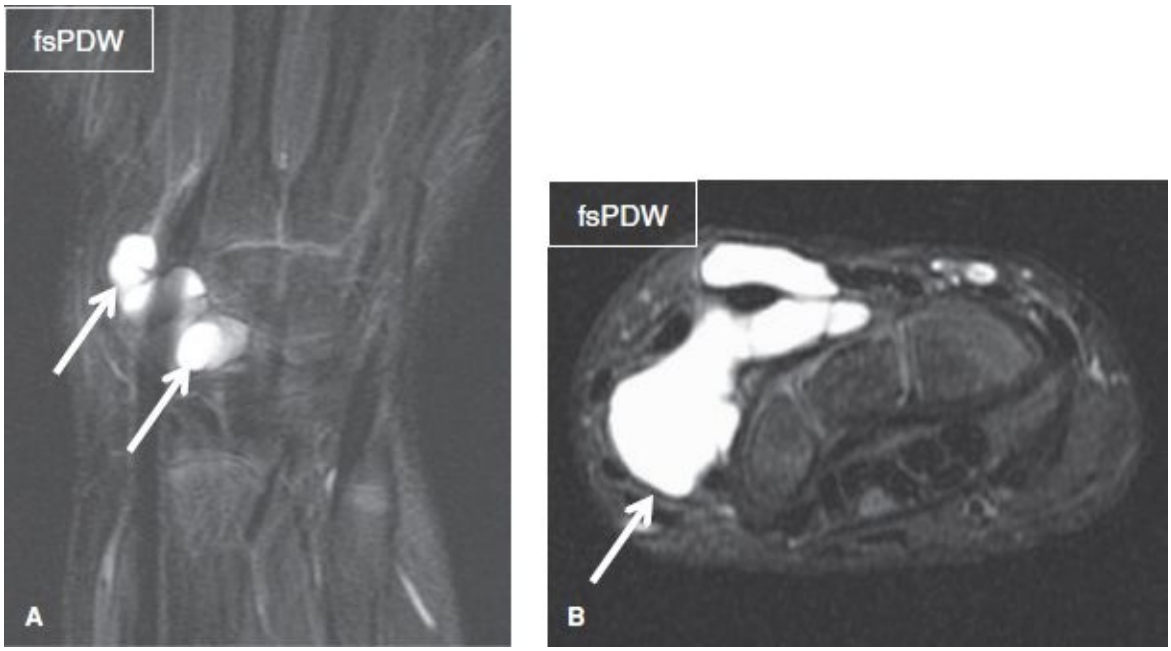

Fig. 51: Distal intersection (decussation) syndrome. Coronal **(A)** and axial **(B)** images reveal a large ganglion cyst (*arrows*) projecting between and around the extensor tendons of

compartments II and III and probably formed as a consequence of chronic friction.

The ECU tendon courses through a groove on the ulnar side of the distal end of the ulna and is held in position by a band of collagen fibers, which is referred to as the ECU subsheath. The subsheath is 1.5 to 2 cm long and is located near the ulnar aspect of the ulnar origin of the TFCC. The ECU tendon sheath is not evident on MR images unless it is filled with fluid. The ECU tendon lies within its groove in the neutral position and pronation and subluxes in supination when there is subsheath rupture (Fig. 52). Minimal perched appearance on the ulnar styloid process can be a normal or asymptomatic variant. Symptomatic subluxations and dislocations are commonly seen in cases of ulnar styloid process fractures, adjacent fascial edema, underlying ECU tendon abnormality, tenosynovitis, and peripheral TFCC tear. Another normal variant should be kept in mind to avoid overdiagnosing ECU pathology. Two heads (humeral and ulnar) of ECU tendon can have a little gap at the wrist, which may mimic a split tear or tendinosis.

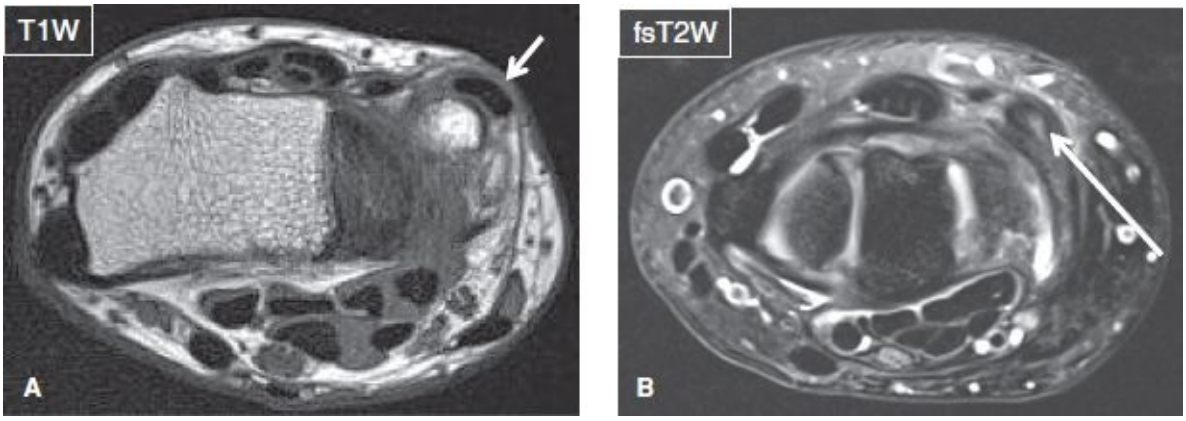

Fig. 52: Extensor carpi ulnaris tendon pathology. Axial images from different cases. **A:** The extensor carpi ulnaris tendon (*arrow*) has been displaced out of its ulnar groove (perched tendon). It can be seen as an asymptomatic variant or can be symptomatic. **B:** A longitudinal split tear (*arrow*) is evident in the extensor carpi ulnaris tendon.

FLEXOR COMPARTMENT:

Flexor retinaculum: [<Normal> <Thickened / Bowed / Discontinuous>]

Flexor tendons: [<Normal / Tenosynovitis / Tendinosis / Tear>]

Carpal tunnel: [<Normal> <Effaced deep fat pad>]

Median nerve: [<Normal> <Hyperintense> <Proximal enlargement with distal flattening>]

Guyon canal: [<Normal> <Hyperintense ulnar nerve>]

Similar to the extensor tendons, the flexor tendons originate in the forearm, cross the wrist

under the flexor retinaculum or adjacent to it, and insert onto the small bones of the hand. They are best evaluated on axial images, where they normally exhibit homogeneous low signal intensity and trace fluid in their sheaths. The flexor retinaculum attaches at the pisiform, hook of hamate, scaphoid tuberosity and trapezium ridge and is normally flat or minimally bulging volarly. A total of nine tendons traverse the carpal tunnel (passing under the flexor retinaculum and its superficial thickening, the transverse carpal ligament), which include the four deep flexor digitorum profundus (FDP) tendons, the four superficial flexor digitorum superficialis (FDS) tendons, and the single flexor pollicis longus (FPL) tendon (Fig. 53).

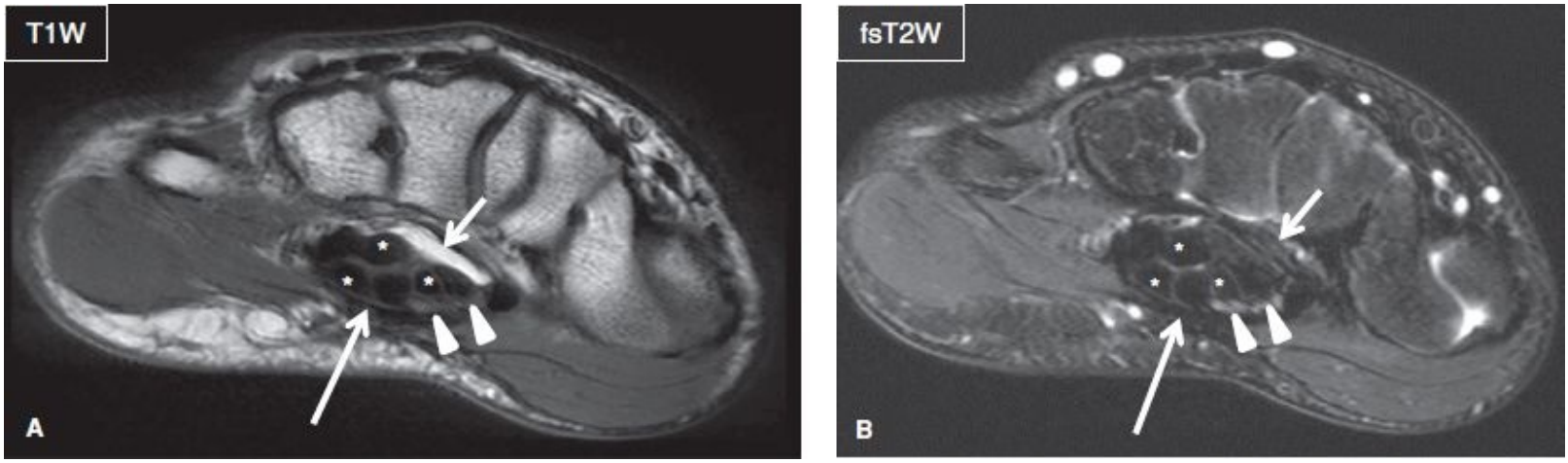

Fig. 53: Normal structures of the flexor compartment at the level of the carpal tunnel. Axial images **(A, B)** demonstrate the flexor tendons (some of them designated with *asterisks*), the flexor retinaculum (*long arrows*), the fat pad (*short arrows*) at the roof of the carpal, and a congenitally bifid median nerve (*arrowheads*).

The FDP originates from the proximal ulna and inserts onto the bases of distal phalanges of the index, middle, ring, & little fingers. The FDS arises from the medial epicondyle and coronoid process of the ulna and inserts onto the middle phalanges of index, middle, ring, & little fingers. The FPL originates from the proximal radius, coronal process and interosseous membrane and inserts onto the bases of distal phalanx of the thumb. The pronator quadratus arises from the medial distal volar ulna and inserts onto the lateral distal dorsal radius. The flexor carpi radialis originates from the medial epicondyle and inserts on the bases of the second and third metacarpal bones. The palmaris longus originates at the medial epicondyle and inserts on the volar flexor retinaculum and aponeurosis. The flexor carpi ulnaris arises from the medial epicondyle and inserts on the pisiform, continuing distally as pisohamate and pisometacarpal ligaments. The above muscles are innervated by the median nerve and its anterior interosseous branch.

Abnormal bowing of the retinaculum is seen in carpal tunnel syndrome. Thickening or discontinuity of the retinaculum is indicative of prior injury or surgery. One should look for flexor tenosynovitis, tendinosis, or tendon tears, which more commonly involve the flexor carpi radialis (located near the radial artery), the palmaris longus (situated centrally under

the subcutaneous tissues), and the flexor carpi ulnaris (located adjacent to the ulnar artery) tendons (Figs. 54, 55). The ulnar bursa encases the FDS and FDP tendon sheaths whereas the radial bursa encases the FPL tendon sheath. The above bursae arise about an inch proximal to the flexor retinaculum and extend into the fingers, thereby limiting the spread of disease, such as collections or infection in the respective compartments. A horseshoe-shaped abscess can be seen involving the forearm and the hand. Because the flexor tendon sheaths of the flexor pollicis longus and the FDP of the little finger extend to the level of the distal forearm, they can rupture and communicate in Parona's space to create a horseshoe-shaped abscess. This requires an aggressive debridement involving digits as well as Parona's space. Flexor tendons may be involved in direct or indirect injuries and tendinosis and, their tears appear similar to the appearances seen with other tendons. Uncommonly, one would see calcific tendinitis with adjacent partial tears of the involved tendon (Fig. 56).

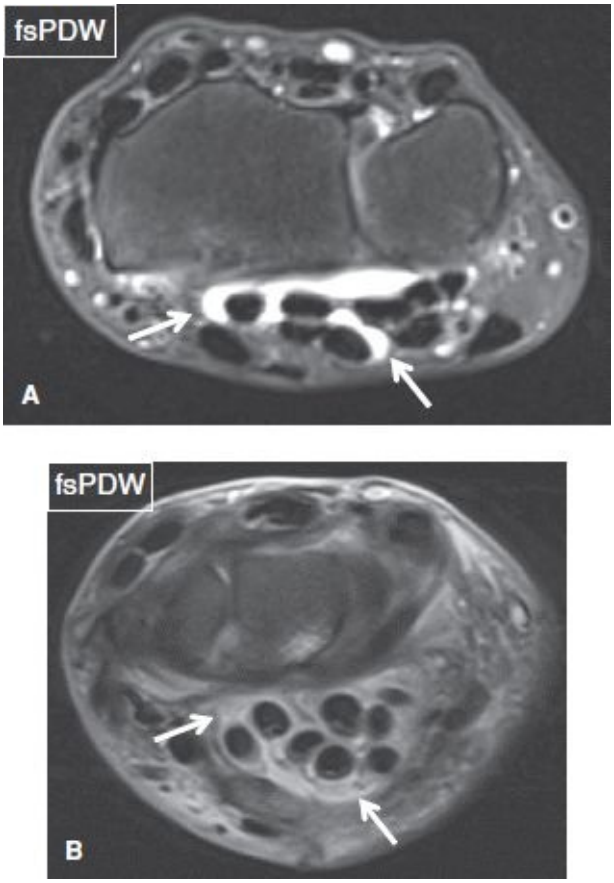

Fig. 54: Flexor tenosynovitis. Axial images demonstrate moderate (*arrows* in **A**) and large amount (*arrows* in **B**) of fluid within flexor tendon sheaths, in keeping with moderate and severe tenosynovitis, respectively. Case in **(A)** is mechanical tenosynovitis, and case in **(B)** is a case of rheumatoid arthritis.

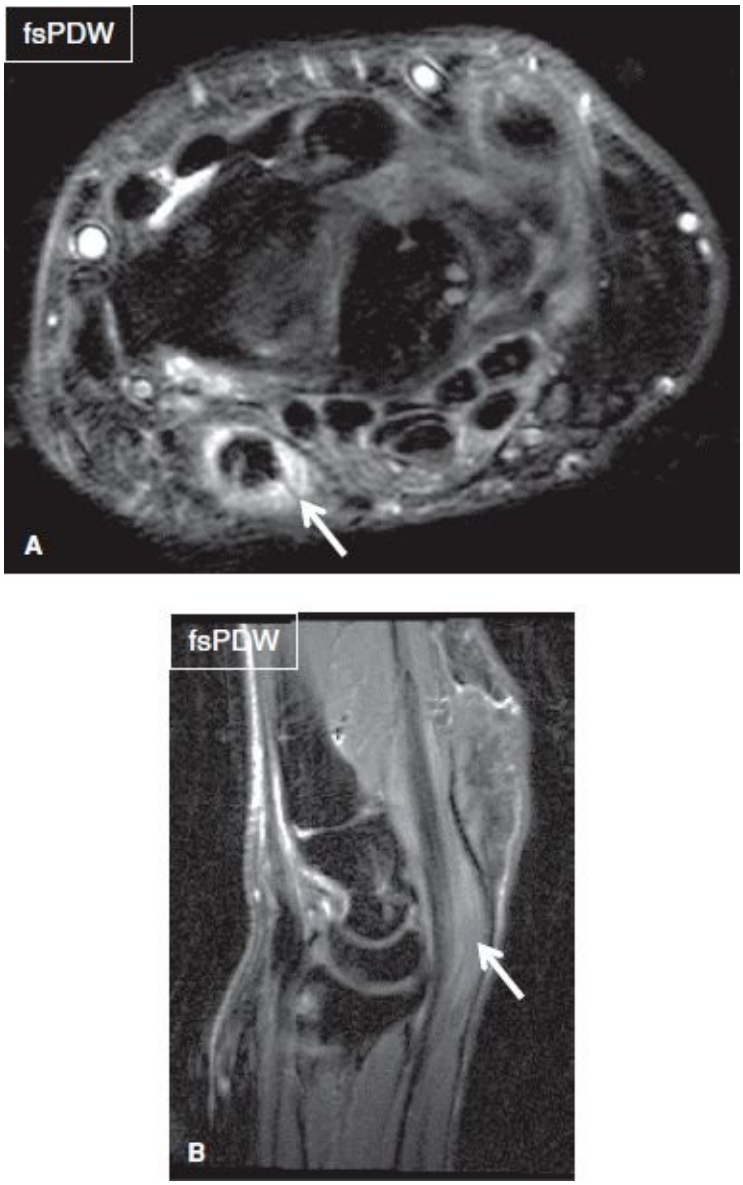

Fig. 55: FPL tenosynovitis. Axial **(A)** and sagittal **(B)** images show moderate tenosynovitis of the FPL tendon with internal hypointense synovial thickening (*arrows*) in this case of rheumatoid arthritis. Also note common flexor and second compartment tenosynovitis confirming the systemic inflammatory process.

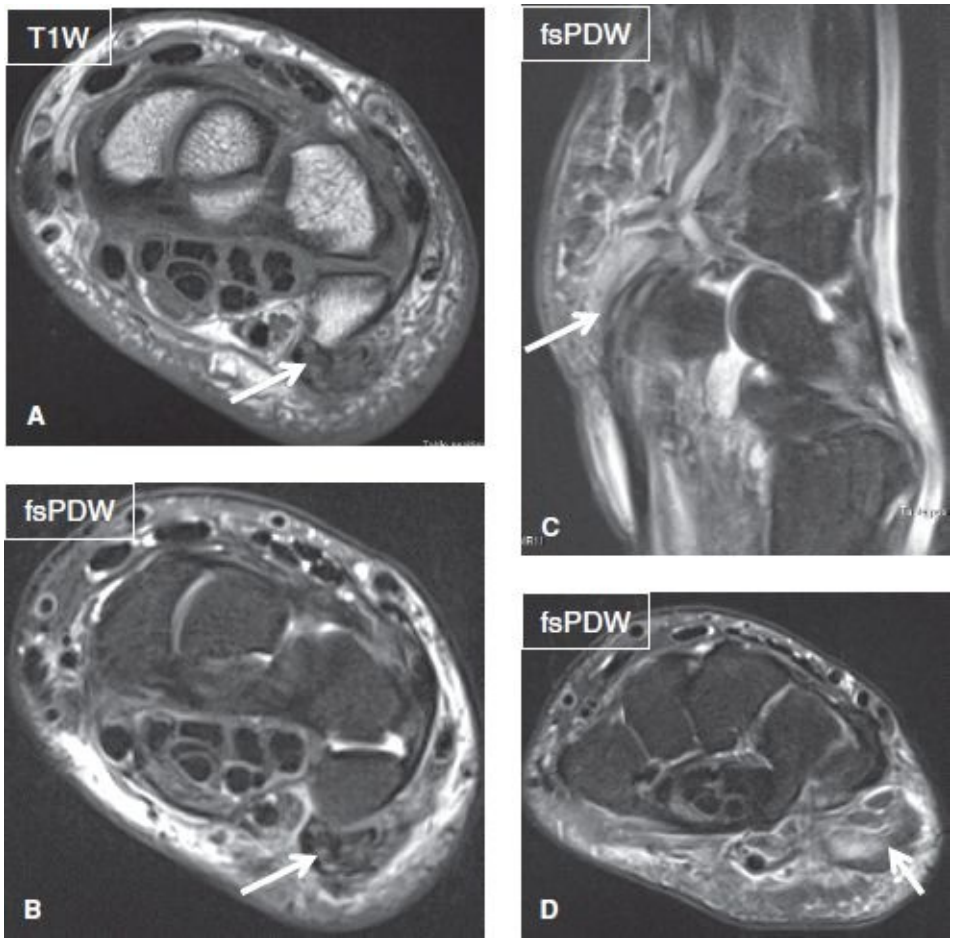

Fig. 56: Calcific tendinitis with tendinosis and split tears of the FCU. Axial **(A, B)** and sagittal **(C)** images exhibit an enlarged and heterogeneous flexor carpi ulnaris tendon (*arrows*), which was associated with regional calcifications on plain film (not shown). **D:** An axial image distal to images in **(A, B)** demonstrates partial tear of the flexor digiti minimi muscle and adjacent fascial edema (*arrow*).

A fat pad is normally present in the dorsal aspect of the carpal tunnel at the pisiform level (Fig. 57). The median nerve is enclosed between the FPL and FDS tendons and changes position within the tunnel on supination (located superficial) and pronation (located deep in the tunnel behind the flexor tendons). The nerve bifurcates proximal to the carpal tunnel in 6% of wrists, within the tunnel in 18%, and distal to the tunnel in the remaining cases. Rarely, it may trifurcate within the tunnel. The thenar muscles include the abductor pollicis brevis (APB, proximal and lateral), opponens pollicis (deep to the APB), flexor pollicis brevis (medial and distal to the APB), and adductor pollicis (further medial and distal to the APB). The median nerve supplies the thenar muscles whereas the ulnar nerve supplies the adductor pollicis and all of the intrinsic muscles of the hand. The median nerve may show mild nonspecific T2 hyperintensity in asymptomatic subjects. In addition, it may be congenitally bifid or assume a course in between the flexor tendons (Fig. 58). In 11% to 20% of wrists, a persistent median artery may be present within the tunnel (Fig. 57).

Fig. 57: Bifid median nerve. Axial images display a bifid median nerve (*short arrows 1* and *2*), as well as a persistent median artery (*long arrows*) in between the two nerve bundles. The patient had undergone partial carpal tunnel release (*open arrow*), and postsurgical fibrous tissue (*asterisk* in **A**) abuts the radial bundle of the nerve (*short arrow 1*), which features enlarged fascicles more than the ulnar bundle, reflecting re-entrapment neuropathy. Denervation edema is evident at the thenar muscles (*asterisk* in **B**). Notice re-emergence of the fat pad deep to the flexor tendons in **(A),** following the transverse carpal ligament release.

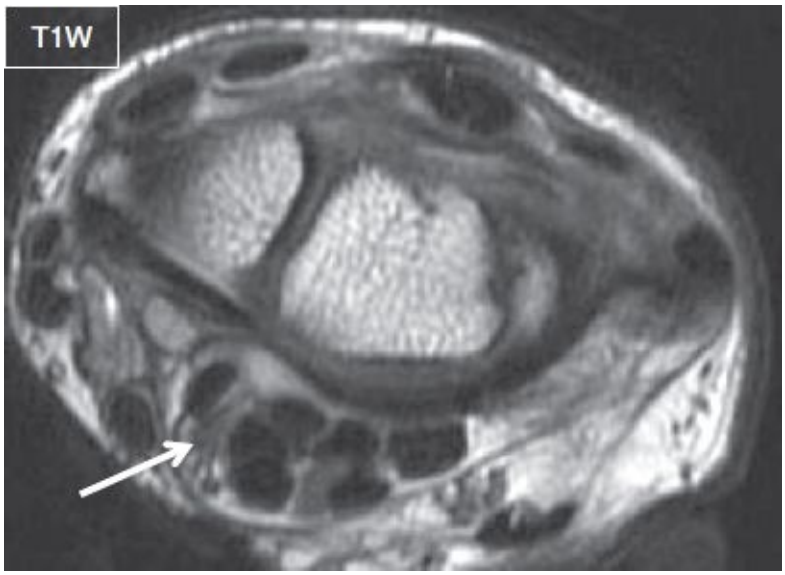

Fig. 58: Intertendinous course of the median nerve. Axial image exhibits the median nerve (*arrow*) coursing between the flexor tendons, a normal variant.

Carpal tunnel syndrome can be suggested when the median nerve is enlarged at the level

of the DRUJ and flattened within the carpal tunnel and concomitantly features abnormal fascicular enlargement and/or high T2 signal, which approaches the signal of the in-plane vascular structures (Figs. 59, 60). The finding becomes even more specific if the signal abnormality extends longitudinally into the median nerve branches, that is, increased longitudinal extent of the signal alteration. Secondary signs include thenar muscle denervation changes, effacement of the deep fat pad in the proximal carpal tunnel at the level of pisiform, abnormal bowing of the flexor retinaculum, and flexor tenosynovitis or any other space-occupying lesion, such as persistent median artery with or without bifid median nerve, bony callous, ganglion cyst, and more proximal origin of the lumbrical muscles within the deep carpal tunnel (22% prevalence), etc.

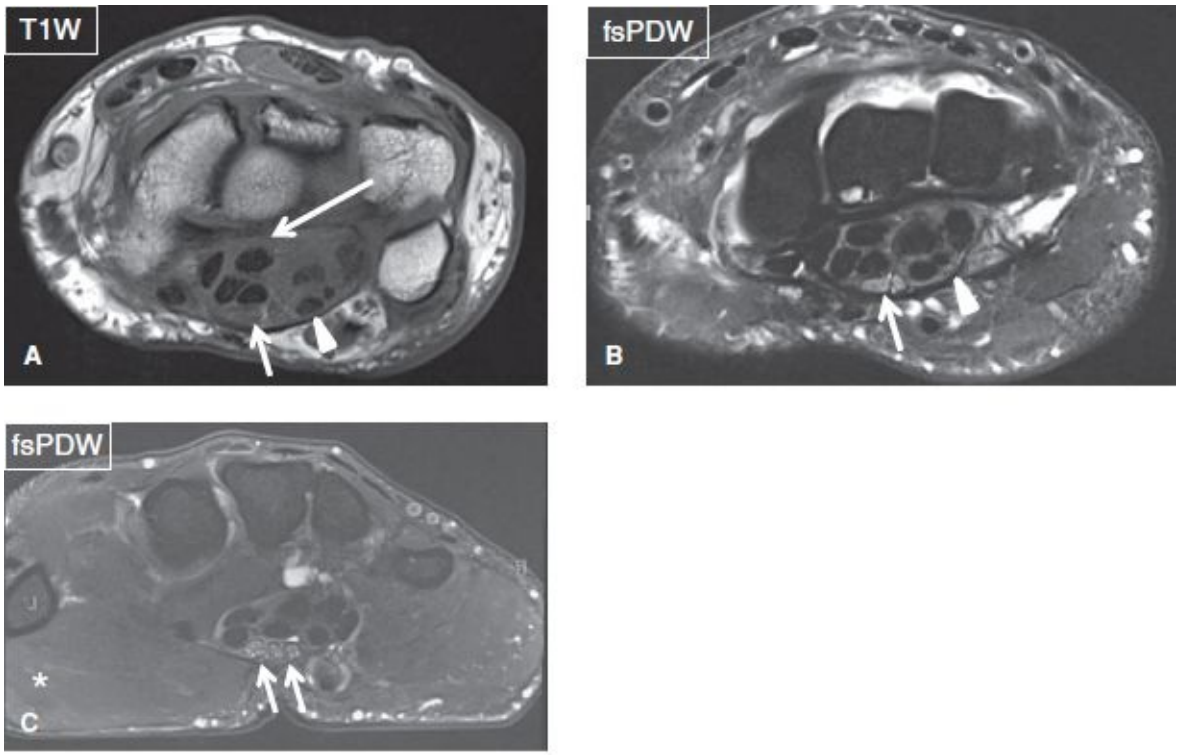

Fig. 59: Carpal tunnel syndrome. Axial images. **A, B:** A bifid median nerve (*short arrows*) is present along with increased bowing of the transverse carpal ligament (*arrowheads*) and effacement of the deep fat pad at the carpal tunnel roof (*long arrow* in **A**). **C:** Distal image shows the median nerve branches (*arrows*) featuring enlarged fascicles and abnormal hyperintensity, reflecting neuropathy. Also note mild denervation edema-like signal (*asterisk*) of the thenar muscles.

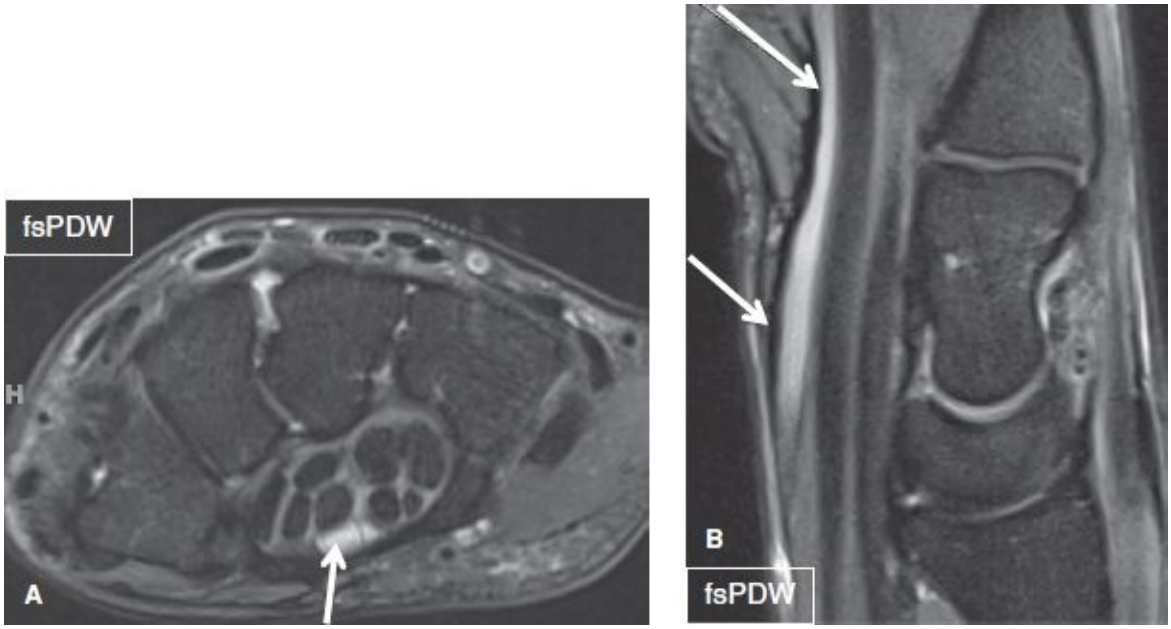

Fig. 60: Acute carpal tunnel syndrome after wrist contusion. Axial **(A)** and sagittal **(B)** images exhibit diffuse abnormal hyperintensity of the median nerve with intraneural edema effacing the fascicles (*arrows*) following a direct contact wrist injury.

In cases of median nerve injury, it is important to report nerve continuity/discontinuity or formation of neuroma in continuity, as the treatment varies whether one would perform decompression, neurolysis, or nerve grafting. Stretch injury or traction neuropathy causes the nerve to become abnormally hyperintense with or without diffuse enlargement and prominent fascicles, though its caliber and signal intensity remains uniformly homogeneous and fascicular architecture is maintained. Acute carpal tunnel syndrome is in the spectrum of traction neuropathy (Fig. 60). Neuroma in continuity appears as focal nerve enlargement and heterogeneous signal intensity due to intraepineurial fibrosis with effaced or disrupted fascicles (Fig. 61). In case of nerve discontinuity, the extent of the nerve gap should be reported, if possible (Fig. 62). Finally, a mass lesion in continuity with the median nerve may reflect a nerve sheath tumor, especially if typical imaging signs are present, such as the tail, fascicular, target, and split-fat signs. The nerve sheath tumor abnormally enhances as compared to neuroma in continuity, which typically does not show appreciable enhancement. Schwannoma of the median nerve is more common than neurofibroma and it more commonly shows cystic changes, calcification, and internal hemorrhage. Other lesions with typical features include intraneural ganglion, which appears as a multilocular cystic lesion; lipoma, which features homogeneous fat signal; and fibrolipomatous hypertrophy, which appears as fibrofatty enlargement of the nerve with prominent fascicular appearance (“coaxial cable” appearance on axial images and “spaghetti appearance” on longitudinal images). The latter entity typically affects the median nerve and can occur in isolation or with macrodystrophia lipomatosa. Hematoma can rarely present as a mass lesion compressing the median nerve (Fig. 63).

Fig. 61: Posttraumatic neuroma of the median nerve branch. Coronal image displays a heterogeneous focal bulbous swelling in keeping with a neuroma in continuity (*long arrow*) of a branch of the median nerve (*short arrow*) in the palm.

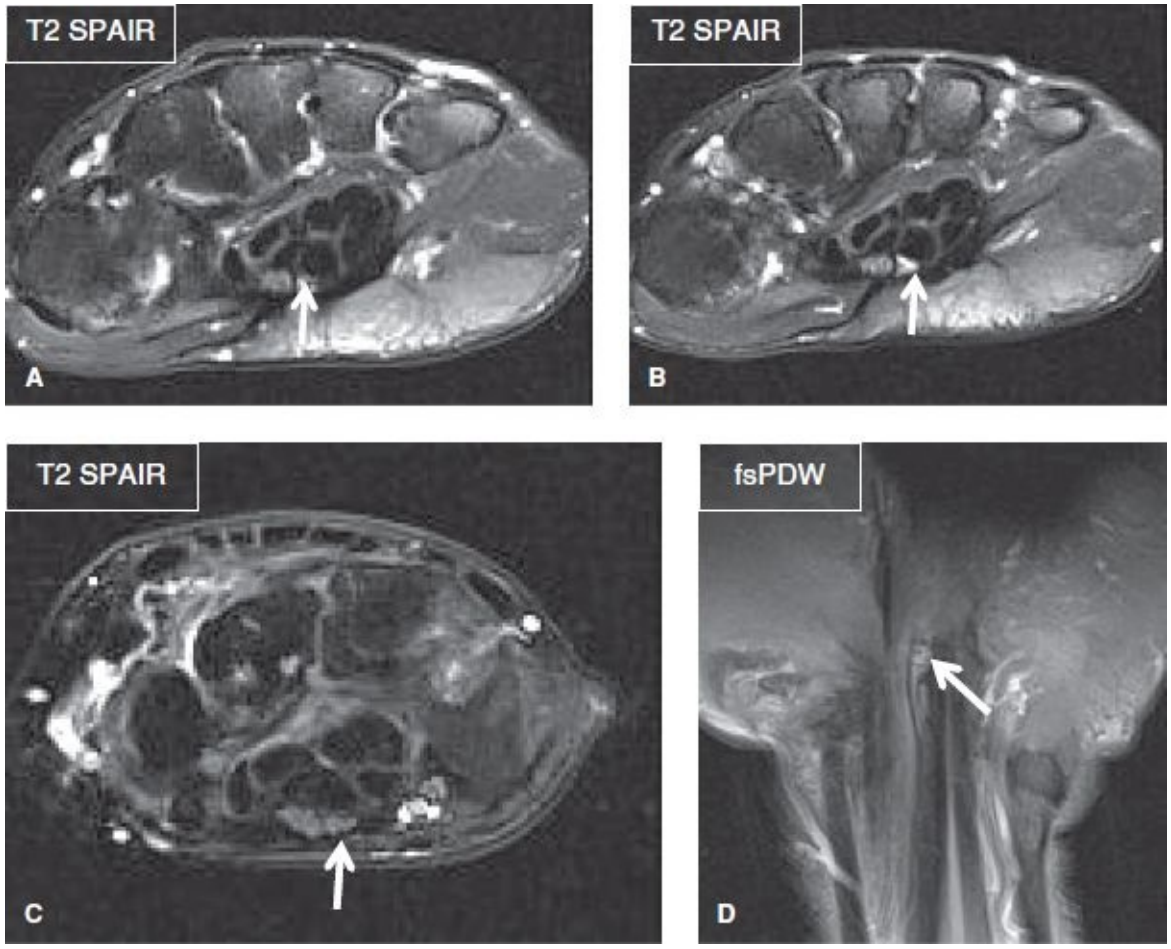

Fig. 62: Neurotmesis of the ulnar bundle of the median nerve. Young woman underwent recent carpal tunnel release, now numb in the middle and ring fingers. **A–C:** Serial axial images show bifid median nerve with end bulb neuromas of the ulnar bundle fascicles (*arrow* in **A**), fluid gap at the iatrogenic transection site (*arrow* in **B**), normal ulnar bundle distally following a gap of 1.1 cm (*arrow* in **C**). **D:** Coronal image shows the end bulb

neuroma (*arrow*).

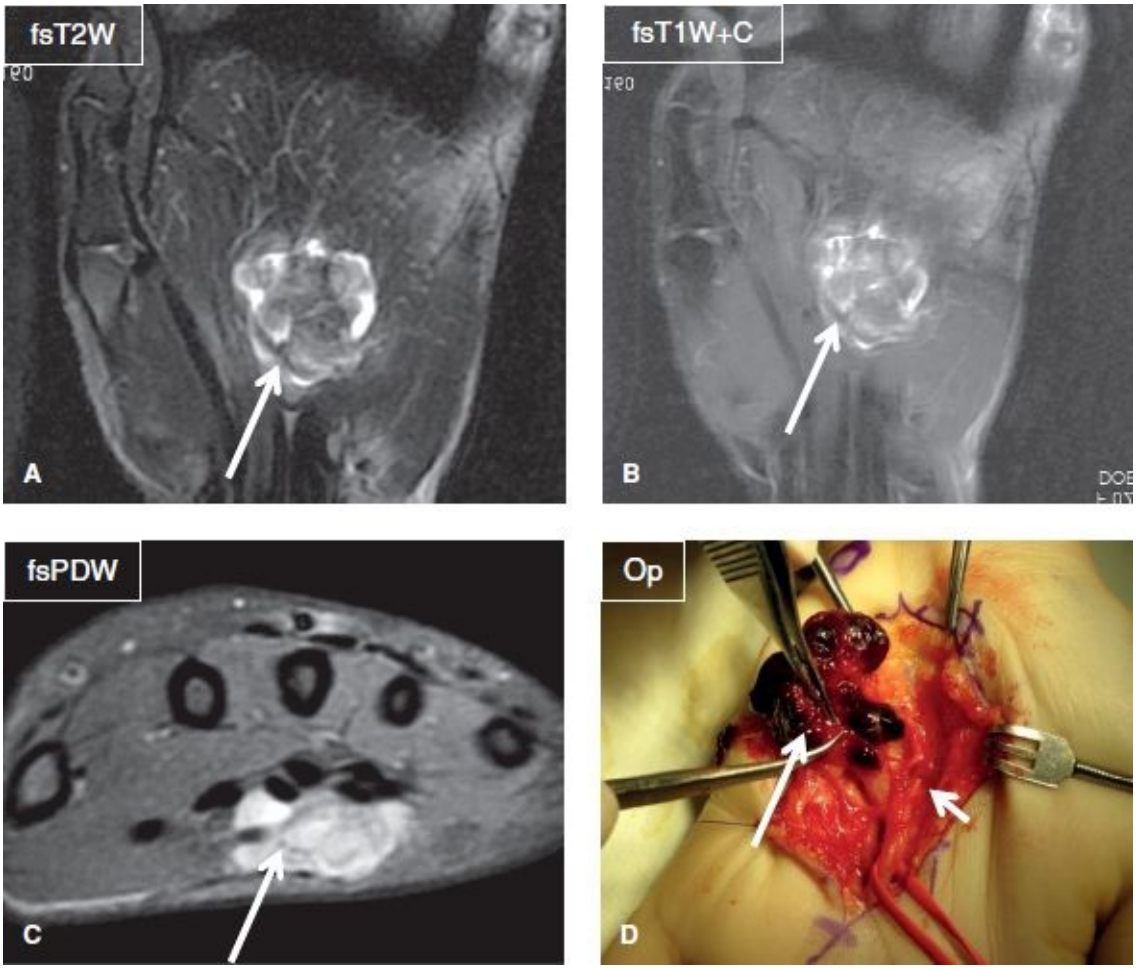

Fig. 63: Hematoma compressing the median nerve. A 20-year-old woman with palmar mass for many months and tingling in fingers. Coronal **(A, B)** and axial **(C)** images show a lobulated heterogeneous peripherally enhancing mass that has invaginated the distal carpal tunnel. **D:** Intraoperative picture shows the hematoma (*long arrow*) and the median nerve (*short arrow*). (Case courtesy Dr Kyung Jin Suh, MD.)

Guyon's canal is a confined anatomic space, which contains the ulnar nerve. The medial border of the canal is formed by the pisiform bone and the hook of the hamate, the roof by the palmar carpal ligament, palmar fascia, and palmaris brevis muscle while the floor is constituted by the FDP tendons, transverse carpal ligament, pisohamate and pisometacarpal ligaments, and opponens digiti minimi muscle. Within the canal, the vessels run superficial and the ulnar nerve deep to the palmar carpal ligament, respectively. Also within the canal, the ulnar nerve divides as follows:

- Superficial branch—first provides motor innervation to the palmaris brevis muscle (located in the subcutaneous and fascial planes) and then divides to provide sensory innervation to the ulnar side of the palm and ring finger, and the entire small finger
- Deep branch—courses more deeply, adjacent to the medial surface of the hook of the hamate and innervates the adductor pollicis, flexor pollicis brevis (deep head), and hypothenar muscles, as well as the interossei and lumbricals to the ring and small fingers

The hypothenar muscles include the abductor digiti minimi (ADM, most medially located), flexor digiti minimi brevis (lateral and distal to the ADM), and opponens digiti minimi (deep and lateral to the ADM). Depending upon the site of entrapment, the symptoms may be sensory, motor, or both.

Various functional causes, such as repeated bicycling or typing on keypads, may lead to ulnar neuropathy. One should look for space-occupying lesions within Guyon's canal, such as ganglion, lipoma, synovial cyst, ulnar artery aneurysm, accessory ADM muscle, etc. (Fig. 64). Symptoms depend on involvement of motor, sensory, or both branches. Imaging findings of ulnar neuropathy include abnormal size of the ulnar nerve (normal diameter = 3–4 mm at the pisiform level); abnormal fascicles that are edematous, disrupted or effaced; and abnormal nerve hyperintensity approaching the adjacent vessel signal intensity. Hyperintensity due to magic angle artifact is common at the sites where the nerve enters the Guyon's canal and where the deep branch of ulnar nerve courses obliquely dorsal to the flexor tendons. Real signal abnormality extends for a longer distance, even if the nerve straightens up along its course and is associated with other findings as above. Secondary signs include regional hypothenar muscle denervation changes (especially of the first interosseous muscle).

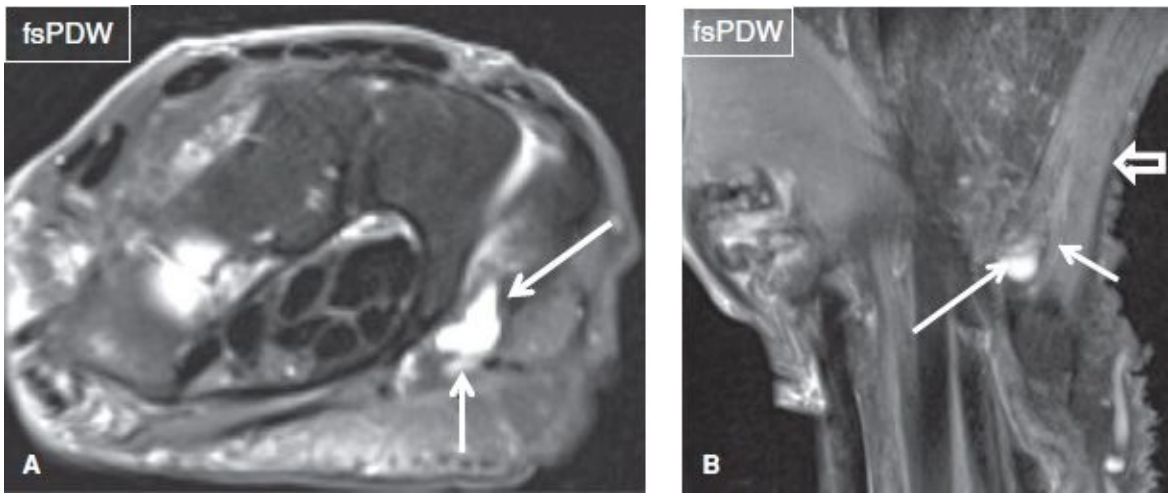

Fig. 64: Ulnar neuropathy. Axial **(A)** and coronal **(B)** images exhibit a ganglion cyst (*long arrows*) flattening the ulnar nerve (*short arrows*), which is abnormally hyperintense, reflecting compression neuropathy. Also note mild denervation edema-like signal of the hypothenar muscles (*open arrow* in **B**).

ARTICULAR:

Thumb–carpometacarpal/Metacarpophalangeal joints: [<Normal> <Osteoarthritis>]

Scaphotrapeziotrapezoidal joint: [<Normal> <Osteoarthritis>]

Pisiform–triquetral joint: [<Normal> <Effusion> <Ganglion>]

One should look for bony productive, cartilage thinning, cystic or erosive changes, and

joint effusion in the small joints of the wrist and other joints included in the field of view, such as the thumb–CMC, MCP, scaphotrapeziotrapezoidal (triscaphe), and PT joints. The most common pathology is osteoarthritis, which predominantly involves the radiocarpal, first CMC, triscaphe, and first MCP joints, and presents as bony productive changes, cartilage thinning and defects, subchondral sclerosis, and subchondral cysts (Fig. 38). The distribution of osteoarthritis usually follows the instability pattern in the wrist, for example, in the commonly acquired SL instability and DISI pattern, it commences at the radioscaphoid joint, progresses to the lunocapitate joint and finally involves the radiolunate joint (Fig. 34).

Rheumatoid arthritis typically involves the wrists bilaterally and symmetrically and is characteristically distributed in the intercarpal, PT, and MCP joints, as well as in the ulnar styloid process. It is associated with diffuse synovial thickening, complex effusion, synovitis and rice body formation. In advanced stage, one would see ligament tears leading to instabilities, such as SL dissociation, VISI, and ulnar-sided carpal translocation (Figs. 10, 23, 44, 54, 5, 65). Role of MRI is to detect the soft tissue and early bony changes not apparent on radiographs; differentiate it from other conditions, such as pigmented villonodular synovitis (PVNS) or synovial chondromatosis; and finally, assess response to immune therapy. In severe cases, rheumatoid nodules may form within the subcutaneous tissues and less commonly in bursae, joints, tendons, or ligaments. These nodules appear isointense to muscle on T1W images and hypointense or hyperintense on T2W images and demonstrate intense enhancement, which is homogeneous in solid nodules and ring shaped in cystic ones.

Calcium pyrophosphate depositional (CPPD) arthropathy is associated with multiple well-defined intraosseous cysts, radiocarpal and capitolunate joint space narrowing, MCP joint involvement, and TFCC chondrocalcinosis. Plain film correlation is useful in arriving at the final diagnosis. PVNS is associated with joint effusion, hypointense nodular mass-like synovial thickening, hemosiderin deposition (blooming on gradient-echo imaging) and eccentric well-defined carpal erosions, and/or bone marrow edema (Fig. 66). Other condition that can mimic RA or PVNS, is amyloidosis. It can also show hypointense synovial thickening or masses with cystic bony changes. Amyloidosis is associated with underlying chronic systematic condition, such as myeloma or chronic renal insufficiency (Fig. 67). Juvenile idiopathic arthritis is seen in young children and is associated with soft tissue swelling, large joint involvement, accelerated maturation, enlarged carpal bones with irregular margins, and ankylosis. As elsewhere in the body, septic arthritis demonstrates complex and, usually large joint effusion with associated synovitis (synovial thickening and intense contrast enhancement), with perisynovial fascial edema and/or fluid (Fig. 68).

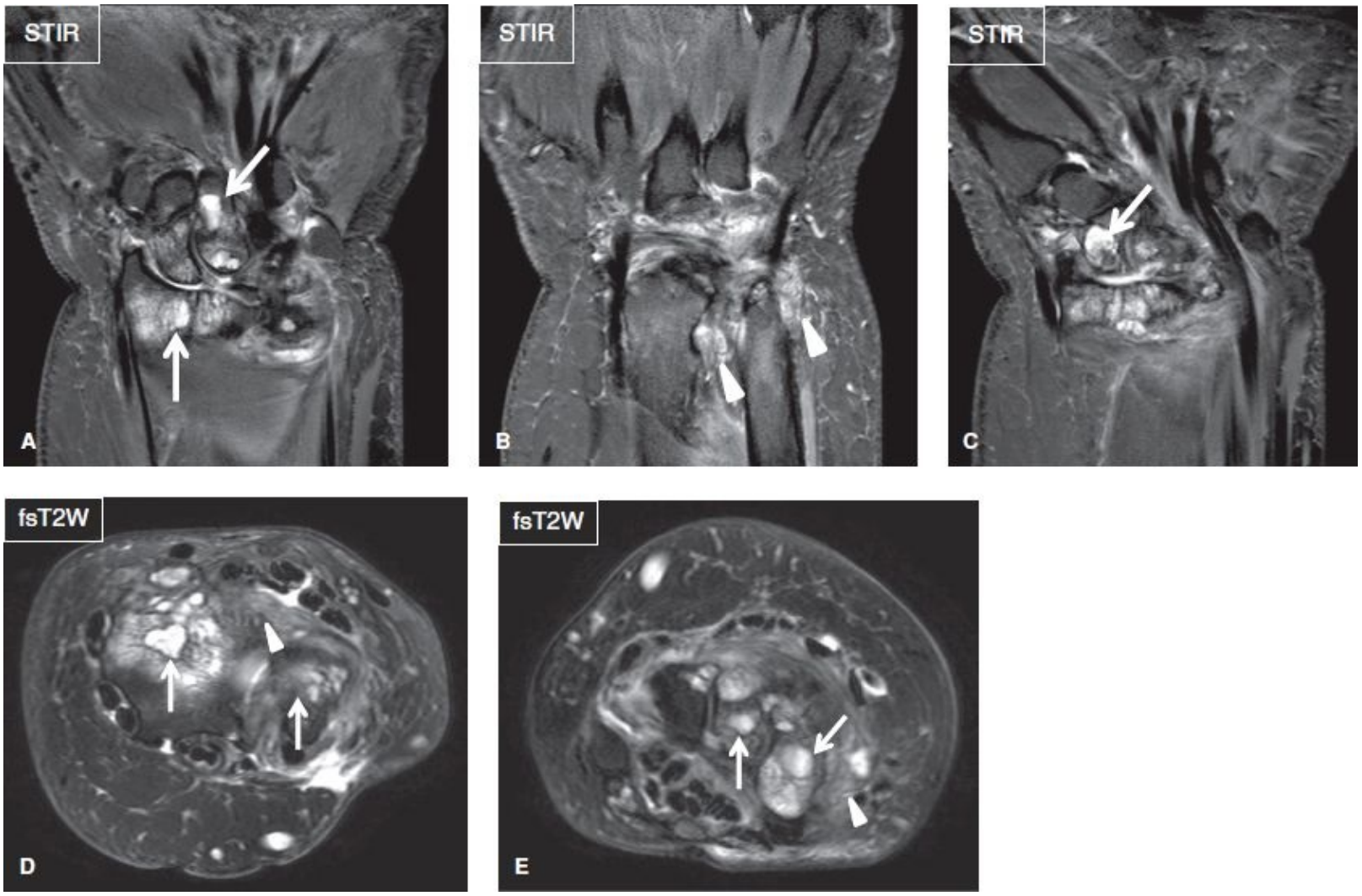

Fig. 65: Rheumatoid wrist. Coronal **(A–C)** and axial **(D, E)** images demonstrate severe, end-stage RA with numerous cystic erosive changes (*arrows*) along with mild tenosynovitis and moderate synovial proliferation (*arrowheads*).

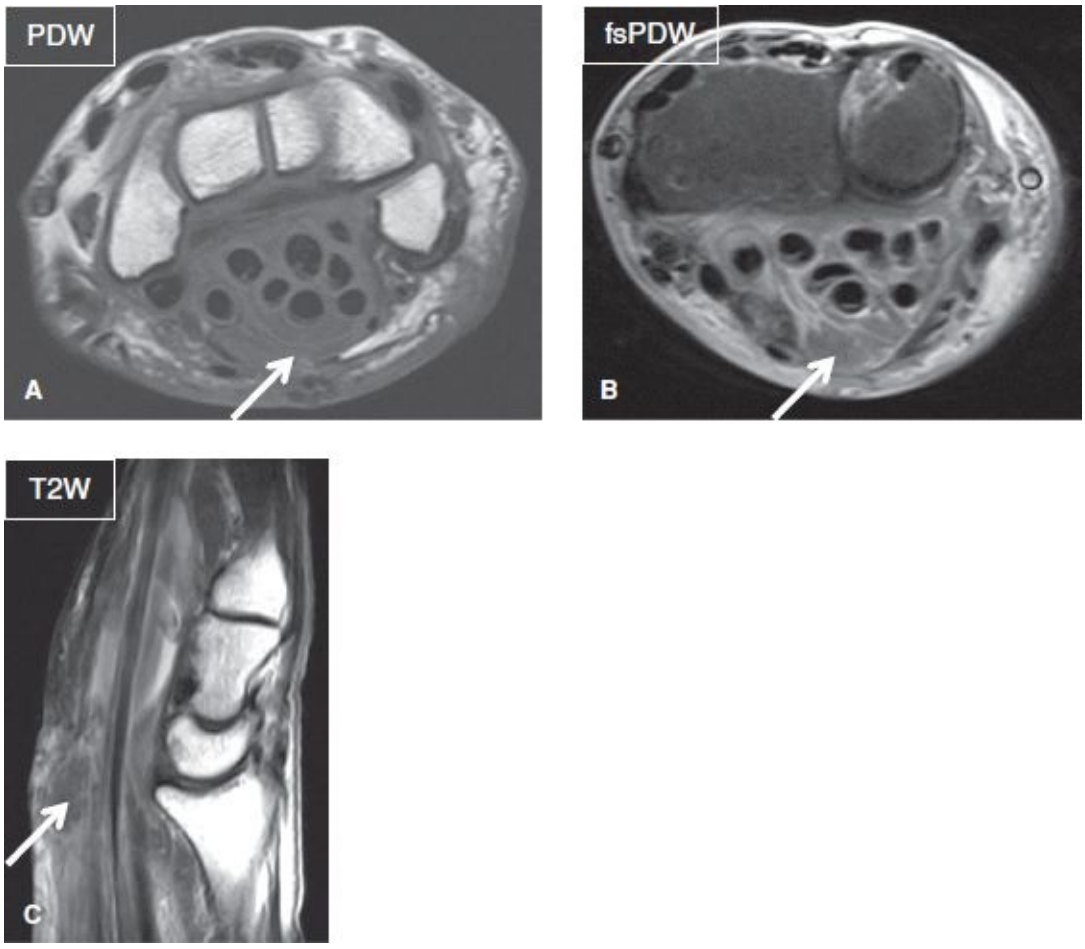

Fig. 66: Pigmented villonodular synovitis. Axial **(A, B)** and sagittal **(C)** images display long flexor tenosynovitis. Also note focal hypointense nodular mass in the volar aspect of the carpal tunnel (*arrows*) in this biopsy-proven monoarticular PVNS case.

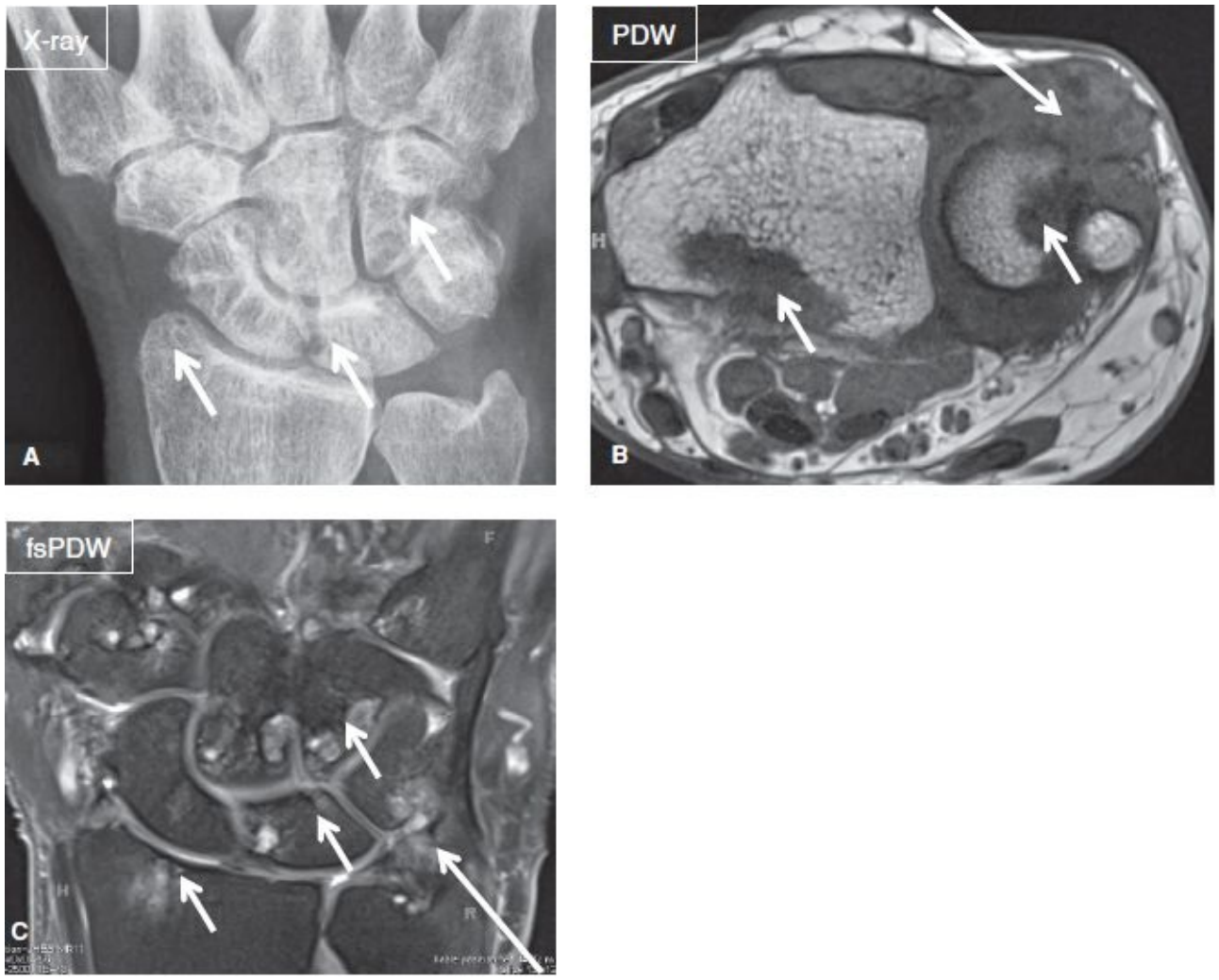

Fig. 67: Amyloid wrist arthropathy. Anteroposterior radiograph **(A),** axial **(B),** and coronal **(C)** MR images reveal multiple subarticular cystic changes with internal hypointensities (*short arrows*) in the radius, ulna, carpal, and metacarpal bones, along with heterogeneous tissue of intermediate-to-dark signal (*long arrows* in **B, C**) surrounding the ulna. The patient had underlying chronic renal insufficiency and the lesions likely represent amyloid deposits.

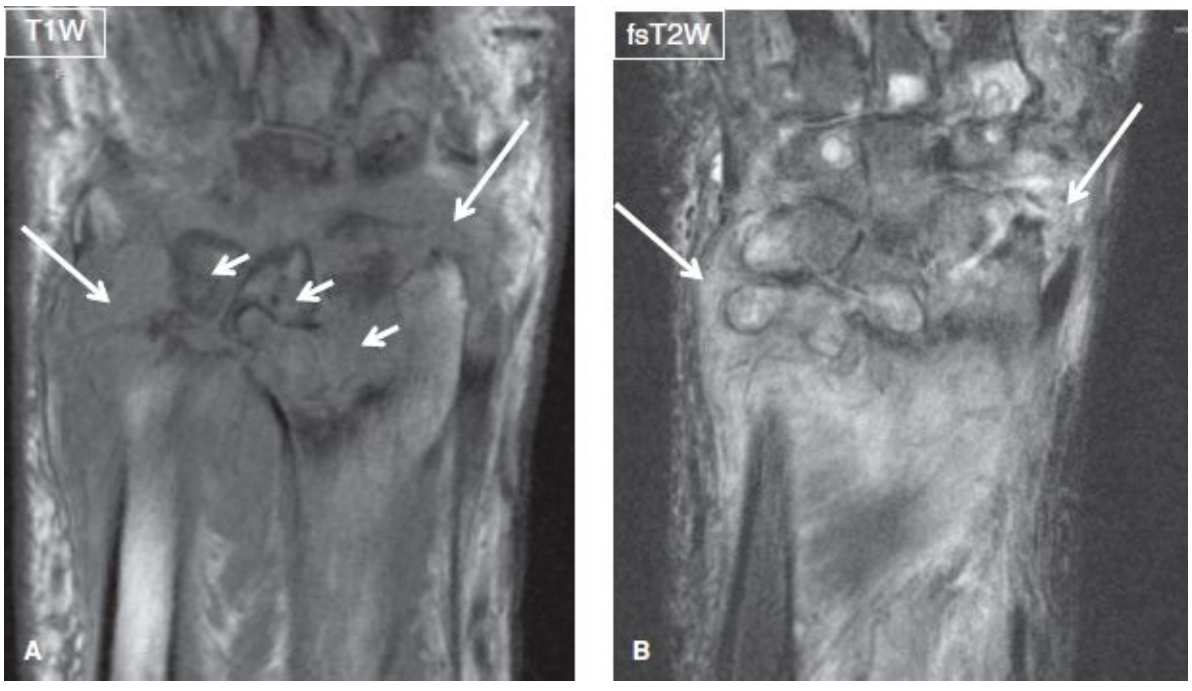

Fig. 68: Septic arthritis. Coronal images **(A, B)** demonstrate heterogeneous moderate carpal joint effusion (*long arrows*). Low T1 marrow signal of affected bones (*short arrows*) with cortical erosions indicate osteomyelitis. Also note diffuse cellulitis and myositis in keeping with widespread infection in this case.

EXTRINSIC LIGAMENTS:

Radial collateral ligament/Ulnar collateral ligament: [<Normal> <Attenuated> <Acute Sprain>]

Dorsal intercarpal ligament/Volar extrinsic ligaments: [<Normal> <Acute Sprain>]

The dorsal and volar radioulnar ligaments originate from the dorsal and volar distal rims of the sigmoid notch of the radius, course toward the ulna and subdivide into superficial and deep components. The superficial limbs attach to the midportion of the ulnar styloid and the deep limbs to the ulnar fovea. The radioulnar ligaments are best assessed on axial images, where they normally feature homogeneous low signal intensity on all pulse sequences (Fig. 69). The DRUJ alignment is best assessed on axial images, as described above. The ulna subluxes volarly in supination and dorsally in pronation with DRUJ instability. One should look for acute sprains or prior injury-related deficiency, attenuation, or thickening of these ligaments. Volar radioulnar ligament is insufficient in dorsal subluxation at DRUJ and vice vera. MRI is good for depiction of static malalignment, while 4D CT currently (Fig. 70) and in future, kinematic MRI (Fig. 71) would be useful in dynamic depiction of these lesions.

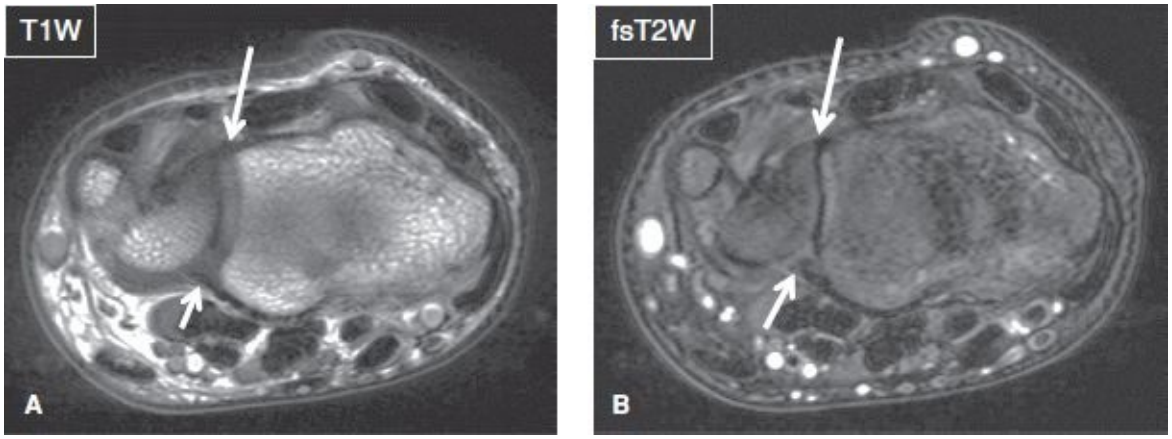

Fig. 69: Normal distal radioulnar ligaments. Axial images **(A, B)** show the dorsal (*long arrows*) and volar (*short arrows*) radioulnar ligaments attaching from bone to bone.

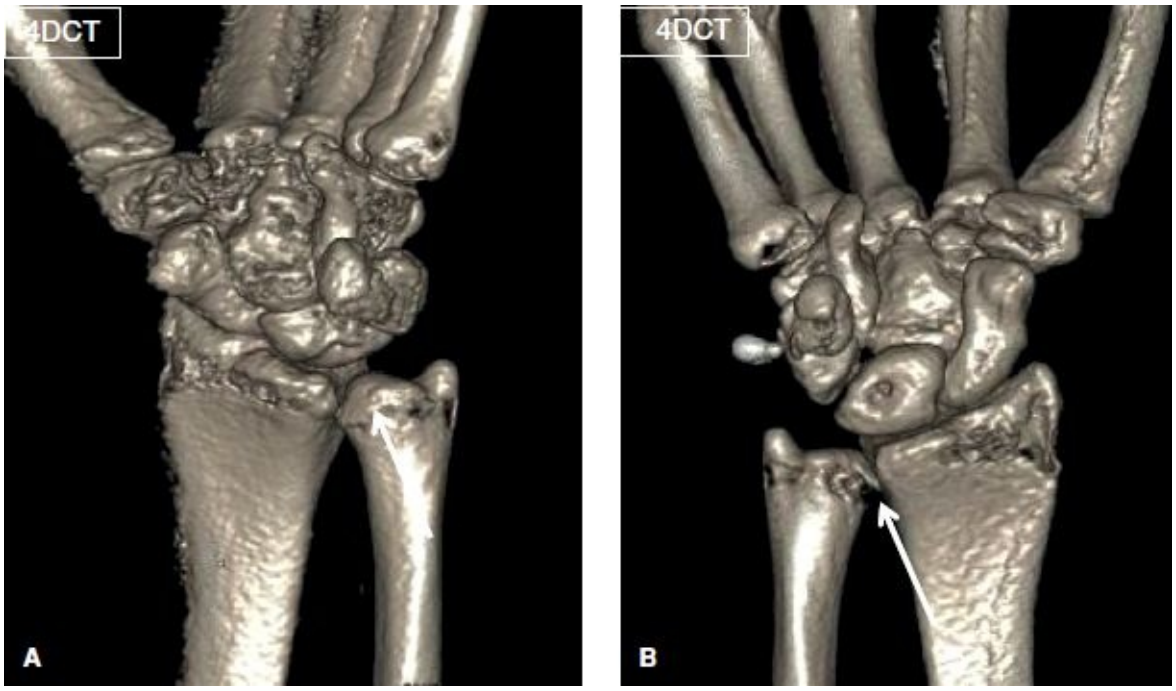

Fig. 70: Four-dimensional CT wrist showing DRUJ subluxation. Coronal volume rendered captures **(A, B)** from kinematic 4D CT from a 320 slice CT scanner show dorsal ulnar subluxation at the DRUJ (*arrows*) on pronation in the right wrist **(A)** versus normal DRUJ on the left side **(B).**

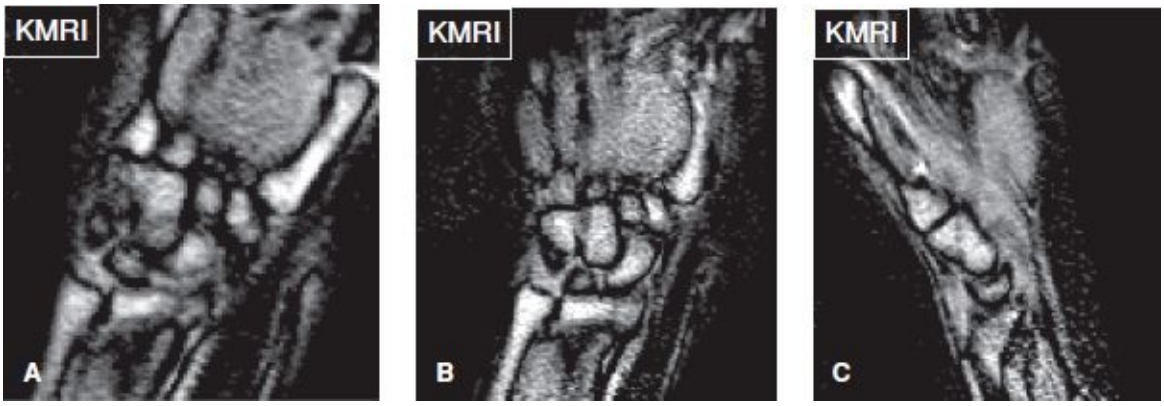

Fig. 71: Kinematic MRI. Multiple captures from a real-time kinematic MRI showing various positions of the wrist during radioulnar deviation **(A, B)** and flexion–extension **(C)** maneuvers performed on a closed 1.5T scanner.

The UCL and the radial collateral ligament (RCL) are thickenings of the ulnar and radial wrist capsules, respectively. The UCL arises from the ulnar styloid process and inserts onto the triquetrum and pisiform, restricting radial deviation of the wrist. The RCL originates from the radial styloid process and has two limbs that insert on the scaphoid waist and trapezium, restricting ulnar deviation of the wrist (Fig. 72). Both are best seen on the coronal images, and secondarily on the axial images, as dark band-like thickenings of the wrist capsule.

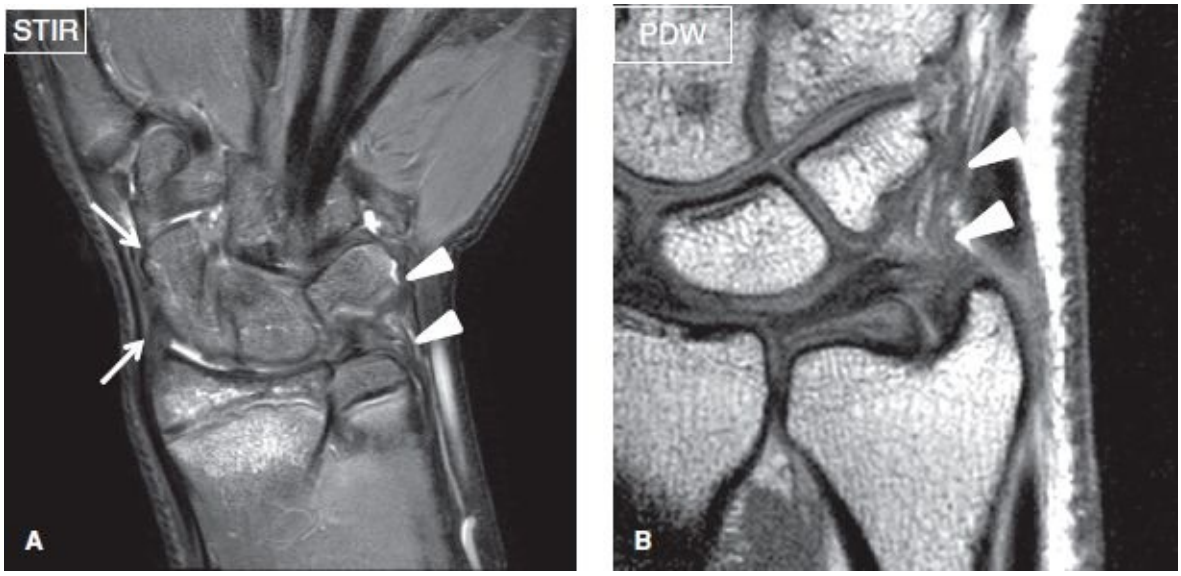

Fig. 72: Wrist collateral ligaments. Coronal images exhibit the radial (*arrows*) and ulnar (*arrowheads*) collateral ligaments.

RCL injuries are common in falls, in which force is exerted on the outstretched hand and are associated with SL ligament tears whereas injuries of the UCL are usually associated with TFCC injuries. Ligament injuries are described as grade I, II, and III sprains; or as partial or complete stripping from the proximal or distal attachments. Other findings include avulsive cystic changes at the ligament attachments with or without thickening, attenuation or deficiency of the ligament, or even ganglion formation (Figs. 34, 35, 73, 74). Small avulsed fragments at the RCL attachment of the scaphoid waist can be mistaken for significant scaphoid fractures by unwary radiologist on radiographs. MR images show the ligament injury as well and confirm the nature of such fractures.

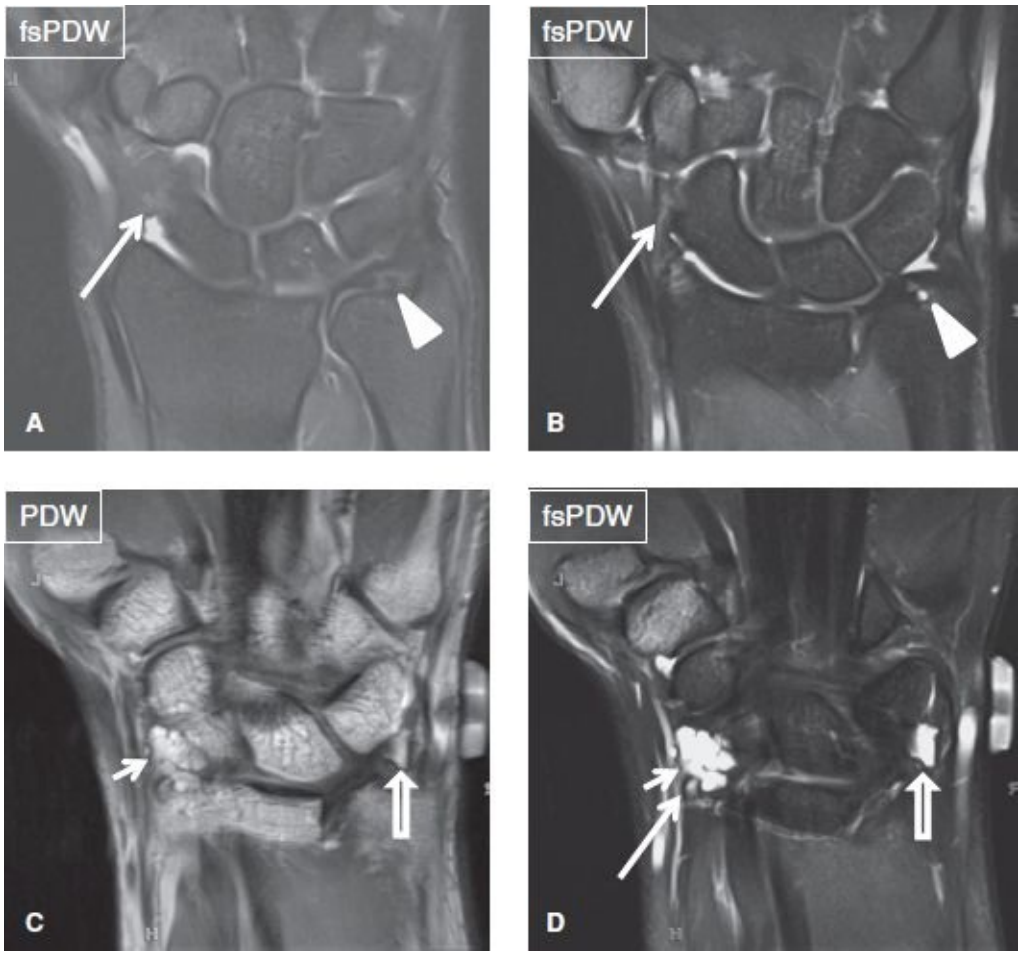

Fig. 73: Radial collateral ligament injury. Coronal images **(A–D)** demonstrate partial tears of the radial collateral ligament (*long arrows*) and foveal attachment of the triangular fibrocartilage (*arrowheads*) with underlying cystic changes. There is also ganglion formation in relation to the radial (*short arrows*) and ulnar (*open arrows*) collateral ligaments.

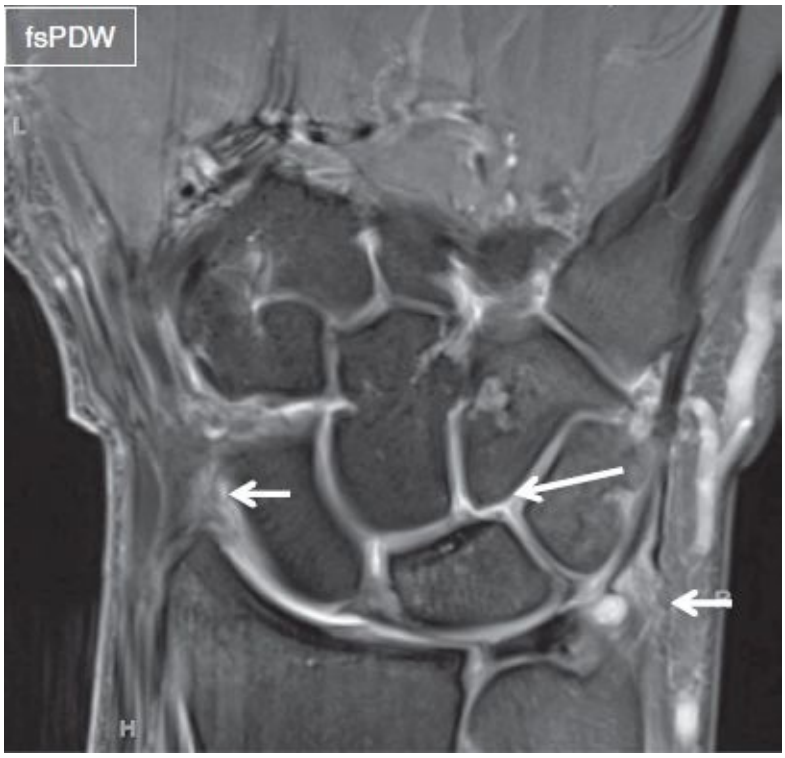

Fig. 74: Chronic radial and ulnar collateral ligament injuries. Coronal image shows an

attenuated radial and ulnar collateral ligament (*short arrows*). Also note incidental hamate–lunate chondromalacia (*long arrow*) and small ganglion related to peripheral TFCC injury.

The volar and dorsal aspects of the wrist feature multiple additional ligaments, which are variably named, but controversy still exists regarding their naming and clinical significance. However, it is generally believed that dynamic wrist instability requires at least partial injury of these ligaments whereas static instability occurs with their full-thickness disruption. According to most authors, the volar extrinsic ligament complex includes the radioscaphocapitate, long radiolunate (radiolunotriquetral), and short radiolunate ligaments. These ligaments connect the palmar aspect of the distal radius to the carpal bones and are best seen on sagittal images at the scaphoid and lunate levels, respectively (Fig. 75). The radioscapholunate neurovascular bundle courses alongside the volar extrinsic ligament complex. The dorsal extrinsic ligament complex (aka DIC ligament) is an important restraint against volar instability and consists of the radiotriquetral, dorsal intercarpal and ulnocarpal ligaments. It is further bound by the extensor retinaculum, with the extensor tendons situated between the latter and the DIC. The DIC is best seen on sagittal and axial images, where it appears as thickening of the dorsal wrist capsule. The normal volar and dorsal extrinsic ligaments show homogeneous low signal intensity on PDW images obtained with or without fat suppression and may feature wavy contours, depending on the position of the wrist (Fig. 76). Similar to other ligaments in the body, these ligament injuries are again described as grade I, II, or III sprains (Fig. 77). More commonly, one will encounter avulsive cystic changes at their bony attachments or ganglion in relation to these ligaments due to prior partial ligament and co-existent adjacent synovial injuries (Figs. 78–80).

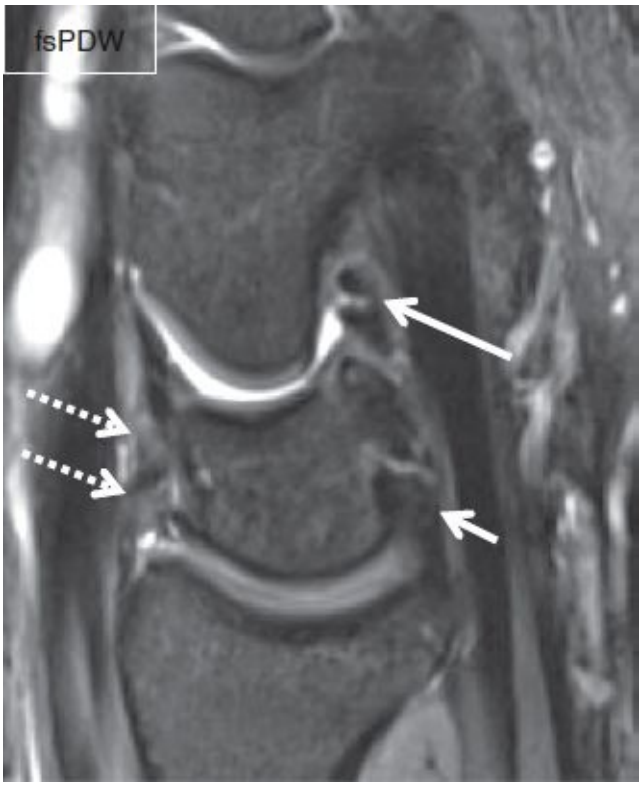

Fig. 75: Normal intrinsic ligaments. Sagittal image exhibits normal short (*small arrow*) and long (*long arrow*) radiolunate ligaments, and dorsal intercarpal ligament (*dotted arrows*).

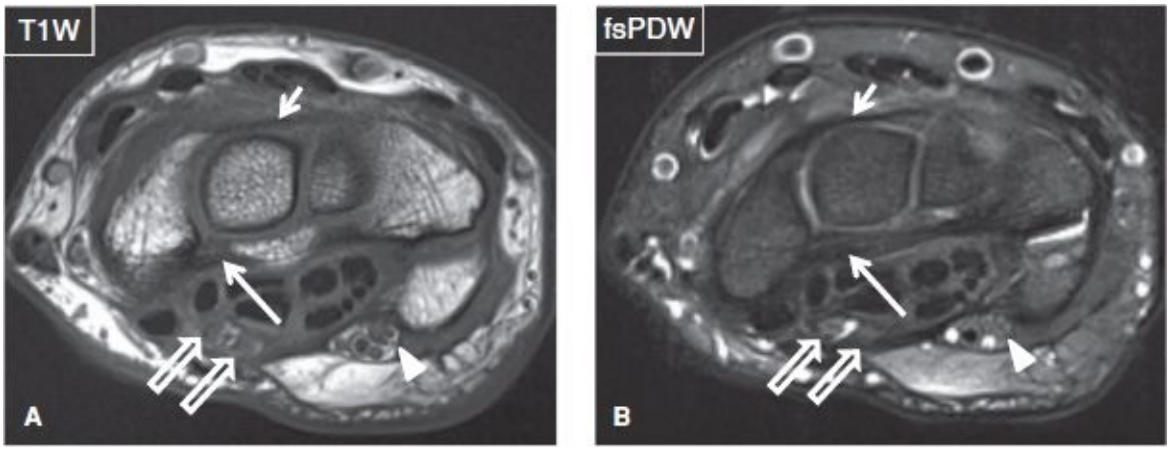

Fig. 76: Normal extrinsic ligaments. Axial images **(A, B)** show normal dorsal (*short arrows*) and volar (*long arrows*) intercarpal ligaments. Also note normal ulnar nerve (*arrowheads*) and bifid medial nerve (*open arrows*) with a persistent median artery.

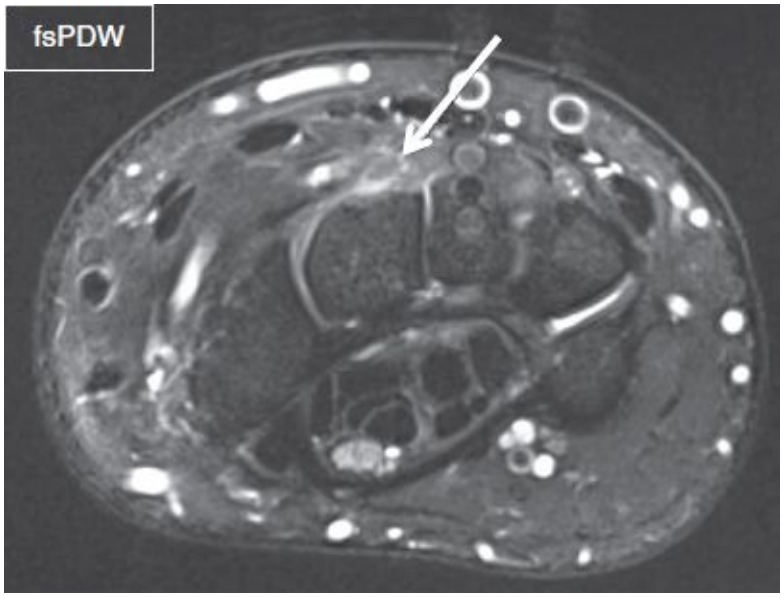

Fig. 77: Dorsal intercarpal ligament injury. Axial image exhibits subacute full-thickness tear (*arrow*) of the dorsal intercarpal ligament with adjacent synovial thickening.

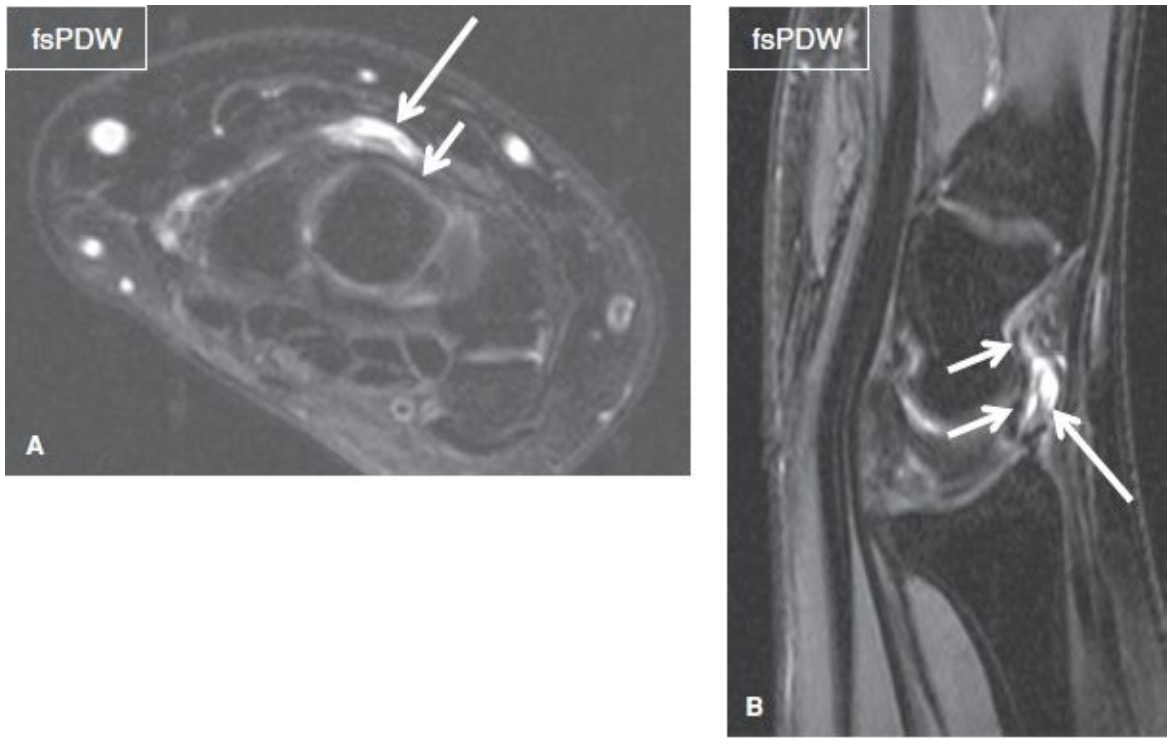

Fig. 78: Ganglion of the dorsal intercarpal ligament. Axial **(A)** and sagittal **(B)** images demonstrate a cystic lesion (*long arrows*) enveloping the dorsal intercarpal ligament (*short arrows*).

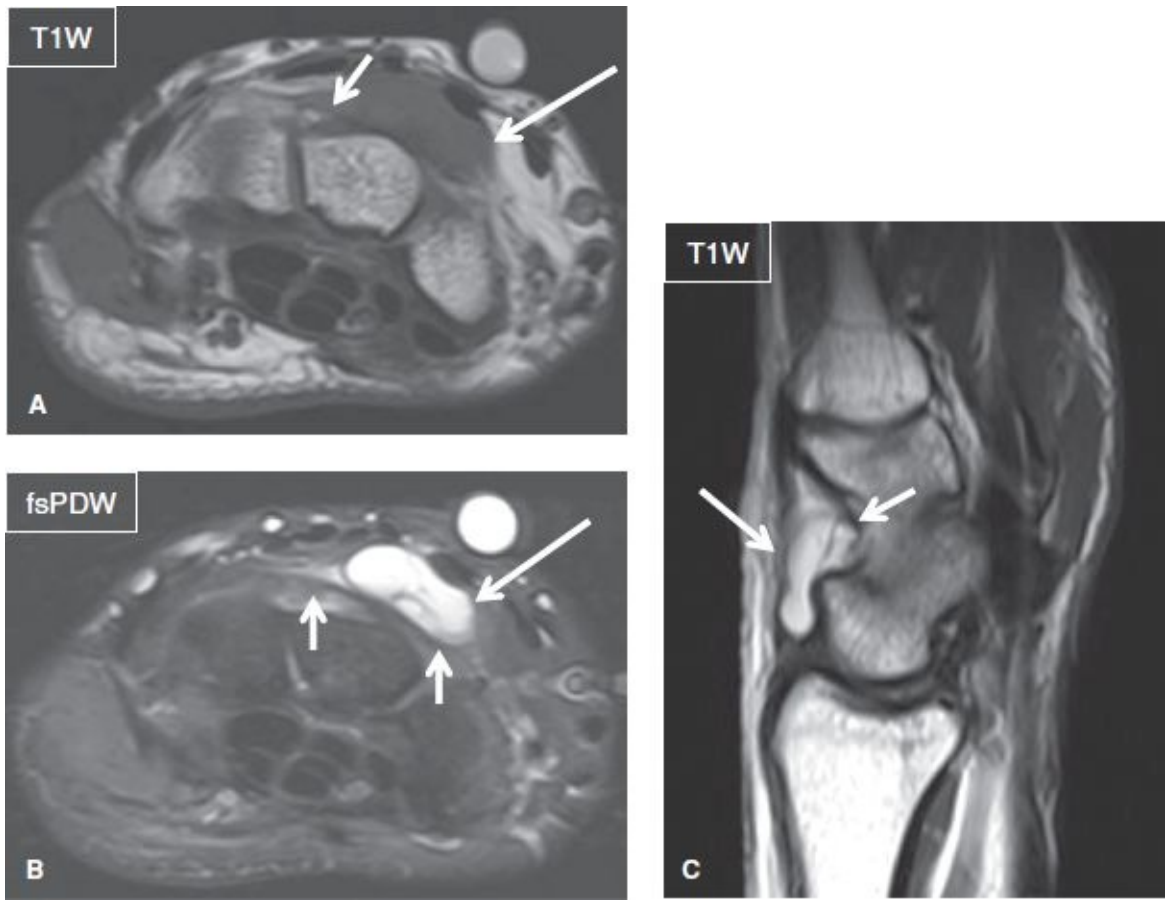

Fig. 79: Ganglion of the dorsal intercarpal ligament. Axial **(A, B)** and sagittal **(C)** images demonstrate a cystic lesion (*long arrows*) with mild thickening of the radial aspect of the dorsal intercarpal ligament (*short arrows*).

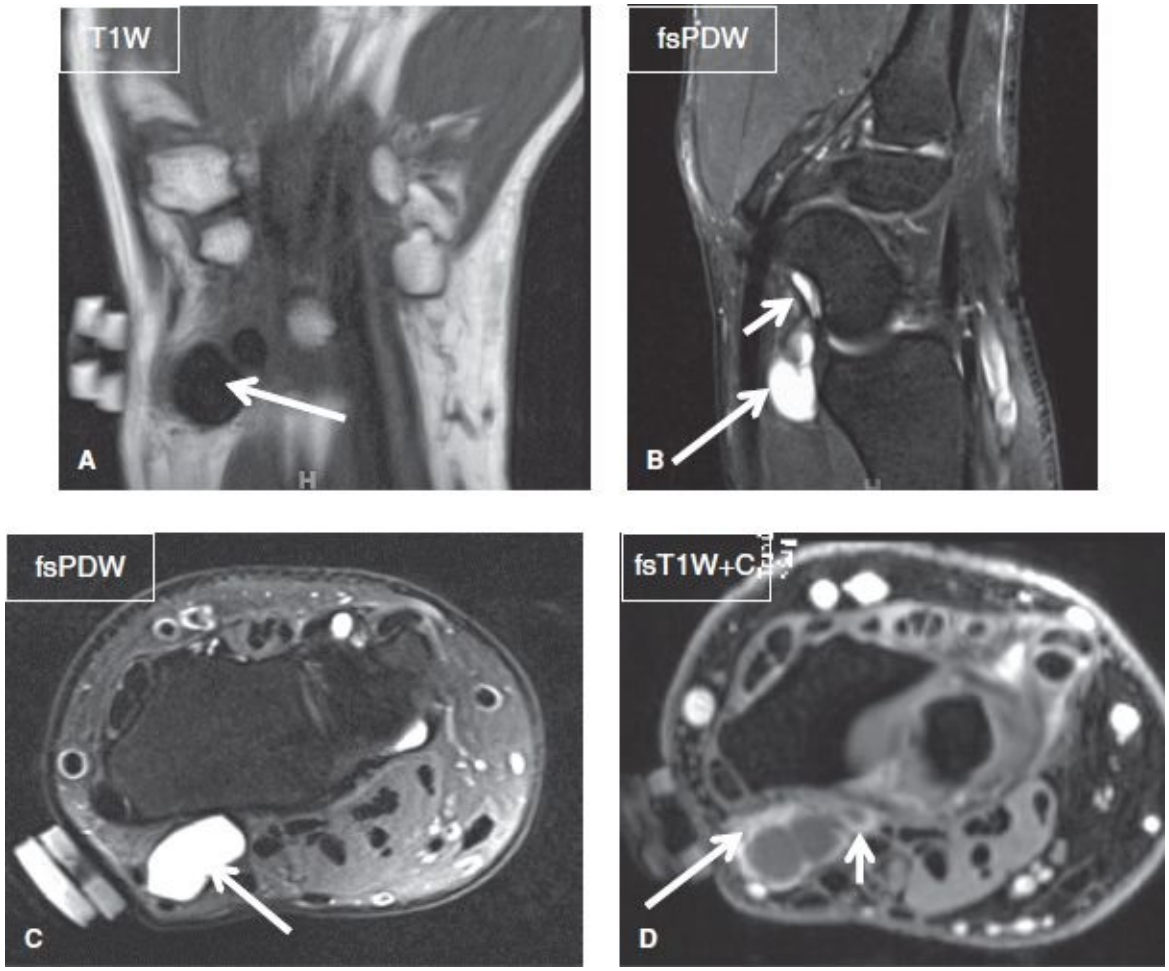

Fig. 80: Ganglion of the volar intercarpal ligament. Coronal **(A),** sagittal **(B),** and axial **(C, D)** images show a cystic lesion (*long arrows*) with its neck abutting the volar intercarpal ligament (*short arrows*).

BONES: [<Normal / Otherwise Normal>]

Congenital bone variations can be encountered incidentally, such as LT coalition (most common) or capitate–hamate coalition (Figs. 81, 82). Madelung deformity refers to small radial epiphysis with foreshortened radius combined with elongated and dorsally subluxed ulna with enlarged ulnar head. Characteristically, the carpus features a triangular configuration with the lunate at the apex. The deformity may appear as a congenital condition (true Madelung deformity) or as an acquired entity (pseudo-Madelung deformity, which can be idiopathic or may be associated with Turner and Leri–Weill syndromes, prior trauma or infection of the radial epiphysis, and multiple hereditary exostosis) (Fig. 83). In such cases, ligaments should be evaluated in multiple planes for confirmation of their integrity to avoid false diagnosis of tear due to altered bony and soft tissue arrangements (Fig. 84).

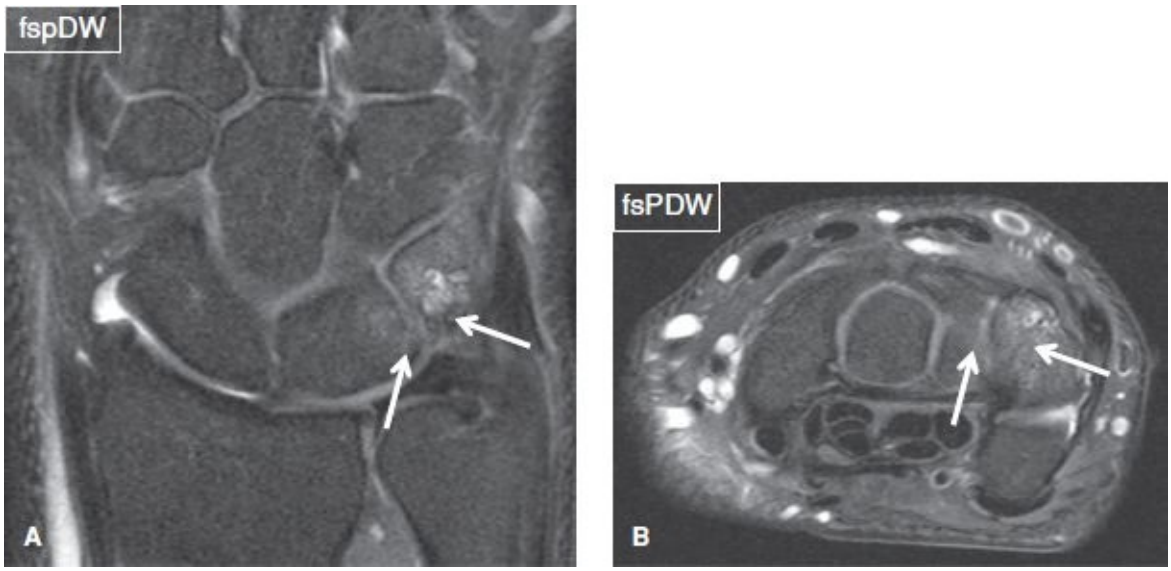

Fig. 81: Fibrous lunotriquetral coalition. Coronal **(A)** and axial **(B)** images show chronic stress-related cystic and edematous changes (*arrows*) due to fibrous coalition at the lunotriquetral articulation.

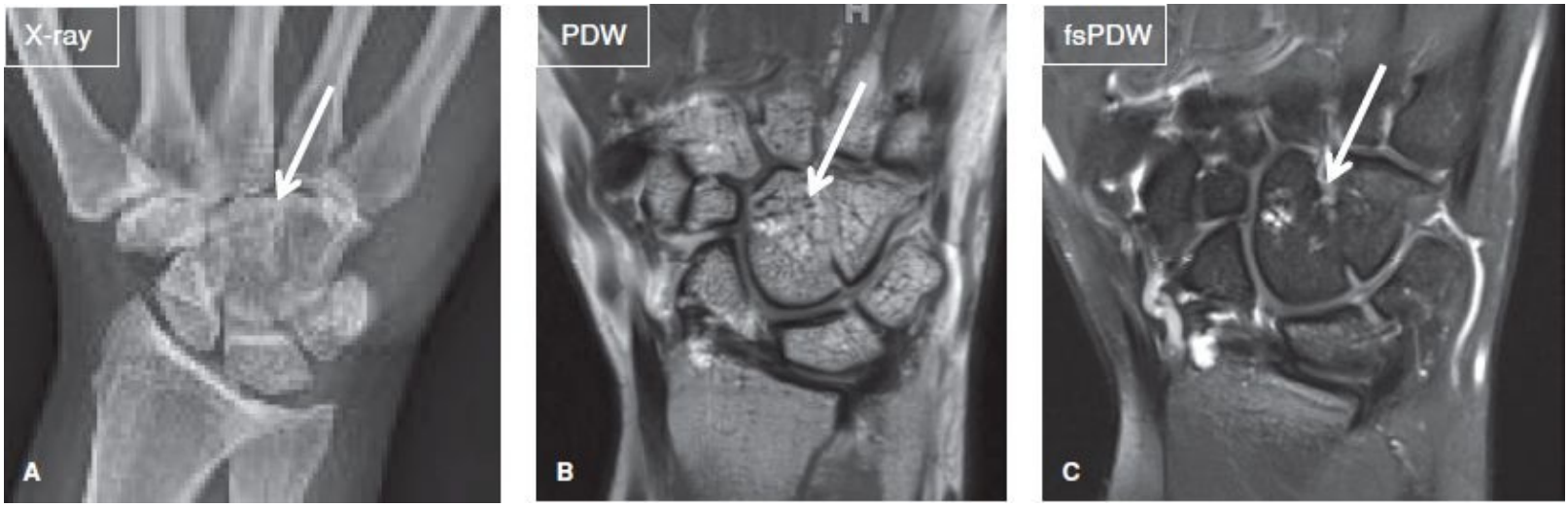

Fig. 82: Fibroosseous capitate–hamate coalition. Anteroposterior radiograph **(A)** and coronal MR images **(B, C)** show chronic stress-related cystic changes at the fibroosseous coalition at the capitate–hamate articulation (*arrows*).

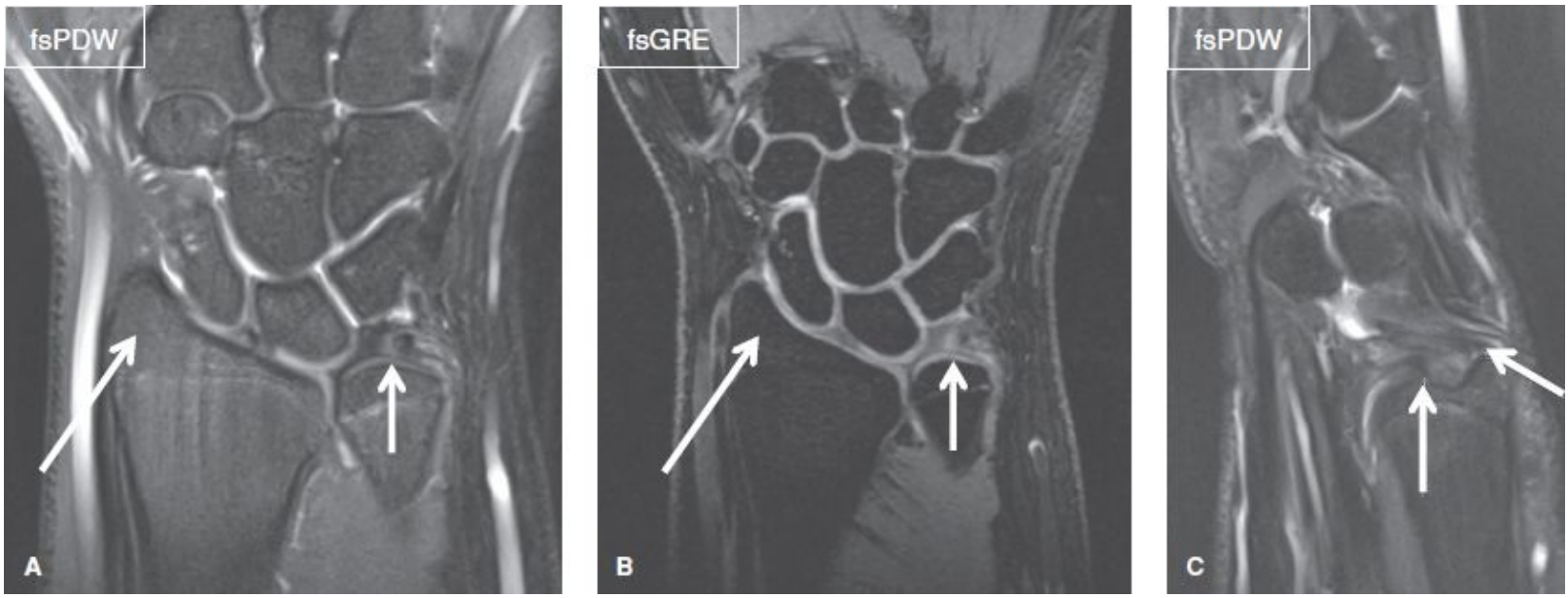

Fig. 83: Pseudo-Madelung deformity. Coronal spin-echo **(A)** and gradient-echo **(B)** images demonstrate a hypoplastic radial epiphysis (*long arrows*), probably as a result of prior Salter injury resembling Madelung deformity. Due to rotation, the triangular fibrocartilage disk is rotated and features internal increased signal (*short arrows* in **A, B**), mimicking a tear. In such cases, the integrity of the disk should be evaluated on the sagittal plane **(C),** and in this patient it was intact (*arrows*). Note scattered few fibrocystic changes in the other carpal bones of little or no clinical significance.

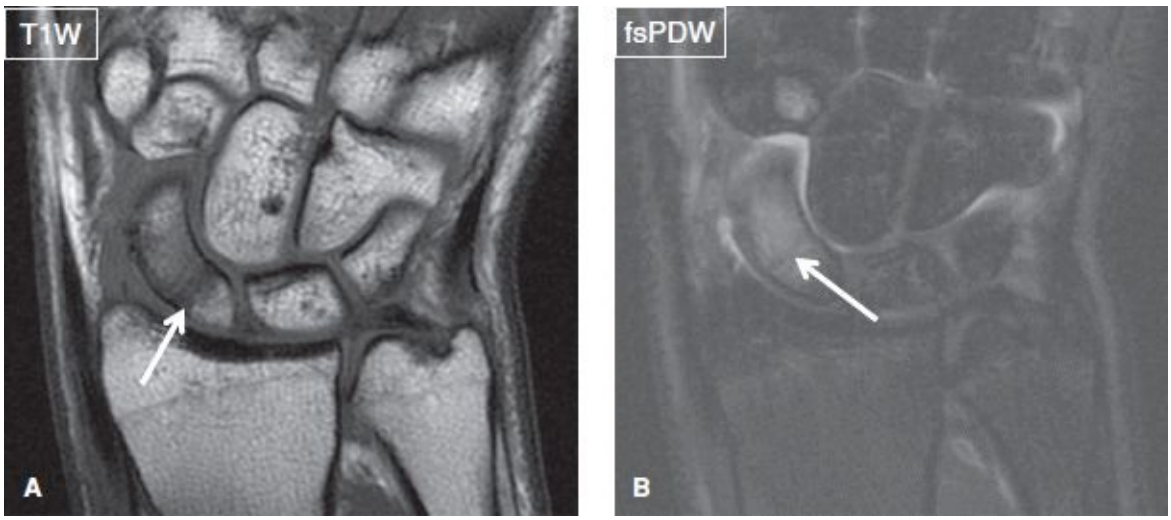

Fig. 84: Radiographically occult scaphoid fracture. Coronal images **(A, B)** show a sharp hypointense line (*arrows*) which is traversing the scaphoid waist and is surrounded by marrow edema. The fracture was not visible on the respective radiographs (not shown).

Bony productive changes are best seen on non-fs images while bone marrow edema and cystic changes are seen on fsPDW/fsT2W images. Non-fs images are useful for differentiating infection, subchondral cysts, infarcts, and fractures (which feature substantial amount of dark marrow signal at the affected sites on T1W/PDW images) from sites of reactive bone marrow edema (which demonstrate hazy intermediate marrow signal at the affected sites only on fs fluid-sensitive sequences without substantial hypointensity on

T1W or PDW images) (Fig. 84). Scattered fibrocystic changes are commonly evident in the carpal bones on MR images, especially at the small intercarpal ligament attachments. In the report, these lesions can be described as "scattered fibrocystic changes of the carpal bones, of little or no clinical significance," indicating that these findings are unlikely to be clinically important (Fig. 83). On the other hand if other findings, such as synovial thickening, fascial edema, bone marrow edema, etc. were to be concomitantly present, these lesions would not only be more pronounced but would also be likely related to one of the conditions in the "spotty carpus" differential. These conditions include sarcoidosis, gout, PVNS, tuberculosis, atypical mycobacterial infection, rheumatoid arthritis, and amyloid (Figs. 65, 67). Clinical and other imaging findings may help in differentiating among these entities. Sarcoidosis mostly affects young or middle-aged women, involves the metacarpal bones and the phalanges and features MCP joint effusions, as well as cystic bony changes, which assume a lacework appearance on plain films. Additional findings include symmetrical mediastinal lymphadenopathy and elevated serum acetylcholinesterase levels. Gout affects older men, features eccentric bone erosions with sclerotic margins on plain films, commonly involves the lower extremities, and is characterized by T2 dark soft tissue and eccentric bony tophi. PVNS affects young males, is typically monoarticular and features eccentric bony erosions and hemosiderin-laden synovial thickening, with blooming effect on gradient-echo sequences. Tuberculosis usually affects immunocompromised or incarcerated individuals and features unilateral joint involvement with effusion, tenosynovitis, erosions, joint space loss, ankylosis, and cold abscess formation. Rheumatoid arthritis mostly affects young and middle-aged women in a bilateral and symmetric fashion and is typically distributed in the carpus, MCP and proximal interphalangeal joints. Imaging findings include tenosynovitis, erosive cystic bony changes, effusions, and periarticular contrast enhancement related to active synovitis and pannus. Amyloidosis usually affects older subjects in the setting of chronic long-standing systemic disease (e.g., multiple myeloma and chronic renal failure) and is associated with T2 dark lesions.

If the pathology is not joint centric, most common bone pathologies include injuries, infections, and tumors. One should carefully look for nondisplaced fractures, which can be radiographically occult. The common sites include scaphoid, lunate, capitate, trapezium, dorsal triquetrum, pisiform, and the hook of the hamate. The detection of radiographically occult fractures is particularly beneficial when they occur in the scaphoid bone, where unless immobilized, they may lead to displacement, avascular necrosis (AVN), SNAC, or nonunion of the proximal scaphoid pole. More proximal the fractures is on scaphoid, more are the chances of AVN. On MR imaging, acute fractures of carpal and adjacent bones are best seen on coronal images and these appear as sharp hypointense bands, which are surrounded by cloud of marrow edema (Figs. 84–88). The bone marrow edema is expected to persist to a varying degree, as the healing progresses. Nonunion can be seen in up to 50% of cases of scaphoid fracture, and is depicted as a high signal intensity gap, with associated sclerosis and cystic changes at the fractured bone margins. Sometimes, on radiographs, a small fleck of bone or minimal cortical infraction may be seen at the lateral

aspect of the scaphoid waist. On MR images, this usually corresponds to isolated avulsive injury at the RCL attachment and may have associated avulsive cystic changes or marrow edema. These findings are relatively inconsequential. Fractures of the epiphyseal (growth) plates are common in the distal radius and ulna, particularly in children and adolescents. These lesions are categorized for prognostic and treatment purposes according to the Salter–Harris classification, where worsening grade of injury or fracture displacement would require more aggressive surgical management (Table 2).

Idiopathic AVN most commonly involves the lunate (Kienböck's disease) and the scaphoid (Preiser's disease). For diagnostic and therapeutic purposes, the entity may be classified into four stages based on imaging findings. In *stage I,* where radiographs are normal, on MRI, there is focal or diffuse intermediate marrow signal on T1W images, and edema-related hyperintensity on fsT2W images. Conservative treatment is recommended at this stage. In *stage II,* where plain films reveal sclerosis or lytic areas, on MRI, marrow signal progressively turns from intermediate to low on T1W images to heterogeneously increased on fsT2W images. In general, low signal intensity on T1W images is highly suggestive of AVN. Focal regions of T2 hyperintensity in isolation usually represent reactive marrow edema, but if such findings are associated with significant or proportionate T1 hypointensity, further assessment with dynamic contrast-enhanced MR (CEMR) imaging should be performed to exclude AVN. On CEMR, enhancing marrow areas represent perfused and viable bone tissue whereas nonenhancing areas correspond to ischemic or necrotic tissue (Fig. 89). CEMR is more useful compared to CT imaging, since sclerosis on CT does not always equate with AVN. Treatment of AVN is surgical, with options including revascularization of the affected bone or in advanced stages, correction of the length discrepancy between the radius and ulna. *Stage III* is characterized by progressive articular surface collapse and fragmentation of the involved bone with decreased T1 and T2 signal intensity (Fig. 90), and *stage IV* reflects superimposed additional generalized arthritic changes at the wrist. In the latter two stages, the disease is considered irreversible, and treatment options include bone excision/prosthesis replacement or carpal fusion.

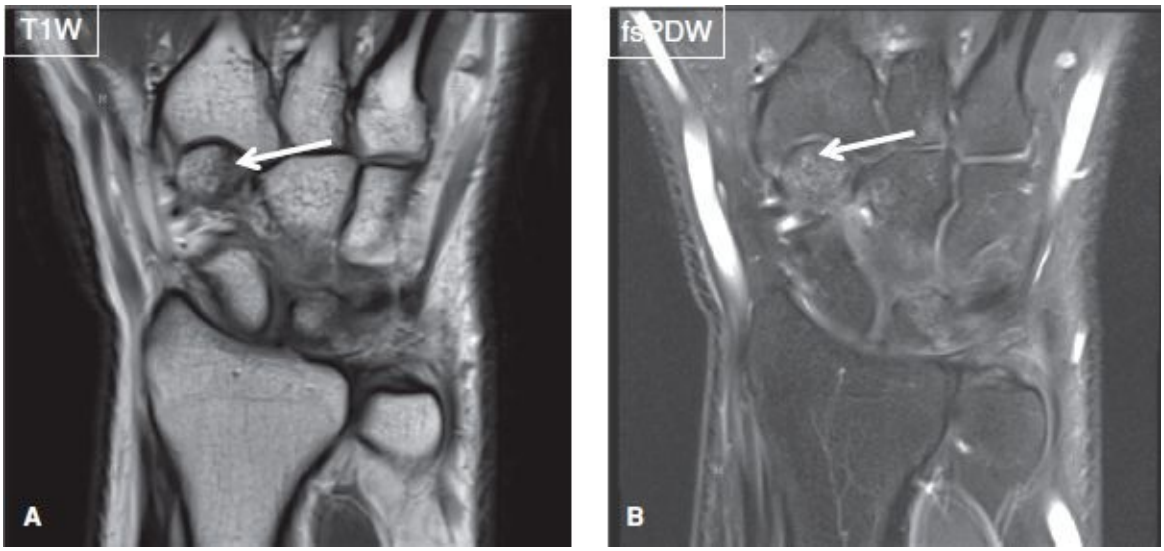

Fig. 85: Intratrabecular wrist fracture. Coronal images **(A, B)** show a nondisplaced fracture

(*arrows*) of the trapezoid, which was occult on plain films. Notice additional impaction-related contusion of the lunate and capitate.

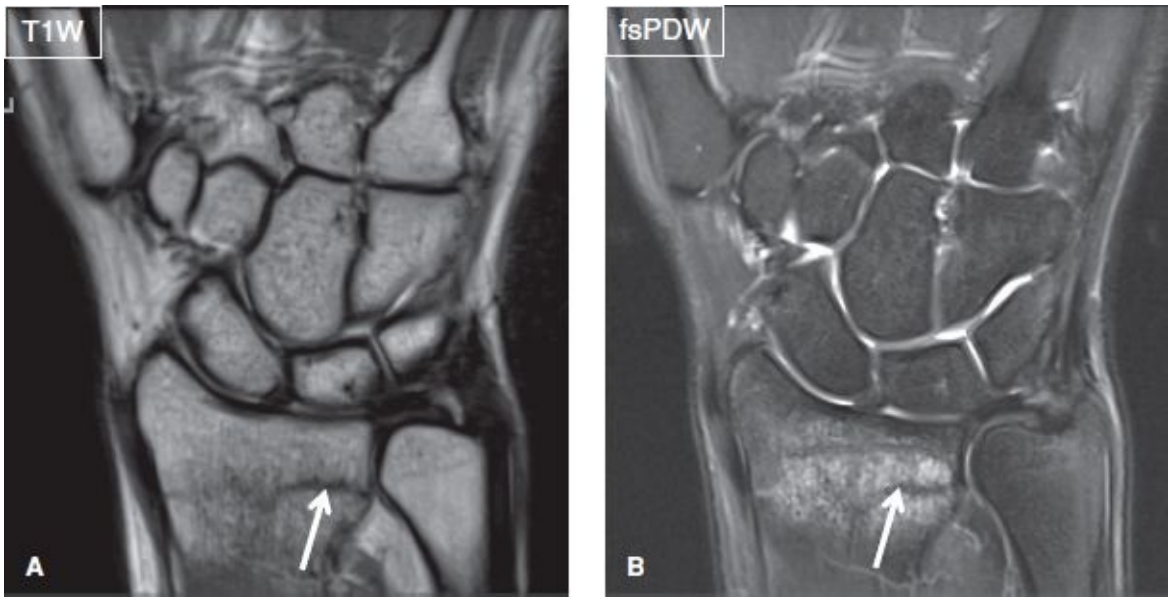

Fig. 86: Acute radial fracture. Coronal images **(A, B)** exhibit a sharp hypointense line (*arrows*), which is traversing the distal radial epiphysis and is surrounded by extensive cloud of marrow edema.

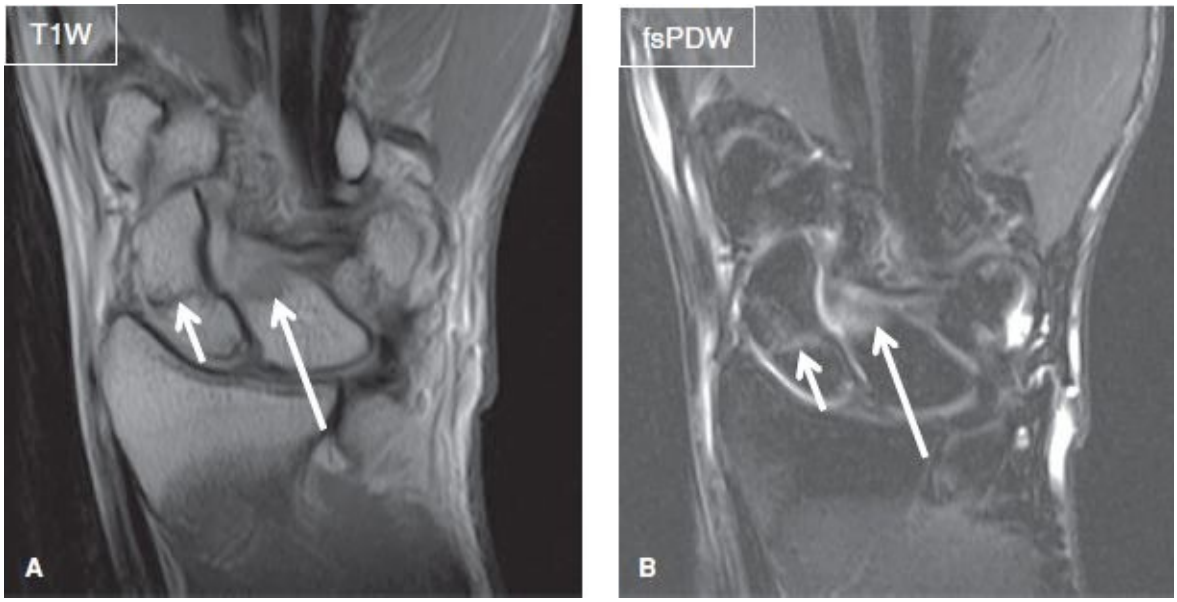

Fig. 87: Multiple wrist fractures. Coronal images **(A, B)** display concomitant fractures of the scaphoid waist (*short arrows*) and distal lunate (*long arrows*). Notice intertrabecular fracture of the proximal capitate as well.

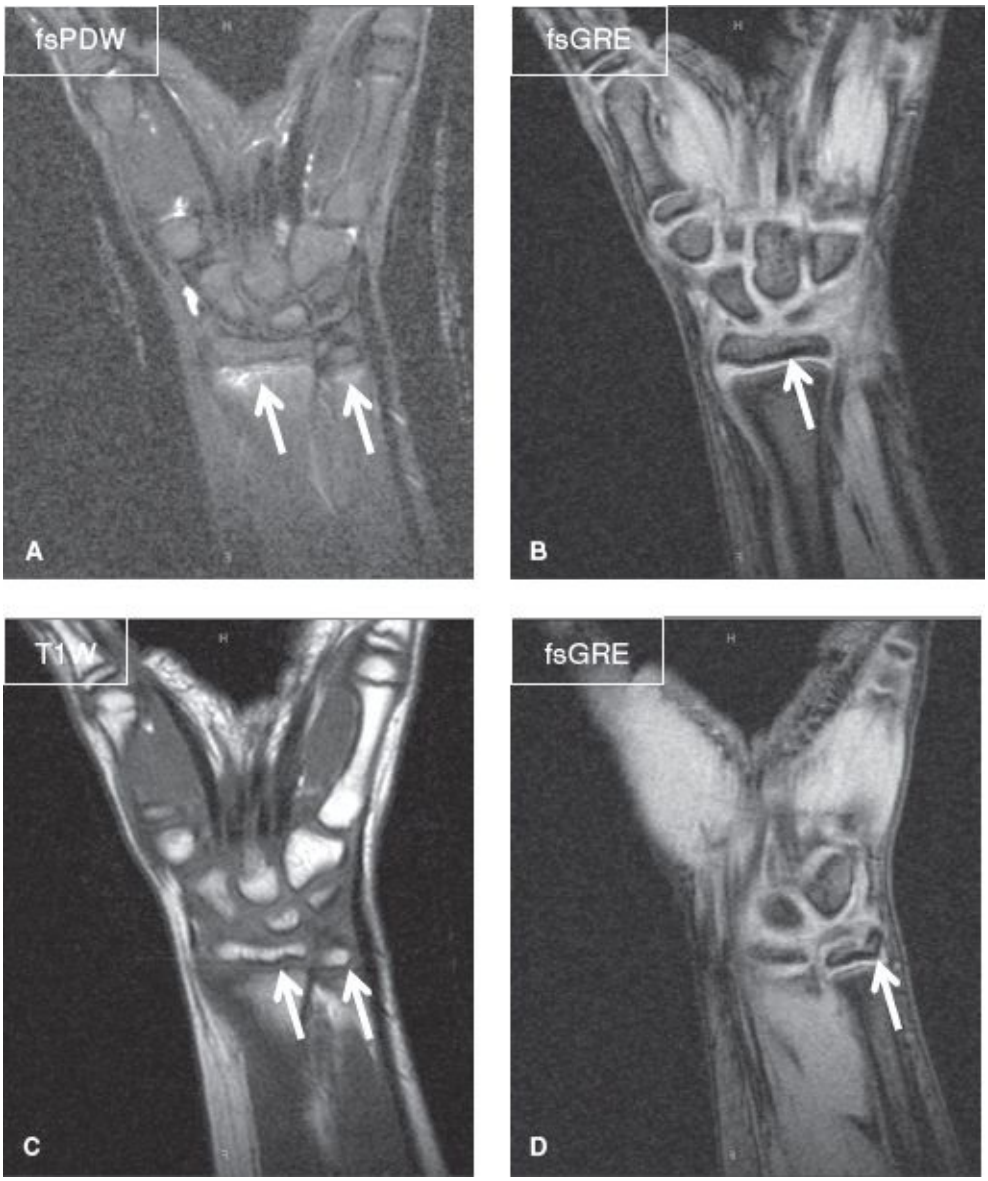

Fig. 88: Salter–Harris type I injury in a gymnast. Coronal spin-echo **(A, C)** and gradient-echo **(B, D)** images reveal widening of the distal growth plates (*arrows*) of the radius and ulna, along with adjacent marrow edema (*arrows* in **A**, classic for gymnast wrist).

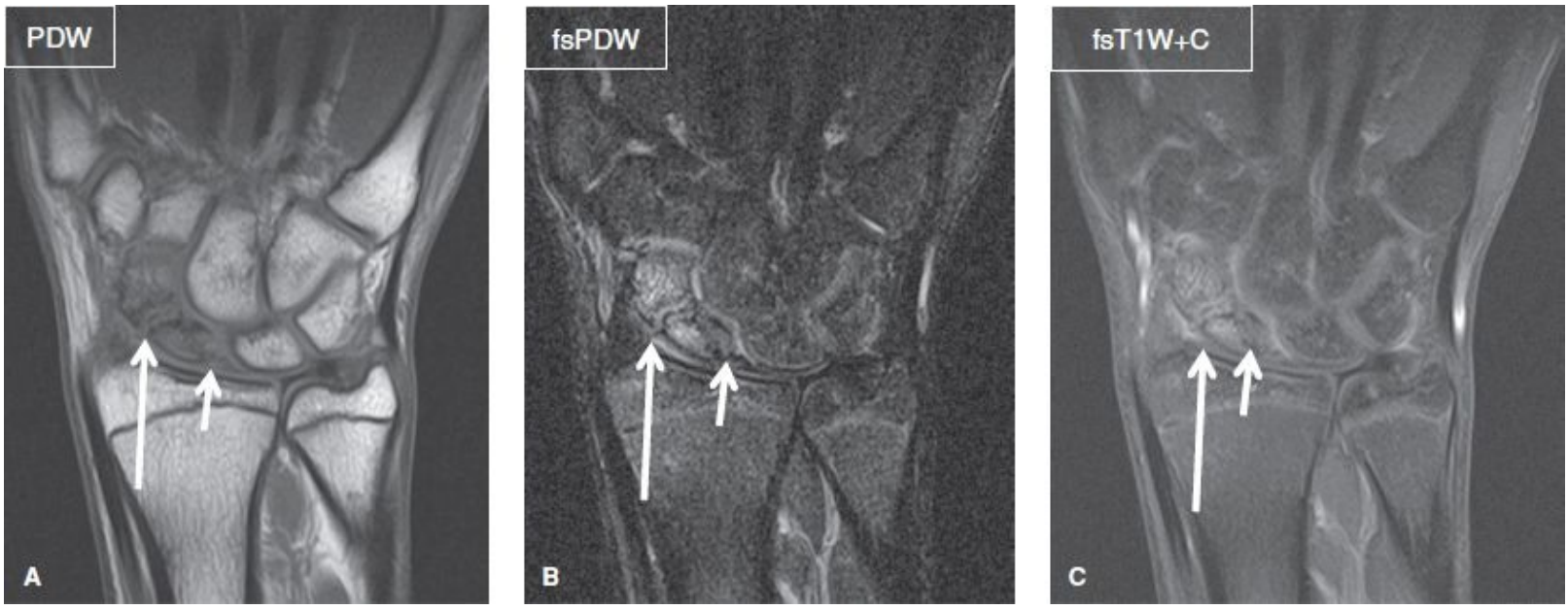

Fig. 89: AVN versus normal healing. Coronal images **(A–C)** show fibrous union at the

scaphoid waist fracture site (*long arrows*) with residual edema from prior injury. Hyperemia around the fracture site is reactive phenomenon on contrast image **(C).** Proximal pole of scaphoid is minimally enhancing since it is not very hyperemic and is relatively normal bone (*short arrows*). Thus, contrast aids in distinguishing normal bone from AVN, which would be expected to enhance minimally similar to other viable bones in the vicinity.

Fig. 90: Kienböck's disease. Anteroposterior radiograph **(A)** and coronal MR images **(B, C)** reveal collapse of the lunate (*arrows*), in keeping with stage III avascular necrosis.

TABLE 2: The Salter–Harris classification for categorizing injuries of the physeal plate

Type	Features	Prognosis
I	Transverse fracture through the hypertrophic zone of the physis/ physis appears widened with surrounding marrow edema	Excellent/rapid healing, usually within 2–3 wks
II	Fracture through the physis and metaphysis/no involvement of the epiphysis	Good/rapid healing/growth rarely disturbed
III	Fracture through the physis and epiphysis	Poor, unless there is early accurate reduction
IV	Fracture through the epiphysis, physis, and metaphysis	Guarded/growth is affected even with perfect reduction
V	Compression or crush injury of the physeal plate/no epiphyseal or metaphyseal fracture	Poor/usually no growth potential

Bone tumors, tumor-like conditions, and infections are not uncommon in the wrist and show similar imaging appearances as elsewhere in the body (Figs. 91, 92).

Fig. 91: Intraosseous benign fatty lesion. **A:** Anteroposterior radiograph reveals a well-defined lucent lesion (*arrow*) with narrow short zone of transition in the distal radius. **B, C:** In the corresponding coronal MR images, the lesion (*arrows*) features signal similar to fat, which represents an old-healed gumma, mimicking a lipoma. Also note marked inflammatory joint changes in the wrist, secondary to chronic syphilis infection.

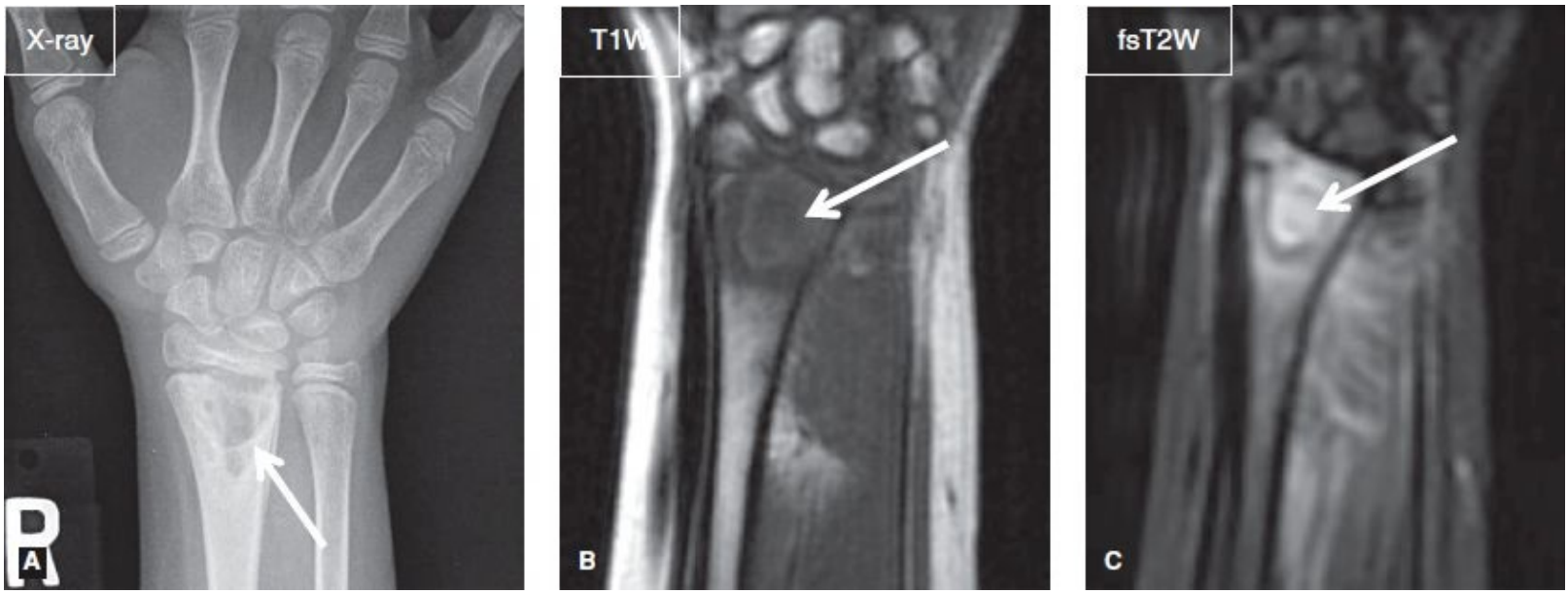

Fig. 92: Osteomyelitis. **A:** Anteroposterior radiograph demonstrates a relatively ill-defined lytic lesion with surrounding fading sclerosis (*arrow*) at the distal radial epi-metaphysis. **B, C:** On coronal MR images, the corresponding lesion (*arrows*) appears multilayered and T1 hypointense and is associated with diffuse bone marrow and fascial contrast enhancement. Findings consistent with a Brodie's abscess.

MUSCLES: [<Normal>]

Apart from denervation changes in thenar and hypothenar muscles, one should look for trauma- or infection-related myositis. Fatty infiltration and atrophy of muscles are best depicted on PDW or T1W images, and edema-like signal on fsPDW images (Fig. 93). In

muscle strains, myopathy or myositis cases, imaging changes are usually focal, involve one or more muscles, abnormalities are not limited to a particular nerve distribution, and there is associated fascial edema. In denervation, changes are usually diffuse, limited to a particular nerve distribution, occur distal to the site of neuropathy consistently lack fascial edema (Fig. 94).

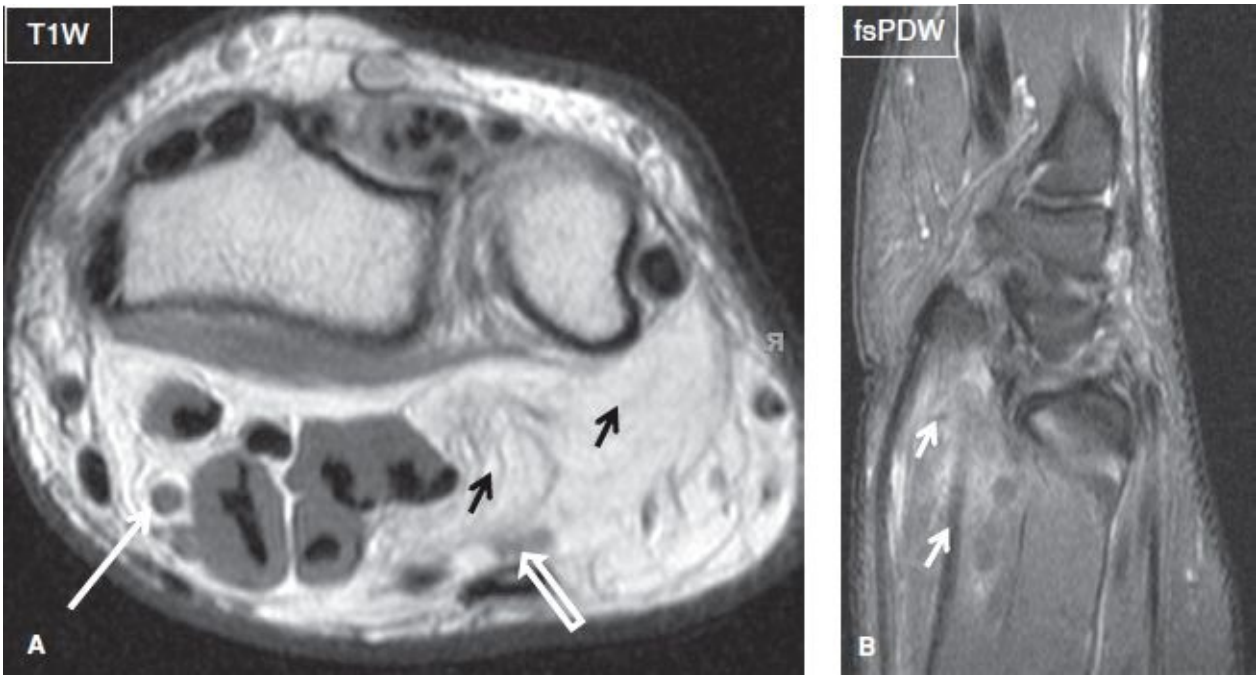

Fig. 93: Chronic poliomyelitis. Axial **(A)** and sagittal **(B)** images reveal varying degrees of fatty replacement, atrophy, and edema-like signal (*short arrows*) of the flexor muscles around the wrist. Also note mild atrophy of the median (*long arrow*) and ulnar (*open arrow*) nerves.

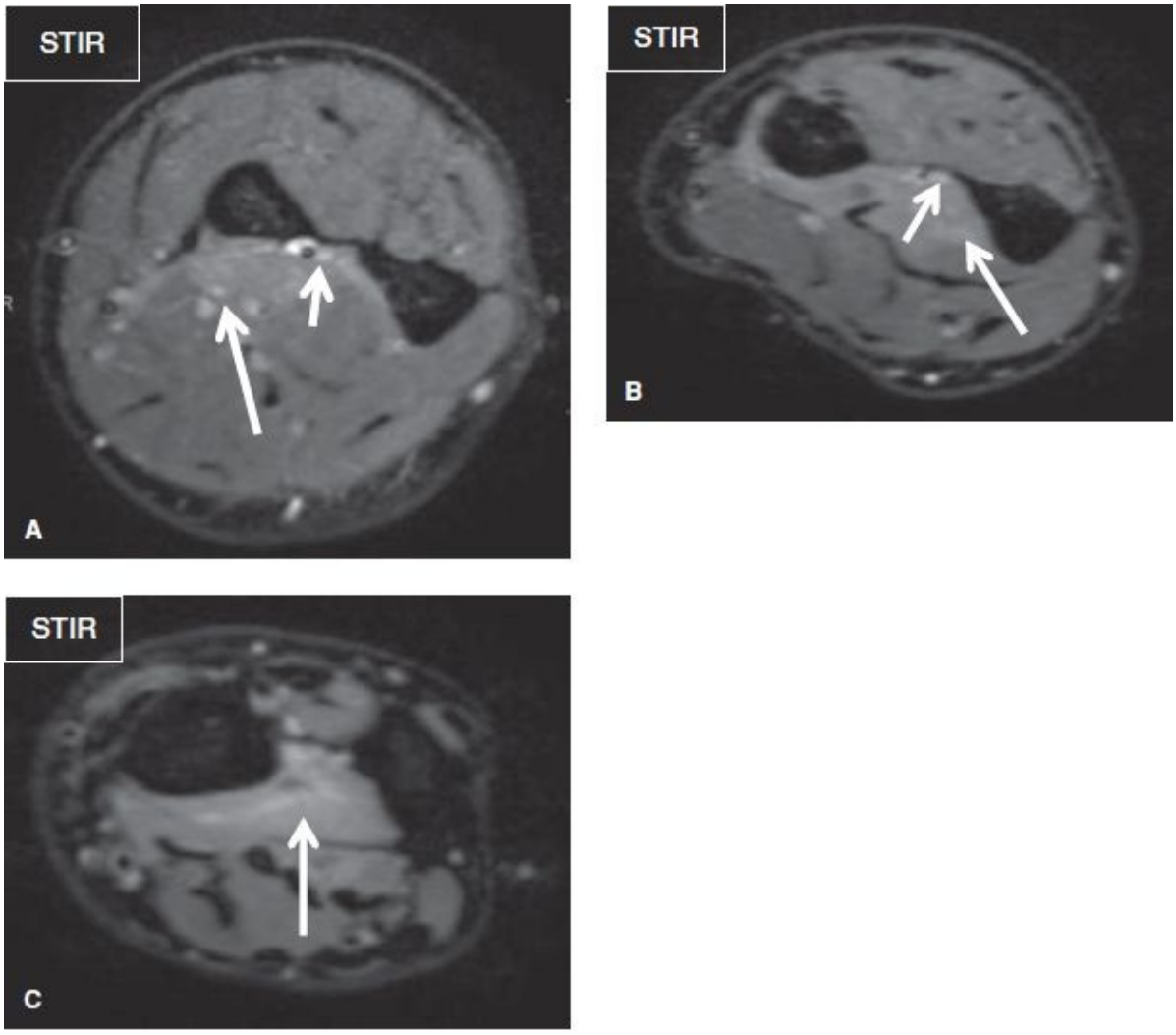

Fig. 94: Anterior interosseous nerve syndrome. Axial images **(A–C)**. The anterior interosseous nerve (*short arrows* in **A, B**) features abnormal T2 hyperintensity, reflecting neuropathy. Edema-like signal of the flexor digitorum profundus (*long arrow* in **B**), flexor pollicis longus (*long arrow* in **A**), and pronatus quadratus (*long arrow* in **C**) reflect muscle denervation changes.

Accessory muscles are common in the wrist and may be seen as incidental findings or may present as soft tissue mass that may result in compression neuropathy. They include (a) the accessory palmaris longus muscle, which is located volar to the flexor tendons and medial to flexor carpi radialis muscle, (b) the extensor digitorum manus brevis muscle (1% to 3%), which lies deep to the metacarpal bones, (c) the accessory extensor carpi radialis muscle, and (d) the accessory abductor digiti minimi muscle (24%) (Fig. 95).

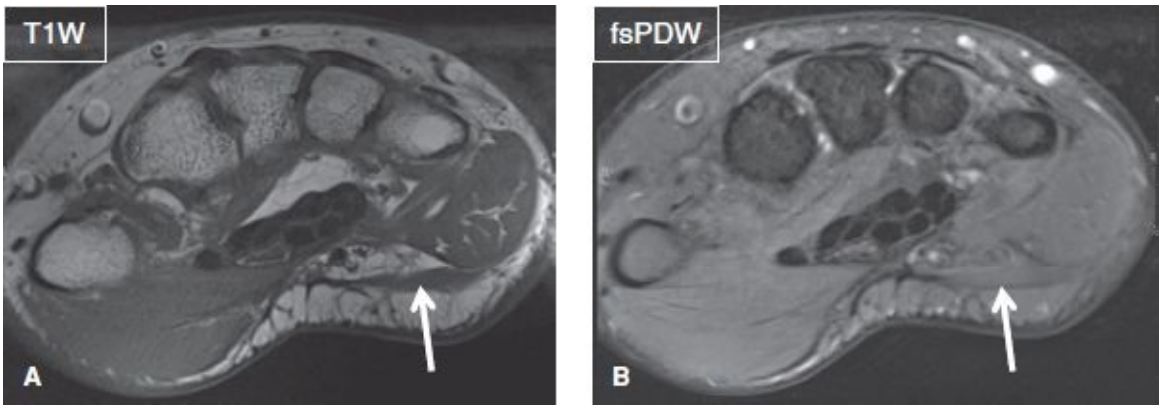

Fig. 95: Accessory abductor digiti minimi muscle. Axial images **(A, B)** demonstrate the accessory muscle (*arrows*), which is located at the palmar aspect of the wrist.

VESSELS: [<Normal>]

Ulnar or radial artery thrombosis or aneurysms can be incidentally encountered (Figs. 96, 97). Hypothenar hammer syndrome involves thrombosis, spasm, or aneurysm of the ulnar artery adjacent to the hook of the hamate, due to chronic repetitive trauma. The aneurysm may compress the adjacent ulnar nerve. There may be associated underlying fibromuscular dysplasia. Rarely, thenar hammer syndrome may also be encountered, which involves similar process in the superficial radial artery. Most patients do well following interposition grafting to restore pulsatile digital artery flow. In patients with an intact palmar arch and isolated radial or ulnar artery involvement, arterial ligation without reconstruction can be performed to prevent further embolization.

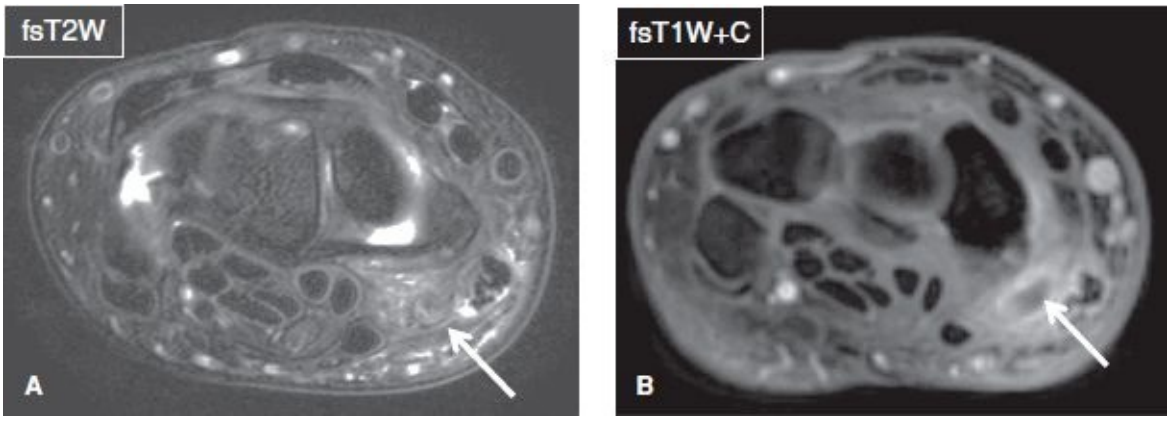

Fig. 96: Radial artery thrombosis. Axial images. **A:** There is absence of flow void (*arrow*) in the radial artery, indicative of thrombosis. Notice abnormal T2 hyperintensity of the surrounding soft tissues, compatible with reactive edema. **B:** Just distal to image **(A),** there is an intraluminal contrast filling defect on intravenous contrast image (*arrow*), which corresponds to the thrombus.

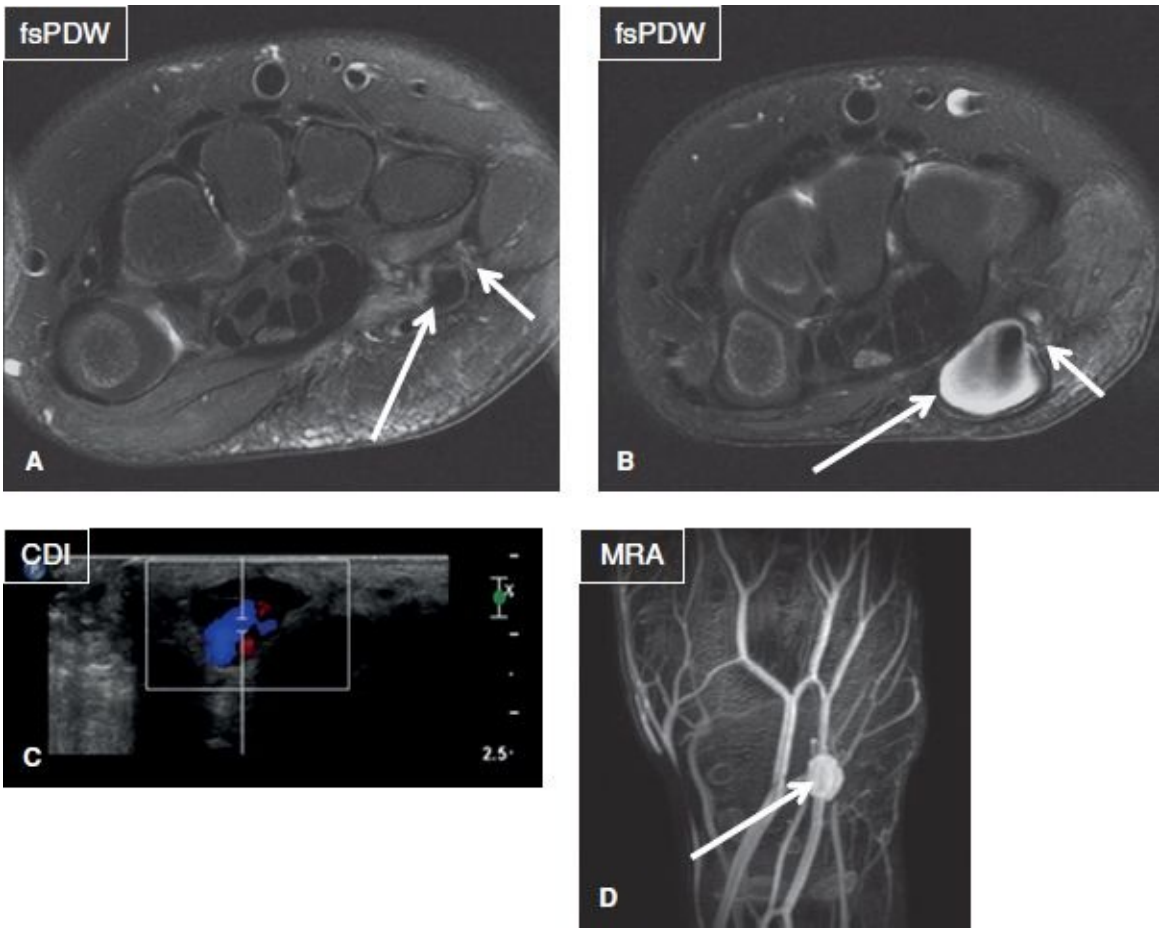

Fig. 97: Ulnar artery aneurysm. **A, B:** Sequential axial images exhibit an aneurysm of the ulnar artery (*long arrows*) at the level of the wrist. The ulnar nerve is displaced dorsally and medially by the lesion (*short arrows*). **C:** Doppler ultrasonography reveals turbulent arterial flow within the vascular lesion. **D:** The aneurysm (*arrow*) is best delineated in this coronal MR angiography image.

Various types of vascular malformations may be encountered and can be differentiated using contrast administration, especially if time-resolved dynamic imaging is available. Venous malformations are the most common in adults (Fig. 98) and these appear as serpiginous clusters of well-circumscribed T2 hyperintense masses, with or without associated phleboliths and pulsation artifacts. The lesions show no surrounding edema, enhance in the late phase of dynamic imaging and do not demonstrate venous shunting in the arterial phase. Arteriovenous malformations (AVMs) appear as enlarged vascular channels, which feature multiple flow voids due to fast flow but do not exhibit a discrete soft tissue mass. Early arteriovenous shunting is the rule. These can have single arterial feeder (simple AVM) or multiple arterial feeders (complex/glomus AVM). Lymphatic malformations appear as non-enhancing or peripherally enhancing septated cysts, which may contain fluid–fluid or blood–fluid levels. Large lymphatic or cavernolymphatic malformations can be seen with Klippel–Trénaunay–Weber syndrome, which is also associated with bones and soft tissues hypertrophy in one limb or one side of body. Capillary malformations typically appear as skin thickening and/or cutaneous channels, without prominent deep vascular channels. Hemangiomas are congenital lesions, which

appear as enhancing soft tissue masses and may encompass arterial feeders. They commonly disappear by the age of 1 to 2 years or mostly by 8 to 10 years. Thus, the most common vascular malformations in adults are venous malformations, and in children, are hemangiomas. Finally, one may encounter dilated subcutaneous venous channels due to deep venous thrombosis or venous insufficiency, and these should not be mistaken for venous malformation, since the treatment is different (embolization or sclerotherapy for venous malformation vs. anticoagulation or stenting for deep venous thrombosis). Other important features of vascular malformations that should be reported include discrete or infiltrative appearance, focal or multifocal, presence or absence of deep venous dysplasia, and involvement of muscle, bone, or joint.

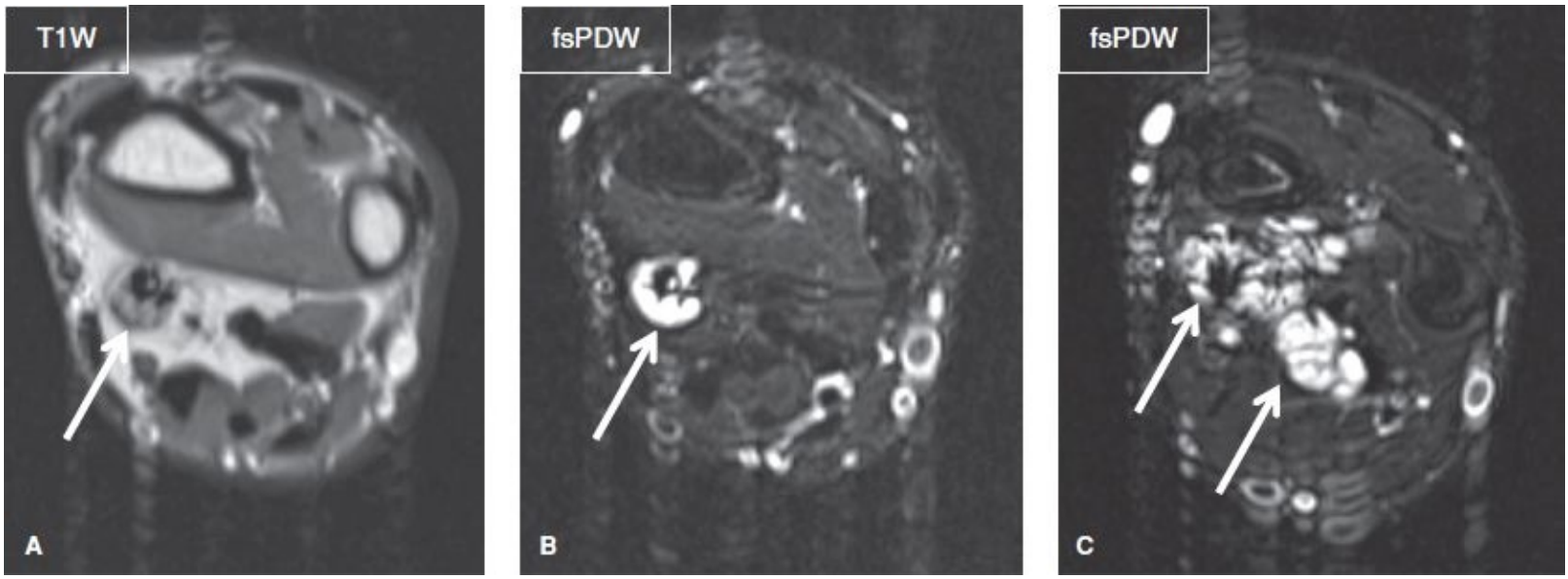

Fig. 98: Venous malformation. Axial images demonstrate clusters of enlarged vessels (*arrows*) with in-plane flow phenomenon reflective of slow flow malformation in the distal forearm. Notice prominent pulsation artifacts.

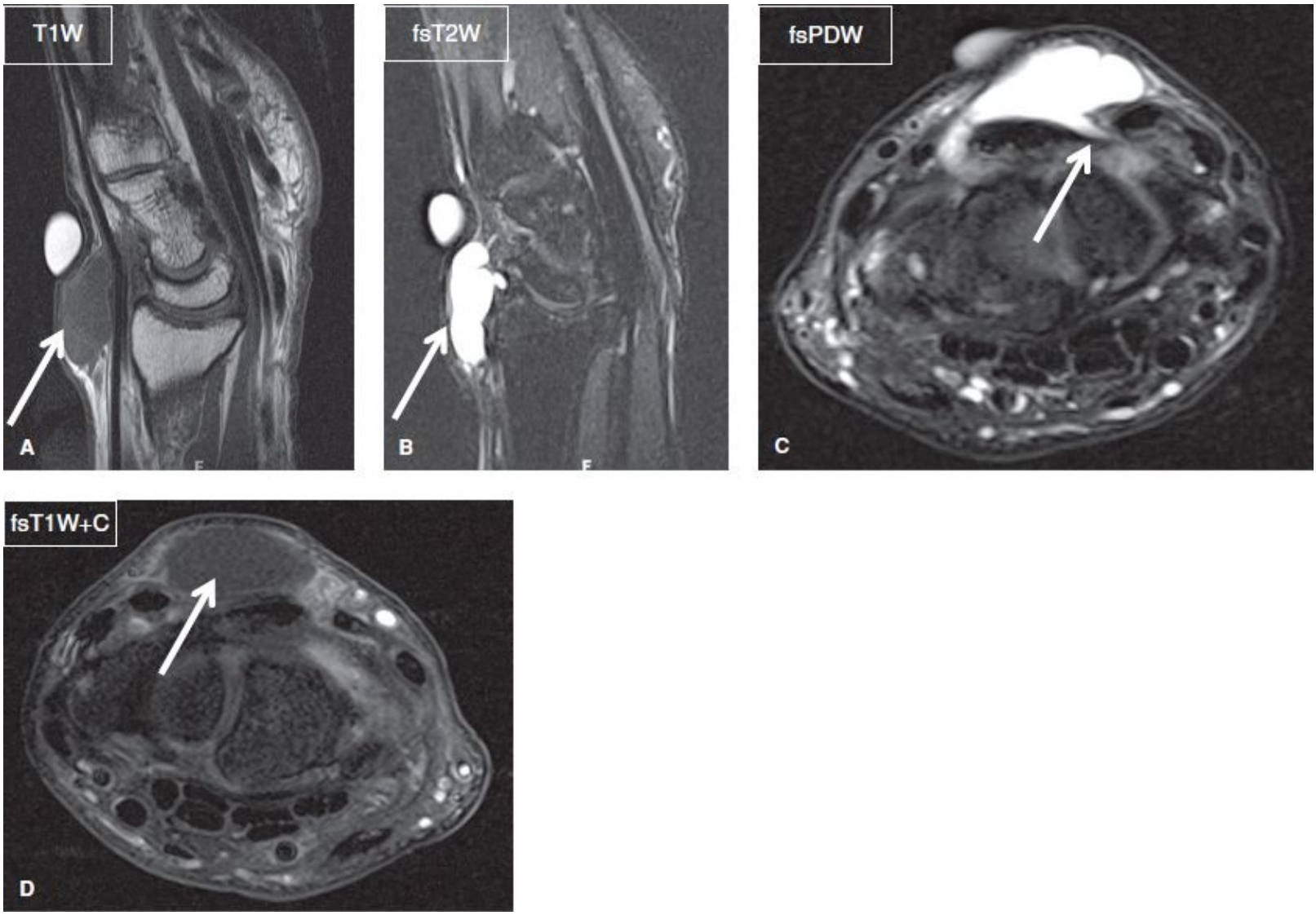

Fig. 99: Ganglion cyst. **A, B:** Sagittal images show the cystic mass (*arrows*) in the dorsal aspect of the wrist. **C, D:** Axial images show the lesion's neck extending under the DIC (*arrow* in **C**), along with peripheral contrast enhancement (*arrow* in **D**) confirming the cystic nature of the lesion.

OTHER: [<None>]

Finally, a search should be made for incidental soft tissue mass. Ganglion cysts typically appear as uni- or multilocular rounded or oval masses, which are located adjacent to joints, tendon sheaths, or ligaments and exhibit fluid-like T2 signal. They are usually hypointense on T1W images, and less commonly iso- or hyperintense on fsT1W images, which reflects their proteinaceous or hemorrhagic contents. After contrast administration, mild enhancement of the thin wall or internal septations may be seen (Figs. 64, 73, 78–80, 99). On identification of a ganglion cyst, careful examination of its neck and the adjacent structures, particularly ligaments, is necessary to detect underlying tear. Large ganglion cysts may erode into the adjacent bony cortex.

Giant cell tumor of the tendon sheath (extra-articular PVNS) is a benign lesion, which usually arises at the volar aspect of the first three digits, and less commonly involves the wrist. Typically, the lesion is located adjacent to or envelops a tendon and appears as a

well-defined mass, which is hypointense on all sequences and demonstrates variable, though most commonly, homogeneous enhancement. Blooming artifact may be evident on gradient-echo sequences due to hemosiderin deposition similar to intra-articular PVNS.

Dupuytren's contracture, also known as palmar fibromatosis, refers to fibrous proliferation and collagen deposition in the palmar aponeurosis and its extensions, which often results in progressive and debilitating flexion contractures of the palm and the fingers. MR images exhibit multiple nodules or cords, which arise from the palmar aponeurosis, extend distally and superficially parallel to the flexor tendons and terminate in the form of fine strands into the subcutaneous tissues at the level of the distal metacarpals. Typically, nodules are isointense and cords are hypointense compared to muscle on T1W and T2W images.

Lipomas typically exhibit high signal on T1W and T2W images, which suppresses on fs images. They may be inconspicuous, particularly when they blend in with normal subcutaneous fat. Intramuscular lipomas assume a more heterogeneous appearance due to interdigitation of normal muscle fibers with fatty lobules. They lack nodular enhancement, though thin internal fibrovascular septations are not uncommon. A simple rule can be followed if the lipoma looks "dirtier" or more strandy than the subcutaneous fat, it should be qualified as atypical lipomatous lesion, a broad term, which includes both atypical lipoma and well-differentiated liposarcoma since both entities show similar clinical behavior, and mere follow-up to stability is enough. On the other hand if the lesion shows nodular enhancement, it should be biopsied to exclude liposarcoma.

Other incidental masses include os styloideum and os centrale. The os styloideum is more common and presents as a variably sized palpable accessory bone, located on the dorsal aspect of the wrist at the level of bases of the second and third metacarpal bones (Fig. 100). Although commonly asymptomatic, it may cause pain and limitation of hand motion due to superimposed trauma, degenerative changes, or recurrent friction and slippage of the extensor carpi radialis longus and brevis tendons (carpal boss syndrome; Fig. 101). Imaging studies demonstrate a small bone, which articulates with the capitate and trapezoid. In symptomatic cases, there is bone marrow edema, osteoarthritic changes, joint effusion, and/or abnormalities of the extensor tendons. The os centrale is adjacent to the dorsal aspect of the scaphoid bone and it may be confused with scaphoid fracture. Presence of well-defined corticated margins aid in differentiation of this variant from an acute fracture that will show bone marrow and fascial edema as well as ill-defined cortex of the bony fragment. Finally, an uncommon entity is radial styloid impingement syndrome. It represents a painful syndrome where a normal-sized or elongated radial styloid process may impinge on the scaphoid leading to impingement-related soft tissue or bone marrow edema and/or bony cystic changes (Fig. 102). More commonly, this entity has been reported as a consequence of proximal row carpectomy or triscaphe arthrodesis. In such cases, prophylactically, radial styloid process may be resected to prevent the development of impingement syndrome or secondary exostosis from scaphoid waist.

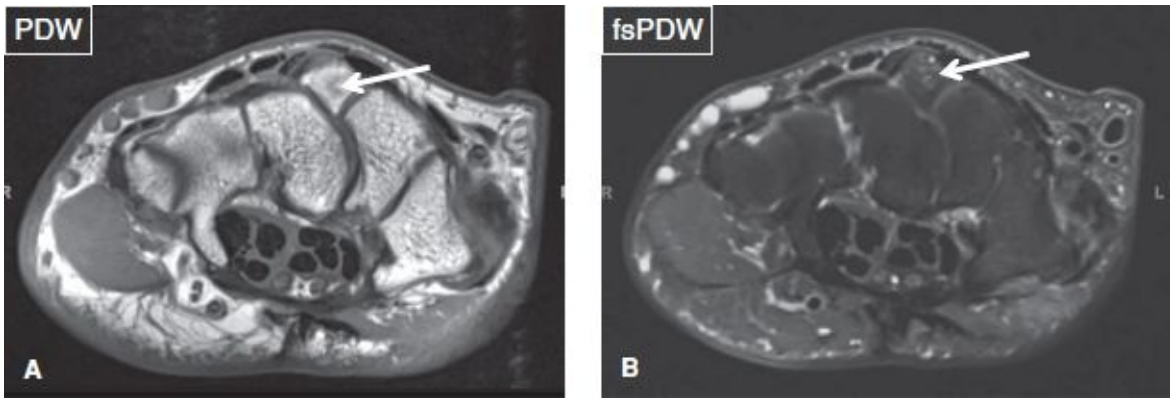

Fig. 100: Os styloideum. Axial images **(A, B)** display an incidentally detected accessory ossicle (*arrows*) located on the dorsum of the wrist at the base of the second and third metacarpal bones.

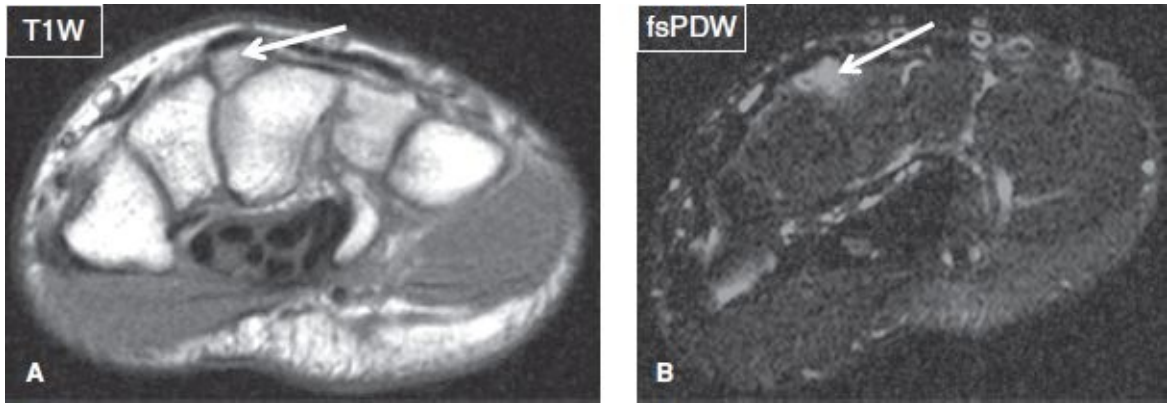

Fig. 101: Carpal boss syndrome. Axial images **(A, B)** display marrow edema within the os styloideum (*arrows*) in this symptomatic subject.

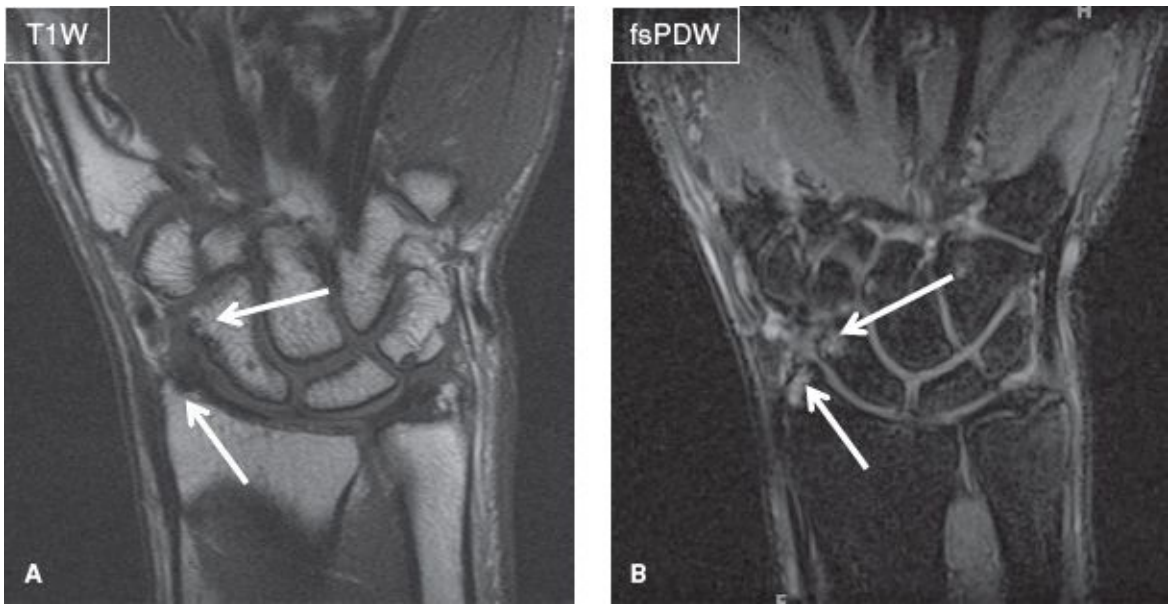

Fig. 102: Radial styloid impingement. Coronal images **(A, B)** show subchondral sclerosis and cysts of the opposing surfaces of the radial styloid process and adjacent scaphoid (*arrows*).

To conclude, the wrist joint encompasses multitude of small bony and ligamentous structures, and a systematic approach in its evaluation is essential for quality reporting.

SUGGESTED READINGS

Buck FM, Gheno R, Nico MA, et al. Ulnomeniscal homologue of the wrist: Correlation of anatomic and MR imaging findings. *Radiology*. 2009;253(3):771–779.

Burns JE, Tanaka T, Ueno T, et al. Pitfalls that may mimic injuries of the triangular fibrocartilage and proximal intrinsic wrist ligaments at MR imaging. *Radiographics*. 2011;31(1):63–78.

Chhabra A, Soldatos T, Thawait GK, et al. Current perspectives on the advantages of 3-T MR imaging of the wrist. *Radiographics*. 2012;32(3):879–896.

Coggins CA. Imaging of ulnar-sided wrist pain. *Clin Sports* Med. 2006;25(3):505–526.

Cunningham PM. MR imaging of trauma: Elbow and wrist. *Semin Musculoskelet* Radiol. 2006;10(4):284–292.

Davis KW, Blankenbaker DG. Imaging the ligaments and tendons of the wrist. *Semin Roentgenol*. 2010;45(3):194–217.

Ergun T, Lakadamyali H, Derincek A, et al. Magnetic resonance imaging in the visualization of benign tumors and tumor-like lesions of hand and wrist. *Curr Probl Diagn Radiol*. 2010;39(1):1–16.

Nobauer-Huhmann IM, Pretterklieber M, Erhart J, et al. Anatomy and variants of the triangular fibrocartilage complex and its MR appearance at 3 and 7T. *Semin Musculoskelet Radiol*. 2012;16(2):93–103.

Shahabpour M, Van Overstraeten L, Ceuterick P, et al. Pathology of extrinsic ligaments: A pictorial essay. *Semin Musculoskelet* Radiol. 2012;16(2):115–128.

Taljanovic MS, Malan JJ, Sheppard JE. Normal anatomy of the extrinsic capsular wrist ligaments by 3-T MRI and high-resolution ultrasonography. *Semin Musculoskelet Radiol*. 2012; 16(2):104–114.

Tanaka T, Ogino S, Yoshioka H. Ligamentous injuries of the wrist. Semin Musculoskelet Radiol. 2008;12(4):359–377.

Theumann NH, Pfirrmann CW, Antonio GE, et al. Extrinsic carpal ligaments: Normal MR arthrographic appearance in cadavers. Radiology. 2003;226(1):171–179.

Weber MA, von Stillfried F, Kloth JK, et al. Cartilage imaging of the hand and wrist using 3-T MRI. Semin Musculoskelet Radiol. 2012; 16(2):71–87.

Weinberg EP, Hollenberg GM, Adams MJ, et al. High-resolution outpatient imaging of the wrist. Semin Musculoskelet Radiol. 2001;5(3):227–234.

Wilson D, Allen GM. Imaging of the carpal tunnel. *Semin Musculoskelet Radiol*. 2012;16(2):137–145.

APPENDIX 1: Sample Completed Structured Report: Wrist: NORMAL

EXAM: MR WRIST [<WITH> OR <WITHOUT>] CONTRAST

HISTORY: []-year-old <patient sex> with <order reason for study>

TECHNIQUE: Imaging was performed [without IV contrast/before and after IV/after intra-articular contrast]. Multiplanar, multisequence MR images of the [right/left] wrist were obtained on a [1.5 or 3] Tesla magnet.

COMPARISON: [<None>]

FINDINGS:

Alignment: [<Normal>]

Ulnar variance: [<Neutral>]

Distal radioulnar joint: [<Congruent>]

Scapholunate dissociation: [<Absent>]

Fluid:

Carpus joint effusion: [<None>]

Distal radioulnar joint effusion: [<None>]

Intrinsic ligaments:

Scapholunate: [<Intact>]

Lunotriquetral: [<Intact>]

Ulnar side:

Triangular fibrocartilage ligament: [<Intact>]

Lunate facet: [<Absent>]

Hamate–lunate joint: [<Normal>]

Ulnocarpal impaction: [<None>]

Extensor compartment:

I: [<Normal>]

II: [<Normal>]

III: [<Normal>]

IV: [<Normal>]

V: [<Normal>]

VI: [<Normal>]

Flexor compartment:

Flexor retinaculum: [<Normal>]

Flexor tendons: [<Normal>]

Carpal tunnel: [<Normal>]

Median nerve: [<Normal>]

Guyon canal: [<Normal>]

Articular:

Thumb–carpometacarpal/Metacarpophalangeal joints: [<Normal>]

Scaphotrapeziotrapezoidal joint: [<Normal>]

Pisiform–triquetral joint: [<Normal>]

Extrinsic ligaments:

Radial collateral ligament/Ulnar collateral ligament: [<Intact>]

Dorsal intercarpal ligament/Volar extrinsic ligaments: [<Intact>]

Bones: [<Normal>]

Muscles: [<Normal>]

Vessels: [<Normal>]

Other:

Impression:

1. [<>]

APPENDIX 2: Sample Completed Structured Report: Wrist: ABNORMAL

EXAM: MR WRIST WITH CONTRAST

HISTORY: [<25-year-old man with right wrist pain>]

TECHNIQUE: Imaging was performed [<after intra-articular contrast>]. Multiplanar, multisequence MR images of the [<right>] wrist were obtained on a [<1.5] Tesla magnet.

COMPARISON: [<Radiographs dated 9/11/2014>]

FINDINGS:

Alignment: [<DISI deformity>]

Ulnar variance: [<Mild negative ulnar variance>]

Distal radioulnar joint: [<Congruent>]

Scapholunate dissociation: [<Present>]

Fluid: Trace

Carpus joint effusion: [<Intra-articular contrast with no body>]

Distal radioulnar joint effusion: [<Trace fluid>]

Intrinsic ligaments:

Scapholunate: [<Complete tear with involvement of all bands. Contrast extends from the radiocarpal space to the midcarpal space>]

Lunotriquetral: [<Intact>]

Ulnar side:

Triangular fibrocartilage ligament: [<Degenerative signal and tear of the styloid attachment of peripheral portion>]

Lunate facet: [<Present>]

Hamate–lunate joint: [<Normal>]

Ulnocarpal impaction: [<Absent>]

Extensor compartment:

I: [<Mild tendinosis>]

II: [<Normal>]

III: [<Normal>]

IV: [<Normal>]

V: [<Normal>]

VI: [<Moderate tendinosis and mild tenosynovitis>]

Flexor compartment:

Flexor retinaculum: [<Mild bowing>]

Flexor tendons: [<Mild tenosynovitis>]

Carpal tunnel: [<Deep fat pad effaced>]

Median nerve: [<Mild enlargement proximally with mild flattening in the tunnel. Moderate hyperintensity with extends in its branches>]

Guyon canal: [<Normal>]

Articular:

Thumb–carpometacarpal/metacarpophalangeal joints: [<Mild osteoarthrosis>]

Scaphotrapeziotrapezoidal joint: [<Normal>]

Pisiform–triquetral joint: [<Normal>]

Extrinsic ligaments:

Radial collateral ligament/ulnar collateral ligament: [<Attenuated with subcortical cystic change at its scaphoid attachment>]

Dorsal intercarpal ligament/volar extrinsic ligaments: [<Ganglion in relation to volar intercarpal ligament measuring 15 × 4 mm>]

Bones: [<Otherwise normal>]

Muscles: [<Normal>]

Vessels: [<Normal>]

Other: [<None>]

IMPRESSION:

1. Complete scapholunate disruption with scapholunate dissociation and DISI deformity.

2. Ganglion in relation to volar intercarpal ligament.

3. Low-grade peripheral TFCC tear.

4. Small carpal effusion.

5. Findings of carpal tunnel syndrome with mild flexor tenosynovitis.

6. ECU tendinosis and tenosynovitis.

9

The Hip ☑

Avneesh Chhabra, Shivani Ahlawat, and Theodoros Soldatos

The hip (or femoroacetabular) joint is a ball-and-socket articulation, which connects the axial skeleton with the lower extremity. It is one of the largest joints in the body and helps retain balance and supports the body's weight in both static and dynamic postures. The concave acetabulum articulates with the convex femoral head permitting a joint space, which is equal at each point with slight deviation to allow adequate lubrication. This symmetry allows for rotation about a fixed axis related to the action of four groups of muscles that permit adduction, abduction, flexion, and extension of the lower extremity.

Various diseases of traumatic, degenerative, infectious, and metabolic origin may affect the hip, similar to any other joint. A systematic imaging analysis and structured reporting is essential for optimal diagnostic assessment of the hip structures. In most situations, unilateral hip imaging provides better spatial and contrast resolution, due to the small field of view and use of a dedicated surface coil. Imaging of both hips as part of pelvis protocol is recommended in suspected osteonecrosis, decubitus ulcer or search for metastases. Intravenous contrast material may be used to determine the tissue viability in osteonecrosis and in cases of suspected infection or tumors. Direct MR arthrography is traditionally indicated in cases of suspected labral pathology, intra-articular bodies, osteochondral lesions, as well as for preoperative assessment of developmental hip dysplasia, especially on low field scanners. Alternatively, indirect MR arthrography can be performed by intravenous injection of gadolinium (1 mmol/kg) followed by 10 to 15 minutes of gentle exercise and subsequent acquisition of fat-saturated (fs) T1-weighted (T1W) images in all three orthogonal planes. With current high resolution and 1.5 T or 3T imaging, indications for arthrography are diminishing. On the most part, MR arthrography is performed if patients need a diagnostic or therapeutic pain injection as well. This chapter discusses the imaging evaluation approach and describes how to fill in the structured checklist in Box 1. Conceptual details of related MR physics and imaging protocol are discussed in the chapter of MR protocol optimization.

IMAGE EVALUATION

The below-outlined stepwise interpretation approach is only a practical guide, and all hip

structures should be evaluated in multiple planes for their optimal assessment. This will also help readers perceive which structures are best depicted and evaluated in which particular plane.

1. Line up the similar plane fs and non-fs images and synchronize them for tandem evaluation. Evaluate the visualized pelvic viscera, sacrum, and spine in all three planes, before assessing the hip for significant pathology or mass lesions.
2. Start with the coronal images and look for possible hip effusion, which will be evident by capsular distention. Evaluate the bones in regards of alignment, presence of femoral head and neck bump, fibrocystic change and shallow acetabulum, os acetabulum, and check the bone marrow for red marrow reconversion or other signal abnormality. Next, rule out cartilaginous or osteochondral bodies and ligamentum teres pathology, and check the gluteal, hamstring, and iliopsoas tendons for anatomic continuity, tears or adjacent insertional abnormalities (e.g., trochanteric bursitis, enthesopathy, avulsive cystic changes). Subsequently, evaluate the superolateral labrum and chondrolabral junction, and look particularly for paralabral cysts. Finally, check the articular cartilage for osteoarthritic changes or osteochondral lesions.
3. On sagittal images, evaluate the anterosuperior and posteroinferior labrum and the respective chondrolabral junctions. This is a good plane to assess for potential joint space loss, cartilage defects, fissures, and subchondral cysts, especially at the anterosuperior joint compartment, the most common site for labro-cartilagenous lesions. Finally, check for iliopsoas bursitis and tendon retraction, if there are gluteal, hamstring, or rectus adductor aponeurosis tears.
4. The axial plane is optimal for the evaluation of the anterior and posterior labrum (check again for paralabral cysts) and iliopsoas bursa, but also provides adequate assessment of the gluteal, hamstring, and iliopsoas tendons and their related bursae. Regional muscles, vessels, and nerves are also best evaluated on the axial images.

BOX 1: The Structured Report: Hip

The checklist for structured reporting of MR imaging of the hip. For each field, *Normal* is considered default in the dictation whereas the rest of the elements describe various pathologies that could be encountered during imaging evaluation. See Appendices 1 and 2 at the end of the chapter for sample completed reports for normal and abnormal examination results.

EXAM: MRI OF THE [<RIGHT / LEFT>] HIP [<WITH / WITHOUT>] CONTRAST

FINDINGS:

Alignment: [<Normal> <Subluxation / Dislocation>]

Femoroacetabular impingement-related anatomy:

Pincer: [<Normal> <Retroversion / Overcoverage / Os acetabulare>]

Cam: [<Normal head-neck offset> <Fibrocystic lesion of femoral neck / Femoral head and neck bump>]

Dysplasia: [<None> <Shallow acetabulum / Labral hypertrophy>]

Fluid: [<Normal> <Small effusion / Moderate effusion / Large effusion> <Synovial hypertrophy>]

Trochanteric bursitis: [<Absent / Present>]

Labrum: [<Normal> <Degenerative fraying> <Tear> <Chondrolabral separation> <Paralabral cyst> <Labral ossification>]

Cartilage:

Femoral: [<Normal> <Low-grade thinning / High-grade thinning> <Low-grade defects/ High-grade defects>]

Acetabular: [<Normal> <Low-grade thinning / High-grade thinning> <Low-grade defects/ High-grade defects>]

Capsule/ligaments: [<Normal> <Thickened or sprained iliofemoral, ischiofemoral, or pubofemoral ligaments>]

Visualized muscles/tendons:

Gluteal: [<Normal> <Strain> <Tendinopathy> <Muscle atrophy> Enthesopathy>]

Adductors: [<Normal> <Strain> <Atrophy>]

Iliopsoas: [<Normal> <Strain>]

Lateral rotators: [<Normal> <Strain> <Piriformis asymmetry> <Ischiofemoral impingement-related edema and/or fatty infiltration of quadratus femoris>]

Hamstrings: [<Normal> <Strain> <Tendinosis> <Enthesopathy>]

Bones: [<Otherwise normal>]

Vessels: [<Normal / Abnormal>]

Nerves: [<Normal / Abnormal>]

Viscera: [<Visualized pelvic structures appear normal. No lymphadenopathy by size criteria. No significant free fluid in the pelvis / Ascites>]

Miscellaneous:

IMPRESSION:

[<In the order of importance with acute findings first>]

HOW TO FILL THE STRUCTURED REPORT

ALIGNMENT: [<Normal> <Subluxation / Dislocation>]

FEMOROACETABULAR IMPINGEMENT-RELATED ANATOMY:

Pincer: [<Normal> <Retroversion / Overcoverage / Os acetabulare>]

Cam: [<Normal head-neck offset> <Fibrocystic lesion of femoral neck / Femoral head and neck bump>]

Evaluation of the bony structures and alignment is best performed on non-fs images, which provide accurate assessment of the bone marrow and cortex, as well as clear depiction of osteophytes. The spherical-shaped femoral head should normally be centered within the acetabular fossa (Fig. 1). In posterior subluxation/dislocation, the femoral head is placed superolaterally with respect to the acetabulum, and the condition may be complicated with injury to the sciatic nerve. In the less common anterior subluxation/dislocation, the femoral head is displaced anteroinferiorly with respect to the acetabulum, and the entity may be associated with injury to the femoral artery and nerve. In central dislocation, the femoral head protrudes into the pelvic cavity, and the entity may be complicated with intrapelvic soft tissue injury and hemorrhage. These can be commonly seen in association with underlying bone insufficiency, such as with osteoporosis, inflammatory arthropathy, or osteomalacia. When associated with femoral head fractures, hip dislocations may be classified according to the Pipkin classification, the key criterion of which is whether the fracture line lies above or below the fovea capitis (Table 1). Spina bifida may be associated with valgus hip posturing (coxa valga) (Fig. 2).

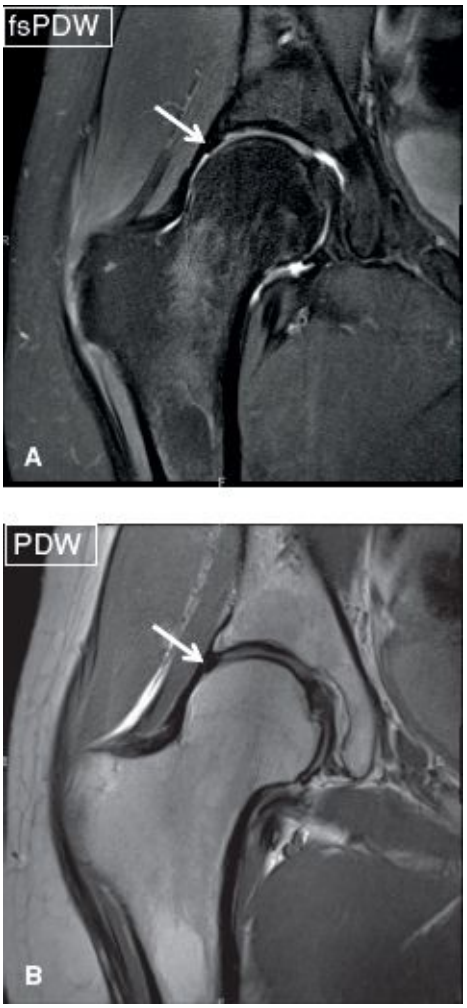

Fig. 1: Normal hip bony alignment. Coronal images **(A, B)** demonstrate the spherical-shaped femoral head centered within the acetabular fossa. Notice normal hypointense appearance of the labrum.

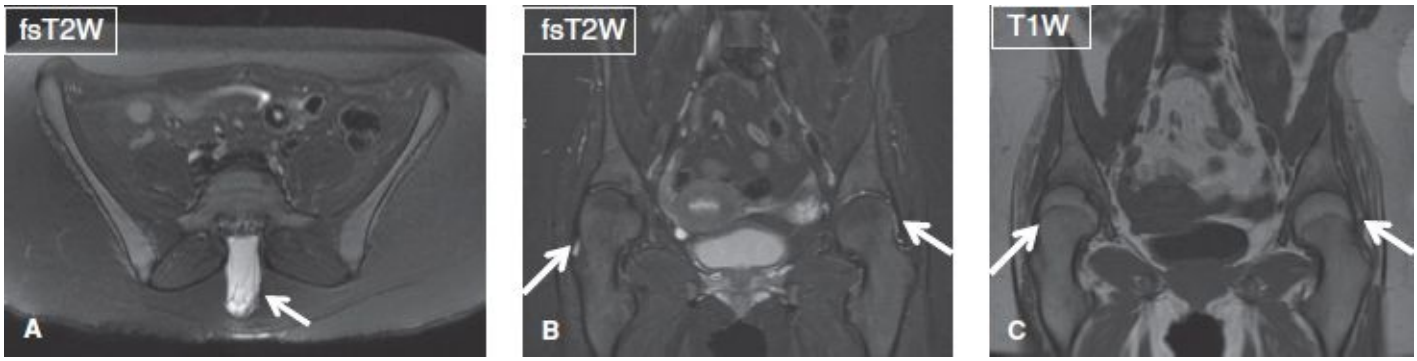

Fig. 2: Abnormal hip alignment. Axial **(A)** and coronal **(B, C)** images show a case of spina bifida (*arrow* in **A**) associated with valgus hip posturing (*arrows* in **B, C**).

TABLE 1: The Pipkin classification of femoral head fractures, when associated with hip dislocation

Type	Features
I	Fracture of the femoral head caudal to the fovea capitis
II	Fracture of the femoral head cephalad to the fovea capitis
III	Type I and type II with associated fracture of the femoral neck
IV	Type I, II, or III with associated fracture of the acetabulum

Femoroacetabular impingement (FAI) refers to chronic pathomechanical abutment of the femoral head–neck junction and acetabulum, which leads to acetabular labral tears and breakdown of the articular cartilage, and subsequent development of early osteoarthritis (OA) in otherwise normal hip. FAI may result from a "too big or posteriorly rotated (retroverted) acetabulum" configuration, which results in excessive coverage of the femoral head globally and anterolaterally, respectively by the acetabulum. It leads to abnormal contact between the acetabular rim and femoral head–neck junction (*pincer-type FAI*). Alternatively, a "too big head" configuration, which refers to a non-spherical femoral head or an inadequate femoral head–neck offset, leads to abnormal compression and stress between the acetabular labrocartilaginous complex and the prominent femoral head–neck junction during hip flexion, adduction, and internal rotation (*cam-type FAI*). Commonly, both mechanisms play together in the course of FAI and/or progression to OA. Prevention of irreversible degenerative joint changes is feasible by surgical intervention only in early stages of the disease; thus, prompt detection and grading of the disease are imperative to improve the patient prognosis. Some subjects depending upon their type and level of activities (e.g., golfing, soccer) may be predisposed to FAI at different degrees of femoroacetabular articulations (dynamic FAI) and the respective degree of correctional surgery may differ, meaning personalized to such subjects. It should be noted that FAI is a clinical diagnosis and it is best to describe the altered anatomy and refer in impression as "anatomy associated with FAI" with associated labrocartilaginous lesions.

Pincer-type FAI may be congenital (e.g., coxa profunda with global overcoverage, or acetabular retroversion with focal overcoverage at the anterolateral margin) or acquired (e.g., prior trauma, os acetabulare and marginal osteophytes). Coxa profunda is diagnosed on radiographs if the acetabular margin extends medial to the ilioischial line and on MRI if the center-edge angle is more than 39 degrees (normal 19 to 39 degrees). One can also draw the lateral center-edge (Wiberg) angle on coronal images, with the vertical and oblique lines intersecting through the center of the femoral head and the lateral acetabular margin, respectively. The angle is small (<19 degrees) in dysplasia and large (>39 degrees) in overcoverage. Another way one might diagnose overcoverage on MRI, would be using the axial images obtained through the midlevel of the femoroacetabular joint, where

the center of the femoral head circumference will lie medial to the line drawn from the anterior to the posterior bony margins at the base of the labrum. A recent study showed that it is quiet common to see this finding on radiographs in asymptomatic subjects and it may not predispose to FAI. Acetabular retroversion is present when the alignment of the acetabular face is not directed in the normal anterolateral direction but inclines more posterolaterally. The condition may be part of a complex dysplasia or a single entity and is established on axial images when the anterior wall margin of the acetabulum is neutral or more lateral as compared to the posterior wall margin whereas in normal hip, the anterior wall lies more medially. This should be assessed on proximal 2 to 4 sections of the hip joint where one sees the complete femoral head. Correlation with available radiographs should be obtained, where one may see a figure-of-eight sign, that is, anterior wall crossing lateral to the posterior wall along the superior aspect of the acetabulum (Fig. 3). Current trend is to obtain pre-operative CT imaging in FAI patients to evaluate the hip anatomy and calculate the acetabular as well as femoral version in the same setting. Femoral version can either protect (antevesion making CAM deformity less likely to impinge) or make it more susceptible (relative retroversion making it more likely to impinge). Similar imaging can be done with MRI but this approach requires more time for acquisition with potential coil movement from hip to knee.

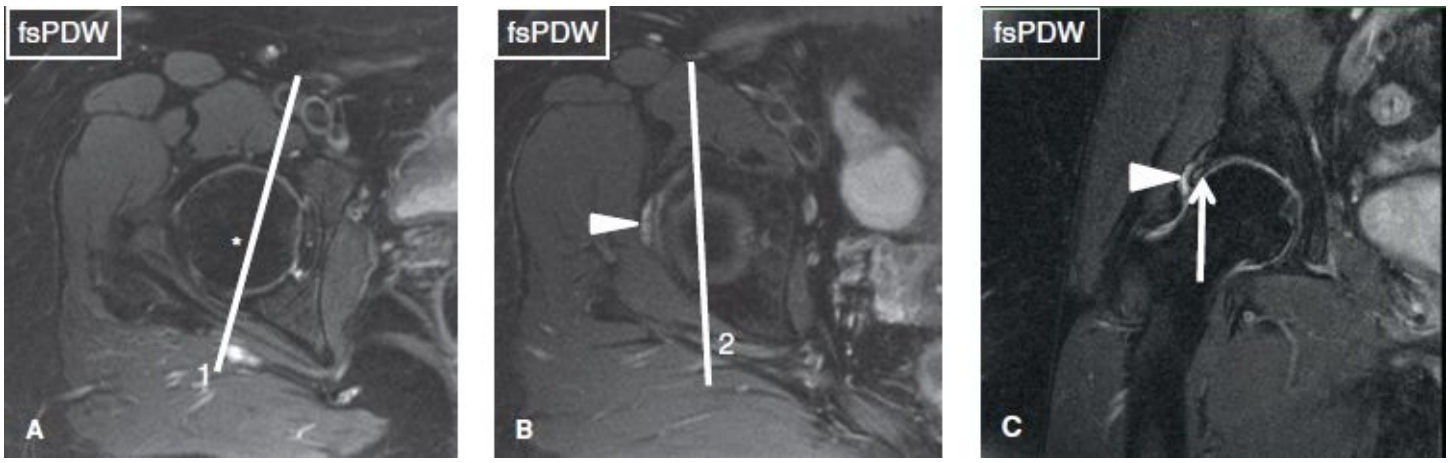

Fig. 3: Pincer-type femoroacetabular impingement presenting with left hip pain. Axial **(A, B)** and coronal **(C)** images. At the midlevel of the femoroacetabular joint **(A),** the center of the femoral head (*asterisk*) is lateral to the line (*1*) drawn from the anterior to the posterior labrum, indicating absence of global overcoverage. In a superior axial image **(B),** one can see anterior wall of acetabulum lateral to the posterior wall, line (*2*). Notice superolabral tear (*arrow* in **C**) with an associated paralabral cyst (*arrowheads* in **B, C**).

Common soft tissue imaging findings in pincer-type FAI include smaller anterosuperior and larger posteroinferior labral lesions (degeneration, truncation, hypertrophy, and tears with/without paralabral cysts), along with associated damage of the acetabular articular cartilage and/or subchondral cyst formation. Absence of large areas of cartilage abnormality or significant arthritis on MR imaging is good predictor of successful outcome in FAI cases. Other osseous findings include intralabral ossification at the lateral margin of

the acetabular dome and the anterior margin of the hip joint, lateral acetabular rim fracture, as well as bony buttering and indentation with or without sclerosis at the femoral neck, due to pinching effect by the large acetabulum. Rim fracture is oriented perpedicular to the acetabular margin as compared to commonly found parallel oriented Os acetabulare. Additional finding of cartilage coverage over the rim is supportive for the diagnosis of a rim fracture. On delayed gadolinium-enhanced MR imaging of cartilage (dGEMRIC), one would see global T1 signal alteration reflective of diffuse glycosaminoglycan loss. The term "os acetabuli" refers to periacetabular ossicles, which should raise the suspicion for underlying labral pathology, especially in adult subjects. They should not be confused with ossification of the acetabular labrum, in which bone marrow signal intensity extends into the substance of the labrum (Fig. 4).

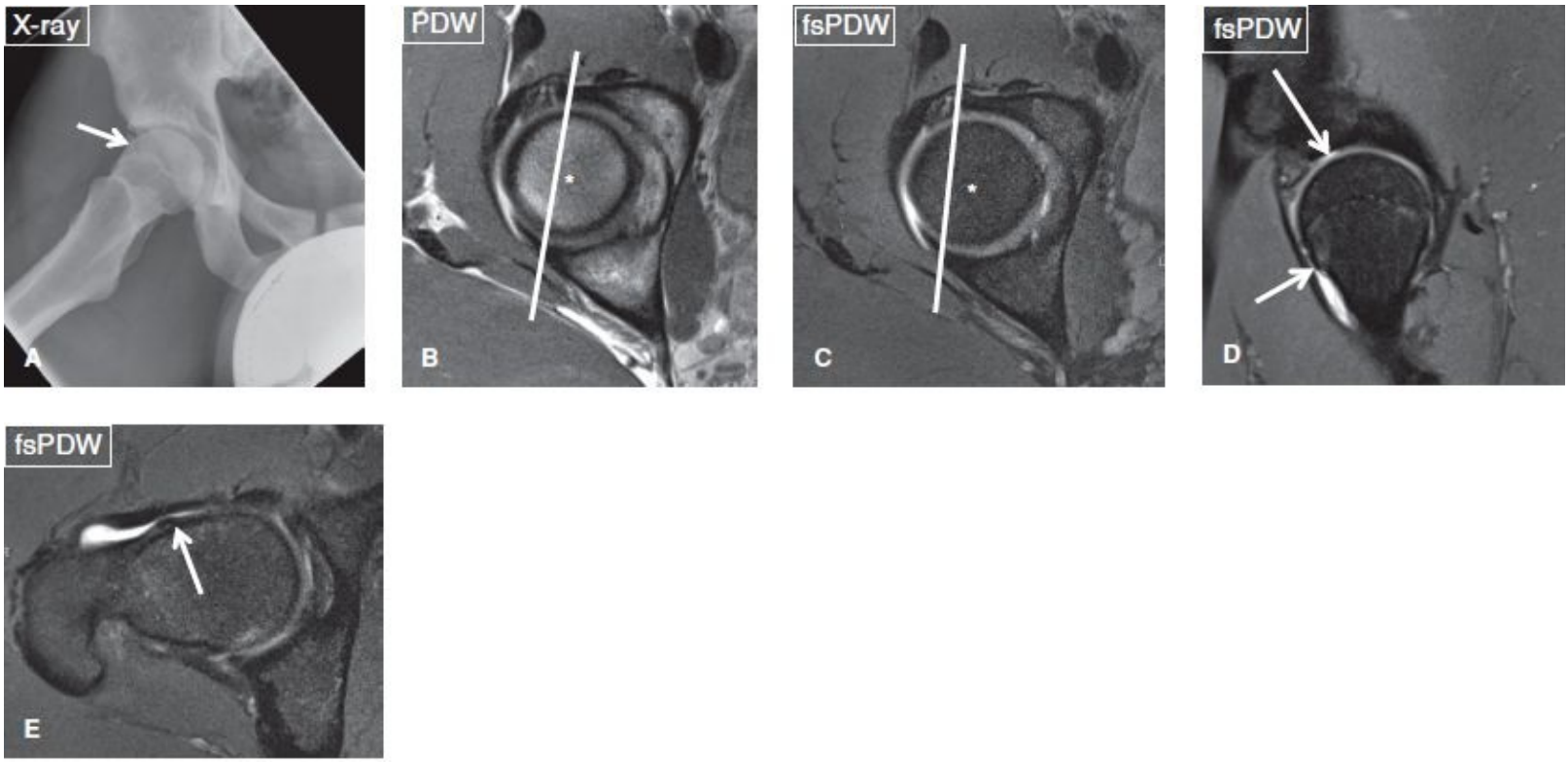

Fig. 4: Mixed (pincer- and cam-type) femoroacetabular impingement. **A:** Anteroposterior radiograph shows overcoverage with labral ossification (*arrow*). **B, C:** On axial images, the center of the femoral head (*asterisks*) is medial to the line drawn from the anterior to the posterior acetabular margins, indicating overcoverage that would cause pincer-type femoroacetabular impingement. **D:** Sagittal images reveal a bump (*short arrow*) at the femoral head–neck junction reflecting cam-type femoroacetabular impingement. Also note a high-grade cartilage defect of the anterosuperior acetabulum (*long arrow*). **E:** The bump (*arrow*) is also confirmed in the axial plane.

In cam-type FAI, a bony bump exists in the femoral head–neck junction, creating lack of normal concave offset (straightening or convex margin), which may be developmental or may be result of prior slipped capital femoral epiphysis (SCFE). The size of the associated fibrocystic change may vary from a tiny, few millimeter lesion (more common) to a giant

lesion >1 cm (Figs. 5, 6). Other acquired etiologies include prior trauma and avascular necrosis (AVN) of the femoral head. The diagnosis can be established on oblique axial non-fs images, when there is decreased anteroposterior distance (<8 mm, normal >11 mm) between the lines drawn as tangents to the femoral head, and neck, respectively. Anterior femoral distance (AFD) may be measured as the distance between lines tangent to the neck and the bump. More than 3.6-mm AFD also confirms CAM-type impingement anatomy. The other widely accepted measurement to establish the abnormality is the alpha angle. The latter is again calculated on the oblique axial image or frog leg lateral view through the fovea by extrapolating one line along the long axis of the femoral neck through the center of the femoral head, and a second line from the center of the femoral head to a point on the anterior femoral head where it exits the radius of the best fit circle on the femoral head. A normal alpha angle is 42 degrees with an upper limit of 55 degrees (Fig. 7). Patients are usually symptomatic when the angle is more than 65 degrees. Depending upon the degree of bony protuberance of the femoral head and neck junction, the findings may be reported as lack of normal concave offset, or bump at the femoral head and neck junction (Fig. 8). Chronic abutment of the acetabulum over the anterosuperior femoral bump can cause small cortical defects on the latter, through which synovial tissue may herniate and create T2 hyperintense subcortical cysts, termed fibrocystic changes or herniations pits (Figs. 5, 6, 8). Other typical findings in cam-type FAI include anterosuperior and superolateral labrum tears (commonly with associated chondrolabral separations), cartilage loss with/without subchondral cysts at the anterosuperior aspect of the acetabular dome and/or femoral head, femoral collar osteophyte formation, thickening of the iliofemoral ligament, and occasionally regional scarring of the synovial lining under the iliofemoral ligament, aka soft tissue CAM lesion. Soft tissue cam lesion is composed of fibrocartilage and synovial proliferation, which may be associated with subcortical bone marrow edema of the femoral head and neck junction or subcortical sclerosis on CT. It basically reflects early stage of FAI, which may be diagnosed in adolescent children and relatively younger adults, before full-blown fibrocystic changes develop in the head and neck area. In advanced stage of FAI, one will see multifocal high-grade and full-thickness cartilage loss (usually worse on the acetabular side), large osteophyte formation, perifoveal osteophytes, joint space loss, intra-articular synovial thickening, and/or loose bodies (Figs. 8, 9). Detection of cartilage abnormality is essential to report since labral teas are virtually the rule in the setting of FAI anatomy and the surgeon would want to know the cartilage status ahead of time before intervening for these labral and bony lesions. Few pitfalls should be kept in mind. The bump and fibrocystic change may be anterior, lateral, or superolateral, therefore, close interrogation of the femoral head and neck junction in all three planes is recommended, ideally with 3D imaging on CT or MRI (Figs. 9, 10). The fibrocystic changes may have different signals of fluid, fibrous tissue, or fat depending upon the temporal evolution and chronicity; thus, evaluation of both fs and non-fs images in tandem is recommended. Other advantages of isotropic 3D imaging include lesion visualization in any arbitrary plane with similar resolution, CT-like bone reconstructions for preoperative mapping, and sharper

definition of labral tears and cartilage fissures (Figs. 10–12). Finally, it should be noted that normal recesses (feature smooth margination) exist around the acetabular labrum underneath the iliofemoral ligament (perilabral sulcus) and at the anteroinferior and posteroinferior labral attachments with the transverse ligament, and these should not be mistaken for tears (irregular shape, intralabral signal alterations, abnormal labral morphology with truncation, and/or paralabral cyst).

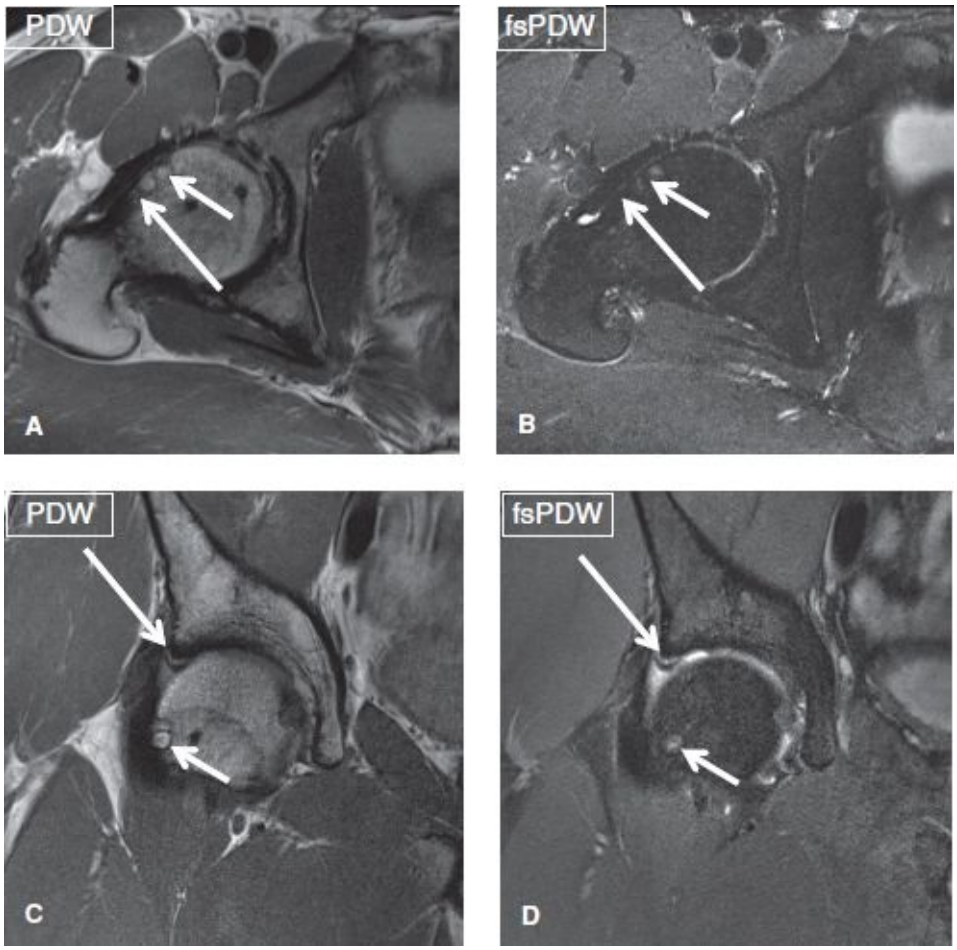

Fig. 5: Cam femoroacetabular impingement. **A, B:** Axial images at the midlevel of the femoroacetabular joint show inadequate femoral head–neck offset (*long arrows*), along with herniation pits (*short arrows*), some cystic and some partially fatty at the anterior aspect of the femoral head. **C, D:** The corresponding coronal images exhibit superolateral chondrolabral separation (*long arrows*). Note again the herniation pit/fibrocystic change (*short arrows*) of the femoral head and neck junction and a full-thickness cartilage defect of the superolateral acetabulum.

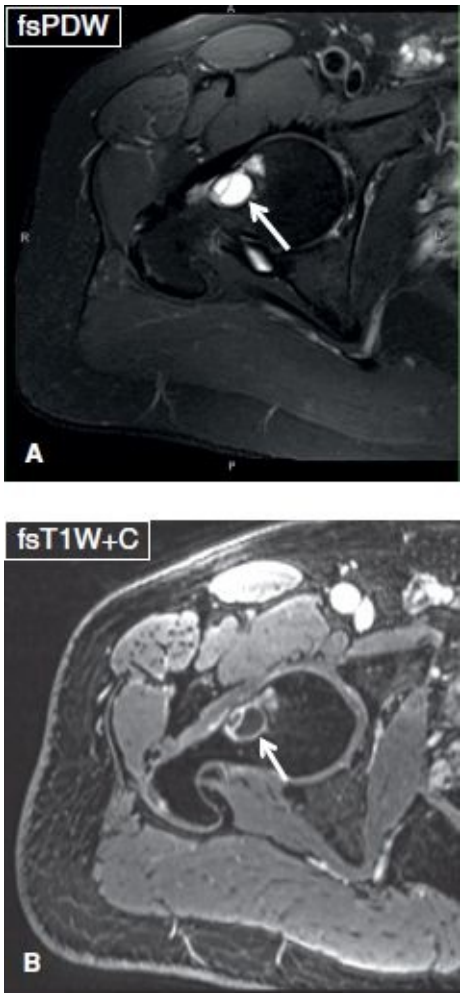

Fig. 6: Giant fibrocystic lesion. Axial images **(A, B)** show a large fibrocystic change (*arrows*) at the femoral head–neck junction, which demonstrates peripheral enhancement, reflecting herniated synovium in the setting of cam-type FAI.

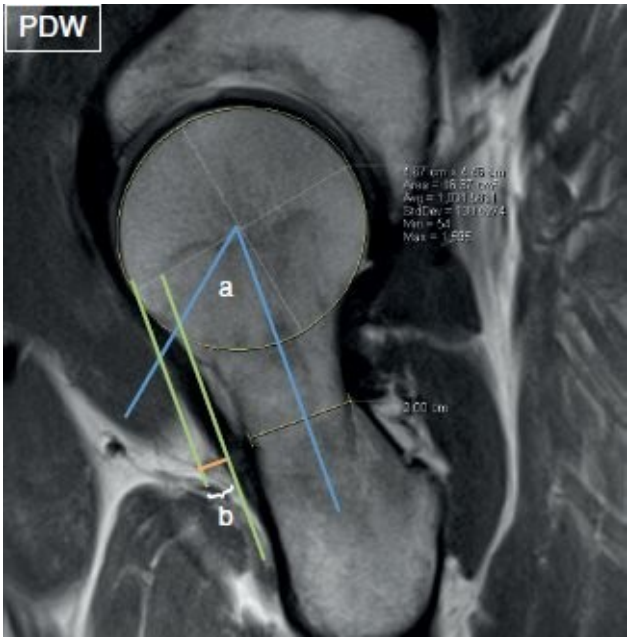

Fig. 7: Measurement of head–neck offset and alpha angle. Image acquired in oblique plane to reveal the full extent of the head–neck anatomic association displays the measurement of the alpha angle (*a*) and head–neck offset (distance *b*).

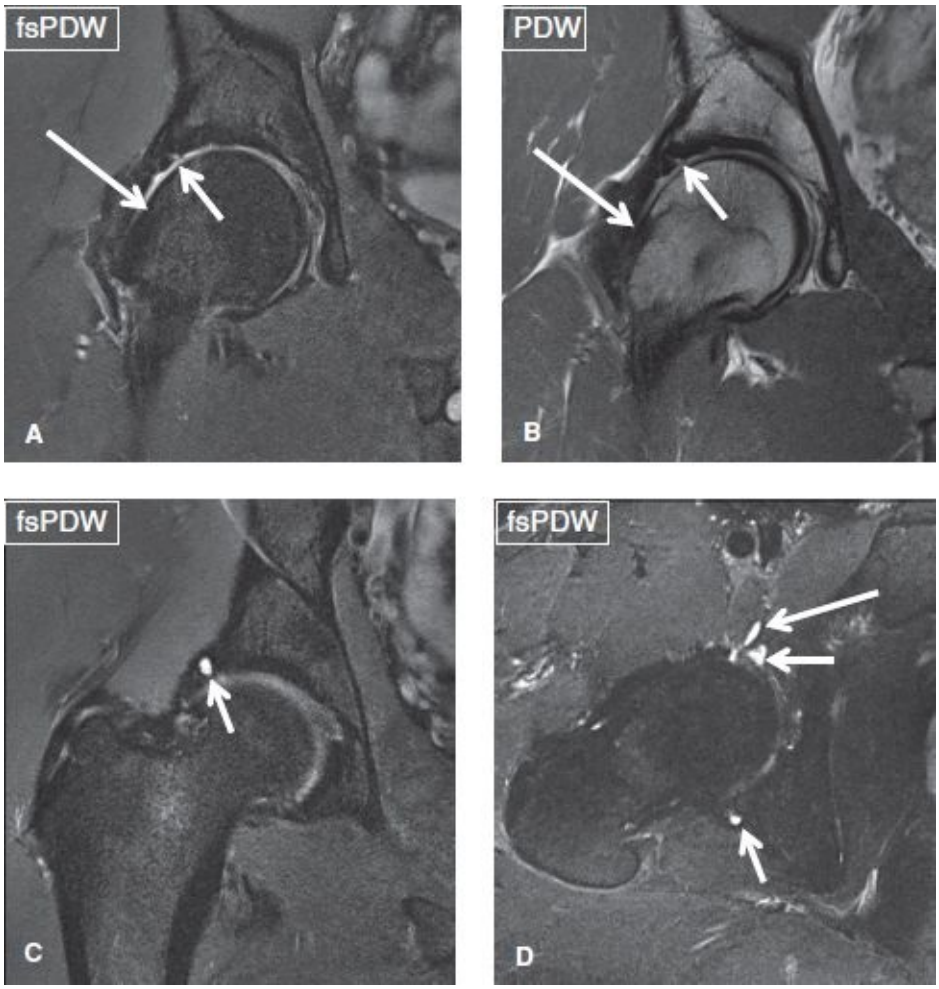

Fig. 8: Cam femoroacetabular impingement. Coronal **(A–C)** and axial **(D)** images exhibit lack of femoral head–neck offset (*large arrows* in **A, B**) and superolateral chondrolabral separation (*short arrows* in **A, B**). Notice intralabral cysts (*short arrows* in **C, D**), anteroinferior paralabral cyst (*long arrow* in **D**) and superolateral acetabular cartilage full-thickness defects with subchondral sclerosis.

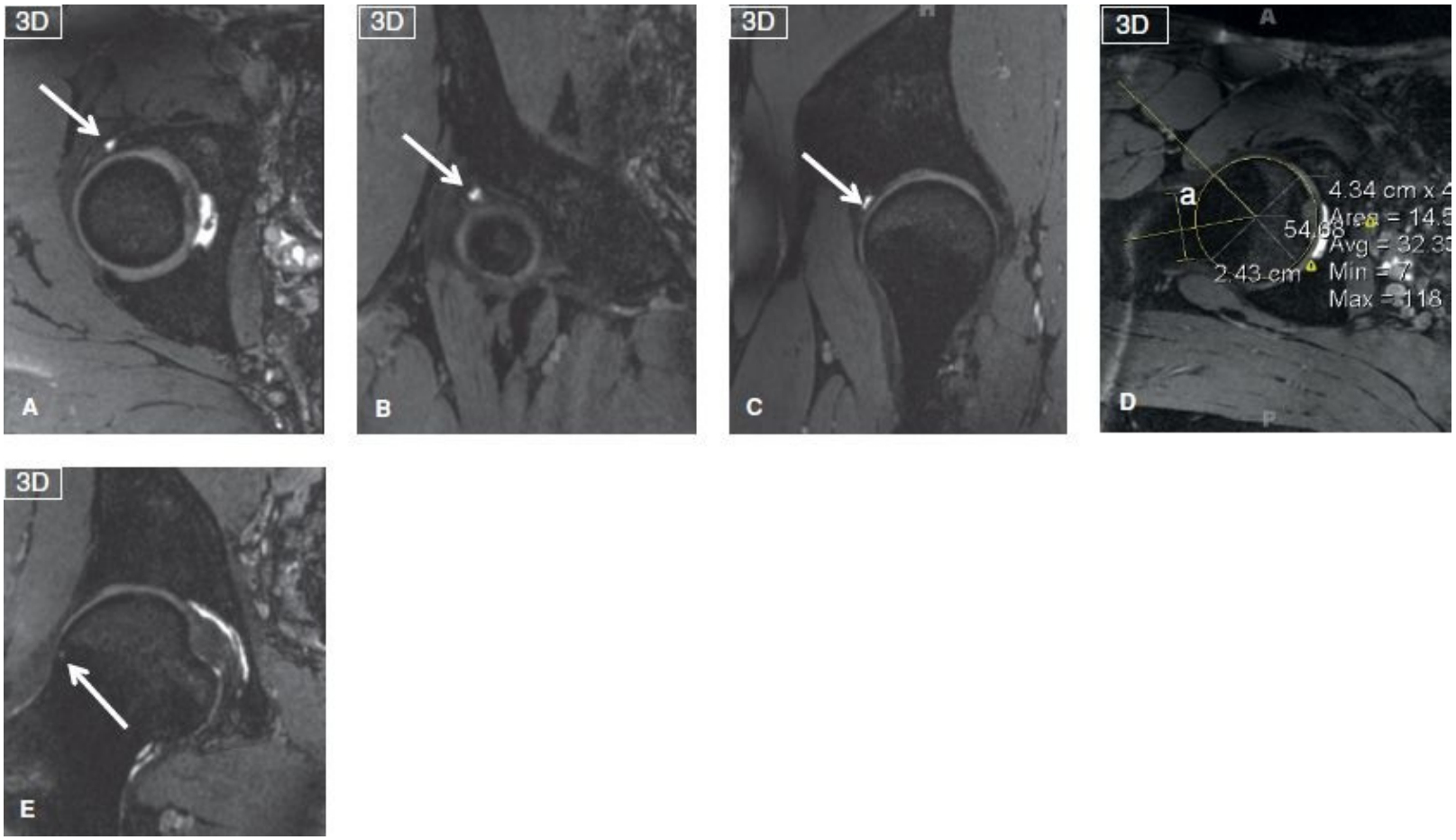

Fig. 9: Mixed (cam- and pincer-) type femoroacetabular impingement. Reconstructions in axial **(A),** coronal **(B),** and sagittal **(C)** planes from a three-dimensional isotropic steady state sequence show femoral head overcoverage, along with a intralabral cyst of the anterosuperior labrum (*arrows*). Reconstruction in oblique axial plane **(D)** shows an alpha angle measurement ($a = 55$ degrees). Another reconstruction in the coronal plane **(E)** exhibits the fibrocystic change (*arrow*) of the femoral head and neck junction.

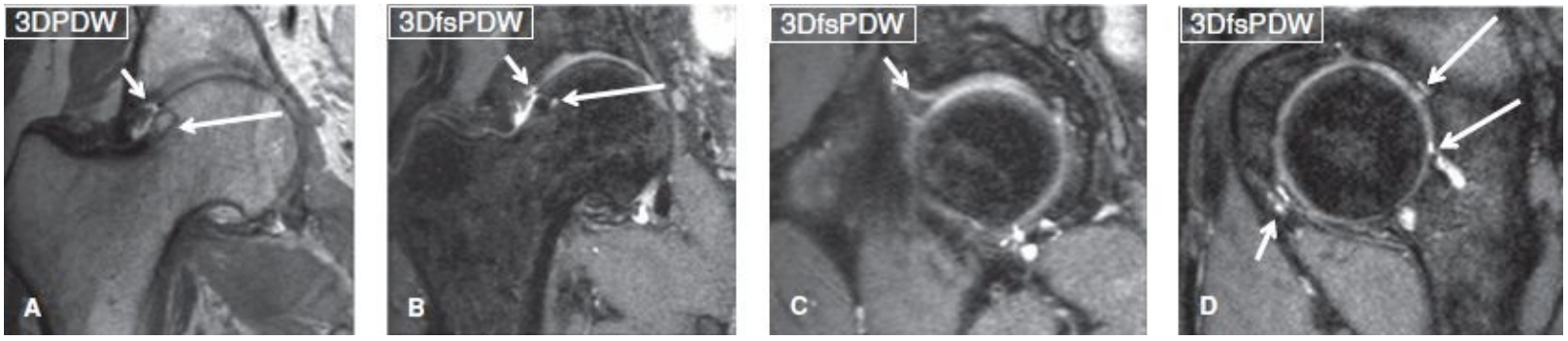

Fig. 10: Mixed (cam- and pincer-) type FAI on 3D isotropic spin-echo PDW and fsPDW images. Notice sharp definition of the superolateral chondrolabral separation (*short arrows*) and fibrocystic change with bump (*long arrows*) in coronal images **(A)** and **(B).** Sagittal images **(C, D)** show additional anterosuperior chondrolabral separation (*short arrow* in **C**), anteroinferior labral tear with intra- and paralabral cyst (*short arrow* in **D**) and full-thickness cartilage defects (*long arrows* in **D**) with multiple subchondral cysts.

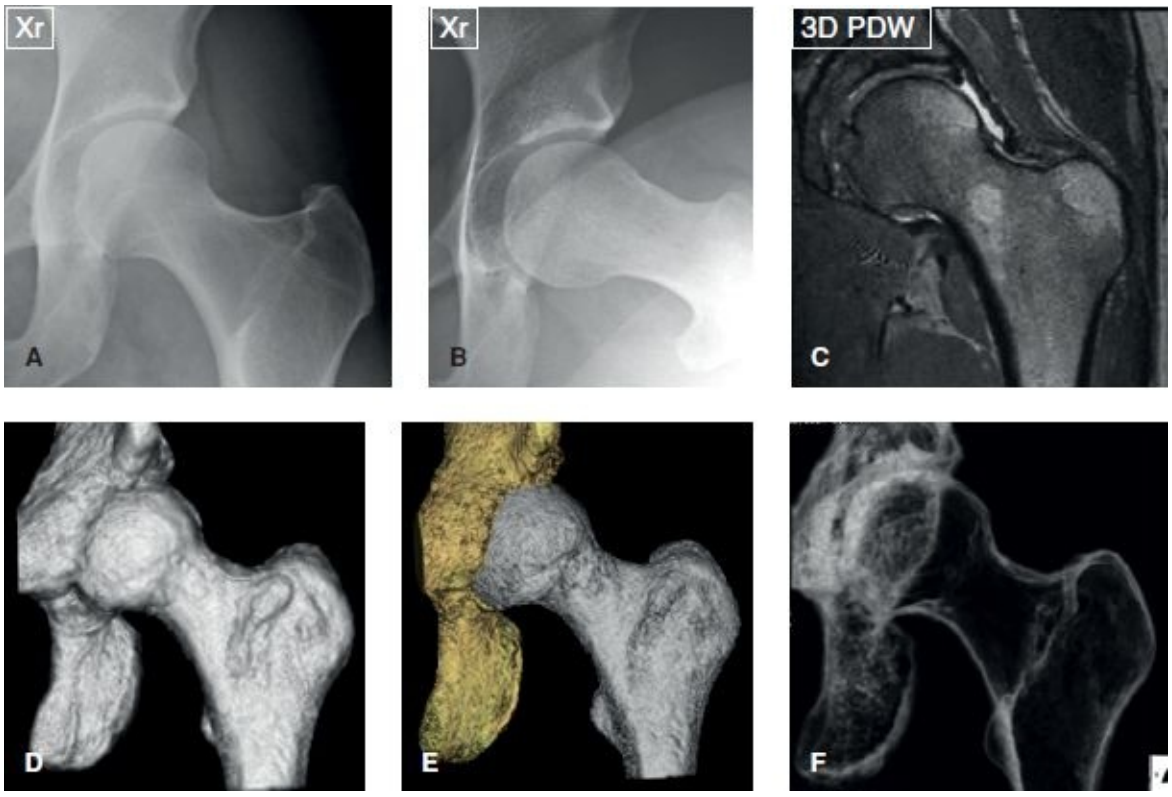

Fig. 11: Radiographs **(A, B)**, respective coronal 3D MR image **(C)** and 3D models generated from the isotropic 3D PDW sequence show the bone modeling in various contrast renderings, producing opaque and radiolucent Xray type views.

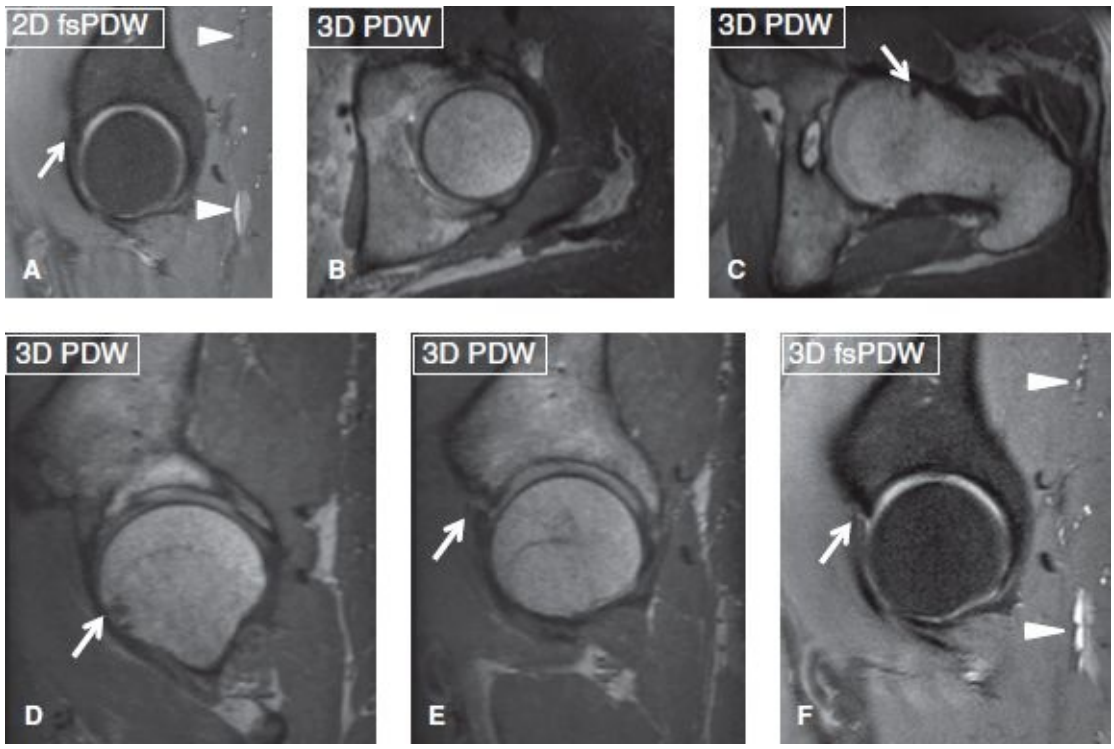

Fig. 12: Two-dimensional versus three-dimensional MRI: 2D coronal image: No labral tear seen. Isotropic 3D PDW **(B–E)** and 3D fsPDW **(F)** reconstructions show no overcoverage **(B)**, bump and fibrocystic change (*arrows* in **C, D**) as well as anterosuperior labral tear **(E, F).** Also note sharper posterior gluteal veins (*arrowheads*) on 3D image **(F)** compared to 2D image **(A).**

Surgeons that specialize in FAI operations may ask for other measurements on CT or MR imaging. The more common ones include, femoral neck-shaft angle, acetabular version and femoral version. The femoral neck-shaft angle is measured on a coronal slice or thick slab through the center of the femoral head between the lines through the center of the femoral neck and the proximal diaphysis. It normally measures 120–140 degrees. The acetabular version is measured on the axial image between the line joining anterior and posterior acetabular bony margins, and the line perpendicular to the plane of the ischial tuberosities. One should correct for the pelvic tilt. The normal measurements are 5, 10 and 15 degrees respectively, at 1:00, 2:00, and 3:00 positions, respectively. The femoral version is measured on the axial image between the lines coursing through the femoral neck and the horizontal. Internal rotation constitutes a negative angle. Next, draw a line between the posterior femoral condyles and the horizontal. External rotation at the knee constitutes a negative angle. Add the two angles.

A single or a combination of surgical procedures may be performed to treat FAI, including femoral head and neck bump resection (osteotomy), labral debridement and/or repair, acetabular chondroplasty, as well as acetabular and/or iliac rotational osteotomies. In the setting of a rim fracture, screw fixation of the acetabular rim should be performed to avoid post-operative acetabular undercoverage. In the postoperative setting, imaging will show sharply concave femoral neck from prior CAM resection, and focal deficiencies of the iliofemoral ligament and joint capsule. The labrum may show post-debridement free edge truncation and fibrocartilage formation at the healed cartilage site (Figs. 13, 14). The role of MR imaging is to assess the adequacy of neck debridement and residual bump, and to detect labral retears (fluid-like signal on fsPDW image, gadolinium imbibition in the labrum or chondrolabral junction, abnormal labral morphology, tear in a location that was previously absent before the surgery, and any progression of chondral loss or new cartilage defects), as well as new complications, including infection, and insufficiency fracture of the femoral neck or acetabulum.

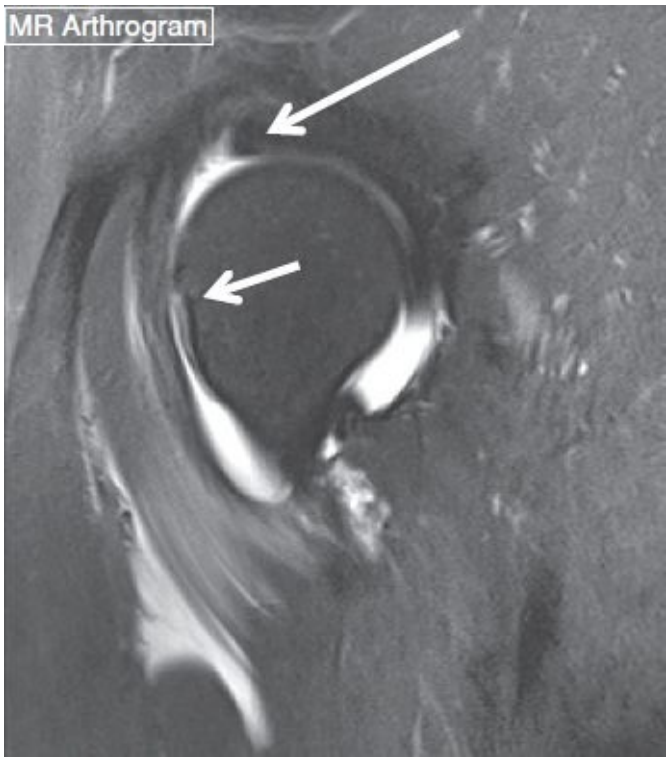

Fig. 13: Postoperative appearance of FAI correction surgery. Postsurgical follow-up sagittal MRA image demonstrates attenuated anterosuperior labrum (*long arrow*). Also note the normal appearance of the femoral osteotomy site (*short arrow*). No contrast imbibition in the labrum was seen on this postarthrogram image.

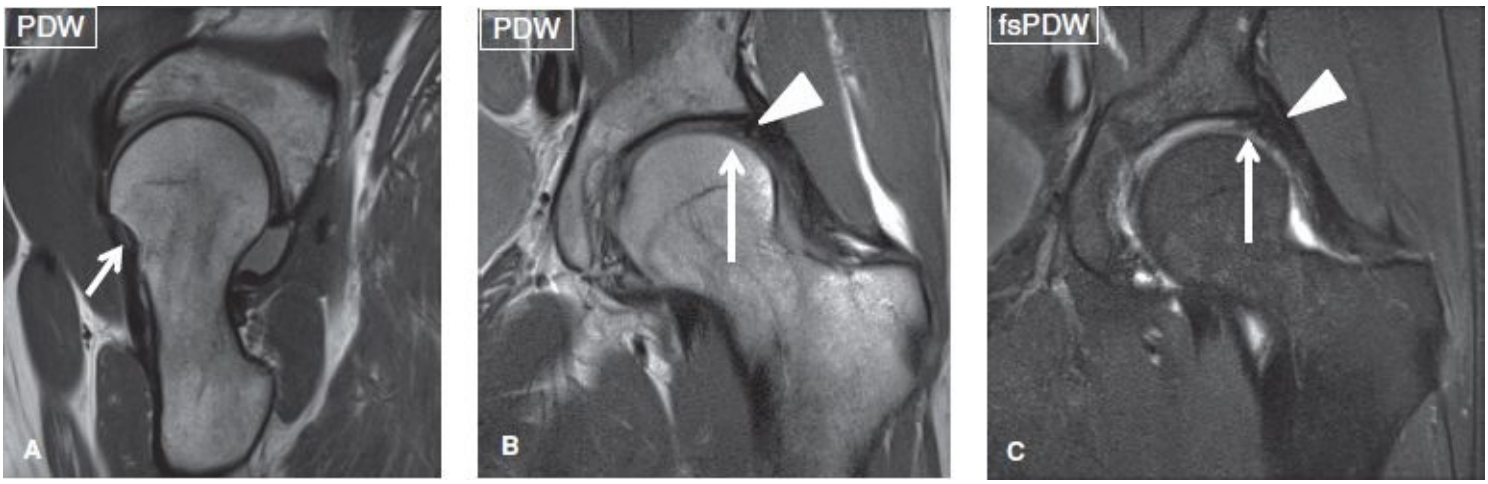

Fig. 14: Normal postoperative appearance. Post-FAI surgery and superolateral labral repair. Sagittal **(A)** image shows the femoral osteotomy site (*small arrow*). Coronal **(B, C)** images show the intact repaired labrum (*arrowheads*) and superolateral acetabular fibrocartilage formation (*long arrows*).

DYSPLASIA: [<None> <Shallow acetabulum / Labral hypertrophy>]

Similar to radiographs, developmental dysplasia of the hip can be diagnosed on coronal MR images by measuring the lateral center edge angle (Wiberg) as above. Shallow acetabulum is established when the angle is less than 19 degrees (19- to 25-degree borderline). One can also draw the acetabular angle, which is formed between the lines drawn horizontally

through the superior aspect of both triradiate cartilages (Hilgenreiner's line) and the superolateral bony edge of the acetabulum, with abnormal values exceeding 25 to 30 degrees. The angle should be measured on non-fs coronal images plane anterior to the fovea, where one sees obturator internus and externus muscles, otherwise the measurement may be falsely low (Fig. 15). In the dysplastic hip, the femoral head is located superiorly in the acetabulum, and the lateral aspect of the acetabular roof is oriented superiorly instead of inferiorly. The femoral head is normally 80% covered by the acetabulum. If more than 20% of the head is out laterally, it is called undercoverage, as observed in the dysplastic hips. If less than 10% is out, it means overcoverage (CE angle greater than 39 degrees), as can be observed in the setting of coxa profunda. In compensatory response to the increased load experienced by the front of the acetabulum, and to improve femoral head coverage and maintain joint lubrication, the labrum often undergoes developmental hypertrophy (and occasionally calcification or ossification and/or inversion), which predisposes it to impingement between the acetabulum and the femoral head, and subsequently further degeneration and tears. Additional soft tissue hypertrophy may be seen in the hyaline cartilage or the pulvinar fat pad. The condition leads to early degenerative joint changes and OA.

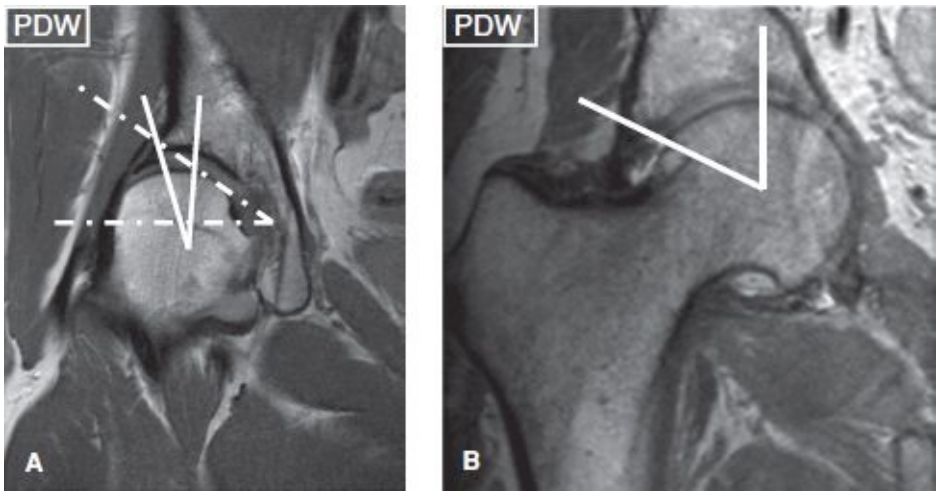

Fig. 15: Lateral center edge angle measurements. Dysplastic hip **(A)** versus overcoverage **(B)** show angles of 16 degrees versus 66 degrees, respectively. Notice abnormally high acetabular angle of 37 degrees (*dashed lines* in **A**).

MR imaging may detect unsuspected dysplasia, labral hypertrophy and/or tears (Fig. 16). It is also indicated in cases of unsuccessful hip reduction, to define the causative soft tissue component, such as an abnormal pulvinar fat pad, labrum intrusion, iliopsoas tendon interposition, and status of hyaline cartilage. In terms of prognosis, the chances of recurrent subluxations, chondral wear, and predisposition to AVN worsen with increasing levels of lateral uncovering (extrusion) of the femoral head (Fig. 17).

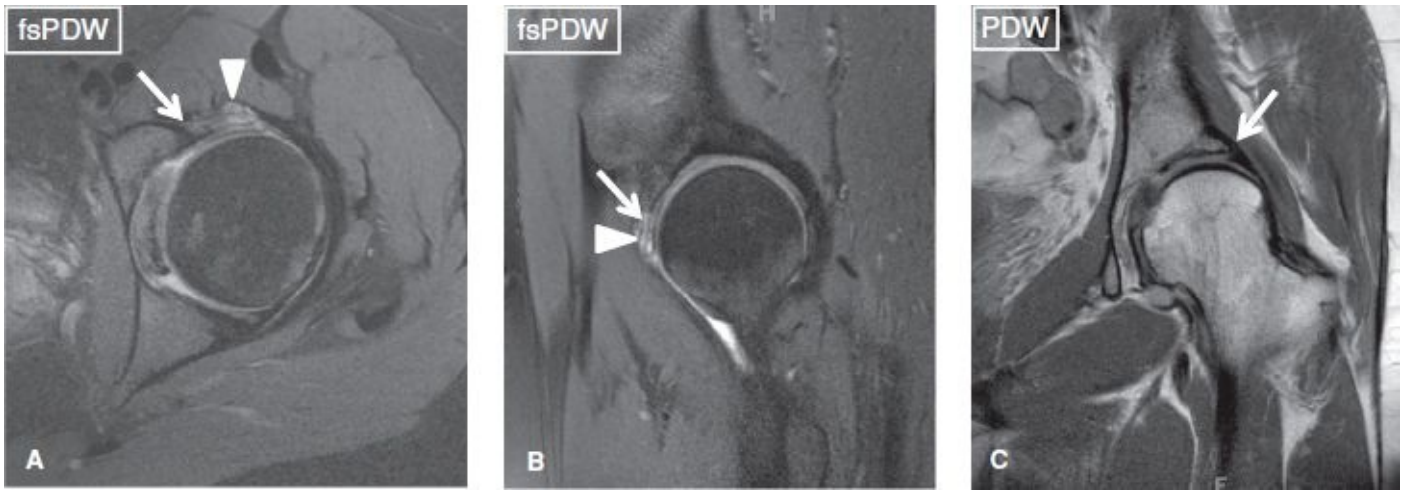

Fig. 16: Developmental dysplasia of the hip. Axial **(A),** sagittal **(B),** and coronal **(C)** images show a diffusely hypertrophied labrum (*short arrows*), which includes an intralabral cyst at its anterosuperior aspect (*arrowheads*). Notice underlying dysplastic hip with undercoverage of anterior femoral head.

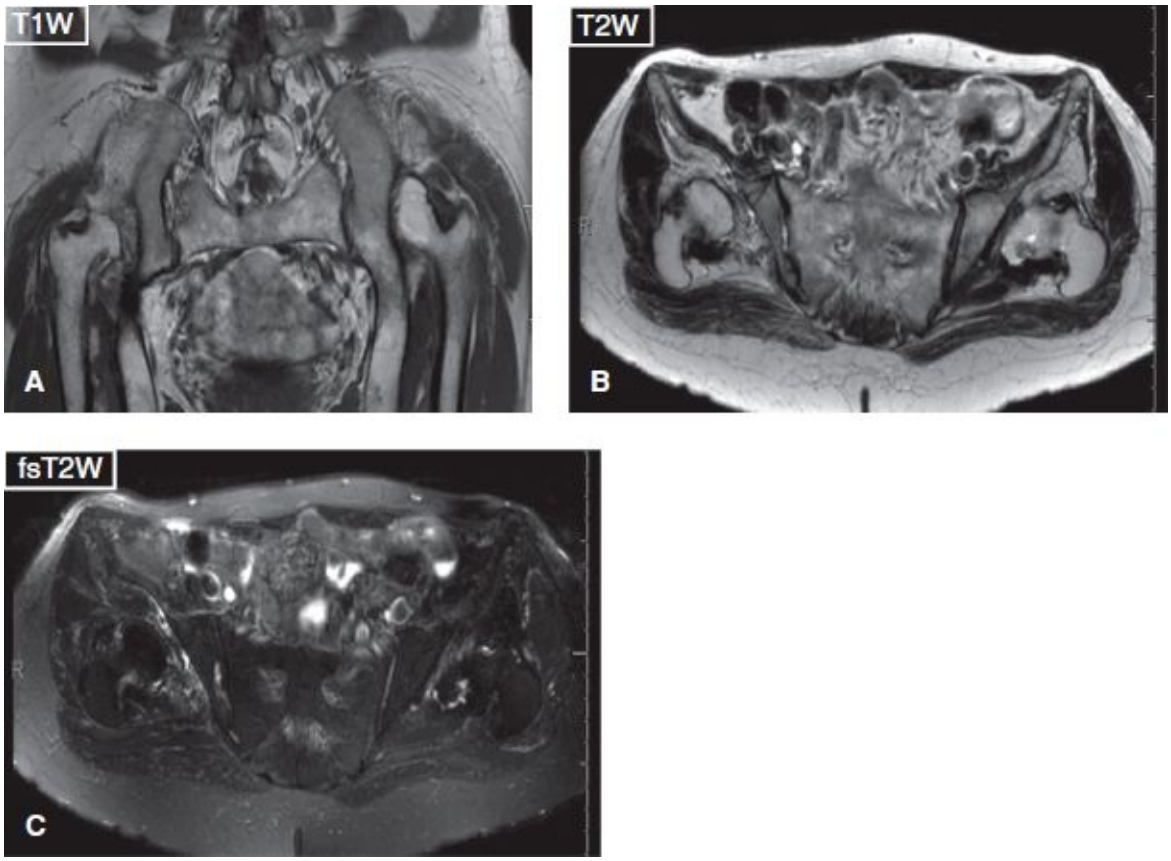

Fig. 17: Developmental dysplasia of bilateral hips. Coronal **(A)** and axial **(B, C)** images exhibit bilateral shallow acetabuli and femoral head deformities, along with right dislocation and left femoral subluxation.

FLUID: [<Normal> <Small effusion / Moderate effusion / Large effusion> <Synovial hypertrophy>]

A small amount of synovial fluid is normally present in the hip joint. Joint effusion is diagnosed when fluid results in bulging of the joint capsule or its recesses, such that a bone

to capsular distance exceeds 3 mm or when the latter distance is more than 2 mm asymmetric between the right and the left hips. Small, moderate, or large effusions are subjectively graded depending upon the distention of increasing number of recesses (inferior, posterior, or iliopsoas) (Fig. 18). Intra-articular strands or nodules of intermediate signal intensity are indicative of synovial thickening. Synovial thickening, debris, intra-articular cartilaginous (intermediate signal) or osteochondral bodies (dark ring with or without internal fatty marrow signal), synovial diverticula(e), and ganglion cysts should be reported, as they usually indicate underlying internal derangement. The bodies typically lodge in the inferior, posterior, or iliopsoas recesses. Numerous similar-sized bodies are seen in primary synovial osteochondromatosis and a small number of irregular-shaped bodies of variable size are seen in the secondary form of the disease. The latter is usually seen in older individuals and is associated with prior trauma or arthritis.

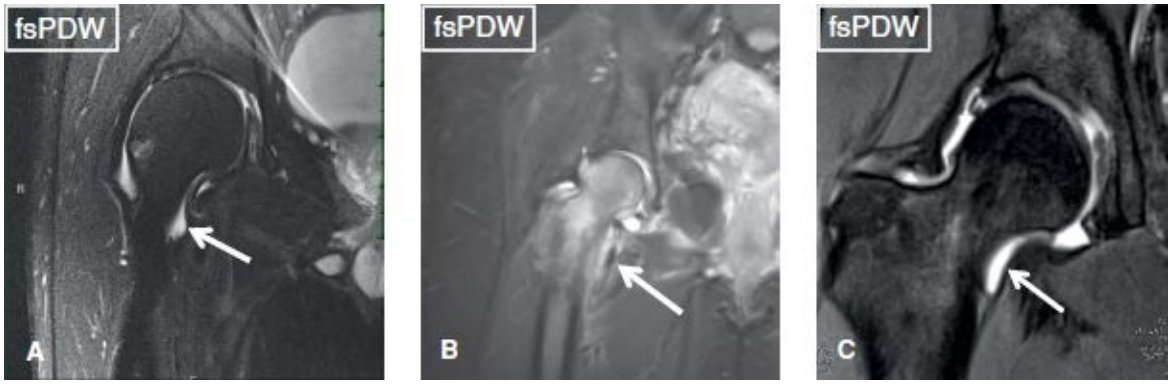

Fig. 18: Hip effusion. Coronal images demonstrate increasing degrees of capsular distention (*arrows*), indicating small **(A),** moderate **(B),** and moderate-to-large **(C)** effusion, respectively.

TROCHANTERIC BURSITIS: [<Absent / Present>]

Three distinct bursae exist around the greater trochanter: (a) The subgluteus medius bursa, which is located laterally and superiorly along the greater trochanter, immediately deep to the gluteus medius tendon muscle, (b) the subgluteus minimus bursa, which is situated anteromedial to the greater trochanter, deep to the superior aspect of the gluteus minimus tendon, and (c) the trochanteric bursa (or subgluteus maximus bursa), which is located along the posterior and lateral aspect of the greater trochanter and covers the insertion of the gluteus medius tendon. With repetitive frictional movements, chronic microinjury to tendons, or with acute trauma, one or more of the aforementioned bursae may become irritated, undergo inflammation, and fill with fluid with or without regional leakage. The bursitis is best depicted on axial or coronal images as fluid signal assuming either a crescentic shape with well-defined margins or an ill-defined configuration with a feathery shape infiltrating into the adjacent soft tissues (Figs. 19–22). Enhancement of the thin bursal wall is often seen after contrast administration as an asymptomatic finding. Trochanteric bursitis is often associated with gluteus medius and minimus tendinopathy and tears, most commonly with lateral facet insertional tears of the gluteus medius. One should

look for tears of these tendons or underlying enthesopathy-related old bony avulsions. The bursitis can also been seen in the postoperative setting, particularly related to particle disease, metallosis, or pseudotumor formation (Fig. 23). Underlying bony findings include enthesopathy, avulsive bone marrow edema, or subcortical cystic changes of the trochanter. Trochanteric bursitis and/or gluteal tendinopathy may be responsible for chronic pain overlying the lateral aspect of the hip, in an entity known as the greater trochanteric pain syndrome. However, mild trochanteric bursitis, as well as T2 hyperintensity (and occasionally contrast enhancement) of the soft tissues lateral to the greater trochanter are found in up to 80% of asymptomatic individuals and should be correlated with the clinical symptoms, before attributing them to greater trochanteric pain syndrome. On the other hand, symptomatic subjects exhibit one or more of a combination of MR imaging findings of gluteal tendinopathy, tears of the gluteus minimus/medius tendons (so-called rotator cuff of hip), and regional peritendinous bone marrow or fascial edema.

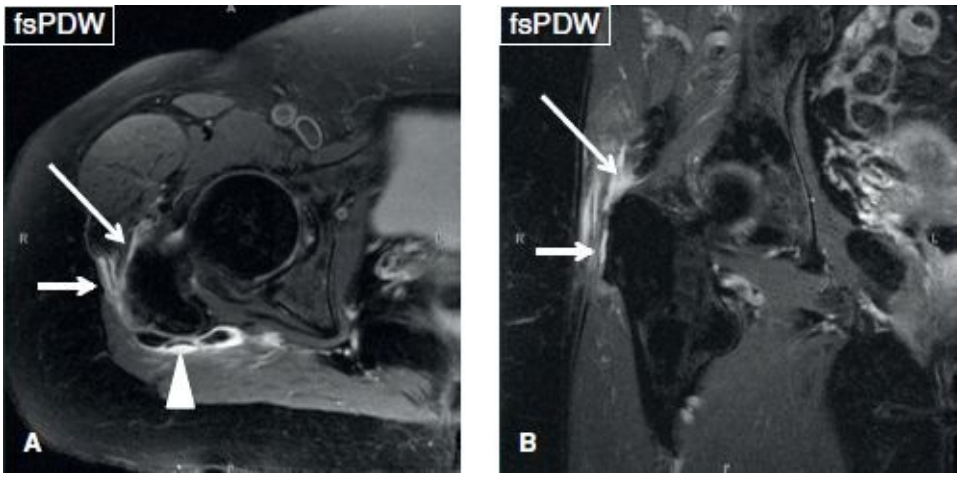

Fig. 19: Moderate trochanteric bursitis. Axial **(A)** and coronal **(B)** images reveal fluid collection within the subgluteus minimus (*long arrows*), subgluteus medius (*short arrows*), and subgluteus maximus (*arrowhead*) bursae.

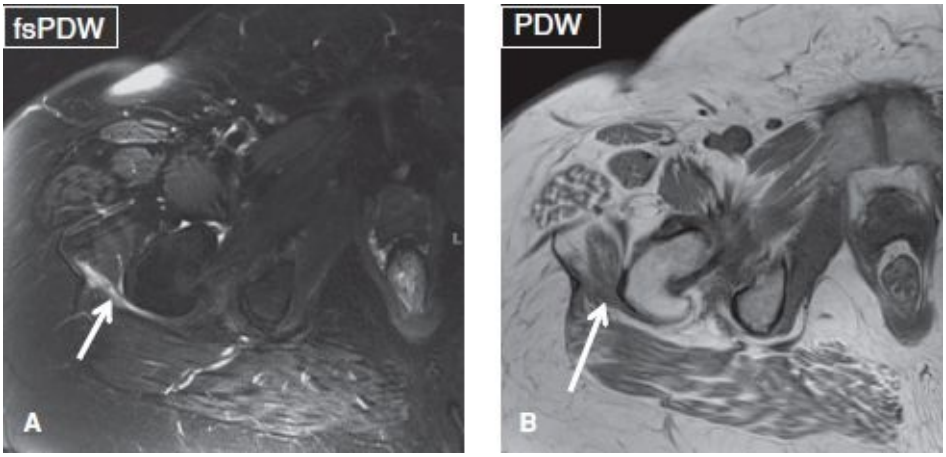

Fig. 20: Subgluteus maximus bursitis. Axial images **(A, B)** show small fluid collection (*arrows*) within the subgluteus maximus bursa.

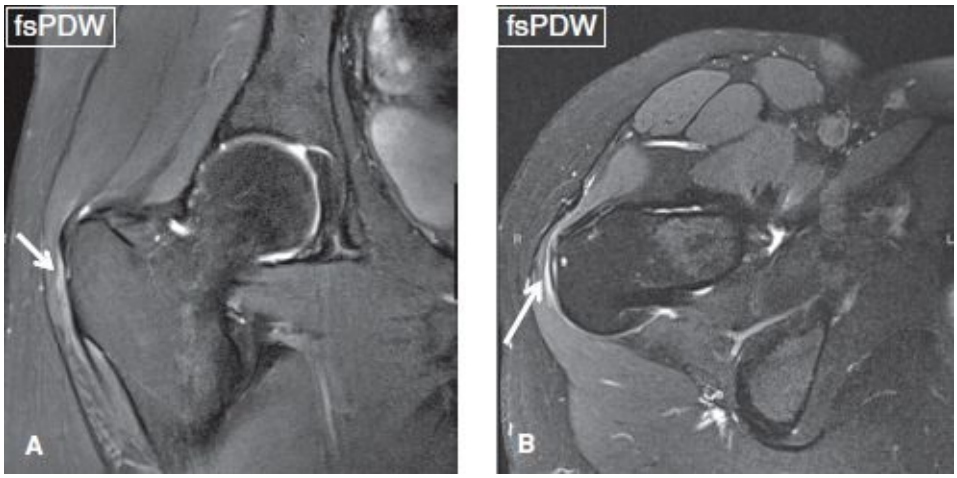

Fig. 21: Subgluteus medius bursitis. Coronal **(A)** and axial **(B)** images exhibit a trace amount of fluid within the subgluteus medius bursa (*arrows*).

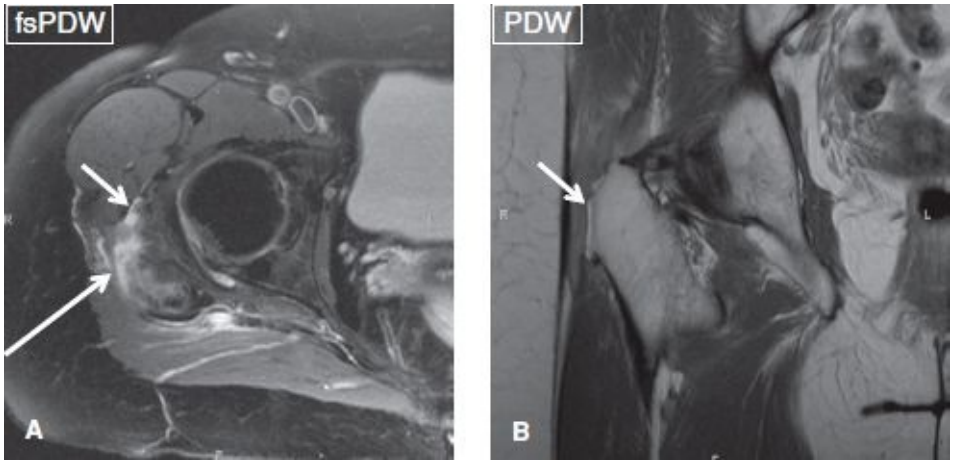

Fig. 22: Gluteus medius and minimus tendon tears with bursitis. Axial **(A)** and coronal **(B)** images demonstrate partial tears of gluteus medius (*long arrow*) and gluteus minimus (*short arrows*) along with moderate trochanteric bursitis. Notice underlying enthesopathy of the greater trochanter (*arrow* in **B**).

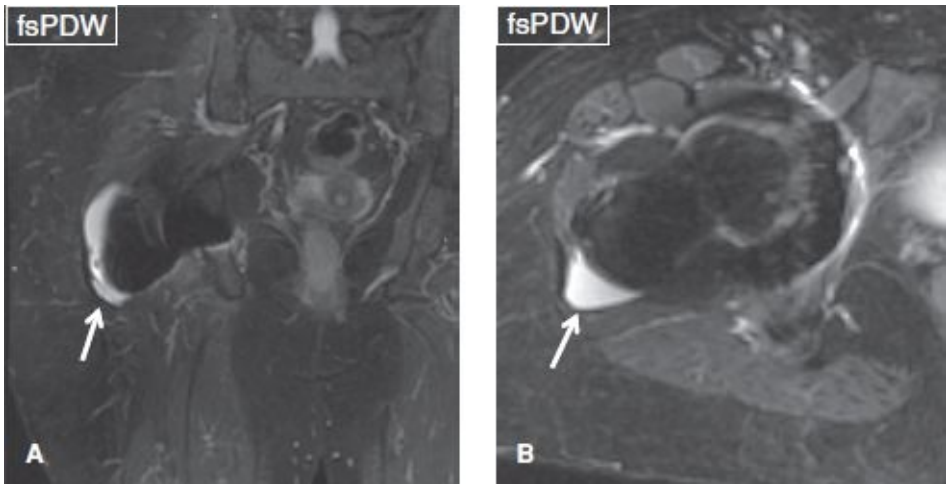

Fig. 23: Postsurgical trochanteric bursitis. Coronal **(A)** and axial **(B)** images show moderate fluid collection (*arrows*) in the trochanteric bursa in this patient with ipsilateral hip replacement.

LABRUM: [<Normal> <Degenerative fraying> <Tear> <Chondrolabral separation> <Paralabral cyst> <Labral ossification>]

The labrum is a fibrocartilaginous structure that is firmly attached to the osseous acetabular rim and overlies its hyaline cartilage, acting both as a static stabilizer, by maintaining negative intra-articular pressure and providing approximately 20% increase in articular surface. The labrum acts as a hyaline cartilage protective seal, keeping the joint fluid in the central compartment, thereby aiding in even the distribution of the compressive forces loading the articular cartilage. Inferiorly, the labrum blends with the transverse ligament at the margins of the acetabular notch, except for a small area where the two structures join and form a sulcus or recess, both anteriorly and posteriorly hosting a small amount of fluid (Fig. 24). The normal labrum is thinner anteriorly and thicker posteriorly, and demonstrates homogeneous low signal on all pulse sequences. It is usually triangular and less commonly round or flat shaped, with the apex pointing laterally. The superolateral and anterosuperior portions of the labrum are best visualized on the coronal images while the anterosuperior and posteroinferior portions are best evaluated on sagittal images. Axial images provide adequate evaluation of the anterior and posterior labrum. The normal recesses should be evaluated in all planes of acquisition before overcalling them as tears (Figs. 24–27).

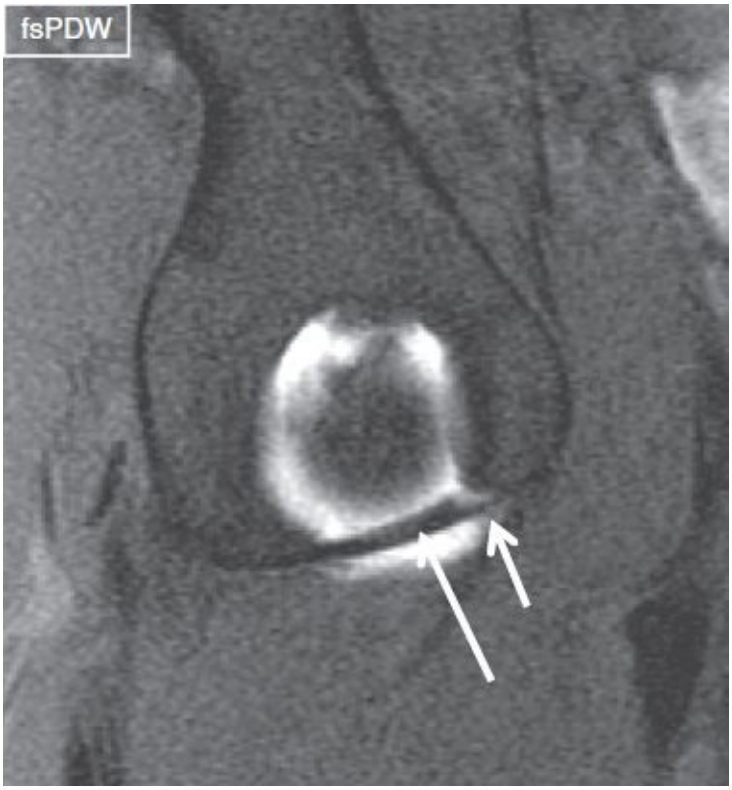

Fig. 24: Normal transverse ligament. Sagittal arthrography image demonstrates a normal transverse ligament (*long arrow*), bridging the anteroinferior and posteroinferior labrum. Notice normal synovial recess between the transverse ligament and the anteroinferior labrum (*short arrow*).

Fig. 25: Normal superolateral labrum and perilabral recess. Midcoronal image of the right hip shows a well-defined, triangular-shaped, and homogeneously hypointense superolateral labrum (*long arrow*). Note normal perilabral recess (*short arrow*).

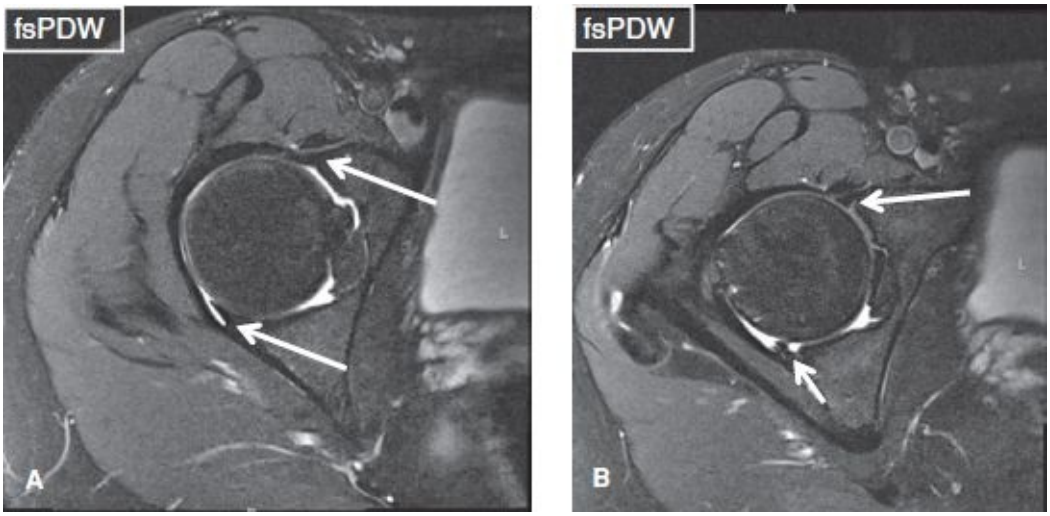

Fig. 26: Normal anterior and posterior labrum. Axial image **(A)** at the midlevel of the hip joint show well-defined, triangular-shaped, and homogeneously hypointense anterior and posterior labrum (*long arrows*). Axial image **(B)** shows a small anterior labral tear (*long arrow*). *Short arrow* in (**B)** exhibits the location of the normal recess at the posteroinferior labrum–transverse ligament junction.

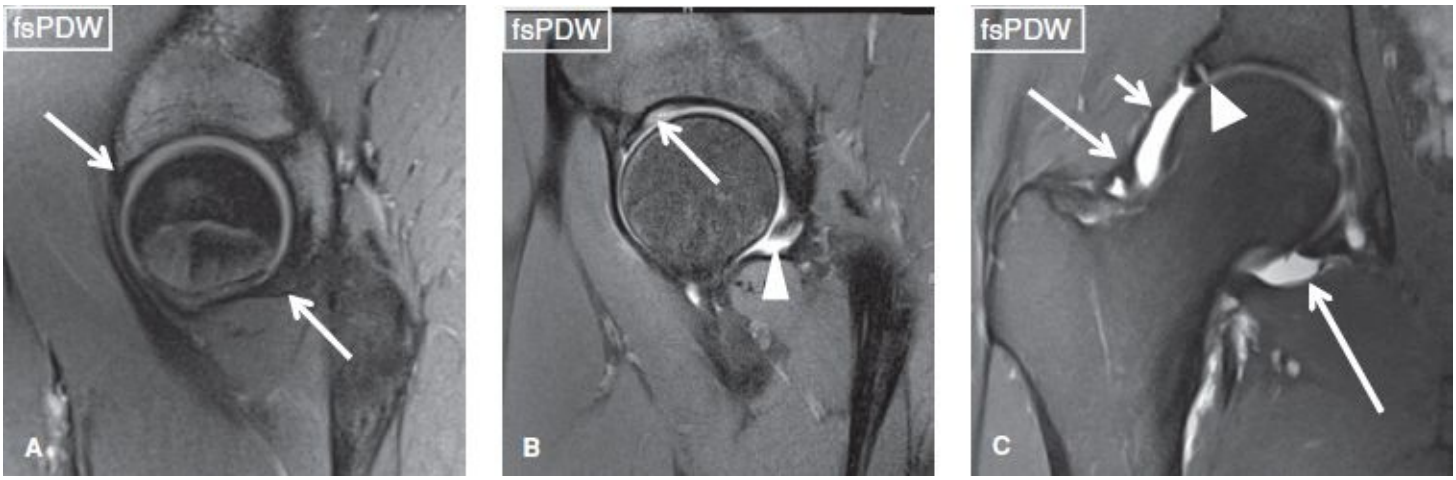

Fig. 27: Normal labrum. Sagittal **(A, B)** and coronal **(C)** images exhibit normal anterosuperior and posteroinferior labrum (*arrows* in **A**) under the iliofemoral and ischiofemoral ligaments, normal posteroinferior perilabral recess (*arrowhead* in **B**), and posterosuperior (*arrowhead* in **C**) sublabral recess. Notice normal cartilage undercutting the base of the labrum (*arrow* in **B**). **C:** Notice normal capsular thickenings, iliofemoral ligament (*short arrow*), zona orbicularis (*medium arrow*), and ischiofemoral ligament (*long arrow*).

In labral degeneration, the labrum demonstrates irregular fraying, attenuation or diffusely increased intrasubstance signal, which does not extend to the articular surface, similar to the meniscal tears. Occasionally, degeneration may be difficult to differentiate from a tear. Labral tears may be caused by acute trauma, FAI, degenerative disease, or capsular laxity. Their location can vary, for example, anterior, posterior, or superior (superolateral). The vast majority (>90%) of tears involve the anterosuperior labrum whereas tears of the posterior labrum are substantially less common and are usually associated with posterior instability, hip dislocation, pincer-type FAI, and underlying dysplasia. Labral tears are seen as (a) surface tears, appearing as linear fluid signal areas that extend to free edge or articular surface, or blunted labral margin (aka radial tear), (b) chondrolabral separation, which appear as focal or extended detachment of the labrum from the cartilage of the acetabulum (aka longitudinal peripheral tear). If it extends longitudinally from anterior to posterior similar to SLAP tear in shoulder, a linear high signal focus is depicted on true coronal images that is surrounded above and below by linear low signal ("reverse oreo cookie" sign), or it may be displaced to appear as flap tear or bucket-handle tear (Figs. 28, 29). Apart from the type of lesion characteristic, other features to report include the estimated length of the tear (small or large, e.g., less than or more than 1 cm), its location(s) either by defining the quadrant involved (anterosuperior, posteroinferior, superolateral, or anterior, etc.) or using a clock-face description, description of associated paralabral cysts, and any cartilage and bony changes, such as subchondral fracture (Fig. 30). Finally, describe any detached or displaced fragments.

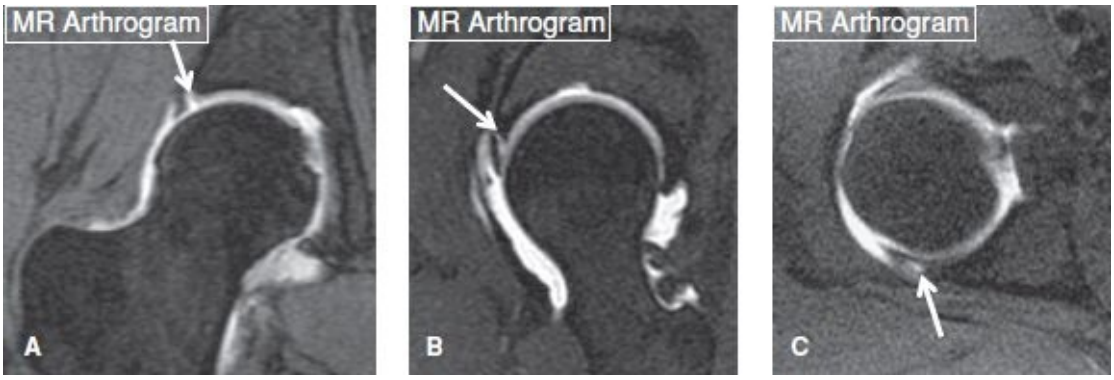

Fig. 28: Labral tears on MR arthrography. Coronal **(A),** sagittal **(B),** and axial **(C)** MRA images from different cases exhibit superolateral (*arrow* in **A**) and anterosuperior (*arrow* in **B**) chondrolabral separations, and posterior labral tear (*arrow* in **C**), respectively.

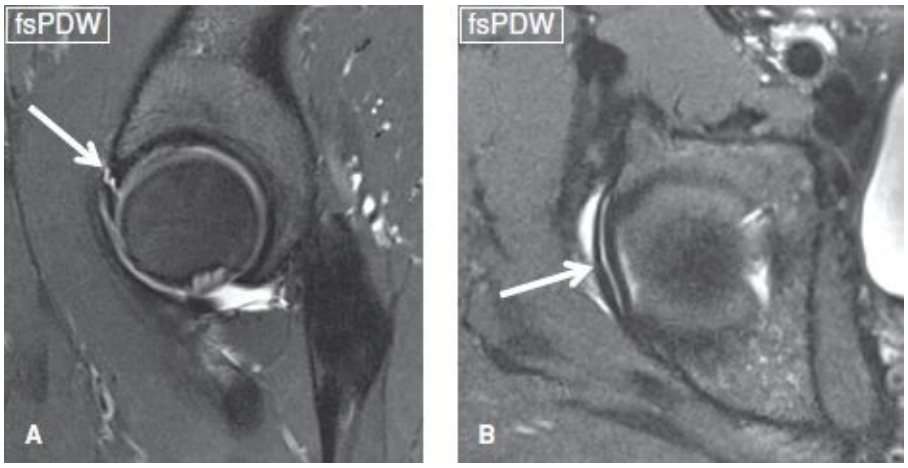

Fig. 29: Bucket-handle labral tear. Coronal **(A)** and axial **(B)** images show a complete longitudinal tear (*arrows*) along the superior labrum, anterosuperior to posterosuperior similar to a SLAP lesion in the shoulder with minimal displacement.

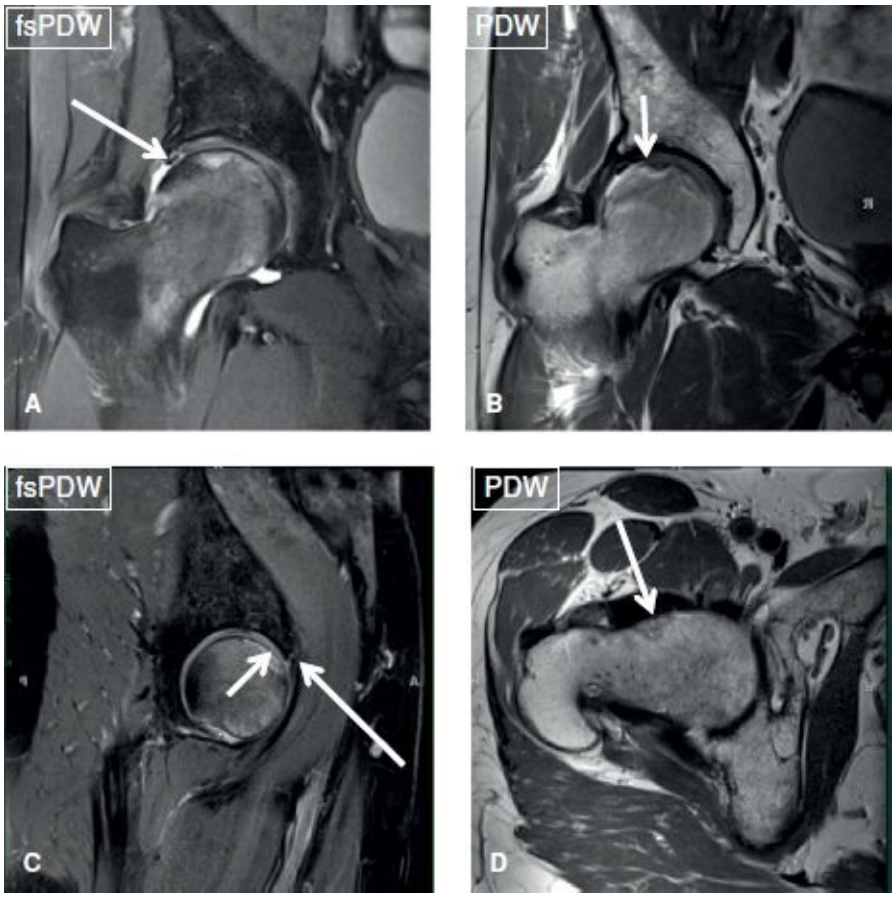

Fig. 30: FAI and associated hip joint abnormalities. Coronal **(A, B),** sagittal **(C),** and axial **(D)** images from the same individual show superolateral and anterosuperior labral tears (*long arrows* in **A, C**), a subchondral insufficiency fracture of the superior femoral head (*short arrows in* **B, C**), along with inadequate femoral head–neck offset with fibrocystic change (*arrow* in **D**), related to CAM-type femoroacetabular impingement.

Labral tears are commonly associated with intra- and paralabral cysts. These cysts confirm the presence of a tear and indicate that the tear has been around for some time. Occasionally, the labrum might show only degenerative fraying, truncation, or partial ossification adjacent to the paralabral cyst without demonstrable clear cut tear. These lesions appear as homogeneous well-circumscribed round or oval structures, usually multilocular, and show iso- to hypointense and hyperintense signal alterations on T1W and T2W images, respectively. The cysts can measure up to 4 to 5 cm in size, and infrequently feature intermediate signal appearance on T2W images due to gelatinous/mucinous material, debris or proteinaceous products (Figs. 3, 8, 31, 32). Long-standing paralabral cysts may cause adjacent bone erosion and form subcortical geodes. The differential diagnosis includes ganglion cyst unrelated to the labral tear, synovial diverticulum, perineural cyst traversing retrograde along innervating intra-articular branch of the adjacent sciatic or less commonly, femoral nerves sheath tumor, and iliopsoas bursitis. Differentiation between the iliopsoas bursitis and a labral tear is based on (1) the location of the lesion since paralabral cysts are usually lateral to the iliopsoas tendon whereas iliopsoas bursal fluid collections are located medial to the iliopsoas tendon, and (2) detection of direct communication of a paralabral cyst with the labral tear or intralabral

cyst while iliopsoas bursitis communicates with the joint effusion. It should be noted that a paralabral cyst, if identified correctly, should always raise a strong suspicion of an underlying labral tear.

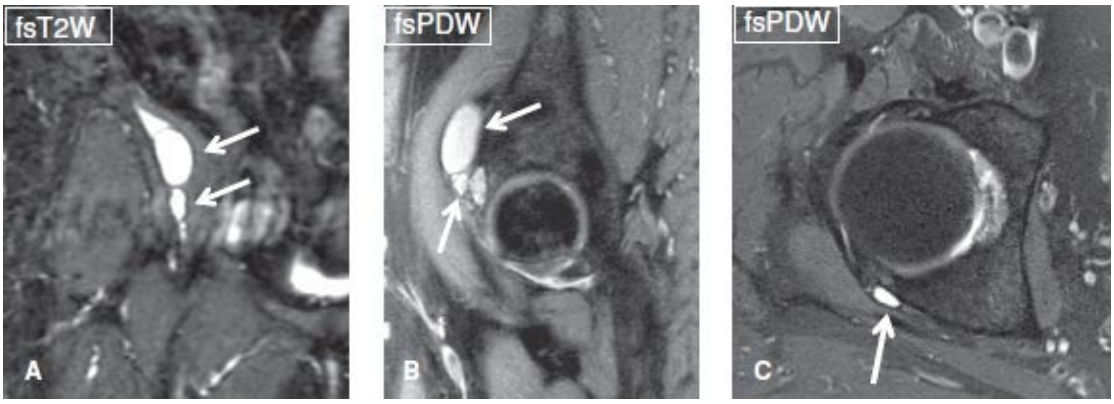

Fig. 31: Paralabral cysts. Coronal **(A),** sagittal **(B),** and axial **(C)** images show typical cases of different paralabral cysts (*arrows*).

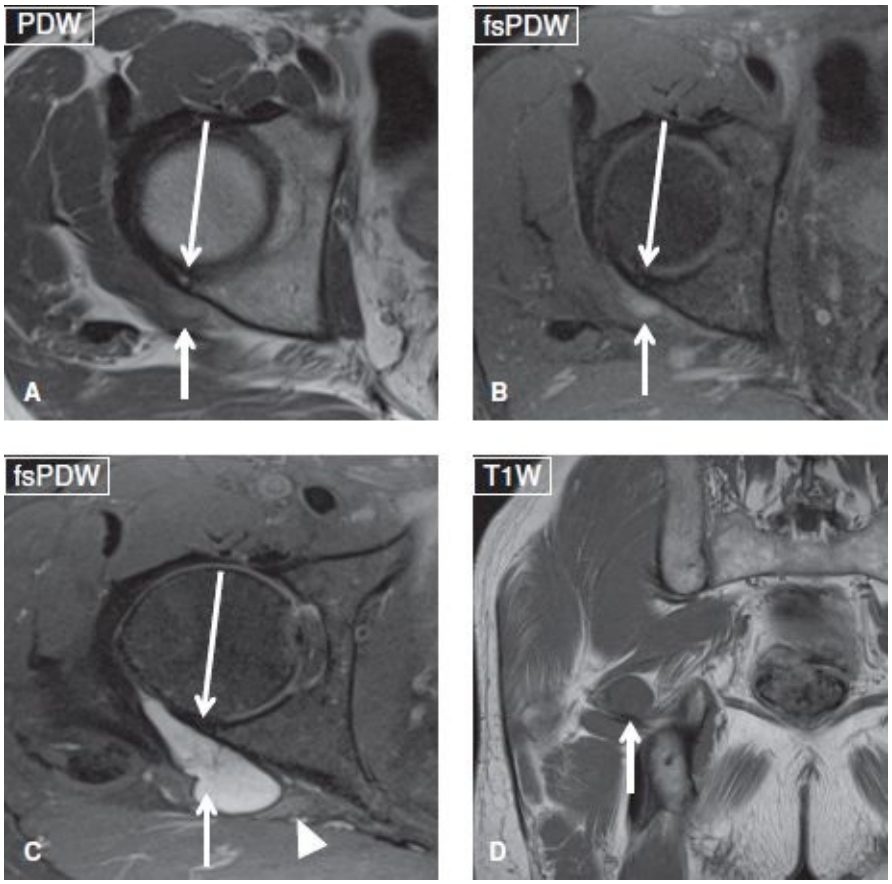

Fig. 32: Large paralabral cyst, asymptomatic. Axial **(A–C)** and coronal **(D)** images from the same individual show a large paralabral cyst (*short arrows*) with minimal degenerative change of the labrum and no clear cut tear (*long arrows*). The cyst displaces and compresses the sciatic nerve (*arrowhead*). The patient had no posterior symptoms and complained of anterior groin pain.

Several pitfalls should be avoided when establishing labral tears:

- The normal perilabral recess, which extends between the joint capsule and the capsular

side of the labrum, most prominent on the coronal images (Fig. 25)

- The sublabral sulcus, which is located under the posterosuperior labrum in up to 18% of individuals and can be differentiated from a tear by its morphology (shallow, sharply marginated, linear in shape, and located posterosuperiorly, beyond 12 o'clock position in contrast to tears, which tend to be deeper, nonlinear, and are anterosuperior or superolateral)
- The labrum–transverse ligament recess, which forms at the junctions of the anteroinferior and posteroinferior labrum with the transverse ligament (Figs. 26, 27)
- Cartilage undercutting refers to mildly increased signal of the labrum–cartilage interface, similar to the glenoid labrum–cartilage interface in the shoulder, and it should not be misinterpreted for a tear since it has uniform intermediate signal and is present on nearly all sequences (Fig. 27)
- The iliopsoas tendon–labrum sulcus, which is created by the tendon as it crosses anterior to the labrum at 12 o'clock position on the axial image and creates a linear hyperintense interface with the latter that can mimic a tear
- Synovial diverticulum from prior capsular injury mimicking paralabral cyst, as the former features smooth margins, is at labrocapsular junction and is unilocular
- Enlarged or hypertrophied labrum in individuals with dysplastic hip (Fig. 16)

CARTILAGE:

Femoral: [<Normal> <Low-grade thinning / High-grade thinning> <Low-grade defects/ High-grade defects>]

Acetabular: [<Normal> <Low-grade thinning / High-grade thinning> <Low- grade defects/ High-grade defects>]

The horseshoe-shaped articular surface of the acetabulum is covered by hyaline cartilage, except (a) at the acetabular fossa, which extends from the central portion down to the acetabular notch, and is filled with fatty tissue, referred to as the pulvinar, (b) the stellate crease, a small bony indentation, which is located slightly superior to the acetabular fossa with an attached ligament (Fig. 33). Similarly, the femoral head is almost entirely covered by articular cartilage, except for a central area, known as the fovea capitis. The articular cartilage of the femoral head becomes thicker from the periphery to the center; whereas, the articular cartilage of the acetabulum becomes thicker from the center to the periphery, though they are both extremely thin, measuring only about 2 mm in thickness. The suprafoveal femoral head articular cartilage and the cartilage over the lateral acetabular dome are assessed primarily on coronal and secondarily on sagittal images whereas the anterior and posterior acetabular cartilages are best evaluated on the axial images.

Fig. 33: Stellate crease. Coronal image demonstrates the acetabular fossa with the ligament (*long arrow*) and the superiorly located stellate crease (*short arrow*).

The normal cartilage demonstrates smooth surface and homogeneous intermediate signal intensity (darker toward the bone surfaces) on all pulse sequences. Defects appear as lesions where fluid signal replaces the normal intermediate signal, more commonly on the acetabular surface as compared to the femoral surface (Figs. 4, 5, 34–36). In FAI, anterosuperior or posteroinferior cartilages are more commonly eroded, as described above. In hip OA, there is multifocal or diffuse cartilage thinning or loss, which is again more prominent at the acetabular roof and superior surface of the femoral head. Cartilage delamination is seen as fluid-like signal undercutting the cartilage–bone interface (debonding of cartilage from bone) with or without buckling of the overlying cartilage. Similar to other joints, the evaluation of the cartilage should include the assessment of the size, location, and grade (low or high) of cartilaginous defects; the subchondral bone interface irregularity; and the subjacent marrow signal alterations of edema, cyst, and/or sclerosis.

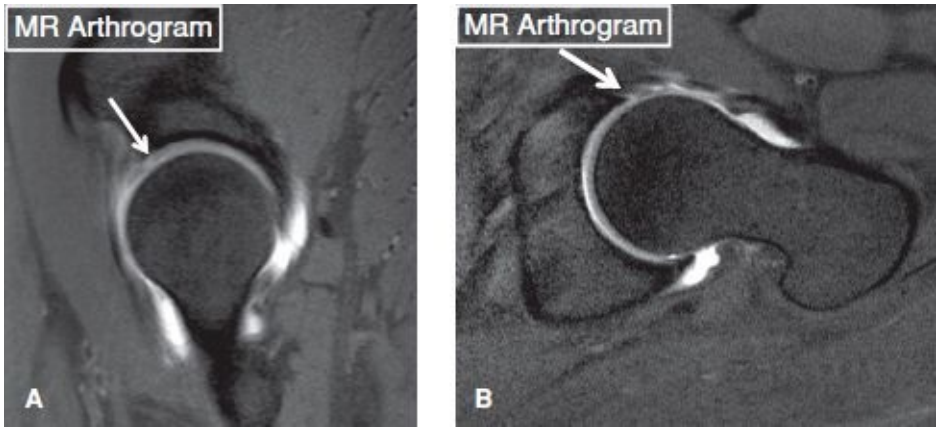

Fig. 34: Acetabular cartilage lesion. **A:** Sagittal MRA image shows a high-grade cartilage defect in the anterior superior aspect of the acetabulum (*arrow*). **B:** Oblique axial MRA image from the same patient demonstrates associated anterior labral tear (*arrow*).

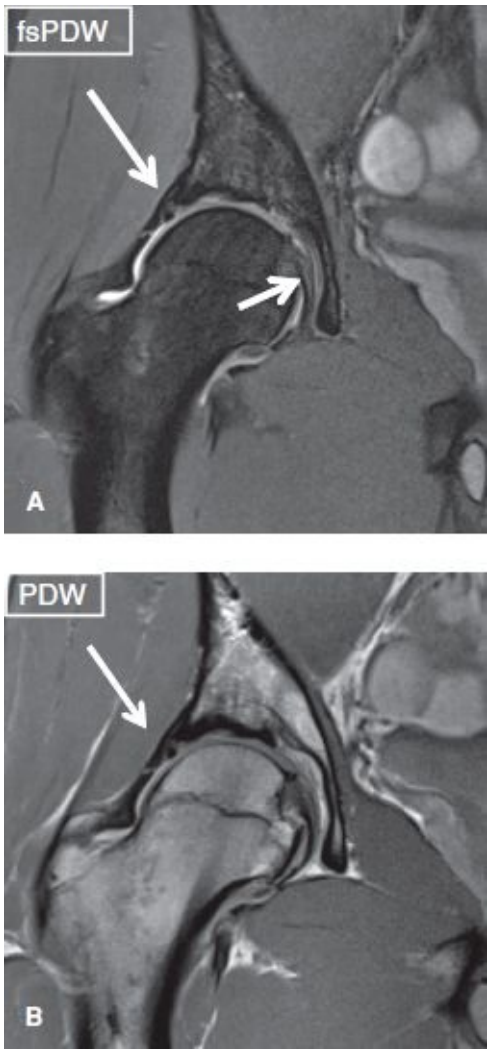

Fig. 35: Labro-cartilage lesion. Coronal images exhibit a high-grade cartilage fissure with associated superolateral labral tear (*long arrows*). Notice normal ligamentum teres (*short arrow*).

Fig. 36: Femoral articular cartilage flap. Coronal MRA image shows a high-grade cartilage flap (*long arrow*) of the femoral head. Also note a superolateral labral tear (*short arrow*).

CAPSULE/LIGAMENTS: [<Normal> <Thickened or sprained iliofemoral, ischiofemoral, or pubofemoral ligaments>]

The joint capsule attaches proximally along the osseous rim of the acetabulum and inserts near the base of the labrum, creating the perilabral recess. Distally, it attaches along the anterior aspect of the femoral neck at the base of the trochanters. Thickened layers of the joint capsule form three longitudinally oriented ligaments, which stabilize the joint, particularly during upright positioning or walking. These include the following.

- The triangular-shaped iliofemoral ligament, the strongest ligament of the body that extends from the ilium (between the anterior-inferior iliac spine and the superior border of the acetabulum) to the intertrochanteric line of the anterior femur and is best visualized transversely in the axial and axial-oblique planes and longitudinally in the sagittal plane
- The pubofemoral ligament, which attaches via a broad base on the iliopubic eminence, superior ramus of the pubis, obturator crest and membrane, extends inferolaterally to attach onto the intertrochanteric line and is best depicted on the sagittal images
- The spiral-shaped ischiofemoral ligament that arises from the inferior part of the ischium and attaches to the femoral neck, which is best depicted on axial and oblique-axial images (Fig. 27).

Injuries to the extracapsular ligaments are rarely reported in the absence of traumatic hip dislocation. Injury to the above ligaments usually occurs following hip dislocation or subtle subluxation (mostly in contact sport activities) and appears as ligament sprain and capsular edema (Fig. 37). Of the three ligaments, the iliofemoral ligament injuries are most commonly observed. Thickened iliofemoral and ischiofemoral ligaments may be normally seen in athletes or in symptomatic FAI subjects and it could potentially lead to decreased range of motion similar to adhesive capsulitis in the shoulder joint.

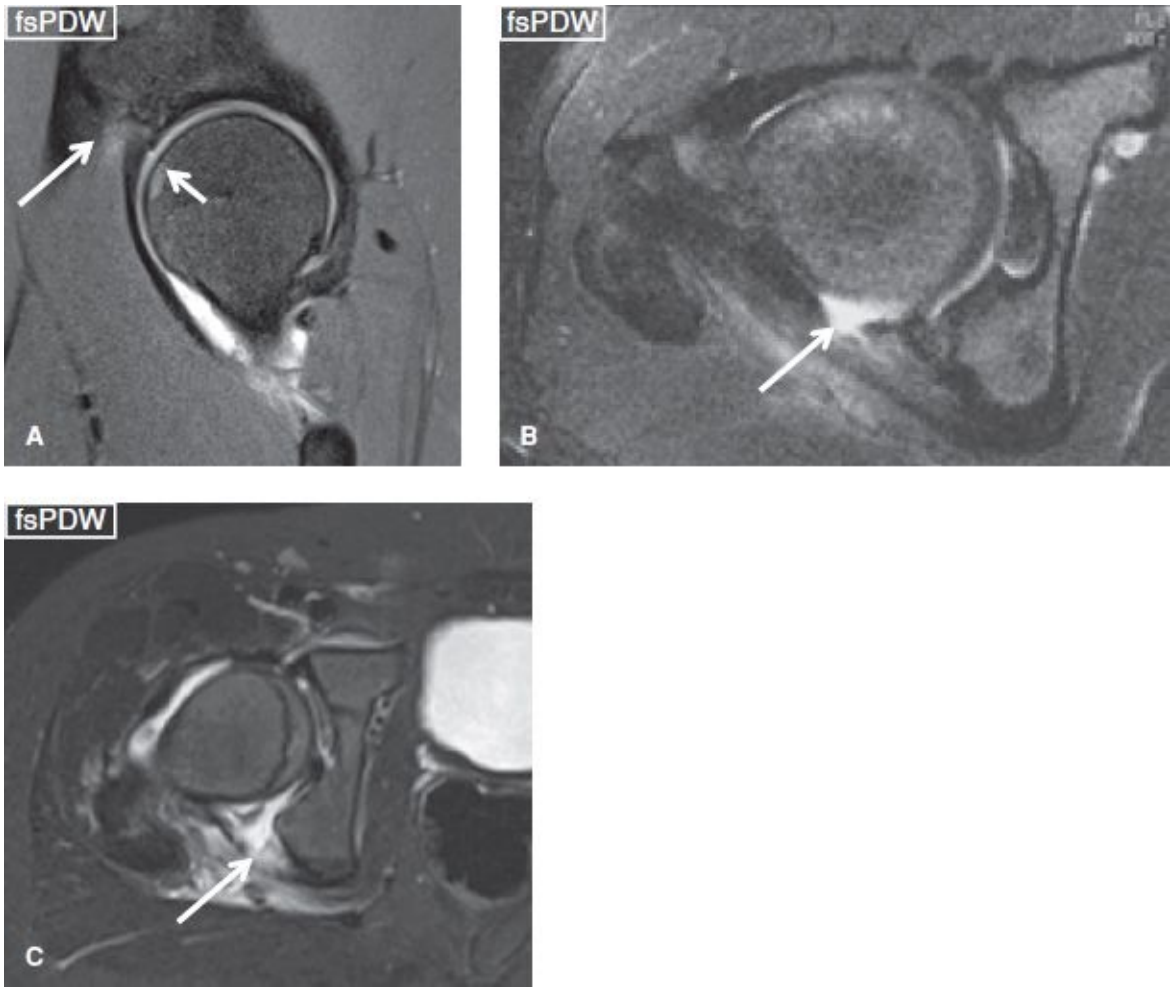

Fig. 37: Hip ligament sprains. Sagittal image **(A)** shows focal hyperintensity (*long arrows*) at the iliac insertion of the iliofemoral ligament in keeping with grade I sprain. Also note the underlying contusion (*short arrow*) of the femoral head from recent injury. Axial images **(B, C)** in two different subjects show grade III sprains of ischiofemoral ligaments from recent posterior hip dislocations.

The zona orbicularis or annular ligament (transverse to the long axis of femur) is another capsular thickening composed of circular layer of capsule fibers, which projects intra-articularly and wraps around the femoral neck, acting as a locking ring and providing hip stability. It is seen as a filling defect at the level of the femoral neck on flouroscopy images during hip arthrogram.

The ligamentum teres is a strong intra-articular ligament consisting of two thick bands, which arise from the fovea capitis and insert at the edges of the acetabular fossa, blending with the transverse ligament. Its shape changes from round or oval proximally to trapezoidal distally. It is an important stabilizer of the hip, resisting joint subluxation forces particularly in adduction, flexion, and external rotation. On MR images, it appears as a relatively homogeneous band, which has smooth contours and features low signal intensity on all pulse sequences (Fig. 35) although areas of slightly increased signal may normally exist at its attachment to the fovea capitis. The ligament may undergo (a) partial tear, or complete tear (or avulsion), which often result from hip subluxation or dislocation, most commonly seen near the fovea capitis. These lesions appear as partial or complete ligament

discontinuity, respectively, with associated joint effusion and subcortical edema and/or cystic changes at the avulsion site, (b) degeneration, in which the ligament demonstrates diffuse T1 and T2 hyperintensity and often irregular contours with or without perifoveal osteophyte or ganglion cyst formation (Fig. 38). In dysplastic hips, the ligament may be thickened, hypertrophied, or elongated. In few individuals, it is congenitally absent and the fovea capitis may be hypoplastic.

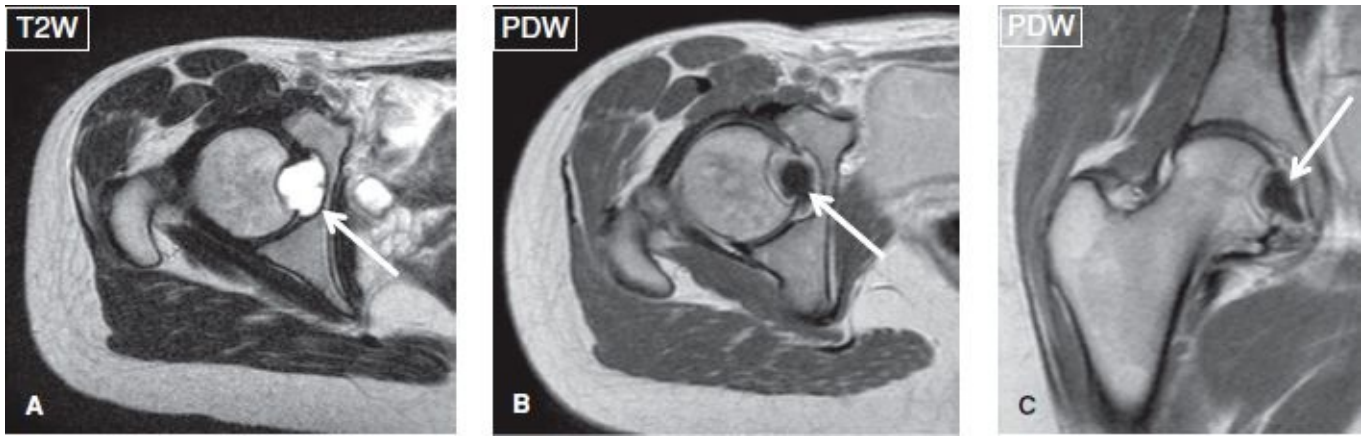

Fig. 38: Ligamentum teres ganglion cyst. Axial **(A, B)** and coronal **(C)** images demonstrate a well-defined lesion (*arrow in* **A**) with fluid signal at the anatomic location of the ligamentum teres. Notice thick ligament (*arrows in* **B, C**) surrounded by ganglion.

Several reflections of the synovial membrane, known as synovial folds or plicae, may be found in the hip joint, particularly in the presence of joint effusion (Figs. 39, 40). The other synovial thickenings include, most commonly encountered retinacula of Weitbrecht, which run medially to the nutrient foramen in the femoral neck and encompass the branches of the medial femoral circumflex artery; and the pectinofoveal fold, which runs along the medial aspect of the femoral neck and inserts into the capsule. There are no morphologic criteria to describe symptomatic plicae, but their relevance remains in avoiding mistaking them for adhesions. Additionally, they are seen attaching at the collar osteophytes of the femoral head, believed to be the cause of these traction osteophytes. Uncommonly, they have been considered as a cause for snapping hip (described below).

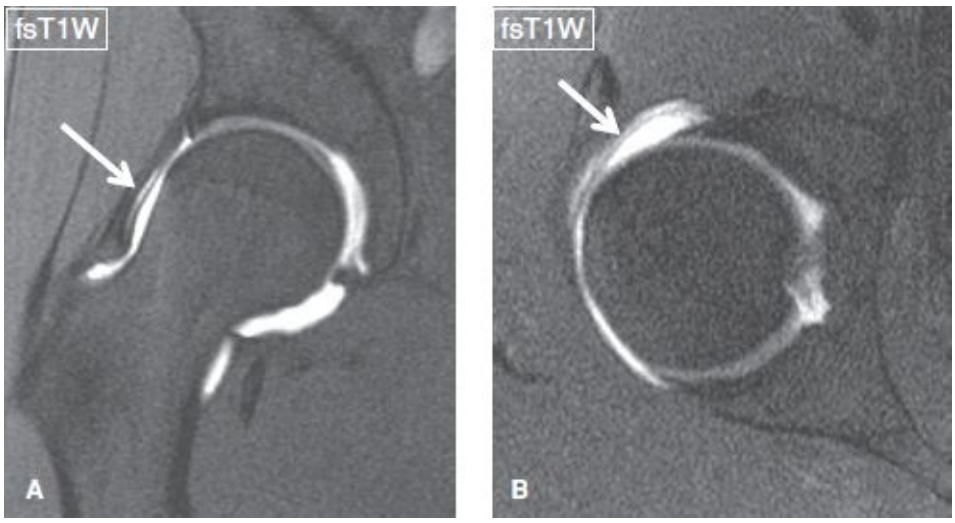

Fig. 39: Superolateral plica: Coronal **(A)** and axial **(B)** arthrography images depict a normal thin superolateral plica (*arrows*).

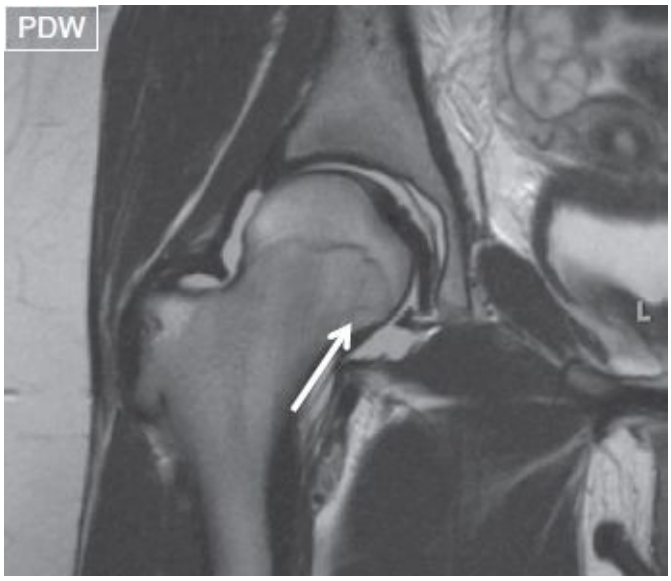

Fig. 40: Superomedial plica. Coronal images **(A, B)** depict a normal thin superomedial plica (*long arrow*). Also note the inferomedial plica along the neck, where traction related femoral head collar osteophyte would arise in degenerative disease or hip instability.

VISUALIZED MUSCLES/TENDONS:

Gluteal: [<Normal> <Strain> <Tendinopathy> <Muscle atrophy> Enthesopathy>]

Adductors: [<Normal> <Strain> <Atrophy>]

Iliopsoas: [<Normal> <Strain>]

Lateral rotators: [<Normal> <Strain> <Piriformis asymmetry> <Ischiofemoral impingement-related edema and/or fatty infiltration of quadratus femoris>]

Hamstrings: [<Normal> <Strain> <Tendinosis> <Enthesopathy>]

The gluteal muscles include the gluteus minimus, medius, and maximus. The gluteus minimus inserts on the anterior facet of the greater trochanter and the gluteus medius has two insertions, the larger one at the superior aspect of the posterior facet and smaller one at the lateral facet. Similar to other locations in the body, strains are classified as follows.

- Grade I—mild injury with preservation of the architecture and appears as a feathery pattern of intramuscular edema
- Grade II—corresponds to partial tear of the muscle belly or musculotendinous junction and appears as partial discontinuity of the muscle fibers with internal hemorrhagic fluid collection
- Grade III—refers to complete disruption of the musculotendinous junction or avulsion from

the attachment site with or without associated retraction and laxity of the torn elements, intra- and extramuscular hemorrhagic fluid and edema (Figs. 41, 42).

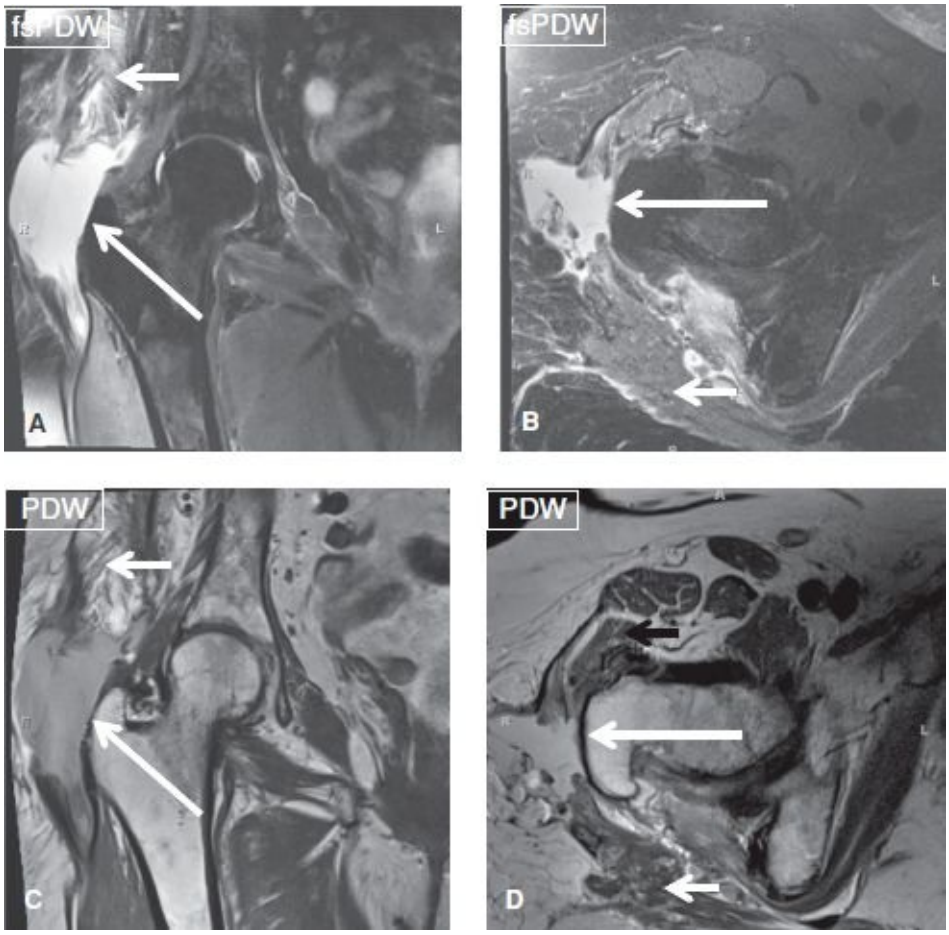

Fig. 41: Gluteus tendons avulsion. Coronal **(A, C)** and axial **(B, D)** images demonstrate complete avulsion of the gluteal tendons from the greater trochanter (*long arrows*), and a large fluid collection in the resultant gap. Notice associated muscle atrophy (*short arrows*).

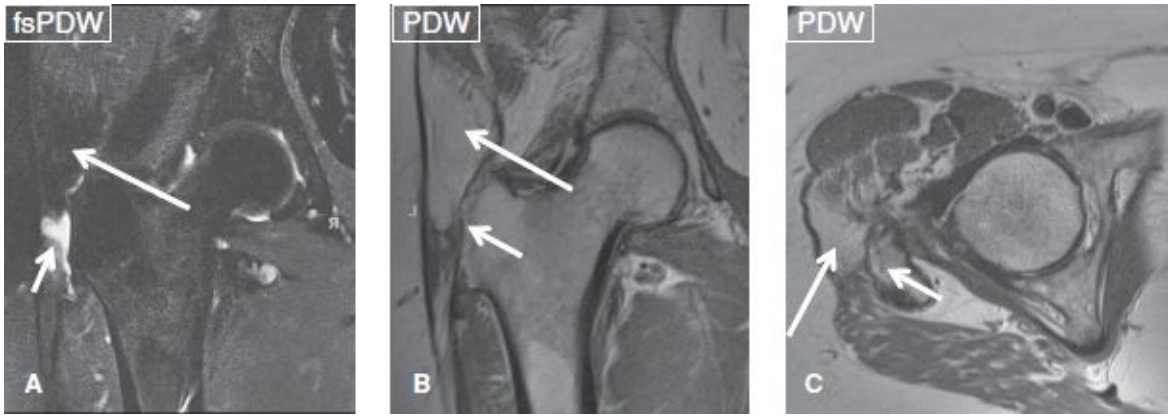

Fig. 42: Gluteus medius avulsions. Coronal **(A, B)** and axial **(C)** images show complete tendon avulsion and fatty degeneration of the gluteus medius muscle (*long arrows*), along with trochanteric bursitis (*short arrow* in **A**). Notice underlying enthesopathy (*short arrows* in **B** and **C**).

The gluteal tendons may be affected by insertional tendinosis, which appears as intratendinous intermediate signal; partial tears, which appear as partial discontinuity of

tendon fibers, most commonly involving the lateral facet attachment of the gluteus medius; or as complete tears, which appear as complete tendon discontinuity with associated retraction. Indirect signs of gluteal tendinopathy include trochanteric bursitis, bony enthesopathy, cystic or avulsive changes at the greater trochanteric attachment, and fatty atrophy of gluteal muscles. Tears of the gluteus minimus and medius tendons have been referred as "rotator cuff tears of the hip" due to the anatomic and functional similarity of the rotator cuff of the shoulder. Finally, gluteus maximus and less commonly, gluteus medius may be involved by calcific tendinitis, where plain film correlation may be beneficial (Figs. 43, 44).

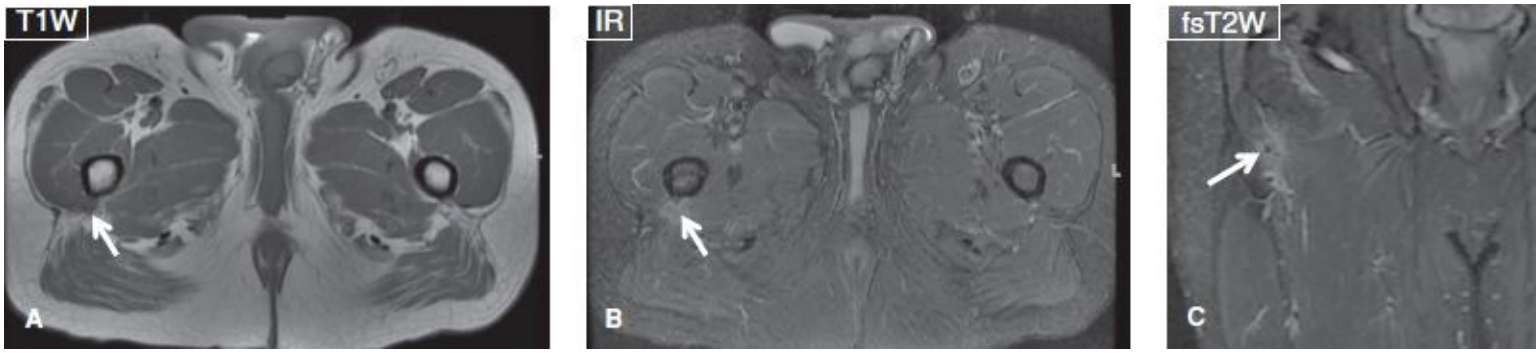

Fig. 43: Calcific tendinitis of the gluteus maximus muscle. Axial **(A, B)** and coronal **(C)** images show tiny hypointense foci (*arrows*) at the right gluteus maximus tendon, which correspond to calcifications and are surrounded by mild soft tissue edema.

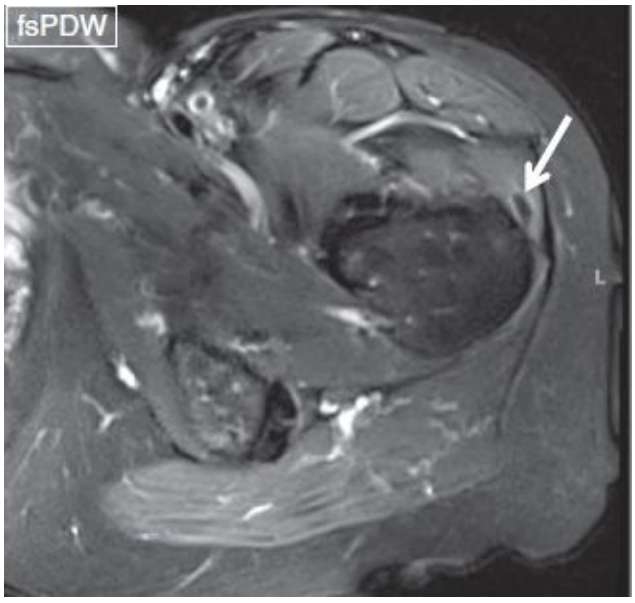

Fig. 44: Calcific tendinitis. Axial image demonstrates a hypointense focus (*arrow*) adjacent to the gluteus medius tendon attachment with adjacent inflammatory edema.

The hip adductors include the adductor longus, brevis and magnus, the obturator externus, the quadratus femoris, the pectineus, and the gracilis. The adductor muscles may be affected by Grade I strains (commonly during sport activities), tendinopathy, partial and complete tears (Fig. 45), as well as calcific tendinitis although differentiating the latter from an injury may prove challenging. "Thigh splints," or adductor insertion avulsion

syndrome, refers to a painful condition involving mild injury at the adductor tendon insertion related to the avulsions of the Sharpey fibers as they blend with the bony cortex. Imaging findings include a thin rim of T2 hyperintensity subjacent to the medial periosteum in the adductor attachments, intermediate signal intensity of the respective tendons, and fascial edema. Finally, injury to the origin of the pectineus, adductor longus, or brevis tendons may be seen as part of adductor variant athletic pubalgia. Athletic pubalgia (aka sports hernia) can broadly present as three different variants.

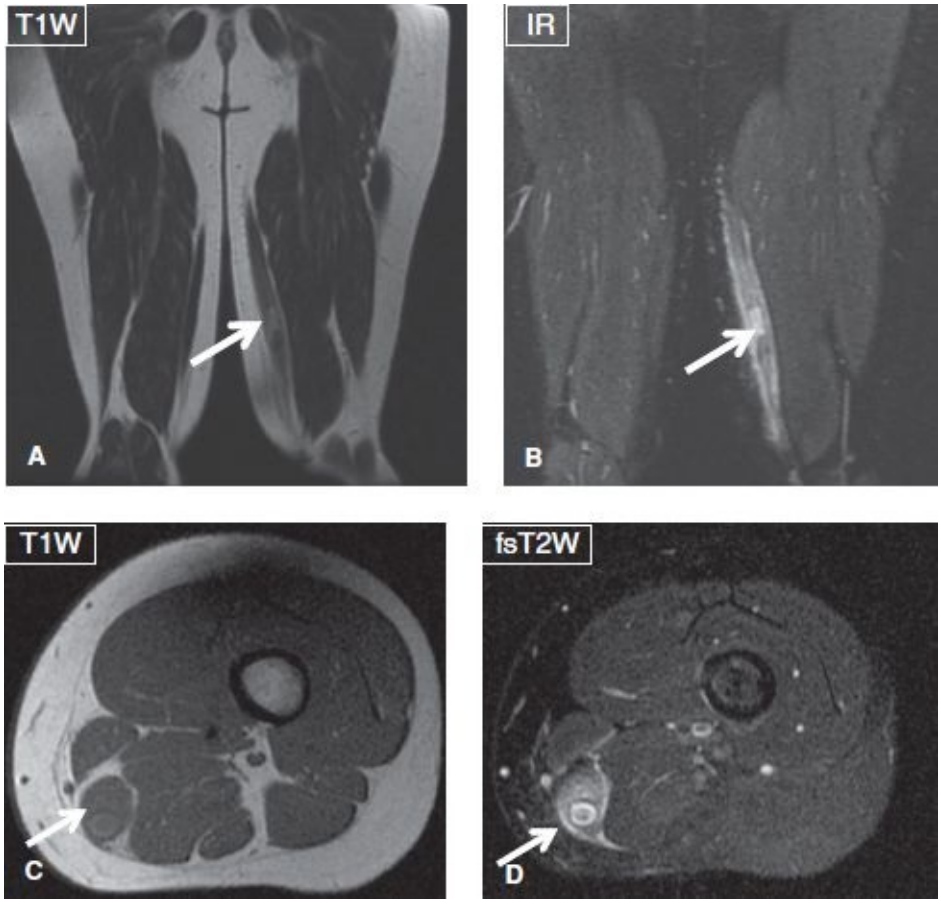

Fig. 45: Gracilis muscle injury. Coronal **(A, B)** and axial **(C, D)** images exhibit diffuse edema of the left gracilis muscle, perimuscular edema as well as an intramuscular region of fibers discontinuity with small fluid collection (*arrows*), in keeping with grade II strain.

- Osteitis pubis, which presents with groin, pubic, or lower abdominal pain. Clinical examination reveals tenderness to palpation over the symphysis pubis, superior pubic ramus, and/or proximal adductor muscles. MR imaging may exhibit extrusion of the symphyseal disc, irregularity of the articular surfaces, subchondral cysts, sclerosis, and bone marrow edema on both sides of the joint (preferentially or more pronounced in anterosuperior aspects of the pubic bones), stress, or insufficiency fractures in the parasymphyseal region, pubic symphysis effusion, and pubic ligament (anterior or inferior) sprains. Occasionally, an osteophyte-like beak is evident on the superior border of the pubic bone indenting the base of the bladder.
- Adductor variant, referring to preferential adductor partial or complete tears with ipsilateral pubic bone marrow or adjacent fascial signal alterations (Figs. 46, 47). On

coronal and axial STIR or fsT2W/fsPDW images, a linear fluid-signal structure may be seen at the inferior border of the symphysis and the pubic bone, contiguous with the primary (central) cleft of the symphysis. This is known as secondary cleft sign, it may extend to the ipsilateral adductor attachments, and its side corresponds to the side of the symptoms in most cases (Fig. 48).

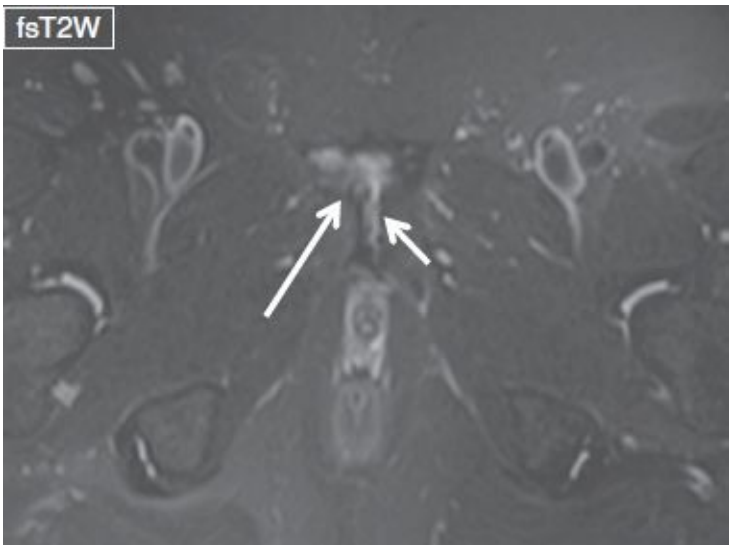

Fig. 46: Adductor variant athletic pubalgia and osteitis pubis. Axial image demonstrates mild pubic symphysis widening with effusion (*short arrow*). Notice high-grade avulsion of right common adductor tendon origin (*long arrow*).

Fig. 47: Bilateral adductor tendon avulsions. Axial image shows fluid signal (*arrows*) at the attachments of the adductor tendons bilaterally, reflecting high-grade avulsions.

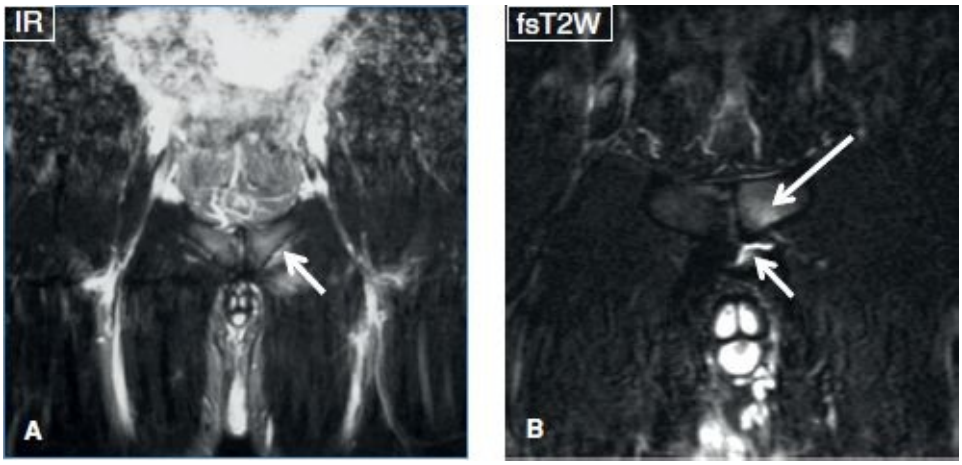

Fig. 48: Athletic pubalgia/adductor variant. Coronal images. **A:** Fluid signal (*arrow*) at the origin of the left adductor longus muscle indicates partial avulsion. Notice edema of the left adductor longus muscle. **B:** A curvilinear fluid (*short arrow*) which is continuous with the symphysis pubis and undermines the inserting structures at the pubis is indicative of avulsion of the adductor longus origin and is referred to as the secondary cleft sign. Also note marrow edema (*long arrow*) of the ipsilateral pubic bone.

- Classic athletic pubalgia, which corresponds to rectus abdominis tear (avulsion) or muscle atrophy with concomitant involvement of common rectus–adductor aponeurosis and adductor tendon tears. These findings are also associated with anterior and inferior pubic ligament sprains and above-described pubic bone and bone marrow signal alterations. One should look carefully on the axial or coronal T1W images for atrophy of the rectus abdominis muscle, which involves its lateral head more and earlier than the medial head (Figs. 49–52).

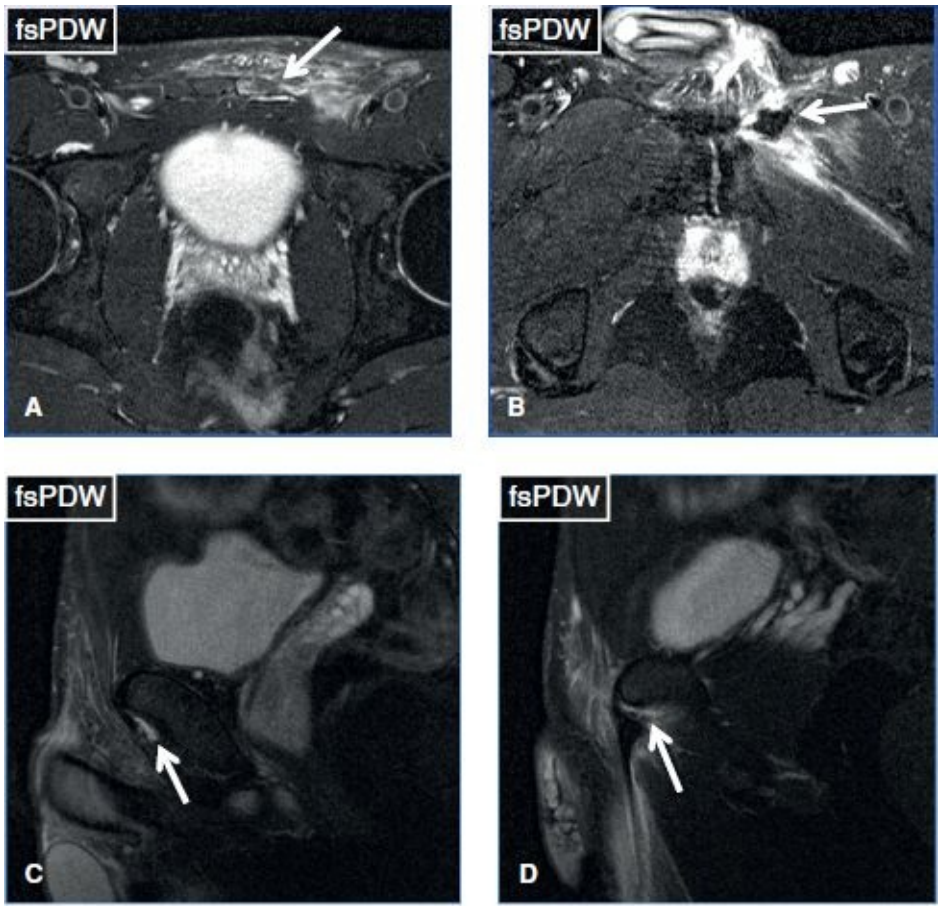

Fig. 49: Classic athletic pubalgia. **A, B:** Axial images demonstrate partial avulsion of the left rectus abdominis insertion (*arrow* in **A**) and complete avulsion of the ipsilateral adductor longus origin (*arrow* in **B**). **C, D:** Sagittal images show site of avulsion of the common rectus abdominis–adductor longus aponeurosis (*arrow* in C) and adductor aponeurosis (*arrow* in **D**).

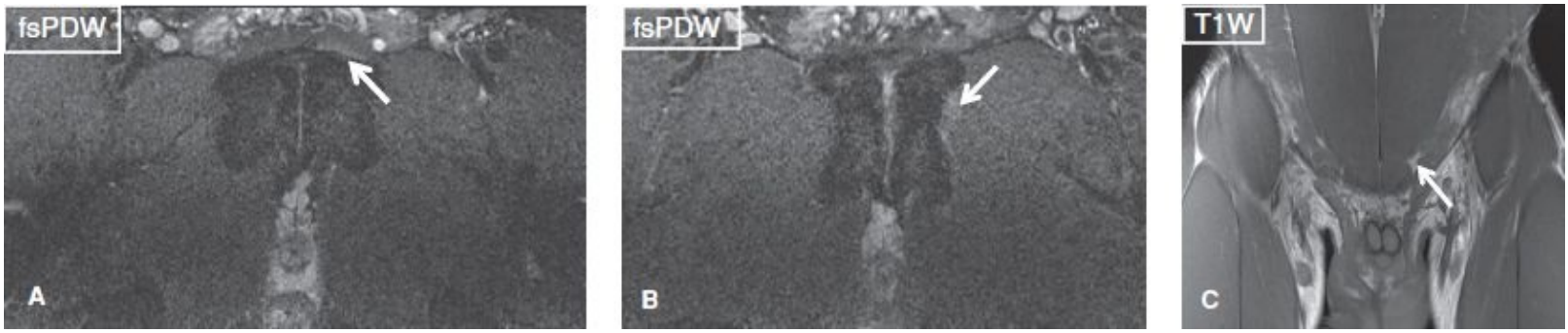

Fig. 50: Classic acute on chronic athletic pubalgia. Axial **(A, B)** images exhibit grade I strains of the left rectus abdominis tendon (*arrow* in **A**) and left common adductor origin (*arrow* in **B**). No frank avulsion is seen and findings are related to Sharpey fiber injury. Notice mild atrophy (*arrow* in **C**) of the ipsilateral lateral head of the rectus abdominis muscle on the coronal T1W image.

Fig. 51: Classic subacute athletic pubalgia with intramuscular cyst. Axial **(A),** coronal **(B),** and sagittal **(C)** images exhibit an intramuscular cyst (*arrows*) within the left rectus–adductor aponeurosis.

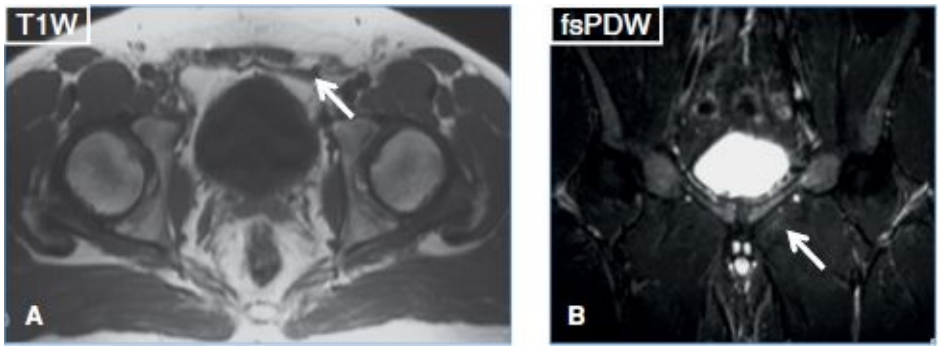

Fig. 52: Acute on chronic athletic pubalgia. Axial image **(A)** exhibits fatty atrophy of the lateral head of the left rectus abdominis muscle, reflecting a chronic process. Coronal image **(B)** from the same patient shows mild edema of the left adductor muscle (*arrow*), compatible with superimposed acute grade I sprain.

Among these variants, the classic pubalgia variant usually requires surgery (modified Bassini or pelvic floor repair), while the others are commonly treated with conservative management of physiotherapy, local anaesthetics and steroids. Nonresponding adductor variant cases may be helped with debridement whereas full-thickness retracted (>2 cm) adductor avulsions will likely need surgery, especially in professional athletes. Postoperatively, secondary cleft sign is a normal finding on MR imaging. One should look for other complications that may mimic groin pain, such as other muscle strains, pubic stress fractures, and infection (Fig. 53). Another variant of athletic pubalgia includes adductor magnus variant, which may appear as chronic atrophy and calcifications of the adductor magnus proximal attachment. The latter is not uncommon in bull riders. Finally, a separate syndrome has been described in the literature, known as baseball pitcher hockey goalie syndrome (BPHGS), which refers to a consequence of epimysial injury of adductor longus muscle in the proximal thigh with consequent muscle hernia causing recurrent inflammations and painful entanglement of a branch of the obturator nerve. On MR imaging, one would see fascial edema along the adductor longus muscle and less commonly, the hernia itself. Of note, the entity is not uncommonly seen in other players (Figs. 54, 55). The term *sports hernia* is a misnomer since most athletic pubalgia entities are related to myotendinous tears, and the only true hernias are BPHGS and spigelian hernia. The

spigelian hernia is basically caused by an upward extension of tear/attenuation of the rectus abdominis and adjacent fascia above the level of inferior epigastric vessels. There is pain and weakening at the linea semilunaris, the line where the sheaths of the lateral abdominal muscles fuse to form the lateral rectus sheath. The surgical treatment requires extension of repair at the spigelian area in addition to the standard anterior pelvic floor repair with rectal release. The MR imaging findings include edema or thinning of rectus abdominis and bulge at the spigelian area consistent with weakening of the fascial layers in this region (Fig. 56). Inguinal or femoral hernias are uncommon cause of athletic pubalgia in these subjects. Finally, other variants are named according to the tendons or myotendinous strains of the respective structures involved, such as rectus femoris, quadratus femoris, pectineus, gracilis, and obturator externus variants of athletic pubalgia (Figs. 45, 57–60). The obturator externus also has a bursa, which communicates with and extends from the posteroinferior aspect of the hip deep to the obturator externus tendon. Similar to iliopsoas bursitis, obturator externus bursitis can be symptomatic or may be affected by synovial processes, such as synovial osteochondromatosis and pigmented villonodular synovitis.

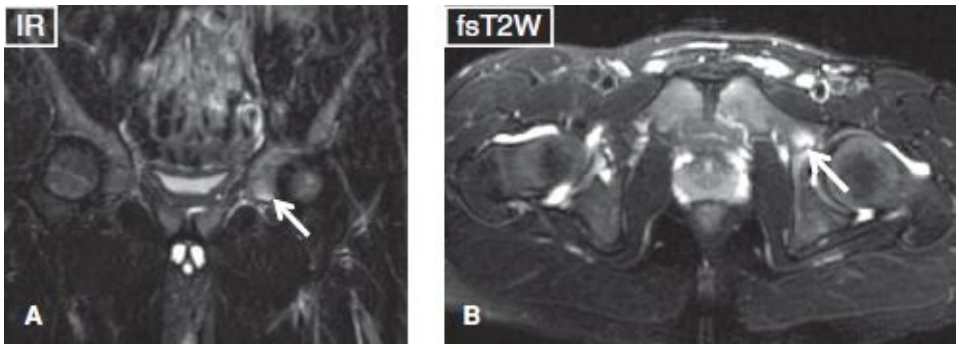

Fig. 53: Unrelated finding postathletic pubalgia surgery. Coronal **(A)** and axial **(B)** images exhibit new cause of left groin pain—a stress fracture of the left ischiopubic ramus (*arrows*).

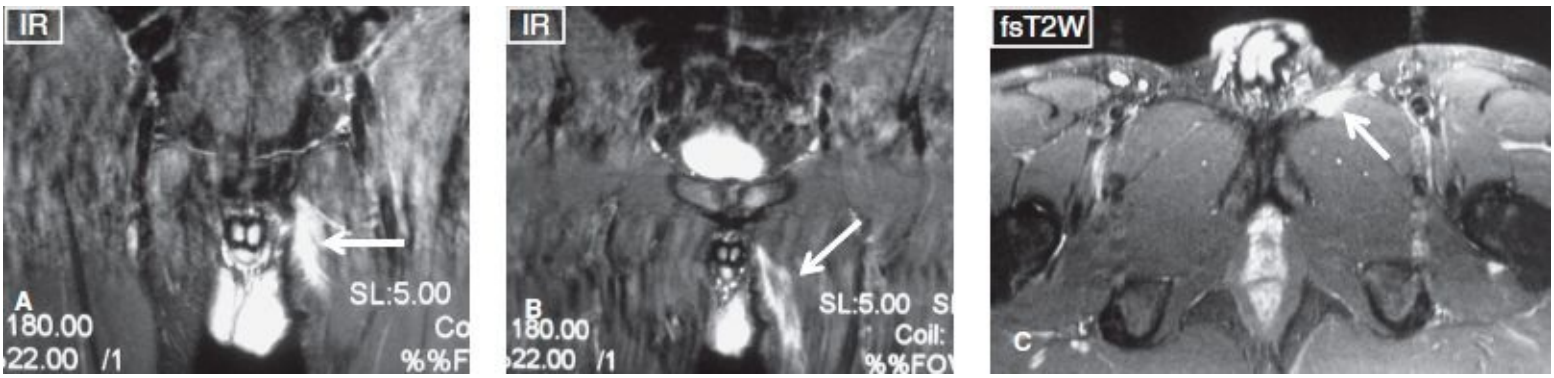

Fig. 54: BPHGS. Coronal **(A, B)** and axial **(C)** images show fascial edema along a clinically proven adductor longus muscle hernia and epimysial injury (*arrows*). This was a 33-year-old hockey player who felt a “pop” during a game 5 months prior with chronic pubic pain. He had tenderness and a cord-like palpable hernia that extended from the pubic symphysis down several inches into the muscle belly.

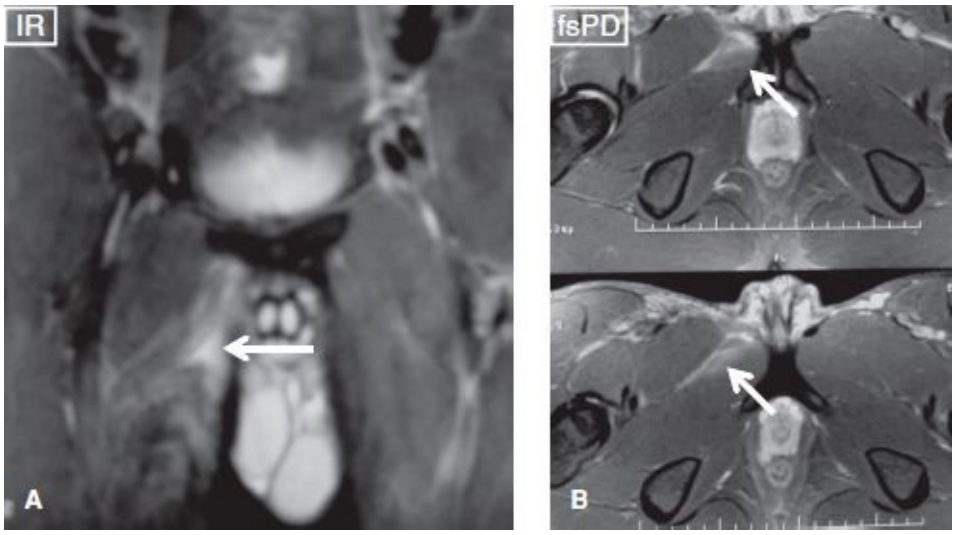

Fig. 55: BPHGS. Coronal **(A)** and axial **(B)** images show fascial edema along the clinically proven adductor longus muscle hernia and epimysial injury (*arrows*). This was a 28-year-old professional hockey player (goalie) with acute right groin pain. He had tenderness along a cord of the adductor longus and at the junction of the longus and pectineus belly several inches inferior to the pubic symphysis.

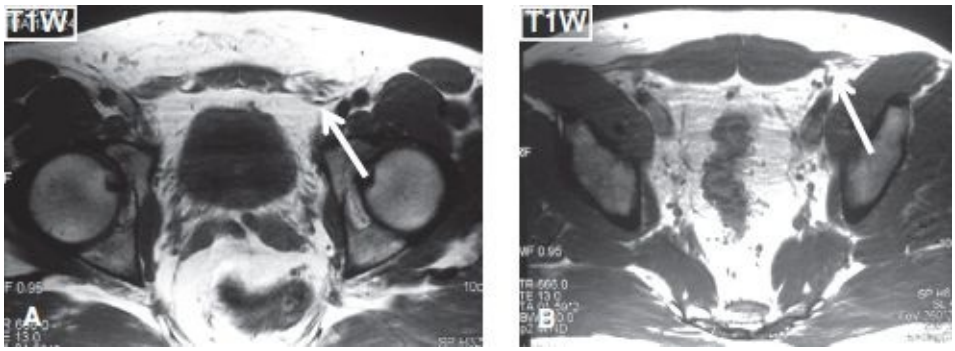

Fig. 56: Spigelian hernia variant. A 39-year-old vigorous karate expert was having significant problems throughout his pelvis and pain in the spigelian area for the last 3 months. Axial MR images demonstrate attenuation of lateral head fibers of left rectus abdominis muscle (*arrow* in **A**) and resultant bulge in the left spigelian area (*arrow* in **B**).

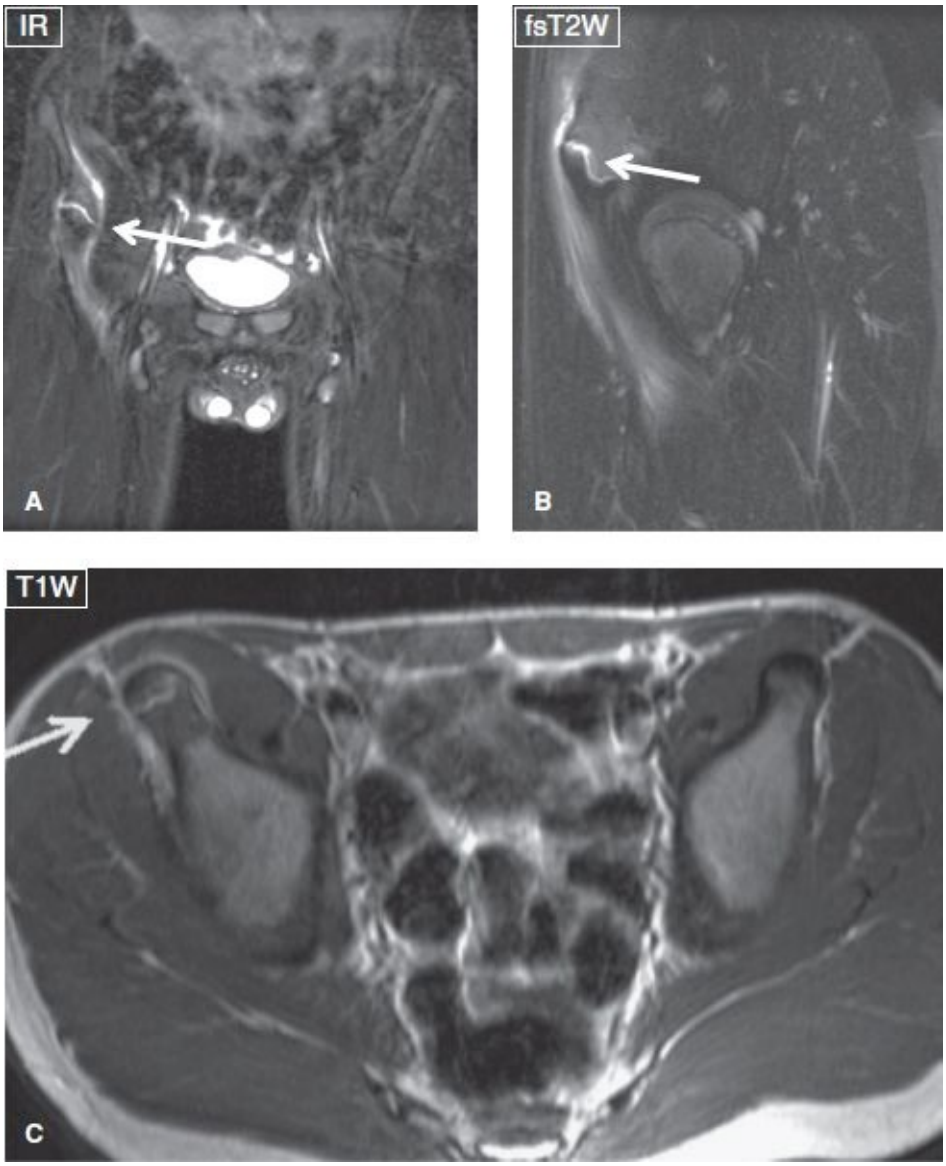

Fig. 57: A 16-year-old runner with acute right groin pain. Sagittal **(A),** coronal **(B),** and axial **(C)** images through the pelvis show avulsion of the anterior-superior iliac spine at the attachment of rectus femoris (*arrows*) with bone marrow and fascial edema.

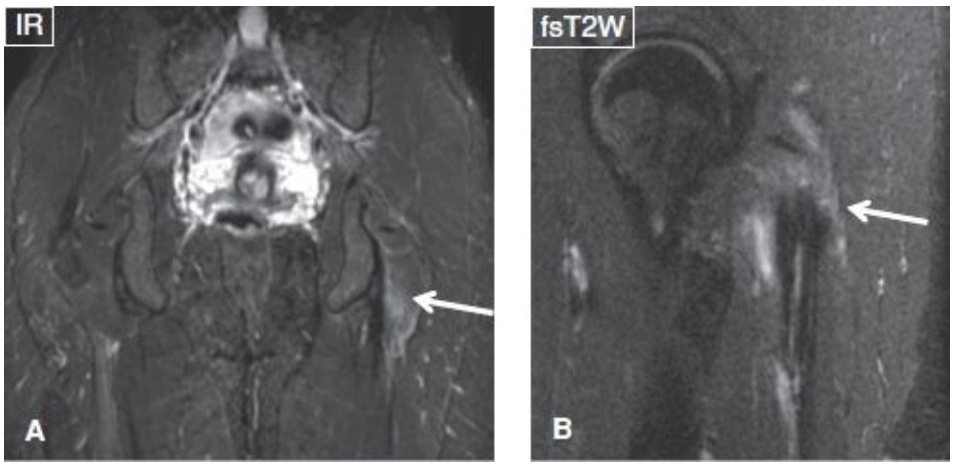

Fig. 58: Quadratus femoris syndrome. A 15-year-old marathon runner complains of left groin and gluteal pain. Coronal **(A)** and sagittal **(B)** images show edema in the left quadratus femoris muscle (*arrows*) consistent with grade I strain.

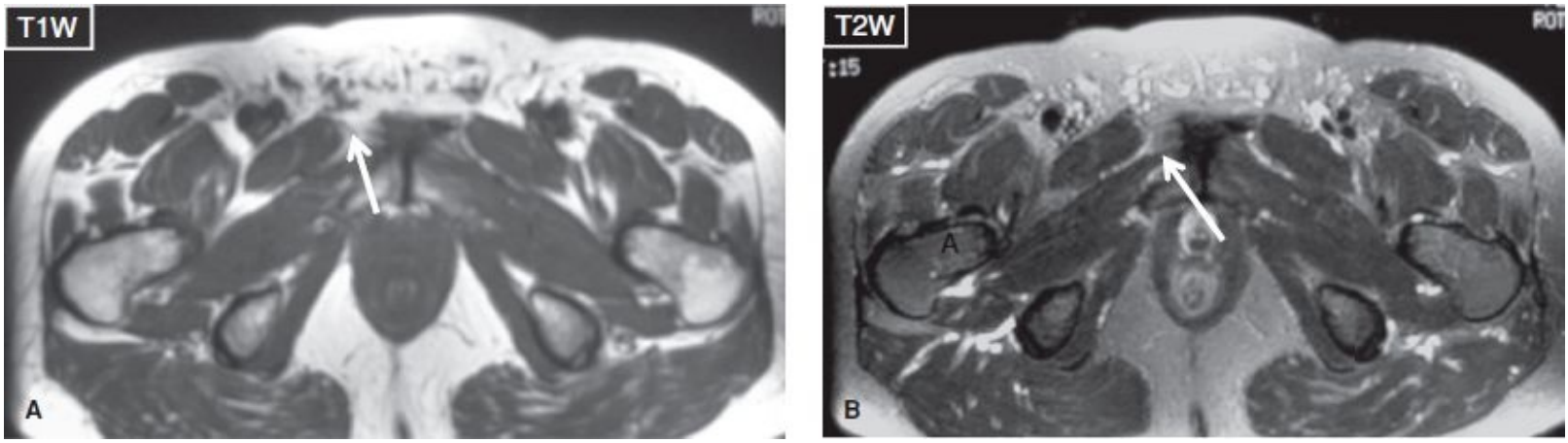

Fig. 59: Pectineus variant. A 66-year-old soccer player with pain in right groin and localized tenderness at the right pubis for few weeks. Axial images **(A, B)** show isolated avulsion and retraction of the right pectineus tendon (*arrows*).

Fig. 60: Obturator externus muscle injury. Coronal images show edema of the obturator externus muscle, along with an intramuscular fluid collection (*arrows*), which signifies partial discontinuity of muscle fibers in keeping with a grade II strain.

At the level of the pelvis, the iliacus and psoas muscles converge to form the iliopsoas muscle, the tendon of which features two parallel bands that run anterior to the hip joint separated by a thin cleft of T1 hyperintense fatty fascia. These insert onto the lesser trochanter and proximal femoral shaft, respectively. The iliopsoas tendon has a bursa, which lies between the musculotendinous portion and the joint capsule, and it communicates with the hip joint in up to 15% of individuals. It is the largest bursa in the body with an average size of 6 × 3 cm when filled with fluid and can have a bilobed configuration. When distended, it may extend into the anterolateral pelvis along the sheath of the iliopsoas tendon. The iliopsoas bursitis may occur in conjunction with strains of the iliopsoas muscle or tendon. It occurs in activities requiring extensive use of the hip flexors including soccer, ballet, running, hiking, and jumping. Acute bursitis and/or strains of the tendon are essentially identical in their clinical presentations with some differences. The pain due to strain or tendonitis usually occurs at the musculotendinous junction during resisted hip flexion or hyperextension. Iliopsoas bursitis is characterized by deep groin pain that sometimes radiates to the anterior hip or thigh and is often accompanied by a snapping sensation (Figs. 61, 62). Partial tears most often involve the lesser trochanter insertion and

appear either as focal fluid within the tendon (split tear) or as focal discontinuity of the tendon fibers. Less commonly, whole muscle may be edematous with areas of discontinuity (Fig. 63). Similar to other tendons, iliopsoas tendinopathy appears as thickening or increased intrasubstance signal of the tendon along its course or at the insertion. Potential associated findings include peritendinous high T2 signal and distention of the iliopsoas bursa. With complete tears, there is total discontinuity of the tendon and variable retraction of the torn fragments. Various other causes of iliopsoas bursitis include trauma, overuse injury, total hip arthroplasty with particle disease, OA, rheumatoid arthritis, pigmented villonodular synovitis, gout, joint infection, and AVN of the femoral head.

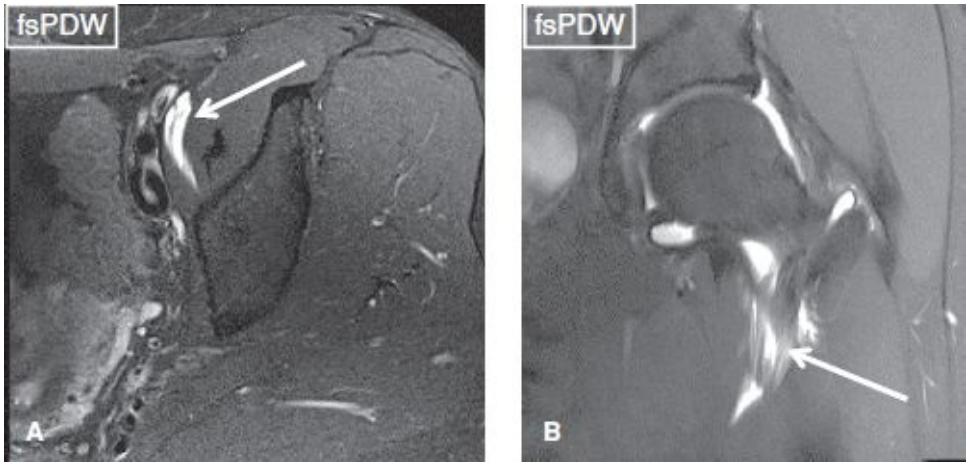

Fig. 61: Iliopsoas bursitis. Axial **(A)** and coronal **(B)** images demonstrate small fluid collection (*arrows*) within the iliopsoas bursa.

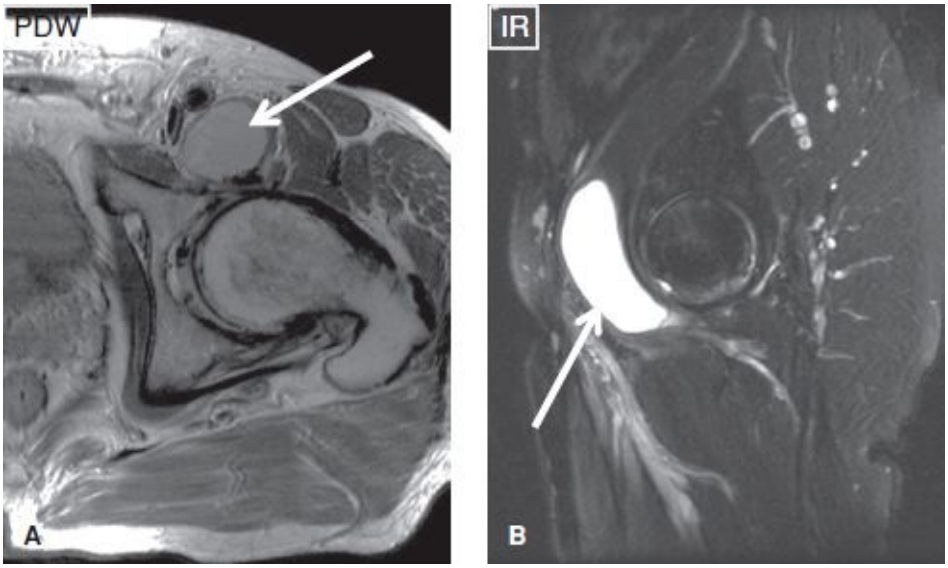

Fig. 62: Iliopsoas bursitis. A 45-year-old runner with chronic left groin pain and snapping sensation. There is complex collection in left iliopsoas bursa. Axial **(A)** and sagittal **(B)** images demonstrate moderate fluid collection (*arrows*) within the iliopsoas bursa.

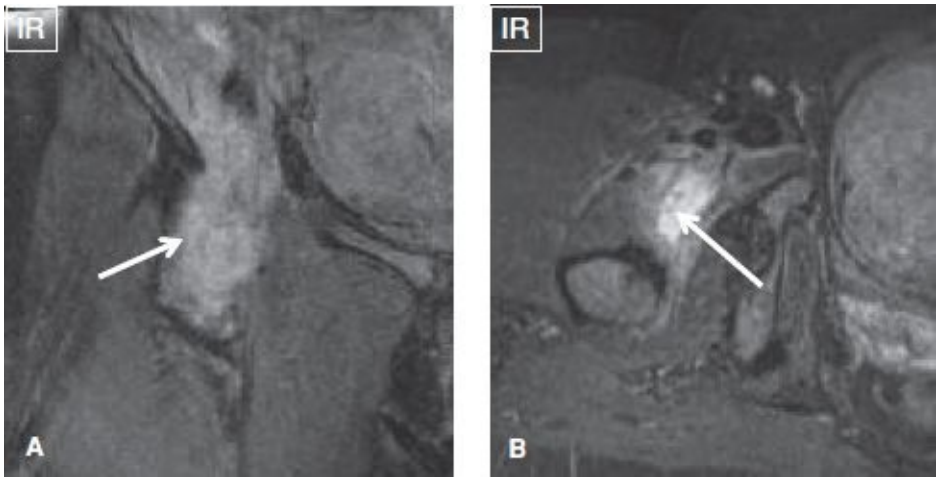

Fig. 63: Iliopsoas muscle injury. Coronal **(A)** and axial **(B)** images show partial discontinuity of iliopsoas muscle fibers with diffuse edema (*arrows*), in keeping with grade II strain.

The lateral rotators include the piriformis, superior and inferior gemelli, and obturator internus muscle although obturator externus and quadratus femoris may also be included in this group. The piriformis muscle can cause sciatic nerve impingement syndrome, conveniently labeled as piriformis syndrome. Patients present with gluteal pain or wallet anesthesia and the muscle may be asymmetrically hypertrophied or atrophied. It should be noted that piriformis is made of many muscle bellies and mild asymmetry is not uncommonly seen as a normal finding. In addition, about 20% of asymptomatic subjects may have split sciatic or intramuscular course of sciatic as a normal variant. To make a case for piriformis syndrome, in the right clinical setting of buttock pain or wallet anesthesia, one should look for abnormal signal hyperintensity of sciatic nerve (approaching adjacent in plane venous signal intensity) with/without contour or caliber change (flattening with proximal enlargement) at the sciatic notch, apart from the variant muscle or sciatic course anatomy (Figs. 64, 65). There are other identifiable pathologies that may exacerbate findings of piriformis syndrome in the setting of underlying variant neuromuscular anatomy. These include superimposed lumbosacral plexopathy causing neural swelling, and double crush syndrome, that is, proximal spine disease affecting the neural elements that constitute the sciatic nerve downstream. These findings are best observed on MR neurography; however, if carefully sought for, one may also notice variant anatomy or nerve signal changes on the dedicated hip MR imaging. One should also note that sciatic nerve is normally mildly bright at the sciatic notch due to magic angle artifact or may appear artifactually brighter than the other side due to suboptimal fat suppression. Therefore, it is prudent not only to compare the nerves side to side for asymmetry in size and signal but also account for nonuniformity of fat suppression while making a call for abnormality.

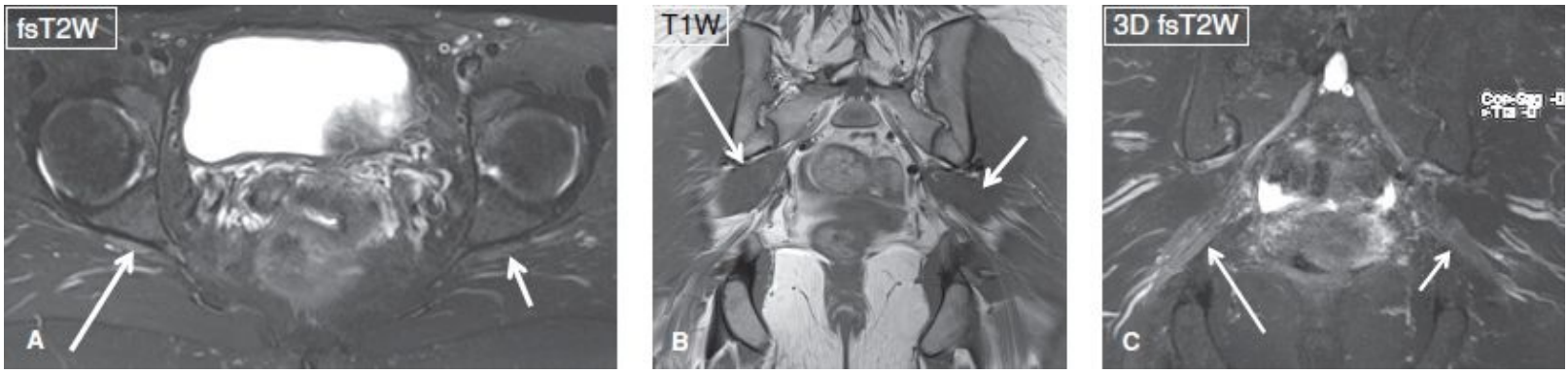

Fig. 64: Piriformis syndrome on MR neurography in a 42-year-old woman with right buttock pain. Axial **(A)** and coronal **(B, C)** images show asymmetric increased signal of the right sciatic nerve (*long arrows* in **A, C**) and increase size (*long arrow* in **C**) relative to the normal left sciatic nerve (*short arrows* in **A, C**). Also note hypertrophy of the right piriformis (*long arrow* in **B**) relative to the normal left piriformis (*short arrow* in **B**).

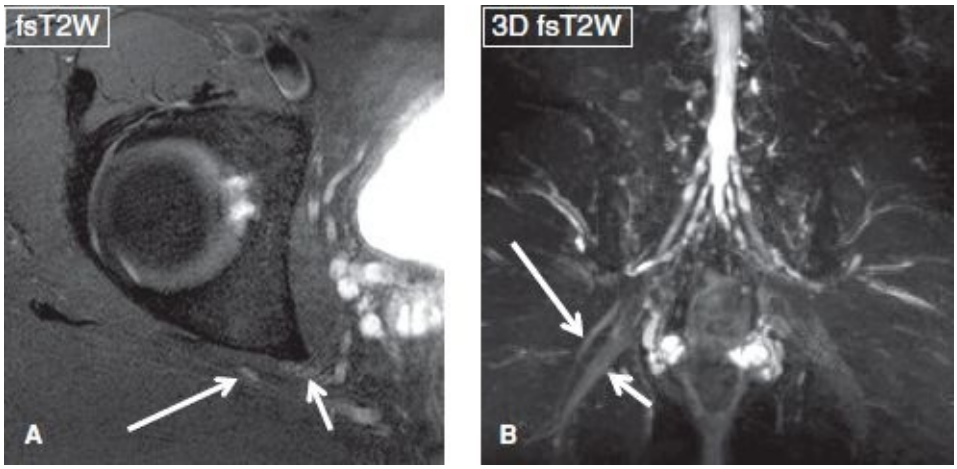

Fig. 65: Piriformis syndrome with split sciatic nerve on MR neurography. Axial **(A)** and coronal MIP reconstruction from 3D fsT2W **(B)** images show split right sciatic nerve with mild hyperintensity of the peroneal component (*long arrows*) and normal tibial component (*short arrows*).

Congenital narrowing of the space between the ischial tuberosity and lesser trochanter may lead to impingement of the quadratus femoris muscle that runs within this space. It may cause hip pain, especially on adduction, extension, and external rotation, and the entity is known as ischiofemoral impingement. On MR imaging it is seen as edema-like signal alteration of the quadratus femoris, which is centered at the site of maximal impingement. The edema may become more severe with increased severity of impingement and it may be associated with variable degrees of atrophy and/or fatty infiltration within the muscle, adventitial bursa formation, and occasionally, mild contrast enhancement (Figs. 66–68). One can measure the ischiofemoral space between the ischial tuberosity and lesser trochanter, or quadratus femoris space (transverse width of the muscle). The measurements are made on non-fs images and the distances are considered abnormal when less than 15–16 and 11–12 mm, respectively. However, since this space can get narrowed dynamically, the

measurement is not always abnormally small, but secondary abnormal soft tissue findings guide the diagnosis. In recalcitrant cases, the space may require surgical widening with debridement of the atrophied, scarred muscle and/or resection of the adventitial bursa. One should note that the MR imaging findings of ischiofemoral impingement are frequently incidentally noted and clinical correlation of the findings is essential. In addition, hamstring peritendinitis may mimic ischiofemoral impingement clinically, or may be seen as a coexistent finding. The inflammatory edema in peritendinitis is usually localized around the tendon and underlying partial tears of the hamstring tendon origin. Enthesopathy of ischial tuberosity is commonly associated with this lesion (Fig. 69). Uncommonly, one might see reverse ischiofemoral impingement, that is, impingement between the greater trochanter of an externally rotated hip with the ischial tuberosity. This entity is seen in exaggerated coxa valga, for example, in cerebral palsy and may lead to sciatic nerve impingement (Fig. 70).

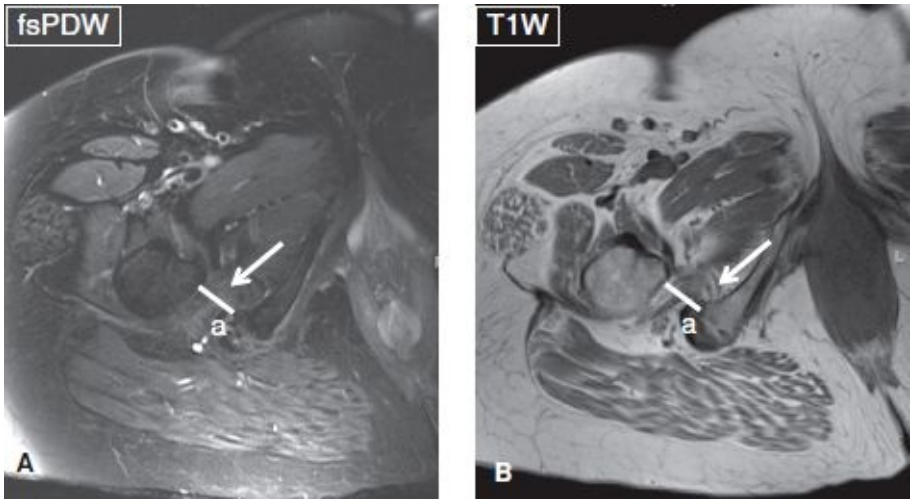

Fig. 66: Ischiofemoral impingement. Axial images **(A, B)** exhibit mild edema-like signal and moderate fatty atrophy of the quadratus femoris muscle (*arrows*) in the abnormally small (12 mm) ischiofemoral space (distance *a*).

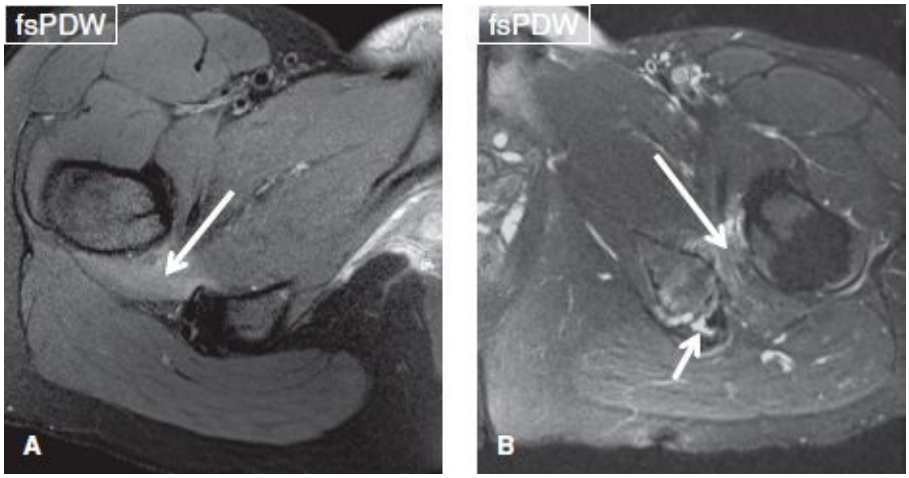

Fig. 67: Ischiofemoral impingement. Axial images from two different patients demonstrate edema of the quadratus femoris muscles (*long arrows*) with normal space measurement **(A)** and small space measurement **(B).** Notice partial tear (*short arrow*) of the left hamstring tendon origin.

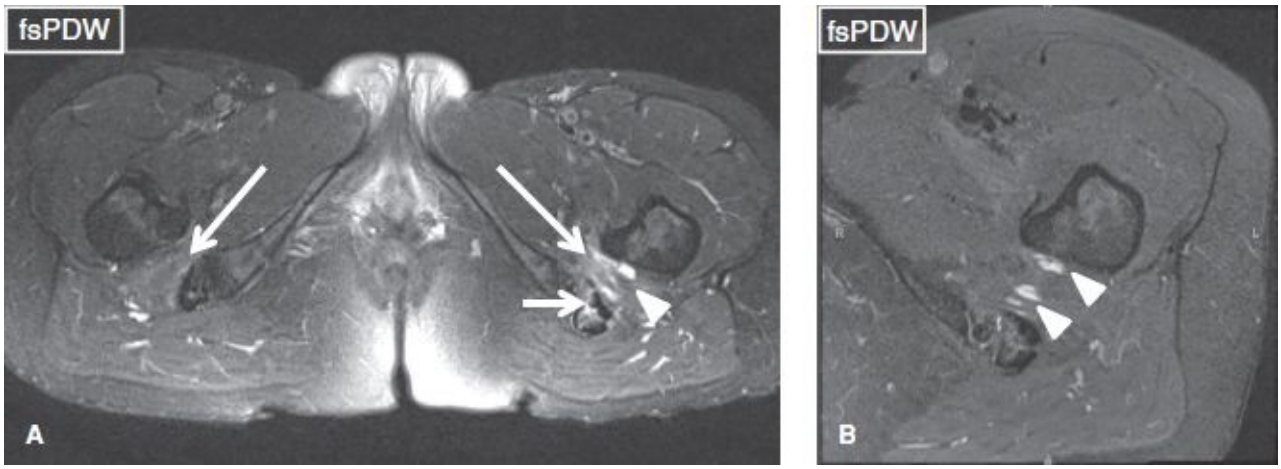

Fig. 68: Ischiofemoral impingement, preoperatively **(A)** and postoperatively **(B). A:** Axial image exhibit bilateral edema of quadratus femoris muscles (*long arrows*) within the ischiofemoral spaces, which are narrow. The edema is most prominent on the left side, where there is also a partial tear of the hamstrings tendon (*short arrow*), along with adventitial bursa formation (*arrowhead*). **B:** Axial image following surgery reveals near-complete resolution of muscle edema, and small residual adventitial bursa (*arrowheads*). Notice the widened ischiofemoral space and healing of hamstring tears.

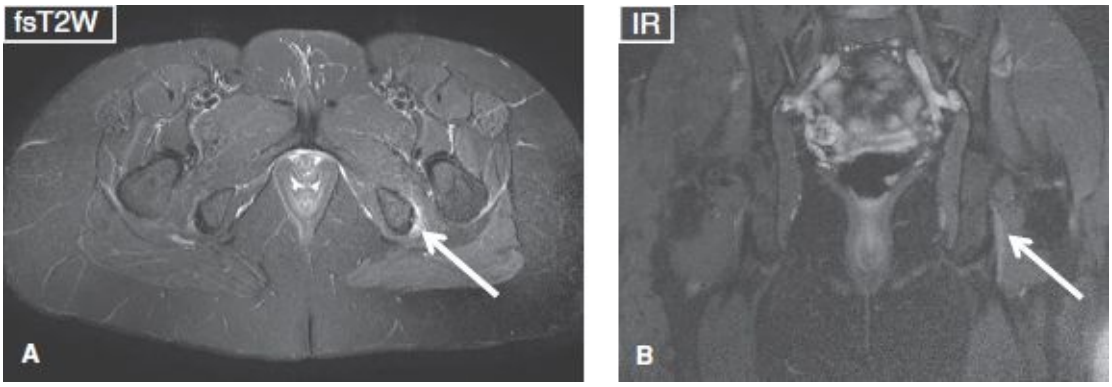

Fig. 69: Hamstring peritendinitis. Axial **(A)** and coronal **(B)** images display moderately high signal (*arrows*) around the hamstring tendons, which are otherwise intact.

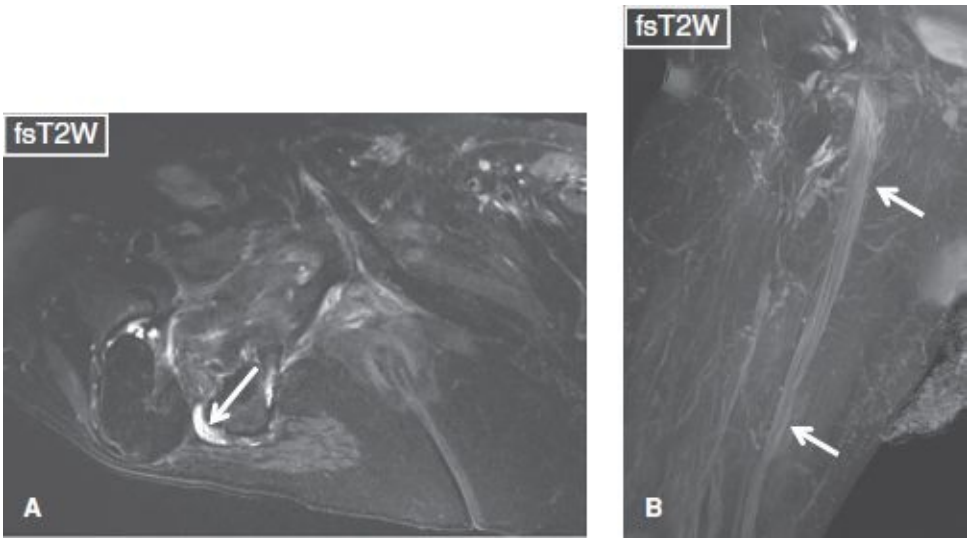

Fig. 70: Reverse ischiofemoral impingement. Axial **(A)** and coronal **(B)** images show bright

and diffusely enlarged sciatic nerve (*arrows* in **B**), impinged (*arrow* in **A**) in a case of reverse ischiofemoral impingement between the greater trochanter and the ischial tuberosity.

The snapping hip syndrome, more commonly seen in women ballet dancers and runners, is a complex of symptoms characterized by an audible and/or palpable snapping with certain hip joint movements usually with flexion and extension. The entity may be caused by intra-articular or extra-articular causes. The intra-articular causes include labral tears, loose bodies, synovial osteochondromatosis, synovial folds, and fracture fragments. There are three different extra-articular variants described in the literature.

- External (lateral) snapping hip syndrome—the iliotibial tract or anterior portion of the gluteus maximus muscle rubs over the greater tuberosity. A patient may experience pain over lateral aspect of the thigh or buttocks due to superimposed inflammation of the greater trochanter or subgluteus maximus bursae.
- Internal (medial) snapping hip syndrome—friction of the iliopsoas tendon on the iliopectineal eminence, lesser trochanter, femur or anterior-inferior iliac spine during hip flexion and extension. There may be associated iliopsoas bursitis causing pain in the anterior groin and hip. Accessory iliopsoas tendinous slips (otherwise a normal variant) and iliopsoas stenosing tenosynovitis can also produce snapping of the tendon.
- Posterior snapping hip syndrome—ischiogluteal bursitis and edema in ischiofemoral space due to friction of the long head of the biceps femoris tendon over the ischial tuberosity or, from prior trauma to ischial tuberosity.

Snapping hip is a clinical diagnosis and can be confirmed with dynamic imaging using ultrasound; however, MR imaging may assist to rule out aforementioned anatomic causes and associated tendon abnormalities. The first-line treatments include muscle stretching, rest, and avoidance of symptoms. It might take 6 to 12 months to resolve. In failed cases, depending upon the type of lesion, the treatments include iliopsoas fractional lengthening (internal), Z-plasty of the IT band or ischiogluteal space widening with bursa resection (external), and hip arthroscopy (intra-articular). In many cases, during FAI surgery, iliopsoas release may also be performed in patients with symptoms of anterior groin pain and medial snapping syndrome. There is no consensus yet, whether to perform release at the iliopsoas tendon, myotendinous junction or muscle itself. Recurrence rates of snapping are also not that low, ranging from 20–40% over 1–2 year postoperative follow-up interval.

The hamstrings muscles, which serve as hip extensors, include the semimembranosus, which originates from the superolateral facet of the ischial tuberosity, and the semitendinosus and biceps femoris, which share a common origin from the ischial tuberosity, located infero medial to the semimembranosus tendon, aka the conjoint tendon. Adductor magnus has the medial most origin from the ischial tuberosity. The hamstring tendons may exhibit tendinosis (a fairly common finding in middle-aged and elderly subjects, depicted as intermediate intrasubstance signal) and may suffer partial tears (usually depicted as fluid-filled cleavage at the origin site), bony avulsions (in children and elderly), or complete tears (which appear as complete tendon discontinuity, along with

associated retraction) (Figs. 71–74). Tendon injuries may be associated with underlying bony changes, such as avulsive edema, cystic changes, enthesopathy or frank avulsion fractures, particularly in skeletally immature patients. Most tears and avulsions typically involve the conjoint tendon with at least partial tearing of the semimembranosus tendon. Hypointense foci within or around the tendinous origins represent calcifications and are indicative of chronic injuries. One should not mistake normally present prominent vessels around the tendon attachments for partial hamstring tears as the former show tortuous branching configuration. Finally, chronic tears may be associated with scarring and significant fatty infiltration of the muscle due to disuse leading to balled up and retracted mass-like lesion, which can mimic neoplasm. Most hamstring injuries are treated in a conservative fashion and factors leading to delayed recovery from injury include higher-grade injuries and edema around the sciatic nerve. Indications of surgery include, more than 2 cm tendon retraction, significant sciatic symptoms, and more than two tendon avulsions.

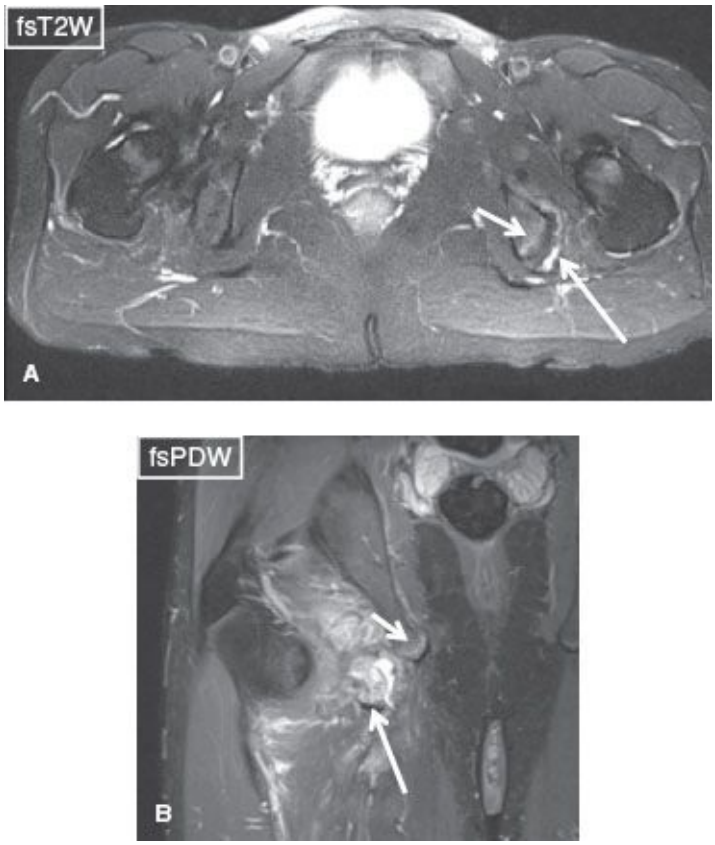

Fig. 71: Hamstring avulsion. **A:** Axial image shows partial avulsion of the common hamstrings tendon (*long arrow*). Also note mild subtendinous bone marrow edema at the attachment site (*short arrow*). **B:** Coronal image in a different patient exhibits complete avulsion and mild distal retraction of the common hamstrings tendon (*long arrow*). Also note mild bone marrow edema at the attachment site (*short arrow*) and edema of the quadratus femoris muscle.

Fig. 72: Hamstring apophyseal avulsion. Coronal image shows apophyseal avulsion of the ischial tuberosity (*arrow*), related to traction by the hamstring muscles in an adolescent boy.

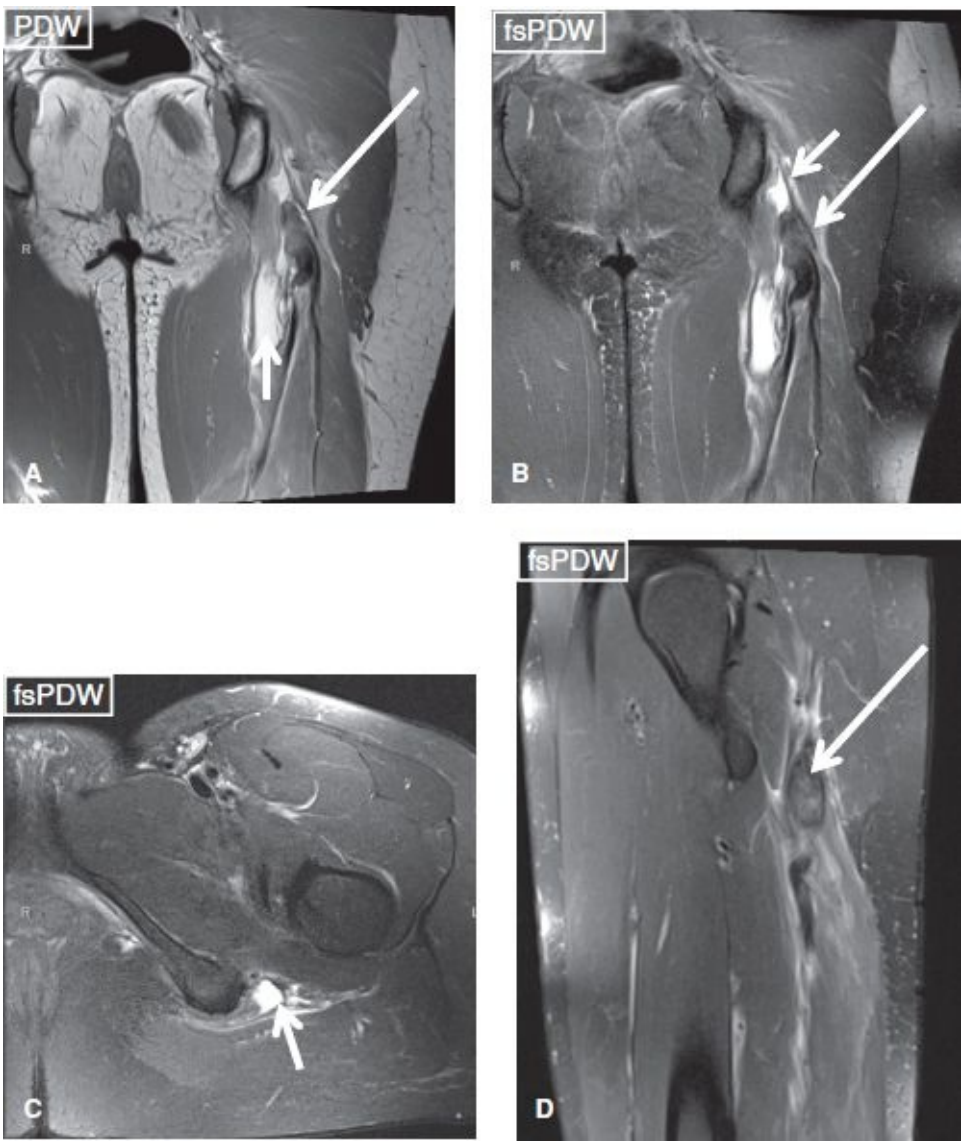

Fig. 73: Hamstring tendon avulsion, surgical case. Coronal **(A, B)** and axial **(C)** images demonstrate a fluid collection (*small arrows*) at the expected anatomic location of the hamstring origin with distal retraction of the tendons (*long arrows*), which was confirmed on

the sagittal image **(D).**

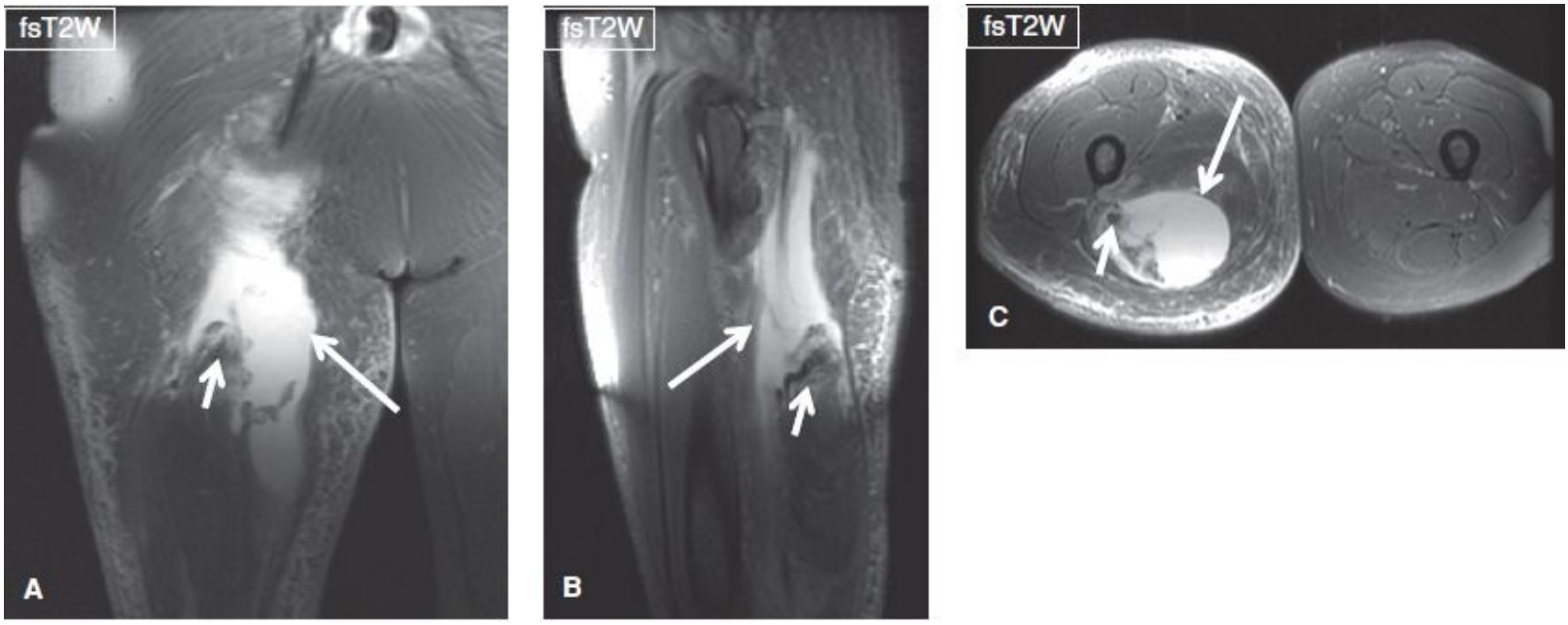

Fig. 74: Hamstring tendon avulsion, surgical case. Coronal **(A),** sagittal **(B),** and axial **(C)** images demonstrate complete avulsion and distal retraction of common hamstrings tendon (*short arrows*), with fluid collection (*long arrows*) filling the gap.

Similar to other areas of the body, the muscles around the hip may be involved by several inflammatory, infectious, and iatrogenic abnormalities. Myopathy, whether idiopathic or due to various causes, such as dermatomyositis, collagen vascular disease, etc. leads to edema-like signal of the muscle with or without fatty replacement and atrophy in multiple compartments of the limb and usually in a symmetric fashion (Figs. 75, 76). Heterotopic ossification could look aggressive with patchy edema-like signal in the muscle and its adjacent fascia in its early stages. However, recent history of trauma or anticoagulation and presence of fascial edema or blood products (hyperintensity on T1W/T2W images and blooming on GRE images) are helpful clues to the diagnosis. One should look for available radiographs or CT scan for peripheral calcifications, which mature over time and may turn into ossifications (Fig. 77). While myopathy and neuropathy causes fatty atrophy, one should also consider underlying motor neuron disease and poliomyelitis in the differential for muscle fatty infiltration or atrophy (Fig. 78). Infectious myositis can be diagnosed in the right clinical setting of toxemia and myofascial changes of edema and intense enhancement. In this setting, non-enhancing areas representing necrosis or early abscess formation may be identified (Fig. 79). Organized abscess will show well-defined multilayered enhancing rim. Finally, rhabdomyolysis or necrotizing myositis may show enlargement of the muscle, intramuscular hemorrhage, bulging epimysium, and nonenhancing areas on contrast imaging with background edematous muscle (Figs. 80, 81). Compartment syndrome may arise in this setting and it may further exacerbate muscle ischemia, swelling, and necrosis. This diagnosis should be clinically correlated as most acute conditions of muscles lead to some degree of muscular swelling. Soft tissue hematoma in

and around the muscles may mimic soft tissue sarcoma. The presence of internal signal hyperintensity on all sequences, recent history of trauma, anticoagulation or surgery and isolated peripheral enhancement on contrast images are helpful clues toward the diagnosis of a benign hematoma (Fig. 82). Subtraction images are particularly helpful in excluding central or nodular enhancement of sarcoma, and better characterizing the enhancement pattern in a T1 hyperintense mass lesion. Indeterminate lesions should be followed up to stability or resolution. Any central or nodular enhancement, however, raises the suspicion of a sarcoma and it should be dealt aggressively with percutaneous or excisional biopsy.

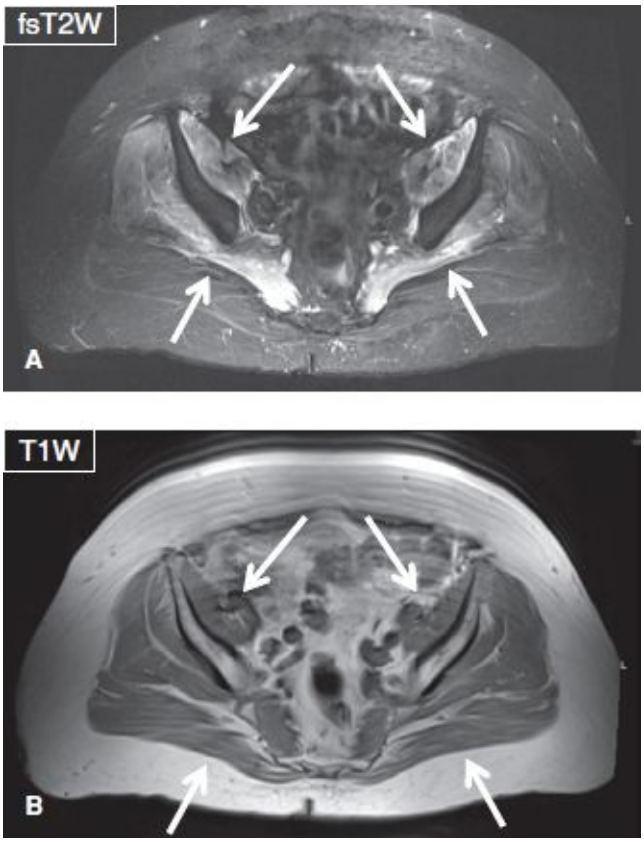

Fig. 75: Dermatomyositis. Axial images. **A:** There is diffuse and symmetric edema-like signal of the gluteus minimus, medius, and iliopsoas muscles (*arrows*). **B:** No significant atrophy or fatty infiltration is evident in the involved muscles (*arrows*).

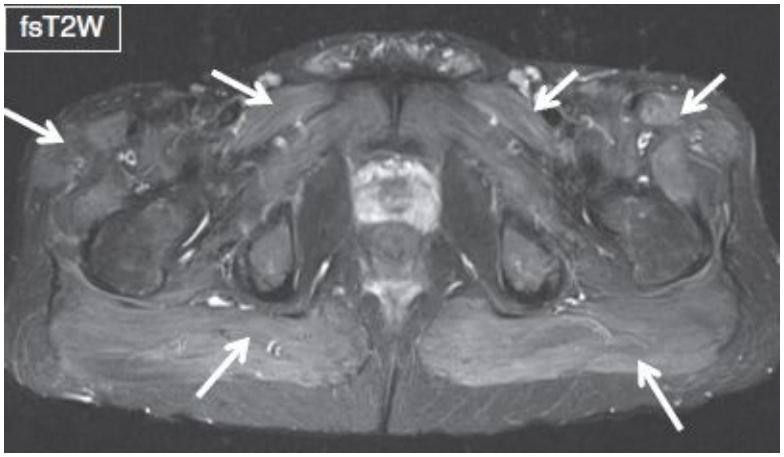

Fig. 76: Idiopathic myositis. Axial image shows mild diffuse and symmetric edema of all skeletal muscles (*arrows*) around the pelvis.

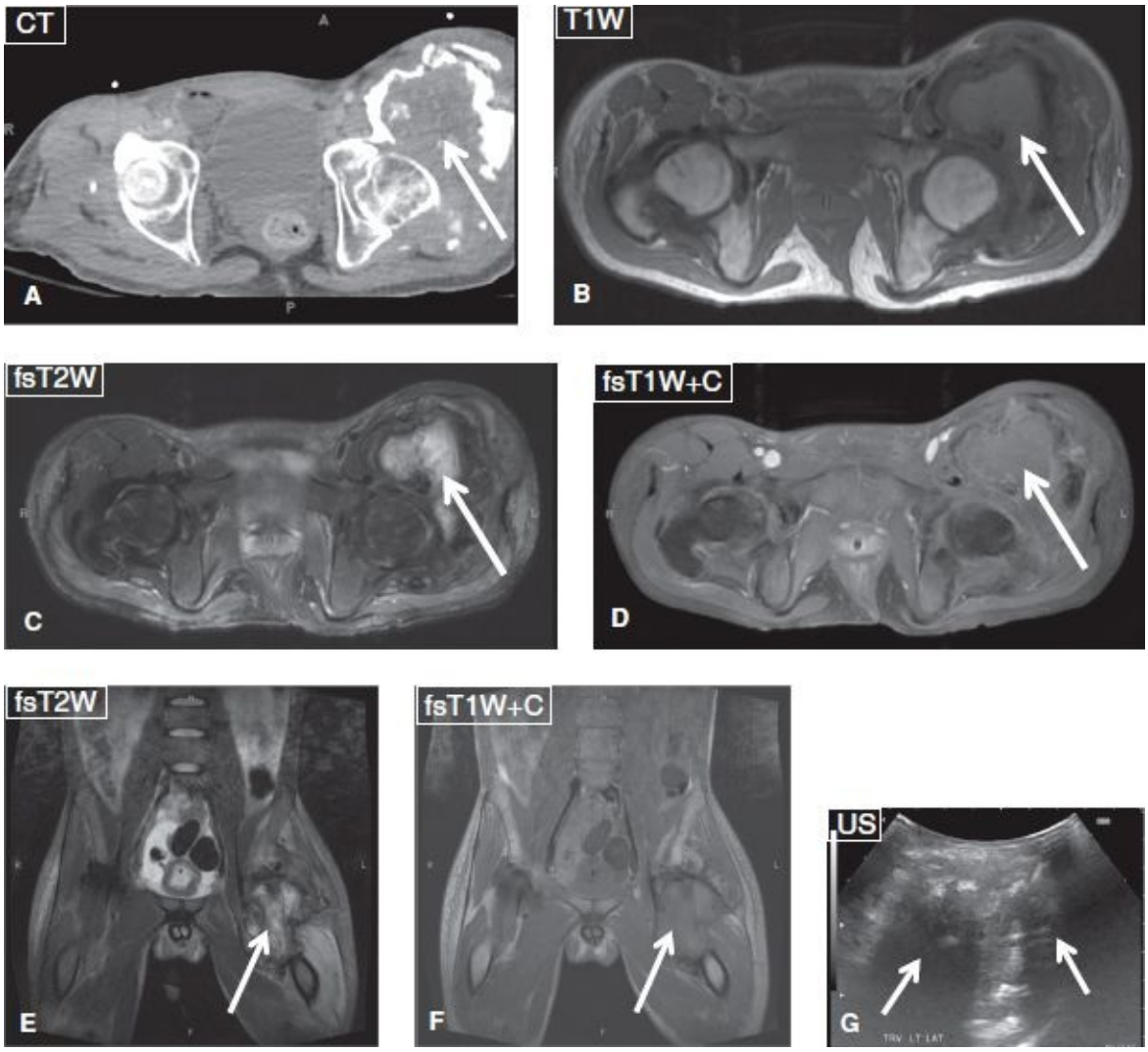

Fig. 77: Heterotopic ossification. Axial CT image **(A)** demonstrates a heterogeneous mass-like lesion (*arrow*) in the muscles of the anterolateral aspect of the proximal thigh, which shows mass effect and extensive peripheral mature calcification. On the corresponding axial **(B–D)** and coronal **(E, F)** MR images, the lesion (*arrows*) features heterogeneous T1 and T2 hyperintense signal, hypointense rim, and no significant enhancement. Notice adjacent fascial edema of the quadriceps muscles. On ultrasound **(G),** the lesion's calcifications cause marked acoustic shadowing (*arrows*).

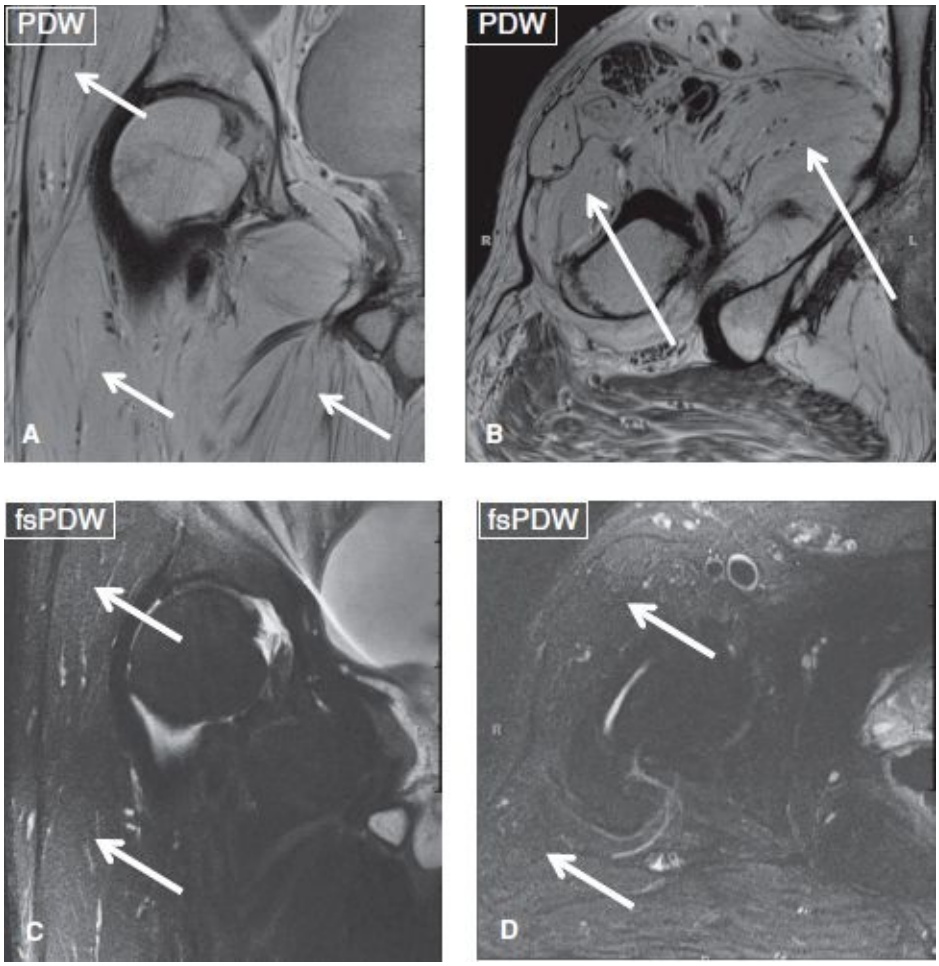

Fig. 78: Poliomyelitis-related muscle fatty replacement. Coronal **(A, C)** and axial **(B, D)** images demonstrate diffuse fatty infiltration of the skeletal muscles (*arrows*) around the hip joint in this known case of long-standing poliomyelitis.

Fig. 79: Infectious myositis and tendinitis. Coronal images in a patient with toxemia demonstrate localized peripherally enhancing fluid collections in the tensor fascia lata tendon (*arrow in* **A**) and iliopsoas muscle (*arrow in* **B**). Notice surrounding hyperemia, fascitis, and myositis.

Fig. 80: Necrotizing myositis. Axial image displays diffuse enlargement and intense contrast enhancement of the left gluteal medius (*long arrow*), part of minimus (*short arrow*), and piriformis (*medium arrow*) muscles, reflecting compartment syndrome due to necrotizing myositis. Notice small areas of nonenhancement in the muscles due to ischemia.

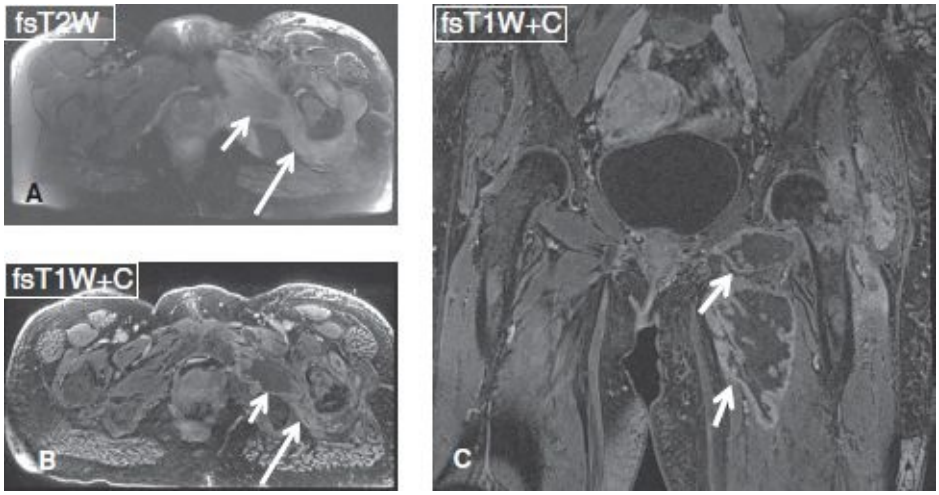

Fig. 81: Tylenol-induced myonecrosis. Axial **(A, B)** and coronal **(C)** images demonstrate edematous enlargement and heterogeneous contrast enhancement (*long arrows*) of the muscles around the left hip joint, reflecting inflammation. Notice multifocal areas of nonenhancement indicative of myonecrosis (*short arrows*).

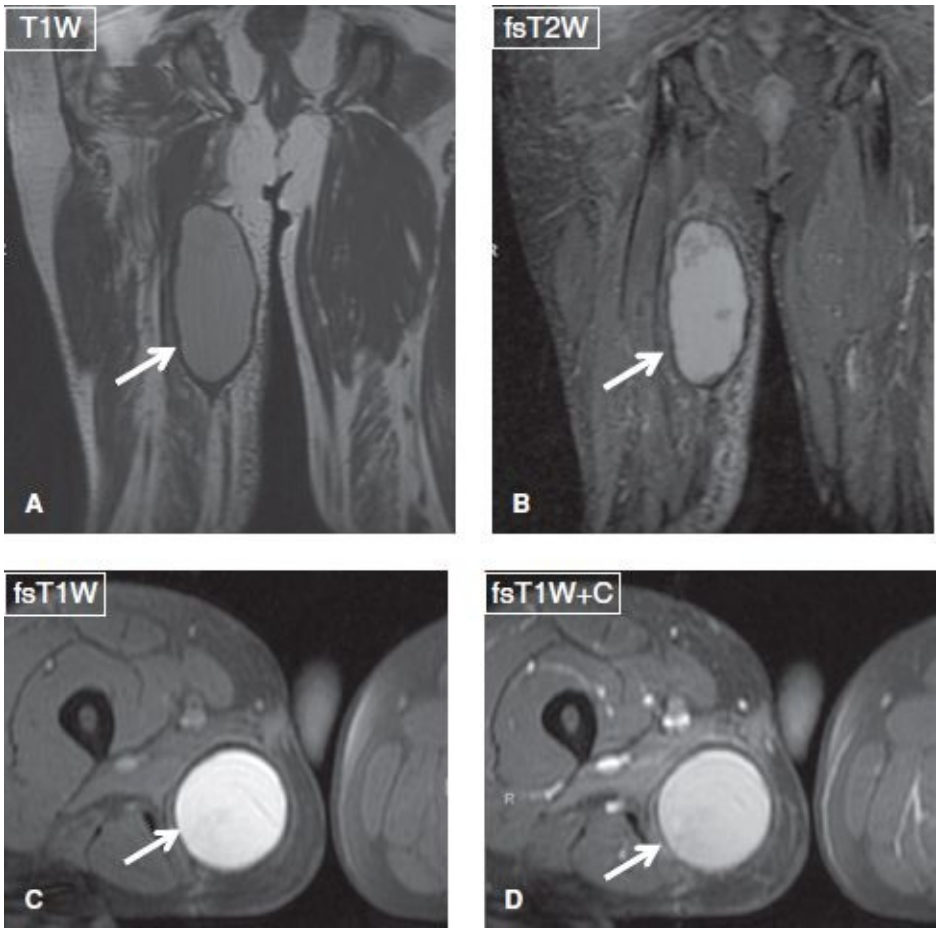

Fig. 82: Postoperative hematoma. Coronal **(A, B)** and axial **(C, D)** images display a well-defined lesion (*arrows*) in the medial aspect of the right thigh, which causes mild mass effect and features homogeneous internal hyperintensity, corresponding to methemoglobin, as well as a smooth, thin, and well-defined hypointense wall with hemosiderin lining, which lacks contrast enhancement.

BONES: [<Otherwise normal>]

Similar to any synovial joint, different types of arthritis can affect the hip joint. OA is the most common and demonstrates as joint space narrowing, which is more apparent in the superior, weight-bearing area. Other findings include femoral collar osteophytes, perifoveal osteophytes, and acetabular osteophytes; degeneration, multifocal tears, or detachment of the labrum; subchondral sclerosis, cystic changes, and marrow edema; and nonspecific joint effusion with or without synovial thickening (Figs. 83, 84). In advanced stages, the femoral head may protrude into the medial wall of the acetabulum due to osteopenia and bone weakening. Generally, mild OA refers to mild capsular or bony hypertrophy and mild joint space loss. Moderate OA refers to significant cartilage loss with subchondral bony changes of edema (ill-defined and mostly seen on fsPDW images), cyst (well-defined and conspicuous on both PDW and fsPDW images), and sclerosis (subchondral hypointensity on all sequences). Severe OA refers to marked bony proliferation, broad areas of cartilage loss or complete denuding and subchondral reactive changes as above. Large subchondral cysts aka geodes may mimic malignancy; however, presence of underlying OA or overlying

cartilage defect, lesion extension to the bony subchondral plate, elongated shape or angulated margination of the lesion, surrounding sclerosis, other satellite cysts or multiloculated appearance, and finally presence of internal fat or air are diagnostic clues of such a lesion (Figs. 85–87).

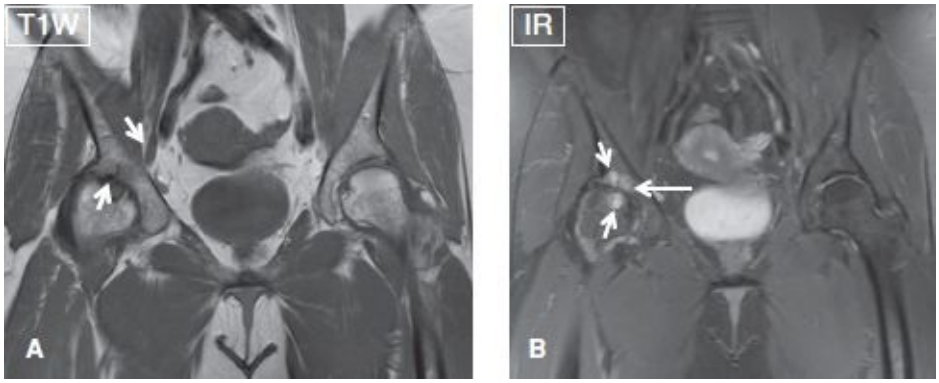

Fig. 83: Moderate-to-severe hip osteoarthritis. Coronal images **(A, B)** show right hip joint space loss and diffuse articular cartilage erosion, subchondral cysts at the acetabulum and femoral head (*short arrows*), as well as subchondral edema of the acetabulum (*long arrow*). Compare to the normal-appearing contralateral hip. Notice cysts are equally well seen on both images whereas edema is relatively ill defined and seen best on the fsPDW image.

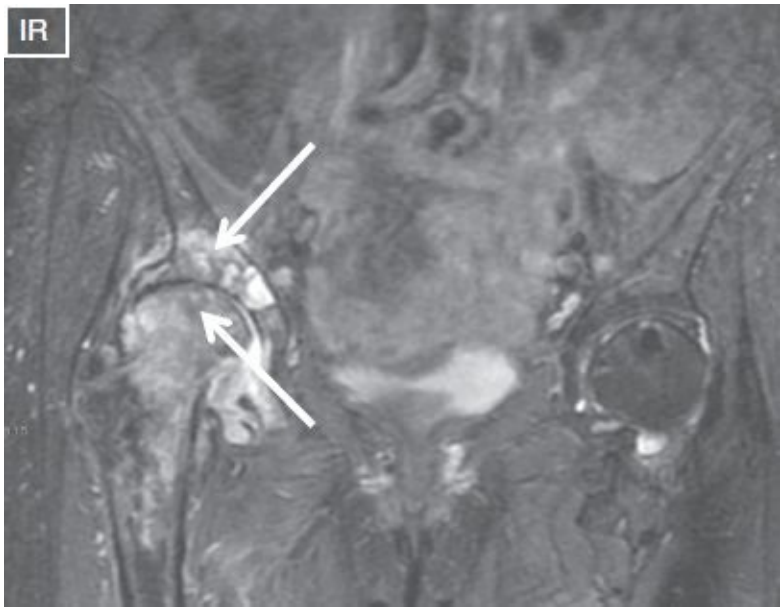

Fig. 84: Severe hip osteoarthritis. Coronal image shows extensive subchondral edema and cyst formation along with complete loss of joint space and articular cartilage (*arrows*) in the right hip, in keeping with severe osteoarthritis. In the left hip, there is also articular cartilage and joint space loss with minimal cyst formation, in keeping with moderate osteoarthritis.

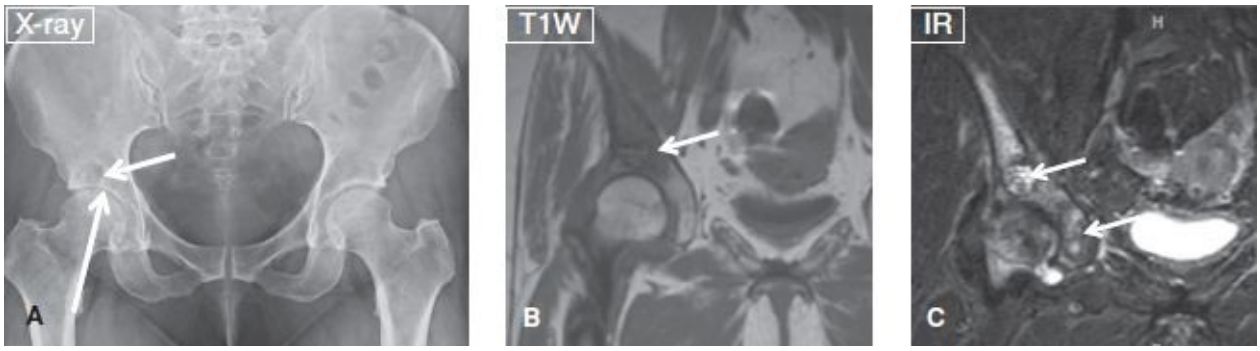

Fig. 85: Acetabular geodes. **A:** Anteroposterior radiograph demonstrates a well-defined subarticular lytic lesion with peripheral sclerosis and angulated margin (*short arrow*) in the right acetabulum. Note the associated joint space loss (*long arrow*) of the ipsilateral hip joint. **B, C:** On coronal images, the lesion shows fluid signal, multiloculated appearance, peripheral hypointense rim, and minimal internal fat. Note surrounding bone marrow edema and another similar lesion in the medial wall of the acetabulum (*arrows*), less well seen on the T1W image due to predominant edema and early cyst formation.

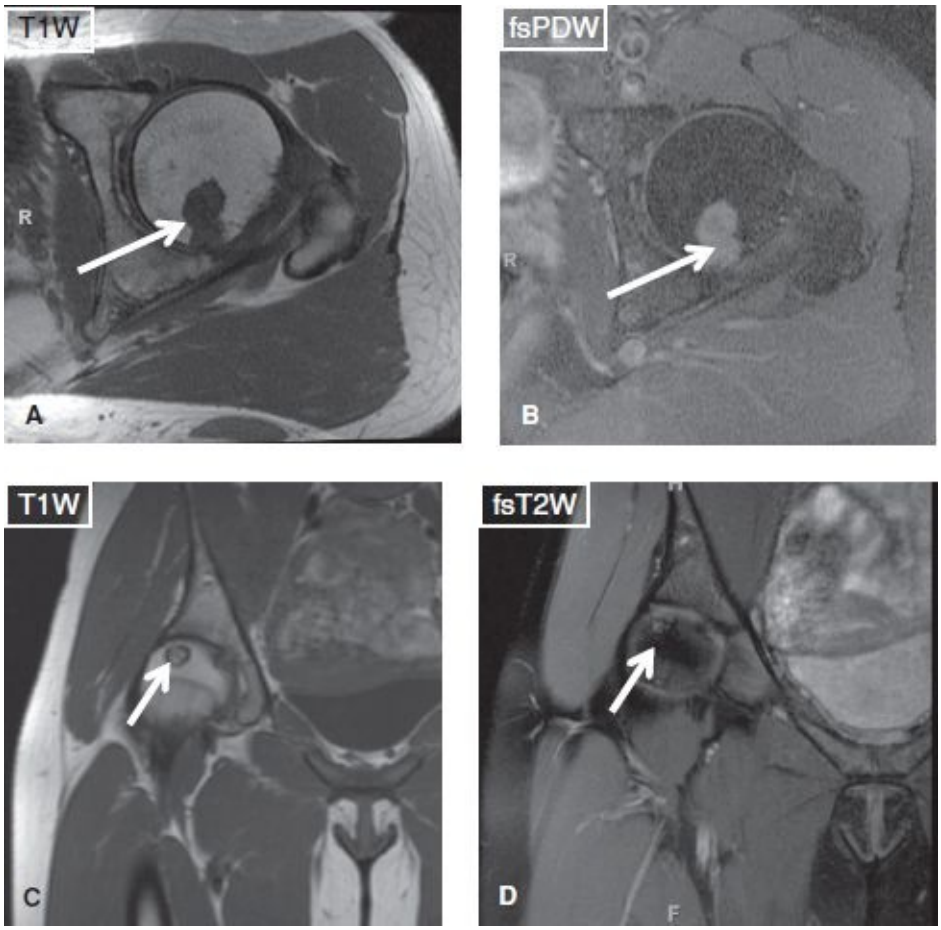

Fig. 86: Femoral head geode. Axial **(A, B)** and coronal **(C, D)** images exhibit a well-defined subarticular femoral head lesion (*arrows*) with fluid signal, internal fat, and elongated shape reaching the overlying cartilage defect.

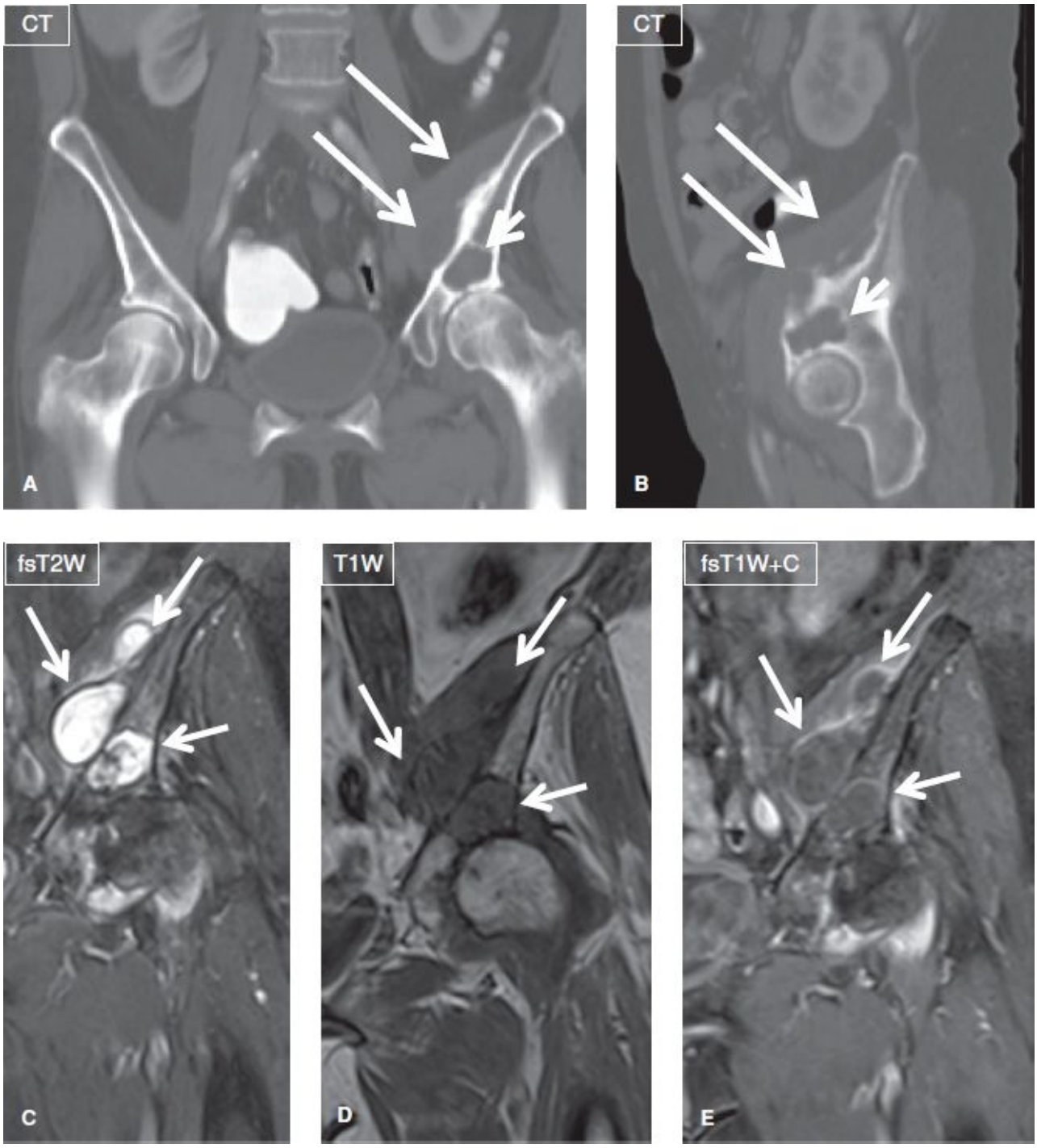

Fig. 87: Atypical acetabular geode. **A, B:** Coronal and sagittal reformation CT images depict an intraosseous subarticular lytic lesion with minimal peripheral sclerosis (*short arrows*) and two extraosseous hypodense lesions, along with periosteal reaction of the iliac bone, raising the suspicion of a malignant process. **C–E:** On the respective coronal MR images, all the lesions (*arrows*) proved cystic with peripheral enhancement, representing acetabular geodes with extraosseous extension. Notice the extension from the articular surface and minimal internal fat, helpful clues to determine the benignity of the lesion.

Synovial chondromatosis presents with multiple nodular cartilaginous or osteochondral deposits, which may become difficult to discern, once the disease becomes confluent and a "cast" of synovium is created. Femoral neck pressure erosions develop rapidly and may lead to bony or joint deformities and stress fractures. The lesions are numerous and are of the

similar size in primary chondromatosis (benign disorder of unknown origin) (Fig. 88); while of variable size and fewer in number in secondary chondromatosis (due to trauma, OA, osteonecrosis, or neuropathic arthropathy). Joint effusion is commonly associated.

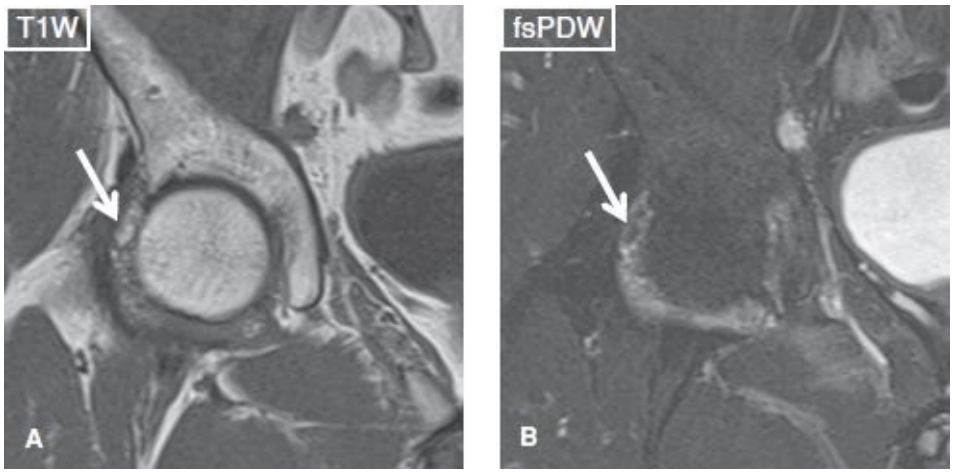

Fig. 88: Primary synovial chondromatosis. Coronal images **(A, B)** show numerous small bodies in the hip joint with small effusion. One might have to change the window width and level to detect these hypointensities, which can otherwise be missed and are hidden in the baggy joint distention due to effusion.

Pigmented villonodular synovitis may present as a focal nodular form, in which a soft tissue mass of intermediate-to-low signal intensity is detected within the joint capsule (Fig. 89), or as a diffuse form, which is characterized by genralized filling of the capsular recesses by intermediate to low signal intensity-laden synovial masses. Associated effusion, well-defined bony erosion(s), and superimposed cartilage loss may be present. The hemosiderin-laden synovial tissue is particularly conspicuous on gradient-echo images, which should be acquired in the event, the entity is suspected. Uncommonly, the lesions may show T1 hyperintensity as well. Other differential diagnoses of low signal intensity synovial lesions include synovial osteochondromatosis, amyloid, hemophilia, and hemorrhage from rheumatoid arthritis. Typically, PVNS is monoarticular and does not calcify. Focal form is amenable to cure by resection however, the diffuse form is difficult to treat and is prone to frequent recurrences. Mitotic inhibitors, such as imitinab may be tried in diffuse cases to stabilize the disease.

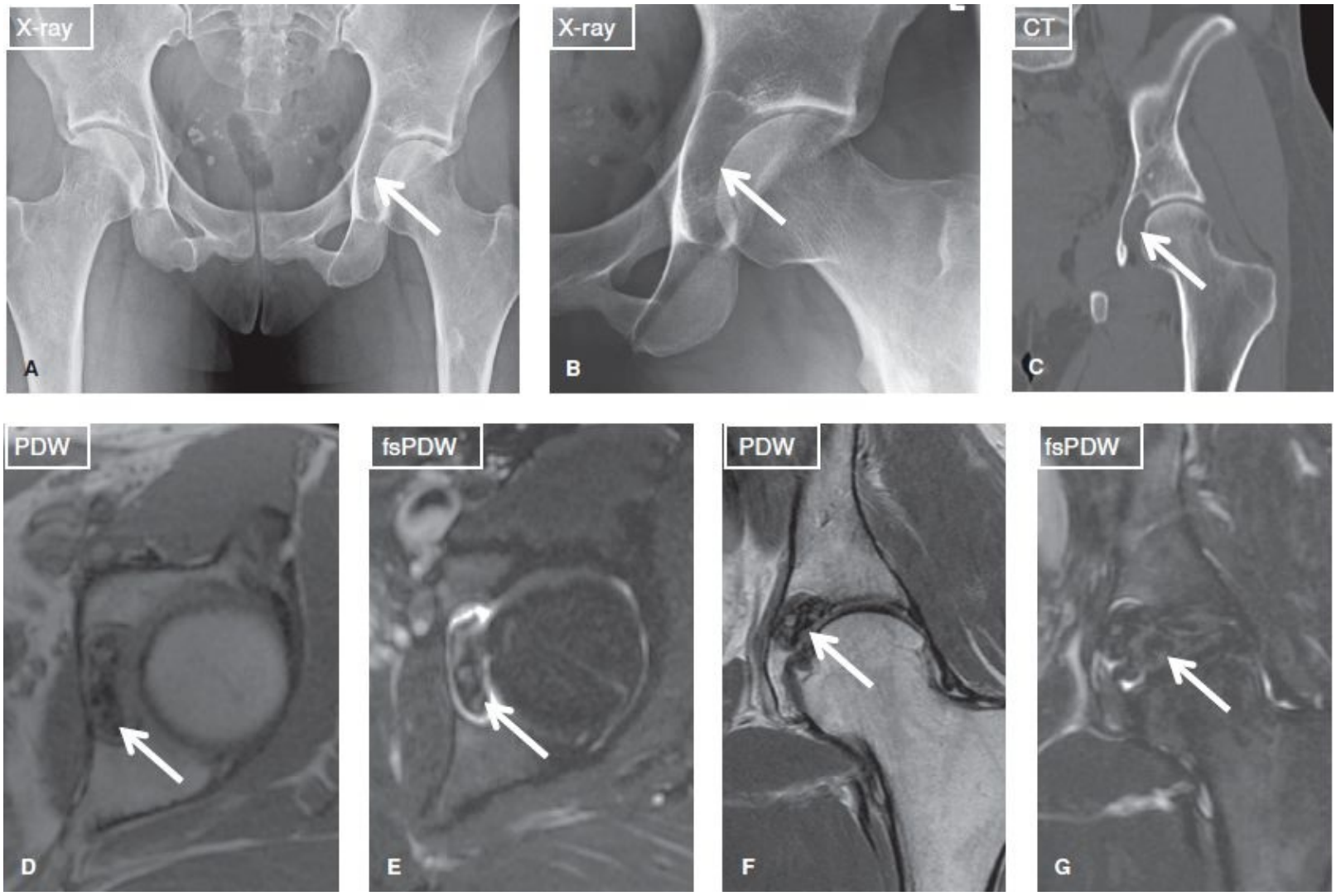

Fig. 89: PVNS, focal. Radiographs of pelvis **(A)** and left hip **(B)** and CT of the left hip **(C)** show well-circumscribed left acetabular erosion (*arrows*). Corresponding axial **(D, E)** and coronal **(F, G)** MR images show focal nodular hypointense mass (*arrows*), biopsy-proven focal PVNS.

Rheumatoid arthritis presents as bilateral, nearly symmetrical involvement, joint effusions and quiet remarkable or nodular synovial thickenings, appearing low and high signal on T1W and T2W images, respectively. In the active phase of the disease, the pannus (synovial mass) displays strong contrast enhancement whereas it becomes fibrotic with patchy enhancement in the chronic phase. Occasionally, there may be deposits of hemosiderin, which are hypointense on all sequences, or hypointense filling defects scattered diffusely within the joint effusion, the so-called rice bodies, which measure few millimeters in diameter and correspond to detachments of fibrotic nodules of the pannus from the synovial membrane. Due to diffuse cartilage loss, the femoral head may migrate superomedially or axially, in contrast to the superolateral migration found in OA. Additional findings may include erosions of the central portion of the femoral head and acetabulum, subchondral edema-like signal, and subchondral cysts (Fig. 90).

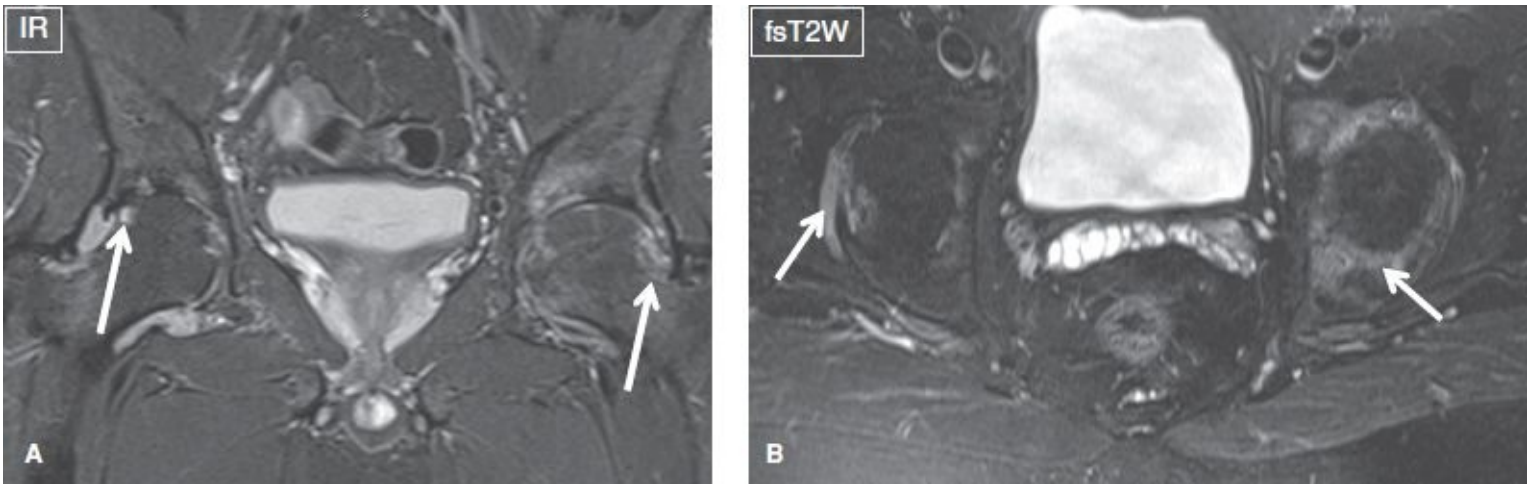

Fig. 90: Rheumatoid arthritis. Coronal **(A)** and axial **(B)** images show bilateral symmetrical diffuse joint space and cartilage loss, bony erosions (*arrows* in **A**) and synovial thickening (pannus; *arrows* in **B**) in this case of known advanced case of rheumatoid arthritis.

AVN of the femoral head is a common cause of musculoskeletal disability, which has been associated with conditions that result in interruption of the blood supply to the femoral head, such as femoral neck fracture and sickle cell anemia, as well as with other causes, such as corticosteroid therapy, alcohol abuse, connective tissue disorders, sickle cell disease, and marrow storage diseases, in which the pathogenesis is still unclear. MR imaging allows early detection of the disease, which is critical for the preservation of the femoral head integrity. In most cases of AVN, the necrotic area involves the anterosuperior aspect of the cephalad, weight bearing, (usually subchondral) portion (10-o'clock to 2-o'clock positions) of the femoral head, and usually has a biconcave, half-moon shaped or planoconcave geographic configuration (Figs. 91–94). One should note that bone marrow edema is not an early manifestation of AVN and the reader should not confuse the more commonly encountered stress reaction or subchondral insufficiency fracture-related edema for AVN. AVN on the other hand, almost always exhibits a nice demarcation zone and if edema is present around the lesion, it may indicate activity in the lesion. Other causes of bone marrow edema pattern include transient osteoporosis of the hip (diagnosis of exclusion and a rare disease), infection, or malignancy, such as leukemia or lymphoma. In the early stage of AVN, if intravenous contrast is used, areas of decreased enhancement may be seen. As the disease progresses, the involved area becomes sharply marginated from the healthy bone, and in about 80% of cases, it demonstrates an inner serpiginous border of high signal intensity and an outer parallel border of low signal intensity (double-line sign) on fsT2W or fsPDW images (Fig. 91, 92). The central signal of the involved area is variable (Fig. 95), may change throughout the disease, and has been shown to correlate with clinical symptoms by some authors (Table 2) (class A = less severe, class D = most severe). In our experience, central fatty area is usually asymptomatic and represents chronic stage of AVN while variable symptoms may be present in other stages. In later stages, one might see a subchondral line of fluid-like T2 hyperintensity corresponding to crescent sign of radiographs. Such finding indicates impending collapse of chondral surface of the bone and

the fragment might become loose body in the joint (Fig. 96). In advanced stages, there is osteochondral fragmentation of the femoral head, along with secondary degenerative joint changes (Figs. 97, 98). Joint effusion or synovitis may also be present in any stage of the disease, and its amount correlates with pain symptoms. MR imaging remains positive throughout the course of the disease, or until the lesion is healed. The modified Ficat and Arlet classification may be used to define the stage of the disease based on MR imaging findings (Table 3). The radiologist should report the location and extent of the necrotic area, usually defined as percentage of the total femoral head articular surface, and any associated subchondral collapse. In terms of prognosis, small lesions (less than one-third of articular surface) and limited to the medial anterosuperior portion of the femoral head, as well as lesions that do not contact the articular surface tend not to collapse and, thus, are amenable to conservative therapy. AVN that does not contact the subchondral margin tends to have a better prognosis regardless of the lesion size. Lesions that involve more than two-thirds of the weight-bearing articular surface area of the femoral head have a high propensity to collapse. Generally, stage II and before are treated with core decompression with curative intent while stage III and beyond require palliative measures, such as hemiathroplasty, resurfacing or total hip replacement. Joint effusion, synovitis, fascial, and bone marrow edema usually correlate with activity and symptoms of pain and/or limited range of motion. Due to the frequent bilateral occurrence of AVN, contralateral hip should also be evaluated. In children (4 to 9 years), one may see AVN related to Legg–Calvé–Perthes disease (idiopathic) and in adolescent children (9 to 15 years), one may see AVN as a complication of SCFE (Fig. 99). Perthes disease is more common in boys and is more commonly bilateral in girls (Fig. 100). It is considered to be multifactorial disease similar to developmental dysplasia of hip (DDH), and represents a diagnosis of exclusion. Other causes of AVN, such as sickle cell disease, steroids, etc. need to be excluded before one makes the diagnosis of Perthes disease. The disease progresses from patchy femoral epiphysis sclerosis and/or lucencies (stage I) to partial collapse (stage II, coxa plana), to bone reconstitution and remodeling (stage III), and to finally, recontouring (stage IV). Healed Perthes disease may result in normal contouring of the femoral head or in some cases, heals with a classic appearance of mushrooming of the femoral head (coxa magna) with foreshortening and varus deformity of the neck (coxa vara) (Figs. 101, 102). The resultant abnormality may predispose to femoral neck stress fracture (Fig. 103). Apart from older age and female gender being the poor prognostic factors, the height of lateral pillar on AP radiographs (lateral one-third of epiphysis) is most frequently believed to determine the prognosis. The respective staging includes, stage A (no height loss of lateral pillar), stage B (less than 50% height loss), stage B/C (about 50% height loss), and stage D (>50% height loss). However, this staging system can only be used in stage II or beyond, as described above. Recently, MRI perfusion has been shown to be useful in the early diagnosis and possible prognostication of this disease. Preserved perfusion in the lateral pillar is probably a good prognostic indicator. Finally, in the setting of systemic causes, one might see areas of osteonecrosis in other pelvic bones and similar appearance of demarcation

zone with or without associated bone marrow edema around the lesions (Fig. 104).

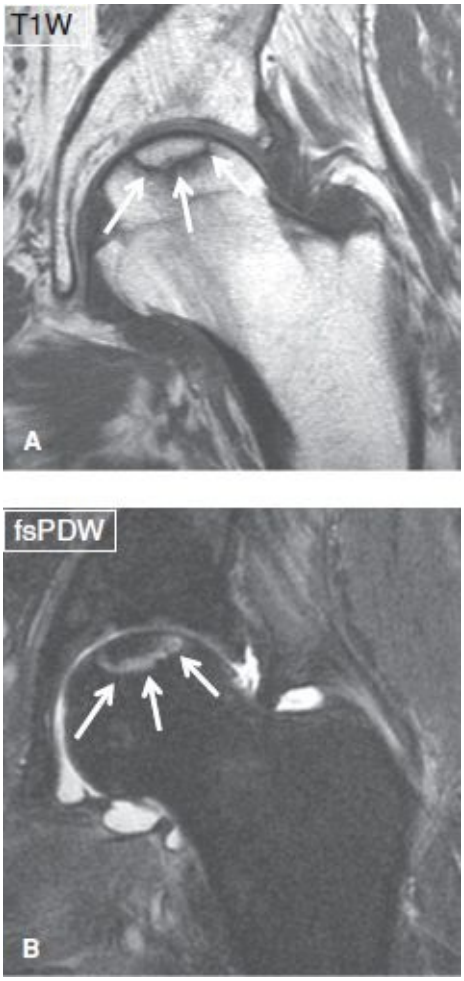

Fig. 91: Avascular necrosis. Coronal images **(A, B)** show a classic half-moon–shaped fat-containing lesion with a double-ring sign in the femoral head in keeping with avascular necrosis (*arrows*). Notice moderate effusion.

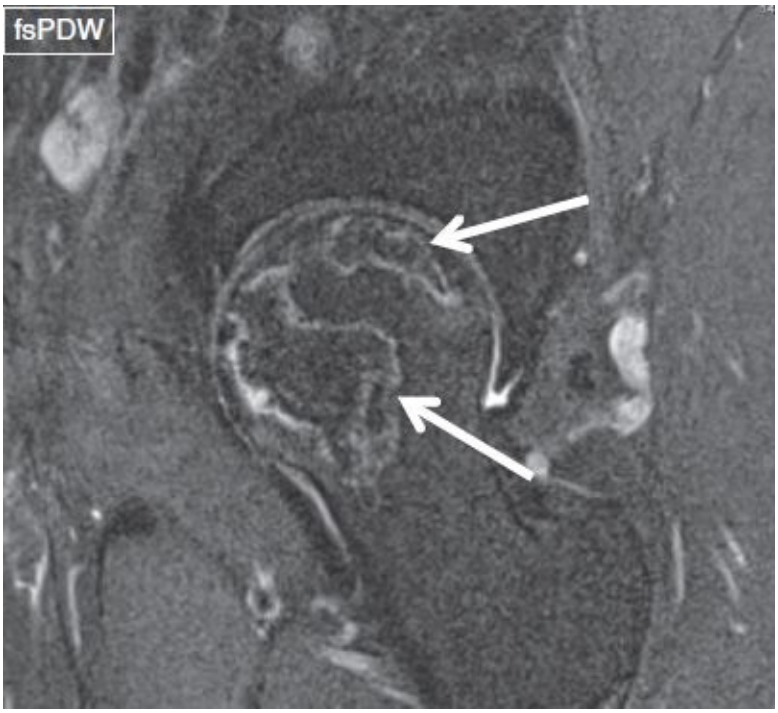

Fig. 92: Chronic infarct of the femoral head. Sagittal image demonstrates two well-

demarcated regions (*arrows*) of double ring sign, geographic borders and internal fat signal intensity, without evidence of marrow edema, synovitis, or effusion. Findings are compatible with chronic avascular necrosis.

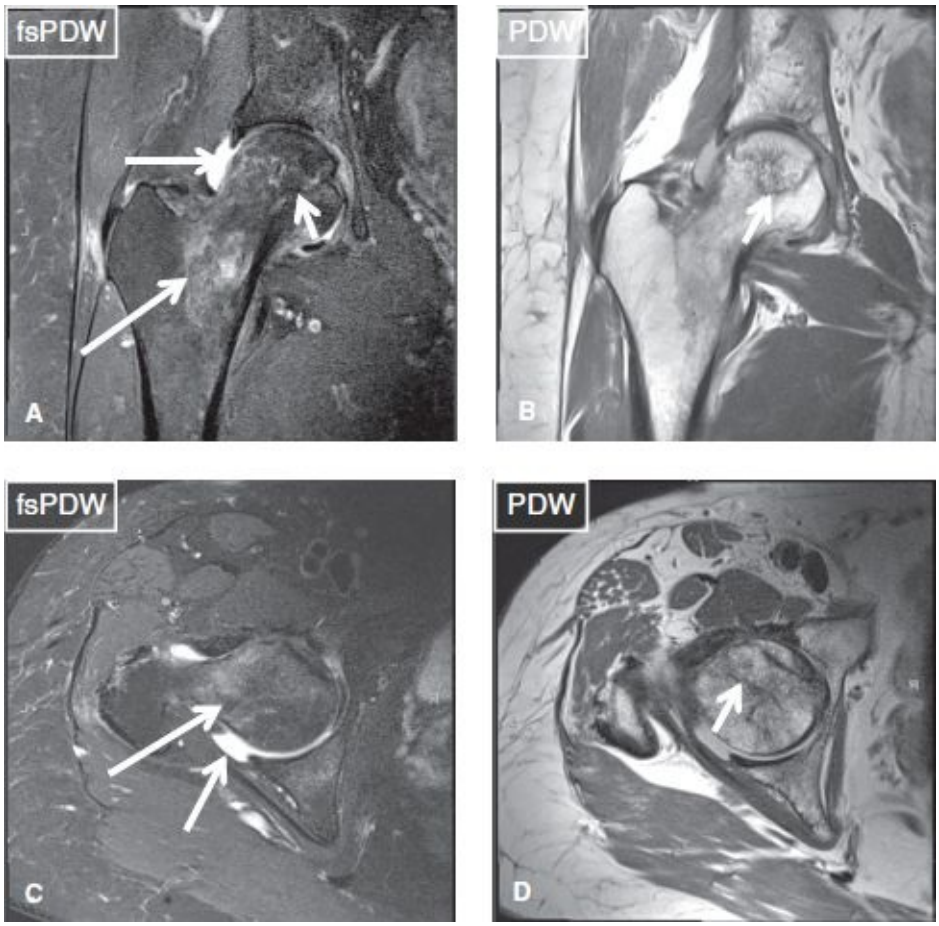

Fig. 93: Active avascular hip necrosis. Coronal **(A, B)** and axial **(C, D)** images demonstrate mild edema of the femoral head and neck (*long arrows* in **A, C**) associated with a well-demarcated region (*short arrows* in **A, B, D**) showing geographic margins and internal fat-like signal at the superior aspect of the femoral head. Also note small joint effusion (*medium arrows in* **A, C**).

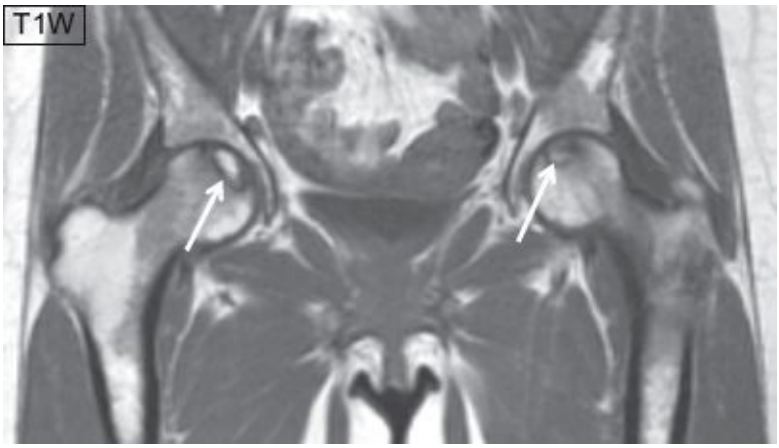

Fig. 94: Bilateral avascular necrosis in a patient with underlying HIV infection. The lesions (*arrows*) again contain internal fat in keeping with chronicity.

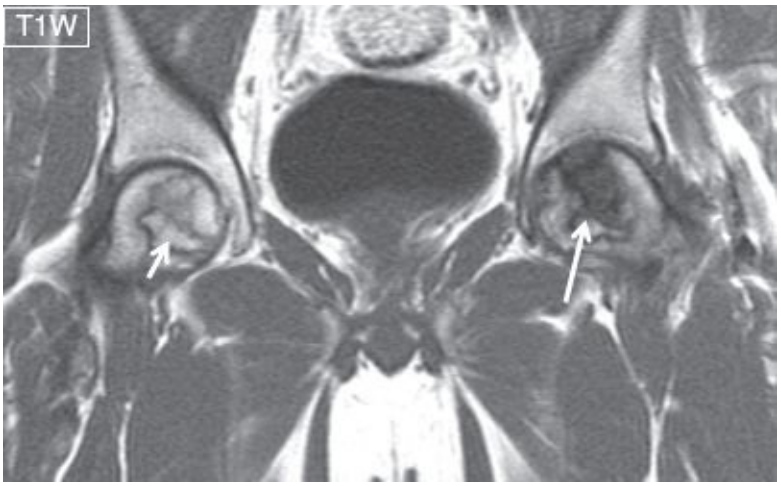

Fig. 95: Bilateral avascular necrosis with early subchondral collapse on left. Notice predominant fat in the right femoral lesion (*small arrow*) and mixed fat and fibrosis in the left femoral lesion (*long arrow*) with early subchondral collapse.

Fig. 96: MR crescent sign. Coronal images from two different subjects with stage III avascular necrosis show subchondral hyperintense crescent sign (*arrows*) with articular surface collapse. Notice reactive bone marrow edema, minimal medial fascial edema, and moderate to large joint effusion in both cases indicating activity.

Fig. 97: Chronic avascular necrosis with moderate degenerative changes. Coronal images **(A, B)** exhibit bilateral well-demarcated regions (*arrows*) of geographic borders and fat and fibrous signal intensity, without evidence of marrow edema. Notice subchondral collapse on the left with moderate osteoarthritis. Small cartilage defect is also present on the right with

bilateral osteophyte formation.

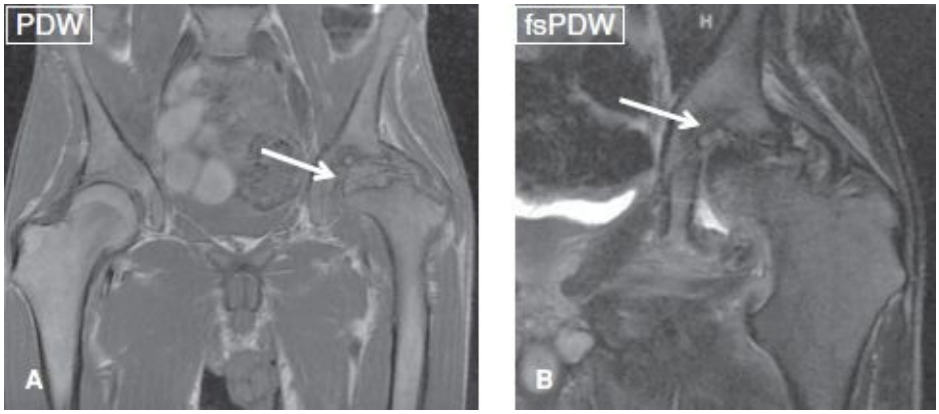

Fig. 98: Chronic avascular necrosis with advanced degenerative changes. Coronal images **(A, B)** exhibit sequel of long-standing avascular necrosis of left femur with subchondral collapse and advanced osteoarthritis (*arrows*).

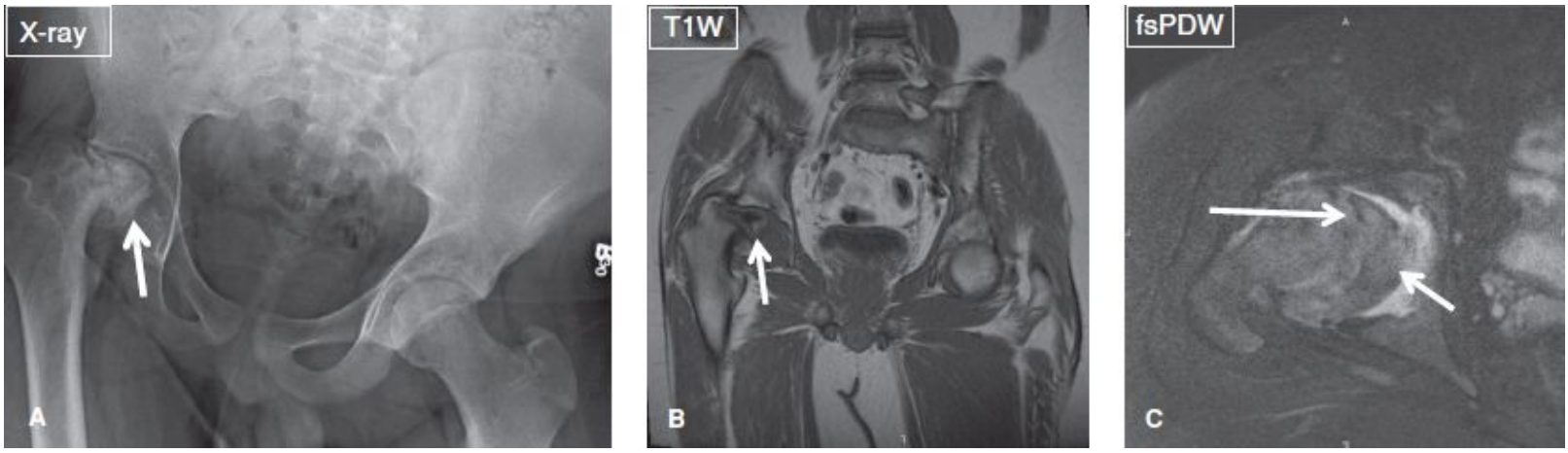

Fig. 99: Avascular necrosis in the setting of chronic slipped capital femoral epiphysis. Anteroposterior radiograph **(A)** demonstrates marked deformity, posteromedial displacement and sclerosis of the partially collapsed right femoral epiphysis (*arrow*). The corresponding coronal **(B)** and axial **(C)** MR images show diffuse marrow edema of the femoral head and neck (*short arrows*) with widening of the physeal plate (*long arrow*) and small effusion.

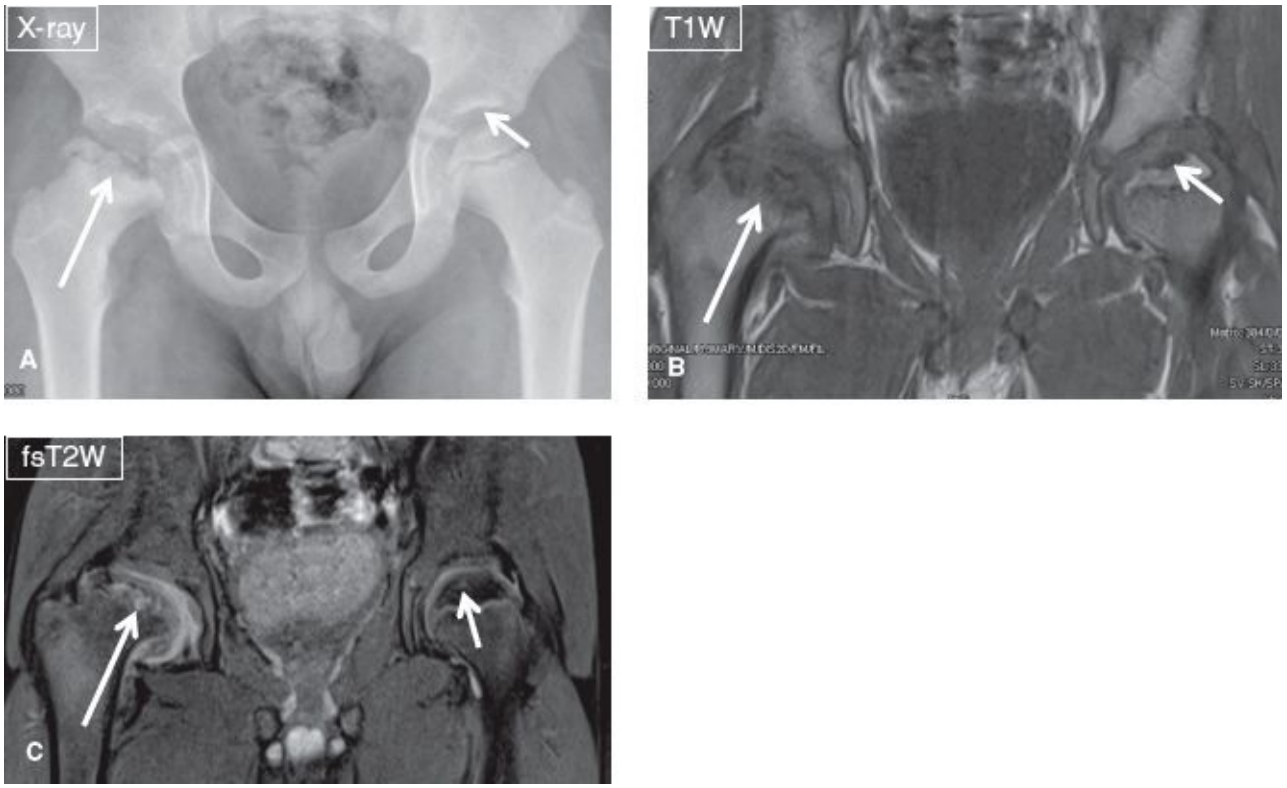

Fig. 100: Perthes disease. AP radiograph of pelvis **(A)** and corresponding coronal MR images **(B, C)** in a 8-year-old girl show collapsed right femoral epiphysis with cystic changes and edema (*long arrows*) and minimal such changes on the left (*small arrows*).

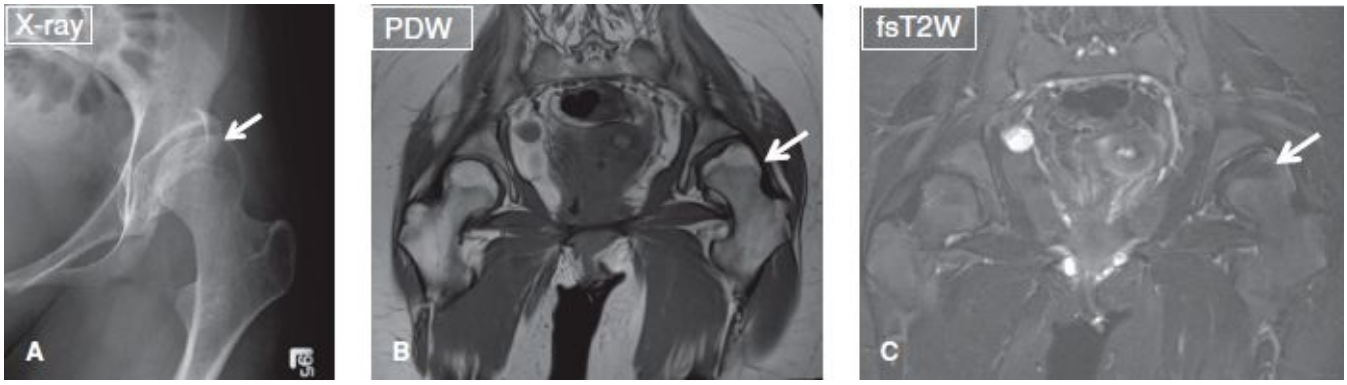

Fig. 101: Old-healed Perthes disease. AP radiograph of left hip **(A)** and corresponding coronal MR images **(B, C)** of the pelvis in a 13-year-old girl show small left femoral epiphysis with mushroom appearance due to foreshortening of the femoral neck (*arrows*). Also note associated DDH.

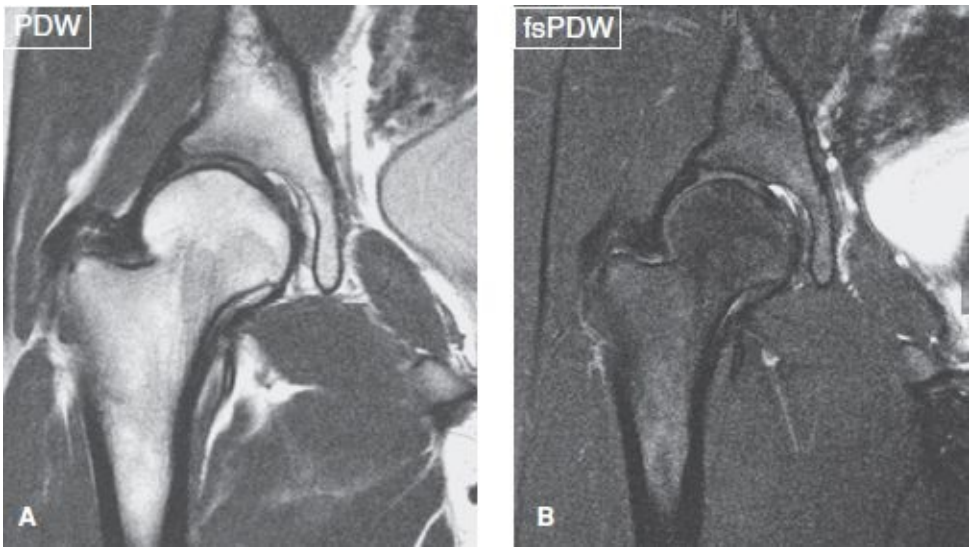

Fig. 102: Old-healed Perthes disease. Coronal MR images **(A, B)** of the pelvis in a young man show mushroom-like appearance of femoral head (coxa magna) with foreshortening of the femoral neck (*arrows*).

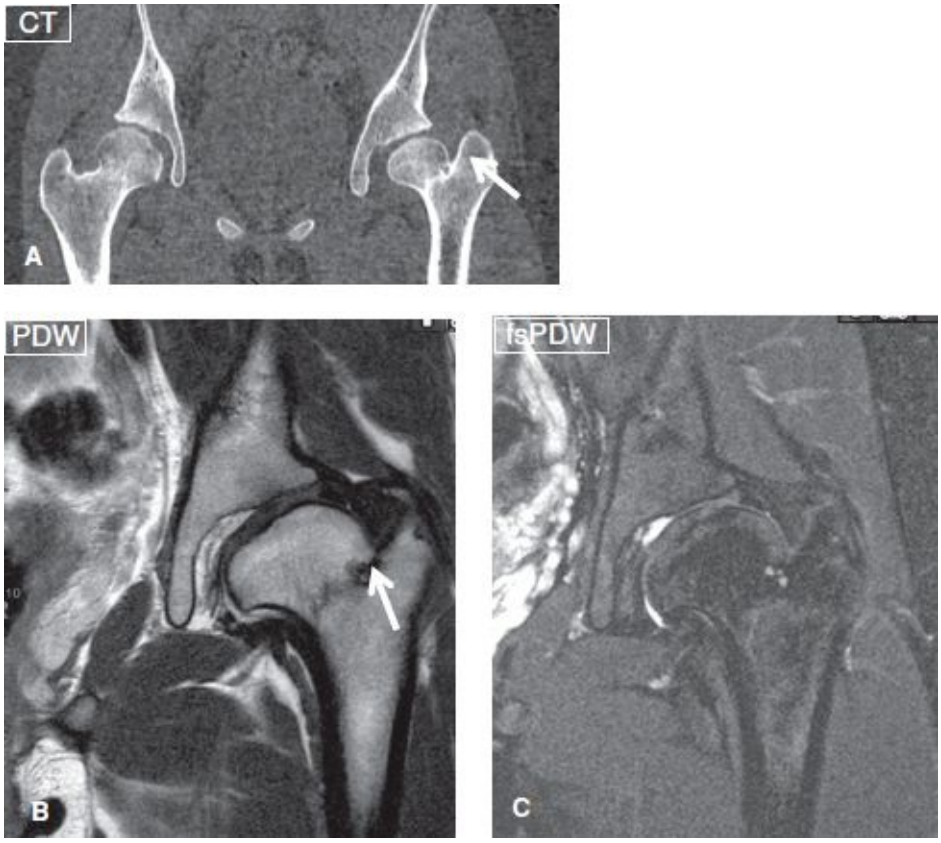

Fig. 103: Old-healed Perthes disease. Coronal CT **(A)** and MR images **(B, C)** of the pelvis in a young man exhibit mushroom-like appearance of femoral heads (coxa magna) with bilateral foreshortening of the femoral necks. Also note bilateral subacute femoral neck stress fractures on CT. The left femoral neck also depicts minimal cyst formation (*arrows*) at the pseudoarthrosis.

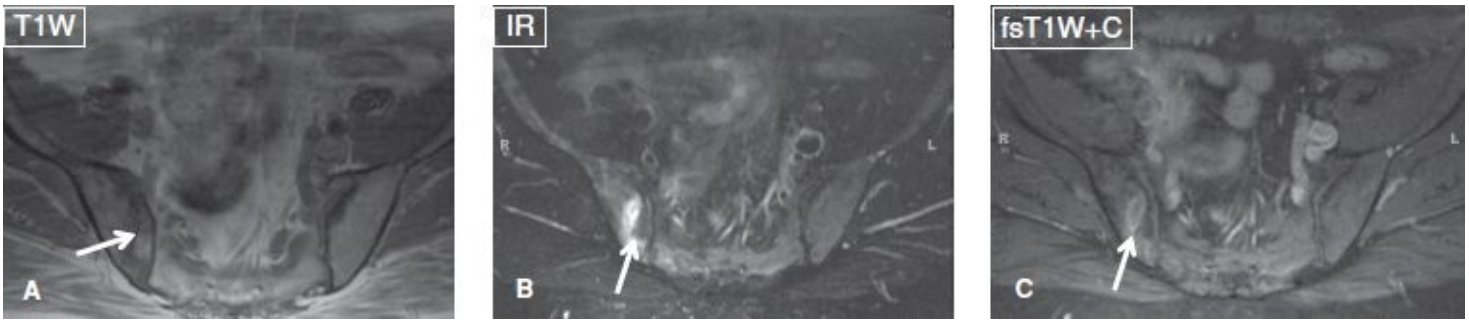

Fig. 104: Idiopathic avascular necrosis of the iliac bone. Axial images **(A–C)** show a well-defined subarticular lesion (*arrows*) in the right iliac bone, which demonstrates thick peripheral enhancement. The biopsies performed from the lesion showed osteonecrosis.

TABLE 2: The Mitchell classification of the signal characteristics of the necrotic bone

Class	T1W Signal	T2W Signal	Simulating
A	Intermediate	High	Fat
B	High	High	Blood
C	Low	High	Fluid
D	Low	Low	Fibrous tissue

TABLE 3: The modified Ficat and Arlet classification for the definition of the clinical stage of AVN of the femoral head based on MR imaging findings

Stage	MR Imaging Findings
0	Demarcation zone and/or double-line sign on T2W and fsPDW images (Radiographs negative)
1	Double-line sign on T2W and fsPDW images and single line on T1W images
2	Demarcated lesion with marrow edema extending from the nonischemic region of the femoral head into the femoral neck
3	Crescent sign or collapse of the femoral head with preservation of the joint space
4	Further collapse of the femoral head with articular cartilage loss and joint space narrowing

Pitfalls to be avoided when evaluating for AVN include the following.

- The fovea capitis, which is located in the medial aspect of the femoral head and is attachment site of the ligamentum teres.
- Subchondral cysts, which are seen in the setting of degenerative joint disease, are circular

in shape, demonstrate smooth and regular margins, rather than serpiginous, and may show internal fibrofatty tissue.

- Foci of red marrow reconversion, which are typically bilateral and demonstrates higher signal than muscle on T1W or PDW images, compared to AVN.
- Synovial herniation pits or fibrocystic changes of FAI, which are around 5 mm in size (may range between 5 and 15 mm), oval or round in shape, located at the anterosuperior aspect of the femoral head and neck junction, and are associated with underlying FAI anatomy.

Transient osteoporosis of the hip (aka bone marrow edema syndrome) is a rare disorder of unknown etiology and is a diagnosis of exclusion among the above-described entities of bone marrow edema pattern. It is characterized by acute onset of disabling bone pain, which resolves spontaneously over the course of few months, and is seen as reversible diffuse bone marrow edema involving the femoral head and neck on MR imaging. It is more common in adult men and the entity may involve one or both femora and could migrate to other bones. This entity can be differentiated from AVN based on more pronounced and diffuse edema pattern, absence of a lesion with demarcation zone and double ring sign, as well as lack of risk factors for AVN. Uncommonly, the latter entity may involve other bone locations around the hip. One should, however, note that most of the cases with such diffuse edema like appearance actually represent subchondral insufficiency fractures with reactive bone marrow edematous changes. The subchondral insufficiency injury is related to excessive stress on a weak bone and the reader should look for underlying focal subchondral hypointensity of fracture in the diffuse cloud of bone marrow edema. Based on imaging findings, stress or insufficiency injuries can be classified into four grades, which correspondingly reflect increasing severity of insult (Figs. 105–108).

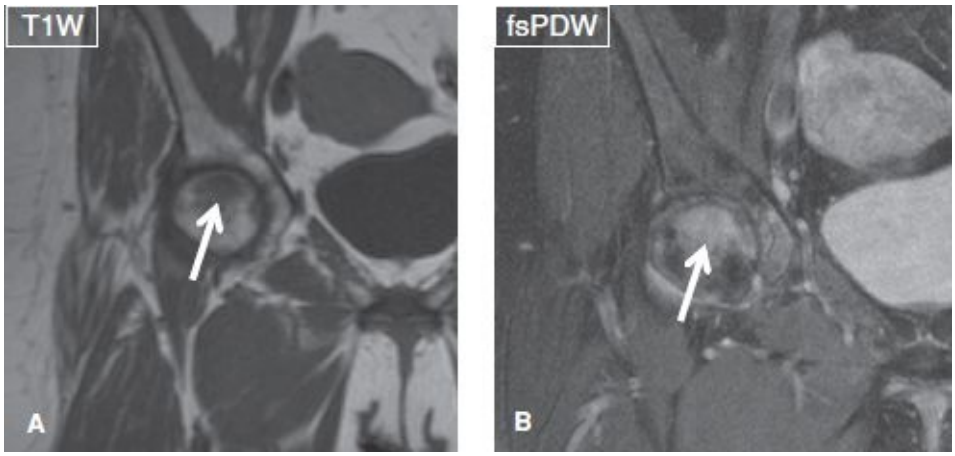

Fig. 105: Subchondral stress injury. Coronal images **(A, B)** display a subchondral region of marrow edema (*arrows*) at the superior aspect of the femoral head in keeping with grade III stress injury.

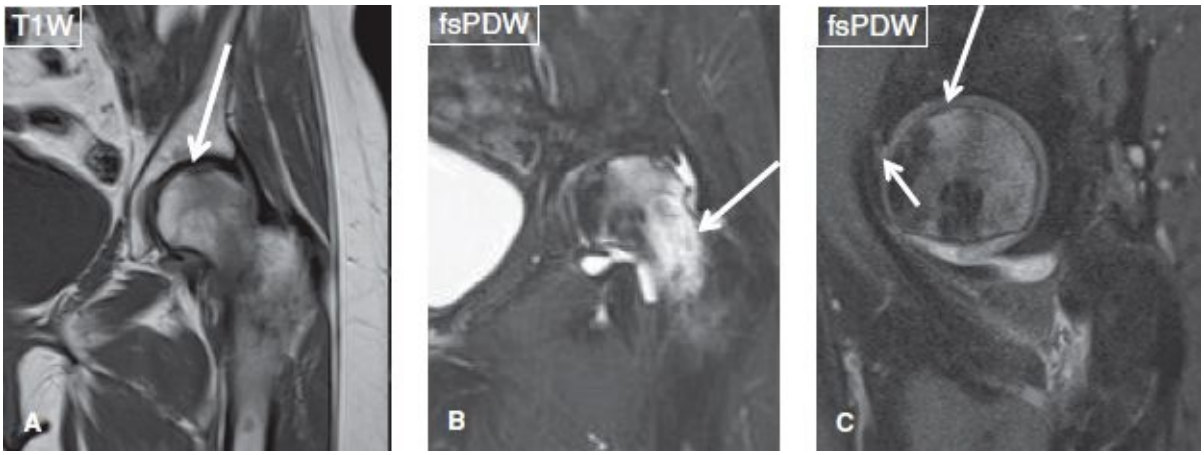

Fig. 106: Subchondral insufficiency fracture of femoral head. **A:** Coronal image shows subchondral fracture (*arrow*) of the right femoral head. **B:** Coronal image shows extensive stress-related reaction bone marrow edema (*arrow*). **C:** Sagittal image shows subchondral fracture (*long arrow*) and anterosuperior labral tear (*small arrow*). Also note moderate hip joint effusion.

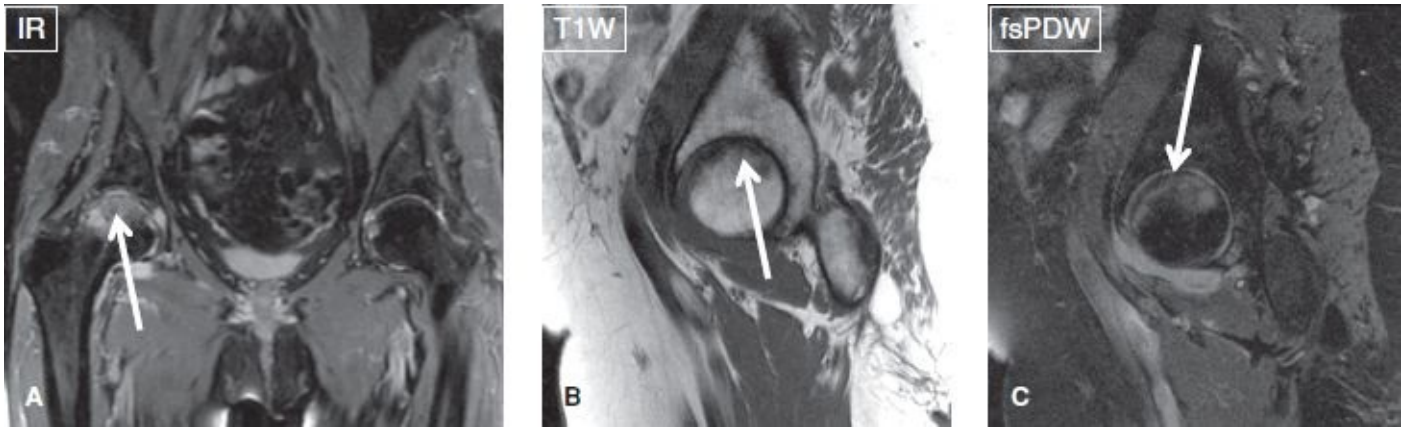

Fig. 107: Subchondral insufficiency fractures of femoral head. Coronal **(A)** and sagittal **(B, C)** images exhibit multiple small subchondral insufficiency fracture lines (*arrows*) paralleling the subarticular surface of the femoral head with associated bone marrow edema. Notice superolateral labral tear on coronal image **(A).**

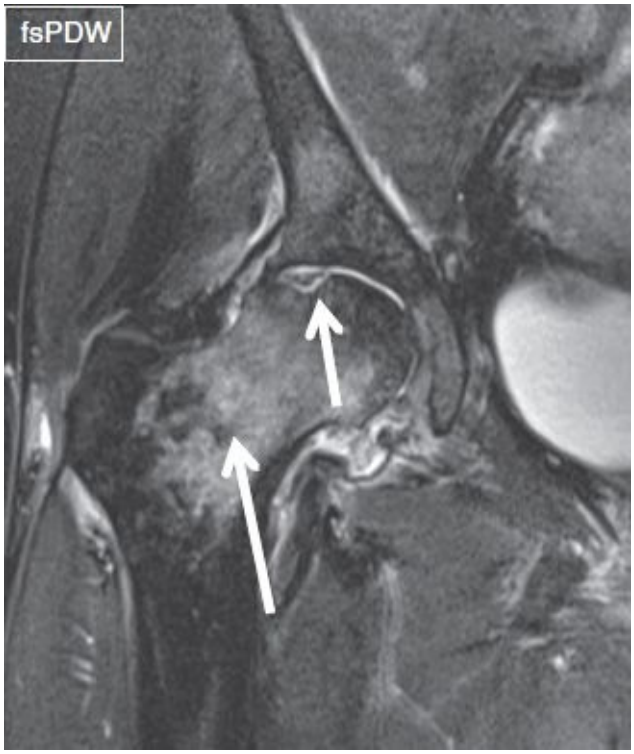

Fig. 108: Subchondral insufficiency fracture with unstable fragment: Coronal image shows marrow edema (*long arrow*) of the femoral head and neck, along with an osseous fragment (*short arrow*) of the superior femoral head surrounded by fluid cleft, in keeping with an unstable in situ osteochondral body.

- *Grade I* injury—subtle subchondral or sub-periosteal edema, vaguely detectable on fluid-sensitive fs sequences
- *Grade II* injury—characterized by larger and more focal marrow edema on fluid-sensitive fat-saturated images and with possible subtle changes on T1W/PDW images
- *Grade III* injury (intertrabecular fracture)—characterized by more prominent marrow edema, evident on all images
- *Grade IV* injury—a discrete fracture line is evident on T1W/PDW images, which is usually linear, immediately subarticular and perpendicular to the orientation of the major trabeculae, with or without subchondral collapse.

These fractures are commonly associated with anterosuperior and superolateral labral tears as well as hip cartilage loss. Apart from the latter location, stress fractures may occur at the medial or concave side (typically fatigue fractures/insufficiency fractures in osteomalacia, Fig. 109) and at the lateral or convex side (typically insufficiency fractures, banana fractures in Paget disease) of the femoral neck. Apart from identifying the fracture, the radiologist should provide an estimation of the extent of the fracture line across the width of the bone (incomplete or complete), as the latter affects treatment. Complete fracture on the concave side and incomplete fracture on the convex side of the femoral neck require surgical fixation. Other locations for insufficiency and stress fractures include the sacrum, acetabulum, pubic bone, and the ischiopubic ramus (Figs. 110–114).

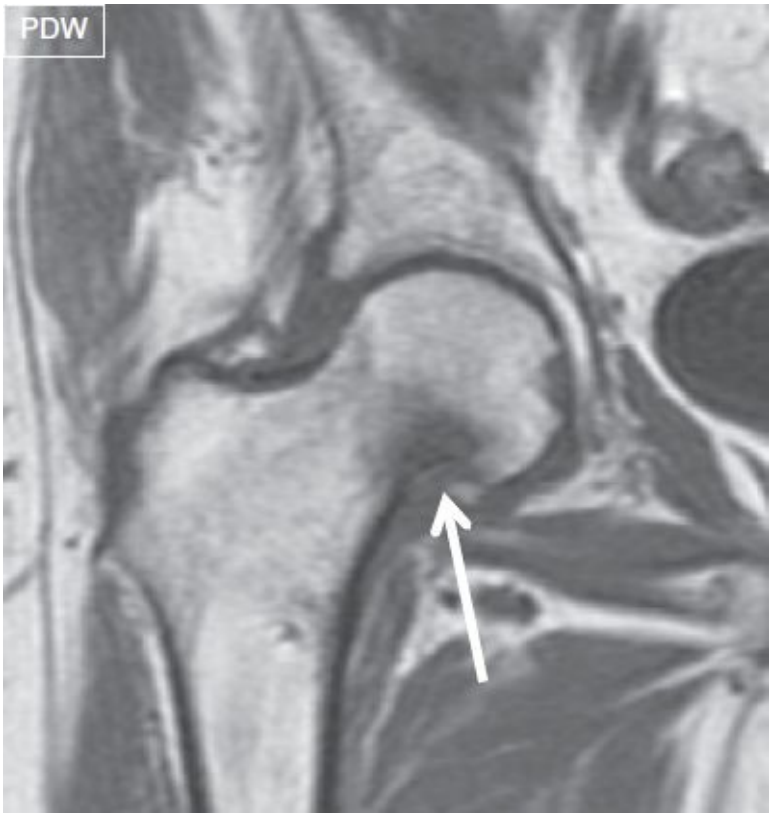

Fig. 109: Stress fracture of femoral neck in osteopenia. Coronal image shows focal marrow edema (*arrow*) of the femoral neck.

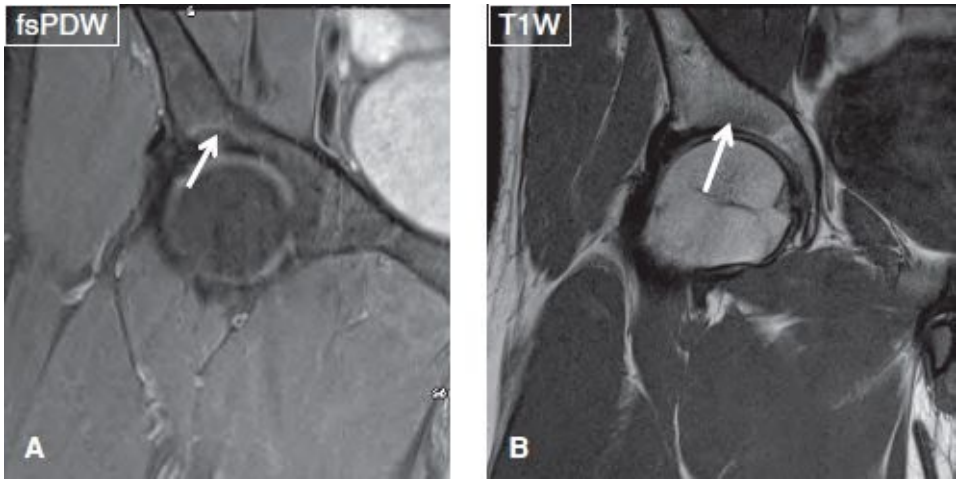

Fig. 110: Subacute acetabular fracture. Coronal images **(A, B)** demonstrate a fracture line (*arrows*) paralleling the acetabular roof, with lack of marrow edema.

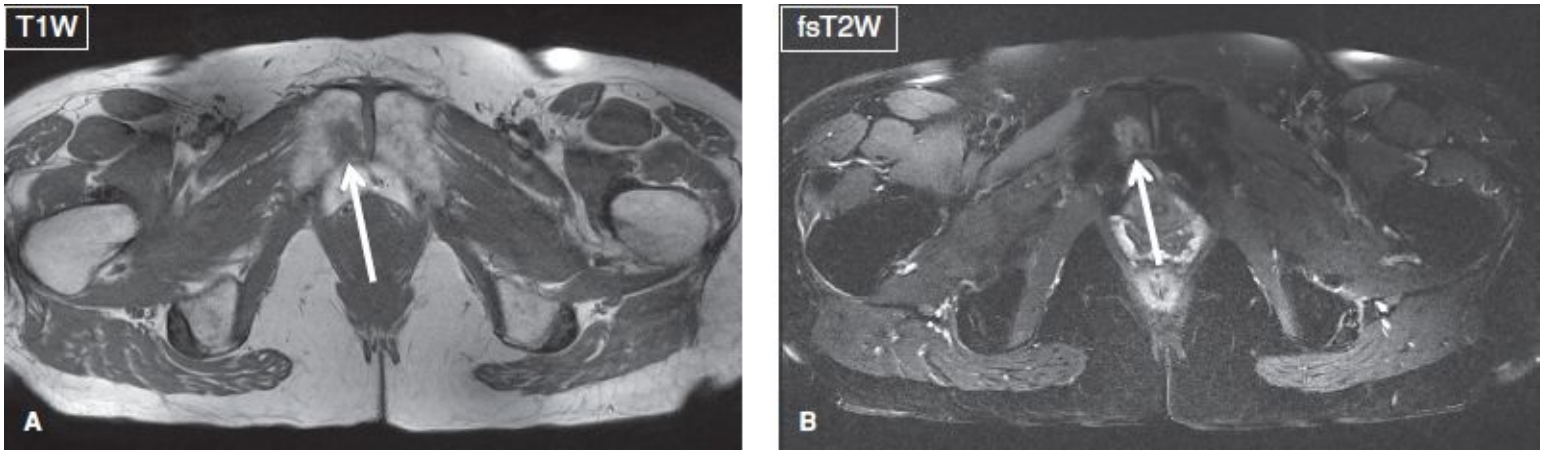

Fig. 111: Pubic bone insufficiency injury. Axial images **(A, B)** exhibit bone marrow edema due to insufficiency injury (*arrows*) of the right pubic bone.

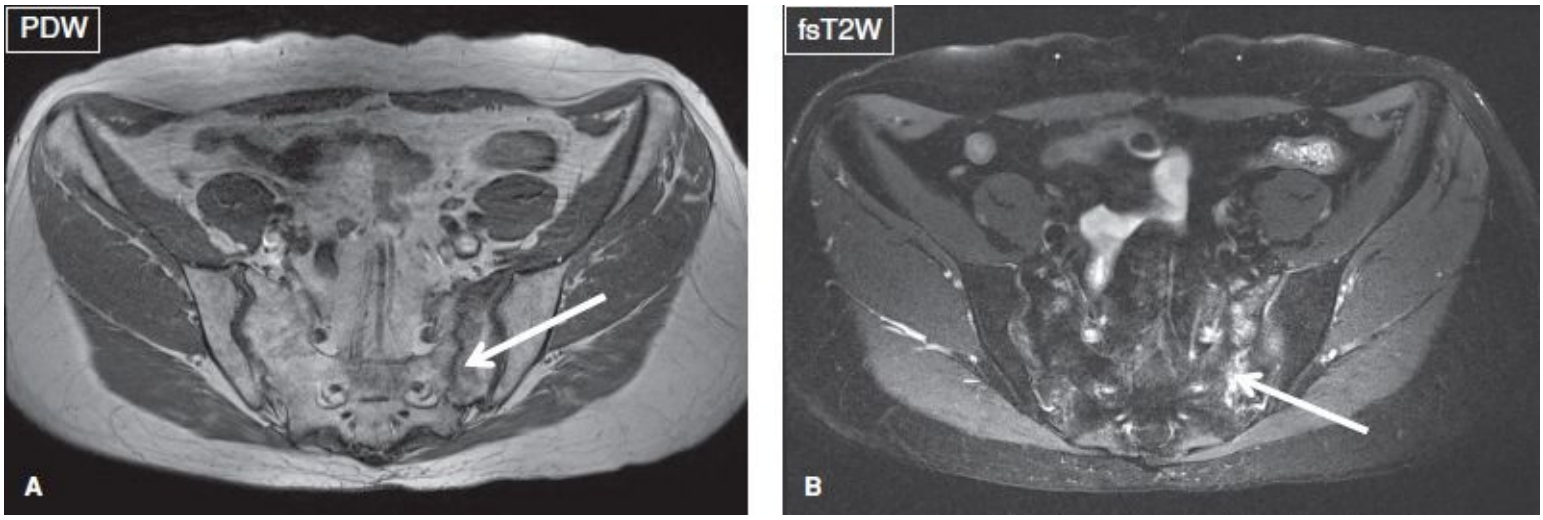

Fig. 112: Sacral insufficiency fracture. Axial images **(A, B)** show bone marrow edema around a fracture line (*arrows*) through the left sacral ala. Minimal injury is also seen in the right sacrum and the left ilium.

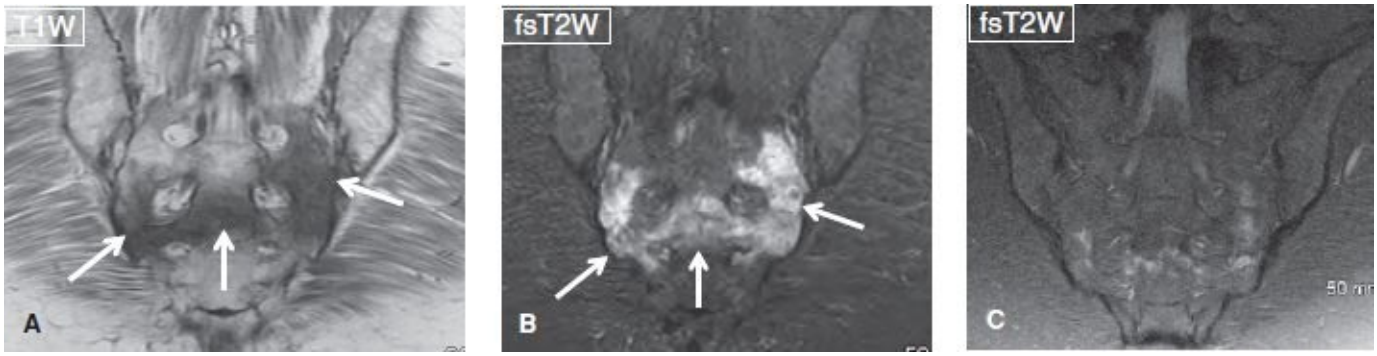

Fig. 113: Sacral insufficiency fracture. Coronal images **(A, B)** show extensive bone marrow edema in keeping with insufficiency injury to the sacrum (Honda sign; *arrows*). **C:** Follow-up scan after 6 weeks shows near-complete resolution of the bone marrow edema.

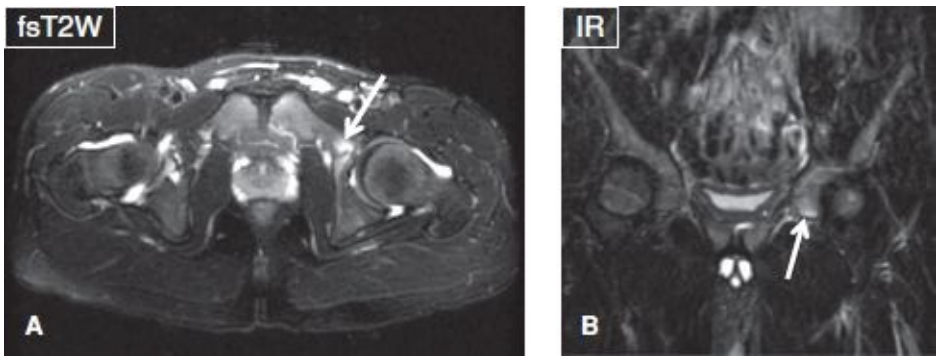

Fig. 114: Ischiopubic ramus stress fracture. Axial **(A)** and coronal **(B)** images exhibit a focus of marrow edema (*arrows*) at the ischiopubic ramus synchondrosis.

Other causes of developmental femoral abnormalities include SCFE, epiphyseal, and

metaphyseal dysplasias. SCFE is a relatively common condition, which affects the proximal femoral physis in skeletally immature individuals. It is essentially a type I Salter–Harris injury, typically seen in adolescent age. Predispositions include obesity, hormonal imbalance, and rapid growth spurt. If it happens as part of birth injury cases, there remains a possibility that the femoral head ossification center would not underdo mineralization, ultimately leading to a dysplastic hip. The entity initially presents with diffuse or globular widening with irregularity and/or ill definition of the physis. This is then followed by acute slip of the epiphysis in a posteromedial direction. Left untreated, the epiphysis becomes sclerotic and osteonecrotic. Many cases will develop into cam-type FAI morphology, eventually leading to premature secondary OA. MR imaging should include the contralateral hip since the entity is frequently bilateral (Fig. 115). MR imaging is useful in detecting subtle cases of physeal injury, detection of contralateral abnormality, response to treatment and complications, such as AVN and osteoarthriitis (Fig. 99). Epiphyseal dysplasia could be localized to epiphysis, such as chondrodysplasia punctate or multiple epiphyseal dysplasia, or it could be a part of spondyloepiphyseal dysplasia (Fig. 116). Usually bilateral epiphyses are involved, in a nearly symmetric fashion. The effect is disordered growth of the limbs, labral tears, cartilage loss, and premature degenerative changes. Metaphyseal and diaphyseal dysplasia are localized to respective portions of the bones (Fig. 117).

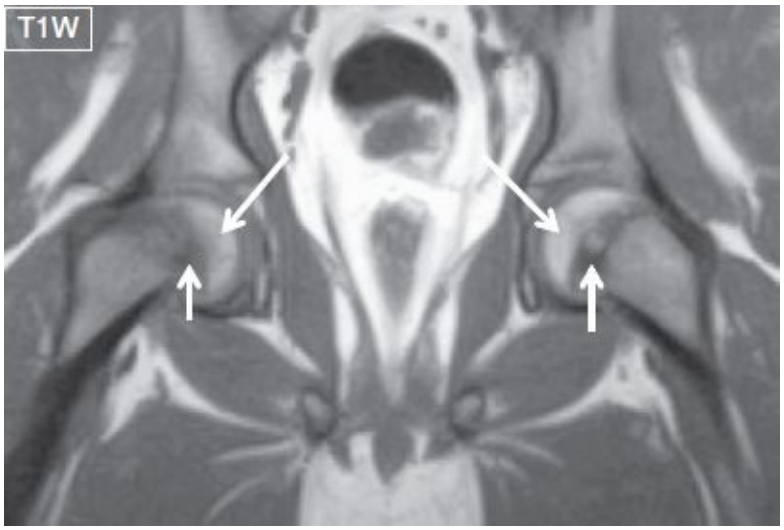

Fig. 115: Bilateral slipped capital femoral epiphyses. Coronal image shows bilateral widening of the growth plates (*long arrows*) and irregularity and blurring of the physeal edges with inferior and posteromedial displacement of the femoral epiphyses (*short arrows*).

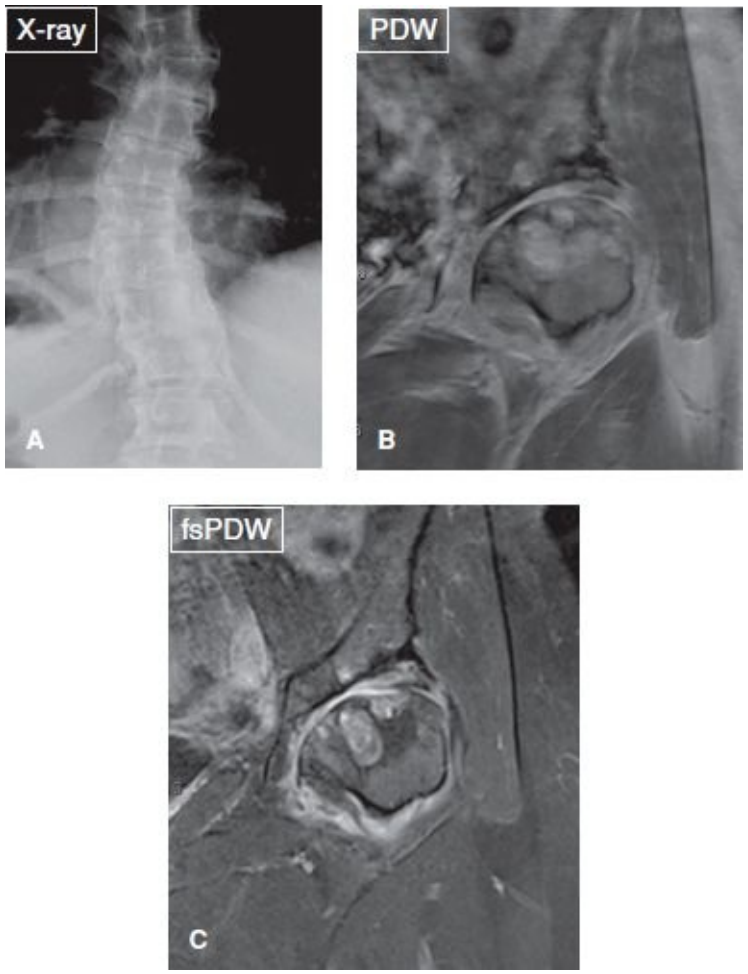

Fig. 116: Spondyloepiphyseal dysplasia. **A:** AP radiograph of the thoracolumbar spine shows multilevel platyspondily and premature degenerative changes in an adolescent child. **B, C:** Coronal images of the left hip in the same patient show severe osteoarthritic changes of the left hip with labral tears, small effusion, and deformed left femoral capital epiphysis.

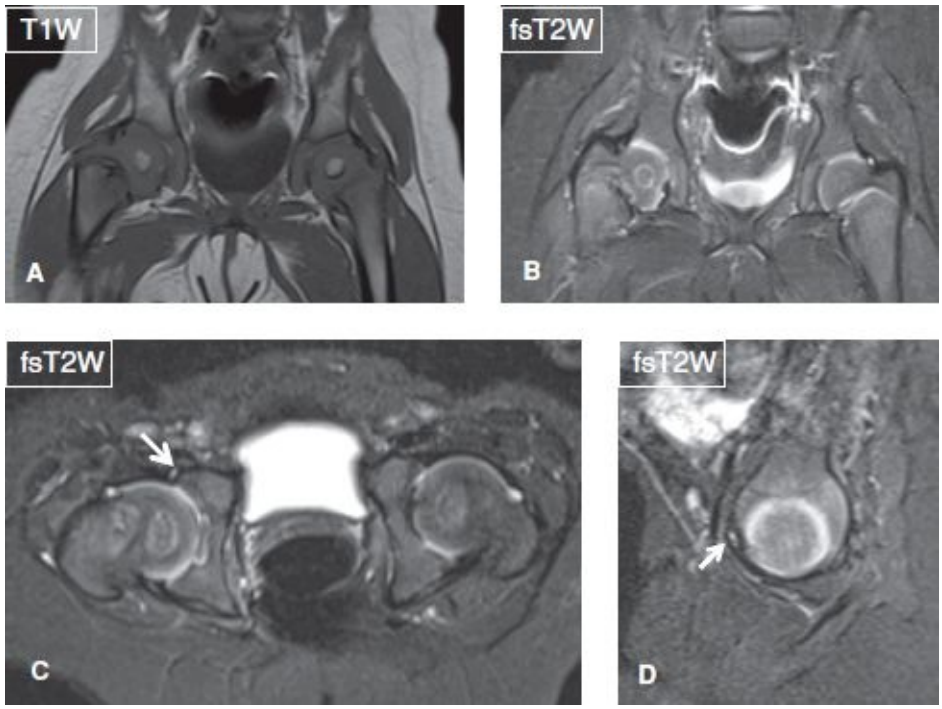

Fig. 117: Pyle's metaphyseal dysplasia. Coronal **(A, B)** images show foreshortened deformed femoral necks with normal capital epiphyses. Axial **(C)** and sagittal **(D)** images show

anterior and anterosuperior labral tears (*arrows*) with intralabral cysts.

Osseus fractures may be related to neoplastic process or non-neoplastic process (Figs. 118, 119). General rules which can be applied in differentiating nonneoplastic process, such as fracture, stress reaction, or red marrow reconversion from neoplastic fractures include, sharp margin of the fracture edges, higher signal on T1W images than muscles, not substantial T2 brightness of the lesion, fascial edema and fluid collection, presence of fracture line, more than 20% loss on chemical shift imaging on the out-of-phase image, only peripheral or no enhancement and no significant diffusion restriction (high ADC values, more than 1.5×10^{-3} mm^2/s). Infections similarly produce excessive fascial or muscle edema, joint effusion, fluid collection, monoarticular involvement, e.g., with unilateral sacroilitis, sinus tract or fistula and peripheral enhancement in a organized collection and, relatively diffuse enhancement in associated cellulitis or myositis (Fig. 120). The bones around the pelvis are common sites of red marrow reconversion (Fig. 121). Diffuse darkening of the marrow on all sequences can be caused by etiologies leading to diffuse bony sclerosis on radiographs, such as osteopetrosis (Fig. 122), renal osteodystrophy, myelofibrosis, fluorosis, etc. Common neoplasms involving the proximal femur include bony cyst, osteoid osteoma (<1.5 cm), osteoblastoma (similar histology to osteoid osteoma, >1.5 cm, more complex ossified lesion with internal calcifications that can rarely metastasize), fibrous dysplasia (mixed, predominantly T2 dark rim or internal hyperintense signals, young age, trabeculated marrow in polyostotic fibrous dysplasia), chondroblastoma (young patient, epiphyseal or apophyseal lesion with lots of bone marrow, periosteal and soft tissue edema), lipoma (simple fat intensity or with internal cystic degeneration), liposclerosing myxofibrous tumor (as the name suggests—complex signal apart from fat, calcification, sclerosis, small malignant potential), chondrosarcoma (cartilaginous matrix, soft tissue mass, cortical destruction or endosteal scalloping more than two-third of the cortex, bone marrow edema, periosteal reaction), hemangioma (trabeculated lesion with T1/T2 hyperintensity, no surrounding bone marrow edema and can be multiple in hemangiomatosis), leukemia or lymphoma (permeative lesion that can appear as bone marrow edema pattern, known history of lymphoproliferative disorder), Ewing sarcoma (caucasian young boy or male, metadiaphyseal lesion, permeative pattern, onion peel periosteal reaction, cortical saucerization due to adjacent soft tissue mass), multiple myeloma, and metastasis (older patients, T2 bright rim to the lesion, bone marrow edema, soft tissue mass being more common with myeloma lesions). Plain film correlation is very useful in the lesion characterization and MR imaging is useful in further depiction of the extent of the lesion (Figs. 123–139).

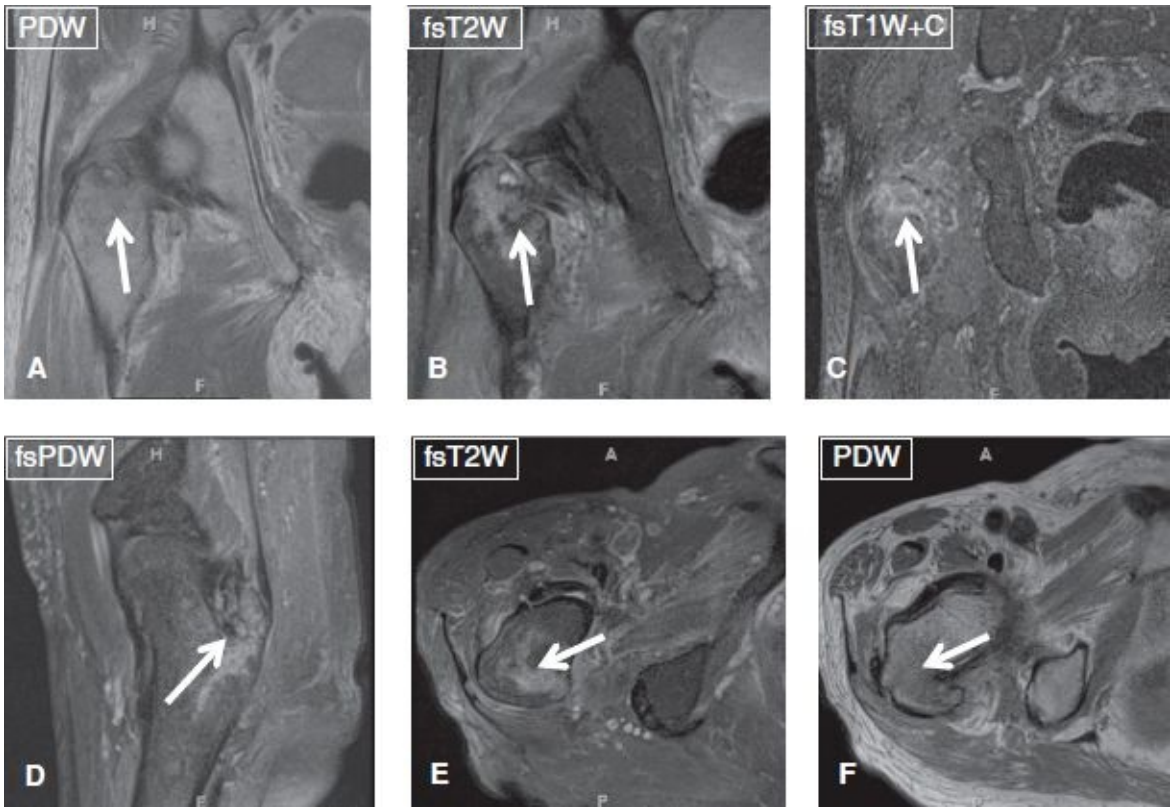

Fig. 118: Benign greater trochanter fracture in a patient with known pancreatic cancer. Coronal **(A–C),** sagittal **(D),** and axial **(E, F)** images demonstrate a fracture (*arrows*) at the base of the greater trochanter, without associated soft tissue mass. Notice no significant darkening on non-fat-saturated image **(A),** fascial edema **(B),** and mostly peripheral enhancement **(C)** at the fracture site. The patient improved on conservative treatment and the imaging findings regressed on 3 month follow-up.

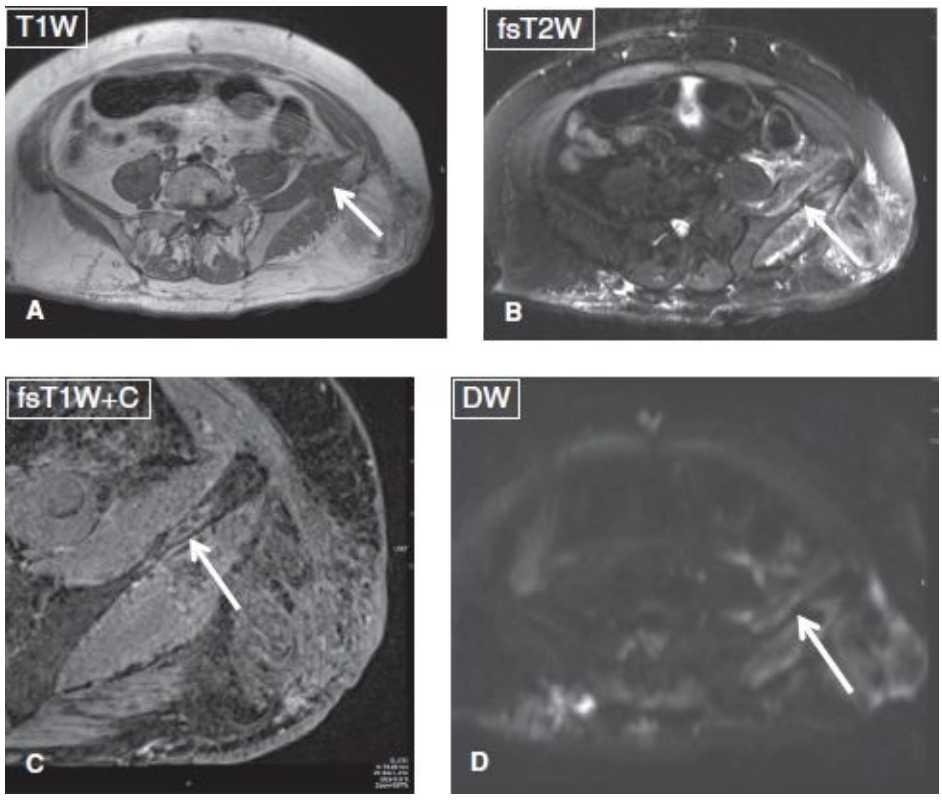

Fig. 119: Nonpathologic iliac bone fracture. Axial images. **A, B:** Notice soft tissue and fascial edema and a fracture (*arrows*) is evident in the left iliac bone. **C, D:** There is only peripheral

contrast enhancement and no restricted diffusion in the involved area (*arrows*) in this case of a benign fracture.

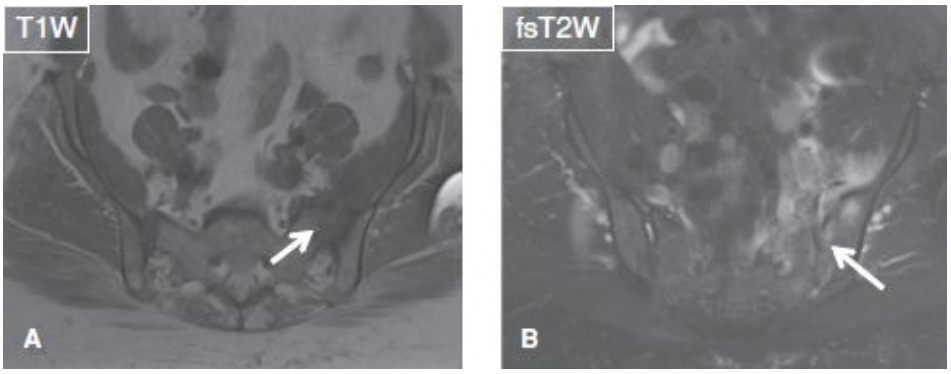

Fig. 120: Infectious sacroilitis. Axial images **(A, B)** exhibit edema of the articular surfaces (*arrows*) of the left sacroiliac joint with surrounding fascial and left iliopsoas muscle edema in this case of tubercular arthritis.

Fig. 121: Red marrow reconversion. Coronal images **(A, B)** show patchy areas (*arrows*) that exhibit T1 hyperintense to muscle and minimally high T2 signal in the femoral metaphysis and diaphysis.

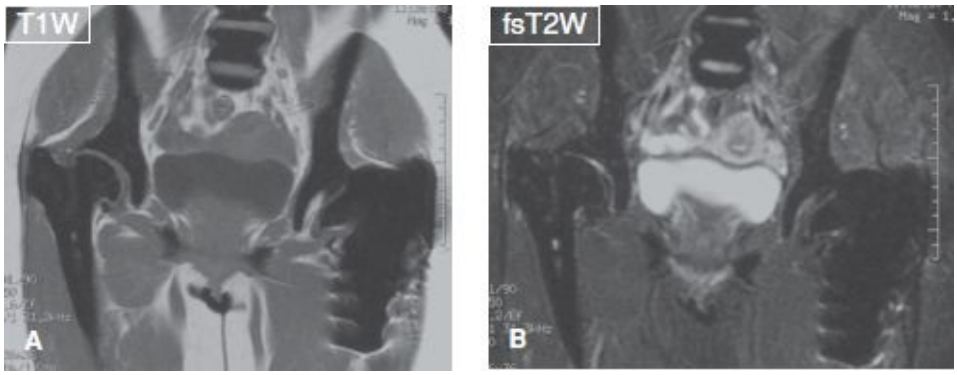

Fig. 122: Osteopetrosis. Coronal images **(A, B)** show diffuse dark signal of the marrow of the pelvis and lumbar spine. Artifacts in the left femur are related to left femoral fracture fixation hardware material.

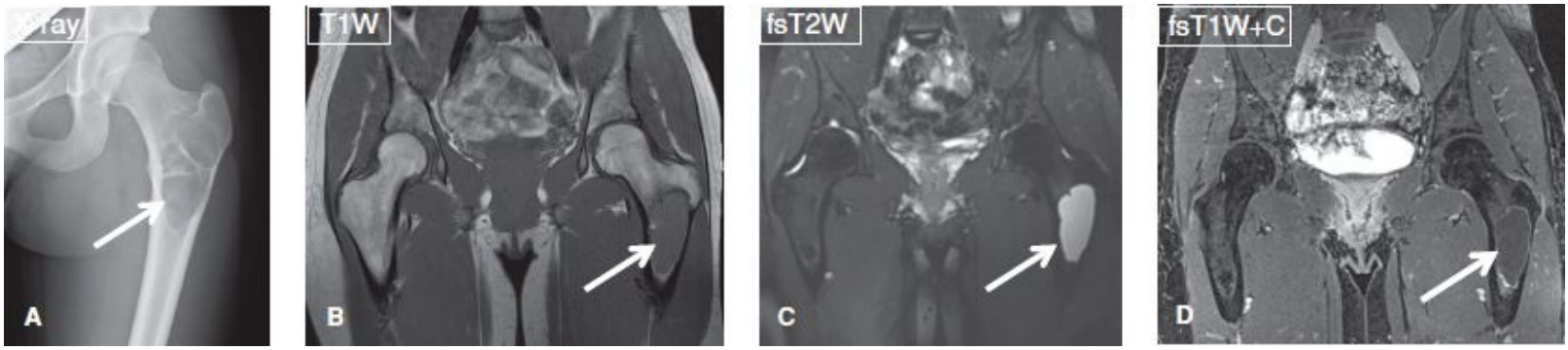

Fig. 123: Simple bone cyst. **A:** Anteroposterior radiograph displays a well-defined lytic lesion in the left femoral metaphysis (*arrow*). **B–D:** On coronal images, the lesion (*arrows*) follows the signal intensity of fluid on all sequences and shows minimal peripheral contrast enhancement.

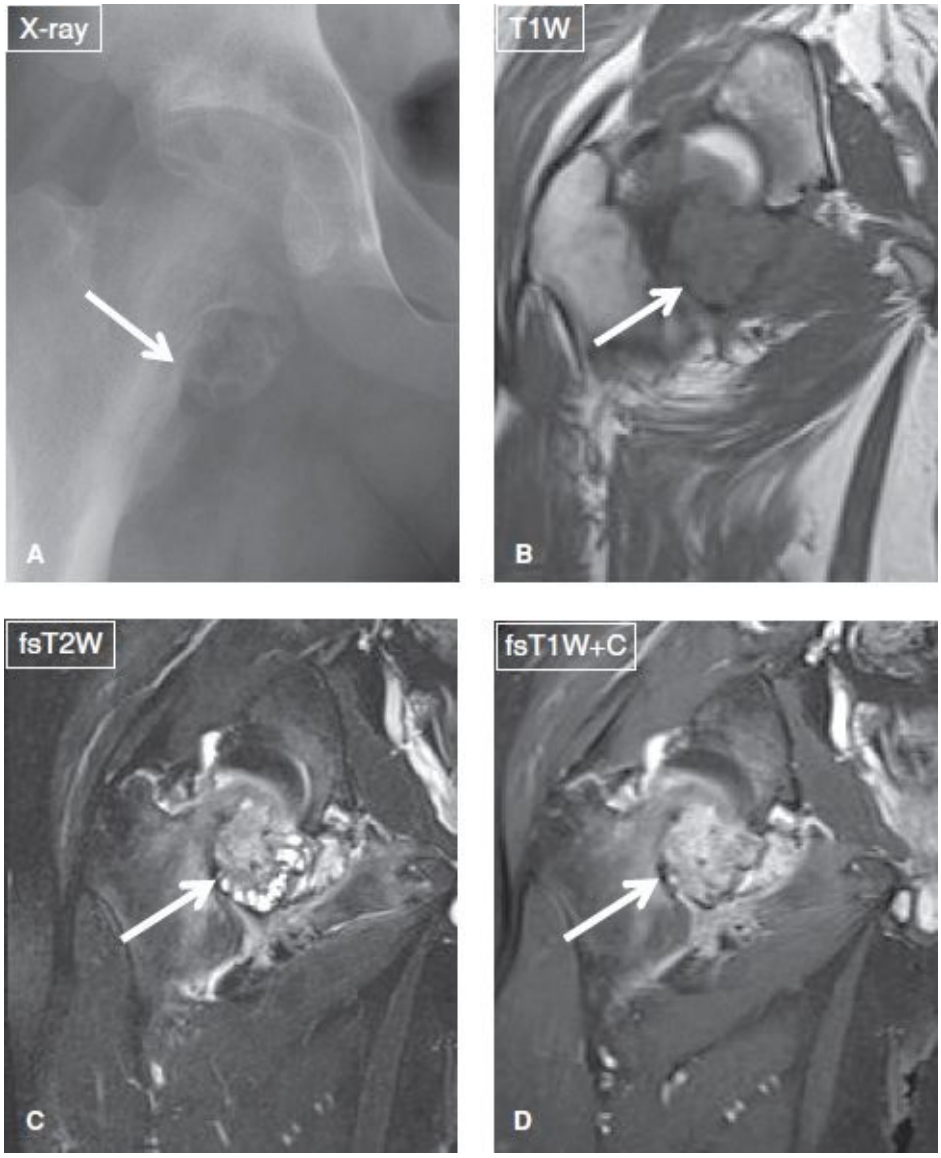

Fig. 124: Osteoblastoma. Anteroposterior radiograph **(A)** and coronal MR images **(B–D)** of right hip show a partially calcified and ossified lesion larger than 1.5 cm with associated bone marrow edema, soft tissue mass and nodular enhancement in a young boy Courtesy Dr. Kyung Jin Suh, MD.

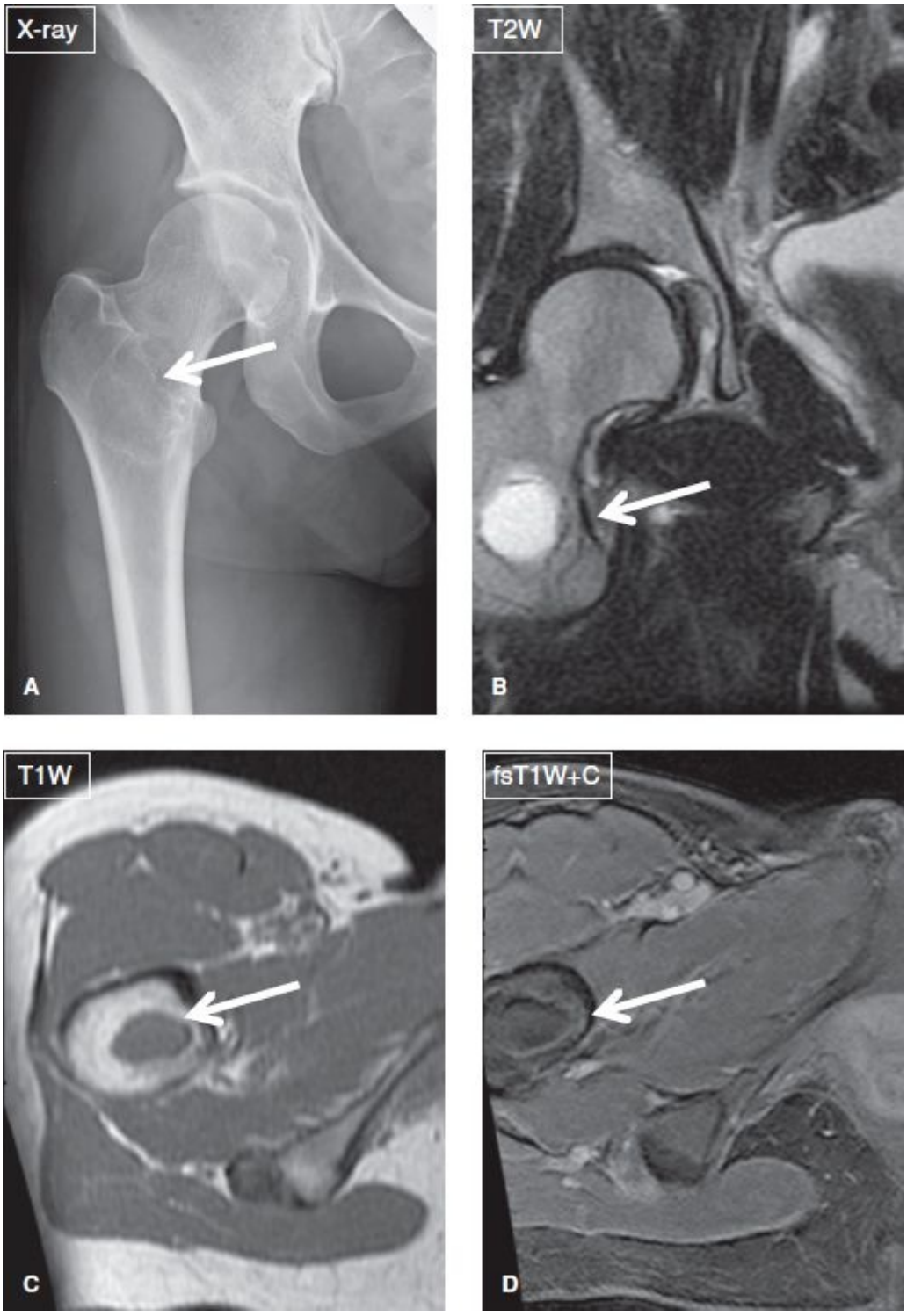

Fig. 125: Lipoma with cystic degeneration. Anteroposterior radiograph **(A)** displays a lytic lesion (*arrow*) with thin, well-defined borders in the femoral metaphysis. On the respective coronal **(B)** and axial **(C, D)** images, the lesion (*arrows*) demonstrates homogeneous internal fluid signal with peripheral fatty component and lacks contrast enhancement.

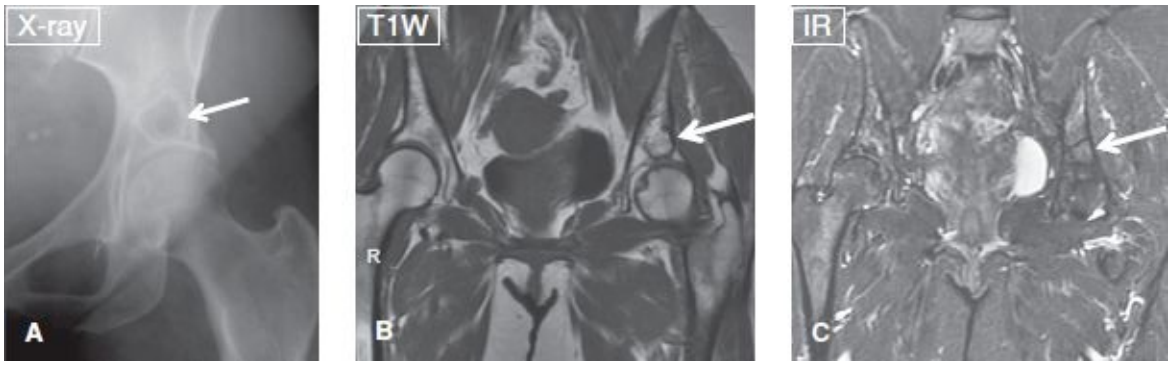

Fig. 126: Intraosseous lipoma. **A:** Anteroposterior radiograph displays a well-defined lytic lesion (*arrow*) in the left acetabulum with sclerotic rim. **B, C:** On coronal images, the lesion (*arrows*) follows the signal intensity of fat on all sequences, in keeping with lipoma. A geode would give similar appearance on fatty metamorphosis, but one should expect to see underlying significant degenerative changes of the hip and osteoporotic bone.

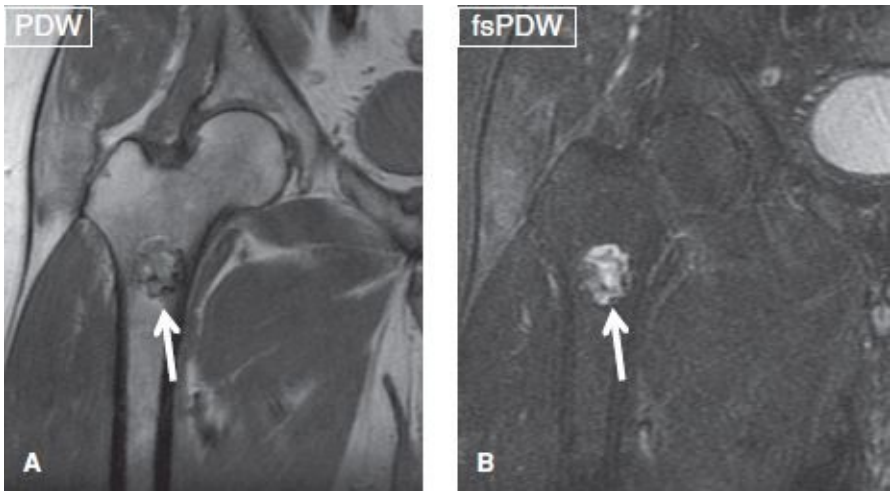

Fig. 127: Enchondroma. Coronal images **(A, B)** exhibit a nonaggressive round intramedullary lesion (*arrows*) with sharp (popcorn-like) contours, and internal chondral (T2 hyperintense) components as well as calcifications in rings-and-arcs pattern.

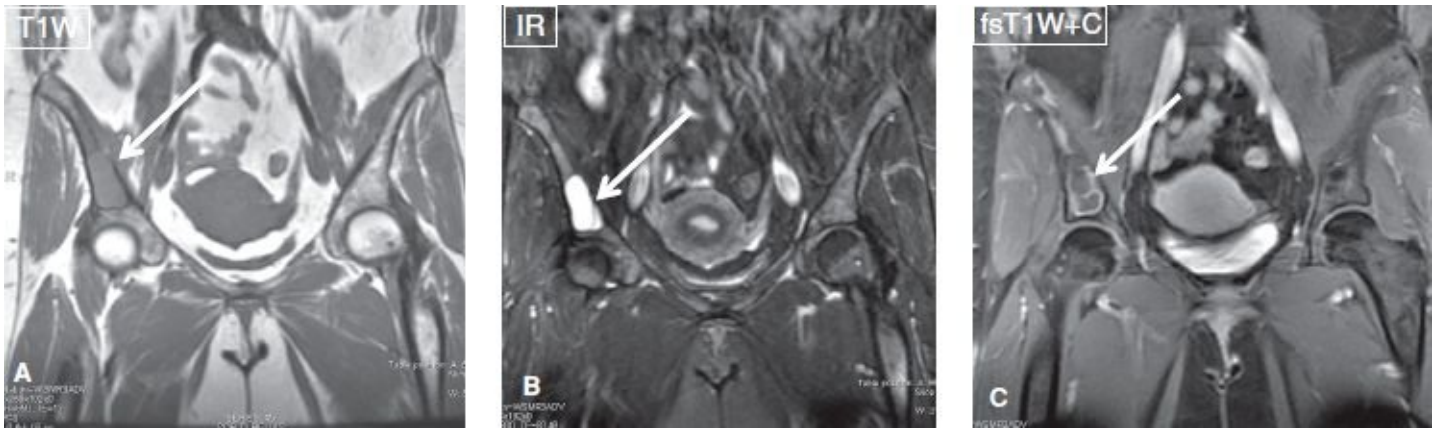

Fig. 128: Monostotic fibrous dysplasia. Coronal images **(A–C)** display a well-defined lesion (*arrows*) in the right iliac bone in a young woman, which shows thin hypointense peripheral rim and enhancement with mild focal bone enlargement.

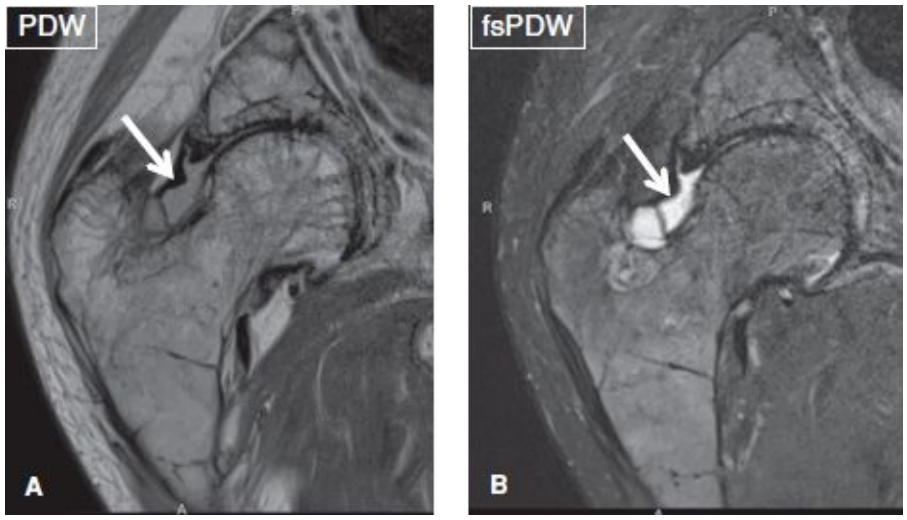

Fig. 129: Polyostotic fibrous dysplasia. Coronal images **(A, B)** show diffuse trabeculated pattern of the bone marrow and mild bone enlargement of the femur and iliac bone, which are involved by fibrous dysplasia. Also note moderate joint effusion (*arrows*).

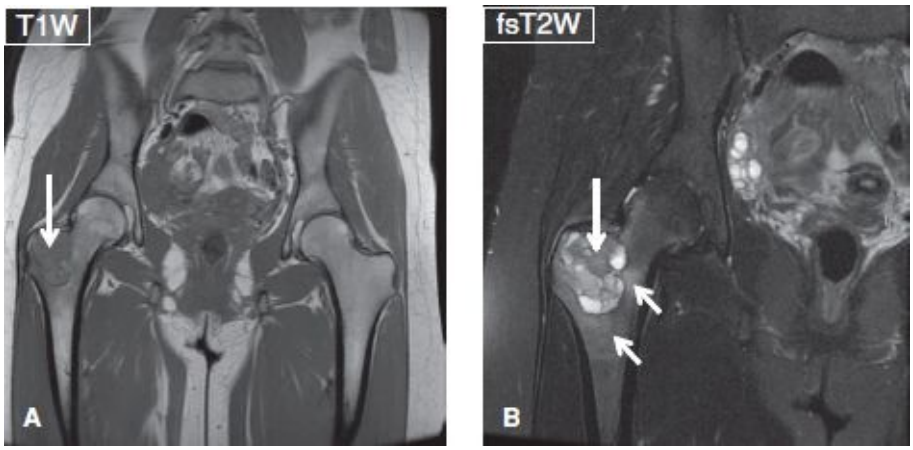

Fig. 130: Chondroblastoma with aneurysmal bone cyst. Coronal images **(A, B)** exhibit a well-defined intramedullary lesion (*long arrows*) in the right greater trochanter, which features internal septae and is associated with surrounding marrow edema (*short arrows*).

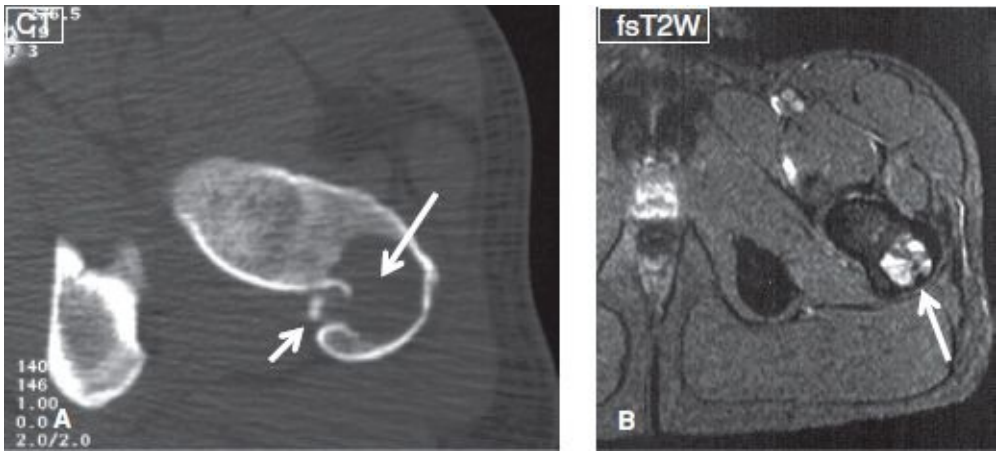

Fig. 131: Chondroblastoma with aneurysmal bone cyst. **A:** Axial CT image demonstrates an intramedullary lytic lesion (*long arrow*) in the left greater trochanter, which has caused focal cortical disruption (*short arrow*). **B:** On the respective axial MR image, the lesion (*arrow*) is well defined and exhibits internal septae and fluid–fluid levels.

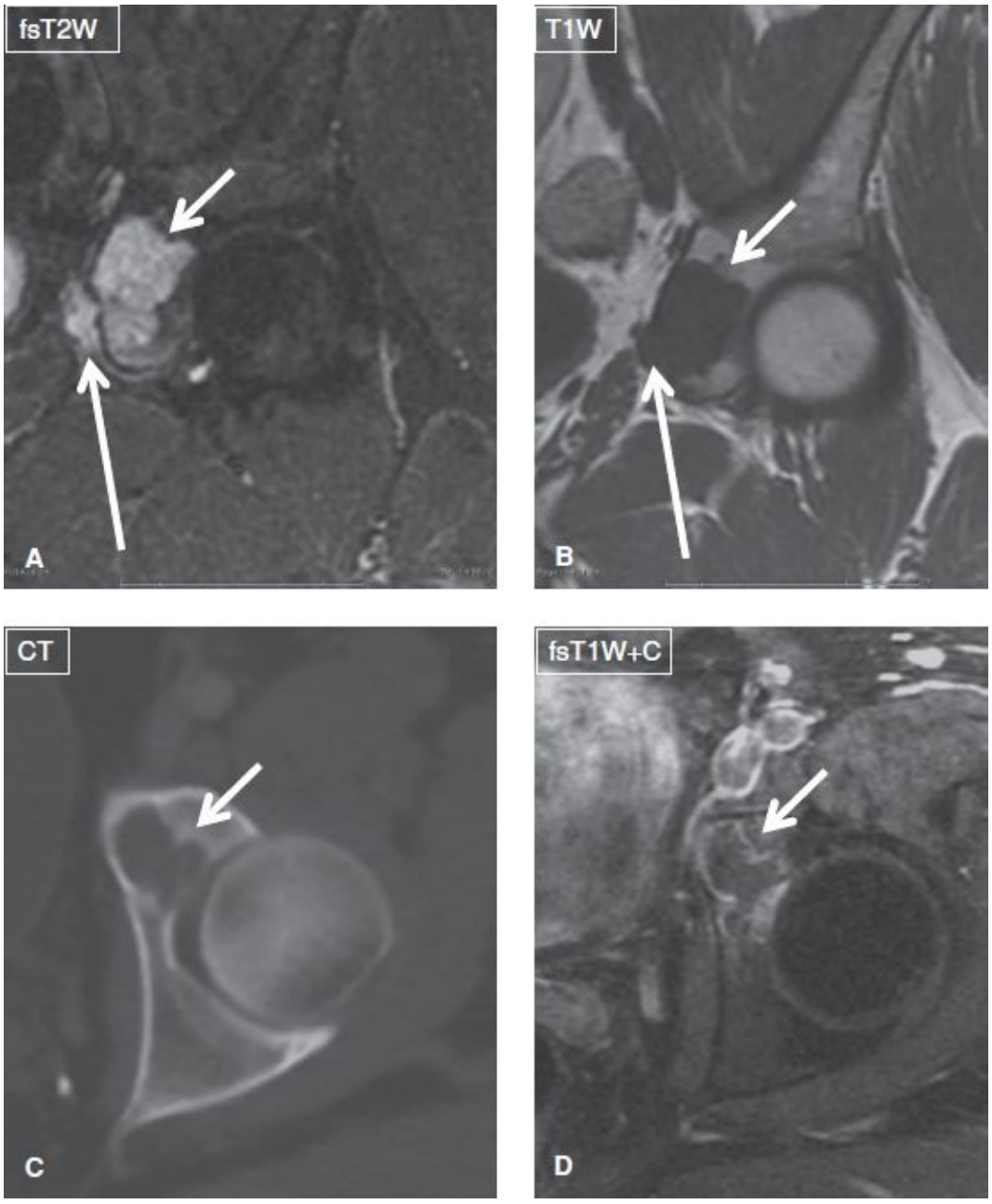

Fig. 132: Chondrosarcoma. Axial MR **(A, B, D)** and CT **(C)** images demonstrate well-defined osteolytic lesion (*short arrows*) in the left acetabulum, which shows mild peripheral contrast enhancement. Notice associated extraosseous soft tissue component (*long arrows*) in this biopsy-proven chondrosarcoma, in this young patient. Similar appearance could be seen with a geode. But, note lack of underlying degenerative changes in the underlying hip joint.

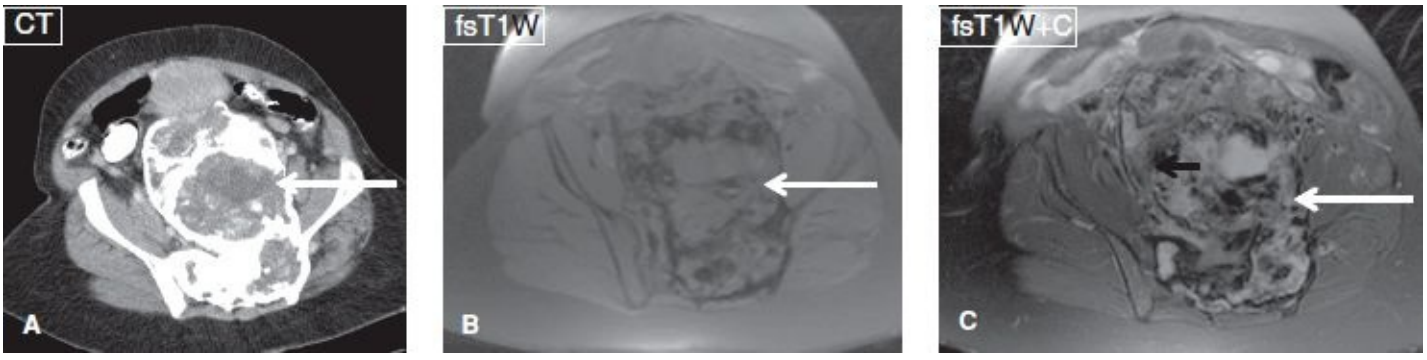

Fig. 133: Chondrosarcoma. Axial CT **(A)** and MR **(B, C)** images demonstrate a large partly calcified heterogeneous destructive soft tissue mass (*arrows*), which emanates from the

sacrum and projects intra-abdominally.

Fig. 134: Chondrosarcoma. Coronal images **(A, B)** show a relatively homogeneous infiltrating marrow lesion (*arrows*) in the right femoral metaphysis, which demonstrates strong and diffuse enhancement in this biopsy-proven primary chondrosarcoma.

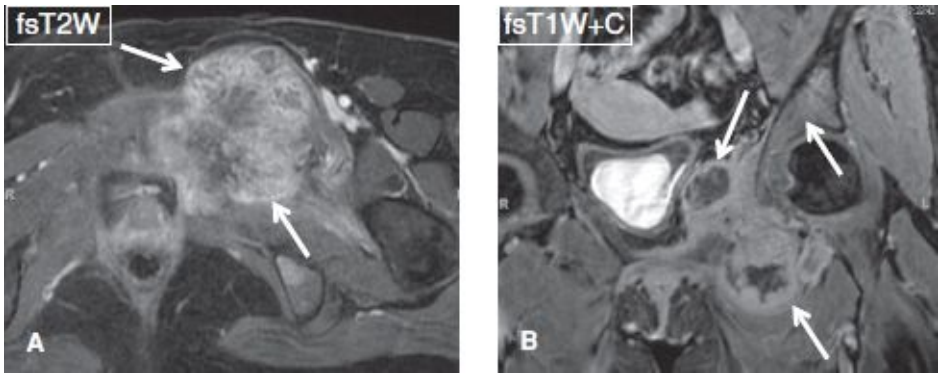

Fig. 135: Chondroblastic osteosarcoma. Axial **(A)** and coronal **(B)** images exhibit a large bony and soft tissue mass (*arrows*), which infiltrates the left adductor muscles and demonstrates heterogeneous signal and enhancement.

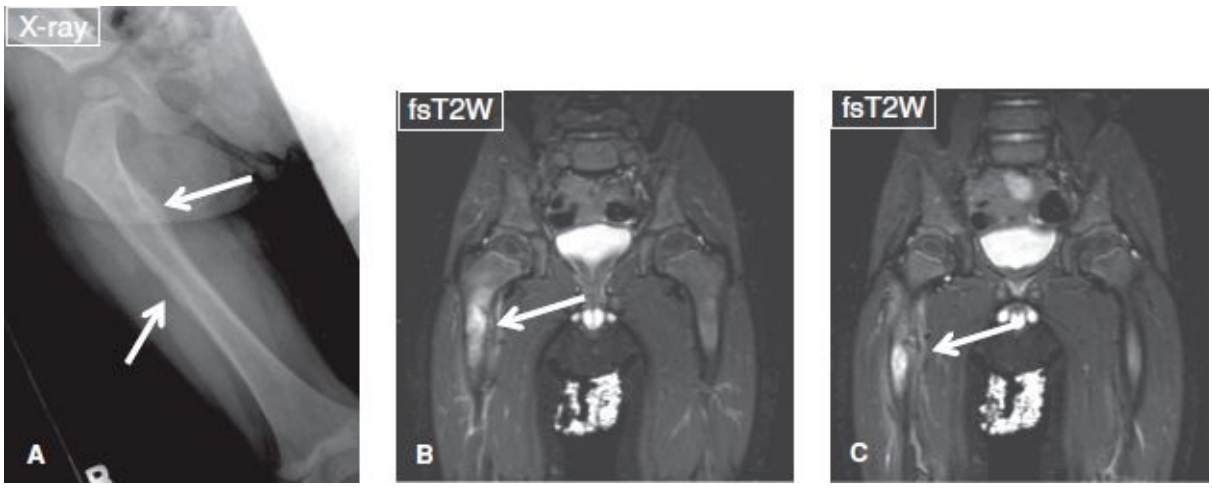

Fig. 136: Ewing sarcoma in a child. **A:** Anteroposterior radiograph demonstrates aggressive onion peel periosteal reaction (*arrows*) at the proximal diaphysis. **B, C:** Coronal images reveal a infiltrating mass (*arrows*) in the corresponding location.

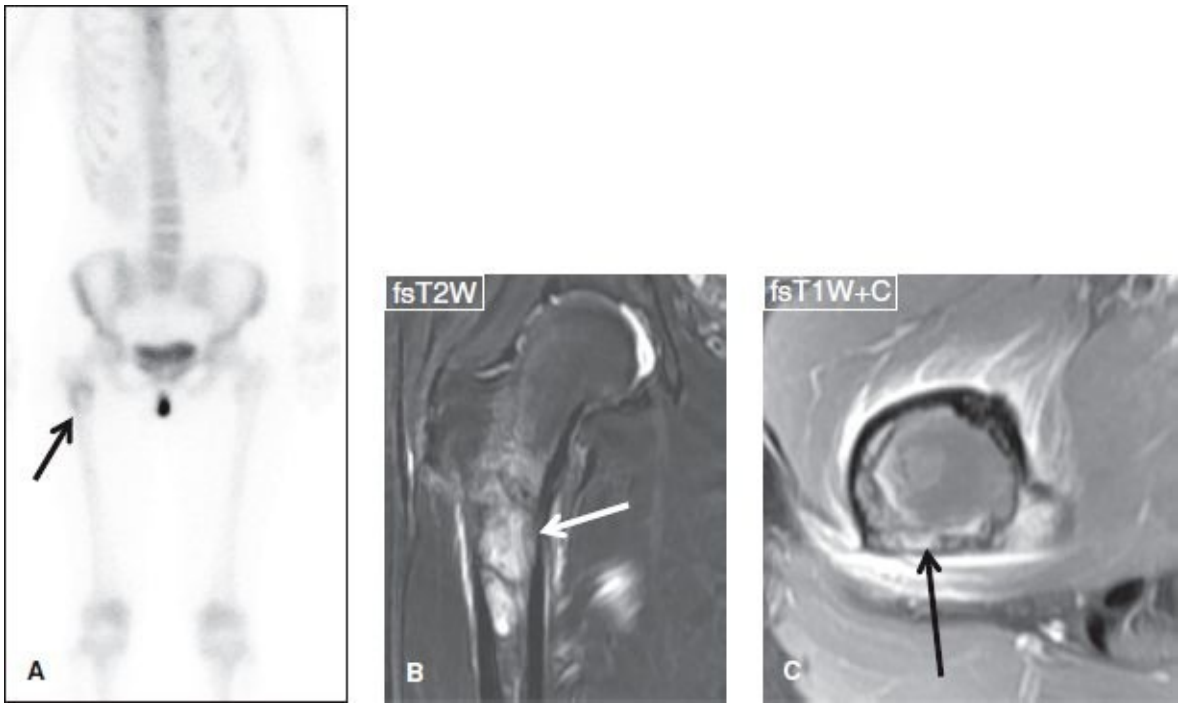

Fig. 137: Leukemia. Tc99m MDP bone scan image **(A)** shows a focal lesion (*arrow*) in the right femoral metadiaphysis. On coronal **(B)** MR image, there is a T2 bright infiltrative lesion with cortical permeation (*arrow*) and adjacent fascial edema. Axial **(C)** image confirms the endosteal and cortical erosions (*arrow*).

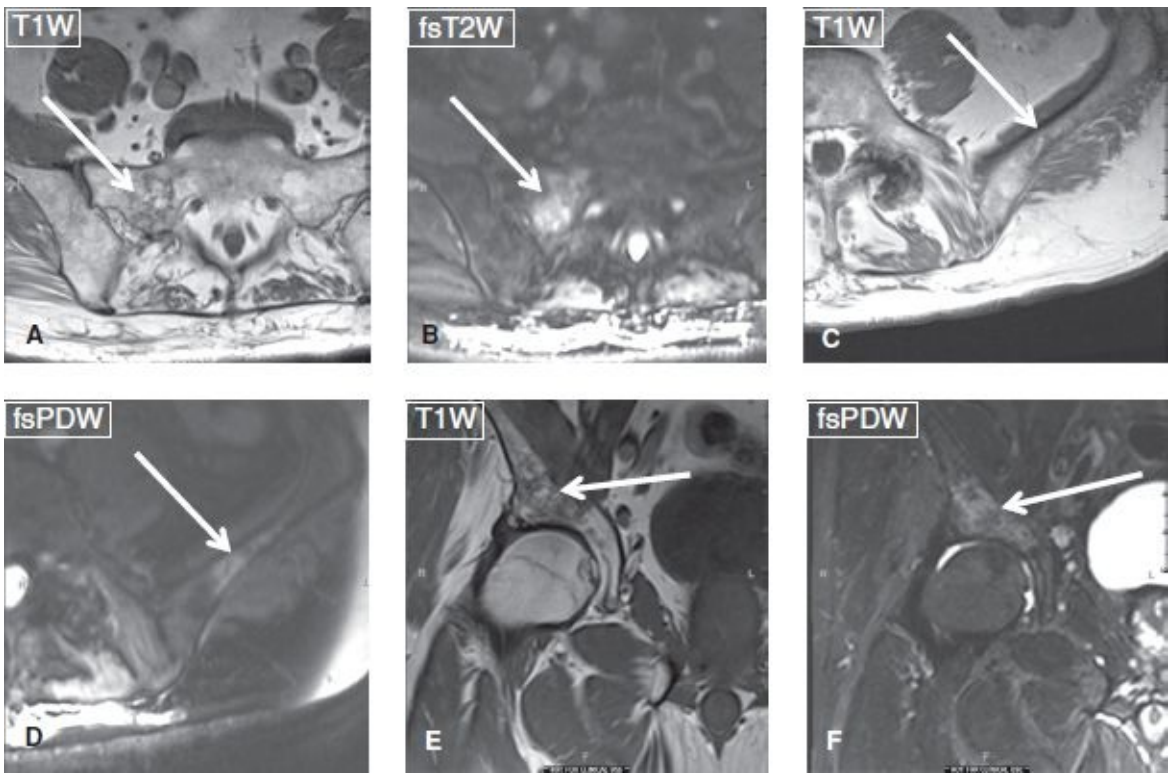

Fig. 138: Skeletal hemangiomatosis. Axial **(A–D)** and coronal **(E, F)** images of the same individual exhibit hemangiomas in the sacrum (*arrows* in **A, B**), left iliac bone (*arrows* in **C, D**), and right iliac bone (*arrows* in **E, F**). Notice the lesions are trabeculated and show both T1 and T2 hyperintensity.

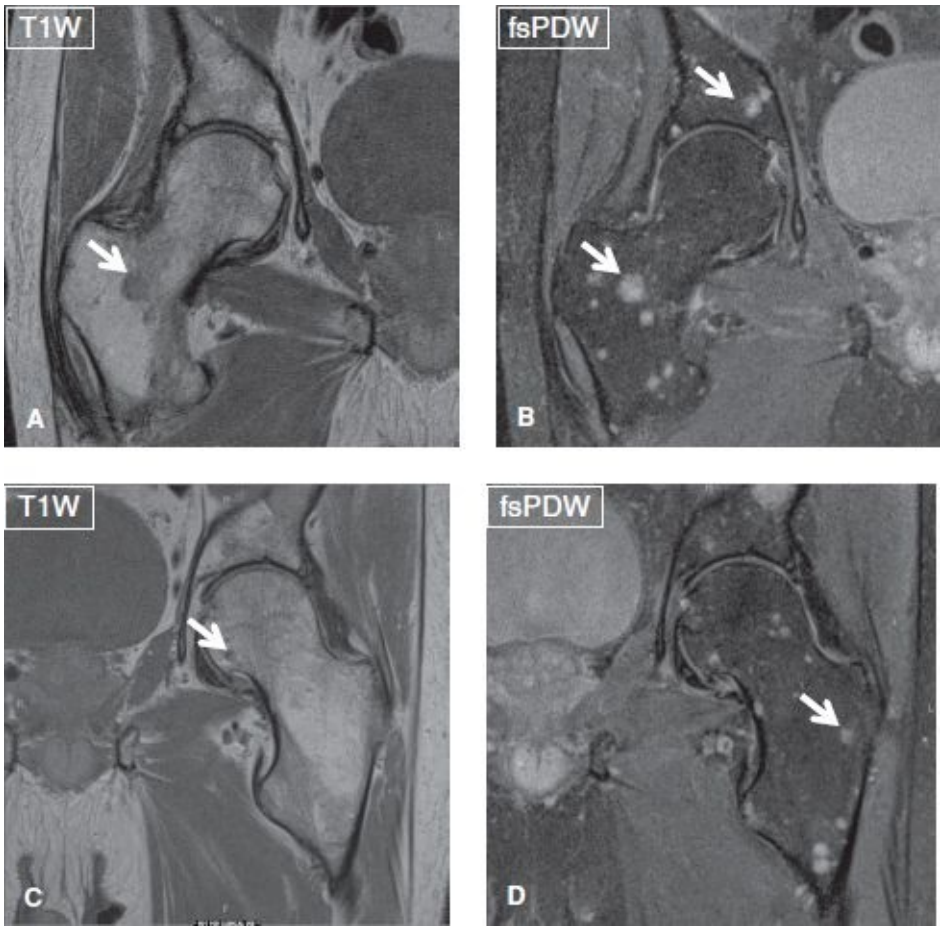

Fig. 139: Metastatic disease. Coronal images **(A–D)** show multiple foci (*arrows*) of abnormal signal in the bone marrow. Lesions are particularly evident on the fluid-sensitive images and were due to melanoma metastases.

Particle disease refers to the bone reaction that occurs in response to debris released from the wear of arthroplasty components. The entity may lead to progressive osteolysis, and therefore, early diagnosis and treatment are essential. The earliest MR finding is joint effusion and synovitis whereas in later stages, there is capsular thickening along with low signal intra-articular debris within and around the joint. Foci of osteolysis demonstrate intermediate signal, similar to or slightly brighter than the skeletal muscle, on all MR sequences, while metallosis leads to reduced signal on all sequences (Fig. 140). Metal MR imaging sequences are more sensitive than radiographs for the detection of particle disease and related pseudotumors (ALVAL, aseptic lymphocyte-dominated vasculitis-associated lesion), especially seen with metal on metal prosthesis. Any surrounding fluid collection with sinus tract or intense enhancement, especially with clinical symptoms of toxemia, should be sampled to rule out underlying infection.

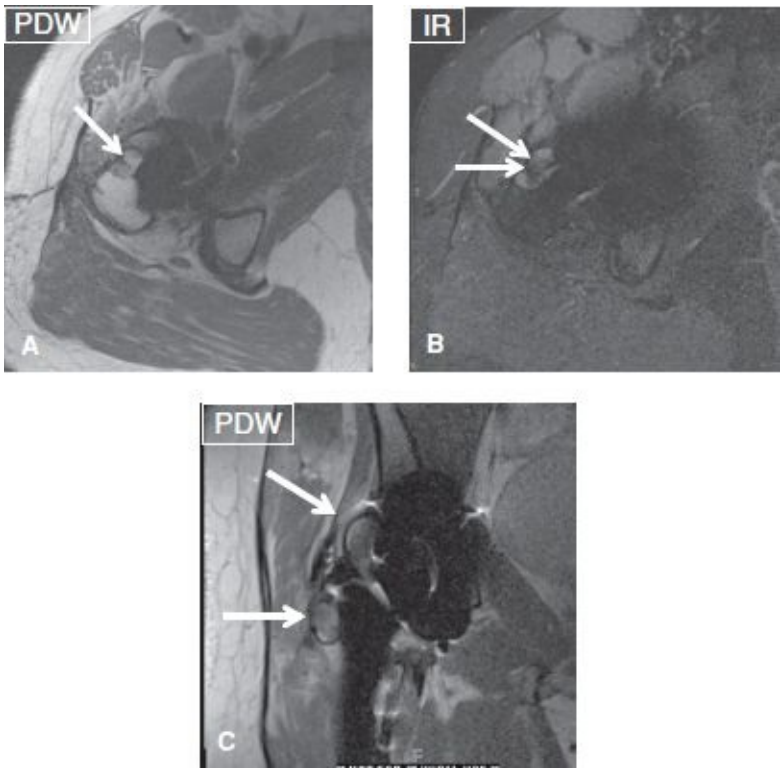

Fig. 140: Particle disease. Axial **(A, B)** and coronal **(C)** images from following prior hip replacement demonstrate hyperintense marrow lesions (*arrows*), reflecting development of granulomatous tissue reaction (Alval) in response to the prosthesis particles.

VESSELS: [<Normal / Abnormal>]

The continuation of common femoral artery, superficial femoral artery, and profunda femoris artery should normally exhibit flow voids, especially on fsPDW or T2W images. One may encounter incidental venous or chronic arterial thrombosis exhibited as loss of normal flow voids. The reader may identify venous varicosities (especially in the setting of pelvic congestion syndrome) and vascular malformations in and around the pelvis. In the absence of flow voids, the malformation would likely be a slow flow vascular malformation (Figs. 141, 142). This could be further confirmed with time-resolved MR angiogram where these lesions will show lack of arteriovenous shunting. In addition, depending upon the type of lesion, it may show delayed enhancement (venous malformation), gradual filling with a soft tissue mass (hemangioma), none or peripheral enhancement (lymphatic malformation), or a combination of these lesions (see Chapter 4 for further details on vascular malformations). Long saphenous vein lies in subcutaneous tissues and is sometimes involved in superficial venous thrombosis. Finally, findings of pelvic congestion syndrome are quiet common and the radiologic diagnosis may not correlate with clinical symptoms. However, current criteria of diagnosis include, more than three pelvic veins (larger than 3 mm each), gonadal vein larger than 7 mm, perivaginal, and perineal varicose veins.

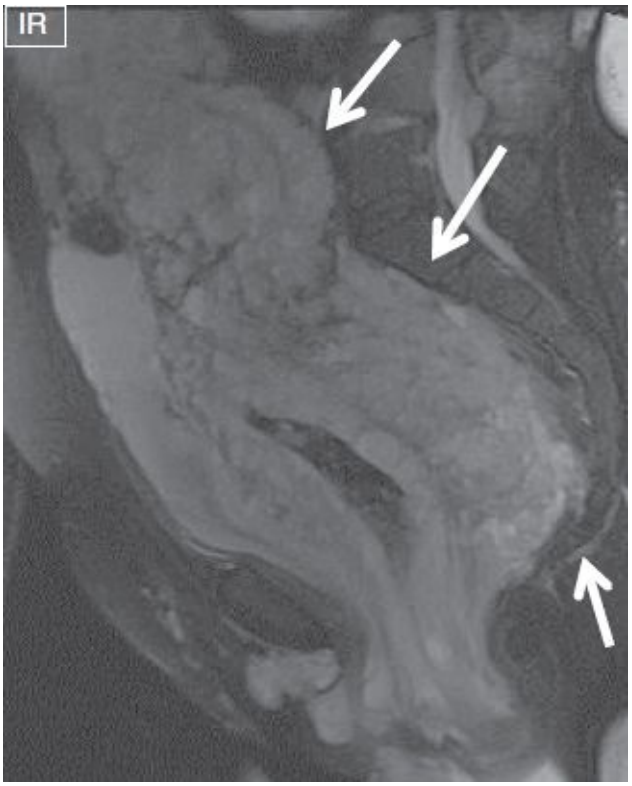

Fig. 141: Large venous malformation. Sagittal image show a markedly hyperintense, large, lobulated, and septated intrapelvic mass (*arrows*), which fills the presacral space and causes mass effect on the uterus and urinary bladder. No flow voids are seen, a typical finding of slow flow venous malformation. Only voids that are expected in this setting, would be rounded to oval foci of phleboliths.

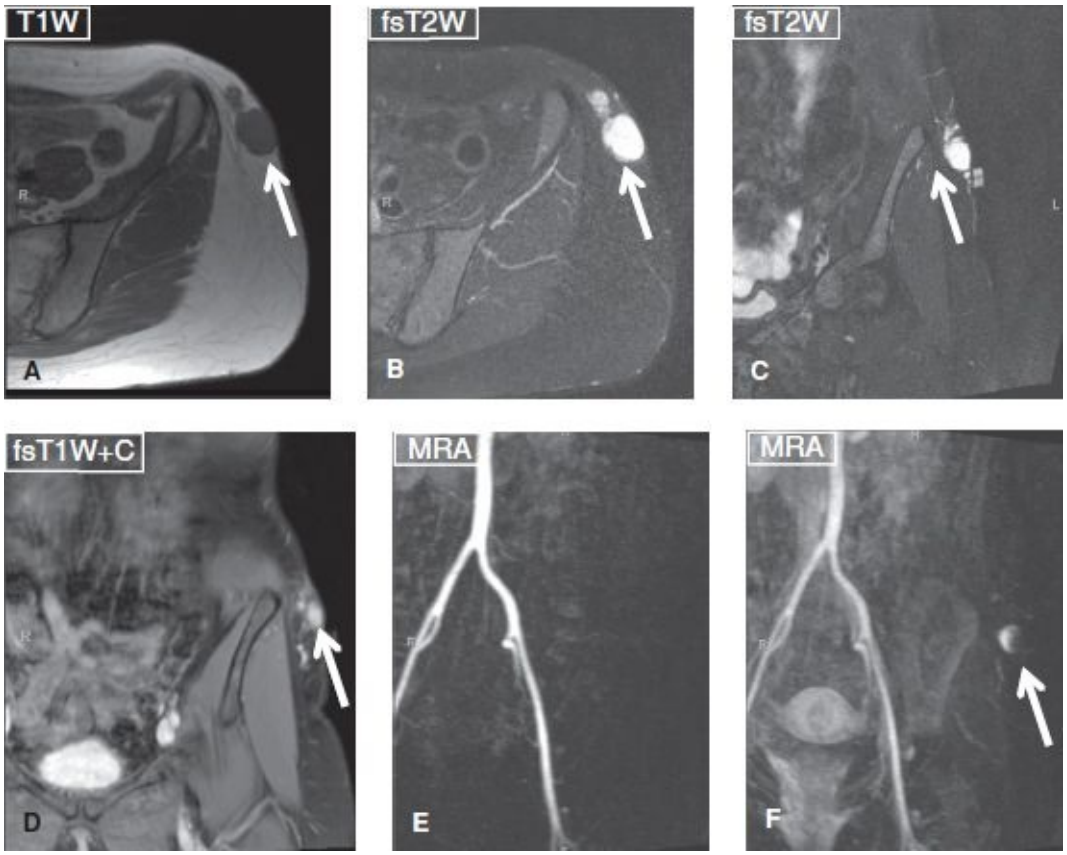

Fig. 142: Venous malformation. Axial **(A, B)** and coronal **(C, D)** MR images demonstrate a lobulated enhancing homogeneously T2 hyperintense subcutaneous lesion (*arrows*) in the

left side of the pelvis. On MR angiography images **(E, F),** the lesion (*arrow* in **F**) enhances during the venous phase of the time-resolved imaging.

NERVES: [<Normal / Abnormal>]

The normal sciatic and femoral nerves are isointense to muscles on T1W images, and mildly hyperintense on fsT2W/fsPDW images in their pelvic course, and isointense on all sequences in the thigh, below the inguinal ligament. Further, the nerves have a clear perineural fat plane and they demonstrate a smooth contour and uniform size throughout their course in and around the pelvis. Alterations in the course, signal intensity, and/or size of these nerves, as well as obliterations of the fat planes around the nerves are radiologic signs of pathology. The nerves may be involved with systemic processes, such as chronic inflammatory demyelinating neuropathy, diabetes mellitus (amyotrophy), and hereditary neuropathy and these lesions may be identified incidentally during ortho hip read outs. And although MR neurography demonstrates these lesions the best, isolated neuropathies can be picked up if one is diligently evaluating neurovascular structures during structured evaluation (Figs. 143, 144). The femoral nerve is susceptible to trauma within the iliopsoas compartment especially with injury (muscle tear, hematoma) or impingement by mass (abscess, neoplasm) (Fig. 145). More distally, the femoral nerve is at risk for injury in the groin due to a variety of iatrogenic causes, such as hernia repair, venous, and arterial punctures for central line placement. The sciatic, obturator, femoral and superior gluteal nerves are susceptible to iatrogenic injury during total hip replacement or other local instrumentation (Figs. 146, 147). Other causes of neuropathy include, pelvic fractures, piriformis syndrome, hematoma, heterotopic ossification and tumors.

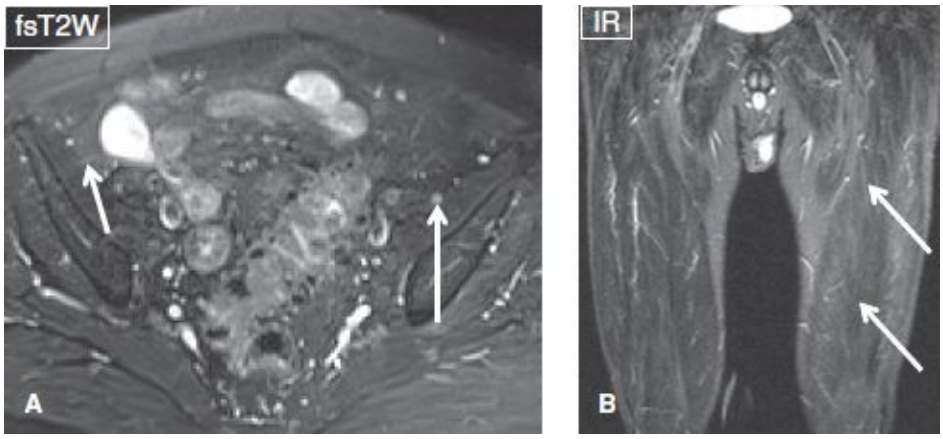

Fig. 143: Diabetic femoral neuropathy. **A:** Axial image reveals normal right femoral nerve (*short arrow*) while enlarged and hyperintense left femoral nerve (*long arrow*). **B:** The corresponding coronal image exhibits diffuse edema-like signal and atrophy of the quadratus femoris muscle (*arrows*), in keeping with subacute denervation, incidentally detected in this patient with left thigh pain and gradual weakness.

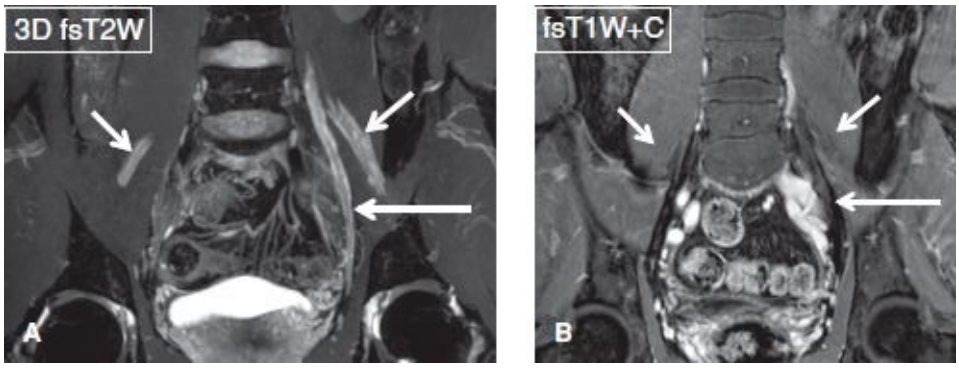

Fig. 144: Chronic inflammatory demyelinating polyneuropathy. Maximum intensity projection coronal MR neurography images **(A, B)** exhibit diffuse and homogeneous thickening and hyperintensity of the femoral nerves (*short arrows*) and left obturator nerve (*long arrows*). In **(B),** notice that there is no contrast enhancement, excluding the possibility of neoplastic conditions, such as lymphoma or perineurioma.

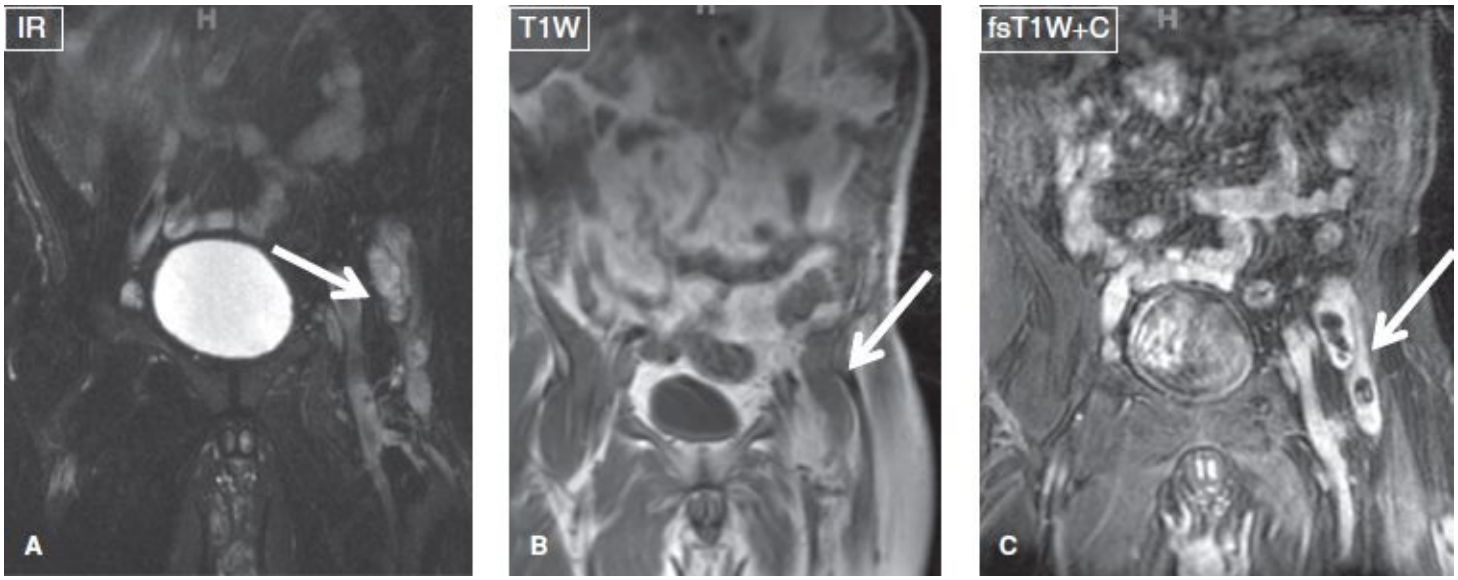

Fig. 145: Malignant peripheral nerve sheath tumor. Coronal images **(A–C)** depict an elongated enhancing lesion (*arrows*) along the left femoral nerve, which shows foci of internal necrosis.

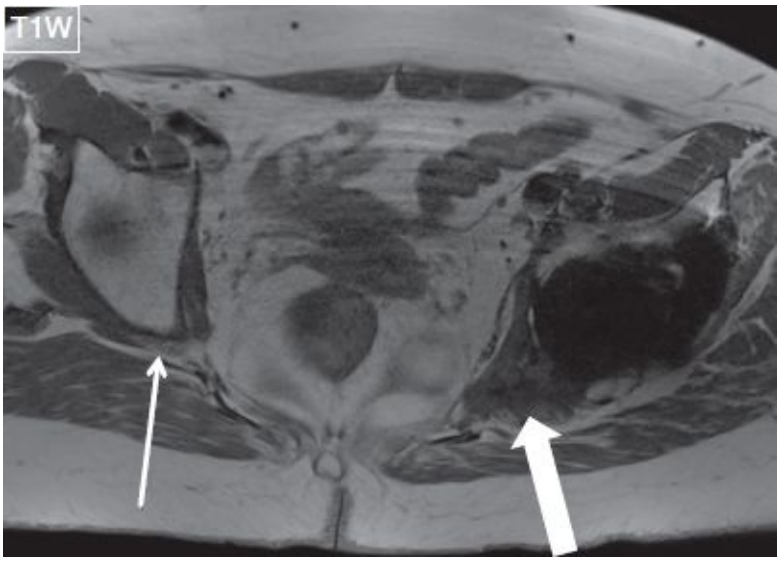

Fig. 146: Sciatic nerve fibrous encasement. Axial image from a patient with prior left hip arthroplasty demonstrates isointense fibrotic tissue (*thick arrow*) encasing the left sciatic nerve. Compare with the normal right sciatic nerve (*thin arrow*).

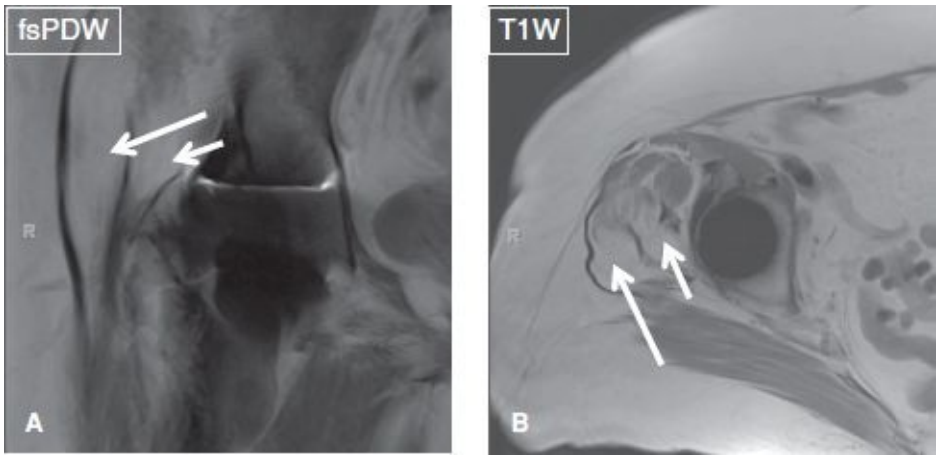

Fig. 147: Superior gluteal nerve neuropathy. Coronal **(A)** and axial **(B)** images from an individual with total right hip replacement demonstrate fatty infiltration and atrophy of the ipsilateral gluteus minimus (*short arrows*) and gluteus medius (*long arrows*) muscles, reflecting chronic denervation from superior gluteal nerve injury.

VISCERA: [<Visualized pelvic structures appear normal. No lymphadenopathy by size criteria. No significant free fluid in the pelvis / Ascites>]

It is important to evaluate the pelvic viscera for abnormal enlargement, such as enlarged prostate or uterus, or for obvious neoplastic lesions. Pelvic lymph nodes larger than 1 cm transverse dimension should be reported. Small amount of physiologic free fluid is common in true pelvis in young women. Significant amount of free fluid extending in false pelvis, complex fluid, or any free fluid in men should be reported. In women, endometriomas may appear in as heterogeneous, hemorrhagic and fibrotic T2 dark masses in intra- and extrapelvic locations (Fig. 148).

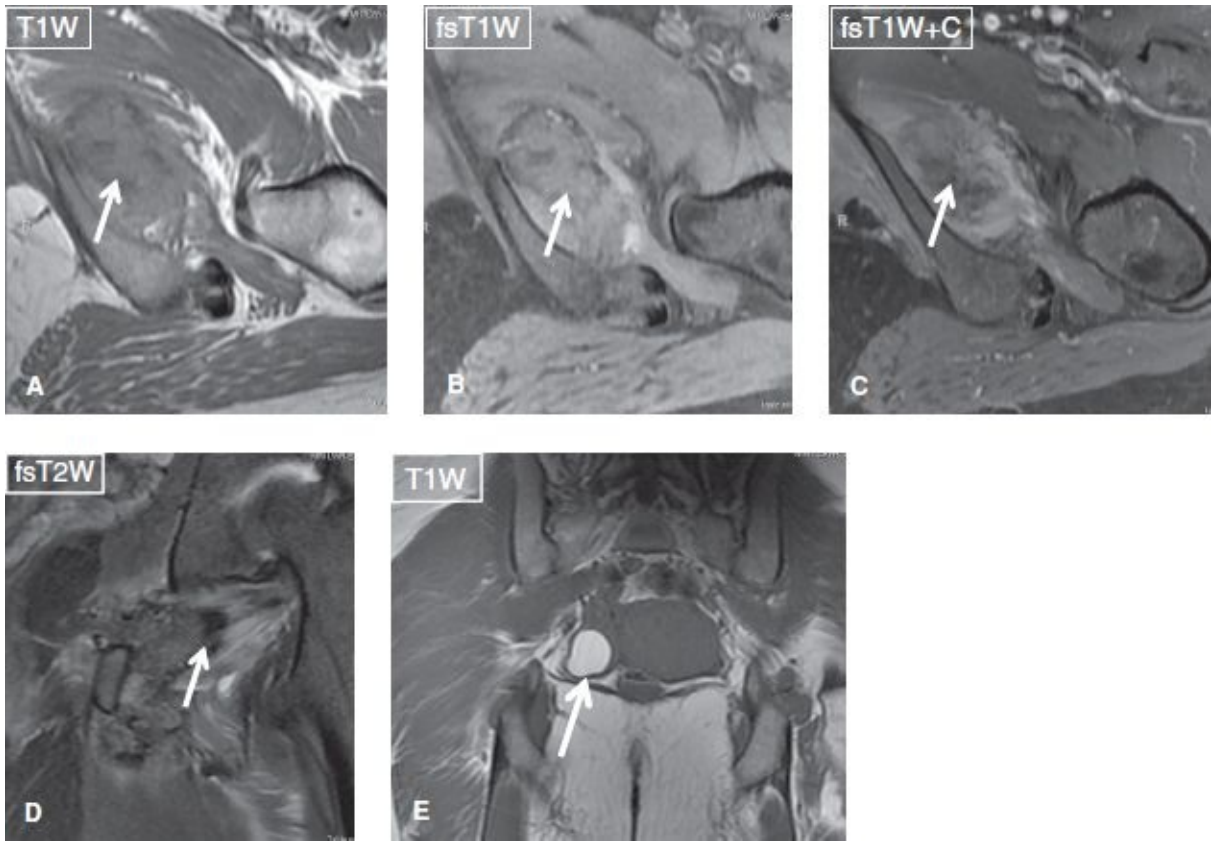

Fig. 148: Endometriosis. Axial **(A–C)** and coronal **(D)** images demonstrate an ill-defined, heterogeneously isointense to hypointense hemorrhagic mass (*arrows*) with heterogeneous enhancement in the left obturator and adductor muscles. On biopsy, the lesion proved to be an endometrioma. **E:** Another coronal image from the same patient exhibits a contralateral hemorrhagic ovarian lesion (*arrow*), compatible with coexistent endometrioma.

MISCELLANEOUS:

Other incidental findings include avulsion fractures, stress fractures, or muscle strains mimicking mass lesions (Fig. 149, 150). Other soft tissue mass that is commonly seen around pelvis is a lipomatous mass. The terminology that should be used includes the following.

Fig. 149: ASIS avulsion mimicking a mass. Axial image demonstrates partial avulsion of the anterior-superior iliac spine (*arrow*), mimicked a mass clinically, due to palpable swelling in this older individual.

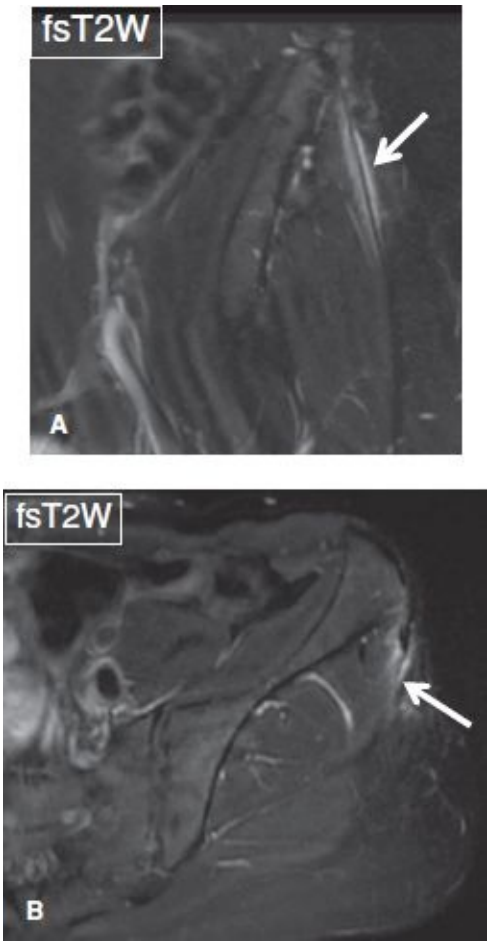

Fig. 150: Strained iliotibial band felt as a knot-like swelling by the patient. Coronal **(A)** and axial **(B)** images show grade I strain of the iliotibial band with mild edema (*arrows*).

- Lipoma—a simple fat-containing lesion with minimal or no fibrovascular septations similar to surrounding subcutaneous fat and no internal enhancement (Fig. 151)

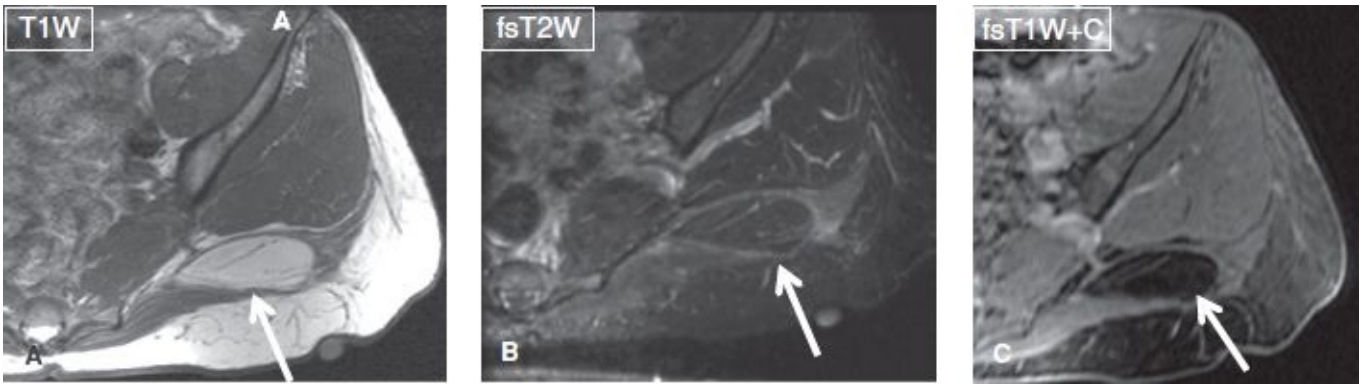

Fig. 151: Lipoma. Axial images **(A–C)** demonstrate a well-defined fat containing lesion (*arrows*) within the left gluteus maximus muscle, which features signal identical to subcutaneous fat and shows no internal enhancement, findings compatible with simple lipoma.

- Atypical lipomatous lesion—scattered thin septations and appearance dirtier than the subcutaneous fat with minimal linear foci of enhancement; includes previously used terms *atypical lipoma* and *well-differentiated liposarcoma* since these are difficult to distinguish even pathologically, and the clinical behavior, growth patterns, and prognosis are similar
- Suspicious for liposarcoma—nodular enhancing foci or thicker enhancing septations (Fig. 152).

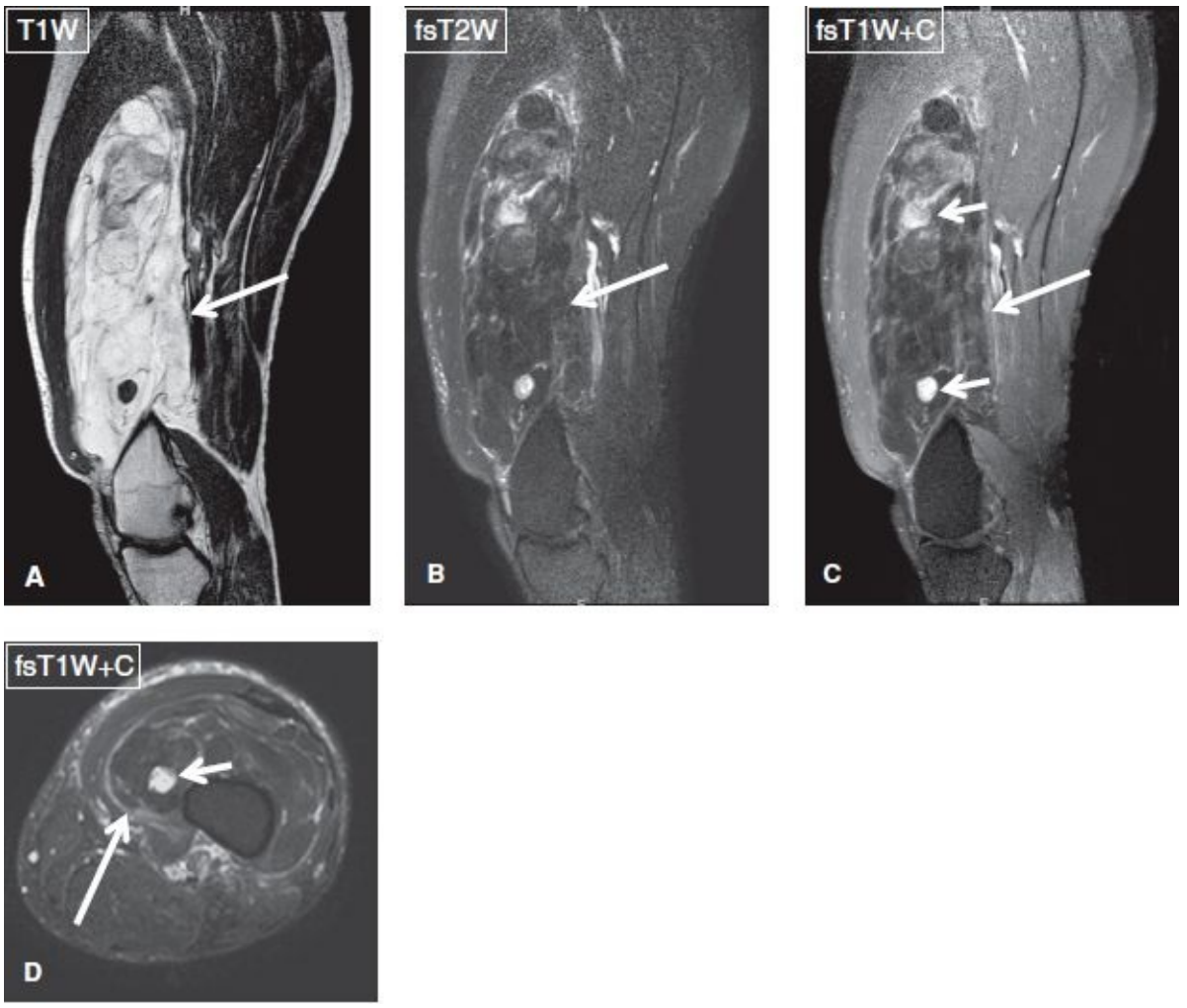

Fig. 152: Liposarcoma. Sagittal **(A–C)** and axial **(D)** images show a large fat-containing

mass (*long arrows*) in the thigh, which features heterogeneous and mostly fat-like signal, but also includes enhancing nodules (*short arrows*).

Another rare fatty lesion is hibernoma which will also show flow voids, which may aid in its characterization (Fig. 153).

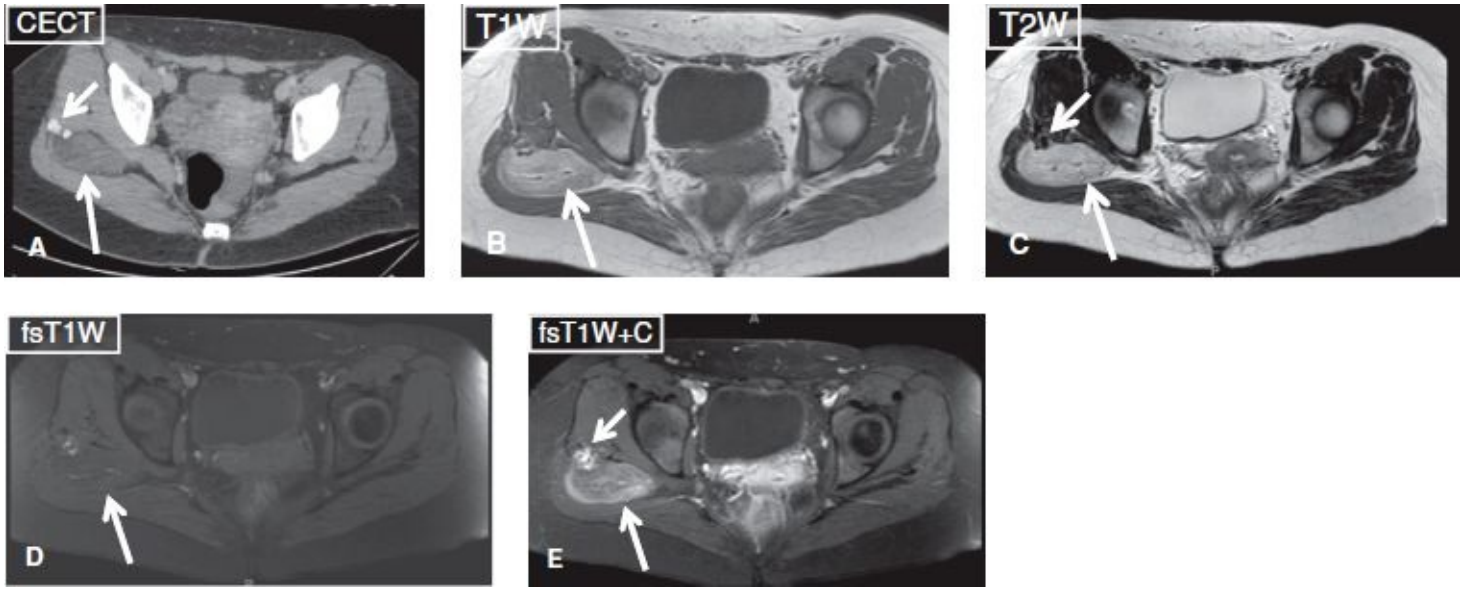

Fig. 153: Hibernoma. **A:** Axial CT image exhibits a well-defined soft tissue mass (*long arrow*) between the right gluteus maximus and medius muscles, which is slightly hypodense compared to skeletal muscles and shows few enlarged vessels (*short arrow*) in its periphery. **B–E:** In the corresponding axial MR images, the lesion (*long arrows*) shows signal almost similar to fat as well as relatively heterogeneous enhancement. Note again the enlarged peripheral vessels (*short arrows*).

To conclude, structured template reporting should be adopted to optimally evaluate the variety of structures around the hip and report the respective abnormalities.

SUGGESTED READINGS

Anderson SE, Siebenrock KA, Mamisch TC, et al. Femoroacetabular impingement magnetic resonance imaging. *Top Magn Reson Imaging.* 2009;20(3):123–128.

Ansede G, English B, Healy JC. Groin pain: Clinical assessment and the role of MR imaging. *Semin Musculoskelet Radiol.* 2011;15(1):3–13.

Bancroft LW, Blankenbaker DG. Imaging of the tendons about the pelvis. *AJR Am J Roentgenol.* 2010;195(3):605–617.

Blankenbaker DG, Ullrick SR, Davis KW, et al. Correlation of MRI findings with clinical findings of trochanteric pain syndrome. *Skeletal Radiol.* 2008;37(10):903–909.

Bui KL, Ilaslan H, Recht M, et al. Iliopsoas injury: An MRI study of patterns and prevalence correlated with clinical findings. Skeletal Radiol. 2008;37(3):245–249.

Cerezal L, Kassarjian A, Canga A, et al. Anatomy, biomechanics, imaging, and management of ligamentum teres injuries. Radiographics. 2010;30(6):1637–1651.

Dillman JR, Hernandez RJ. MRI of Legg-Calve-Perthes disease. AJR Am J Roentgenol. 2009; 193(5):1394–1407.
Gold SL, Burge AJ, Potter HG. MRI of hip cartilage: Joint morphology, structure, and composition. Clin Orthop Relat Res. 2012;470(12):3321–3331.
Hwang B, Fredericson M, Chung CB, et al. MRI findings of femoral diaphyseal stress injuries in athletes. AJR Am J Roentgenol. 2005; 185(1):166–173.
MacMahon PJ, Hogan BA, Shelly MJ, et al. Imaging of groin pain. Magn Reson Imaging Clin N Am. 2009;17(4):655–666, vi.
Mamisch TC, Bittersohl B, Hughes T, et al. Magnetic resonance imaging of the hip at 3 Tesla: Clinical value in femoroacetabular impingement of the hip and current concepts. Semin Musculoskelet Radiol. 2008;12(3):212–222.
McMahon SE, Smith TO, Hing CB. A systematic review of imaging modalities in the diagnosis of greater trochanteric pain syndrome. Musculoskeletal Care. 2012;10(4):232–239.
Mengiardi B, Pfirrmann CW, Hodler J. Hip pain in adults: MR imaging appearance of common causes. Eur Radiol. 2007;17(7):1746–1762.
Parker BJ, Clifford PD. Acetabular labral tears. Am J Orthop. 2008;37(12):636–637.
Petchprapa CN, Rosenberg ZS, Sconfienza LM, et al. MR imaging of entrapment neuropathies of the lower extremity. Part 1. The pelvis and hip. Radiographics. 2010;30(4):983–1000.
Potter HG, Schachar J. High resolution noncontrast MRI of the hip. J Magn Reson Imaging. 2010;31(2):268–278.
Sutter R, Zanetti M, Pfirrmann CW. New developments in hip imaging. Radiology. 2012;264(3):651–667.
Torriani M, Souto SC, Thomas BJ, et al. Ischiofemoral impingement syndrome: An entity with hip pain and abnormalities of the quadratus femoris muscle. AJR Am J Roentgenol. 2009;193(1):186–190.
Wagner FV, Negrao JR, Campos J, et al. Capsular ligaments of the hip: Anatomic, histologic, and positional study in cadaveric specimens with MR arthrography. Radiology. 2012;263(1):189–198.
Zilkens C, Miese F, Jager M, et al. Magnetic resonance imaging of hip joint cartilage and labrum. Orthop Rev (Pavia). 2011;3(2):e9.
Zoga AC, Mullens FE, Meyers WC. The spectrum of MR imaging in athletic pubalgia. *Radiol Clin North Am.* 2010;48(6):1179–1197.

APPENDIX 1: Sample Completed Structured Report: Hip: NORMAL

EXAM: MRI OF THE [<RIGHT/LEFT>] HIP [<WITH/WITHOUT>] CONTRAST

HISTORY: []-year-old <patient sex> with <order reason for study>

TECHNIQUE: Imaging was performed [<without IV contrast> <before and after IV / after intra-articular contrast>]. Multiplanar, multisequence MR images of the [<right / left>] hip were obtained on a [1.5 or 3] Tesla magnet.

COMPARISON: [<None>]

FINDINGS:

Alignment: [<Normal>]

Femoroacetabular impingement-related anatomy:

Pincer: [<Normal>]

Cam: [<Normal head-neck offset>]

Dysplasia: [<None>]

Fluid: [<Normal>]

Trochanteric bursitis: [<Absent>]

Labrum: [<Normal>]

Cartilage:

Femoral: [<Normal>]

Acetabular: [<Normal>]

Capsule/ligaments: [<Normal>]

Visualized muscles/tendons:

Gluteal: [<Normal>]

Adductors: [<Normal>]

Iliopsoas: [<Normal>]

Lateral rotators: [<Normal>]

Hamstrings: [<Normal>]

Bones: [<Normal>]

Vessels: [<Normal>]

Nerves: [<Normal>]

Soft tissues: [<Normal>]

Viscera: [<Visualized pelvic structures appear normal. No lymphadenopathy by size criteria. No significant free fluid in the pelvis>]

Miscellaneous:

Sacroiliac joint: [<Normal>]

Pubic symphysis: [<Normal>]

IMPRESSION:

1. [< >]

APPENDIX 2: Sample Completed Structured Report: Hip: ABNORMAL

EXAM: MRI OF THE LEFT HIP WITH CONTRAST

HISTORY: [<33-year-old man with right hip pain>]

TECHNIQUE: Imaging was performed [<after intra-articular contrast>]. Multiplanar, multisequence MR images of the [<right>] hip were obtained on a [<1.5>] Tesla magnet.

COMPARISON: [<Radiographs dated 7/5/2014>]

FINDINGS:

Alignment: [<Normal>]

Femoroacetabular impingement-related anatomy:

Pincer: [<Present. Retroversion present>]

Cam: Femoral head and neck bump present with fibrocystic change>]

Dysplasia: [<None>]

Fluid: [<Intra-articular contrast with no body>]

Trochanteric bursitis: [<Mild present>]

Labrum: [<Anterosuperior chondrolabral separation. Posterior-inferior labral fraying. No paralabral cyst>]

Cartilage:

Femoral: [<Normal>]

Acetabular: [<Focal high-grade thinning anterosuperiorly over 5 × 4 mm>]

Capsule/ligaments: [<Normal>]

Visualized muscles/tendons:

Gluteal: [<Low-grade partial tear gluteus medius at lateral facet attachment. Enthesophyte formation>]

Adductors: [<Normal>]

Iliopsoas: [<Normal>]

Lateral rotators: [<Normal>]

Hamstrings: [<Mild tendinosis. Enthesophyte formation>]

Bones: [<Otherwise normal>]

Vessels: [<Normal>]

Nerves: [<Normal>]

Soft tissues: [<Normal>]

Viscera: [<Visualized pelvic structures appear normal. No lymphadenopathy by size criteria. No significant free fluid in the pelvis>]

Miscellaneous:

Sacroiliac joint: [<Normal>]

Pubic symphysis: [<Normal>]

IMPRESSION:

1. Mixed CAM and Pincer-type deformity of right hip with anterosuperior chondrolabral separation and focal acetabular high-grade chondrosis.

2. Partial tear gluteus medius tendon with mild trochanteric bursitis.

10

The Knee

Avneesh Chhabra, Vibhor Wadhwa, Ty K. Subhawong, and Theodoros Soldatos

The knee is a pivotal hinge joint, which connects the bones of the upper and lower leg, and allows flexion and extension, as well as limited medial and lateral rotation. It is stabilized by a complex arrangement of ligaments, tendons and muscles.

The knee is arbitrarily divided into medial and lateral compartments, in which the medial and the lateral femoral condyles articulate with the respective articular surfaces of the tibial plateau, and patellofemoral compartment, in which the patella articulates with the femoral trochlea. The three compartments share a common joint capsule, composed of a strong outer fibrous layer, with local thickenings, which form ligaments, and a thin inner synovial membrane. Superiorly, the capsule attaches to the femur, immediately proximal to the articular margins of the condyles, and inferiorly on the tibia, distal to the cartilage. Anteriorly, the synovial membrane is separated from the capsule, which attaches to the patella and lines the posterior surface of infrapatellar fat pad. The synovial membrane extends posteriorly through the joint space and surrounds the two cruciate ligaments, rendering them extrasynovial. Posteriorly, the capsule attaches at the cartilaginous margins of the femoral condyles. The capsule is deficient on the lateral condyle, allowing the popliteus tendon to exit the joint.

Figures 1 to 6 show the normal MR appearance of important knee joint structures. A systematic image analysis and structured reporting is prudent for optimal diagnostic assessment of the knee structures. This chapter discusses the imaging evaluation approach and describes how to fill in the structured checklist (Box 1). Conceptual details of related MR physics and imaging protocol are discussed in the chapter on MR protocol optimization.

IMAGE EVALUATION

The below-outlined stepwise interpretation approach is only a practical guide, and all structures of the knee should be evaluated in multiple planes for optimal assessment. This will also help readers perceive which structures are best depicted/evaluated in which particular plane.

1. Line up the similar-plane fat-saturated (fs) and non-fs images and synchronize them for

tandem evaluation.

2. Start with the sagittal and axial images to look for possible knee effusion or Baker cyst. Check on sagittal and coronal images for marrow abnormalities, such as red marrow reconversion, fracture, contusion, or mass lesion. Subsequently, check for cartilaginous or osteochondral bodies and assess the bony alignment.
3. For the internal structures, use coronal and sagittal images. Coronal images are useful for assessing free edge abnormalities of the meniscal bodies, evaluating the anterior and posterior meniscal roots, and detecting displaced flap or bucket-handle components of meniscal tears. The anterior cruciate ligament (ACL) and posterior cruciate ligament (PCL) are also best seen on coronal images and different bundles can be outlined. Anterior-most coronal images show patellofemoral cartilage erosion-related marrow abnormalities, whereas posterior most images are good for detecting Baker cyst rupture-related fluid leakage and the popliteal neurovascular bundle. Mid-coronal images are useful for the evaluation of the medial collateral ligament (MCL) complex and lateral collateral ligament (LCL) complex.
4. Sagittal images are useful for secondary look at the meniscal horns and roots. The normal ACL should parallel the roof of the intercondylar notch (Blumensaat line) on these images. All fat pads are well evaluated on sagittal images and secondarily on axial images, including Hoffa's, quadriceps, and prefemoral fat pads. Synovial thickening, debris, bodies, and abnormality of plicae are also well seen on these images. The posterior joint capsule, patellar tendon, quadriceps tendon, and semimembranosus (especially the pars distalis) tears are nicely seen on sagittal images. Finally, sagittal images are essential for establishing patella alta and abnormal tibial translation.
5. Axial images are useful for the evaluation of patellofemoral malalignments (tilt and subluxation). While coronal and sagittal images are ideal for tibiofemoral articuar cartilage (coronal and sagittal both) and trochlear cartilage (sagittal images), axial images are ideal for evaluation of the cartilage of patella and apex of the trochlear sulcus. Capsular thickenings of anterior and posterior knee (including the medial and lateral retinaculae, medial and LCLs, posterior oblique ligament, oblique popliteal ligament, and arcuate ligament) are best seen on the axial images. Finally, the axial images are optimal for assessing the gastrocnemius, popliteus, pesanserinus and semimembranosus tendons, muscles, 2nd look at the collateral and cruciate ligaments, regional mass lesions and evaluation of the neurovascular bundles.

BOX 1: The Structured Report: Knee

The checklist for structured reporting of MR imaging of the knee. For each field, *Normal* is considered default in the dictation whereas the rest of the elements describe various

pathologies that could be encountered during imaging evaluation. See Appendices 1 and 2 at the end of the chapter for a sample completed reports of normal and abnormal examination results.

EXAMINATION: MRI OF THE [RIGHT/LEFT] KNEE [WITH/WITHOUT] CONTRAST

FINDINGS:

Fluid: [<Normal> <Small effusion> <Moderate effusion> <Large effusion> <Baker cyst (present / partially ruptured)> <Synovial hypertrophy> <Cartilaginous or osteochondral bodies>]

Medial compartment:

Medial meniscus: [<Normal> <Degenerative free edge fraying> <Incomplete or complete radial tear/Oblique tear/Horizontal tear/Longitudinal tear/Flap tear/Displaced bucket-handle tear>]

Medial collateral ligament: [<Normal> <Thickened> <Acute sprain>]

Medial femoral condyle cartilage: [<Normal>]

Medial tibial plateau cartilage: [<Normal>]

Posteromedial corner:

Semimembranosus tendon: [<Normal> <Tendinosis> <Tear>]

Posterior oblique ligament: [<Intact> <Acute Sprain>]

Lateral compartment:

Lateral meniscus: [<Normal> <Degenerative free edge fraying> <Incomplete or complete radial tear/Oblique tear/Horizontal tear/Longitudinal tear/Flap tear/Displaced bucket-handle tear>]

Lateral collateral ligament: [<Normal> <Thickened> <Acute sprain>]

Lateral femoral condyle cartilage: [<Normal>]

Lateral tibial plateau cartilage: [<Normal>]

Posterolateral corner:

Popliteus tendon: [<Normal> <Tendinosis> <Partial tear>]

Popliteofibular ligament: [<Intact> <Acute sprain>]

Arcuate ligament: [<Intact> <Acute sprain>]

Proximal tibiofibular joint: [<Normal> <Osteoarthrosis> <Effusion>]

Anterior compartment:

Alignment: [<Normal> <Patella alta/Patella infera> <Patellar tilt> <Lateral/Medial patellar subluxation>]

Quadriceps tendon: [<Normal> <Tendinosis> <Tear> <Enthesopathy> <Quadriceps fat pad edema/Prefemoral fat pad edema>]

Patellar tendon: [<Normal> <Tendinosis> <Tear> <Enthesopathy>]

Patellar cartilage: [<Normal>]

Trochlear groove: [<Normal> <Shallow> <Prominent lateral ridge>]

Trochlear cartilage: [<Normal>]

Plica: [<Normal / Thickened> <Sprained ligamentum mucosum>]

Hoffa fat pad: [<Normal> <Superolateral edema> <Shearing injury>]

TT–TG distance: [__] cm

Intercondylar compartment:

Anterior cruciate ligament: [<Normal> <Mucoid degeneration> <Sprain>]

Posterior cruciate ligament: [<Normal> <Mucoid degeneration> <Sprain>]

Bones: [<Otherwise normal>]

Muscles: [<Normal>]

Vessels: [<Normal>]

Nerves: [<Normal>]

Other:

IMPRESSION:

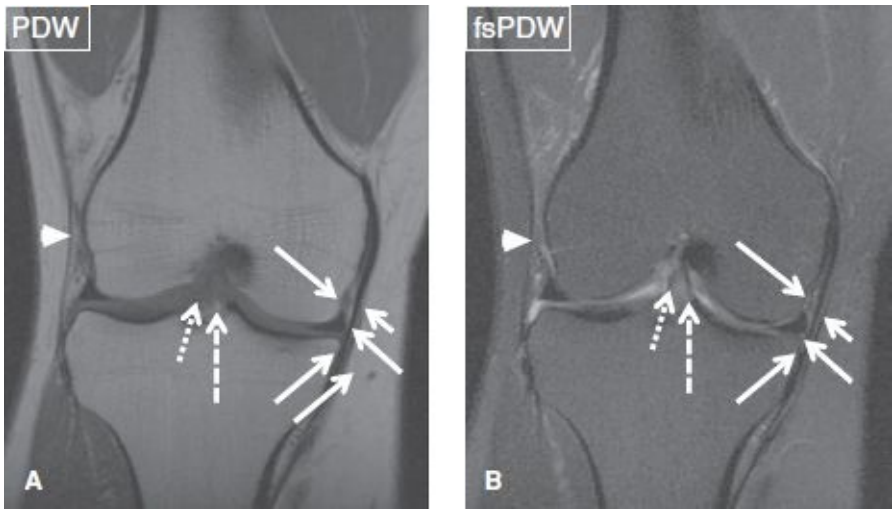

Fig. 1: Normal knee MR anatomy. Anterior coronal images **(A, B)** demonstrate the iliotibial band (*arrowheads*), 1st layer of the medial collateral ligament (*short arrows*), superficial (*medium arrows*) and deep (*long arrows*) medial collateral ligament, as well as the anteromedial (*dashed arrows*) and posterolateral (*dotted arrows*) bundles of the anterior cruciate ligament.

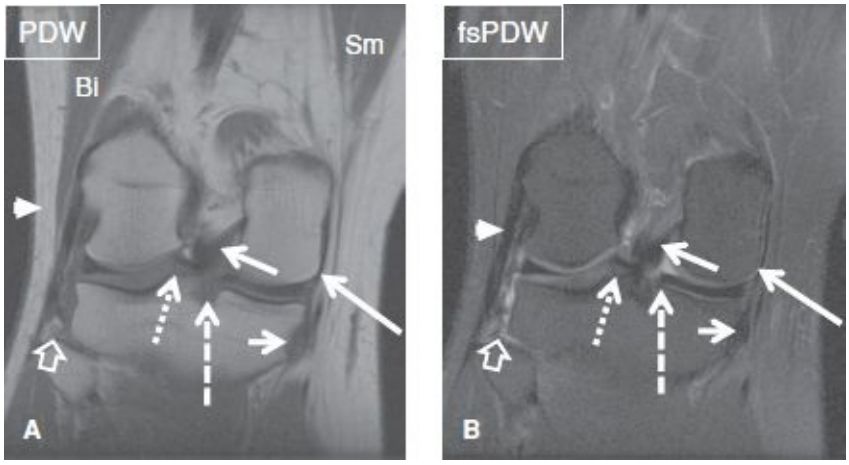

Fig. 2: Normal knee MR anatomy. Posterior coronal images **(A, B)** show the lateral collateral ligament (*arrowheads*), popliteofibular ligament (*open arrows*), posterior oblique ligament (*long arrows*), posterior cruciate ligament (*medium arrows*), posterior root of the medial (*dashed arrows*) and lateral (*dotted arrows*) meniscus, semimembranosus muscle (Sm), semimembranosus tendon (*short arrows*) and biceps femoris muscle (Bi).

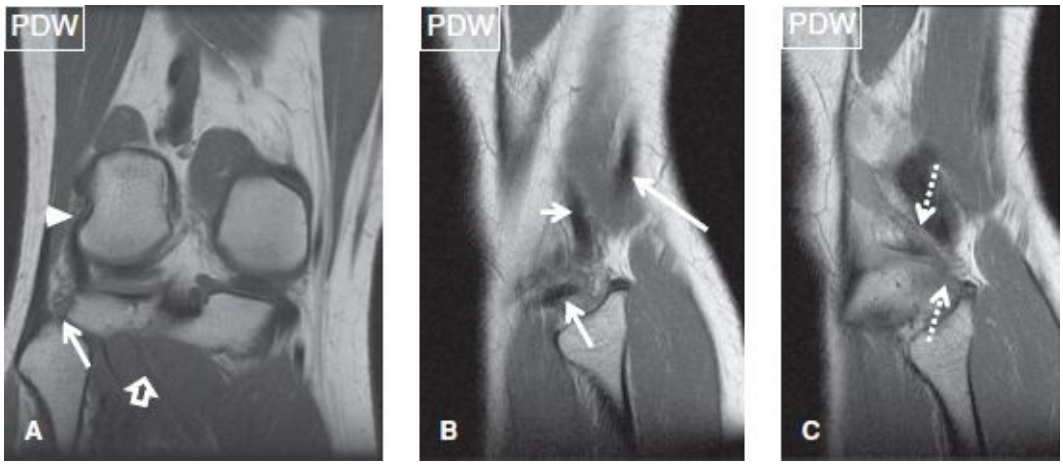

Fig. 3: Normal knee MR anatomy. Posterior coronal **(A)** and sagittal **(B, C)** images show the popliteus tendon (*arrowhead*) and myotendinous junction (*open arrow*), biceps femoris tendon (*long arrow*), popliteofibular ligament (*medium arrows*), lateral collateral ligament (*short arrow*), and arcuate ligament (*dotted arrows*) arising from the tip of styloid process.

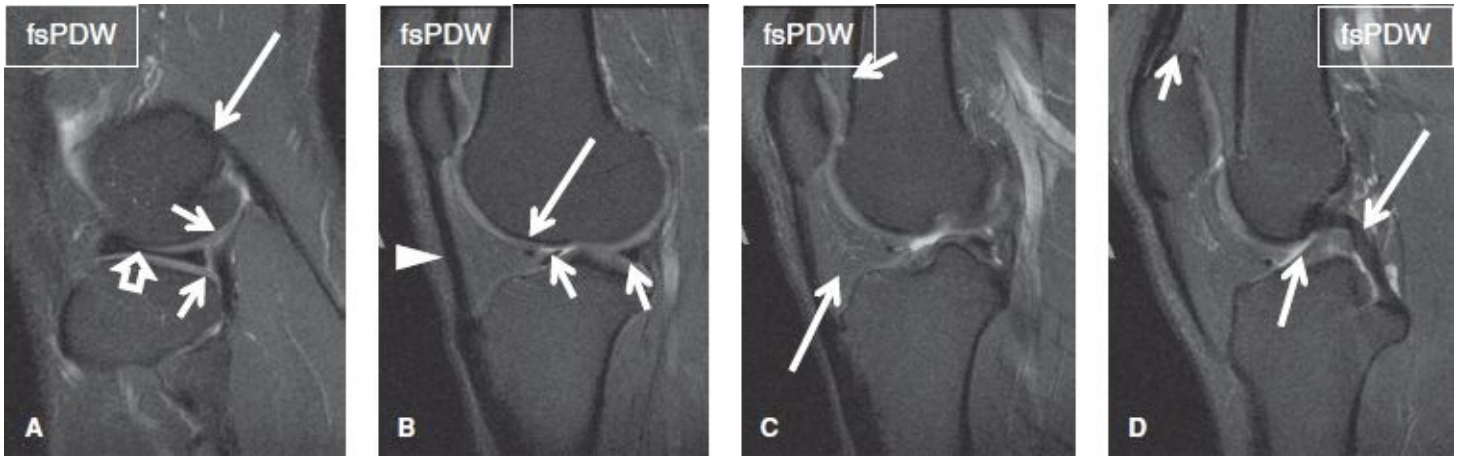

Fig. 4: Normal MR knee anatomy. Sequential lateral sagittal images. **A:** *Open arrow,* body of the lateral meniscus; *short arrows,* superior and inferior popliteomeniscal fasciculi; *long arrow,* origin of the lateral head of the gastrocnemius muscle. **B:** *Short arrows,* anterior and posterior horns of the lateral meniscus; *long arrow,* transverse meniscal ligament; *arrowhead,* patellar tendon. **C:** *Long arrow,* Hoffa's fat pad; *short arrow,* prefemoral fat pad. **D:** *Short arrow,* quadriceps fat pad; *medium arrow,* anterior cruciate ligament; *long arrow,* posterior cruciate ligament.

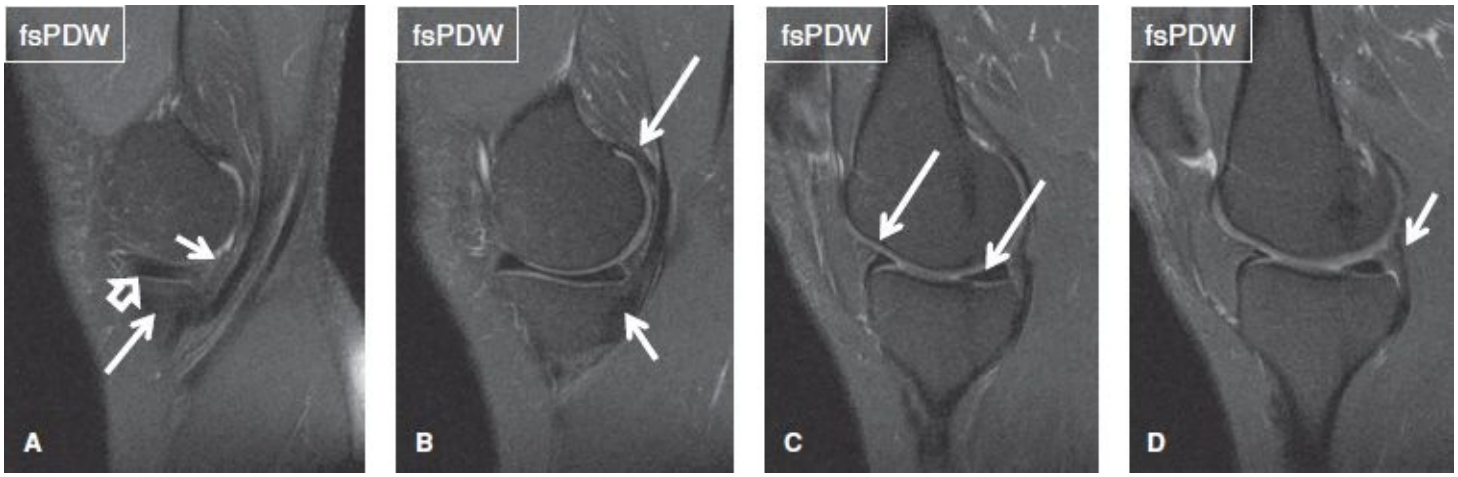

Fig. 5: Normal knee MR anatomy. Sequential medial to sagittal images. **A:** *Open arrow,* body of the MM; *short arrow,* meniscocapsular junction; *long arrow,* pars reflexa of the semimembranosus tendon. **B:** *Short arrow,* pars distalis of the semimembranosus tendon; *long arrow,* medial head of the gastrocnemius muscle. **C:** *Arrows,* anterior and posterior horns of the MM. **D:** *Arrow,* posterior oblique ligament and capsular reflection of the semimembranosus tendon.

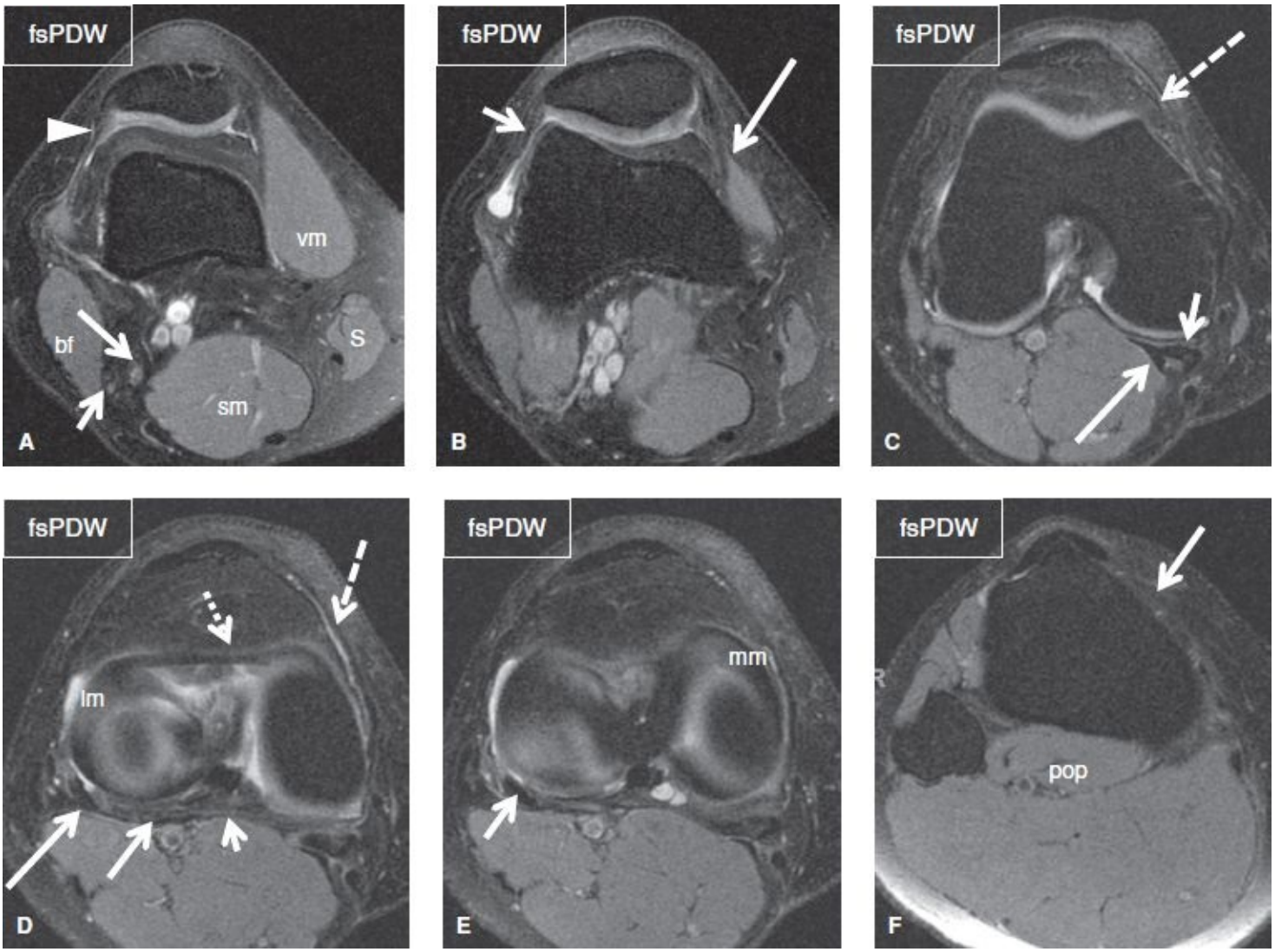

Fig. 6: Normal knee MR anatomy. Sequential axial images. **A:** *Arrowhead,* vastus lateralis obliquus; *short arrow,* common peroneal nerve; *long arrow,* tibial nerve; vm, vastus medialis muscle; S, sartorius muscle; sm, semimembranosus muscles; bf, biceps femoris muscle. **B:** *Short arrow,* lateral patellofemoral ligament; *long arrow,* medial retinaculum. **C:** *Dashed arrow,* medial patellofemoral ligament; *short arrow,* semimembranosus tendon; *long arrow,* medial head of the gastrocnemius tendon. **D:** *Dashed arrow,* medial patellomeniscal ligament; *dotted arrow,* transverse meniscal ligament; lm, lateral meniscus; *short arrow,* oblique popliteal ligament; *medium arrow,* medial bundle of the arcuate ligament; *long arrow,* lateral bundle of the arcuate ligament. **E:** *Arrow,* popliteus tendon underneath the lateral bundle of the arcuate ligament; mm, medial meniscus. **F:** *Arrow,* medial patellotibial ligament; pop, popliteus muscle.

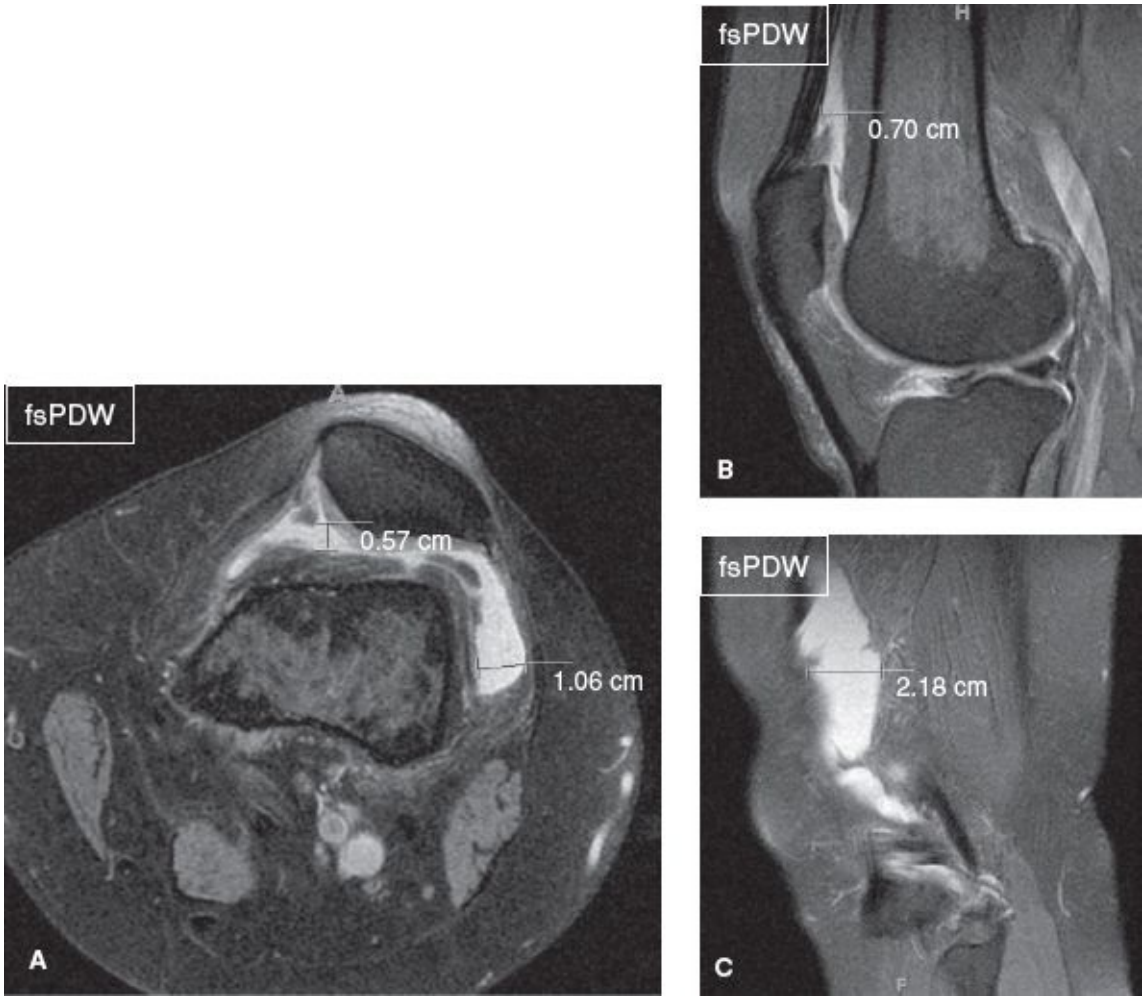

Fig. 7: Small joint effusion. On axial **(A)** and midsagittal **(B)** images, the anteroposterior distance of the effusion at its widest point in the midline of the suprapatellar pouch exceeds 5 mm and transverse diameter exceeds 10 mm in the lateral recess. **C:** On the respective far-lateral sagittal image, the anteroposterior distance of the effusion at its widest point in the lateral aspect of the suprapatellar pouch also exceeds 10 mm.

HOW TO FILL THE STRUCTURED REPORT

FLUID: [<Normal> <Small effusion> <Moderate effusion> <Large effusion> <Baker cyst (present / partially ruptured)> <Synovial hypertrophy> <Cartilaginous or osteochondral bodies>]

Typically, effusion in the knee joint first accumulates in the suprapatellar bursa, a potential space, which normally contains minimal amount of fluid. Joint effusion is established on sagittal images when the anteroposterior distance of the effusion at its widest point in the midline of the suprapatellar pouch is more than 5 mm or when the transverse distance of the effusion at its widest point in the lateral recesses on the axial image exceeds 10 mm (Fig. 7). Joint effusion can be graded as small (minimally exceeding the criteria as described), moderate (distending anterior and posterior recesses), and large (substantial distention of all recesses). Additional components, such as fat-fluid level or hematocrit level indicating recent intra-articular fracture, should be identified (Figs. 8, 9). The normal

synovium is a thin imperceptible layer. With worsening internal derangement, whether mechanical or inflammatory, it may undergo thickening, with or without associated fibrofatty proliferation of the prefemoral fat pad. Synovial thickening can be graded as mild, moderate, or extensive. The suprapatellar bursa is the most frequent site of lipoma arborescens (villous lipomatous proliferation), a rare benign intra-articular lesion of unknown etiology, which is characterized by diffuse replacement of the subsynovial tissue by mature fat cells. On MR imaging, the entity appears as frond-like proliferation of the synovium, which features fat-like signal on all sequences. Visualization of the fronds is improved in case effusion co-exists. Chemical shift artifact is sometimes evident at the fat–fluid interface on gradient-echo images (Figs. 9, 10). This diagnosis should be made in younger individuals and they may benefit from synovectomy. In older subjects, partial (uni-compartmental) or bicompartmental joint involvement with lipoma arborescence is usually a manifestation of worsening internal derangement.

Fig. 8: Moderate and large knee joint effusion. Compared to Figure 7, these sagittal midline images demonstrate increased amount of synovial fluid, corresponding to moderate **(A)** and large **(B)** joint effusion.

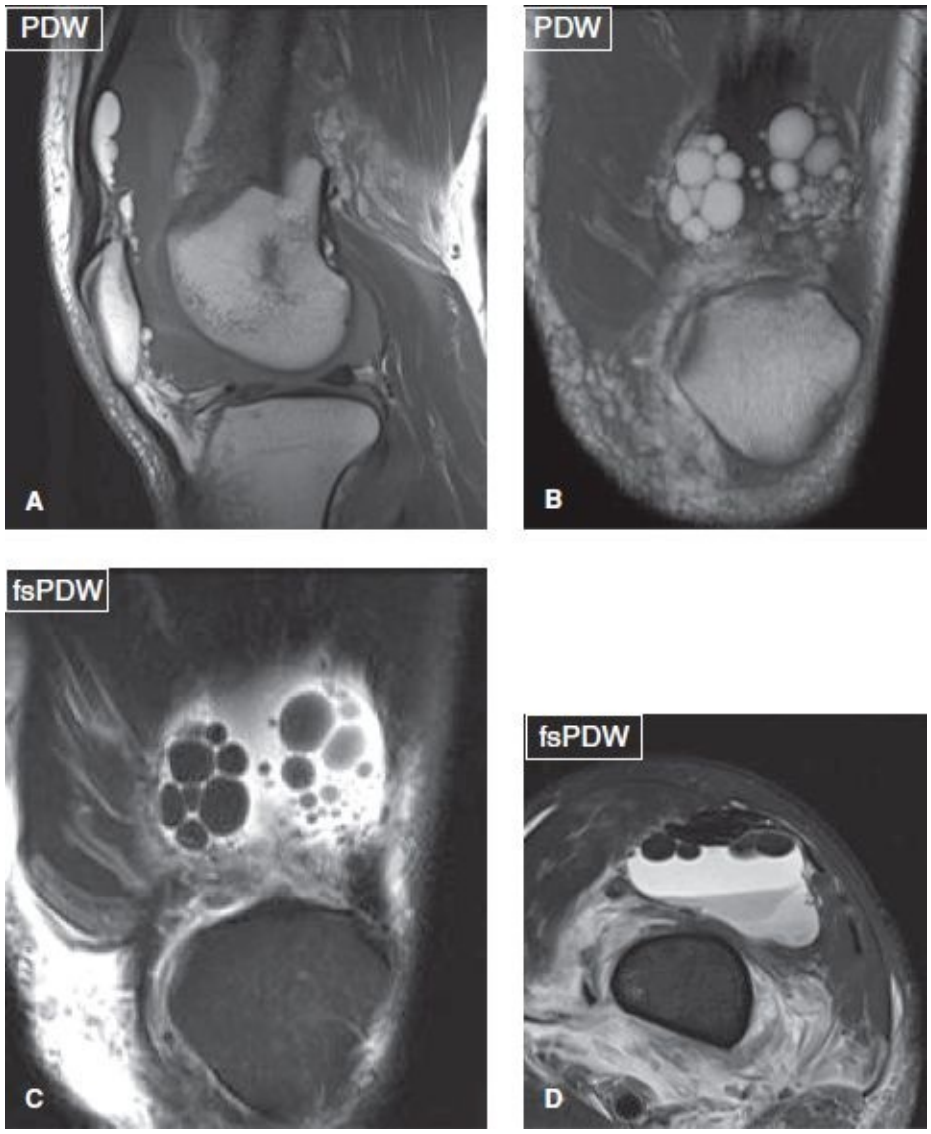

Fig. 9: Moderate lipohaemarthrosis. On sagittal **(A),** coronal **(B, C),** and axial **(D)** images, a femur fracture and lipohaemarthrosis with multiple fat globules can be seen.

The knee is a common location for pigmented villonodular synovitis, in which the synovium is focally or diffusely thickened and features nodularity and low signal on all sequences (even more evident on gradient-echo images related to blooming artifacts) due to hemosiderin deposition. Joint effusion is typically present. The entity is usually mono-articular, involves large joints, and is infrequently associated with bone erosions (Figs. 11–14). Differentiation from hemophilic arthropathy is difficult and is usually based on clinical history (Fig. 15). Other causes of joint hemorrhage include rheumatoid arthritis and prior arthroscopy. Other causes of hypointense synovial thickening or lesions include gout and amyloidosis; however, these entities are predominantly para-articular rather than intra-articular. A thorough search should be performed for intra-articular loose bodies. The latter may be a) cartilaginous, featuring intermediate signal on T1W and PDW images, or b) osteochondral, demonstrating variable signal, depending on the degree of ossification, but usually showing hypointense cortical lining and internal marrow signal. In case one or two bodies are detected, the articular surfaces should be checked for potential donor sites. Multiple loose bodies in the knee are commonly encountered in primary and secondary

synovial osteochondromatosis (Figs. 16, 17). In the primary variety, the bodies are numerous and similar sized with no obvious predisposing pathology or internal derangement. The secondary variety usually affects older individuals with a predisposing underlying cause or internal derangement, such as trauma or arthritis and the bodies are of variable size and fewer in number.

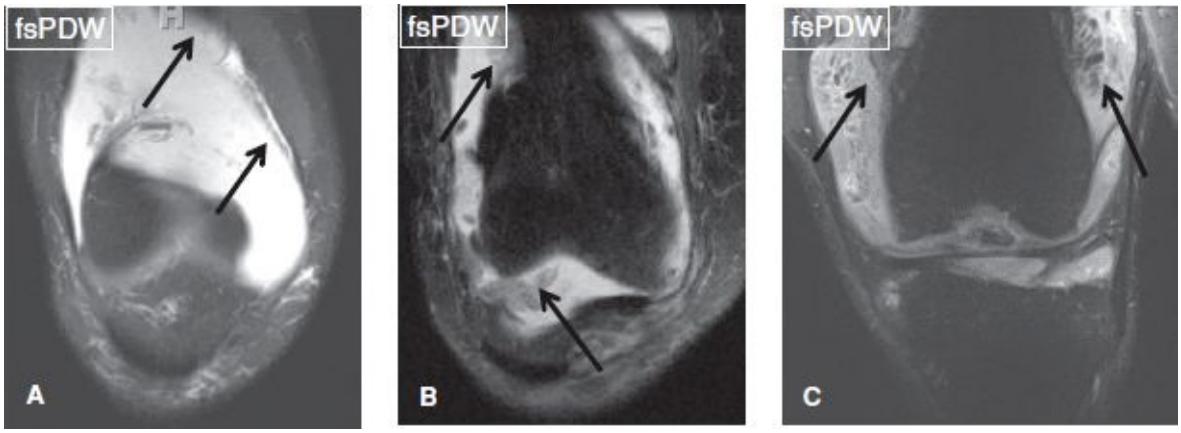

Fig. 10: Synovial thickening. Coronal images from different cases demonstrate mild **(A),** moderate **(B),** and severe **(C)** synovial thickening (*arrows*). The frond-like projections of the synovium in **C** are named as lipoma arborescens.

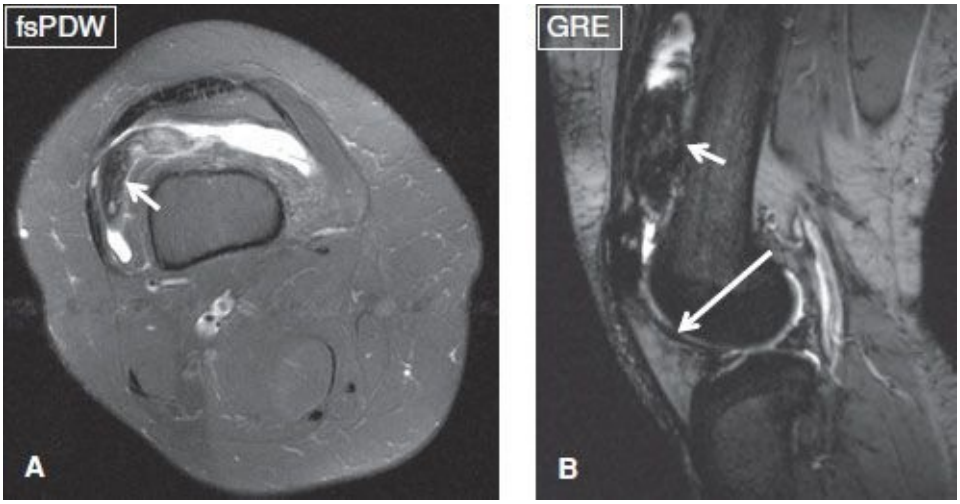

Fig. 11: Pigmented villonodular synovitis. Axial spine echo **(A)** and sagittal gradient echo **(B)** images from the same subject demonstrate focal PVNS (*short arrows*) with blooming artifact on GRE from internal hemorrhages. Notice diffuse hypointensity (*long arrow*) of the adjacent synovium from hemosiderin lining, a reflection of prior episodes of recurrent hemorrhages.

Fig. 12: Pigmented villonodular synovitis. Axial **(A)** and sagittal **(B)** images show a large erosion (*long arrows*) of the femoral metaphysis with bone marrow edema, associated with internal hypointensity (*short arrows*) within the hypertrophied synovium, a biopsy-proven case of focal PVNS.

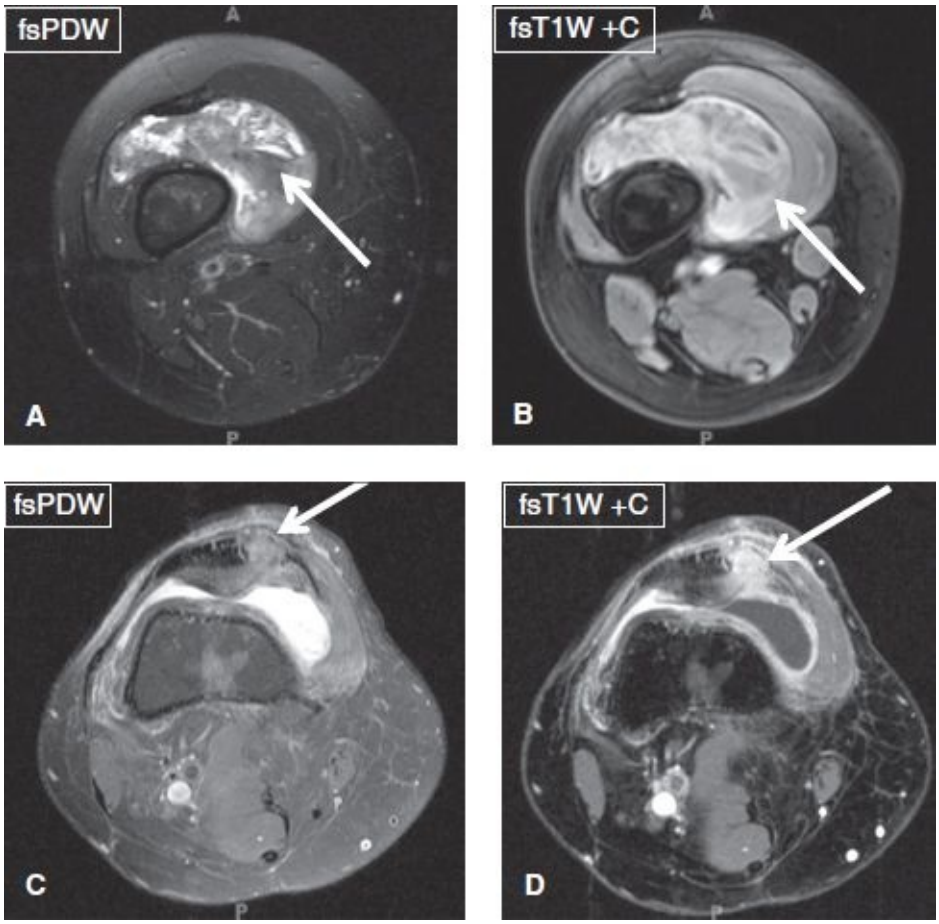

Fig. 13: Diffuse pigmented villonodular synovitis. **A, B:** Axial images demonstrate diffuse hypointense synovial thickening that enhances on contrast (*arrows*). **C, D:** Images obtained after synovectomy show recurrence at the surgical site (*arrows*).

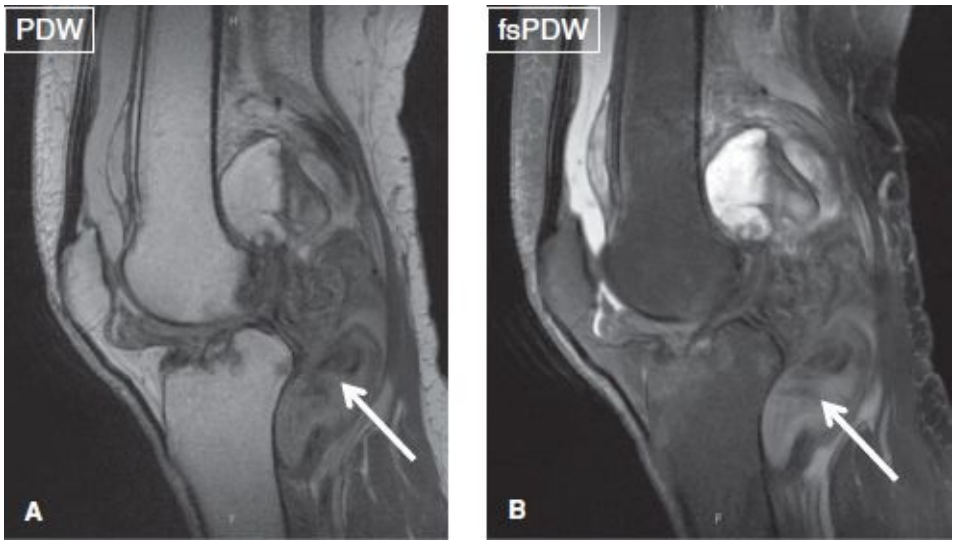

Fig. 14: Diffuse pigmented villonodular synovitis. Sagittal images demonstrate diffuse hypointense synovial thickening (*arrows*), a biopsy-proven PVNS.

Baker (popliteal) cyst is the most commonly encountered cyst about the knee and is considered a sign of internal derangement or degenerative disease. It is located in the posteromedial aspect of the joint and represents abnormal accumulation of joint fluid within a normally present synovial bursa, which lies between the medial head of the gastrocnemius tendon and the semimembranosus tendon. Typically, uncomplicated Baker cysts have thin low-signal wall and homogeneous high T2 signal intensity and extend in the inferomedial direction, respecting the intermuscular planes. The cysts are qualified as small (<3 cm), moderate (4 to 6 cm), and large (>6 cm) based on the length. Sagittal images demonstrate the extent of the cyst, posterior coronal images show potential leck whereas axial images reveal the cyst's neck, which is essential for the diagnosis (Fig. 18). Popliteal cysts are asymptomatic but can undergo rupture and dissect along or into adjacent structures, clinically simulating thrombophlebitis. Rupture typically results in edema in the surrounding fascial planes and subcutaneous fat, with fluid tracking inferiorly along the medial side of the medial gastrocnemius muscle plane (Fig. 19). Blood products from intracystic hemorrhage or protein-rich synovial fluid may result in increased signal on T1W images and the cysts can extend variable distances along the knee; however, they can be distinguished from more ominous lesions based on identification of the neck location, multiloculated cystic appearance (usually following multiple prior episodes of rupture and chronicity), and peripheral enhancement on contrast. Uncommonly, popliteal cysts contain debris, loose (cartilaginous or osteochondral) bodies, or pigmented villonodular synovitis (PVNS) (Fig. 20).

MEDIAL COMPARTMENT:

Medial meniscus: [<Normal> <Degenerative free edge fraying> <Incomplete or complete radial tear/Oblique tear/Horizontal tear/Longitudinal tear/Flap tear/Displaced bucket-handle tear>]

Medial collateral ligament: [<Normal> <Thickened> <Acute sprain>]

Medial femoral condyle cartilage: [<Normal>]

Medial tibial plateau cartilage: [<Normal>]

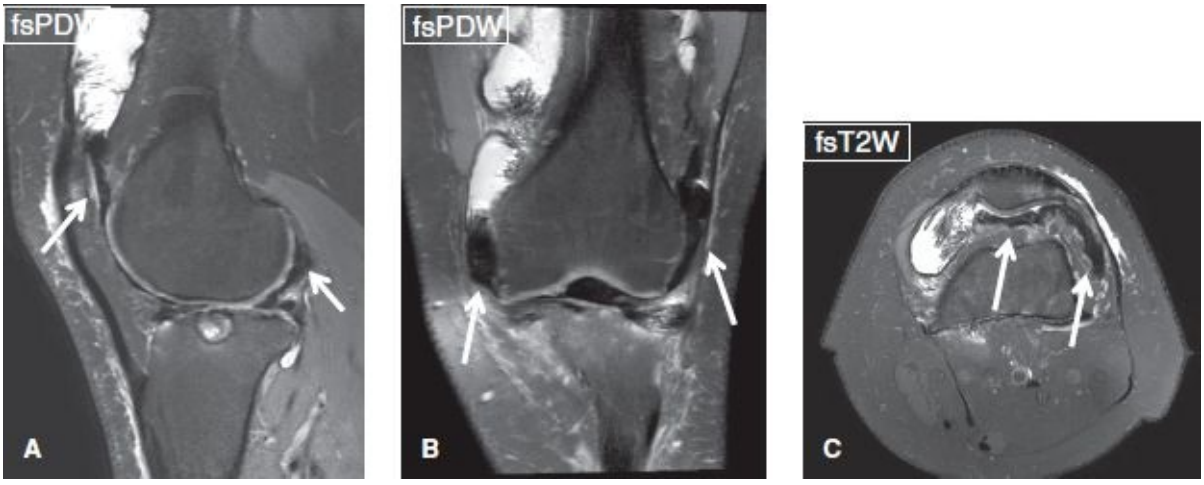

Fig. 15: Hemophilic arthropathy. Sagittal **(A),** coronal **(B),** and axial **(C)** images demonstrate diffuse hypointensity of the synovium (*arrows*), reflecting hemosiderin deposits due to repeated haemarthrosis.

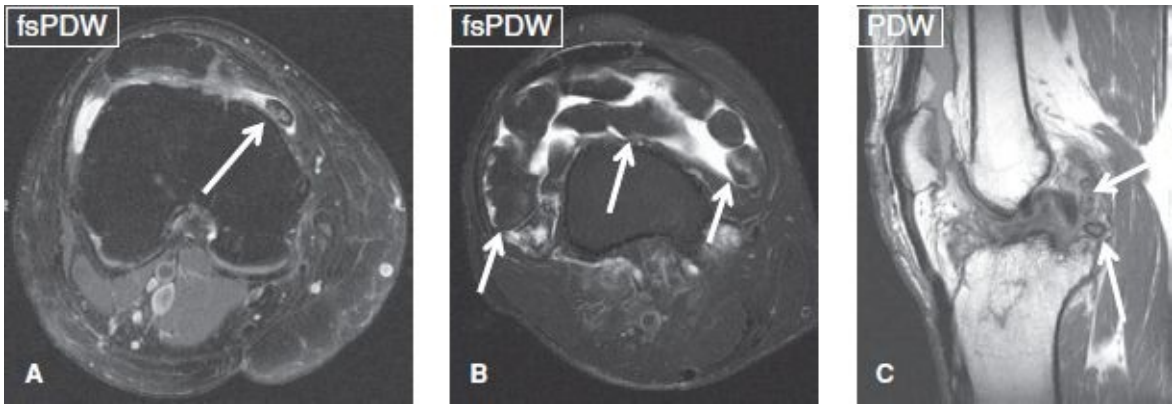

Fig. 16: Loose intra-articular bodies. Axial images. **A:** A single osteochondral body (*arrow*) is evident anterior to the medial femoral condyle. **B:** Multiple osteochondral bodies (*arrows*) of approximately the similar size are present in the suprapatellar bursa, in this case of primary osteochondromatosis. **C:** Two osteochondral bodies (*arrows*) of different size are evident in the posterior aspect of the joint space, in this case of secondary osteochondromatosis. Notice prior ACL graft failure changes.

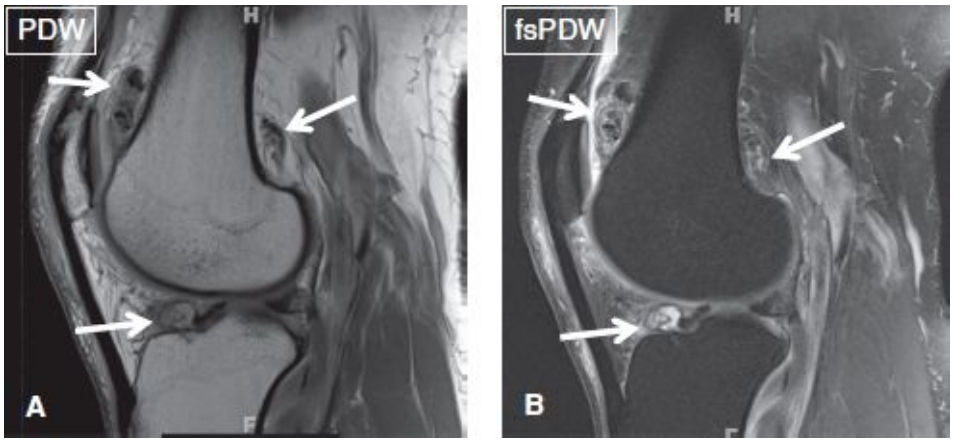

Fig. 17: Secondary osteochondromatosis. Sagittal images **(A, B)** show multiple intra-articular loose bodies (*arrows*) of different sizes in the suprapatellar bursa, intercondylar notch, and gastrocnemius recess.

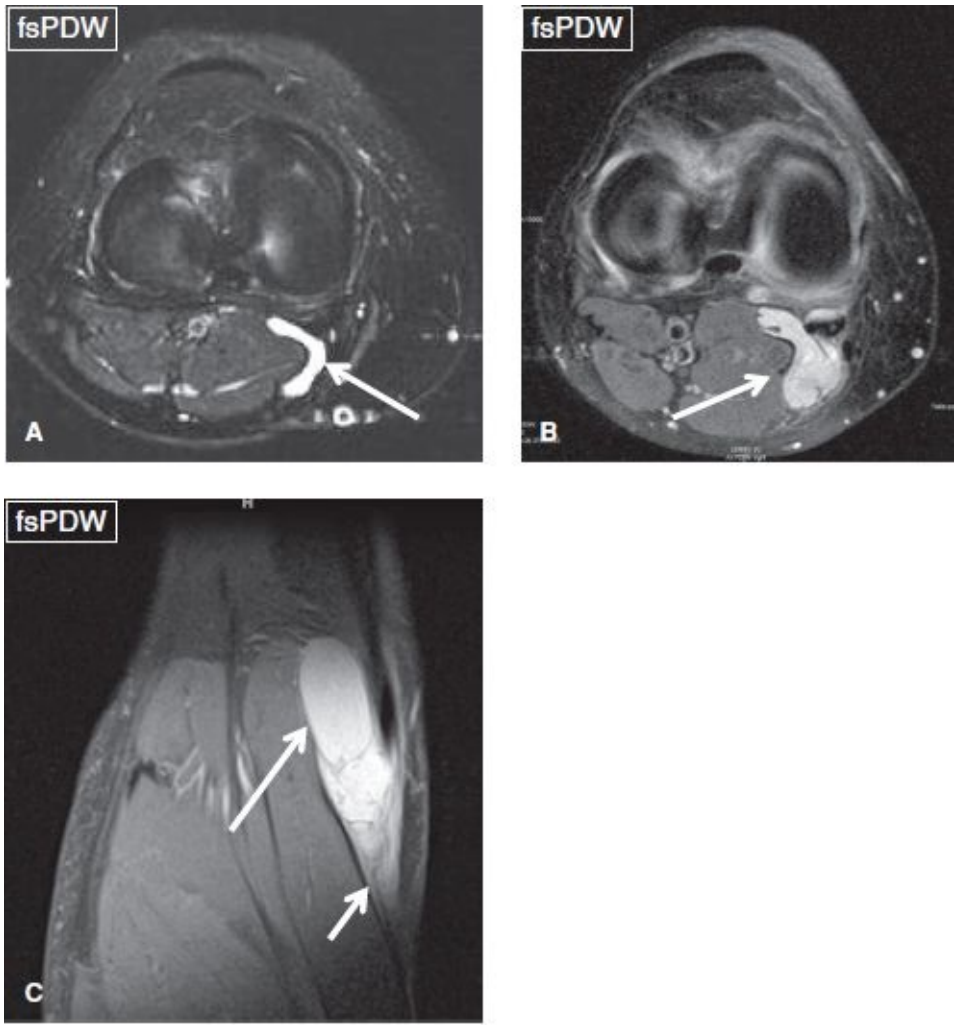

Fig. 18: Baker cyst. Axial **(A, B)** and coronal **(C)** images exhibit small, moderate, and large Baker cysts (*arrows*), respectively. Notice peri-cyst fascial edema and fluid related to recent leak from the cyst in **C** (*short arrow*).

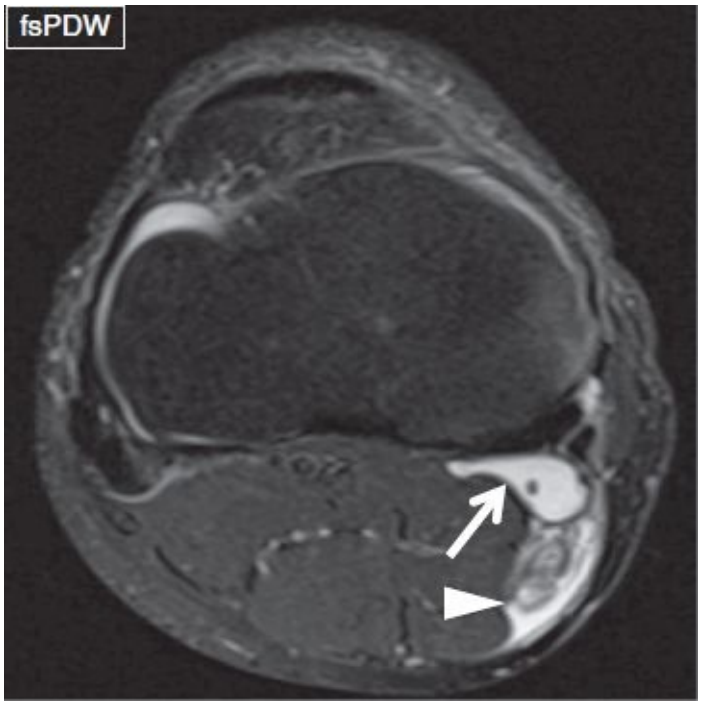

Fig. 19: Ruptured Baker cyst. Axial image shows a small Baker cyst (*arrow*), with fluid (*arrowhead*) extending posteriorly beyond the cyst margins and dissecting into adjacent muscles, indicating recent leak/rupture.

The medial meniscus (MM) and the lateral meniscus (LM) are C-shaped fibrocartilaginous structures, which are interposed between the femoral condyles and the tibial plateau. They are composed of type I collagen and encompass 65% to 75% water. The menisci bear 70% of the weight and provide proprioceptive stability, lubrication, cartilage protection, and shock absorption to the joint. Each meniscus consists of an anterior horn, a body, and a posterior horn and is triangular in cross-section, being thicker at the periphery and tapering to a thin free edge centrally. Each meniscus is fixed in the central tibial plateau by anterior and posterior roots, which represent fibers originating from the respective horns. Anteriorly, the menisci are connected via the transverse intermeniscal ligament. The MM is firmly attached to the deep medial collateral ligament (MCL) (aka meniscotibial or coronary ligament) along its entire peripheral circumference. The oblique meniscomeniscal ligament, a normal variant, originates from the anterior horn of one meniscus and inserts into the posterior horn of the contralateral meniscus. Oblique meniscomeniscal ligaments are defined as medial or lateral, based on their anterior origin, and their prevalence is about 3% to 4% (Fig. 21). Unilateral meniscomeniscal ligament is also a known variant, which connects the anterior horn of one meniscus to the posterior horn of the same meniscus. It may lead to formation of what may be called as the ring meniscus variant.

Fig. 20: PVNS localized to a Baker cyst. Axial **(A),** coronal **(B),** and sagittal **(C)** images show Baker cyst filled with hypointense material (*arrows*) in a biopsy-proven case of PVNS. **D:** Diffuse contrast enhancement is seen on intravenous gadolinium administration (*arrow*).

The normal menisci demonstrate smooth margins and uniform low signal on all imaging sequences, except in children and young adults, in whom intermediate or high intrasubstance signal in the periphery may be present, which represents normal vascularity, and should not be interpreted as abnormal. Menisci are best evaluated on non-fs proton density-weighted (PDW) sequences. The latter provide high signal to noise ratio and sharper images. However, fs-PDW provide higher specificity in detecting meniscal tears in post-meniscectomy or meniscal repair cases. Combined examination on sagittal and coronal images is essential, where the normal menisci feature smooth margins and sharp edges. In cross-section, they are triangular, with concave superior surface, flat inferior surface, convex outer curve, and apex pointing to the intercondylar notch. In the sagittal plane, provided that 4- or 5-mm thick slices have been obtained, the two most peripheral images reveal the body of the meniscus, which appears as a bow-tie or an elongated rectangle whereas the three or four more medial images show the opposing triangular shapes of the anterior and posterior horns. The posterior horn of the MM is larger than the anterior horn. As a rule, the anterior horn should never be larger than the posterior.

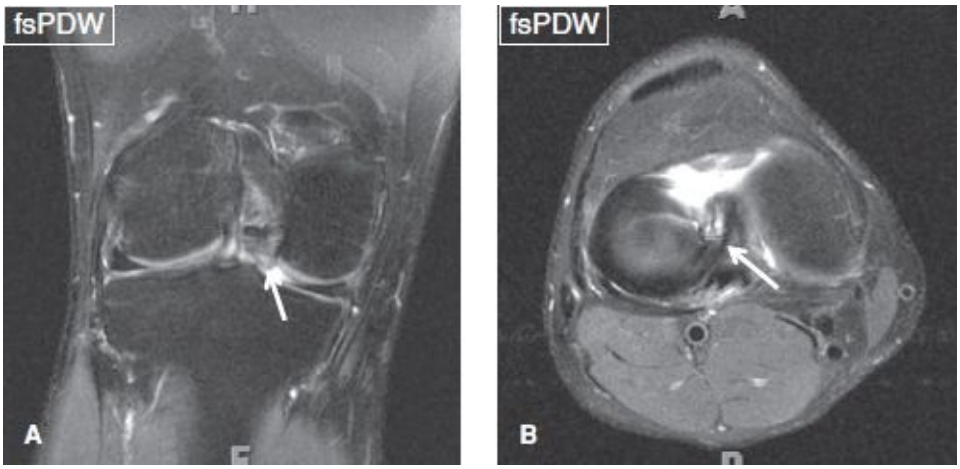

Fig. 21: Medial oblique meniscomeniscal ligament. Coronal **(A)** and axial **(B)** images demonstrate a medial oblique meniscomeniscal ligament (*arrows*), which extends from the anterior horn of the medial meniscus to the posterior horn of the lateral meniscus. Three structures in the intercondylar notch (in addition to normal ACL and PCL) raise the suspicion of a flipped bucket-handle tear, which can be mimicked by this ligament.

Fig. 22: Intrameniscal cyst. Coronal images display well-defined near fluid-like signal (*arrow*) within the posterior horn of the medial meniscus with minimal expansion.

Meniscal tears are uncommon in individuals younger than 10 years of age. In young adults, the most common mechanism is twisting injury, while in older individuals, meniscus tears result from fall or sudden squatting. The diagnostic criteria used for establishing degeneration and tears of the MM are similar to those of the LM. Clinically, there may be pain (due to inflammation around the tear) or symptoms of locking (relating to flap or bucket-handle tears) and clicking. Assessment of a possible meniscal tear is usually done clinically by locating pain and crepitation along the joint line (most sensitive signs). The palpation for these symptoms must be done while simultaneously applying a valgus or

varus stress to the knee at 30 degrees of flexion. Positive findings on clinical exam suggest meniscal tear or an articular cartilage flap.

Provocative pain in the posterior aspect of the knee with maximal flexion is usually indicative of a posterior horn meniscal tear. The McMurray test, also known as the McMurray circumduction test is a rotation test for demonstrating torn meniscus of the knee in a fully flexed position, while hand is placed at the joint line. The MM is tested in external rotation with lateral force (mnemonic *mel*) while the LM is tested in internal rotation with medial force. A tear in the meniscus may cause a pedunculated tag of the meniscus which may become jammed between the joint surfaces. This would result in a palpable or audible click on extension of the knee. Deep posterior knee pain with squatting is also indicative of a meniscal tear.

MR imaging signs of meniscal degeneration include a) intrasubstance focal or diffuse intermediate signal on all sequences, which does not abut the articular surface, and b) fraying of the free edge, which results from multiple chronic radial microtears, best depicted on coronal images. However, any fluid-like or near fluid-like signal on the fs images warrants closer look at the meniscal surface, since in that case, a tear is likely. If the fluid-like or near-fluid-like signal is relatively well-defined and is associated with some expansion of the meniscus, it is referred to as an intrameniscal cyst (Fig. 22). With three-dimensional (3D) high resolution (0.6 to 0.7 mm isotropic) imaging, many microcysts are seen within the meniscus, which, on two-dimensional (2D) images look like a larger intrameniscal cyst (Fig. 23). Since a radiology consultant is trying to help the orthopod decide whether to go or not to go for surgery and meniscal degenerative changes are so common, it is paramount that one should carefully identify meniscal tears and not spend too much time looking for or deciding whether degenerative changes are present or absent.

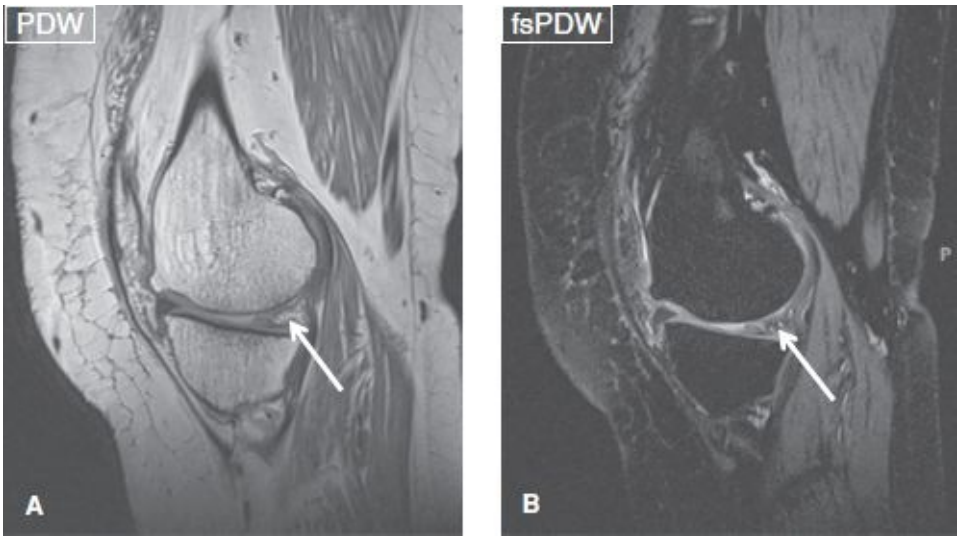

Fig. 23: Intrameniscal microcysts. Sagittal images **(A, B)** show microcysts within the posterior horn of the medial meniscus (*arrows*).

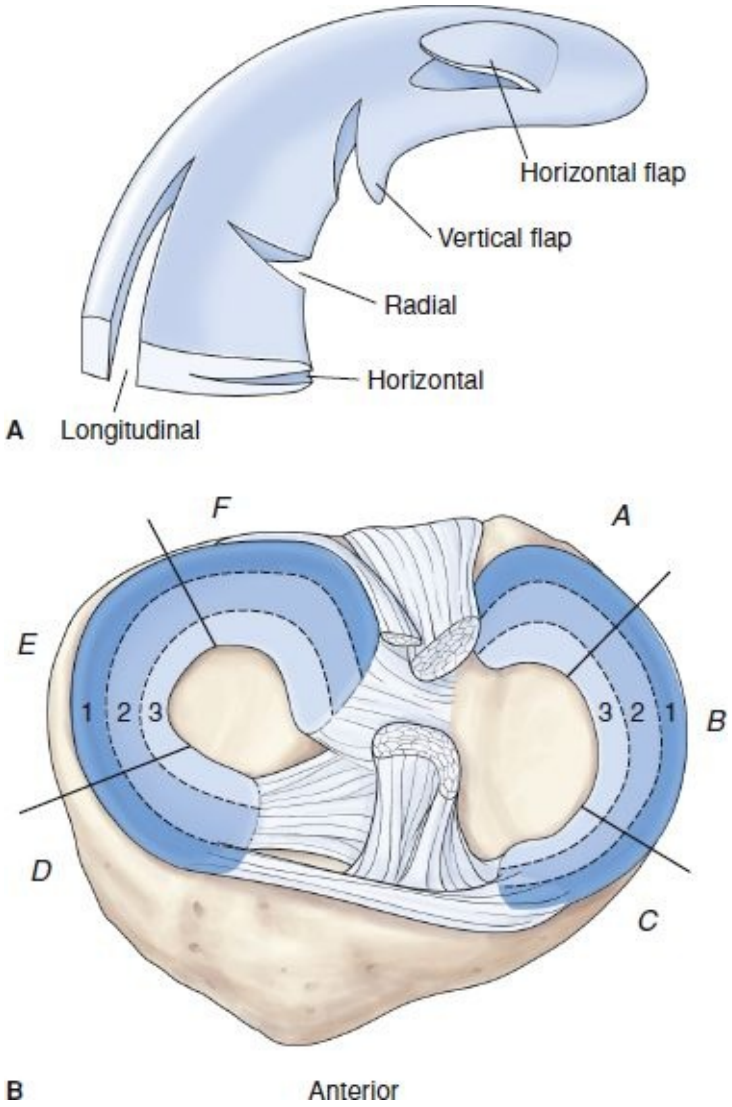

Fig. 24: Classification of meniscal tears as developed by the Knee Documentation Committee of the International Society of Arthroscopy, Knee Surgery and Sports Medicine (ISAKOS). **A:** Types of tears. **B:** Location. The meniscal parts are referred to as *A, B,* or *C* for one meniscus and *D, E,* or *F* for the other meniscus; and *1, 2,* and *3* are used for the different layers of the width of the meniscus: the red, pink, and white zones, respectively.

Meniscal tears appear as: a) fluid-like signal or sharp intermediate signal clearly contacting the articular surface on at least one image and/or b) as abnormal morphology of the meniscus. The latter criterion may not apply to menisci which have undergone prior surgery. Tears can involve the anterior horn (or root), the body, or the posterior horn (or root) of the meniscus. Recently, the International Society of Arthroscopy, Knee Surgery, and Sports Medicine (ISAKOS) has made a push for standardization of terminology used for the description of meniscal tears. The Society recommends using the following terminology for different types of tears: radial, longitudinal, horizontal, horizontal flap, and vertical flap; the meniscal parts are referred to as A, B, or C for one meniscus and D, E, or F for the other meniscus; and finally, 1, 2, or 3 for different layers of the width of the meniscus, zone 1 (tears of the meniscosynovial junction or a tear with a rim of less than 3 mm), zone 2 (tears with a rim of 3 to <5 mm), and zone 3 (tears with a rim width of 5 mm or more). The use of the terms red-red, red-white, white-white is discouraged, because of the variable vascular

supply of the menisci (Fig. 24). Conceptually, there are simple, complicated and complex tears. Based on shape, simple tears are classified into radial, longitudinal, horizontal, horizontal flap, and vertical flap. Further A and B qualifiers can be added depending upon the tear extends to one surface (incomplete) or both meniscal surfaces (complete). Finally, the committee discourages the use of the terms acute, subacute, and chronic tears.

Radial tears extend from the free edge perpendicularly to the meniscal circumference and appear as cleft on one imaging plane, and as truncation of the free edge on the other. They are characterized as incomplete or complete, based on whether they run through a part or the entire thickness of the meniscus, respectively (Fig. 25). Although radial tears may be small, consequences can be devastating: in acute radial tears, subchondral insufficiency fractures may develop as a result of twisting injury (Fig. 26). On the other hand, these are the most common tears in young adults and develop at points of weakening or change in directionality of meniscal fibers, that is, at the junction of anterior or posterior horn with the body. These progress to oblique (aka parrot beak or coapted flap) tears with increasing age (Fig. 27). In fact, the most common tears in a 40 to 60 year old individuals are oblique tears. The latter may further progress to displaced flaps in the medial (coronary recess) or lateral gutters, with resulting progressive thinning of the opposing articular cartilages over time (Figs. 28, 29). Finally, another type of radial tear is the root tear, which most commonly involves the posterior root of the MM and the anterior root of LM. Associated findings in root tears include subcortical cysts or fatty change (due to prior partial root avulsion), degenerative appearance of the meniscal root and medial extrusion of the meniscal body (Fig. 30). Less commonly, one sees avulsive subcortical linear or flame-shaped bone marrow edema, bony foot plate avulsion, and partial or complete avulsion of the root with medial extrusion of the body and/or insufficiency injury of the overlying femoral or tibial condyles (Figs. 31, 32). With partial tears, it is usually the anterior superior one-third to two-thirds of the root that is affected. The root tear itself is best seen on the sagittal and coronal images while bone marrow changes (cysts and edema) are best seen on the coronal images. One should not mistake these for the bone marrow changes at the PCL tibial attachment. Most times, the PCL-related avulsive changes are usually at the femoral attachment. Sometimes, prominent vessels at the posterior root tibial attachment may mimic these cysts as well; therefore, one should carefully look at the root before overcalling meniscal roots as abnormal. When incomplete, radial tears are one of the worst types of acute tears, as they make the meniscus deficient to tolerate hoop stress. Finally, the readers should be aware that the anatomy dictates the pathologic appearance. Since the MM and LM roots are anatomically different, the appearances of their tears also differ. MM anterior and posterior roots appear as dark uniform bands at the attachment, except on the high resolution images, when a uniform speckled appearance of the roots may be evident. Therefore, it is easy to identify focally increased signal or secondary bony changes, and the diagnosis of tear can be accomplished. On the other hand, the LM evaluation is little more challenging, in the sense that a speckled appearance is pretty common in the anterior root, whereas the posterior root shows two slips of attachment, on either side of the lateral tibial

spine (Fig. 33). Therefore, one should carefully look for the individual slips of attachment and associated bony findings before arriving at the diagnosis of root tears. Free edge radial tears can be debrided on surgery while root tears may need repair.

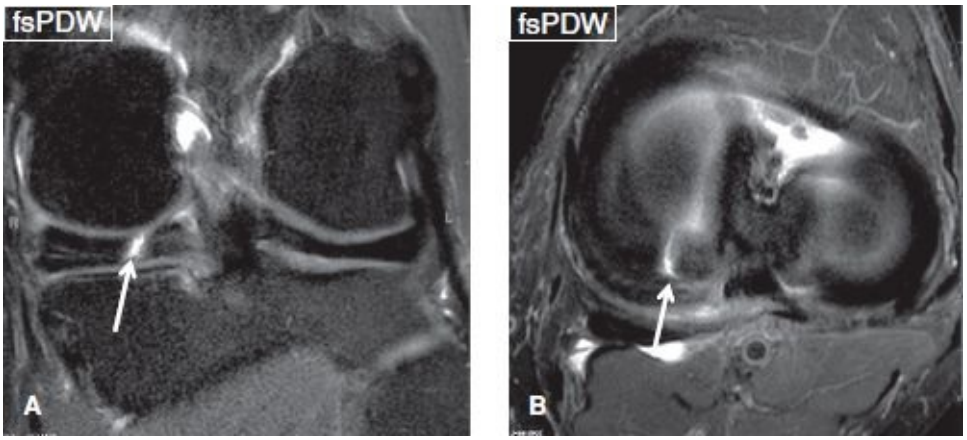

Fig. 25: Radial meniscal tear. Coronal **(A)** and axial **(B)** images show fluid-like signal (*arrows*), which runs perpendicular to the meniscal circumference and traverses nearly its entire thickness. Zone 2 and 3 are involved.

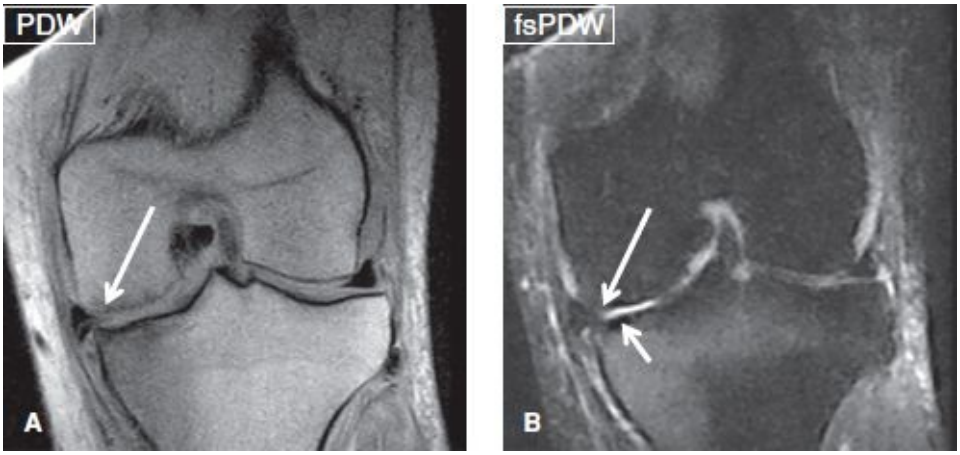

Fig. 26: Incomplete radial tear. Coronal images **(A, B)** display an incomplete radial tear (*long arrows*) as truncation of the free edge and extrusion of the body of the medial meniscus. Also note a subchondral insufficiency fracture of the medial tibial plateau (*short arrow*) with full-thickness cartilage defects.

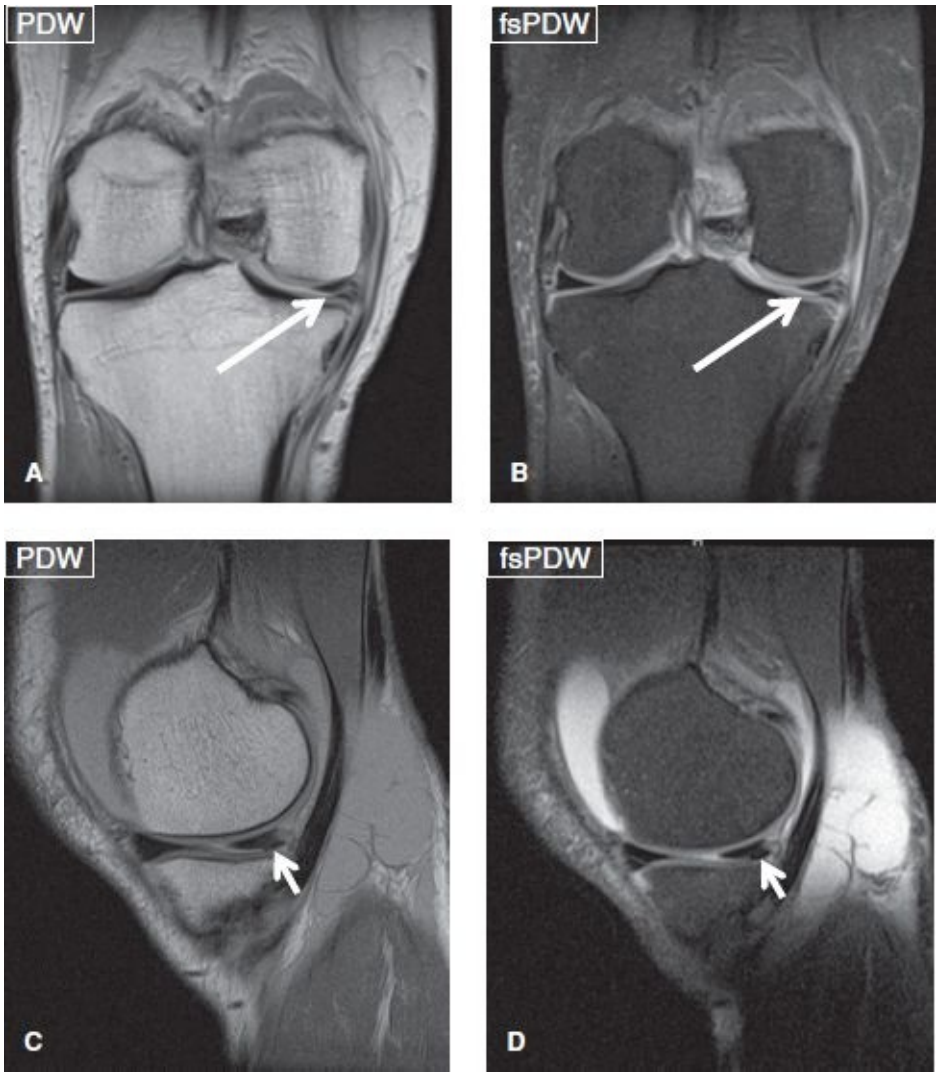

Fig. 27: Oblique (aka parrot beak/coapted flap) meniscal tear. Coronal **(A, B)** and sagittal **(C, D)** images demonstrate an oblique tear (*arrows*) at the junction of body and posterior horn of the medial meniscus, a classic and common location.

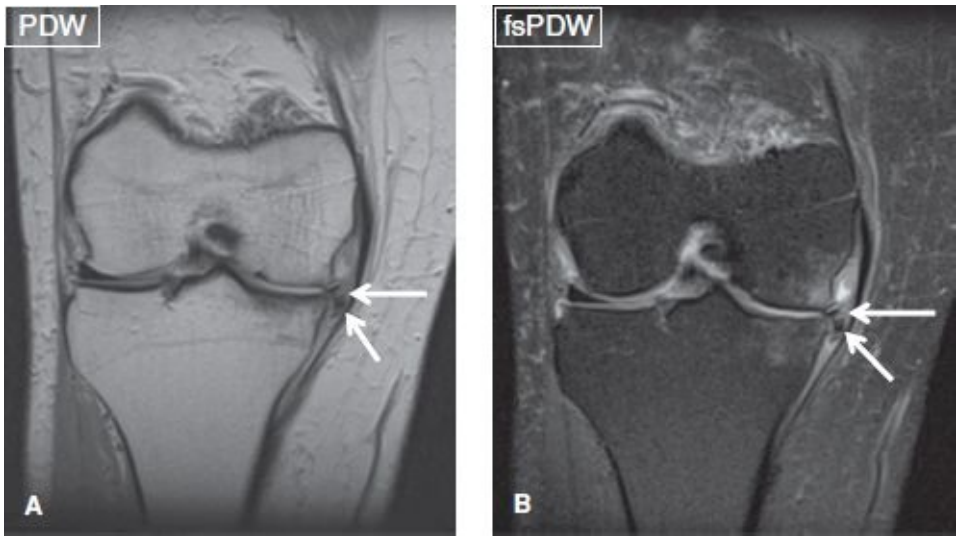

Fig. 28: Displaced flap tear. Coronal images **(A, B)** show extruded meniscus with a meniscal fragment (*arrows*) displaced within the coronary recess.

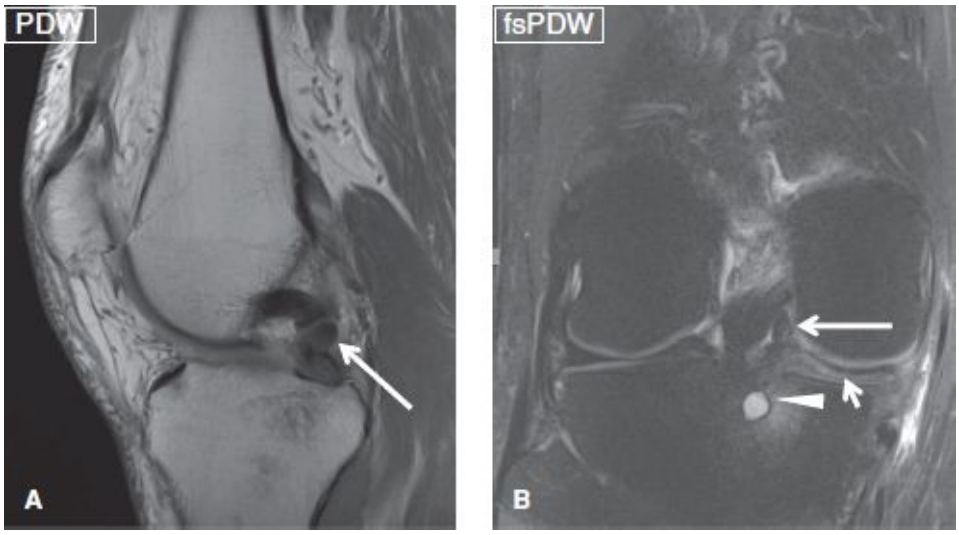

Fig. 29: Displaced flap tear. Sagittal **(A)** and coronal **(B)** images demonstrate a superiorly displaced flap tear of the posterior horn of the medial meniscus (*long arrows*). **B:** Note avulsive cystic change and bone marrow edema (*arrowhead*) at the posterior root attachment of the MM from incomplete radial tears and an additional horizontal tear of the posterior horn (*short arrow*).

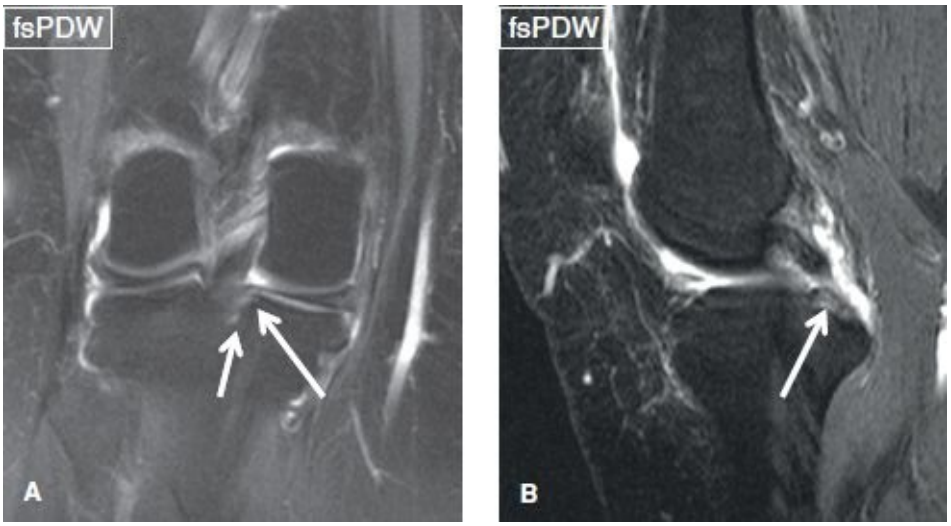

Fig. 30: Incomplete posterior root tear. Coronal **(A)** and sagittal **(B)** images exhibit fluid-like signal (*long arrows*) within the posterior root of the medial meniscus, corresponding to a partial radial/root tear. Also note avulsive cystic change (*short arrow*) adjacent to the root attachment indicating its subacute nature. Partial tears usually involve anterosuperior one-third to two-thirds of the posterior root.

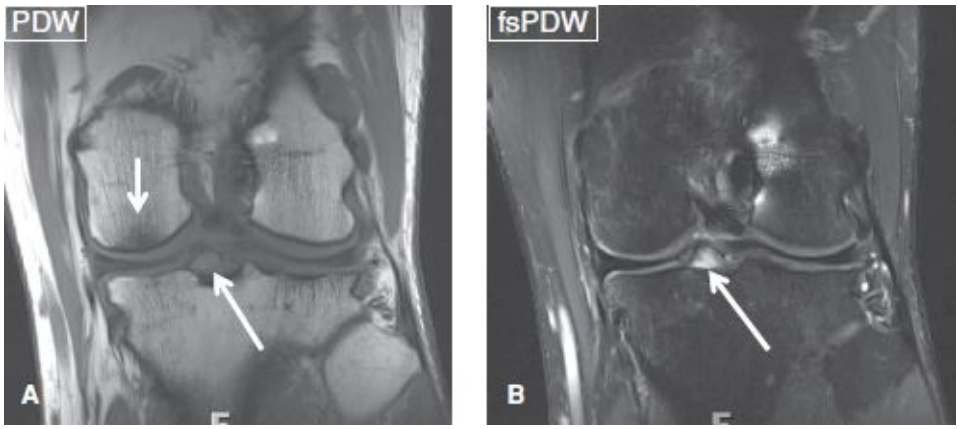

Fig. 31: Posterior root bony avulsion. Coronal images **(A, B)** show avulsion (*long arrows*) of the posterior root foot plate of the medial meniscus. Notice prior ACL repair–related artifacts and subchondral sclerosis (*short arrow*) from prior insufficiency injury of the medial femoral condyle (*short arrow*).

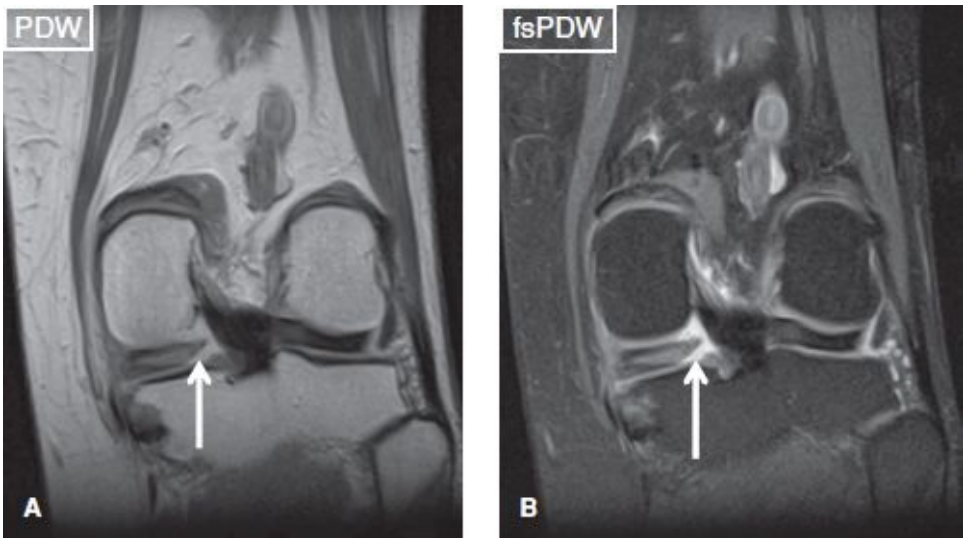

Fig. 32: Posterior root avulsion. Coronal images **(A, B)** show complete avulsion (*arrows*) of the posterior root of the medial meniscus.

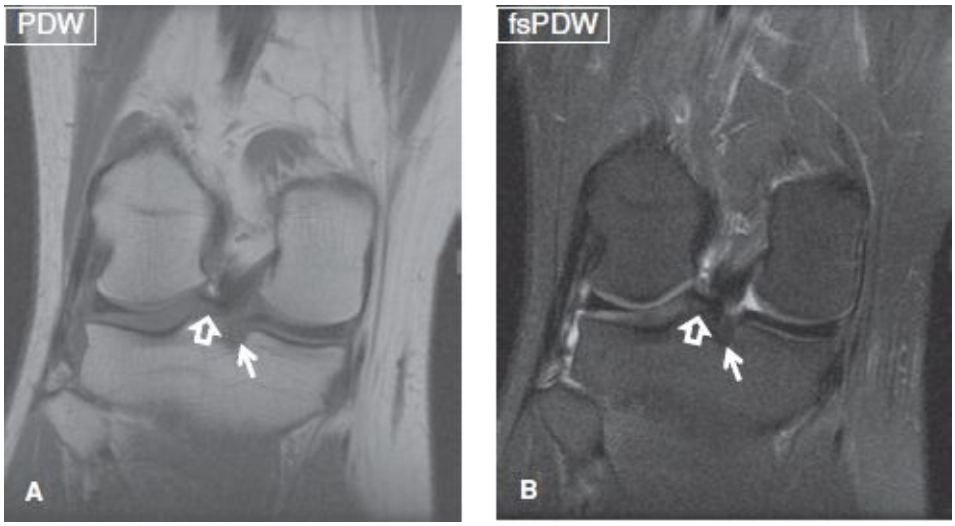

Fig. 33: Normal posterior root anatomy. Posterior coronal images **(A, B)** exhibit the two slips of the posterior root of the lateral meniscus across the lateral tibial spine (*open arrows*)

as well as posterior root of the medial meniscus as a thick dark band (*solid arrows*).

Longitudinal tears have a vertical axis, running parallel to the C-shaped circumference of the meniscus. These tears appear as a vertical line in the mid-substance of the meniscus, which separates the latter into inner and outer parts, and spares the free edge (Fig. 34). They are usually associated with twisting–translational injuries, such as ACL injuries, and typically involve the peripheral one-third of the meniscus (zone 1). The reader may encounter cases where the surgeon chose to reconstruct the ACL but leave the (complete or incomplete) longitudinal tear of the MM posterior horn to partially heal. In such cases, the fibrous tissue fills the gap between the torn meniscal edges, and appears as linear intermediate signal strands. Meniscal tears are considered stable if they are incomplete, short (<1 cm long) and demonstrate less than 3 mm displacement on arthroscopy probing. In a recent orthopaedic study, these lesions were named as "ramp lesions." It was found that their prevalence increased over two years from ACL injury, probably due to underlying knee instability and the lesions were more prevalent in young males. Repair of ramp lesions at the time of the ACL reconstruction may be needed but these lesions may heal on their own. Larger tears are more likely to require surgical repair to heal fully. Smaller or non-displaced (stable) tears can heal without repair. In cases where the inner part is displaced into the joint space, the tear is called bucket-handle tear (Figs. 35, 36). On sagittal images, the bucket-handle fragment may be seen as a dark band anterior to the posterior cruciate ligament (PCL). The appearance is known as "double PCL" sign (Fig. 35). It should be noted that the above sign can also be produced by a complete tear of the anterior cruciate ligament (ACL) tear. Alternatively, the displaced meniscal fragment may be seen posterior to the native anterior horn or anterior to the native posterior horn, a sign known as "flipped meniscus" or "anterior/posterior double delta" sign (Figs. 37, 38). This sign is common in LM bucket-handle tears since the ACL obstructs the displacement under the PCL. However, if one sees double PCL sign in bucket-handle tear of LM, ACL would be likely completely disrupted. Bucket-handle tears can be distinguished from flap tears, since the latter do not involve the whole circumference of the meniscus as the former would do. Finally, a large displaced bucket-handle tear can be easily repaired and sewed back to the torn edges despite looking ominous on images. Subsequently the meniscus may look normal on imaging and the lesion may heal pretty well due to good regional vascularity. On the other hand, a complex bucket-handle tear with irregular or displaced fragments may need major meniscectomy to prevent locking and other painful knee symptoms. The current surgical concept is to preserve as much meniscus as possible in order to protect the cartilage maintain the shock-absorbing ability of the meniscus.

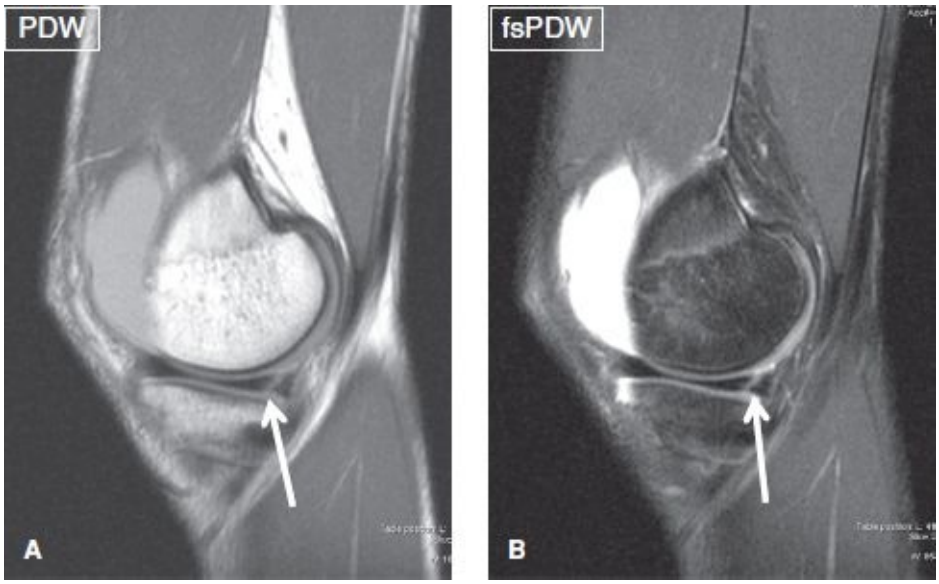

Fig. 34: Longitudinal meniscal tear. Sagittal images **(A, B)** display a vertical fluid-like signal (*arrows*), typically in the red–pink (peripheral–central) zone of the meniscus.

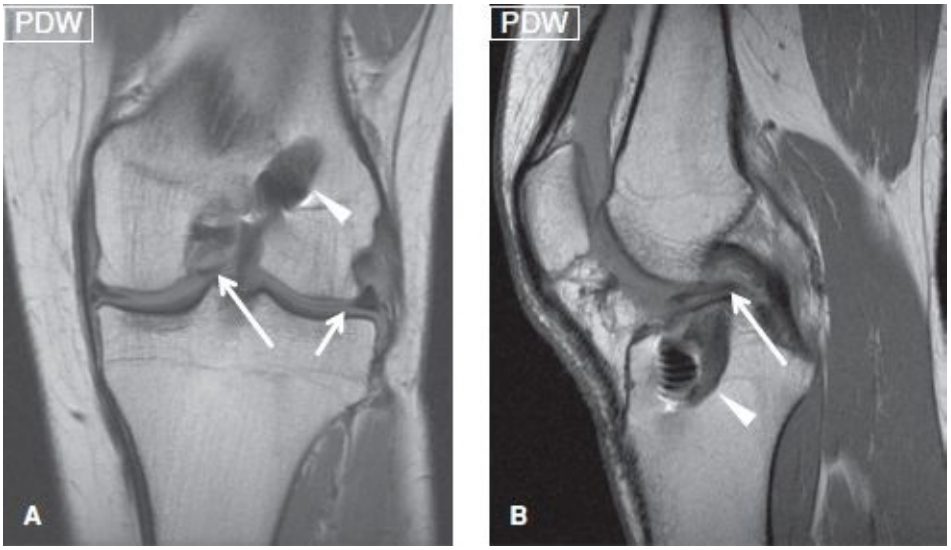

Fig. 35: Displaced bucket-handle medial meniscal tear. Coronal **(A)** and sagittal **(B)** images exhibit a bucket-handle tear of the medial meniscus, with the inner part (*long arrows*) displaced into the intercondylar space. In **B,** the displaced fragment projects anterior to the posterior cruciate ligament, forming a “double posterior cruciate ligament” sign. Also note an incomplete radial tear of the body of the lateral meniscus (*short arrow*), and postsurgical changes (*arrowheads*) from anterior cruciate ligament reconstruction.

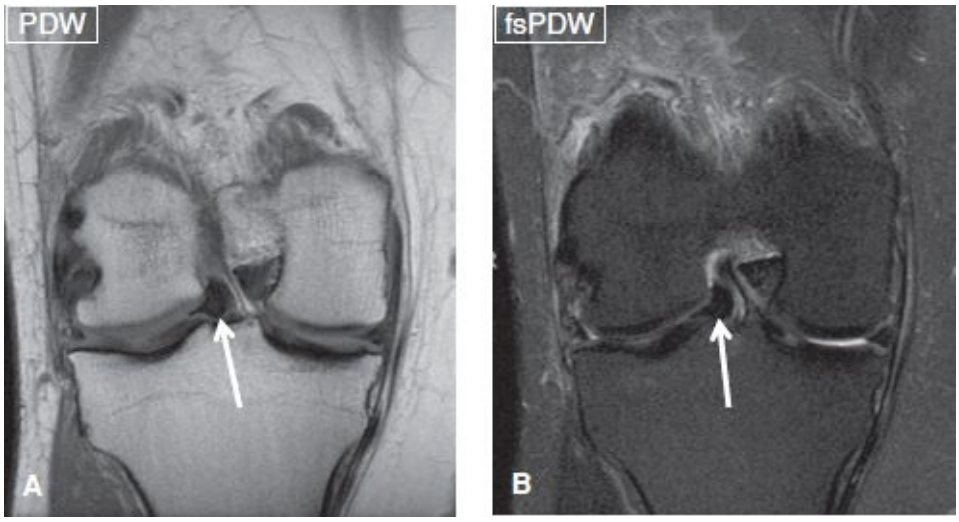

Fig. 36: Displaced bucket-handle lateral meniscal tear. Coronal images **(A, B)** demonstrate a bucket-handle tear (*arrows*) of the lateral meniscus. Note that the displaced fragment is obstructed by the ACL.

Fig. 37: Displaced bucket-handle lateral meniscal tear. Sagittal image shows the bucket-handle fragment (*short arrow*) located posterior to the native anterior horn (*long arrow*) producing the “flipped meniscus” or “anterior double delta” sign.

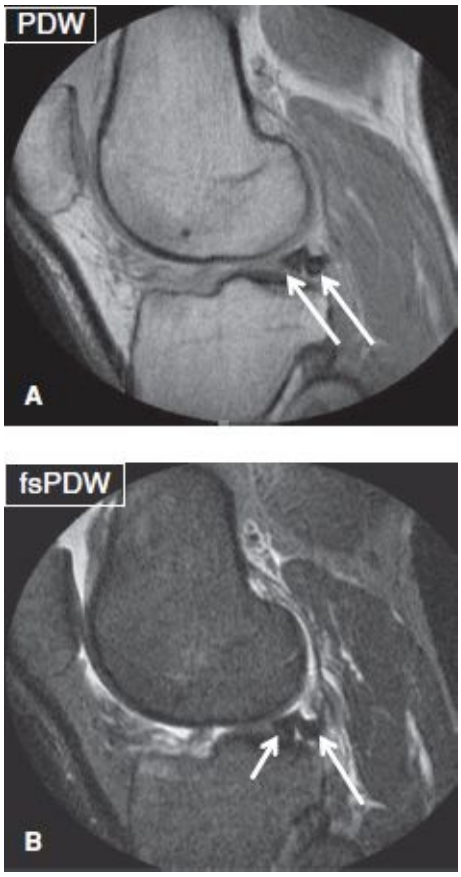

Fig. 38: Displaced bucket-handle lateral meniscal tear. Sagittal images **(A, B)** show the bucket-handle fragment (*short arrow*) located anterior to the native posterior horn (*long arrows*) producing the "flipped meniscus" or "posterior double delta" sign.

Fig. 39: Horizontal meniscal tear. Coronal image shows a horizontal near fluid-like signal (*arrows*), which runs parallel to the circumference of the meniscus.

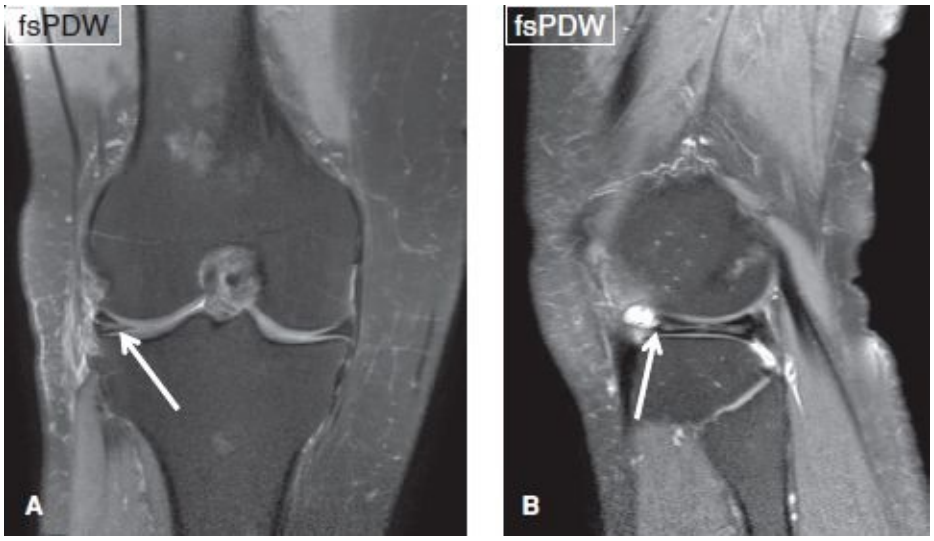

Fig. 40: Horizontal meniscal tear. Coronal **(A)** and sagittal **(B)** images exhibit linear near fluid-like signal (*arrows*) within the body of the lateral meniscus, which runs parallel to the tibial plateau and separates the meniscus into upper and lower parts. Notice parameniscal cyst anteriorly on the sagittal image.

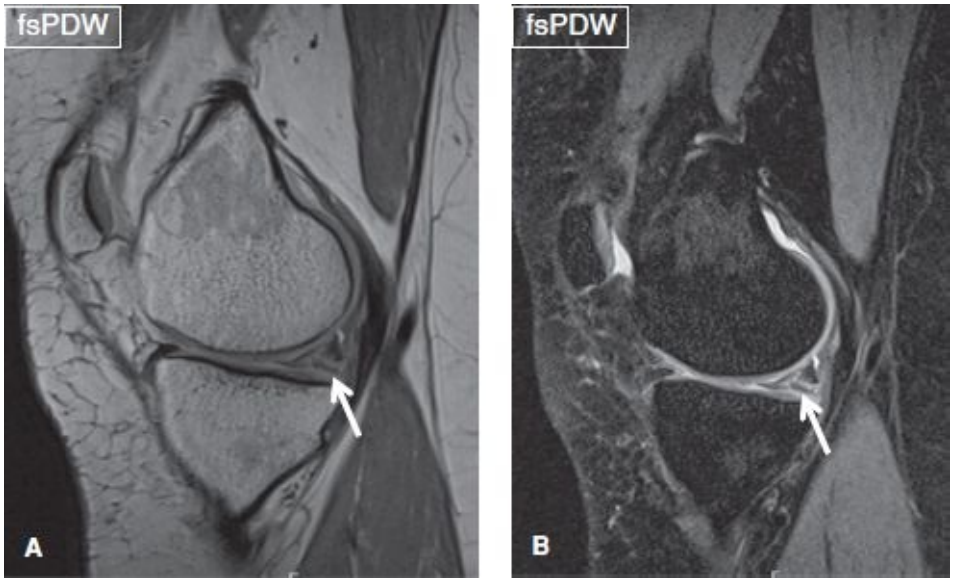

Fig. 41: Complex meniscal tear. Sagittal images show a complex tear (*arrows*) of the posterior horn of the medial meniscus, which features both longitudinal and oblique components.

Horizontal tears run parallel to the tibial plateau and appear as a horizontal line, which separates the meniscus into upper and lower parts (Figs. 39, 40). They are usually degenerative in origin and are uncommon. Treatment is conservative (leave alone) or surgical debridement. One should not mistake oblique or flap tears for a horizontal tear. Horizontal tears open the meniscus apex akin to fish mouth on the sagittal images, whereas oblique or flap tears contact the undersurface of the meniscus and do not extend to the apex. In case any of the parts is displaced into the intercondylar notch or into the lateral joint recess, the tear is referred to as a flap tear. These tears are most commonly associated with intra- and parameniscal cysts. Once the surgeon debrides the tear, the intra- and

parameniscal cysts partially or completely decompress into the joint or para-articular soft tissues.

Complicated tears conceptually represent a combination of two directions. Now, we have understood the three primary directions of meniscal tears (radial, vertical, horizontal) and three complicated directions of meniscal these lesions (radial leads to oblique or coapted flap; longitudinal leads to bucket-handle or vertical flap; horizontal leads to horizontal flap). Anything with two or more directions would be a complex tear according to ISAKOS classification (Fig. 41) as described below. In complex tears, the predominant tear direction and any full-thickness radial components or displaced flaps should also be described for treatment purposes. Parrot-beak, bucket-handle, and flap (horizontal or longitudinal) are considered unstable. Additional features suggesting instability include a tear that is greater than 10 mm in length and tears with complex patterns.

Chronic degenerative tears may result in severe deformity (maceration) and small size (truncation) of the menisci. This appearance is commonly seen with moderate–severe osteoarthritis. Apart from osteoarthrosis, the differential diagnosis for diminutive meniscus includes post-operative partial meniscectomy change, in which case the MR reader should look for relevant history or previous arthroscopy-related scarring in the Hoffa fat pad. Generally, in post-meniscectomy or post repair cases, menisci retain a triangular shape and the internal fluid-like signal resolves. The differential diagnosis also includes bucket-handle meniscal tear with flipped fragment, which may be located in the intercondylar notch, or in the anterior, posterior, or meniscotibial recesses.

Meniscal extrusion refers to the situation where a portion of the meniscus is overhanging the tibial plateau, usually by >2–3 mm on the medial side and >1 mm on the lateral side. It is associated with chronic posterior or anterior root degeneration, underlying osteoarthritis, as well as with radial and longitudinal tears. Other findings related to meniscal tears include fascial edema (more common with radial and vertical tears, indicating relative acuity of the lesion), intra- and parameniscal cysts, overlying cartilage loss, subjacent bone marrow stress reactions, insufficiency fractures, and finally dissection of the fluid into the adjacent bursae leading to MCL bursitis, iliotibial band (ITB) bursitis, tibial collateral ligament semimembranosus bursitis or pes anserinus bursitis. Whenever one notices fluid distention of these bursae, carefully evaluate adjacent meniscus tear. Many a times, multiple bursae may be distended with larger meniscal tears.

Parameniscal cysts are fluid accumulations, which result from fluid extrusion through (usually horizontal or complex) meniscal tears. They are typically located at the meniscal–capsular interface and are associated with intra-meniscal cysts (Figs. 42–44). They are considered strong indicators of meniscal tears, and, therefore, once identified, a thorough search should be performed to find the tear, which is usually adjacent to the cyst, and often displays a stalk toward the meniscus. Long-standing large parameniscal cysts rarely may also result in erosions or scalloping of the adjacent bony structures.

Fig. 42: Parameniscal cyst. Coronal image exhibits a parameniscal cyst (*arrowhead*), associated with a horizontal tear and intrameniscal cyst (*arrow*) of the body of the medial meniscus.

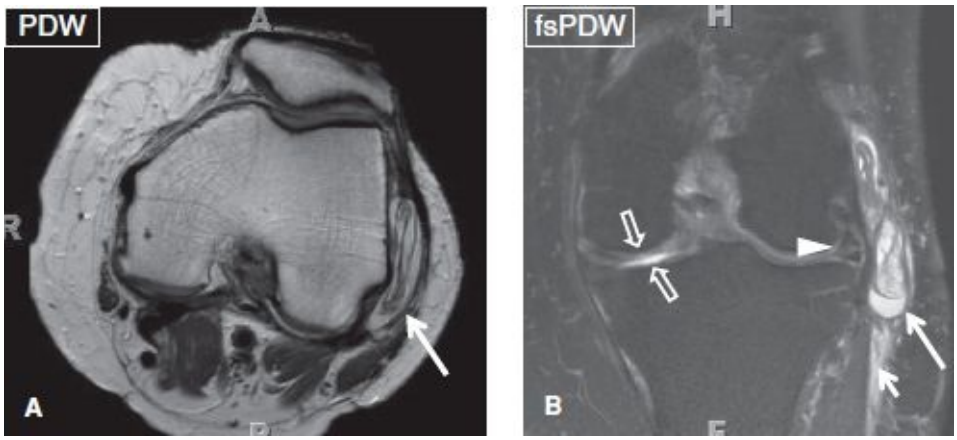

Fig. 43: Leaking parameniscal cyst with extension into the iliotibial band bursa. Axial **(A)** and coronal **(B)** images demonstrate a large parameniscal cyst (*long arrows*), which is associated with a horizontal tear of the lateral meniscus (*arrowhead*) and shows evidence of leaking (*short arrow*). Note high-grade cartilage lesions (*open arrows*) of the medial compartment.

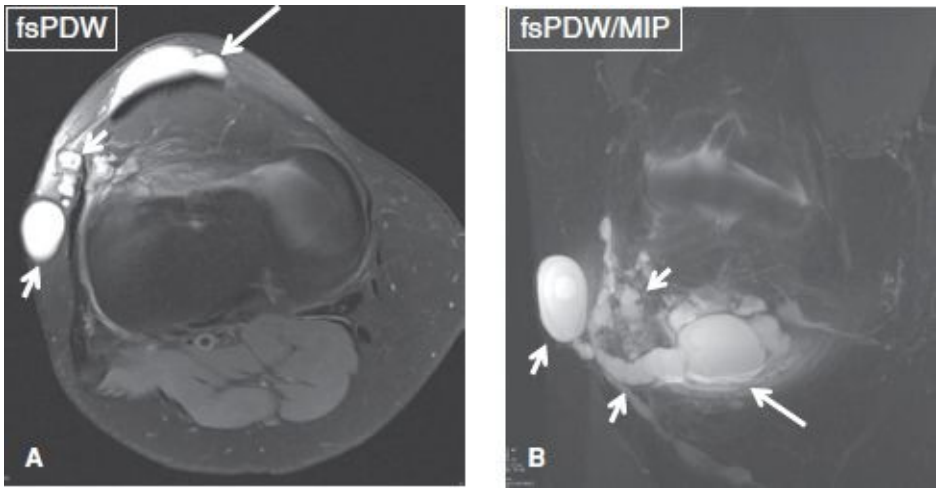

Fig. 44: Parameniscal cyst. Axial conventional **(A)** and coronal maximum intensity projection **(B)** images an elongated, multiloculated parameniscal cyst (*short arrows*) projecting in the subcutaneous tissues across the lateral retinaculum and extending into the prepatellar bursa (*long arrows*).

Ideally, in every meniscal tear, the radiologist should define the location, shape and size of the tear, and underlying meniscus tissue quality (degenerative changes). It is also important to report the following:

- Whether the tear is peripheral (zone 1/2) or central (zone 3).
- Parameniscal cysts, which may not be identifiable on arthroscopy
- Meniscal extrusion, and whether a meniscal fragment has been displaced into the medial or the lateral synovial recess

Pitfalls to be avoided when evaluating for meniscal tears include the following.

- The transverse ligament insertion on the meniscus, which can be followed on sequential sagittal images, interconnecting the two anterior horns
- The meniscofemoral ligament insertion on the LM, which can also be followed on sequential sagittal images, extending between the posterior horn of the LM and the medial femoral condyle (MFC)
- The frequent speckled anterior horn of the LM and sometimes, posterior horn of the MM
- The popliteus tendon pseudotear, which is depicted on sagittal images at the level where the respective tendon crosses the capsule and runs adjacent to the posterior horn of the LM
- The pulsation artifact from the popliteal artery, which can be confirmed by changing the phase and frequency direction from superior to inferior rather than anterior to posterior
- The magic angle phenomenon, occasionally depicted as diffuse haziness of the posterior horn of the LM on T1W and PDW images, but disappears on T2W images
- The oblique meniscomeniscal ligament or unilateral meniscomeniscal ligament, as described above
- Gibbs artifact due to undersampling that may mimic blurring of meniscal edges.

Other pathologic and anatomic variants include:

- Meniscal ossicles (0.15% prevalence): They correspond to small ossific foci that are usually considered post-traumatic in origin. They are typically found in the posterior horn of the MM, related to prior meniscal tears, usually root tears. They demonstrate bone marrow signal on all sequences.
- Meniscal flounce (0.2%–6% prevalence): A transient physiologic distortion/wavy configuration of the free edge of the meniscus, which is identified when the knee is in 10 degrees of flexion, and resolves nearly 50% of the times when the knee is flexed maximally, and completely when the knee is extended (Fig. 45). The clinical relevance of the flounce is that it can appear truncated on coronal images and simulate tear or degeneration. Flounce can also be associated with co-incidental meniscus tear but it does not predispose the meniscus itself to a tear.

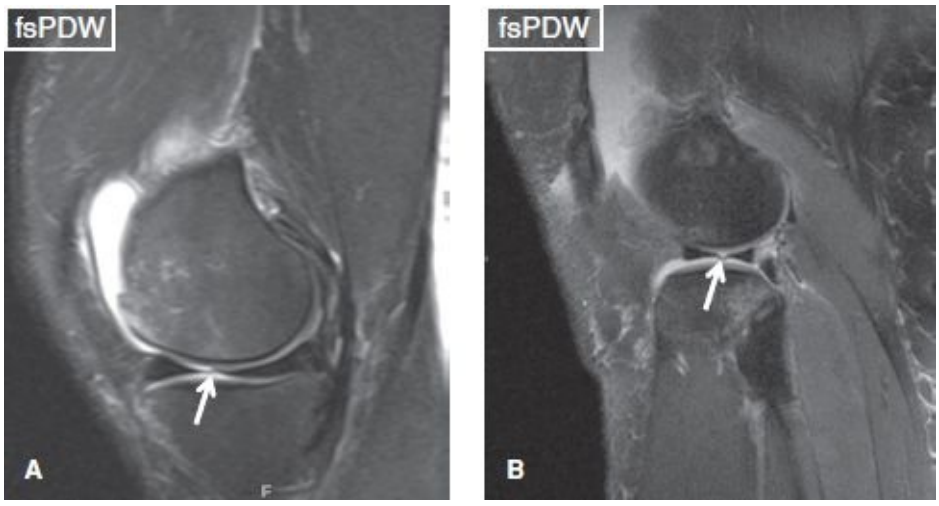

Fig. 45: Meniscal flounce. Sagittal images from different cases show wavy configuration (*arrows*) of the free edge of the medial meniscus **(A)** and lateral meniscus **(B).**

- Meniscal contusion: With adjacent bone contusions, a meniscus can become impacted and show diffuse increased signal approaching the surface of the meniscus, referred to as contusion or meniscal bruise (Fig. 46). Any sharp signal abnormality or fluid-like cleft should however be called a tear.

Fig. 46: Sagittal image from a patient with recent MVA shows bone contusions of the tibia and femur. Notice diffuse increased signal of the meniscus (*arrow*) approaching the meniscal surface, in keeping with a meniscal contusion.

The MCL is the strongest and most important of the knee supporting structures. It acts as the primary restraint to knee valgus stress at 30 degrees, as well as a secondary restraint to anterior tibial translation and external rotation. The MCL is a broad and flat membranous band composed of (1) a superficial fascial layer, which is an extension of the crural fascia overlying the vastus medialis and sartorius muscles; (2) a superficial MCL layer, which is attached proximally to the posterior aspect of the medial femoral condyle immediately below the adductor tubercle, and distally to the medial aspect of the tibial metaphysis, 4–5 cm distal to the tibial joint line; and (3) a deep layer, consisting of capsular thickenings, the meniscofemoral and meniscotibial extensions, which attach to the meniscus and to the proximal femur and tibia, respectively. The latter two layers are separated by a small bursa and minimal peribursal fat. The MCL is best depicted on coronal images, where it normally appears as a thin, taut, well-defined, linear band, which is homogeneously hypointense on all sequences. Coursing along a straight superoinferior direction, the ligament is typically seen in its entirety on a single coronal image. The sprains are best assessed on both coronal and axial images.

MCL injuries are common and most frequently represent grade II sprains. These occur following a valgus force, and most often involve the femoral attachment or its midportion. The injuries are assessed clinically using a “valgus stress test” that can be performed at 0 and 30 degrees. For isolated MCL injury, the test is performed with the knee at 30 degrees of flexion and it measures the amount of joint line opening of the medial compartment. The fingers of one hand are placed directly over the joint line to evaluate the amount of joint-line opening. The amount of joint line opening can be quantified as 0 to 5 mm, 5 to 10 mm, and greater than a centimeter. This would roughly correlate with MR imaging grade I, II,

and III sprains of the MCL, respectively. It is also important to recognize that stability testing using valgus stress test or varus stress test (for LCL) need to be compared to the normal contralateral knee. The same test, if positive at 0 degrees, i.e., an increase of valgus opening in extension, would likely mean combined MCL and ACL/PCL injury.

For primary MCL injuries, MR imaging may not be needed, since the clinical diagnosis is easy, and most of these entities are treated non–operatively using a hinged brace. Similar to other ligaments of the body, MCL injuries are classified on imaging as *grade I* sprains, which correspond to microscopic tears or stretch injury and appear as T2 hyperintense soft tissue edema surrounding an intact MCL, that otherwise features normal thickness and intact bone attachments; *grade II* sprains, which correspond to partial tears, and appear as thickening and/or partial disruption of the MCL, along with increased T2 hyperintensity of the surrounding soft tissues, reflecting edema and hemorrhage; or *grade III* sprains, which correspond to complete tears, and appear as complete disruption of the ligament with waviness, along with surrounding soft tissue edema and hemorrhage (Fig. 47). Avulsion injuries are typically associated with minor bony edema at the attachment site. In chronic MCL tears, the ligament is ill-defined and thickened, maintains low signal on T1W and T2W images, and occasionally ossifies at its femoral attachment (Pellegrini–Stieda lesion). However, one should not overcall MCL sprains, since soft tissue edema is common in the fascial planes of the medial side of the knee, simply as a result of Baker cyst rupture, meniscal tears, or bony contusions/stress injuries. Following conservative treatment, return to sports usually happens within 2 to 6 weeks. With combined ACL and PCL injuries, most advocate non-operative healing of the MCL and reconstruction of the ACL when the range of motion is regained. The ACL reconstruction is intentionally delayed for 2–4 weeks to prevent post-operative stiffness. Some advocate reconstruction of the ACL and primary repair of the MCL. With combined MCL and PCL injuries, most advocate primary repair of the MCL and reconstruction of the PCL. Another recently recognized lesion of MCL is referred to as the Stener like-lesion of the MCL, akin to Stener lesion of the 1st metacarpophalangeal joint of the thumb. The lesion represents disruption of the superficial fibers of the medial collateral ligament of the knee without tearing of the deep fibers. The anterior superficial fibers may thus displace over the pes anserinus tendons and healing back to the tibial attachment site may be jeopardized. Since, the deep fibers are intact, the knee will show increased valgus laxity only in flexion with no clear end point at 30 degrees of flexion. The clinical findings are confusing, the medial swelling and ecchymosis may be remarkable, and the MR imaging will show short bunched up superficial MCL over the pes tendons. Surgery may be required to prevent residual laxity, even with isolated partial MCL injury.

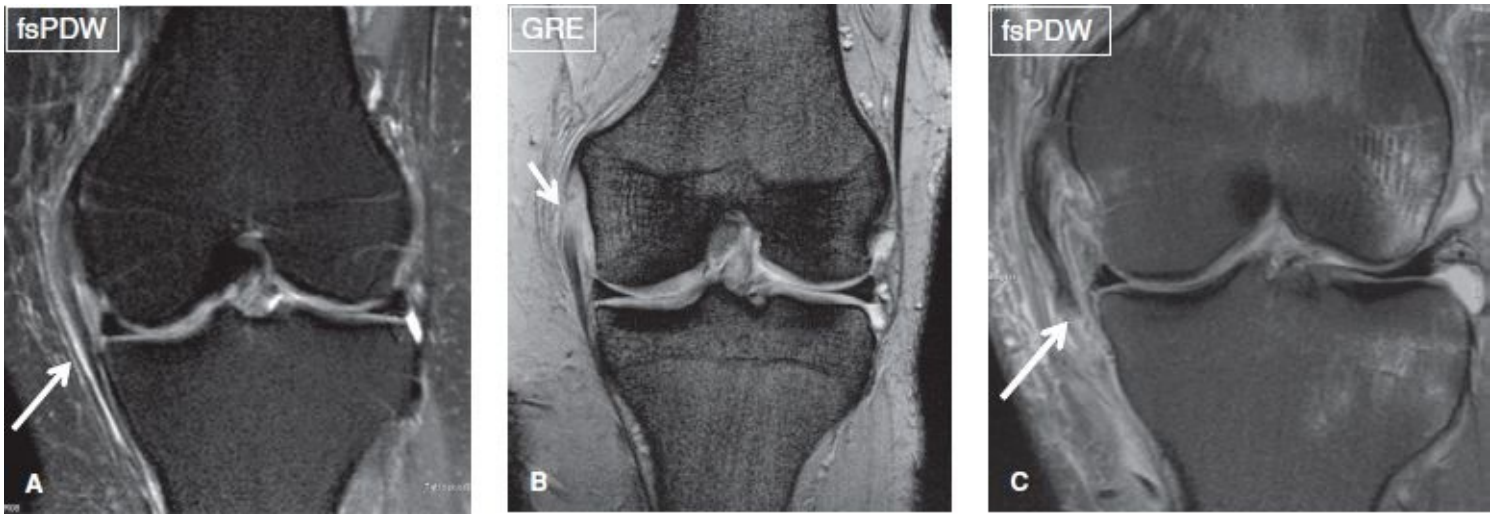

Fig. 47: Medial collateral ligament sprains. Coronal images. **A:** Edema (*arrow*) of the soft tissues superficial to and deep to the (otherwise intact) medial collateral ligament indicates a grade I sprain. **B:** Partial discontinuity (*arrow*) of the medial collateral ligament corresponds to grade II sprain. **C:** Complete rupture (*arrow*) of the medial collateral ligament is synonymous with grade III sprain.

The MCL bursa is located between the superficial and the deep portions of the MCL. MCL bursitis is a cause of medial knee pain and appears on coronal images as a vertically elongated well-defined fluid collection which extends adjacent to the femoral and tibial cortexes (Fig. 48). On axial images, the anterior margin of the bursa is located adjacent to the anterior edge of the superficial portion of the MCL whereas its posterior margin is outlined by the junction between the superficial and deep portions of the MCL. The above description assists in differentiating MCL bursitis from other fluid collections of the medial knee. The differential diagnosis includes

Fig. 48: Medial collateral ligament bursitis. Coronal image exhibits a vertically elongated well-defined fluid collection (*arrow*) among the superficial layers of the MCL.

- Pes anserinus bursitis, with the distended bursa located distal to the joint line, deep to the pes anserinus tendons, and superficial to the MCL (Fig. 49)

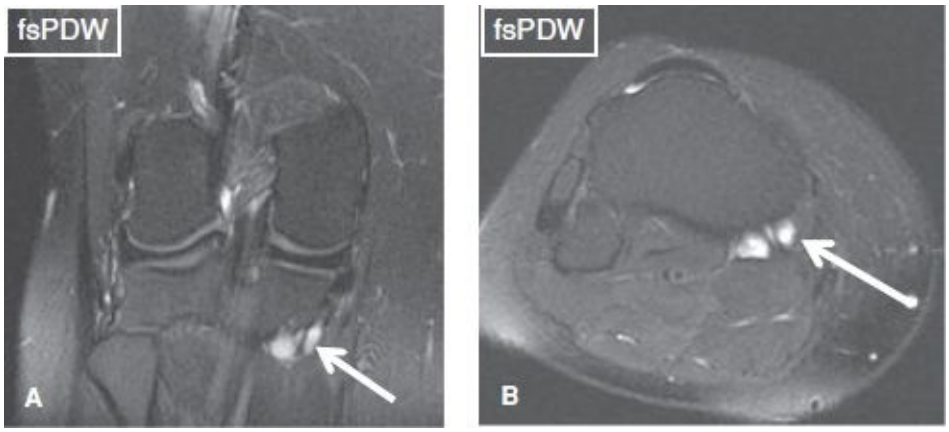

Fig. 49: Pes anserinus bursitis. Coronal **(A)** and axial **(B)** images show a small fluid collection (*arrows*), located distal to the joint line, deep to the pes anserinus tendons.

- Meniscocapsular separation, in which the fluid collection is ill-defined and located adjacent to the posterior horn of the MM
- Parameniscal cysts, which are associated with meniscal tears, often have a communicating stalk or neck with the tear and are usually round or oval and multiloculated
- Ganglion cysts, which are often septated and lobulated and are unlikely to be confined to the location of the MCL bursa.

The articular cartilage of the femoral condyles and tibial plateau is evaluated on sagittal and coronal images. Similar to other joints, it normally features homogeneous thickness and smooth margins, appears slightly less hyperintense to joint fluid on fsPDW images and shows intermediate signal on PDW images (Fig. 50). The cartilage shows graded intensity, with deeper layers (radial zone) appearing darker than the superficial layers (intermediate and superficial layers). The radial zone is more concentrated in the central weight-bearing portions of the femoral and tibial condyles. Cartilage lesions may result from acute trauma, degeneration, or inflammatory arthritis. The cartilage is avascular and aneural, and derives nutrition from the synovial fluid. Cartilage-related pain is generally due to inflammatory tissue around the cartilage lesions, inflammation adjacent to the meniscal lesion or from stress-related bone marrow edema. Typically, acute traumatic lesions have sharp margins and are oriented perpendicular to the bone surface. They can occur on both weight-bearing and non–weight-bearing surfaces, and are associated with subjacent bone marrow edema. Degenerative lesions tend to be shallower and demonstrate wide, horizontal, or obtuse margins with respect to the bone surface. They typically occur in the weight-bearing portions of the joint and result in nonuniform joint space narrowing. If the defects extend to the bone, subchondral bone marrow edema, cysts, or sclerosis may result. In inflammatory arthritis, cartilage loss is usually diffuse and uniform, resulting in symmetric joint space narrowing. The cartilage and its associated bony lesions should be evaluated on

both PDW and fsPDW images in tandem. Subchondral stress edema is disproportionately seen as an ill-defined bright signal on fsPDW images; subchondral cysts are well-defined and are seen as proportionate intermediate signal on PDW and bright on fsPDW images; finally, subchondral sclerosis and fatty metamorphosis of these lesions are only seen on the PDW images.

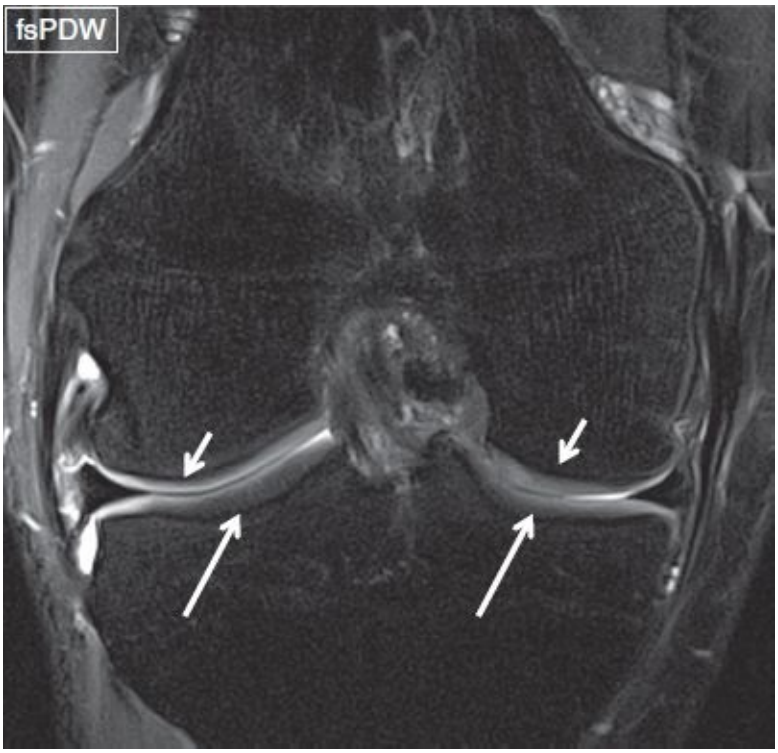

Fig. 50: Normal articular cartilage. Coronal image shows normal articular cartilage of the femoral condyles (*short arrows*) and tibial plateau (*long arrows*), appears slightly less hyperintense to joint fluid and featuring homogeneous thickness and smooth overlying hypointense margins (lamina splendens). The cartilage shows graded intensity with deeper layers (radial zone) darker than the superficial layers (intermediate and superficial layers). The radial zone is more concentrated in the central weight-bearing portions of the femoral and tibial condyles.

Chondromalacia (blistering, softening) is the earliest stage of cartilage injury and appears as focal or diffuse areas of T2 hyperintensity with overlying intact-appearing lamina splendens. Chondromalacia is a non-specific finding, which can also be seen in asymptomatic subjects (Fig. 51). Small imperceptible areas of fissuring leading to focal or diffuse fluid imbibation are thought to cause this signal alteration. In some areas of the knee, magic angle artifact or relative collagen orientation in the cartilage may falsely produce this appearance e.g., far posterior or anterior femoral condyle surfaces on sagittal images. Concurrent underlying marrow signal abnormality, T2 mapping and persistence on high TE images increases diagnostic specificity. Fibrocartilage, which is formed as a repair response to cartilage injury, appears as hypointense areas within the cartilage on fluid-sensitive images similar to areas of cartilage degeneration or chondrocalcinosis. Cartilage surface fibrillation and erosions represent the next stage of degeneration and are

characterized by uneven articular surface of the cartilage, which otherwise relatively maintains normal thickness. Diffuse cartilage thinning is the result of normal age-related cartilage degeneration or the result of chronic/recurrent cartilage injury. The cartilage is homogeneously thin and features no focal defects. In cartilage fissure, a linear (≤2 mm thick) T2 hyperintense signal with vertical or near-vertical orientation is noted disrupting the articular surface whereas in flap, the fissure is obliquely oriented and is associated with elevation of superficial semi-separated cartilage layers. Fissures and flaps are further subdivided into low- or high-grade lesions based on whether they involve less or more than 50% (50% to 99%) of the cartilage thickness, respectively. Cartilage defects appear as fluid-filled hyperintense lesions, which are greater than 2 mm in width, and are again described as low- or high-grade similar to fissures (Fig. 52). In full-thickness defects, there is exposure of the subchondral bone (100%) with or without associated bone marrow edema, cysts, sclerosis, and articular surface irregularity or depression. Cartilage delamination is characterized by separation (debonding) of the cartilage from the subchondral bone at the tidemark zone (calcifying radial layer), with fluid dissection or cartilage buckling (Fig. 53). It is one of the worst types of acute cartilage lesions, which does not normally heal. Cartilage denudation results from acute on chronic progressive complete cartilage loss and appears as complete absence of cartilage on the articular surface, with the bone directly exposed to synovial fluid (Fig. 54). Again, bone marrow edema, cysts, sclerosis, and articular surface irregularity or depression may be evident whereas if the entity is present at the opposing articular surfaces, painful bone-on-bone apposition may occur (Fig. 55). The Outerbridge classification is the most commonly used system for grading osteoarthritis (Table 1). Further details are available in Chapter 5 dedicated to cartilage imaging.

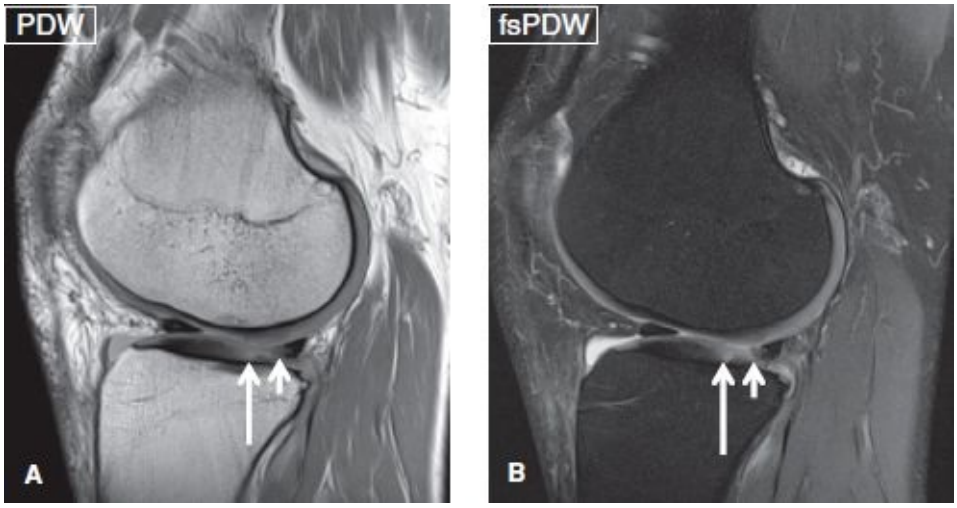

Fig. 51: Chondromalacia. Sagittal images **(A, B)** show focal T2 hyperintense signal of the tibial plateau cartilage (*long arrows*) with overlying intact appearing lamina splendens, in keeping with chondromalacia. Also note an incomplete radial tear (*short arrows*) of the posterior horn of the lateral meniscus and focal fibrocartilage formation of the opposing femoral condyle surface.

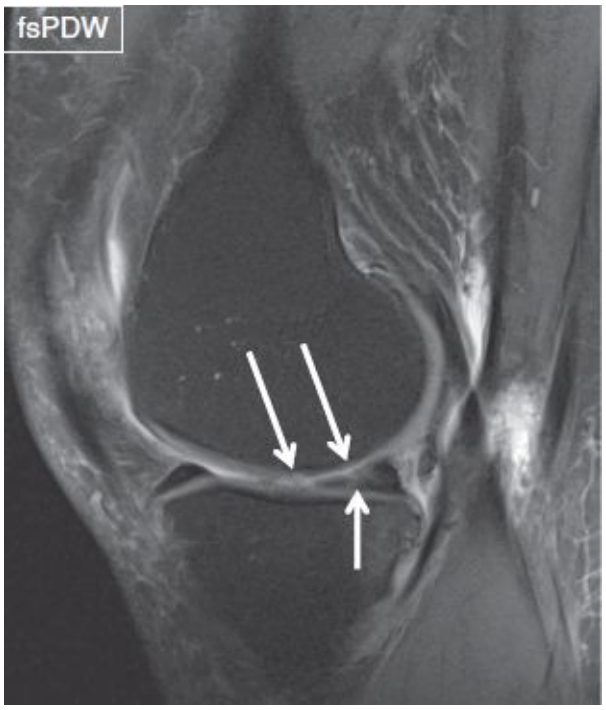

Fig. 52: Cartilage defects. Sagittal image demonstrates high-grade cartilage defects (*long arrows*) of the central medial femoral condyle. Also note a complex tear (*short arrow*) of the posterior horn of the medial meniscus.

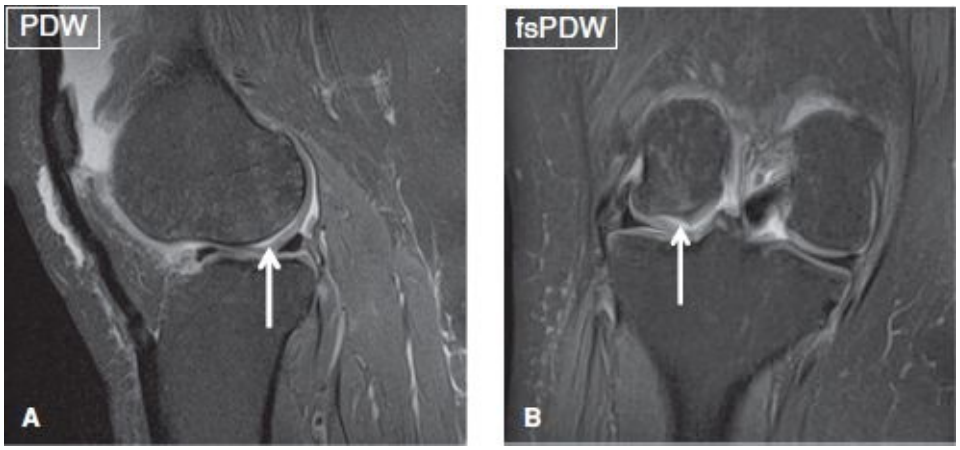

Fig. 53: Cartilage delamination. Sagittal **(A)** and coronal **(B)** images exhibit separation (debonding) of the lateral femoral condyle cartilage (*arrows*) from the subchondral bone.

Fig. 54: Cartilage denudation. Sagittal images **(A, B)** demonstrate areas of complete cartilage loss (*arrows*) at the weight-bearing aspects of the femoral condyle and tibial plateau with subchondral edema, cysts, and sclerosis.

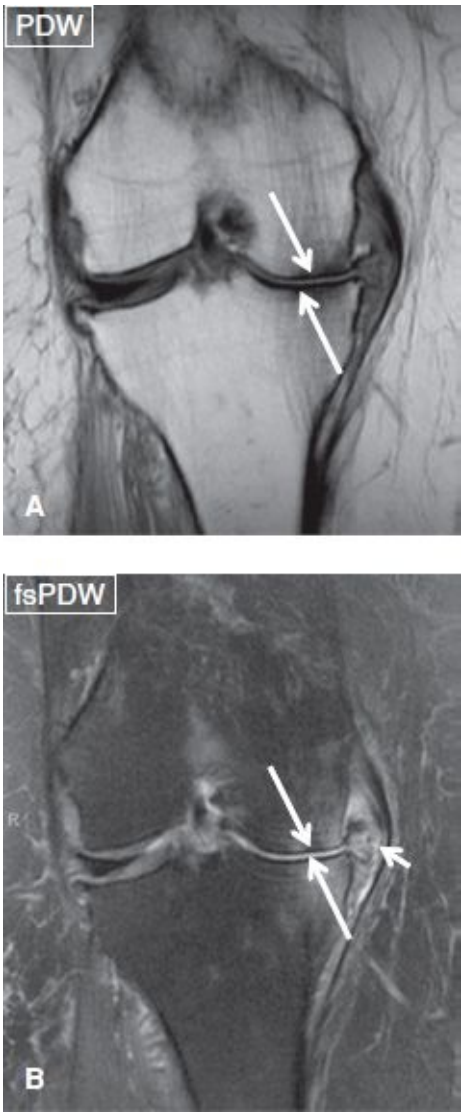

Fig. 55: Severe osteoarthritis. Coronal images **(A, B)** exhibit complete cartilage loss (*long arrows*) in the medial joint compartment, with severe loss of the joint space and sclerosis, edema, and cysts of the opposing articular surfaces, assuming a bone-on-bone articulation. Also note the macerated extruded medial meniscus (*short arrow*).

In osteochondral fractures, there is T1 hypointense fracture line in the subchondral bone, which is associated with extensive surrounding marrow edema and erosion of the overlying articular cartilage. The severity of the lesions can be assessed based on the Anderson classification (Table 2). Osteochondritis dissecans refers to a disorder of the secondary physis, which lies underneath the articular cartilage, and is distinct from the primary physis that lies between the metaphysis and epiphysis. Osteochondritis dissecans is common in adolescents and results in aseptic separation of an osteochondral fragment with gradual fragmentation of the articular surface. The osteochondral fragment typically shows half-moon configuration and the overlying articular cartilage may be proud or flush with the native cartilage but might show fissuring, defects, or fibrocartilage formation. The role of imaging is to determine the potential instability of the defect. Findings indicating instability include large areas of deficient articular cartilage, undercutting of osteochondral fragment with fluid signal, osteochondral defect with fluid-filled cavity, size larger than 1 cm, and extensive cystic changes deep to the lesion. The entity can be graded based on the ICRS

classification (Table 3).

TABLE 1: The Outerbridge classification for grading osteoarthritis

Grade	Imaging Feature(s)
0	No abnormality
1	Softening
2	Shallow ulceration or blister-like swelling
3	Partial-thickness fibrillation or deep ulceration not extending to the bone or thinning
4	Exposure of the subchondral bone

Meniscocapsular injury refers to sprain or frank disruption of the normal tight attachment of the MM to the joint capsule and its thickenings, including the MCL, posterior oblique ligament, and oblique popliteal ligament. The diagnosis is best established on coronal and sagittal fluid-sensitive images. In meniscocapsular sprain, there is edema (T2 hyperintensity) of the interface between the MM and the capsule, which otherwise remain attached to each other. In meniscocapsular separation, there is fluid intersecting between the MM and the capsular layers, which show irregular outlines. Secondary, though less accurate, criteria include displacement of the MM relative to the tibia, peripheral meniscal tear extending to the superior or inferior corner of the MM, tears of the meniscofemoral or the meniscotibial extensions of the MCL extending to the meniscal periphery, increased distance between the MM and the MCL, and stripping of the capsule from the tibial attachment and tears of semimembranosus tendon (Figs. 56, 57). In contrast to meniscocapsular sprain, which may not be clinically important, meniscocapsular separation is associated with meniscal hypermobility and loss of peripheral vascularity, which may be clinically significant.

TABLE 2: The Anderson classification for grading osteochondral injuries

Stage	Imaging Feature(s)
I	Bone marrow edema
IIa	Subchondral cyst formation
IIb	Incomplete separation of the osteochondral fragment
III	Fluid around an undetached, undisplaced osteochondral fragment
IV	Displaced osteochondral fragment

TABLE 3: The IRCS classification for grading osteochondritis dissecans

Stage	Imaging Feature(s)
I	Intact cartilage over the osteochondral fragmentation
II	Partial discontinuity of the cartilage over the osteochondral fragmentation
III	Complete discontinuity of the cartilage over the osteochondral fragmentation; fragment not displaced
III	Fluid around an undetached, undisplaced osteochondral fragment
IV	Dislocated fragment or loose body

POSTEROMEDIAL CORNER:

Semimembranosus tendon: [<Normal> <Tendinosis> <Tear>]

Posterior oblique ligament: [<Intact> <Acute sprain>]

The distal semimembranosus tendon courses deep to the semitendinosus and long head of biceps muscles, and fans out distally with six insertions, which attach to the far medial proximal tibial plateau (pars reflexa), posteromedial tibial plateau distally (pars distalis), oblique popliteal ligament, posteromedial capsule and posterior horn of MM, posterior oblique ligament (POL), and aponeurosis of the popliteus muscle. It provides flexion and internal rotation of the knee, as well as dynamic stability to the joint and its posteromedial corner. During flexion, the semimembranosus tendon pulls the posterior horn of the MM out of the joint during flexion, thus, preventing impingement of the meniscus between the tibia and the femur. Similar to other tendons, semimembranosus tendinosis appears as intermediate signal within the tendon on PDW and fsPDW images whereas partial- and full-thickness appear as partial or complete tendon discontinuity, respectively, that may be associated with T2 hyperintensity of the peritendinous soft tissues, reflecting edema, and/or hemorrhage. In case of avulsion of the tendinous insertion, mild marrow edema and/or subcortical cystic change is evident in the adjacent bone with underlying enthesopathy from prior episodes of partial tears. Wrapping around the distal semimembranosus tendon, the semimembranosus bursa is located deep to the medial collateral ligament and distal to the joint line featuring a comma-shaped or horse-shoe–shaped configuration when filled with fluid (Fig. 58). The entity is commonly associated with medial meniscal tears and is referred to as tibial collateral ligament–semimembranosus bursitis.

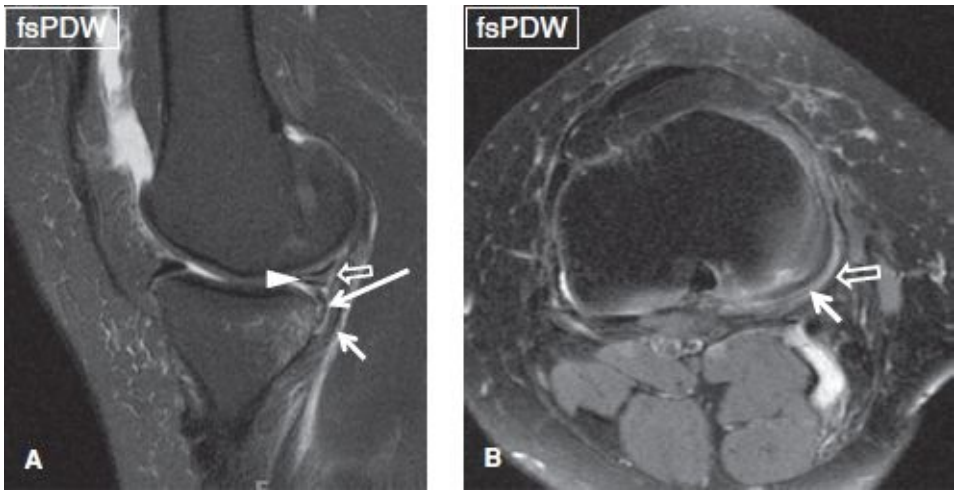

Fig. 56: Meniscocapsular sprain due to recent twisting injury. Sagittal **(A)** and axial **(B)** images show capsular stripping of the tibia (*long arrow*), edema of the meniscocapsular interface (*open arrows*), edema of the soft tissues overlying the posterior oblique ligament indicating grade I sprain (*short arrows*), as well as a horizontal tear (*arrowhead*) of the posterior horn of the medial meniscus.

In the posteromedial aspect of the joint, the superficial and deep portions of MCL blend together and form the POL, which is attached from the adductor tubercle to the posterior aspect of the proximal tibia, posterior MM and is inseparable from the capsule. The oblique popliteal ligament arises medially from the semimembranosus and the capsular arm of the POL, courses superolaterally along the posterior joint capsule, and inserts to the arcuate ligament and the lateral gastrocnemius head, thus, connecting the posterior medial and lateral knee and completing the circle of capsular thickenings along with medial and lateral retinaculae and collateral ligaments.

Posteromedial corner injuries are caused by valgus and hyperextension forces. The spectrum of imaging findings may include one or more of the following: POL injury (described below); fluid collection posterior to the semimembranosus tendon, which should be differentiated from ruptured Baker cyst; tear of the posterior third of the MM; stripping of the posterior capsule from the tibia; and semimembranosus tendon tears.

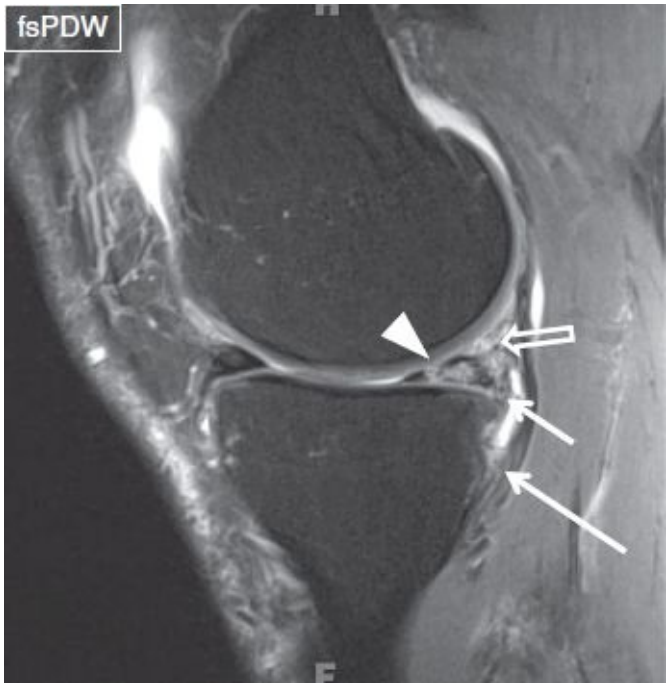

Fig. 57: Meniscocapsular sprain. Sagittal image shows capsular stripping of the tibia (*short arrow*), partial tear of the pars distalis portion of semimembranosus (*long arrow*), edema of the meniscocapsular interface (*open arrow*), and complex tear (*arrowhead*) of the posterior horn of the medial meniscus.

Based on severity, POL injuries may be classified into *grade I* sprains (microscopic tears), in which the POL is intact and features normal thickness but is surrounded by edema of the adjacent extracapsular soft tissues; *grade II* sprains (partial tears), which are characterized by thickening of the POL, partial disruption of its fibers, and increased amount of surrounding edema/hemorrhage; and *grade III* sprains (complete tears/avulsions), in which there is complete disruption of the POL, along with extensive surrounding edema/hemorrhage (Figs. 59, 60). Uncommonly, POL pathology may present as calcific tendinitis (Fig. 61).

LATERAL COMPARTMENT:

Lateral meniscus: [<Normal> <Degenerative free edge fraying> <Incomplete or complete radial tear/Oblique tear/Horizontal tear/Longitudinal tear/Flap tear/Displaced bucket-handle tear>]

Lateral collateral ligament: [<Normal> <Thickened> <Acute sprain>]

Lateral femoral condyle cartilage: [<Normal>]

Lateral tibial plateau cartilage: [<Normal>]

The anterior and posterior horns of the LM are equal in size. The LM is attached to the capsule with superior and inferior popliteo-meniscal fascicles or struts forming a popliteal tunnel, through which courses the popliteus tendon. The anterior and posterior

meniscofemoral ligaments are variably present and extend from the medial aspect of the intercondylar notch to the posterior horn of the LM, after passing anterior (ligament of Humphrey) or posterior (ligament of Wrisberg) to the PCL, respectively. These supplement the PCL, stabilize the posterior horn of the LM, and prevent posterior drawer of tibia.

The discoid LM is a normal variant, in which the body of the meniscus is larger than normal due to failure of resorption of its central discal portion, leading to disc-like meniscal shape and meniscal instability as well as dysfunction. The condition is suspected when the body (bow tie) of the meniscus appears on three or more 4-mm-thick sagittal images, and is confirmed on coronal images when the minimal meniscal width is greater than 14 mm. Discoid menisci are characterized as complete or incomplete, based on whether they completely or partially cover the lateral tibial plateau, respectively (Figs. 62, 63). The variant may be associated with widening of the lateral joint space, cupping of the lateral tibial plateau (which is normally flat or slightly convex) and/or hypoplasia of the lateral femoral condyle or tibial spine. Another discoid variant is the Wrisberg-type discoid LM, in which the meniscus lacks attachments to the capsule or the tibia (meniscotibial ligament), allowing the bulky meniscus to sublux into the joint and cause symptoms of locking. The variant is suspected in the absence of popliteomeniscal and meniscotibial ligaments, and/or if the posterior horn of the LM is separated from the tibial plateau by fluid and is elevated by more than 4 mm. Discoid MM is rare (<1%) as compared to the discoid LM (4%) (Fig. 64). In discoid menisci, the signal alteration does not have to extend to the articular surface to suggest the diagnosis of tear. Extensive increased signal in discoid menisci signifies cavitation. Other conditions which may mimic discoid meniscus include vacuum in the joint space and chondrocalcinosis (Figs. 65, 66). The anterior horn of the LM and less commonly posterior horn of the MM assume a speckled appearance near their attachments (Fig. 67), which should not be mistaken for tear. The imaging criteria for MM and LM tears and re-tears are otherwise the same. Parameniscal cysts of the anterior root of LM can be challenging to distinguish from mucoid degeneration of the ACL, which can lead to cysts adjacent to the anterior root region. Location of the cysts in and around the anterior root, its subjacent bone involvement, and abnormal morphology of the anterior root itself are useful pointers in identifying meniscal pathology, which is otherwise less common than the ACL mucoid degeneration.

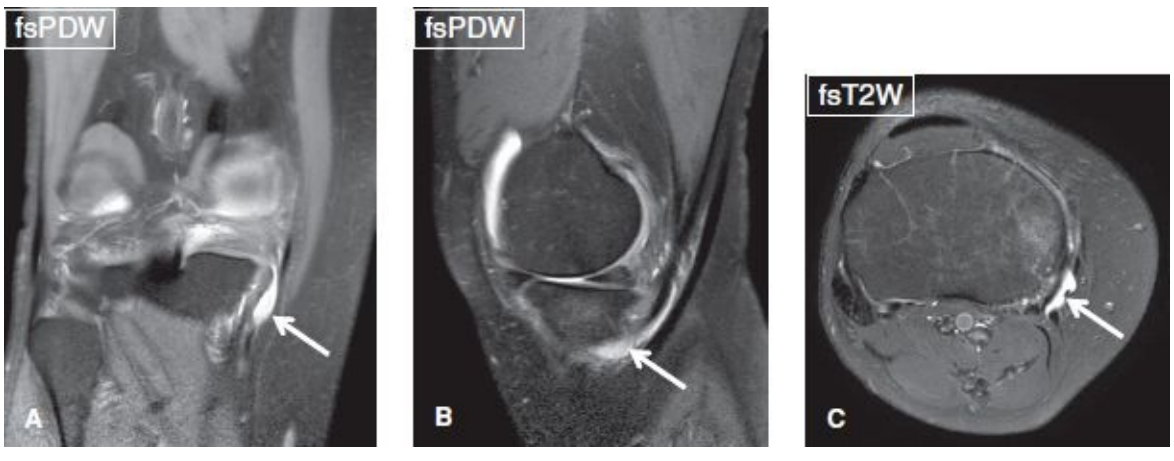

Fig. 58: Semimembranosus bursitis. Coronal **(A),** sagittal **(B),** and axial **(C)** images demonstrate a well-defined comma-shaped fluid collection (*arrows*) wrapping around the distal semimembranosus tendon.

Fig. 59: Posterior oblique ligament avulsion. Axial **(A)** and coronal **(B)** images demonstrate avulsion of the posterior oblique ligament (*arrows*) along with mild edema of the surrounding soft tissues.

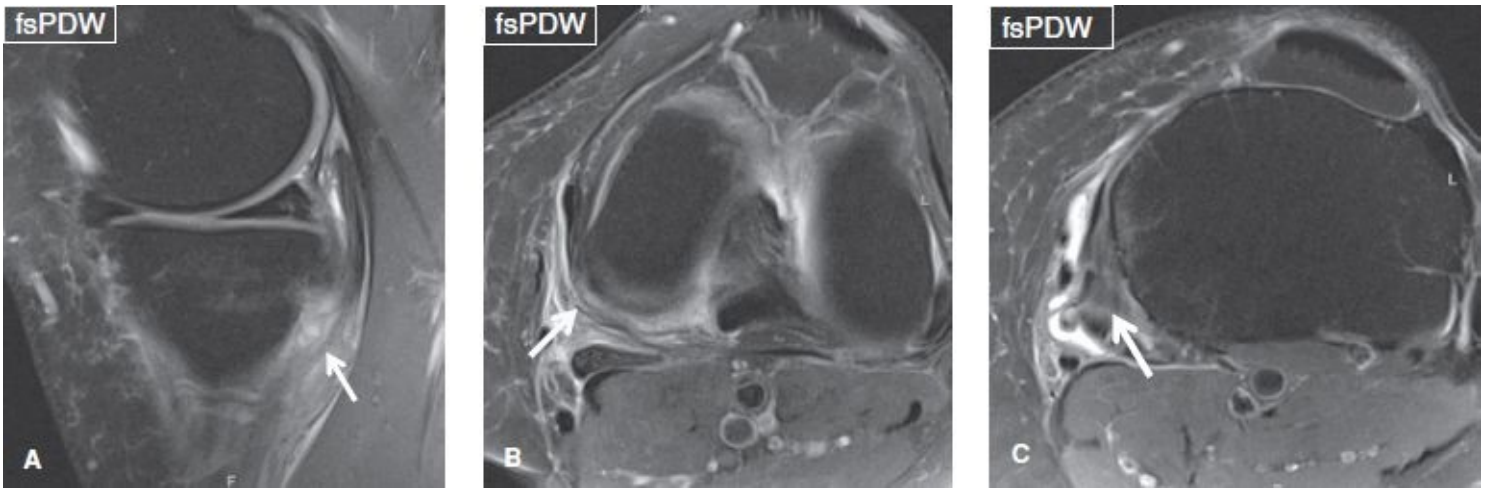

Fig. 60: Posteromedial corner injury. Sagittal **(A)** and axial **(B, C)** images show grade II sprain of the pars distalis portion of the semimembranosus tendon (*arrows* in **A, C**) and posterior oblique ligament (*arrow* in **B**).

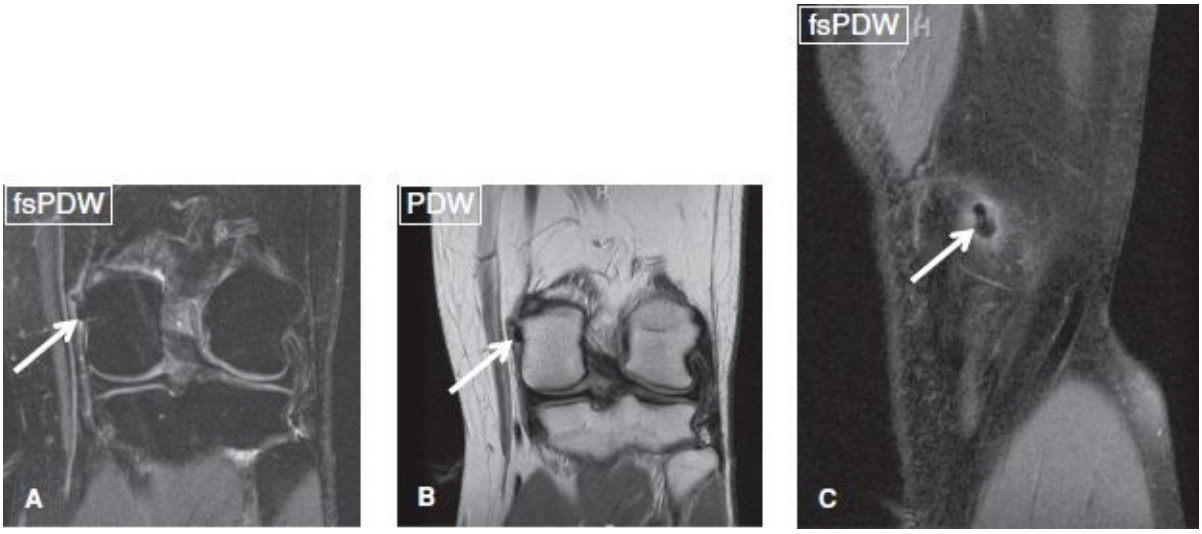

Fig. 61: Calcific tendinitis of the posterior oblique ligament. Coronal **(A, B)** and sagittal **(C)** images demonstrate ovoid lesion with signal void (*arrows*) and mild surrounding inflammatory edema in the anatomic location of the posterior oblique ligament.

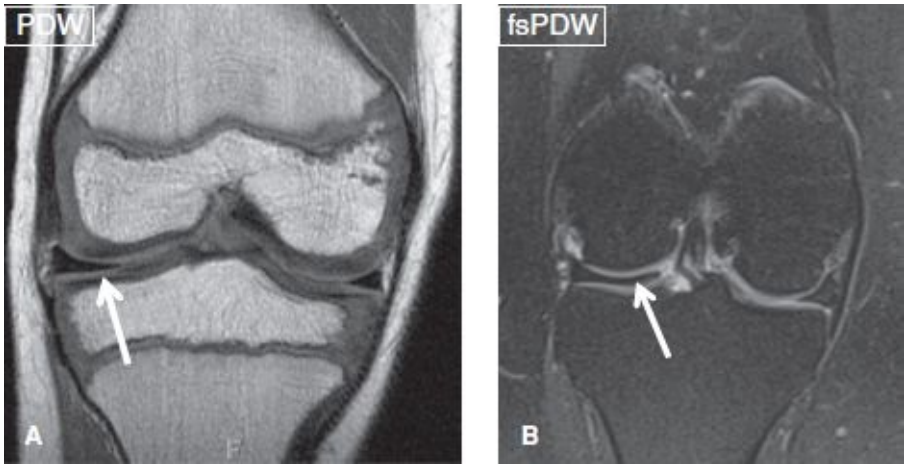

Fig. 62: Discoid meniscus. Coronal images from different cases demonstrate discoid lateral menisci (*arrows*), which partially **(A)** and completely **(B)** cover the ipsilateral tibial plateau.

The LCL complex serves as the primary restraint to varus stress of the knee at 30 degrees of flexion and external rotation of the tibia. It is comprised of the ITB anteriorly, the LCL in the middle and the biceps femoris tendon posteriorly. The LCL is extracapsular, 5–7 cm long, originates from the lateral femoral epicondyle, and converges distally with the biceps femoris tendon to form a conjoined tendon, which inserts to the anterior and lateral aspect of the fibular head (Fig. 68). Compared to the MCL, the LCL is more rounded and narrow, lacks any meniscal attachments, and is seldom seen entirely on one coronal image, due to its posterior oblique direction. If the LCL is seen entirely on one image, one should suspect abnormal anterior tibial translation and underlying ACL tear. On the sagittal view, the LCL and biceps femoris tendon form a V-shaped structural construct. Acute LCL tears may involve the proximal, mid-substance, or the tibial insertion, and appear as a serpiginous or lax ligament with discontinuous fibers (or avulsed fibular head), often without associated thickening of the ligament. In addition, due to its extracapsular location, LCL tears do not

result in much extravasation of joint fluid, and, therefore, are not associated with substantial T2 hyperintensity or edema of the surrounding soft tissues. In complete tears, one can identify the missing arm of the V construct on sagittal images (Fig. 69). The most common setting of LCL injury is in association with ACL and posterolateral (PL) corner injuries. Partial tears are better seen on axial and coronal images and are not uncommon in ACL injuries. Isolated LCL injuries are uncommon and can be seen with unusual falls, motor vehicle accidents, or wrestling injuries. Grade I and II LCL injuries are treated non-operatively; however grade III injuries require primary repair or reconstruction. In combined LCL and cruciate ligament injuries, both ligaments are reconstructed. In chronic microtears, the ligament becomes thickened and maintains low to intermediate signal intensity on T1W and T2W images. This finding is not uncommon in degenerative knees. The lateral compartment of the knee is further supported anteriorly by the ITB and posteriorly by the biceps femoris tendon. The ITB is an extension of the fascia lata and ends at Gerdy tubercle, which is located on the anterolateral surface of the tibia. ITB (friction) syndrome is a common cause of anterolateral knee pain related to intense physical activity that can be associated with repeated knee flexion and extension, such as in cyclists. These activities result in repeated inflammations, when an excessively tight or stressed ITB moves posteriorly and rubs against the femoral epicondyle, irritating the lateral synovial recess and/or the ITB bursa that lies between the ITB and the lateral femoral condyle. Imaging findings include ill-defined T2 hyperintensity (edema) of the fatty tissue interposed between the ITB and the lateral femoral condyle and/or well-defined fluid collection(s) in the same location, representing primary ITB or secondary (adventitious) bursitis. Chronic cases are characterized by diffuse ITB thickening (Figs. 70, 71). Tears of the ITB rarely occur in isolation and are usually associated with injuries to multiple ligaments of the knee, including the ACL and LCL (Fig. 72).

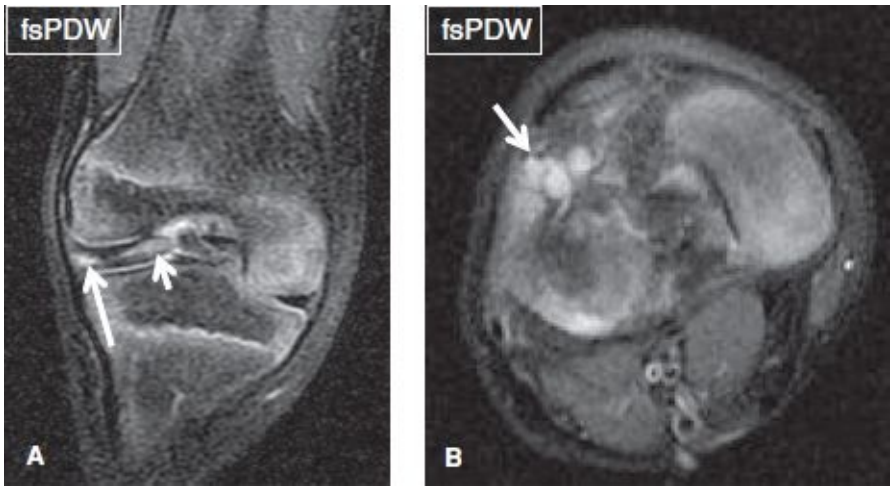

Fig. 63: Discoid meniscus. Coronal **(A)** and axial **(B)** images show a complete lateral discoid meniscus (*short arrow* in **A**) and associated intrameniscal (*long arrow* in **A**) and parameniscal (*arrow* in **B**) cysts.

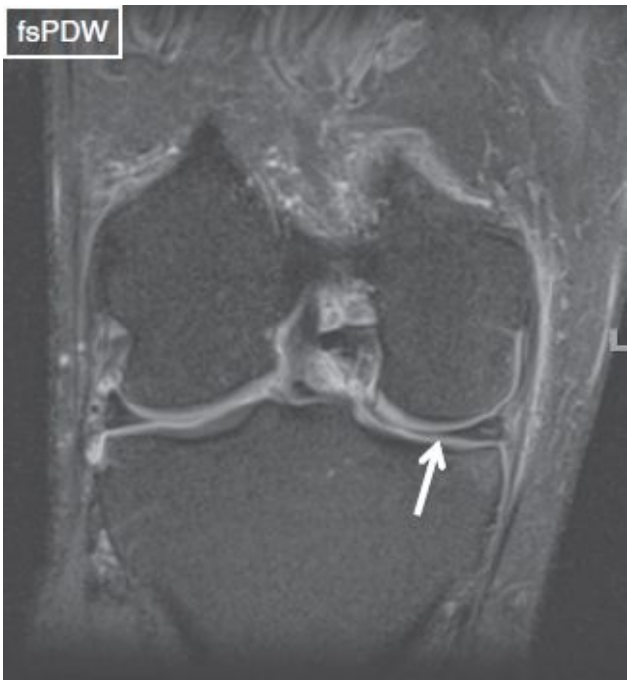

Fig. 64: Discoid medial meniscus. Coronal image shows increased width of the body of the medial meniscus (*arrow*).

Fig. 65: Chondrocalcinosis: Anteroposterior radiograph **(A)** and coronal MR images **(B, C)** show artifactual appearance of incomplete discoid meniscus, mimicked by chondrocalcinosis (*arrows*).

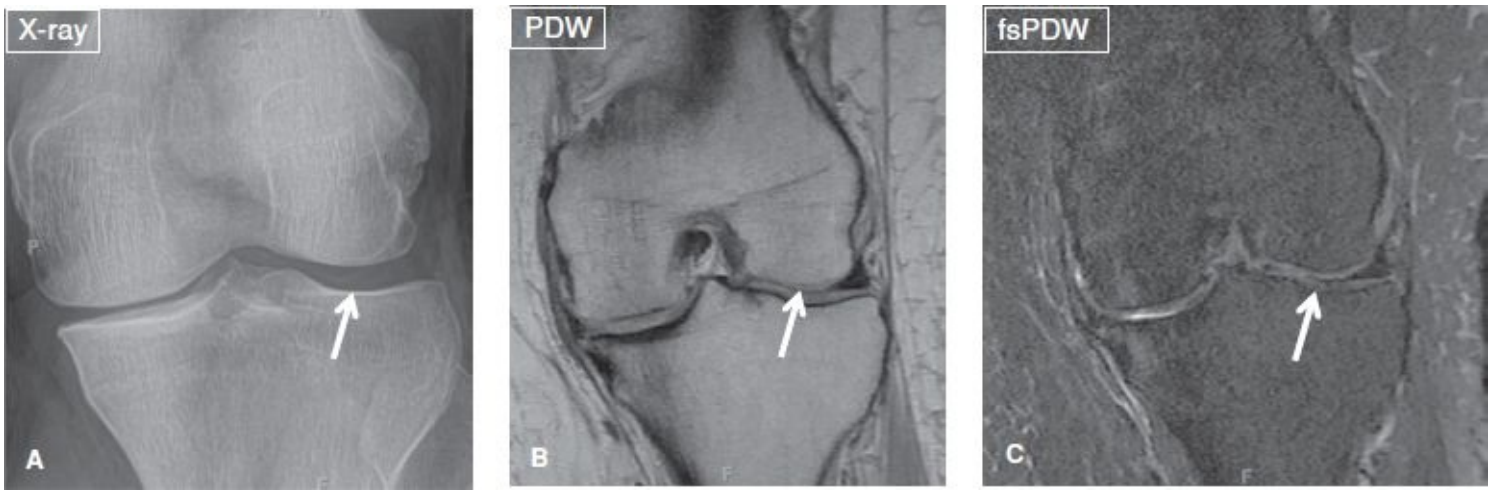

Fig. 66: Vacuum phenomenon. Sagittal **(A)** and coronal **(B)** images show artifactual appearance of incomplete discoid meniscus, mimicked by vacuum in the joint space (*arrows*).

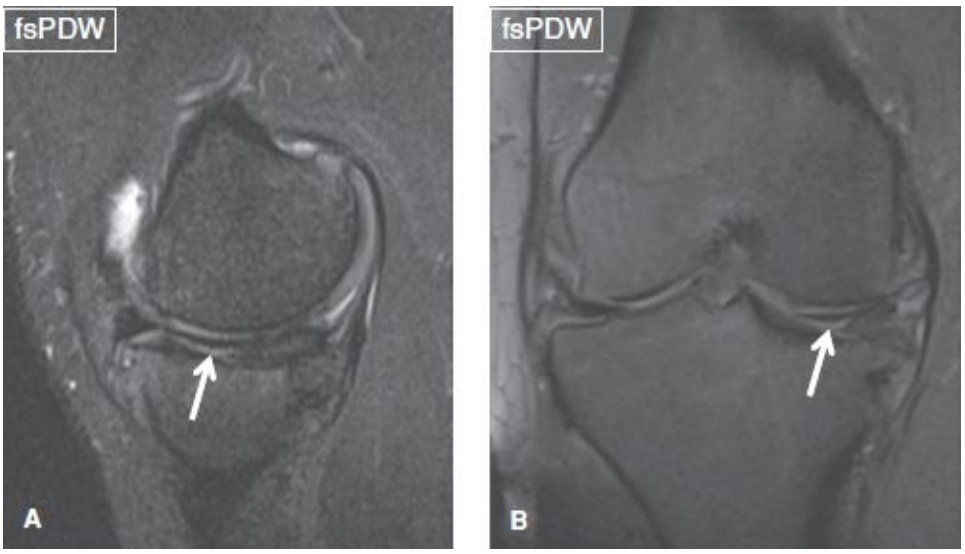

Fig. 67: Speckled appearance of the anterior horn of the lateral meniscus. Coronal image shows a speckled appearance (*arrow*) of the anterior horn attachment of the lateral meniscus, which is much more pronounced than what can be seen with the posterior horn of the medial meniscus.

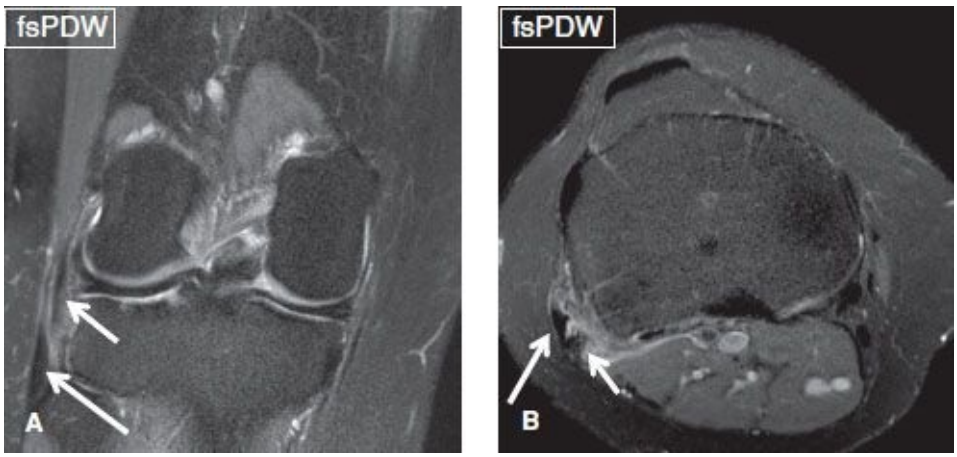

Fig. 68: Conjoined tendon formed by the lateral collateral ligament and biceps femoris

tendon. Coronal **(A)** and axial **(B)** images show the lateral collateral ligament (*long arrows*) lying proximal to the biceps femoris tendon (*short arrows*), just proximal to their convergence.

The biceps femoris is a strong flexor of the knee joint and the most lateral of the hamstring muscles. A long head arising (together with the semitendinosus muscle) from the ischial tuberosity as a conjoint tendon, and a short head originating from the linea aspera of the femur join and form a long common tendon, which inserts into the fibular head (after converging with the LCL, as described above), crural fascia, and proximal tibia. Biceps femoris tendinopathy appears as intermediate signal within the tendon on T1W and T2W images. Similar to other tendons in the body, injuries to the biceps femoris tendon are characterized as *grade* I (peritendinous edema), II (partial tear), and III (complete tear) sprains. In cases of tendon avulsion, mild bone marrow edema may be evident at the attachment site (Fig. 72).

POSTEROLATERAL CORNER:

Popliteus tendon: [<Normal> <Tendinosis> <Partial tear>]

Popliteofibular ligament: [<Intact> <Acute sprain>]

Arcuate ligament: [<Intact> <Acute sprain>]

Proximal tibiofibular joint: [<Normal> <Osteoarthrosis> <Effusion>]

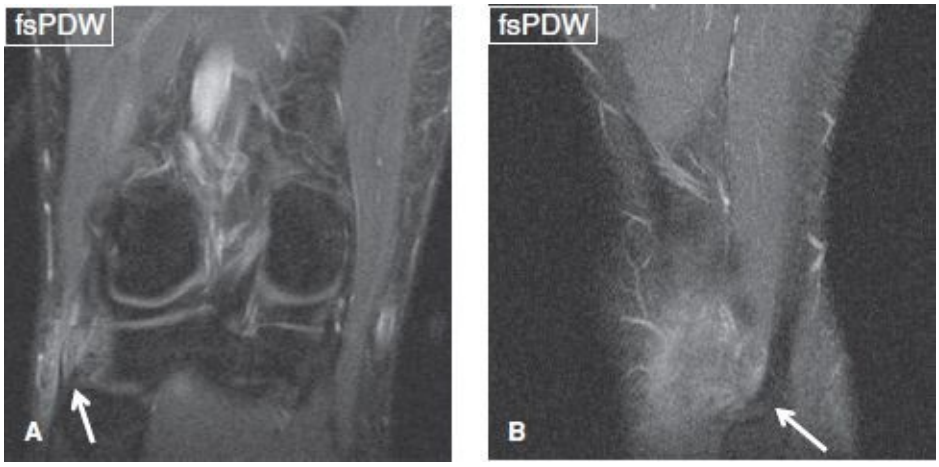

Fig. 69: LCL tear (Grade III sprain). Coronal **(A)** and sagittal **(B)** images show the insertions of the conjoined tendon (*arrows*) at the fibular head with absent anterior arm of the V, the lateral collateral ligament.

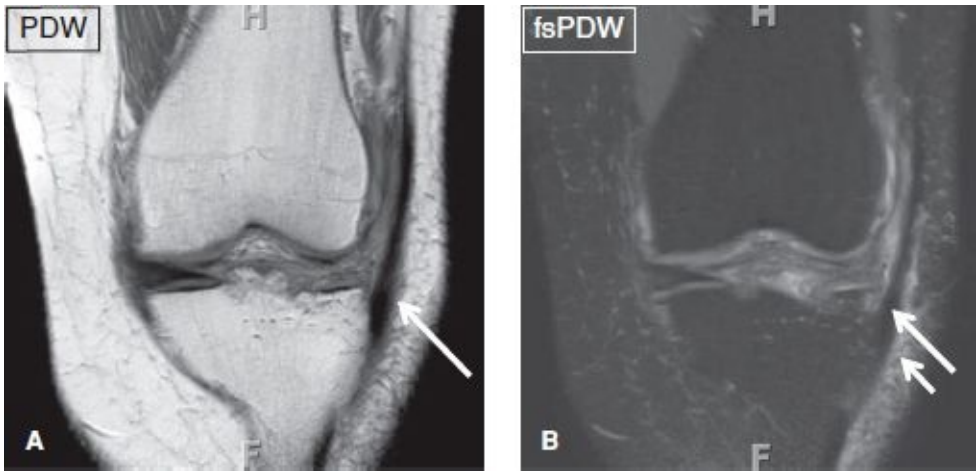

Fig. 70: Acute on chronic iliotibial band syndrome. Coronal images **(A, B)** show a diffuse thickening of the iliotibial band (*long arrows*), indicating remodeling from chronic microtrauma and inflammation, as well as edema of the subjacent and the surrounding soft tissues (*short arrow*), suggesting superimposed acute inflammation.

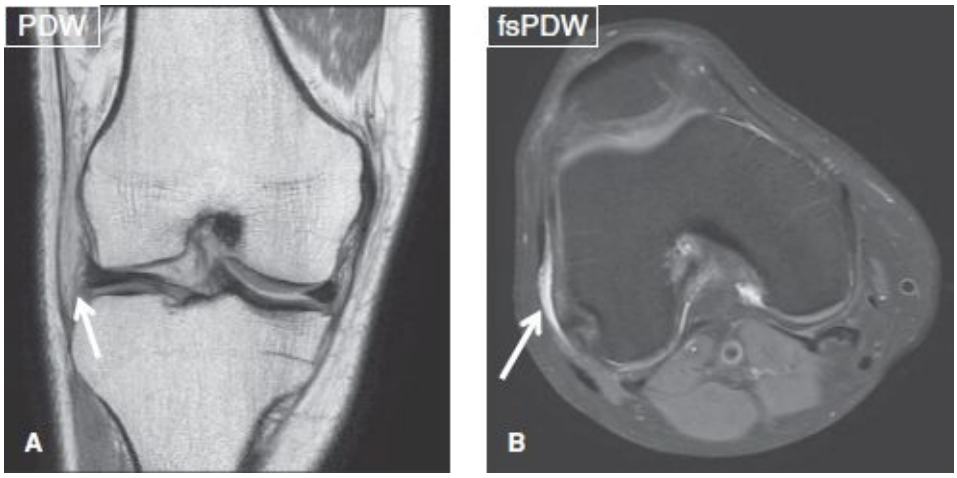

Fig. 71: Iliotibial band bursitis. Coronal **(A)** and axial **(B)** images show a well-defined fluid collection (*arrows*) interposed between the iliotibial band and the lateral femoral condyle, corresponding to fluid-filled iliotibial bursa.

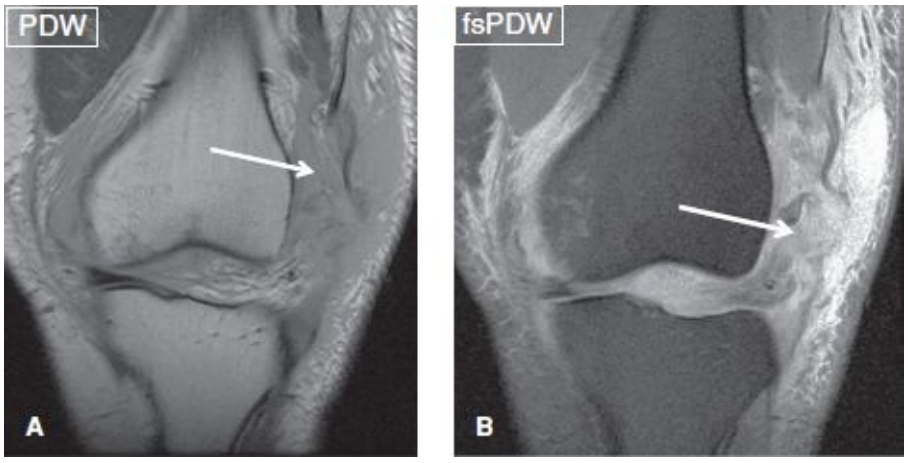

Fig. 72: ITB rupture: Coronal MR images **(A, B)** of a patient with recent MVA show complete rupture of the ITB (*arrows*) adjacent to Gerdy tubercle. Patient also had ACL, LCL, and posterolateral corner injury (not shown).

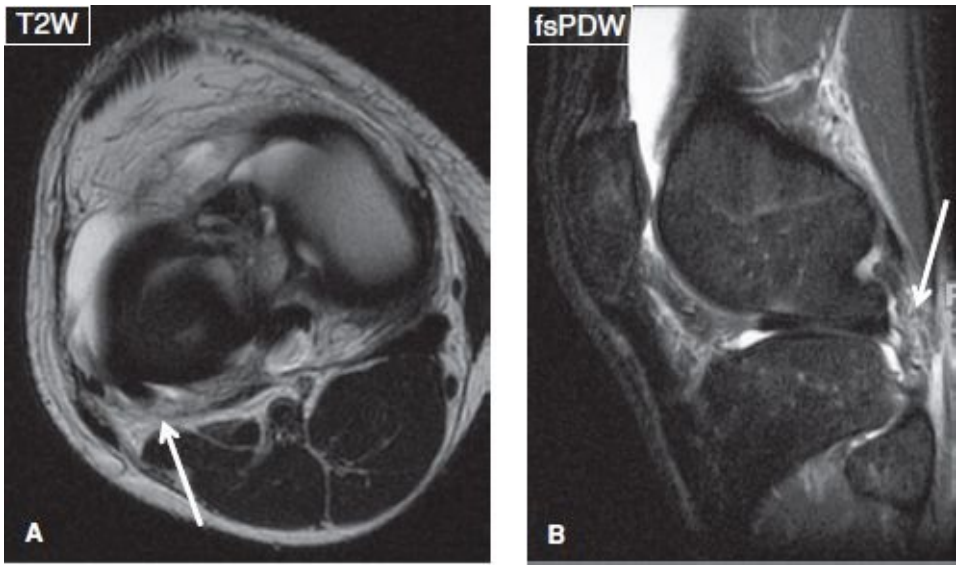

Fig. 73: Grade II sprain of the arcuate ligament. Axial **(A)** and sagittal **(B)** images show partial discontinuity (*arrow* in **A**) of the arcuate ligament, with associated edema (*arrow* in **B**) of the surrounding soft tissues. One should note the posterolateral fascial edema is almost never associated with popliteal cyst rupture.

The stability of the posterolateral (PL) corner of the knee is provided by capsular and non-capsular structures that function as static and dynamic stabilizers, including the arcuate ligament, the popliteus muscle, the popliteofibular and the fabellofibular ligament and the LCL. Failure to identify PL corner injuries can have consequences of chronic instability, predispose to cruciate graft failure, and contribute to significant post-traumatic osteoarthritis. In addition, if unrecognized and one performs arthroscopy in the acute stage of injury, most of the intra-articular fluid injected during arthroscopy can leak into the calf soft tissues and predispose to development of compartment syndrome. PL corner injury is clinically identified using a number of tests.

- In the external rotation recurvatum test, one looks for increased knee extension, or recurvatum +/–varus, as an indication of severe ligamentous injury. This test is usually positive in patients who have a combined PL corner injury and/or ACL and PCL injury. In this test, the examiner uses one hand to stabilize the distal femur while the other hand is placed around the great toe or foot and is used to lift it off the examining table. The relative amount of increased hyperextension is compared to the contralateral knee.
- In the varus stress test, one applies varus stress with the knee flexed at 30 degrees. Mild (0–5 mm), moderate (5–10 mm), or severe (>10 mm) lateral compartment opening, compared to the normal knee, is usually indicative of at least PL knee injury and potentially ACL and/or PCL injury.
- In the PL drawer test, a posterior and externally rotated force is applied through the fingers to assess for PL translation of the tibia on the femur. This test determines the degree of PL corner injury, and can be grossly positive even with an intact posterior cruciate ligament.
- The dial test, which provides an assessment of a possible PL knee injury. It is performed with the knee either flexed at 30 or 90 degrees. One hand is used to stabilize the distal

femur while the other is used to externally rotate the foot. A positive dial test at 30 degrees with an increased amount of external rotation (>15 degrees) compared to the contralateral normal knee is indicative of a PL corner injury. A positive dial test at 30 and 90 degrees of knee flexion would indicate that there is concurrent PCL injury in addition to the PL corner injury.

There is no strict definition of PL corner injury on imaging, and the diagnosis is typically clinical. However, one should carefully look for various PL corner structures in the event of PL fascial edema, especially for LCL, conjoint tendon, and popliteus tendon injuries. Once identified, they should be reported and clinical correlation for potential PL instability should be recommended.

The arcuate ligament is a thickening of the PL capsule and essentially the lateral sided equivalent of the POL. It is a Y-shaped structure with medial and lateral limbs, both of which insert distally at the top of the fibular styloid process, as opposed to the conjoint tendon, which inserts on the side of the fibular styloid process. The POL is best depicted on axial images at the level of the joint line as a low-signal linear band at the PL aspect of the joint (Fig. 6D,E). Injuries to the arcuate ligament are graded similar to POL injuries as grade I, II, and III sprains (Fig. 73). Arcuate fracture (arc-like crescentic fracture) of the fibular styloid process is seen with arcuate ligament avulsion and it is associated with PL capsular injury (60%), both cruciate ligaments (50%), and posterior cruciate ligament (90%) injuries (Fig. 74).

Fig. 74: Arcuate fracture. Sequential sagittal images **(A, B)** demonstrate avulsion of the arcuate ligament attachment with arcuate fracture (*arrows*) from the fibular styloid process. The corresponding far-lateral sagittal image **(C)** displays an intact conjoined tendon (*arrow*).

The popliteus tendon and lateral head gastrocnemius tendons are dynamic stabilizers of the PL corner. The popliteus muscle arises from the posteromedial aspect of the proximal tibia, and extends superiorly and laterally to form a tendon that continues into the joint through the popliteal hiatus or tunnel. The tendon inserts at the popliteal sulcus of the LFC,

the posterior horn of the LM, and the fibular head. The popliteus tendon is the primary restraint to external rotation at 30 degrees and is best depicted on axial and coronal images, featuring low and intermediate signal, respectively (Figs. 3, 6 (D,E)). The intermediate signal is related to oblique course and magic angle artifact. The spectrum on abnormalities include tendinopathy, which appears as intermediate signal within the tendon with thickening on PDW and fsPDW images; partial tear of the musculotendinous junction, which appears as amorphous increased T2 signal within the tendon and muscle, frank disruption of fibers and/or enlargement of the muscle belly; and partial or complete avulsion from the femoral attachment, which appears as a lax and retracted popliteus tendon, occasionally associated with mild bone marrow edema and/or cystic changes and enthesopathy at the attachment site (Figs. 75, 76).

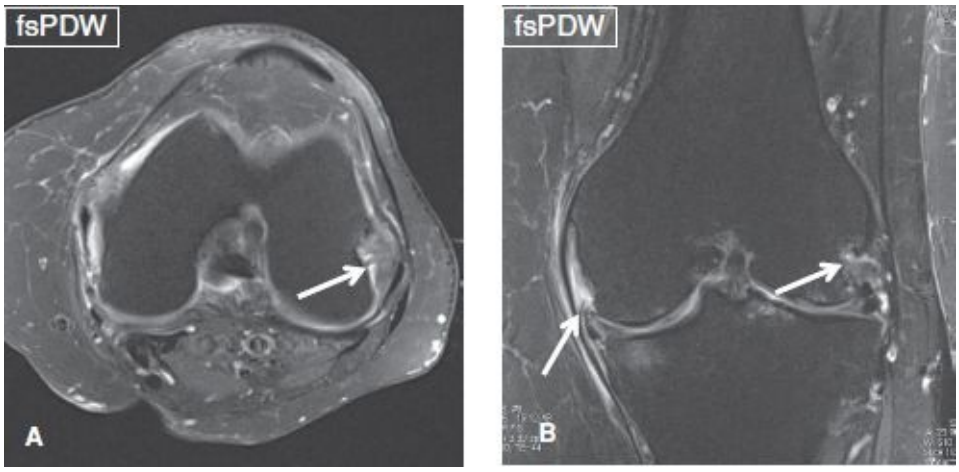

Fig. 75: Subacute partial tear popliteus tendon. Axial **(A)** and coronal **(B)** images exhibit partial avulsion of the popliteus tendon (*arrows*) from its femoral attachment with subjacent subcortical cystic changes.

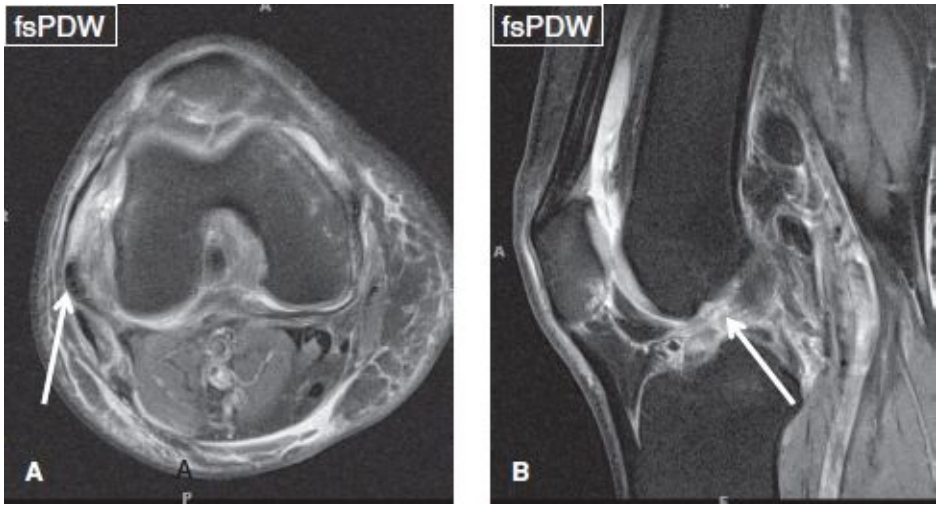

Fig. 76: Popliteus tendon complete avulsion. **A:** Axial image exhibits complete avulsion of the popliteus tendon (*arrow*) with mild subcortical edema and an associated complete avulsion of the lateral retinaculum from the femoral attachment. **B:** The corresponding sagittal image demonstrates complete anterior cruciate ligament disruption (*arrow*).

The popliteofibular ligament represents the attachment of the popliteal tendon to the fibular head. It is invariably visualized as a small hypointense structure on coronal and sagittal images (Figs. 2, 3). Injury may be detected as increased signal within the ligament, discontinuity, or avulsion of the ligament off the fibular styloid process (Fig. 77).

The fabellofibular ligament arises from the fibular styloid process and inserts on the PL aspect of the fabella. The fabella is a sesamoid bone, which is situated inside the tendon of the lateral gastrocnemius head, with a prevalence of about 25%. The fabellofibular ligament is occasionally visualized on coronal images as a hypointense structure located posterior to LCL. Evidence of injury includes distal avulsion from the fibular styloid process, which is sometimes associated with avulsion of the biceps femoris tendon, thickening, and increased signal intensity. The thickness of fabellofibular ligament is reported to be inversely proportional to the arcuate ligament thickness.

The “arcuate sign” or “arcuate fracture” can be caused by injury to one or more of the attaching ligaments (arcuate, popliteofibular, fabellofibular) (Figs. 74, 77). Even in cases without a frank fracture, edema may be localized at the fibular styloid process, suggesting popliteofibular, fabellofibular, and/or arcuate ligament injury, or more diffuse edema may be evident at the lateral aspect of the fibular head, indicating injury to the LCL and/or the biceps femoris tendon. With PL corner injuries, one should carefully assess the common peroneal nerve for injuries, such as stretch injury (most common), neuroma in continuity or transection (Fig. 78).

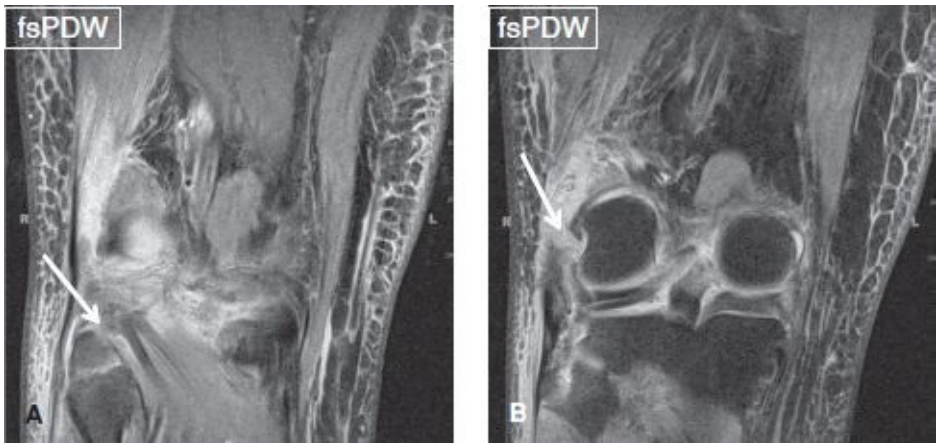

Fig. 77: Popliteofibular ligament injury. **A:** Coronal image shows disruption of the popliteofibular ligament (*arrow*) in its mid-portion. Notice arcuate fracture of the fibula and posterolateral fascial edema in keeping with findings of posterolateral coroner injury. **B:** Sequential coronal image anterior to the latter shows complete rupture of the lateral collateral ligament and popliteus tendon (*arrow*) from the femoral attachments.

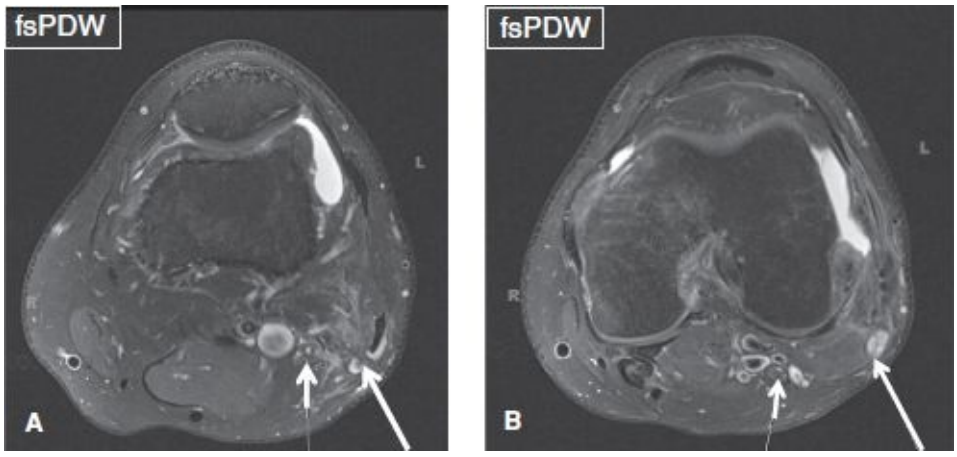

Fig. 78: CPN injury. Sequential axial MR images **(A, B)** through the knee in a case of ACL and posterolateral corner injury. Notice abrupt changes in caliber and hyperintense CPN (*long arrows*) in keeping with a neuroma in continuity from high-grade injury. Mild hyperintensity of the tibial nerve (*short arrows*) is in keeping with mild stretch injury.

The proximal tibiofibular joint is an often overlooked source of lateral knee pain. It functions in dissipating lower leg torsional stresses and lateral tibial bending moments as well as in transmitting axial loads in weight-bearing. The proximal tibiofibular joint normally features thin hypointense anterosuperior and posterosuperior ligaments and occasionally a small amount of joint fluid. The anteroinferior and posteroinferior ligaments form part of the syndesmotic ligament complex of the ankle along with interosseous ligament. The proximal tibiofibular joint may be involved by osteoarthritis, featuring osteophytes, subchondral cysts, subchondral sclerosis, and joint space narrowing; direct trauma, which may include fracture, dislocation, ligament strains and tears, and injury to the peroneal neurovascular bundle; ganglion cysts (Fig. 79), which often result from degeneration of the proximal tibiofibular joint and may extend extraneurally or intraneurally with retrograde extension along the intra-articular branch causing chronic or repeated compression of the common peroneal nerve (Fig. 80); or pigmented villonodular synovitis, which is characterized by large, globular areas of low T1 and T2 signals outlining the hypertrophied synovium.

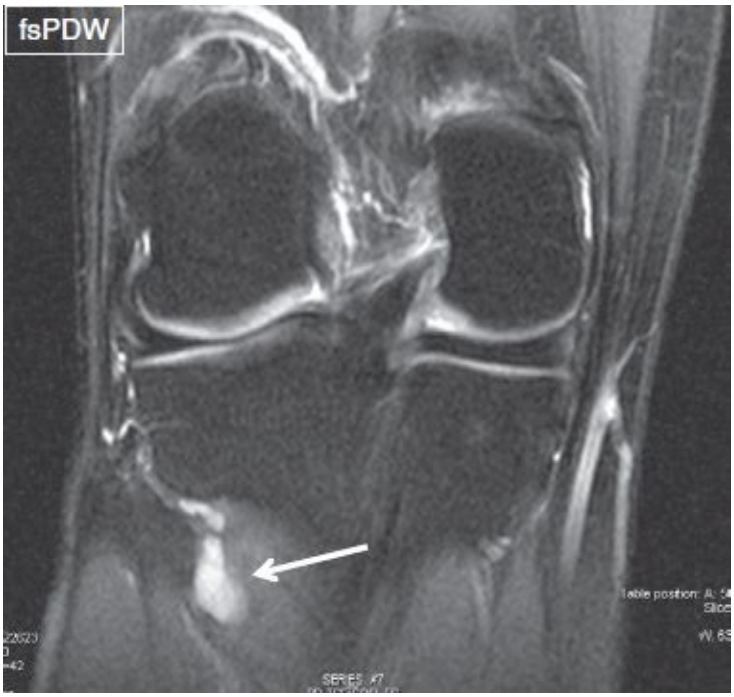

Fig. 79: Proximal tibiofibular joint ganglion. Coronal image shows increased synovial fluid (*arrow*) loculated adjacent to the tibiofibular joint in keeping with a ganglion cyst.

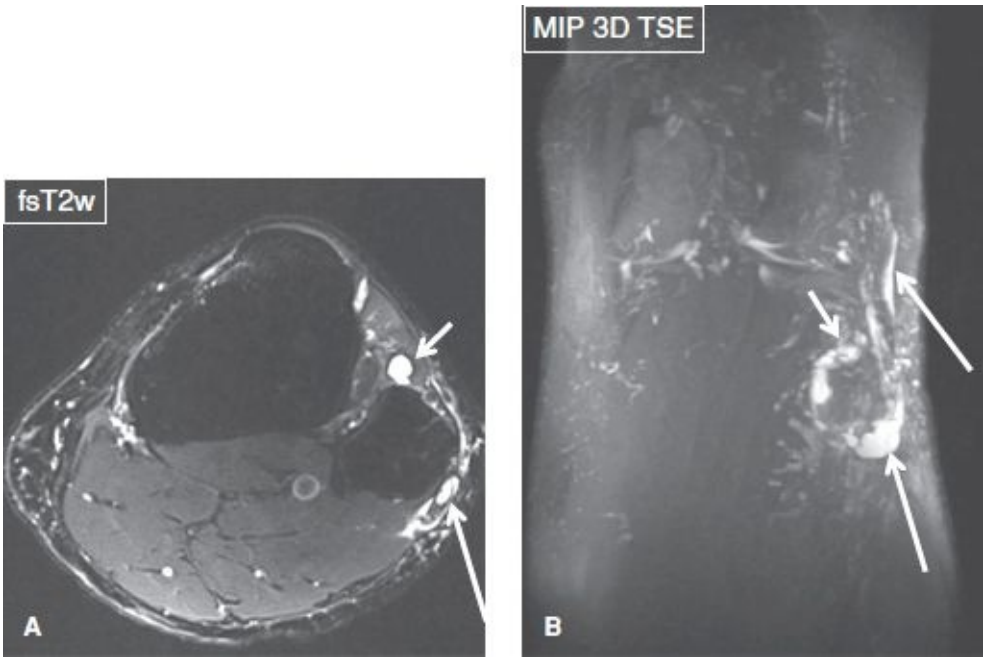

Fig. 80: CPN ganglion. Axial fsT2W **(A)** and coronal MIP image from a 3D TSE sequence **(B)** show retrograde extension of a ganglion cyst from the proximal tibiofibular joint (*short arrows*) via an intra-articular branch to envelop and invade the proximal common peroneal nerve (*long arrows*).

ANTERIOR COMPARTMENT:

Alignment: [<Normal> <Patella alta/patella infera> <Patellar tilt> <Lateral/medial patellar subluxation>]

Quadriceps tendon: [<Normal> <Tendinosis> <Tear> <Enthesopathy> <Quadriceps

fat pad edema/prefemoral fat pad edema >]

Patellar tendon: [<Normal> <Tendinosis> <Tear> <Enthesopathy>]

Patellar cartilage: [<Normal>]

Trochlear groove: [<Normal> <Shallow> <Prominent lateral ridge>]

Trochlear cartilage: [<Normal>]

Plica: [<Normal/thickened> <Sprained ligamentum mucosum>]

Hoffa fat pad: [<Normal> <Superolateral edema> <Shearing injury>]

TT–TG distance: [__] cm

The patella sits into the trochlear groove of the distal femur, and acts as a fulcrum, which increases the force exerted by the quadriceps muscle when the knee extends. It is held in position by (1) the quadriceps tendon, which attaches into the superior pole of the patella, and has a trilaminar configuration, with a superficial layer of the rectus femoris, a middle layer of the vastus lateralis and medialis, and a deeper layer of the vastus intermedius; (2) the patellar tendon (or ligament), which extends from the inferior pole (apex) of the patella to the tibial tuberosity, and is mainly composed of rectus femoris fibers that course over the patella; and (3) the medial and lateral patellar retinaculae (MPR, LPR), which extend obliquely and transversely from the medial and lateral patellar margins to the femur and tibia. The retinaculae contribute to the static stability. Dynamic stability is provided by the vastus lateralis obliquus (VLO) and vastus medialis obliquus (VMO). The MPR is composed of (1) a superficial layer, which is formed by the vastus medialis oblique sheath and the investing layer over the sartorius muscle; (2) a middle layer, which is formed by the superficial MCL, and the medial patellofemoral, medial patellomeniscal, and medial patellotibial ligaments, which are thickenings of the joint capsule and are arranged according to their names at the respective craniocaudal levels of medial femoral condyle, MM, and medial tibial plateau, respectively (the medial patellofemoral ligament constitutes the main passive restraint to the lateral patellar translation); and (3) a deep layer, which is formed by the deep portion of the MCL, meniscotibial, and meniscofemoral ligaments. The LPR is composed of (1) a superficial layer, which is formed by the vastus lateralis oblique sheath and the ITB; and (2) a deep layer, which is formed by the lateral patellofemoral ligament (or epicondylopatellar band), lateral patellomeniscal (or transverse) ligament, and lateral patellotibial ligament (or band). Similar to the MPR, the above are arranged according to their names at the respective levels of lateral femoral condyle, LM, and lateral tibial plateau, respectively, from superior to inferior (Fig. 6).

Clinically, patients with lateral patellar instability are tested using the lateral patellar apprehension test. This test evaluates patellar subluxation or dislocation as one compares to

the opposite knee. In this test, the examiner flexes the knee to approximately 45 degrees and tries to mobilize the patella from medial to lateral in the trochlear groove. If the patella subluxes laterally outside the trochlear groove, it is considered lateral patellar subluxation. In some instances, the patella may actually dislocate. When a patient exhibits a small degree of subluxation, it is important to compare clinical findings with the contralateral knee. If the patient feels that the patella is about to dislocate or expresses pain and apprehension, this is considered a positive lateral patellar apprehension test. The medial patellar apprehension test is performed for medial instability, which almost always a result of prior surgery. The knee is started in full extension and then flexed through an arc of about 0 to 40 degrees. The patella will commonly catch on the top of the medial trochlear groove and a visible clunk and/or patient's pain can be reproduced as the patella is observed reducing back into the confines of the trochlear groove after 35 to 40 degrees of flexion.

Injuries to the patellar retinaculae may result from patellar dislocation or direct impaction. In the vast majority of cases, patellar dislocations occur in the lateral direction, and typically result from twisting injuries in flexed foot and knee positions. Medial dislocation occurs due to iatrogenic reasons, such as overzealous attempt at lateral retinacular release or medial retinacular plication. Because dislocation almost always reduces spontaneously, it is referred to as transient patellar dislocation. Typical (and pathognomonic) areas of impaction injuries or fractures include the anterolateral aspect of the lateral femoral condyle (LFC) and the inferior aspect of the medial pole of the patella. In most situations, the diagnosis is clinically obvious. The role of radiologist is to define the degree and extent of the retinacular injuries, and detect potential ostochondral injuries and fractured loose bodies. Injuries to the patellar retinaculae are graded in the same way as any other ligament injury, namely *grade I* (microscopic tear, depicted as periligamentous edema), *grade II* (partial tear, depicted as with edema-like signal within and around the ligament), and *grade III* (complete tear, depicted as complete disruption of the ligament, which is lax and retracted, along with contralateral patellar dislocation). Most commonly, injuries involve the medial patellofemoral ligament. Partial injuries may be isolated to the inferior portions of the retinaculum, such as medial patellomeniscal and medial patellotibial ligaments. In avulsion injuries, bone marrow edema is evident at the attachment site. Subacute injuries manifest as a combination of resolving bone marrow and fascial edema, hematoma or ganglion formation in the soft tissues and within the retinaculum, bony avulsive deformity at the retinacular attachments, and thickening/attenuation as well as remodeling of the retinaculum along its transverse span (Figs. 81–83). Chronic injuries manifest with one or more of the following findings: fibrosed/thickened/attenuated retinaculum and/or ganglion formation; bony productive changes at a retinacular attachment, especially contour irregularity of the inferior aspect of the medial pole of the patella; partial ossification of the retinacular layers; or chronic patellar malalignment (abnormal tilt and subluxation as described below). Commonly, chronic altered stress of patellar malalignment leads to thickening of the lateral retinaculum, and attenuation of the

medial retinaculum.

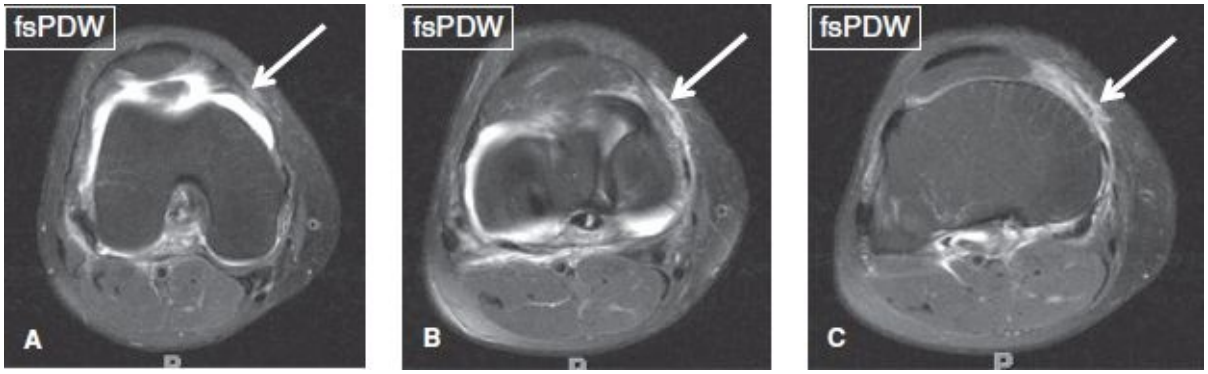

Fig. 81: Acute on chronic transient patellar dislocation. Axial images at the levels of the trochlea **(A),** knee joint line **(B),** and tibiofibular joint **(C)** demonstrate attenuated superior part of the medial retinaculum (*arrow* in **A**) and fascial edema (*arrows* in **B, C**), most prominent at the lower aspect of the medial patellar retinaculum (in the region of the medial patellomeniscal and medial patellotibial ligaments), in keeping with acute on chronic grade II sprains.

Fig. 82: Transient patellar dislocation. **A:** Axial image of a patient with an acute transient patellar dislocation shows foci of postimpaction marrow edema (*short arrows*) at the medial patellar facet and lateral femoral condyle, along with fascial edema (*long arrow*) superficial to the medial patellar retinaculum, in keeping with grade II sprain. Sagittal **(B)** and axial **(C)** images of a patient with a subacute transient patellar dislocation exhibit postimpaction marrow edema at the medial patellar facet (*short arrows*), along with hematoma formation (*long arrow*), deep to the medial patellar retinaculum.

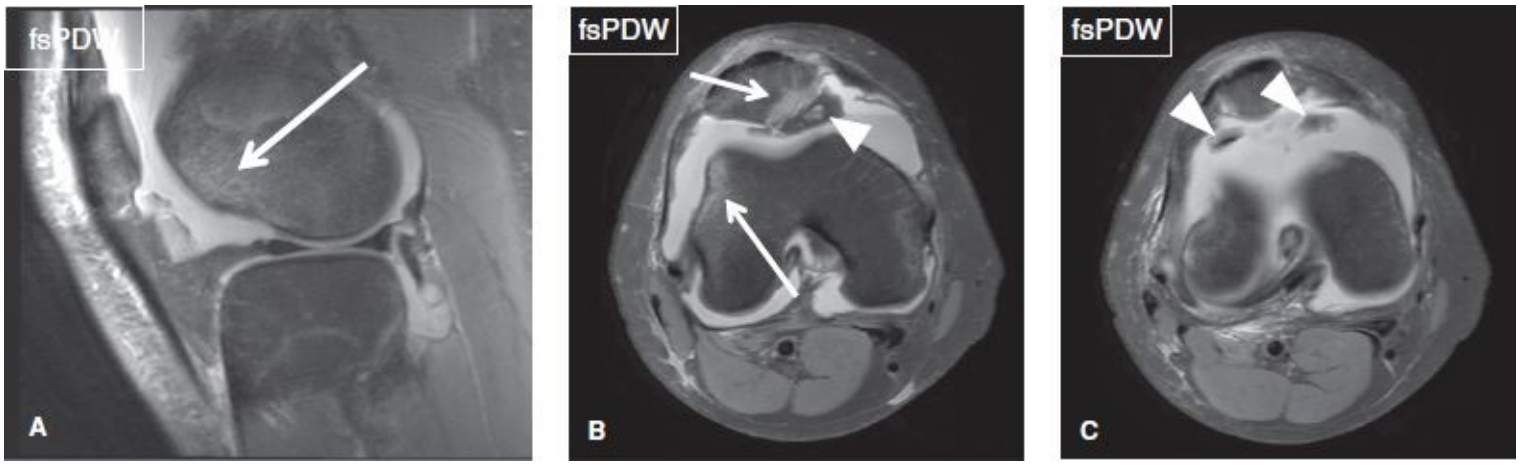

Fig. 83: Transient patellar dislocation associated with osteochondral injury. Sagittal **(A)** and axial **(B, C)** images demonstrate large hemarthrosis, fracture of the Hoffa's fat pad, osteochondral impaction injuries of the lateral femoral condyle (*long arrows*), inferior aspect of the medial pole of the patella (classic location, *short arrow*). Notice osteochondral displaced fragments (*arrowheads*) into the anterior joint recess and torn medial retinaculum (grade III sprain of medial patellofemoral ligament).

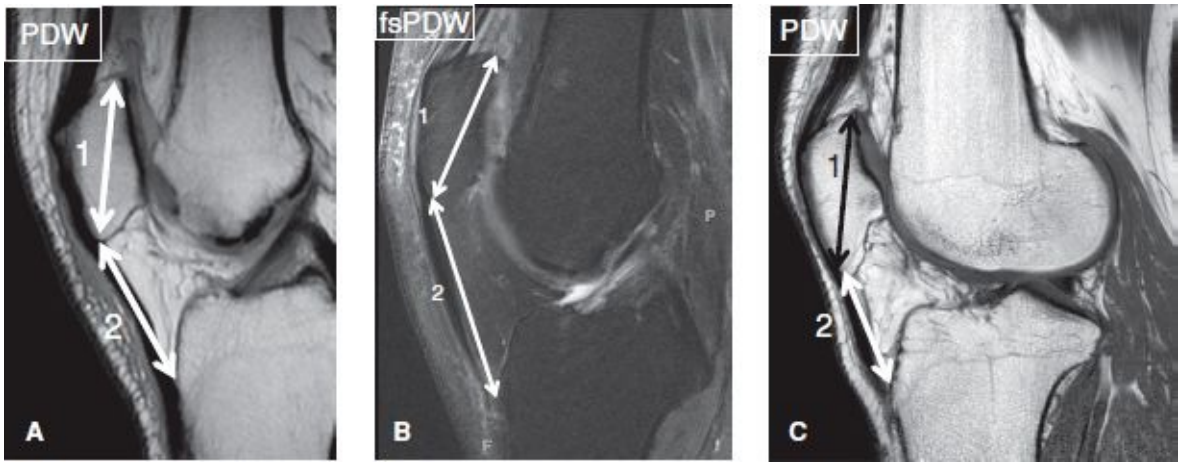

Fig. 84: Normal and abnormal patellofemoral alignment. On midline sagittal images, the ratio of the patellar tendon length (*distance 2*) to the maximal diagonal length of the patella (*distance 1*) is normal (between 0.8 and 1.2) in **A,** and abnormal (exceeding 1.2, in keeping with patella alta) in **B,** and (less than 0.8, in keeping with patella infera) in **C.**

The alignment on the patella with respect to the trochlea should be assessed on the sagittal and axial images. On the midline T1W sagittal image, the ratio of the patellar tendon length (inferior border of patella to top of tibial groove) to the maximal diagonal length of the patella is calculated, with normal values ranging between 0.8 and 1.2 (Insall–Salvatti ratio). Values greater than 1.2 indicate abnormally high position of the patella (patella alta) whereas values less than 0.8 indicate abnormally low position of the patella (patella infera or baja) (Fig. 84). Subsequently, axial images are used to measure the distance between perpendicular lines drawn from the medial edge of the patella through the most anterior point of the medial condyle (Fig. 85). The above distance should normally measure up to 2 mm, otherwise mild (distance 3–5 mm), moderate (distance 5–10 mm), or

severe (distance >10 mm) patellar subluxation (translation) exists. It should be remembered that joint effusion in itself might cause or exaggerate patellar subluxation. One could also match up the apex of the patella with the apex of the trochlear sulcus concavity, which should normally be within 2 mm of each other. Most patellofemoral pain syndromes are usually associated with lateral rather than medial patellar subluxation. Subsequently, the radiologist should check for abnormal patellar tilt, by measuring the patellofemoral angle, which is formed by the lines drawn along the bony lateral patellar facet and the tangent to the anterior femoral condyles. In general, the patellofemoral angle measures more than 8 degrees and opens laterally. Medial opening or an angle of less than 8 degrees qualifies as abnormal tilt (Fig. 86). Other simple gestalt way of finding tilt is by comparing the tangents to the body of patella with the posterior femoral condyle, which should normally be parallel. It is noteworthy that abnormal tilt may be present with or without patellar translation. The latter case is usually caused by a tight LPR (known as excessive lateral pressure syndrome) which results in abnormal lateral patellar tilt and exaggerated pressure in the lateral aspect of the patellofemoral joint. This may be associated with friction-related superolateral Hoffa's fat pad edema, lateral aspect prefemoral fat pad edema (excessive lateral friction syndrome, ELFS), and early patellofemoral osteoarthritis. ELFS may also develop due to overzealous attempts of MPR plication, underlying persistent trochlear dysplasia, and prior ACL repairs with consequent patellar tendinosis from graft harvest. However, edema like T2 signal is common in superolateral Hoffa's fat pad, lateral aspect of the prefemoral fat pad, and quadriceps fat pad, and these fat pad edema might not cause symptoms (Fig. 87). Excessive fat pad edema, formation of adventitial bursa and associated patellofemoral malalignments are more commonly associated with symptoms.

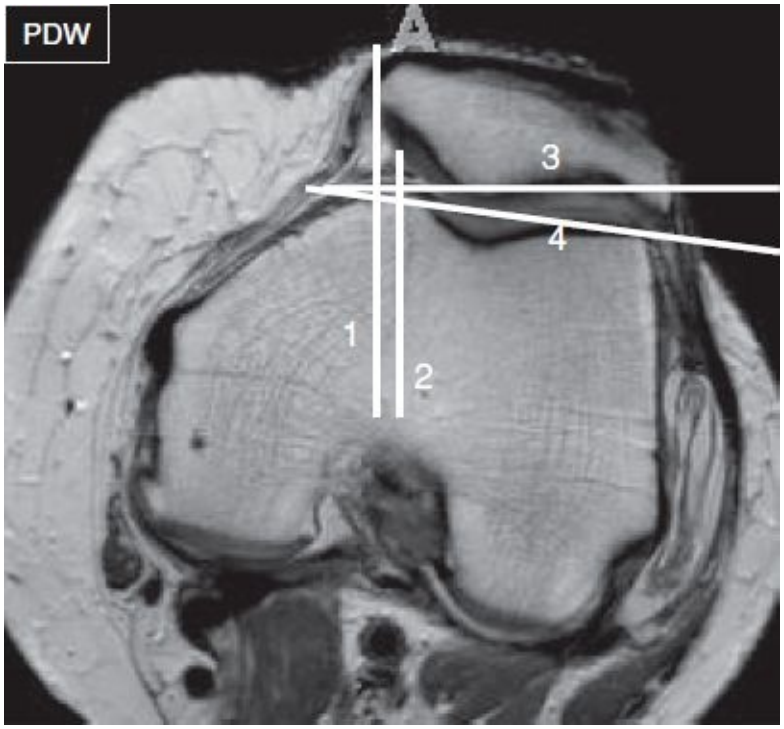

Fig. 85: Normal patellofemoral alignment. Axial image at the level of the trochlea or thickest patellar and trochlear cartilage, approximately at the femoral physeal scar level show normal distance (≤2 mm) between perpendicular lines drawn through the medial

edge of the patella (*line 1*) and through the most anterior point of the medial femoral condyle (*line 2*), and normal lateral opening of the angle (>8 degrees) formed by lines drawn along the bony lateral patellar facet (*line 3*) and tangent to the anterior femoral condyles (*line 4*).

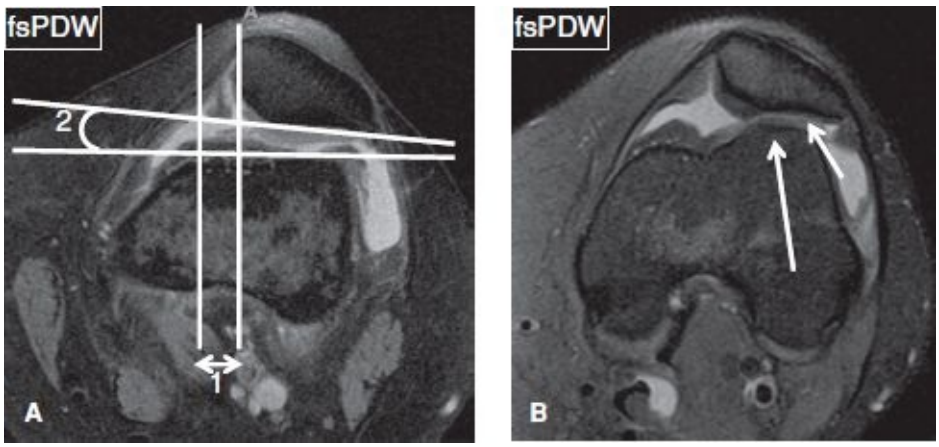

Fig. 86: Patellar translation and tilt. Axial images. **A:** Increased distance (*line 1*) between the lines crossing through the medial edge of the patella and the medial femoral condyle indicates lateral translation. The patellofemoral angle (*angle 2*) opens medially, in keeping with tilt. **B:** A similar case to **A,** but exaggerated due to a prominent lateral trochlear ridge (*long arrow*), and associated with high-grade cartilage thinning (*short arrow*) of the lateral patellar facet.

The normal quadriceps tendon appears as a relatively straight low signal band measuring approximately 8 and 35 mm in sagittal and coronal planes, respectively. On sagittal images, it features a laminated configuration, with three parallel layers (Fig. 87). Occasionally, it may appear bilaminar or quadrilaminar; however, smooth fat layers should be present between the hypointense tendon layers. In quadriceps tendinosis, there is ill-defined intermediate signal alteration within the distal tendon, along with partial effacement of the laminated appearance and/or tendon thickening. Tears most often involve the teno-osseous junction at the superior patella. These injuries occur with eccentric contraction (such as partially flexed knee with foot in planted position), standing from sitting position, and prior surgery (such as total knee replacement or prior LPR release). Partial tears appear as partial discontinuity of tendon fibers, associated with edema and hemorrhage of the anterior soft tissues (Fig. 88). These should be distinguished from prominent vessels, which can mimic small interstitial tears. Any focal non-branching fluid-like T2 hyperintensity with or without tendon fiber discontinuity and associated fascial edema indicates a tear (Fig. 89). In complete tears, the tendon is completely torn, lax, and retracted, and patella infera may result. In some cases, quadriceps tendon traction may lead to avulsion fracture of the superior patellar pole or detachment of a pre-existing enthesophyte (Fig. 90). In 20% cases, tendon tears can be bilateral and spontaneous with minimal injury. The underlying etiologies may include pre-existing tendinosis due to gout, collagen vascular disease, anabolic steroids, renal insufficiency, etc. Quadriceps

enthesopathy refers to inflammation of the tendon insertion, which results from recurrent traction-related injury and appears as T2 hyperintensity (edema) of the quadriceps–patella interface, with or without associated T2 hyperintensity of the overlying subcutaneous tissues (Fig. 91). It should be distinguished from prominent vessels that may be sometimes observed anterior to the patella. Chronic traction-related injuries result in formation of enthesophytes at the teno-osseous junction and anterior aspect of the patella, best seen on non-fs images or radiographs.

The patellar tendon (or ligament) extends from the anterior aspect of the inferior pole of the patella to the tibial tubercle. It is best evaluated on sagittal images, where it normally does not exceed 6 mm in thickness and demonstrates homogeneous low signal intensity on all sequences, except from the posterior margins of the proximal and distal attachments, which occasionally demonstrate mild focal intermediate signal, due to interspersed nontendinous fibers and magic angle phenomenon (Figs. 4, 92). The tendon is semilunar to half round in geometry, and features convex anterior border and a well-defined straight posterior border. In patellar tendinosis, there is focal or diffuse thickening (>6 mm thickness) and intermediate signal intensity of the tendon, occasionally with ill-definition of the posterior margin, and edema of the adjacent Hoffa's fat pad. More severe cases tend to involve the full length of the tendon. However, any intratendinous fluid-like T2 hyperintensity reflects a tear (Fig. 93). With chronicity, there may be ossification in the tendon or intra-tendinous ganglion formation (Figs. 94, 95). Traumatic partial or complete tears show coexistent edema and hemorrhage of the adjacent tissues, and/or associated retinacular injuries. The injuries could be due to direct forces, indirect tensile forces, in the setting of prior ACL repair with graft harvest and total knee replacement. Patella alta may or may not be evident in cases of complete tears depending upon the lack or presence of integrity of the retinaculae, respectively (Fig. 96). The term "jumper's knee" refers to the phenomenon of repeated insertional injuries of the proximal, central third (and inner third) fibers of the patella tendon, where they insert onto the inferior pole of the patella. It usually affects jumping athletes (e.g., basketball and volleyball players) but can also be encountered in patients with rheumatoid arthritis, seronegative arthropathies or in patients on treatment with exogenous steroids. In the initial stages, MR images show thickening and hyperintensity of the proximal (most commonly the central and inner third of the tendon). As the disease progresses, the abnormality extends to involve the other parts of the tendon, with the posterior tendon border gradually becoming instinct (Figs. 97, 98).

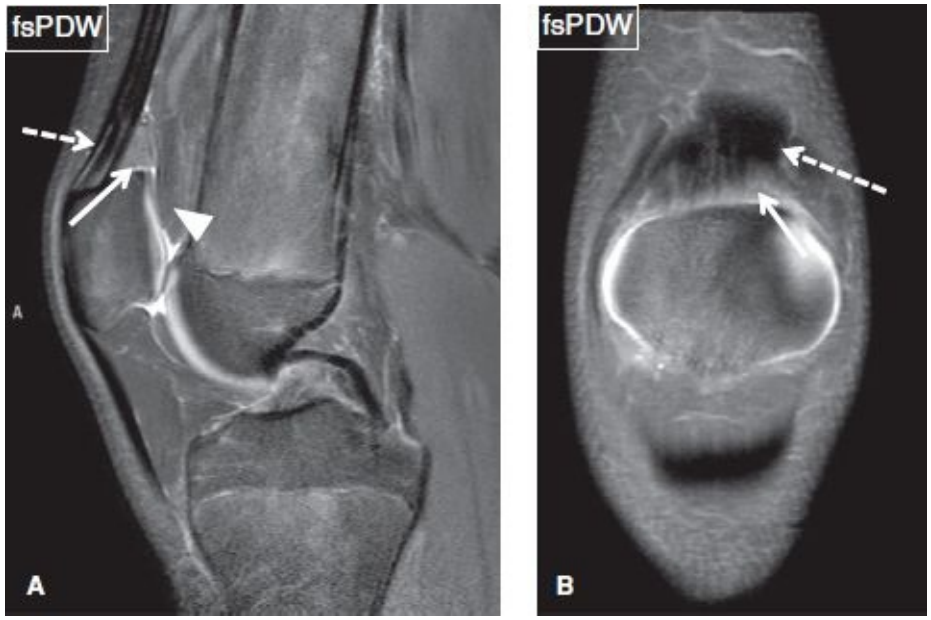

Fig. 87: Normal trilaminar quadriceps tendon. Sagittal **(A)** and coronal **(B)** images demonstrate a normal trilaminar distal quadriceps tendon (*dashed arrows*). Notice edema in

the quadriceps fat pad, a nonspecific and commonly asymptomatic finding (*solid arrows*) and normal prefemoral fat pad (*arrowhead*).

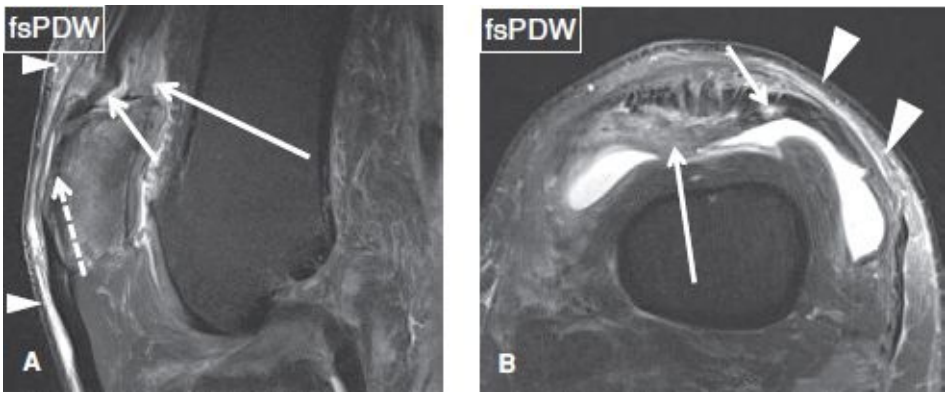

Fig. 88: Quadriceps tendon partial tear. Sagittal **(A)** and axial **(B)** images show low-grade small tear of distal quadriceps tendon fibers (*short arrows*), along with edema of the surrounding subcutaneous fat planes (*arrowheads*) and suprapatellar or quadriceps fat pad (*long arrows*). Notice anterior enthesopathy of the patella (*dashed arrow*).

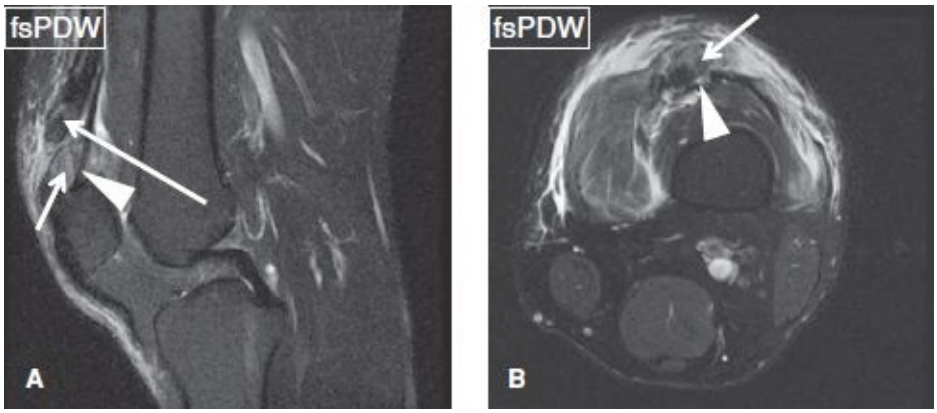

Fig. 89: Near-complete tear of the quadriceps tendon. Sagittal **(A)** and axial **(B)** images show near-complete tear (*short arrows* in **A, B**) of the quadriceps tendon from the attachment site, along with proximal tendinous retraction and edema (*long arrow* in **A**). Notice intact vastus intermedius tendon (*arrowheads*).

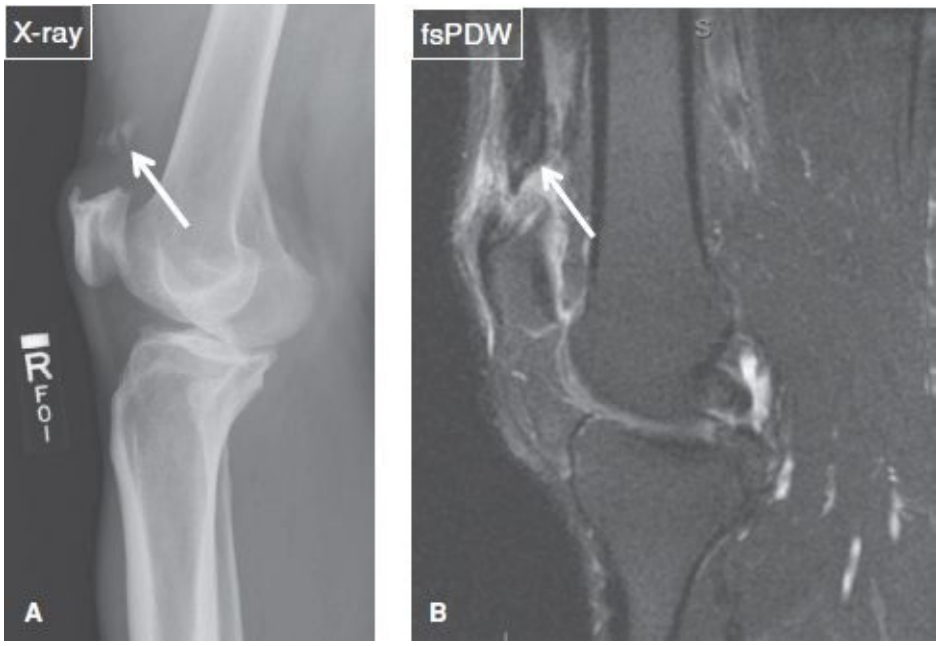

Fig. 90: Complete quadriceps tendon tear. **A:** Lateral radiograph shows an avulsive fracture (*arrow*) of the superior patellar pole related to detached enthesophyte. **B:** Sagittal MR image confirms the complete tendon tear with retraction (*arrow*).

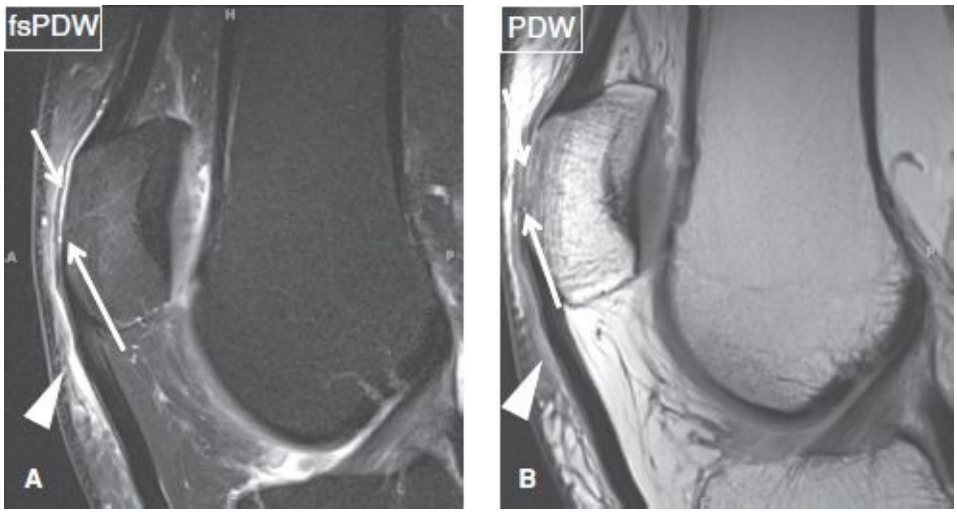

Fig. 91: Quadriceps tendon acute on chronic enthesopathy. Sagittal images demonstrate hyperintensity reflecting edema of the quadriceps–patella interface due to minor tendon stripping (*short arrows;* acute component), with associated edema of the overlying subcutaneous tissues (*long arrows*). Notice underlying bony productive change at the anterior border of the patella (*arrowheads,* chronic component).

Fig. 92: Normal variant. Sagittal image show focal T2 hyperintensity (*arrows*) at the proximal patellar tendon, which lacks tendon thickening or edema of the surrounding soft tissues, and is considered a normal finding, attributed to interspersed nontendinous fibers and/or magic angle phenomenon.

Osgood–Schlatter disease is a traction-related injury in adolescent or pre-adolescent age groups. It is a result of repetitive quadriceps contractions through the patellar tendon at its insertion on the skeletally immature tibial tubercle. In the acute setting, MR images demonstrate thickening and edema of the inferior patellar tendon, again involving the inner and central third of the latter, associated soft tissue swelling anterior to the tibial tuberosity, loss of the sharp posterior-inferior margin of the Hoffa's fat pad and/or coexistent infrapatellar bursitis. In the subacute setting, there is cartilaginous damage to the tibial tuberosity and injury to the secondary ossification center. More severe lesions may extend into the tibial epiphysis as Salter type III fractures (Figs. 99–101). In the chronic stage, the avulsed bone fragments are pulled superiorly and become separated, forming discrete ossicles. However, larger gaps may remain, with the avulsed fragments maturing to form separate ossicles within the patellar tendon. An important other acute cause of extensor mechanism failure is patellar fracture. The latter may be transverse (50–60%), stellate (30–35%), vertical (12–17%), or marginal (tendon avulsions). It may also occur in the form of periosteal sleeve avulsion (in children or adolescents) and osteochondral fracture (in patellar subluxation or direct impact injury, such as fall on the anterior knee) (Figs. 83, 102). In bipartite patella, the non-united bony fragment and associated synchondrosis may be located in the inferior, medial, or superolateral aspects of the parent bone. It should be differentiated from patellar fracture, which will show the fragments that would fit with each other forming a full patella (Fig. 103). Similar to os acromiale in the shoulder or os naviculare in ankle, one should look for stress-related bone marrow edema, cystic changes, or disruption of the synchondrosis.

The patellar and the trochlear articular cartilage are best evaluated on axial and sagittal

images, respectively, except that the region of apex of the trochlear sulcus is best evaluated on the axial image. Criteria for determining pathology are identical to those applied for evaluating the cartilages of the medial and lateral joint compartments (Figs. 104, 105).

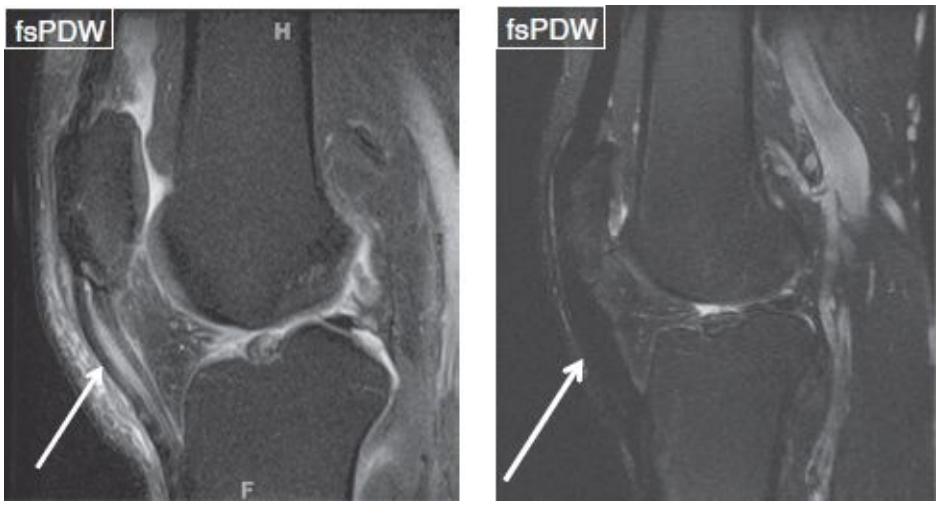

Fig. 93: Patellar tendon lesions. Sagittal images. **A:** The patellar tendon (*arrow*) shows diffuse thickening and hyperintensity (*arrow*), along with hyperintensity of the surrounding soft tissues, in this case of acute interstitial tear. These are common in the setting of underlying chronic diseases, such as gout in this case. **B:** Diffuse thickening of the patellar tendon (*arrow*), though without evident signal change, corresponds to chronic patellar tendinosis.

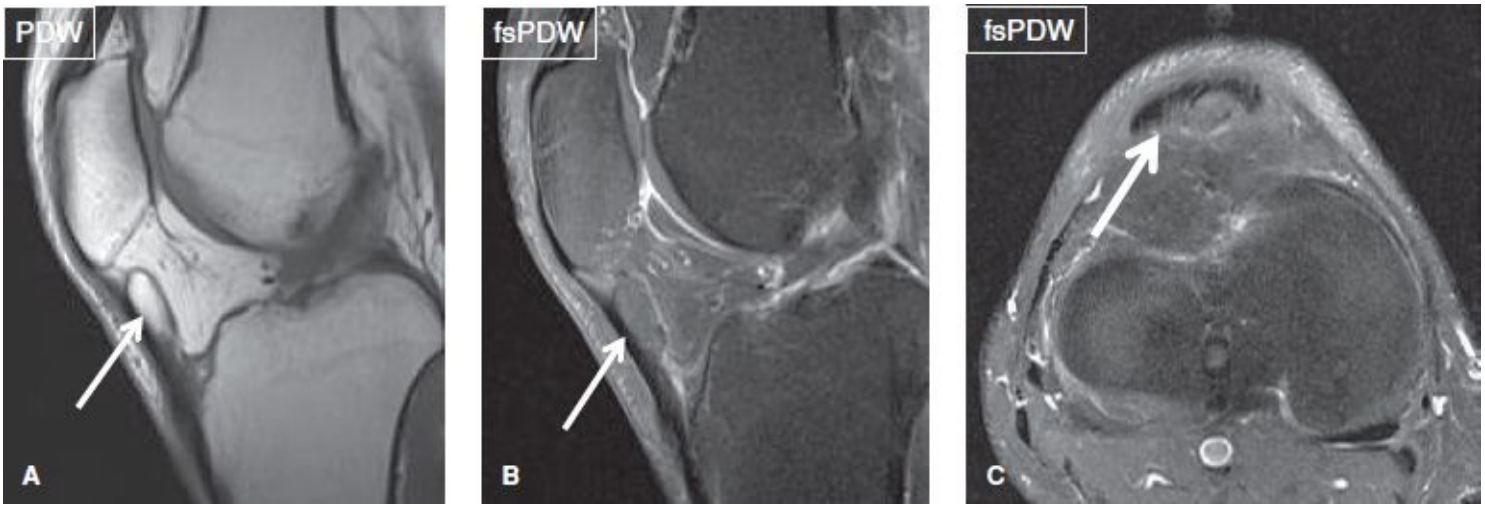

Fig. 94: Patellar tendon lesions. Sagittal images **(A, B)** and axial image **(C)** show a rounded bony fragment (*arrows*) in relation to the patellar tendon suggesting a sesamoid bone. Old avulsed fragment with chronic overgrowth can produce similar appearance.

Fig. 95: Ganglion of patellar tendon. Sagittal images **(A, B)** show a cystic fluid collection within the patellar tendon (*arrowheads*) in keeping with an intratendinous ganglion along with old avulsive changes from the tibial tubercle and soft tissue edema in the peritendinous fascial planes.

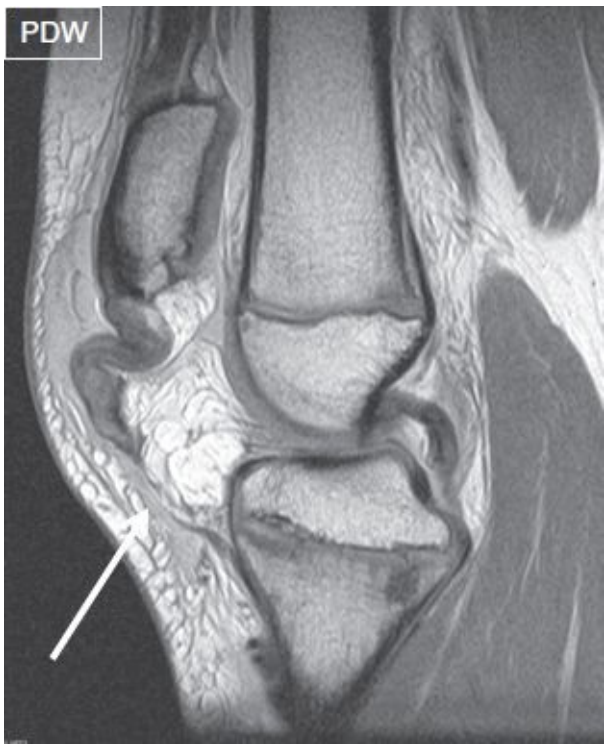

Fig. 96: Complete tear of the patellar tendon. Sagittal image demonstrates complete discontinuity (*arrow*) of the patellar tendon, along with patella alta.

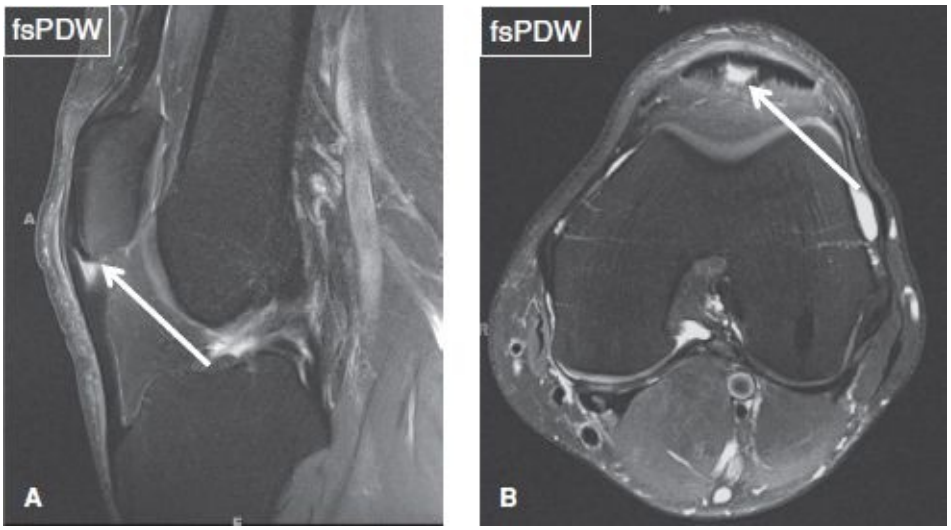

Fig. 97: Acute-on-chronic jumper's knee. Sagittal **(A)** and axial **(B)** images demonstrate focal T2 hyperintensity (*arrows*) involving the posterior and central thirds of the proximal patellar tendon indicating a partial tear. Notice underlying thickening of the proximal portion of the tendon indicating chronic tendinosis.

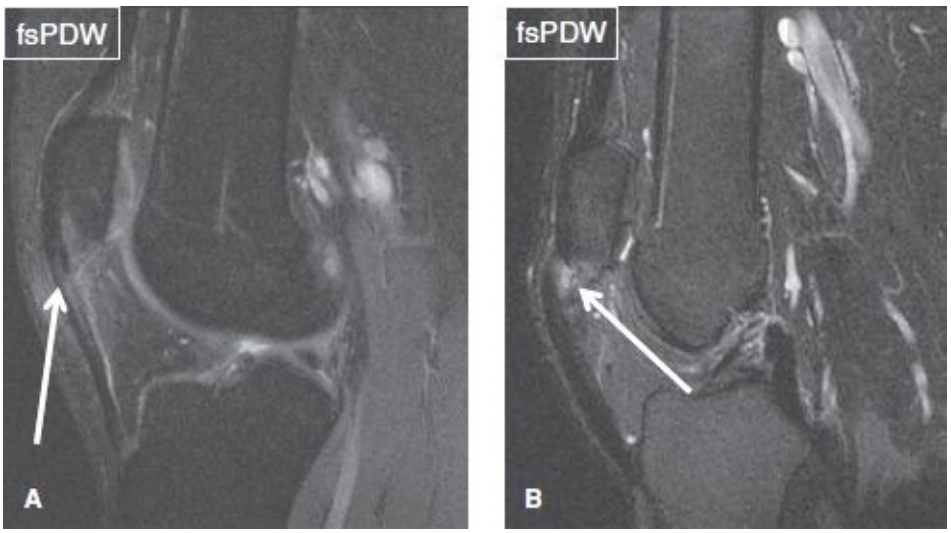

Fig. 98: Jumper's knee. Sagittal images. **A:** Intratendinous and peritendinous edema (*arrow*) of the proximal third of the patellar tendon corresponds to acute–subacute stage of tendinosis. **B:** An insertional partial tear (*arrow*) is evident at the proximal attachment of the patellar tendon, along with diffuse moderate tendon thickening, signifying acute-on-chronic injury.

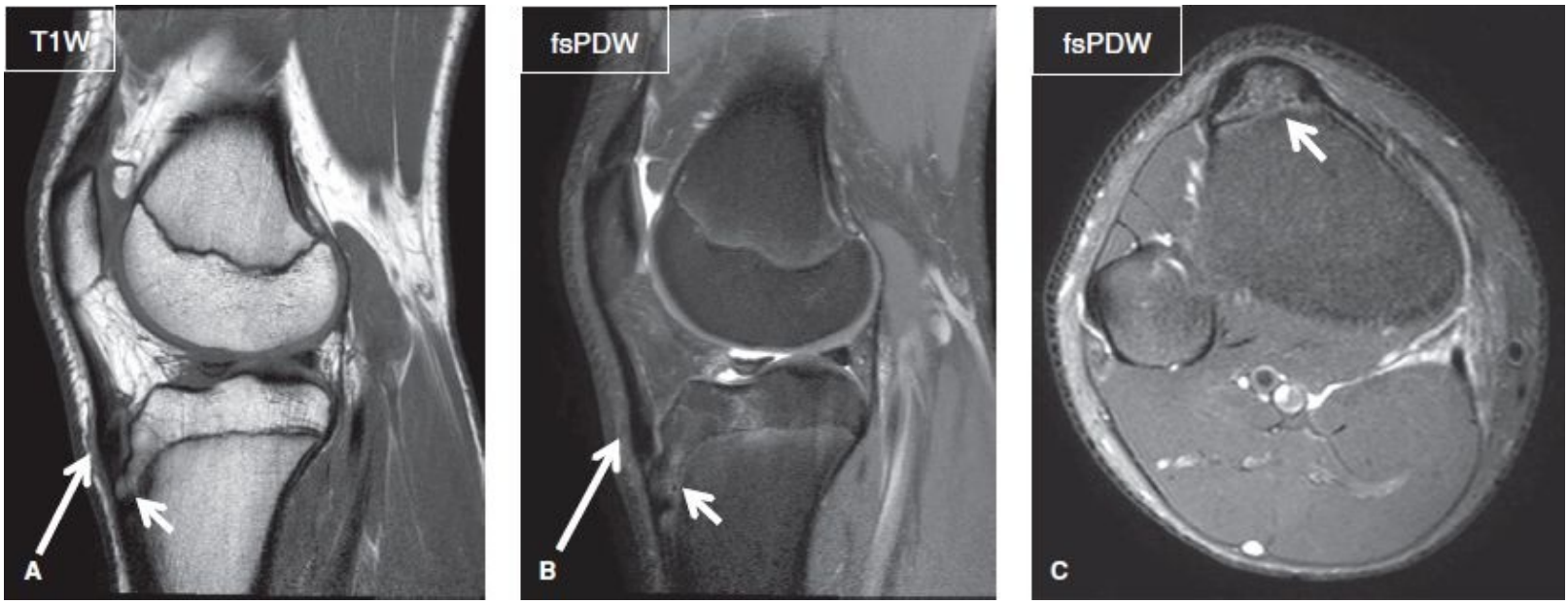

Fig. 99: Osgood–Schlatter disease. Sagittal **(A, B)** and axial **(C)** images demonstrate intratendinous and peritendinous edema of the distal patellar tendon (*long arrows*) with edema of the tibial tuberosity (*short arrows*).

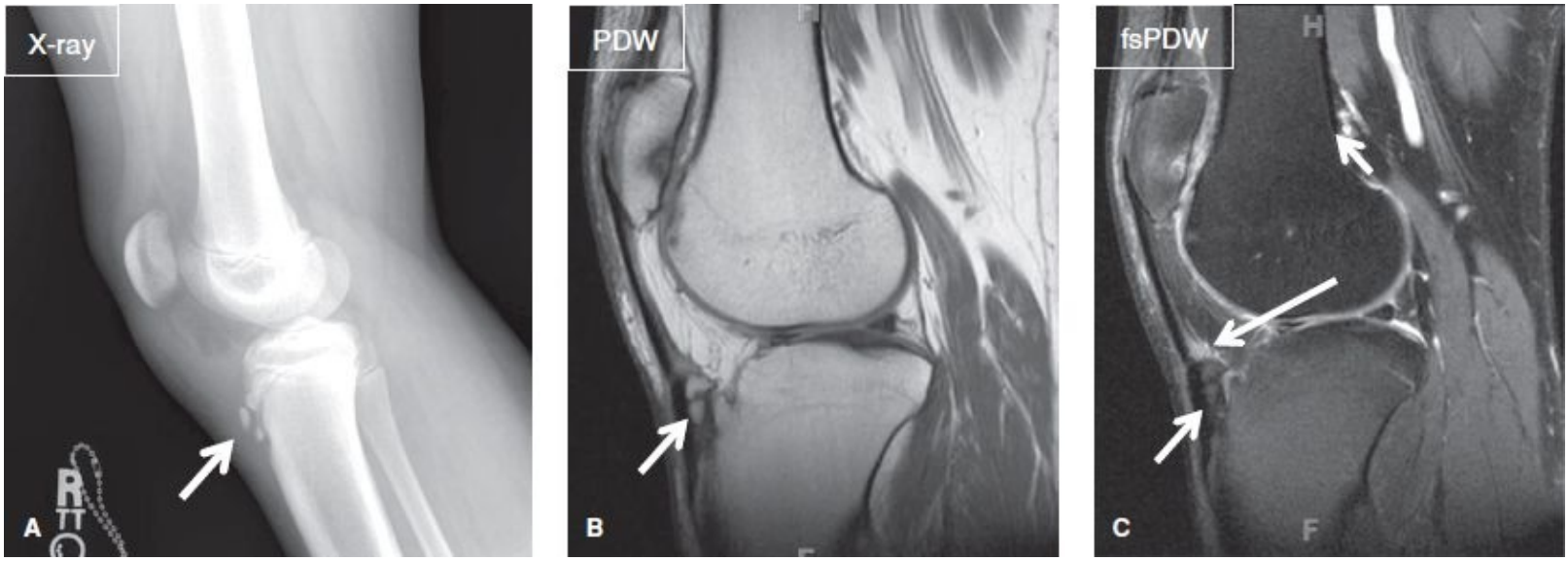

Fig. 100: Osgood–Schlatter disease. **A:** Lateral radiograph shows fragmentation and chronic avulsions (*arrow*) of the tibial tuberosity. **B, C:** The corresponding sagittal MR images confirm the plain film finding (*short arrows*) and additionally demonstrate focal adjacent distention (*long arrow* in **C**) of the deep infrapatellar bursa.

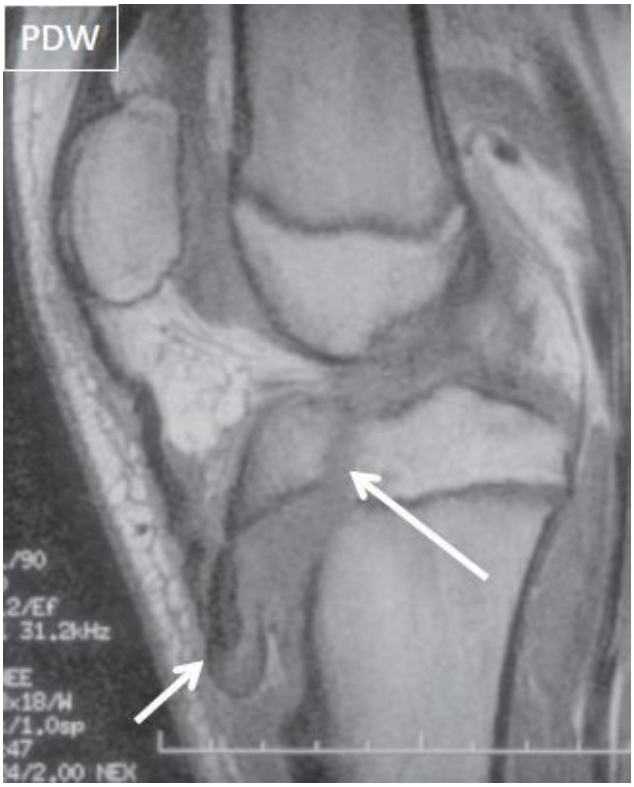

Fig. 101: Osgood–Schlatter disease. Sagittal image exhibits avulsive fracture of the tibial tuberosity (*short arrow*). The fracture line (*long arrow*) extends superiorly through the tibial epiphysis, resulting in a Salter–Harris type III injury.

The trochlear sulcus angle and trochlear depth should be measured in suspected cases of trochlear hypoplasia. The trochlear sulcus angle is measured in the axial plane, approximately 3 cm above the lateral tibial plateau or at the physeal scar level between the lines paralleling anterior cortices of the trochlea. The trochlear depth is measured on the same image (usually at the level of the thickest patellar cartilage) as the shortest distance from the deepest point of the trochlear groove to the line joining the most anterior margins of the medial and lateral facets (Fig. 106). The latter line is tangent to the line joining the posterior femoral condyles. A sulcus angle greater than 144 degrees and/or a depth of less than 3 to 5 mm indicate hypoplasia or dysplasia. There are many types of trochlear dysplasias described in the literature, with a variety of ways by which, these measurements can be obtained. The above-described measurements are simple to obtain in a busy practice and are very reliable. One should also report if the trochlear groove is convex rather than concave (dysplastic facet) and if there is a prominent lateral ridge of the trochlear facet (Fig. 107).

Fat pads are masses of encapsulated adipose tissue, which act as cushions that absorb forces generated across the joint. The infrapatellar (Hoffa's) fat pad is intracapsular and extrasynovial. It is bordered by the patella sueriorly, the tibia and infrapatellar bursa inferiorly, the patellar tendon and joint capsule anteriorly, and the synovium-lined joint cavity posteriorly. The suprapatellar (aka quadriceps) fat pad is triangular in shape and is located superior to the patella and posterior to the distal quadriceps tendon. The prefemoral fat pad is situated immediately anterior to the femur. In shearing injuries of Hoffa's fat pad,

the latter demonstrates irregular posterior contour, as well as intrasubstance, often linear fluid collection at the level of the menisci (Fig. 108). The entity is frequently associated with ACL tears, where it is also a sign of hemorrhagic synovitis. Generally, in simple joint effusions without synovitis, the posterior border of the Hoffa fat pad is smoothly contoured. In the subacute and chronic setting, low signal intensity foci within the fat pad may appear, corresponding to fibrin deposits or calcifications whereas the fat pad itself may show distortion and/or puckering (Fig. 109). Edema of the superolateral portion of Hoffa's fat pad has been related to patellar tendon impingement on the femoral condyle during knee flexion due to underlying patellar malalignment or maltracking. Although the finding could be seen in asymptomatic subjects, one should evaluate patellofemoral cartilage carefully in such instances. The entity is best demonstrated on sagittal and axial fluid-sensitive images, on which Hoffa's fat pad may also be enlarged (bulging contours) and extend into the lateral gutter on axial images (Fig. 110). Edema of the suprapatellar or lateral aspect of prefemoral fat pad is also commonly associated with patellofemoral malalignment and is reflective of repeated quadriceps tendon-lateral femoral condyle friction (Figs. 111, 112). Isolated edema of suprapatellar fat pad is also a secondary finding in quadriceps tendinosis and, substantial amount of edema should direct the reader to look for underlying quadriceps interstitial tears. All above fat pads may develop focal fluid collections from adventitial bursa formation in occasional cases and may be subject to synovial processes, such as PVNS or synovial osteochondromatosis.

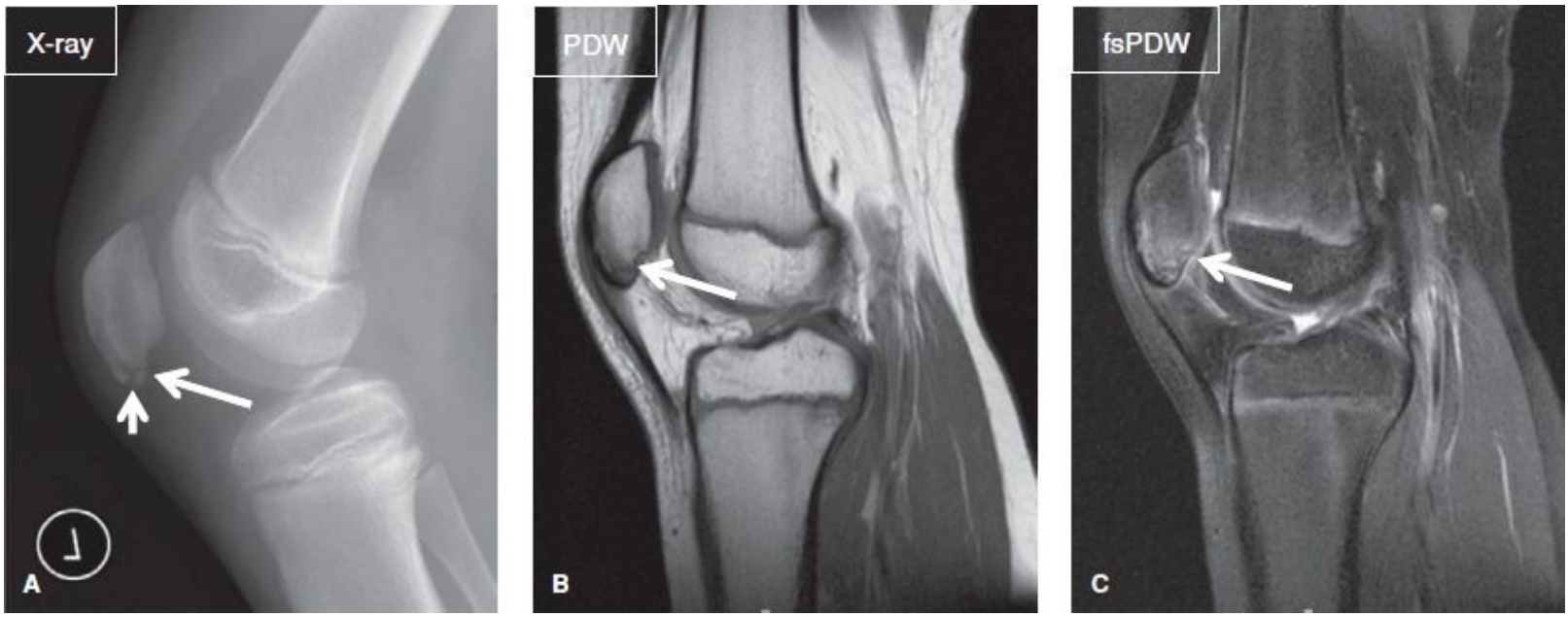

Fig. 102: Periosteal sleeve avulsion. **A:** Lateral radiograph shows elevation of the inferior patellar periosteum (*long arrow*), with fragmentation (*short arrow*). **B, C:** Sagittal images confirm the periosteal elevation (*arrow* in **B**) and additionally show marrow edema (*arrow* in **C**) of the inferior patellar pole.

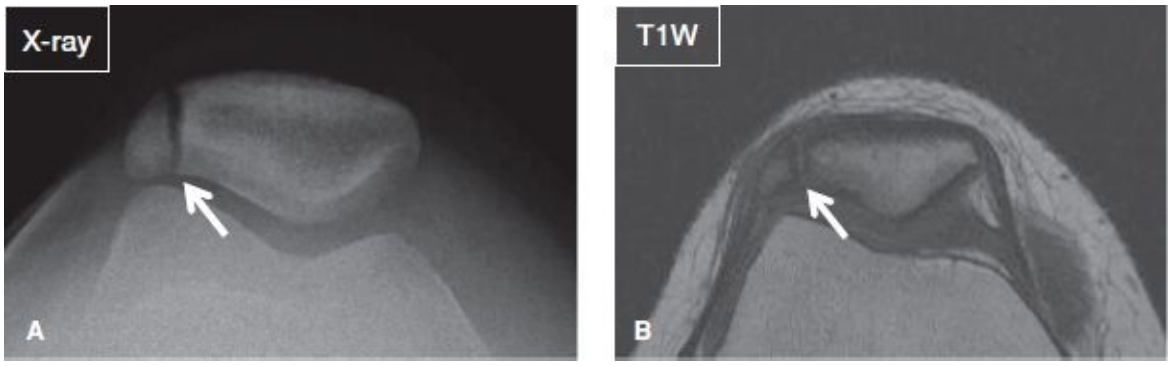

Fig. 103: Bipartite patella versus fracture. **A:** Axial radiograph shows superolateral fragment of the patella (*arrow*). **B:** Axial MR image shows minimal sclerosis (*arrow*) of the bony margins across the gap. The fragments nearly fit into each other and the findings are compatible with a fracture non-union.

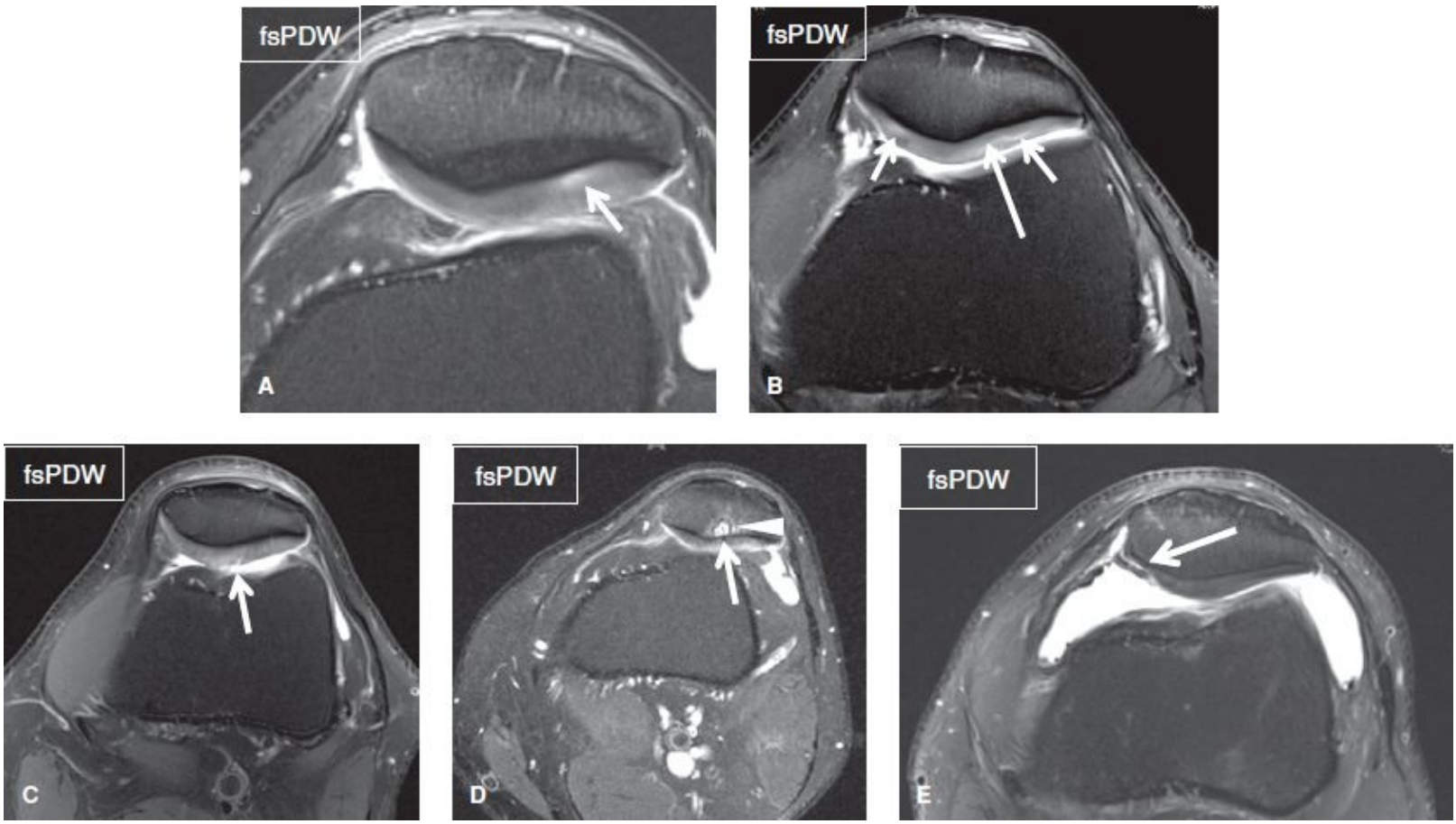

Fig. 104: Patellar cartilage pathology. Axial images. **A, B:** Focal (*arrow* in **A**) and multifocal/diffuse hyperintensity (*short arrow* in **B**) of the patellar cartilage is indicative of chondromalacia. Notice superimposed low-grade cartilage defect in the lateral facet (*long arrow* in **B**). **C, D:** Low-grade fissures (*arrow* in **C**) and high-grade defects (*arrow* in **D**) in the patellar cartilage. In **D,** also note subchondral cyst formation (*arrowhead*) and lateral patellar subluxation. **E:** Cartilage delamination (*arrow*) is seen in the medial patellar facet reflecting debonding from the underlying bony surface).

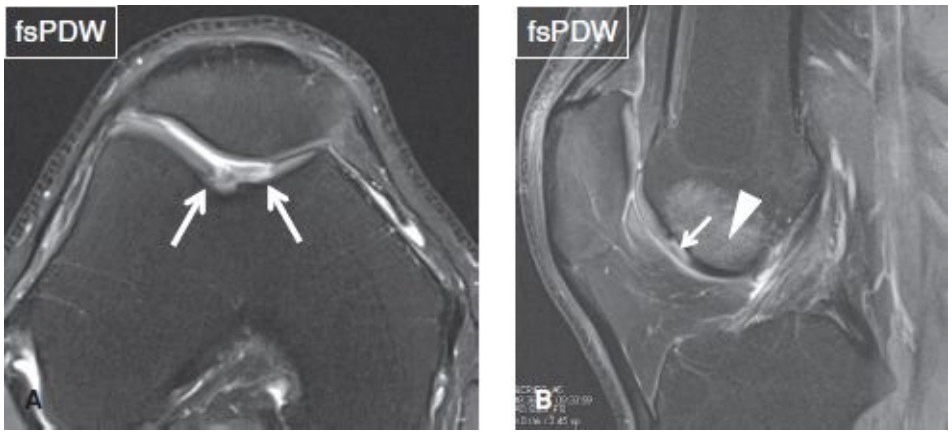

Fig. 105: Trochlear cartilage pathology. Axial **(A)** and sagittal **(B)** images demonstrate high-grade cartilage defects (*arrows*) of the trochlea with full-thickness fissure along the medial facet. Notice subjacent bone marrow edema (*arrowhead* in **B**).

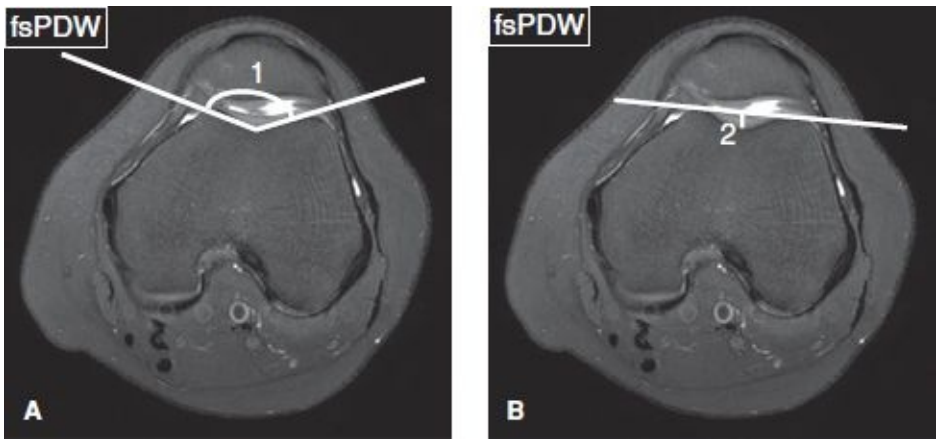

Fig. 106: Evaluation of the trochlear groove morphology. Axial images approximately 3 cm above the joint line demonstrate the measurement of the trochlear sulcus angle (*angle 1*) and trochlear sulcus depth (*distance 2*).

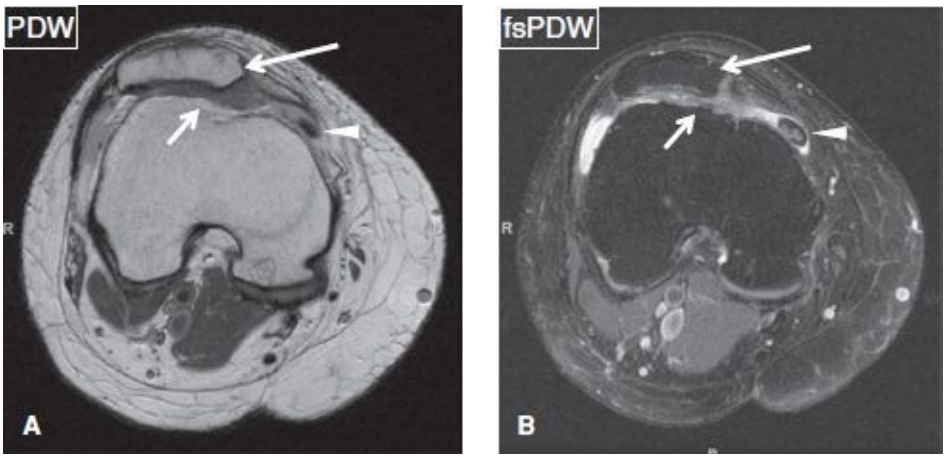

Fig. 107: Dysplastic trochlear groove. Axial images exhibit a very shallow, barely perceptible trochlear groove with a prominent lateral ridge (*short arrows*). Also note a loose intra-articular osteochondral body (*arrowheads*), and that the patella (*long arrows*) is laterally subluxed and features an almost flat articular surface with multifocal high-grade cartilage defects.

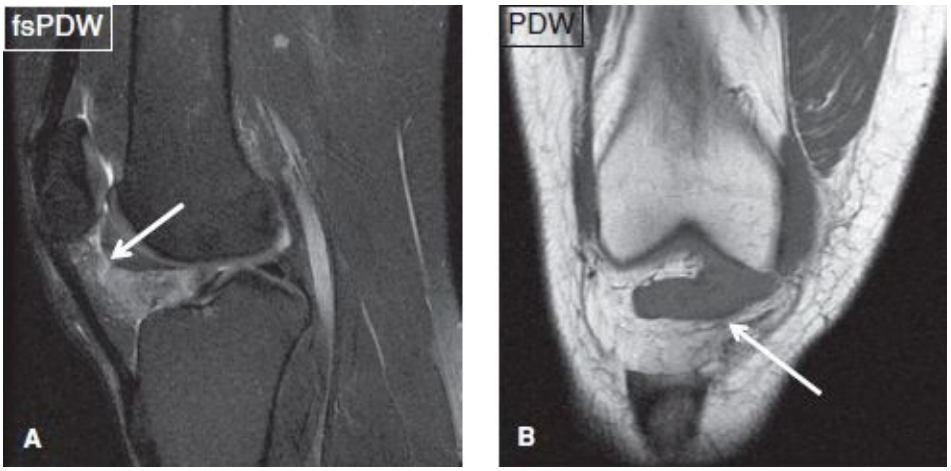

Fig. 108: Shearing injury of Hoffa's fat pad. Sagittal **(A)** and coronal **(B)** images show heterogeneous edema and hemorrhage (*arrows*) within Hoffa's fat pad.

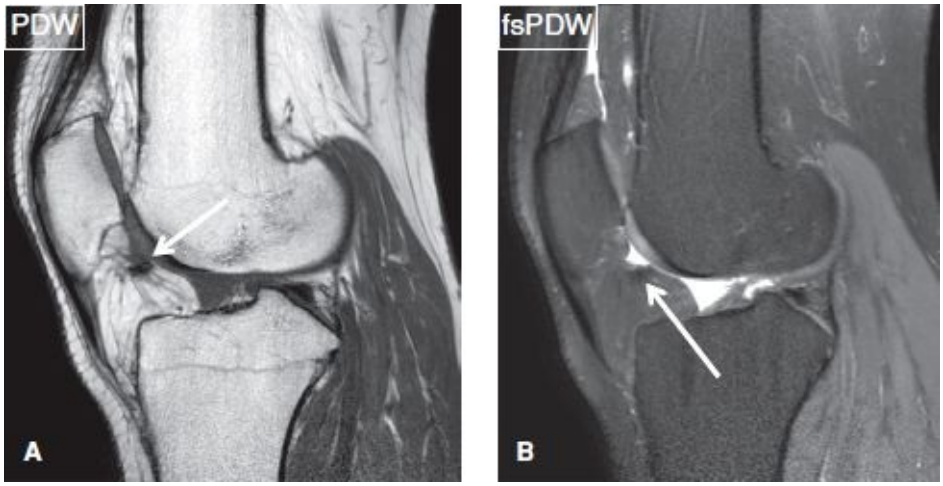

Fig. 109: Chronic Hoffa's disease. On sagittal images, Hoffa's fat pad appears contracted, puckered, and features central fibrosis (*arrows*), reflecting sequel of prior shearing injury.

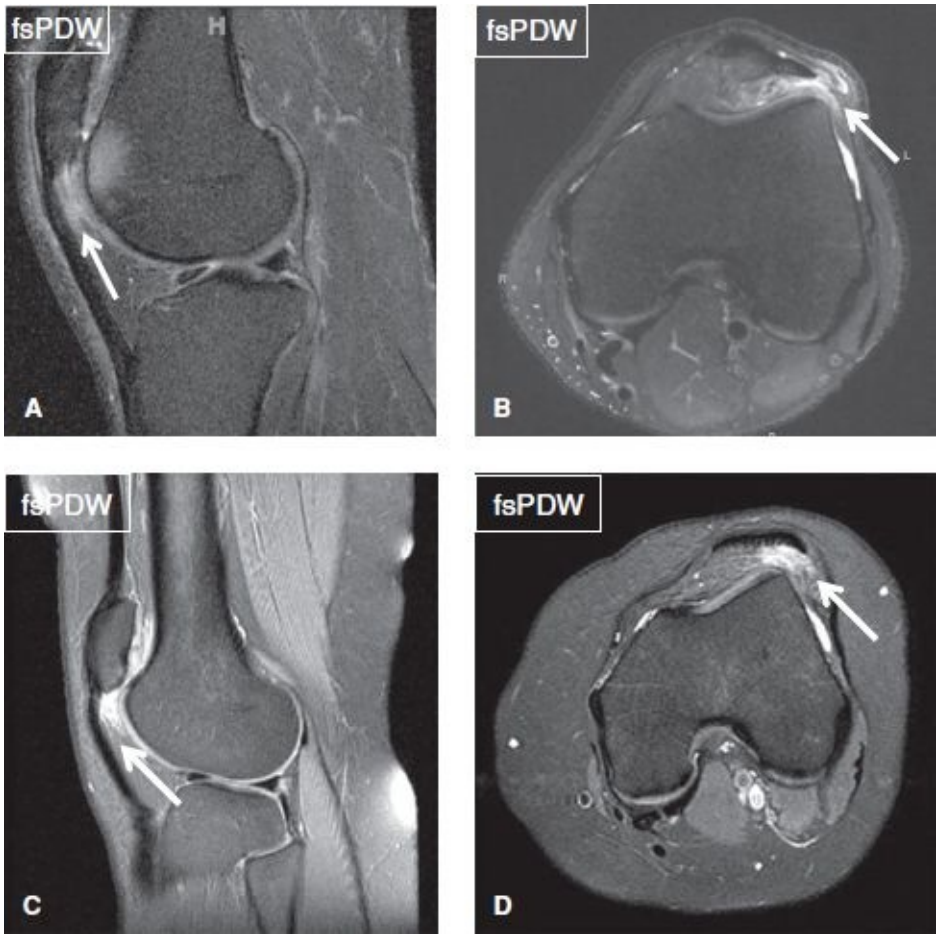

Fig. 110: Superolateral Hoffa's fat pad edema. Sagittal **(A)** and axial **(B)** images from a patient with anterior knee pain, as well as respective images **(C, D)** from another subject with similar symptoms reveal edema (*arrows*) of the superolateral portion of Hoffa's fat pad, along with underlying patellar malalignment findings of patella alta and lateralized patellar tendon. Notice extension of the hypertrophied Hoffa's fat pad into the lateral gutter.

Synovial plicae are remnants of embryologic normal synovial folds. Although, the size and location of the plicae are variable, four plicae are encountered in variable frequency, and are best seen on axial and sagittal images: The superior (or suprapatellar) plica is typically located 2 cm superior to the patella as a crescentic fold, and is the most consistently present. The medial plica (plica synovialis) arises on the medial wall of the synovial pouch or under the medial retinaculum and courses in a coronal plane, parallel to the medial border of the patella, to insert distally on the infrapatellar fat pad. It ranges in size from a small ridge to a shelf or well-formed cord. The inferior plica (or infrapatellar plica or ligamentum mucosum) originates from the intercondylar notch, courses immediately anterior to the ACL, and then curves gently upward to attach to the infrapatellar fat pad or the inferior pole of the patella. The lateral plica, which is the least commonly encountered of all plicae, is located in the lateral aspect of the patellofemoral joint space, under the LPR. The normal plicae appear as homogeneous hypointense linear bands, and feature a thickness of 1–2 mm (Fig. 113). Minimal fluid extension along the inferior plica is a normal finding as these ligaments are covered by synovium. However,

irregular edema around the ligament or notched inpouching of the posterior inferior or superior Hoffa's fat indicates sprain of the ligamentum mucosum. Symptomatic plica may be thicker than 2 mm, with or without surrounding edema. It might be, associated with erosion of the patellar and trochlear cartilage, or ganglion formation (Figs. 114–116). One should note, however, that more than 2 mm of thickening is normal in the post-operative state or following arthroscopy.

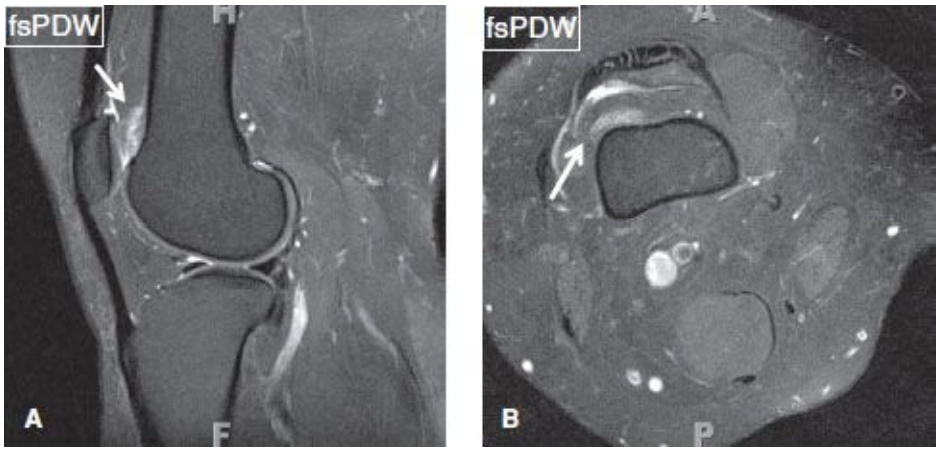

Fig. 111: Prefemoral fat pad edema. Sagittal **(A)** and axial **(B)** images exhibit a focus of edema (*arrows*) of the lateral aspect of the prefemoral fat pad in this case of patellar malalignment.

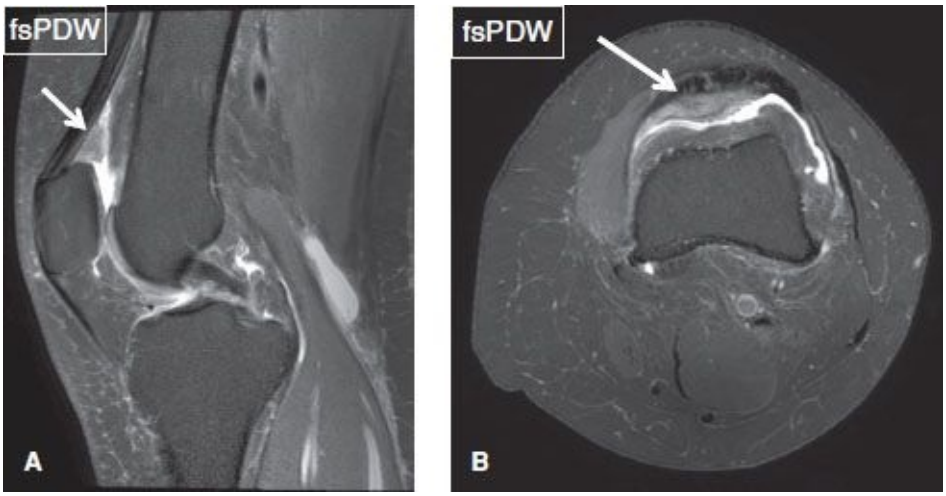

Fig. 112: Quadriceps or suprapatellar fat pad edema. Sagittal **(A)** and axial **(B)** images exhibit diffuse hyperintensity (*arrows*), signifying edema of the suprapatellar fat pad.

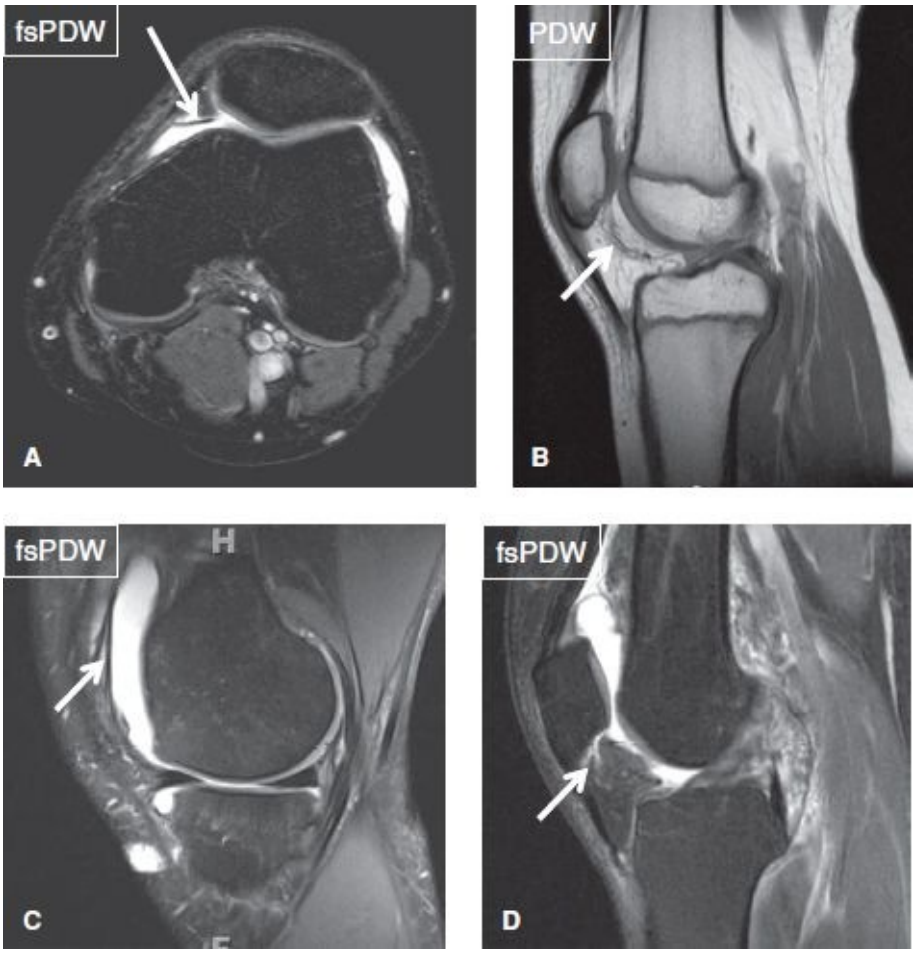

Fig. 113: Normal and abnormal synovial plicae. Axial **(A)** and sagittal **(B)** images show normal medial (*arrow* in **A**) and inferior (*arrow* in **B**) plicae. **C, D:** Sagittal images in different subjects show thick medial plica (*arrow* in **C**) and absent inferior plica with inpouching of the superior aspect of Hoffa fat pad (*arrow* in **D**), pathognomonic finding of prior inferior plica tear.

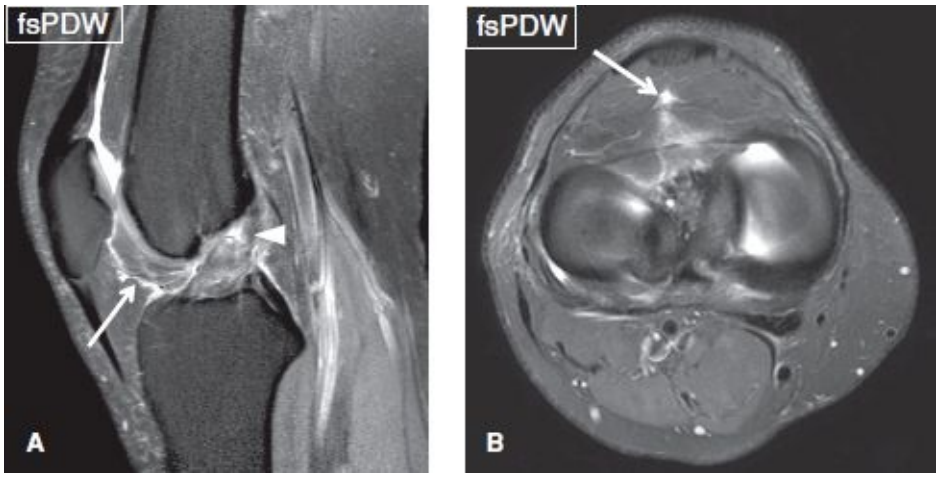

Fig. 114: Acute infrapatellar plica injury. Sagittal **(A)** and axial **(B)** images from a patient with recent knee trauma show fluid-like signal (*arrows*) along the anatomic course of the infrapatellar plica, indicating sprained ligamentum mucosum, not uncommon with rotational injuries. Also note near-complete tear of the proximal anterior cruciate ligament (*arrowhead*).

Fig. 115: Ganglion of ligamentum mucosum. Sagittal image exhibits fluid-like thickening of the infrapatellar plica (*long arrow*), along with adjacent fluid and soft tissue edema (*short arrow*), reflective of acute on chronic injury and ganglion formation (*arrowhead*).

Fig. 116: Postoperative plica thickening. Sagittal image shows mild thickening of the infrapatellar plica (*arrow*) and irregular contour of the posterior Hoffa fat pad, a normal finding postoperatively.

An abnormally lateralized tibial tubercle is considered a potential cause of patellar

instability. The location of the tibial tubercle can be assessed by measuring the tibial tubercle to trochlear groove (TT–TG) distance: On axial images and at the level where the femoral condyles fuse, a first line is drawn through the deepest trochlear groove that is perpendicular to a line drawn across the backs of the condyles. At the level of the tibial tubercle, a second line is drawn though the tibial tubercle or center of patellar tendon exactly parallel to the trochlear groove line (Fig. 117). The TT–TG distance is the distance between the aforementioned lines, should normally be equal to or less than 1.1 cm, and is considered abnormal when greater than 1.5 cm. The TT–TG distance should be included in the report whenever patellar maltracking is suspected. It is a surrogate marker of the Q angle (clinically formed between the lines joining the anterior superior iliac spine, center of the patella, and the tibial tuberosity). Generally, surgeries for patellofemoral malalignment correction, such as LPR release, medial retinacular plication, medialization of tibial tuberosity, or trochleoplasty are performed when the TT–TG distance is more than 1.5–2 cm, depending upon the surgeon's preference. It should be noted that the TT–TG distance varies with patient coil positioning (body coil vs. knee coil), tibial or femoral torsion (toe pointing up in the magnet or to the side), and the degree of knee flexion. Further research is needed to establish the standardized way of measuring and threshold values that should be employed for treatment of patellofemoral pain syndromes.

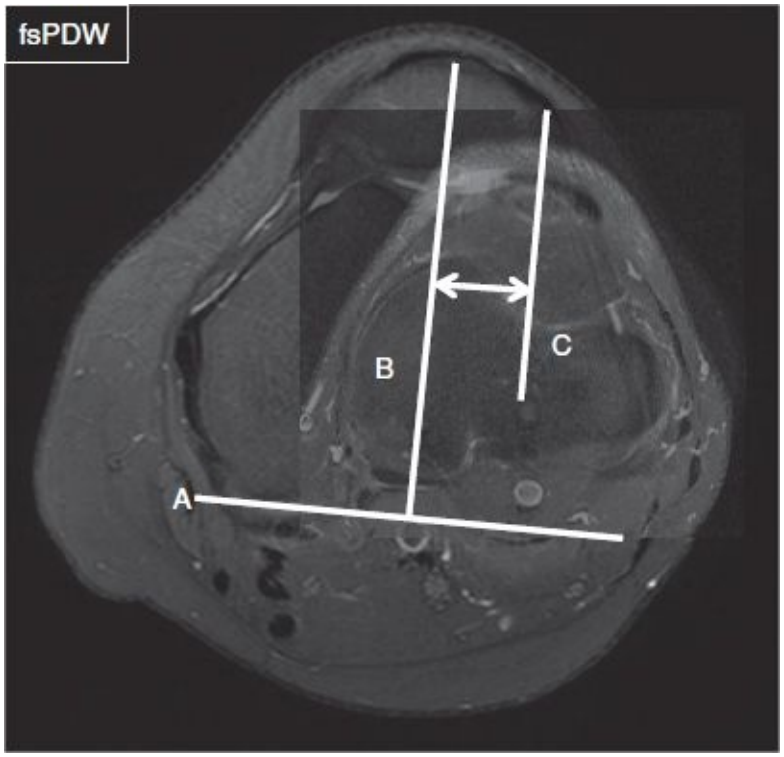

Fig. 117: TT–TG distance measurement. Superimposed axial images through the trochlear groove and tibial tuberosity show the correct way of measuring the TT–TG distance between lines **B** and **C** perpendicular to line **A,** which is tangent to the posterior border of the femoral condyles.

INTERCONDYLAR COMPARTMENT:

Anterior cruciate ligament: [<Normal> <Mucoid degeneration> <Sprain>]

Posterior cruciate ligament: [<Normal> <Mucoid degeneration> <Sprain>]

The cruciate ligaments are strong ligamentous bands, which extend from the tibial plateau, cross each other like the limbs of an X, and attach into intercondylar notch of the femur. The ACL extends in an inferior, anterior, and medial direction from its origin on the posterior aspect of the lateral wall of the medial femoral condyle to its insertion on the front of the intercondylar eminence of the tibia. It resists anterior translation and medial rotation of the tibia. The ACL consists of the anteromedial and the posterolateral bundles, which are named according to their insertions in relation to the tibial spine. The anteromedial bundle controls translation and flexion, while the posterolateral bundle controls rotation. The PCL extends in an inferior, posterior, and lateral direction from its origin on the anterolateral aspect of the medial femoral condyle to its insertion on the far posterior aspect of the tibial plateau and provides restraint to posterior translation and external rotation of the tibia. It is also composed of two bundles, the anterolateral and the posteromedial.

Clinically, the ACL and PCL are tested using a simple “Drawer test.” The patient is placed in supine position with the hips flexed to 45 degrees, the knees flexed to 90 degrees, and the feet flat on table. This position accomplishes complete relaxation of the hamstrings; otherwise, false-negative result may occur. A firm, but gentle, grip on the proximal tibia is achieved and an anterior or posterior force is then applied comparing it to the normal contralateral knee. Excessive displacement of the tibia anteriorly indicates ACL deficiency, whereas excessive posterior displacement indicates PCL deficiency. The “Lachman test” is a variation with the knee in 30 degrees flexion and is the most sensitive test for ACL injury. Another commonly used test is the pivot shift test. It involves basic principles of applying a valgus internal rotation force to the leg. The knee is started out in full extension and then is gently flexed to about 30–40 degrees. In a patient with a positive pivot shift test, the joint starts out subluxed in full extension and then is reduced back into its normal position by the action of the ITB pulling the anterolaterally subluxed tibia back against the femur when the knee courses through approximately 30 degrees of knee flexion. This test is most specific for ACL injury.

The ACL is best evaluated on sagittal and coronal images. On the former, the ligament appears as a straight and taut band, which features up to three–four striations and runs parallel to the roof of the intercondylar notch (Blumensaat line) although minimal sagging inferior convexity may be normally present. Coronal images are best for the evaluation of the ACL, with the two bundles seen adjacent to the tibial attachment anteriorly; these join together in the mid-coronal section as an Indian greeting “Namaste” and finally a dark thick band is seen attaching to the inner margin of the lateral femoral condyle on the posterior coronal image. On axial images, the proximal portion is elliptical in shape and gradually splits into fan-shaped array of fascicles as it approaches its tibial insertion. On coronal T1W or PDW images, linear bands of fat are normally interposed between the ACL

fibers (Fig. 1).

The ACL can become pathologic as a consequence of acute rotational injury or chronic microtrauma related to the instability of the knee. In the latter case, one may encounter early or exaggerated development of what is known as the mucoid degeneration of the ACL. Since the ACL is extrasynovial, recurrent minor rotational injuries associated with knee instability lead to small tears of the synovium and/or minor fiber disruption of ACL. Consequent articular fluid leakage into the ACL substance leads to mucoid degeneration appearance. The fluid may accumulate to larger proportions in the ACL substance leading to a visible intra-substance ganglion. Further manifestation of the same process includes ganglion in the adjacent intercondylar notch and/or ACL micro-avulsion bony attachment site(s). These findings are commonly seen in middle-aged or older patients and affect more women than men. The patients with deranged knee due to underlying instability, such as patellofemoral malalignment or maltracking, may demonstrate mucoid degeneration of the ACL and/or PCL at a relatively younger age. The earliest imaging signs of ACL mucoid degeneration include partial or complete effacement of the normal fat in between the ACL bundles on the coronal images with/without traction cysts at the bony attachment sites. The cysts should be distinguished from prominent vessels, which may be normally present at the ACL attachment sites. With worsening degree of mucoid degeneration, one will see increasing T2 hyperintensity of the ACL with intra-substance ganglion producing a striated (celery stalk or drumstick appearance) and finally, development of a notch ganglion (Figs. 118–120). In a minority of these cases, PCL mucoid degeneration and/or ganglion cyst may also be associated (Fig. 121). These findings cause locking in terminal extension and are treated by debridement or rehabilitation. These lesions should not be overcalled as acute tears, since no repair or reconstruction is performed or needed in these lesions. In acute or subacute partial or complete ACL tears, there will be a history of recent twisting injury, and one will see hemorrhage and edema in the intercondylar notch, posterior capsular injury, bony contusions and frank discontinuity of the fibers and finally, with absent expansion of ACL fibers and intraosseus cystic changes, which are rather commonly observed with mucoid degeneration of the ACL.

Fig. 118: Mucoid degeneration of the anterior cruciate ligament. Sagittal image demonstrates expanded anterior cruciate ligament, which has become isointense to the skeletal muscles and shows intrasubstance and notch ganglions as well as bony cysts at the attachment.

Fig. 119: Anterior cruciate ligament ganglion cyst. Sagittal image shows a large ganglion cyst (*arrow*) emanating from the anterior cruciate ligament and eroding into the femoral bone. Also note intra-substance ganglion.

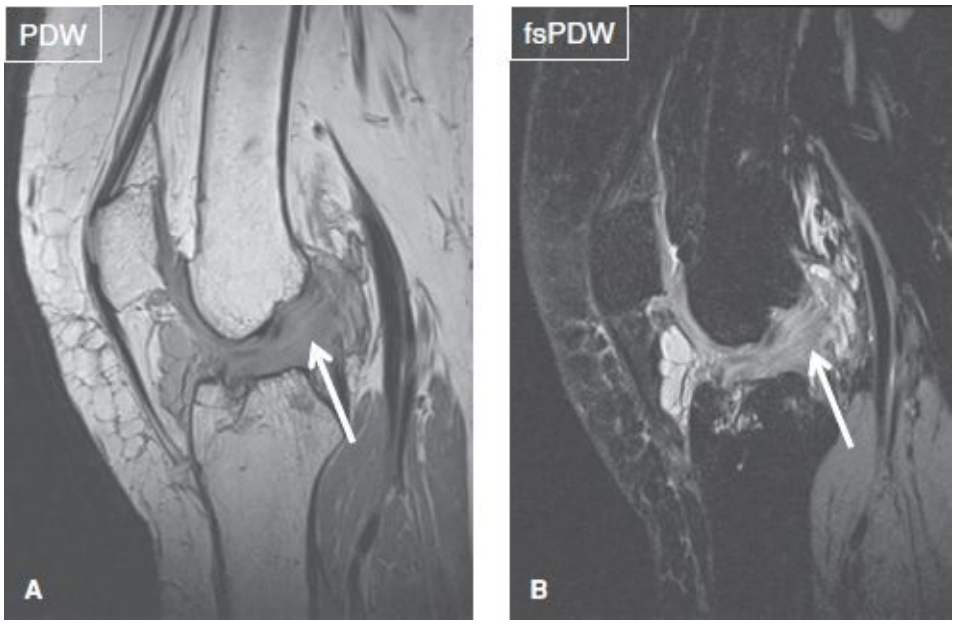

Fig. 120: Anterior cruciate ligament ganglion cyst. Sagittal images demonstrate diffuse enlargement of the anterior cruciate ligament (*arrows*), which has assumed a drumstick-like configuration with intrasubstance, notch, and intraosseus ganglion cysts.

Fig. 121: Intercondylar notch ganglion cyst and posterior cruciate ligament ganglion cyst. Sagittal image shows a multi-septated ganglion cyst (*arrow*) situated in the posterior half of the intercondylar notch and is contiguous with the cyst in the posterior cruciate ligament.

Acute or subacute ACL disruptions usually occur in young or middle ages. Full-thickness tears are much more common than partial tears. In complete ACL tears, there are primary imaging signs related to the ligament injury itself, and secondary signs reflecting injuries to associated structures and joint derangement. The primary imaging signs, which provide

high accuracy in diagnosing ACL injury, even in the absence of secondary signs, include the following:

- Non-visualization of the ACL, usually with ill-defined edema and hemorrhage in the expected location of the ligament (Fig. 122)
- Disruption of the mid-substance of the ACL by abnormal increased T2 signal or foot plate avulsion (Fig. 123)
- Horizontalization of the distal portion of the ACL ("fallen ACL" sign or "lazy ACL"), which is detected on sagittal images as a difference of more than 15 degrees relative to the roof of the intercondylar fossa or an angulation of less than 45 degrees to the tibial plateau (Figs. 122, 124)

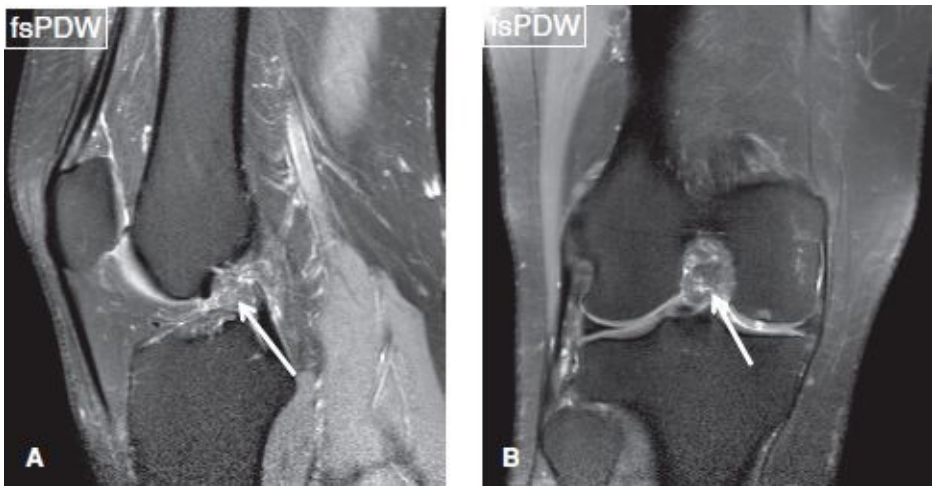

Fig. 122: Anterior cruciate ligament disruption and nonvisualization. On sagittal **(A)** and coronal **(B)** images, the ACL is not visualized in its expected anatomic location (*arrows*). Also note irregular soft tissue from prior hemorrhage and posterior capsular disruption.

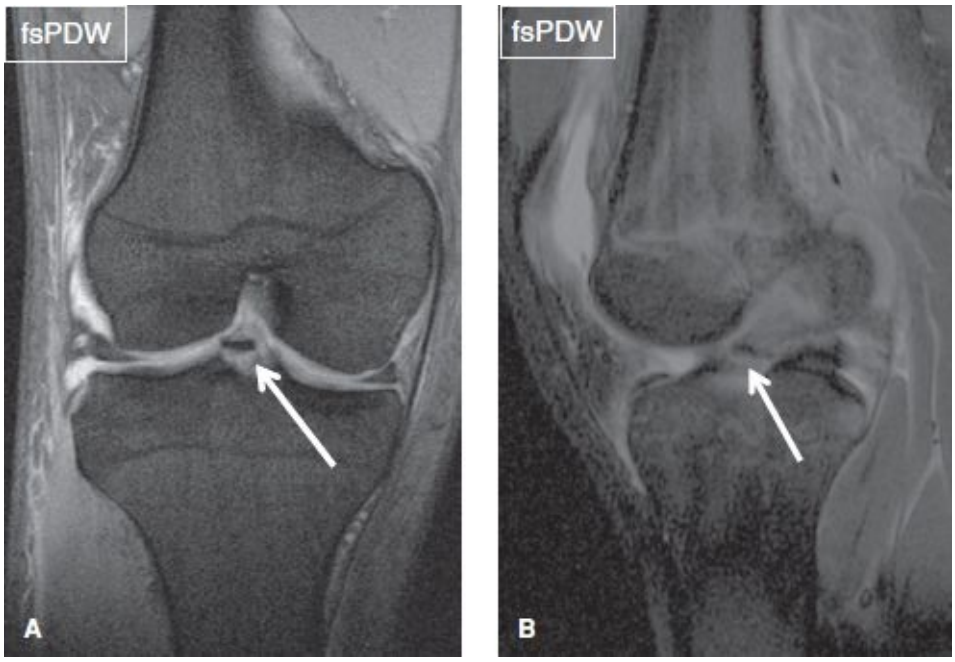

Fig. 123: Complete anterior cruciate ligament foot plate avulsion. Coronal **(A)** and sagittal **(B)** images exhibit a near-complete avulsion (*arrows*) of the distal foot plate attachment of the anterior cruciate ligament.

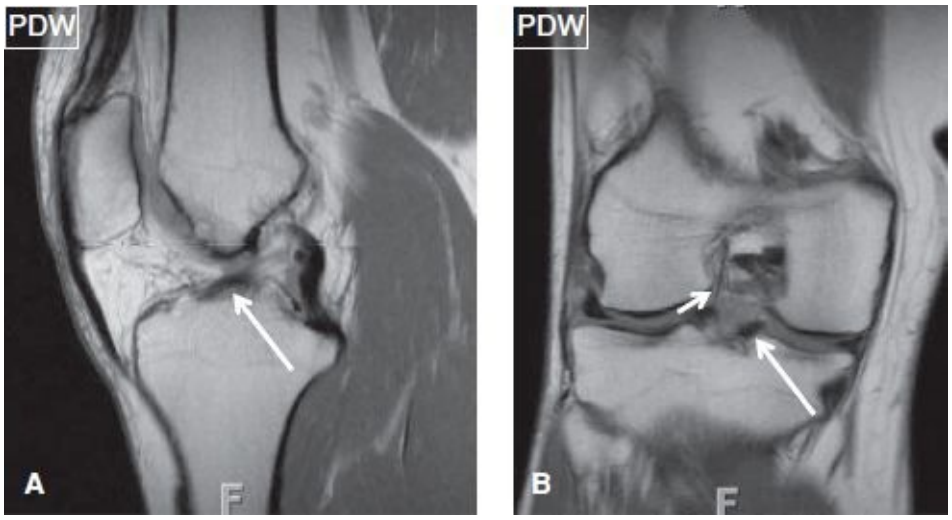

Fig. 124: Fallen anterior cruciate ligament sign. **A:** Sagittal image demonstrates horizontalization of the distal portion of the anterior cruciate ligament (*long arrow*) and missing bundles proximally. **B:** Coronal image confirms absence of anteromedial bundle (*long arrow*) and diffusely attenuated posterolateral bundle, probably representing mostly scar tissue (*short arrow*).

- Irregular, fuzzy, ill-defined contours and thickening of the ACL due to subacute tear and scarring
- An ill-defined mass with abnormal signal in the intercondylar fossa

On coronal and axial images, the linear hypointense band representing the proximal ACL may be attenuated, fragmented, completely or partially replaced by hemorrhage, or displaced away from the lateral wall of the intercondylar notch. The above-described anterior to posterior configuration of ACL on coronal images cannot be followed when there is an ACL tear. On coronal images, one or both bundles may be absent near the tibia, they may not join ("no namaste") in the mid portion, or may not hug the femoral condyle proximally and posteriorly. Lack of femoral hugging or partial separation from femoral condyle is a very useful sign and, if not recognized on coronal or axial images, proximal partial tears may be missed.

The diagnosis of complete ACL tear may be supported by secondary signs, which include the following:

- The "double PCL" sign, which is seen on midline sagittal image as a hypointense band that is parallel and anteroinferior to the PCL, with the differential diagnosis also including the more commonly encountered displaced bucket-handle meniscal tear (Fig. 125)

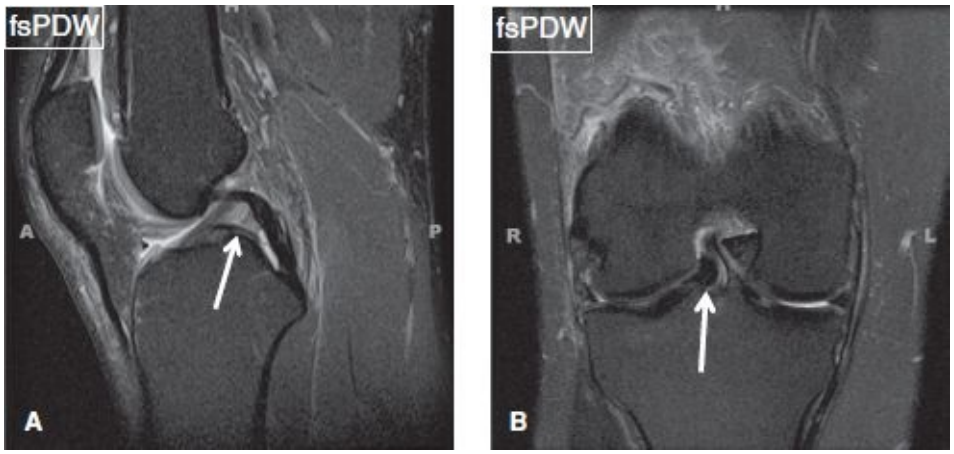

Fig. 125: Double posterior cruciate ligament sign. Sagittal **(A)** and coronal **(B)** images display a hypointense band (*arrows*) that is parallel and anteroinferior to the posterior cruciate ligament, corresponding to the upper portion of the torn posterolateral bundle of the anterior cruciate ligament. Notice ACL horizontalization and disruption from the femoral attachment. The lateral meniscus showed free edge degenerative truncation.

- The "buckled PCL" sign, which occurs when any portion of the PCL is concave posteriorly on the sagittal images
- Anterior tibial translation, which is established on sagittal images when the distance between vertical tangent lines through the posterior margins of the femur and tibia exceeds 5–7 mm (MR drawer sign or better named MR Lachman sign). As a result of the translation, the LCL may be visualized in its entire craniocaudal extent on a single coronal image, and buckling of the patellar tend on may be seen due to shortening of the distance between the patella and the tibial tuberosity (Fig. 126)

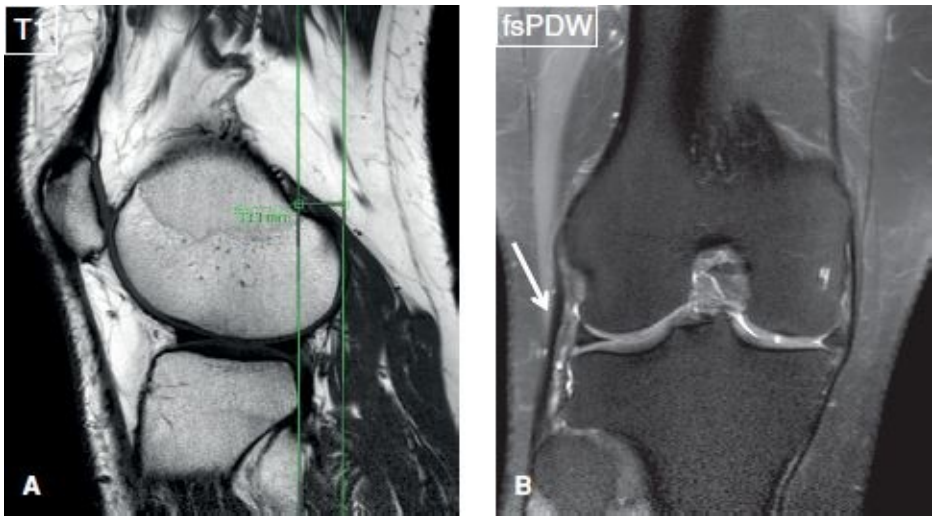

Fig. 126: MR drawer sign. **A:** On the sagittal plane, the distance between vertical tangent lines through the posterior margins of the femur and tibia measures 13 mm, reflecting anterior tibial translation. **B:** As a result of the translation, the fibular collateral ligament (*arrow*) is visualized in its entire craniocaudal extent on a single coronal image. Notice nonvisualized ACL in the notch.

- Segond fracture refers to cortical avulsion of the tibial insertion of the middle third of the lateral capsular ligament. Imaging studies display an elliptical, vertical, up to 10 mm bone fragment. It parallels the lateral tibial cortex about 3 to 4 mm distal to the plateau capsular ligament (Fig. 127). The finding has approximately 70% sensitivity for the diagnosis of complete ACL tears. The fracture is easier to diagnose on radiographs as compared to MRI

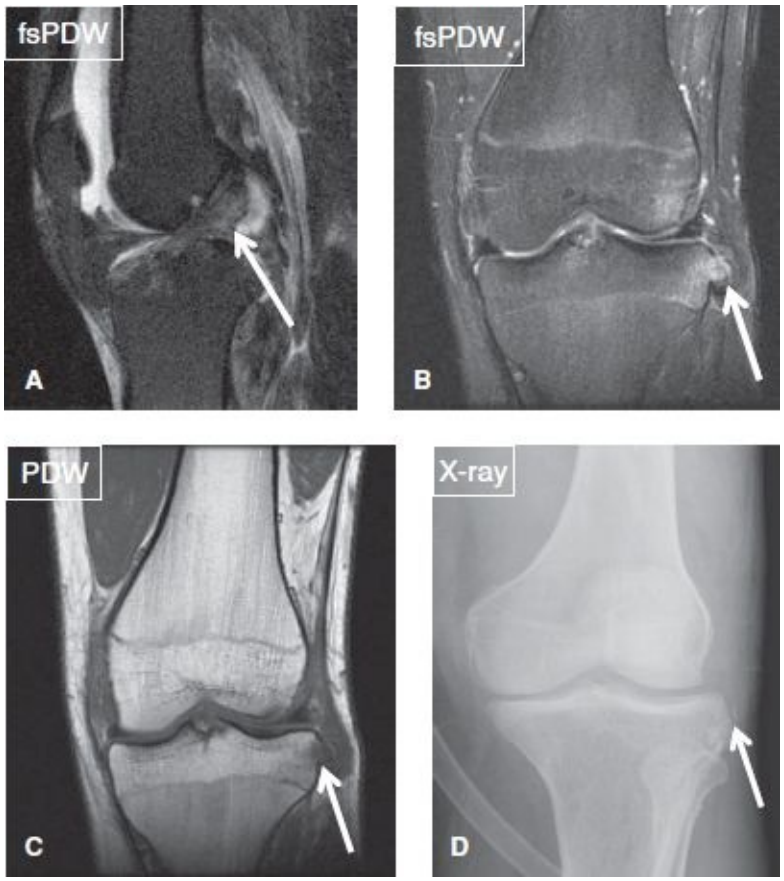

Fig. 127: Segond fracture. **A:** Sagittal image show tear of the anterior cruciate ligament with hemorrhage in the notch and hematocrit level in the joint (*arrow*). **B, C:** Coronal images demonstrate a focus of cortical avulsion (*arrows*) at the tibial insertion of the middle third of the lateral capsular ligament with a kissing contusion of the lateral femoral condyle. **D:** An elliptical bone fragment (*arrow*) is evident at the respective location in a anteroposterior radiograph in keeping with a Segond fracture.

- Kissing femoral and tibial bone contusions (Fig. 128), which are common in rotational translational event that happens during ACL injury (aka clipping injury). The typical locations of coup contusions are posterolateral tibial platue and anterior or central-lateral femoral condyle, while the counter-coup contusions occur at the posteromedial tibia at the semimebranosus attachment and central-medial femoral condyle. The posterolateral tibia is usually the most affected and the injury may vary from simple bone contusion to intra-trabecuar fracture, to osteochondral fracture with depression.

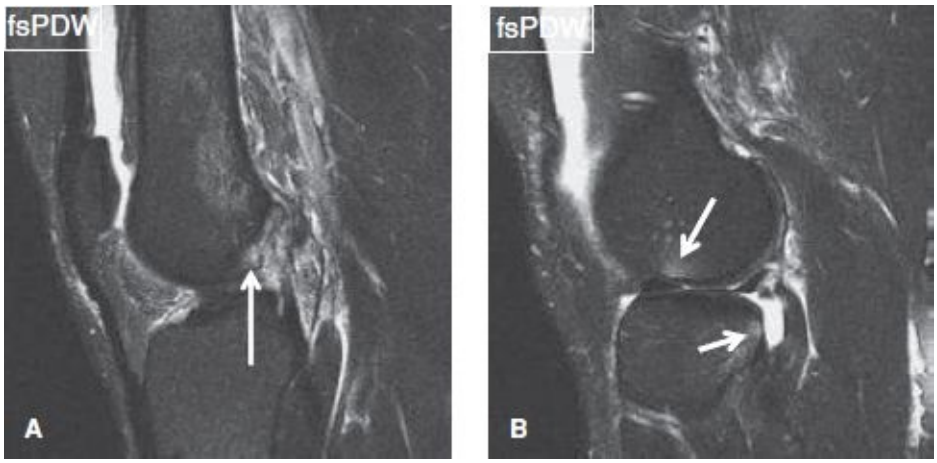

Fig. 128: Kissing bone contusions associated with anterior cruciate ligament tear. Sagittal images show complete tear of the anterior cruciate ligament (*arrow* in **A**), along with bone contusions (*arrows* in **B**) at the lateral femoral condyle and posterolateral tibial plateau, which are considered typical for this injury and recent translational and rotational event.

- Deep sulcus sign, which describes an exaggerated depression (>1.5 mm) of the condylopatellar sulcus (aka sulcus terminalis), due to impaction of the lateral femoral condyle with the posterior aspect of the lateral tibial plateau
- Wrisberg rip, a term referring to a longitudinal or oblique tear of the superior surface of the posterior horn of the LM that extends far laterally (>12 mm) from the normal Wrisberg ligament attachment
  - i) tibial uncovering of the posterior horn of the LM
  - j) concurrent MCL sprain and MM tear, which, along with the ACL tear, comprise the so-called O'Donoghue triad, not so commonly observed as previously described
- Hemorrhagic synovitis, seen as shearing injury of Hoffa's fat pad with ill-defined posterior contour and/or sprained ligamentum mucosum. Humphery hitch or transverse meniscal-ligament rip (meniscal tears at respective ligament attachments) may also be seen with ACL transational injuries.

ACL tears may also be complicated with posteromedial or PL corner injuries as described above in the respective sections (Figs. 129, 130).

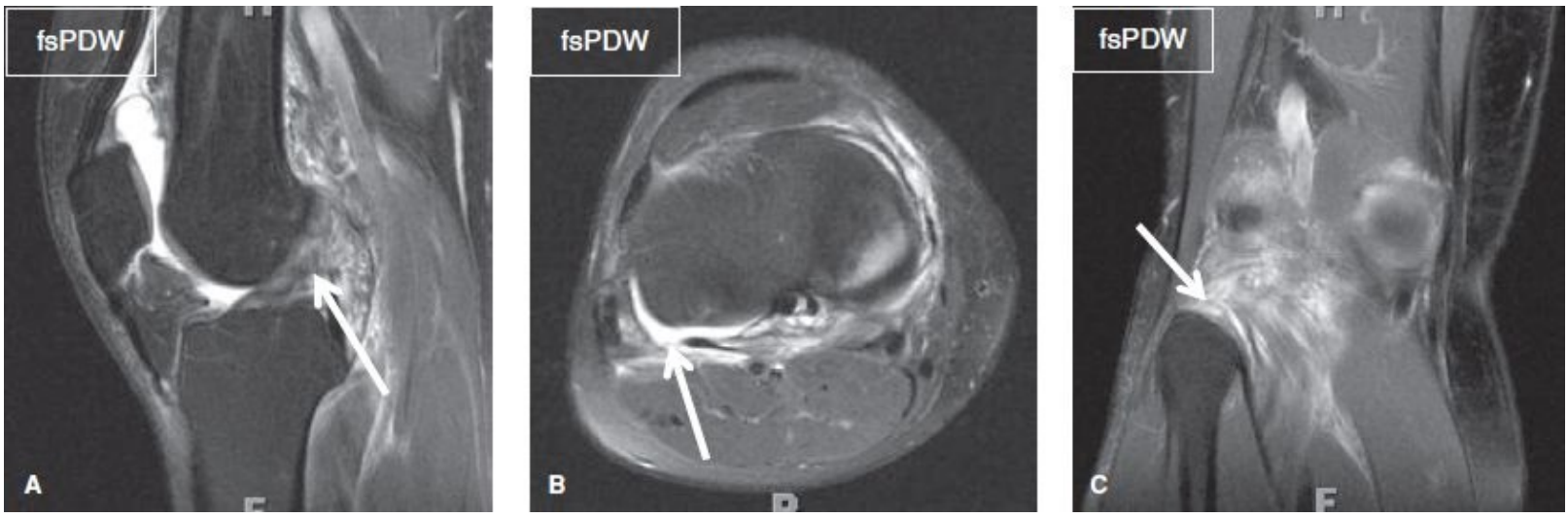

Fig. 129: Anterior cruciate ligament tear complicated with posterolateral corner injury. Sagittal **(A),** axial **(B),** and coronal **(C)** images display complete tear of the anterior cruciate ligament (*arrow* in **A**), along with arcuate ligament tear, and popliteofibular ligament tear (*arrows* in **B** and **C**), in keeping with posterolateral corner injury.

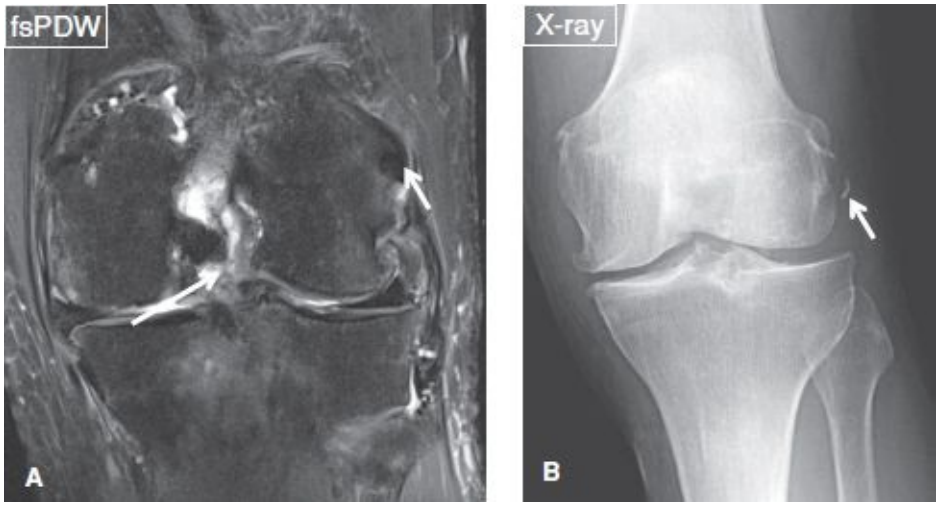

Fig. 130: Anterior cruciate ligament tear complicated with lateral collateral ligament avulsion. **A:** Coronal image shows complete disruption of the mid portion of the anterior cruciate ligament (*long arrow*), along with bony avulsion of the femoral insertion of the lateral collateral ligament (*short arrow*), and popliteus tendon avulsion (partially shown). **B:** Anteroposterior radiograph confirms cortical avulsion (*arrow*).

Differentiation between high-grade partial tears and complete tears of the ACL is sometimes challenging on MR imaging. Coronal and axial images are particularly useful in this setting. The anteromedial bundle provides the most (about 80%) strength to the ACL and is essential to evaluate on the coronal images. Low-grade partial tears should be suspected in cases where a) full continuity can not be established on coronal images b) the ACL exhibits abnormal focal signal, attenuation, or focal thickening. c) secondary signs of complete ACL tear are present but the ACL appears intact (Fig. 131). Most of these grade I and II sprains are treated conservatively, especially if clinically stable. Foot-plate avulsion is an interesting scenario, which if nondisplaced, will likely heal with conservative management or if displaced, would heal with simple pinning rather than complicated ligament reconstruction (Fig. 123).

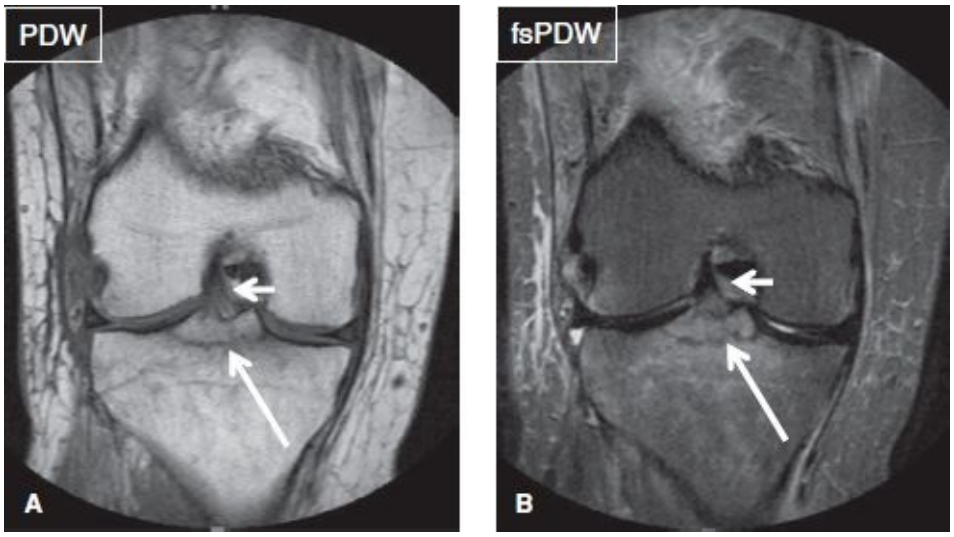

Fig. 131: Traction-related foot plate fracture of the intercondylar notch. Coronal images exhibit a transverse fracture (*long arrows*) of the base of the intercondylar eminence related to traction by the anterior cruciate ligament (*short arrows*). Notice minimal attenuation of the anteromedial bundle, which should be thicker than the posterolateral bundle.

In chronic ACL deficiency, one might see scarred fragmented ACL or complete non-visualization of the ligament, with mostly fat signal in the lateral intercondylar notch (Fig. 132). If the PCL is also concomitantly deficient, it is referred to as “empty notch” sign. In some cases however, hypointense mature scar tissue envelops a chronic non-displaced ACL tear that may render the ligament tear difficult to detect on imaging, with the only sign confirming the tear being a subtle angulated contour or flattened axis of the ACL. Finally, ACL injury may be predisposed by underlying mucoid degeneration of the ligament and one abrupt twisting injury event may completely disrupt the ligament (Fig. 133).

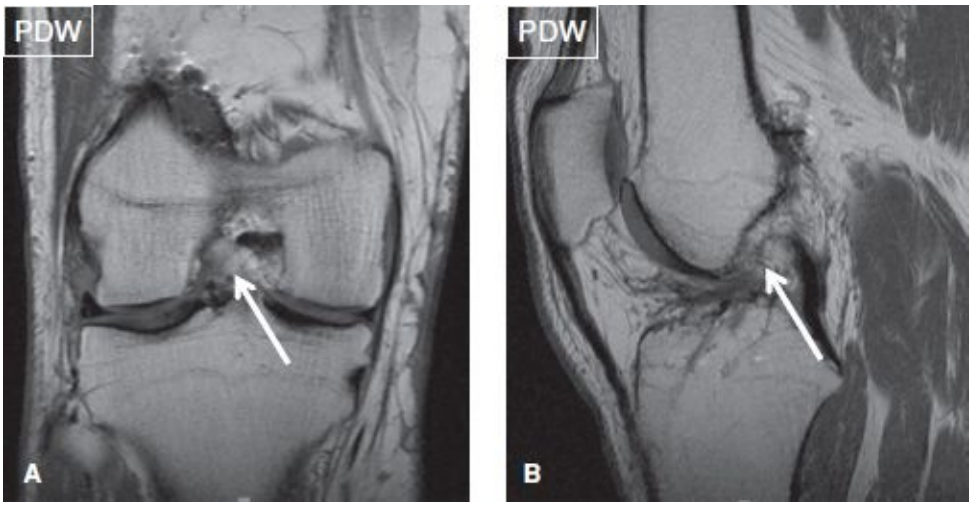

Fig. 132: Chronic anterior cruciate ligament deficiency. On coronal **(A)** and sagittal **(B)** images, there is complete nonvisualization of the anterior cruciate ligament, with only fat signal (*arrows*) evident in the lateral intercondylar notch.

Fig. 133: ACL disruption with underlying mucoid degeneration. Sagittal image shows completely disrupted ACL with posterior capsular injury and edema. Notice underlying cystic changes at the ACL attachments with expansion of the torn ACL reflecting underlying chronic mucoid degeneration.

The PCL also contains two bundles, the anterolateral (larger, controls flexion) and the posteromedial (smaller, controls extension). The normal PCL has uniform low signal intensity and lacks the striations observed in the normal ACL. The ligament has a gentle convex posterior margin in extension or minimal flexion. Minimal buckling is normal in different knee positions. The most common mechanisms of injury include direct blow to the anterior tibia (dashboard injury) in a flexed knee with foot planter flexed, forced hyperextension (could be bicruciate injury), or posterior rotatory force. Combined ACL and PCL injuries are more common than isolated PCL injuries. The PCL may be injured in different areas depending on the mechanism, such as at the tibial attachment in dashboard injury, at the femoral attachment in hyperextension, or at the mid-portion in extreme flexion. The posterior drawer test, as described above, is the most sensitive test. When the test is attempted, it is important to quantitate whether the tibia remains anterior to the distal femur (grade I), is in line with it (grade II), or is displaced posterior to it (grade III PCL tear). Posterior translation of the proximal tibia posterior to the distal femur indicates a significant amount of posterior instability and is usually indicative of a combined PCL and PL corner injury. The “tibial drop back or sag test” provides a static view of the amount of posterior translation caused by gravity in a knee with a PCL tear. This test can usually be performed on most patients, as it does not usually cause pain. In this test, the knee is flexed to 90 degrees and is evaluated from its lateral aspect. In the normal knee, the anterior tibia is normally 1 cm anterior to the femoral condyles. In the PCL deficient knee, there is

posterior displacement of the tibia with loss of the normal anterior tibial plateau outline. Finally, quadriceps active test, is a dynamic test and helps to assess for partial and complete PCL tears. The starting position for the test is the tibial drop test and the patient is asked to contract quadriceps muscle in an attempt to straighten the leg. If the tibia is subluxed posteriorly compared to normal, the quadriceps contraction will create anterior reduction force on the proximal tibia. A positive quadriceps active test is indicative of at least partial PCL tear.

Degeneration and partial tears usually involve the central fibers of the ligament without complete loss of PCL continuity (Fig. 134). In high-grade and complete mid-substance tears with an intact synovial sheath, the ligament usually maintains continuity as a single structure but demonstrates apparent thickening (anteroposterior diameter of the vertical portion greater than 7 mm), as well as high signal intensity on PDW and T2W images (Fig. 135). In case of complete PCL tears with a torn sheath, complete discontinuity is evident on imaging (Figs. 136, 137). In PCL avulsions, there is focal interruption of the ligament fibers, and alterations of the PCL contour, occasionally an avulsed bony fragment (Fig. 138). In chronic PCL tears, the ligament may maintain partial continuity due to scarring, but one can see attenuated caliber, thickened ligament and/or buckled contour. PCL repair is not commonly performed unless complete disruption is present or it is part of a multiligamentous injury in a high-performance athlete, since the meniscofemoral ligaments serve as secondary stabilizers of the posterior knee and the repairs have not shown to alter the progress to osteoarthritis. Primary reattachment is performed in avulsions from the tibial or femoral attachment sites using endobuttons, and reconstruction is performed in mid-portion full-thickness tears. In general, varus or valgus laxity in full extension is an indicator of a combined ligament injury (cruciate plus collateral). Neurovascular injuries are common in this scenario. Bicruciate or multiligament injury involving three or more ligaments should be considered a spontaneously reduced knee dislocation.

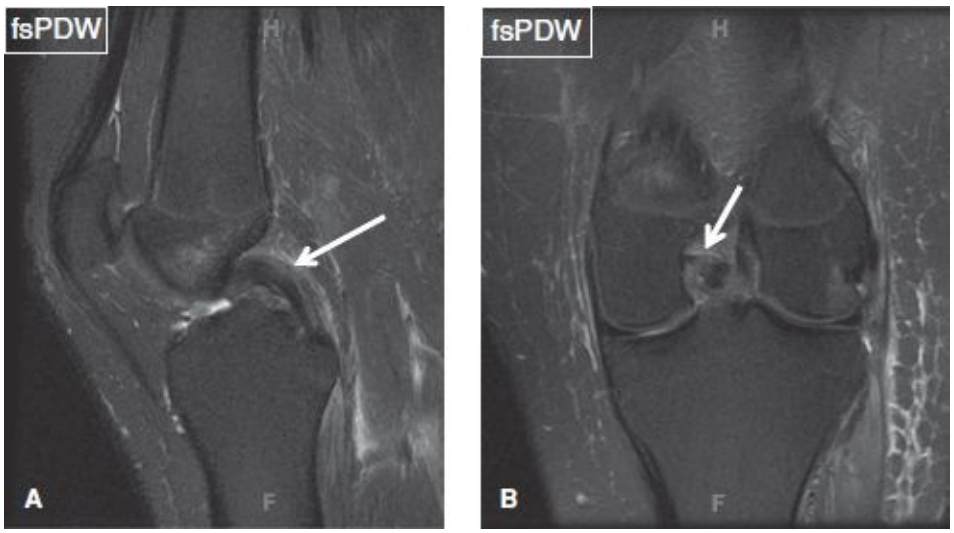

Fig. 134: Low-grade partial tear of the posterior cruciate ligament. Sagittal **(A)** and coronal **(B)** images show internal hyperintensity in the dorsal portion of the otherwise continuous posterior cruciate ligament in keeping with a interstitial tear.

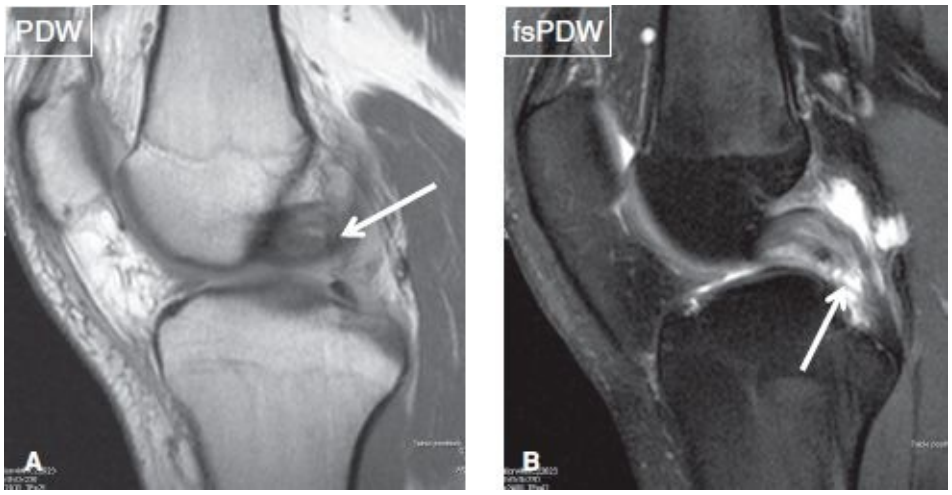

Fig. 135: High-grade partial, near full-thickness tear of the posterior cruciate ligament. On sagittal images, the ligament is diffusely thickened and heterogeneously hyperintense with near complete discontinuity of fibers.

Fig. 136: Complete disruption of the posterior cruciate ligament. Sagittal image shows complete discontinuity (*arrow*) of the distal portion of the posterior cruciate ligament and irregular posterior joint capsule from subacute injury.

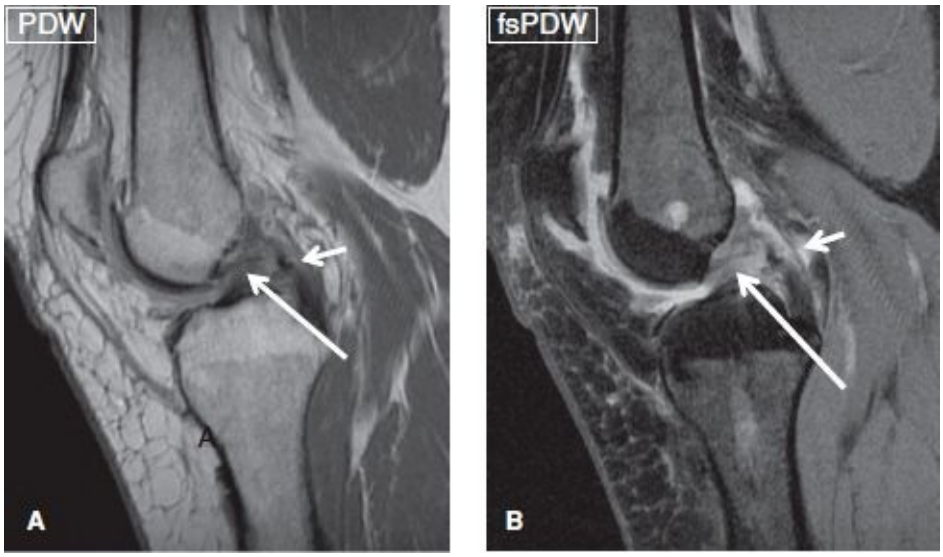

Fig. 137: Concomitant anterior and posterior cruciate ligament disruptions. Sagittal images demonstrate simultaneous complete tears of the anterior (*long arrows*) and posterior (*short arrows*) cruciate ligaments. Notice small cartilage rest in the distal femoral metaphysis, not uncommon adjacent to the physeal scar.

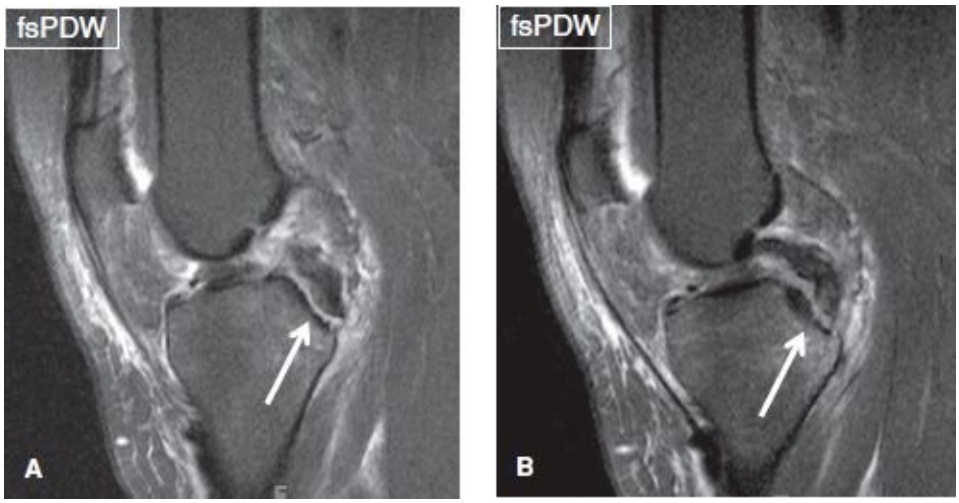

Fig. 138: Posterior cruciate ligament foot plate avulsion. Sagittal images exhibit avulsion of the tibial attachment of the posterior cruciate ligament at the foot plate with avulsive bone marrow edema (*arrows*) and posterior capsular tear.

BONES: [<Otherwise normal>]

The bones should be checked for cortical and marrow abnormalities, such as red marrow reconversion, benign and malignant marrow infiltrative processes, cortical and subchondral fractures, osteochondral lesions, infarcts and neoplasms. T1W images are optimal for the evaluation of bone marrow, and should be included in at least in one imaging plane in every "ortho" joint MR imaging protocol. Red marrow reconversion process is mildly hyperintense to muscle on T1W and PDW images, and usually spares the epiphysis and apophysis. Deeper involvement of the epiphysis, apart from the normal subchondral red marrow area may require correlation with radiographs and/or supplemental chemical shift imaging. More than 20% loss of signal intensity on the out-of-phase images indicates

presence of microscopic fat within the lesion in question and likely benignity, such as red marrow reconversion. In clinical practice, chemical shift imaging is only occasionally needed, since most of the times, marrow signal more than the skeletal muscle on T1W imaging is enough to qualify it as red marrow reconversion (Figs. 139, 140). Other marrow infiltrative or replacement processes include Erdheim–Chester disease (histiocytic infiltration, systemic symptoms including diabetes insipidus, sclerotic bones on radiographs, mixed diffuse infiltrative marrow signal changes with nearly symmetrical appearance bilaterally), leukemia and lymphoma (peripheral smear abnormality, underlying known lymphoproliferative disorder, patchy or diffuse T1 isointense or hypointense marrow infiltration, cortical permeation, soft tissue mass, regional or systemic lymphadenopathy), hematopoetic disorders, such as sickle cell disease, hemophilia, chronic renal insufficiency and myelodysplastic syndromes (known disorder, genetic predisposition, red marrow reconversion, and hemosiderosis), sarcoidosis (known sarcoid, speckled or reticular marrow infiltration multifocal T2 iso- or hypo-intense lesions, female gender), and finally myeloma and metastasis (known primary tumor, hypercalcemia, anemia, abnormalities on electrophoresis, bone lesions on radiographs, focal, multifocal or diffuse marrow infiltration, endosteal scalloping, cortical erosions, peri-lesional bone marrow edema with metastasis, and soft tissue mass, especially with myeloma) (Figs. 141, 142).

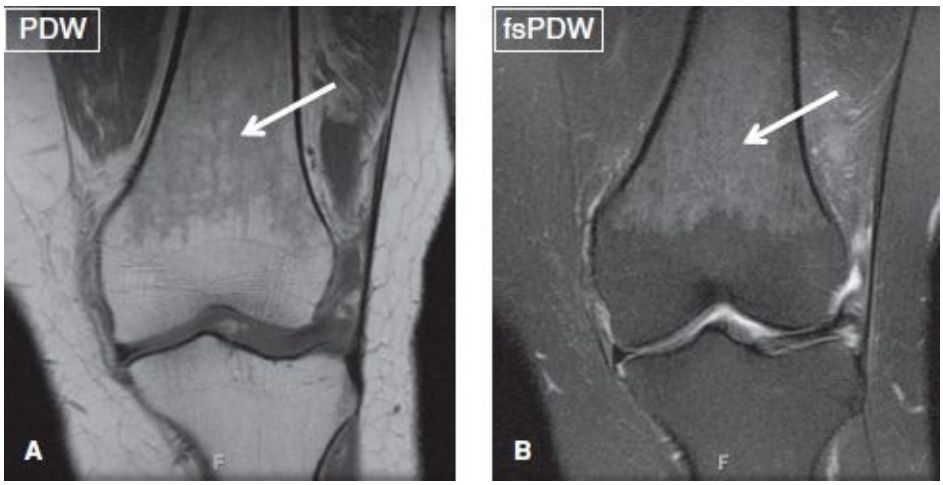

Fig. 139: Red marrow reconversion. Coronal images show diffuse intermediate T1 signal alteration higher than the adjacent muscles and slightly high T2 signal of the bone marrow (*arrows*) of the femoral diaphysis and metaphysis in keeping with red marrow reconversion.

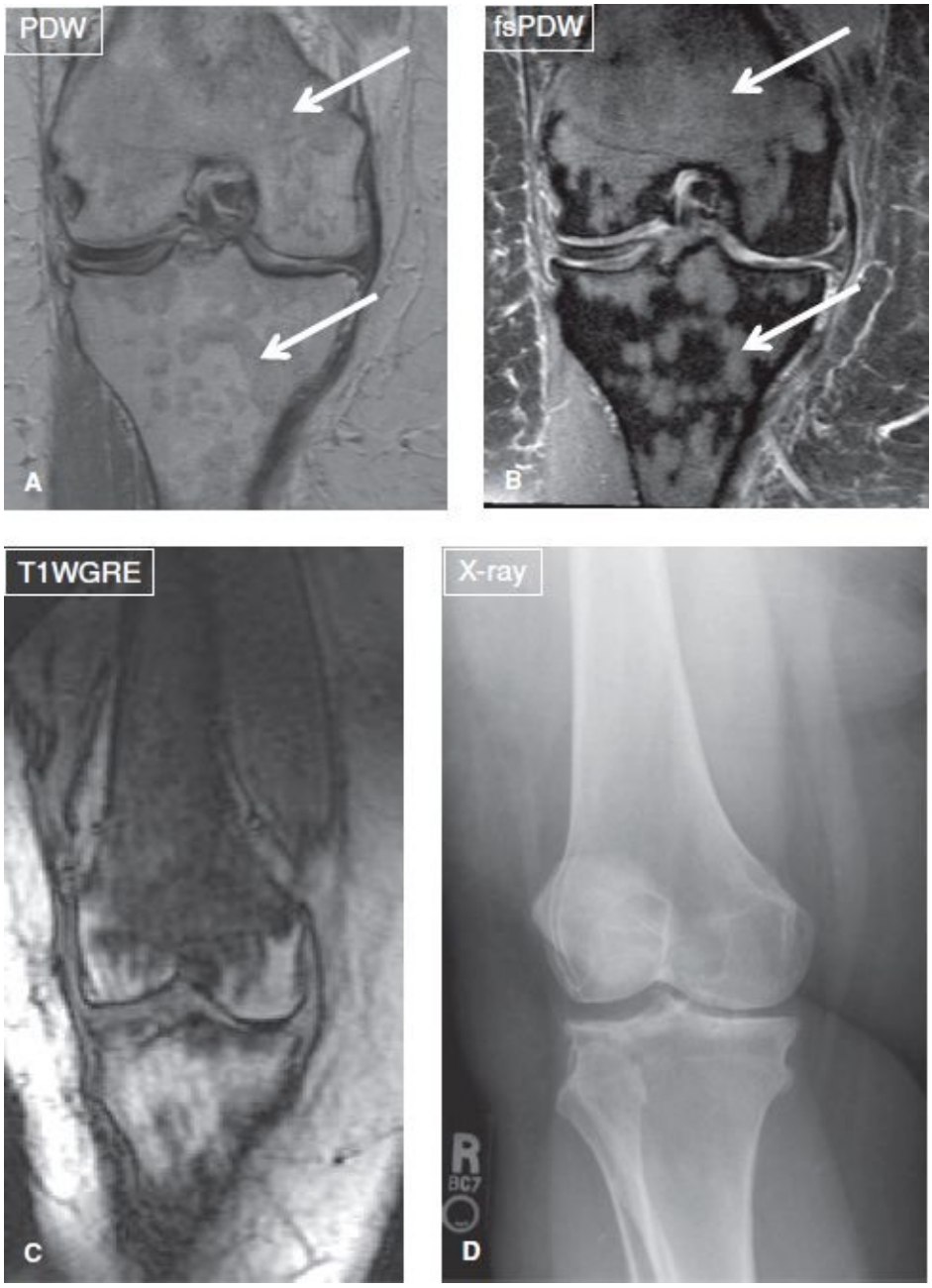

Fig. 140: Red marrow reconversion. Coronal images **(A, B)** show multifocal areas of intermediate signal (*arrows*) in the femur and tibia, again hyperintense as compared to the regional muscles. The areas demonstrate signal drop in the corresponding opposed-phase image **(C)** due to intracellular lipid and are compatible with scattered foci of red marrow reconversion. The respective anteroposterior radiograph **(D)** is normal.

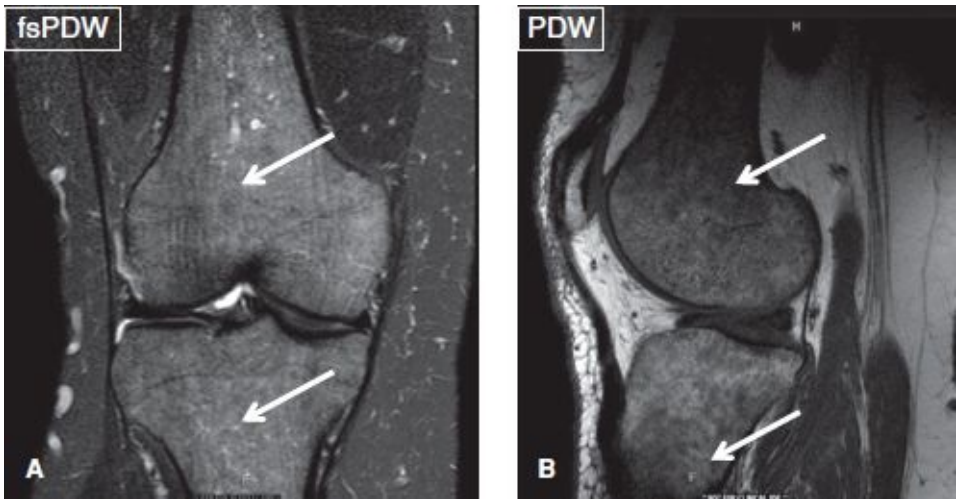

Fig. 141: Erdheim–Chester disease. Coronal **(A)** and sagittal **(B)** images show diffuse low signal involving all areas of bone marrow including epiphyses with heterogeneity and isointense signal to the adjacent muscles (*arrows*), corresponding to histiocytic infiltration in this case of Erdheim–Chester disease.

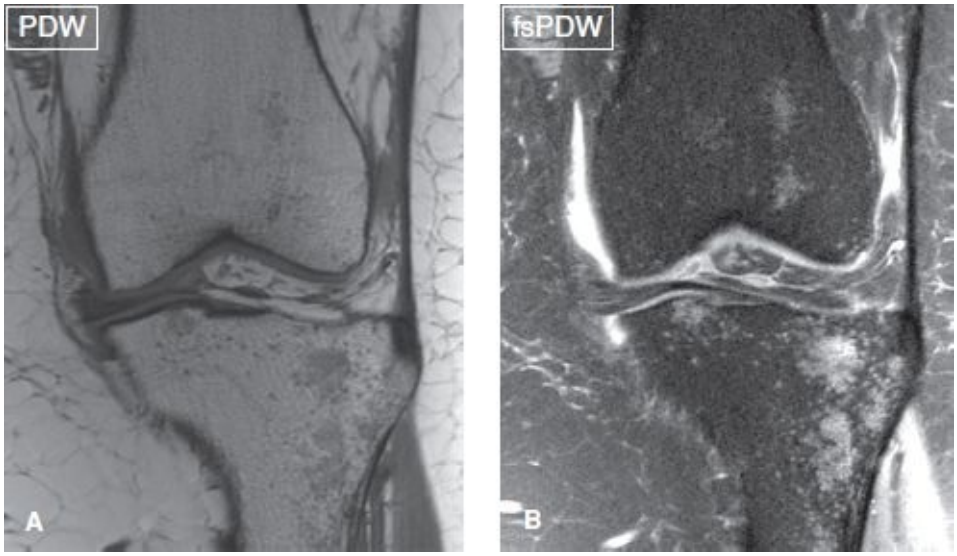

Fig. 142: Sarcoid arthropathy. Coronal images **(A, B)** demonstrate small effusion and multifocal speckled marrow infitrative changes in biopsy proven case of osseous sarcoidosis.

Subchondral insufficiency fractures of the knee (previously referred to as spontaneous osteonecrosis of the knee) most often affect elderly and osteoporotic subjects and present with sudden onset of pain, without a history of major trauma. The entity is typically unilateral, and involves the medial and, less commonly, the lateral femoral condyle, but may also involve the lateral tibial condyle. It is seen as a low signal intensity focus beneath the articular surface on T1W or PDW images with extensive (usually >2 cm area) marrow edema within the femoral condyle on fsT2W or fsPDW images. One should look for the common association of underlying meniscal tear, particularly radial tear of the free edge of the body/posterior horn or the posterior root (Fig. 143). Osteochondral lesions are not uncommonly identified as incidental or symptomatic findings and they are discussed in detail in the cartilage chapter (Figs. 144–146). These may be related to prior trauma in

most ages, except in adolescents, in whom they are believed to represent disorders of the secondary physis (zone of provisional calcification). Signs of potential instability include large size (>1.5 cm), extensive cystic changes at the base of the lesion, in situ body with overlying high-grade cartilage fissuring or loss, and clear fluid signal, lucency on radiographs, or intra-articular gadolinium undercutting the lesion. The lesions may heal spontaneously or operative intervention may be needed in symptomatic subjects. Upon healing, the bone marrow edema and/or cystic changes show fatty metamorphosis or sclerosis. Therefore, it is essential to use both PDW and fsPDW images in tandem to detect these lesions (Fig. 146).

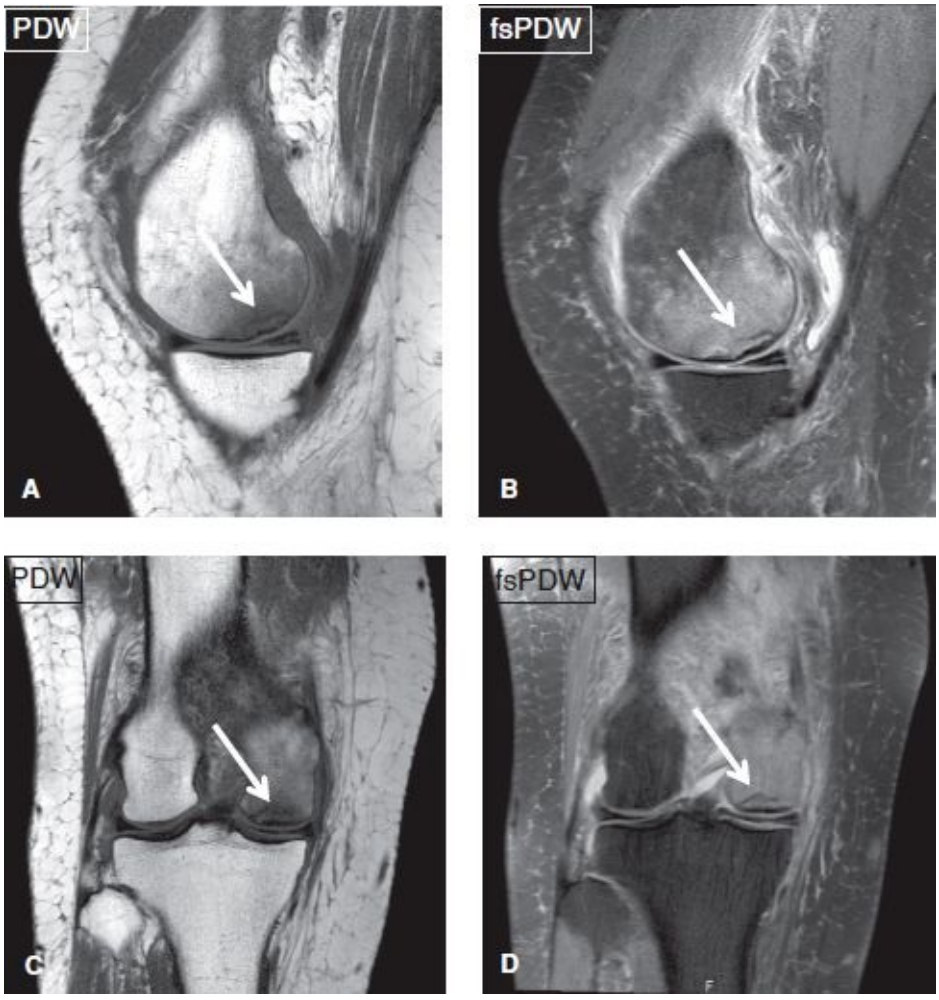

Fig. 143: Subchondral insufficiency fracture. Sagittal **(A, B)** and coronal **(C, D)** images demonstrate a subchondral hypointense fracture line (*arrows*) paralleling the articular surface of the medial femoral condyle. Notice extensive (>2 cm) bone marrow edema and small free edge radial tear of the posterior horn.

Fig. 144: Osteochondral lesion (OCL). **A:** Lateral radiograph shows an OCL of the femoral condyle (*long arrow*), with complete lucency around an in situ body (*short arrow*). **B:** Sagittal MR image confirm the OCL (*long arrow*) with in situ body (*short arrow*). **C:** Another OCL following dislocated body and remaining full-thickness cartilage defect (*arrow*).

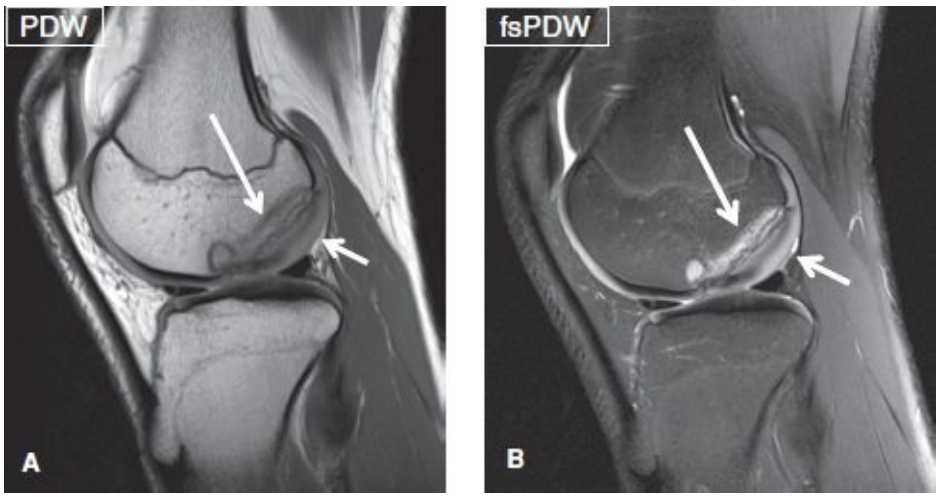

Fig. 145: Osteochondral lesion. Sagittal images demonstrate a large OCL of the lateral femoral condyle (*long arrows*) with subjacent cystic changes. The overlying cartilage appears mildly proud relative to normal cartilage (*short arrows*).

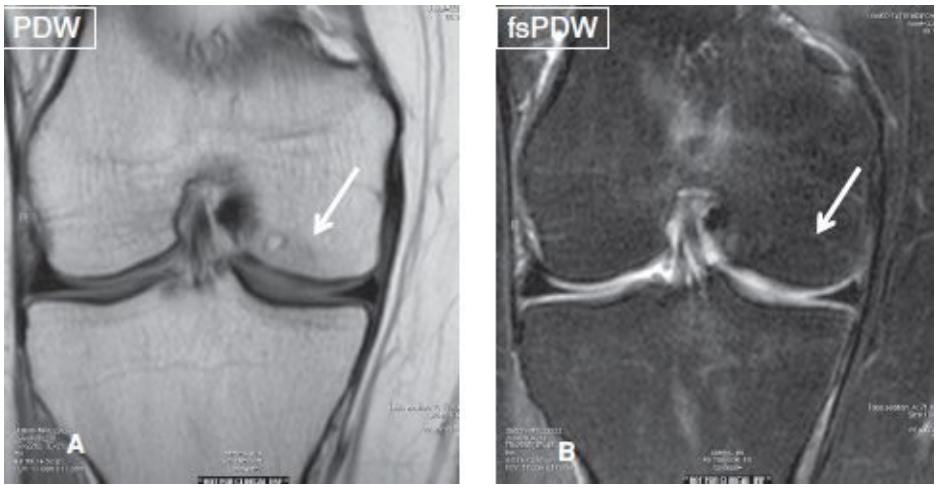

Fig. 146: Chronic osteochondral lesion on coronal knee MR images. Better seen on nonfat suppressed PDW image **(A)** due to fatty metamorphosis of the cystic changes, a barely visible osteochondral lesion (*arrows*) is present in the medial femoral condyle. Absence of surrounding marrow edema indicates a chronic healed lesion.

The knee bones may be fractured due to stress injuries or from direct or indirect trauma. Stress injuries are common in the tibia, whereas insufficiency injuries are common in femur. Whenever, one sees extensive bone marrow edema (>2 cm area), one should look for underlying dark line that would correspond to the fracture line (Figs. 147, 148). In most circumstances, the bone marrow edema resolves after 3 months from injury although less commonly, it may take more than 3 months for the edema to resolve despite good fracture healing. However, the fascial edema resolves quickly within 2 to 4 weeks, and periostitis may appear suggesting subacute nature of the lesion (Figs. 148, 149). Salter–Harris injuries are fractures of the epiphyseal plate in pediatric population. Their classification is based on the involvement of the physis, metaphysis, and epiphysis, and is important because it affects patient treatment and provides clues to possible long-term complications (Table 4). Type III/IV fractures require open reduction and internal fixation. Type V fractures are usually diagnosed late. One should look for periosteal or collateral ligament entrapment within the lesion that may prevent healing (Figs. 150, 151). These lesions are important, as they can result in altered growth, or more commonly, premature closure of the growth plate, with subsequent limb shortening and abnormal growth (Fig. 152). Bony bridge from premature fusion is common in the tibia and distal femur and is better seen on 3D MR or CT imaging as osseous bridge across the physis with a metaphyseal cartilaginous tongue. The earlier the age of the injury and more angular the deformity, the higher are the chances that leg length discrepancy will result and surgery may be needed. Lower limb lesion, lesion in distal femur and tibia, varus deformity, and extension lesions are less well tolerated as compared to the upper limb lesion, lesion around the hip, valgus deformity, and flexion lesions. More than 5 degrees of varus or valgus angulations or more than 10–20 degrees of posterior angulation usually require intervention. In cases of leg length discrepancy of more than 1 cm or less than 4 cm, the bony bridge is resected on the affected side and/or epiphysiodesis can be performed by drilling or staples on the contralateral normal side to attempt premature fusion and equalize the limb lengths. The site of bony bridge or bar may determine the growth of the bone: for example, a medial bony bar in the distal femur will lead to lateral overgrowth and varus knee deformity. More than 4 cm discrepancy will likely require resection and allograft placement to lengthen the limb.

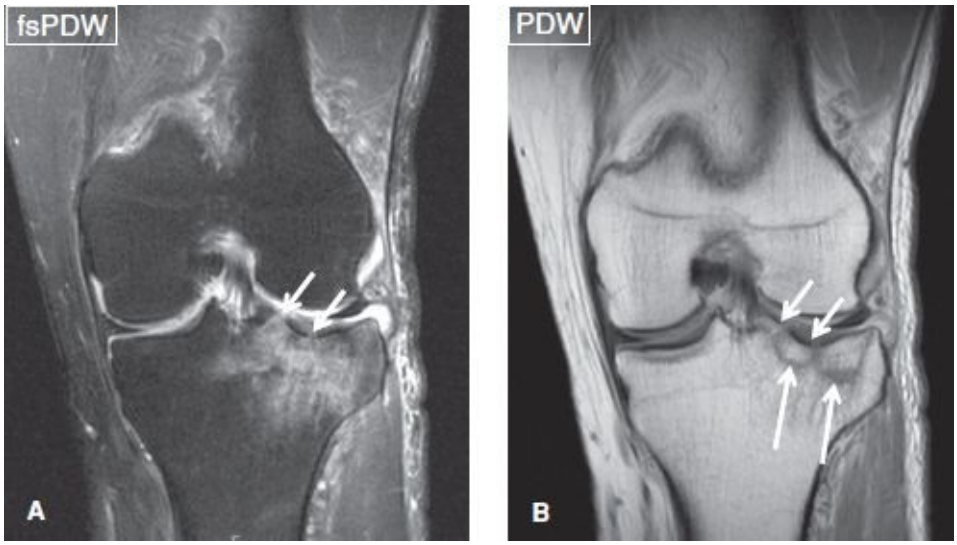

Fig. 147: Tibial plateau compression fracture from motor vehicle accident. Coronal images **(A, B)** show depression and focal cortical interruptions (*short arrows*) of the lateral tibial plateau, due to hypointense fracture lines (*long arrows*) in a cloud of extensive bone marrow and adjacent fascial edema.

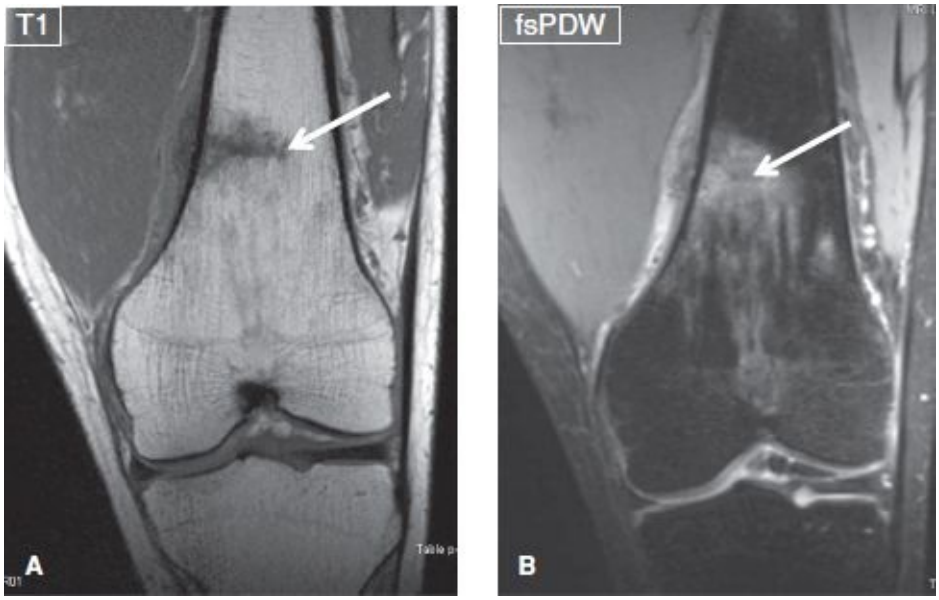

Fig. 148: Femoral shaft fracture. Coronal images **(A, B)** show a transverse hypointense incomplete fracture line (*arrows*) across the distal femoral shaft, which is surrounded by marrow edema and periostitis from subacute insufficiency fracture in this subject with osteopenia.

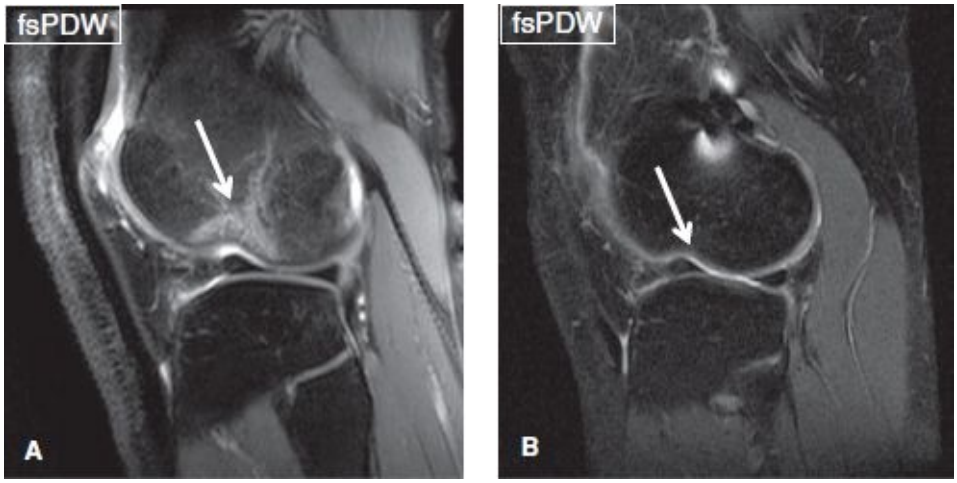

Fig. 149: Compression fracture of the lateral femoral condyle. Sagittal images. **A:** A compression fracture (*arrow*) is evident at the anterior lateral femoral condyle, surrounded by marrow edema. **B:** A few months later, there is complete resolution of marrow edema, signifying healing of the fracture (*arrow*). Residual cortical depression is still evident.

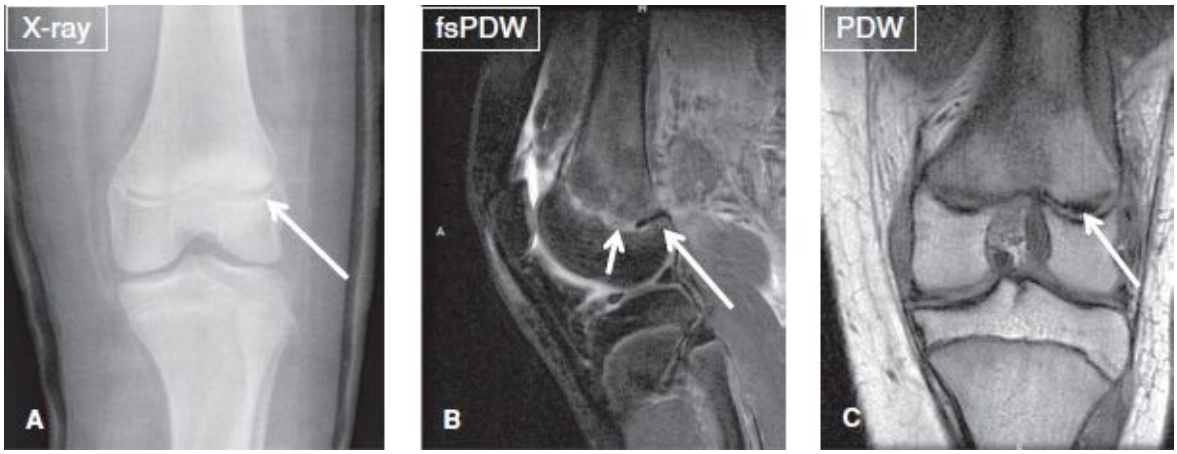

Fig. 150: Salter–Harris type I injury with entrapped periosteum. **A:** Anteroposterior radiograph demonstrates widening of the lateral distal femoral physis (*arrow*). The corresponding sagittal **(B)** and coronal **(C)** MR images confirm mild widening and fluid signal at the physis (*short arrow* in **B**) as well as a linear hypointense structure in the lateral physis (*long arrows*), representing displaced periosteum from the ipsilateral femoral metaphysis entrapped in the physis.

Fig. 151: Salter–Harris type IV injury. Coronal image exhibits a physeal fracture (*long arrow*) involving the epiphysis and metaphysis. Note the wavy configuration of the medial collateral ligament (*short arrow*) due to avulsion of its distal attachment.

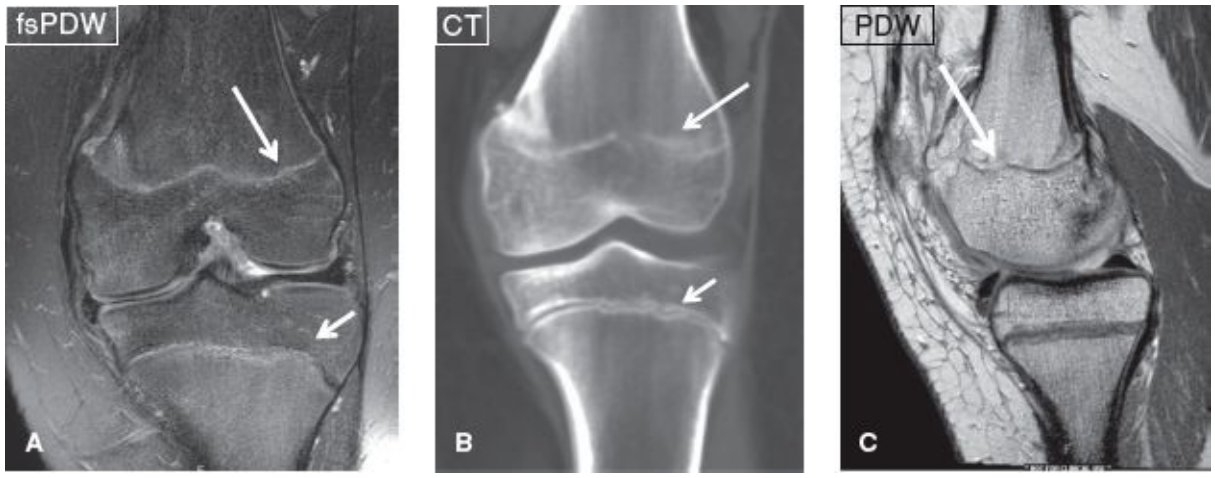

Fig. 152: Healed Salter–Harris injury with physeal fusion. Coronal fat-saturated image shows fusion of the lateral tibial plateau physis (*short arrow* in **A**), which is much better seen on the CT image (*short arrow* in **B**). Femoral physeal fusion (*long arrows*) is also better seen on CT and non–fat-saturated image **(C)**.

Tumors and pseudolesions around the knee are common, due to high vascularity of these bones, susceptibility of this flexible joint to injuries, and commonly found islands of residual red marrow. The lesions should be classified as benign or indolent (do not touch lesions or those that can be safely followed up), malignant or aggressive (malignancy unless proven otherwise, and indeterminate (requiring short-term, 6- to 12-week follow-up or biopsy). The MR imaging findings should be correlated with plain films, wherever available. Benign lesions include cortical desmoid (tug lesion at the tendon or ligament attachments), fibrous cortical defect (<1.5 cm, cortical-subcortical lesion with peripheral sclerosis), non-ossifying fibroma (>1.5 cm cortical-subcortical lesion with peripheral thick sclerosis, may contain cystic areas, bone marrow edema is uncommon), bone infarct (double ring sign or well-defined demarcation zone), subperiosteal hematoma (recent trauma, location, fascial or bone marrow edema, mixed signal intensity fluid collection in the subperiosteal area with peripheral enhancement), chondroblastoma (extensive edema, epiphseal location, periostitis, young age, peripheral sclerosis, secondary ABC may co-exist with fluid–fluid levels), ganglion cyst (T2 bright lesion with peripheral enhancement and neck in relation to synovial lining), aneurysmal bone cyst (metaphyseal, fluid–fluid levels), osteoid osteoma (bone marrow, fascial edema and cortical thickening, enhancing nidus, increased perfusion in arterial phase imaging), enchondroma (T2 bright cartilage matrix and internal mineralization, endosteal scalloping, proximity to the physeal plate), osteochondroma (bone marrow and cortical continuity, cartilage cap <1.5 cm), giant cell tumor (subarticular location, areas of T2 hypointensity), etc. (Figs. 153–162). Malignant or aggressive lesions show cortical destruction, aggressive periostitis, large size and multicompartment involvement, for example osteosarcoma, Ewing sarcoma, myeloma, metastasis, lymphoma, etc. (Figs. 163, 164). Indeterminate lesions show mixture of MR imaging features. For example, T1 isointense marrow replacement, or enchondroma with more than one-half cortex endosteal scalloping or lesions with bone marrow edema. In such

cases, short-term follow-up or biopsy may be performed for further management (Fig. 165). Infections may mimic all three (benign, indeterminate and potentially malignant categories), and therefore correlation with the clinical picture is important. The infected bone may show extensive periostitis and cortical destruction. Other helpful signs include, presence of a multilayered lesion that abuts the physeal plate, adjacent fluid collection or sinus tract, and the underlying setting of systemic toxemia (Fig. 166).

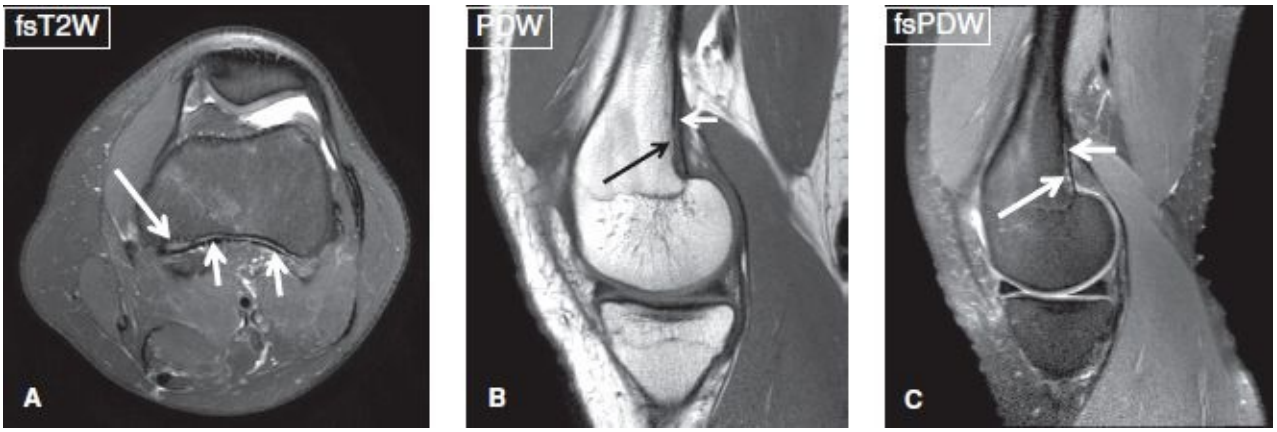

Fig. 153: Cortical desmoid. Axial **(A)** and sagittal **(B, C)** images demonstrate a cortically based lesion (*long arrows*) at the posteromedial aspect of the distal femoral metaphysis, which basically represents cortical avulsive deformity at the gastrocnemius origin. Note concomitant metaphyseal stripe (*short arrows*), which is distributed along the entire posterior portion of the femur.

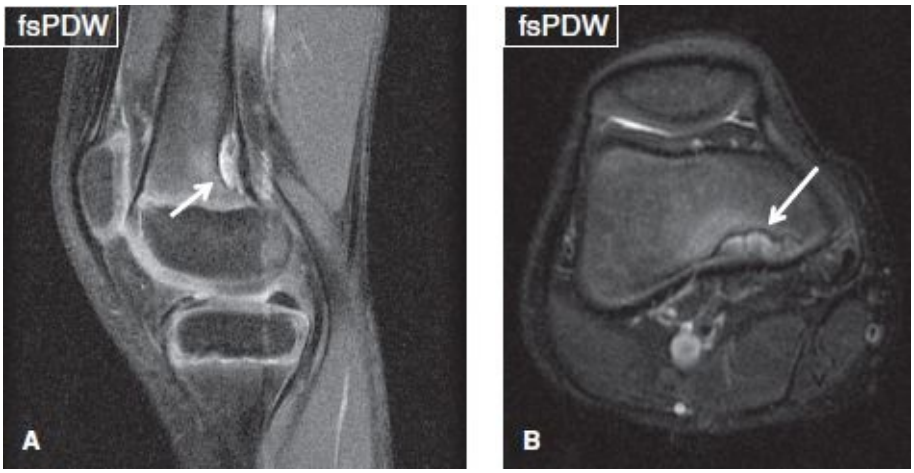

Fig. 154: Non–ossifying fibroma. Sagittal **(A)** and axial **(B)** images from a child exhibit a well-defined cortical–subcortical hyperintense lesion (*arrows*), which features a hypointense rim and is surrounded by mild marrow edema. The findings are virtually pathognomonic for the diagnosis. By definition, lesions <1.5 cm in size are termed fibrous cortical defects whereas lesions >1.5 to 2 cm are termed non–ossifying fibromas.

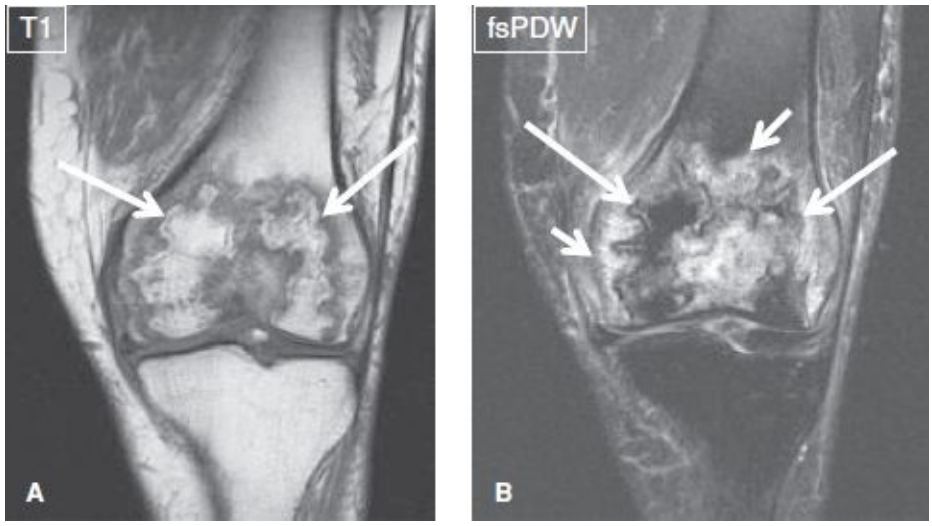

Fig. 155: Bone infarct. Coronal images **(A, B)** show bicondylar well-defined medullary lesions (*long arrows*), which have geographic margins, show internal signal which is similar to fatty marrow surrounded by double ring sign. Notice perilesional bone marrow and fascial edema (*short arrows*), indicating active process.

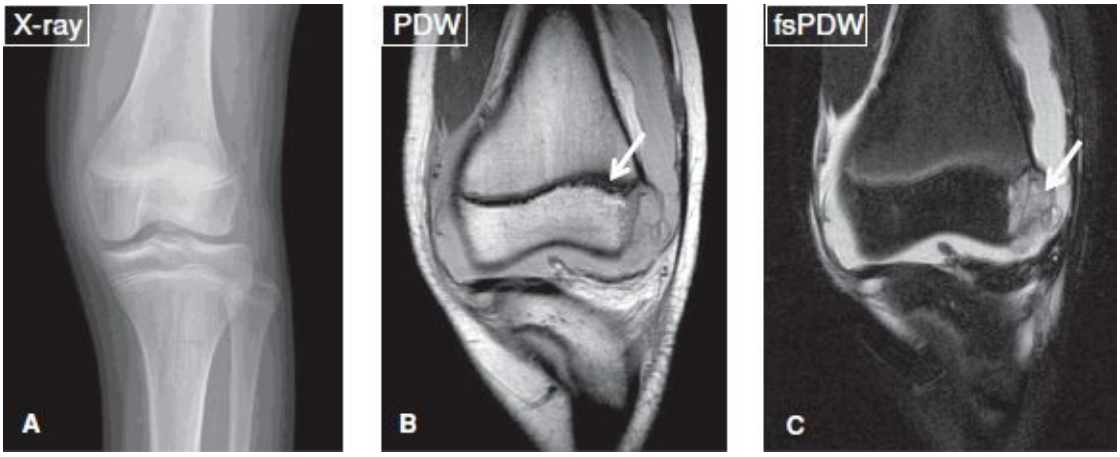

Fig. 156: Subperiosteal hematoma. AP **(A)** and coronal **(B, C)** images show a subperiosteal fluid collection (*arrows*) with minimal elevation of periosteal- cortical hypointensity of the lateral femoral condyle on non–fat suppressed image due to cortical shear injury. Notice moderate knee effusion.

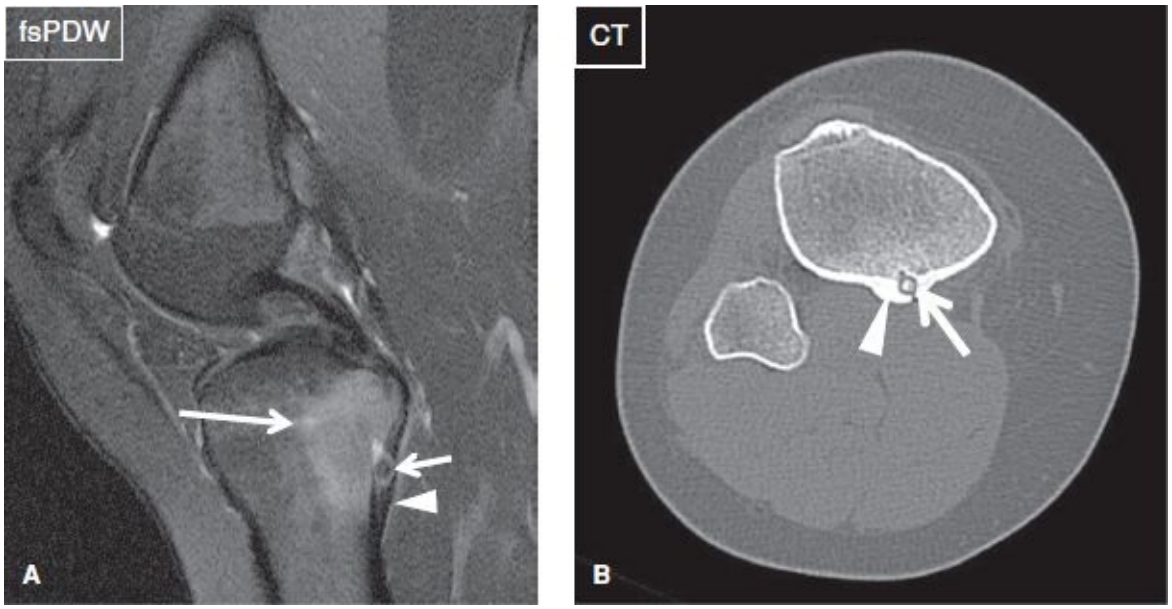

Fig. 157: Osteoid osteoma. **A:** Sagittal MR image shows a well-defined area of marrow edema (*long arrow*) in the tibial epiphysis and metaphysis. Notice underlying posterior peripheral cortical thickening (*arrowhead*) and an intracortical hyperintense ovoid lesion with internal focal hypointensity (*short arrow*). **B:** Axial CT image confirms cortical thickening and sclerosis (*arrowhead*) and reveals a well-defined and round partially mineralized nidus (*arrow*).

Fig. 158: Enchondroma. Small T1 isointense and T2 hyperintense lesion (*arrows*) abutting the physeal scar, a classic location for cartilage rest (<1 cm) and enchondroma (>1 cm and/or internal mineralization). No aggressive features, such as bone marrow edema, periosteal reaction, cortical destruction, soft tissue mass, or large size are evident confirming benignity of the lesion.

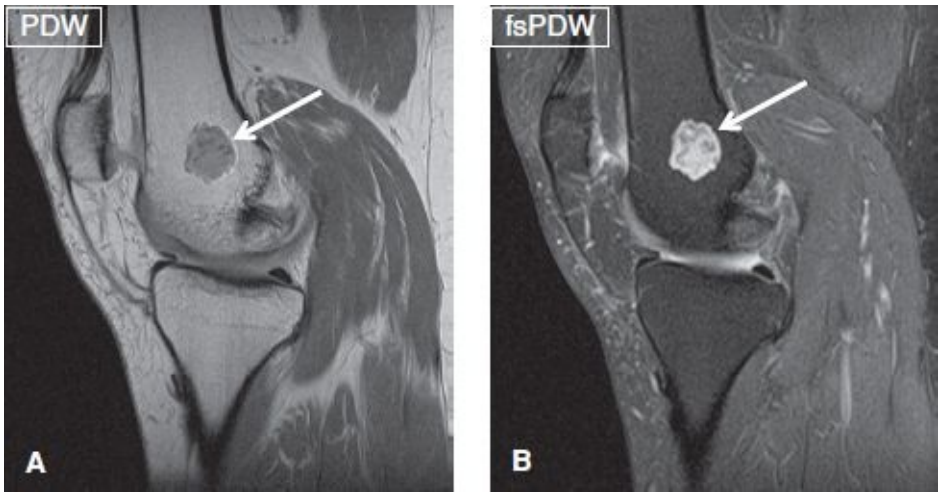

Fig. 159: Enchondroma. Sagittal images demonstrate a well-defined somewhat lobulated T2 hyperintense lesion (*arrows*) with foci of signal drop within the lesion that correspond to calcifications within the cartilaginous matrix.

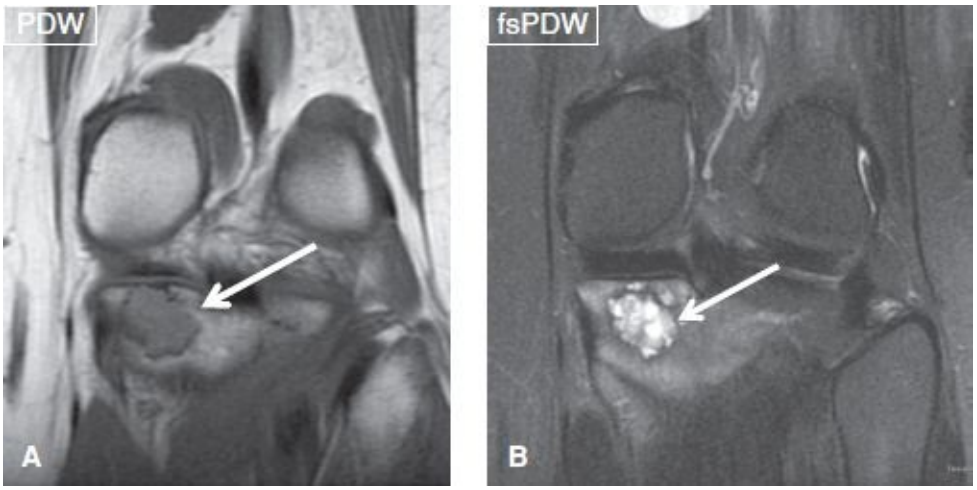

Fig. 160: Chondroblastoma. Coronal images. Focal lobulated T2 hyperintense epiphyseal lesion (*arrows*) with extensive perilesional bone marrow edema, a biopsy-proven chondroblastoma.

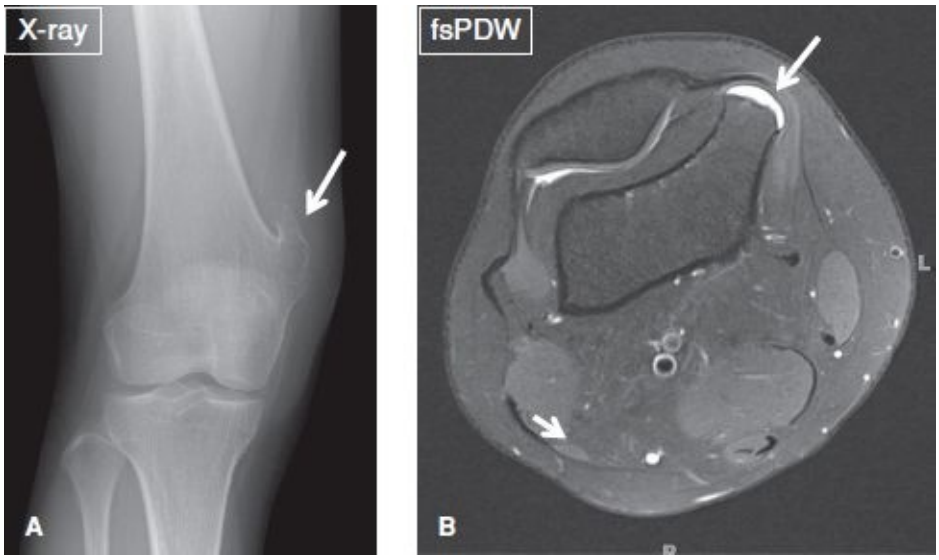

Fig. 161: Osteochondroma. **A:** Anteroposterior radiograph demonstrates a broad-based

sessile bone lesion (*arrow*), which is typically arises from the metaphysis and projects away from the epiphysis. **B:** Axial MR image, which has been acquired to evaluate cartilage cap thickness and exclude malignant transformation, shows the cap is thin and well defined, indicating a benign lesion (*arrow*).

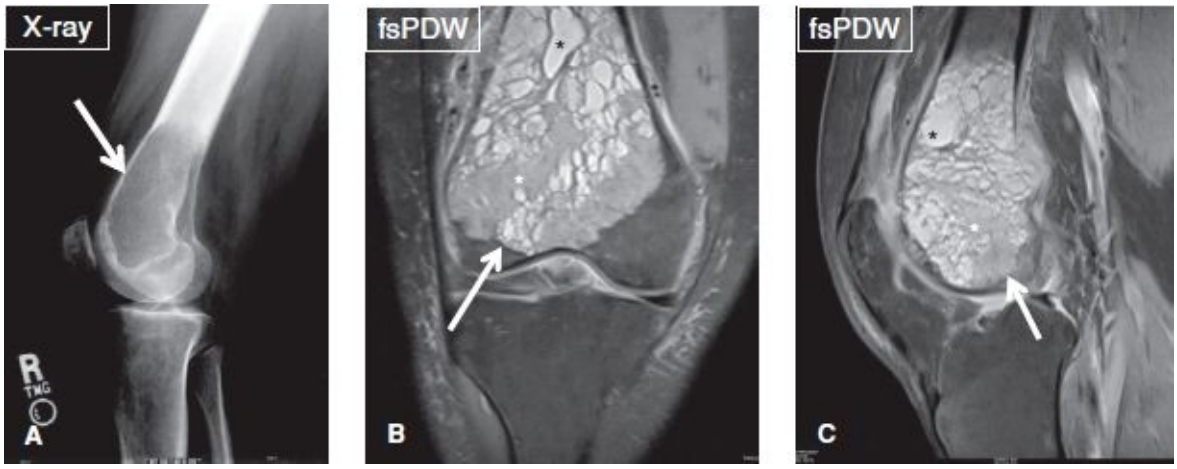

Fig. 162: Giant cell tumor. **A:** Lateral radiograph shows a well-defined lytic lesion with nonsclerotic margins (*arrow*), which abuts the articular surface and involves an individual with closed growth plates. On coronal **(B)** and sagittal **(C)** MR images, the lesion features low signal intensity margins (*arrows*) and heterogeneous high T2 signal with areas of intermediate to dark signal solid areas (*white asterisks*) and markedly hyperintense cystic components (*black asterisks*).

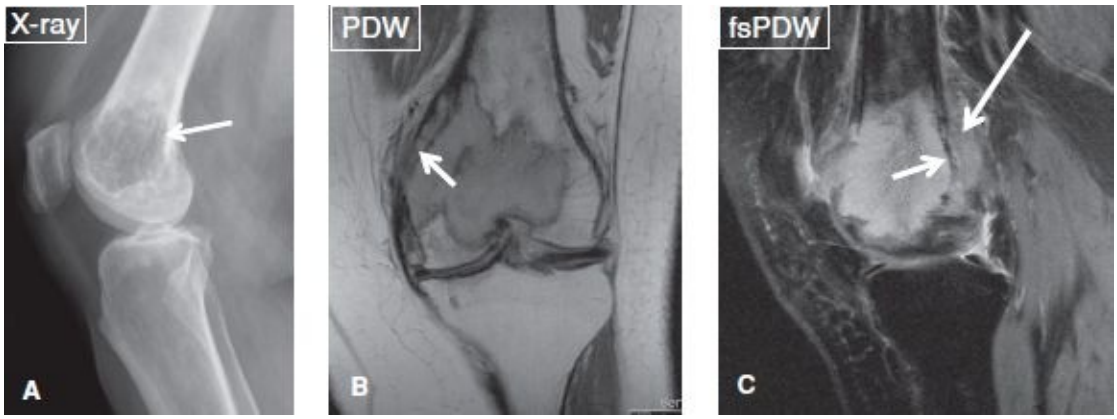

Fig. 163: Metastatic lesion. **A:** Lateral radiograph shows a lytic lesion (*arrow*) with patchy sclerosis and wide zone of transition in an adult subject. **B, C:** MR images show medial and posterior cortical erosions (*short arrows*) along with an adjacent small soft tissue mass (*long arrow* in **C**) in this malignant lesion.

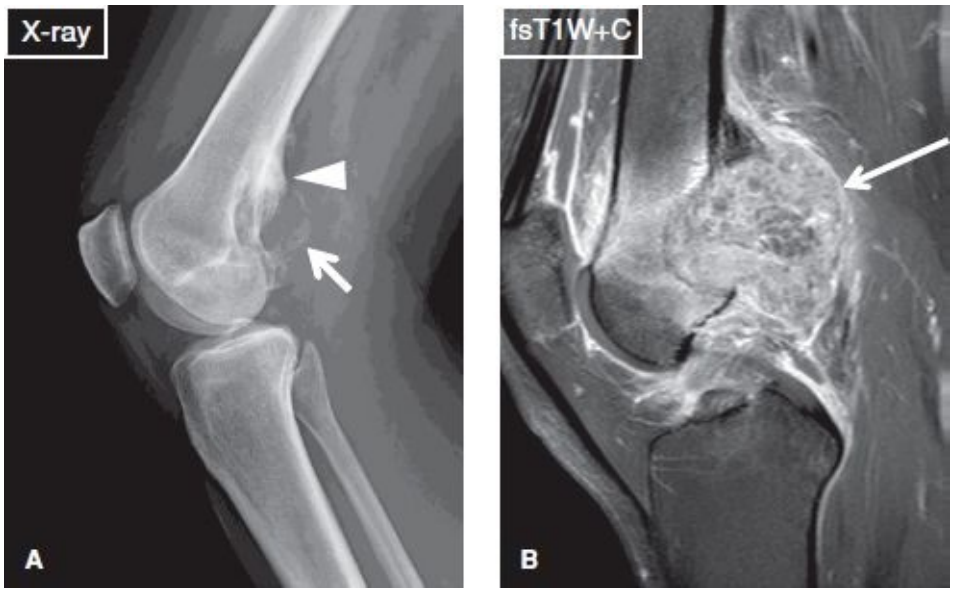

Fig. 164: Periosteal osteosarcoma. **A:** Lateral radiograph exhibits a broad-based soft-tissue lesion at the femoral metaphysis, which shows peripheral mineralization (*arrow*) and Codman triangle (*arrowhead*). **B:** Sagittal MR image demonstrates an aggressive infiltrating enhancing heterogeneous mass (*arrow*), which has intramedullary and extramedullary components and is surrounded by hyperemia of the adjacent marrow and soft tissues.

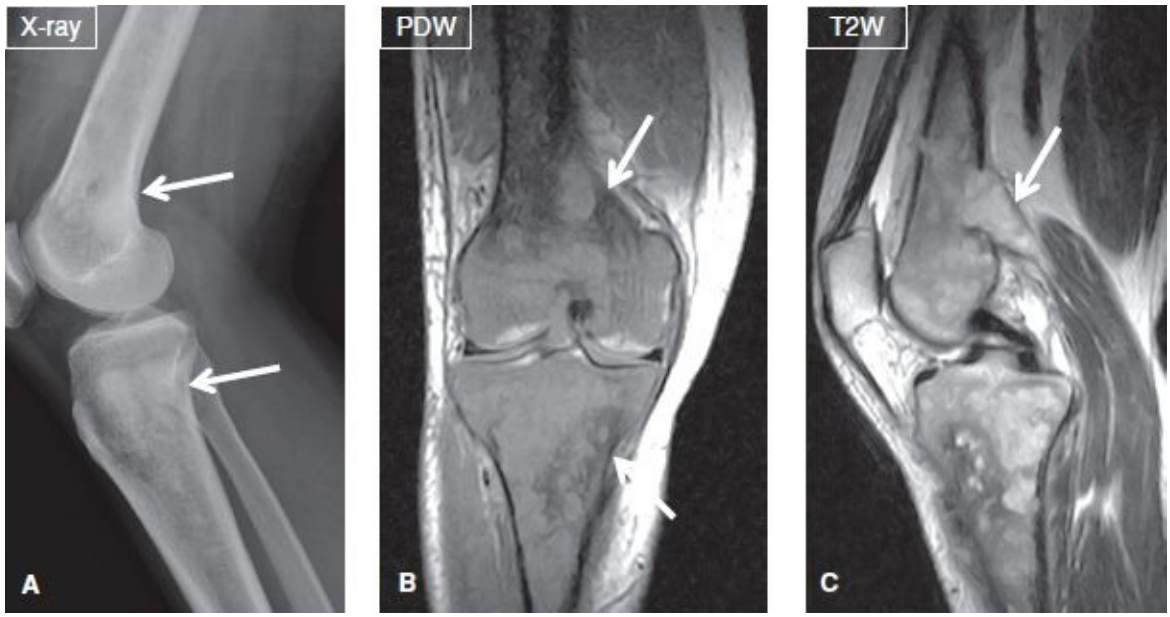

Fig. 165: **A:** Lateral radiograph of knee shows patchy sclerosis of the distal femur and proximal tibia. Coronal **(B)** and sagittal **(C)** MR images show extensive marrow replacement process (*arrows* in **B**). Notice cortical destruction posteriorly with soft tissue mass (*arrow* in **C**). The lesions are indeterminate and may represent metastatic disease, lymphoproliferative disorder, or Erdheim–Chester disease (diagnosis in this case).

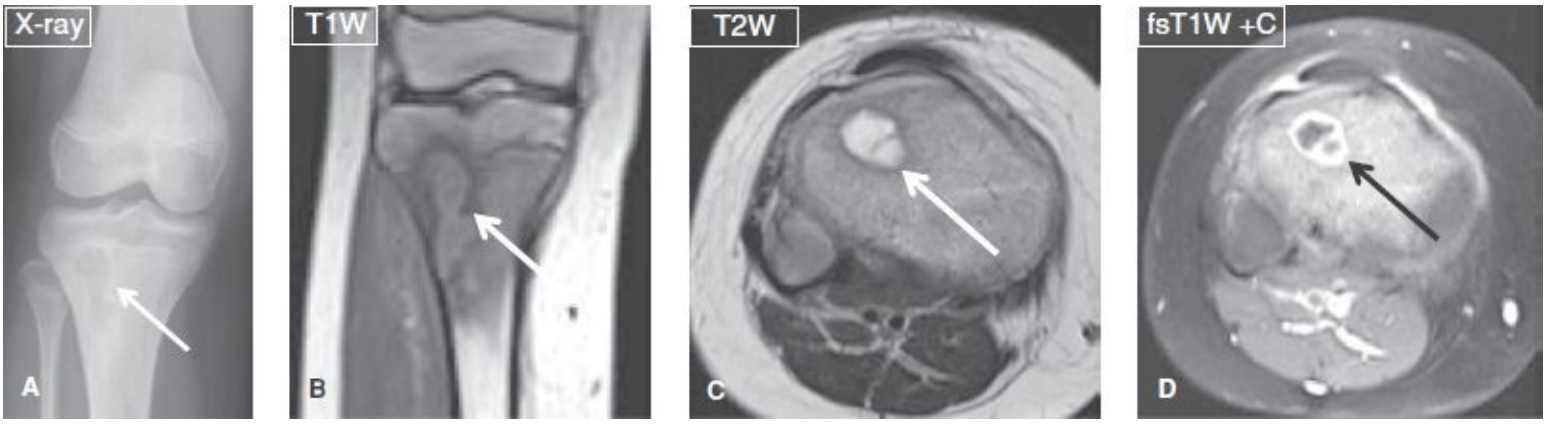

Fig. 166: Brodie abscess. Anteroposterior radiograph **(A)** and coronal **(B)** and axial **(C, D)** MR images show an elongated lesion (*long white and black arrows*) abutting the physeal plate. The lesion has multiple layers and exhibits coalescing daughter lesions (areas of necrosis) constituting a large Brodie abscess in the tibia. Perilesional fascial edema and enhancement is present, findings commonly seen in the setting of infections.

TABLE 4: The classification of Salter–Harris injuries

Injury Type	Features
I	Transverse fracture through the physis, the width of which is increased
II	Fracture through the physis and metaphysis, without involvement of the epiphysis
III	Fracture through the physis and epiphysis
IV	Fracture through the epiphysis, physis, and metaphysis
V	Compression or crush injury of the epiphyseal plate, with no epiphyseal or metaphyseal fracture

MUSCLES: [<Normal>]

The muscles around the knee should be evaluated for possible sprains, infections, myositis, and neoplasms, as well as for evidence of denervation, including edema, fatty infiltration, and atrophy. The muscle signal alterations can be broadly divided in 3 separate categories: a) Diffuse muscle signal change with associated fascial edema (muscle strain, myositis, infection) b) Diffuse muscle signal change with no fascial edema (denervation [limited to nerve distributions], polio, motor neuron disease, Pompe disease, DIabetes mellitus and some myositis [multi-compartment and bilateral disease]) c) Patchy muscle signal change (infection, contusion, strain, tumor and tumor like condition, such as hemangioma). Muscle sprains usually involve fast twitch muscles and muscles that extend across two joints and

these lesions are caused by direct or indirect (eccentric contraction against resistance) injuries. Sprains are graded similar to ligament lesions as grade I (fascicular edema), grade II (partial tear seen as focal intramuscular fluid collection or discontinuity of fibers), and grade III (complete tear) (Fig. 167A). Grade II tears can be further subdivided into low-grade or high-grade partial tears. Generally deeper hematomas resolve slowly or might need aspiration, while superficial hematomas quickly resolve on their own and quite quickly. Myotendinous injuries are usually treated by rehabilitation, whereas tendon avulsions may need re-attachment in professional athletes or if there is >2 cm retraction. Based on their locaton, muscle sprains can also be described as peripheral (myofascial) and central (myotendinous, tendinous, myo-osseus). Myo-osseous tears are usually seen in muscles with a small tendon at the bony attachment, such as the adductor magnus distally, triceps medial head, and pectineus. Central sprains heal slower than peripheral sprains. Apart from central or peripheral locations of involvement, in high-performance athletes, return to play is also determined by the cross-sectional area (CSA) of muscle involvement (<25%, 1 week; 25% to 75%, 1 to 3 weeks; >75%, >3 weeks), as well as the proximal or distal tendon involvement (distal and central lesions being the worse prognostic indicators). Other worse prognostic indicators associated with delayed return to play e.g., in hamstring tendon injuries include degree of tendon retraction (>2 cm), number of tendon involvement (>1 tendon), and surrounding fascial fluid around the neurovascular bundles.

Other causes of muscle injury include compartment syndrome (usually a clinical diagnosis, recent extreme or severe exercise, such as yoga, cycling, etc., bulging fascia, increased intra-compartmental pressures, myonecrosis in later stages of the disease process) and myositis or myopathy, which can be caused by idiopathic, or a variety of genetic, metabolic, and vascular etiologies. While compartment syndrome related muscle edema and swelling are limited to the affected limb compartment, myositis usually involves multiple muscle compartments, can be bilateral, and it may be associated with fascial edema or enhancement. Generally, myopathies are conceptually divided onto four different types: eosinophilic fasciitis or dermatomyositis, which may predominantly affect peripheral myocapsular junction; other myositis, which shows patchy involvement of muscle fibers; inclusion body myositis, which shows inclusion bodies in the muscles fibers; and vasculitis, where arterioles are primarily affected and inflammation spills over to the muscle fibers secondarily. On imaging, one should report the abnormal muscle or fascial findings, which may help the clinician to select the biopsy site and aid in correlation of clinical, histologic, and serology findings to arrive at a particular diagnosis. Generally, muscle denervation changes are in the distribution of a regional nerve, are diffuse, show nerve abnormality proximal to the site of muscle denervation and finally, are not associated with any fascial edematous changes (Fig. 167B).

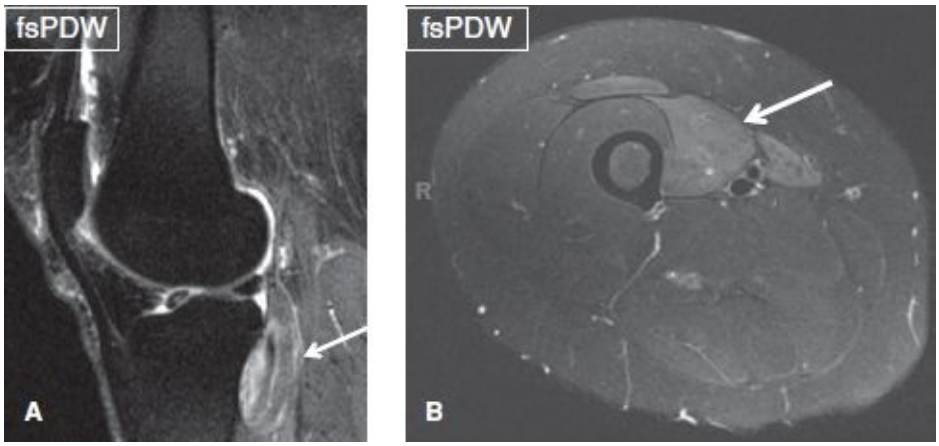

Fig. 167: Grade I muscle strain versus denervation edema like signal. **A:** Diffuse reticular edema in the popliteus muscle with surrounding fascial edema (*arrow*) in keeping with grade I strain. **B:** Diffuse muscle edema-like signal without reticular appearance and lack of fascial edema (*arrow*) in a case of femoral neuropathy.

VESSELS: [<Normal>]

Vascular lesions that are commonly encountered around the knee include vascular malformations, popliteal artery and vein aneurysms, popliteal vein thrombosis, and commonly venous varices in the gastrocnemius muscle and subcutaneous fat (Figs. 168, 169).

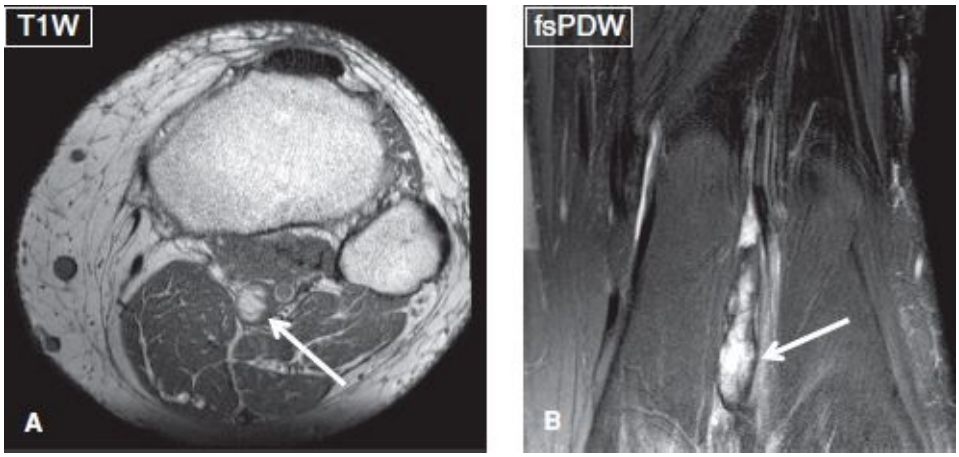

Fig. 168: Popliteal vein thrombosis. On axial **(A)** and coronal **(B)** images, the popliteal vein (*arrows*) is relatively enlarged and shows lack of normal flow void, compatible with acute–subacute thrombosis.

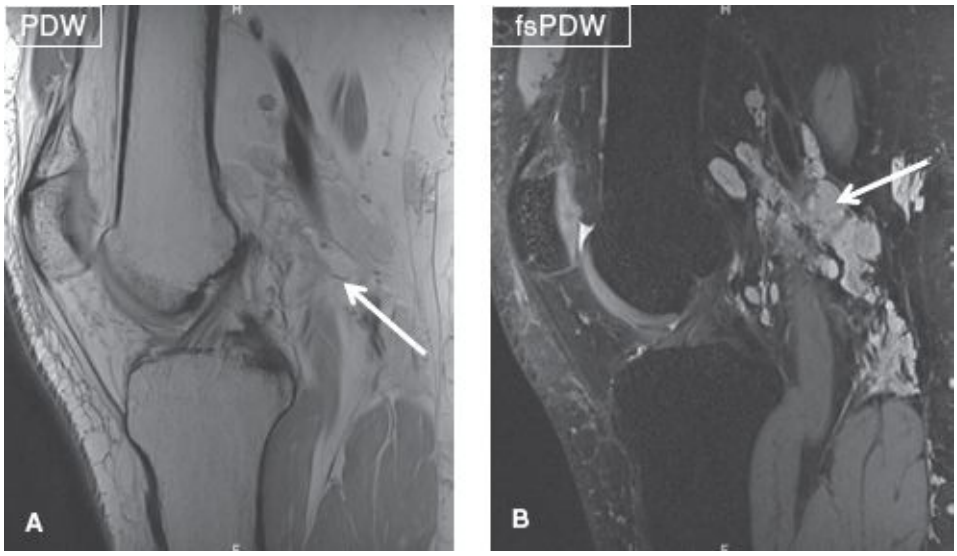

Fig. 169: Venous malformation. Sagittal images **(A, B)** exhibit a large multilobular infiltrative T2 hyperintense lesion (*arrows*) in the popliteal fossa with no flow voids in keeping with a slow flow (venous) malformation.

NERVES: [<Normal>]

The tibial nerve (TN) and the common peroneal nerve (CPN) should be evaluated in terms of size, course, signal intensity, and fascicular morphology. The normal TN is isointense to muscles on all sequences whereas the CPN may show minimally increased T2 signal intensity as it travels obliquely. The signal returns to isointensity, as the nerve lies beneath the deep fascia of the posterior knee and in the region of the peroneal tunnel. The two nerves are prone to direct or penetrating trauma and can be involved by nerve sheath tumor, or compression/involvement by ganglion cyst, large Baker cyst, soft-tissue tumors, osteochondroma and other bony tumors, malunited fracture, post-traumatic hematoma, postsurgical scar, and posterior tibial artery aneurysm. The CPN in particular is subject to entrapment within the peroneal tunnel. Typically, the entrapped nerve demonstrates T2 hyperintensity at and immediately proximal to the compression site, along with flattening at the site of entrapment, and potentially regional muscle denervation changes (Fig. 170).

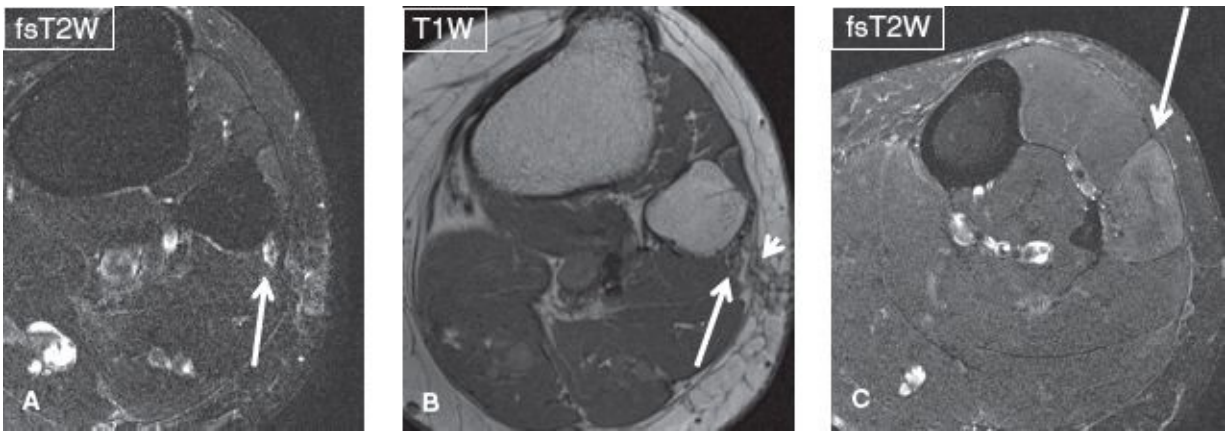

Fig. 170: CPN entrapment. Axial MR images show enlarged CPN proximal to the entrapment at the fibular tunnel (*long arrows* in **A, B**) with thickened fascia of the fibular

tunnel (*short arrow* in **B**). Notice denervation change of the peroneal muscles (*arrow* in **C**).

As elsewhere in the body, peripheral nerve sheath tumors appear as round or ovoid well-defined T2 hyperintense lesions, which demonstrate homogeneous contrast enhancement (Figs. 171, 172). Additional features that aid in the diagnosis of these lesions include the tail-, target-, fascicular and split-fat signs.

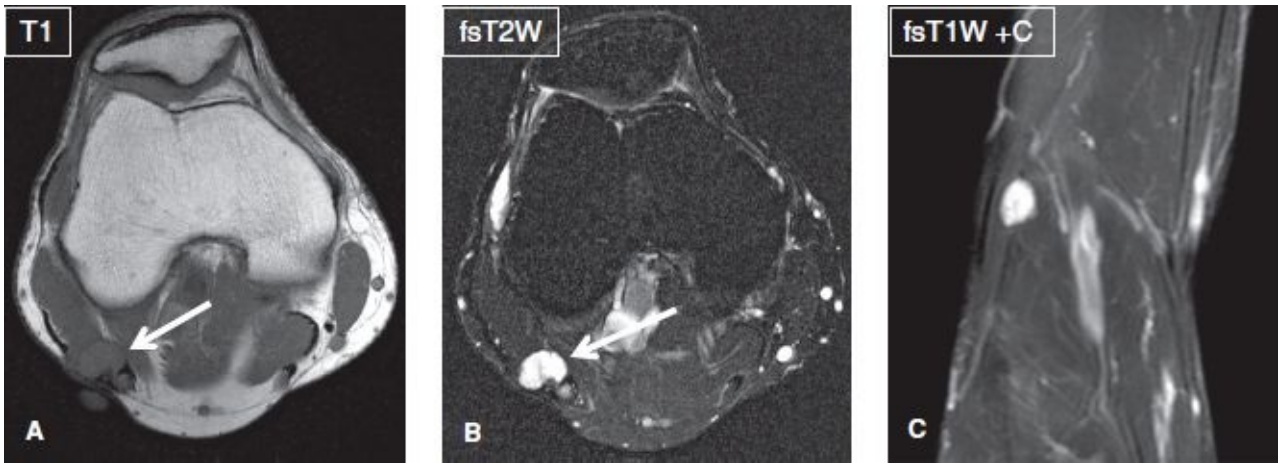

Fig. 171: Peripheral nerve sheath tumor. **A, B:** Axial images show a well-defined T1 isointense and T2 hyperintense ovoid mass lesion involving the common peroneal nerve, which is markedly hyperintense. **C:** On the postcontrast sagittal image, the lesion enhances homogeneously.

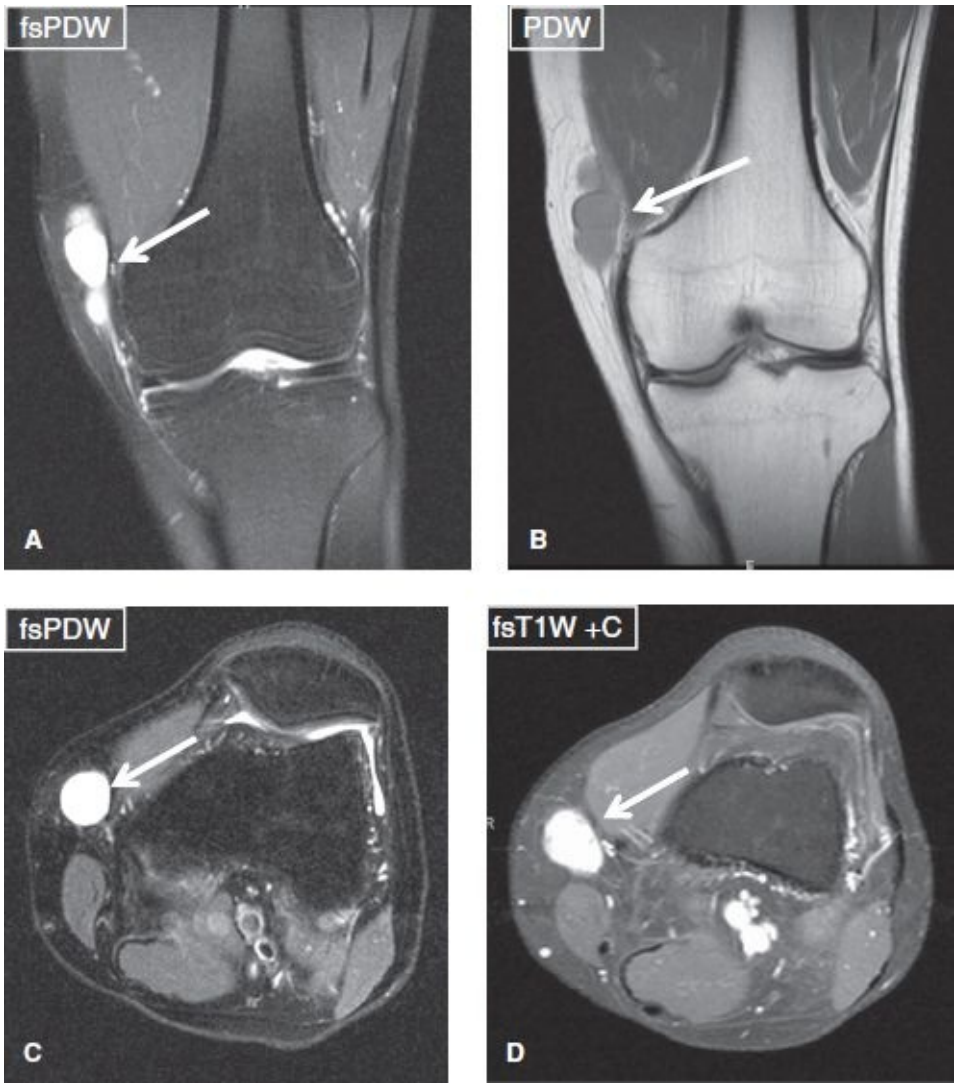

Fig. 172: Peripheral nerve sheath tumor. Coronal **(A, B)** and axial **(C)** images show a well-defined T2 hyperintense ovoid lesion (*arrows*) at the anatomic location of the saphenous nerve. **D:** On the postcontrast axial image, the lesion enhances homogeneously.

OTHER:

In case of anterior knee contact trauma, fluid commonly accumulates in the prepatellar and/or infrapatellar bursae, which do not communicate with the joint. If the fluid seems to extend beyond the confines of the bursa, possibility of a degloving (Morel-Lavallée) lesion should be entertained (Figs. 173, 174). These lesions occur due to shear injury of the subcutaneous fascial layers and their major complication is a non-resolving swelling or overlying skin induration/necrosis due to the persistent hemo-lymphatic collection for prolonged periods of time. Subcutaneous fat interposition is commonly seen in subacute/chronic lesions of such nature aiding in their differentiation form other lesions. None, peripheral or septal enhancement is seen after contrast administration. Ganglion cysts are typically located adjacent to ligaments, tendons, and joint capsule, and represent accumulation of synovial fluid through a ball-valve mechanism. They commonly arise from the gastrocnemius sub-tendinous bursae, especially with increasing age and worsening severity of the internal derangement (Fig. 175). When visible, the communicating pedicle or

neck with the adjacent synovial space should be reported. Popliteal lymph nodes are commonly encountered in the popliteal fossa, and unless abnormally enlarged (short axis diameter >1 cm), they need not be interpreted as pathologic (Fig. 176). Other benign fluid collections around the knee include anteriorly located prepatellar bursitis, superficial and deep infrapatellar bursitis on either side of the distal aspect of the patellar tendon, TCL-semimembranosus bursitis (posteromedial at the joint line), pes anserinus bursitis (anteromedial knee at the level of the tibia under Sartorius, gracilis, and semitendinosus) and finally, popliteofibular bursitis (Figs. 177–179). Any other T2 bright lesion mimicking a collection around the knee should be closely interrogated, since it will likely need intravenous contrast to exclude soft tissue sarcoma. The latter shows central or nodular enhancement in most cases.

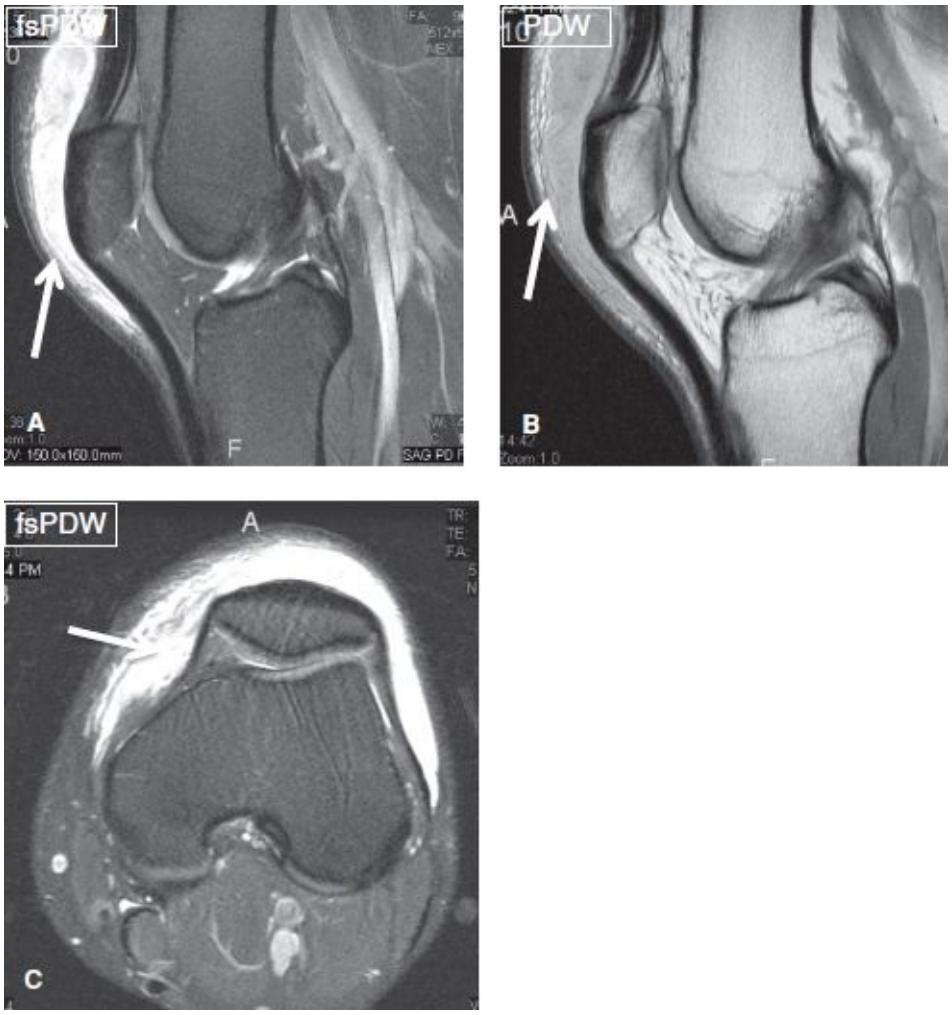

Fig. 173: Acute–subacute degloving lesion. Sagittal **(A, B)** and axial **(C)** images demonstrate a complex hemorrhagic large fluid collection (*arrows*) extending beyond the confines of the prepatellar bursa with surrounding fascial edema.

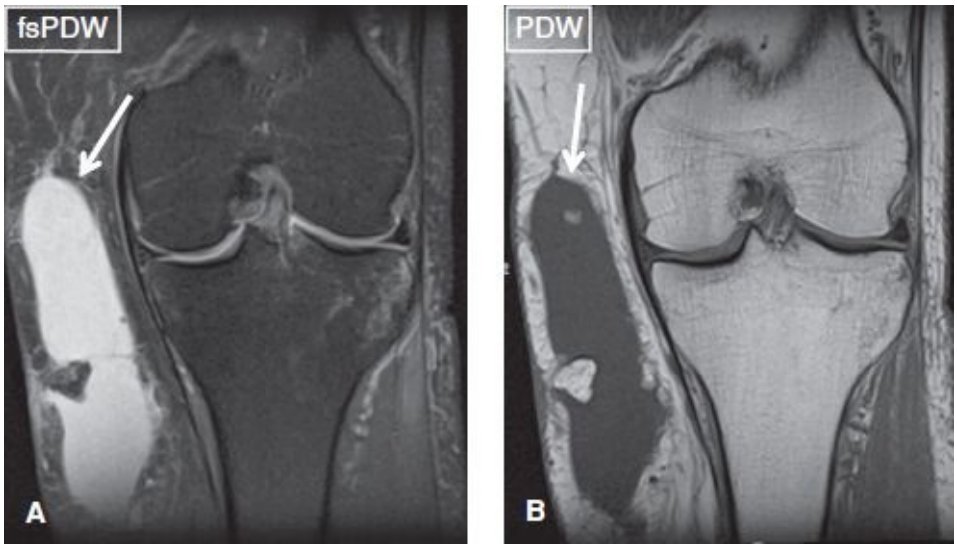

Fig. 174: Subacute–chronic degloving injury on coronal images **(A, B)**. An elongated fluid collection (*arrows*) is evident in the subcutaneous soft tissues, which features well-defined borders and tapering margins. Notice fat interposition in the lesion that can be commonly seen with more chronic lesions.

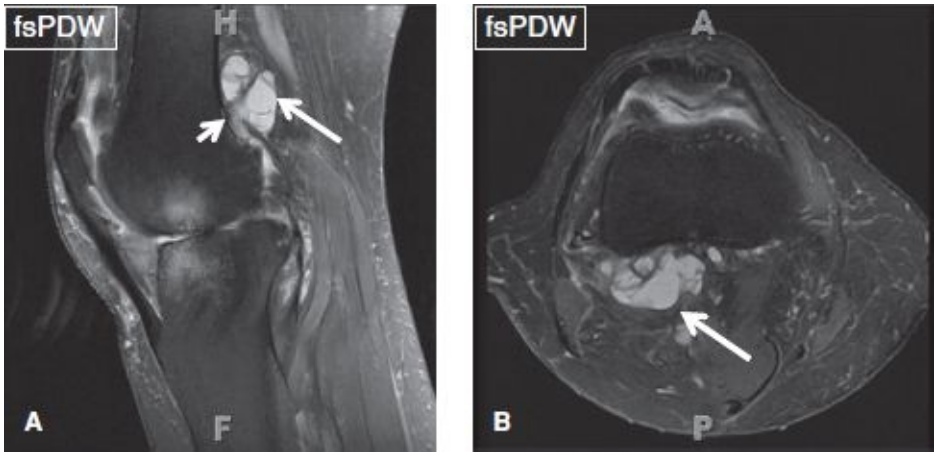

Fig. 175: Ganglion cyst from the gastrocnemius sub-tendinous bursa. Sagittal **(A)** and axial **(B)** images exhibit a multi-loculated cystic lesion (*long arrows*), which features intra- and extra-articular components, crossing through a small opening (*short arrow*) of the posterior superior recess of the joint capsule adjacent to the lateral head gastrocnemius subtendinous bursa.

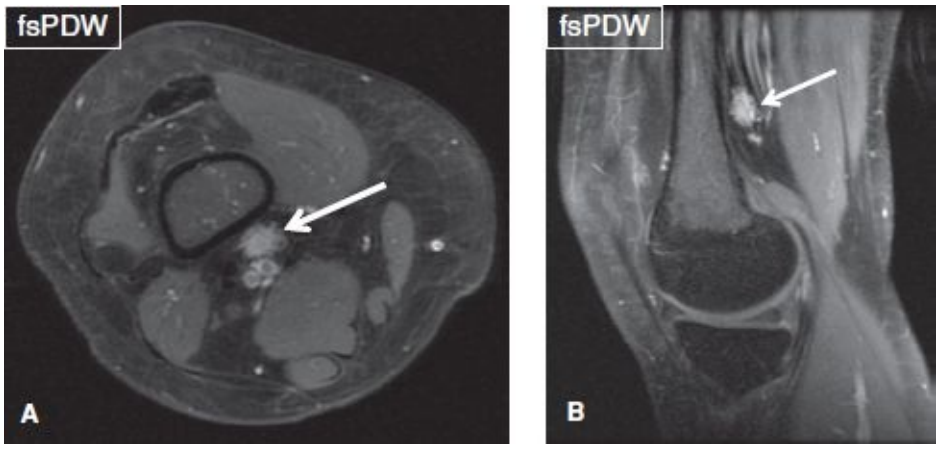

Fig. 176: Popliteal lymph node. Axial **(A)** and sagittal **(B)** images display an ovoid lesion (*arrows*) in the popliteal fossa, with irregular margins and minimal internal fat in keeping with a small reactive lymph node.

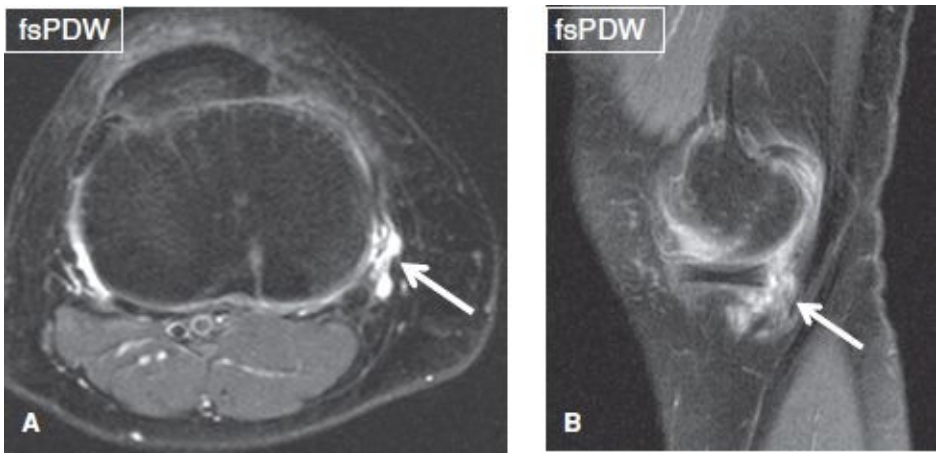

Fig. 177: TCL-semimembranosus bursitis. Axial images **(A, B)** show a horseshoe-shaped collection at the joint line extending posteriorly under the semimembranosus tendon in keeping with a TCL-semimembranosus bursitis.

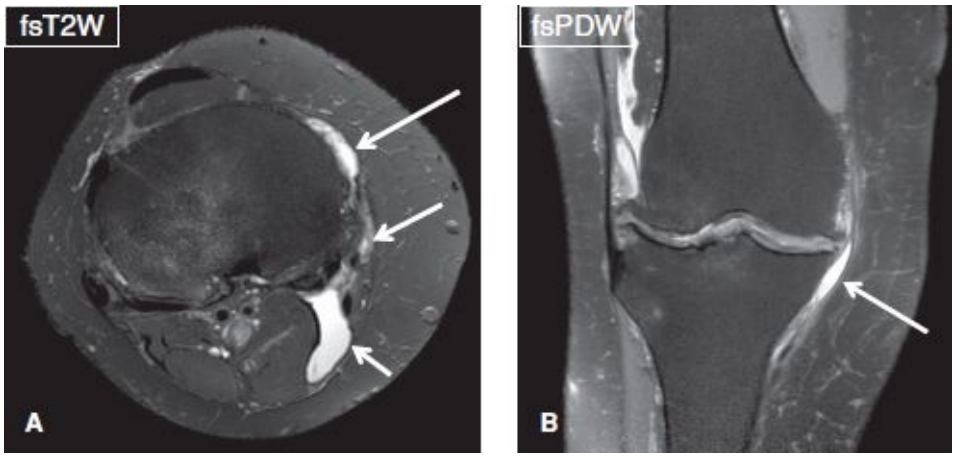

Fig. 178: Multiple bursitis. Axial **(A)** and coronal **(B)** images show multiple fluid collections, a small fluid collection anteriorly (pes anserinus bursitis; *long arrows*), minimal distention of the TCL-semimembranosus bursa (*medium arrow*), and small Baker cyst (*short arrow*). These are not uncommonly encountered in the setting of meniscal tears or in chronically deranged knees, where a parameniscal cyst fills multiple adjacent knee bursae.

Fig. 179: Popliteofibular bursitis. Sagittal MR image shows moderate distention of the popliteofibular bursa with minimal leaking. These should be differentiated from proximal tibiofibular effusion and associated ganglion cysts.

POSTOPERATIVE KNEE

Imaging features indicating prior arthroscopy include a) a linear area of low signal intensity in Hoffa's fat pad, representing the footprint of the arthroscopic cannula b) a rounded low signal on each side of the patellar tendon, corresponding to the scope scar c) intra-articular susceptibility artifacts from metallic hardware or microscopic metallic fragments.

Meniscal tears can be treated surgically or by non-operative means. Non-operative management is dictated by patient's lack of significant symptoms, stable small tears as described above or degenerative tears with osteoarthritis, such as horizontal tears, free edge fraying, and truncation. In symptomatic subjects, the free edge lesions are debrided while flaps are resected or repaired. Lesions in the Zones 1 and 2, such as longitudinal or bucket-handle tears, may be repaired. Partial meniscectomy is performed in symptomatic subjects with unstable tears (larger than 1 cm, flaps, complex tears, more than 3 mm of instability on probing), irreparable tears, or in ACL deficient knees. The goals are to debride unstable tissue, balance remaining rim, maintain hoop fibers, and eliminate stress risers. There are three types of repairs, inside-out, outside-in, and all-inside repairs. Vertical suturing is shown to perform better than the horizontal suturing. Inside-out repair is the gold standard and it is performed for posterior tears, from the level of the collateral ligaments to the gastrocnemius origin. This kind of repair may cause injury to the saphenous or common peroneal nerves. Outside-in repair is performed for more anterior and middle tears and is relatively difficult for posterior tears. Although the risk of nerve injury is less with these, articular cartilage can sustain damage during the repair. All-inside repair requires no

posterior incision and is also considered to be safer. Bioabsorbable meniscal implants are also available currently; however, there are efficacy concerns and reports of implant failure, breakage, migration, chondral injury, and saphenous nerve irritation. Meniscus repair has a success rate of 80% in stable knees and more than 90% in conjunction with ACL reconstruction. In unstable knees, the success rate of meniscus repair can go down to 30% to 70%.

Menisci that have undergone surgical repair appear truncated on MR images (provided that greater than 25% of their substance was resected), and display mildly irregular margins and/or cleft at the area of the previous tear (Figs. 180, 181, 182). Due to bony overload, subchondral insufficiency fractures may develop postoperatively similar to the native meniscal tears. Criteria for diagnosing meniscus re-tear include, high signal intensity joint fluid imbibed into the meniscus, a displaced meniscal fragment, a new tear in a different location, and new irregularity of meniscal edges. These days, meniscus debridements are more commonly performed than repair as the latter is more complicated, may lead to more morbidity, and lesser number of patients are eligible for repair. One can perform MR arthrogram (MRA) but false-negatives can also occur with MRA, since the fluid may not imbibe into the tear due to partial healing and interspersed fibrous tissue. In most circumstances, non–MRA images are sufficiently diagnostic when using high resolution imaging.

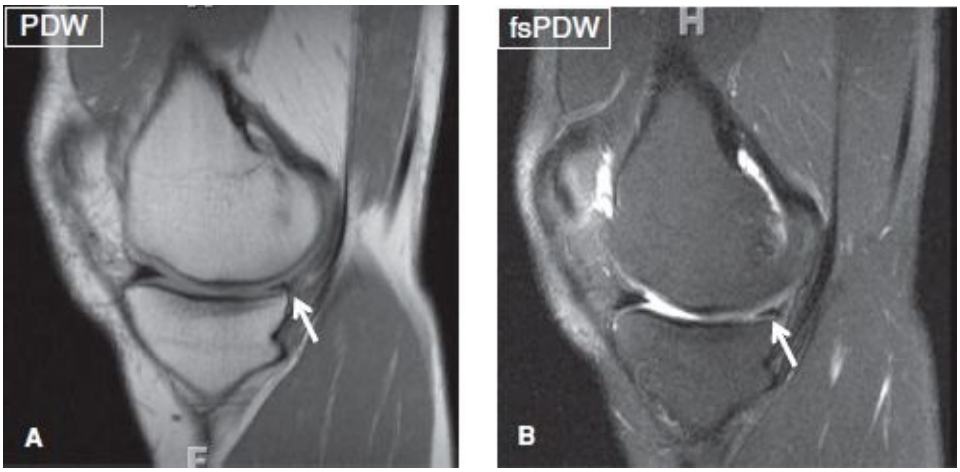

Fig. 180: Partial meniscectomy. On sagittal images **(A, B)**, the posterior horn of the lateral meniscus (*arrows*) appears small; however, it maintains its triangular shape. There is no evidence of recurrent tear.

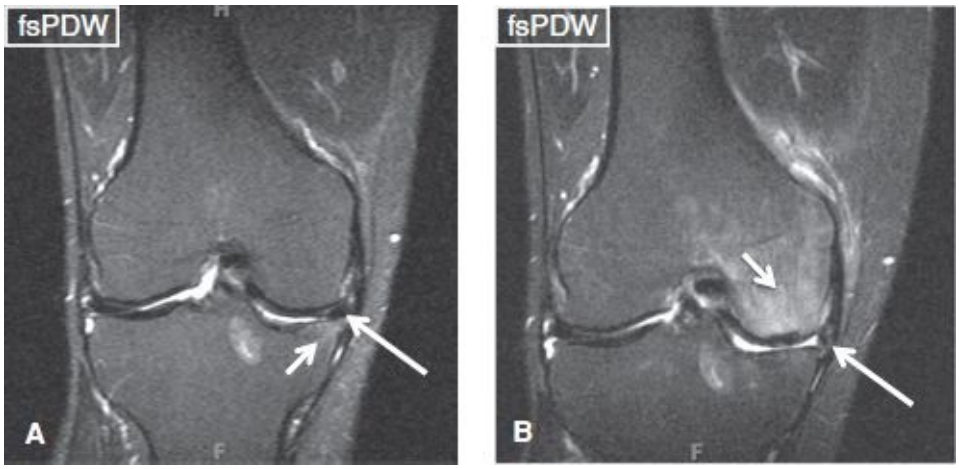

Fig. 181: Partial meniscectomy. Coronal images. **A:** There is an incomplete radial tear (*long arrow*) of the body of the medial meniscus, which was debrided. Notice mild stress reaction of the ipsilateral tibial condyle (*short arrow*). **B:** On postoperative follow-up examination, the body of the medial meniscus (*long arrow*) appears truncated from interval partial meniscectomy. Also note a new subchondral insufficiency fracture (*short arrow*) of the ipsilateral femoral condyle from bony overload.

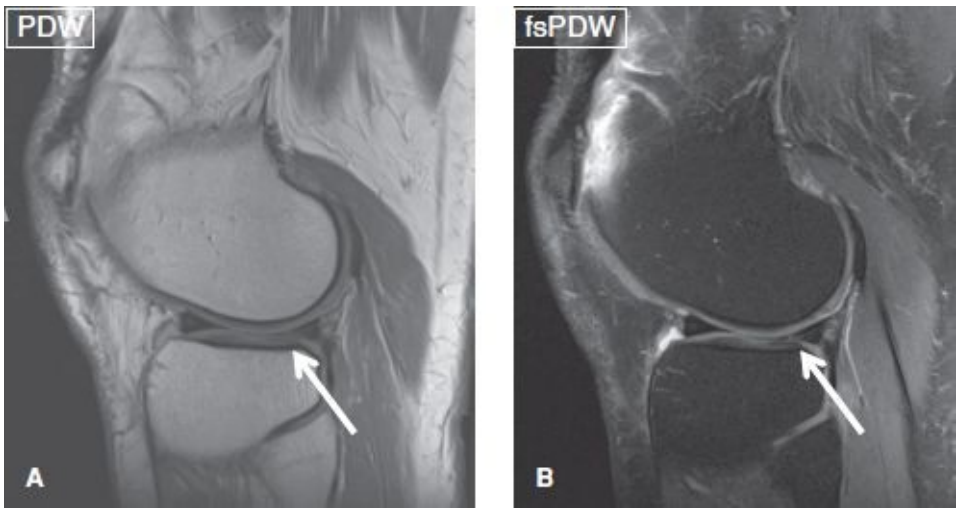

Fig. 182: Postrepair evaluation of the lateral meniscus. Sagittal images **(A, B)** show mild undersurface irregularity of the posterior horn of the medial meniscus (*arrows*) related to prior repair. Notice there is no fluid cleft to suggest re-tear.

Meniscus allografts are also being used; however, there might be up to 50% failure rate of this surgery. The indications include young (<50 years) with pain, s/p total meniscectomy and, stable, grade 3, or less chondral damage. Contraindications include uncorrected extremity malalignment, instability, significant chondral change. On imaging, these should show native meniscus like morphology with anterior horn, body, and posterior horn. In author's experience, various types of tears as described above can also be seen with these allografts, including flap and bucket-handle tears (Fig. 183).

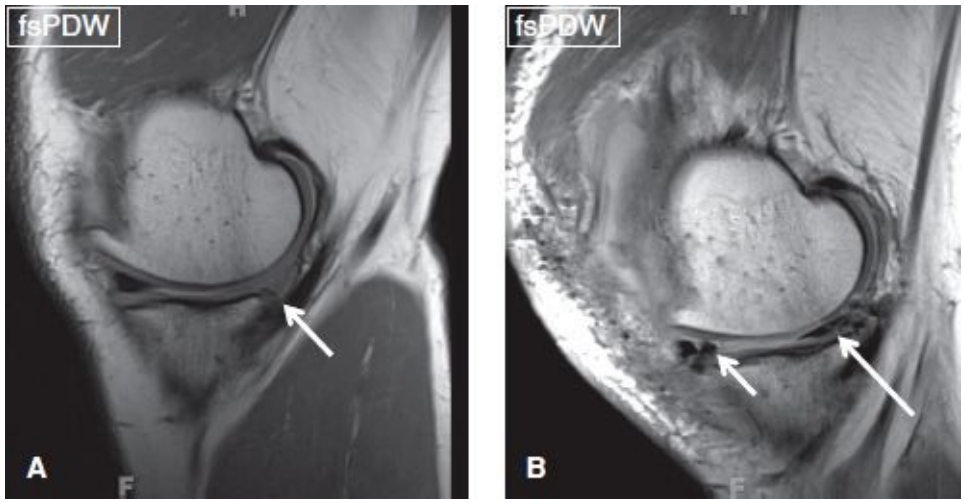

Fig. 183: Re-tear of meniscal allograft. Sagittal images. Notice absent posterior horn (*arrow* in **A**) with displaced meniscal fragment anteriorly (*short arrow* in **B**) and undersurface tears of the remaining posterior horn (*long arrow* in **B**) in keeping with a bucket-handle meniscal tear.

ACL reconstruction should be delayed for 2 to 4 weeks for the hemorrhagic synovitis to resolve and range of motion to return. Otherwise stiffness may occur post-operatively, which is a disturbing complication. The reconstruction can be performed using allograft, bone–patellar–tendon bone graft or hamstring graft. There is no superiority shown with any particular graft. However, double bundle reconstruction is considered to be a better stabilizing procedure. In cases of ACL reconstruction, imaging features to evaluate include the following:

- The ACL graft itself, which should normally be continuous and feature low or intermediate signal on fluid-sensitive images (Figs. 184, 185). The hamstring grafts may show thicker layered appearance, a normal finding. In complete tears, there is absence of intact graft fibers and increased signal intensity similar to that of fluid within the expected region of the graft (Fig. 186). In chronic deficiency of the graft, no fibers are seen and fat fills the ACL fossa (Fig. 187). In partial ACL graft tears, areas of increased signal intensity affect a portion of the graft, which otherwise maintains some intact fibers.

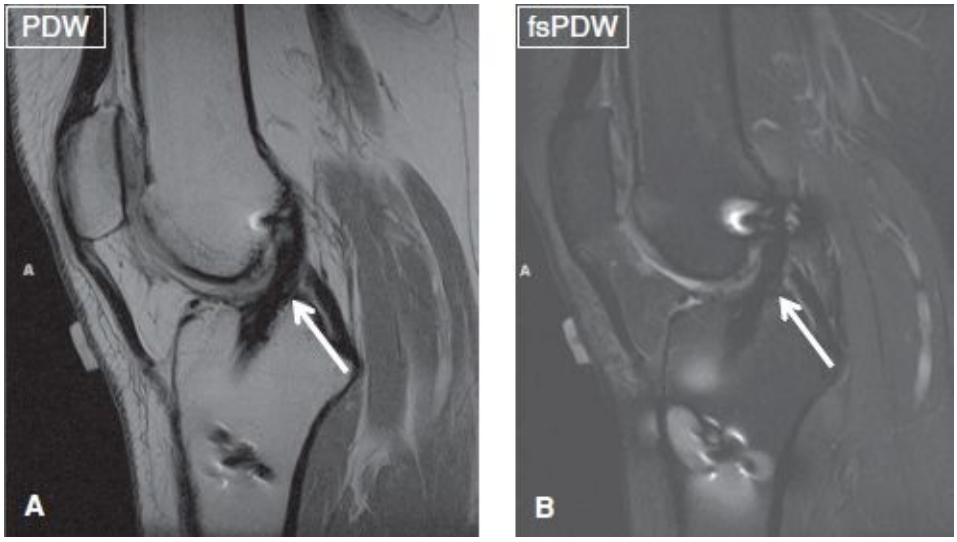

Fig. 184: Anterior cruciate ligament reconstruction. Sagittal images **(A, B)** demonstrate a normally positioned intact graft (*arrows*).

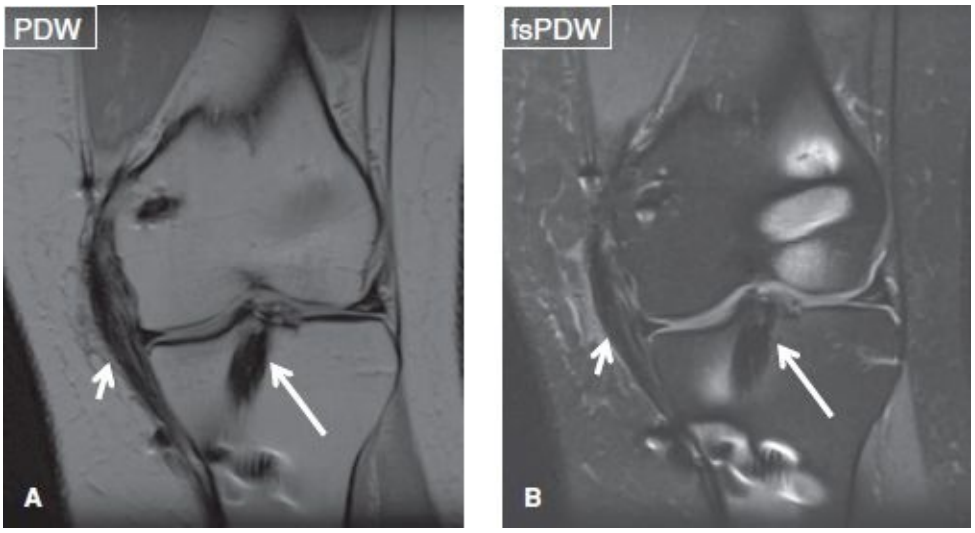

Fig. 185: Anterior cruciate and medial collateral ligaments reconstruction. Coronal images **(A, B)** exhibit anatomic continuity of the anterior cruciate (*long arrows*) and medial collateral (*short arrows*) ligament grafts. Mild to moderate thickening of the graft is a common asymptomatic finding of no consequence as long as there is no gap in the ligament. ACL signal alterations also evolve from intermediate signal to hypointensity with time and graft maturity. It might take 1.6 years post-operatively for the graft to return to uniformly dark signal.

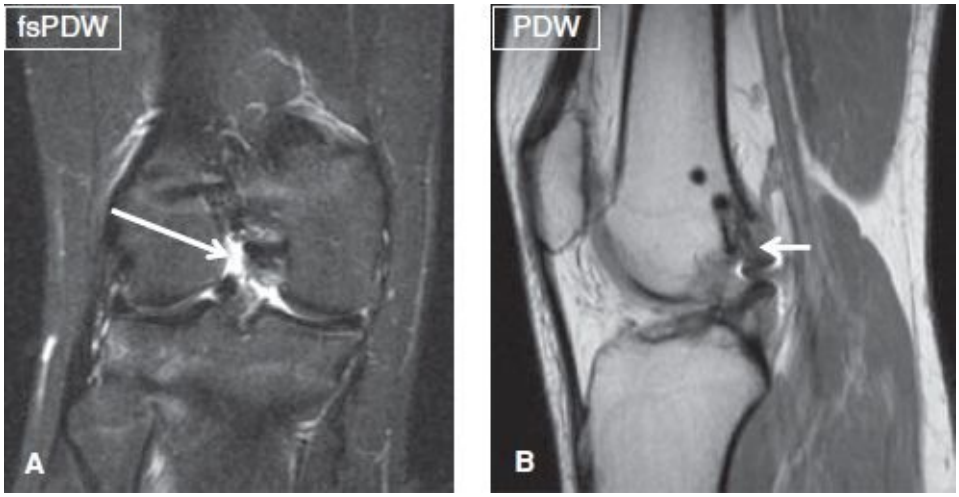

Fig. 186: Anterior cruciate ligament graft disruption. Sagittal **(A)** and coronal **(B)** images show complete discontinuity (*arrow* in **A**) of the graft with fluid gap and inferiorly retracted interference screw (*arrow* in **B**).

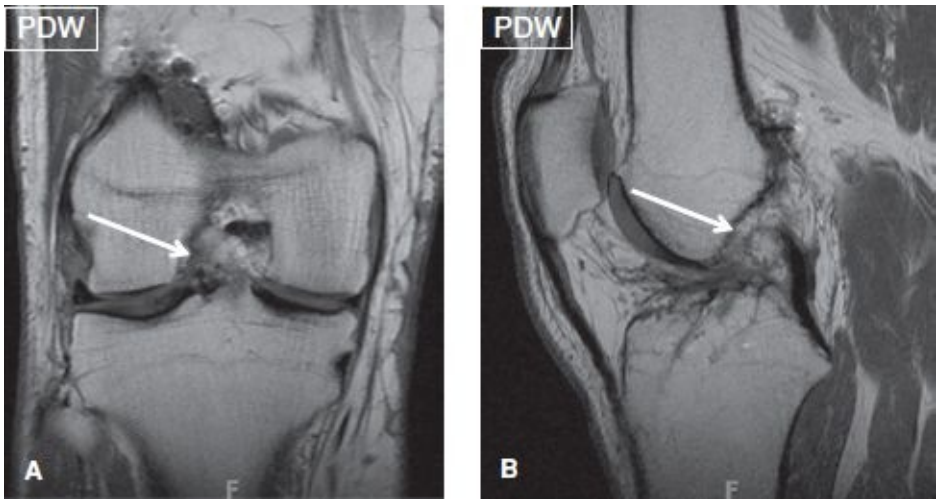

Fig. 187: Chronic anterior cruciate ligament graft deficiency. Coronal **(A)** and sagittal **(B)** images show chronic deficiency (*arrows*) of the graft with empty ACL fossa.

- The position of the femoral tunnel, which should normally be at the intersection of the posterior femoral cortex and the posterior physeal scar, as depicted on sagittal images, and at the 11 o'clock and 1 o'clock positions in the right and left knees, respectively, on coronal images. Along the anterior–posterior axis of the metaphysis adjacent to the physeal scar on the sagittal image, if one divides the scar in four parts, the femoral tunnel should be in the posterior one-fourth of the metaphysis. The femoral tunnel positioning is important for isometry and if the femoral tunnel is too anteriorly placed, it reduces flexion and may lead to graft failure.
- The position of the tibial tunnel, which should be parallel but posterior to the slope of the intercondylar roof on sagittal images and should open to the intercondylar eminence on coronal MR images. Similar to the femoral tunnel positioning, if the tibial plateau is divided into four parts, the tibial tunnel should be in the second part from the anterior tibial border. If the tunnel is in the first part, it would be located too anteriorly. The latter may lead to roof impingement, in which the graft contacts the intercondylar roof, reduces extension and may lead to mucoid degeneration and eventual graft failure. On imaging, the graft appears to be draped over the anterior inferior edge of the intercondylar roof or be posteriorly bowed (Fig. 188). A tibial tunnel located too posteriorly, that is, in the fourth part, may lead to graft laxity and joint instability (Fig. 189). Technical shortcomings resulting in ACL graft failure, thus, include, nonanatomical tunnel placement, graft impingement, improper tensioning of the graft, and inadequate fixation of the graft in the osseous tunnels. Anterior placement of the femoral tunnel is the most common surgical error when a one-incision endoscopic technique is used.

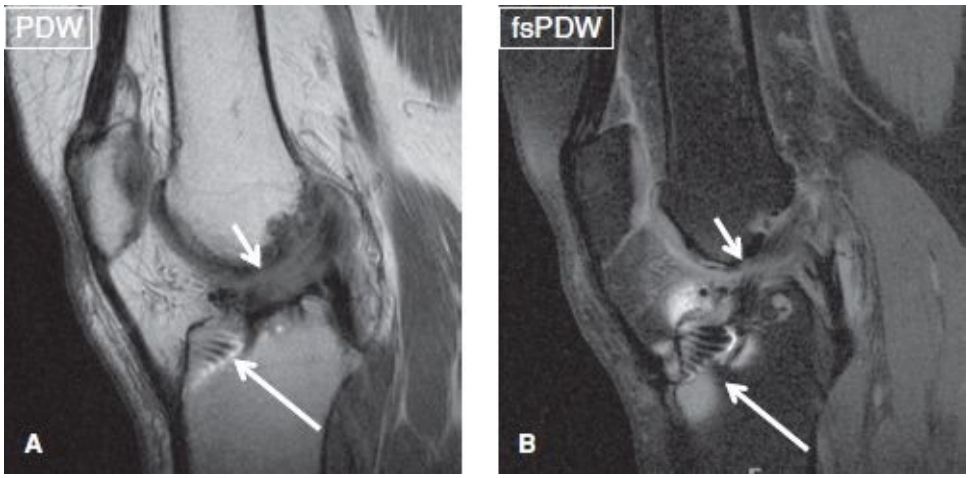

Fig. 188: Anterior cruciate ligament graft roof impingement. Sagittal images **(A, B)** demonstrate a tibial tunnel located too anteriorly (*long arrows*), with the graft (*short arrows*) appearing draped over the anterior inferior edge of the intercondylar roof. Notice degenerative mucoid signal in the graft.

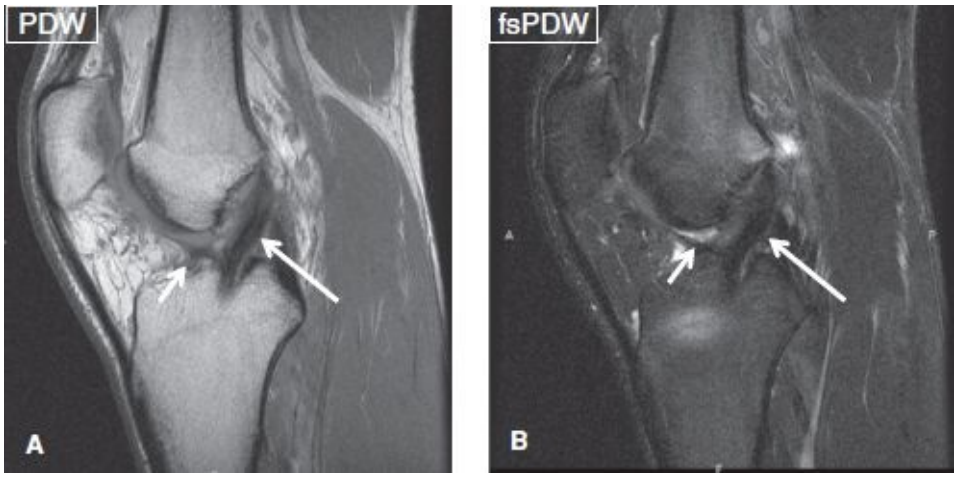

Fig. 189: Anterior cruciate ligament graft laxity. Sagittal images **(A, B)** display a tibial tunnel located too posteriorly, along with a wavy configuration of the graft (*long arrows*), indicating mild laxity. Intermediate signal anterior and surrounding the graft corresponds to small amount of arthrofibrosis (*short arrows*).

- Localized anterior arthrofibrosis, aka “cyclops lesion,” is seen anterior to or attached to the distal portion of the ACL graft, and appears as a focal nodular mass like lesion of low signal on T1W images and heterogeneous signal on T2W images with/without cystic changes from synovitis and granulation tissue intermingled with fibrous tissue (Fig. 190). The cyclops lesion can cause inability to fully extend the knee (knee locking at terminal extension) or pain at extension. Small areas of arthrofibrosis anterior or around the graft are not uncommon and may not be symptomatic (Fig. 189). Also note that cyclops lesions may occur without ACL surgery as well.

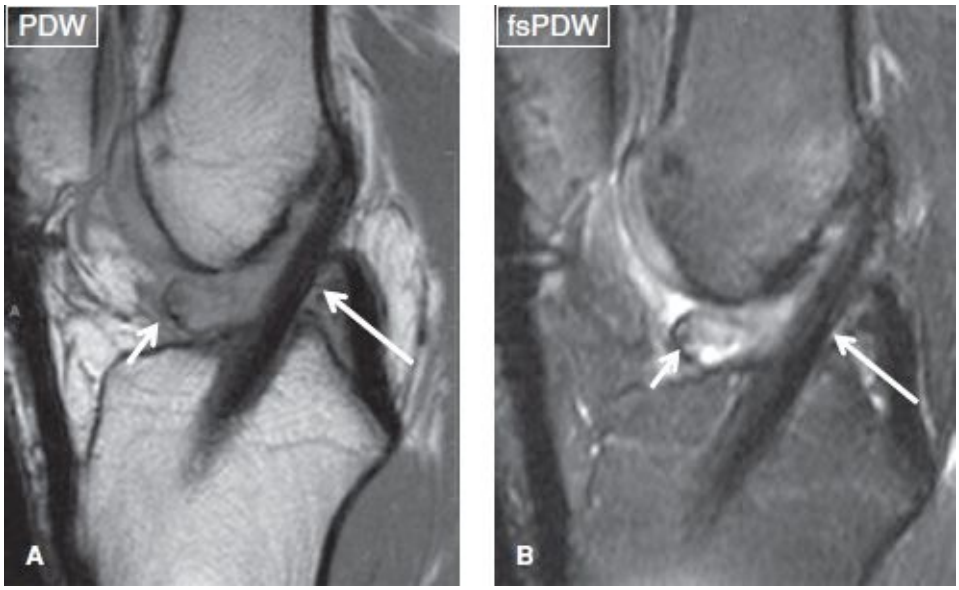

Fig. 190: Cyclops lesion. Sagittal images **(A, B)** show an ovoid lesion (*short arrows*) anterior to an intact anterior cruciate ligament graft (*long arrows*) in keeping a cyclops lesion.

- ACL graft ganglia, refer to cyst formation in the graft substance, tunnel or outside the tunnel, which can cause pain and mechanical symptoms (Fig. 191). Small amounts of fluid along the course of a graft can be normal, particularly within the tibial tunnel; however, symptomatic graft ganglia are typically large and may cause expansion of the osseous tunnels, disruption of the ACL graft, and even bone destruction with associated mass like subcutaneous swelling. These may be associated with bony productive change in the intercondylar notch reflecting instability and graft impingement.

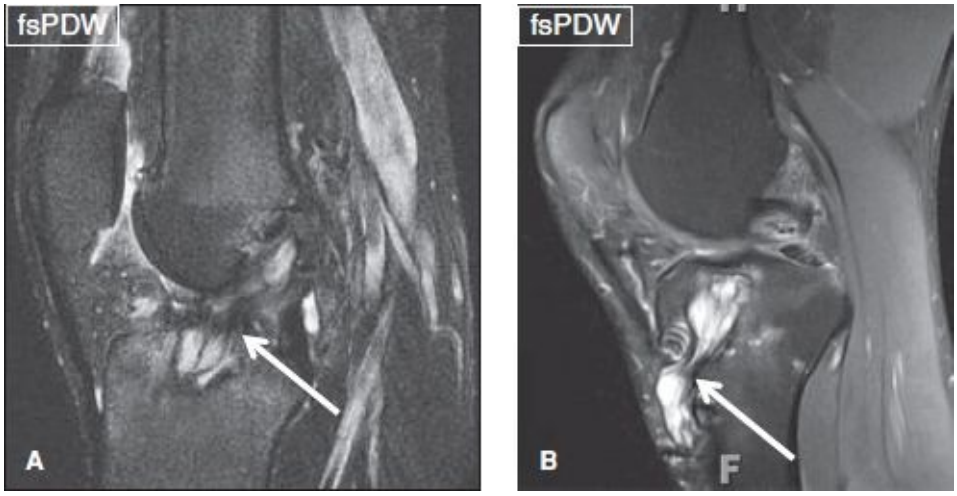

Fig. 191: Ganglion cysts of anterior cruciate ligament graft. Sagittal images **(A, B)** from two different cases exhibit mucoid degeneration with ganglion formation of the ACL grafts (*long arrows*). Notice soft tissue ganglion protruding out of the tibial tunnel mimicking a soft tissue mass lesion (*arrow* in **B**).

- Hardware failure or migration, which can lead to mechanical symptoms, graft insufficiency, or damage to other knee structures due to the displaced hardware (Fig. 186).

- Signs of infection, such as extensive fascial edema, persistent bone marrow edema, sinus tract, tunnel destruction or erosions, complex effusion, clinical signs of toxemia, etc. (Fig. 192).

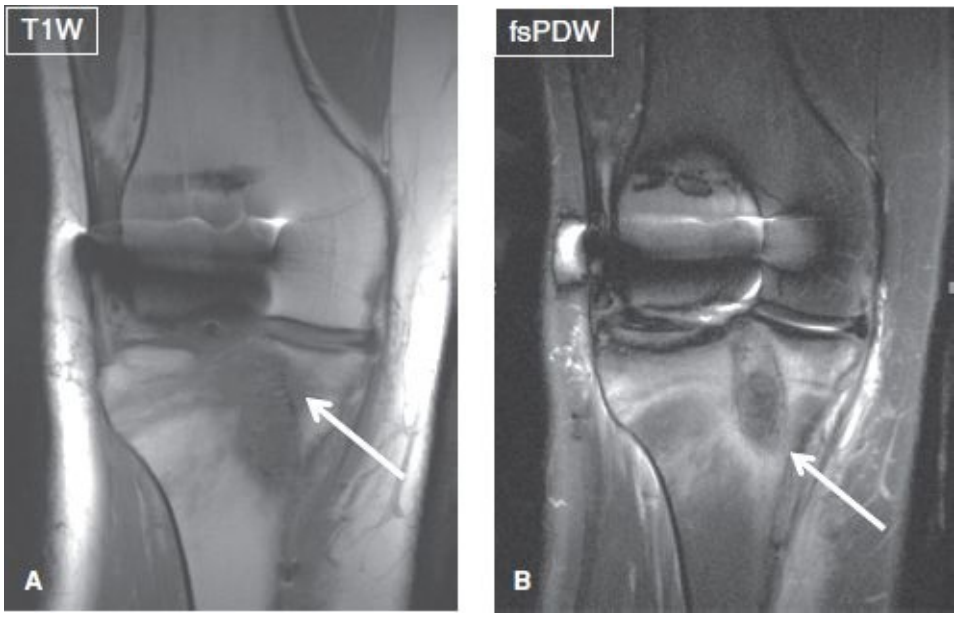

Fig. 192: Postanterior cruciate ligament reconstruction infection. Coronal images **(A, B)** show areas of T1 hypointensity/T2 hyperintensity in the tibial epiphysis and metaphysis surrounding the tibial tunnel with erosion of the inferior cortical margin of the tibial tunnel (loss of normal hypointensity; *arrows*), in keeping with osteomyelitis. Notice surrounding marked fascial edema.

- Particle disease, which was common with older Dacron grafts and is now uncommon with bone—tendon–bone allografts (Fig. 193).

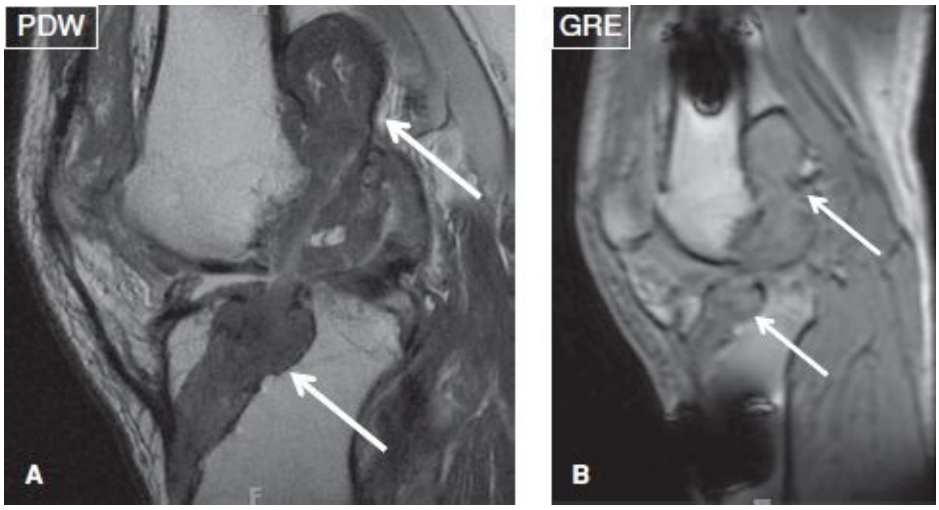

Fig. 193: Particle disease. Sagittal images show large amount of intermediate signal tissue along the expected course of the previously placed Dacron-based ACL graft (*arrows*) in keeping with particle disease. Notice no appreciable signal loss on gradient echo image excluding the possibility of PVNS, which would be in the differential diagnosis.

The operative reconstruction of the anterior cruciate and non-operative healing of the medial collateral ligament offers similar results to the approach if one were to operate on both ACL and MCL, with regards to valgus instability. Reconstruction of the ACL, a secondary valgus stabilizer, done in a timely manner will increase the quality of healing of the medial collateral ligament. The concern is the timing of repair of the ACL. ACL reconstruction performed within 2 to 4 weeks after injury increases the risk of post-operative stiffness. Waiting for full, pain-free motion will lessen the risk of arthrofibrosis and still afford healing of the medial collateral ligament.

Isolated PCL injuries are managed nonoperatively with quadriceps strengthening and relative rest for 4 to 6 weeks. Grade III injuries may be repaired or reconstructed in young athletes. Restoring quadriceps strength is essential in such cases; however, there is shown to be increased incidence of medial and patellofemoral arthrosis over time with nonoperative management. Surgical intervention should be reserved for those who fail conservative treatment, and patients with combined ligamentous injuries (PCL plus MCL, PCL plus LCL, PCL plus PL corner injury, three or more ligament injuries, that is, knee dislocation cases, or those with multidirectional instability). Hamstring strengthening should be delayed in patients undergoing PCL reconstruction, since the pull of the hamstrings is also posterior. Therefore, most surgeons place knee in extension for 6 weeks postoperatively.

Timing of ligament repair is controversial. However, most people advocate immediate repair within 2 to 3 weeks if one encounters disruptions of ACL plus PCL plus LCL; PCL plus LCL; ACL plus PCL plus MCL (grade III injuries/distal tears); and PCL plus MCL (grade III injuries/distal tears). The surgery is commonly delayed, if there is disruption ACL plus PCL (intact collaterals) or ACL plus PCL plus grade I–II MCL (where PCL is intact).

PL corner injury can be repaired if less than 3 weeks out of injury while reconstruction is a better option if more than 3 weeks have passed, since, otherwise it becomes difficult to identify the various structures in the PL corner due to scarring. Reconstruction using allografts is a better choice in severe injuries and significant PL instability. The common peroneal nerve should be carefully isolated during the repair of those injuries. For chronic PL corner and LCL injuries, if there is significant varus deformity, the varus malalignment should be corrected first with osteotomy and bony reconstruction, and subsequently, the ligament reconstruction should be attempted.

For patellar malalignment, initially rehabilitation is recommended for 3 to 6 months. Following failure of conservative management in patients with recurrent instability, one may attempt to realign patella by doing LPR release or tibial tubercle mobilization. Medial patellofemoral reconstruction is attempted using the semitendinosus or gracilis tendons in situations with no underlying malalignment, patella alta, or trochlear dysplasia. If there is patella alta, distal tibial tubercle transfer is attempted. In excessively lateralized tibial tuberosity (TT-TG distance >2 cm; Q angle >15 degrees in male, and >18 degrees in female), Fulkerson anteromedialization can be performed. In case of abnormal femoral or tibial torsion, correction with derotational osteotomy is performed. Lateral retinacular release will be seen as focal defect in the lateral retinaculum, which may be combined with

medial retinacular plication. One should look for re-tear of retinaculum in reconstructed case, which will be seen as laxity or focal discontinuity of the ligament. Medial patellar subluxation or medial compartment degenerative disease may also develop due to overcorrection.

Knee chondral repair can be performed by a variety of techniques depending on the size of the defect, local skill, and cost involved. MOCART grading should be used to describe these repair sites as discussed in detail in the cartilage chapter. As a generally accepted diagnostic algorithm, for lesions no larger than 1 cm, options include observation, abrasion chondroplasty, microfracture, osteochondral autograft transfer; for lesions 1 to 2 cm, options include abrasion chondroplasty, microfracture, and osteochondral autograft transfer; for lesions 2 to 3.5 cm, options include fresh osteochondral allograft and autologous chondrocyte implant and ACI; but for lesions 3.5 to 10 cm or multiple lesions, the only current good option is ACI.

- Bone marrow stimulation techniques, such as microfracture or abrasion chondroplasty
  - Normal findings
  - Complete filling of the defect with an uninterrupted interface between the repair tissue and the native cartilage
  - Well-defined smooth surface of the repair tissue. Initially, the repair tissue may be slightly thinner than the native cartilage, but this should fill in and become flush with the native cartilage surface over the following 2 years. Signal differences between the repair tissue and the native cartilage are considered to be within normal limits due to expected fibrocartilage formation with these techniques. The subchondral bone often has a thin and more irregular appearance as compared to the adjacent bone, and demonstrates reactive marrow edema, which gradually resolves.
  - Abnormal findings
  - Repair tissue that is persistently thinner compared relative to the native adjacent cartilage for more than 2 years following surgery
  - Incomplete filling of the defect with gaps between the repair tissue and the adjacent native cartilage
  - Significant thinning or surface irregularity of the repair tissue
  - Chondral flaps
  - Progressive thinning on subsequent examinations or progressive widening of the initial chondral defect
  - Bare areas with chondral osteophyte formation, subchondral cystic changes, or increasing edema
- Autologous osteochondral transplants
  - Normal findings
  - A smoothly congruent articular surface in the region of repair (with a cortical bone offset considered normal as long as the cartilaginous surfaces are congruent)
  - A graft signal, which is usually the same as the native cartilage or slightly heterogeneous

- Bone marrow edema and enhancement in the donor and recipient sites, which usually resolves by 12 months postoperatively but may be mildly persistent for up to 2 years
- Abnormal findings
- Step-offs in the interface of the native cartilage and graft
- Degeneration of the chondral surface, depicted as surface irregularity, fissures, and thinning over time
- Graft subsidence, depicted as changes in the step-off of the cortical surface of the graft relative to the native cortex although the graft cartilage may itself maintain its normal thickness and smooth surface
- Graft motion and failure of incorporation, suggested if the marrow signal changes do not diminish to minimal after 9 months following surgery

- Autologous chondrocyte implantation
  - Normal findings include a defect which is completely filled with a smooth transition between the surface contour of the native cartilage and the repair tissue. The transplant tissue is homogeneous in signal at the initial stage and heterogeneous at later stages.
  - Abnormal findings include incomplete filling of the defect, surface irregularity or fissuring, or surface incongruity relative to the native cartilage, a protuberant contour in the region of repair, delamination of the repair tissue, depicted as a linear region of fluid-like T2 hyperintensity between the repair tissue and the underlying bone, chondral osteophytes or increasing bone marrow changes, and finally failure of incorporation at the border zones with the native cartilage.

To conclude, one should compartmentalize and use structured reporting system to evaluate and describe knee anatomy and pathology.

SUGGESTED READINGS

1. Fox MG. MR imaging of the meniscus: Review, current trends, and clinical implications. *Radiol Clin North Am.* 2007;45(6):1033–1053, vii.
2. Balcarek P, Jung K, Frosch KH, et al. Value of the tibial tuberosity-trochlear groove distance in patellar instability in the young athlete. *Am J Sports Med.* 2011;39(8):1756–1761.
3. Diederichs G, Issever AS, Scheffler S. MR imaging of patellar instability: Injury patterns and assessment of risk factors. *Radiographics.* 2010;30(4):961–981.
4. House C, Connell D, Saifuddin A. Posteromedial corner injuries of the knee. *Clin Radiol.* 2007;62(6):539–546.
5. Beaman FD, Peterson JJ. MR imaging of cysts, ganglia, and bursae about the knee. *Magn Reson Imaging Clin N Am.* 2007;15(1):39–52.
6. De Smet AA, Graf BK, del Rio AM. Association of parameniscal cysts with underlying meniscal tears as identified on MRI and arthroscopy. *AJR Am J Roentgenol.* 2011;196(2):180–186.
7. Kijowski R. Clinical cartilage imaging of the knee and hip joints. *AJR Am J Roentgenol.*

2010;195(3):618–628.
8. Vieira RL, Rosenberg ZS, Kiprovski K. MRI of the distal biceps femoris muscle: Normal anatomy, variants, and association with common peroneal entrapment neuropathy. *AJR Am J Roentgenol.* 2007;189(3):549–555.
9. Vinson EN, Major NM, Helms CA. The posterolateral corner of the knee. *AJR Am J Roentgenol.* 2008;190(2):449–458.
10. Hartley KG, Damon BM, Patterson GT, et al. MRI techniques: A review and update for the orthopaedic surgeon. *J Am Acad Orthop Surg.* 2012;20(12):775–787.
11. Saggin PR, Saggin JI, Dejour D. Imaging in patellofemoral instability: An abnormality-based approach. *Sports Med Arthrosc.* 2012;20(3):145–151.
12. Xu L, Hayashi D, Roemer FW, et al. Magnetic resonance imaging of subchondral bone marrow lesions in association with osteoarthritis. *Semin Arthritis Rheum.* 2012;42(2):105–118.
13. Thawait SK, Soldatos T, Thawait GK, et al. High resolution magnetic resonance imaging of the patellar retinaculum: Normal anatomy, common injury patterns, and pathologies. *Skeletal Radiol.* 2012;41(2):137–148.
14. De Maeseneer M, Shahabpour M, Pouders C. MRI spectrum of medial collateral ligament injuries and pitfalls in diagnosis. *JBR-BTR.* 2010;93(2):97–103.
15. Forster BB, Lee JS, Kelly S, et al. Proximal tibiofibular joint: An often-forgotten cause of lateral knee pain. *AJR Am J Roentgenol.* 2007;188(4):W359–W366.
16. Chhabra A, Subhawong TK, Carrino JA. A systematised MRI approach to evaluating the patellofemoral joint. *Skeletal Radiol.* 2011;40(4):375–387.
17. Subhawong TK, Eng J, Carrino JA, et al. Superolateral Hoffa's fat pad edema: Association with patellofemoral maltracking and impingement. *AJR Am J Roentgenol.* 2010;195(6):1367–1373.
18. Wangwinyuvirat M, Dirim B, Pastore D, et al. Prepatellar quadriceps continuation: MRI of cadavers with gross anatomic and histologic correlation. *AJR Am J Roentgenol.* 2009;192(3):W111–W116.
19. Roemer FW, Guermazi A, Zhang Y, et al. hoffa's fat pad: Evaluation on unenhanced MR images as a measure of patellofemoral synovitis in osteoarthritis. *AJR Am J Roentgenol.* 2009;192(6):1696–1700.
20. Guenoun D, Le Corroller T, Amous Z, et al. The contribution of MRI to the diagnosis of traumatic tears of the anterior cruciate ligament. *Diagn Interv Imaging.* 2012;93(5):331–341.
21. Abdelhamid MF, Sandler B, Awad RW. Ischaemic lumbosacral plexopathy following aorto-iliac bypass graft: Case report and review of literature. *Ann R Coll Surg Engl.* 2007;89(5):W12–W13.
22. Recht MP, Kramer J. MR imaging of the postoperative knee: A pictorial essay. *Radiographics.* 2002;22(4):765–774.
23. McCauley TR. MR imaging evaluation of the postoperative knee. *Radiology.* 2005;234(1):53–61.

24. Polster J, Recht M. Postoperative MR evaluation of chondral repair in the knee. *Eur J Radiol.* 2005;54(2):206–213.
25. Choi YS, Potter HG, Chun TJ. MR imaging of cartilage repair in the knee and ankle. *Radiographics.* 2008;28(4):1043–1059.

APPENDIX 1: Sample Completed Structured Report: Knee: NORMAL

EXAMINATION: MRI OF KNEE [<WITH>/<WITHOUT>] CONTRAST

HISTORY: [] year-old <<Patient sex>> with <<Order reason for study>>

TECHNIQUE: Imaging was performed [without IV contrast/before and after IV/after intra-articular contrast]. Multiplanar, multisequence MR images of the [right/left] knee were obtained on a [1.5 or 3] Tesla magnet.

COMPARISON: [<None>]

FINDINGS:

Fluid: [<Normal>]

Medial compartment:

Medial meniscus: [<Normal>]

Medial collateral ligament: [<Normal>]

Medial femoral condyle cartilage: [<Normal>]

Medial tibial plateau cartilage: [<Normal>]

Posteromedial corner:

Semimembranosus tendon: [<Normal>]

Posterior oblique ligament: [<Normal>]

Lateral compartment:

Lateral meniscus: [<Normal>]

Lateral collateral ligament: [<Normal>]

Lateral femoral condyle cartilage: [<Normal>]

Lateral tibial plateau cartilage: [<Normal>]

Posterolateral corner:

Popliteus tendon: [<Normal>]

Popliteofibular ligament: [<Intact>]

Arcuate ligament: [<Intact>]

Proximal tibiofibular joint: [<Normal>]

Anterior compartment:

Alignment: [<Normal>]

Quadriceps tendon: [<Normal>]

Patellar tendon: [<Normal>]

Patellar cartilage: [<Normal>]

Trochlear groove: [<Normal>]

Trochlear cartilage: [<Normal>]

Plica: [<Not thickened>]

Hoffa fat pad: [<Normal>]

TT-TG distance: [_] cm

Intercondylar compartment:

Anterior cruciate ligament: [<Normal>]

Posterior cruciate ligament: [<Normal>]

Bones: [<Otherwise normal>]

Muscles: [<Normal>]

Vessels: [<Normal>]

Nerves: [<Normal>]

Other:

IMPRESSION:

APPENDIX 2: Sample Completed Structured Report: Knee: ABNORMAL

EXAMINATION: MRI OF KNEE WITHOUT CONTRAST

HISTORY: [<25-year-old man with recent soccer injury, pain and swelling>]

TECHNIQUE: Imaging was performed [<without IV contrast>]. Multiplanar, multisequence MR images of the [<right>] knee were obtained on a [<3.0 Tesla magnet>]

COMPARISON: [<Radiographs dated 11/11/2014>]

FINDINGS:

Fluid: [<Moderate effusion with fat-fluid-hemorrhage level>]

Medial compartment:

Medial meniscus: [<Complex tear posterior horn measuring 5 × 7 mm with associated meniscocapsular sprain and fascial edema>]

Medial collateral ligament: [<Grade II sprain>]

Medial femoral condyle cartilage: [<Normal>]

Medial tibial plateau cartilage: [<Normal>]

Posteromedial corner:

Semimembranosus tendon: [<Partial tear pars distalis portion with fascial edema>]

Posterior oblique ligament: [<Intact>]

Lateral compartment:

Lateral meniscus: [<Peripheral incomplete inferior surface vertical tear measuring 3 × 3 mm at the meniscocapsular junction. Tears of the superior and inferior popliteomeniscal fasciculi>]

Lateral collateral ligament: [<Mid substance grade III sprains of iliotibial band and fibular collateral ligament>]

Lateral femoral condyle cartilage: [<Contusion over impaction injury centrally>]

Lateral tibial plateau cartilage: [<Contusion over impaction injury posterior>]

Posterolateral corner:

Popliteus tendon: [<Partial tear at the attachment>]

Popliteofibular ligament: [<Torn with fascial edema>]

Arcuate ligament: [<Torn lateral band with posterolateral fascial edema>]

Proximal tibiofibular joint: [<Normal>]

Anterior compartment:

Alignment: [<Mild patella alta. Lateral patellar tilt exaggerated by effusion>]

Quadriceps tendon: [<Intact>]

Patellar tendon: [<Intact>]

Patellar cartilage: [<Mild chondromalacia lateral facet>]

Trochlear groove: [<Shallow>]

Trochlear cartilage: [<Normal>]

Plica: [<Torn inferior plica>]

Hoffa fat pad: [<Diffuse edema>]

TT–TG distance: [<1.8 cm>]

Intercondylar compartment:

Anterior cruciate ligament: [<Complete disruption with hemorrhage and edema in the notch>]

Posterior cruciate ligament: [<Intact>]

Bones: [<Contusions and subcortical nondisplaced impaction fractures central lateral femoral condyle and posterolateral tibial plateau. Additional contusion posteromedial tibial plateau>]

Muscles: [<Grade I strain popliteus muscle>]

Vessels: [<Normal>]

Nerves: [<Normal>]

Other: [<Grade II sprains of the medial and lateral retinaculae from the femoral attachments>]

IMPRESSION:

1. Grade III sprains of ACL, lateral collateral ligament complex with findings of posterolateral corner injury as described. Please correlate clinically for instability.

2. Grade II sprains of MCL and patellar retinaculae.

3. Medial and lateral meniscal tears.

4. Moderate lipohaemarthrosis and bony injuries from recent translational event as above.

11

The Ankle

Avneesh Chhabra, Jared Kasper, Colby Engar, and Theodoros Soldatos

The ankle joint is constituted by multiple ligaments and supporting tendons, which are subject of various pathologies that can affect them in isolation or in combination with other structures. For systematic imaging analysis and structured reporting, the ankle can be divided into medial, lateral, anterior, and posterior compartmental structures. This chapter discusses the imaging evaluation approach and describes how to fill in the structured checklist in Box 1. Conceptual details of related MR physics and imaging protocol are discussed in the chapter on MR protocol optimization.

IMAGE EVALUATION

The below-outlined stepwise interpretation approach is only a practical guide, and all ankle structures should be evaluated in multiple planes for their optimal assessment. The discussion below will help the reader perceive which structures are best depicted and evaluated in which particular plane.

1. Line up the similar-plane fat-saturated (fs) and non-fs images and synchronize them for tandem evaluation. From three-dimensional (3D) isotropic images, the technologist should create reconstructions in pre-specified planes to save the reading time.
2. Start with the sagittal images to look for possible tibiotalar, talonavicular, and subtalar joint effusions, integrity of the tibiotalar capsule and dorsal talonavicular ligament. Subsequently, evaluate for possible talar fault, pes planus/alta, Stieda process, os trigonum, Achilles tendon (AT) pathology, retrocalcaneal and/or retroachilles bursitis, as well as for Kager fat pad abnormalities. Then, evaluate sinus tarsi, Gissane angle, lateral process of talus, the anterior process of calcaneus, and bifurcate ligament moving from medial to lateral images. Look for plantar enthesophyte (spur), and for plantar fascia, and heel pad pathology. Finally, check for any obvious lesions, such as hindfoot or midfoot osteochondral lesion (OCL), osteoarthritis, mass lesion, or fracture. Although the sagittal plane is not ideal for ligament evaluation, the anterior and posterior talofibular ligaments can be seen on the far-lateral images as moustache-like structures extending from the fibula to the calcaneus (Fig. 1).

Fig. 1: Normal ankle anatomy on sagittal images. **A:** *Long arrow,* bifurcate ligament; *short arrow,* sinus tarsi; *star,* Achilles tendon. **B:** *Long arrow,* bifurcate ligament; *medium arrow,* posterior intermalleolar ligament; *short arrow,* dorsal talonavicular ligament. **C:** *Long arrow,* posterior talofibular ligament; *short arrow,* anterior talofibular ligament.

3. On the coronal plane, moving from anterior to posterior images, look for anteromedial talonavicular uncovering, ankle mortise asymmetry, talocalcaneal coalition, and hindfoot valgus. On the medial side, evaluate the medial malleolus, the three bands of the spring ligament (superomedial, medial plantar oblique, and inferoplantar), as well as the superficial and deep portions of the deltoid ligament. After reassessing the sinus tarsi, move to the lateral side, where the syndesmotic ligaments above the tibiotalar joint line (interosseous, anterior distal tibiofibular, and posterior distal tibiofibular), posterior intermalleolar (at the joint line), posterior talofibular (PFL), and calcaneofibular ligaments (CFL) (below the joint line) can be assessed from superior to inferior on a single image. Subsequently, evaluate the lateral malleolus, look for OCL in the talus or tibia, and check the three (medial, central, and lateral) cords of the plantar fascia bordering the plantar muscles. Finally, check the peroneus longus (PL) tendon insertion on the first metatarsal base, as it courses under the foot arch from lateral to medial (Figs. 2, 3).

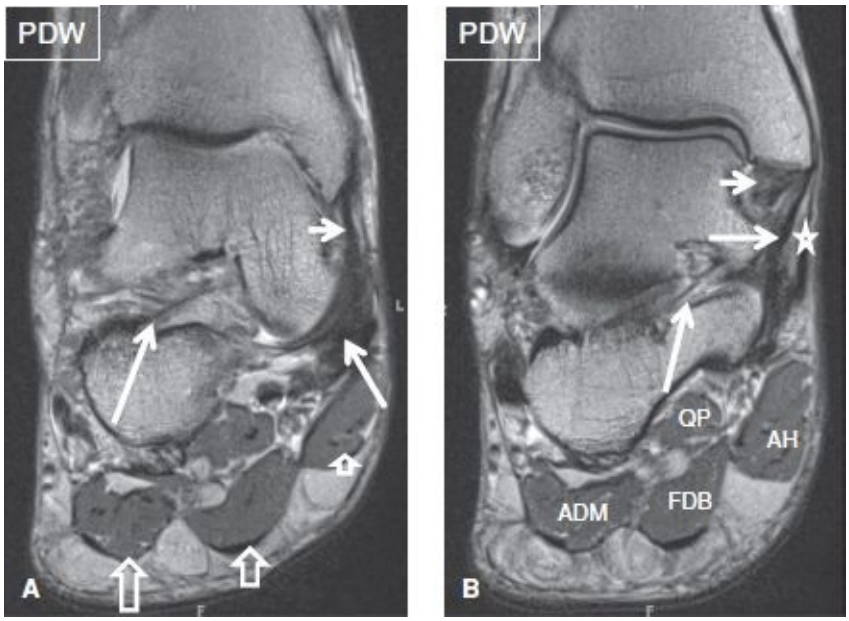

Fig. 2: Normal ankle anatomy on coronal images. **A:** *Long arrow,* cervical ligament; *medium arrow,* superomedial band of spring ligament; *short arrow,* tibiospring ligament; *long open arrow,* lateral cord of plantar fascia; *medium open arrow,* central cord of plantar fascia; *short open arrow,* medial cord of plantar fascia. **B:** *Long arrow,* interosseous talocalcaneal ligament; *medium arrow,* tibiocalcaneal ligament; *short arrow,* posterior deep tibiotalar ligament; *star,* flexor retinaculum; AH, abductor hallucis; FDB, flexor digitorum brevi; ADM, abductor digiti minimi; QP, quadratus plantae.

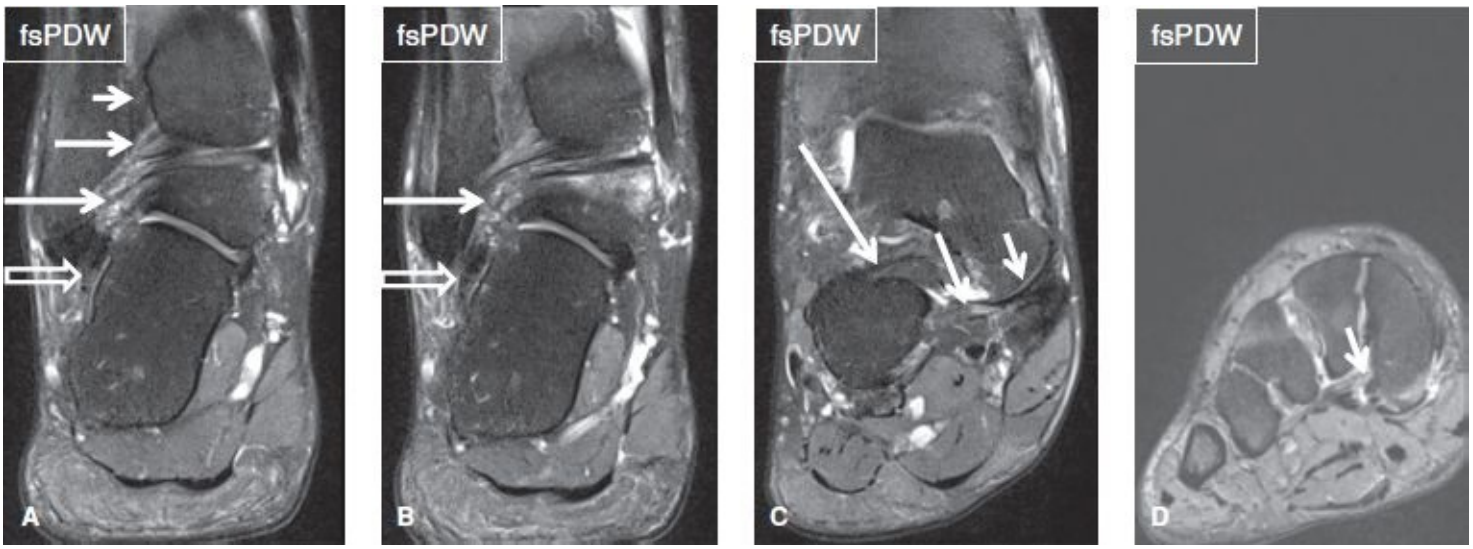

Fig. 3: Normal ankle anatomy on coronal images. **A:** *Open arrow,* calcaneofibular ligament; *long arrow,* posterior talofibular ligament; *medium arrow,* PIML; *short arrow,* posterior distal tibiofibular ligament. **B:** *Open arrow,* calcaneofibular ligament; *long arrow,* posterior talofibular ligament. **C:** *Long arrow,* inferoplantar band; *medium arrow,* medioplantar oblique band; *short arrow,* superomedial band of spring ligament. **D:** *Arrow,* normal striated insertion of the peroneus longus tendon.

4. The axial plane is best for ligament and tendon assessment. The interosseous, anterior distal tibiofibular, and posterior distal tibiofibular ligaments should be again evaluated

above the joint line, the posterior intermalleolar ligament (PIML) at the joint line, and the deltoid, spring, anterior talofibular ligament (AFL), and PFLs below the joint line. All tendons should be traced from above the ankle to their insertions. Vessels, nerves, and tarsal tunnel are also best evaluated on the axial plane. Finally, axial plane is excellent for measuring the osteochondral lesions and mass lesions in the transverse axes (Fig. 4).

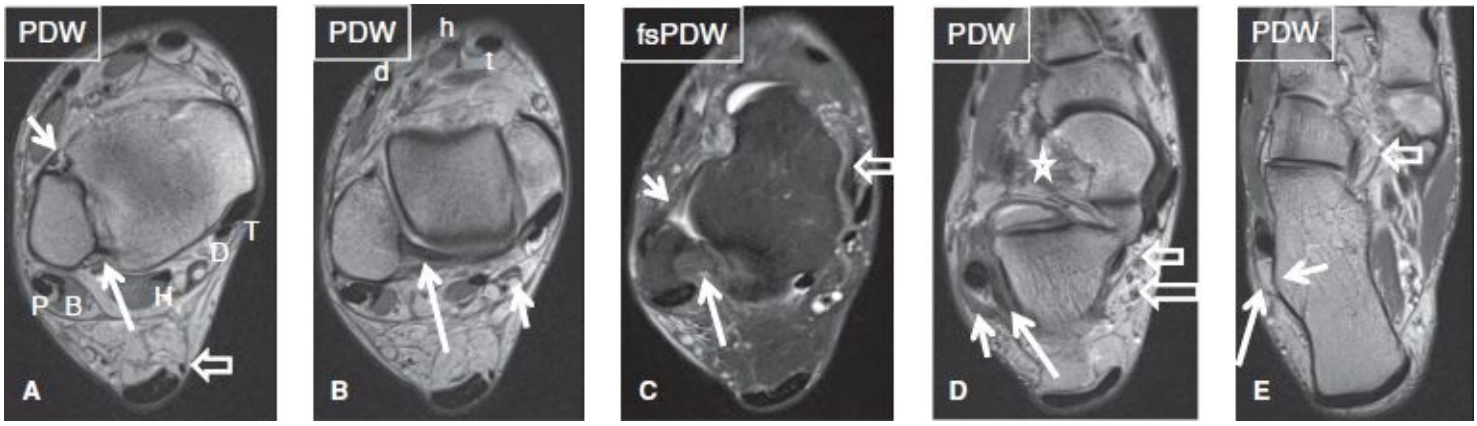

Fig. 4: Normal ankle anatomy on axial images. **A:** *Long arrow,* posterior distal tibiofibular ligament; *short arrow,* anterior distal tibiofibular ligament; *open arrow,* plantaris tendon; T, tibialis posterior; D, flexor digitorum longus; H, flexor hallucis longus; P, peroneus longus; B, peroneus brevis. **B:** *Long arrow,* posterior intermalleolar ligament; *short arrow,* tibial nerve; t, tibialis anterior; h, extensor hallucis; d, extensor digitorum. **C:** *Long arrow,* posterior talofibular ligament; *short arrow,* anterior talofibular ligament; *open arrow,* superomedial band of spring ligament. **D:** *Long open arrow,* lateral plantar nerve; *short open arrow,* medial plantar nerve; *long arrow,* calcaneofibular ligament; *short arrow,* superior peroneal retinaculum; *star,* sinus tarsi. **E:** *Long arrow,* inferior peroneal retinaculum; *short arrow,* peroneal tubercle; *open arrow,* recurrent slip of tibialis posterior.

BOX 1: The Structured Report: Ankle

The checklist for structured reporting of MR imaging of the Ankle. For each field, *Normal* is considered default in the dictation whereas the rest of the elements describe various pathologies that could be encountered during imaging evaluation. See Appendix 1 and 2 at the end of the chapter for a sample completed reports of the normal and abnormal examination results.

Examination: MRI of Ankle [<With/Without>] Contrast

FINDINGS:

Alignment: [<Normal> <Talonavicular uncovering> <Talar fault> <Hindfoot valgus> <Pes planus> <Pes alta>]

Fluid:

Tibiotalar joint: [<Normal> <Small effusion> <Moderate effusion> <Large effusion>]

Posterior subtalar joint: [<Normal> <Small effusion> <Moderate effusion> <Large effusion>]

Talonavicular joint: [<Normal> <Small effusion> <Moderate effusion> <Large effusion>]

Calcaneonavicular joint: [<Normal> <Small effusion> <Moderate effusion> <Large effusion>]

Medial structures:

Medial malleolus: [<Normal> <Enthesopathy> <Contusion>]

Tendons:

Posterior tibial tendon: [<Normal> <Tendinosis> <Tenosynovitis> <Split tear> <Complete tear>]

Flexor digitorum longus: [<Normal> <Tendinosis> <Tenosynovitis> <Split tear> <Complete tear>]

Flexor hallucis longus: [<Normal> <Tendinosis> <Tenosynovitis> <Split tear> <Complete tear>]

Ligaments:

Deltoid ligament complex—superficial: [<Intact> <Thickened> <Acute sprain>]

Deltoid ligament complex–deep: [<Intact> <Thickened> <Acute sprain>]

Spring (plantar calcaneonavicular) ligament: [<Intact> <Thickened> <Attenuated> <Acute sprain>]

Lateral structures:

Lateral malleolus: [<Normal> <Enthesopathy> <Contusion>]

Retromalleolar groove: [<Concave> <Flat> <Convex>]

Tendons:

Peroneus longus: [<Normal> <Tendinosis> <Tenosynovitis> <Split tear> <Complete tear>]

Peroneus brevis: [<Normal> <Tendinosis> <Tenosynovitis> <Split tear> <Complete tear>]

Superior peroneal retinaculum: [<Intact> <Thickened> <Deficient>]

Ligaments:

Interosseous (syndesmosis): [<Intact> <Thickened> <Acute sprain>]

Anterior inferior tibiofibular (syndesmosis): [<Intact> <Thickened> <Acute sprain>]

Posterior inferior tibiofibular (syndesmosis): [<Intact> <Thickened> <Acute sprain>]

Anterior talofibular ligament: [<Intact> <Thickened> <Attenuated> <Acute sprain>]

Calcaneofibular ligament: [<Intact> <Thickened> <Attenuated> <Acute sprain>]

Posterior talofibular ligament: [<Intact> <Thickened> <Mucoid degeneration> <Acute sprain>]

Bifurcate ligament: [<Intact> <Thickened> <Acute sprain>]

Posterior structures:

Posterior talus: [<Normal> <Os trigonum> <Stieda process>]

Posterior intermalleolar ligament: [<Intact> <Thickened>]

Achilles tendon: [<Normal> <Tendinosis> <Tear> <Kager fat pad edema> <Enthesophyte> <Retrocalcaneal bursitis> <Retroachilles bursitis>]

Plantar fascia: [<Normal> <Thickened> <Tear> <Perifascial edema> <Enthesophyte> <Heel pad edema>]

Anterior structures:

Tendons:

Anterior tibial tendon: [<Normal> <Tendinosis> <Tenosynovitis> <Split tear> <Complete tear>]

Extensor hallucis longus: [<Normal> <Tendinosis> <Tenosynovitis> <Split tear> <Complete tear>]

Extensor digitorum longus: [<Normal> <Tendinosis> <Tenosynovitis> <Split tear> <Complete tear>]

Ligaments:

Dorsal talonavicular ligament: [<Intact> <Thickened> <Enthesopathy>]

Tibiotalar joint: [<Normal> <Osteochondral lesion> <Osteoarthritis>]

Subtalar joint: [<Normal> <Osteochondral lesion> <Osteoarthritis>]

Bones (other than subarticular marrow and malleoli): [<Normal> <Midfoot enthesopathy> <Midfoot osteoarthritis>]

Muscles: [<Normal>]

Nerves and tarsal tunnel: [<Normal> <Hyperintense medial plantar nerve>]

Sinus tarsi: [<Normal> <Edema> <Sinus tarsi syndrome>]

Vessels: [<Normal>]

Other: [<None>]

Impression:

[<In the order of importance with acute findings first>]

HOW TO FILL THE STRUCTURED REPORT

Alignment: [<Normal> <Talonavicular uncovering> <Talar fault> <Hindfoot valgus> <Pes planus> <Pes alta>]

Evaluation of bony structures and bone alignment is best performed on non fs images, as one can clearly see the fatty marrow, bony cortices, and osteophytes. Normal alignment means bony articulation congruency at the tibiotalar, subtalar, and talonavicular joints. It

is easy to remember the rule of 2–4–6: The medial and lateral mortise (tibiotalar articular) spaces are symmetrical with less than 2 mm side-to-side difference. The medial clear space (medial gutter) between the medial malleolus and the talus is less than 4 mm whereas the syndesmotic space (between the distal tibia and the fibula at 1 cm above the tibial plafond) is less than 6 mm. The central axis of the talus should correspond to the visualized base and shaft of the first metatarsal bone, and the central axis of the calcaneus should align with the base and shaft of the fourth metatarsal bone. The angle between these two lines is 20–40 degrees. Less than 20 degrees qualifies as hindfoot varus while more than 40 degrees as hindfoot valgus. Talar fault is best seen on sagittal images, where the talus inferiorly subluxes relative to the first metatarsal bone axis. Anteromedial uncovering, best seen on axial or coronal images, is established when there is loss of congruency at the talonavicular joint with anteromedial translation of talar head. Hindfoot valgus is best assessed on the posterior ankle images, where the angle between the lines drawn along the tibial and talar axes is greater than 6–8 degrees (Figs. 5, 6). Hindfoot varus and valgus can also be diagnosed on the axial image through the calcaneus, where the tibial axis should match up with the calcaneus axis, if no varus or valgus exists. Alternatively, it is assessed on the sagittal image by drawing lines along the talus and calcaneus axis (valgus: lateral talocalcaneal angle >50 degrees, varus: lateral talocalcaneal angle <35 degrees).

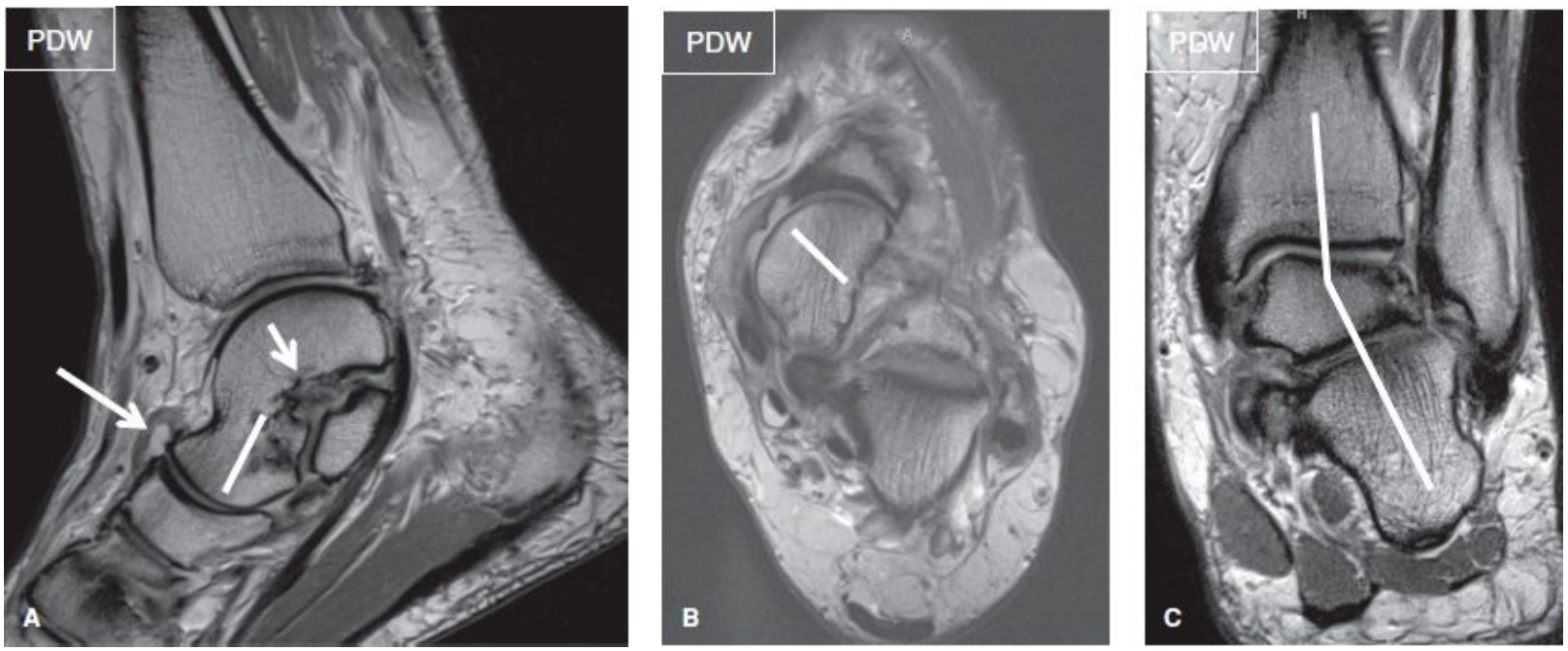

Fig. 5: Ankle malalignments. **A:** *Line,* mild talar fault; *long arrow,* thickened dorsal talonavicular ligament; *short arrow,* subcortical cysts at the sinus tarsi ligament attachment. **B:** *Line,* anteromedial uncovering of talus. **C:** Abnormally increased talocalcaneal angle indicates hindfoot valgus.

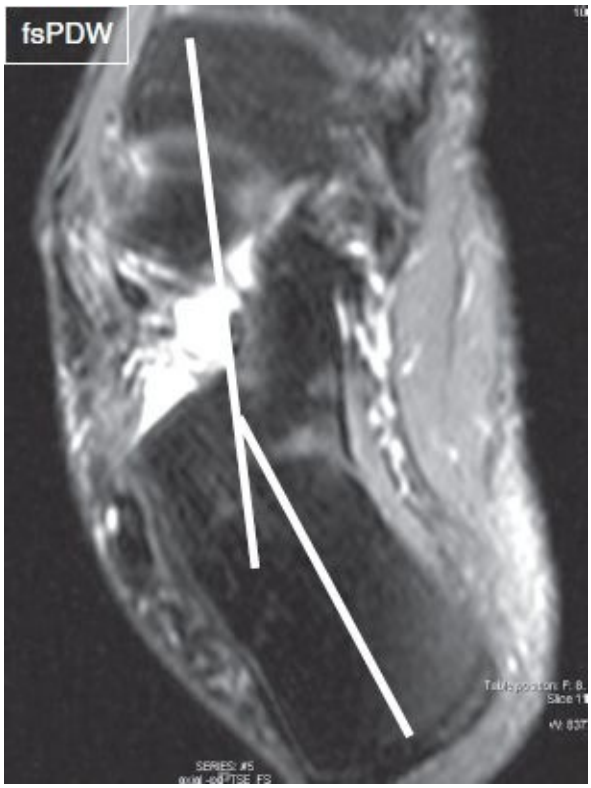

Fig. 6: Hindfoot varus on axial image. The angle between the central axis of the calcaneus and the shaft of the fourth metatarsal bone is less than 20 degrees.

Although weight-bearing imaging studies are the best for detecting malalignment, features suggesting various ankle instabilities (sensation of "giving way") can also be seen on MR images. These instabilities can be lateral (typically inversion sprain), medial (typically eversion sprain), subtalar (related to pes planus), or rotational (with multidirectional malalignments). Lateral instability results from injury to two or more of lateral collateral ligaments, usually of the AFL and CFL, and leads to anterior translation and varus tilt to talus. Deltoid ligament injury is also common in these injuries, observed in 40% to 50% cases. Medial instability results from deltoid ligament injury and is seen as widening of medial gutter and valgus tilt of talus. Syndesmotic ligament injuries may also be associated due to similar mechanism leading to high ankle sprain. Subtalar instability results from CFL or sinus tarsi ligament tears and is associated with lateral translation of calcaneus with valgus positioning. Another important measurement is the calcaneal pitch (angle between horizontal along the heel and inferior calcaneus surface (normal angle = 20 to 25 degrees, pes alta >25 degrees, pes planus <20 degrees).

FLUID:

Tibiotalar joint: [<Normal> <Small effusion> <Moderate effusion> <Large effusion>]

Posterior subtalar joint: [<Normal> <Small effusion> <Moderate effusion> <Large effusion>]

Talonavicular joint: [<Normal> <Small effusion> <Moderate effusion> <Large

effusion >]

Calcaneonavicular joint: [<Normal> <Small effusion> <Moderate effusion> <Large effusion >]

The tibiotalar, posterior subtalar, talonavicular, and calcaneonavicular joints have thin synovial lining and small amount of fluid for nutrition and lubrication, which does not normally distend (convex margins) the capsule. Since the ankle is imaged in prone position, small amount of fluid in the posterior tibiotalar and subtalar recesses is normal. There is a normal communication between the tibiotalar and the posterior subtalar joints. To call the joint effusion, one should look for distention of the capsule (especially at the anterior, non-dependent portion of the capsule) and grade it as small (distension either anterior or posterior), moderate (distention both anterior and posterior), or large (distention anterior, posterior, and lateral) (Fig. 7). Associated synovial thickening, debris, intra-articular cartilaginous or osteochondral bodies, synovial diverticulae, and ganglion cysts should be reported, as they usually indicate underlying internal derangement. Capsular injuries may occur from recent or prior trauma, and manifest as irregularity, attenuation, and/or thickening of the capsules (Fig. 8). The articular cartilage normally appears as a 1–2 mm thick smooth continuous lining.

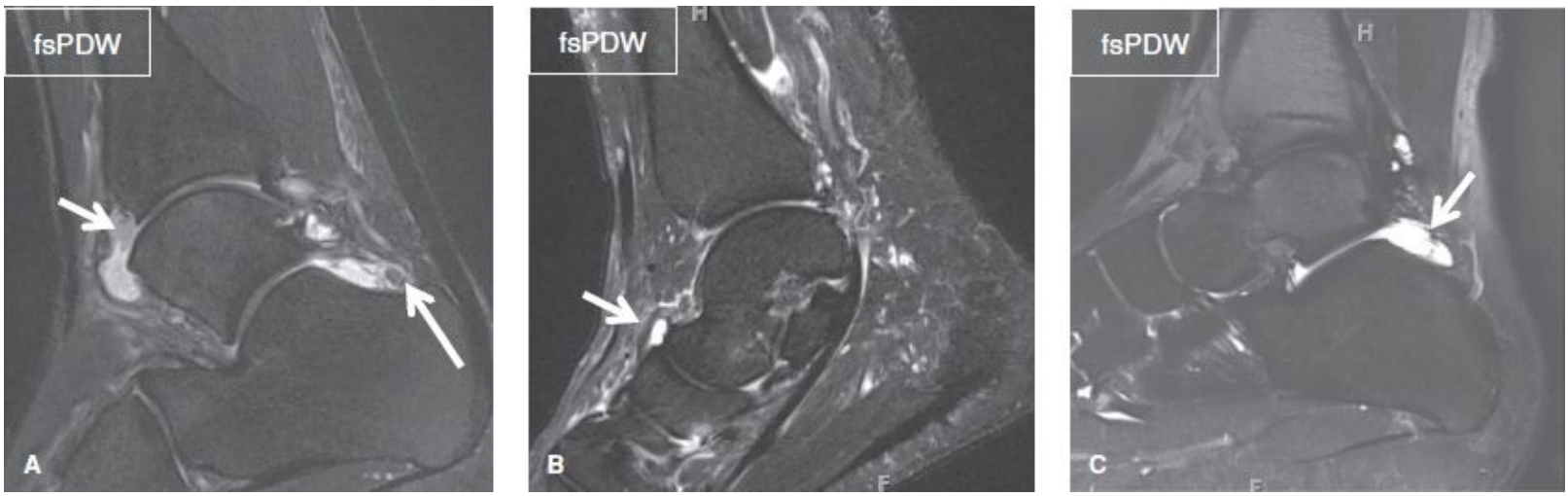

Fig. 7: Joint effusion on sagittal images. **A:** Moderate tibiotalar and small posterior subtalar effusion. *Long arrow,* loose body; *short arrow,* synovial thickening. **B:** Small talonavicular effusion (*arrow*). **C:** Small posterior subtalar effusion (*arrow*).

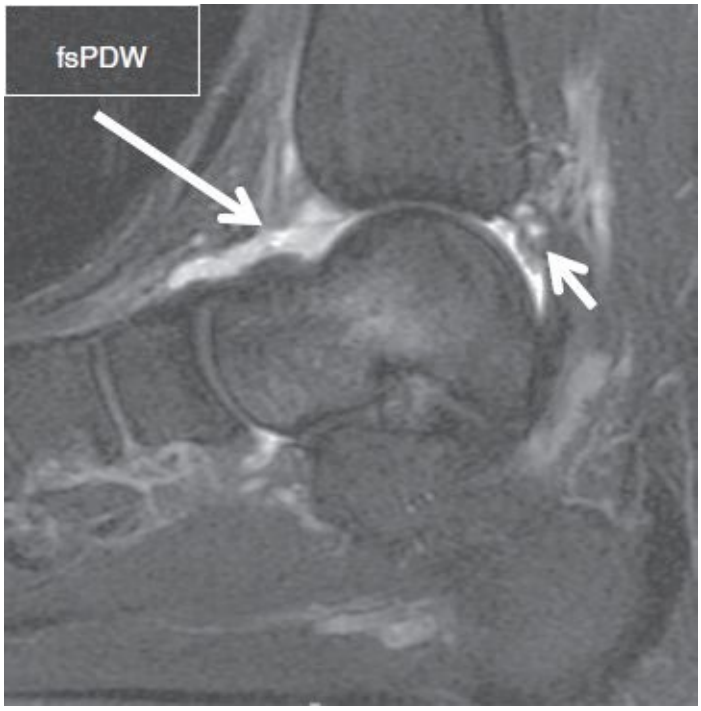

Fig. 8: Capsular rupture. Sagittal image demonstrates absent anterior joint capsule (*long arrow*) and irregular posterior joint capsule (*short arrow*) as well as an adjacent ill-defined fluid collections (*short arrow*).

MEDIAL STRUCTURES:

Medial malleolus: [<Normal> <Enthesopathy> <Contusion>]

TENDONS:

Posterior tibial tendon (PTT): [<Normal> < Tendinosis> <Tenosynovitis> <Split tear> <Complete tear>]

Flexor digitorum longus (FDL): [<Normal> < Tendinosis> <Tenosynovitis> <Split tear> <Complete tear>]

Flexor hallucis longus (FHL): [<Normal> < Tendinosis> <Tenosynovitis> <Split tear> <Complete tear>]

LIGAMENTS:

Deltoid ligament complex—superficial: [<Intact> < Thickened> <Acute sprain>]

Deltoid ligament complex—deep: [<Intact> < Thickened> <Acute sprain>]

Spring (plantar calcaneonavicular) ligament: [<Intact> <Thickened> <Attenuated> <Acute sprain>]

The bony contours are best assessed on coronal non–fs images for enthesopathy (Fig. 9), old

or recent fractures (irregular edge/fragment fits the fracture site/bone marrow edema/acute angle with the fracture site) or accessory ossicles (round corticated unfused fragment with obtuse angle). The fat-suppressed images are useful for detecting subcortical avulsive cystic changes or bone marrow edema from flexor retinaculum or deltoid ligament avulsion, contusion or fracture. Beware of poor fat saturation images, especially on low-field scanners or frequency-selective fs images to avoid overcalling bone marrow edema (Fig. 10). Inversion recovery images perform better than frequency-selective fs images on low-field scanners for this purpose.

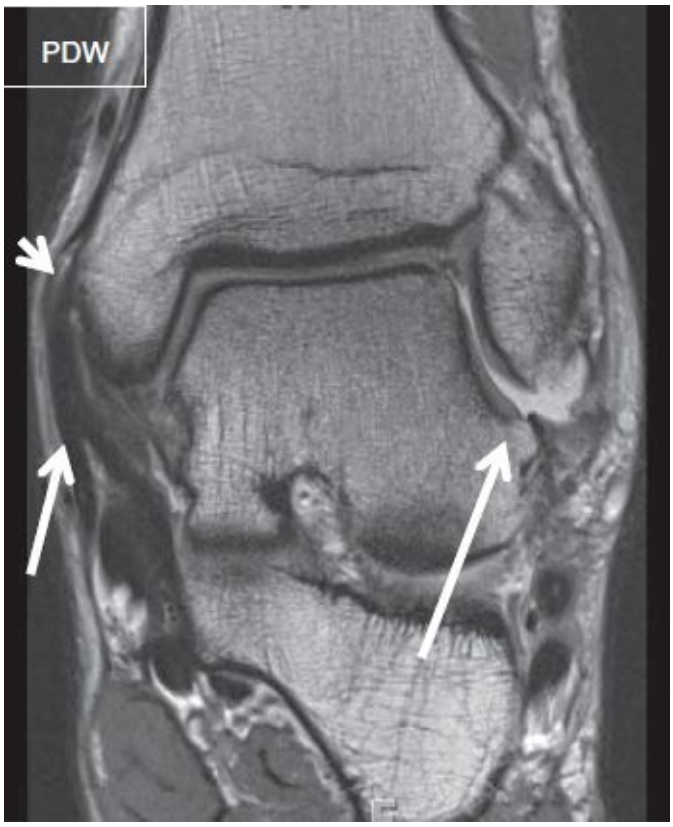

Fig. 9: Enthesophytes. Coronal image demonstrates an enthesophyte (*short arrow*) at the medial aspect of the medial malleolus with thickened flexor retinaculum (*medium arrow*) from prior injury. Also note enthesophyte at lateral process of talus from prior injury to calcaneofibular ligament (*long arrow*).

Fig. 10: Inadequate fat saturation on frequency-selective fat-suppressed axial image. High signal at the medial and lateral malleolus (*arrows*) is due to poor fat saturation, which should not be erroneously interpreted as marrow edema.

The medial tendons are best evaluated on the axial images. Liniing up, from anterior to posterior, are the PTT, FDL tendon, and FHL tendon, which are all bounded by the flexor retinaculum. Accessory muscles, such as accessory FHL or accessory FDL may be incidentally present and these follow the respective tendons. The flexor retinaculum attaches to medial malleolus and is proximally continuous with deep fascia of leg and distally with plantar aponeurosis and abductor hallucis (AH) fascia. If flexor tendons are torn, the retraction is best measured on the sagittal images. Trace fluid is normal along the dependent portions of the tendons. Tendons also have 1–2 remnant linear bands of synovial layers within their sheath, called mesotenon(s). The findings indicative of tenosynovitis include, any fluid that is circumferential around the tendon, or more than 2 mm thickness in the nondependent portion, or if it is associated with synovial thickening/debris (Fig. 11). Although infection leads to abnormal synovial thickening, fascial edema, and/or surrounding tissue reaction, it is often difficult to define the cause of tenosynovitis (mechanical, infection, inflammatory, or post-traumatic). If there is clinical suspicion for infection, synovial fluid should be aspirated. Stenosing tenosynovitis is diagnosed when multiple septations, asymmetric pooling of fluid and/or fluid loculations exist within and along the tendon sheath. FHL stenosing tenosynovitis has been associated with os trigonum syndrome. As elsewhere in the body, tendinosis reflects incompletely healed microtears. Mild tendinosis is seen as increased signal in the tendon on the proton density-weighted (PDW) images without fluid-like bright signal. Moderate tendinosis is seen as increased signal and tendon thickening. Severe tendinosis is seen as near fluid-bright signal, marked tendon thickening, and edge

irregularities, often difficult to differentiate from tendon tears. Tendon tear shows up as fluid-bright signal (partial or complete tear) or as longitudinal split with or without distal reconstitution, or as complete tear with retracted edges. Tendinosis predisposes to tears, as normal tendons do not tear spontaneously, unless transected by a penetrating injury. Therefore, it is important to describe both quality of the tendon and tear, as mild/moderate/severe tendinosis with superimposed partial/complete tear. FHL tenosynovitis is common at the sites of anatomic constrictions, at os trigonum/Stieda process, at the Henry knot (crossing of FHL and FDL), and at level of the hallux sesamoid bones (Fig. 12). It should be noted that the submalleolar portions of the medial flexor tendons are prone to magic angle artifacts, and minimal increased signal may be normally seen on low echo time images.

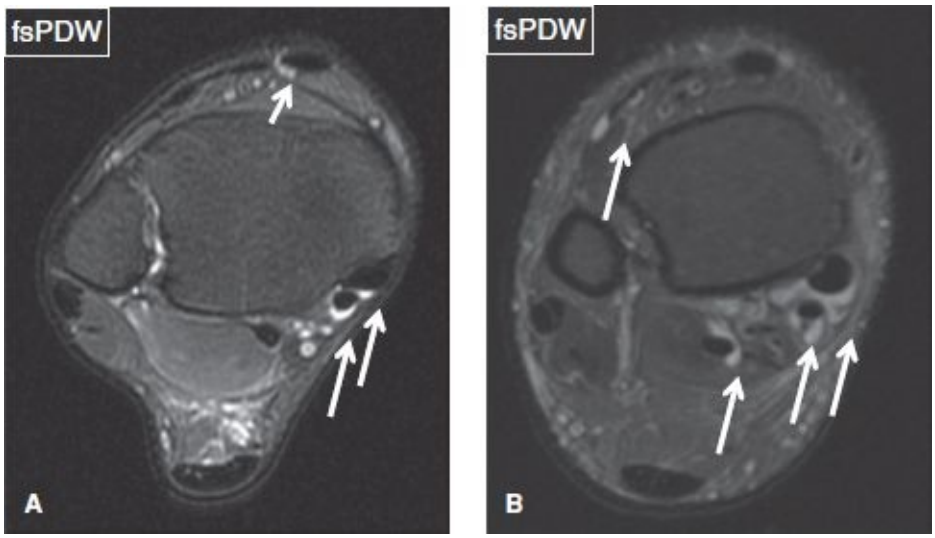

Fig. 11: Physiologic versus pathologic tendon sheath fluid on axial images. **A:** Normal trace fluid along the dependent portions of the posterior tibial and flexor digitorum longus tendons (*long arrows*). Normal vessels mimicking fluid adjacent to tibialis anterior tendon (*short arrow*). **B:** Circumferential and greater than 2 mm in thickness fluid around the posterior tibial, flexor digitorum longus, flexor hallucis longus, and extensor digitorum tendons (*arrows*) indicating tenosynovitis.

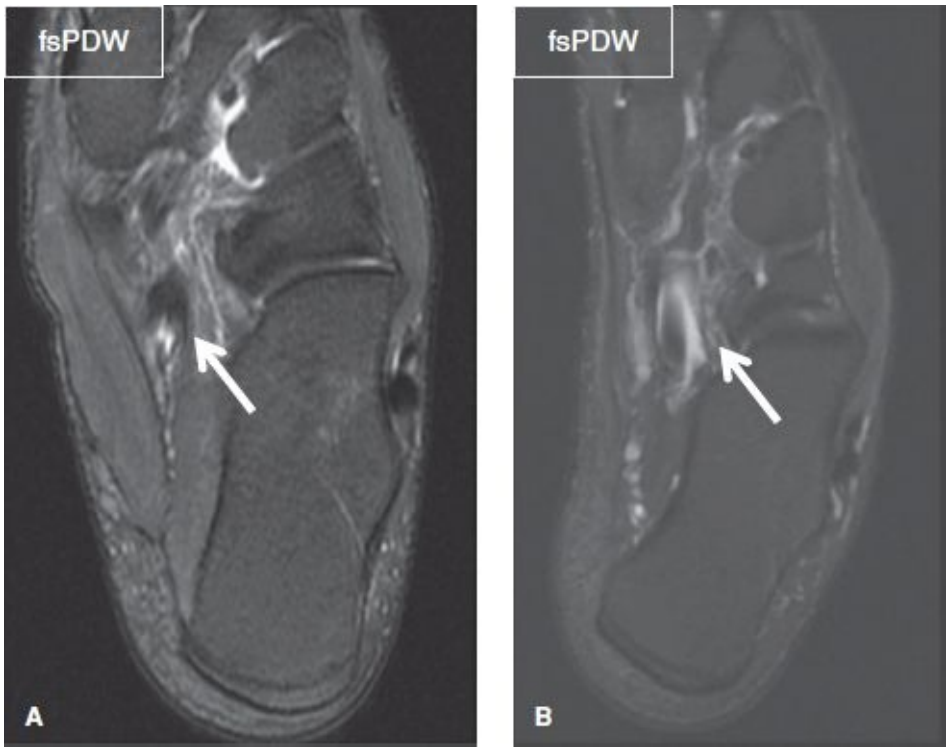

Fig. 12: Henry knot on axial images. **A:** Trace fluid is a common finding at Henry knot (*arrow*), where the flexor digitorum longus and flexor hallucis longus tendons cross each other. **B:** Circumferential fluid (*arrow*) around the flexor hallucis longus tendon at the level of Henry knot, without ankle effusion, corresponds to tenosynovitis.

The PTT is the most commonly injured and biomechanically important medial tendon. It is the anterior most medial tendon in the retromalleolar grove, coursing beneath the flexor retinaculum along with two other medial tendons, to terminate as multiple layers that insert on the navicular tuberosity, cuneiforms, metatarsals, and sustentaculum talus. It is the primary invertor of the foot, aids in plantar flexion, and supports the medial longitudinal arch with assistance from FHL and FDL. On axial images, normal PTT is about 1.5 to 2 times the size of the FDL tendon. The PTT overlies the superomedial band of the spring ligament and is separated from the latter by a connective tissue layer (gliding zone). At its insertion, the PTT fans out to insert on navicular tuberosity, cuneiforms, sustentaculum talus, and bases of second to fourth metatarsals. At the insertion, it commonly shows minimal thickening and/or increased signal, which are normal findings. However, fluid and edema surrounding this distal 1–2 cm segment (paratenonitis) is abnormal, since there is no normal synovial sheath around this distal part of the tendon.

An accessory ossification center for the navicular, known as os naviculare, may be identified along the insertional fibers of the PTT. Type I os naviculare (os tibiale externum) is a small (few mm) sesamoid bone within the distal PTT. Type II (prehallux) is a triangular or heart-shaped ossicle which measures up to 12 mm and is connected to the navicular tuberosity by fibrocartilage or hyaline cartilage (synchondrosis). Type III (cornuate naviculum) is a partially (medially) fused ossicle that is connected to the navicular by a medial bony ridge (Fig. 13). Type II os naviculare is most commonly implicated in pathology. Painful os naviculare syndrome involves one or a more of the following

findings: presence of os naviculare (commonly type II); bony hypertrophy of the accessory ossicle and navicular tuberosity; bone marrow edema; soft tissue edema; formation of adventitial bursa over the bony prominence; frank disruption and widening of the synchondrosis with fluid-like cleft; PTT tendinosis and/or tear (Fig. 14).

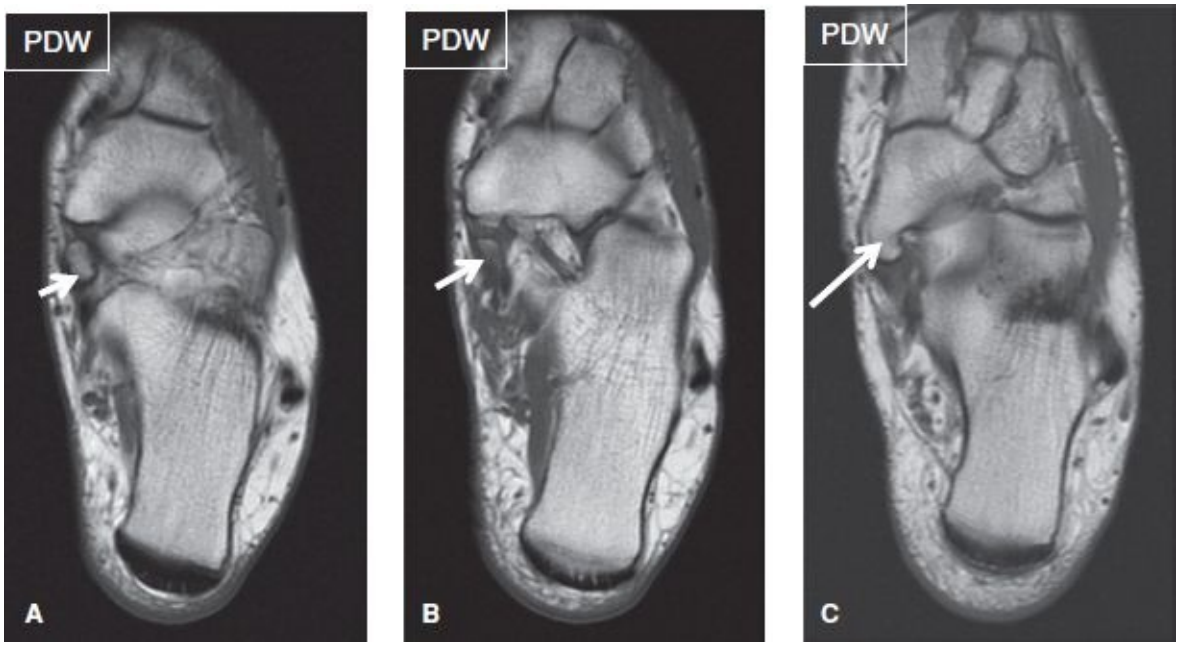

Fig. 13: Os naviculare types on axial images. **A:** Type I os naviculare (os tibiale externum): 6 mm sesamoid bone (*arrow*) within the distal posterior tibial tendon. **B:** Type II os naviculare (prehallux): a triangular or heart-shaped ossicle (*arrow*) which is connected to the navicular tuberosity by fibrocartilage (synchondrosis). **C:** Type III os naviculare (cornuate naviculum): a partially fused ossicle (*arrow*), which is connected to the navicular by a medial bony ridge.

Fig. 14: Painful os naviculare. Axial images **(A, B)** demonstrate a type II os naviculare

(*arrows*), associated with bone marrow edema on both sides of the synchondrosis.

Insertional PTT tendinosis is best seen on axial and coronal images. It presents with moderate thickening and/or signal alteration of the tendon (Fig. 15). PTT tears most commonly occur at or just distal to the level of the medial malleolus, rather than more distally, and have been classified into three types, based on severity:

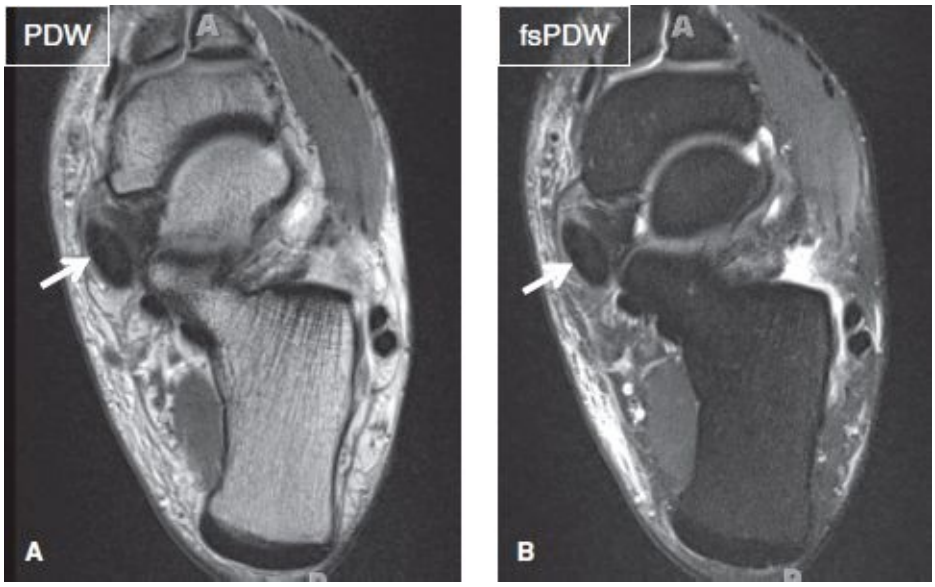

Fig. 15: Posterior tibial tendinosis. Axial images **(A, B)** exhibit moderate thickening and intermediate signal in the distal posterior tibial tendon (*arrows*).

- In *type I* tears, there is fusiform tendon enlargement ($>2\times$ the size of FDL tendon) with varying degrees of increased intrasubstance tendon signal that histologically represent chronic tendinopathy with superimposed areas of longitudinal split tears. With current imaging techniques, the splits can be easily identified in most cases.
- In *type II* tear, there is thinning ($<1.5\times$ the size of the FDL tendon) and elongation of the affected tendon segment with variable amounts of increased intrasubstance signal intensity. In some cases, the tendon splits completely into two subtendons (Figs. 16–18).

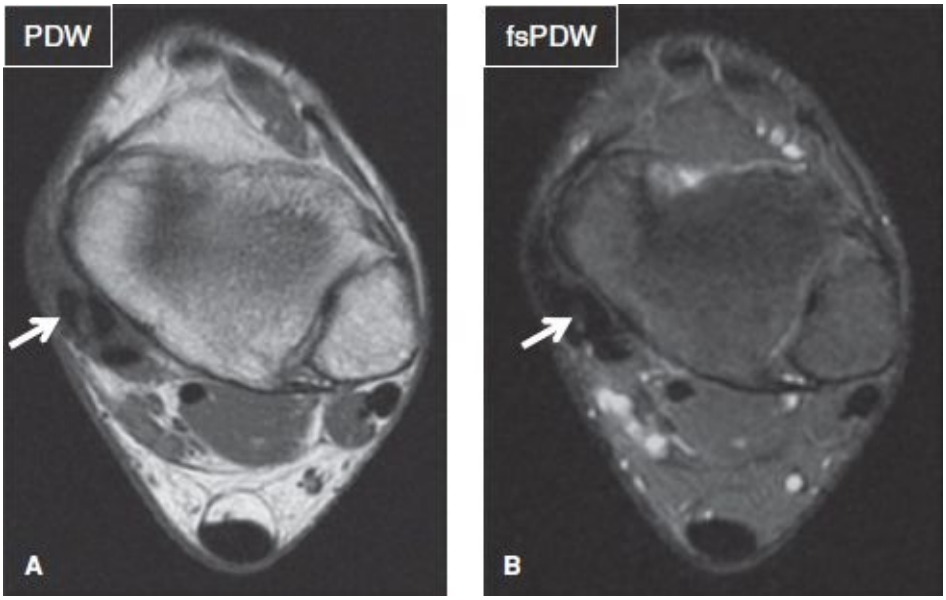

Fig. 16: Longitudinal split tear of the posterior tibial tendon, creating the “four-tendon sign.” Axial images **(A, B)** demonstrate four (instead of three) distinct tendons at the medial side of the ankle joint. The two most anteromedial tendinous structures (*arrows*) represent longitudinal splitting and separation of the original posterior tibial tendon.

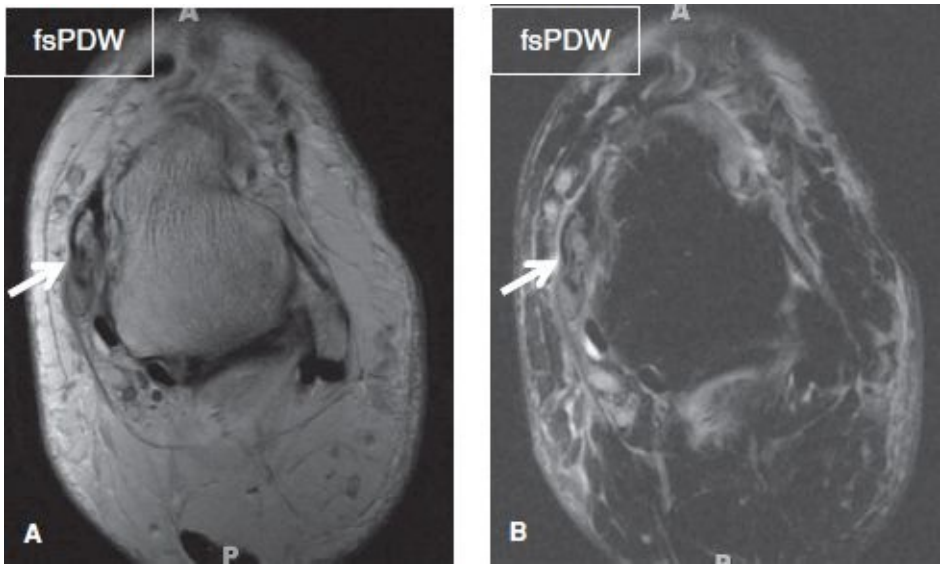

Fig. 17: Multifocal split tears of the posterior tibial tendon. Axial images **(A, B)** demonstrate multiple linear fluid-like signals within the distal posterior tibial tendon fragments (*arrows*).

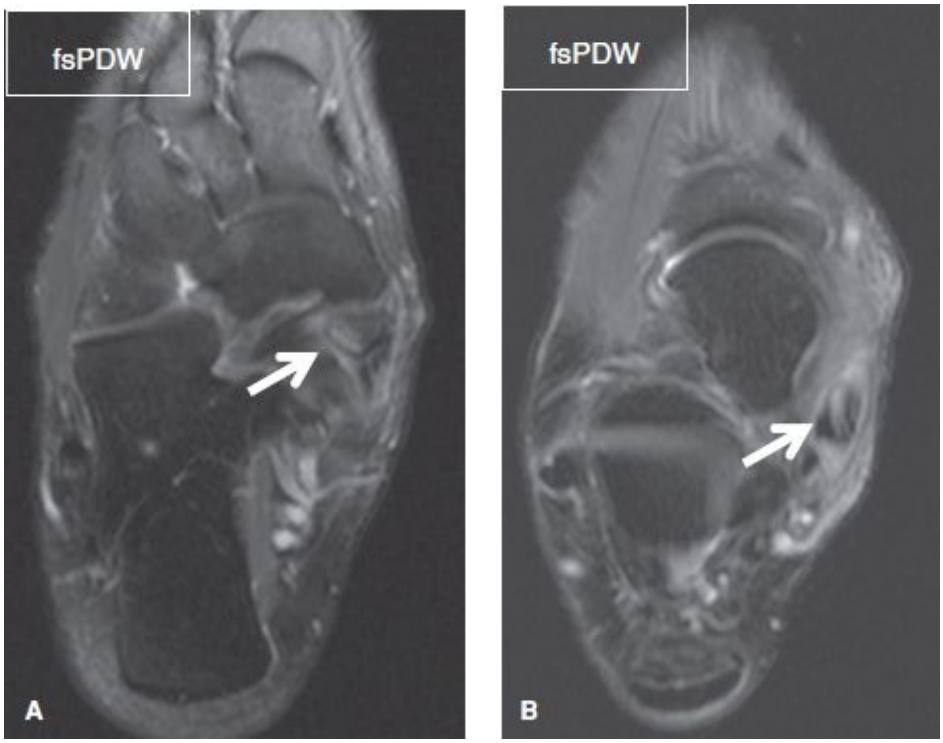

Fig. 18: Posterior tibial tendon tear in the presence of os naviculare. **A:** Axial image demonstrates an os naviculare type II (*arrow*) with mild bone marrow edema at the posterior tibial tendon insertion. **B:** More proximally, the posterior tibial tendon exhibits a longitudinal split tear (*arrow*).

- In *type III* tears, there is complete tendon disruption with fluid signal intensity within the

tendon gap (Fig. 19).

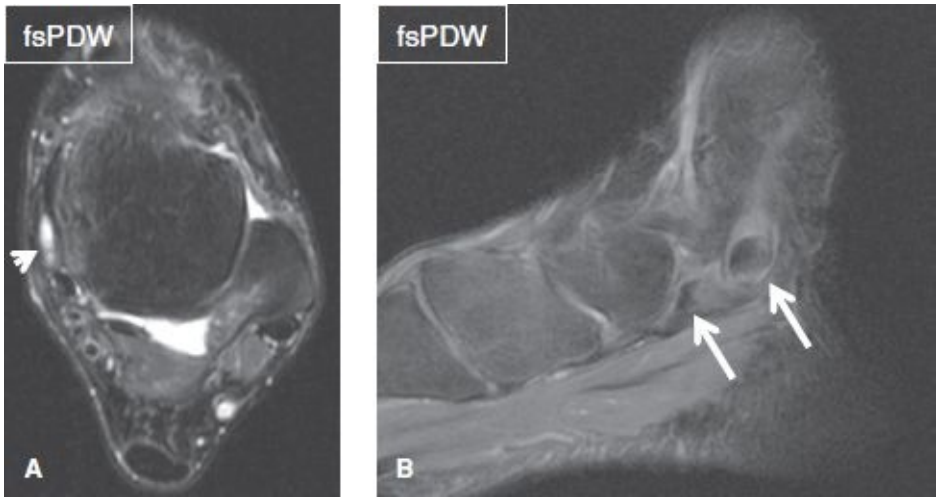

Fig. 19: Complete posterior tibial tendon disruption. **A:** In the axial plane, only fluid is identified at the expected position of the posterior tibial tendon (*arrow*). **B:** Sagittal image shows complete disruption of the posterior tibial tendon, with associated retraction of the torn fragments (*arrows*).

In all three types, additional findings may include tenosynovitis, flexor retinaculum thickening or attenuation, partial tear of the superomedial portion of the spring ligament, marginal osteophytes of the medial malleolus (retromalleolar groove), and/or marrow edema of the medial talus (Fig. 20). Thickened tenosynovium, focal fluid distensions of the tendon sheath and complex septations within the fluid are indicative of stenosing tenosynovitis (Fig. 21).

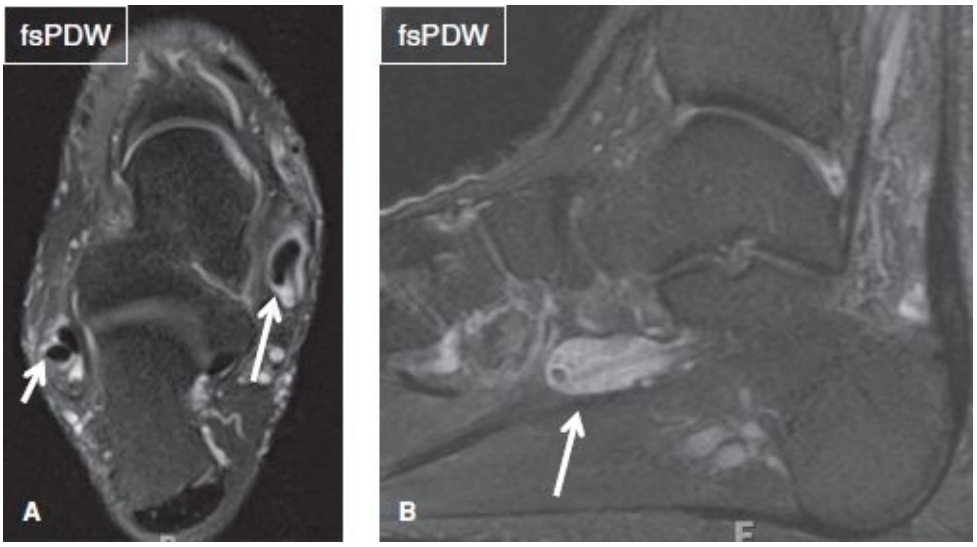

Fig. 20: Posterior tibial tenosynovitis. **A:** Circumferential fluid along the posterior tibial tendon (*long arrow*) is indicative of tenosynovitis, in this case of rheumatoid arthritis. Note concurrent peroneus longus tenosynovitis (*short arrow*). **B:** A large fluid collection along with multiple tiny hypointense foci within the flexor hallucis tendon sheath (*arrow*) is due to synovial chondromatosis and stenosing tenosynovitis.

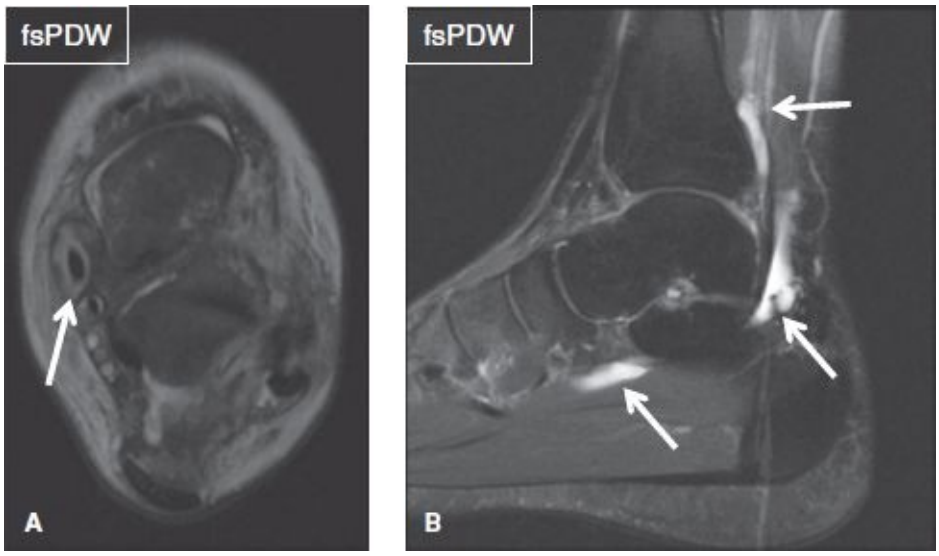

Fig. 21: Post-traumatic synovitis and stenosing tenosynovitis. **A:** Axial image acquired after recent ankle injury demonstrates circumferential fluid (*arrow*) around the posterior tibial tendon and diffuse soft tissue edema, corresponding to post-traumatic tenosynovitis. **B:** Sagittal image exhibits focal fluid distensions and septations within the flexor hallucis longus tendon sheath, which are indicative of stenosing tenosynovitis.

The PTT may rarely undergo subluxation or dislocation in an anteromedial direction relative to the medial malleolus. PTT dislocation may be associated with stripping or avulsion of the overlying flexor retinaculum, seen as a fleck of bone near the medial malleolus or enthesopathy at its expected attachment. Isolated spring ligament tears and flexor retinaculum injuries may clinically mimic PTT abnormality. Degeneration of the PTT may be associated with secondary abnormalities of multiple ligaments, joint capsule, fascia, articulations, and bony structures of the ankle, hindfoot, midfoot, and forefoot, in a syndrome known as PTT dysfunction (described below, in a separate paragraph).

The FHL tendon is the posterior-most tendon of the ankle. It is located between the medial and the lateral tubercles of the ankle, and features a long muscle belly, which is commonly visible at the tibiotalar joint level. The tendon courses along the undersurface of the sustentaculum talus (typical location for tendon identification on the sagittal view) and between the sesamoid bones of the first toe to insert at the base of the great toe distal phalanx. It is a weak plantar flexor of the ankle, maintains the first toe pad on ground when the foot is on ground, and plantar flexes the phalanges of the great toe when the foot is off ground. In 20–40% of individuals, the FHL tendon sheath communicates with the tibiotalar joint, and therefore, the reader should not overcall FHL tenosynovitis unless the tendon sheath fluid is disproportionate to the ankle joint effusion and/or more complex. In most situations, the FHL tendon shows more fluid than the PTT and the FDL tendon. The FDL and FHL tendons cross each other at the hindfoot–midfoot junction (Henry's knot), where their tenosynovial sheaths communicate, and it is common to see fluid loculation or ganglion cyst formation at that site. FHL tenosynovitis/tears are most commonly seen in ballet dancers. Other settings include os trigonum syndrome, fracture of posterior process of talus (medial tubercle, Cedell fracture; lateral tubercle, Shepherd fracture) and accessory

FHL muscle. The typical locations of pathology include, behind the ankle, at Henry's knot, and in the inter-sesamoid space. The latter is commonly associated with first metatarsophalangeal degenerative changes and/or hallux valgus deformity.

The FDL tendon is located posterior to the PTT under the flexor retinaculum. The tendon then runs laterally, across the plantar arch, crosses superficial to the FHL tendon, and inserts on the plantar base of all lesser toe distal phalanges. It divides into four slips, which give origin to lumbricals that assist in plantar flexion of foot. When the foot is on ground, it maintains pads of lesser toes whereas when the foot is off ground, it flexes second to fifth phalanges. It is relatively well protected and is rarely involved in pathologies. Its most common pathology is tenosynovitis whereas tears are uncommon. Small amount of tenosynovial fluid at the level of the ankle joint is a normal finding, as is at the Henry's knot, particularly if there is FHL tenosynovial fluid more proximally.

The deltoid ligament is a very strong ligament, composed of superficial and deep components. The superficial components are best depicted on the axial and coronal images and include the following, from anterior to posterior:

- The tibionavicular ligament is a thin, homogenous hypointense band, which is 0.5 to 1 cm wide, and extends from the medial malleolus to the navicular tuberosity
- The tibiospring ligament is the most superficial component, which extends from the medial malleolus to the superior border of the spring ligament (Fig. 22)

Fig. 22: Normal spring and tibiospring ligaments. Coronal images **(A, B)** demonstrate the superomedial band of the spring ligament (*long arrows*), which connects the medial surface of sustentaculum talus to naviculum and merges superiorly with tibiospring ligament (*short arrows*), which extends superiorly to the medial malleolus.

- The tibiocalcaneal ligament is 2 to 3 mm thick and represents the strongest superficial

component. It originates from the medial aspect of the anterior colliculus, descends vertically, and inserts on the medial border of the sustentaculum tali. It interlaces with those of the superomedial band of the spring ligament (Fig. 23)

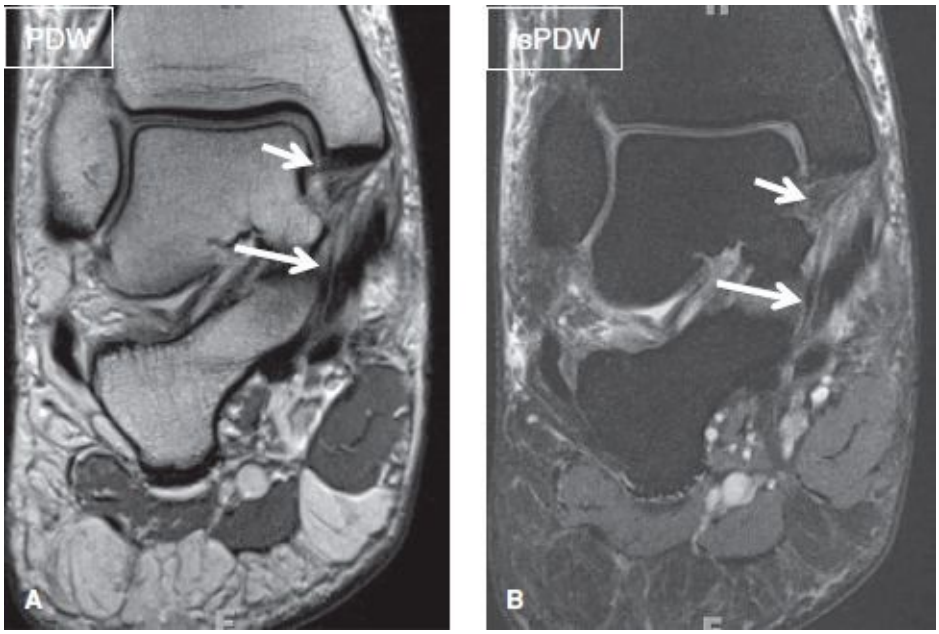

Fig. 23: Normal tibiocalcaneal and posterior deep tibiotalar ligaments. Coronal images **(A, B)** demonstrate the tibiocalcaneal ligament (*long arrows*), which extends from the medial malleolus to the sustentaculum tali, as well as the thick and normally striated posterior deep tibiotalar ligament (*short arrows*), which extends from the medial surface of the talus to the posteromedial talar tubercle.

- The superficial posterior tibiotalar ligament is a thin hypointense band, which originates from the posterior part of the medial surface of the anterior colliculus. It courses posteriorly, inferiorly, and laterally, and inserts on the posteromedial talar tubercle.

Of these components, the tibiocalcaneal ligament is the thickest, and the tibiospring is the only one that attaches to the spring ligament; the other bundles connect adjacent bones. The deep components of the deltoid ligament include a) the anterior deep tibiotalar ligament, which appears as a 2–3 mm thick striated band that extends from the anteromedial portion of the medial malleolus and inserts onto the talar neck (Fig. 24) b) the deep posterior tibiotalar ligament, which appears as a 5–15 mm thick striated band with broad attachment to the medial surface of the talus, as far posteriorly as the posteromedial talar tubercle (Fig. 23).

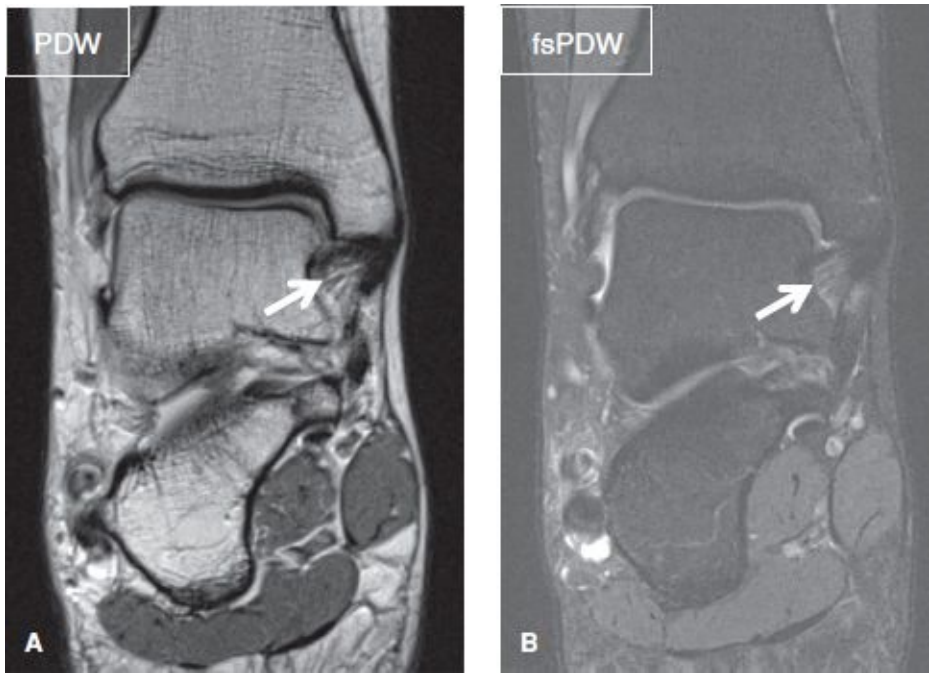

Fig. 24: Normal anterior deep tibiotalar ligament. Coronal images **(A, B)** demonstrate the anterior deep tibiotalar ligament as a striated band (*arrows*), extending from the anteromedial portion of the medial malleolus to the talar neck.

Rotational and translation injuries are the most frequent mechanisms for deltoid ligament injury. Acute tears of the deltoid ligament usually result from significant pronation/eversion injuries, involve both the superficial and the deep portions, and are commonly associated with lateral ligament injuries. Clinically, patients present with medial ankle pain, tenderness, and instability. Tears of the deep posterior tibiotalar component often occur with medial malleolus fractures, and are associated with local hemorrhage. Acute ligament sprains are classified as follows.

- Grade I (ligament stretch): Appears as thickening and/or loss of the fatty striations of the ligament on PDW or T1-weighted (T1W) images, along with periligamentous edema. With chronic injury or repeated sprains, it may lead to diffuse thickening of the ligament from remodeling (Figs. 25, 26)

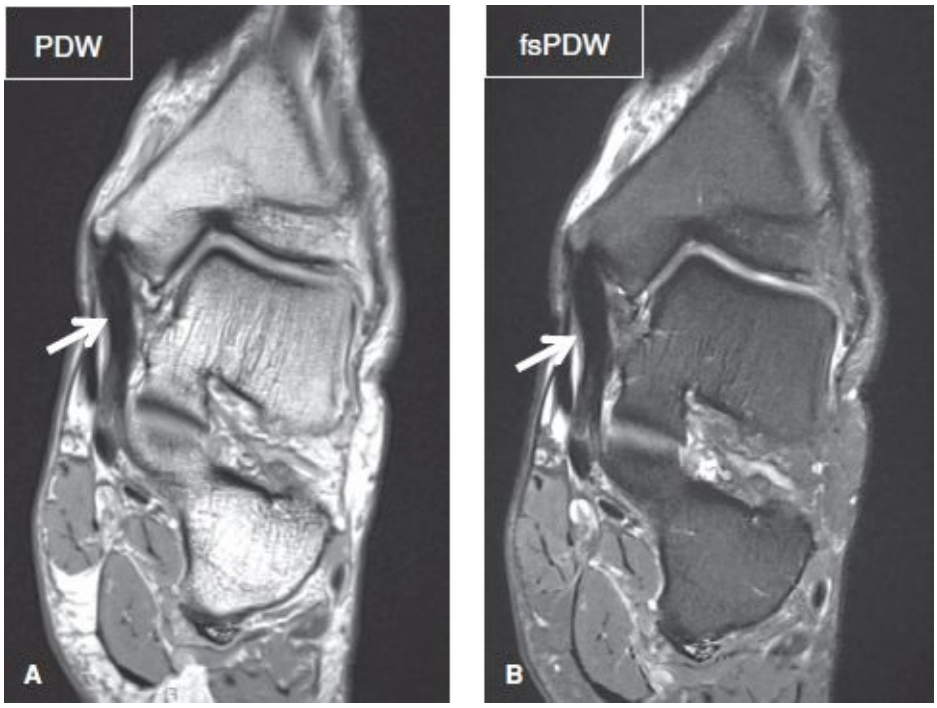

Fig. 25: Chronic sprain of the tibiospring ligament. Coronal images **(A, B)** show homogeneous thickening and remodeling of the tibiospring ligament with proximal enthesopathy (*arrows*).

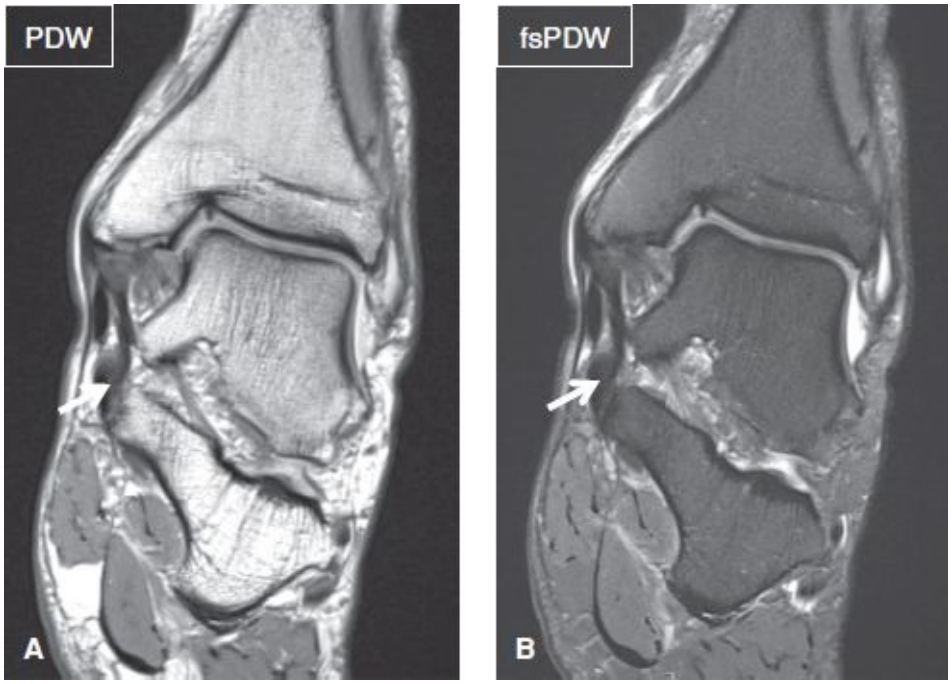

Fig. 26: Chronic sprain of tibiocalcaneal ligament. Coronal images show mild diffuse thickening of the tibiocalcaneal ligament with distal enthesopathy (*arrows*).

- Grade II (partial tear): Appears as intraligamentous increased signal on fat-suppressed PDW or T2-weighted (T2W) images (Figs. 27–29)

Fig. 27: Grade II sprain of the tibiospring ligament. Coronal image exhibits thickening and ill definition of the tibiospring ligament, which maintains partial continuity (*arrow*). Findings correspond to a partial tear.

Fig. 28: Grade II sprain of the tibiocalcaneal ligament. Coronal image demonstrates a near full-thickness tear of the tibiocalcaneal ligament (*arrow*).

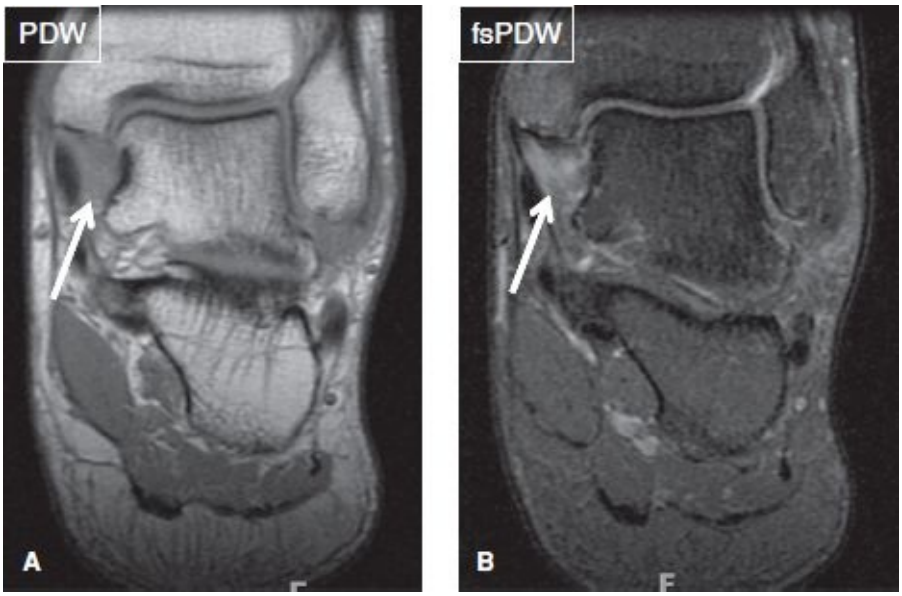

Fig. 29: Grade II sprain of the deep deltoid ligament. Coronal images **(A, B)** exhibit an ill-defined deep deltoid ligament, which lacks its normal striated configuration (*arrows*). Notice medial malleolar avulsive edema.

- Grade III (complete tear): Characterized by discontinuity and wavy contours of the torn ligament (Figs. 30, 31)

Fig. 30: Grade III sprain of the tibiocalcaneal (superficial) deltoid ligament. Coronal images **(A, B)** demonstrate discontinuity of the tibiocalcaneal (*long arrows*) ligament. Notice chronic enthesopathy and cystic changes of the calcaneal attachment site (*short arrows*).

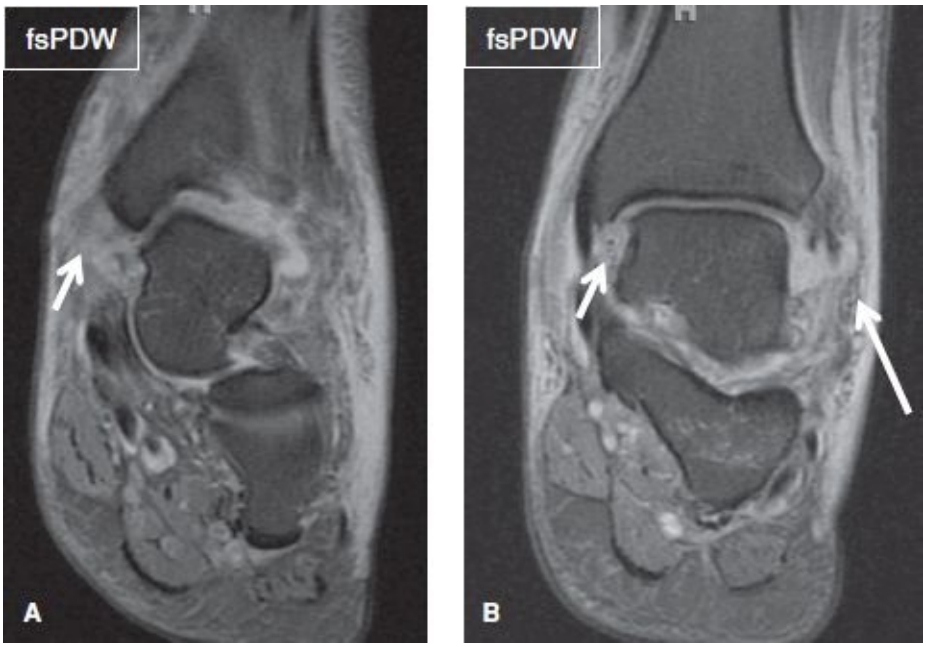

Fig. 31: Grade III sprain of the deltoid ligament. On coronal images **(A, B)**, there is extensive soft-tissue edema around the ankle, and particularly at the medial aspect of the joint, where the tibiospring and deep posterior tibiotalar ligaments are not visualized at their expected location (*short arrows*). Also note complete lateral collateral ligament disruption (*long arrow*).

Acute ligament sprains may also be associated with syndesmotic ligament injuries (occasionally with posterior malleolar fracture), flexor retinaculum tears (occasionally with bony avulsion), enthesopathic changes of the medial clear space (i.e., of the medial malleolus and medial process of talus or calcaneus), PTT and/or spring ligament injuries, lateral collateral ligament injuries and Weber type A, B, or C (Maisonneuve) fibular fractures, and ganglion cyst formation (Fig. 32). If there is ankle dislocation with medial sided injury, such as malleolus fracture, deltoid ligament would be definitely torn. Treatment wise, superficial deltoid or associated spring ligament injuries can be repaired; deep deltoid injury is managed conservatively with immobilization; and syndesmotic ligament injury is fixed with syndesmotic screws.

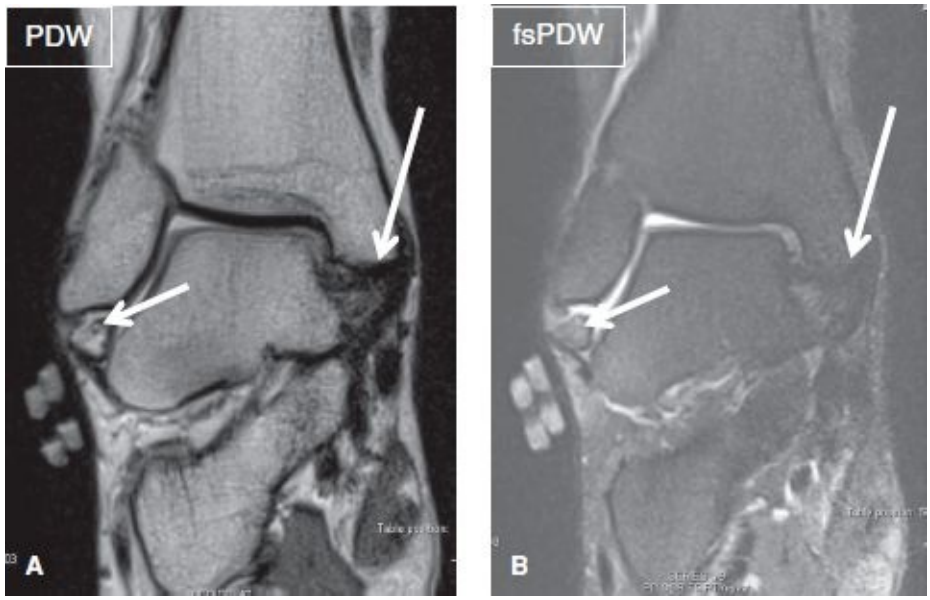

Fig. 32: Chronic Weber type A fracture. Coronal images **(A, B)** show a bone fragment inferior to the lateral malleolus, corresponding to a chronic Weber type A fracture (*short arrows*). Notice mild thickening of superior portion of the deep posterior tibiotalar ligament (*long arrows*).

The spring (or plantar calcaneonavicular) ligament extends from the calcaneus to the navicular bone and is composed of the superomedial, medioplantar oblique, and inferoplantar bands. It is normally 2–5 mm thick, features a small synovial recess between the superomedial and medioplantar oblique band. The superomedial band connects to the tibiospring ligament superiorly (Fig. 22). A fibrocartilaginous portion of the ligament lies superficial to the talar head. The superomedial band connects the medial surface of sustentaculum talus to the naviculum and merges superiorly with tibiospring ligament. Inferoplantar band connects the body of calcaneus to the naviculum, and medioplantar oblique connects the anterior margin of sustentaculum talus to the naviculum. The three bands are best assessed on axial and coronal images, though the medioplantar oblique and inferoplantar bands can also be evaluated on sagittal images. Acute injuries of the spring ligament most often involve the superomedial band, and these are commonly associated with deltoid ligament sprains. Because of the proximity of the spring ligament to the PTT and its integral function in stabilizing the plantar arch, spring ligament injuries are almost always associated with PTT dysfunction. Spring ligament injuries are classified similarly to deltoid ligament sprains (Figs. 33–35). Degeneration of the spring ligament is more common than acute sprains. Ganglions in relation to the spring ligament are usually encountered between the superomedial and the medial plantar oblique bands at the site of the plantar recess site, and in deltoid ligament among its deep fibers (Figs. 36, 37).

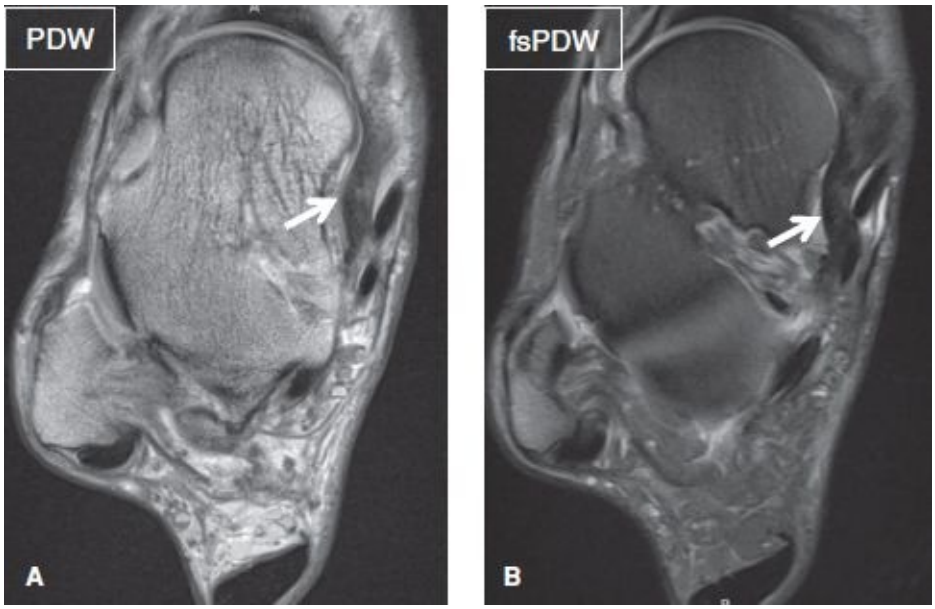

Fig. 33: Chronic sprain of the spring ligament. Axial images **(A, B)** show homogeneous thickening of the superomedial band of the spring ligament (*arrows*).

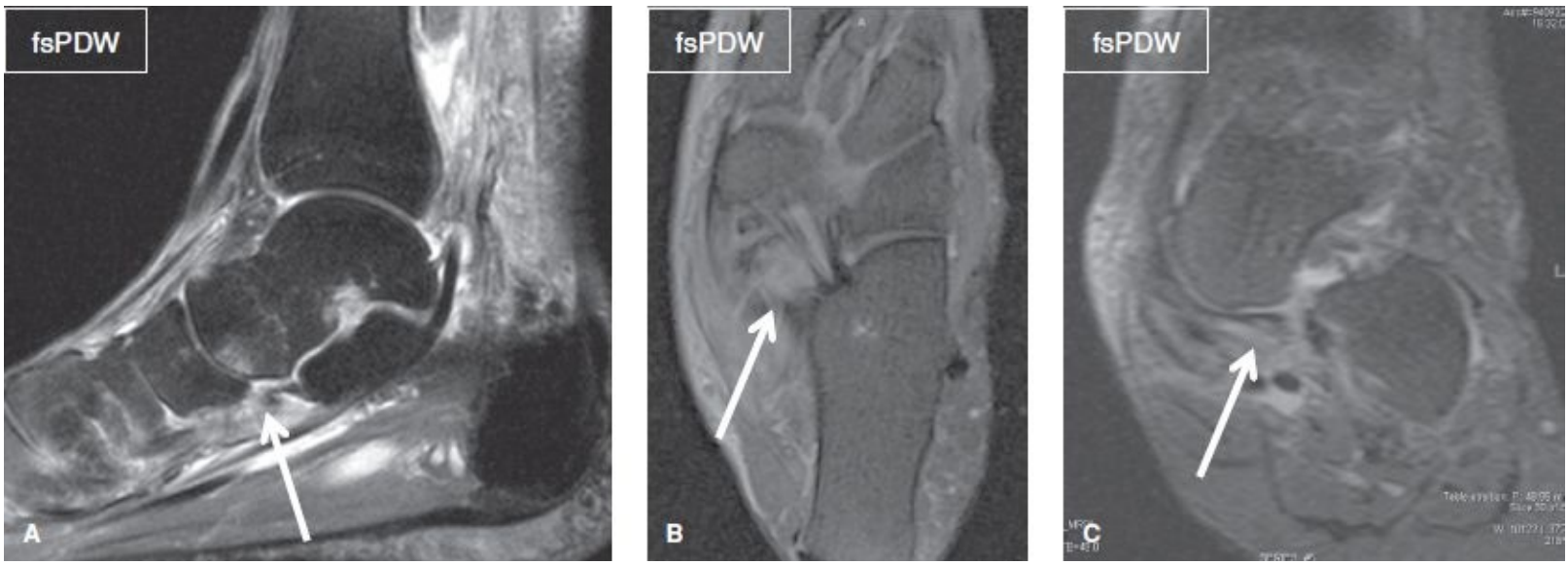

Fig. 34: Grade II sprain of the spring ligament. Sagittal **(A),** axial **(B),** and coronal **(C)** images demonstrate a partial thickness tear of the medioplantar oblique band of the spring ligament (*arrows*) with adjacent fascial edema.

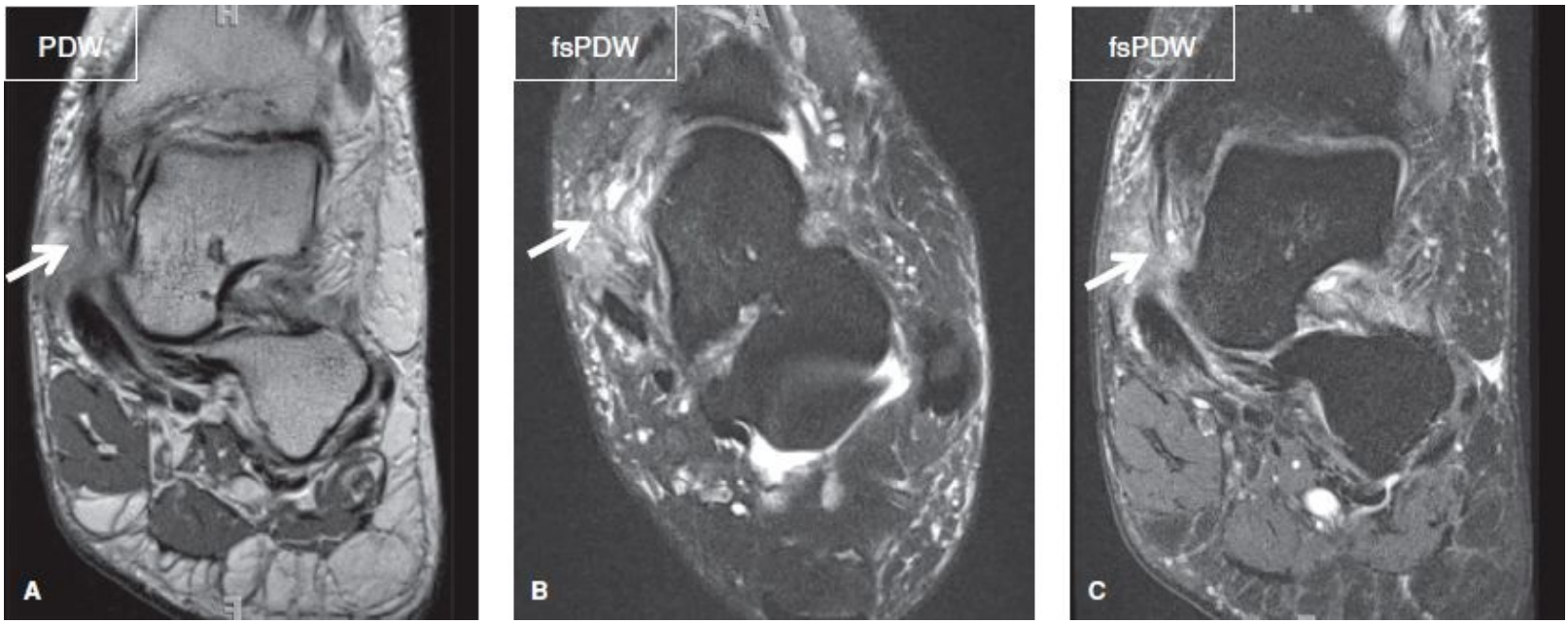

Fig. 35: Grade III sprain of the tibiospring ligament and superomedial band of the spring ligament. Coronal **(A, C)** and axial **(B)** images exhibit discontinuity of the tibiospring ligament and superomedial band of the spring ligament (*arrows*), as well as edema of the surrounding soft tissues. Notice edema and scarring suggesting sinus tarsi syndrome.

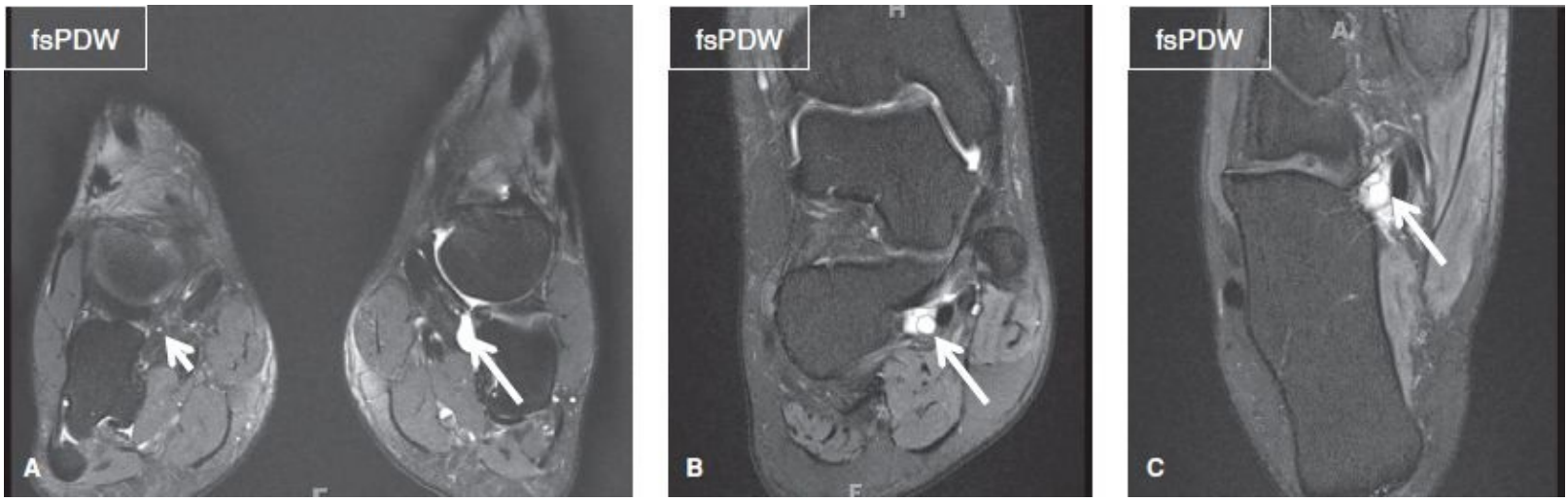

Fig. 36: The plantar recess of the spring ligament. Coronal image **(A)** of both ankles demonstrates the normal recess of the spring ligament (*short arrow*), located between its superomedial and medial plantar oblique bands in the right ankle and small synovial diverticulum (*long arrow*) in the left ankle. Coronal **(B)** and axial images **(C)** in another individual show a multiloculated ganglion (*arrows*) at the expected recess.

Fig. 37: Ganglion of the deltoid ligament. Coronal image exhibits a ganglion (*arrow*) within the substance of the deltoid ligament, related to chronic ligamentous and adjacent synovial injury.

LATERAL STRUCTURES:

Lateral malleolus: [<Normal> <Enthesopathy> <Contusion>]

Retromalleolar groove: [<Concave> <Flat> <Convex>]

TENDONS:

PL: [<Normal> < Tendinosis> <Tenosynovitis> <Split tear> <Complete tear>]

Peroneus brevis (PB): [<Normal> <Tendinosis> <Tenosynovitis> <Split tear> <Complete tear>]

Superior peroneal retinaculum (SPR): [<Intact> < Thickened> <Deficient>]

LIGAMENTS:

Interosseous (syndesmosis): [<Intact> <Thickened> <Acute sprain>]

Anterior inferior tibiofibular (syndesmosis): [<Intact> <Thickened> <Acute sprain>]

Posterior inferior tibiofibular (syndesmosis): [<Intact> <Thickened> <Acute sprain>]

AFL: [<Intact> <Thickened> <Attenuated> <Acute sprain>]

CFL: [<Intact> <Thickened> <Attenuated> <Acute sprain>]

PFL: [<Intact> <Thickened> <Mucoid degeneration> <Acute sprain>]

Bifurcate ligament: [<Intact> <Thickened> <Acute sprain>]

The lateral malleolus is also best assessed on coronal non–fs images for enthesopathy, old/recent fractures, or accessory ossicles. Fat-suppressed images are useful for detection of subcortical avulsive cystic changes or bone marrow edema from extensor/peroneal retinaculum or ligament avulsion, contusion, and fracture. Beware of poor fat saturation images, especially on low-field scanners to avoid overcalling bone marrow edema. Inversion recovery images perform better than frequency-selective fat saturation images on low field scanners. The retromalleolar groove is best assessed on the axial images, about 1 cm proximal to the tip of the fibula. In 82% of individuals it is smooth and concave, though less commonly it assumes a flat or convex configuration with or without irregular contour. The latter predisposes to peroneal tendon subluxation or dislocation and mechanical attrition (Fig. 38). The SPR, a thickening of the deep fascia, extends from the lateral malleolus to the deep fascia of foot or the calcaneus. The inferior peroneal retinaculum (IPR) extends from the posterior surface of the lateral malleolus to the peroneal tubercle (trochlea) of the lateral calcaneus, distal to the retrotrochlear eminence, where the CFL inserts (Fig. 39).

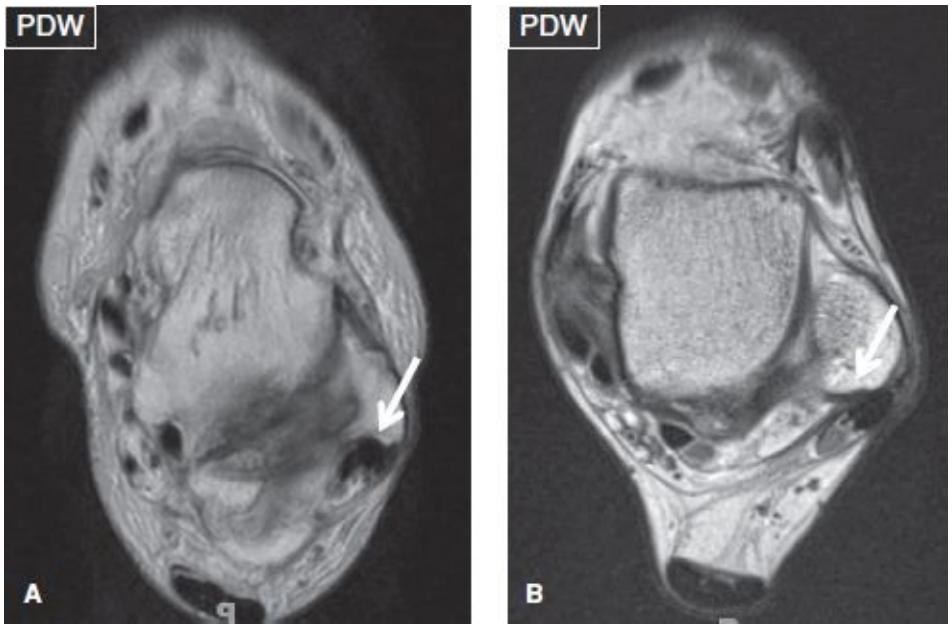

Fig. 38: Morphology of the retromalleolar groove. Axial images demonstrate a concave (*arrow* in **A**) and a flat (*arrow* in **B**) retromalleolar groove.

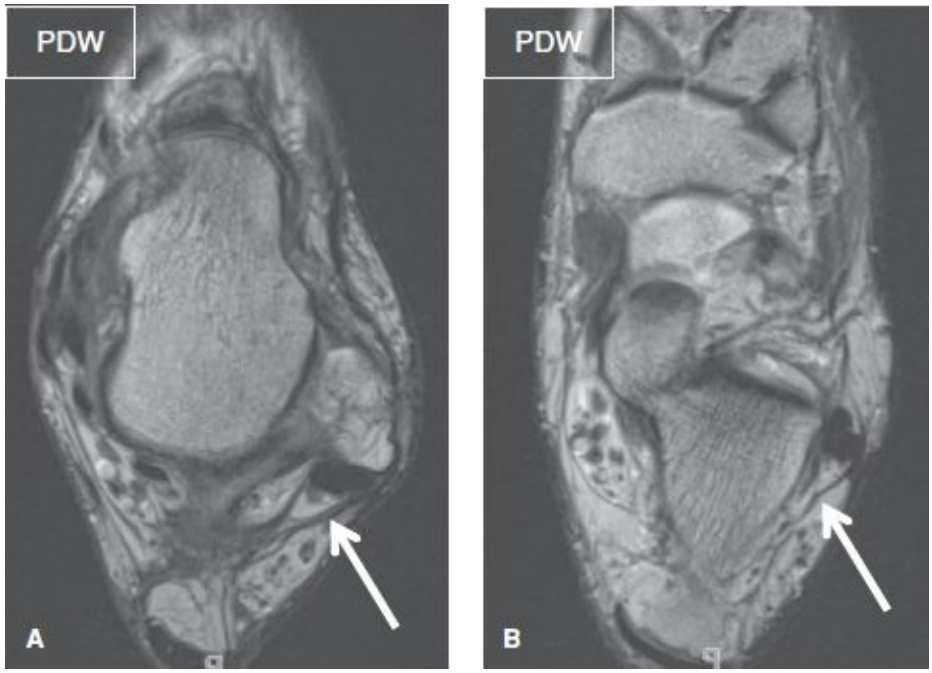

Fig. 39: Axial images **(A, B)** show the normal SPR (*arrow* in **A**) and IPR (*arrow* in **B**).

Similar to other tendons, the peroneal tendons are best evaluated on the axial images. The PL tendon is superficial to the PB tendon, the muscle belly of which extends inferiorly to the level of the malleolus (Fig. 40). Both tendons are contained at the retromalleolar groove by the SPR, and adjacent to the calcaneal tubercle by the IPR. They have a common tendon sheath at the level of the SPR, and separate sheaths at the level of the IPR. The PL tendon curves under the foot, courses through the cuboid sulcus and inserts as multiple fibers at the lateral aspect of the base of the first metatarsal and medial cuneiform. The PB tendon insets at the base of the fifth metatarsal bone. The PL plantarflexes the ankle, everts the foot, and supports the longitudinal and transverse foot arches during ambulation. The PB lies deep to PL and everts the foot. An accessory muscle, the peroneus quartus, may be present in up to 20% individuals (Figs. 41, 42). This accessory muscle originates from the distal fibula, PL or PB and has variable insertions on the lateral foot bones, including the peroneal retinaculum.

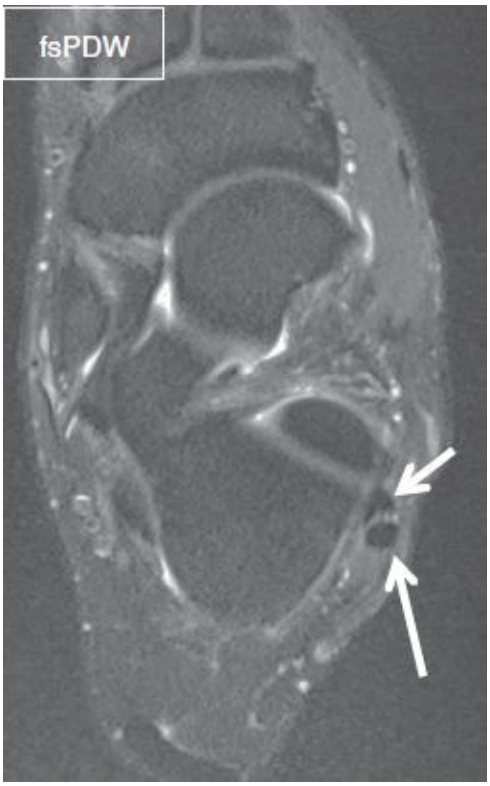

Fig. 40: Normal peroneal tendons. Axial image shows a normal crescentic-shaped peroneal brevis tendon (*short arrow*) and a normal oval-shaped peroneal longus tendon (*long arrow*).

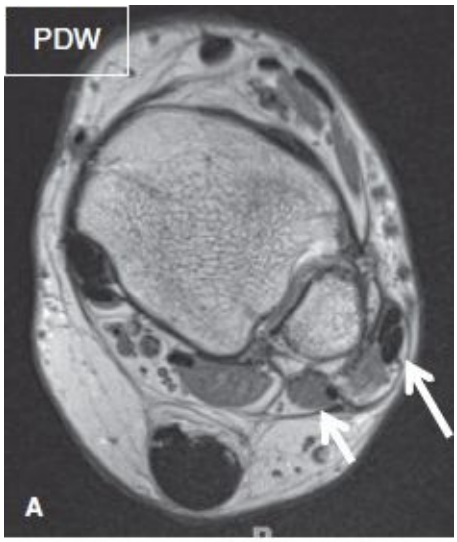

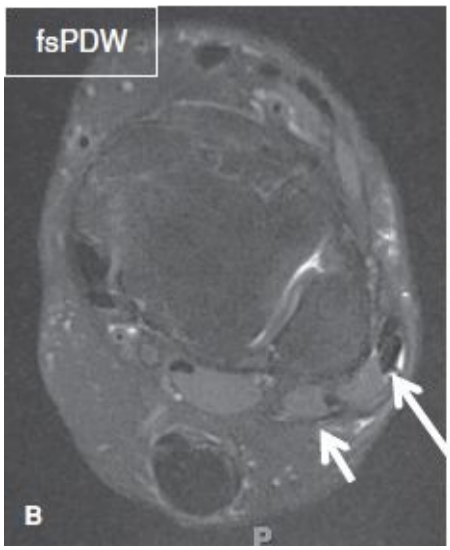

Fig. 41: Axial images **(A, B)** show peroneus quartus muscle (*short arrows*) posterior to the PL and PB tendons (*long arrows*).

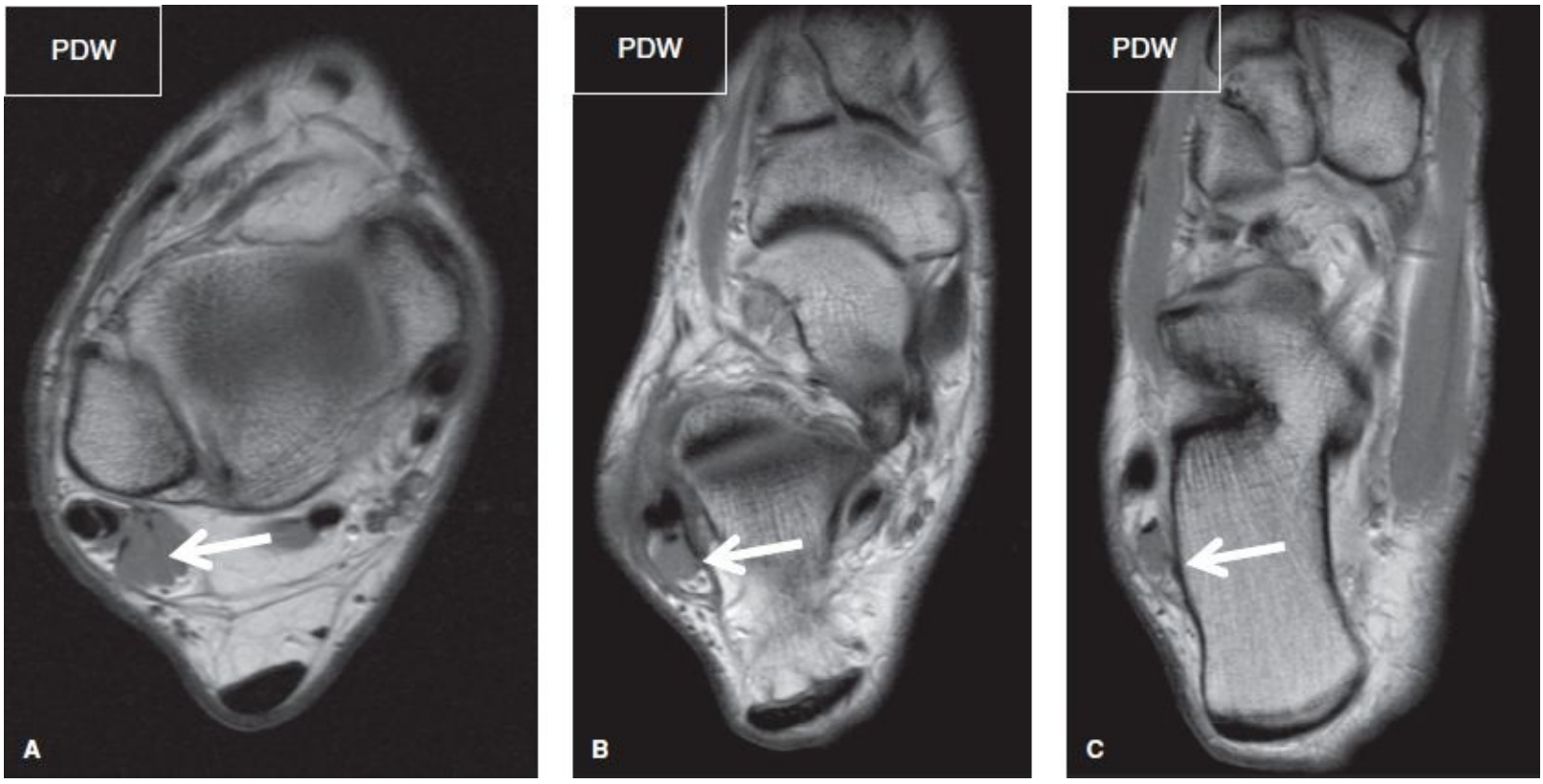

Fig. 42: Peroneus quartus muscle. Axial images **(A–C)**. An accessory muscle is present in the lateral compartment (*arrows*) posterior to the peroneus longus and brevis.

The peroneal tendons frequently undergo injuries including tendinosis, tenosynovitis, tear, and dislocation. A small amount of fluid may normally be present within the peroneal tendon sheath. The fluid is considered pathologic when a) it correlates to the patient's site of maximal pain, or b) is, circumferential about the tendon, or is greater than 2 mm in thickness when measured from the tendon edge to the synovial sheath. Apart from tenosynovitis, fluid could accumulate in the peroneal sheath in the setting of a torn CFL, which forms the floor of the peroneal tendons, or with calcaneus fracture. Peroneal tendinosis manifests as increased intrasubstance signal with or without tendon thickening. The PB and PL are considered thickened if they are equal to or larger in size than the PTT.

The PB tendon undergoes tears much more commonly than the PL tendon. Longitudinal (split) tears of the PB tendon often originate within the fibular groove, where the tendon can get entrapped between the PL tendon and the lateral malleolus. Conditions predisposing to split tear include SPR tear or laxity, flat or convex posterior aspect of the lateral malleolus, low-lying PB muscle belly (extending inferior to the tip of the lateral malleolus), peroneal tubercle hypertrophy, and presence of the accessory peroneus quartus muscle. When split, the PB tendon partially envelops the PL tendon and the split fragments encircle on either side of PL that are 2.5–5 cm in length and reconstitute distally along the length of the tendon, proximal to its insertion (Fig. 44). This creates a "Mickey Mouse ears"

configuration, where the face is formed by the PL tendon and the ears by the PB subtendons. A C-shaped or boomerang (pre-split) configuration below the lateral malleolus is a degenerative variant on MR imaging and should not be overcalled as split tear. In acute cases, marrow edema of the lateral calcaneus at the retinacular attachment site may be present. One should be aware of the bifid PB or bifid peroneus quartus tendons, normal variants, in which the two tendons simulate the subtendons of a PB tendon split tear. The key to avoid misdiagnosis is the identification of separate muscle fibers about each of the bifurcated tendons (Fig. 45). In children, the PB tendon may avulse from the base of the fifth metatarsal. The bony fracture assumes a transverse orientation, which can be distinguished from the normal ossification center that is longitudinally oriented.

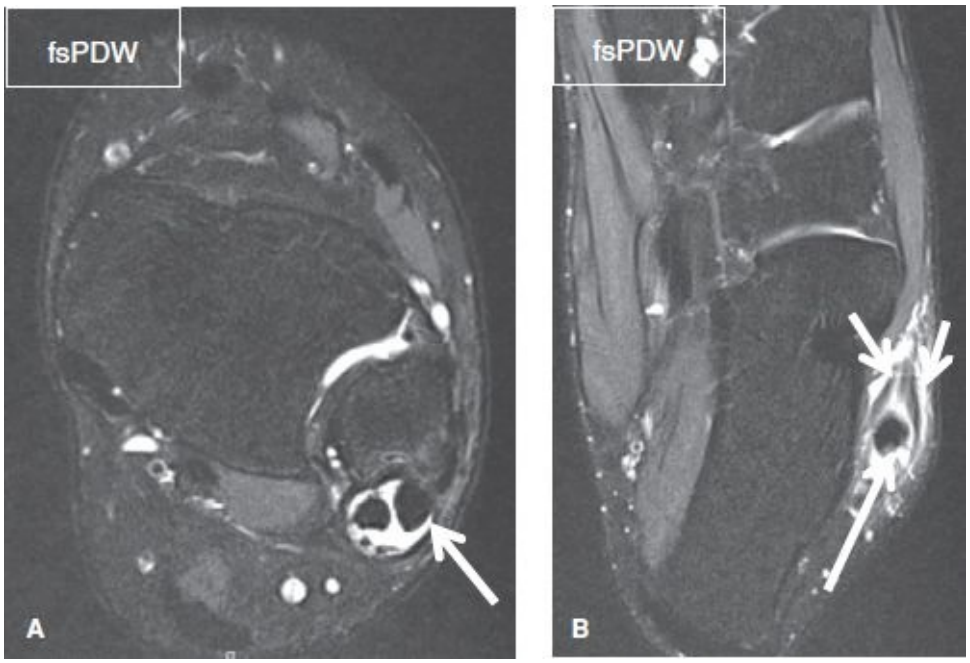

Fig. 43: Peroneal tenosynovitis and longitudinal split tear of the peroneus brevis tendon on the axial images. **A:** Circumferential fluid collection is evident within the common peroneal tendon sheath (*arrow*), in keeping with tenosynovitis. **B:** The peroneus brevis tendon has been divided into two separate subtendons (*short arrows*) which partially envelope the peroneus longus tendon (*long arrow*), in this case of peroneus brevis longitudinal split tear.

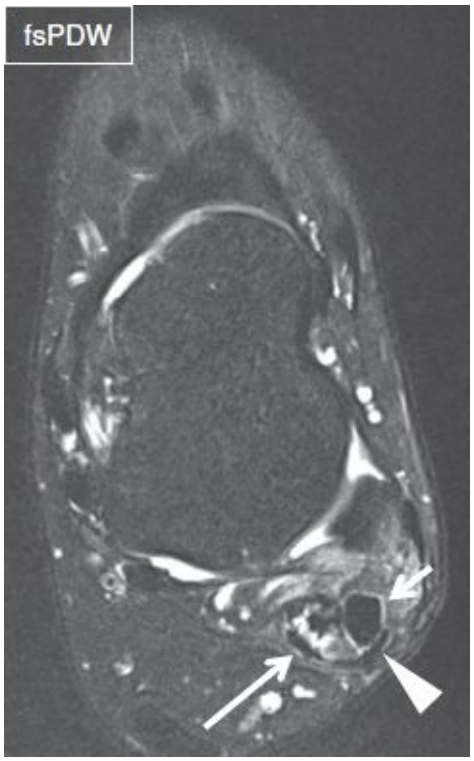

Fig. 44: Peroneus brevis tendon with multiple split tears (shredded tendon). Axial image demonstrates a normal peroneus longus tendon (*short arrow*), as well as multiple subtendons in the expected location of the peroneus brevis tendon (*long arrow*), in keeping with multiple split tears. The superior peroneal retinaculum is torn (*arrowhead*).

Fig. 45: Bifid peroneus brevis tendon. Axial image demonstrates the two tendons (*arrows*) of the peroneus brevis muscle, which originate from separate muscle fibers.

The PL tendinosis is much more common than the frank tears. PL tendinosis can be present at the retromalleolar groove or immediately above the cuboid sulcus. One should

also be aware of the magic angle artifact that may cause artifactual alteration of the signal intensity of the PL tendon just above the cuboid sulcus. PL tendon tears most often occur at the level of the peroneal tubercle or the cuboid tunnel, and may be associated with lateral collateral ligament sprains and marrow edema of the cuboid or the lateral calcaneus (Figs. 46, 47). In complete PL tendon rupture, sagittal images can be prudently used to measure the tendon retraction. An os peroneum is a small round or oval-shaped accessory ossicle located immediately proximal to the base of the fifth metatarsal and within the substance of the PL tendon, adjacent to the calcaneocuboid joint (Fig. 48). Os peroneum is very common, present in about 26% of feet, may be uni- or multi-partite, and should not be erroneously interpreted as an avulsion fracture. When multi-partite, it features a synchondrosis less than 2 mm thick. The term painful os peroneum syndrome (POPS) presents as acute or chronic lateral pain, tenderness, and swelling along the course of the PL tendon. It can be caused by a wide spectrum of pathologies including os peroneum fracture, hypertrophic healing of a fractured os peroneum, diastases of a multi-partite os peroneum, attrition or tear of the PL tendon proximal or distal to the sesamoid bone, or an enlarged painful peroneal tubercle. Common imaging findings include an edematous and fragmented ossicle within the substance of a thickened partially torn PL tendon, with diastasis and retraction of the proximal fragment (Figs. 49, 50). Similar to the PB tendon, the PL tendon is more prone to tears in the setting of a peroneus quartus accessory muscle. PL tendon and PB tendon split- or complete tears can also occur simultaneously (Fig. 51). The relevant differential diagnoses include fifth metatarsal fracture, cuboid fracture, or SPR injury.

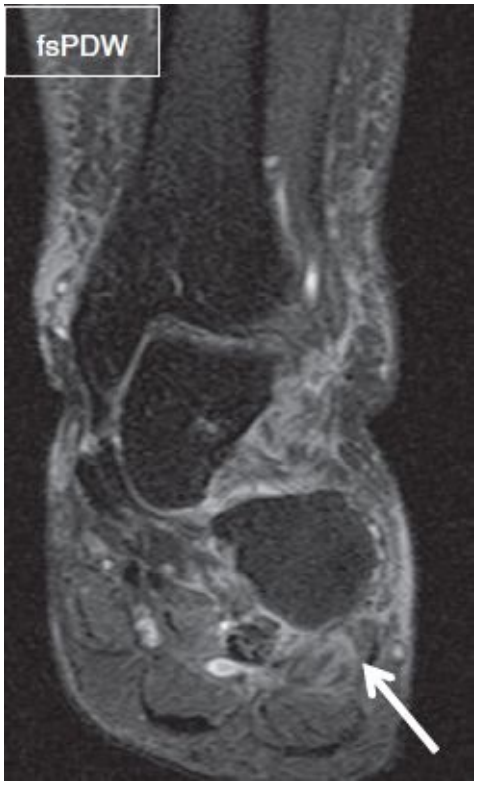

Fig. 46: Split tear of the peroneus longus tendon. Coronal image exhibits a high-grade split tear of the peroneus longus tendon (*arrow*) at the level of the cuboid sulcus.

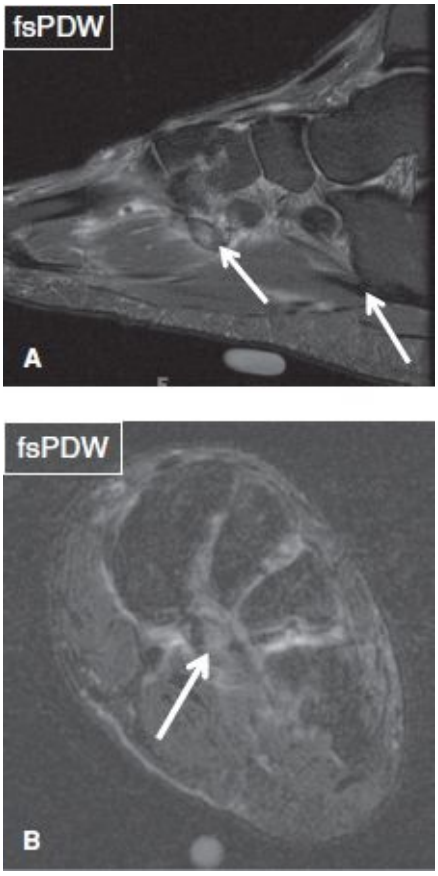

Fig. 47: Split tear of the peroneus longus tendon. Sagittal **(A)** and coronal **(B)** images exhibit a split tear of the peroneus longus tendon (*arrows*) under the arch of the foot.

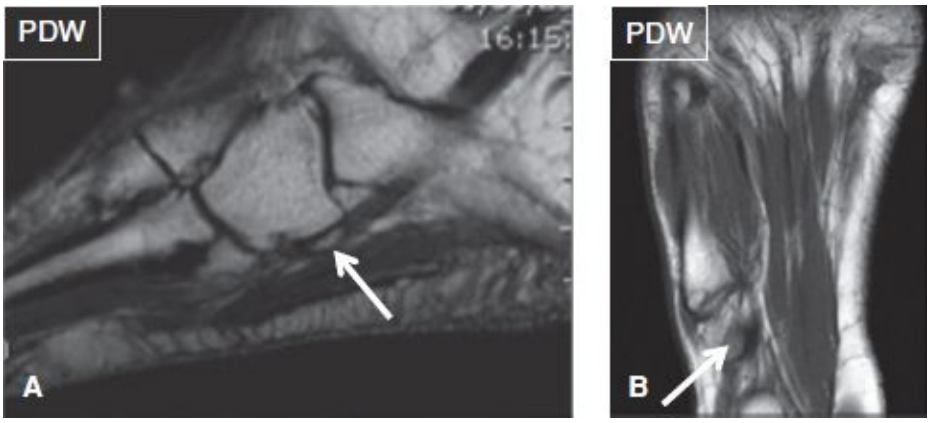

Fig. 48: Normal os peroneum. Sagittal **(A)** and axial **(B)** images demonstrate a normal os peroneum (*arrows*) as a small oval-shaped ossicle located within the substance of the distal peroneus longus tendon.

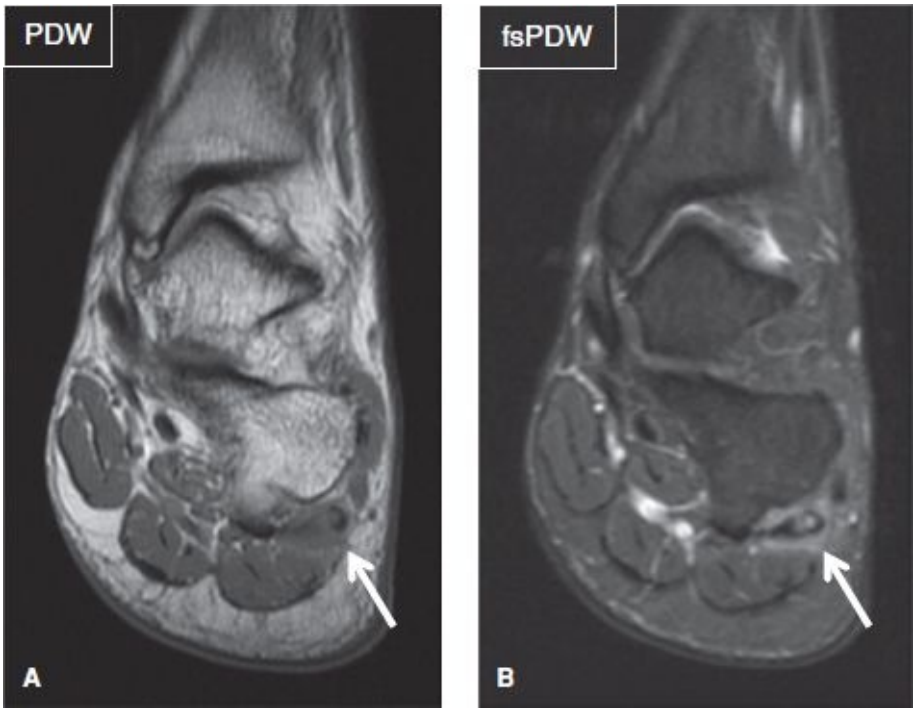

Fig. 49: Painful os peroneus syndrome. Coronal images exhibit an edematous os peroneum along with a partial tear of the distal peroneus longus tendon (*arrows*).

Fig. 50: Painful os peroneus syndrome. Sagittal image shows an edematous os peroneum (*short arrow*) and a completely torn and retracted peroneus longus tendon (*long arrow*).

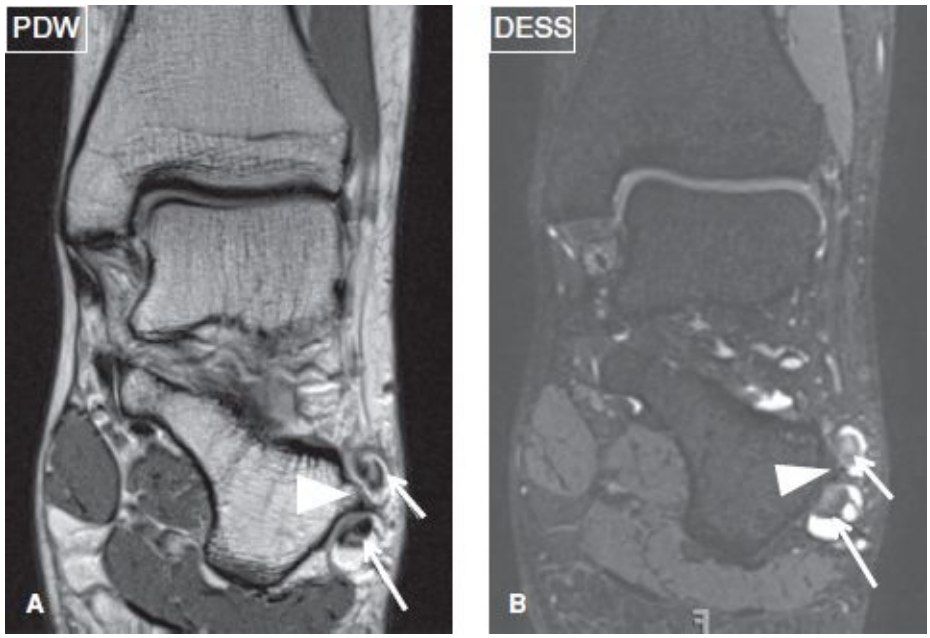

Fig. 51: Concomitant split tears of the peroneus longus and brevis tendons in the setting of a prominent peroneal tubercle. Coronal images **(A, B)** show tenosynovitis and longitudinal split tears of the peroneus longus (*long arrows*) and peroneal brevis (*short arrows*) tendons. Note the prominent peroneal tubercle (*arrowheads*), which predisposes to the peroneal tendons injury.

Dislocation of the peroneal tendons from the retromalleolar groove may occur following disruption of the SPR with or without associated bony avulsion fleck or stripping of the periosteum at its attachment from the fibula, and sometimes with calcaneal fractures. On axial images, the peroneal tendons are located anterior and lateral to the distal fibula and are often found within a "pouch" formed by the partially ripped SPR. Associated findings may include tenosynovitis or tears of the peroneal tendons, convex fibular groove, avulsion fracture of the distal fibula, and tear of the lateral collateral ligament (Fig. 52). SPR and IPR pathologies are rare, and more commonly, these are seen as abnormal thickenings with or without underlying enthesopathy in the setting of prior injury or repeated episodes of ankle instability (Fig. 53).

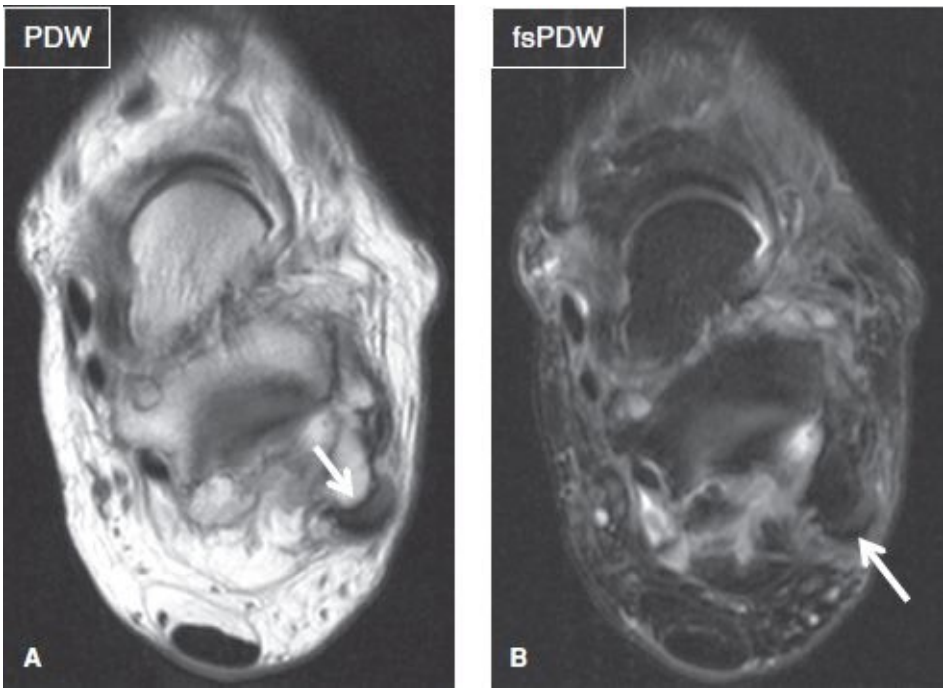

Fig. 52: Peroneal tendons subluxation at the setting of convex retromalleolar groove on the axial images. **A:** The retromalleolar groove has a posterior convex configuration **B:** The peroneal tendons (*arrows*) are subluxed over the retromalleolar groove, and are inhomogeneous, in keeping with tendinosis.

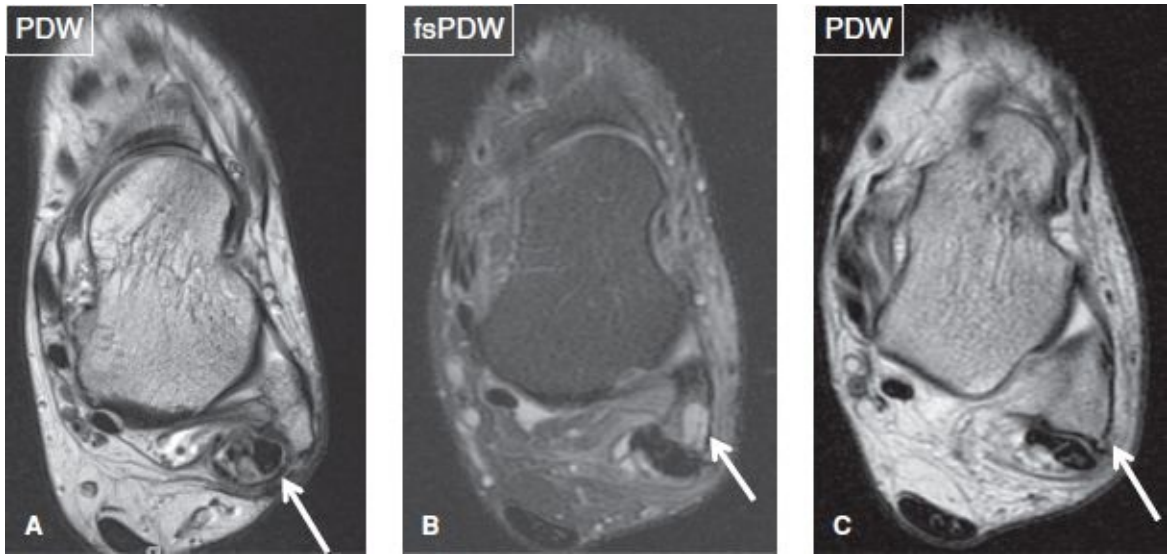

Fig. 53: Chronic superior peroneal retinaculum injury. **A, B:** Axial images from one patient show a thickened superior peroneal retinaculum (*arrow* in **A**) and a focal avulsive cystic change at the malleolar attachment (*arrow* in **B**). **C:** Axial image from another patient demonstrates enthesopathic changes at the superior peroneal retinaculum malleolar attachment.

The syndesmotic ligaments bind the distal tibiofibular articulation. These include the interosseous, the anterior distal tibiofibular ligament (ATFL), and the posterior distal tibiofibular (PTFL) ligament. The interosseous ligament is a thickening of the interosseous membrane, formed approximately 1.5 cm above the joint line and borders the tibiotalar synovial recess. The ATFL and PTFL are 3–5 mm thick, and are oriented obliquely above the

joint line. These are best seen on coronal and axial images. On straight axial images, fat planes around the multi-layered ATFL and PTFL contribute to partial volume averaging, and the ligaments assume a striated configuration, similar to the deltoid ligament (Figs. 54–57).

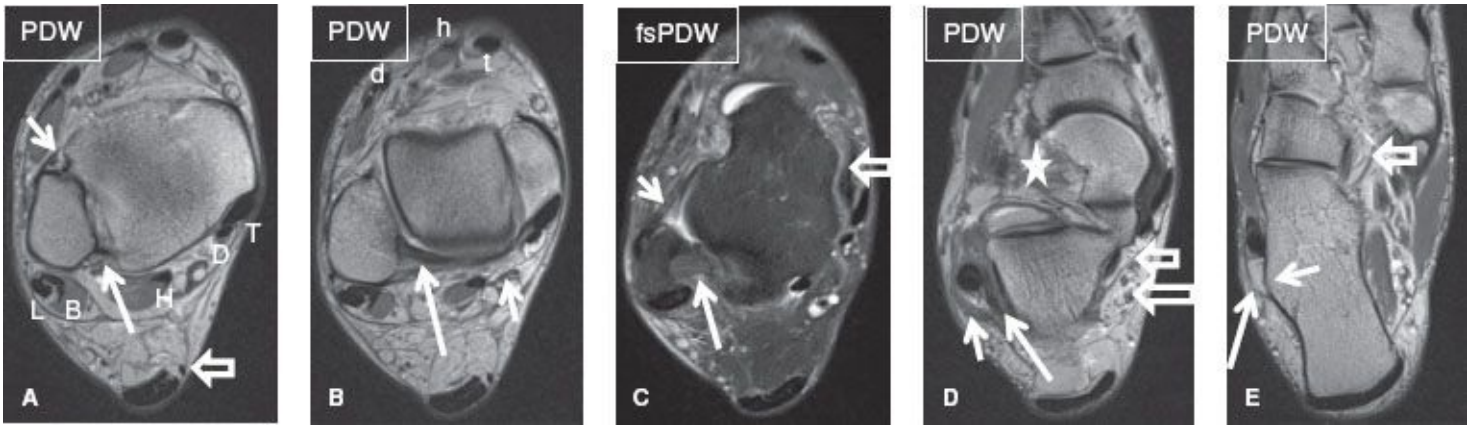

Fig. 54: Normal anatomy. Consecutive axial images from the level of the ankle joint to the level of the calcaneonavicular joint. **A:** *Short arrow,* anterior distal tibiofibular ligament; *long arrow,* posterior distal tibiofibular ligament; *open arrow,* plantaris tendon; B, peroneus brevis tendon/muscle; L, peroneus longus tendon; T, tibialis posterior tendon; D, flexor digitorum longus tendon; H, flexor hallucis longus tendon. **B:** *Long arrow,* posterior intermalleolar ligament; *short arrow,* tibial nerve; d, extensor digitorum longus tendon; h, extensor hallucis longus tendon; t, tibialis anterior tendon. **C:** *Long arrow,* posterior talofibular ligament; *short arrow,* anterior talofibular ligament; *open arrow,* posterior tibial tendon. **D:** *Long arrow,* calcaneofibular ligament; *short arrow,* inferior peroneal retinaculum; *star,* sinus tarsi; *small open arrow,* medial plantar nerve; *large open arrow,* lateral plantar nerve. **E:** *Long arrow,* inferior peroneal retinaculum; *short arrow,* peroneal tubercle of the calcaneus; *open arrow,* recurrent slip of tibialis posterior tendon.

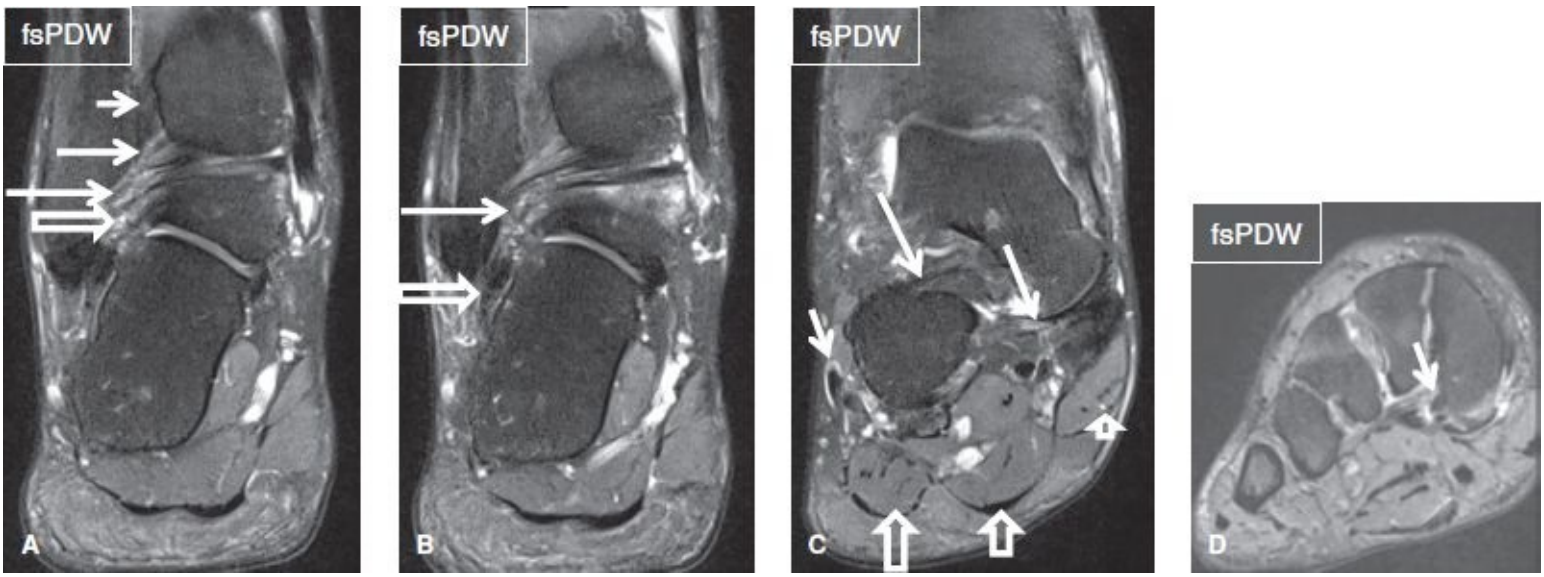

Fig. 55: Normal anatomy on coronal images. **A:** *Short arrow,* interosseous ligament; *medium arrow,* posterior distal tibiofibular ligament; *long arrow,* posterior intermalleolar ligament; *open arrow,* posterior talofibular ligament. **B:** *Long arrow,* posterior intermalleolar ligament;

open arrow, calcaneofibular ligament. **C:** *Long arrow,* cervical ligament; *medium arrow,* plantar calcaneonavicular (spring) ligament; *short arrow,* peroneal tendons; *long open arrow,* abductor digiti minimi muscle; *medium open arrow,* flexor digitorum brevis muscle; *short open arrow,* abductor hallucis muscle. **D:** Peroneus longus tendon insertion (*arrow*).

Fig. 56: Normal anatomy on sagittal images. **A:** *Long arrow,* bifurcate ligament; *short arrow,* sinus tarsi; *star,* Achilles tendon. **B:** *Long arrow,* bifurcate ligament; *medium arrow,* posterior interosseous ligament; *short arrow,* dorsal talonavicular ligament. **C:** *Long arrow,* posterior talofibular ligament; *short arrow,* anterior talofibular ligament.

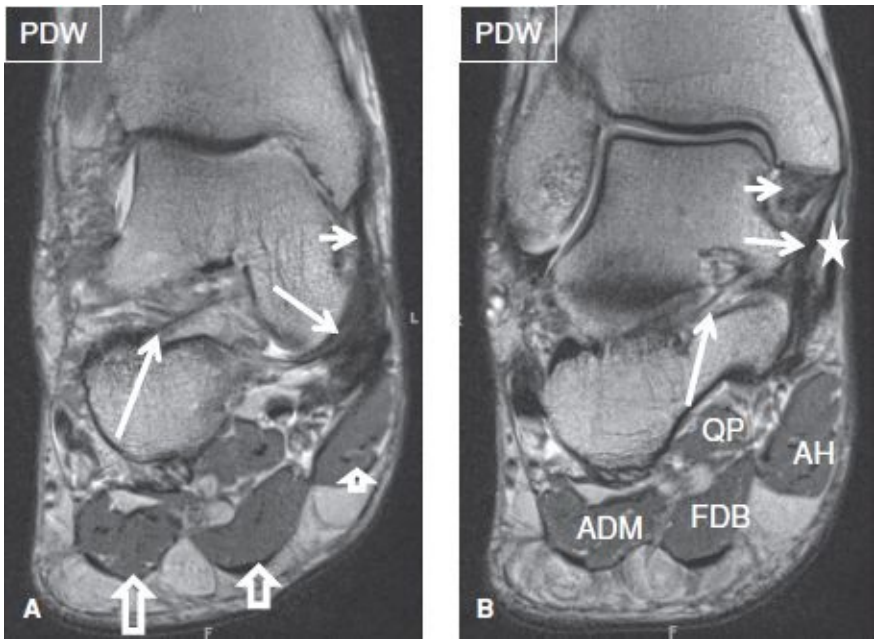

Fig. 57: Normal anatomy on coronal images. **A:** *Long arrow,* cervical ligament; *medium arrow,* spring ligament; *short arrow,* tibiospring ligament; *long/medium/short open arrows,* lateral/middle/medial cords of the plantar fascia. **B:** *Long arrow,* interosseus talocalcaneal ligament; *medium arrow,* tibiocalcaneal ligament; *short arrow,* posterior deep tibiotalar ligament; *star,* posterior tibial tendon; QP, quadratus plantae muscle; ADM, abductor digiti minimi muscle; FDB, flexor digitorum brevis muscle; AH, abductor hallucis muscle.

Syndesmotic ligament injury is referred to as “high ankle sprain.” A syndesmotic ligament injury or “high ankle sprain” can be isolated or may occur in conjunction with injury of other ligament groups, and Weber B or C ankle fractures. Acute ligament injuries are classified as grade I, II, and III sprains, similar to other ligament injuries in the body (Figs. 58, 59). On radiographs, one may see greater than 6 mm widening of the syndesmotic space. Secondary signs include fluid within the tibiofibular space extending more than 1–1.5 cm above the tibial plafond level with or without tibiofibular space diastasis; associated medial or posterior malleolar fractures and osteochondral injury of the talar dome. In subacute and chronic cases, ligament thickening or attenuation is evident with enthesopathy and/or subcortical cystic changes at the bony attachment sites, with sometimes associated hypointensity of the interosseous membrane due to heterotopic ossification. Related fractures are termed, Volkmann fracture (PTFL avulsion from lateral aspect of posterior malleolus) and Tillaux fracture (avulsion of ATFL from lateral margin of anterior tibia). The Tillaux fracture is a Salter III injury and is distinguished from trimalleolar fracture due to lack of fracture component in the coronal plane. Associated synovial injury can result in formation of a synovial diverticulum (unilocular) or a ganglion cyst (multilocular), which may present clinically as soft-tissue lesions (Fig. 60).

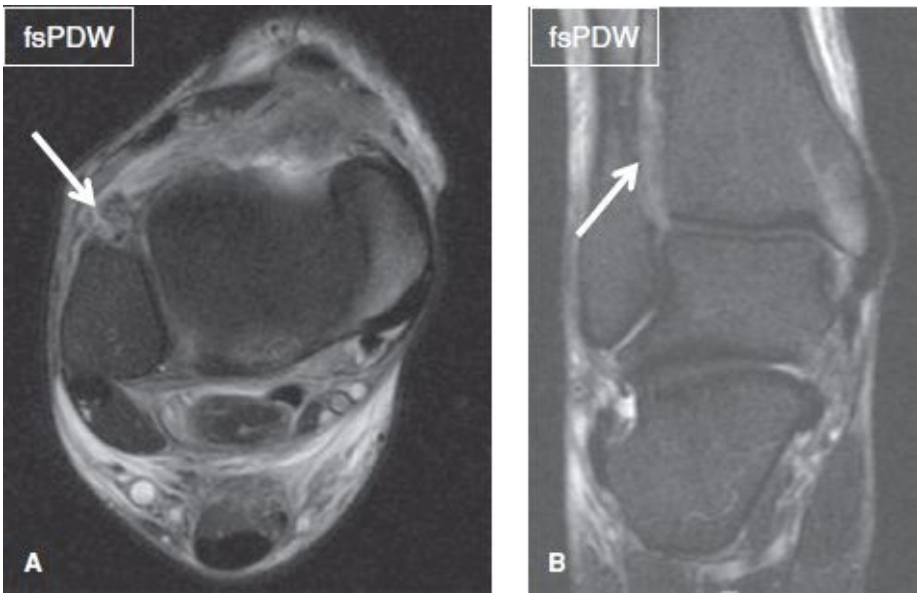

Fig. 58: Acute anterior syndesmotic injury. Axial **(A)** and coronal **(B)** images exhibit a partial tear of the anterior distal tibiofibular ligament (*arrows*), consistent with a grade II sprain.

Fig. 59: Syndesmotic ligament injury ("high ankle sprain"). Coronal **(A)** and axial **(B)** MR arthrogram images exhibit a complete tear (grade III sprain) of the anterior distal tibiofibular ligament (*short arrows*). Notice small ganglion in relation to interosseus talocalcaneal ligament (*long arrow*).

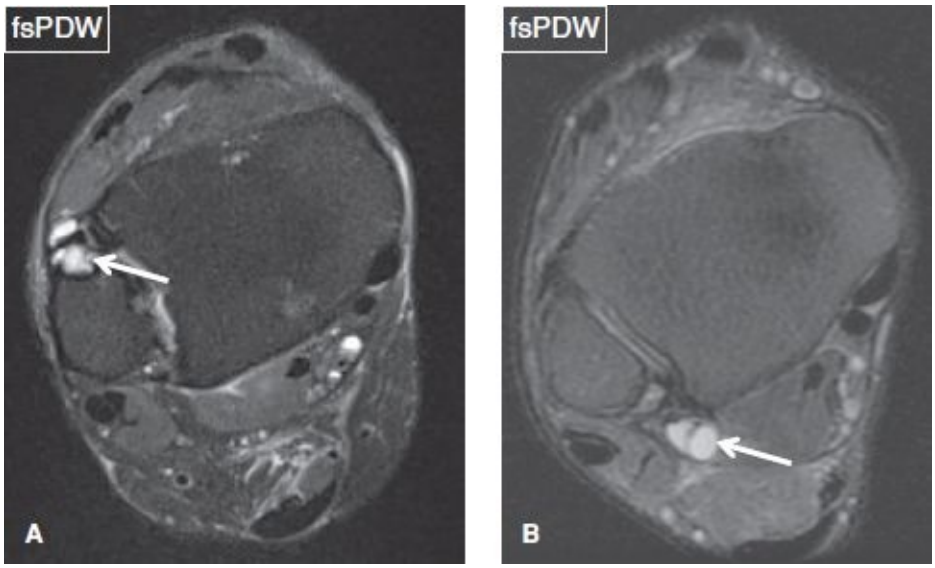

Fig. 60: Chronic syndesmotic ligament injury with associated ganglion formation. Axial images from different cases show ganglions of the anterior **(A)** and posterior **(B)** distal tibiofibular ligaments, related to chronic injuries.

The lateral ligament complex is comprised of the AFL, CFL, and PFL, which are adequately imaged on the axial and coronal images. The AFL and PFL are seen inferior to the level of the joint line, and almost at the mid-level of the lateral malleolus. The AFL is 2–3 mm thick, and appears as a triangular or flat band of low signal intensity, which extends from the anterior margin of the lateral malleolus, 1 cm above its tip, and inserts just anterior to the fibular articular surface of the talus. Intimately related to the joint capsule, the AFL also forms the superficial margin of the articular recess known as the anterolateral gutter. The AFL provides protection from anterior translation, inversion, and internal

rotation. The PFL is thicker (4–6 mm) than the AFL, attaches from lateral malleolar fossa to lateral talar tubercle, and has a striated configuration on axial images, similar to that of the deep deltoid ligament or anterior cruciate ligament of the knee (Fig. 54). The CFL is similar in thickness to the AFL and is best seen on sequential coronal and axial images, underneath the peroneal tendons. It extends from the tip of the lateral malleolus to the retrotrochlear eminence and forms the floor of the peroneal tunnel, separating the tendons from the ankle joint fluid or joint effusion. On axial images, the ligament is identified as a hypointense thin band paralleling the lateral calcaneal wall, though it is more consistently visualized on the coronal images, where it is depicted in cross-section as a ovoid, homogeneous, hypointense structure that can be followed up on sequential images from its fibular origin to its calcaneal insertion site (Fig. 61). The CFL is key to lateral subtalar and ankle stability and protects against inversion sprain.

Fig. 61: Normal calcaneofibular ligament. Axial image demonstrates the normal calcaneofibular ligament (*arrows*), as a thin hypointense band, which extends from the tip of the lateral malleolus to the retrotrochlear eminence.

In inversion ankle sprain (the most usual type of ankle injury), the sequence of ligament injury is usually AFL (the weakest of the ligaments and therefore it can the most frequently torn), followed by the CFL, subsequently the sinus tarsi ligaments, and finally the PFL (rarely torn). Acute ligamentous injuries are classified as grade I, II, and III sprains, similar to other ligaments in the body (Fig. 62). Because the AFL is a thickening of the joint capsule, acute complete AFL disruption is associated with leakage of joint fluid into the anterolateral soft tissues (Fig. 63). In subacute and chronic cases, ligament thickening or attenuation is evident with enthesopathy and/or cystic changes at the bony attachment site.

Associated synovial injury may result in formation of a synovial diverticulum or a ganglion cyst, which may clinically present as a soft-tissue lesion (Fig. 64). When injured, the CFL is thickened and heterogeneous, and additional findings may include localized edema and/or hemorrhage, peroneal retinacular thickening, peroneal tendon(s) tenosynovitis and/or subluxation (Figs. 65–68). Complete PFL tear is very rare, the most common finding is ligament thickening with loss of striations and mucoid degeneration with or without ganglion formation, reflective of repeated partial tears and associated synovial injuries (Fig. 69). Complete AFL disruption is associated with forward displacement of the talus and with additional rupture of the CFL, medial tilting of the talus and progressive widening of the lateral joint space will be seen. As a consequence of chronic injury, hyalinization of tissue in the anterolateral recess, a meniscoid lesion, may result from AFL injury and it can contribute to anterolateral impingement (Fig. 70).

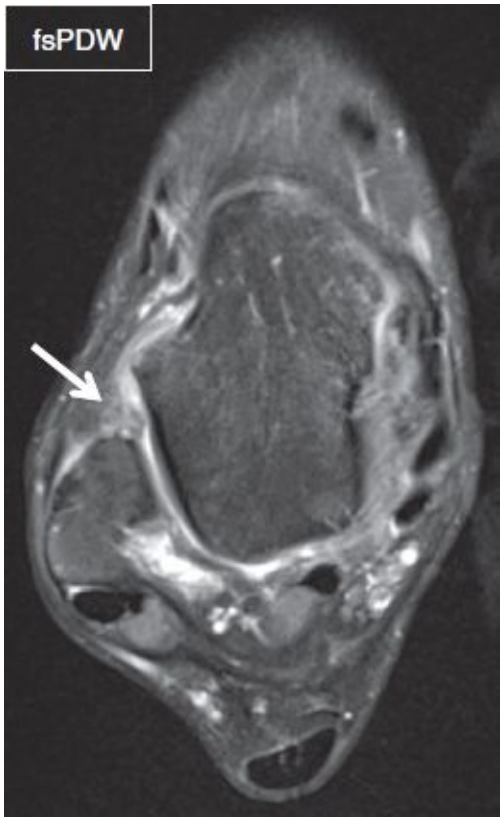

Fig. 62: Grade III sprain of the lateral ligament complex. Axial image demonstrates complete tear of the anterior talofibular ligament (*arrow*).

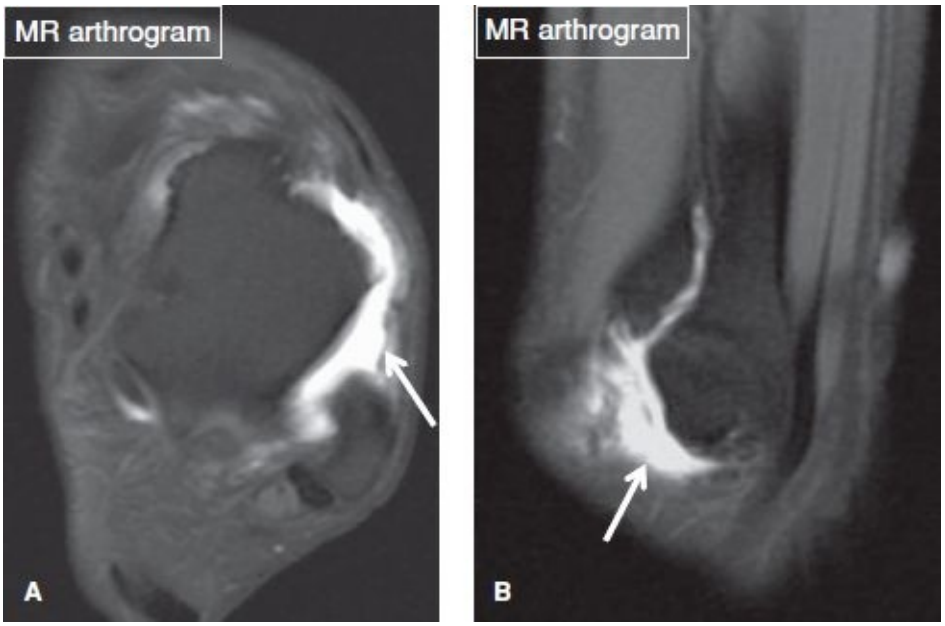

Fig. 63: Grade III sprain of the lateral ligament complex: Axial **(A)** and sagittal **(B)** MR arthrographic images demonstrate leakage of contrast medium (*arrows*) into the anterolateral soft tissues, in this case of anterior talofibular ligament complete tear.

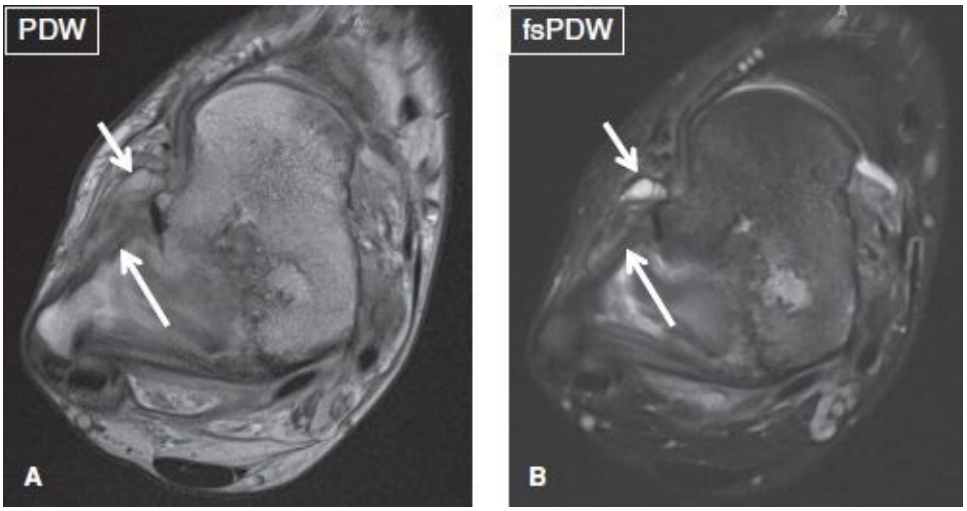

Fig. 64: Chronic injury of the anterior talofibular ligament. Axial images **(A, B)** show a thickened anterior talofibular ligament (*long arrows*), as well as a small adjacent ganglion (*short arrows*).

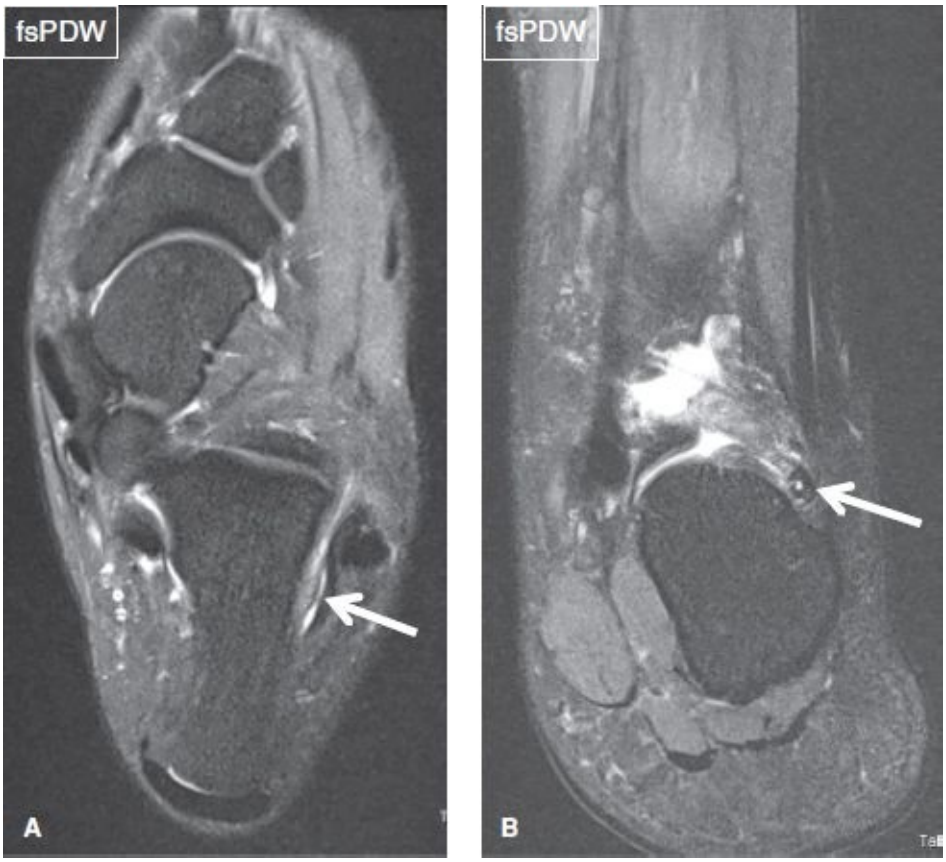

Fig. 65: Tear of the calcaneofibular ligament. Axial **(A)** and coronal **(B)** images exhibit a longitudinal split tear of the calcaneofibular ligament (*arrows*).

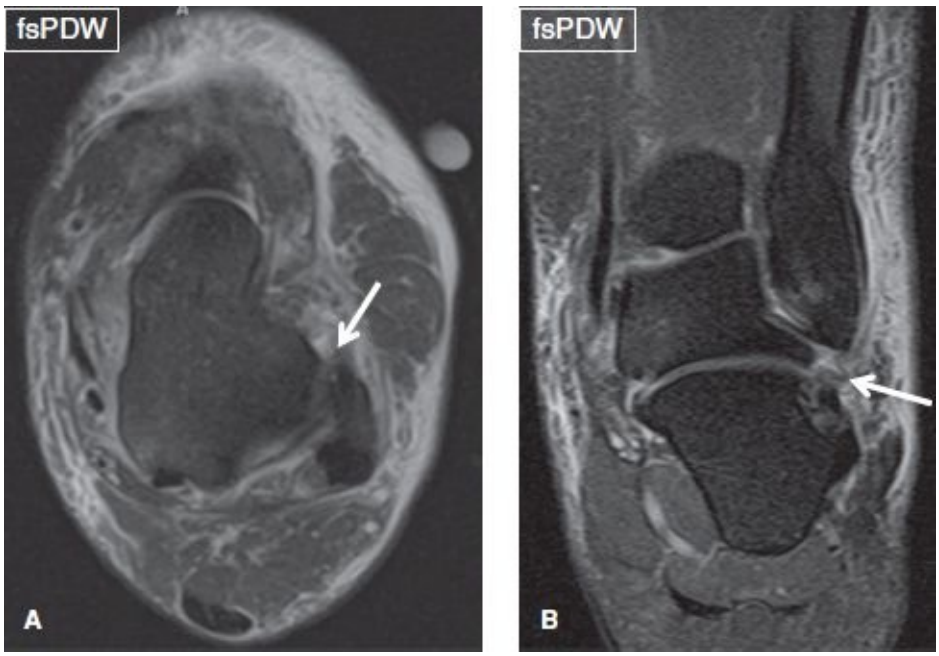

Fig. 66: Lateral ligament complex injury. The anterior talofibular (*arrow* in **A,** axial image) and calcaneofibular (*arrow* in **B,** coronal image) ligaments are completely torn and retracted. Edema of the adjacent soft tissues indicates a recent injury.

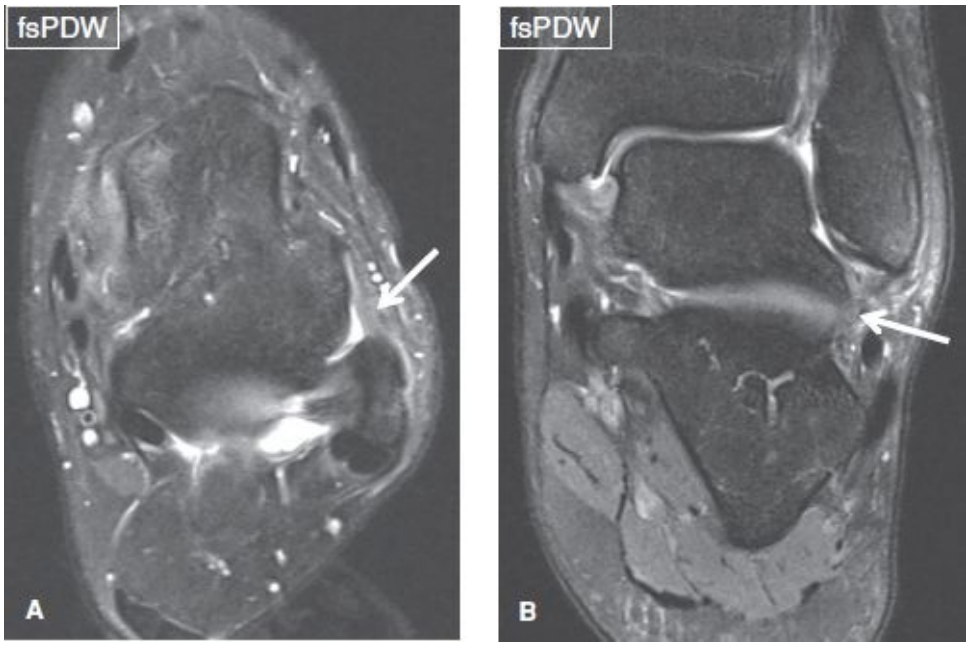

Fig. 67: Remote complete lateral ligament complex injury. Non-visualization of anterior talofibular (*arrow* in **A,** axial image) and calcaneofibular (*arrow* in **B,** coronal image) ligaments is compatible with complete tears. Absence of edema of adjacent soft tissues indicates a remote injury.

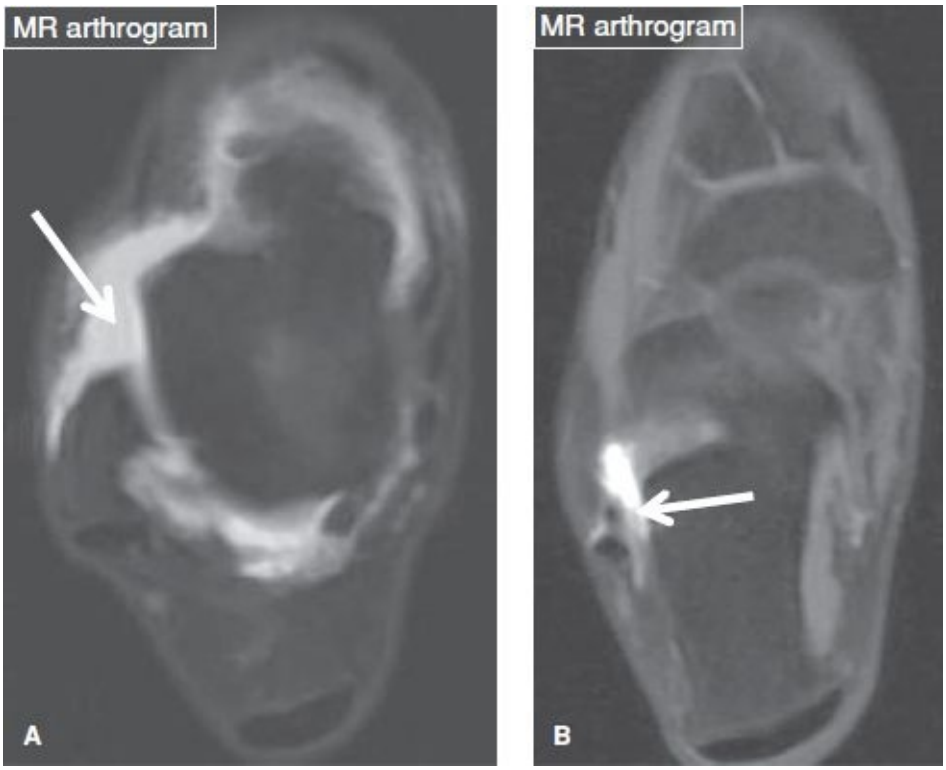

Fig. 68: Lateral ligament complex injury on axial MR arthrographic images. **A:** The anterior talofibular ligament is not visualized (*arrow*). Leakage of contrast medium is apparent in the anterolateral soft tissues. **B:** Contrast medium is abutting the peroneal tendons, indicating complete tear of the calcaneofibular ligament.

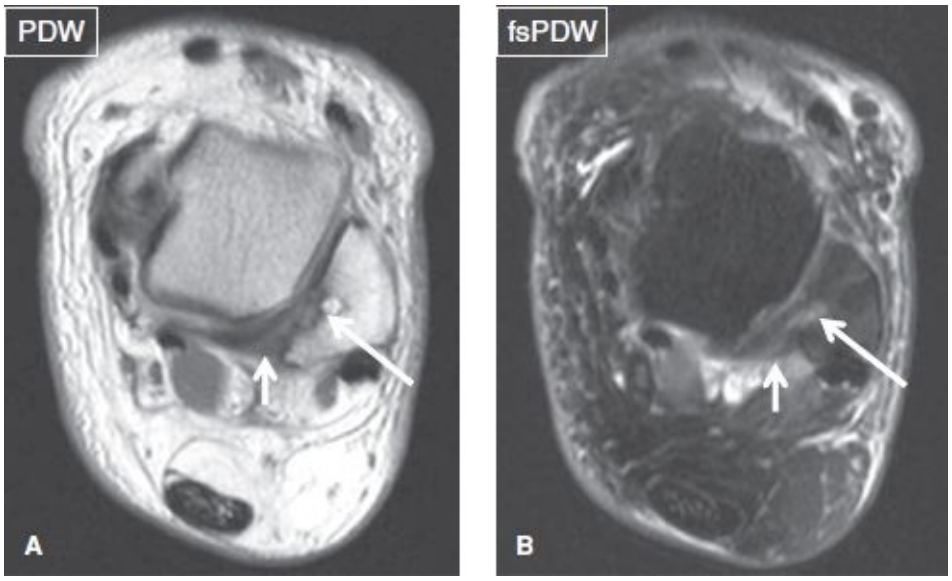

Fig. 69: Mucoid degeneration of the posterior talofibular ligament. Axial images **(A, B)** demonstrate loss of the fatty striations of the posterior talofibular ligament (*short arrows*) and an associated ganglion (*long arrows*) at the fibular attachment site.

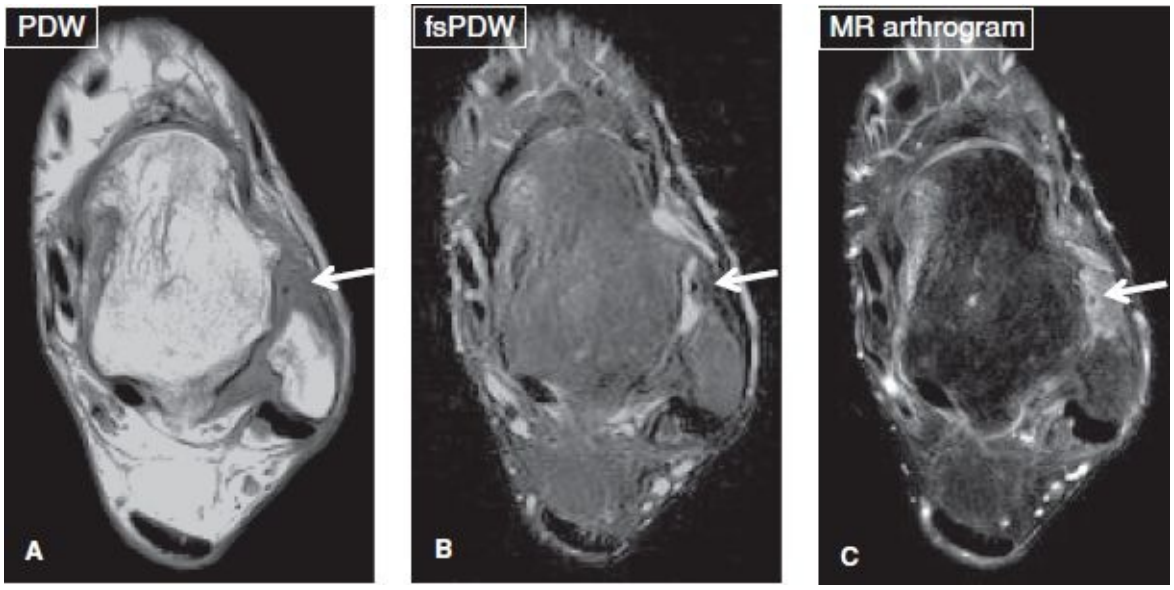

Fig. 70: Anterolateral impingement on axial images. The anterolateral gutter is occupied by soft tissue of intermediate signal (*arrows* in **A, B**), which enhances after contrast administration (*arrow* in **C**).

The V-shaped bifurcate ligament (or ligament of Chopart) has attachments on the anterior process of calcaneus, the dorsolateral aspect of the cuboid, and the lateral aspect of the naviculum. It is 2–3 mm thick and is best seen on the sagittal images. Isolated fracture of the anterior calcaneal process is usually related to avulsive force of the bifurcate ligament (Fig. 71). Acute ligament injury is classified as grade I, II, and III sprains, similar to other ligaments in the body. In subacute and chronic cases, ligament thickening or attenuation is associated with enthesopathy and/or cystic changes at the bony attachment site (Fig. 72). Fascial edema and fluid are absent in remote injury cases. The calcaneocuboid ligament is a thickening of the lateral capsule of the joint, and is less commonly injured as

compared to the bifurcate ligament. Symptomatic joint usually shows osteoarthritis and effusion, however, uncommonly synovial diverticulum, or a ganglion cyst may be seen projecting laterally to the calcaneocuboid joint.

Fig. 71: Acute calcaneal fracture. Sagittal reconstructed CT image **(A)** and sagittal MR image **(B)** show an acute fracture of the anterior calcaneal process (*arrows*), related to avulsive force of the bifurcate ligament.

Fig. 72: Chronic injury of the bifurcate ligament. Avulsive cystic changes (*arrow*) are evident at the calcaneal attachment of the bifurcate ligament, indicating chronic ligamentous injury.

POSTERIOR STRUCTURES:

Posterior talus: [<Normal> <Os trigonum> <Stieda process>]

PIML: [<Intact> <Thickened>]

AT: [<Normal> <Tendinosis> <Tear> <Kager fat pad edema> <Enthesophyte> <Retrocalcaneal bursitis > <Retroachilles bursitis>]

Plantar fascia: [<Normal> <Thickened> <Tear> <Perifascial edema> <Enthesophyte> <Heel pad edema>]

The posterior talus process has lateral and medial tubercles, with the former being slightly larger than the latter. The lateral tubercle might feature elongated/pointed appearance (Stieda process) or might have an unfused accessory ossicle with synchondrosis (os trigonum) (Figs. 73, 74). This is best seen on the axial and sagittal planes. Stieda process and os trigonum may be associated with FHL tear or tenosynovitis, aka os trigonum syndrome. The latter entity, also known as the posterior ankle bony impingement syndrome, results from compression of an osseous structure (Stieda process or os trigonum between tibia and calcaneus with or without soft tissue impingement during plantar flexion). One might observe downward sloping posterior lip of the tibia, osteophyte from the posterior distal tibia, prominent posterior process of the calcaneus or, less commonly, a soft-tissue component (thickened posterior joint capsule, post-traumatic scar tissue, or calcifications of the posterior joint capsule) and loose bodies in the posterior part of the ankle joint. In most cases, the cause of the syndrome is the presence of os trigonum, and the entity manifests as one or a combination of findings, including hypertrophied ossicle, bone marrow edema, cystic changes, fascial or Kager fat pad edema, and frank disruption and widening of the synchondrosis with fluid-like cleft (Fig. 75). Shepherd fracture refers to a fracture of the lateral tubercle of the talus, which can be differentiated from an os trigonum by the lack of corticated margins (Fig. 76).

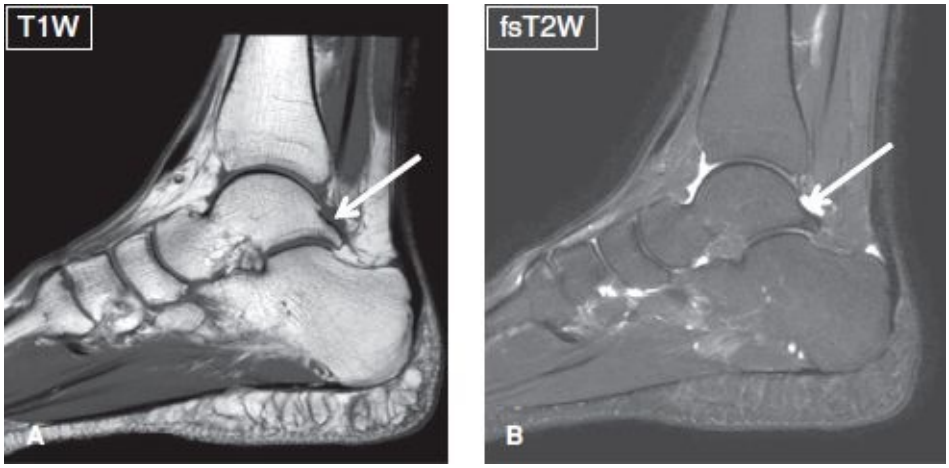

Fig. 73: Stieda process on sagittal images **(A, B)**. The lateral tubercle of the talus is elongated and pointed (*arrows*).

Fig. 74: Normal os trigonum. Sagittal images show an unfused accessory ossicle (*arrows*), at the site of the lateral tubercle of the talus.

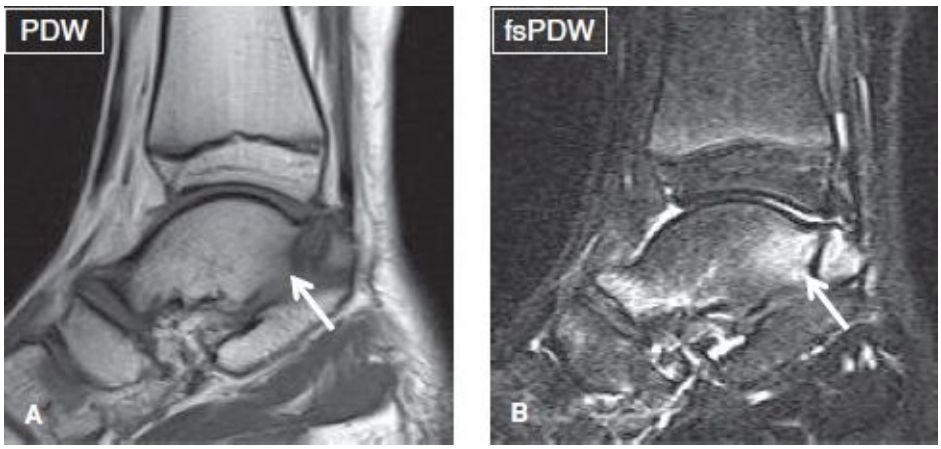

Fig. 75: Os trigonum syndrome. On sagittal images **(A, B)**, marrow edema is evident across the synchondrosis between the os trigonum and the lateral tubercle of the talus (*arrows*), in this case of posterior bony impingement. Also note anterior talar contusion from recent injury.

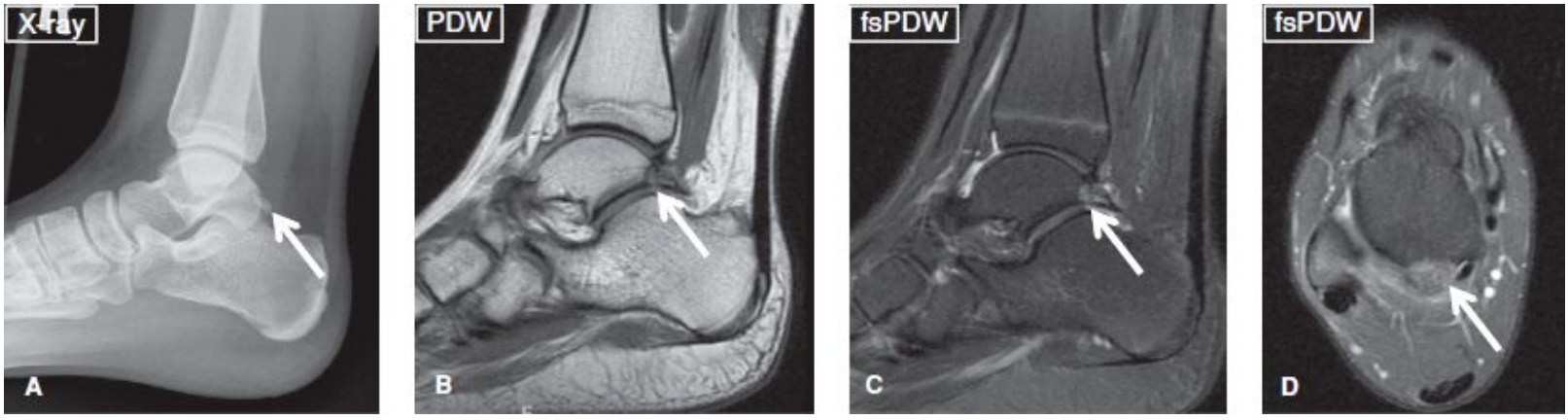

Fig. 76: Shepherd fracture. Lateral radiograph **(A)** and sagittal MR images **(B–D)** show a fracture of the lateral tubercle of the talus (*arrows*), with minimal displacement and fascial edema. No corticated margins are evident across the fracture line.

The PIML, also known as transverse tibiofibular ligament, labrum or meniscus of the

ankle, is a 2–4 mm thick ligamentous interconnection between the medial and lateral malleoli, and is located at the level of the tibiotalar joint line. PIML injuries are usually evident in subacute or chronic stages as ligament thickening, posterior ankle ganglion cyst, or posterior soft tissue impingement (Figs. 77, 78).

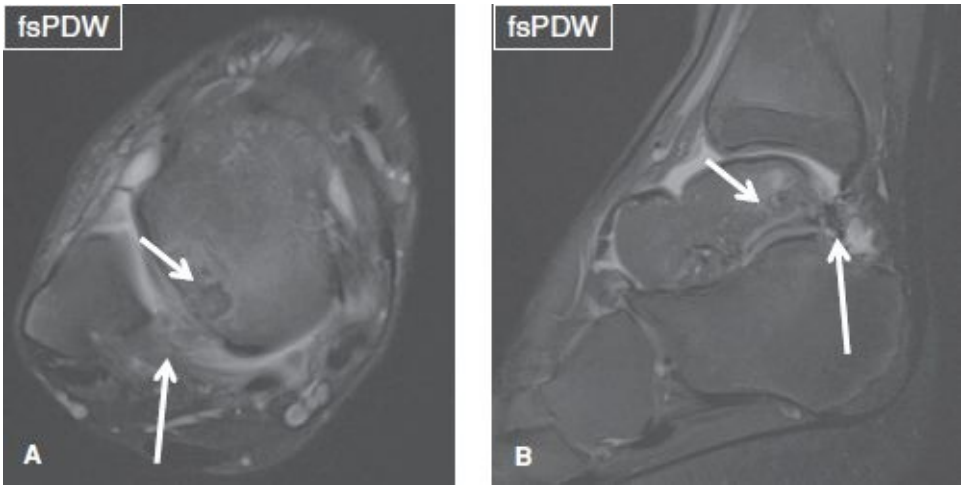

Fig. 77: Chronic injury of the posterior intermalleolar ligament. Axial **(A)** and sagittal **(B)** images demonstrate a thickened posterior intermalleolar ligament (*long arrows*). Note subcortical arthropathy changes in the posterior subtalar joint (*short arrows*).

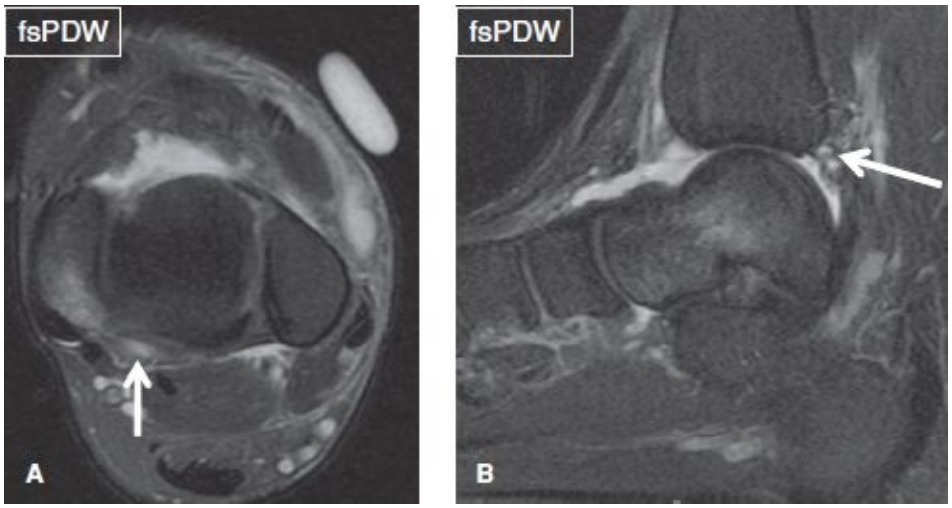

Fig. 78: Grade II sprain of the posterior intermalleolar ligament. Axial **(A)** and sagittal **(B)** images show a partial tear of the posterior intermalleolar ligament (*arrows*) at the tibial attachment.

The AT is the major plantar flexor of the foot and represents the largest tendon (~15 cm length) around the ankle. It is formed by the tendons of the two heads of the gastrocnemius muscles and the soleus muscle, and attaches to the dorsum of the calcaneus at the calcaneal tubercle. On the sagittal images, it normally features almost parallel anterior and posterior margins, whereas on the coronal images, both sides are fairly straight and the tendon widens as it extends distally (Fig. 79). On the axial images, the tendon is normally up to 5–8 mm thick and has anterior flat or concave margin. A focal convexity shifting from the lateral side of the proximal tendon to the medial side of the distal tendon is a normal

finding, and should not to be regarded as abnormal thickening. In addition, proximally at and immediately above the soleus insertion, the tendon may normally be convex or focally bulbous. The AT is usually devoid of signal (appears dark) on all imaging sequences although its normal fascicular anatomy may be visible as a single line and can mimic an interstitial tear. This fascicular signal is usually not evident or fades on T2W images. Small punctate areas of high signal within the tendon represent normal findings and correspond to interfascicular membranes and penetrating vessels (Fig. 80). The AT lacks a tendon sheath, but is instead surrounded by a paratenon. At its lower third, the AT is devoid of muscle fibers and is bordered anteriorly by the Kager fat pad, which should normally feature homogeneous fat signal with no edema, scar tissue, or mass, though it may be partially obliterated by a low-lying soleus muscle belly or an accessory soleus muscle. The retrocalcaneal bursa may normally exhibit small amounts of fluid and should measure less than 6 mm, 3 mm and 2 mm in superoinferior, transverse and anteroposterior diameters, respectively. Convex margins or significant distention indicate retrocalcaneal bursitis (Fig. 81). Fluid or edema in the retro-Achilles bursa is always abnormal (Fig. 82). Another slender anteromedial tendon i.e., plantaris inserts on the calcaneus and can mimic an AT tear (Fig. 54).

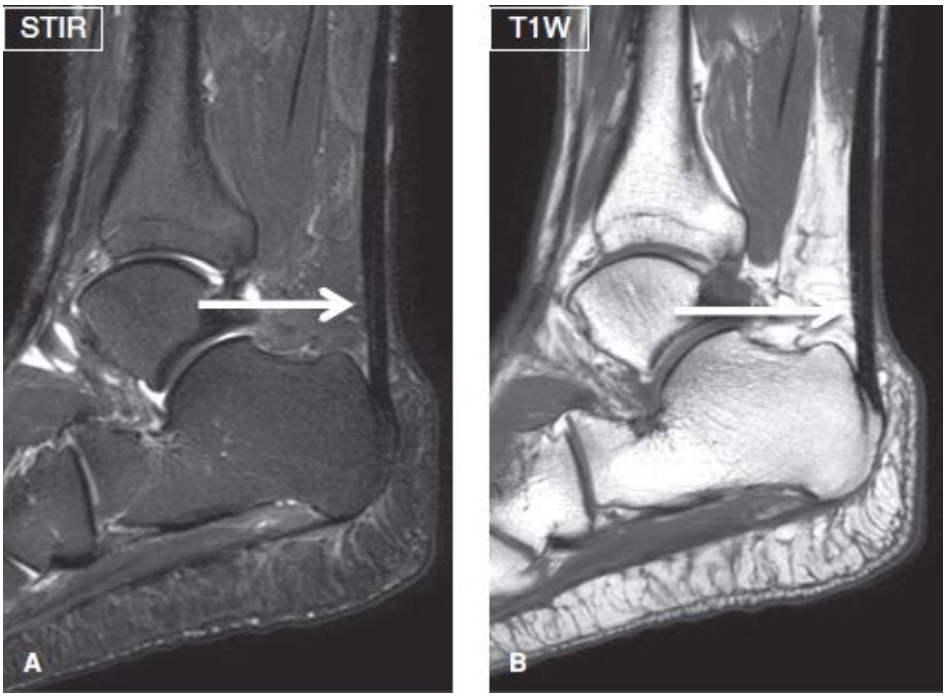

Fig. 79: Normal Achilles tendon. On sagittal images, the normal Achilles tendon features (*arrows*) almost parallel anterior and posterior margins, and is almost devoid of signal. A slightly hyperintense intrasubstance single line corresponds to normal fascicular anatomy.

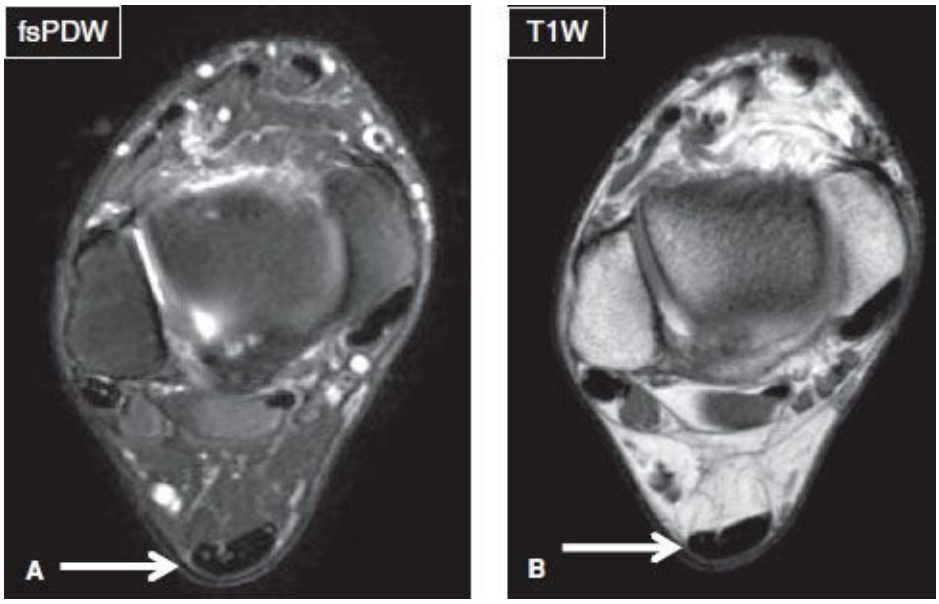

Fig. 80: Normal Achilles tendon. Axial images display a normal Achilles tendon, which features concave anterior margin (*arrows*). Note small intrasubstance linear and punctate areas of high signal, which correspond to interfascicular membranes and penetrating vessels.

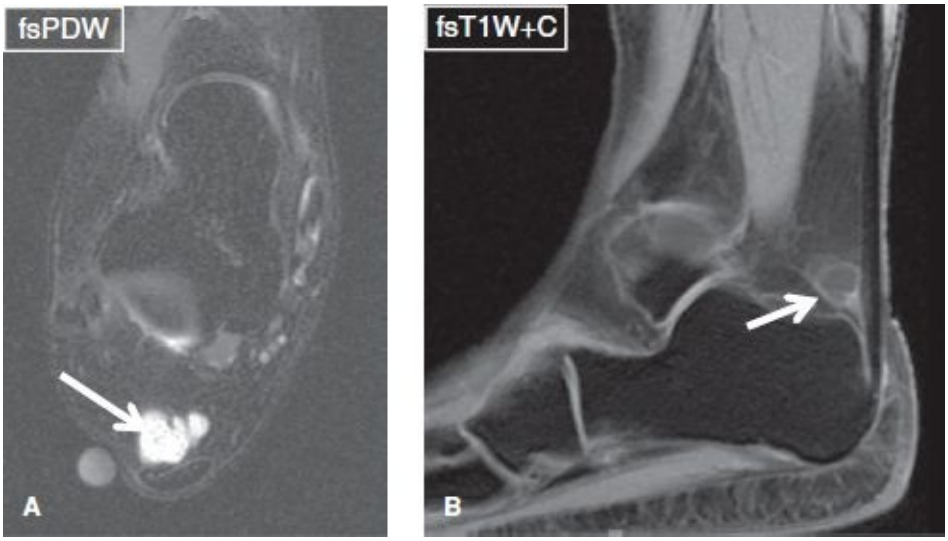

Fig. 81: Retrocalcaneal bursitis. **A:** Axial image demonstrates fluid collection within the retrocalcaneal bursa (*arrow*). **B:** On the sagittal image, the thin wall of the bursa (*arrow*) enhances after contrast administration.

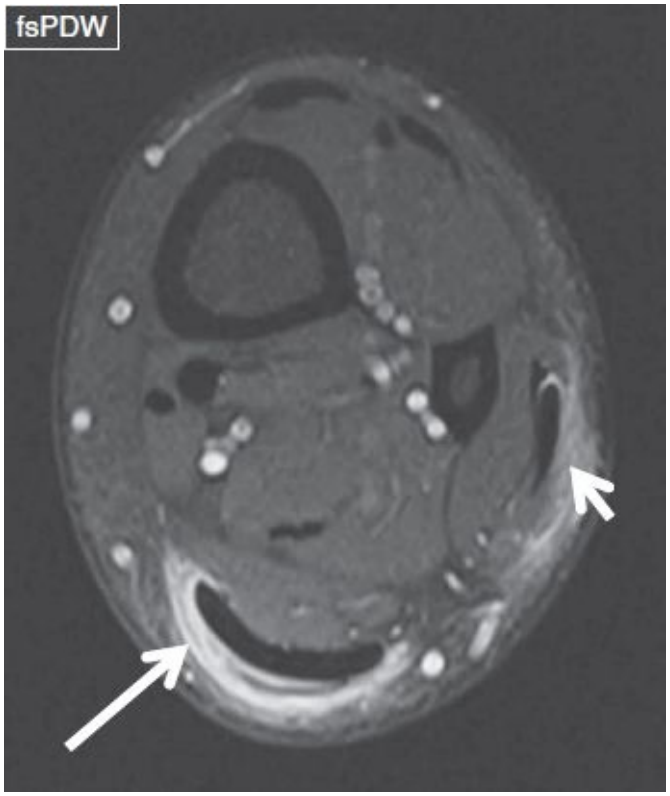

Fig. 82: Achilles peritendinitis. Axial image shows edema of the soft tissues (*long arrow*) around the Achilles tendon. Also note grade I sprain of the peroneus longus tendon with fascial edema (*short arrow*).

Inflammation within Kager fat pad is referred to as peritendinitis and is depicted as linear or irregular areas of altered signal intensity, which indicate edema and/or scarring. Inflammation of the connective soft tissue envelope, which immediately surrounds the AT is termed paratenonitis. The latter may be related to AT tear or may be mimicked by lipodystrophy (e.g., from steroid treatment), in which case it will likely be bilateral.

In Achilles tendinosis, the tendon is focally or diffusely thickened to more than 8 mm and features anterior convex margin. Achilles degeneration can be of various types, such as hypoxic degeneration (dark signal on PDW and fat-suppressed PDW images), mucoid degeneration (mildly increased signal on PDW/T1W and intermediate signal on fat-suppressed PDW images), lipoid degeneration (mildly increased striated signal on PDW and mixed dark signal on fat-suppressed PDW images, commonly associated with hypercholesterolemia, especially type II), and calcific degeneration (intermediate signal on T1W, intermediate to dark signal on PDW and fat-suppressed PDW images due to calcified streaks) (Figs. 83–85). Chronic Enthesopathy at the AT attachment is common and is typically asymptomatic. It is best depicted on sagittal T1W or PDW images.

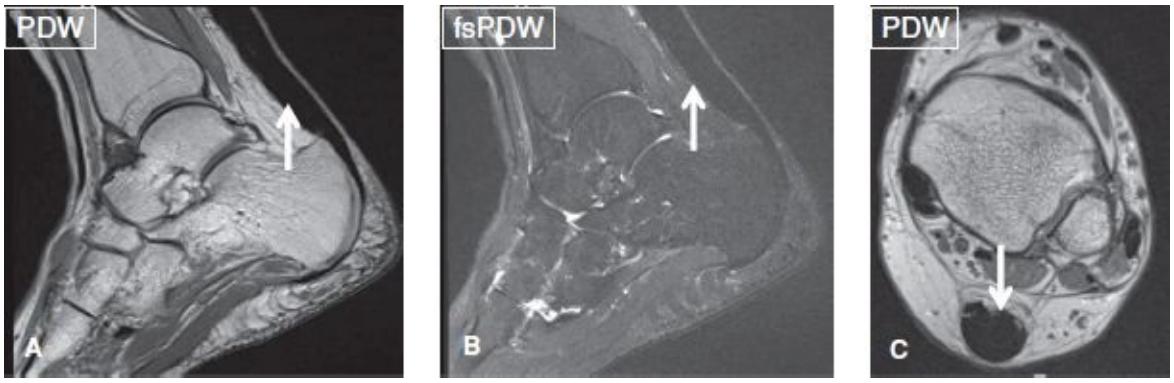

Fig. 83: Achilles tendinosis related to hypoxic degeneration. **A, B:** On sagittal images, the Achilles tendon is moderately thickened (*arrows*) and features homogeneous dark signal. **C:** Anterior convex margin (*arrow*) is evident on the corresponding axial image.

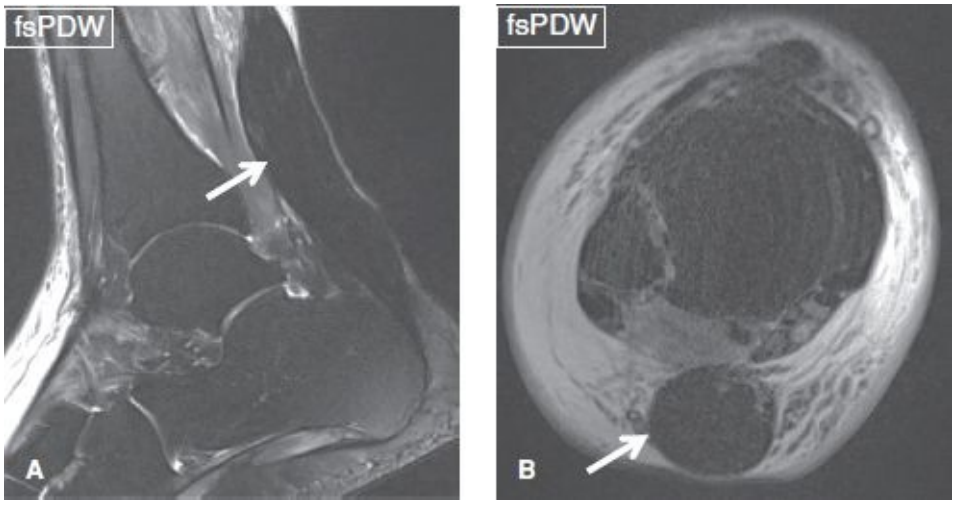

Fig. 84: Marked Achilles tendinosis related to severe hypoxic degeneration. Sagittal **(A)** and axial **(B)** images demonstrate marked hypointense enlargement of the Achilles tendon (*arrows*).

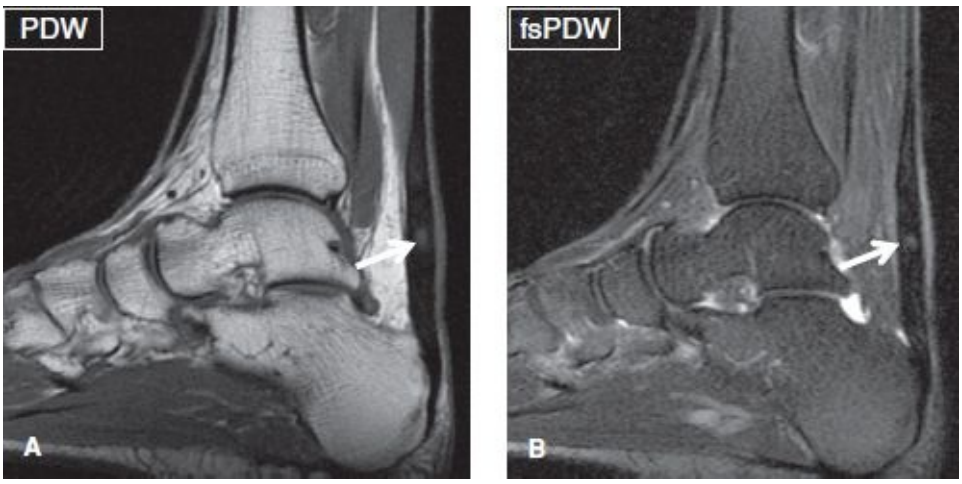

Fig. 85: Achilles tendinosis due to combination of hypoxic and mucoid degeneration. Sagittal images **(A, B)** show thickening and hypointensity of the Achilles tendon, related to hypoxic degeneration, as well as a focus of intermediate signal (*arrows*), corresponding to intermixed area of mucoid degeneration.

Achilles tendinosis may be insertional or non-insertional. Non-insertional tendinosis usually affects middle-aged individuals, young runners and dancers whereas insertional tendinosis mostly involves old sedentary individuals or subjects with inflammatory arthropathy. Insertional tendinosis is often associated with retrocalcaneal and/or retro-Achilles bursitis and hypertrophic spurring of the calcaneal attachment site. It is particularly common in individuals with Haglund deformity. The latter refers to any bony projection of the posterosuperior calcaneus above the line tangential to its superior border and paralleling its inferior border. Individuals with Haglund syndrome (less commonly encountered than isolated Haglund deformity) demonstrate Achilles insertional tendinosis and/or tears, calcaneal marrow edema, as well as retrocalcaneal and retro-Achilles bursitis (Figs. 86, 87). Haglund syndrome is more common in females, who wear high-heel shoes, and presents clinically with focal pain at the AT insertion site. Apart from Haglund deformity, insertional tendinosis/tendinitis may also occur in the setting of reactive arthritis, rheumatoid arthritis, ankylosing spondylitis, and gout. In the latter entities, there may be associated synovial hypertrophy and cortical erosions. Other differentials for mass-like lesions in this region of Kager fat pad include pigmented villonodular synovitis and fibroma, both commonly exhibit areas of intermediate to dark signal on PDW and fs PDW images.

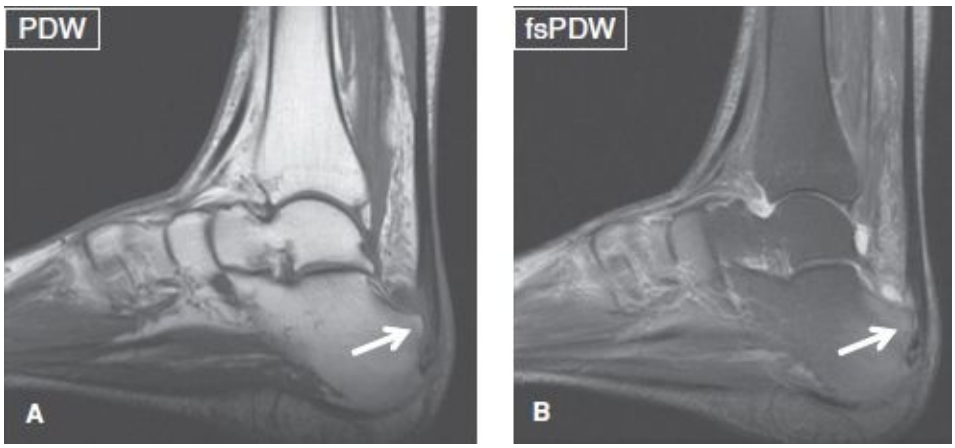

Fig. 86: Haglund syndrome. Sagittal images **(A, B)** demonstrate a bony protuberance (*arrows*) of the posterosuperior calcaneus, compatible with Haglund deformity. There is associated retrocalcaneal bursitis, Kager fat pad edema, and insertional partial tear of the Achilles tendon.

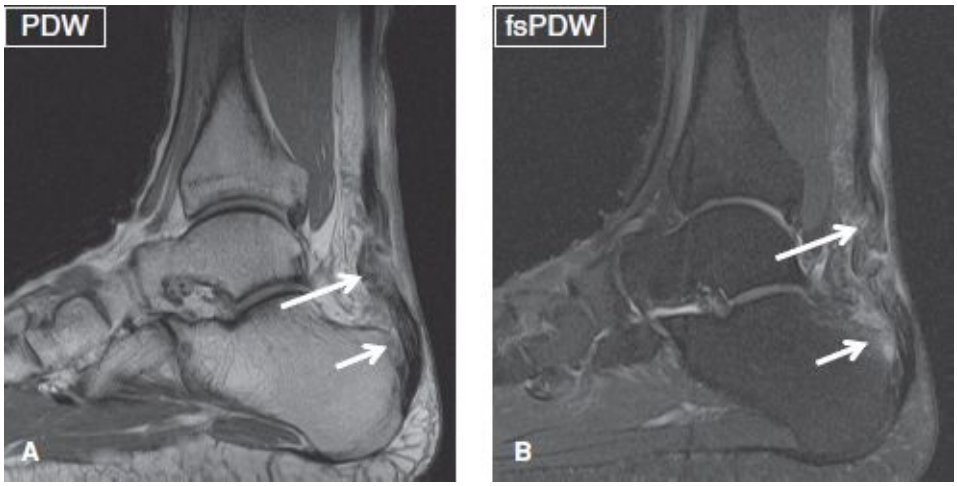

Fig. 87: High-grade partial tear of the Achilles tendon in the setting of Haglund syndrome. Sagittal **(A, B)** images display a near-complete tear of the Achilles tendon (*long arrows*), as well as a bony prominence of the posterosuperior calcaneus (*short arrows*) and retrocalcaneal bursitis, in keeping with Haglund syndrome.

Any fluid-like increased signal within the AT on T2W or fs PDW images reflects an interstitial tear. In partial AT tears, the tendon is thickened and features heterogeneous signal, without complete interruption. These are often associated findings of subcutaneous edema, hemorrhage within Kager fat pad, and intratendinous hemorrhage (Figs. 88, 89). In complete AT rupture, there is discontinuity with fraying and retraction of the torn edges of the tendon. In acute cases, the tendon gap demonstrates intermediate and high signal intensity on T1W and T2W images, respectively, reflecting edema and hemorrhage, whereas in chronic cases, scar or fat fills the gap. At the tear site, the tendon ends are enlarged, assuming often a bulbous contour, which my increase with greater tendon diastasis (Figs. 90, 91). Typically, in both partial and complete tears, the remainder of the tendon is almost always abnormal because of underlying long-standing tendinopathy.

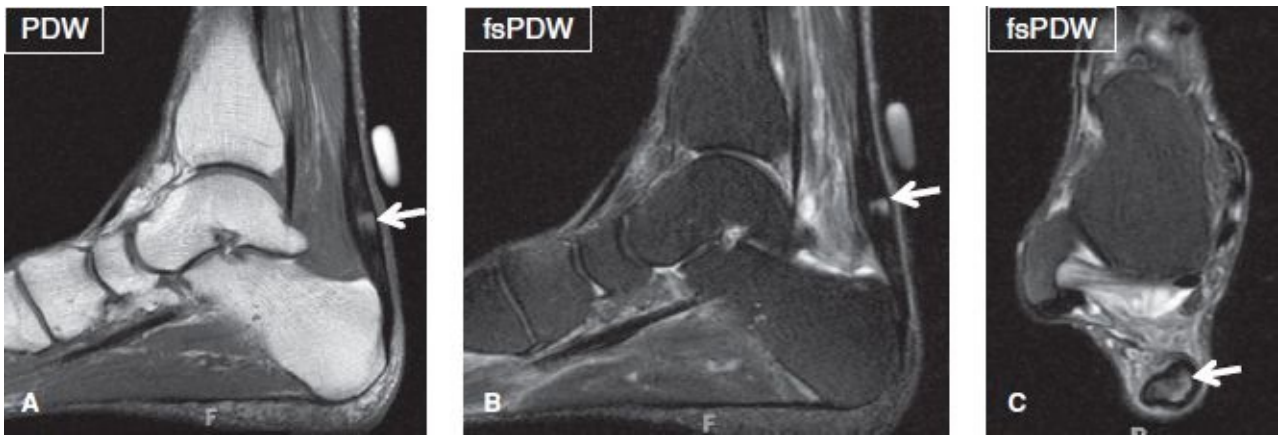

Fig. 88: Achilles tendinosis and with superimposed partial tear and associated lipodystrophy of Kager fat pad. Sagittal **(A, B)** and axial **(C)** images exhibit apparent thickening and heterogeneity of the Achilles tendon, corresponding to mucoid degeneration, as well as an intrasubstance focus of high signal intensity (*arrows*), indicating a partial interstitial tear. There is also extensive edema of Kager fat pad reflecting lipodystrophy. The patient was on

steroid treatment.

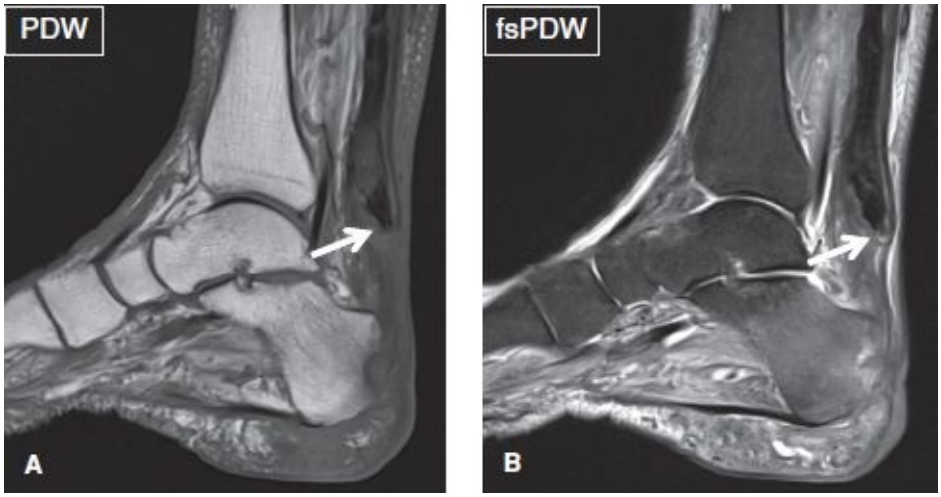

Fig. 89: Near-complete tear of the Achilles tendon in the setting of osteomyelitis. Sagittal images **(A, B)** display a near-complete tear of the Achilles tendon, with proximal retraction of the torn fragment (*arrows*), in this case of osteomyelitis of the calcaneus, which features extensive marrow edema and cortical erosions.

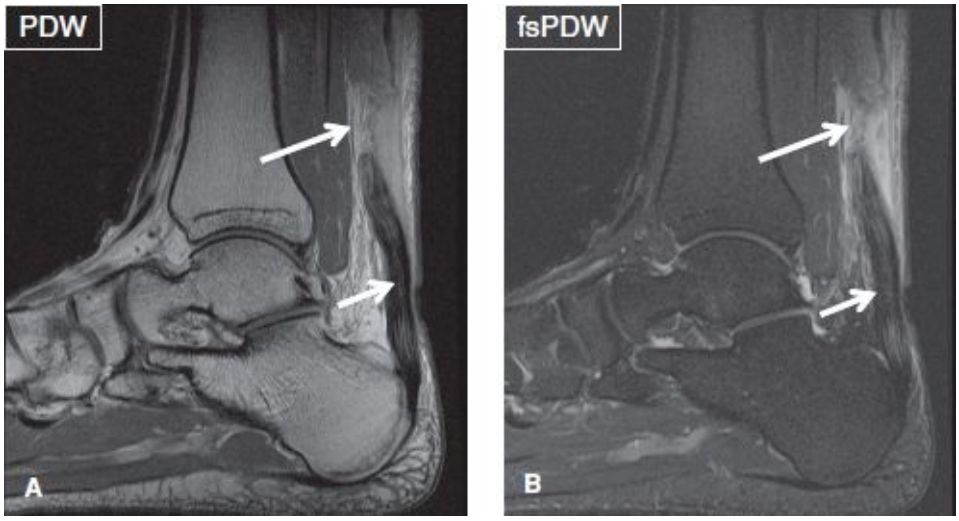

Fig. 90: Complete tear of the Achilles tendon. Sagittal images **(A, B)** demonstrate discontinuity of the Achilles tendon, with a hyperintense gap (*long arrows*) at the tear site, filled with edema and hemorrhage. Heterogeneity of the distal fragment (*short arrows*) indicates tendinosis.

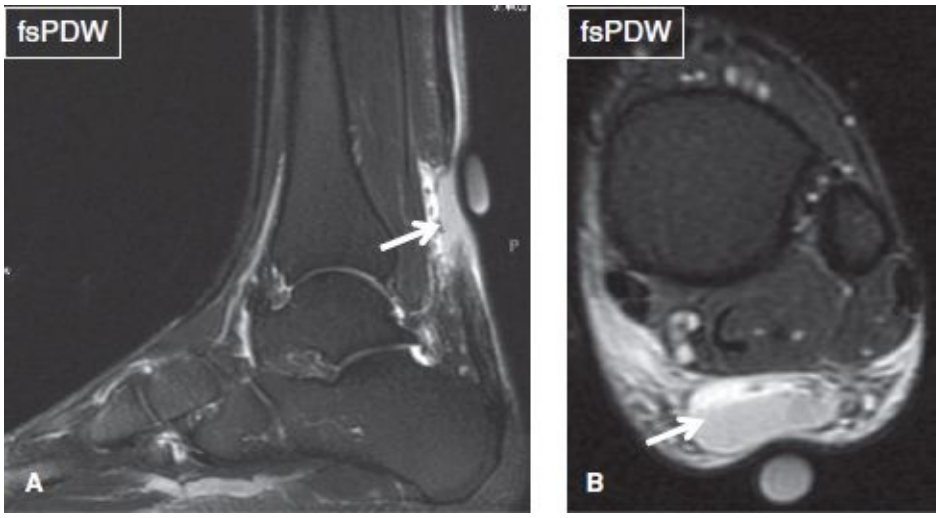

Fig. 91: Complete tear of the Achilles tendon. Sagittal **(A)** and axial **(B)** images exhibit complete discontinuity of the Achilles tendon (*arrows*) along with a loculated hemorrhagic fluid collection at the tendinous gap containing a fluid–fluid level.

In AT tears, features to report include the site of the tear (insertional or noninsertional), the degree of retraction and fraying of the tendon edges, and the extent of the tear in the transverse axis (i.e., medial, lateral, and/or central third of the tendon involved) and in the anteroposterior axis (low-grade when involving less than 50% of the tendon width, high-grade when involving 51% to 99% of the tendon width, or full-thickness tear). Alternatively, measurements of the tear in three dimensions can be reported. Associated findings may include underlying tendinosis, insertional enthesophyte, paratenonitis, calcaneal bone marrow edema, avulsion fracture, retrocalcaneal, and retro-Achilles bursitis (Figs. 92, 93). A calcaneal stress fracture, usually centered slightly anterior to the posterior border of calcaneus is in the differential diagnosis of AT rupture, particularly in athletes. Because AT degeneration and tears most often occur within the tendon 2–6 cm proximal to its calcaneal insertion, the field of view on sagittal images must be large enough to include this region. One would see hemorrhage and edema in the acute stage and muscle atrophy in the chronic stage. Sagittal images should also include at least the last 3 cm of the distal soleus muscle to detect muscle atrophy or strain.

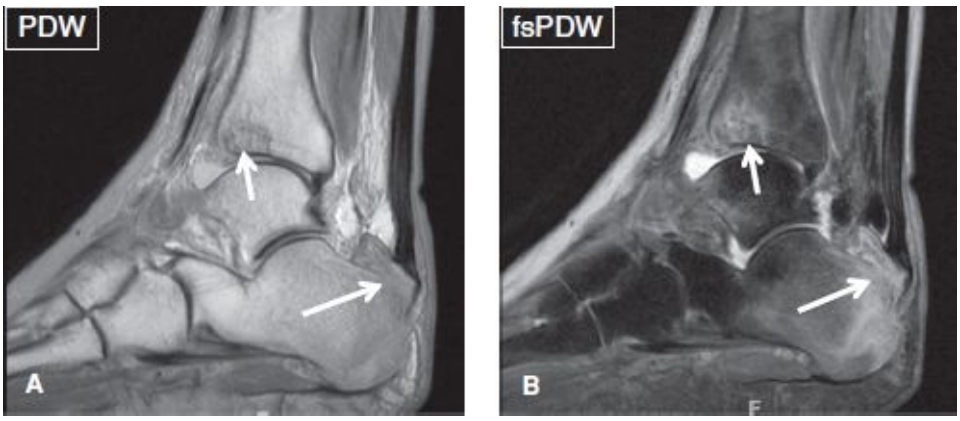

Fig. 92: Avulsion fracture of the posterosuperior calcaneus: Sagittal images **(A, B)** show avulsion of the calcaneal tuberosity (*long arrows*), caused by acute contraction of the Achilles

tendon. Also not osteochondral injury (*short arrows*) of the anterior tibial plafond.

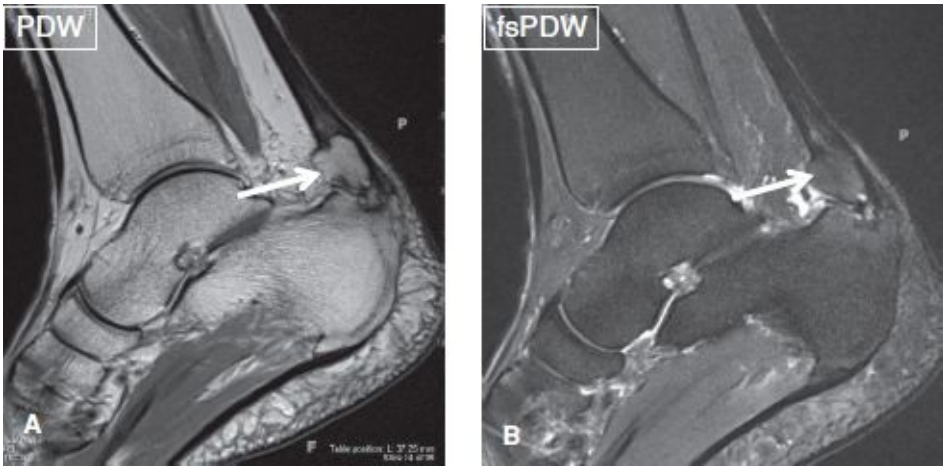

Fig. 93: Chronic avulsion fracture of the calcaneal tuberosity. Sagittal images **(A, B)** demonstrate an avulsed nonunited fragment (*arrows*) from the calcaneal tuberosity at the Achilles tendon attachment site.

When imaged during healing, ATs are expected to be thickened and feature moderate intratendinous heterogeneity, because of scarring, (Fig. 94). A small subset of patients may also exhibit edema, tendon defects, and peritendinous reactions. However, intratendinous fluid signal intensity and/or fiber discontinuity are highly suspicious for recurrent tearing, regardless of the age of the repair and these are best detected on fs PDW or T2W images.

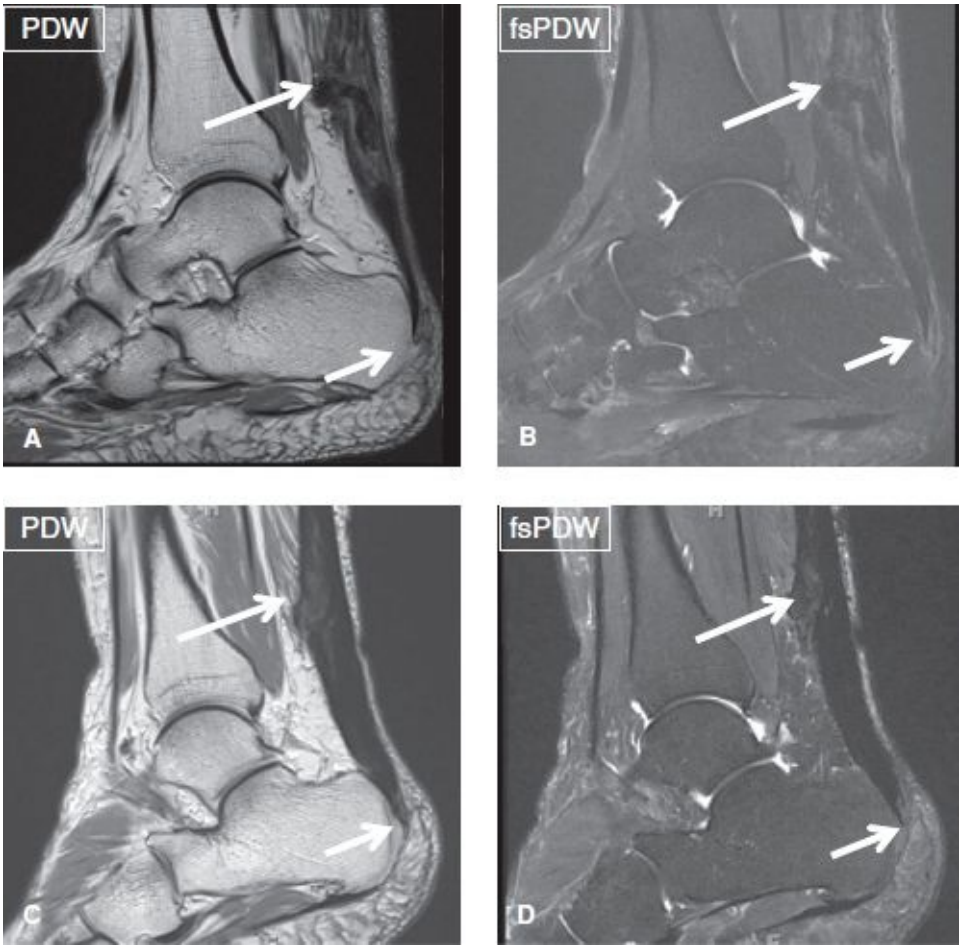

Fig. 94: Healing of AT tear. Sagittal images. A high-grade partial tear (*long arrows* in **A, B**) is evident in the AT. On follow-up examination, the respective area shows moderate heterogeneity (*long arrows* in **C, D**) due to scar tissue formation. Note healing enthesopathy changes (*short arrows*) at the AT insertion site.

The accessory soleus muscle is a rare anatomical variant, found in 0.7%–5.6% of cadaveric specimens. It inserts on the AT and on the medial and lateral calcaneus, and is most commonly an incidental finding. It may be associated with posterior ankle pain due to coexisting Achilles tendinopathy, impingement, compressive tibial neuropathy, or compartment syndrome (Figs. 95, 96).

Fig. 95: Low-lying soleus muscle. On sagittal images **(A, B)**, the anatomic area of Kager fat pad is occupied by a low-lying soleus muscle (*arrows*), which shows mild edema, corresponding to grade I strain.

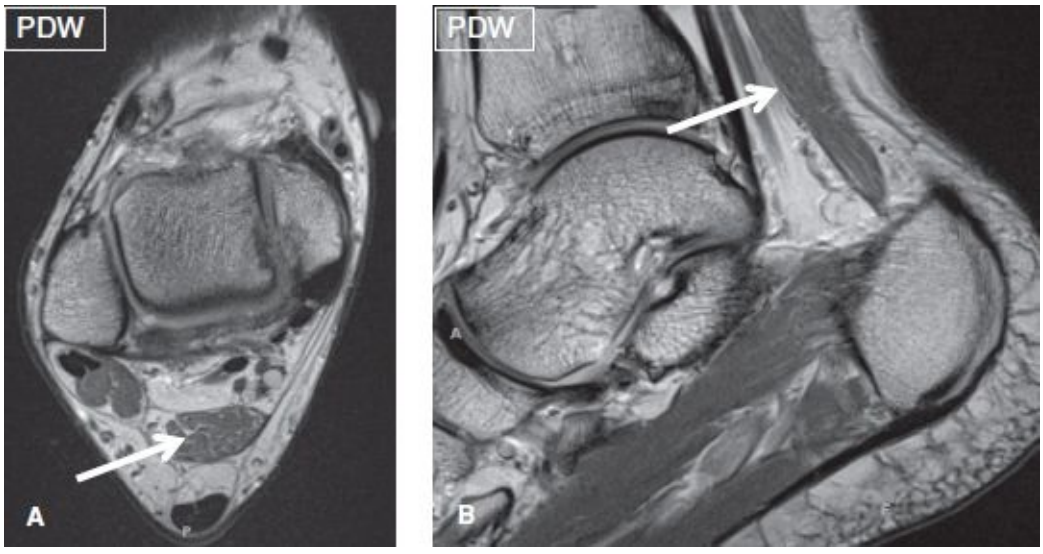

Fig. 96: Accessory soleus muscle. Axial **(A)** and sagittal **(B)** images demonstrate an accessory soleus muscle (*arrows*), which inserts on the posterior calcaneus.

The plantar fascia is a multilayered subcutaneous fibrous structure, extending as a thick, strong, dense tissue from the calcaneus posteriorly to the region of the metatarsal heads anteriorly. It is composed of three portions, the medial, central, and lateral cords, which are

best separated out on coronal images, as thickenings of the fascia underneath the AH, flexor digitorum brevis (FBD), and abductor digiti minimi (ABDM) muscles, respectively. Typically, the central cord is mildly thicker than the lateral cord. The plantar fascia is also nicely seen on sagittal images, normally less than 4 mm thick featuring homogeneous low signal intensity on all pulse sequences. It is subject to focal partial tears and inflammatory or infectious fasciitis, which mostly involve the calcaneal attachment, high-grade or complete tears, which typically occur 1 to 2 cm distal to the calcaneal attachment, and fibromatosis or fibroma, which occur at the midfoot level.

Plantar fasciitis most commonly involves the central cord and less commonly both the central and the lateral cords whereas the medial cord is rarely involved. When inflamed, the fascia demonstrates fusiform thickening (>4 mm), as well as intermediate signal intensity on T1W and PDW images and high signal intensity on T2W images, commonly due to partial tears (Fig. 97). The entity is typically associated with calcaneal enthesophyte (indicating a subacute or chronic process), and a variety of acute and/or subacute findings, such as fluid-like signal at the calcaneal attachment, heel pad edema and/or bone marrow edema, as well as perifascial and/or FDB muscle edema. It should be noted that plantar spur is not synonymous with plantar fasciitis. Many patients have spur or inferior calcaneal enthesophyte without fasciitis. Acute rupture of the plantar fascia, typically a sports-related injury, demonstrates as complete or partial disruption of the fascia, with large intervening areas of prominent increased signal-intensity on T2W images, indicating edema, hemorrhage, and perifascial fluid collection (Figs. 98–101). Associated tears of the FDB or strains of the other plantar muscles may also be evident. Chronic tears appear as focal fascial thickening and intrafascial scar tissue, which show low signal intensity on all pulse sequences whereas perifascial edema is absent.

Fig. 97: Plantar fasciitis. Sagittal **(A)** and coronal **(B)** images demonstrate thickening and intermediate signal of the medial and central cords of the plantar fascia (*arrows*), along with edema of the overlying soft tissues. Notice low grade partial tears at the calcaneal attachments of all 3 cords.

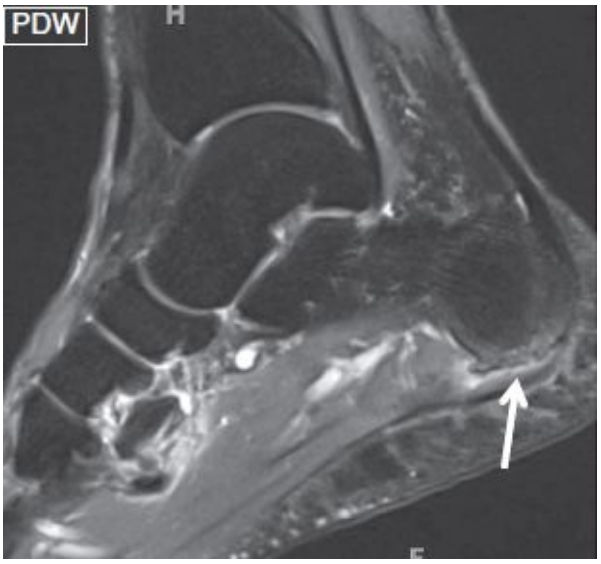

Fig. 98: Partial tear of the plantar fascia. Sagittal image shows a thin linear fluid-like signal (*arrow*) within the origin of the plantar fascia, in keeping with a low-grade partial tear. Note overlying irregular plantar calcaneal enthesophyte.

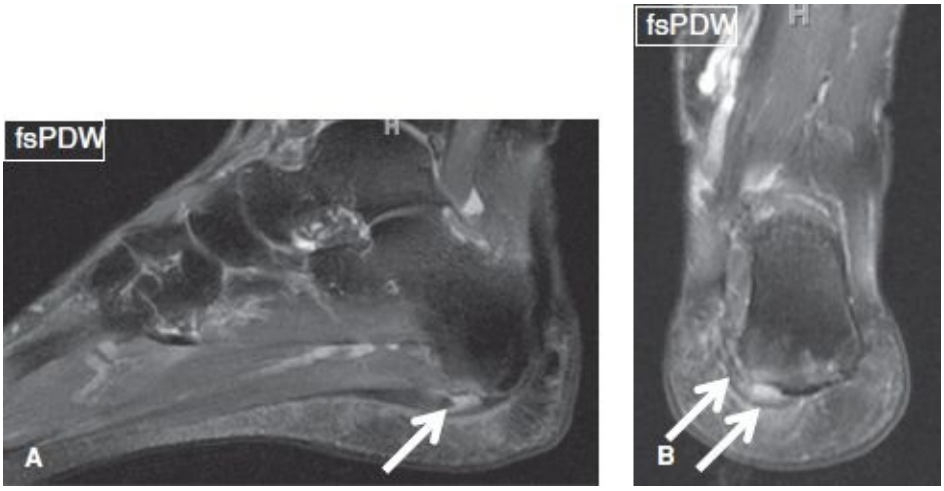

Fig. 99: Partial tear of the plantar fascia. Sagittal **(A)** and coronal **(B)** images exhibit a thick linear fluid-like signal (*arrows*) within the origin of the medial and central cords of the plantar fascia, in keeping with high-grade partial tear. Notice subjacent bone marrow edema and perifascial edema.

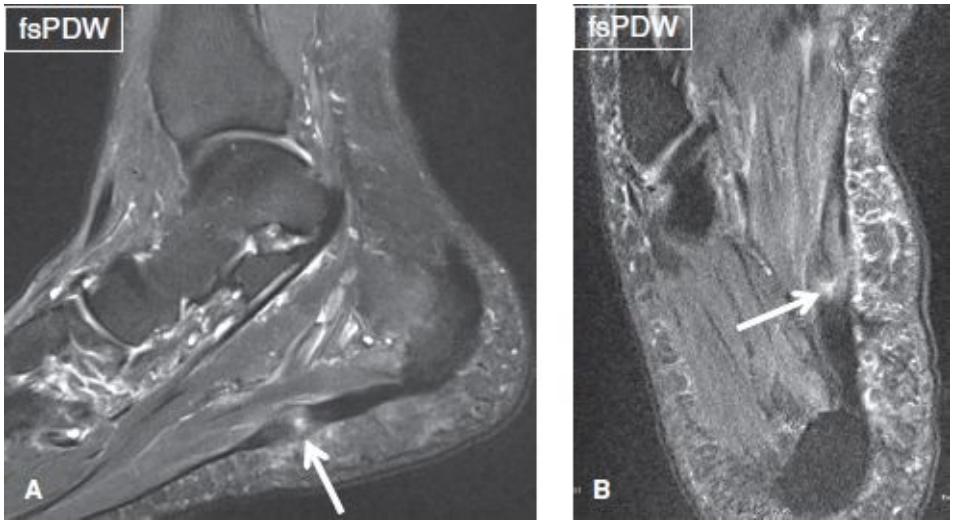

Fig. 100: Partial tear of the plantar fascia. Sagittal **(A)** and axial **(B)** images show a thick linear fluid-like signal within the middle segment of medial and central cords of the plantar fascia (*arrows*), in keeping with a high-grade partial tear.

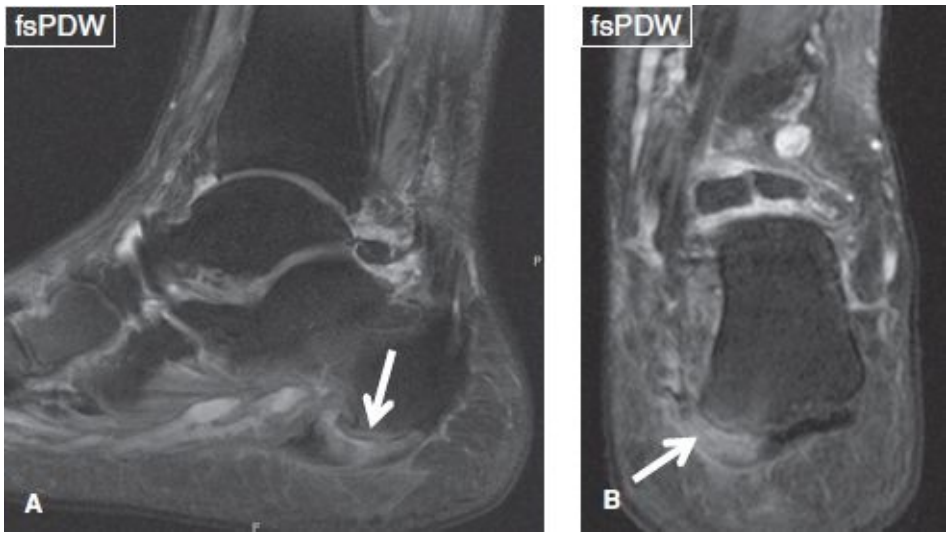

Fig. 101: Full-thickness tears of the plantar fascia. Sagittal **(A)** and coronal **(B)** images show edema and full-thickness tears of the medial and central cords of the plantar fascia at its origin (*arrows*).

Plantar fibroma manifests as a focal pea-shaped thickening of the plantar fascia, typically less than 3 cm in size, which is predominantly isointense to slightly hypointense to skeletal muscle on T1W images, intermediate to minimally increased signal intensity on T2W, and features mild hyperintensity on STIR images. In most cases, the lesions enhance intensely following gadolinium administration (Fig. 102). The patients complain of painful walking, as if marching on marbles. Plantar fibromatosis (Ledderhose disease) refers to multiple such nodules arising along the plantar fascia, often in non–weight-bearing locations, which are infiltrative in their upper margin and may expand into the deeper compartment of the foot. These remain well demarcated and outlined by subcutaneous fat at their lower margin.

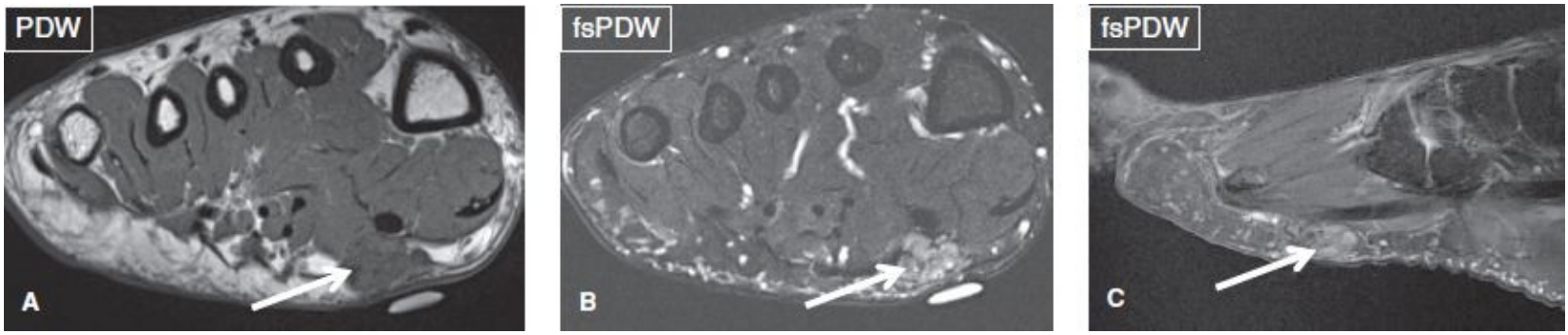

Fig. 102: Plantar fibroma. Coronal **(A, B)** and sagittal **(C)** images show pea-shaped nodular thickening of the plantar fascia (*arrows*), a biopsy proven plantar fibroma.

ANTERIOR STRUCTURES:

Tendons:

Anterior tibial tendon: [<Normal> <Tendinosis> <Tenosynovitis> <Split tear> <Complete tear>]

Extensor hallucis longus (EHL): [<Normal> < Tendinosis> <Tenosynovitis> <Split tear> <Complete tear>]

Extensor digitorum longus (EDL): [<Normal> < Tendinosis> <Tenosynovitis> <Split tear> <Complete tear>]

LIGAMENTS:

Dorsal talonavicular ligament: [<Intact> < Thickened> <Enthesopathy>]

The tibialis anterior (TA), EHL, and EDL tendons course beneath thickenings of the deep fascia, referred to as extensor retinaculae. The superior extensor retinaculum is located a few cm above the ankle joint and extends from the anterior distal tibia and fibula to the inferior extensor retinaculum. The latter extends into the sinus tarsi adjacent to the sinus tarsi ligaments and overlies the dorsalis pedis artery and the deep peroneal nerve.

The TA dorsiflexes the ankle, inverts the foot and supports the medial longitudinal arch while walking. Its tendon inserts onto the first metatarsal base and the medial cuneiform. On axial images, the TA tendon is round or oval at the ankle joint level and becomes flat distally. It should normally be 5 mm or less in thickness within 3 cm of its insertion, and smaller than the PTT. The EHL extends the phalanges of the first toe and dorsiflexes the foot. Its tendon inserts onto the base of the distal phalanx of the great toe. The EDL dorsiflexes the ankle and extends the toes. Its tendon divides into four slips along the dorsum of the foot, each of which splits into three parts, with the central part inserting onto the base of the middle phalanx and the other two reuniting and inserting onto the bases of the second to fifth distal phalanges.

The anterior tendons of the ankle are uncommonly affected by pathology. Normally, synovial fluid is not evident around them; therefore, even trace amount of fluid within their sheath reflects tenosynovitis. TA tendinosis and tendon tears (split or complete) usually involve middle-aged and elderly females, and appear as thickening, attenuation, and/or increased intrasubstance signal (Figs. 103–105). Complete rupture of the TA tendon usually occurs between the extensor retinaculum and the tendon insertion. The tendon retraction is limited to the level of the ankle joint due to the inferior extensor retinaculum and is best measured on sagittal images (Fig. 106). Imaging findings include a fluid-filled tendon gap with retracted, frayed, and thickened tendon ends located between the superior and inferior extensor retinaculae. Associated findings may include tenosynovitis, as well as thickening of the synovium and dorsal osteophytes in the medial tarsometatarsal joint. Similar to the peroneal and medial tendons, the TA tendon is prone to magic angle artifact on short TE

images. The EDL tendon is usually involved by mild mechanical tenosynovitis and partial tears. The EDL and EHL may also get injured during penetrating injuries to the foot (Figs. 107, 108). In about 80% to 90% of individuals, the tendon of an accessory muscle, the peroneus tertius, may travel along with the EDL tendon in the anterior compartment and insert onto the base of the fifth metatarsal.

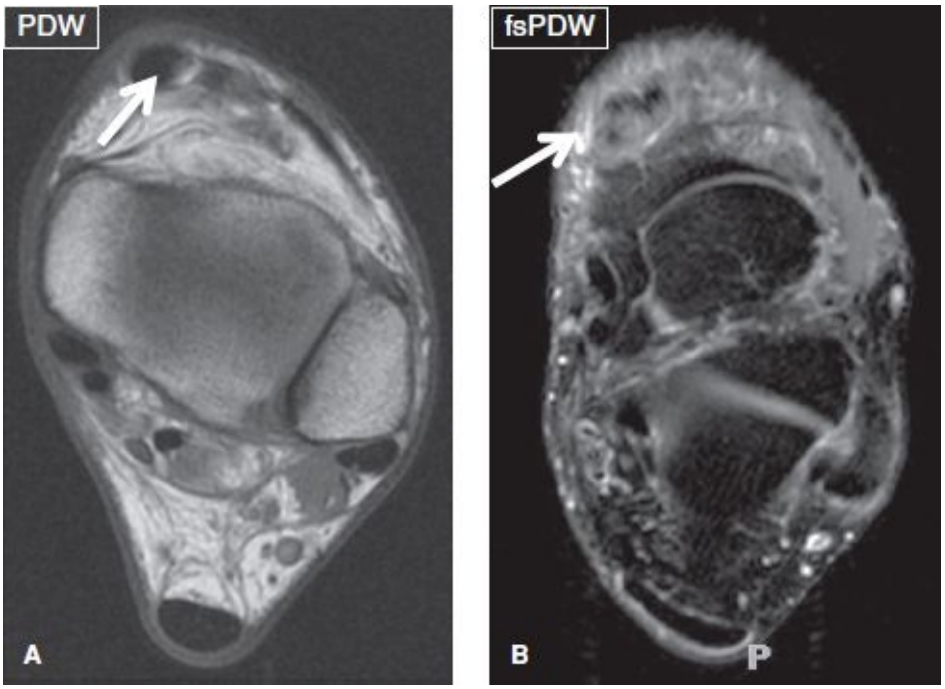

Fig. 103: Tibialis anterior tendinosis. Axial images **(A, B)** demonstrates thickening and intermediate signal (*arrows*) within the tibialis anterior tendon at **(A)** and below **(B)** the level of the ankle, in keeping with tendinosis.

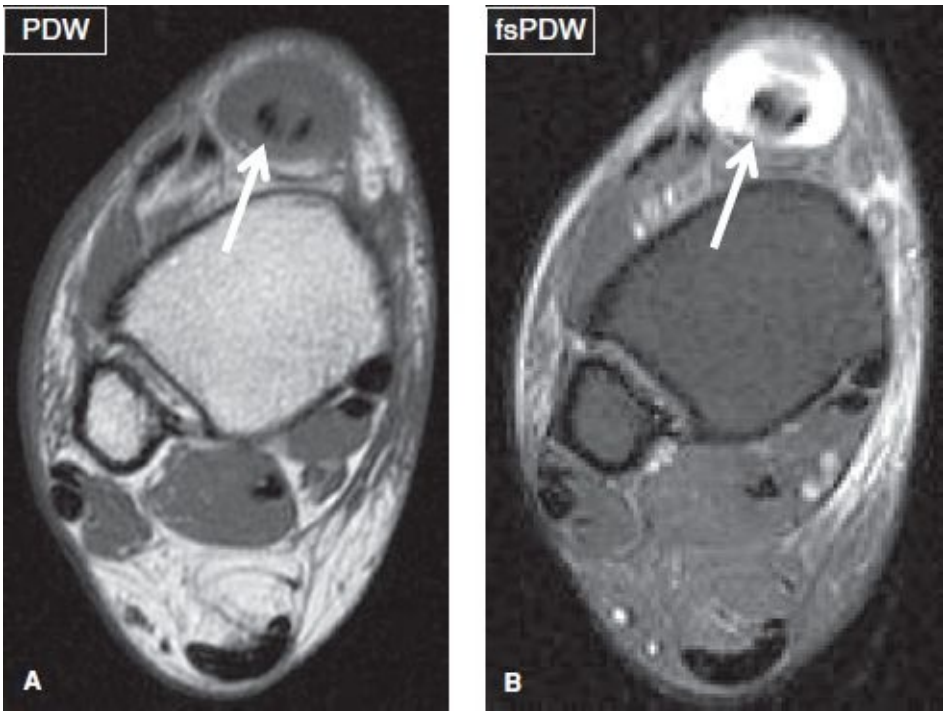

Fig. 104: Tibialis anterior tendon split tear. Axial images **(A, B)** show multifocal splits (*arrows*) in the tibialis anterior tendon with thickening of the tendon. There is concomitant complex tenosynovitis.

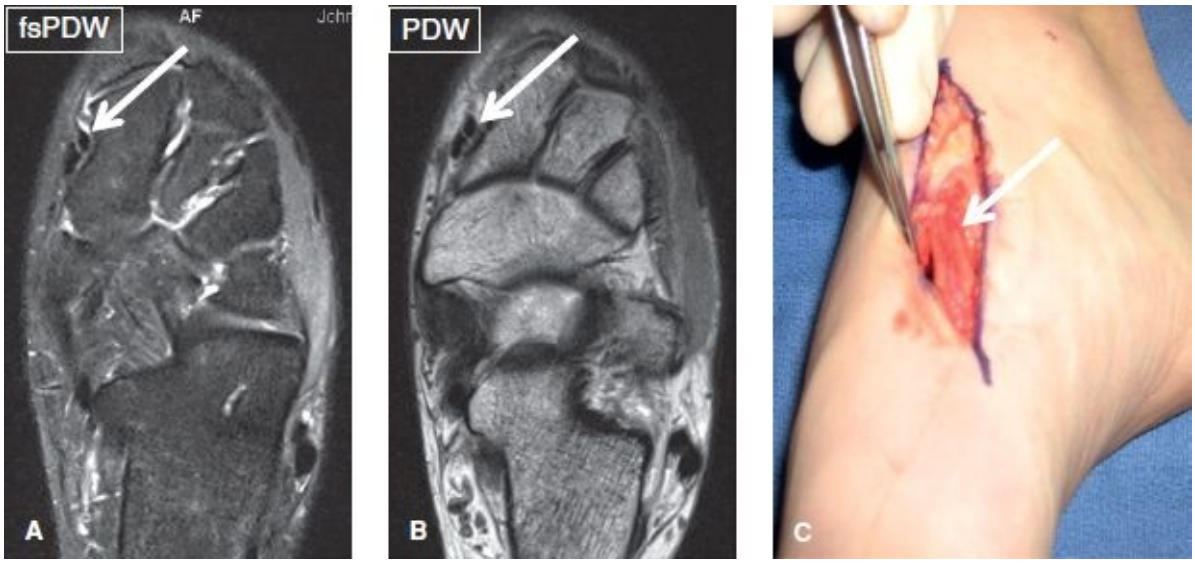

Fig. 105: Split tear of the tibialis anterior tendon. Axial images **(A, B)** display a longitudinal split tear of the tibialis anterior tendon (*arrows*). The finding was confirmed at surgery (*arrow* in **C**).

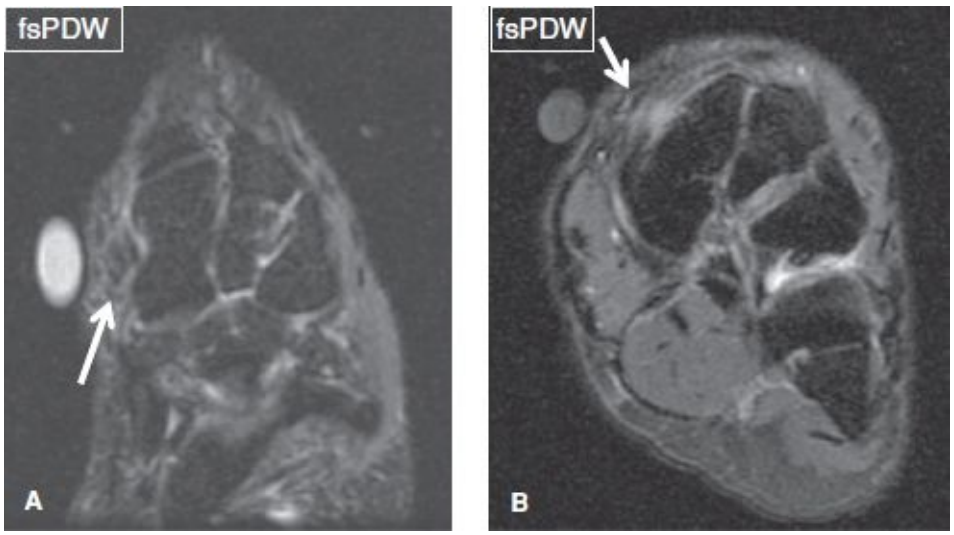

Fig. 106: Near-complete tear of the tibialis anterior tendon. Axial **(A)** and coronal **(B)** images demonstrate near-complete tear of the tibialis anterior tendon (*arrows*), which is partially retracted at the level of the proximal medial cuneiform.

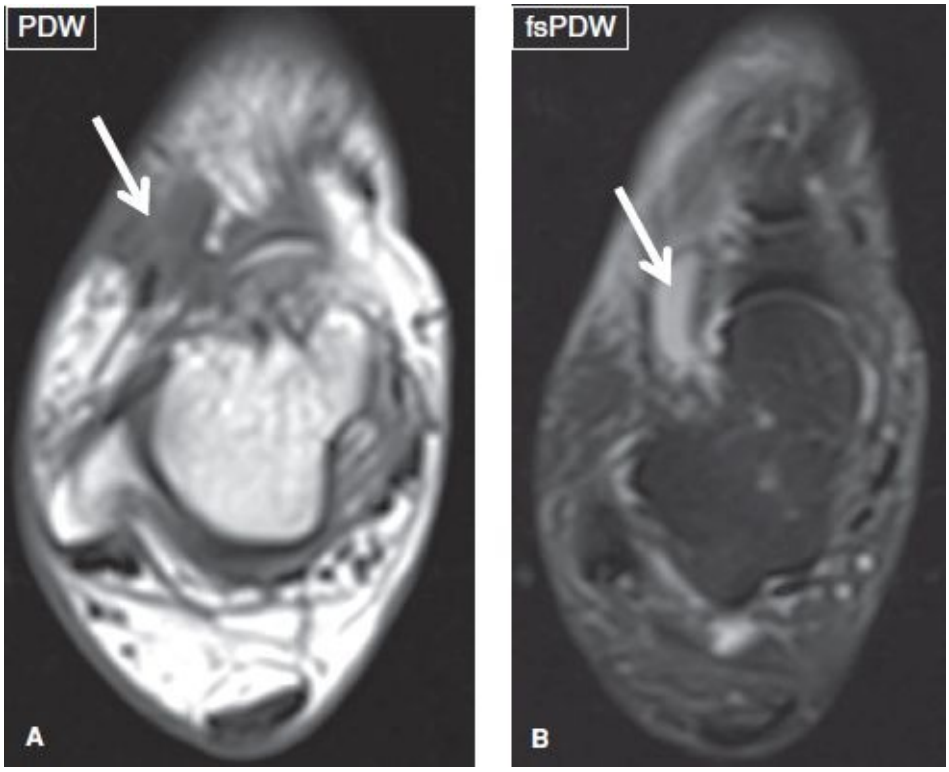

Fig. 107: Laceration of the extensor digitorum longus tendon. Axial images **(A, B)** demonstrate near-complete laceration of the extensor digitorum longus tendon (*arrows*) from a knife injury.

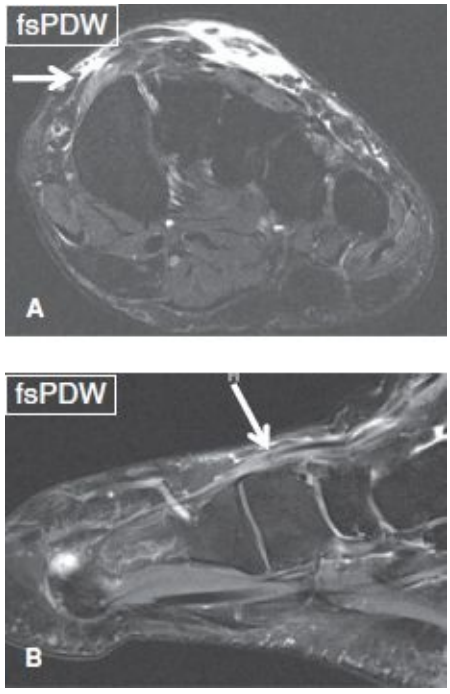

Fig. 108: Laceration of the extensor hallucis longus tendon. Coronal **(A)** and sagittal **(B)** images show complete tear or the extensor hallucis longus tendon, which has been retracted at the level of the tarsometatarsal joints (*arrows*).

Thickenings of the talonavicular joint capsule form the plantar, medial, lateral, and dorsal talonavicular ligaments. Of them, the dorsal talonavicular ligament is most commonly involved with pathology, which can appear as thickening or attenuation of the

ligament, enthesophyte, avulsion fracture or avulsive cystic changes of the superior naviculum, bone marrow edema at the attachment sites, synovial diverticulum, and ganglion cyst formation (Figs. 109–112). Abnormalities of this ligament are commonly associated with talar fault, pes planus, hindfoot bony coalitions (with classic talar beak) and PTT dysfunction.

Fig. 109: Partial tear of the dorsal talonavicular ligament. Sagittal image demonstrates partial discontinuity of the dorsal talonavicular ligament, in keeping with a grade II sprain (*arrow*).

Fig. 110: Ganglion of the dorsal talonavicular ligament. Sagittal images show a well-defined ganglion (*arrows*) within the distal dorsal talonavicular ligament.

Fig. 111: Chronic avulsion fracture of the anterosuperior talus. Sagittal images **(A, B)** demonstrate an ossicle (*short arrows*), which corresponds to chronic avulsion fracture of the talus, related to traction-related injury of the dorsal talonavicular ligament. Also note the chronic osteochondral injuries of the talar dome (*long arrows*).

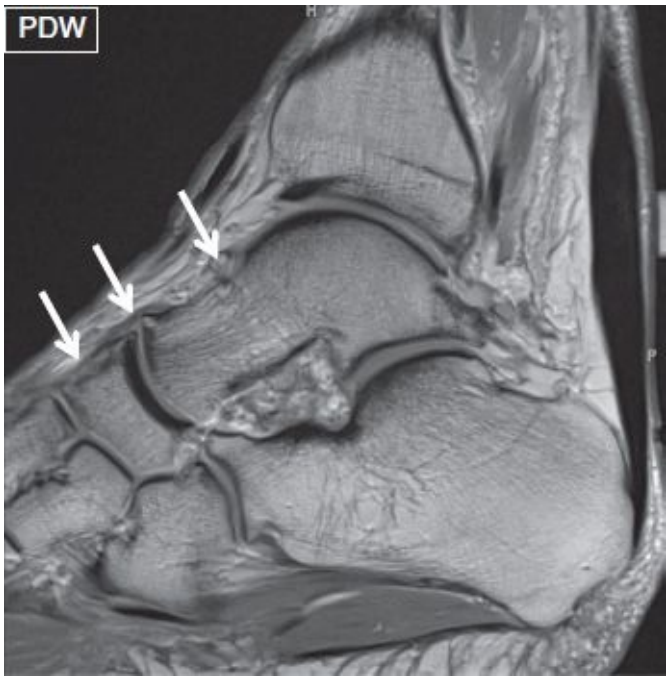

Fig. 112: Enthesopathic changes of the dorsal midfoot. Sagittal images shows small enthesopathic changes (*arrows*), associated with chronic traction-related changes of attachments of tibiotalar joint capsule and dorsal talonavicular ligament.

Tibiotalar joint: [<Normal> <Osteochondral lesion> <Osteoarthritis>]

Subtalar joint: [<Normal> <Osteochondral lesion>

The tibiotalar and posterior subtalar joints are approximately equal in space and feature homogeneous thin (1–2 mm) articular cartilage. They may be involved by osteoarthritis, which manifests as cartilage loss, joint space narrowing, osteophytes, subchondral sclerosis and cysts, and less commonly with effusions and synovial thickening (Fig. 113). The tibiotalar and posterior subtalar joints may also be involved by rheumatoid arthritis (demonstrated as juxta-articular osteoporosis, multiple, bilateral and symmetrical joint space loss, erosions, effusions, and pannus formation), gout (manifested as preserved joint space till late, well-corticated eccentric erosions—simulating rat bites, eccentric soft-tissue masses, and typical location, such as the first metatarsophalangeal and tarso-metatarsal joints, as well as the Achilles insertion), and neuropathic (Charcot) joint (demonstrated as joint destruction, disorganization, debris, dislocation, hypointense signal intensity on all sequences and typical patient population with neuropathy or diabetes and bilateral involvement of subtalar joints and midfoot) (Figs. 114–116). In pigmented villonodular synovitis, the hyperplastic synovium demonstrates multiple amorphous or nodular intra-articular masses, which feature low signal on all pulse sequence due to hemosiderin deposition; the deposits are particularly evident as blooming artifacts on gradient-echo images, and enhancement is seen after gadolinium administration. Erosions of the joint surfaces may also be present in the advanced cases (Figs. 117, 118).

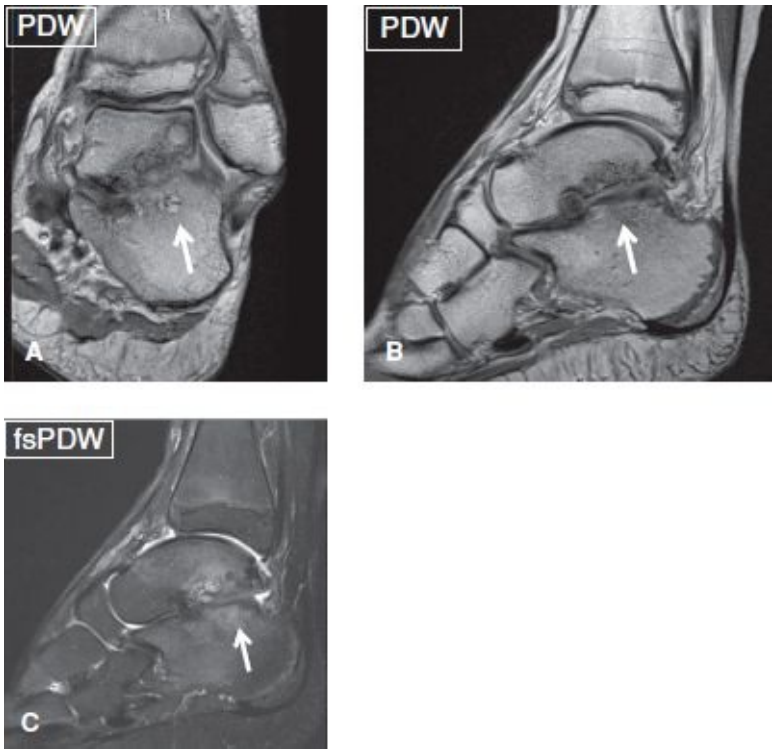

Fig. 113: Subtalar joint osteoarthritis. Coronal **(A)** and sagittal **(B, C)** images exhibit multifocal erosions of the joint surfaces, joint space loss, subchondral edema and cyst formation (*arrows*) at the posterior subtalar joint, in keeping with severe secondary osteoarthritis in this patient with known connective tissue disorder. Secondary OA typically shows diffuse joint space loss if superimposed on inflammatory arthropathy.

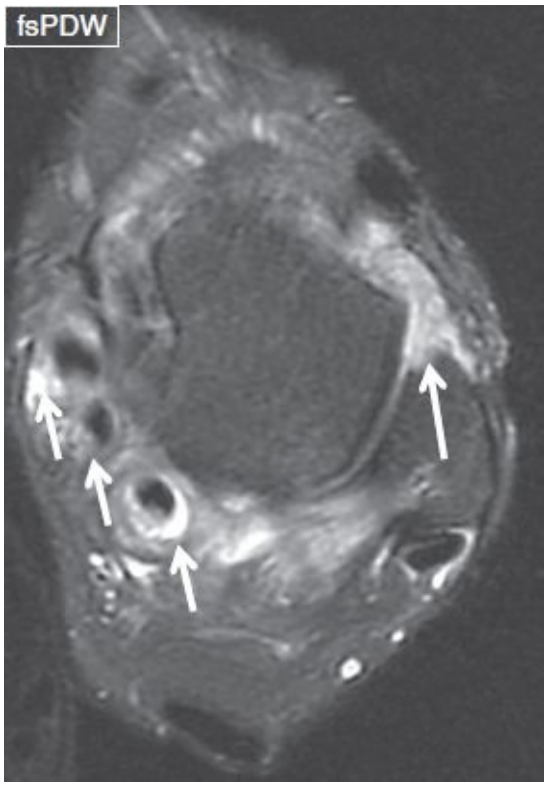

Fig. 114: Rheumatoid arthritis. Axial image shows joint effusion and synovial proliferation in the ankle joint (*long arrow*), along with tenosynovitis of the flexor tendons (*short arrows*).

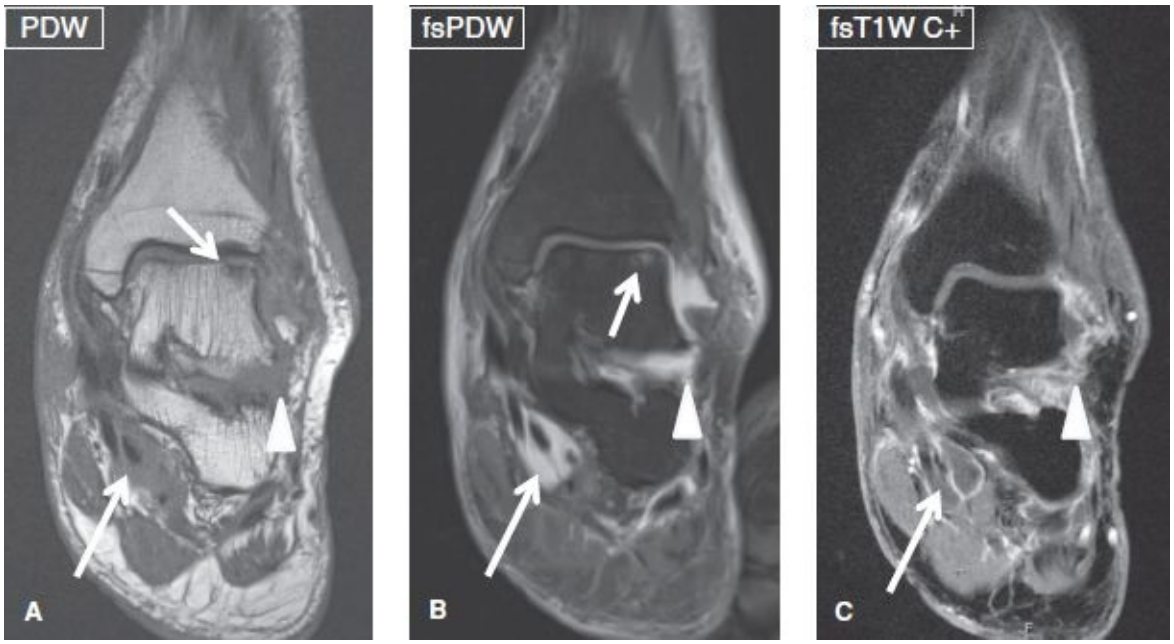

Fig. 115: Gout. Coronal images **(A–C)** display an eccentric erosion (*short arrows*) of the lateral talar dome, fluid distension of the ankle joint (*arrowheads*), as well as flexor hallucis longus tenosynovitis (*long arrows*). Joint aspiration revealed gouty crystal deposits.

Fig. 116: Neuropathic (Charcot) ankle joint. Sagittal images **(A, B)** demonstrate extensive destruction of the ankle joint (*long arrows*). There is diffuse soft-tissue edema of the forefoot, as well as a well-circumscribed ovoid lesion, compatible with an abscess (*short arrows*).

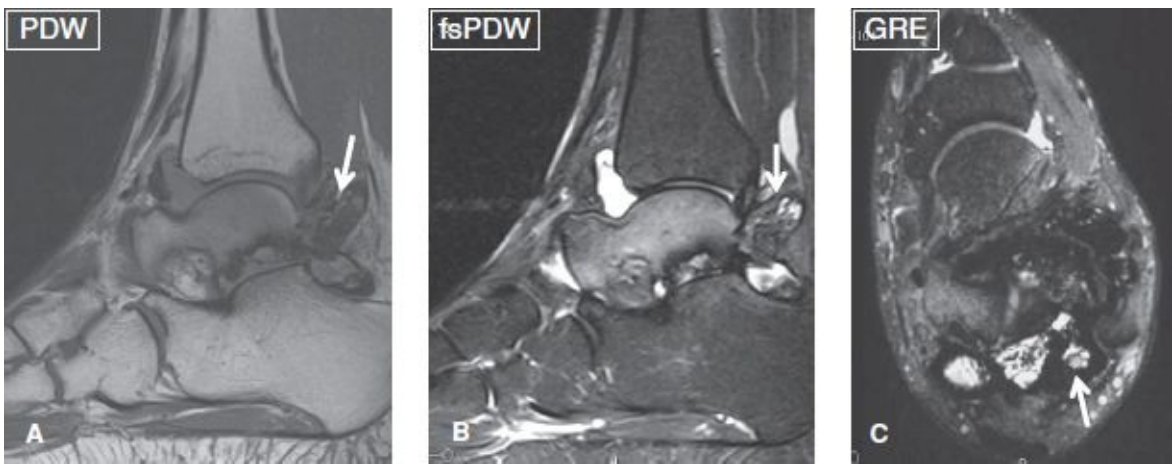

Fig. 117: Pigmented villonodular synovitis of the ankle. Sagittal **(A, B)** and axial **(C)** images show fluid distention of the ankle joint, which contains amorphous hypointense lesions (*arrows*), corresponding to hyperplastic synovium with hemosiderin deposition. Notice blooming on the GRE image.

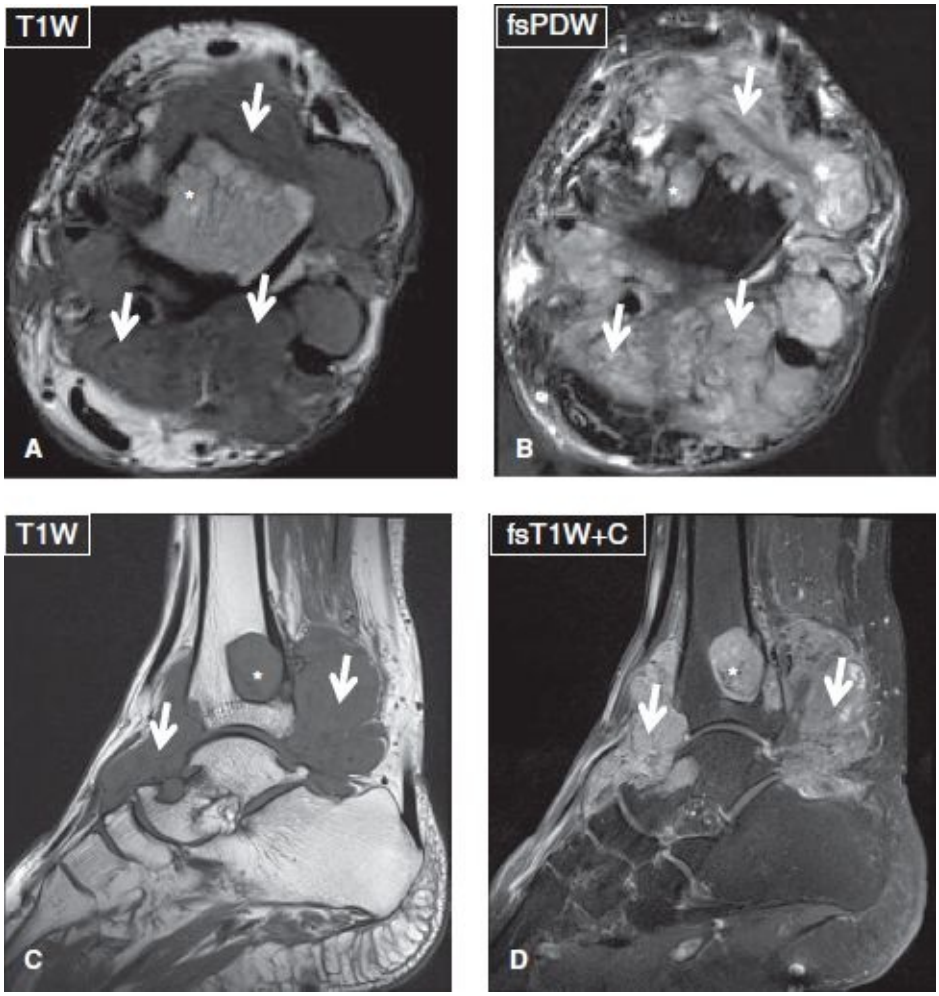

Fig. 118: Pigmented villonodular synovitis of the ankle. Axial **(A, B)** and sagittal **(C, D)** images demonstrate distention of the ankle joint by multiple T1 hypointense masses (*arrows*), which enhance after gadolinium administration. The lesions cause cortical erosions in the tibia and talus, and one of them (*asterisks*) has a subcortical location within the distal tibia.

The term OCL is best reserved for one or two focal lesions of the osteochondral complex. In the acute stage, the lesion may be termed osteochondral contusion injury/fracture, and in adolescents, it might represent osteochondritis dissecans. Obviously, a patient can develop multiple OCLs, diffuse lesions, or even lesions on both sides of the joint, which are best referred to as osteoarthritis. The patients usually develop osteochondral injury during ankle sprain and present with pain on activity. The description of the lesion should include the location (medial, central or lateral, and anterior or posterior; tibial plafond or talar dome); the size in three dimensions; the status of the overlying and adjacent cartilage (heterogeneous signal, low-, high- or full-thickness fissure, defect, flap or delamination); articular bony plate irregularity or depression; subjacent bone marrow changes (edema, cyst, sclerosis); and any signs of potential instability, such as fluid cleft at the base of the lesion, in situ body, loose body, gadolinium undercutting the lesion on arthrography, large (>1 cm) lesion and extensive cystic changes at the base of the lesion. OCLs of the lateral talar dome tend to be thin and shallow, with the surface fragment greater in width than in depth whereas lesions of the medial dome usually have a deeper, crater-like appearance

(Figs. 119–124). Sources of diagnostic pitfalls include fibrous or synovial bands abutting the tibial plafond anteromedially at the notch of Harty, or synovial fringes at the posteromedial or posterolateral aspect of the ankle, which can mimic OCL. Talar dome OCLs can be graded according to the classification by Berndt and Harty, in which *stage I* lesions are restricted to the subchondral bone, with apparent preserved integrity of the overlying articular cartilage, *stage II* lesions feature a partially detached fragment of articular cartilage and subchondral bone, *stage III* lesions demonstrate a completely detached fragment, which is still located within the defect produced (in situ body), and *stage IV* lesions consist of a completely detached osteochondral fragment, which is located in a joint recess away from the lesion site. Another practical classification for describing the lesion that encompasses most imaging findings would be: a) stable lesion (small [<1 cm] area of subchondral cyst, edema, sclerosis, cartilage irregularity); b) potentially unstable (>1 cm, extensive subchondral cysts or marrow edema at the base of the lesion, in situ body, large cartilage flaps/delamination); and c) unstable lesion (free body, gadolinium or fluid undercutting the lesion).

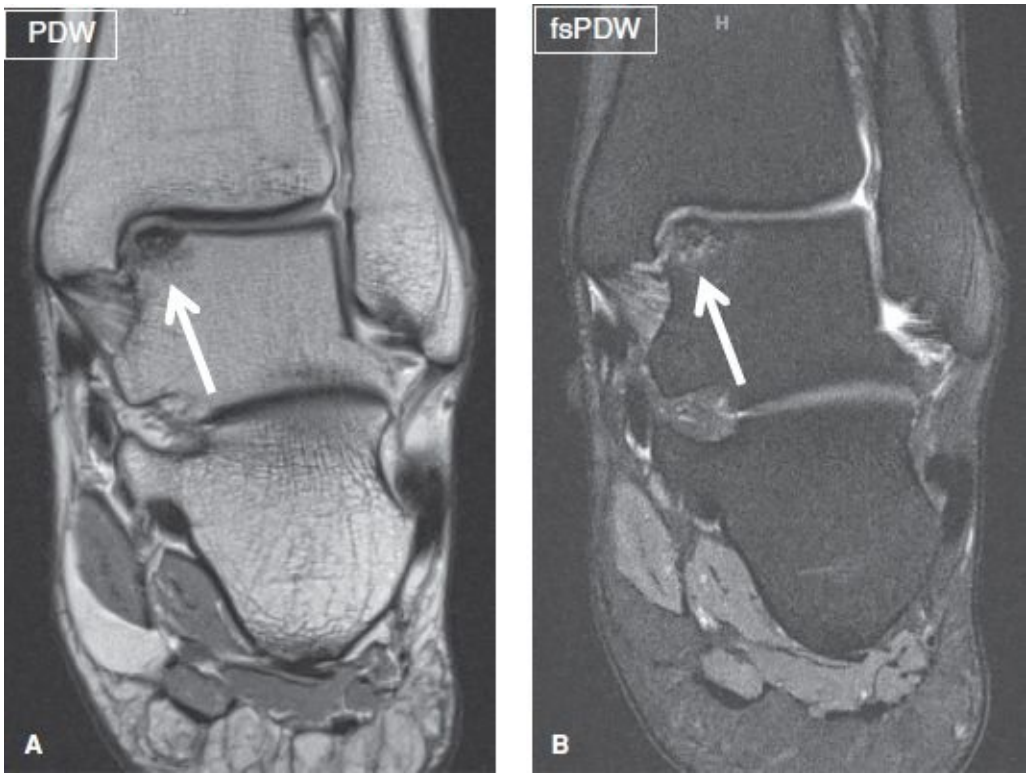

Fig. 119: Osteochondral lesion of the talus. Coronal images **(A, B)** display an osteochondral lesion (*arrows*) of the medial talar dome. Extensive cystic changes underneath the bone fragment and overlying cartilage irregularity indicate that the lesion is potentially unstable.

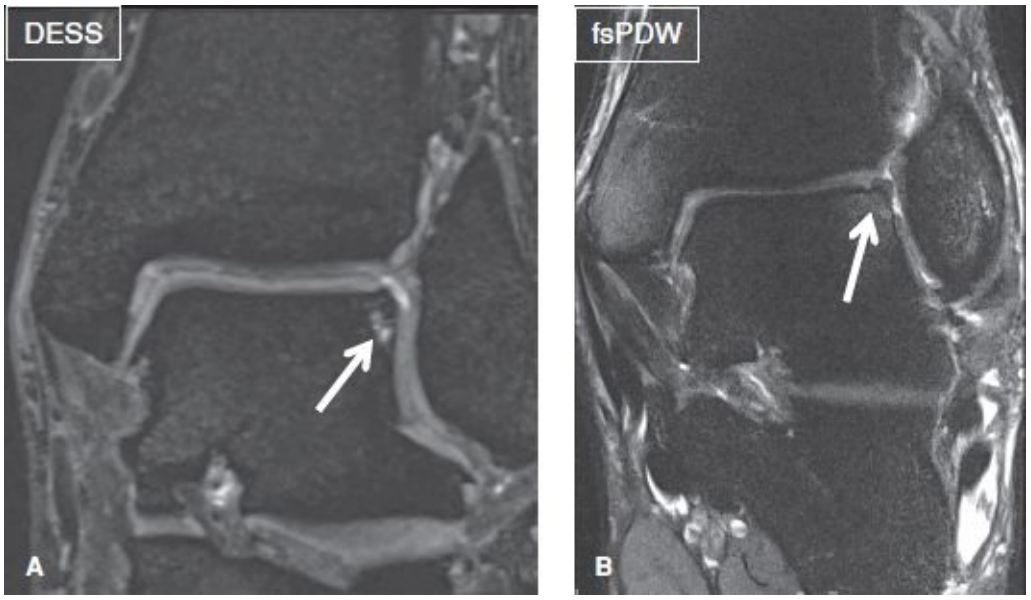

Fig. 120: Small osteochondral lesions of the talar dome on coronal images. Two different subjects. **A:** Subcortical cysts (*arrow*) are evident in the lateral talar dome, with associated focal delamination of the overlying articular cartilage. **B:** A focus of mild bone marrow edema (*arrow*) is present in the lateral talar done, with overlying cartilage flap.

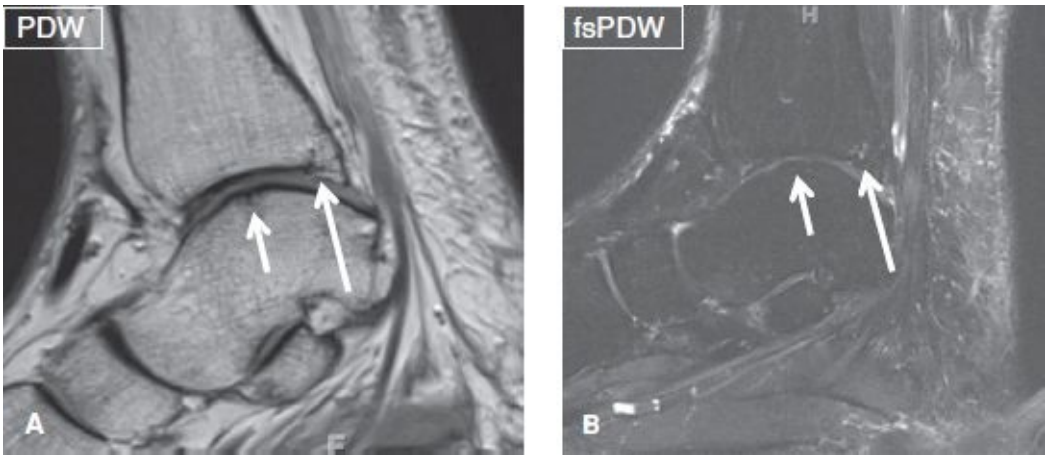

Fig. 121: Chronic osteochondral lesion of the talus. Sagittal images **(A, B)**. A focal flattening of the cortex with associated subchondral cysts (*short arrows*) is evident at the central aspect of the talar dome. This reflects a chronic osteochondral lesion, caused by an old fracture of the posterior malleolus with additional OCL (*long arrows*).

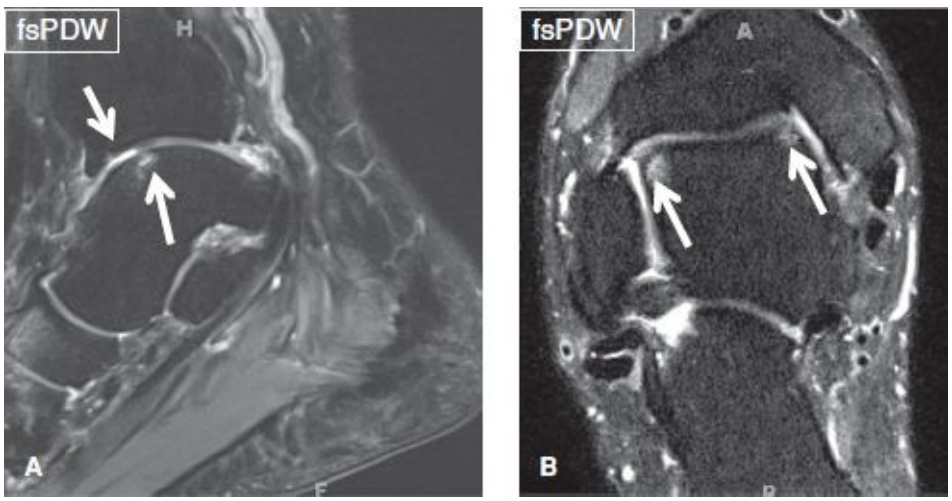

Fig. 122: Osteochondral lesions of the talus and tibia. Sagittal **(A)** and coronal **(B)** images demonstrate multiple OCLs with associated subchondral cysts (*arrows*) at the talar dome and tibial plafond. Notice large area of full-thickness cartilage loss of the anterior tibia.

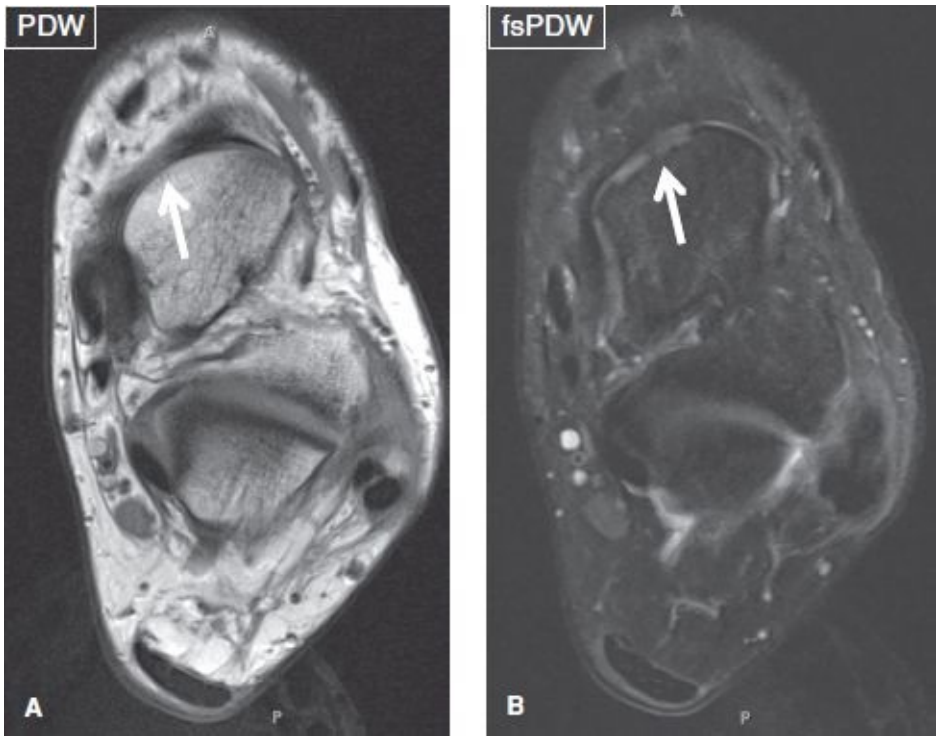

Fig. 123: Osteochondral lesion of the talus. Axial images **(A, B)** show a large full-thickness cartilage defect at the anterior joint surface of the talus (*arrows*), with no underlying marrow edema, in keeping with a chronic osteochondral lesion.

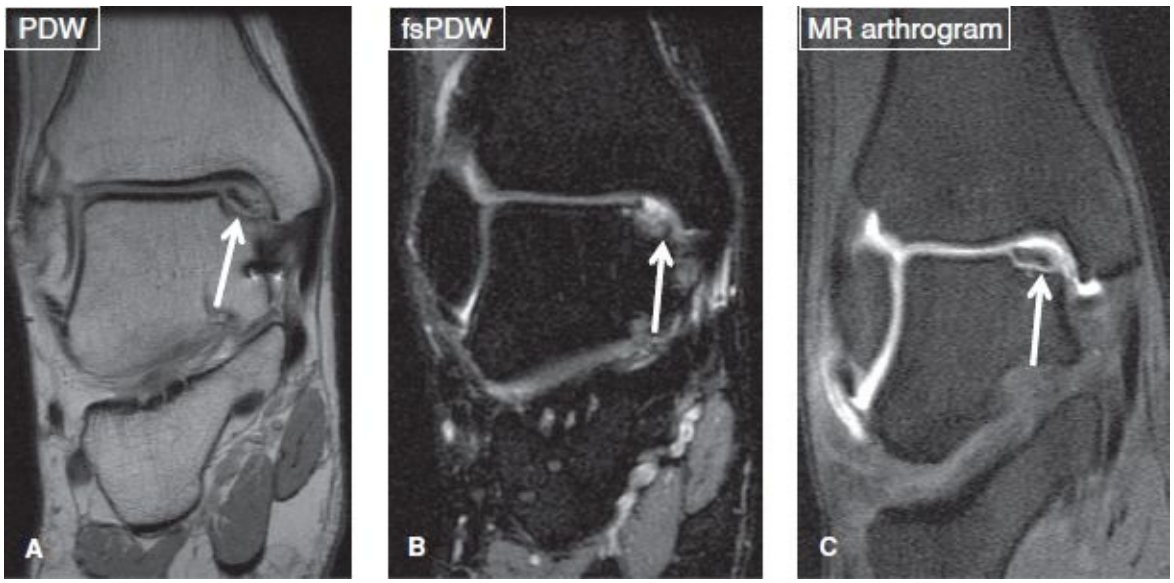

Fig. 124: Osteochondral lesion of the talus. Coronal images **(A–C)** exhibit an avulsed cortical in situ bone fragment at the medial aspect of the talar dome with fluid and gadolinium undercutting at the base of the lesion, in keeping with an unstable osteochondral lesion.

Bones (other than subarticular marrow and malleoli): [<Normal> <Midfoot

enthesopathy> <Midfoot osteoarthritis>]

Important lesions to identify include bone contusions, fracture, osteomyelitis, tumor, or avascular necrosis. Bone marrow edema and cystic changes are best seen on fs images, while bony productive changes and sclerosis are best identified on non–fs images. Non–fs T1W and PDW images are useful to differentiate infection, subchondral cysts, infarcts, and fractures from reactive bone marrow edema, since the reactive bone marrow change is predominantly evident on fat-suppressed images (Fig. 125). Osteomyelitis typically demonstrates ill-defined T1 hypointense bone marrow area, which enhances following gadolinium administration (Figs. 126, 127). Associated findings may include sinus tract reaching the bone, cellulitis, myositis, and soft-tissue abscess. In adults, if there is no ulcer, there is very little chance of osteomyelitis (Figs. 128, 129).

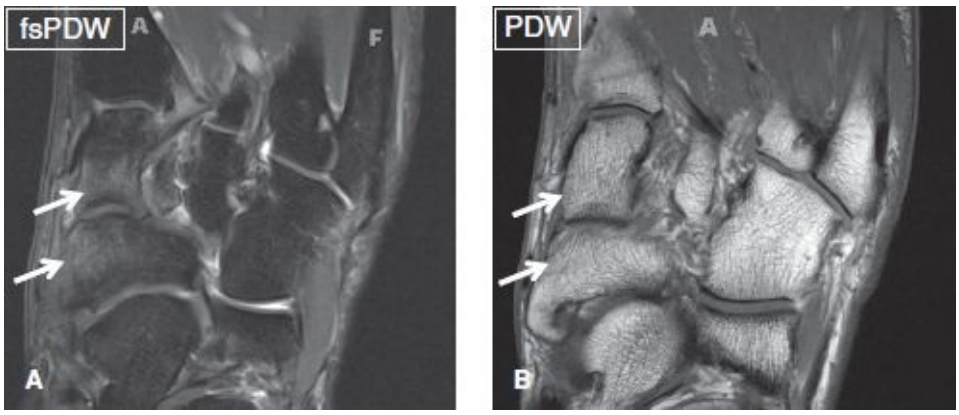

Fig. 125: Bone contusions on axial images. **A:** The fat-suppressed image shows mild hyperintensity, compatible with marrow edema and contusions at the navicular and medial cuneiform bones (*arrows*). **B:** No corresponding marrow signal change is apparent in the non–fat-suppressed image (*arrows*) suggesting no superimposed fracture.

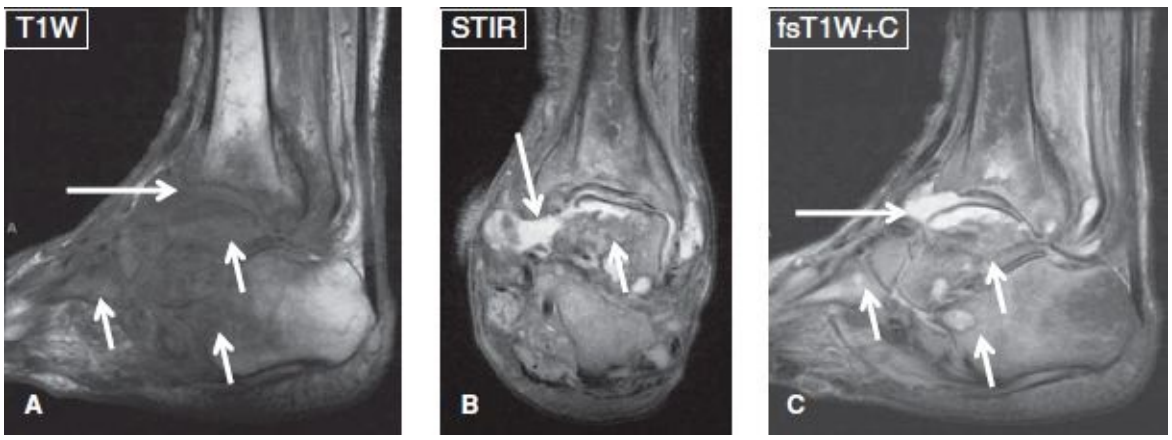

Fig. 126: Osteomyelitis and septic arthritis. Sagittal **(A, C)** and coronal **(B)** images show extensive marrow changes of T1 hypointensity in the bones of the hind- and midfoot and corresponding hyperintensity on fluid-sensitive image **(B),** which enhance after contrast administration (*short arrows*), in keeping with osteomyelitis. Deformity and fluid distention of the tibiotalar joint (*long arrows*) suggest septic arthritis.

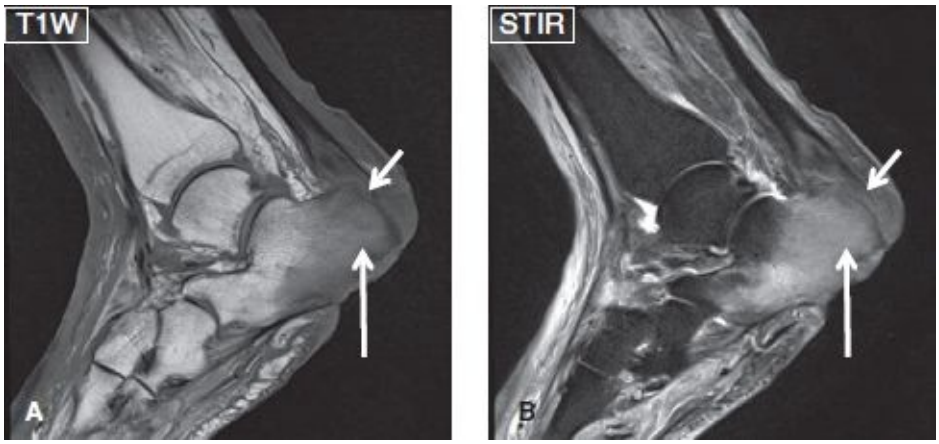

Fig. 127: Osteomyelitis of the calcaneus. Sagittal images exhibit T1 hypointensity and T2 hyperintensity of the marrow of the posterior calcaneus (*long arrows*) with loss of cortical hypointensity at the site of the ulceration. Thickening and hyperintensity of the distal Achilles tendon corresponds to tendinitis (*short arrows*).

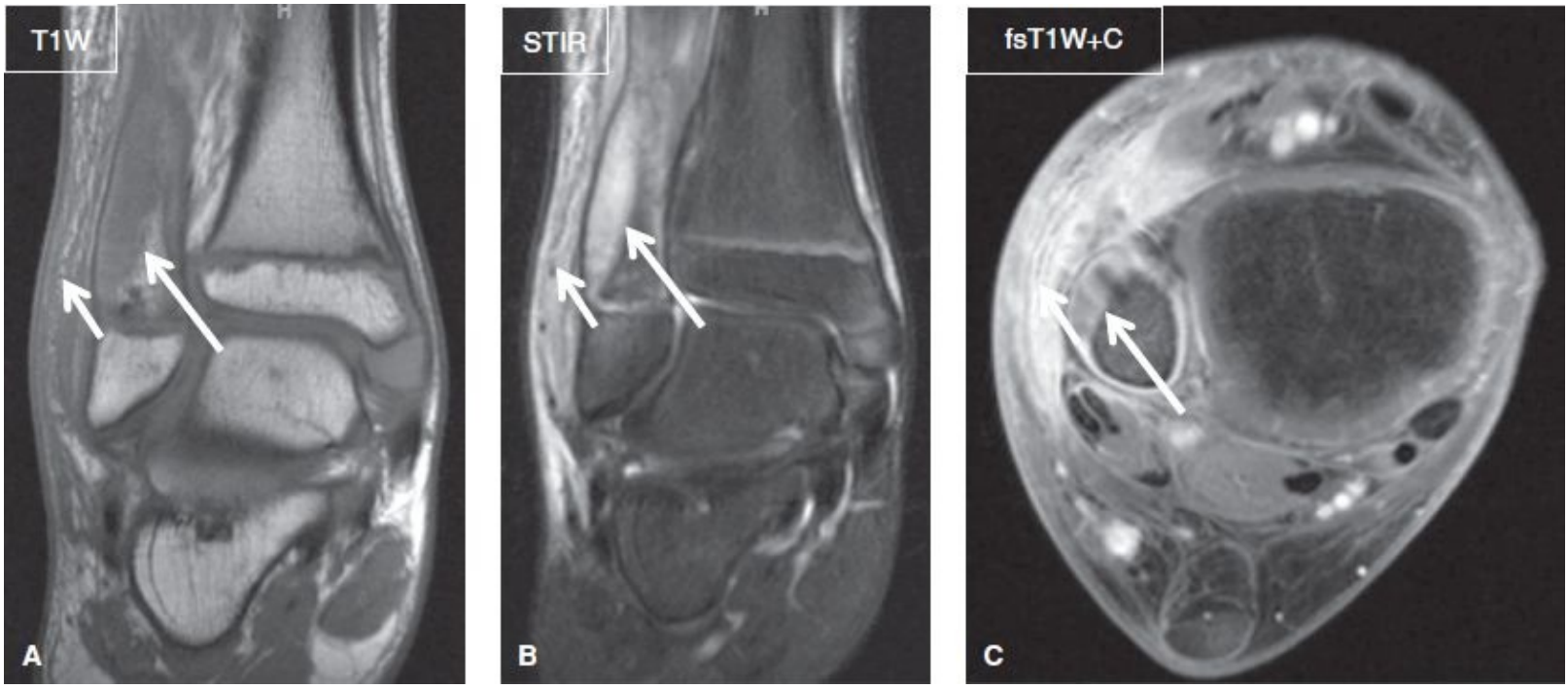

Fig. 128: Subperiosteal abscess. Coronal **(A, B)** and axial **(C)** images show well-circumscribed partially enhancing subperiosteal fluid collection (*long arrows*) at the distal fibula. There is associated edema and contrast enhancement of the adjacent fascia and muscle (*short arrows*), in keeping with fasciitis and myositis.

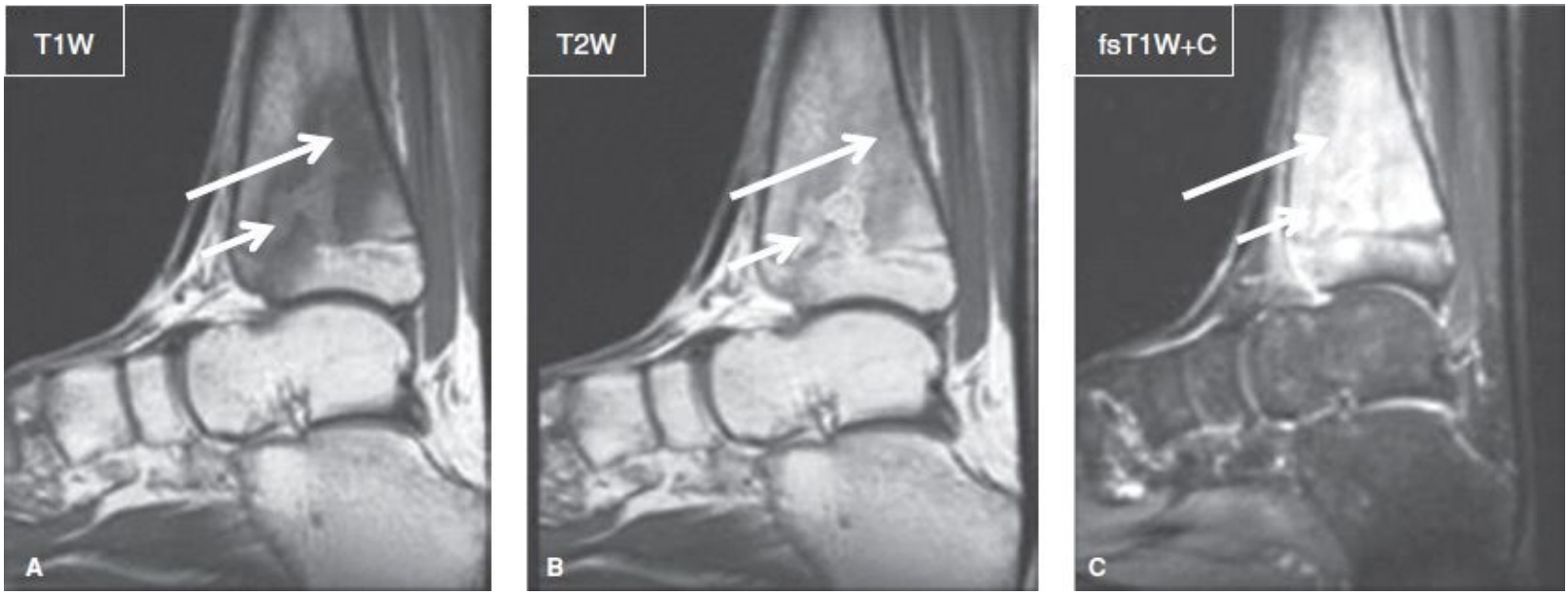

Fig. 129: Brodie abscess. Sagittal images **(A–C)** demonstrate a relatively well-circumscribed lesion with fluid-like internal signal and enhancing geographic borders in the tibial metaphysis (*short arrows*). There is T1 hypointensity and enhancement of the surrounding marrow (*long arrows*), in keeping with osteomyelitis.

Young patients presenting with painful flat (peroneal spastic) feet might have calcaneonavicular or talocalcaneal coalitions, which appear as fibrous union (dark on fs PDW and fs PDW images), cartilaginous union (intermediate on non–fs PDW, fs PDW, and fs T2W images), mixed fibrocartilaginous union (mixed signals), or frank bony union (marrow continuity). The union may be associated with stress-related subchondral cystic changes, bone marrow edema, pes planus, hind foot valgus, and secondary degenerative changes of the posterior subtalar joint. In calcaneonavicular coalition, there is elongation of the anterior process of calcaneus ("ant eater" sign) and adjacent naviculum ("reverse ant eater" sign) (Figs. 130–134). In talocalcaneal coalition, the "drunken waiter" sign is evident with medial elongation or protrusion of the united dysplastic middle facet of the subtalar joint (Fig. 135). In general calcaneonavicular coalition is much easier to identify on MR imaging as compared to the talocalcaneal coalition. Talar beak at the dorsal talonavicular ligament attachment is also more common in calcaneonavicular coalition (50%) as compared to the talocalcaneal coalition (25%).

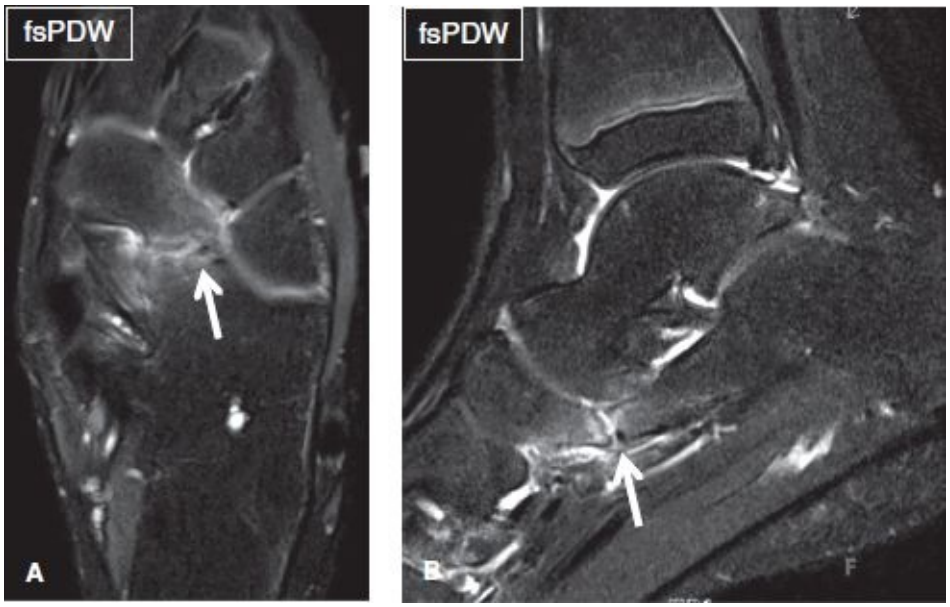

Fig. 130: Calcaneonavicular coalition. Axial **(A)** and sagittal **(B)** images display pseudo-articulation (cartilagenous union) between the anterior process of the calcaneus and the navicular bone, with associated marrow edema across the articulating surfaces and partial disruption of synchondrosis (*arrows*). Notice the “ant eater” and “reverse ant eater” signs.

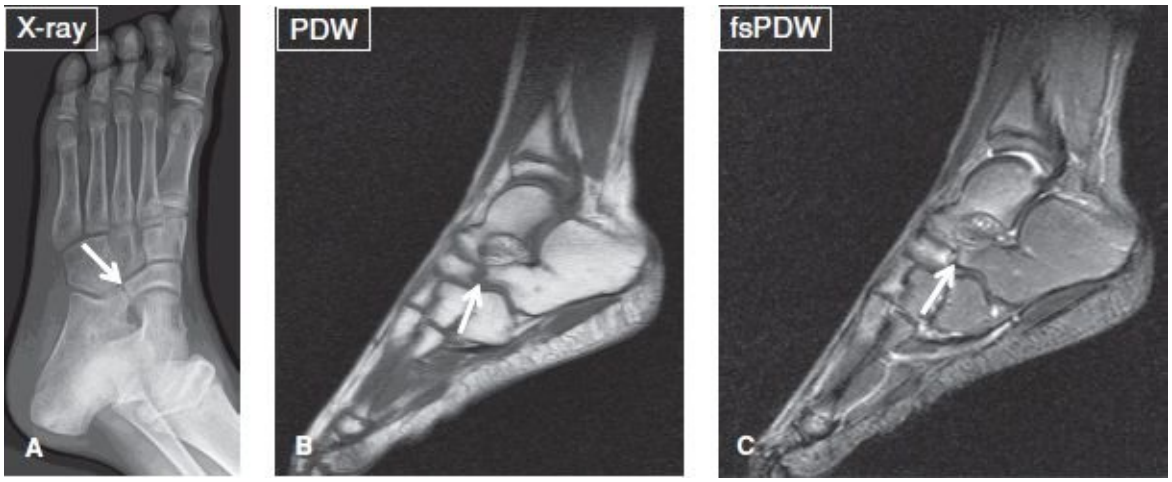

Fig. 131: Calcaneonavicular coalition. **A:** Lateral radiograph shows pseudoarticulation (*arrow*) band marrow edema between the anterior process of the calcaneus and the navicular bone. **B, C:** On sagittal MR images, hypointensity across the articulating surfaces (*arrows*) indicates a fibrous coalition. Notice mild stress related edema at the synchondrosis.

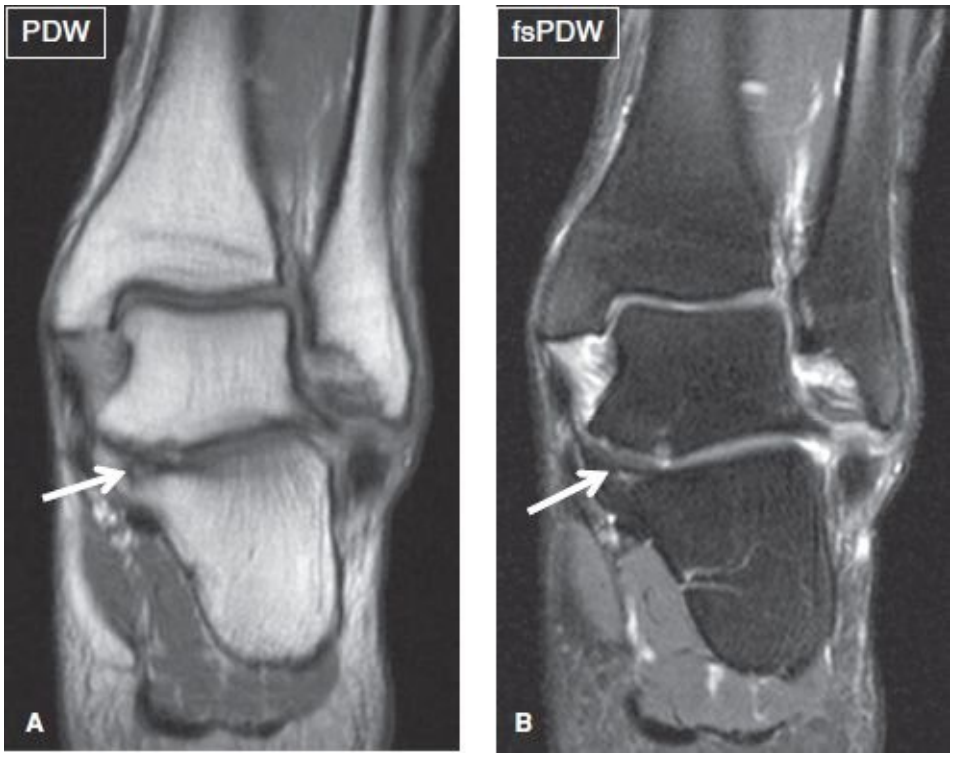

Fig. 132: Subtalar coalition. Coronal images **(A, B)** show fibrocartilaginous coalition of the middle facet of the subtalar joint (*arrows*), demonstrating intermediate to dark signal across the coalition surface.

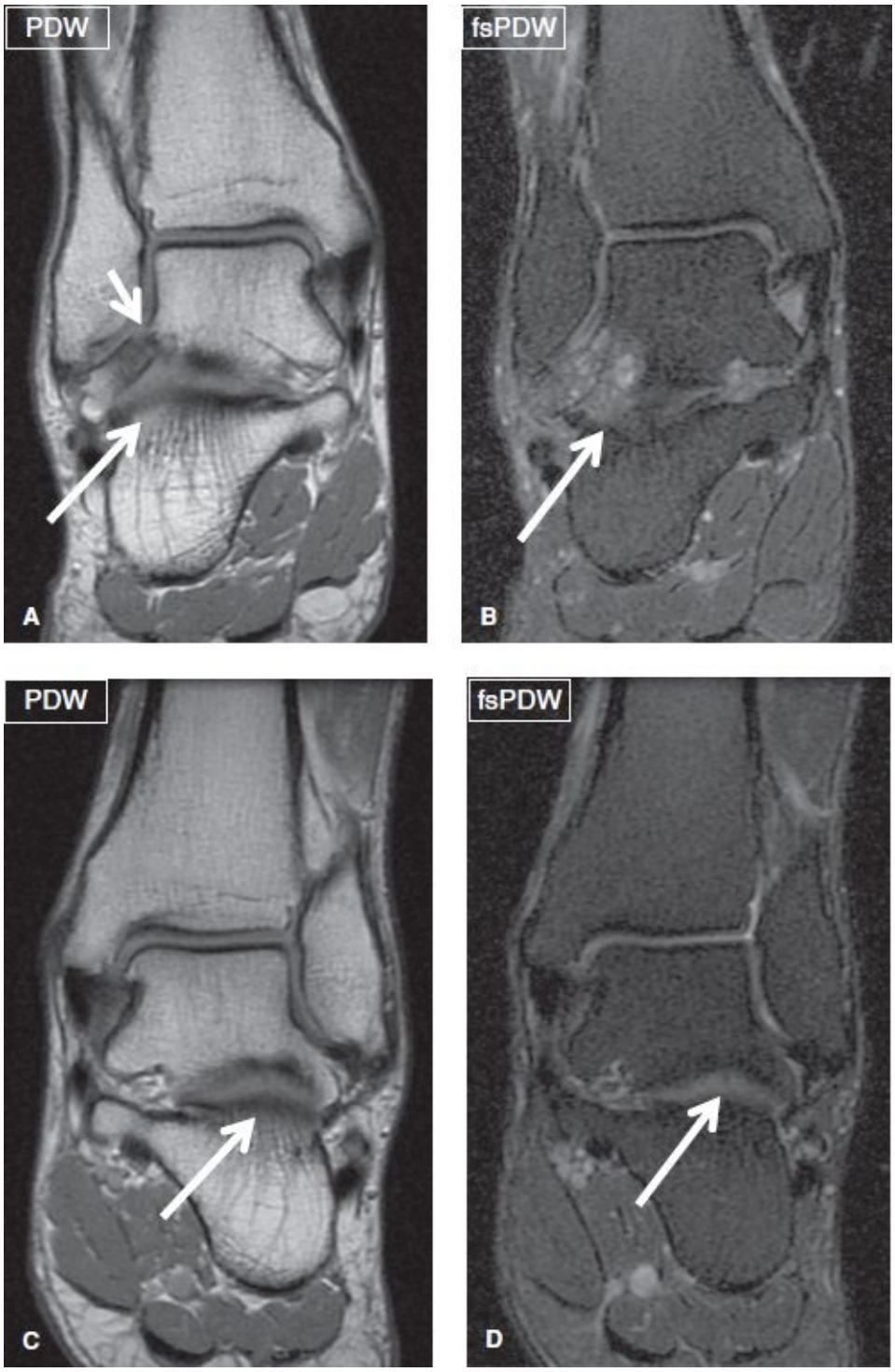

Fig. 133: Subtalar coalition. Coronal images **(A, B)** show cartilaginous coalition of the posterior facet of the subtalar joint (*long arrows*), demonstrating intermediate signal across the coalition surface. Notice elongated lateral process of talus with partial nonunion from old fracture (*short arrow*). The contralateral ankle **(C, D)** in the same patient shows milder changes of posterior subtalar coalition and elongated lateral process of talus.

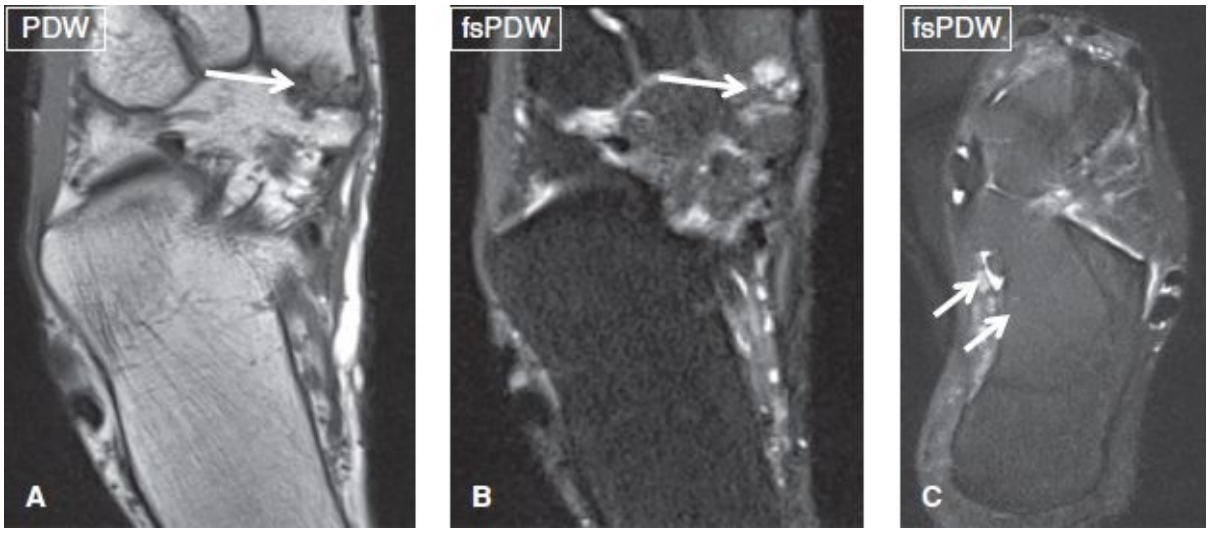

Fig. 134: Navicular–cuneiform coalition on axial images. **A, B:** A fibrous coalition is evident between the navicular and the medial cuneiform bones (*arrows*) with stress-related cystic changes across the synchondrosis. **C:** On a more inferior level, co-existing hyperintensity of the medial and lateral plantar nerves (*arrows*) is indicative of traction neuropathy.

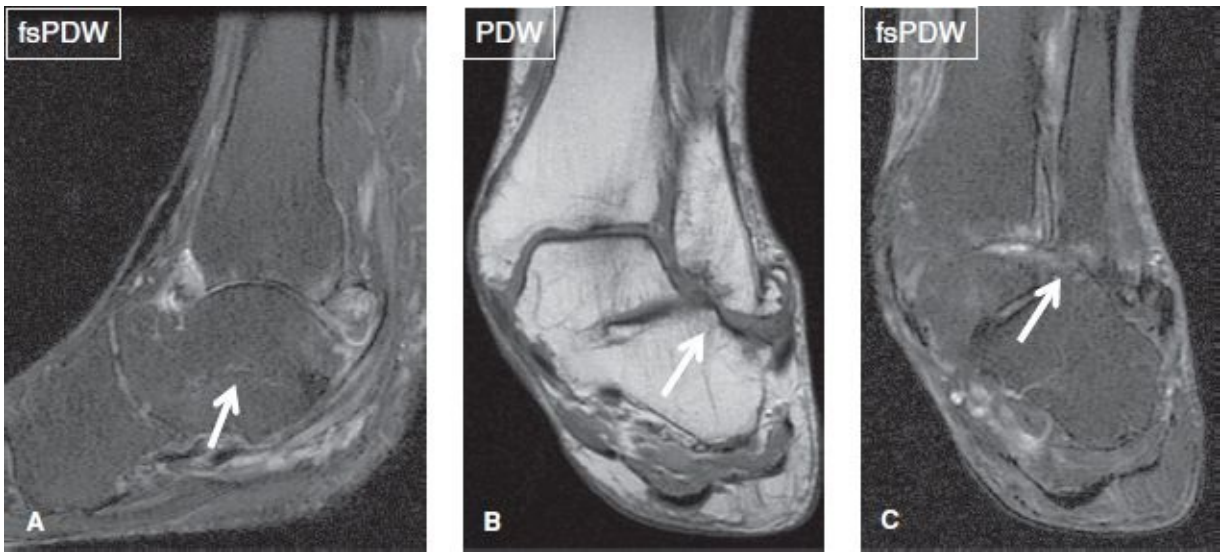

Fig. 135: Talocalcaneal coalition. **A:** Sagittal image exhibits continuation of bone marrow signal across the talocalcaneal joint (*arrow*), indicating a bony coalition. **B, C:** On coronal images, there is hindfoot valgus with calcaneofibular impingement (*arrows*) apart from findings of bony subtalar middle facet coalition. Note the dysplastic sustenticulum talus, aka "drunken waiter sign".

A physeal bar (premature physeal arrest) is the result of trauma (Salter–Harris injury) or infection of the unfused physis. It consists of a bridge, which crosses the growth plate, and it may be fibrous, osseous, or contain granulation tissue. Bony bars are isointense to bone marrow whereas fibrous or dense bony bars are typically hypointense on all pulse sequences. In the acute and subacute setting, granulation tissue forms within the healing site, featuring hypointensity and hyperintensity on T1W and fluid-sensitive images, respectively. It becomes hypointense on all sequences with chronicity (Fig. 136).

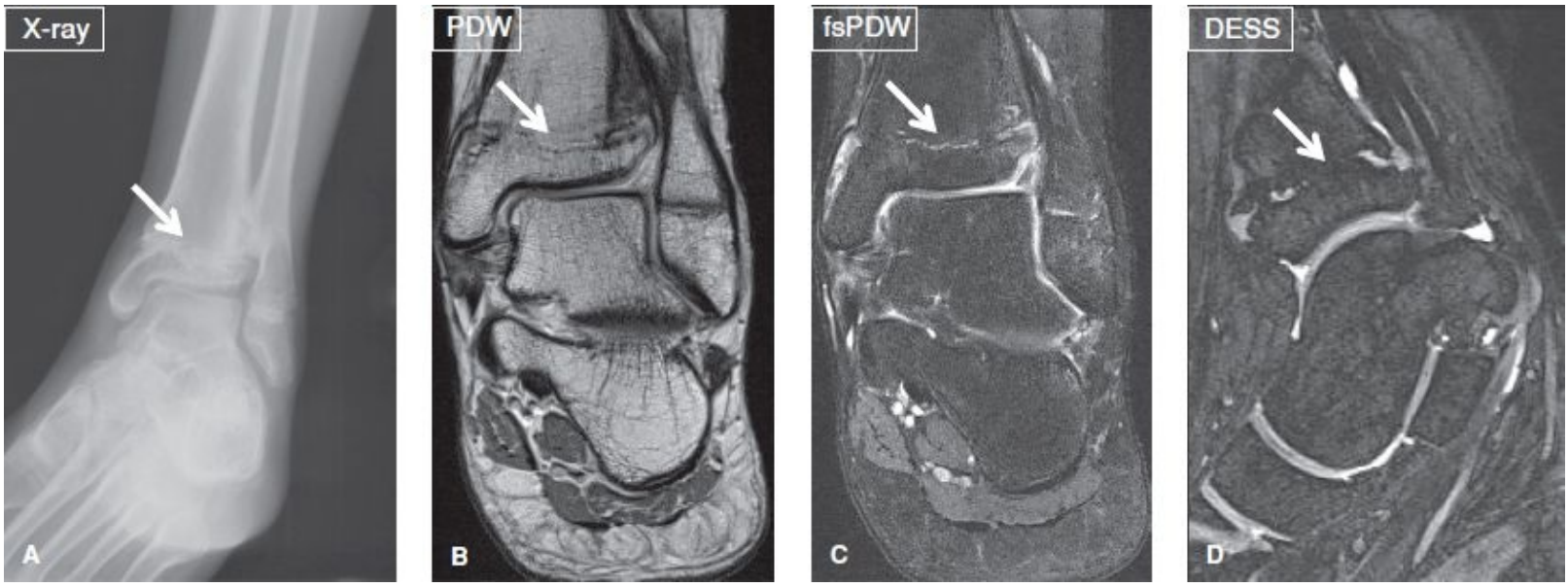

Fig. 136: Physeal bar. Anterosuperior radiograph **(A)** demonstrates a transversely oriented thin radiodense bridge (*arrow*) at the central aspect of the distal tibial metaphysis. On coronal **(B, C)** and sagittal **(D)** images, the bridge (*arrows*) is readily identified.

Multi-focal, patchy reticular or "starry sky"-like bone marrow edema is seen with disuse osteoporosis or complex regional pain syndrome (CRPS), the differentiation of which depends on the clinical setting (Fig. 137). For example, in case of a patient who was recently (days or weeks) casted at the knee or calf, the edema-like signal at the ankle would reflect disuse osteoporosis, whereas in the case of a subject who develops hyperesthesia or dysesthesia following a recent trauma, surgery, or a similar inciting event, the changes might be indicative of CRPS. Depending upon the stage, the latter entity presents with different imaging appearances, including soft-tissue edema initially, followed by bone marrow edema like changes, and finally featuring soft tissue atrophy (atrophic stage). The bone marrow signal alterations demonstrate a sharp transition from normal to abnormal, and the abnormal marrow changes are also evident distally throughout the ankle and foot. After contrast administration, decreased perfusion may be seen in the affected foot. A triple-phase nuclear scan could also be used to confirm the diagnosis. In asymptomatic children, patchy foci of normal red bone marrow may simulate the aforementioned imaging appearances, therefore, disuse osteoporosis or CRPS should not be overdiagnosed and the clinical findings should be carefully taken into consideration.

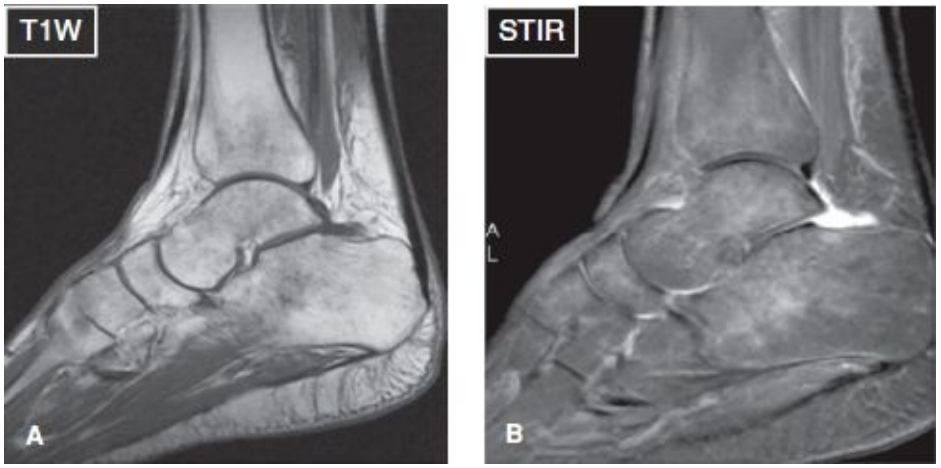

Fig. 137: Complex regional pain syndrome. Sagittal images **(A, B)** exhibit diffuse reticular marrow edema in the bones of the hind- and midfoot.

Stress reactions as well as stress and insufficiency fractures most often involve the calcaneus, talus, and naviculum. Marrow edema related to stress reaction is seen as increased signal on T2W/fs PDW/fs T2W images without substantial low signal on non fs T1W/PDW images (Fig. 138). To diagnose actual fracture, one should look for a hypointense line in the cloud of edema or a confluent area of T1 hypointensity, which would suggest inter-trabecular injury (Figs. 139, 140). Ankle pilon and trimalleolar fractures require surgical fixation in the following instances, unstable fracture, significant deltoid ligament injury, articular surface step off of more than 2 mm, posterior malleolar fracture involving more than 25% of the tibial plafond articular surface, and posterior talar translation.

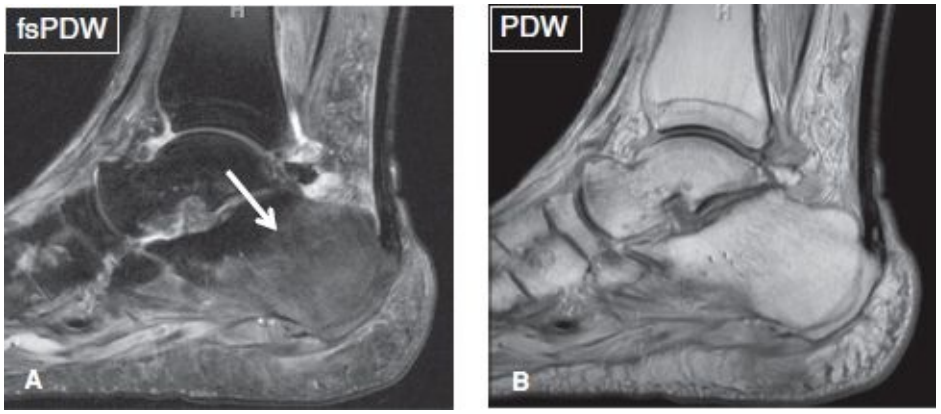

Fig. 138: Stress reaction of the calcaneus. Sagittal images. **A:** A diffuse area of hyperintensity, representing stress related marrow edema (*arrow*), is evident in the middle and posterior calcaneus, without a frank fracture line. **B:** The respective non–fat-suppressed image confirms absence of fracture line.

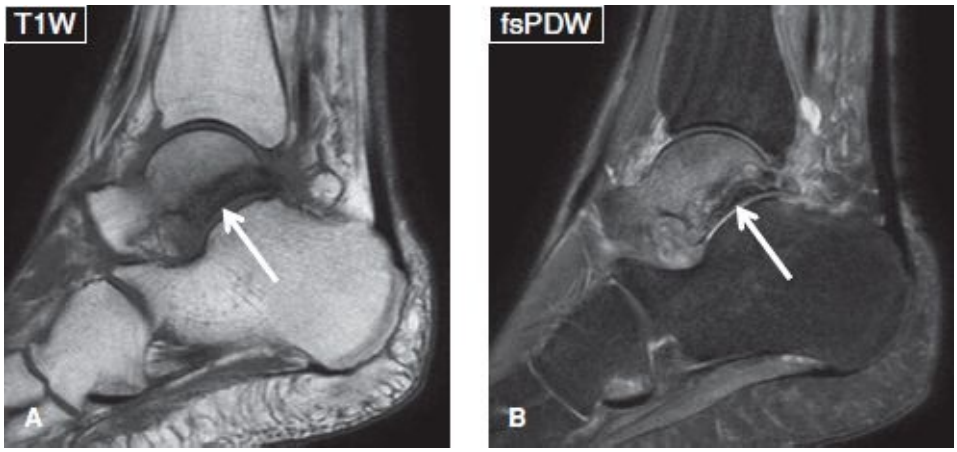

Fig. 139: Stress fracture of the talus. Sagittal images **(A, B)** demonstrate marrow edema in the talus, as well as a fracture line (*arrows*), paralleling the posterior subtalar facet.

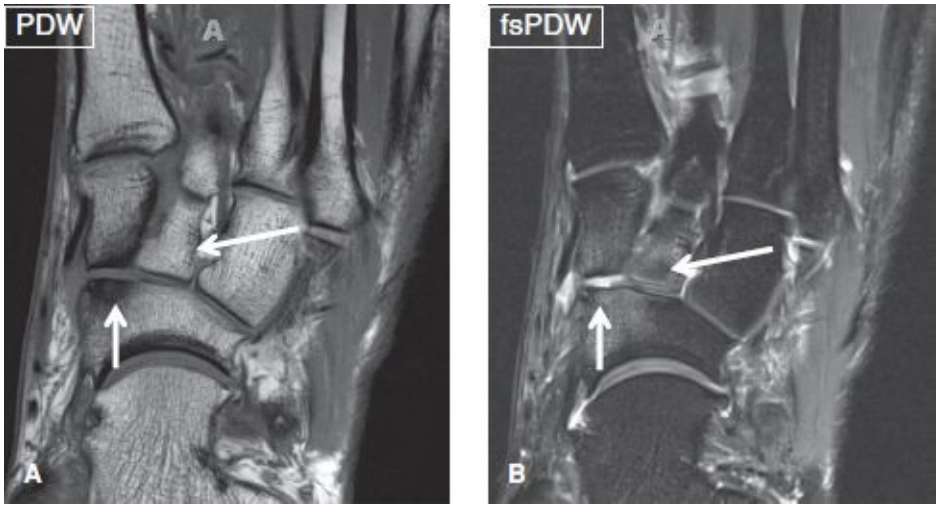

Fig. 140: Subchondral fractures of naviculum and medial cuneiform. Axial images **(A, B)** demonstrate subchondral fractures of naviculum and medial cuneiform with full-thickness cartilage defects (*short arrows*). Notice stress reaction of the intermediate cuneiform (*long arrows*).

Pilon (tibial plafond) fractures are seen in young adults with high energy trauma and axial load mechanism from foot up. They are classified as a) extra-articular, b) partially intra-articular, and c) complete intra-articular or metaphyseal dysjunction. Generally, it results in 3 major bone fragments, medial, anterolateral and posterolateral. The medial, anterolateral (Chaput) and posterolateral (Volkmann) fragments are at the deltoid ligament, anterior inferior distal tibiofibular and posterior inferior distal tibiofibular ligament attachments, respectively. About 75% have associated fibular fractures. Operative treatment is required with >2 mm displacement. Pilon fracture treatment involves restoring the limb length with external fixator, reducing fibular shortening, and subsequent internal fixation in the 2nd stage. During internal fixation, it is important to reduce the posterolateral fragment 1st to convert the complete fracture to partial intra-articular, and then fix anteriorly. Varus malunion and fibular shortening should be avoided.

Calcaneal fractures classically exhibit two major bone fragments, a lateral tuberosity

fragment and a medial sustenticulum fragment, resulting in hindfoot varus. Degree of medial displacement of the fracture should be reported as well as fracture extensions to the tibiolalar and calcaneocuboid joints. The Sanders classification system is used to evaluate the intraarticular fractures, which involve the posterior facet of the calcaneus. This classification is based on the number of intraarticular fracture lines and fragments, and is useful in predicting outcome. As on moves from type 1 to type 4 injuries, expected outcomes become progressively worse. Type 1 includes all intraarticular fractures that have less than 2 mm of articular displacement, regardless of the number of fracture lines/fragments present. Type 2 involves one primary fracture line and two fragments. Type 3 involves two primary fracture lines and 3 fragments, and it usually presents with depression of the central fragment. Type 4 involves three or more primary fracture lines with greater than 2 mm of articular displacement, and is therefore severely comminuted. When Bohler's angle is less than 0 degrees, only option is joint fusion.

Talar fractures may involve neck, head, body or its medial, lateral or posterior processes. Talar neck fractures predispose to AVN. Hawkins classification is used to predict the chances of AVN. Hawkins I is a non-displaced fracture (chance of AVN: 0–13%). Hawkins II involves subtalar dislocation (chance of AVN: 20–50%). Hawkins III involves subtalar and tibiotalar dislocations (chance of AVN: 20–100%). Hawkins IV involves subtalar, tibiotalar and talonavicular dislocations (chance of AVN: 70–100%). Hawkins IV is also associated with posteromedial dislocation and deltoid ligament injury. Any other complex fracture also classifies as Hawkins IV. The main mechanism of injury is dorsiflexion. One should place the ankle in equinus and plantar flexion and reduce any varus or valgus malalignment. Operative intervention is necessary, if there is joint incongruity or displaced fragment in the joint. Early operative intervention and mobility are important to reduce ankle stiffness and the goal is to avoid varus malignment. Bad reduction would lead to malunion, varus hindfoot malalignment, medial column shortening and lateral foot overload, which would require calcaneal osteotomy. AVN if asymptomatic requires no surgical intervention. However, if symptomatic, ankle fusion would be needed. Talar head fracture occurs with plantar flexion mechanism. It may associated with mid foot injuries and talonavicular dislocation. Treatment differs if more than or less than 50% of the talar head is affected. Lateral process fracture results from avulsion (inversion and plantar flexion mechanism) or impaction (eversion and dorsiflexion mechanism) injuries. The fracture may be fixed or the fragment may be surgically removed. Finally, subtalar dislocations can occur medially (more common, club foot like appearance to the foot) or laterally (uncommon, high energy trauma and pes planus appearance to the foot). During reduction, medial dislocation may be blocked by PTT or talonavicular impaction, while lateral dislocation may be blocked by extensor digitorum brevis tendon or talonavicular impaction.

Osteonecrosis (avascular necrosis) in the ankle most often involves the talus, commonly as a consequence of a talar neck fracture, and the navicular bone, usually without defined etiology (Fig. 141). In the latter case, the entity (referred to Köhler disease in the pediatric population and Mueller–Weiss syndrome in the adult population) is associated with severe

pain, disability, and progressive foot deformity. In children, the navicular bone undergoes sclerosis, irregularity, and fragmentation whereas in adults, deformity and collapse begin in the lateral aspect of the bone, which assumes a comma-like configuration, and is associated with superior protrusion of the fragments (Figs. 142, 143). Similar to the femoral head, the osteonecrotic area demonstrates heterogeneous signal, may contain fat or sclerosis in chronic stages, does not enhance after contrast administration and is demarcated by a hypointense band, which is sometimes paralleled by a hyperintense band on T2W images (double line sign). Later stages are characterized by subchondral fracture, collapse, and secondary osteoarthritis. One should look for history of underlying cause, such as trauma, alcoholism, steroid intake, sickle cell disease, Gaucher disease, etc. (Fig. 144).

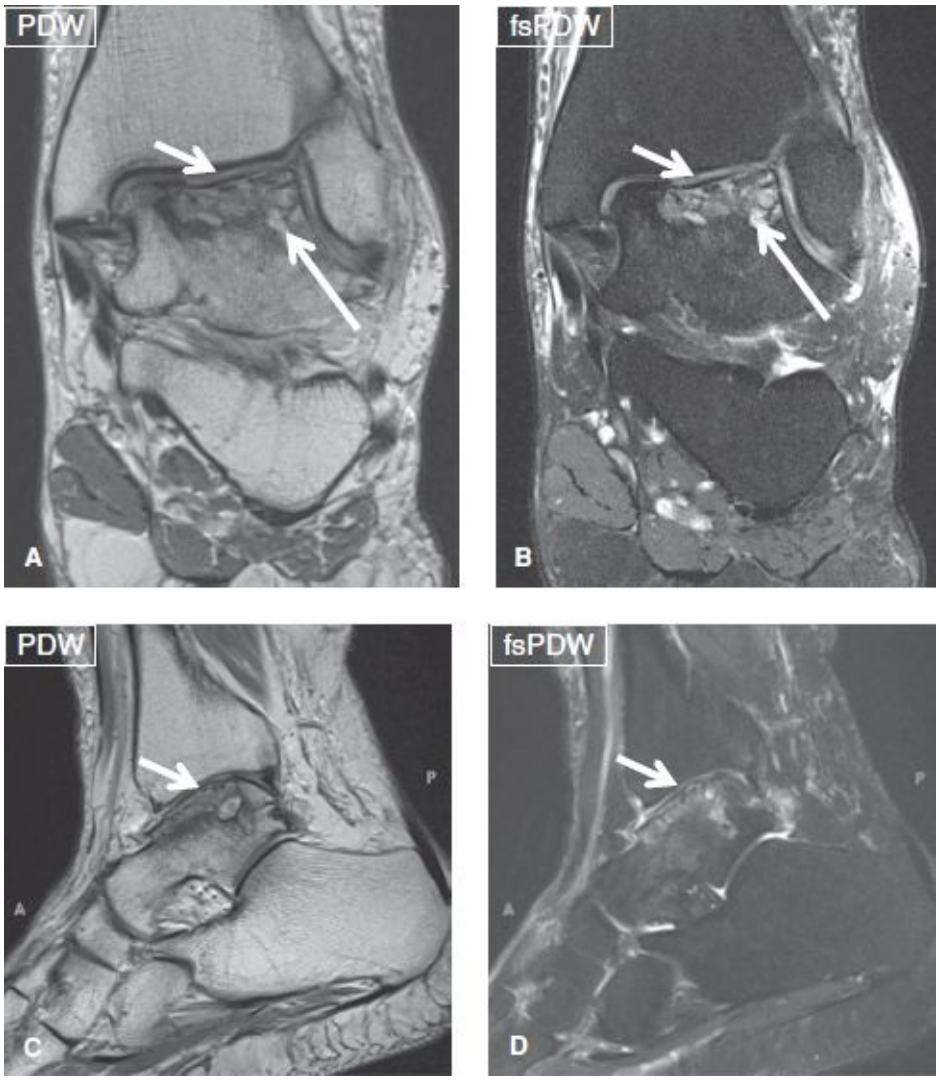

Fig. 141: Avascular necrosis of the talus. Coronal **(A, B)** and sagittal **(C, D)** images exhibit collapse and flattening of the talar dome (*short arrows*) as a sequelae of post-traumatic osteonecrosis, along with multiple associated subchondral cysts (*long arrows*).

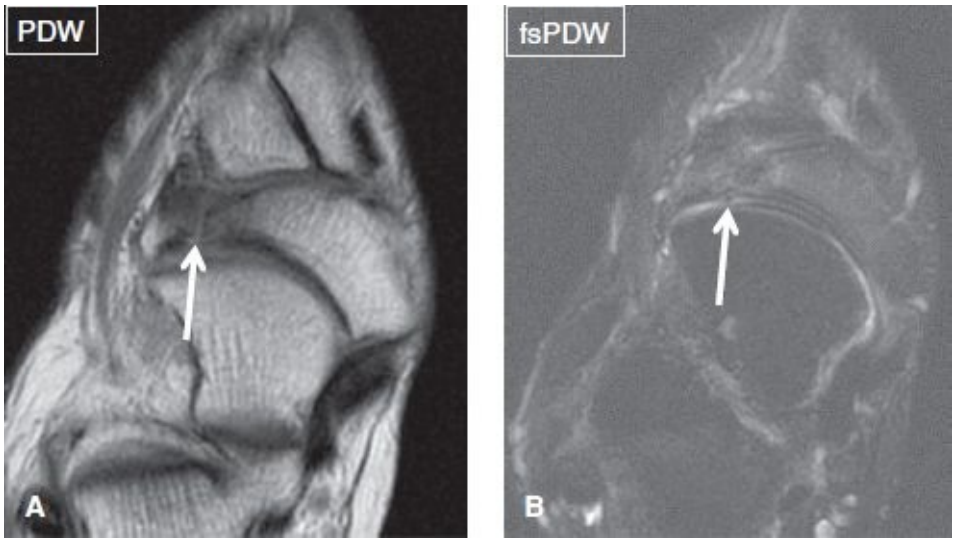

Fig. 142: Mueller–Weiss syndrome. Axial images demonstrate hypointensity and spontaneous collapse of the lateral aspect of the navicular bone, in which a transverse fracture line is evident (*arrows*).

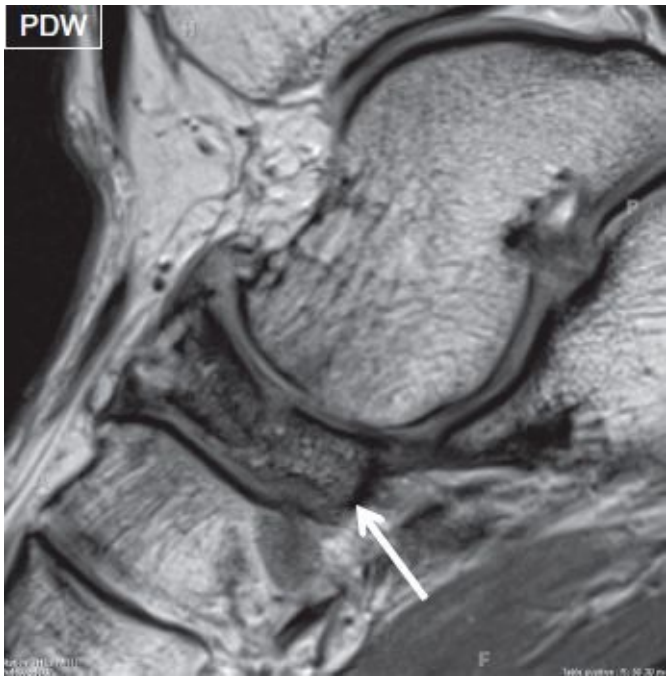

Fig. 143: Mueller–Weiss syndrome. Sagittal image shows deformity, collapse, and diffuse marrow hypointensity of the navicular bone (*arrow*), reflecting chronic avascular necrosis.

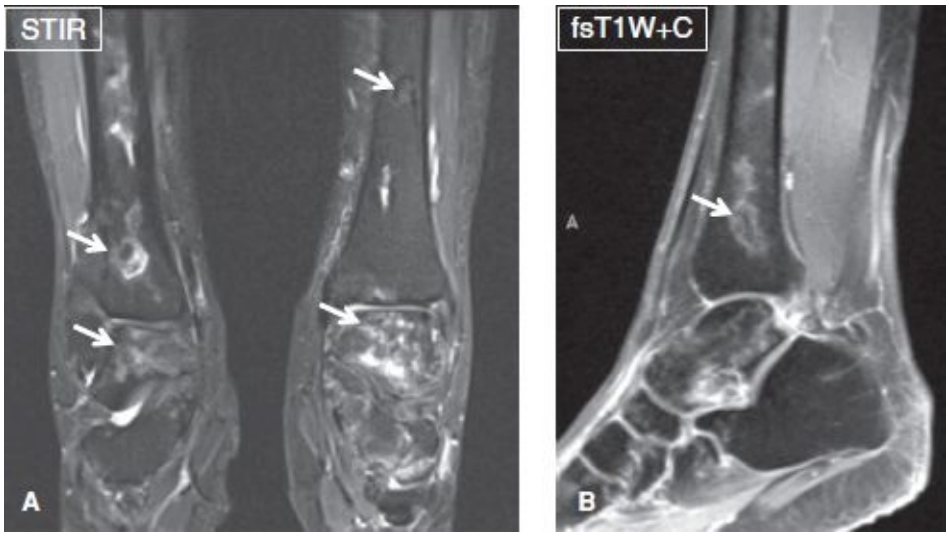

Fig. 144: Bone infarcts secondary to sickle cell disease. Coronal **(A)** and sagittal **(B)** images demonstrate multiple irregular serpiginous fat containing hyperintense lesions (*arrows*) in the tibia and talus, featuring geographic enhancing borders.

The midportion of the calcaneus is not an uncommon location for simple (unicameral) bone cyst, lipoma (may show internal calcification), aneurysmal bone cyst (fluid–fluid levels), giant cell tumor (T2 dark lesion, no sclerosis on radiographs), and lymphoma (T1 and T1 iso- to mildly hyperintense, soft tissue mass, permeative lesion on radiographs) (Fig. 145). The talus and the calcaneus are also common locations for osteoid osteoma, the enhancing nidus of which can be associated with periosteal reaction, as well as edema of the surrounding bone marrow and soft tissues (Fig. 146).

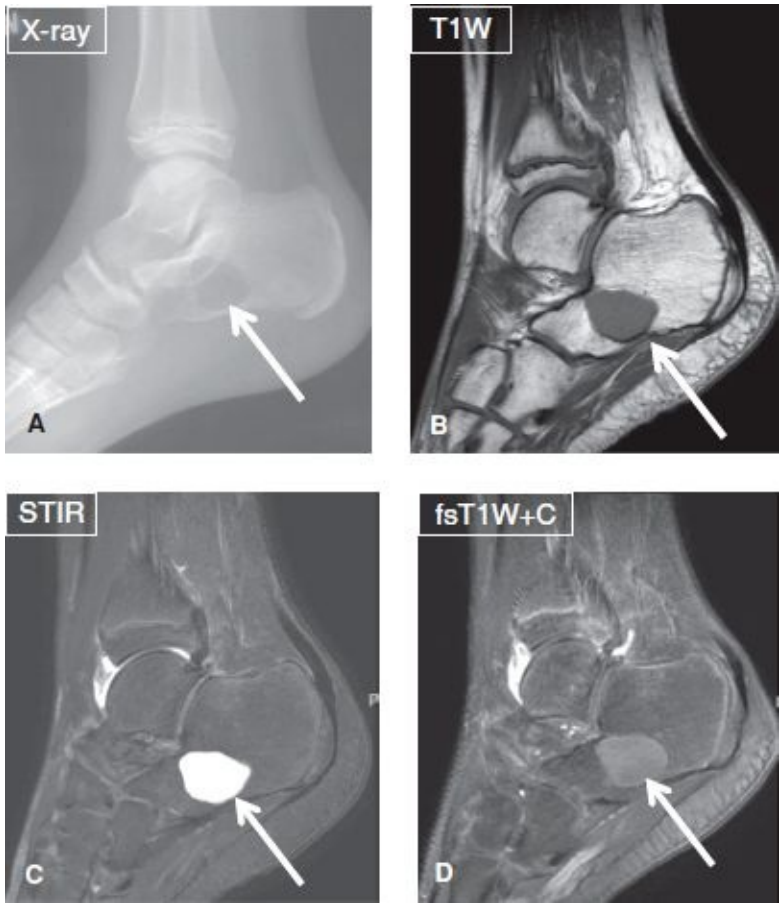

Fig. 145: Unicameral cyst of the calcaneus. Lateral radiograph **(A)** and sagittal MR images **(B–D)** display a well-defined nonenhancing cystic lesion (*arrows*) within the calcaneus.

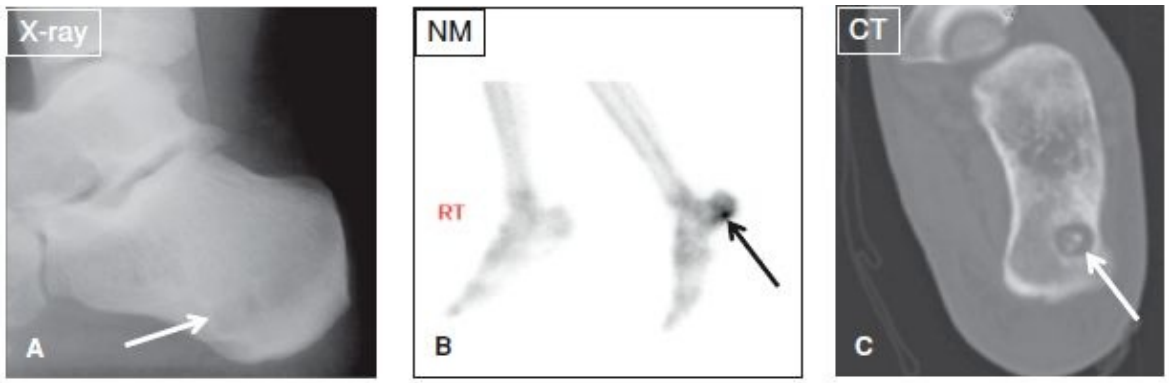

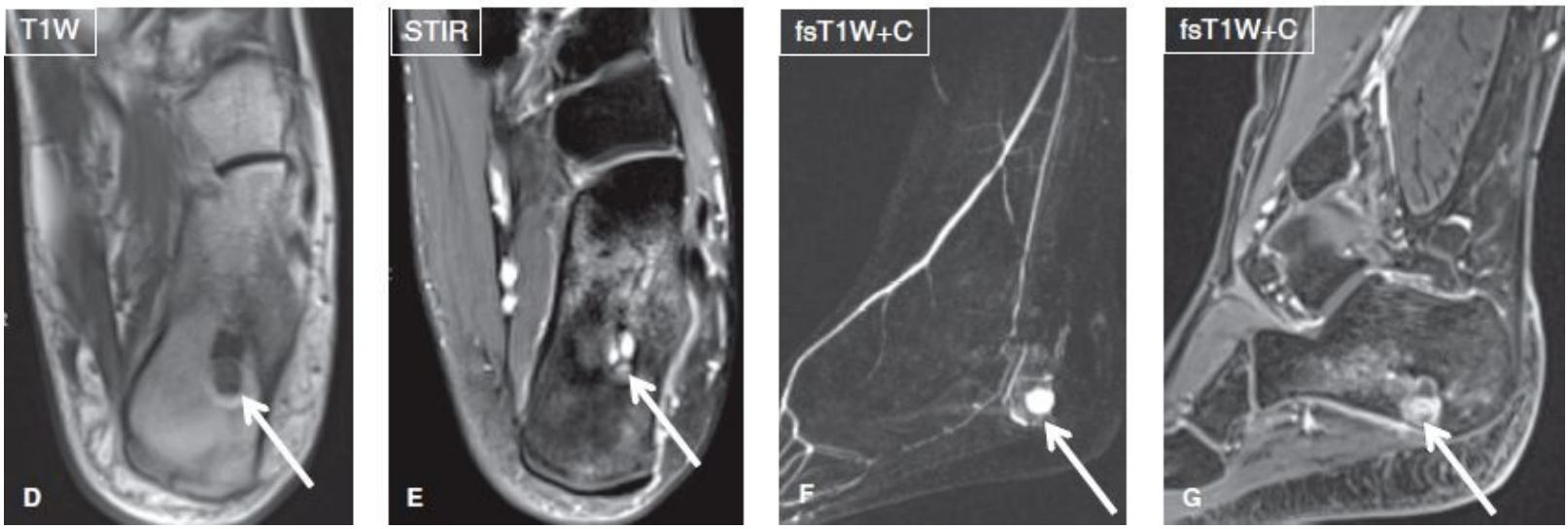

Fig. 146: Osteoid osteoma. **A:** Lateral radiograph demonstrates a well-defined lytic lesion (*arrow*) within the calcaneus. **B:** Lateral projection of scintigraphy bone scan exhibits radionuclide uptake in the lesion (*arrow*). **C:** Axial CT scan shows a subcortical lesion (*arrow*), with a well-defined relatively sclerotic border and a radiolucent center, with a sclerotic nidus. On T1W **(D)** and STIR **(E)** images, the lesion (*arrows*) shows low and high signal intensity, respectively. On dynamic postcontrast imaging **(F, G)** the lesion (*arrows*) demonstrates early and prolonged contrast enhancement with mild wash out.

Muscles: [<Normal>]

The reader should evaluate the dorsally located extensor digitorum brevis muscle (EDB), as well as the four plantar foot muscles, which include the AH, FDB, ABDM, and quadratus plantae (QP). Although the nerve innervation may vary, the EDM is innervated by the deep peroneal nerve, the AH and FDB by the medial plantar nerve (MPN), and the ABDM and QP by the lateral plantar nerve (LPN).

Normal muscles should feature homogeneous and isointense intermediate signal on PDW and fat-suppressed PDW images. Fatty infiltration and atrophy of muscles are best depicted on PDW and T1W images, while edema-like signal is best seen on the fat-suppressed PDW images. In cases of muscle strain, myopathy, or myositis, the changes are usually focal,

involve one or more muscles (not in a particular nerve distribution) and are associated with fascial edema. In denervation or diabetic myopathy, the changes are usually diffuse in a particular nerve distribution, distal to the site of neuropathy, and lack fascial edema (Fig. 147).

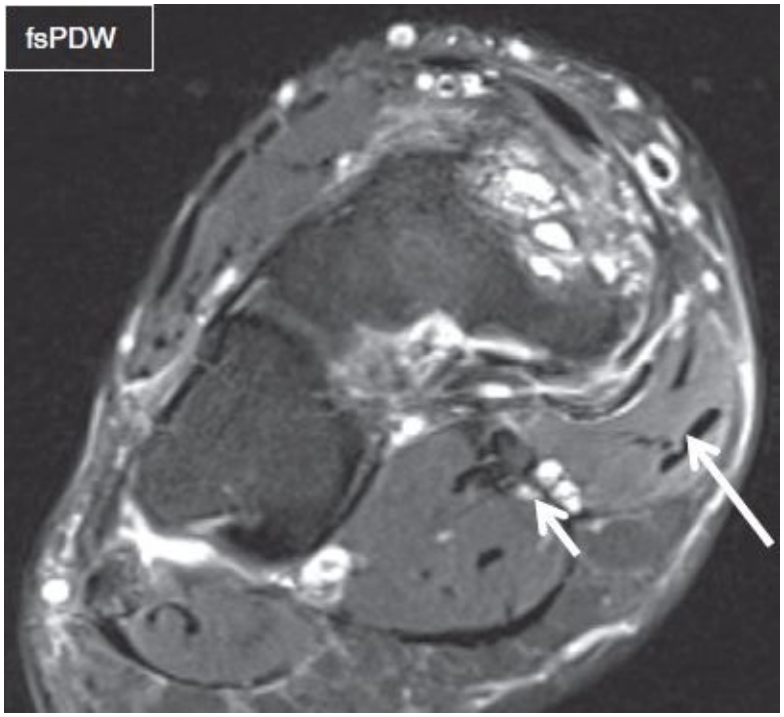

Fig. 147: Denervation of the abductor hallucis muscle. Coronal image demonstrates mild diffuse edema of the abductor hallucis muscle (*long arrow*), associated with abnormal hyperintensity of the medial plantar nerve (*short arrow*), in this case of medial plantar neuropathy. Degenerative cystic changes of the navicular–cuneiform joint related to fibrous coalition at this joint.

Isolated denervation changes in the ABDM (though sometimes also involving the FDB and QP) indicate entrapment/inflammation/injury of the Baxter nerve, which is the first (mixed motor and sensory) branch of the LPN. The entity is termed Baxter neuropathy, and most cases are detected in chronic stage of nerve entrapment with fatty replacement and/or atrophy of the ABDM. Gadolinium enhancement within muscle and edema-like T2 signal alteration may be seen in the acute to subacute phases of denervation. Entrapment may occur between the deep fascia of the AH and the medial plantar margin of the QP or, more distally, along the anterior aspect of the medial calcaneal tuberosity. In the latter case, plantar fasciitis and/or calcaneal plantar enthesophyte may also contribute to entrapment and/or injury (Fig. 148). In addition, patients who fail the treatment for plantar fasciitis might have undiagnosed Baxter neuropathy, related to idiopathic or iatrogenic causes. MR imaging can easily diagnose the muscle denervation change related to Baxter neuropathy.

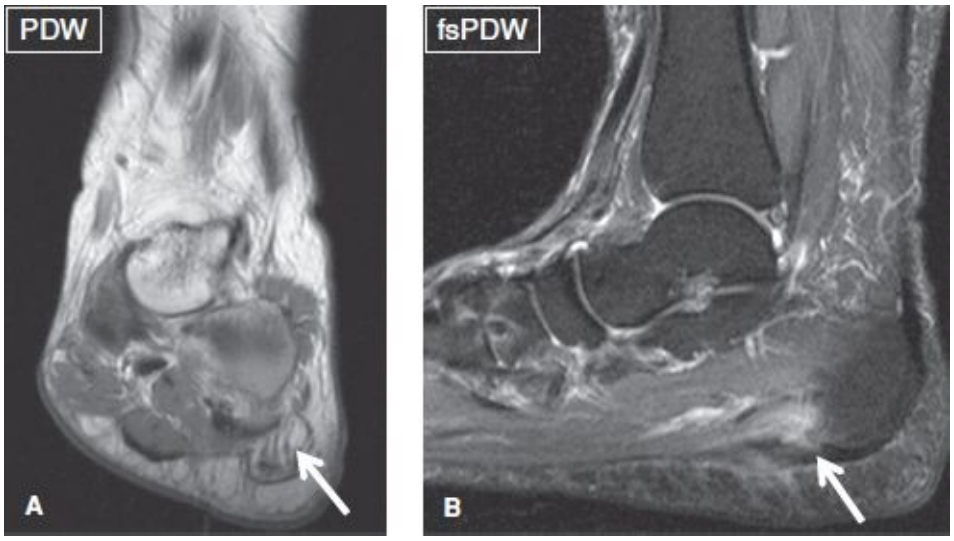

Fig. 148: Baxter neuropathy. **A:** Coronal image demonstrates isolated fatty infiltration of the abductor digiti minimi muscle (*arrow*), suggestive of Baxter (inferior calcaneal nerve) neuropathy. **B:** Sagittal image shows associated plantar fasciitis (*arrow*), which may contribute to the entrapment and inflammation.

Nerves and tarsal tunnel: [<Normal> <Hyperintense medial plantar nerve>]

The tarsal tunnel is a fibro-osseous tunnel, located posterior and distal to the medial malleolus, and is formed by the medial aspect of the talus, the calcaneus, the overlying flexor retinaculum, and the AH aponeurosis. The tarsal tunnel is filled with fat, contains the flexor tendons and the tibial nerve and its branches, and is best evaluated on the axial images (Fig. 149).

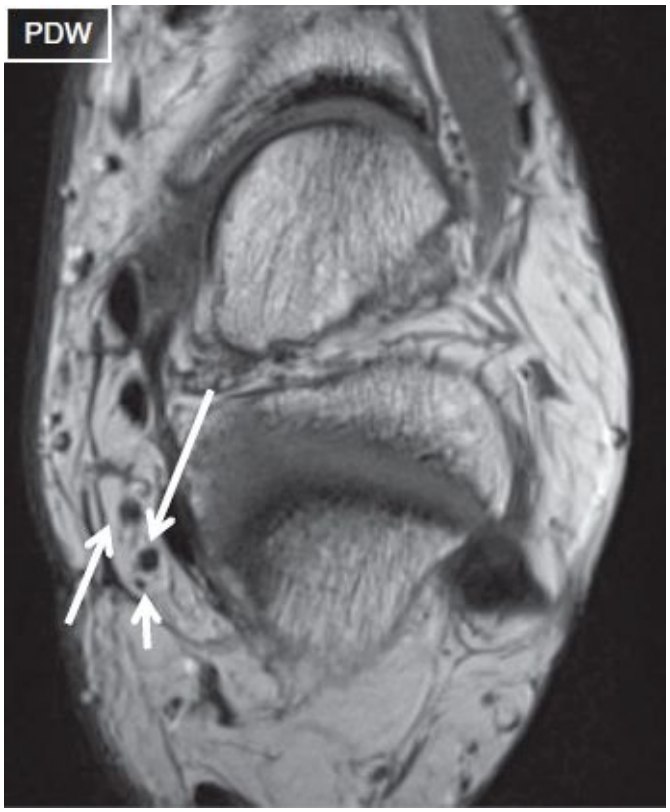

Fig. 149: Normal tarsal tunnel. Axial image shows a normal tarsal tunnel, which is devoid

of space-occupying lesions, and is filled with homogeneous fat delineating the flexor tendons of the ankle and the various nerves (*medium arrow,* medial plantar; *long arrow,* lateral plantar; *short arrow,* calcaneal nerve).

The normal tibial nerve is always isointense to muscles on PDW and fs PDW images. In most cases, the nerve trifurcates within the tunnel into the medial calcaneal nerve(s), which provide(s) sensory innervation to the skin of medial heel, the MPN and the LPN. Separated by a thin septum, the MPN and LPN course in their own respective tunnels and provide motor innervate to the foot muscles. Mild hyperintensity of the MPN and LPN is commonly evident on fs PDW images and could reflect subclinical neuropathy or more commonly, it might be due to magic angle artifact, attributed to their oblique course.

Tarsal tunnel syndrome refers to neuropathy due to entrapment or compression of the tibial nerve or one of its branches at the fibro-osseous tunnel beneath the flexor retinaculum and caudal to the medial malleolus. In most cases, the cause is focal fibrosis from prior injury; however, other etiologies could account for the syndrome, such as tight or thick overlying retinaculum or fascia, prominent venous varicosities, bony callous, intra- or extraneural ganglion, tenosynovitis, hematoma, neoplastic lesion or anomalous muscles (usually an accessory FDL) although up to 50% of cases are idiopathic (Fig. 150). The entity presents clinically with burning, unremitting pain radiating into the toes, paresthesia and/or numbness whereas severe cases demonstrate atrophy of intrinsic foot musculature with alterations in gait. On imaging, one should look for the causative space occupying lesion; and neuropathic changes, which manifest as moderate to severe hyperintensity (signal intensity approaching or exceeding that of the adjacent in-plane veins) and enlargement and/or fascicular abnormality of the tibial nerve or more commonly, its branches including medial and LPNs. Associated muscle denervation changes might be evident.

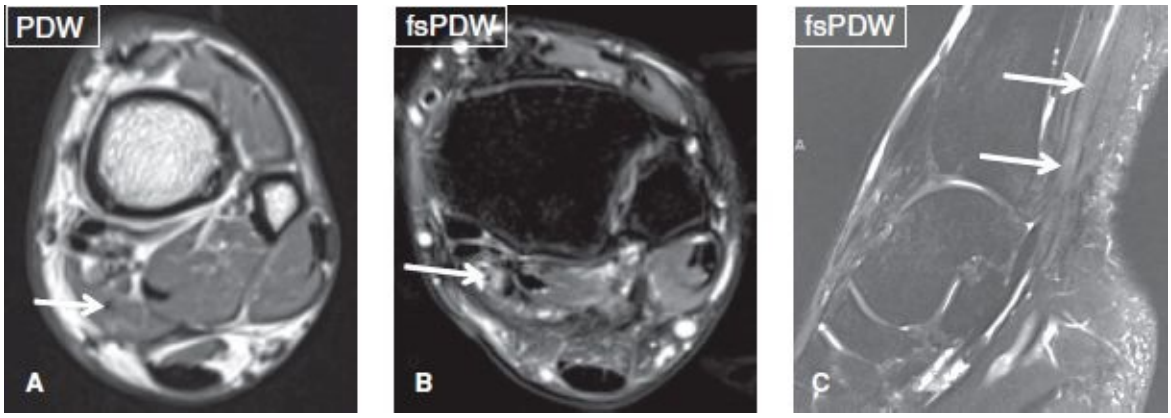

Fig. 150: Tarsal tunnel syndrome associated with accessory flexor digitorum longus muscle. Axial image **(A)** shows an accessory flexor digitorum longus muscle (*arrow*) within the tarsal tunnel. Axial **(B)** and sagittal **(C)** images demonstrate abnormal hyperintensity of the tibial nerve (*arrows*), suggesting compressing neuropathy. As opposed to MPN, TN is usually never normally hyperintense and is immune to magic angle artifacts.

Sinus tarsi: [<Normal> <Edema> <Sinus tarsi syndrome>]

The sinus tarsi is a cone-spaced space located between the talus and the calcaneus, which features a narrow part medially and wider part opening laterally. It contains fat, the medial, intermediate, and lateral layers of the inferior extensor retinaculum, neurovascular structures, as well as the interosseous talocalcaneal ligament medially and the cervical ligament laterally, which provide subtalar stability.

Sinus tarsi syndrome is caused by hemorrhage or inflammation of the synovial recesses of the sinus tarsi with or without tears of the associated ligaments. The entity commonly (70%) occurs following an inversion injury and is often associated with tears of the lateral collateral ligaments but may also be related to rheumatologic disorders and abnormal biomechanics, such as flat foot deformity or secondary to PTT dysfunction. Mild injury of the sinus tarsi ligaments is common in ankle sprains; therefore, edema-like signal within the sinus tarsi space and traction-related bone marrow edema and cystic changes at the sinus tarsi ligament attachments at the talus and calcaneus are commonly encountered. Whereas bone marrow edema and sinus tarsi edema are best seen on fs PDW images, ganglion cysts are equally well seen on PDW and fs PDW images. Sometimes, sinus tarsi ganglion cysts may extend into the soft tissues and present as mass lesions (Figs. 151, 152). Sinus tarsi syndrome should be diagnosed about a month or more after the trauma, if the edema does not resolve, and particularly, if there is partial or complete obliteration of the sinus tarsi fat with decreased definition of the ligaments on T1W or non–fs PDW images (Figs. 153, 154). A large lateral recess effusion of the ankle or the posterior subtalar joint extending into the sinus tarsi should not be misinterpreted as sinus tarsi syndrome. Frank disruption of the sinus tarsi ligaments may be evident in severe acute rotational injuries. The advanced cases are associated with ligament ossification, ganglion formation, and subtalar joint osteoarthritis. The syndrome presents clinically with hindfoot instability and pain along the lateral aspect of the foot. When sinus tarsi syndrome is evident on imaging, the lateral collateral ligaments and PTT should be evaluated for abnormalities. Other top differential diagnoses for sinus tarsi pain include bifurcate ligament tear and talar neck stress fracture. The syndrome is treated with subtalar arthroscopy and debridement.

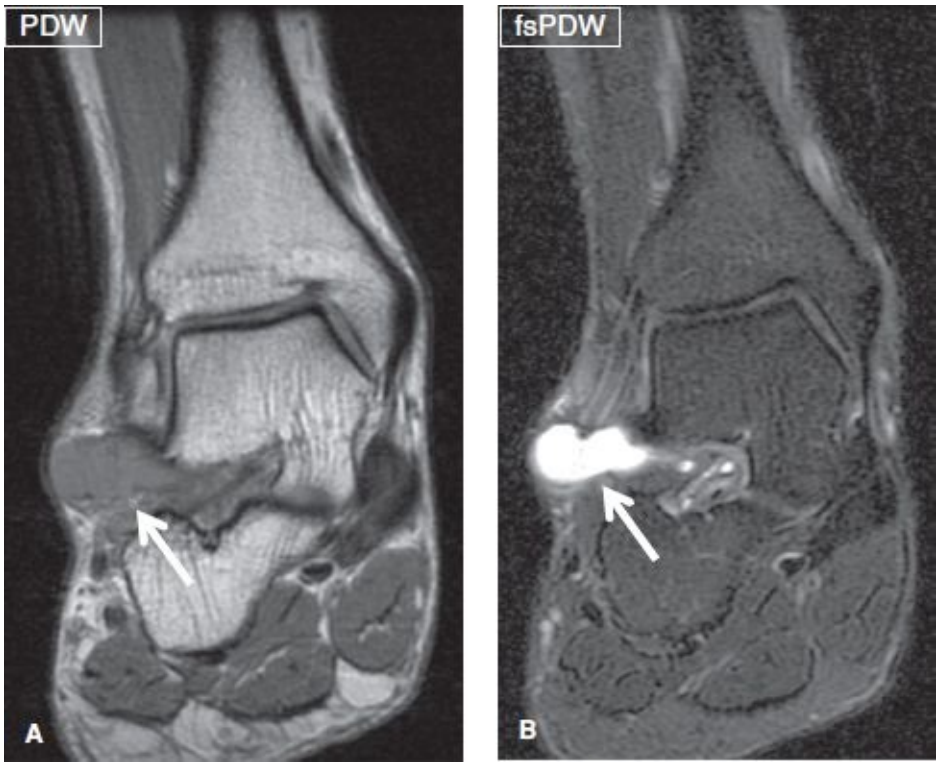

Fig. 151: Ganglion cyst of the sinus tarsi. Coronal images **(A,B)** demonstrate a ganglion (*arrows*) originating from the sinus tarsi and projecting to the subcutaneous soft tissues.

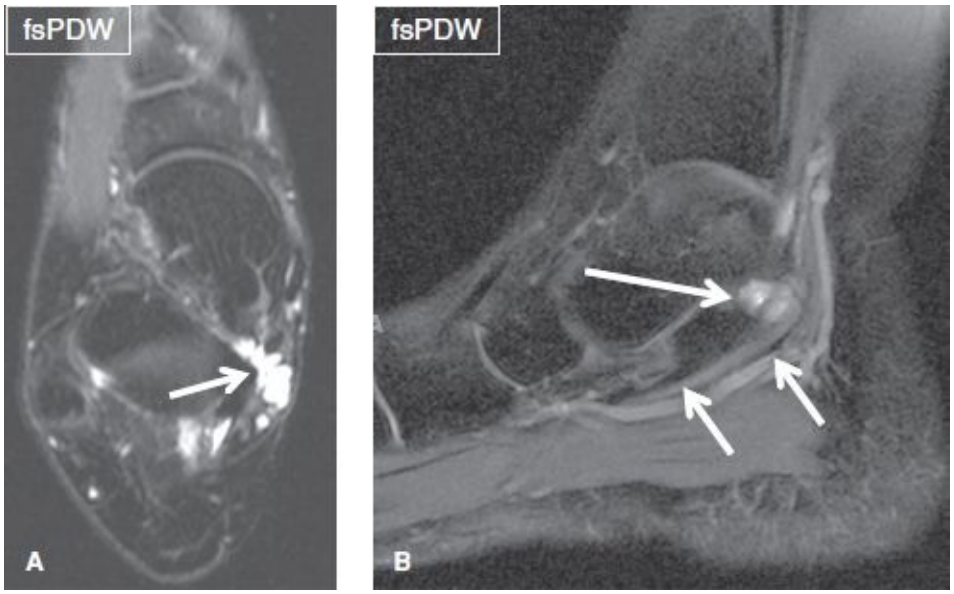

Fig. 152: Ganglion cyst of the sinus tarsi causing medial plantar neuropathy. Axial **(A)** and sagittal **(B)** images exhibit a ganglion (*long arrows*), which originates from the sinus tarsi and projects into the tarsal tunnel. The ganglion abuts the mildly hyperintense medial plantar nerve (*short arrows*).

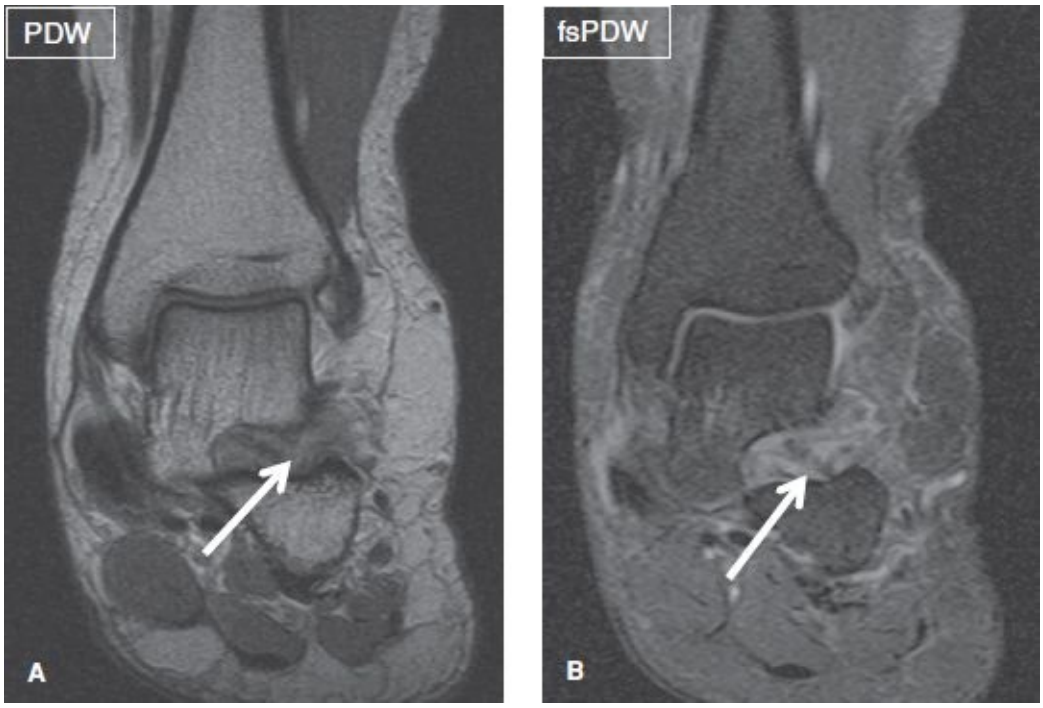

Fig. 153: Sinus tarsi syndrome. Coronal images **(A, B)** demonstrate obliteration of the normal sinus tarsi fat (*arrows*) and poor definition of its ligaments, compatible with sinus tarsi syndrome.

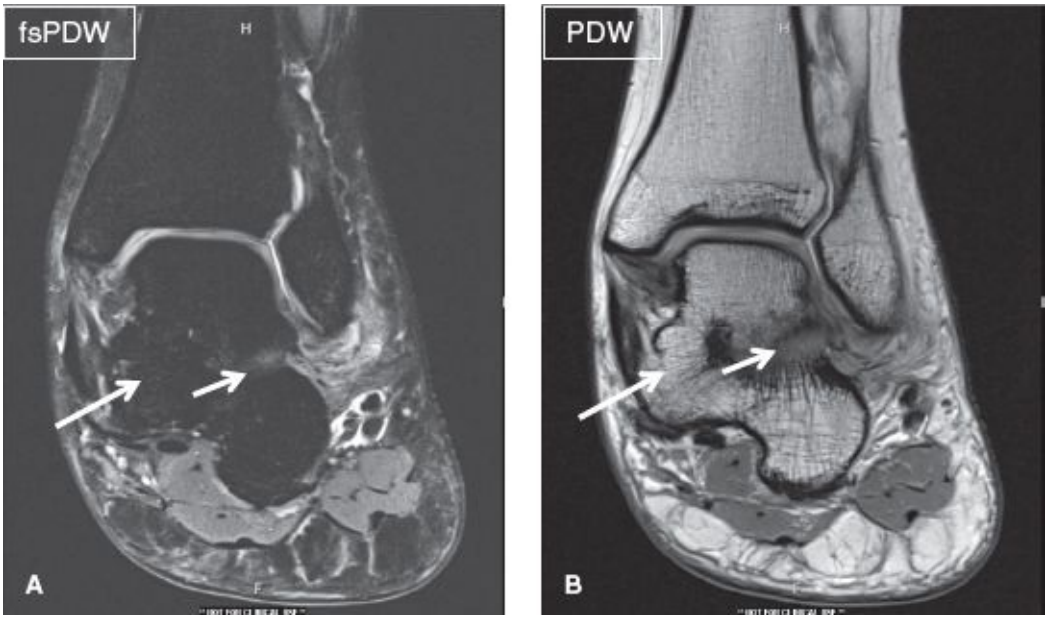

Fig. 154: Sinus tarsi syndrome. Coronal images **(A, B)** demonstrate obliteration of the normal sinus tarsi fat (*short arrows*) compatible with sinus tarsi syndrome. Also note middle facet talocalcaneal bony coalition (*long arrows*).

Vessels: [<Normal>]

The anterior and posterior ankle arteries should normally exhibit flow voids. If present, prominent venous varicosities and vascular malformations should be reported (Fig. 155). Although not included in the structured report, the following two sections include post-operative ankle, spectrum of findings that can be seen in the setting of PTT dysfunction ad

various ankle impingement syndromes.

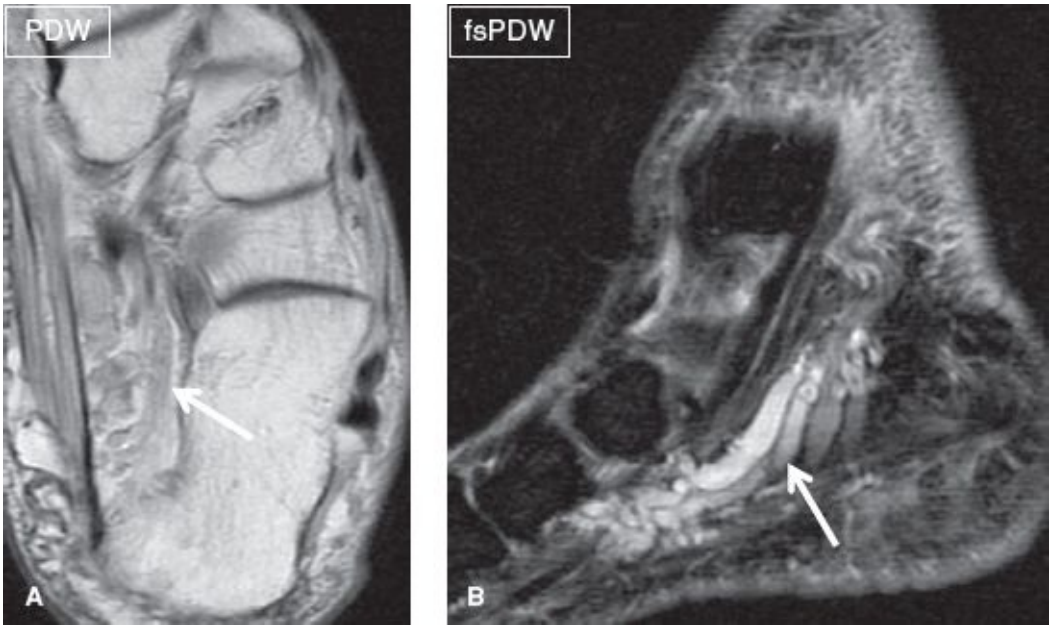

Fig. 155: Venous varicosities within the tarsal tunnel. Axial **(A)** and sagittal **(B)** images demonstrate enlarged varicose veins (*arrows*) within the tarsal tunnel, causing symptoms of medial plantar neuropathy.

POSTOPERATIVE FINDINGS

The musculoskeletal reader should be aware of the common surgical procedures performed in different areas of the ankle for various structures. In general, reconstructed tendons and ligaments should follow their normal course, feature anatomic continuity, and should not demonstrate fluid-like signal (Fig. 156). Mild–moderate intermediate signal alteration or thickening is a common postoperative finding, and should gradually resolve over many months after the surgery, as the tendon/ligament heal and mature. In some settings however, such as in the case of the AT, the latter may remain thickened, simulating chronic tendinosis, even after normal signal intensity has returned (Fig. 157). Recurrent tears may occur due to re-injury or incomplete resection of the Haglund bump (Fig. 158). Surgical transfer of the FDL tendon attachment to the calcaneal tuberosity has been used for the treatment of incompetent AT (Fig. 159). Plantar fascia release surgery involves cutting part of the plantar fascia ligament to release tension and relieve inflammation (Fig. 160).

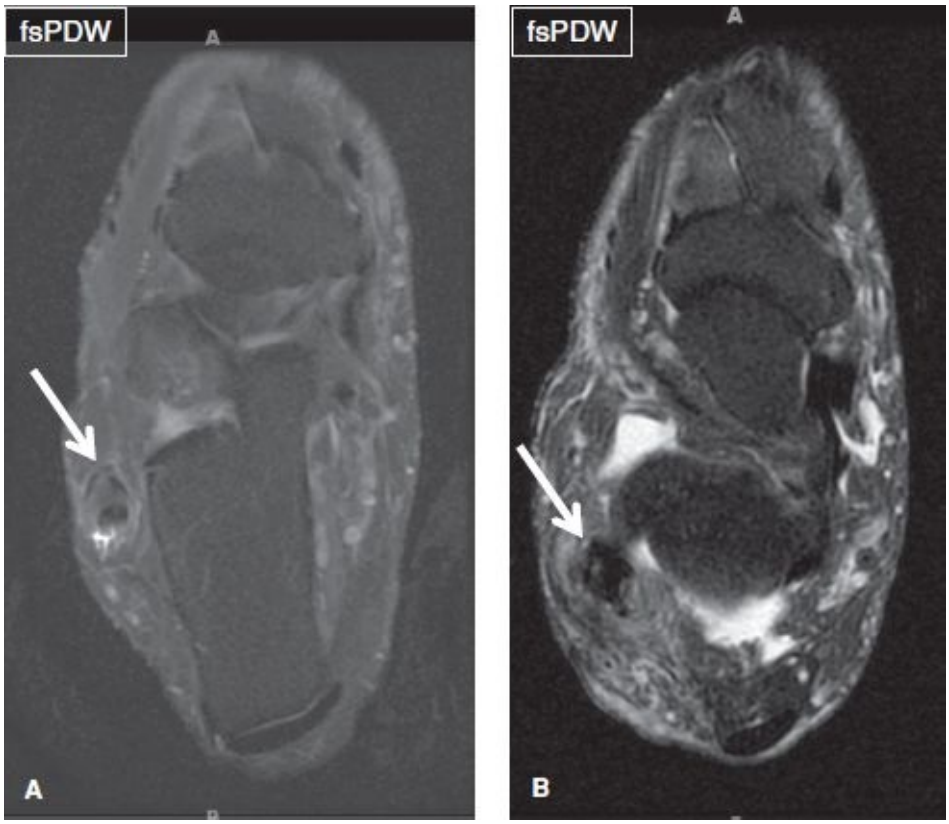

Fig. 156: Peroneus brevis tendon post-op changes on axial images. **A:** Arrow demonstrates a high-grade longitudinal split tear of the peroneus brevis tendon. **B:** Postoperative image shows surgical repair of the tear (*arrow*) with nearly similar configuration.

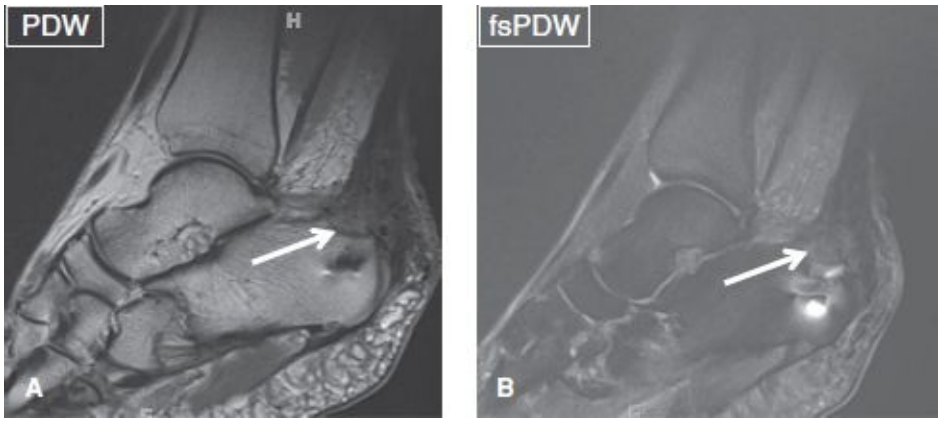

Fig. 157: Surgical repair of torn Achilles tendon. On sagittal images **(A, B)**, the Achilles tendon exhibits normal course and anatomic continuity, with no intrasubstance fluid-like signal. Intermediate signal alteration and considerable thickening at the attachment site (*arrows*) can be normal postoperative findings.

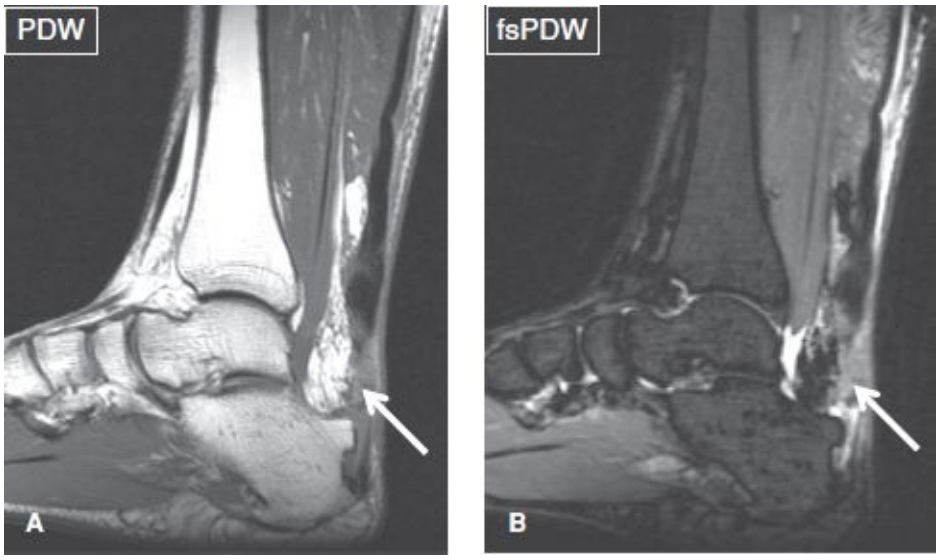

Fig. 158: Achilles tendon retear. Sagittal images **(A, B)** exhibit complete discontinuity of the distal Achilles tendon (*arrows*), in this case of prior surgical Achilles tendon tear repair.

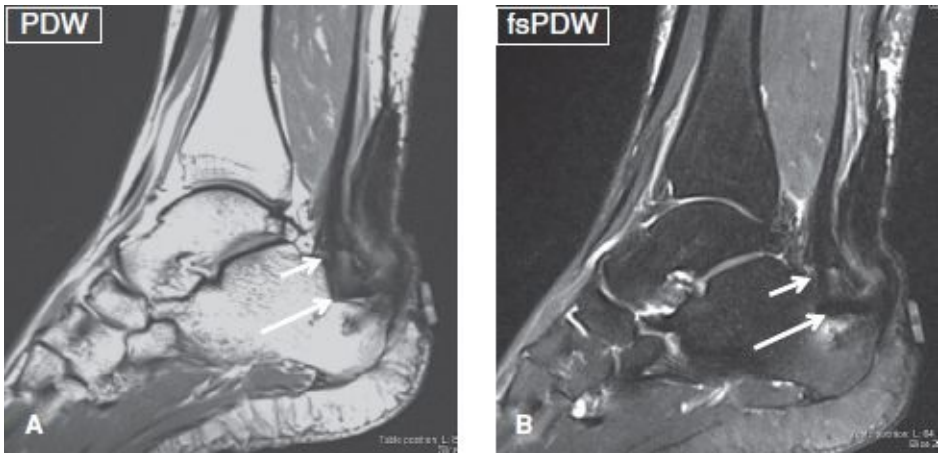

Fig. 159: Flexor digitorum longus transfer for treatment of incompetent Achilles tendon. Sagittal images **(A, B)** exhibit limited calcaneal osteotomy (*long arrows*). The transferred FDL tendon (*short arrows*) attaches at the osteotomy site without retear.

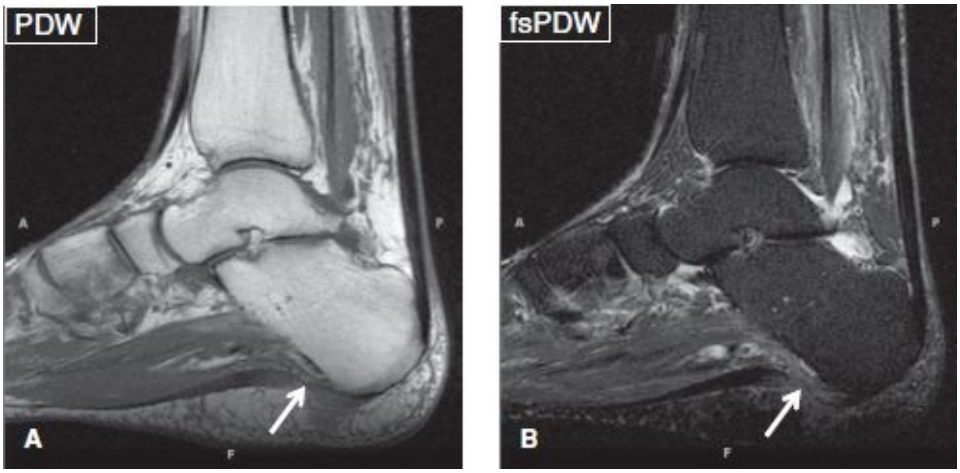

Fig. 160: Surgical release of the plantar fascia. Postoperative sagittal images **(A, B)** demonstrate partial detachment of the plantar fascia from the calcaneus (*arrows*), performed to reduce the effects of plantar fasciitis.

Osteochondral Lesion

It can be treated by microabrasion or drilling, osteochondral implant placement (OCI), mosaicoplasty (multiple osteochondral implants bundled together), autologous cartilage implantation (ACI), or juvenile cartilage cell implantation (JCI). Generally, treatment is recommended for unstable or symptomatic lesions, larger than 1 cm in size. In the ankle, the most common procedures are microabrasion, OCI, and JCI. In OCI, a plug from the non–weight-bearing area of the bone is retrieved and implanted into a hole, created by drilling into the talar or tibial surfaces. In JCI, the hole is filled with juvenile cartilage cells (known to contain adequate glucosamine glycogen levels) and glue in an attempt to regain hyaline cartilage at the site of treatment. Similar to the knee, the postoperative imaging evaluation of osteochondral lesion repair is based on the MOCART scoring scale. In terms of analysis, the most important features to evaluate are the quality of the regenerated cartilage (hyaline/fibrocartilage, atrophic, hypertrophic, or flush with the native cartilage); the binding of the regenerated cartilage at the border zone with the native cartilage; the binding of the regenerated cartilage with the subchondral plate (any exposure of the subchondral surface); the presence of subchondral bony reaction (edema, cysts, or chondral osteophyte); and the presence of joint effusion and/or synovitis (Fig. 161).

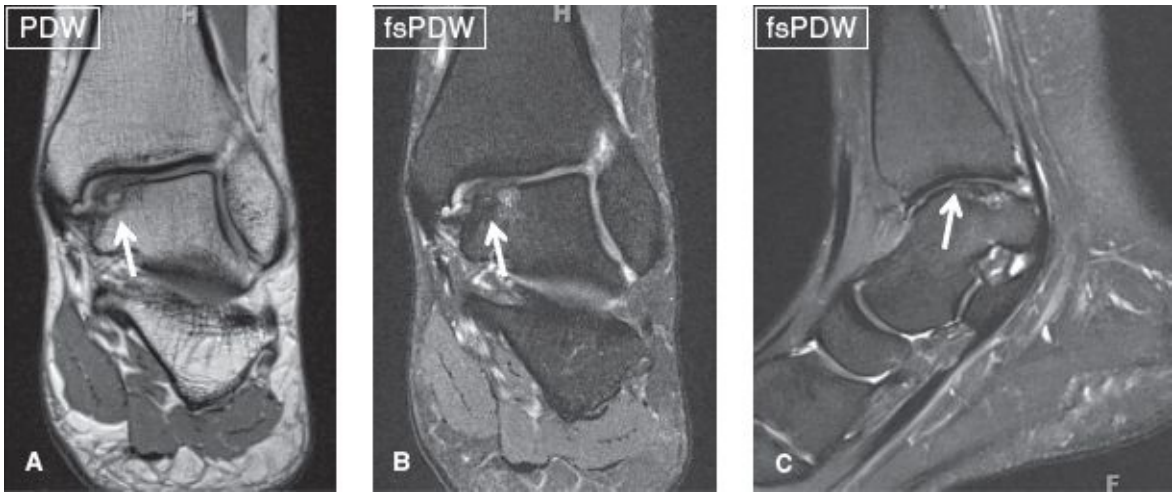

Fig. 161: Surgical repair of osteochondral lesion of the talus. **A, B:** Coronal images show adequate application of the juvenile cartilage implant in the osteochondral defect of the medial talar dome (*arrows*). No subchondral exposure. The cartilage appears mildly proud. **C:** On the sagittal plane, the implant exhibits small anterior flap tear (*arrow*).

PTT Dysfunction

The PTT is the major dynamic stabilizer of the foot, with its primary function being adduction of the transverse tarsal joint. It secondarily assists inversion of the subtalar joint, which causes elevation of the medial longitudinal arch. Static stabilizers include the deltoid ligament, spring ligament, plantar fascia, talocalcaneal interosseous ligaments, and the capsules of the talonavicular and naviculocuneiform joints. PTT dysfunction can be caused by pes planus, rheumatoid arthritis, obesity, or underlying os naviculare, especially type II.

The entity progresses through four stages, which involve the aforementioned structures in various combinations:

- Stage I (is characterized by PTT tenosynovitis and insertional tendinosis. There is no deformity on radiographs.)
- Stage II involves type I (thickening and one or two longitudinal splits) or type II (heterogeneity, attenuation, and wider longitudinal splits) PTT injury, tendinosis and/or tenosynovitis, spring ligament abnormality and sometimes talar fault and/or flexible hindfoot valgus. There is pes planus and forefoot abduction ("too many toes sign")
- Stage III involves type II or type III (complete or near-complete tear) injury with severe tendinosis and/or tenosynovitis, talar uncoverage, rigid hindfoot valgus, spring and tibiospring ligament abnormality, early signs of talocalcaneal and/or calcaneofibular impingements due to bony abutments with edema and sclerosis of lateral margins of talus, calcaneus (at Gissane angle), and lateral malleolus related to pronated foot, peroneal tendon split tears, and subtalar joint osteoarthritis. Sinus tarsi syndrome is commonly associated.
- Stage IV is characterized by stage III findings plus chronic superficial and deep deltoid ligament compromise, severe sinus tarsi pain, talar tilt in ankle mortise, tibiotalar, and subtalar joint osteoarthritis, as well as talocalcaneal and calcaneofibular impingement (Fig. 162).

Fig. 162: Imaging features of posterior tibial tendon dysfunction. **A:** Sagittal image shows mild talar fault (*arrow*). **B:** Hindfoot valgus (*arrow*) is evident in the coronal plane. **C:** Axial image demonstrates posterior tibial insertional tendinosis (*arrow*). **D:** Coronal image show sinus tarsi and adjacent bone marrow edema (*arrow*).

Treatment varies from conservative options to surgical resection of the os naviculare (Kidner procedure), limited calcaneal osteotomy and FDL tendon transfer, osseous fusion (subtalar or triple arthrodesis), and transverse osteotomy of the anterior process of the calcaneus proximal and parallel to the calcaneocuboid joint (Evans osteotomy; Fig. 163). Reconstructed tendons should appear continuous and attach to the navicular tuberosity,

following an expected near-anatomic course (Fig. 164). Immediate postoperative complications include hematoma and abscess formation whereas the most common late complication is FDL or FHL tendon transfer failure, in which the reconstructed tendon shows partial or complete discontinuity with associated fibrosis or soft tissue thickening (Figs. 165, 166). Secondary signs of talar uncovering and/or hindfoot valgus may be present. In some cases, tissue reaction to the suture material or the interference screw can lead to symptomatic tendinitis, which appears as abnormal tendon thickening and features hypervascularity on Doppler ultrasound imaging.

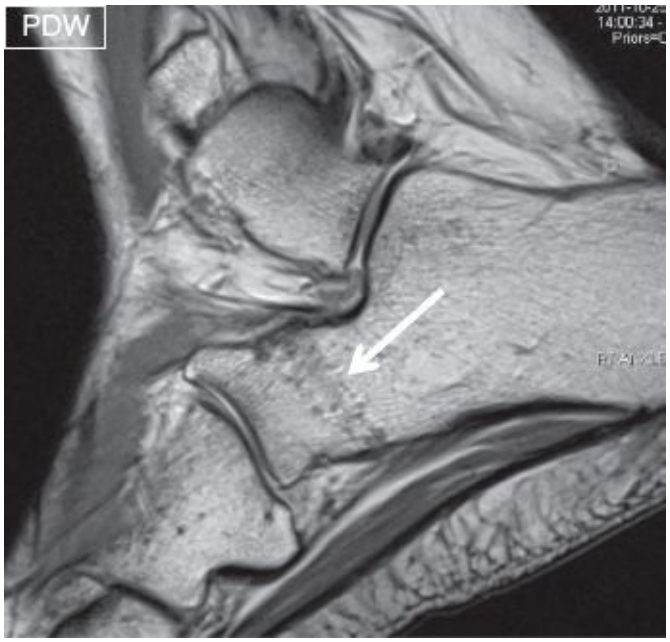

Fig. 163: Evans osteotomy. Postoperative sagittal image demonstrates the site of the transverse osteotomy of the anterior process of the calcaneus (*arrow*), proximal and parallel to the calcaneocuboid joint.

Fig. 164: Flexor digitorum longus transfer for the treatment of posterior tibial tendon dysfunction. Axial **(A),** sagittal **(B),** and coronal **(C)** images demonstrate a flexor hallucis longus tendon (*arrows*), anteromedially transferred and attached on to the navicular bone.

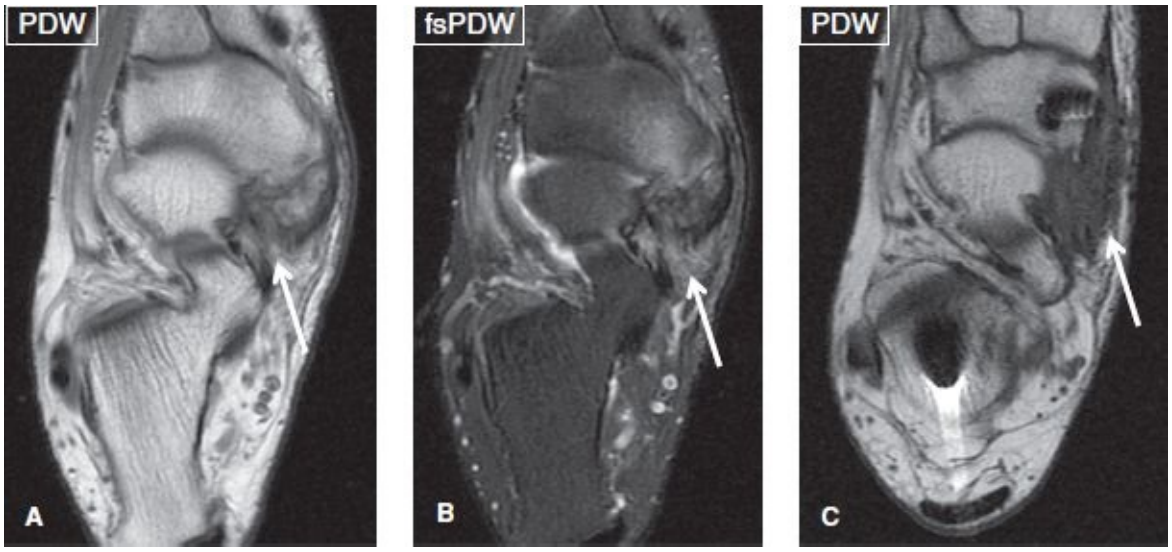

Fig. 165: Complete tear of transferred flexor digitorum longus tendon for PTT dysfunction surgery. **A, B:** Axial images show type II os naviculare with chronic stress-related bony productive and edematous changes. Note high-grade insertional tears of tibialis posterior tendon (*arrows*). FDL transfer was performed which failed in 1 year. **C:** Axial post-operative image shows complete discontinuity of the fibers (*arrow*).

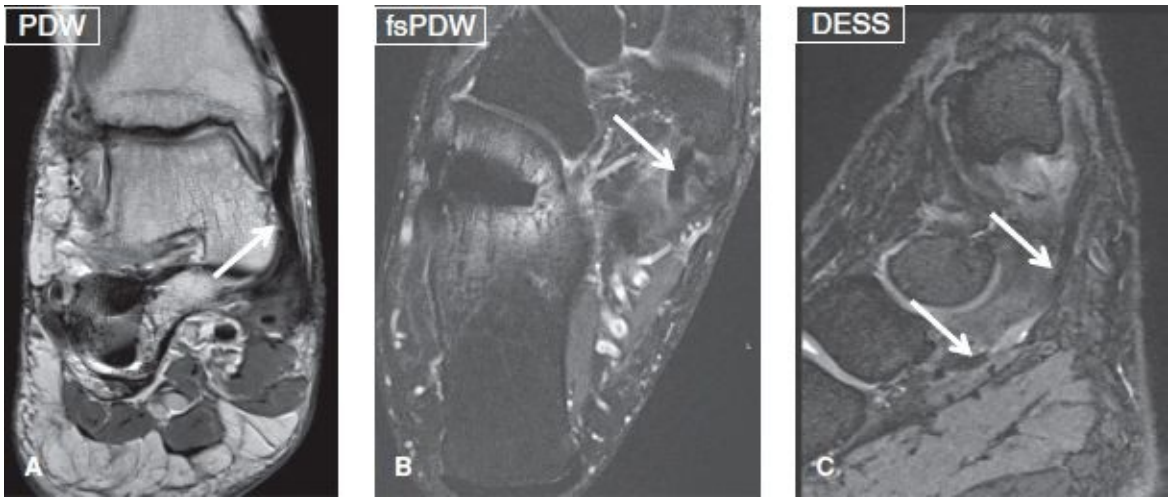

Fig. 166: Complete tear of transferred flexor digitorum longus tendon for PTT dysfunction surgery. Coronal **(A)** and axial **(B)** images show an anteromedially transferred flexor digitorum longus tendon (*arrows*), which attaches on to the navicular tuberosity. On the sagittal plane **(C),** there is complete discontinuity of the tendon, without apposition of the torn fragments (*arrows*).

Lateral Ankle Ligaments

On a daily basis, one person in 10,000 suffers an injury to the lateral ankle ligaments, of which, 90% of the individuals recover but 10% develop chronic instability and might need surgery. The injured ligament may be repaired or reconstructed using either an allograft or patient's peroneal or FDL tendons (Broström procedure; Fig. 167). Again, anatomic continuity of the ligament is the most important feature to evaluate, and any attenuation, partial or complete discontinuity should be reported (Figs. 168, 169).

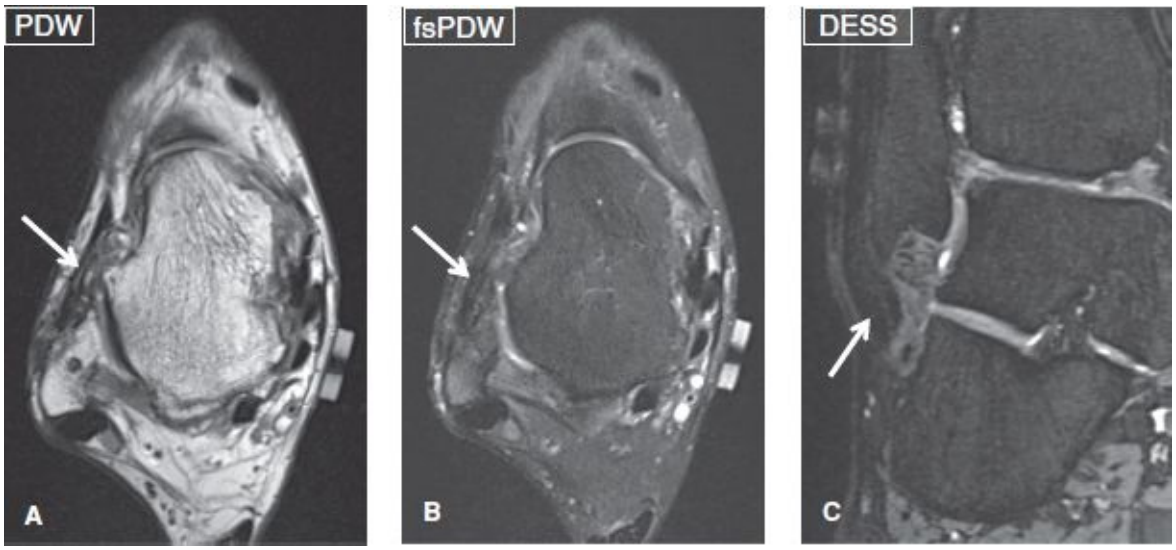

Fig. 167: Broström procedure. Axial **(A, B)** and coronal **(C)** images show an intact allograft at the anatomic location of the anterior talofibular ligament (*arrows*).

Fig. 168: Allograft failure in Broström procedure. Axial images **(A, B)** show a partial tear of a flexor digitorum longus tendon (*arrows*), which has been used as an allograft for surgical repair of the anterior talofibular ligament.

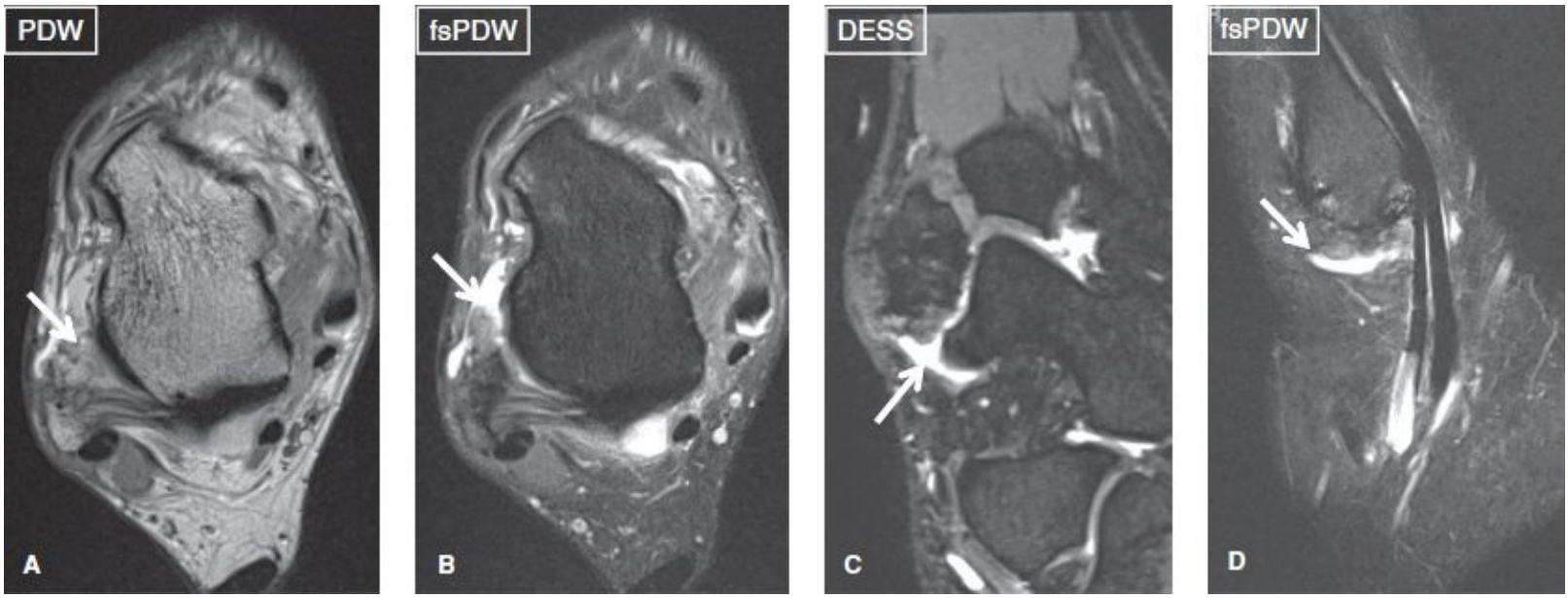

Fig. 169: Allograft failure in Broström procedure. On axial **(A–C)** and sagittal **(D)** images, there is nonvisualization (*arrows*) of the allograft used for surgical repair of the anterior talofibular ligament, corresponding to complete allograft tear.

SYNDROMES

Apart from sinus tarsi syndrome, POPS and painful os naviculare syndrome as described above, a variety of impingement syndromes may occur in the ankle. The impingement syndromes usually involve to subacute or chronic injury of one or more of regional stabilizing ligaments, which leads to recurrent instability. Associated synovial injury or synovial metaplasia results in soft tissue thickening, proliferative granulation tissue, fibrosis, ganglion formation, and bony productive changes. The patients present with localized regional pain, instability, and decreased range of motion due to soft tissue or bony impingement. OCLs can also be seen with the impingement syndromes, particularly with posteromedial impingement. Table 1 outlines the pathophysiology and imaging features of the various ankle impingement syndromes. It should be noted that the imaging findings described are not pathognomonic, and these can also be present in asymptomatic individuals; therefore, accurate diagnosis requires correlation with the clinical picture (Figs. 170–173). The reader should however, recognize the respective subacute/chronic ligament injury as deficiency, attenuation and/or thickening of the ligament, soft tissue thickening, bony productive changes in the adjacent fascial planes, and associated tibial or talar OCLs, which could be seen in the setting of different impingement syndromes as described above.

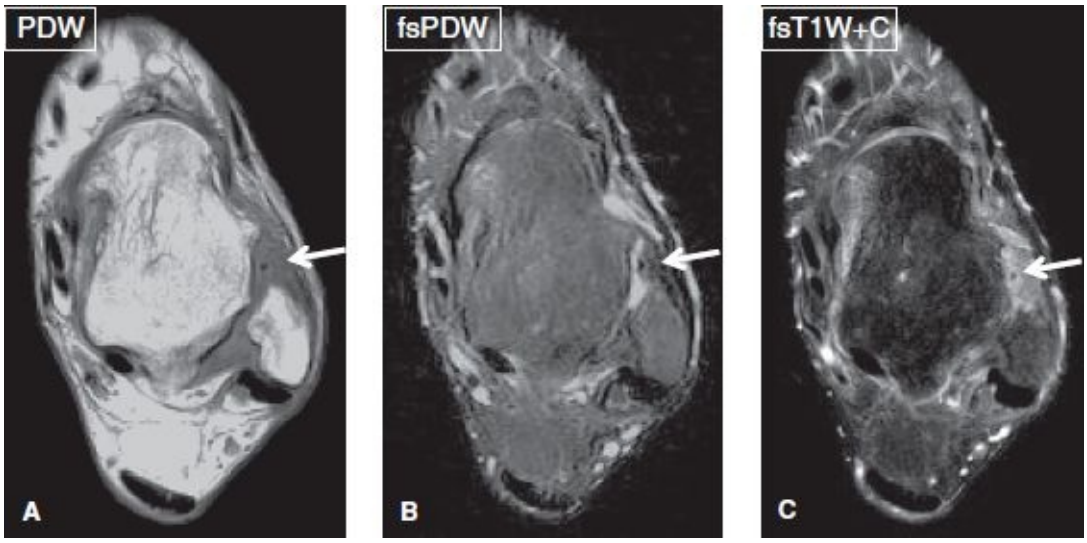

Fig. 170: Anterolateral impingement. Axial images. The normal fat of the anterolateral gutter has been replaced by tissue of intermediate signal (*arrows* in **A, B**), which enhances (*arrow* in **C**) after gadolinium administration, corresponding to synovial hypertrophy, granulation tissue and scarring.

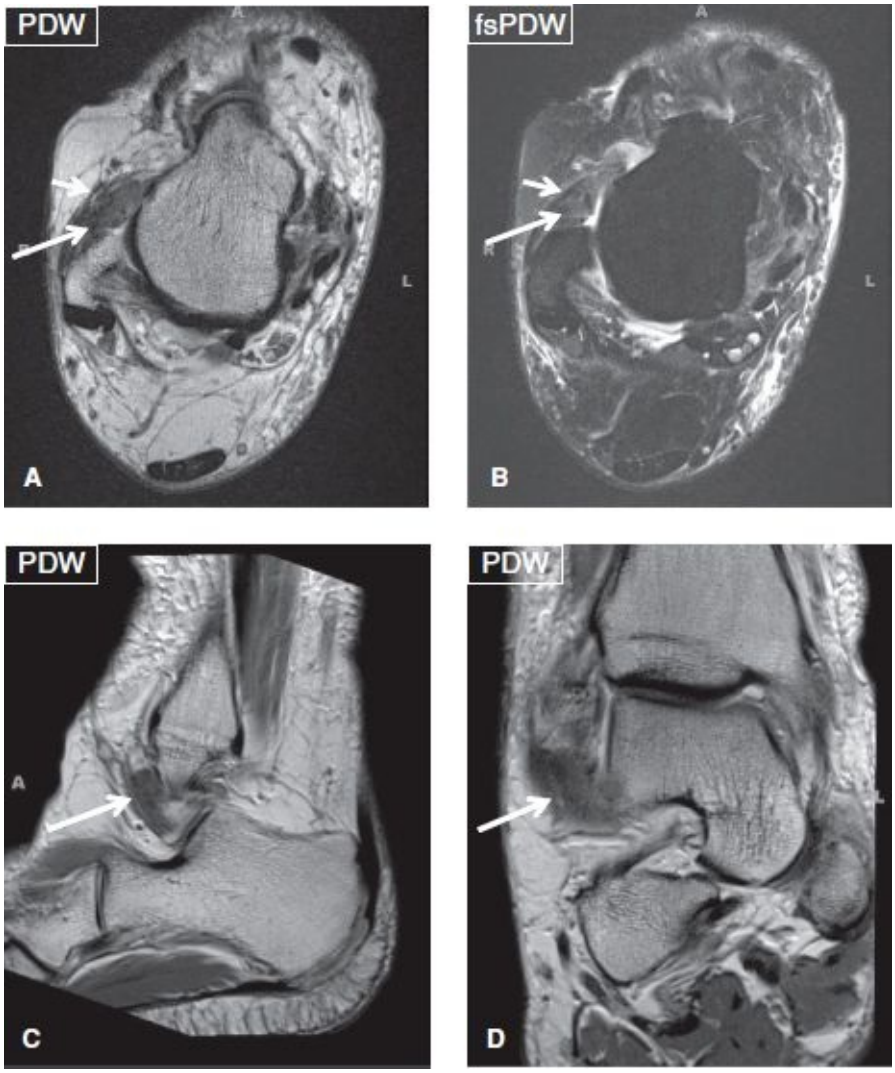

Fig. 171: Anterolateral impingement. Axial **(A, B),** sagittal **(C),** and coronal **(D)** images exhibit replacement of the normal fat of the anterolateral gutter by tissue of intermediate signal (*long arrows*). Note associated attenuation and poor visualization of the anterior

talofibular ligament (*short arrows* in **A, B**).

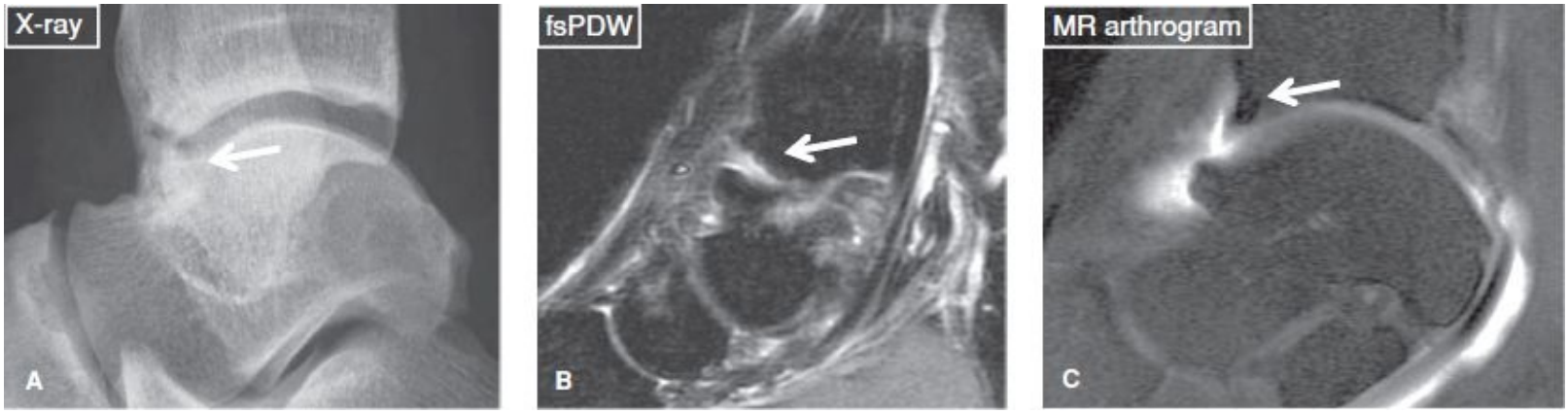

Fig. 172: Anterior impingement. Lateral radiograph **(A)** exhibits osseous overgrowth (*arrow*) of the anterior tibial plafond and anterior talar dome. Sagittal MR image **(B)** and MR arthrogram **(C)** image demonstrate osteophytes and soft tissue edema in the anterior recess (*arrows*).

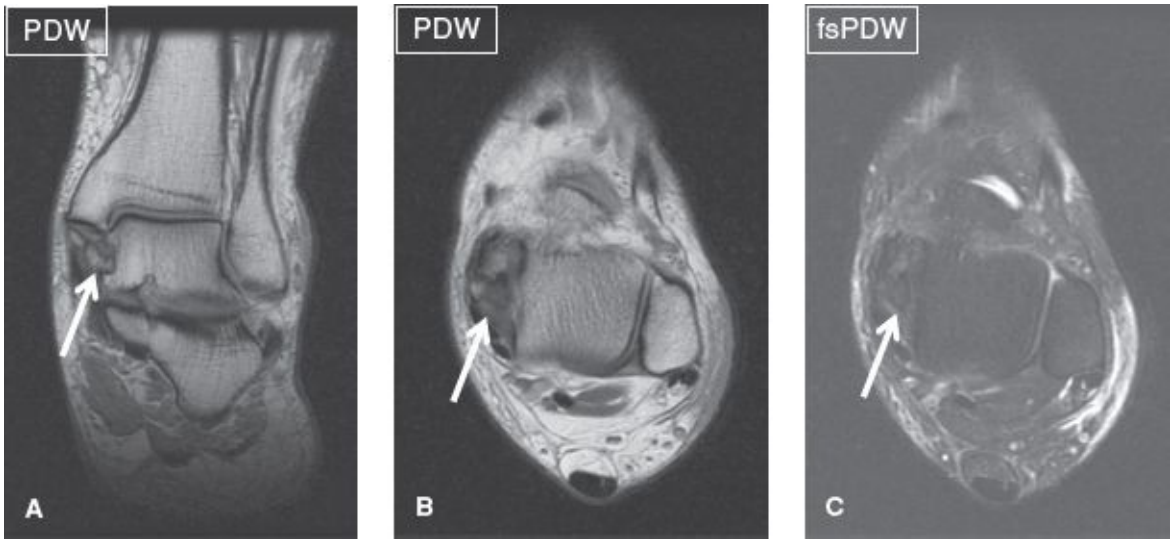

Fig. 173: Anteromedial impingement. Coronal **(A)** and axial **(B, C)** images exhibit heterotopic ossifications with loss of normal striated appearance of deep deltoid ligament in the medial gutter, particularly its anterior tibiotalar portion (*arrows*).

To conclude, structured reporting is the key to remember the bony and soft tissue architecture of the ankle and facilitate its systematic imaging assessment.

TABLE 1: The pathophysiology and MR imaging features of the various ankle impingement syndromes

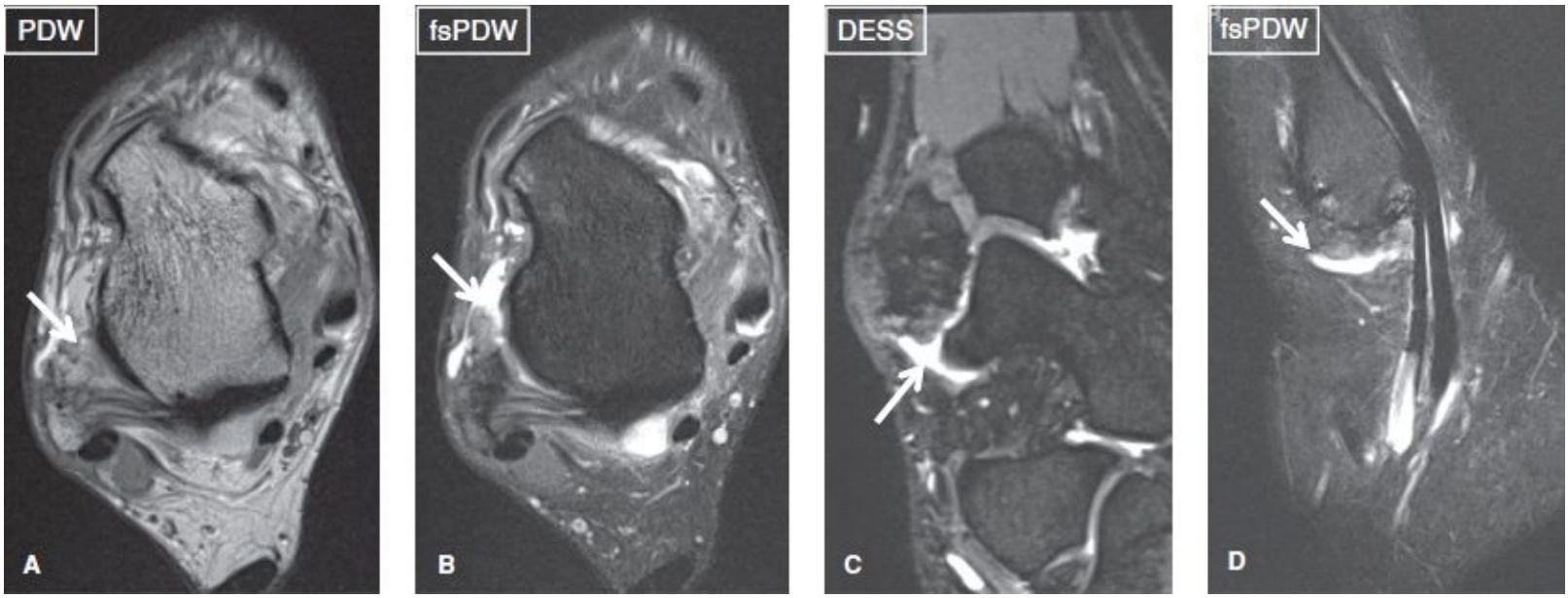

SUGGESTED READINGS

Campbell SE, Warner M. MR imaging of ankle inversion injuries. *Magn Reson Imag Clin North Am.* 2008;16(1):1–18.

Chhabra A, Soldatos T, Chalian M, et al. Current concepts review: 3 T magnetic resonance imaging of the ankle and foot. *Foot Ankle Int.* 2012;33(2):164–171.

Chhabra A, Soldatos T, Chalian M, et al. 3-Tesla magnetic resonance imaging evaluation of posterior tibial tendon dysfunction with relevance to clinical staging. *J Foot Ankle Surg.* 2011;50(3):320–328.

Collins MS, Felmlee JP. 3 T magnetic resonance imaging of ankle and hindfoot tendon pathology. *Top Magn Reson Imaging.* 2009; 20(3):175–188.

Donovan A, Rosenberg ZS. MRI of ankle and lateral hindfoot impingement syndromes. *AJR Am J Roentgenol.* 2010;195(3):595–604.

Helms CA, Major NM, Anderson MW, et al. *Foot and Ankle. Musculoskeletal MRI.* 2nd ed. Philadelphia, PA: Saunders Elsevier; 2009: 384–430.

Hintermann B. What the orthopaedic foot and ankle surgeon wants to know from MR Imaging. *Semin Musculoskelet Radiol.* 2005; 9(3):260–271.

Linklater J. Ligamentous, chondral, and osteochondral ankle injuries in athletes. *Semin Musculoskelet Radiol.* 2004;8(1):81–98.

Muhle C, Frank LR, Rand T, et al. Collateral ligaments of the ankle: High-resolution MR imaging with a local gradient coil and anatomic correlation in cadavers. *Radiographics.* 1999;19(3):673–683.

Narvaez JA, Cerezal L, Narvaez J. MRI of sports-related injuries of the foot and ankle: Part 1. *Curr Probl Diagn Radiol.* 2003;32(4):139–155.

Narvaez JA, Cerezal L, Narvaez J. MRI of sports-related injuries of the foot and ankle: Part 2. *Curr Probl Diagn Radiol.* 2003;32(5):177–193.

Perrich KD, Goodwin DW, Hecht PJ, et al. Ankle ligaments on MRI: Appearance of normal and injured ligaments. *AJR Am J Roentgenol.* 2009;193(3):687–695.

Petersen B, Fitzgerald J, Schreibman K. Musculotendinous magnetic resonance imaging of

the ankle. *Semin Roentgenol.* 2010;45(4):250–276.
Riley GM. Magnetic resonance imaging in the evaluation of sports injuries of the foot and ankle: A pictorial essay. *J Am Podiatr Med Assoc.* 2007;97(1):59–67.
Rosenberg ZS, Beltran J, Bencardino JT. From the RSNA Refresher Courses. Radiological society of North America. MR imaging of the ankle and foot. *Radiographics.* 2000;(20 Spec No):S153–S179.
Sarrafian SK, Kelikian AS, eds. Syndesmology. *Sarrafian's Anatomy of the Foot and Ankle: Descriptive, Topographic, Functional.* 3rd ed. Philadelphia, PA: Lippincott Williams & Wilkins; 2011: 163–223.
Stoller DW. *The Ankle and Foot. Magnetic resonance imaging in orthopaedics and sports medicine*. 3rd ed. Baltimore, MD: Lippincott Williams & Wilkins; 2007:733–1051.

APPENDIX 1: Sample Completed Structured Report: Ankle: NORMAL

Examination: MRI of Ankle [<With/Without>] Contrast

HISTORY: [] year-old [<Patient Sex>] with [<Order Reason for Study>]

TECHNIQUE: Imaging was performed [<without IV contrast> <before and after IV> <after intra-articular contrast>]. Multiplanar, multisequence MR images of the [right/left] ankle were obtained on a [1.5 or 3.0] Tesla magnet.

COMPARISON: [<None>]

FINDINGS:

Alignment: [<Normal>

Fluid:

Tibiotalar joint: [<Normal>]

Posterior subtalar joint: [<Normal>]

Talonavicular joint: [<Normal>]

Calcaneonavicular joint: [<Normal>]

Medial structures:

Medial malleolus: [<Normal>]

Tendons:

Posterior tibial tendon: [<Normal]

Flexor digitorum longus: [<Normal]

Flexor hallucis longus: [<Normal]

Ligaments:

Deltoid ligament complex—superficial: [<Intact]

Deltoid ligament complex—deep: [<Intact]

Spring (plantar calcaneonavicular) ligament: [<Intact]

Lateral structures:

Lateral malleolus: [<Normal>]

Retromalleolar groove: [<Concave>]

Tendons:

Peroneus longus: [<Normal>]

Peroneus brevis: [<Normal>]

Superior peroneal retinaculum: [<Intact>]

Ligaments:

Interosseous (syndesmosis): [<Intact>]

Anterior inferior tibiofibular (syndesmosis): [<Intact>]

Posterior inferior tibiofibular (syndesmosis): [<Intact>]

Anterior talofibular ligament: [<Intact>]

Calcaneofibular ligament: [<Intact>]

Posterior talofibular ligament: [<Intact>]

Bifurcate ligament: [<Intact>]

Posterior structures:

Posterior talus: [<Normal>]

Posterior intermalleolar ligament: [<Intact>]

Achilles tendon: [<Normal>]

Plantar fascia: [<Normal>]

Anterior structures:

Tendons:

Anterior tibial tendon: [<Normal>]

Extensor hallucis longus: [<Normal>]

Extensor digitorum longus: [<Normal>]

Ligaments:

Dorsal talonavicular ligament: [<Intact>]

Tibiotalar joint: [<Normal>]

Subtalar joint: [<Normal>]

Bones (other than subarticular marrow and malleoli): [<Normal>]

Muscles: [<Normal>]

Nerves and tarsal tunnel: [<Normal>]

Sinus tarsi: [<Normal>]

Vessels: [<Normal>]

Other: [<None>]

Impression:

[<In the order of importance with acute findings first>]

☑ APPENDIX 2: Sample Completed Structured Report: Ankle: ABNORMAL

Exam: MRI of Ankle Without Contrast

HISTORY: [<45-year-old man with left medial ankle pain and instability>]

TECHNIQUE: Imaging was performed [<without IV contrast>]. Multiplanar, multisequence MR images of the [<left>] ankle were obtained on a [<3.0>] Tesla magnet.

COMPARISON: [<Radiographs dated 11/11/2014>]

FINDINGS:

Alignment: [<Talar fault and hindfoot valgus>]

Fluid:

Tibiotalar joint: [<Small effusion>]

Posterior subtalar joint: [<Normal>]

Talonavicular joint: [<Normal>]

Calcaneonavicular joint: [<Normal>]

Medial structures:

Medial malleolus: [<Small enthesophytes.

Tendons:

Posterior tibial tendon: [<Longitudinal split tear at the retromalleolar groove with distal reconstitution. Underlying moderate tendinosis>]

Flexor digitorum longus: [<Normal>]

Flexor hallucis longus: [<Small amount of fluid>]

Ligaments:

Deltoid ligament complex—superficial: [<Thickened tibiocalcaneal portion and tibiospring portion>]

Deltoid ligament complex–deep: [<Thickened posterior deep tibiotalar portion>]

Spring (plantar calcaneonavicular) ligament: [<Thickened superomedial band>]

Lateral structures:

Lateral malleolus: [<Normal>]

Retromalleolar groove: [<Flat>]

Tendons:

Peroneus longus: [<Normal>]

Peroneus brevis: [<Normal>]

Superior peroneal retinaculum: [<Intact>]

Ligaments:

Interosseous (syndesmosis): [<Intact>]

Anterior inferior tibiofibular (syndesmosis): [<Intact>]

Posterior inferior tibiofibular (syndesmosis): [<Intact>]

Anterior talofibular ligament: [<Attenuated>]

Calcaneofibular ligament: [<Thickened>]

Posterior talofibular ligament: [<Mucoid degeneration with subcortical cyst at fibular attachment>]

Bifurcate ligament: [<Intact>]

Posterior structures:

Posterior talus: [<Os trigonum present>]

Posterior intermalleolar ligament: [<Intact>]

Achilles tendon: [< Normal>]

Plantar fascia: [<Thickened central cord. Plantar spur>]

Anterior structures:

Tendons:

Anterior tibial tendon: [<Normal>]

Extensor hallucis longus: [<Normal>]

Extensor digitorum longus: [<Normal>]

Ligaments:

Dorsal talonavicular ligament: [<Enthesophytes and small ganglion>]

Tibiotalar joint: [<Normal>]

Subtalar joint: [<Diffuse low grade thinning>]

Bones (other than subarticular marrow and malleoli): [<Subcortical sclerosis at the Gissane angle>]

Muscles: [<Mild fatty infiltration of abductor digiti minimi>]

Nerves and tarsal tunnel: [<Normal>]

Sinus tarsi: [<Diffuse soft tissue thickening with replacement of normal fat signal. Traction subcortical cysts at the sinus tarsi ligament attachments of the talus and calcaneus>]

Vessels: [<Normal>]

Other: [<None>]

Impression:

1. Ankle malalignment, sinus tarsi syndrome and findings of PTT dysfunction with chronic talocalcaneal abutment.

2. Old low-grade lateral collateral ligament injury.

3. Mild chronic plantar fasciitis.

12

Magnetic Resonance Neurography

Avneesh Chhabra, Theodoros Soldatos, and John A. Carrino

Magnetic resonance neurography (aka MR neurography or MRN) is a modified version of current MR imaging techniques, which depicts peripheral nerves with greater conspicuity and in multiple different planes using a combination of high resolution and high contrast two-dimensional (2D) and three-dimensional (3D) imaging techniques. It is being increasingly employed in the diagnostic algorithm of peripheral neuropathy patients for the evaluation of nerve injury, entrapment, inflammation, and mass lesions. Since MRN provides sub -0.5 mm resolution on 2D imaging sequences and sub -1.5 mm resolution on 3D imaging sequences, the regional musculotendinous and joint structures are well seen on these sequences. Generally MRN is primarily performed for neurogenic symptoms, however, non-specific clinical symptoms suggesting sensory neuropathy or non-specific pain symptoms at times are better explained by the findings of regional joint derangement or inflammatory/autoimmune myopathy while the regional nerves might show normal appearance. Therefore, the reader should pay due diligence in the evaluation of various structural abnormalities in the field of view, and employ a structured reporting template to elegantly and accurately describe all the relevant abnormalities that may have the potential to guide patient's treatment and management. This chapter discusses the imaging evaluation approach and describes how to fill the structured checklists in Boxes 1–3. These three checklists are relevant to the evaluation of brachial plexus, lumbosacral (LS) plexus, and generic MRN that could be used for any particular extremity areas. The generic MRN template can be used in isolation for a specific site, for example, carpal tunnel, tarsal tunnel, forearm neurography, etc; or if additional extremity site was performed as part of the plexus examination, for example, one would use brachial plexus and generic template for reporting of MRN examination of brachial plexus and right arm. Conceptual details of related MR physics and imaging protocol are discussed in the MR protocol optimization chapter.

IMAGE EVALUATION

Similar to any other MR examination, a systematic approach to image evaluation is essential. The reader should try to glean relevant information from any available clinical

findings or electrophysiology results to better evaluate and interpret the imaging findings. The below-outlined stepwise interpretation approach is only a practical guide, and all regional soft tissue structures should be evaluated in multiple planes for their optimal assessment. This will also help the readers perceive which structures are best depicted/evaluated on which particular plane.

1. During extremity neurography evaluation, first assess the long axis 2D and 3D images for gross bone or soft tissue injury or any mass lesion. Then, evaluate the muscles for any regional denervation changes. It is important to use good and uniform fat-suppression techniques to detect subtle edema-like signal changes in the denervated or myopathic muscles. This can be followed by assessment of regional joints for effusion, ganglion cyst, gross ligament injuries, labral and meniscal tears. Then, line up the similar-plane axial fat-saturated (fs) fluid sensitive and non-fs T1W images and synchronize them for tandem evaluation (Fig. 1). Diligently interrogate the regional muscles and nerves for signal intensity alterations, course, caliber, fascicles, and perineural fat planes. If there is an incidental finding of a mass lesion, further define its perineural extent, intraneural extension and fascicular involvement, etc. (Fig. 2). Compare the affected nerves to other regional nerves with regards to morphologic and signal alterations. Once a neural abnormality is detected, again look at the anatomically innervated downstream muscles for subtle denervation changes. Finally, in the light of available clinical findings, make a final impression of whether there is nerve injury (grade it), mass lesion (characterize it), entrapment (grade it), or polyneuropathy condition suggesting systemic or polyneuropathy causes, such as hereditary neuropathy, neurocutaneous syndrome, or inflammation.

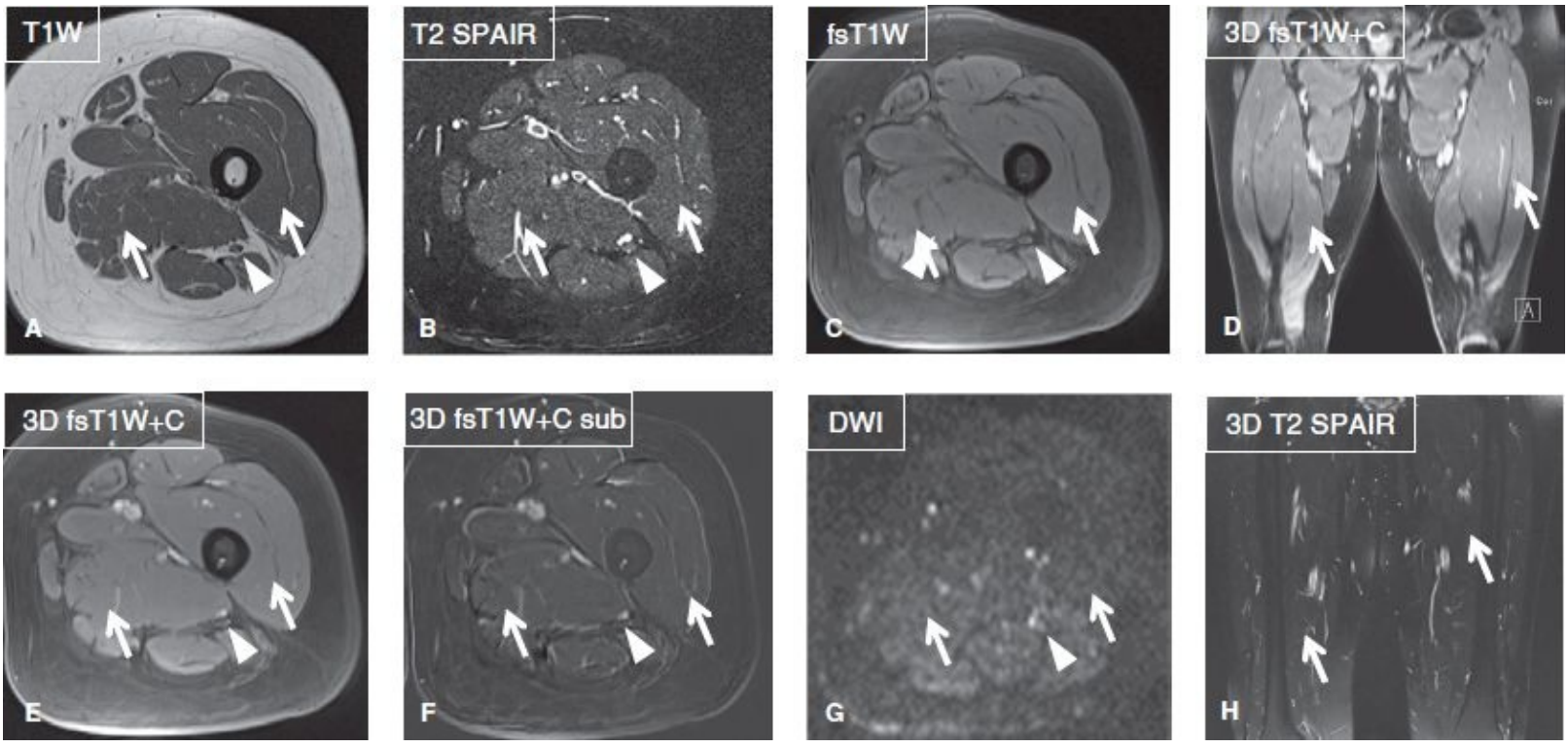

Fig. 1: Normal MRN appearance of peripheral nerves and skeletal muscles. Axial **(A–C, E–**

G) and coronal **(D, H)** images demonstrate normal homogeneously intermediate signal intensity of skeletal muscles (*short arrows*) and sciatic nerves (*arrowheads*). The muscles and nerves lack abnormal enhancement or diffusion abnormality.

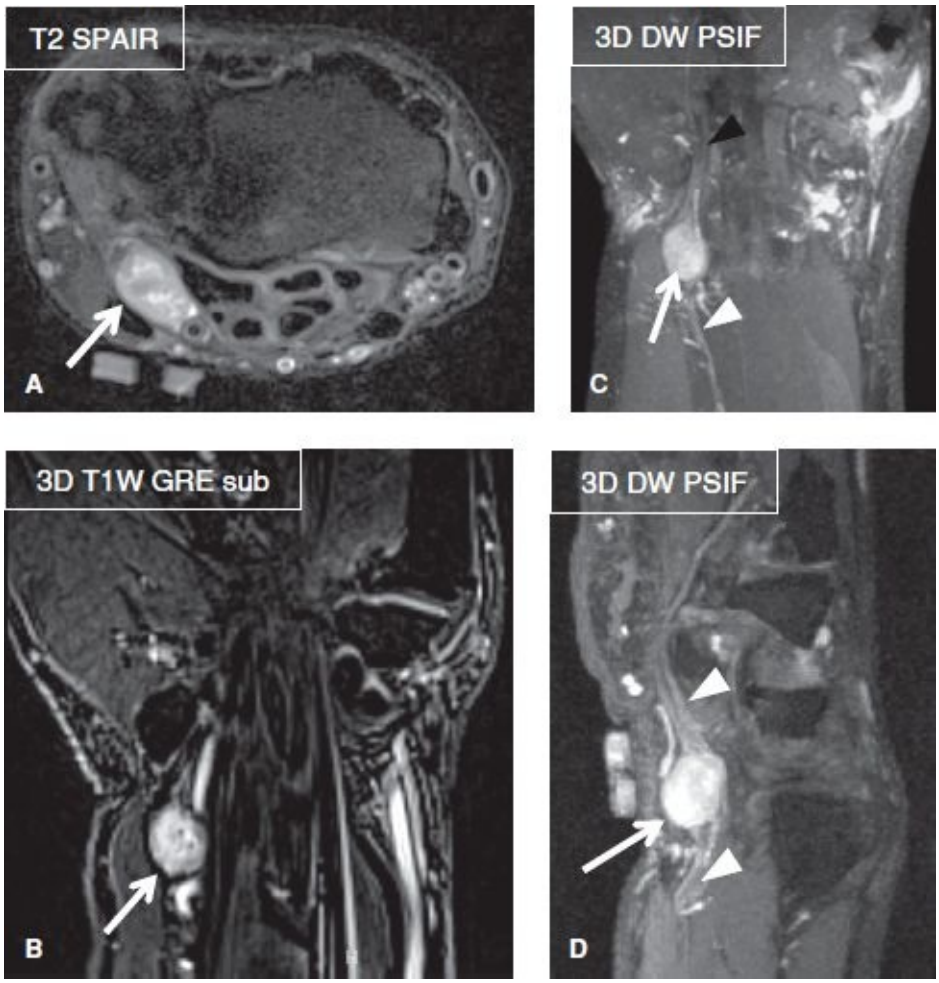

Fig. 2: Schwannoma of the ulnar nerve. Axial **(A),** coronal **(B, C),** and sagittal **(D)** images at the wrist exhibit a well-defined T2 hyperintense homogeneously enhancing mass (*arrows*), which features tail sign (*arrowheads*) and eccentric involvement of the ulnar nerve.

2. During the brachial or LS plexus evaluation, first look at the long axis 3D images for gross bony or soft tissue injury, or any mass lesion. Then, evaluate the muscles for gross regional denervation changes. This should be followed by systematic assessment of the spine (cervical or lumbar) and spinal cord, since spine pathology can be a major clinical confounder in the diagnosis of plexus pathology (Fig. 3). Look carefully for spinal cord or thecal sac impingement, cord edema or myelomalacia, severe neural foraminal stenosis, or other lesions that might explain patient symptoms or might contribute to downstream plexopathy or nerve entrapment (double crush syndrome). This should be followed by assessment of regional joints for effusion, ganglion cyst, gross ligament injuries or paralabral cysts suggesting labral tears. Then, line up the similar-plane axial fat-saturated (fs) fluid sensitive and non-fs T1W images during lumbar plexus evaluation and synchronize them for tandem evaluation. Diligently interrogate the regional muscles and nerves for alterations of signal intensity, course, caliber, fascicles, and perineural fat

planes. If there is a regional mass lesion, further interrogate to define its extent, intraneural extension, fascicular involvement, etc. Compare the affected nerves to the regional nerves with regards to signal and morphologic alterations, since bilateral symmetry in the normal LS plexus and brachial plexus is quite remarkable (Fig. 4). Once a neural abnormality is detected, again look at the anatomically innervated downstream muscles for subtle denervation changes. During the brachial plexus evaluation, it is essential to evaluate sagittal inversion recovery images for side to side comparison with regards to signal and size alterations, as well as to distinguish among different segments of the brachial plexus (Fig. 5). Finally, in the light of the available clinical findings, make a final impression whether there is nerve injury (grade it), mass lesion (characterize it), entrapment (grade it), or one of the systemic/polyneuropathy condition, such as hereditary neuropathy, neurocutaneous syndrome, or inflammation.

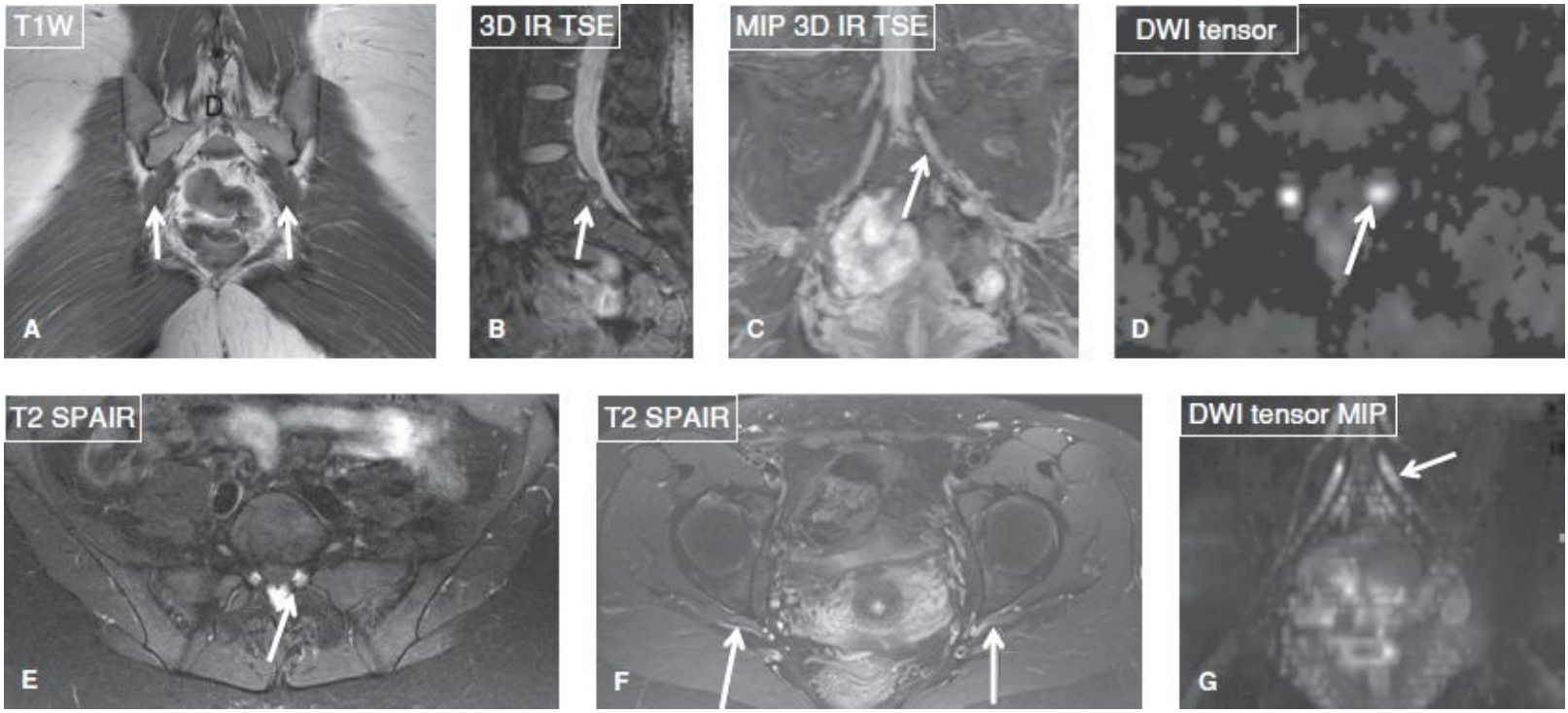

Fig. 3: Spine disease with left sciatica. **A:** Coronal image through pelvis shows normal symmetric piriformis muscles bilaterally (*arrows*). **B:** 3D sagittal reconstructed image shows disc herniation at L5–S1 level (*arrow*). **C:** 3D coronal MIP reconstructed image shows enlarged left S1 nerve (*arrow*). **D, E:** Axial images also confirm the abnormality. **F:** Axial image shows symmetrical appearance of the sciatic nerves (*arrows*) excluding pathology due to piriformis syndrome. **G:** MIP reconstruction from diffusion tensor image shows the subtle nerve enlargement along the long axis.

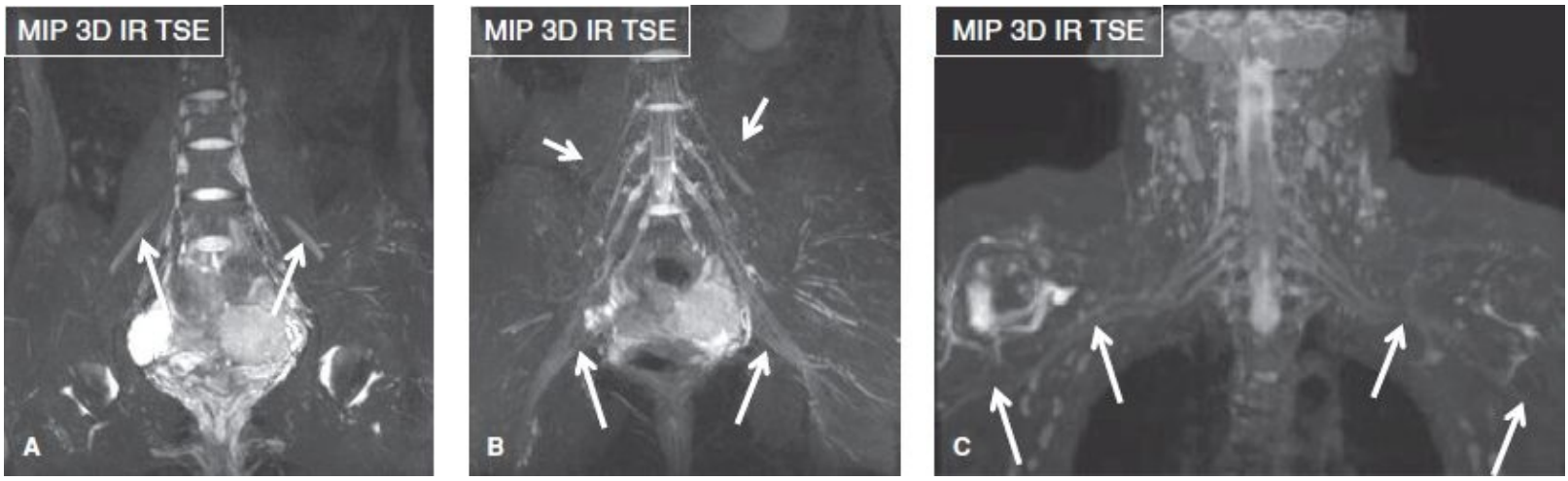

Fig. 4: Symmetrical versus asymmetrical plexus appearance. Coronal images **(A, B)** of the LS plexus show normal femoral nerves (*arrows* in **A**), sciatic nerves (*long arrows* in **B**), and the lateral femoral cutaneous nerves (*short arrows* in **B**). Coronal image **(C)** of the brachial plexus in a patient with a recent motor vehicle accident and associated ipsilateral humeral head fracture demonstrates asymmetric T2 hyperintensity of the right brachial plexus cords and peripheral branches (*arrows*), reflecting traction (Sunderland grade I–II) injury.

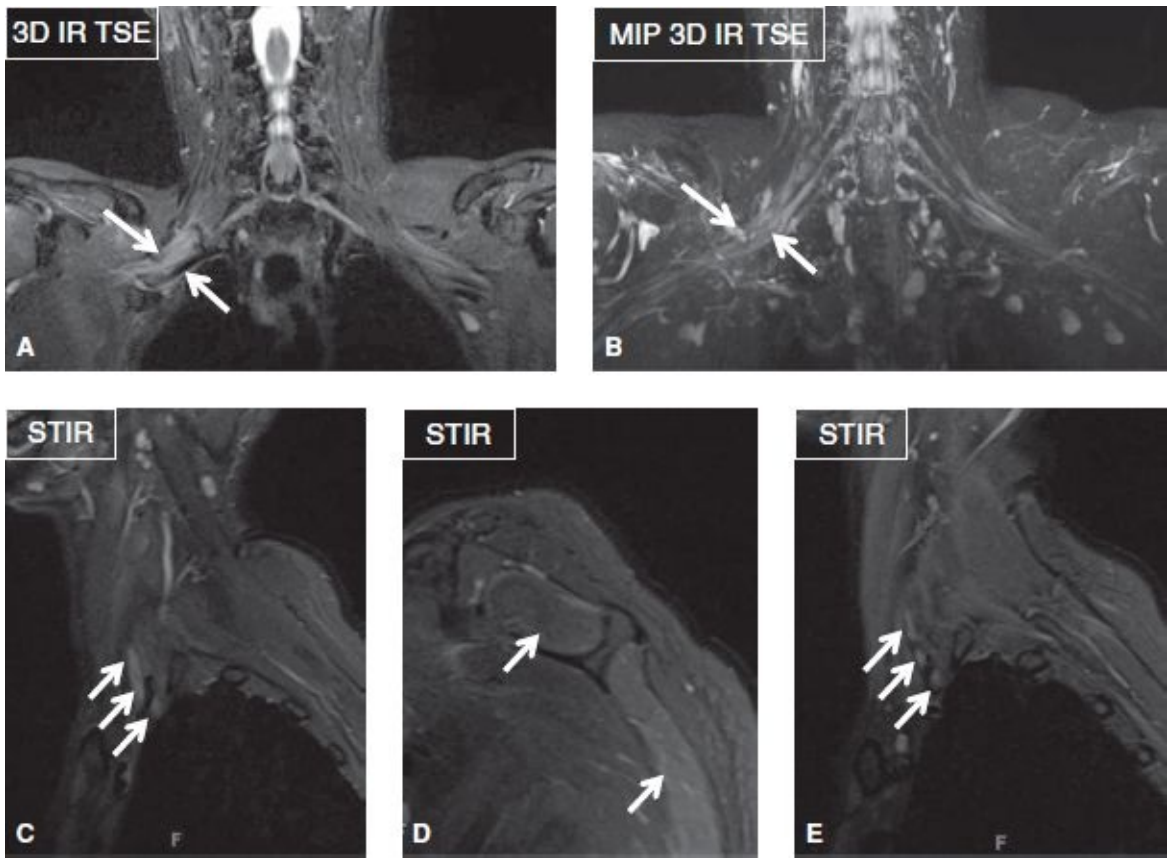

Fig. 5: Importance of sagittal images during brachial plexus evaluation. Brachial plexus iatrogenic stretch injury (Sunderland grade II/III injury). Coronal **(A, B)** and sagittal **(C, D)** images demonstrate asymmetric hyperintensity and thickening of the right brachial plexus (*arrows*) with predominant involvement of the upper and middle trunks, as well as edema of the ipsilateral infraspinatus muscle (*asterisk*). Notice normal trunks on the left side (*arrows* in **E**).

BOX 1: The Structured Report: MRN of the Brachial Plexus

The checklist for structured reporting of MR neurography of the brachial plexus. For each field, *Normal* is considered default in the dictation, whereas the rest of the elements describe various pathologies that could be encountered during imaging evaluation. See Appendices 1 and 2 at the end of the chapter for a sample completed report.

Examination: MR Neurography of Brachial Plexus

FINDINGS:

Nerves:

Spinal cord: [<Normal> <Cord compression> <Cord edema> <Cord hemorrhage> <Myelomalacia>]

Brachial plexus: Preganglionic: [<Normal> <Nerve root avulsion> <Pseudomeningocele>]

Brachial plexus: Postganglionic: [<Normal> <Thickening> <Asymmetrical or abnormal hyperintensity> <Laceration or rupture> <Nodularity> <Mass lesion>] of [<Nerve roots> <Trunks> <Divisions> <Cords> <Proximal peripheral nerves>]

Muscles/Tendons:

Scalenes: [<Normal> <Asymmetrical hypertrophy or Atrophy>]

Rotator cuff muscles: [<Normal> <Edema like signal> <Fatty replacement> <Atrophy>]

Other muscles: [<Normal> <Paraspinal muscles> <Trapezius> <Latissimus dorsi> <Serratus anterior>]

Bones:

Cervical ribs: [<Absent> <Present> <Pseudoarthrosis with first rib>]

C7 transverse processes: [<Normal> <Elongated>]

Marrow signal: [<Normal> <Bone contusion or fracture> <Hemangioma> <Mass lesion>]

Joints:

Cervical spine:

Alignment: [<Normal> <Straightening> <Exaggerated lordosis> <Listhesis>]

Spinal Canal: Developmental stenosis: [<Absent> <Present in lower cervical spine or diffusely short pedicles>]

Occipital-C1 and atlantoaxial (C1–C2) articulations: [<Normal> <Osteoarthritis> <Effusion> <Atlantodental bursitis> <Pannus>]

C2–C3:

- Central canal: [<Patent> <Mild/moderate/severe narrowing>]
- Neural foramina: Right: [<Normal> <Mild/moderate/severe narrowing>]

Left: [<Normal> <Mild/moderate/severe narrowing>]

- Intervertebral disc: [<Normal> <Dessication> <Decreased height> <Bulge> <Herniation> <Disc–osteophyte complex>]
- Facet joints: [<Normal> <Mild/moderate/severe facet hypertrophy>]
- Uncovertebral joints: [<Normal> <Hypertrophy>]
- Ligamentum flavum: [<Normal> <Hypertrophy>]

C3–C4:

- Central canal: [<Patent> <Mild/moderate/severe narrowing>]
- Neural foramina: Right: [<Normal> <Mild/moderate/severe narrowing>]

Left: [<Normal> <Mild/moderate/severe narrowing>]

- Intervertebral disc: [<Normal> <Dessication> <Decreased height> <Bulge> <Herniation> <Disc–osteophyte complex>]
- Facet joints: [<Normal> <Mild/moderate/severe facet hypertrophy>]
- Uncovertebral joints: [<Normal> <Hypertrophy>]
- Ligamentum flavum: [<Normal> <Hypertrophy>]

C4–C5:

- Central canal: [<Patent> <Mild/moderate/severe narrowing>]
- Neural foramina: Right: [<Normal> <Mild/moderate/severe narrowing>]

Left: [<Normal> <Mild/moderate/severe narrowing>]

- Intervertebral disc: [<Normal> <Dessication> <Decreased height> <Bulge> <Herniation> <Disc–osteophyte complex>]

- Facet joints: [<Normal> <Mild/moderate/severe facet hypertrophy>]
- Uncovertebral joints: [<Normal> <Hypertrophy>]
- Ligamentum flavum: [<Normal> <Hypertrophy>]

C5–C6:
- Central canal: [<Patent> <Mild/moderate/severe narrowing>]
- Neural foramina: Right [<Normal> <Mild/moderate/severe narrowing>]

Left: [<Normal> <Mild/moderate/severe narrowing>]
- Intervertebral disc: [<Normal> <Dessication> <Decreased height> <Bulge> <Herniation> <Disc–osteophyte complex>]
- Facet joints: [<Normal> <Mild/moderate/severe facet hypertrophy>]
- Uncovertebral joints: [<Normal> <Hypertrophy>]
- Ligamentum flavum: [<Normal> <Hypertrophy>]

C6–C7:
- Central canal: [<Patent> <Mild/moderate/severe narrowing>]
- Neural foramina: Right: [<Normal> <Mild/moderate/severe narrowing>]

Left: [<Normal> <Mild/moderate/severe narrowing>]
- Intervertebral disc: [<Normal> <Dessication> <Decreased height> <Bulge> <Herniation> <Disc–osteophyte complex>]
- Facet joints: [<Normal> <Mild/moderate/severe facet hypertrophy>]
- Uncovertebral joints: [<Normal> <Hypertrophy>]
- Ligamentum flavum: [<Normal> <Hypertrophy>]

C7–T1:
- Central canal: [<Patent> <Mild/moderate/severe narrowing>]
- Neural foramina: Right: [<Normal> <Mild/moderate/severe narrowing>]

Left: [<Normal> <Mild/moderate/severe narrowing>]
- Intervertebral disc: [<Normal> <Dessication> <Decreased height> <Bulge> <Herniation> <Disc–osteophyte complex>]
- Facet joints: [<Normal> <Mild/moderate/severe facet hypertrophy>]
- Uncovertebral joints: [<Normal> <Hypertrophy>]
- Ligamentum flavum: [<Normal> <Hypertrophy>]

Sternoclavicular joints: [<Normal> <Osteoarthritis> <Effusion>]

Acromioclavicular joints: [<Normal> <Osteoarthritis> <Effusion>]

Glenohumeral joints: [<Normal> <Osteoarthritis> <Effusion>]

Thoracic outlet/Cervicothoracobrachial junction/Spaces:

Interscalene triangle: [<Normal> <Narrowed> <Mass>]

Costoclavicular space: [<Normal> <Narrowed> <Mass>]

Retropectoralis minor space: [<Normal> <Narrowed> <Mass>]

Vessels:

[<Within normal limits> <Vascular kinking> <vascular thrombosis> <vascular malformation>]

Masses:

[<None>]

Other:

[<None> <Incidental posterior fossa brain findings> <Cervical lymphadenopathy> <Thyroid mass> <Prevertebral edema>]

Postgadolinium discussion: [<No abnormal enhancement>]

Impression

1. [< >]

BOX 2: The Structured Report: MRN of the Lumbosacral Plexus

The checklist for structured reporting of MR neurography of the lumbosacral plexus. For each field, *Normal* is considered default in the dictation, whereas the rest of the elements describe various pathologies that could be encountered during imaging evaluation. See Appendices 3 and 4 at the end of the chapter for a sample completed report.

Examination: MR Neurography of Lumbosacral Plexus

FINDINGS:

Nerves:

Lower cord and conus: [<Normal> <Low lying or tethered cord> <Cord edema or compression> <Thickening or clumping of cauda equina>]

Lumbosacral plexus:
- Size: [<Normal> <Enlarged> <Atrophic>]
- Signal: [<Normal> <Asymmetrically or abnormally hyperintense> <Asymmetrically or abnormally hypointense>]
- Course: [<Normal> <Deviated> <Impinged>]

Sciatic nerve:
- Size: [<Normal> <Enlarged> <Atrophic> <Mass>]
- Signal: [<Normal> <Asymmetrically or abnormally hyperintense> <Hypointense>]
- Course: [<Normal> <Variant intramuscular course> <Deviated> <Impinged>]
- Fascicles: [<Normal> <Asymmetrically enlarged or atrophic> <Effaced>]

Femoral and obturator nerves:
- Size: [<Normal> <Enlarged> <Atrophic> <Mass>]
- Signal: [<Normal> <Asymmetrically or abnormally hyperintense> <Hypointense>]
- Course: [<Normal> <Variant intramuscular course> <Deviated> <Impinged>]
- Fascicles: [<Normal> <Asymmetrically enlarged or atrophic> <Effaced>]

Lateral femoral cutaneous nerves:
- Size: [<Normal>]
- Signal: [<Normal>]
- Course: [<Normal>]

Other specific nerves in question: [<Pudendal/genitofemoral>]: [<Normal>]

Muscles/Tendons:

Psoas major:
- Bulk: [<Normal> <Atrophy> <Hypertrophy>]
- Intramuscular signal: [<Normal> <Edema-like signal>]
- Iliopsoas bursa: [<Normal> <Mild/moderate/severe bursitis>]

Piriformis:
- Bulk: [<Normal> <Atrophy> <Hypertrophy>]
- Intramuscular signal: [<Normal> <Edema-like signal>]
- Iliopsoas bursa: [<Normal> <Mild/moderate/severe bursitis>]

Gluteal:

- Bulk: [<Normal> <Atrophy> <Hypertrophy>]
- Intramuscular signal: [<Normal> <Edema-like signal>]
- Trochanteric bursa: [<Normal> <Mild/moderate/severe bursitis>]
- Gluteal tendon: [<Normal> <Tendinosis> <Tear>]

Hamstring tendon: [<Normal> <Tendinosis> <Tear>]

Adductor: [<Normal> <Atrophy> <Edema-like signal> <Tear>]

Other: [<Quadriceps femoris> <Quadratus femoris/ischiofemoral impingement> <Paraspinal muscles, edema-like signal, atrophy>]

Bones:

Sciatic notches: [<Normal> <Mass lesion>]

Marrow signal: [<Otherwise normal>]

Joints:

Lumbosacral spine: Alignment: [<Normal> <Straightening> <Exaggerated lordosis> <Listhesis> <Transitional vertebra present>]

Spinal canal: Developmental stenosis [<Absent> <Present in lower lumbar spine or diffusely short pedicles>]

L1–L2:
- Central canal: [<Patent> <Mild/moderate/severe narrowing>]
- Neural foramina: Right: [<Normal> <Mild/moderate/severe narrowing>]

Left: [<Normal> <Mild/moderate/severe narrowing>]
- Intervertebral disc: [<Normal> <Dessication> <Decreased height> <Bulge> <Herniation> <Disc–osteophyte complex>]
- Facet joints: [<Normal> <Mild/moderate/severe facet hypertrophy> <Synovial cyst>]
- Uncovertebral joints: [<Normal> <Hypertrophy>]
- Ligamentum flavum: [<Normal> <Hypertrophy>]

L2–L3:
- Central canal: [<Patent> <Mild/moderate/severe narrowing>]
- Neural foramina: Right: [<Normal> <Mild/moderate/severe narrowing>]

Left: [<Normal> <Mild/moderate/severe narrowing>]
- Intervertebral disc: [<Normal> <Dessication> <Decreased height> <Bulge>

<Herniation> <Disc–osteophyte complex>]
- Facet joints: [<Normal> <Mild/moderate/severe facet hypertrophy> <Synovial cyst>]
- Ligamentum flavum: [<Normal> <Hypertrophy>]

L3–L4:
- Central canal: [<Patent> <Mild/moderate/severe narrowing>]
- Neural foramina: Right: [<Normal> <Mild/moderate/severe narrowing>]

Left: [<Normal> <Mild/moderate/severe narrowing>]
- Intervertebral disc: [<Normal> <Dessication> <Decreased height> <Bulge> <Herniation> <Disc–osteophyte complex>]
- Facet joints: [<Normal> <Mild/moderate/severe facet hypertrophy> <Synovial cyst>]
- Ligamentum flavum: [<Normal> <Hypertrophy>]

L4–L5:
- Central canal: [<Patent> <Mild/moderate/severe narrowing>]
- Neural foramina: Right: [<Normal> <Mild/moderate/severe narrowing>]

Left: [<Normal> <Mild/moderate/severe narrowing>]
- Intervertebral disc: [<Normal> <Dessication> <Decreased height> <Bulge> <Herniation> <Disc–osteophyte complex>]
- Facet joints: [<Normal> <Mild/moderate/severe facet hypertrophy> <Synovial cyst>]
- Ligamentum flavum: [<Normal> <Hypertrophy>]

L5–S1:
- Central canal: [<Patent> <Mild/moderate/severe narrowing>]
- Neural foramina: Right: [<Normal> <Mild/moderate/severe narrowing>]

Left: [<Normal> <Mild/moderate/severe narrowing>]
- Intervertebral disc: [<Normal> <Dessication> <Decreased height> <Bulge> <Herniation> <Disc–osteophyte complex>]
- Facet joints: [<Normal> <Mild/moderate/severe facet hypertrophy> <Synovial cyst>]
- Ligamentum flavum: [<Normal> <Hypertrophy>]

Sacroiliac joints: [<Normal> <Osteoarthritis> <Effusion>]

Pubic symphysis: [<Normal> <Osteoarthritis> <Effusion>]

Hip joints: [<Normal> <Osteoarthritis> <Effusion> <Paralabral cyst>]

Vessels: [<Normal>]

Masses: [<None>]

Other (pelvic viscera): [<None> <Physiologic free fluid in pelvis> <Fibroid/prostate enlargement/adnexal mass/lymphadenopathy>]

Postgadolinium discussion: [<No abnormal enhancement>]

Impression

1. [< >]

BOX 3: The Structured Report: MRN Generic (Extremity/Tunnel)

The checklist for structured reporting of MR neurography of the extremity or tunnel. For each field, *Normal* is considered default in the dictation, whereas the rest of the elements describe various pathologies that could be encountered during imaging evaluation. See Appendices 5 and 6 at the end of the chapter for a sample of completed reports of the normal and abnormal examination results.

Examination: MR Neurography of Extremity/Carpal, Cubital, or Tarsal Tunnel

FINDINGS:

Nerves:

Size: [<Normal> <Enlarged> <Atrophic> <Mass>]

Signal: [<Normal> <Asymmetrically or abnormally hyperintense> <Asymmetrically or abnormally hypointense>]

Course: [<Normal> <Deviated> <Impinged> <Injured>]

Fascicles: [<Normal> <Asymmetrically enlarged or atrophic> <Effaced>]

Variant anatomy: [<Absent> <Present>]

Perineural fat: [<Normal> <Effaced>]

Muscles/Tendons: [<Normal > <Muscle atrophy or hypertrophy> <Edema-like

signal> <Tendinosis> <Tear>]

Bones: [<Normal > <Contusion> <Fracture> <Mass>]

Joints: [<Normal > <Effusion> <Osteoarthritis> <Ligament sprains> <Parameniscal or paralabral cyst>]

Vascular: [<Normal > <Varicosity> <Vascular malformation>]

Masses: [<None> <Intraneural mass> <Extraneural mass> <Neuroma in continuity> <End bulb neuroma>]

Other: [<None> <Ganglion cyst> <Thickened fascia> <Perineural fibrosis>]

Postgadolinium discussion: [<No abnormal enhancement>]

Impression

1. [< >]

How to Fill the Structured Report

This chapter will be dedicated to MRN imaging interpretation as to how to report abnormalities of peripheral nerves and the regional muscles. The evaluation of specific joints has been discussed separately in different chapters in the book.

Nerves:

Size: [<Normal> <Enlarged> <Atrophic><Mass>]

Signal: [<Normal> <Asymmetrically orabnormally hyperintense> <Asymmetrically or abnormally hypointense>]

Course: [<Normal> <Deviated> <Impinged><Injured>]

Fascicles: [<Normal> <Asymmetricallyenlarged or atrophic> <Effaced>]

Variant anatomy: [<Absent> <Present>]

Perineural fat: [<Normal> <Effaced>]

Muscles/Tendons: [<Normal> <Muscle atrophy or hypertrophy> <Edema-like signal> <Tendinosis> <Tear>]

Normal Peripheral Nerves

Peripheral nerves are most often part and parcel of neurovascular bundles, which makes it convenient to identify their location, but harder to distinguish them from the adjacent veins on conventional MR imaging due to the frequently present in-plane flow phenomenon and frequently encountered pulsation artifacts. The in-flow phenomenon renders the veins hyperintense on the fat-suppressed fluid sensitive images, similar in signal intensity to what the abnormal nerve would appear. Additionally, poor fat suppression can cause artifactual increase in the regional nerve signal intensity. Therefore, one should use optimal techniques to suppress these artifacts and diligently learn the neuromuscular anatomy before embarking upon the interpretation of these examinations. The technical details of extremity and plexus MRN have been discussed in detail in Chapter 2 of this book (Technical considerations). A normal nerve is made up of axons and various connective tissue sheaths in a well-organized architecture. The axons are covered by Schwann cells, endoneurial fluid, and a connective tissue layer, referred to as the endoneurium. The bundles of axons are clustered together in a fascicle, which is covered by another layer, called the perineurium. The latter forms the blood–nerve barrier and prevents the enhancement of a normal nerve on intravenous contrast examination. Multiple fascicles are arranged in another covering layer, called as the epineurium (Fig. 6). The outer epineurium covers the nerve and the internal epineurium contains the supporting fatty tissue and vascular supply to the nerve, called the vasa nervosa. On MRN, one can see the pencil thin hypointense epineurium and fascicles in most nerves larger than 3 mm. The fascicular bundles are uniformly arranged with symmetrical signal intensity and minimal intra-epineurial fat interspersed around them (Fig. 7). The nerves generally travel a straight course along the extremity and oblique course in the plexus without any abrupt focal deviations or kinks. The nerve caliber is nearly similar or smaller than the adjacent arteries with minimal variations as the nerve turns around the joints.

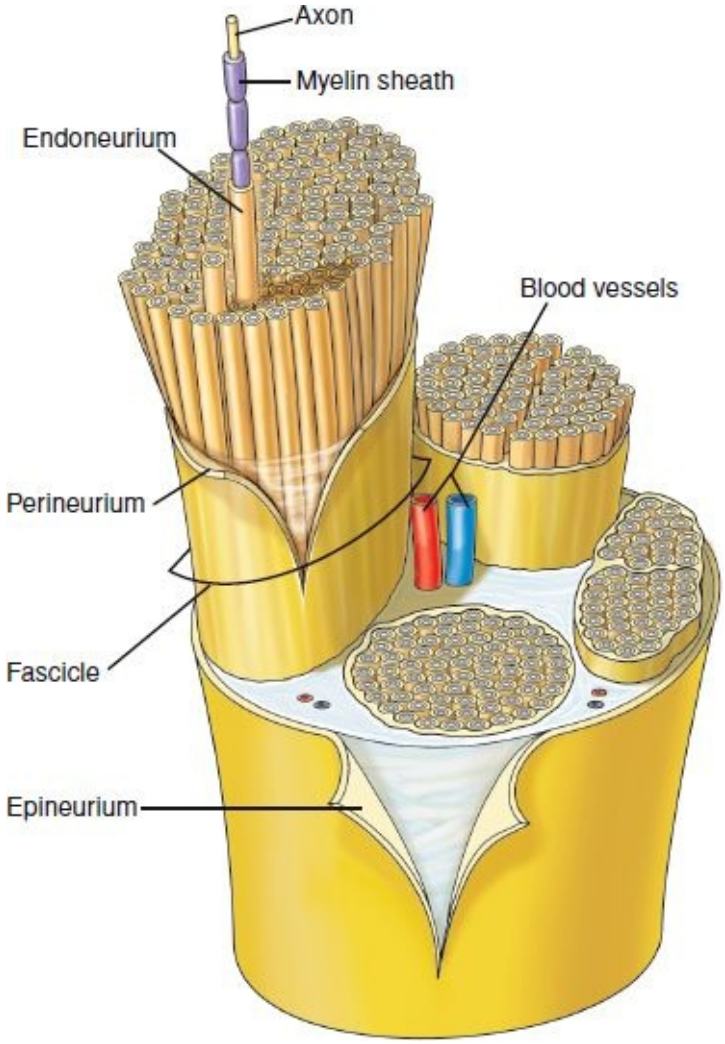

Fig. 6: Peripheral nerve showing axon, endoneurium, perineurium, and outer and inner epineurium.

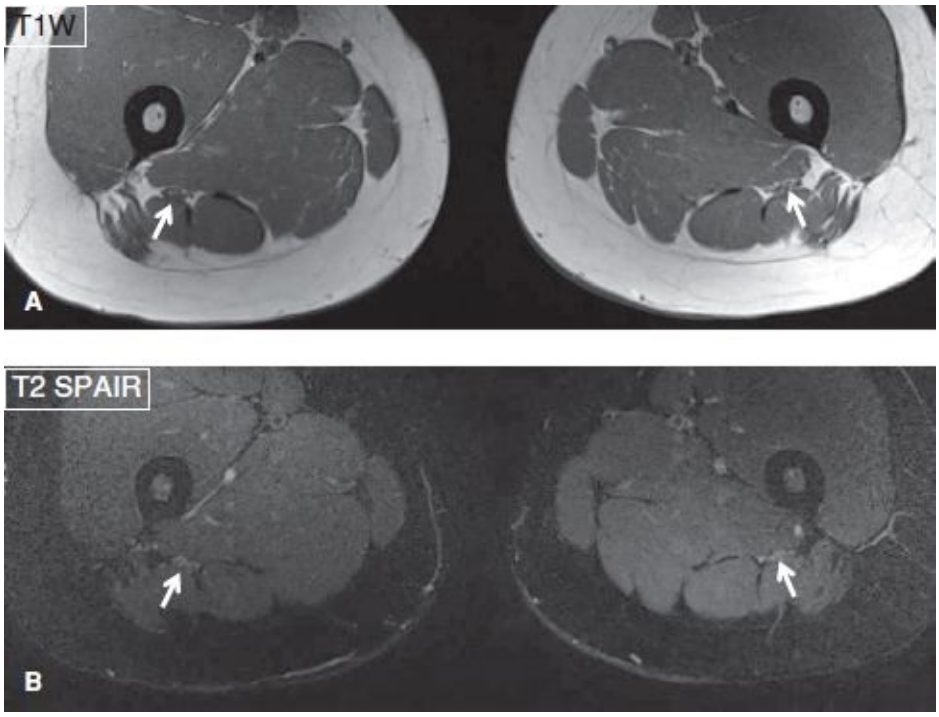

Fig. 7: Normal sciatic nerves. Axial images **(A, B)** through the thighs exhibit bilateral normal sciatic nerves (*arrows*), which appear isointense and mildly hyperintense to skeletal muscles

on T1W and T2W images, respectively.

Nerve Imaging Abnormalities and Related Pitfalls in Interpretation

Nerve Enlargement and Enhancement

Any focal enlargement or distal diffuse caliber increase usually correlates with neuropathy (Fig. 8). It may represent a post-traumatic effect, intra-neural mass lesion, or a perineural mass lesion mimicking nerve enlargement. One should look carefully for displacement or involvement of the fascicles, which would then confirm intra-neural location of the mass lesion. If there is polyneuropathy condition manifested as multiple nerve abnormalities and/or diffuse nerve enlargement, consider hereditary cause (that would lead to symmetrical abnormalities), systemic causes, or autoimmune/inflammatory neuropathy (that commonly leads to patchy asymmetrical or, less commonly, symmetrical abnormalities) (Fig. 9). Contrast administration becomes essential, if there is no clear cut history of trauma or if the enlargement of nerve is away from the site of entrapment. Since normal nerves do not enhance, the enhancement characteristics may aid in diagnosis (e.g., heterogeneous enhancement in malignancy or degenerated schwannoma, patchy enhancement in amyloidosis and dense nodular enhancement in lymphoma, diffuse enhancement in radiation neuropathy, and no significant enhancement in subacute CIDP, post-traumatic neuroma or chemotherapy related toxic neuropathy) or suggest the potential site of activity, which could be biopsied to obtain the definitive diagnosis. If one finds nodular mass lesion(s) or nodular enhancement, consider other diagnostic possibilities, such as lymphoma, neurocutaneous syndrome, endometriosis, or amyloid (Fig. 10). Other patterns of enhancement include uniform fascicular enhancement and enlargement of perineurioma (honey comb pattern) (Fig. 11), lacework-type mild enhancement in fibrolipomatous hypertrophy of the nerve (Fig. 12), and targetoid enhancement of a peripheral nerve sheath tumor (PNST) (Fig. 13).

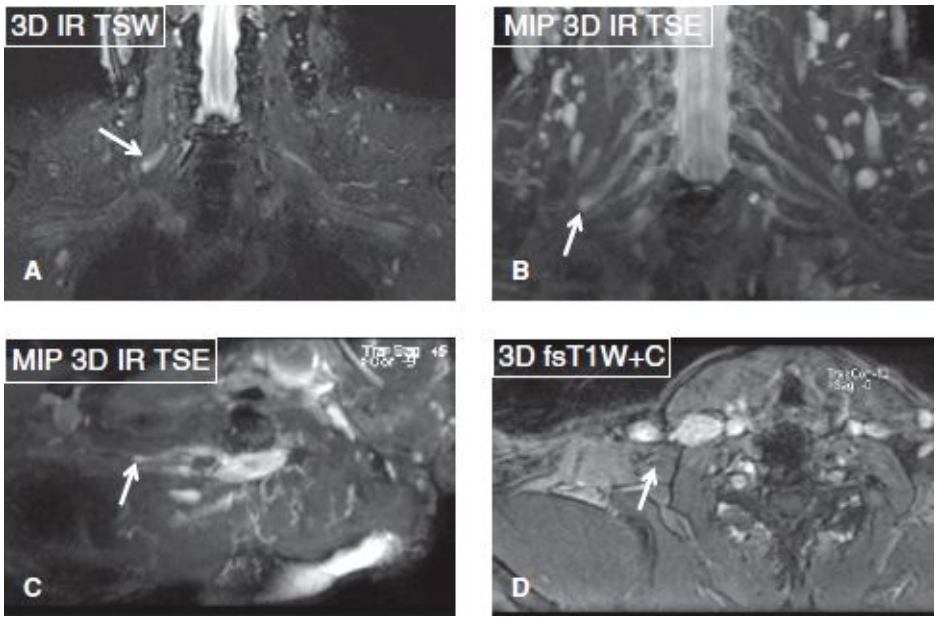

Fig. 8: Post-traumatic neuroma in continuity (Sunderland grade IV injury). Coronal **(A, B)** and oblique axial **(C, D)** images exhibit a neuroma in continuity of the right C6 nerve root (*arrows*) with no enhancement on contrast image **(D).**

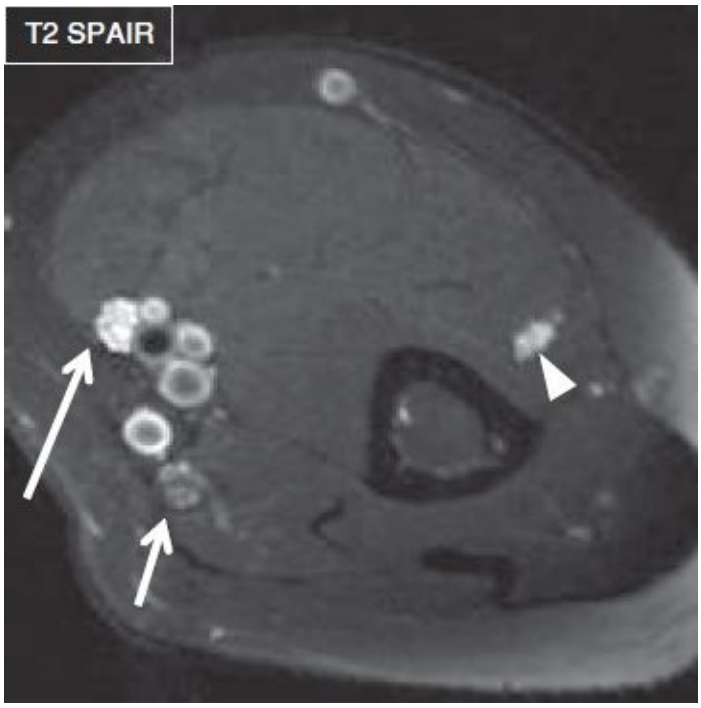

Fig. 9: Polyneuropathy. Multifocal motor neuropathy. Axial image through the arm shows enlarged and abnormally hyperintense peripheral nerves. The median nerve is most affected (*long arrow*) as compared to the ulnar nerve (*short arrow*) and the radial nerve (*arrowhead*).

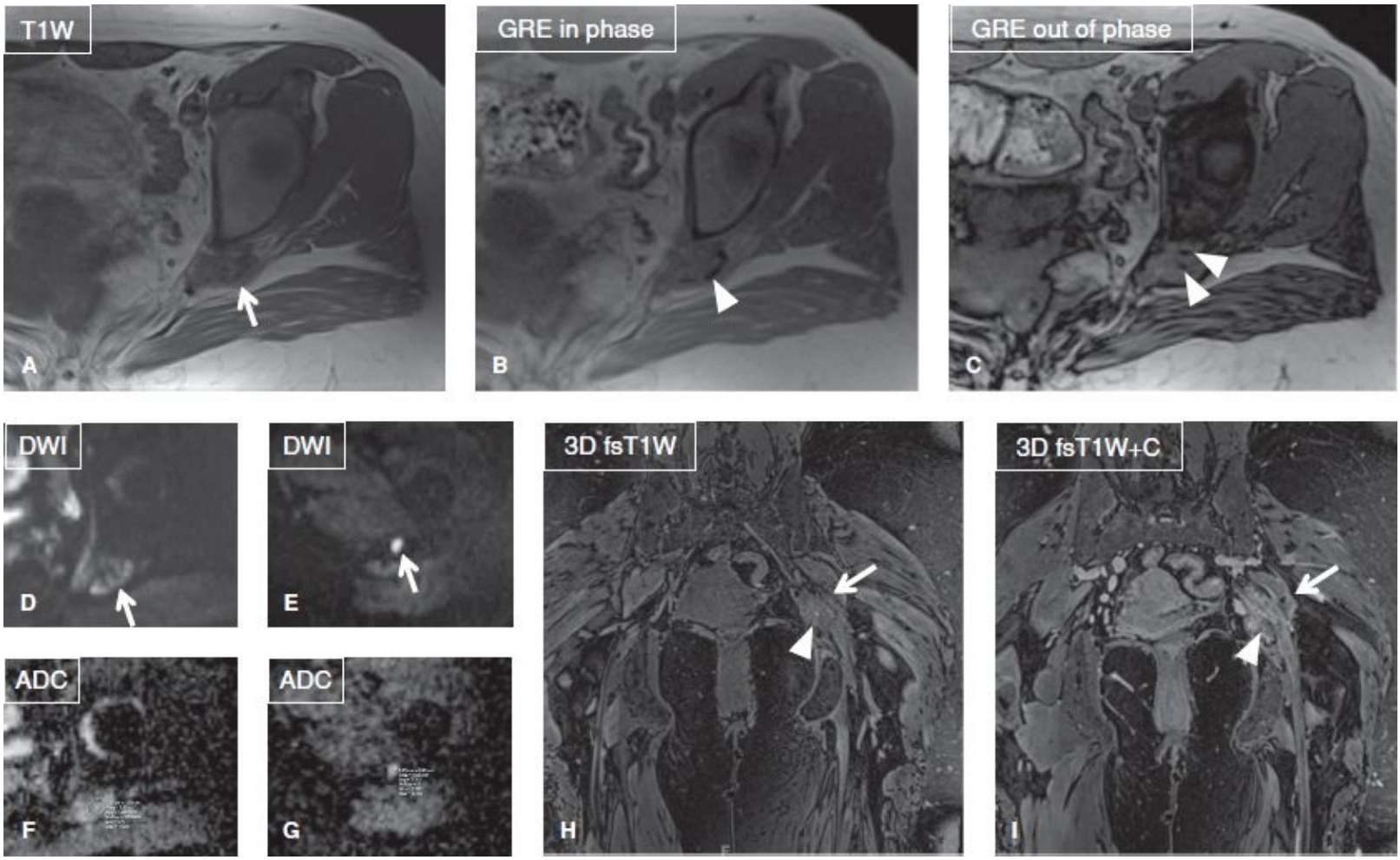

Fig. 10: Endometriosis causing sciatic neuropathy. Axial images **(A–C)** show a mass-like lesion (*arrows*) of intermediate T1/T2 signal at the left greater sciatic foramen, which features hypointense foci (*arrowheads*) on GRE images, indicative of blood products. ADC value of the lesion was 1.4 to 2 × 10^{-3} mm2/s **(D–G).** On the respective coronal images **(H, I),** the lesion (*arrowheads*) shows patchy contrast enhancement, indicative of hyperemia/inflammation. The findings are classic for sciatic endometriosis in a patient with symptoms of cyclical sciatica.

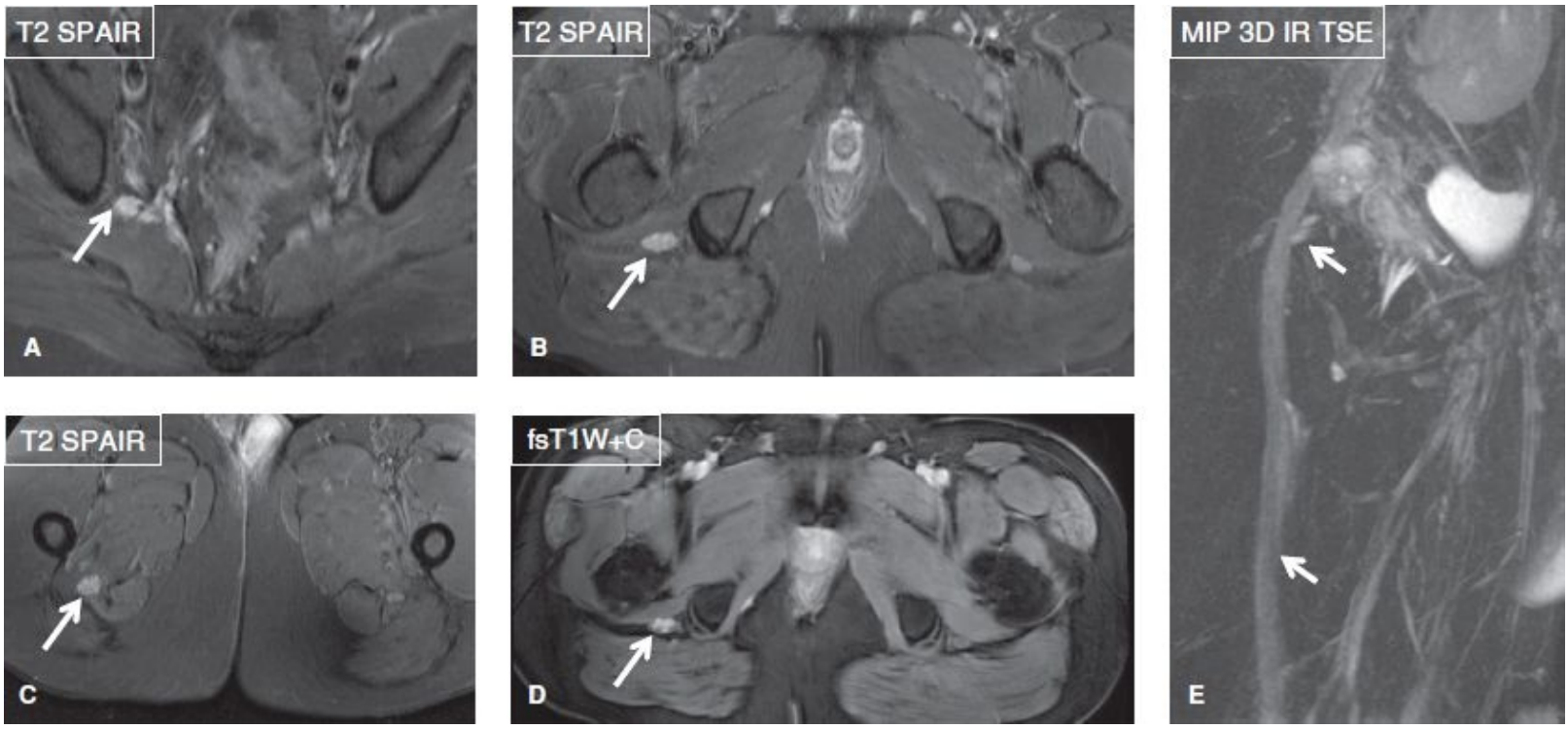

Fig. 11: Perineurioma of the sciatic nerve in a young woman. Axial **(A–D)** and oblique sagittal **(E)** images demonstrate diffuse thickening, abnormal T2 hyperintensity, uniform "honey comb" fascicular enlargement and intense enhancement of the right sciatic nerve (*arrows*).

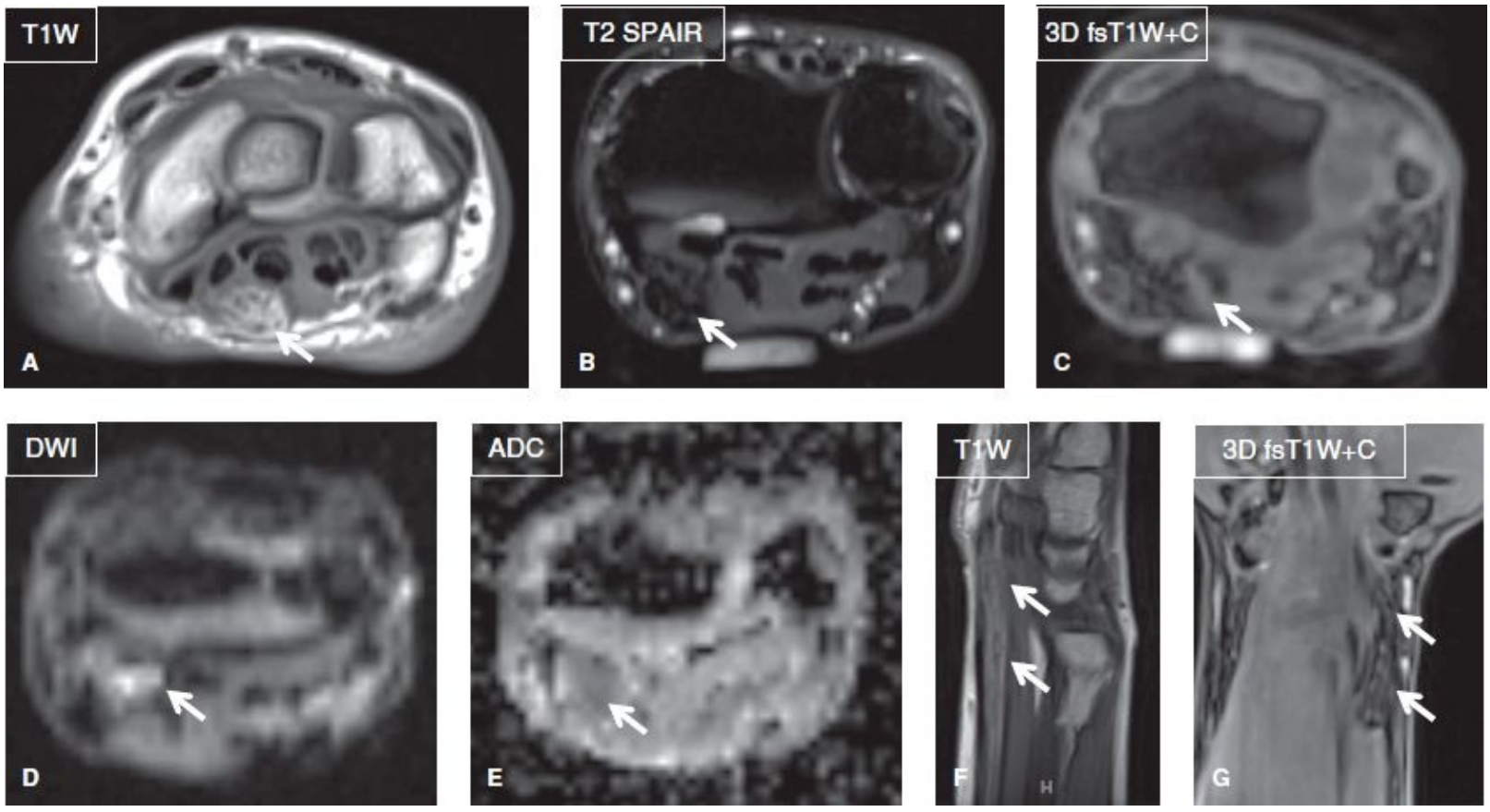

Fig. 12: Fibrolipomatous hamartoma of the median nerve. Axial **(A–E),** sagittal **(F),** and coronal **(G)** images exhibit diffuse enlargement of the median nerve (*arrows*), which contains fatty tissue, responsible for diffusion restriction. Notice "coxial cable" appearance

on axial image **(A)** and "spaghetti appearance" on the long axis image **(F).**

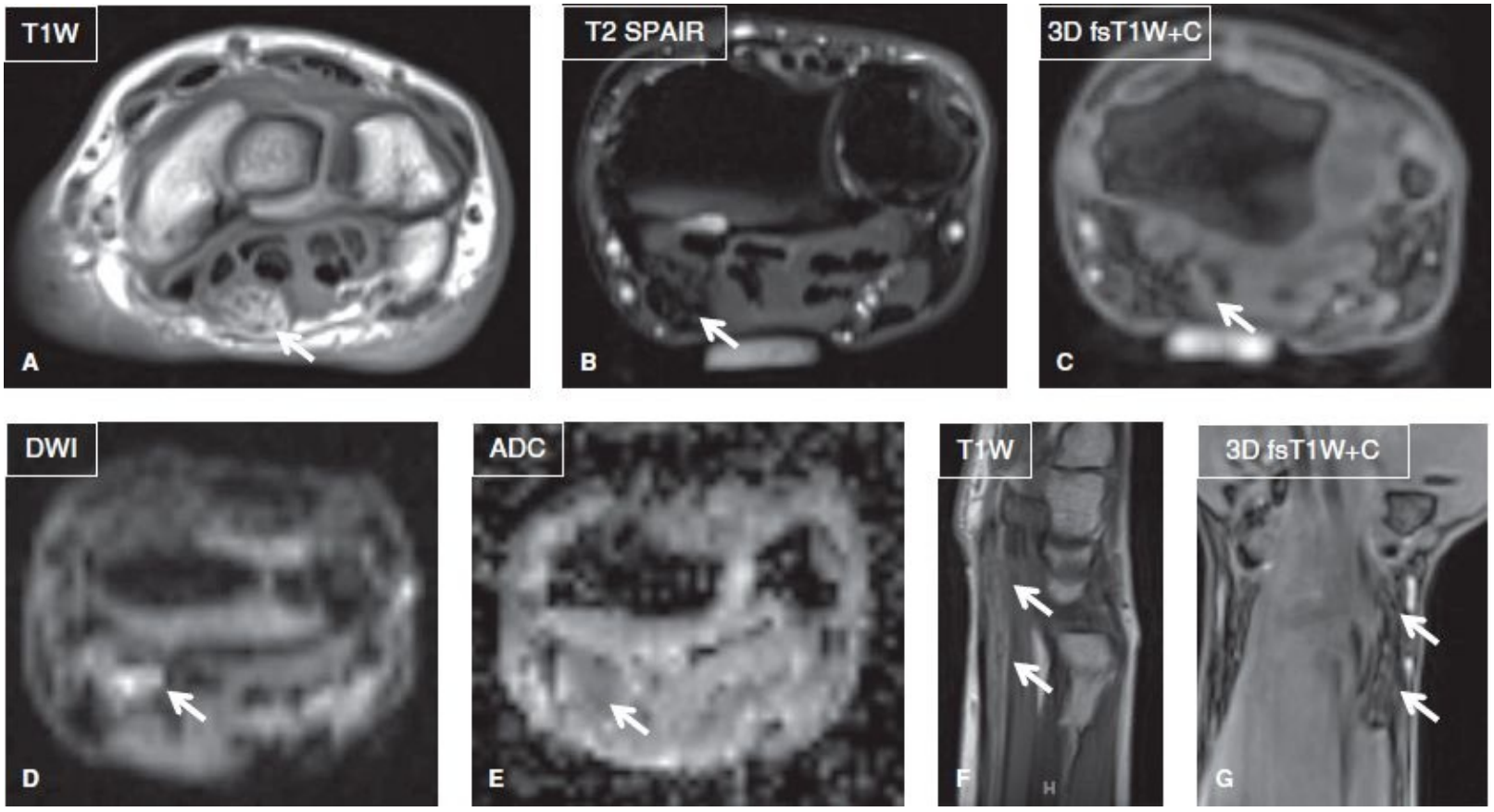

Fig. 13: Neurofibroma. Coronal image shows a well-defined lesion (*arrow*) at the anatomic location of the right brachial plexus trunks, demonstrating targetoid contrast enhancement.

Nerve Signal

The nerve signal is usually isointense on non-fs T2W images while mild hyperintense signals might be normally observed due to good fat suppression on fat-saturated fluid sensitive images. The signal alteration is reflective of enhancement of the endoneurial fluid (Fig. 7). In addition, obliquely traversing nerves can be normally bright due to the magic angle artifact. However, this artifact occurs in expected location(s) along the fixed course of the peripheral nerves and in the plexus. For example, the femoral and sciatic nerves as well as all LS plexus nerves are symmetrically bright in the abdominopelvic region (Fig. 4), while these peripheral nerves outside the pelvis appear isointense to muscles when they have assumed relatively straight course in the extremities. Similar signal alteration may be seen for short segments in otherwise normal peripheral nerves, such as the ulnar nerve at the Guyon canal, medial plantar nerve at the tarsal tunnel, pudendal nerve at the entry into the lesser sciatic foramen, and lateral femoral cutaneous nerve (LFCN) at the iliac spine. Mild, moderate, and severe hyperintensity respectively refer to signal alterations of the nerve, higher than the skeletal muscle or adjacent nerves but considerably less than the regional in-plane venous signal, approaching the regional in-plane venous signal, and similar or higher than the venous signal (Figs. 14, 15). In the brachial or lumbar plexuses,

the nerve roots appear uniformly bright, but symmetrical in signal and size bilaterally. To detect abnormal signal alteration, compare the signal intensity of the dorsal nerve root ganglion (DRG) to the nerve root distally. Normally, DRG is the most bright structure along the nerve (about two times the signal of the distal postganglionic segment of the nerve) and distally, the nerve signal gradually fades along its course. With neuropathy, the T2 signal of the postganglionic segment approaches the DRG ($\sim <1.5$ times) or may exceed it sometimes, leading to inconspicuous appearance of the DRG. One should note that mild nerve signal alterations are not uncommon at the sites of everyday friction, for example, in median nerve at the carpal tunnel, ulnar nerve at the cubital tunnel, sciatic nerve at the sciatic notch, and C8, T1 nerves at the thoracic outlet. Such findings in isolation should be reported as non-specific nerve hyperintensity, to be correlated clinically for significance. The peripheral nerves become increasingly hyperintense with worsening severity of lesion(s); however, with chronicity of neuropathy, the nerves may become atrophic and lose the bright signal alteration. Other signal characteristics that help in further characterization of intraneural lesion include fat (lipoma, fibrolipomatous hypertrophy, chronic atrophic neuropathy, e.g., in diabetes mellitus), fibrosis (neuroma in continuity, Sunderland grade IV–VI injury as described below), hemorrhage (endometriosis, synovial sarcoma), calcification (Leprosy), and hyperintense pseudomass formation (hereditary demyelinating neuropathy, Charcot–Marie–Tooth disease—CMT type 1A) (Fig. 16).

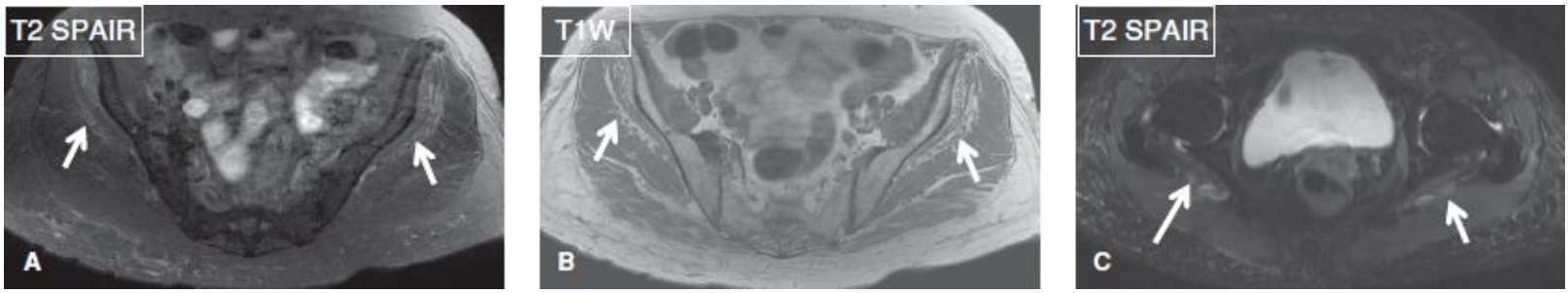

Fig. 14: Mild sciatic hyperintensity in a case of diabetic neuropathy. Gluteus minimus atrophy bilaterally and mild bilateral sciatic neuropathy. Axial images **(A–C)** show symmetric mild edema like signal (*arrows* in **A**) with fatty infiltration and atrophy (*arrows* in **B**) of the gluteus minimus muscles due to long standing diabetes. Mild T2 hyperintensity the sciatic nerves (*arrows* in **C**) are noted bilaterally in this case with recent symptoms of bilateral sciatica **(left > right).** Compare sciatic nerve signal to adjacent muscles and vessels.

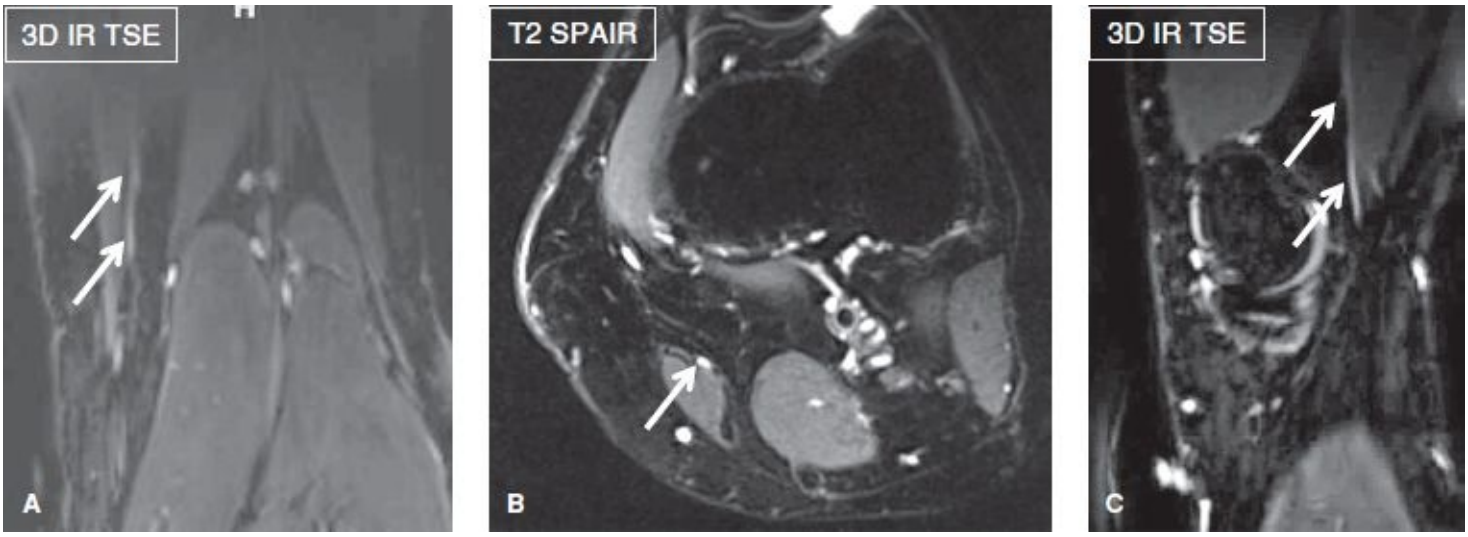

Fig. 15: Moderate nerve hyperintensity. Saphenous neuropathy. Coronal **(A),** axial **(B),** and oblique sagittal **(C)** images through the knee demonstrate a moderately hyperintense saphenous nerve (*arrows*). Compare nerve signal to the adjacent vessels.

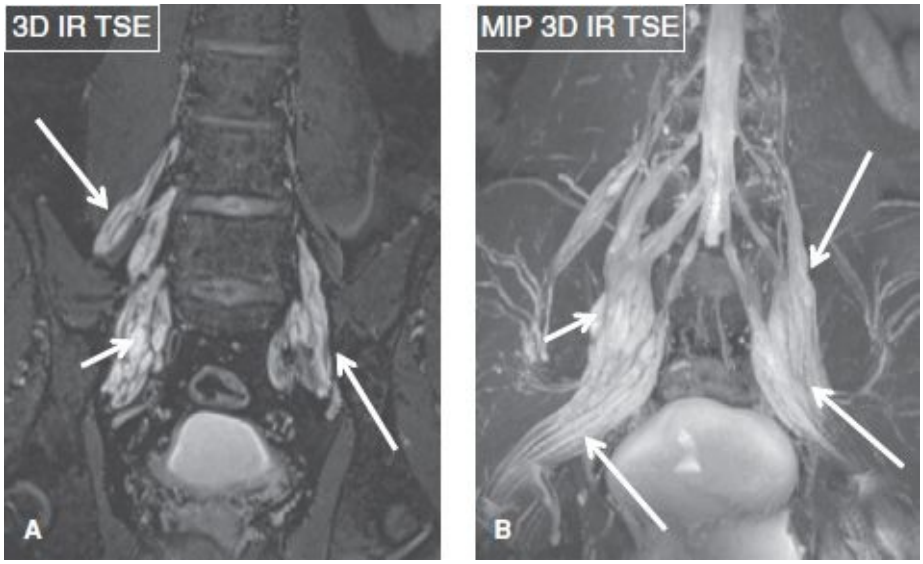

Fig. 16: CMT type 1A with pseudomass. Coronal images **(A, B)** show diffusely thickened lumbosacral plexus nerves (*long arrows*) and increased signal (the signal of the nerve exceeds the DRGs, making them inconspicuous) with interspersed pseudomasses (*short arrows*).

Nerve Course: One should look for course deviations that can result from a space occupying lesion, such as focal mass, fracture callous, ganglion cyst, accessory muscle, peri- and intra-neural scarring from prior injury or surgery, and anatomic variation (Fig. 17). Anatomic variations are not uncommon, for example, up to 20% to 25% normal subjects have split sciatic nerves, accessory anconeus muscles, bifid median nerve with persistent median artery, intramuscular course through scalene muscle and ulnar nerve subluxations, while only 3% to 4% are reported to become symptomatic from these developmental variations (Figs. 18–20). These anomalies are important to report, as they might have implications with regards to regional surgery or perineural injection. In addition, developmental variations may predispose to symptomatic state of disabling motor and/or

sensory loss, when neuropathy from another superimposed etiology contributes to swelling of the nerve coursing through a confined space. In such a case, otherwise asymptomatic anatomic variation may become clinically significant. During thoracic outlet evaluation, one should look for neurovascular kinks, especially in the lower scalene triangle, which may indicate the presence of fibrous band. Elongated c7 transverse process or full-developed cervical ribs are easily apparent. Superman (overhead arm evaluation) positioning is also performed in many institutes including ours for TOS evaluation (Figs. 21–23). One could detect neurovascular kinking in this positioning that would confirm the diagnosis of thoracic outlet syndrome.

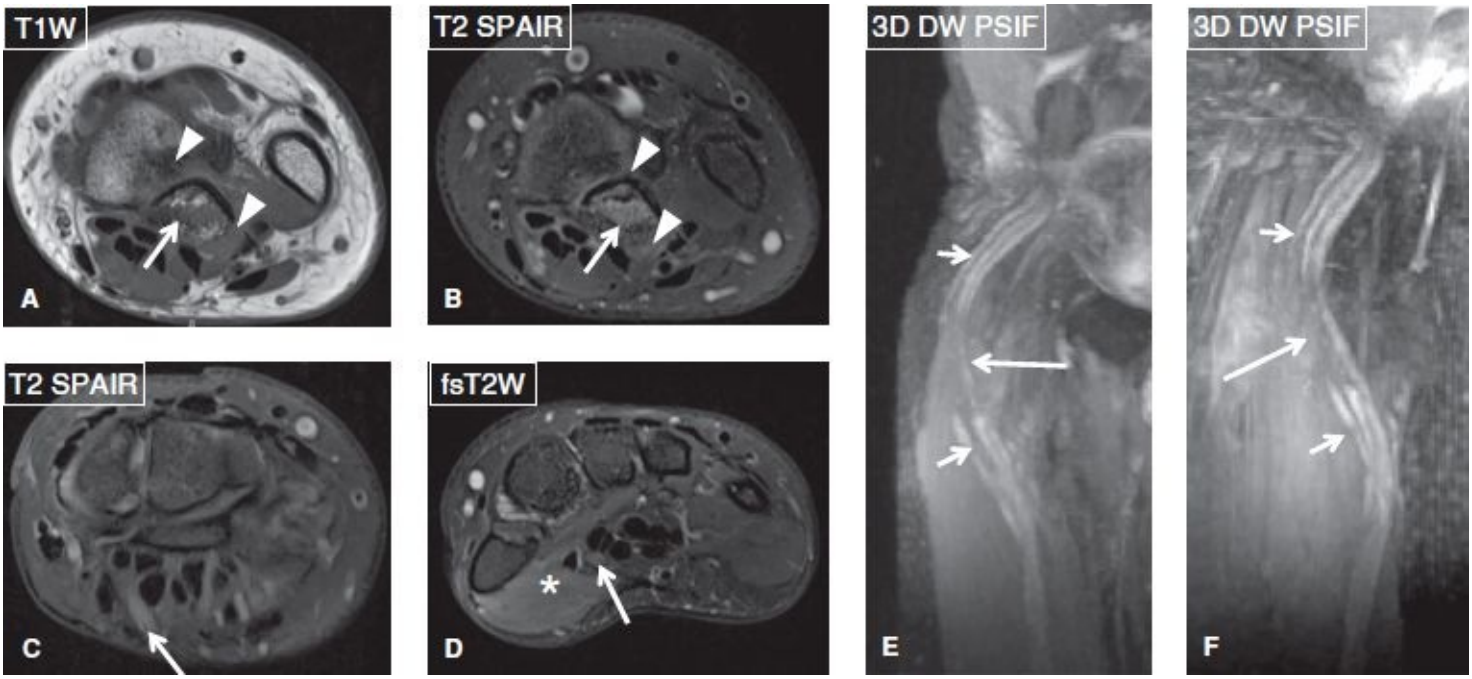

Fig. 17: Sunderland grade VI injury due to radial fracture: median nerve course deviation. Axial images **(A, B)** at the level of the distal forearm demonstrate a significantly enlarged and moderately T2 hyperintense median nerve (*arrows*), which also features prominent fascicles. Also note the adjacent radial fracture with scarring (*arrowheads*). On axial images **(C, D)** at more distal levels, the signal and morphology of the nerve (*arrows*) return to normal, though there is tortuosity of its course. Note edema-like signal of the thenar muscles (*asterisk*), indicating denervation. Oblique sagittal and coronal reconstructed images **(E, F)** confirm course deviation (*short arrows*) and scarring (*long arrows*) of the median nerve.

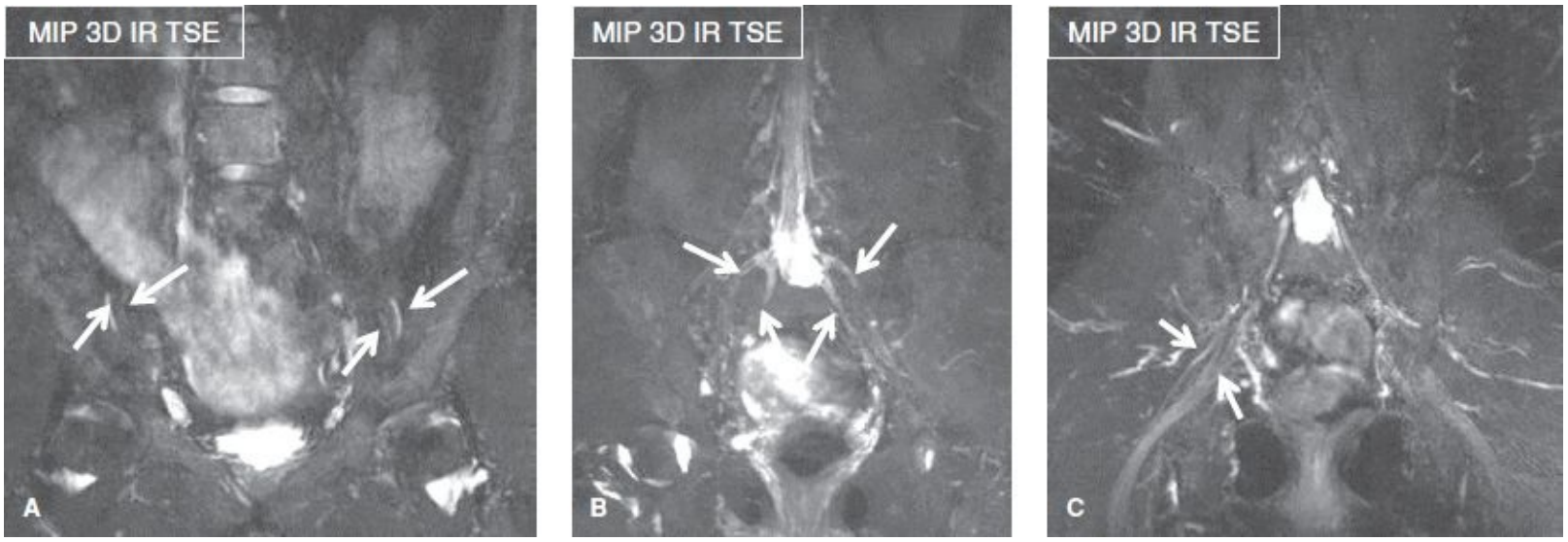

Fig. 18: Normal variants. Coronal images show split femoral nerves (*arrows* in **A**), conjoint right L5 and S1 roots (*arrows* in **B**), and split right sciatic nerve (*arrows* in **C**).

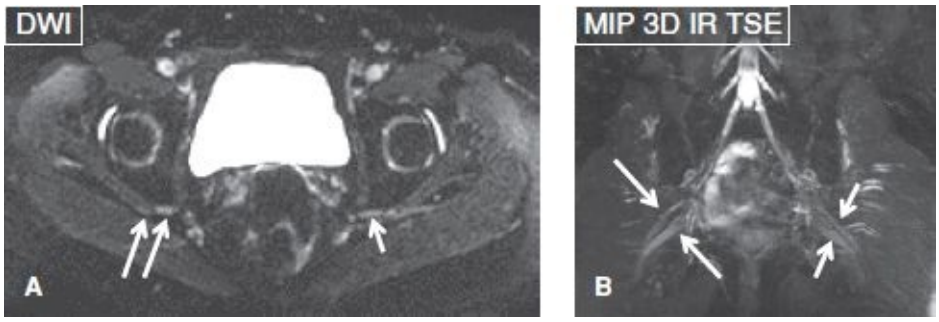

Fig. 19: Piriformis syndrome associated with developmentally split right > left sciatic nerves. Axial **(A)** and coronal **(B)** images show a split right sciatic nerve (*long arrows*) with abnormal increased signal as compared to the normal compact left sciatic nerve (*short arrows*), best seen on 3D image.

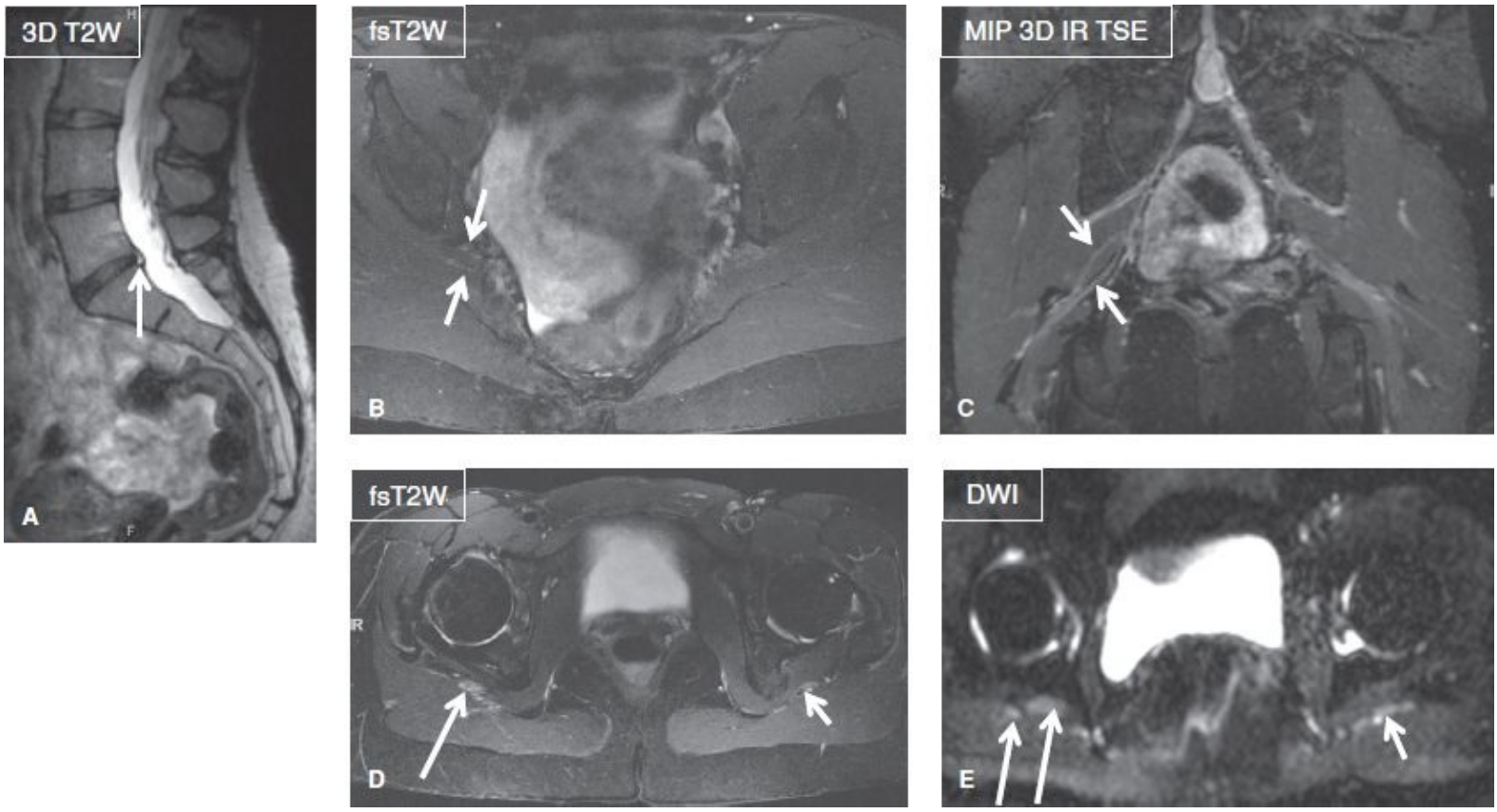

Fig. 20: Piriformis syndrome in a 52-year-old female who presented with right leg weakness and intermittent foot drop over the last 2 years. EMG revealed right sciatic neuropathy, whereas outside MRI examinations of the lumbosacral spine, pelvis, and right lower extremity showed no causative factor. Sagittal **(A)** image of the lumbar spine reveal only a small right paracentral extrusion (*arrows*) at the L5–S1 level. Axial **(B)** and coronal **(C)** MRN images exhibit a split right sciatic nerve (*arrows*). More distal axial images **(D, E)** demonstrate abnormal T2 hyperintensity and enlargement of the right sciatic nerve (*long arrows*) as compared to the left sciatic nerve (*short arrow*).

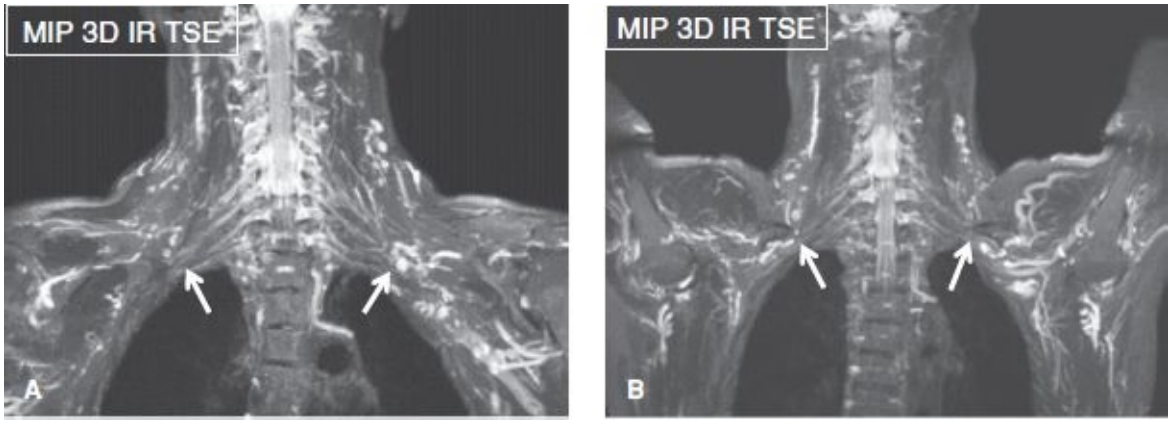

Fig. 21: Normal MRN imaging on 1.5 T. Coronal images with arms in down **(A)** and up **(B)** positions provide limited contrast and spatial resolution for the evaluation of the brachial plexuses (*arrows*). 3D imaging might not come out as robust as on 3 T due to lower SNR and the nerves could be partially obscured by prominent vessels.

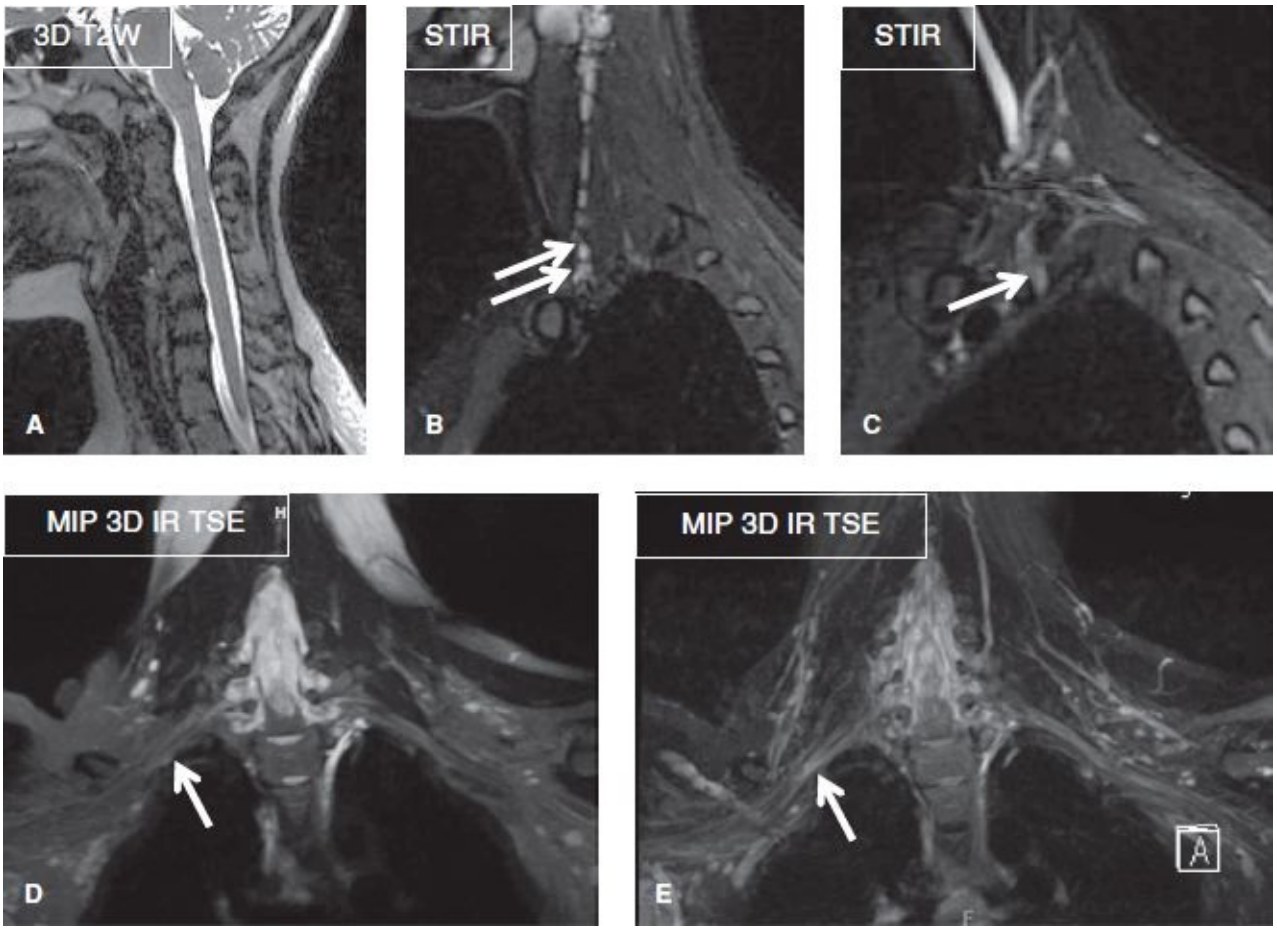

Fig. 22: Thoracic outlet syndrome (TOS). Sagittal image **(A)** of the cervical spine demonstrates loss of normal lordosis with no significant spondylosis changes. Sagittal MRN images **(B, C)** of the right brachial plexus show asymmetric hyperintensity of the C8 and T1 nerve roots (*arrows* in **B**) and lower trunk (*arrows* in **C**). Coronal images with arms up **(D)** and down **(E)** position reveal persistent T2 hyperintensity of the lower trunk (*arrows*). No nerve kinking was seen indicating a mild case of TOS.

Fig. 23: Known inflammatory neuropathy with marked left ulnar nerve weakness (multifocal motor neuropathy), suspected thoracic outlet syndrome. Coronal images with arms down **(A)** and up **(B)** positions reveal patchy increase signal (the signal of the nerve approaches the DRGs, making them inconspicuous) and thickening of multiple brachial plexus segments **(left > right)** (*arrows*) from underlying neuropathy. No superimposed nerve kinking or anatomy was seen to suggest TOS.

Nerve Fascicles

The fascicles should be carefully interrogated for abnormality. If the nerve is enlarged for some reason, e.g. due to inflammation, entrapment, or hereditary neuropathy, the fascicles should become more prominent unless they are damaged by injury or effaced by significant congestion or edema within the nerve (Fig. 24). Chronic neuropathy on the other hand, leads to fascicular atrophy and the intra-epineurial perifascicular fat within the nerve becomes more prominent than the fascicles themselves (Fig. 25). In case of nerve sheath tumor, one should look for fascicular displacement versus involvement. Generally, in a schwannoma, there is mono- or bi-fascicular continuity with the eccentric mass lesion (Fig. 26). Multifascicular involvement is common in neurofibroma and perineuroma, which may make the tumor unresectable in the involved segment(s) of the nerve (Figs. 11, 27). The latter would require auto- or allografting of the resected nerve segment.

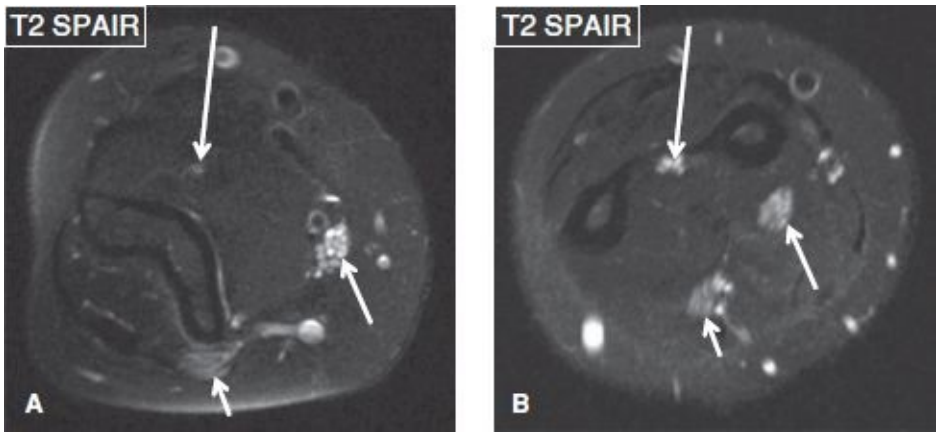

Fig. 24: Charcot–Marie–Tooth type-1A disease with enlarged peripheral nerves and prominent fascicles. Axial images at the level of the distal humerus **(A)** show abnormally hyperintense and enlarged ulnar (*short arrow*), median (*medium arrow*), and radial nerves (*long arrow*). A distal axial image **(B)** at the level of the forearm shows similar abnormality of the ulnar (*short arrow*), median (*medium arrow*), and anterior interosseous nerves (*long arrow*).

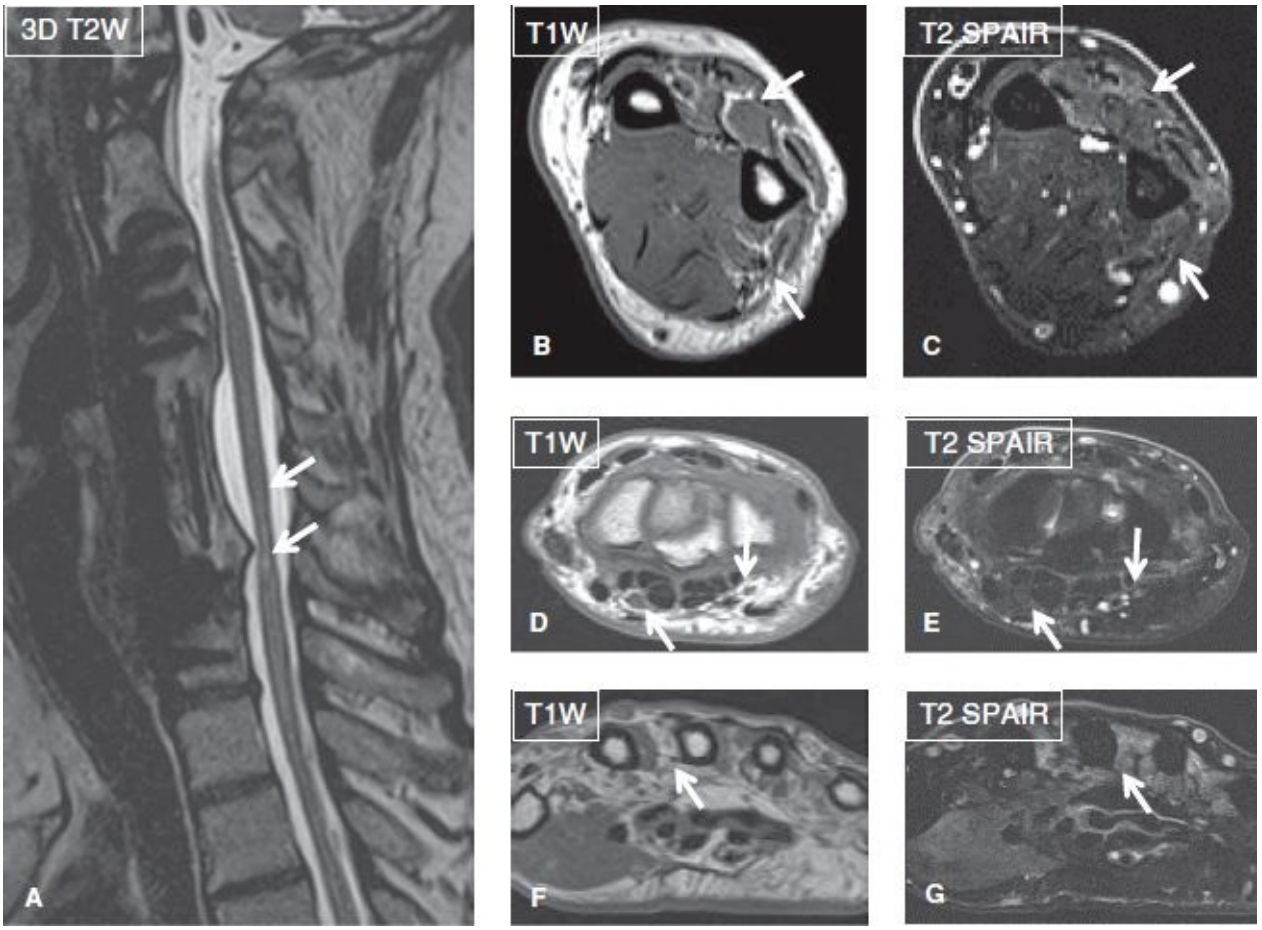

Fig. 25: Chronic atrophic peripheral neuropathy due to myelomalacia. Sagittal image **(A)** demonstrates foci of myelomalacia (*arrows*) in the lower cervical cord. Sequential axial images **(B–G)** show chronic atrophic changes in the extensor and ulnar sided muscles with mild edema-like T2 signal (*arrows* in **B, C**), atrophic nerves, ulnar > median (*arrows* in **D, E**) and chronic denervation related muscle atrophy and edema-like signal change of the intrinsic hand muscles (*arrows* in **F, G**).

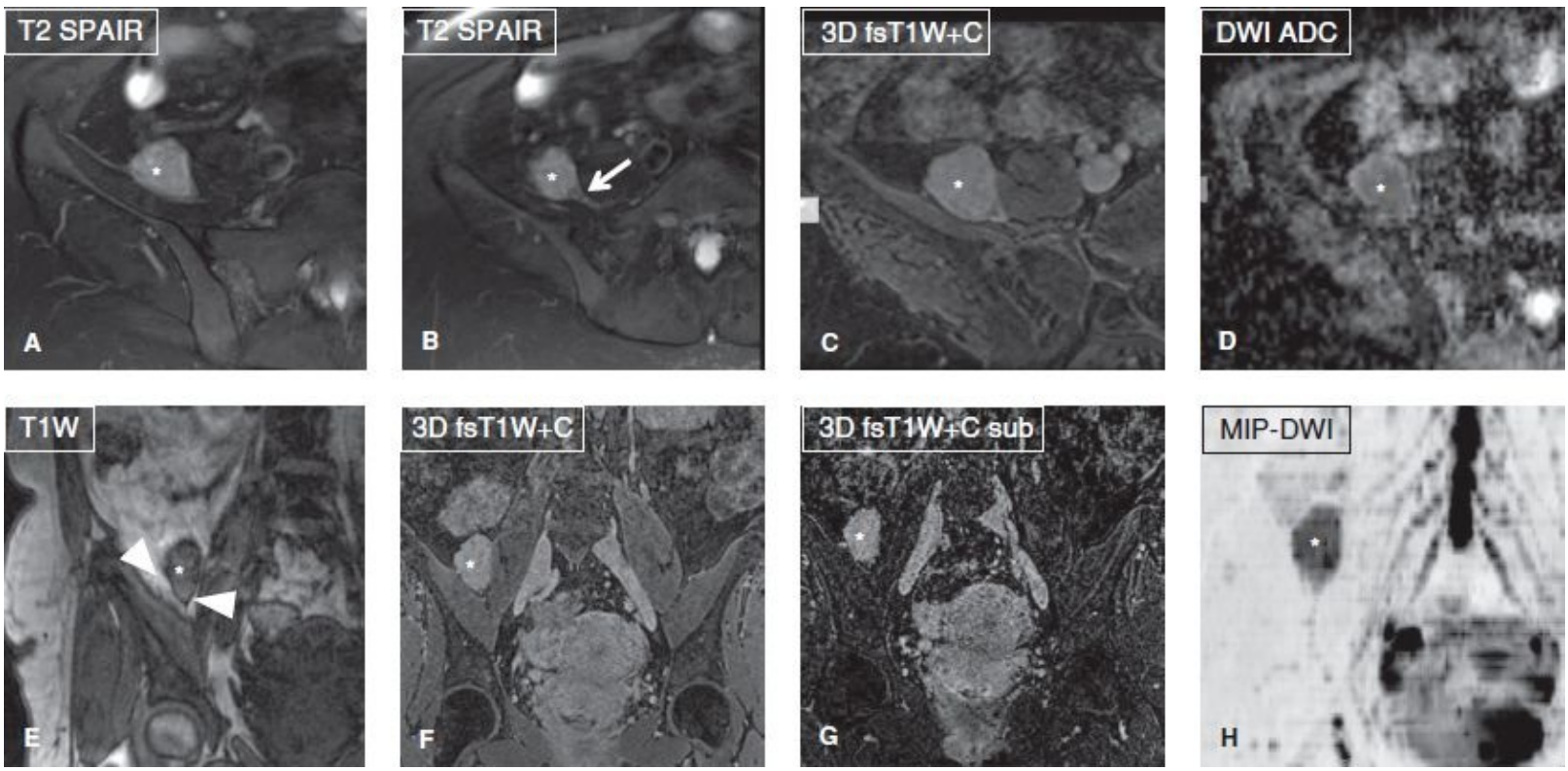

Fig. 26: Femoral nerve schwannoma in a middle-aged woman. Axial **(A–D)** and coronal **(E–H)** images exhibit a well-defined ovoid T2 hyperintense lesion (*asterisks*), which is situated eccentric and attached to the right femoral nerve, and demonstrates tail sign (*arrows*) and split-fat sign (*arrowheads*). The ADC value of the lesion measured 1.6 × 10−3 mm2/s.

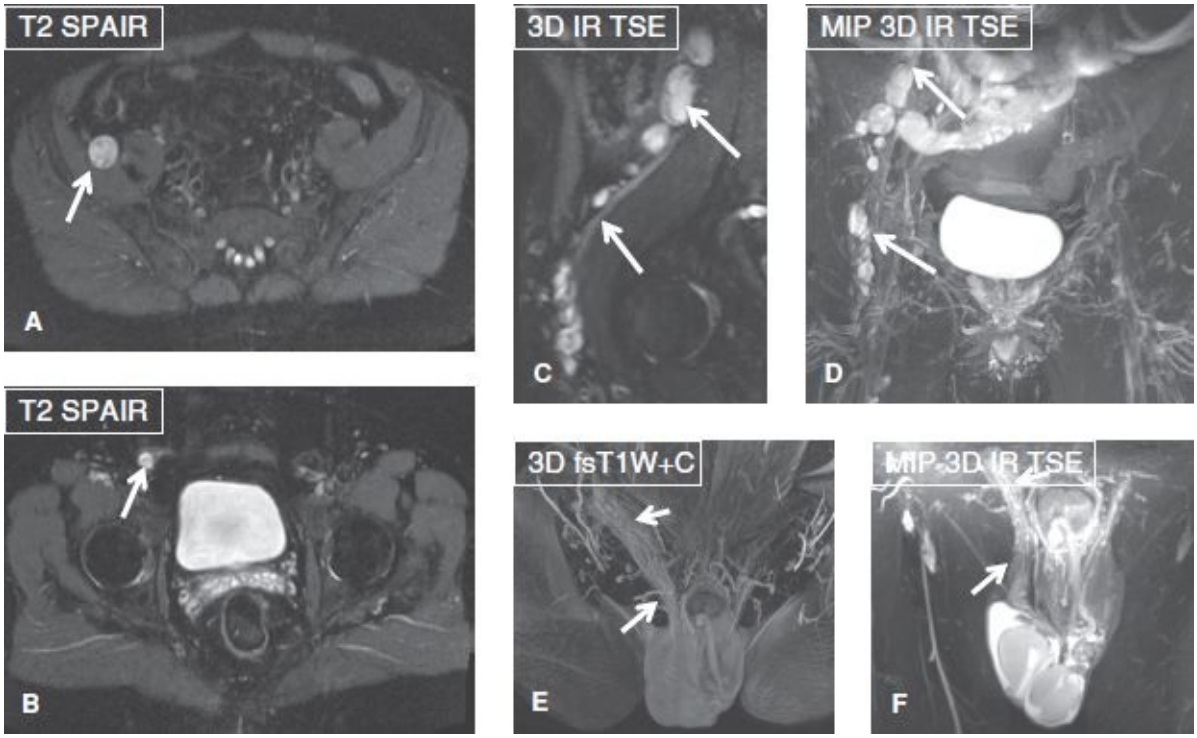

Fig. 27: Neurofibromatosis type-1 in an individual with chronic right groin pain. Notice nerve sheath tumors of the right femoral nerve (*arrow* in **A**) and genitofemoral nerve **(B).** The genitofemoral nerve lesion was removed. Subsequent images show additional multiple nerve sheath tumors of the femoral nerve on the reconstructed oblique sagittal **(C)** and coronal **(D)** images. In addition, notice plexiform neurofibroma of the right genitofemoral nerve (*arrows* in **E, F**).

Perineural Fat Planes: The fat planes around the nerves should be normally clean and uniform, and are best seen on T1W images (Fig. 7). Mass lesion or perineural fibrosis/other space occupying lesions could efface the perineural fat planes or encase the nerve completely (Fig. 28).

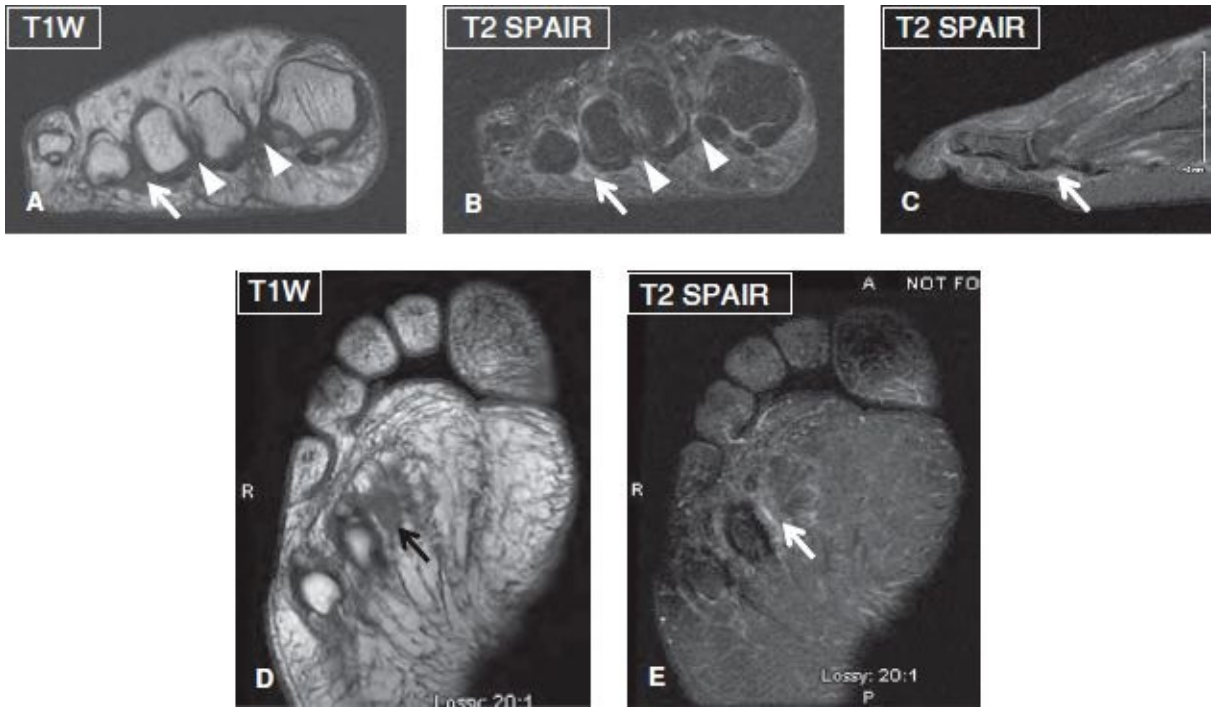

Fig. 28: Morton neuroma. Axial **(A, B),** sagittal **(C),** and coronal **(D, E)** images reveal a dumbbell-shaped intermediate T1/high T2 lesion (*arrows*) between the third and fourth metatarsal bones, which extends into the plantar soft tissues in keeping with a Morton neuroma (exuberant perineural fibrosis). There is also mild perineural fibrosis (*arrowheads*) in the first and second web spaces.

To summarize, any significant nerve signal alteration (hyperintensity or hypointensity), focal or diffuse caliber change (enlargement or atrophy), course deviation (focal or diffuse), fascicular abnormality (enlargement, effacement, or atrophy), abnormal enhancement and perineural abnormality (scar or mass lesion) should be searched, since these findings in isolation or in combination might be important for neuropathy diagnosis and/or clinically significant.

Regional Muscle/Tendon Evaluation

The regional muscles should be carefully assessed for any signal alterations, fatty replacement, atrophy, hypertrophy, accessory slips, or accessory muscles. The imaging appearance of muscle denervation change manifests as an edema-like signal on T2W images in acute stage, which progresses to fatty replacement and atrophy with chronicity (Fig. 29). The edema-like T2 signal change has been reported to be related to perfusion alterations and relative shift of intra- and extra-compartmental fluid within the muscle. Therefore, unlike edema from muscle strain or infection, it may persist for long periods of time, even in chronic stages of muscle denervation. One should carefully look in T1W images for signs of chronic denervation and not weigh in too much on edema-like T2 signal, if fatty replacement or muscle atrophy are present (Fig. 25). Following the release of nerve entrapment or recovery from nerve injury, the muscle edema-like T2 signal has been shown to reverse to normalcy. Sometimes it may be challenging, but most times, one should be

able to distinguish muscle denervation change from other causes of muscle signal change, such as myopathy (autoimmune or inflammatory), infectious myositis, and muscle strains from injury. Myopathy is usually bilateral, it involves multiple muscle compartments of the limbs and underlying nerves show normal appearance. It does not correspond to one nerve territory (Fig. 30). Muscle injury due to trauma or infection usually shows patchy distribution and it may have associated fluid collection(s) (Fig. 31). Finally, fascial edema may be seen in all of the above entities, except with muscle denervation change. As a rule, in denervation, the muscle abnormality is localized to the territory of the involved nerve, is usually diffuse without associated fascial edema or fluid collection, and finally, is classically observed at and below the site of neuropathy. Therefore, if one sees muscle denervation change in the first few scans of the limb, further imaging of the proximal site in the limb or plexus may be required to evaluate the actual injury site. Regional tendons should be evaluated for a number of reasons. Tendon tears may point to the cause as muscle strain or injury rather than denervation. Tendon injury causing instability may lead to local traction neuropathy and one might surmise that repairing or treating the tendon injury would be more important in such a case rather than trying to release the suspected nerve entrapment.

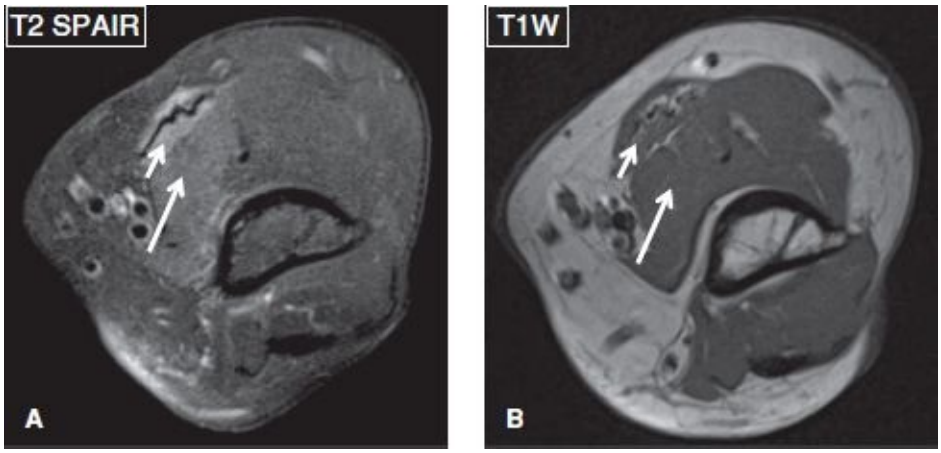

Fig. 29: Muscle denervation. Axial images **(A, B)** through the humerus show edema-like signal of the biceps (*short arrows*) and brachialis (*long arrows*) muscles without much fatty replacement, indicative of recent musculocutaneous neuropathy. Characteristically, the muscle edema follows the respective nerve distribution, is diffuse, and also without associated fascial edema.

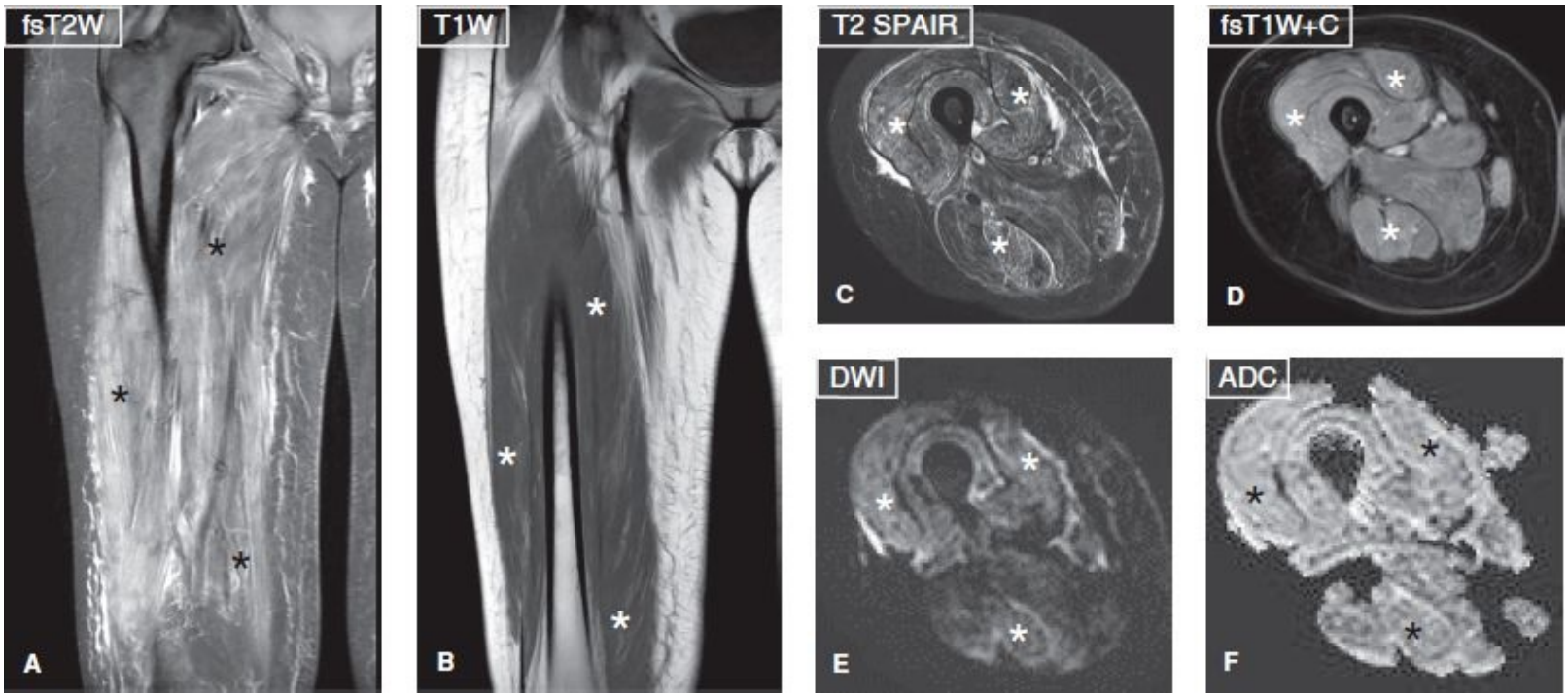

Fig. 30: Dermatomyositis. Coronal **(A, B)** and axial **(C–F)** images exhibit multicompartment diffuse edema-like signal of the muscles, adjacent fascial edema, as well as mild contrast enhancement and no significant diffusion restriction of the thigh muscles (*asterisks*), most prominent in the anterior compartment.

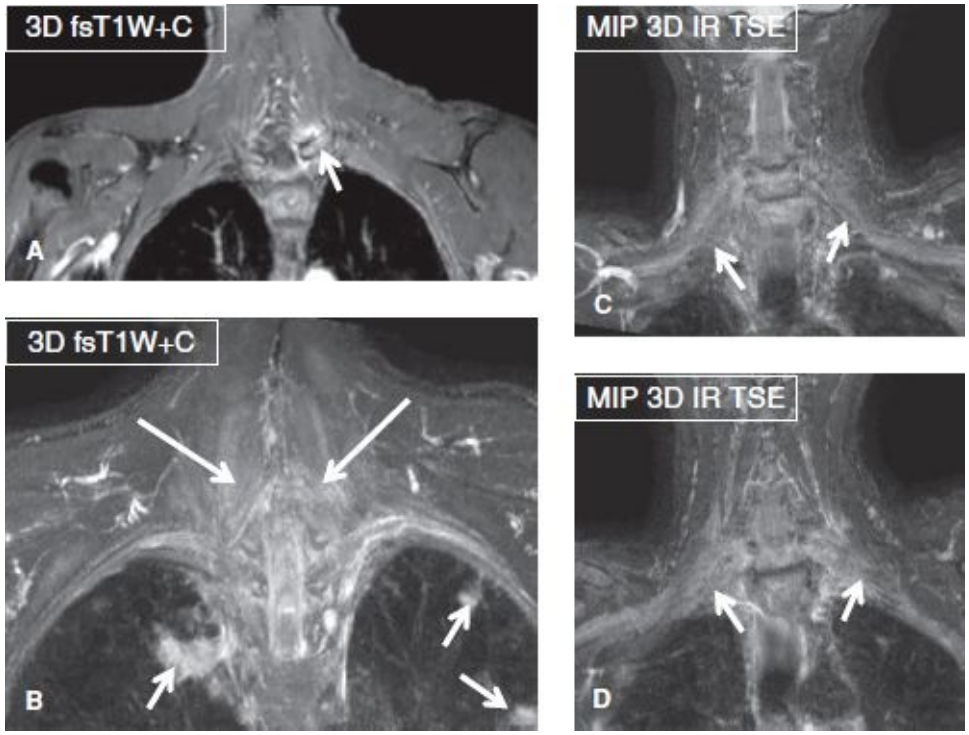

Fig. 31: Inflammatory brachial plexitis from facet joint spinal infection and septic lung emboli. Coronal images **(A–D)** exhibit soft-tissue edema around an edematous lower spinal facet joint (*arrow* in **A**). **B:** Diffuse paraspinal edema (*long arrows*) as well as peripheral opacities in the upper lungs (*short arrows*), corresponding to septic emboli. The brachial plexuses (*arrows* in **C, D**) are bilaterally ill defined, thickened, and abnormally hyperintense (the signal of the nerve exceeds the DRGs, making them inconspicuous).

Systemic Etiologies of Neuropathy

Numerous systemic causes may lead to neuropathy, such as Guillain–Barré syndrome (GBS), parsonage turner syndrome, chronic inflammatory demyelinating neuropathy (CIDP), multifocal motor neuropathy (MMN), Hirayama disease, drug induced neuropathy, metal toxicity, hereditary neuropathy (Charcot–Marie–Tooth disease [CMT]), vasculitis, diabetes mellitus, thyroid disorders, amyloidosis, neurocutaneous syndromes, hyperlipidemia, etc. Clinical findings supplemented by electrophysiology play a major role in the specific diagnosis of these entities. However, one might encounter these entities incidentally during imaging studies or, in some instances, imaging may be obtained in confusing clinical scenarios for exclusion or confirmation of neuropathy. Finally, in patients with known conditions, such as CIDP or CMT, imaging may be performed for the assessment of superimposed entrapment, underlying neuropathy predisposing condition, such as multiple myeloma lesions of the bone marrow, or for superimposed complications, such as development of lymphoma (nodular masses in the nerve with or without adjacent lymphadenopathy). During imaging evaluation, the reader should make use of all available clinical and electrophysiology information to make an informed decision and suggest the most appropriate definitive or differential diagnosis. There are many pointers on imaging that help the reader to label the nerve abnormality as caused by a systemic etiology, such as multiple nerve involvement or multifocal nerve abnormality in the imaging field of view, diffuse nature of the abnormality away from the entrapment sites, pseudomasses in hereditary demyelinating type neuropathy (Figs. 16, 23, 24, 31, 32), and finally, nodularity or focal/multifocal nerve thickening that further points to the diagnosis of lymphoma, amyloid deposition, or neurocutaneous syndrome (Fig. 27). There are other helpful clinical and imaging features that may aid in the diagnosis of systemic etiologies. These entities, include GBS (monophasic acute illness, usually viral illness followed by autoimmune response leading to weakness and tingling in extremities that may progress to extreme whole body weakness, but the entity usually resolves within few weeks of onset; MRN shows diffuse nerve thickening, such as in cauda equina nerve roots); CIDP (downhill chronic course of weakness, elevated CSF protein, lower limb > upper limb involvement, mild–moderate diffuse and patchy nerve thickening, underlying multiple myeloma may be predisposing, and the condition would likely need treatment with intravenous immunoglobulin, corticosteroids, or plasmapheresis treatment) (Fig. 33); MMN (predominant upper limb involvement, distal > proximal involvement and motor loss, mild–moderate diffuse median, ulnar, or radial nerve enlargement with denervation changes (Figs. 9, 23, 34, 35), should be distinguished from motor neuron disease, focal motor neuron disease (Hirayama disease), polio, CIDP, or amyotrophic lateral sclerosis clinically. MMN responds remarkably to immunoglobulins, while no good response is seen to steroids or plasma exchanges as opposed to CIDP, electrophysiologically—MMN manifests as multifocal motor demyelination, specifically partial motor conduction blocks and there is laboratory evidence of high serum anti-GM1 IgM antibodies); CMT (different

varieties in the spectrum of CMT types, with most nerve thickening seen with demyelinating variety, CMT type 1A, which also accounts for two-thirds of CMT cases, familial predisposition, high plantar arches, foot deformities, early age of onset of disease, the nerve thickening is usually diffuse and bilaterally symmetric. In CMT type 1A, pseudomasses may be seen mimicking neurofibromatosis) (Figs. 9, 23, 24, 32, 36); HNPP (another hereditary neuropathy variant where the affected person is predisposed to entrapments at different tunnels in the limbs) (Fig. 37); vasculitis or chemotherapy-induced neuropathy (bilateral patchy neuropathy due to systemic vasculopathy or drug toxicity, usually in sciatic distribution) (Fig. 38); diabetes mellitus (lower limb more than upper limb involvement, diffuse nerve thickening, and hyperintensity, intraepineurial fat deposition with chronicity resulting in persistently thickened nerves, diabetic LS plexopathy aka amyotrophy can occur even with mildly elevated HBA1C levels, and femoral and anterior compartment involvement > sciatic or posterior compartment involvement) (Fig. 39); Amyloidosis (usually in the setting of chronic longstanding disease, for example, multiple myeloma, presents with bilateral sciatic nerve thickening with or without nodularity and patchy enhancement); Neurocutaneous syndromes (genetic predisposition, diffuse nerve thickening is seen with neurofibromatosis and multifocal nodularity may be associated, while schwannomatosis shows multiple focal mass lesions that may show cystic, hemorrhagic, or necrotic changes) (Figs. 40, 41).

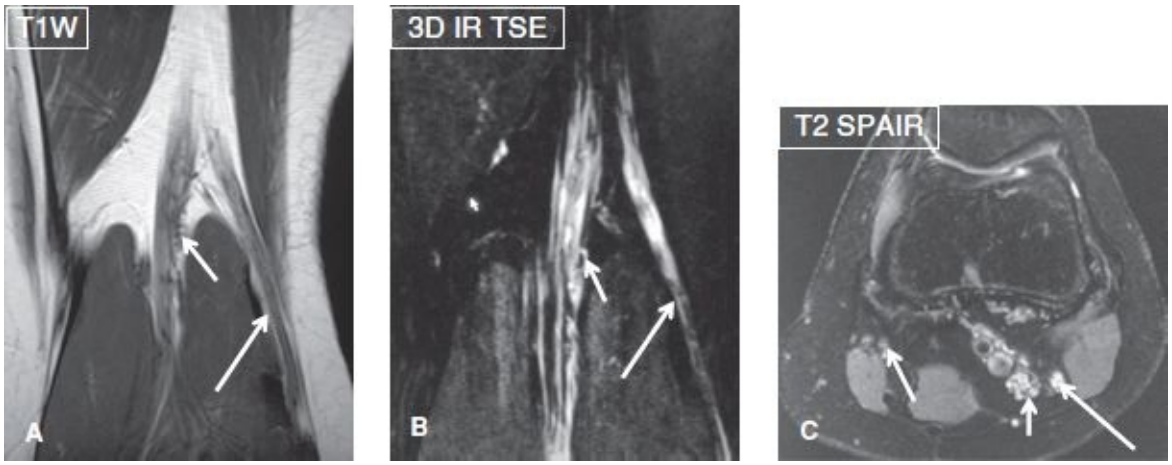

Fig. 32: Charcot–Marie–Tooth type-1A disease. Coronal **(A, B)** and axial **(C)** images exhibit diffuse enlargement and T2 hyperintensity of the tibial (*short arrows*), saphenous (*medium arrows*), and common peroneal (*long arrows*) nerves.

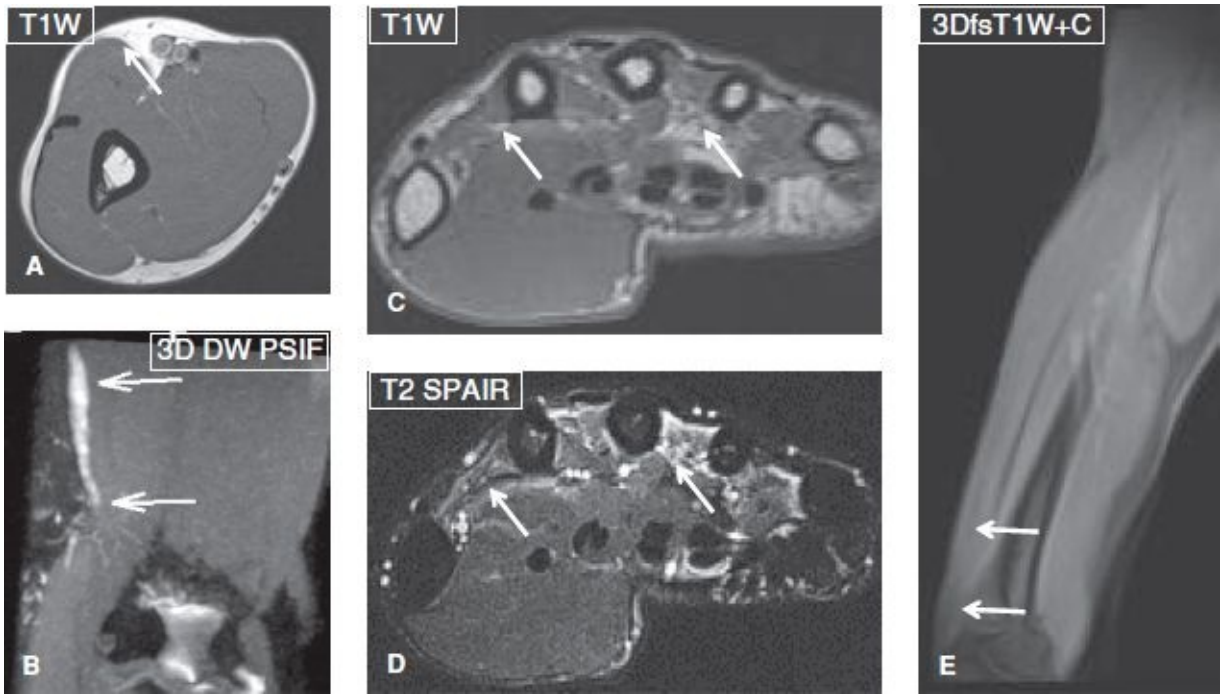

Fig. 33: Chronic inflammatory demyelinating polyneuropathy. Axial **(A, C, D)** and coronal **(B, E)** images show abnormal moderate thickening of the ulnar nerve (*arrows* in **A, B**) with effacement of the fascicular appearance. Notice denervation changes of all intrinsic muscles (*arrows* in **C, D**) including first dorsal interosseous (ulnar innervated) with sparing of the median nerve innervated thenar muscles. No abnormal enhancement is seen, classic for CIDP.

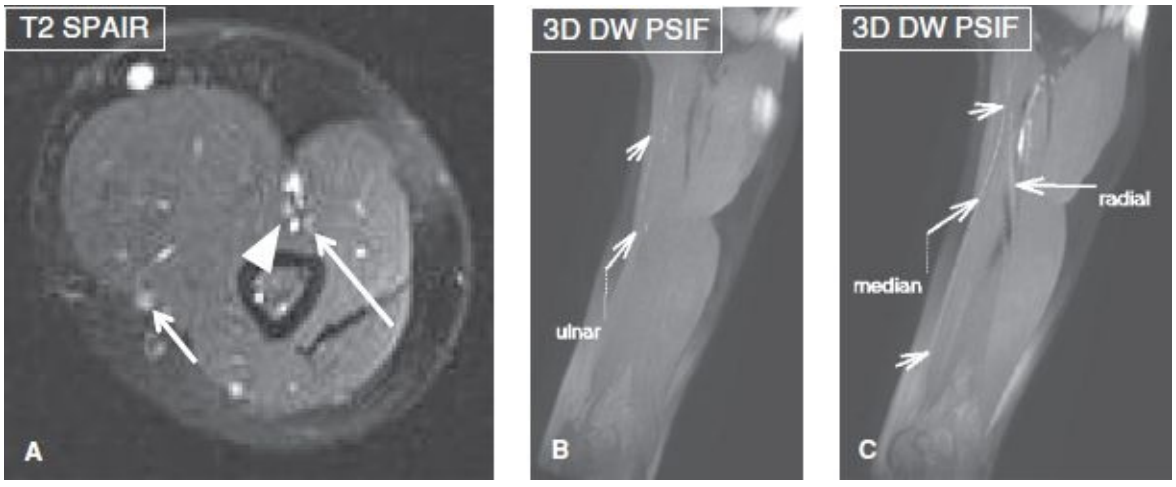

Fig. 34: Multifocal motor neuropathy. Axial image **(A)** demonstrates mild–moderate hyperintensity of the ulnar (*long arrow*), radial (*short arrow*), and median (*arrowhead*) nerves. Findings are confirmed on the respective oblique coronal images **(B, C)** with diffuse hyperintense nerves labeled with arrows.

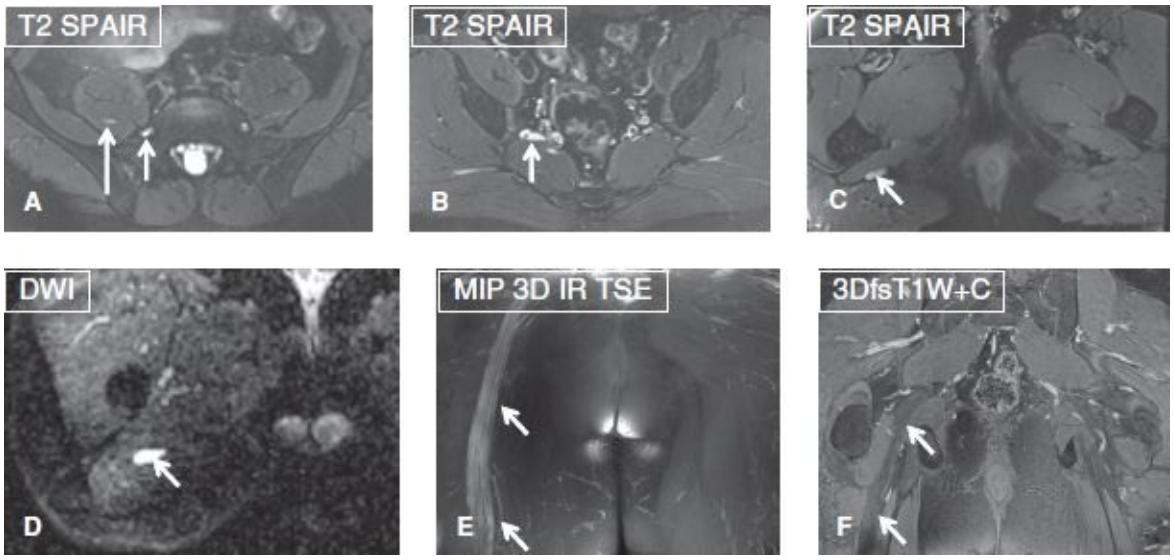

Fig. 35: Multifocal motor neuropathy. Axial **(A–D)** and coronal **(E–F)** images of the pelvis and proximal thighs demonstrate diffuse T2 hyperintensity and mild thickening of the right L5 nerve root (*short* arrow in **A**), ipsilateral femoral nerve (*long arrow* in **A**), sciatic plexus (*arrow* in **B**), sciatic nerve (*arrows* in **C, E**), which additionally shows restricted diffusion (*arrow* in **D**). Notice no abnormal enhancement on the postcontrast image (*arrows* in **F**).

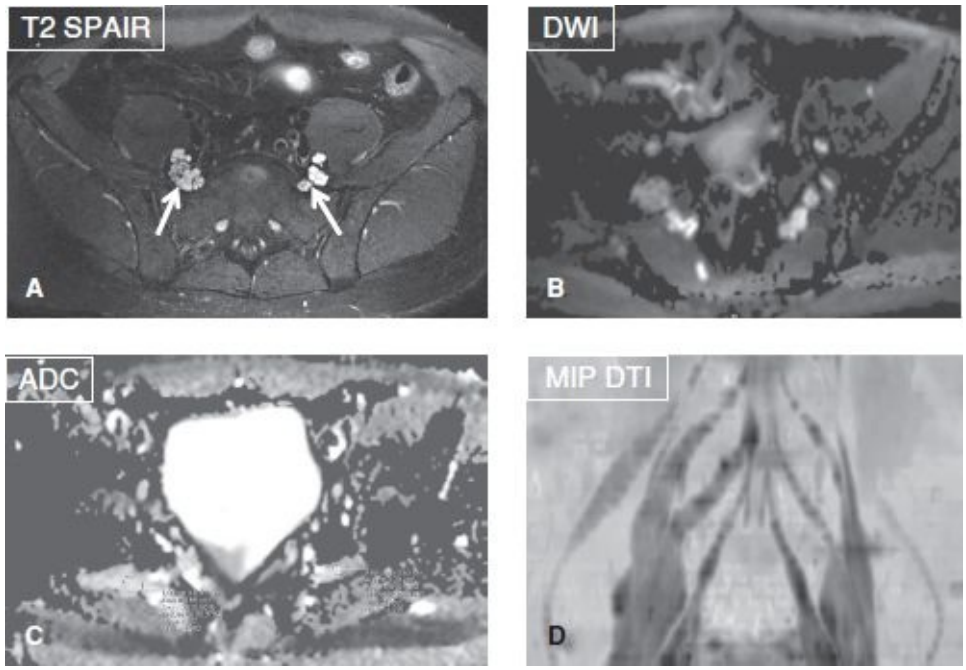

Fig. 36: CMT type 1A. Axial images **(A–C)** show symmetrical bilateral nerve thickening and abnormal hyperintensity. Notice high ADC value (2.1 × 10⁻3 mm2/s) in keeping with benign nerve thickening. Coronal MIP tensor image **(D)** with inverted scale shows the full extent of the abnormality with selective demonstration of bilateral LS plexus nerves.

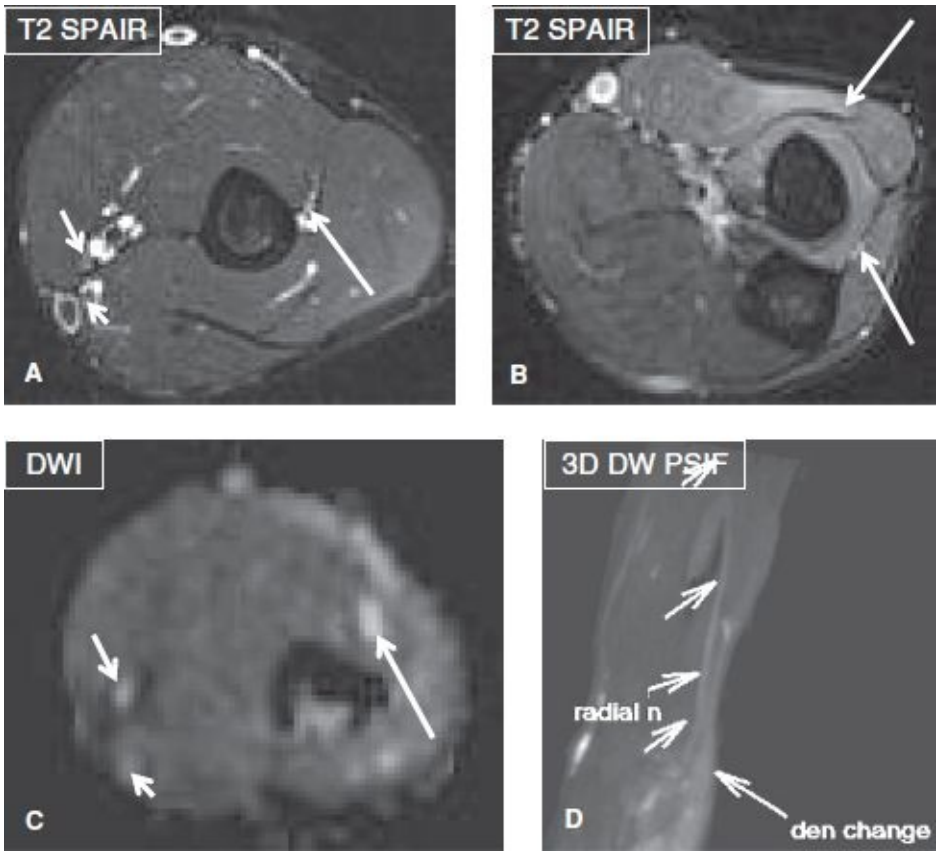

Fig. 37: Hereditary neuropathy with liability to pressure palsies (HNPP). Axial **(A–C)** and oblique coronal **(D)** images demonstrate mild hyperintensity of the ulnar nerve (*short arrow*), median (*medium arrow*) nerve and moderate hyperintensity of the radial nerve (*long arrows*), with associated muscle edema (*long arrows*) of the extensor muscles of the forearm, indicating denervation. Long axis 3D image shows diffuse radial nerve signal changes starting at the spiral groove (*arrows* in **D**) suggesting entrapment.

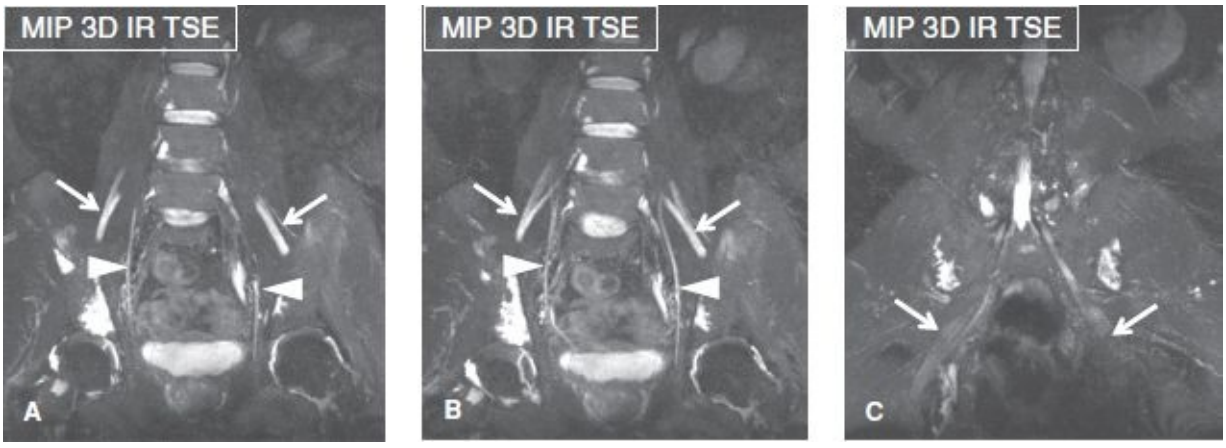

Fig. 38: Chemotherapy-induced neuropathy in a patient with multiple myeloma, who complained of anterior leg and groin pain. Coronal images **(A–C)** exhibit prominent T2 hyperintensity of the femoral nerves (*arrows* in **A, B**) and obturator nerves (*arrowheads* in **A, B**). The sciatic nerves (*arrows* in **C**) show normal signal, showing good correlation with the clinical symptoms.

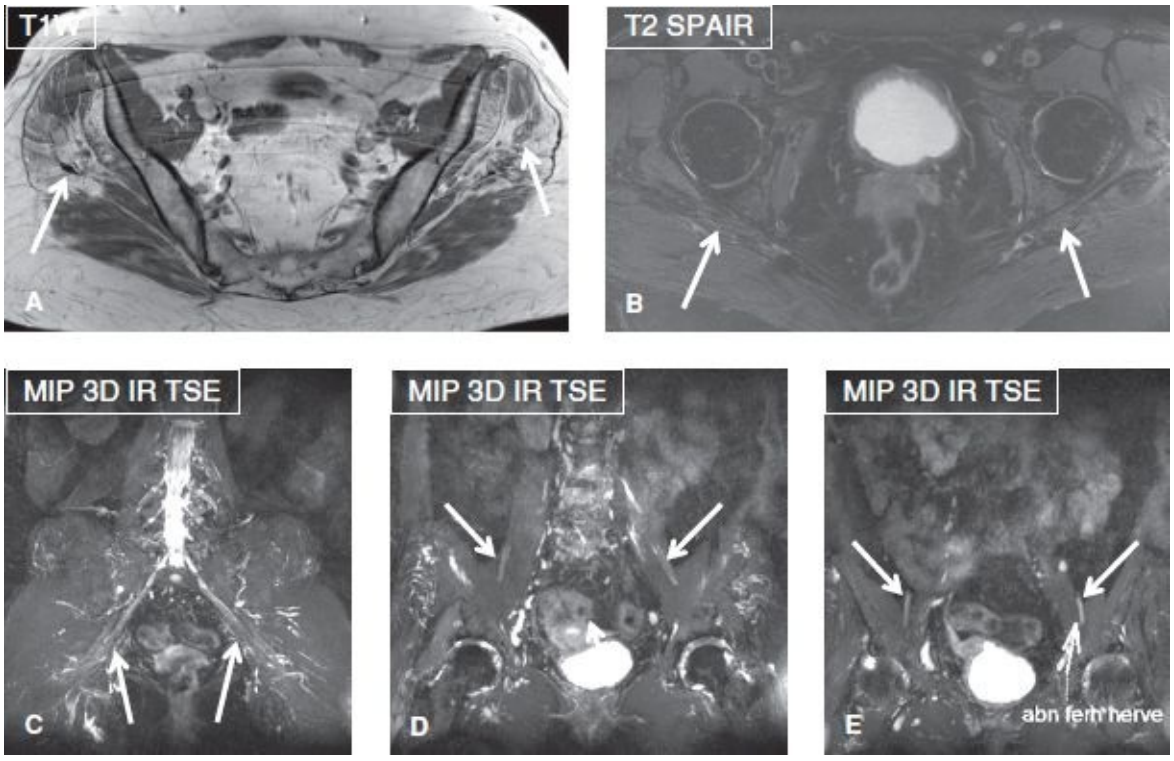

Fig. 39: Diabetic plexopathy and neuropathy. A 48-year-old man with mildly high HBA1C level and type II diabetes mellitus. Complains of severe shooting pains in the anterior left leg with mild foot weakness and leg locking. Axial images **(A, B)** through the pelvis show bilateral symmetrical atrophy of the gluteal muscles (*arrows*) suggesting chronic plexopathy. Coronal images **(C–E)** normal sciatic plexuses (*arrows* in **C**) with maintained DRG to nerve signal ratio. Note asymmetric hyperintensity and enlargement of the left femoral nerve (*arrows* in **D, E**) in keeping with diabetic neuropathy (amyotrophy).

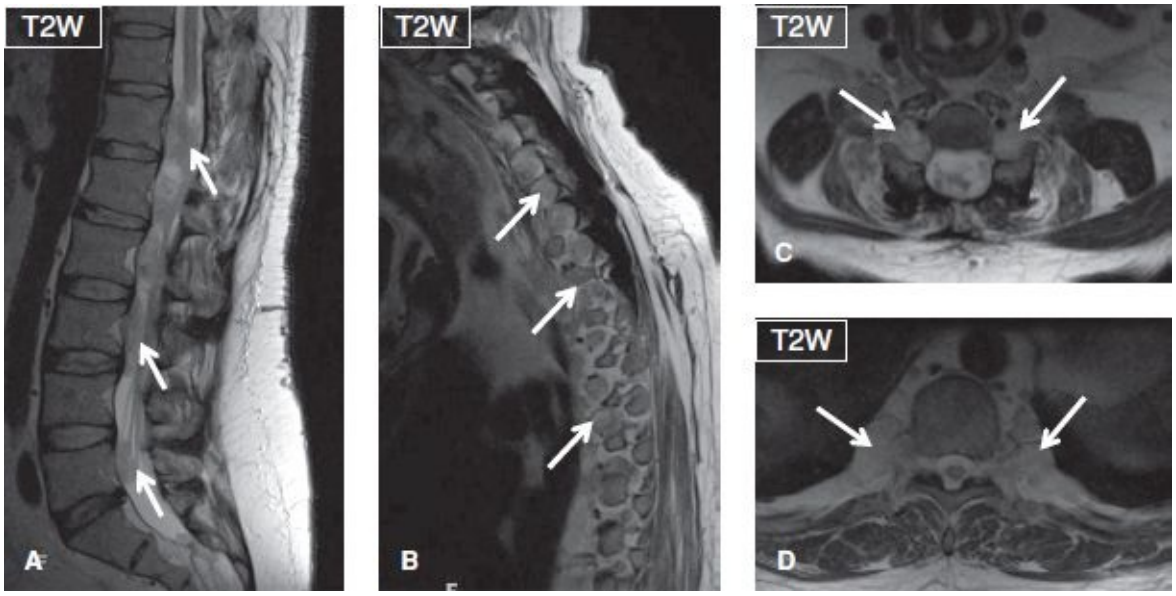

Fig. 40: Schwannomatosis. Numerous peripheral nerve sheath tumors of the thoracolumbar spine. Sagittal **(A, B)** and axial **(C, D)** images exhibit numerous T2 hyperintense lesion (*arrows*) within both the spinal canal and the neural foramina, compatible with schwannomas, in this patient with known schwannomatosis.

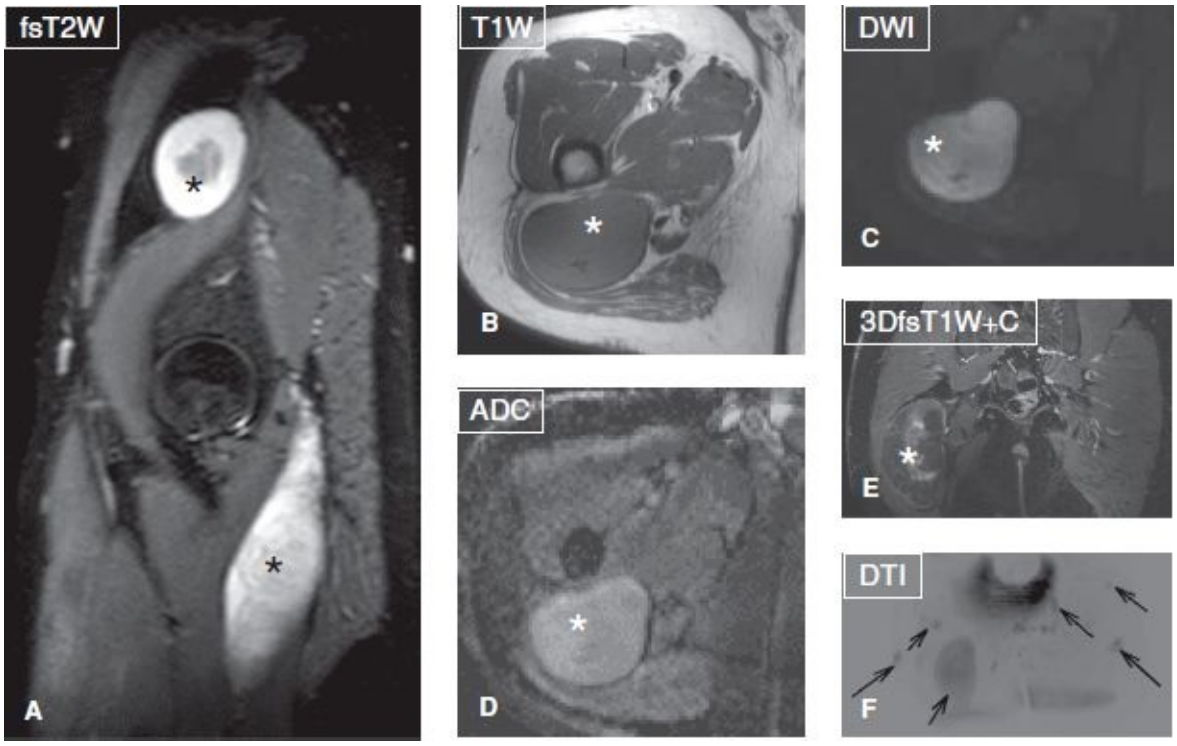

Fig. 41: Neurofibromatosis type-1. Sagittal **(A),** axial **(B–D),** coronal **(E, F)** images demonstrate two well-circumscribed ovoid T2 hyperintense targetoid and centrally enhancing lesions (*asterisks*) involving the femoral and sciatic nerves. The lesions showed high ADC values in keeping with benignity. The respective MIP DTI **(F)** image reveals multiple other similar lesions (*arrows*) in the pelvis, a typical appearance of neurocutaneous syndrome.

Nerve Entrapment

Nerve entrapment can occur as a transient finding, from dynamic causes or it could result from diffuse limb swelling as observed in the compartment syndrome. More commonly, it results from a space occupying lesion or thickened fascia in close proximity to the nerve. The entrapment can occur at expected location(s) where the nerves passes through the confined space(s) of known anatomic tunnels, or in an unexpected area where a space occupying lesion might be present in the vicinity of the course of the nerve. The various tunnels and known entrapment sites along the course of the commonly imaged peripheral nerves are described in Table 1. In general, sensory fascicles are arranged peripheral to the motor fascicles in the mixed nerves. Therefore compressive neuropathy is likely to cause sensory symptoms earlier and with more intensity as compared to the motor symptoms. Currently, the peripheral nerve entrapment is commonly graded based on symptoms, clinical examination results, and electrodiagnostic findings. Mild entrapment refers to (sensory changes clinically and mildly decreased nerve conduction velocity reflecting early demyelination), moderate entrapment refers to (more pronounced sensory changes with or without mild motor changes, moderately decreased nerve conduction velocity and amplitude changes reflecting axonal degeneration), and severe entrapment refers to (more profound and persistent motor and/sensory loss with soft tissue atrophy, absent or severely

reduced conduction velocity and axonal degeneration changes).

MRN is an anatomic study that has shown good correlations with clinical findings and electrodiagnostic results. Various hypothesized mechanisms have been reported that explain nerve signal and/or caliber alterations seen as a consequence of nerve entrapment. These include blockade of normal to and fro axoplasmic flow of endoneurial fluid within the nerve fascicles, venous congestion due to compression of vasa nervosa and hyperemia in acute–subacute stages of nerve impingement. Worsening entrapment leads to local demyelination, which is followed by axonal damage, and consequent increased water content as well as free space within the nerve. Chronic nerve entrapment leads to fascicular atrophy and/or peri- and intraneural fibrosis. On MRN, one would see a variety of imaging findings depending upon the stage of the disease, for example, hyperintensity due to increased water content initially to hypointensity related to fibrosis in more advanced stages. In most cases, in mild entrapment, one would expect to see abnormal hyperintensity of the nerve (usually mild–moderate) and mild flattening of the nerve at the entrapment site (Figs. 42, 43). No muscle denervation changes are expected. In moderate entrapment, one would see proximal enlargement of the nerve with distal flattening, prominent fascicles (outer sensory > motor), moderate to severe hyperintensity, and nerve course deviations (Figs. 44, 45). Muscle denervation changes may become apparent. In both mild and moderate entrapment, the signal abnormality is maximum just above and at the site of entrapment, which gradually fades to near-normal signal intensity distally along the course of the nerve in a uniform fashion, while on the contrary, electrodiagnostic study may show velocity alterations all along the nerve. Therefore, MRN is very good for localization of the nerve entrapment site. In severe entrapment, one would see proximal and distal nerve enlargement in an hourglass configuration and abrupt signal alterations, progressing from hyperintensity to hypointensity (bright—black—bright, triple B sign) along the length of the nerve from proximal to distal due to mixed edema, ischemia and fibrotic changes. One may see abnormal kinks of the nerve (zig-zag deformity) due to perineural fibrosis (Figs. 46, 47). Finally, muscle denervation change is usually the rule in moderate to severe degrees of mixed nerve or motor nerve entrapment (Figs. 44, 45). It is important for the reader to be aware of the regional muscle innervation patterns to increase their reading accuracy while evaluating these studies.

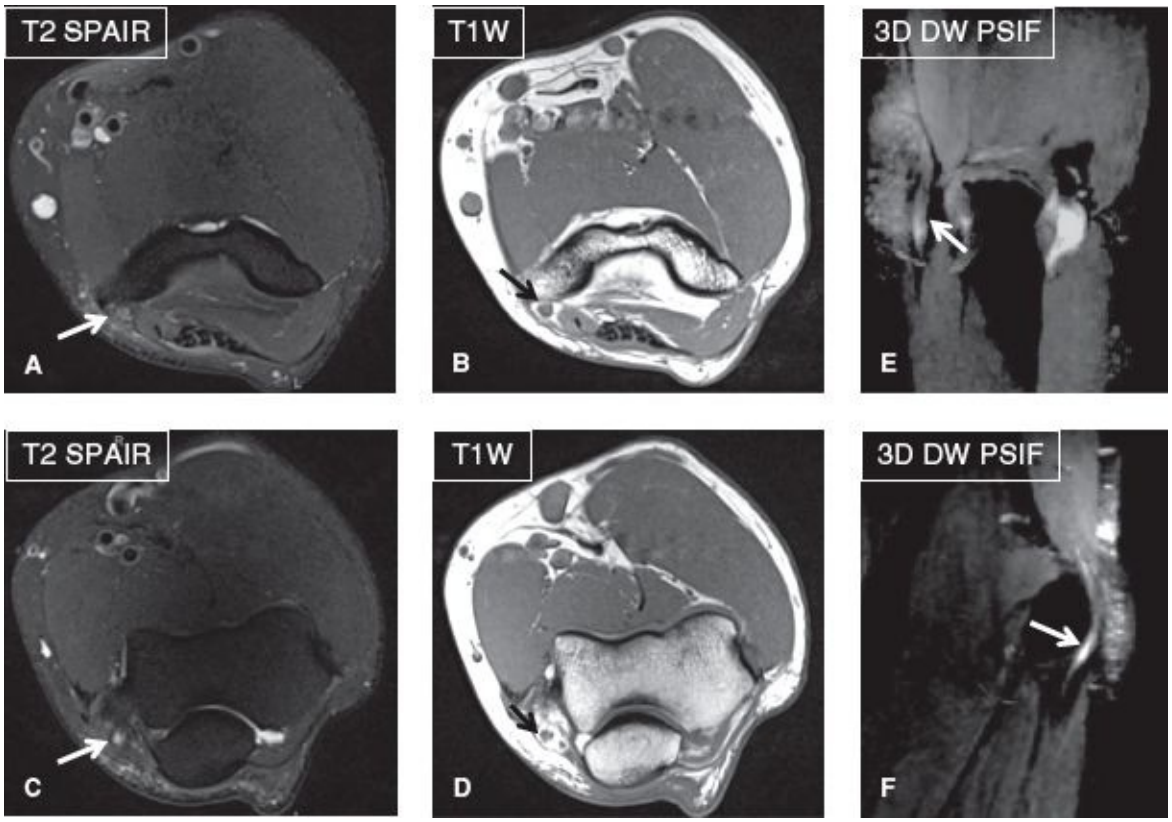

Fig. 42: Mild ulnar neuropathy. Axial images at **(A–D)** at the cubital tunnel demonstrate abnormal mild–moderate T2 hyperintensity of the ulnar nerve (*arrows*). The signal abnormality of the nerve and distal flattening is also delineated on the respective coronal **(E)** and sagittal reformatted 3D images (*arrows* in **E, F**).

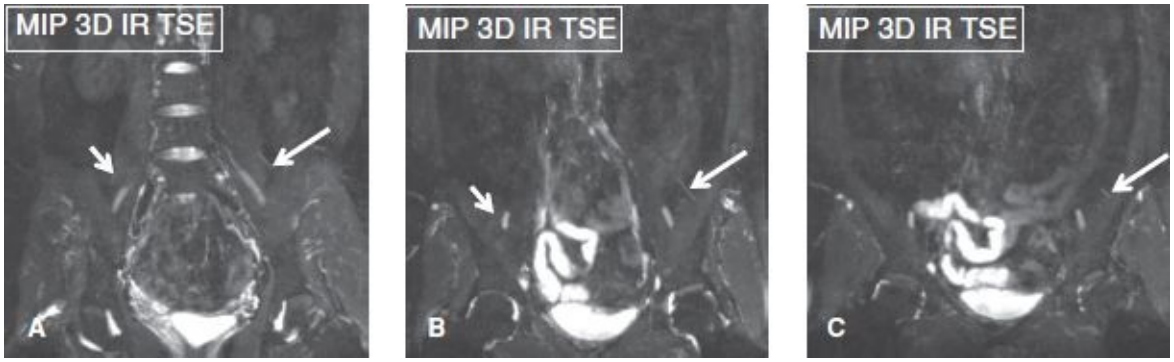

Fig. 43: Mild left lateral femoral cutaneous neuropathy in a patient presenting with left anterolateral pain. Sequential coronal images **(A–C)** exhibit abnormal asymmetric hyperintensity of the left lateral femoral cutaneous nerve (*long arrows*) as compared to the normal right nerve (*short arrows*), whose signal intensity fades at the inguinal ligament. This nerve is best seen on 3D MIP images.

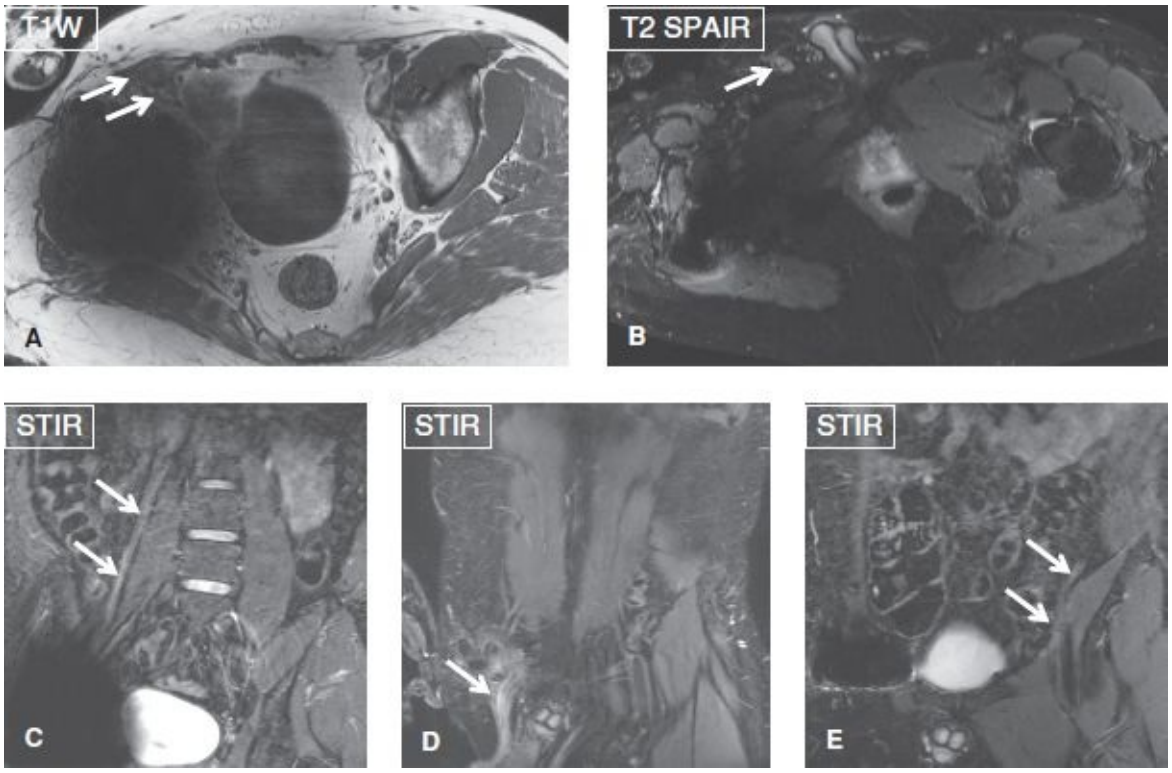

Fig. 44: Moderate bilateral genitofemoral nerve entrapment, right side clinically worse than left, in a patient with prior hernia repairs and right hip replacement. Axial images **(A, B)** show artifacts from postsurgical changes at the right hip and scarring of the ipsilateral groin (*arrows* in **A**), as well as edema of the right cremasteric muscle (*arrows* in **B**), indicative of denervation. The coronal MRN images **(C–E)** exhibit abnormal T2 hyperintensity and enlargement of the genitofemoral nerves (*arrows* in **C, E**) and denervation edema of the right cremastric muscle with surrounding scarring (*arrow* in **D**).

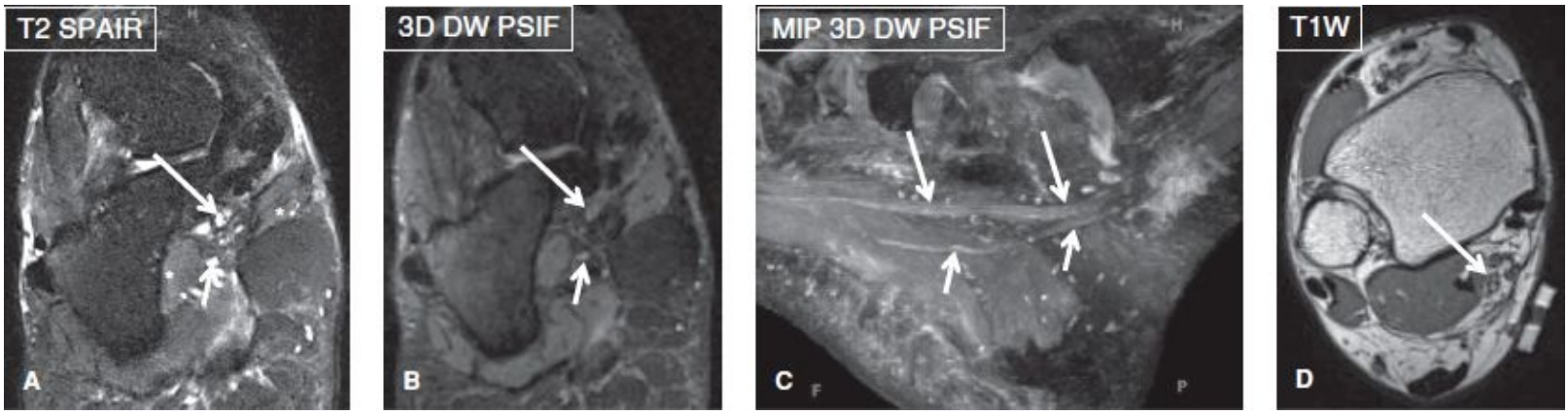

Fig. 45: Moderate medial and lateral plantar neuropathy—recurrent Tarsal tunnel syndrome. Oblique short axis images **(A, B)** and sagittal reconstructed image **(C)** show moderate to severe hyperintensity of medial (*long arrows*) and lateral (*short arrows*) plantar nerves with enlargement of the medial plantar nerve from recurrent entrapment. Notice denervation edema of the abductor hallucis and quadratus plantae muscles (*asterisks*). The tibial nerve (*arrow* in **D**) shows fascicular atrophy with intra-epineurial fatty deposition. Notice overlying subcutaneous scarring.

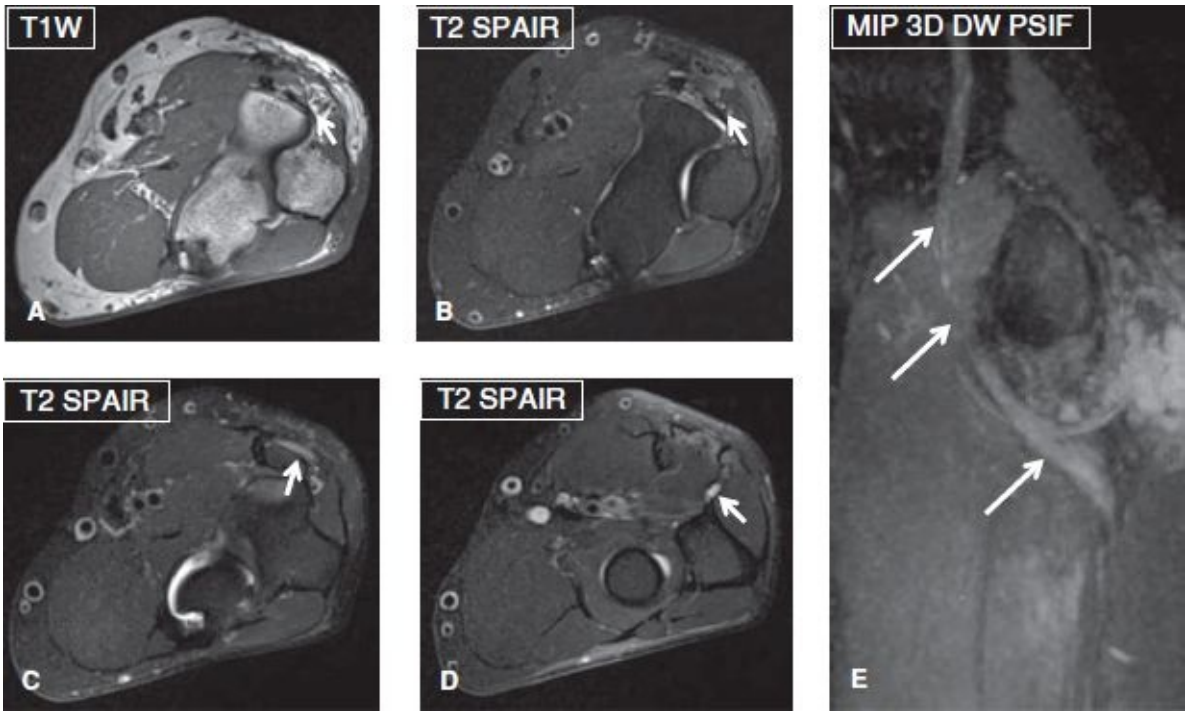

Fig. 46: Ulnar nerve re-entrapment in a patient with prior cubital tunnel release with severe neuropathy. Axial images **(A–D)** at the level of the elbow and oblique axial 3D image **(E)** demonstrate moderate to severe T2 hyperintensity of the anteriorly transposed ulnar nerve (*arrows*) with altered course (*arrow* in **C**). 3D image shows abrupt alterations of signals from bright–black–bright (triple B sign) (*arrows* in **E**) in keeping with severe re-entrapment neuropathy.

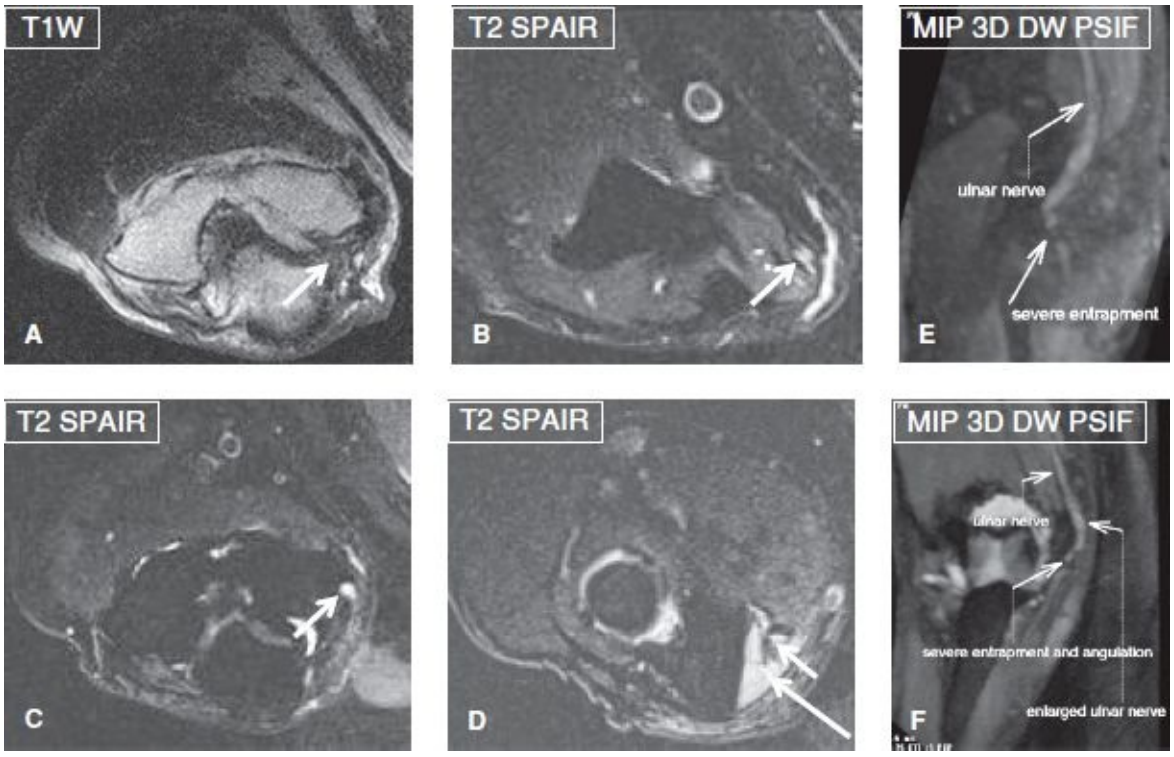

Fig. 47: Ulnar nerve re-entrapment from prior cubital tunnel release and anterior transposition. Axial **(A–D)** show scarring in the cubital tunnel from prior surgery. Notice moderate to marked T2 hyperintensity of the nerve (*short arrows*) and denervation edema of the flexor carpi ulnaris muscle (*long arrow*). Oblique reconstructed sagittal **(E)** and coronal

(F) images show the extent of the abnormality with triple b sign and acute angulation (zig-zag deformity) of the ulnar nerve from severe entrapment neuropathy (*arrows* in **E, F**).

TABLE 1: The various tunnels and known entrapment sites along the course of the commonly imaged peripheral nerves

Peripheral Nerve	Anatomic Region	Compressive Structures and Mechanism	Additional Comments
Brachial plexus lower trunk	Superolateral thorax, supraclavicular region	Cervical rib, elongated C7 transverse process, or fibrous band between C7 transverse process and first thoracic rib; static compression or dynamic compression as with droopy neck syndrome (T2 vertebra visible on lateral spine radiograph)	Thoracic outlet syndrome
Suprascapular nerve	Scapula, shoulder	Ligamentous roof of suprascapular notch (transverse scapular ligament) or spinoglenoid notch (paralabral cyst)	Entrapment leads to focal abnormality while inflammation, such as Lyme disease would lead to diffuse abnormality
Ulnar nerve	Medial elbow, cubital tunnel	Osborne band between two heads of flexor carpi ulnaris mm.; dynamic compression with subluxation; low insertion of medial head of triceps; ulnar collateral ligament injuries	Cubital tunnel syndrome
	Wrist	Guyon canal; static compression from a ganglion cyst or ulnar artery aneurysm	
Median nerve	Wrist, carpal tunnel	Flexor retinaculum or transverse carpal ligament; static compression from flexor tenosynovitis, ganglion	Carpal tunnel syndrome; most common entrapment
	Elbow, distal humerus	Ligament of Struthers or supracondylar bony process; static compression	Relatively uncommon
	Upper forearm	Pronator teres or flexor digitorum superficialis tendon (FDS) sheath; dynamic compression	Anterior interosseous nerve entrapment may be seen with FDS sheath entrapment or accessory (Gantzer) muscle
Radial nerve	Wrist	Radial sensory nerve; static from ganglion cyst or thickened fascia; dynamic in cyclists (Wartenberg syndrome)	
	Mid humerus	Spiral groove: static due to thickened lateral intermuscular septum or tight lateral head of triceps	
	Elbow and proximal forearm	Supinator fascial edge (Arcade of Frohse) leading to posterior interosseous neuropathy	Radial tunnel syndrome with purely sensory findings
Sciatic nerve	Pelvis	Piriformis muscle: static or dynamic	The muscle and nerve might be normally split in 20–30% of population
Femoral nerve	Pelvis	Inguinal ligament	Split femoral nerve or long segment passage through the psoas muscle are normal variants
Lateral femoral cutaneous nerve	Hip, near anterior superior iliac spine	Inguinal ligament; static compression Dynamic compression in obese, tight waist belts and in pregnancy	Meralgia paresthetica; surgical correction risks hernia formation
Common peroneal nerve	Knee, proximal fibula	Fibular neck, peroneus longus muscle; static or dynamic compression	Superficial peroneal nerve as it exits the fascia at the junction of upper two-thirds and lower one-third of lower leg
Posterior tibial nerve	Foot, tarsal tunnel	Flexor retinaculum between medial malleolus and calcaneus; static or dynamic compression; tibial nerve at the level of the soleus sling	Tarsal tunnel syndrome Medial or lateral plantar nerves entrapped in their respective tunnels in the hindfoot
Interdigital nerve	Foot	Intermetatarsal space	Morton neuroma

Generally, intravenous contrast is not required for the evaluation of nerve entrapment case due to their subacute nature of presentation. Although, there exists an acute clinical condition, i.e. acute carpal tunnel syndrome; the authors have not seen abnormal nerve enhancement in that instance as well. One would commonly see abnormal muscle enhancement with denervation. However, in muscle denervation, edema-like signal is easily apparent on the T2W images and contrast is usually not necessary to detect the muscle signal alterations. If one suspects a mass lesion or if there is known space occupying lesion in the vicinity of the nerve, one should give contrast to characterize it further. Common such masses include ganglion cyst, hematoma, abscess or tumor (Fig. 48).

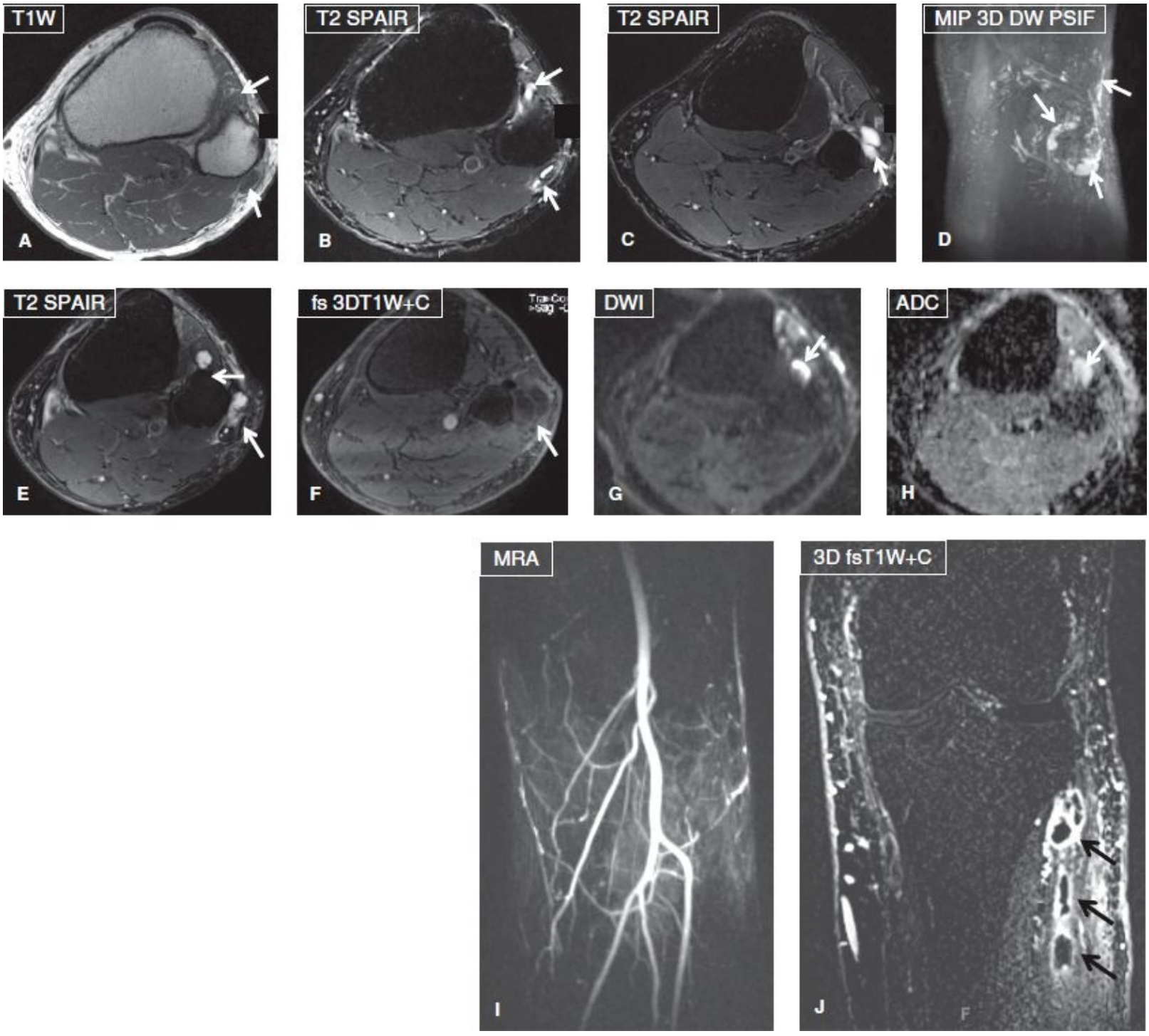

Fig. 48: Common peroneal nerve intra-neural and extra-neural ganglion. Axial **(A–C)** and

coronal **(D)** images show a multilobular cystic lesion (*arrows*) arising from the proximal tibiofibular joint with retrograde extension along the path of the least resistance via the intra-articular branch of the common peroneal nerve (CPN) intraneurally and perineurally (*arrows* in **D**). The patient underwent removal of the ganglion cyst and ligation of the articular branch of the above nerve. There were two branches and only one was ligated. Axial **(E–H)** images from a follow-up scan few months after the baseline exhibit recurrence of the ganglion (*arrows*) with peripheral enhancement and apparent diffusion restriction due to T2 shine through. Coronal MRA delayed postcontrast subtraction **(I, J)** images show no abnormal vascularity and only peripheral enhancement of the lesion.

Some pitfalls and additional clues have to be remembered while evaluating and reporting the nerve entrapment cases. Mild hyperintensity of nerve is common at the friction sites of tunnels. It could be subclinical traction neuropathy or a magic angle artifact in expected locations, as the nerve turns obliquely, as described above. One should increase the window width and make the image greyish to compare the signal alteration with adjacent in plane veins. If the signal abnormality approaches the venous signal, it would be likely abnormal. If it does not and is seen as an isolated finding, this mild signal change should be reported as a non-specific signal alteration to be correlated clinically, since it might not mean much clinically or it might be the only finding explaining the patient symptoms. Usually, clinically symptomatic neuropathy or imaging abnormality that correlates with electrodiagnostic results generally manifests with longer extent of signal alteration along the length of the peripheral nerve. In the latter case, other findings of alterations of nerve course, caliber, and/or fascicular morphology should be looked for apart from regional or distal muscle denervation change. Abnormal nerve findings other than nerve signal alteration, as described above increase the specificity neuropathy diagnosis. The diagnostic accuracy rates for MRN range in 90s among larger nerves, such as sciatic and femoral nerves and 80s for the smaller nerves, such as the common peroneal nerve. The most sensitive sign of neuropathy is T2 hyperintensity while most specific signs are fascicular abnormality, nerve caliber change, and muscle denervation change. Depending upon different entrapment sites under evaluation, other indirect imaging signs contributing to in association with neuropathy might be present, for example, effacement of deep carpal tunnel fat pad, flexor tenosynovitis and bowing of overlying retinaculum in the setting of median neuropathy; thickened ligaments at the ischial spine or tuberosity in cases of pudendal neuropathy; or paralabral cyst in the setting of sciatic or suprascapular neuropathy. Regional muscle alterations, such as accessory muscle or split nerve may be present as developmental variants. Only a minor percentage of such cases exhibit nerve entrapment or are clinically symptomatic due to the anatomic variation per se. One should however, carefully look for imaging signs of neuropathy in such cases, since the findings of signal alteration can be subtle (Figs. 19, 20). In many instances, such anomalies become symptomatic when the nerve coursing through the confined space becomes entrapped due to neural swelling caused by other superimposed causes, such as lumbosacral plexopathy or

proximal spine disease (aka double crush syndrome). In chronic nerve entrapment, the nerve loses water signal, may become ischemia with development of fibrotic changes as well as fascicular atrophy (Fig. 45). Therefore in such cases, the nerve does not show significant increased signal but will show flattening at the entrapment site with more than 50% caliber change and/or proximal enlargement. Finally, pos operatively, the nerve signal and size should decrease within 4 to 8 weeks following surgery returning to near normal after a few months (Fig. 49). Mild signal hyperintensity may persist for long periods of time following surgery. Preoperative studies, if available, are particularly helpful to evaluate the postsurgical response by comparing the signal intensity, size, and fascicular alterations. Re-entrapment or persistent entrapment would lead to increasing nerve signal hyperintensity, persistent fascicular abnormality, perineural fibrosis, triple B sign, or zig-zag deformity as described above (Figs. 45–47). The regional denervated muscles will also undergo progressive fatty replacement and atrophy. Double crush syndrome is another entity, where a proximal pathology or entrapment of the nerve may predispose to distal entrapment. The distal entrapment site might manifest in a more pronounced fashion clinically. Imaging helps to sort out the clinical conundrum by showing the entrapment-related findings at the involved sites (Fig. 50). Sensory neuropathies are difficult to diagnose by electrodiagnostic examinations. A combination of clinical findings and imaging is very useful in their diagnosis, especially in deep pelvic neuropathies. The MRN study may show the neural abnormality similar to imaging signs as described above or might merely show the cause, such as a tumor in the expected location of a sensory nerve or scar entrapment (Figs. 51–54). LS radiculopathy imaging findings are also similar to peripheral nerve entrapment. The most common cause is a disc herniation, which leads to abnormal hyperintensity of the impinged DRG and post ganglionic nerve segment, which fades distally. The downstream nerves, such as femoral, obturator or sciatic nerves may also show signal and/or caliber change with increasing severity of impingement (Figs. 55, 56). Therefore, MRN offers much more than a regular lumbar spine study would reveal and increases the diagnostic confidence of the radiologist in pin pointing the site of exact abnormality, where multiple disc herniations might be present. The appearance is different in inflammation or traction injury of the nerve, where the abnormality is more diffuse and does not conform to the site of neural foraminal stenosis (Fig. 57).

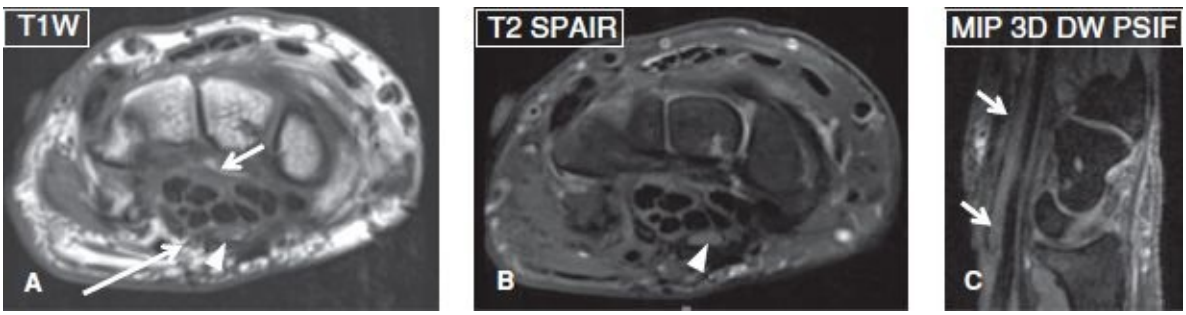

Fig. 49: Normal postoperative appearance. Axial **(A, B)** images show discontinuity of the flexor retinaculum (*long arrows*) from prior surgery, return of the normal deep carpal tunnel fat pad (*short arrow*) and normal oval shaped isointense median nerve (*arrowheads* in **A, B;**

arrows in **C**).

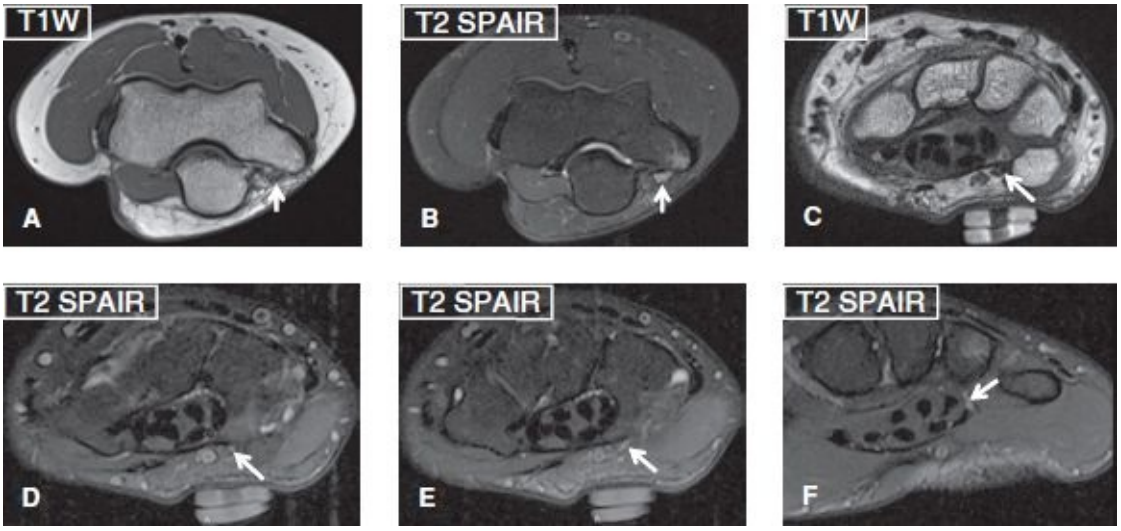

Fig. 50: Double crush syndrome. Axial images **(A, B)** at the level of the elbow demonstrate moderate T2 hyperintensity and mild prominence of the ulnar nerve (*arrows*) within the cubital tunnel, indicative of entrapment neuropathy. Notice mild edema in the medial epicondyle from stress injury. On axial images **(C–F)** at the level of the wrist and hand, there is additional T2 hyperintensity of the deep branch of the ulnar nerve (*arrows*). The patient presented with pain and Tinel sign over the Guyon canal.

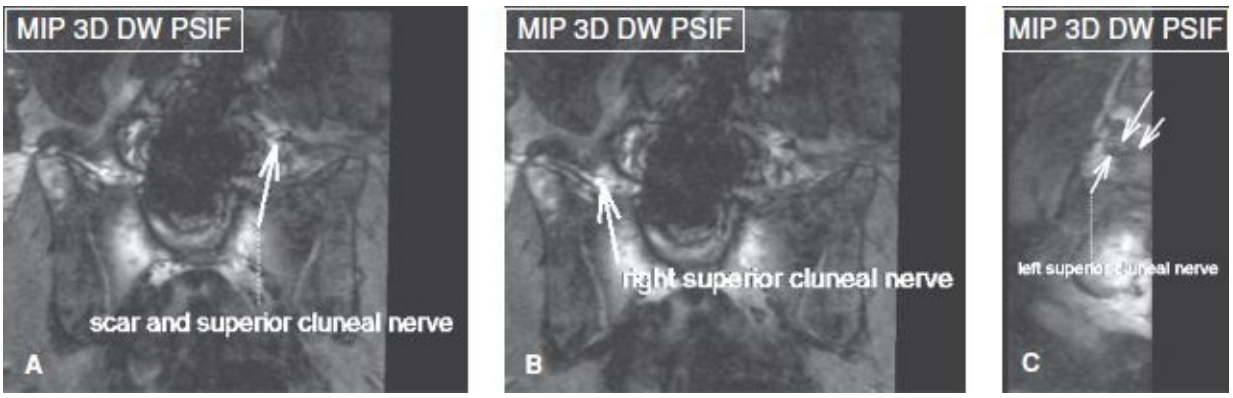

Fig. 51: Scar entrapment of the left posterior superior cluneal nerve after lumbar fusion and right iliac bone graft harvest, presenting with left flank pain. Coronal **(A, B)** and sagittal **(C)** reconstructed images from a vessel suppressed 3D acquisition show artifacts from lower lumbar spine hardware. Notice scar entrapment of the left superior cluneal nerve (*arrows* in **B,C**) and normal course of the right counterpart.

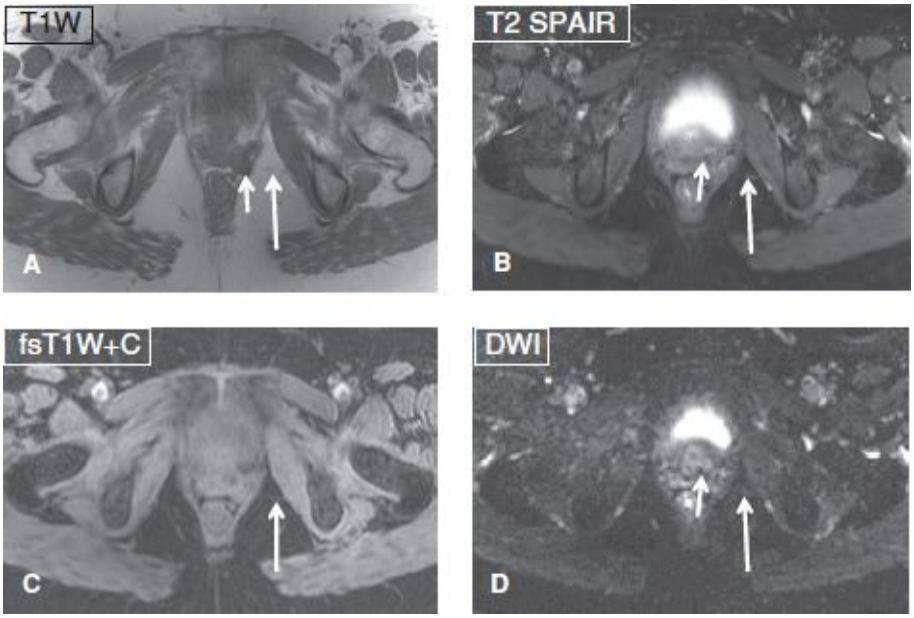

Fig. 52: Left inferior hemorrhoid neuropathy clinically presenting with rectal pain. Prior pelvic floor surgery with mesh placement and removal. Axial images **(A–D)** demonstrate left perineal scarring and perineal body distortion due to prior surgeries (*short arrows*). Notice residual mesh material seen as linear distorted hypointensity (*short arrows* in **B, D**). The left inferior hemorrhoidal nerve is minimally prominent (*long arrows*). CT-guided perineural injection was performed for pain relief. It is important to carefully look on DWI images and available contrast images to differentiate nerve (seen on DWI and nonenhancing on contrast) from a vessel (disappears on DWI and enhances on contrast).

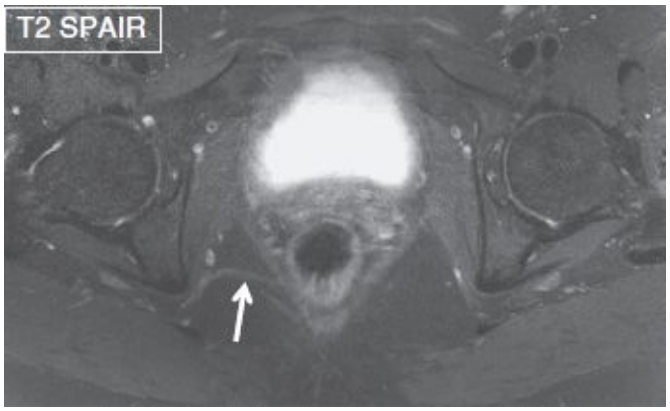

Fig. 53: Inferior hemorrhoid neuropathy. Axial image in another case with rectal pain exhibits enlarged and mildly hyperintense right inferior hemorrhoidal nerve (*arrow*), as it traverses the ischiorectal fat after arising from the right pudendal nerve.

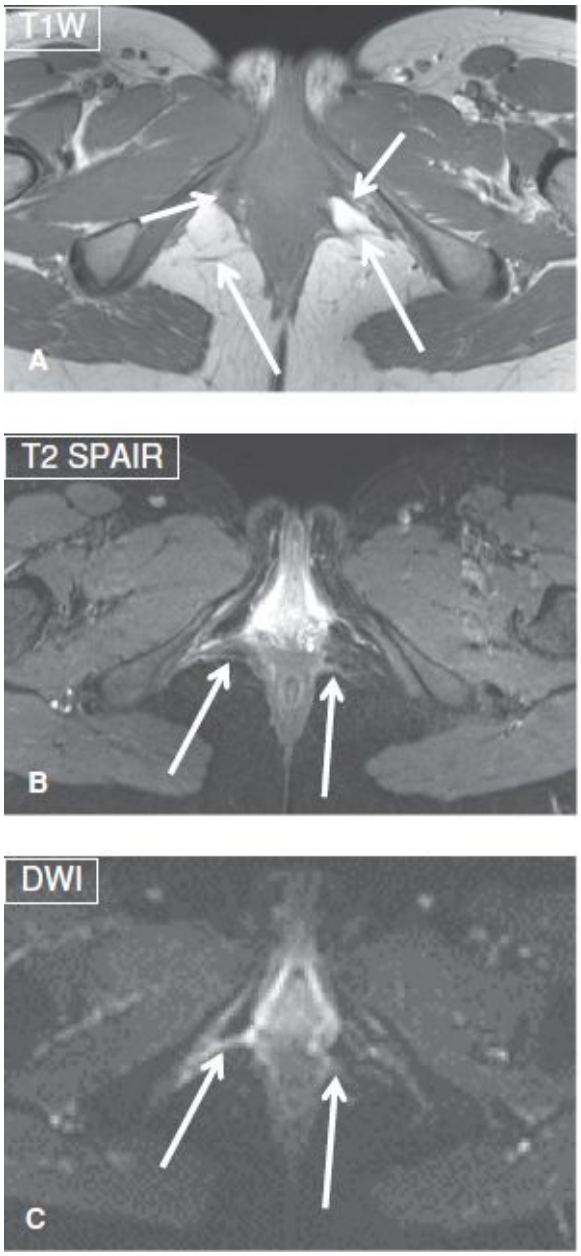

Fig. 54: Perineal branch pudendal neuropathy in a patient presenting with vaginal and perineal pain. Axial images demonstrate bilateral perineal scarring (*short arrows*), left greater than right, with enlarged hyperintense perineal branches of the pudendal nerves (*arrows*).

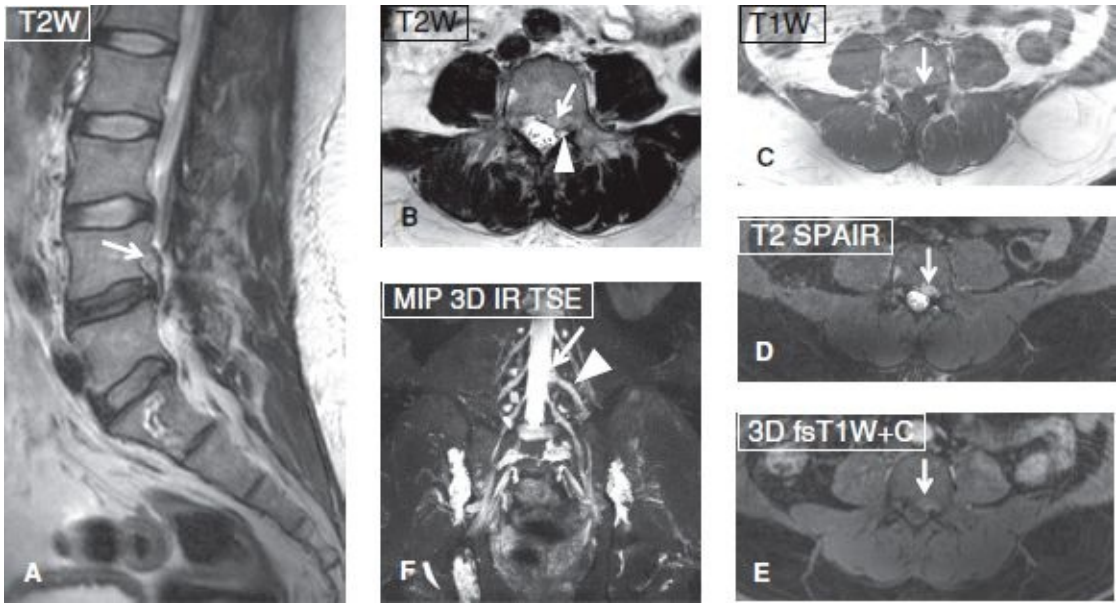

Fig. 55: Radiculopathy. Sagittal **(A)** and axial **(B)** images of the lumbar spine portion of LS plexus MRN show the left paracentral disc herniation (extrusion) at L4–L5 level (*arrows*) compressing the ipsilateral traversing L4 nerve root (*arrowhead* in **B**). On axial MRN images **(C–E),** notice the peripherally enhancing disc herniation (*arrows*). On coronal MRN image **(F),** the herniated disc (*arrow*) is seen effacing the fat triangle between the thecal sac and neuropathic enlarged and hyperintense L4 nerve root (*arrowhead*) due to impingement. Also note bright lesions of the pelvic bones from underlying myeloma infiltration.

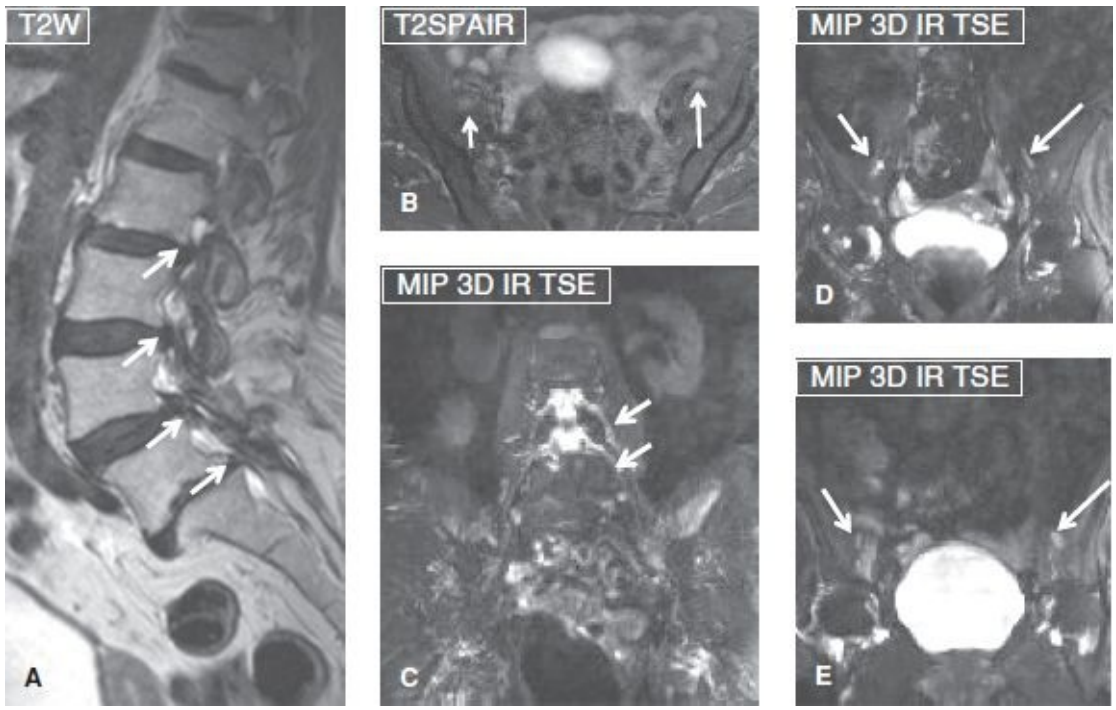

Fig. 56: Radiculopathy and left femoral neuropathy. Old patient with known multilevel lumbar spondylosis presenting with left anterior thigh and knee pain. Oblique sagittal image **(A)** shows stenosis of multiple lumbar neural foramina (*arrows*). The respective axial **(B)** and coronal **(C–E)** MRN images reveal asymmetric T2 hyperintensity of the left L3 and L4 nerve roots (*arrows* in **C**) as well as of the ipsilateral femoral nerve (*arrows* in **D, E**) with mild prominence of these nerves consistent with radiculopathy and neuropathy. MRN pin

points the site of neural abnormalities despite multilevel neural foraminal stenosis.

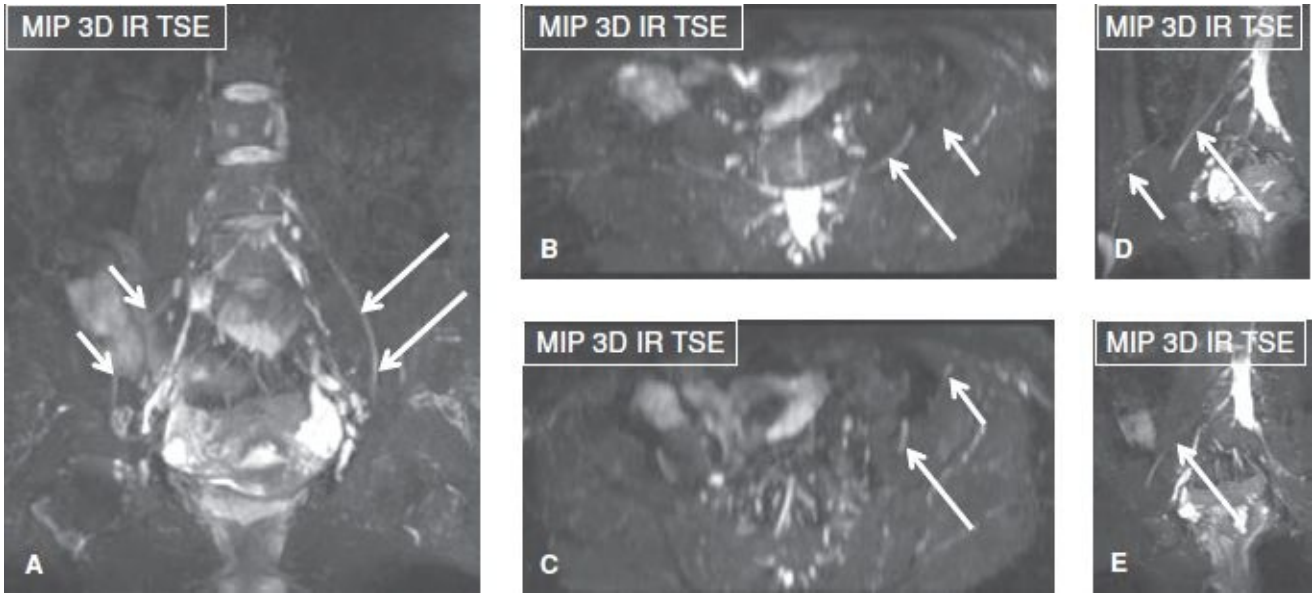

Fig. 57: Inflammatory lumbosacral plexopathy in a patient with left-sided anterior and lateral leg pain. Coronal **(A)** image shows diffuse asymmetric hyperintensity and mild enlargement of the left femoral nerve (*long arrows*) as compared to the normal right femoral nerve (*short arrows*). Reconstructed axial **(B, C)** images show abnormal left femoral (*long arrows*) and lateral femoral cutaneous nerves (*short arrows*). Oblique sagittal images **(D, E)** show abnormal left femoral and LFCN (*arrows* in **D**) as compared to normal right femoral nerve (*long arrow* in **E**). The right LFCN is not visible due to normal isointense signal.

Nerve Injury

Peripheral nerve injury can be caused by indirect or direct trauma. In indirect trauma, such as knee dislocation leading to common peroneal nerve injury or brachial plexus injury due to motor vehicle accident, various mechanisms of traction, shear stress and ischemia, in isolation or combination play a role in the pathophysiology, and different imaging findings may be seen depending upon the amount of nerve congestion, edema, fibrosis, and axonal or gross nerve discontinuity. There is typically an inside-out model of nerve injury as described in the Sunderland grading system, which is based on the nerve architectural anatomy. The oldest and simplest classification of nerve injury was proposed by Seddon, who categorized nerve injuries into three grades, from least severe to most severe, as neurapraxia, axonotmesis, and neurotmesis (Table 2). The Sunderland classification (Table 3) followed it and is currently used by most peripheral nerve surgeons for management purposes. It has five grades and the first grades are similar to Seddon classification while the last 3 grades correspond to progressive severity of neurotmesis, that is, based on the inside-out model, injury to endoneurium, perineurium, and epineurium, respectively. Dellon and MacKinnon added the sixth grade that describes partial and mixed injuries. In partial lesions, only a portion of the nerve fibers (circumference) may be injured while the remaining fibers are intact. In mixed (combined) injuries, all parts of the nerve are affected,

with some areas more severely affected than others. Fascicles in continuity can contain fibers with neurapraxia, axonometosis, or both types of injuries inside the same bundle. The duration, course, and quality of recovery depend on the severity, number, and type of injury to each individual nerve fiber or fascicle.

TABLE 2: The Seddon classification of peripheral nerve injury

Grade	Pathology	Clinical Findings	Prognosis
Neurapraxia	• Mild injury • Intact axon	• Mostly sensory deficits • Initial EMG negative. NCV may be prolonged	Complete spontaneous recovery usually occurs within weeks to months
Axonotmesis	• Internal disruption of axons, loss of axon continuity, and demyelination • Epineurium, perineurium, and endoneurium remain intact	• Motor and sensory deficits. NCV and amplitude changes reflecting higher grade of injury and muscle denervation changes. In the early phase of injury, it is difficult to distinguish axonotmesis from neurotmesis on a clinical basis due to similar deficits • In both lesions, initial electrical studies show no conduction distal to injury • After 3 wks, EMG can show fibrillations and denervation potentials distal to the injury site	• Spontaneous recovery occurs at a regeneration rate of ~1 mm/day (~1 in/mo). • It is usually complete
Neurotmesis	Complete severance of nerve trunk	• Nerve function is completely absent • Proximal sprouting axons that do not reach their target tissues can form neuromas • EMG will show fibrillations and active denervation potentials distal to the injury site	Wallerian degeneration occurs but spontaneous regeneration is less likely, especially if there is significant intervening scar tissue

EMG, electromyography; NCV, nerve conduction velocity.

Table 4 combines essence of the two classification systems with description of expected MRN findings on imaging. Grade I injury is characterized by temporary conduction block and presents acutely with no associated muscle denervation change. Grade II injury encompasses axonal loss and grade III involves injury to covering endoneurium. Since endoneurium is not visible on MRN, grade II and III injuries are difficult to distinguish. Although fascicular abnormality, abnormal nerve hyperintensity, and nerve enlargement findings are more pronounced in grade III injury as compared to grade II injury. Clinically, both grade II and III injuries are treated medically (Figs. 58–60). Grade IV injury is characterized by injury to perineurium and it demonstrates a neuroma in continuity, which is seen as focal heterogeneous nonenhancing enlargement of the nerve with fascicular discontinuity and/or thickened/disrupted perineurium. Neuroma in continuity is constituted by conglomeration of regenerating nerve sprouts and intervening fibrous tissue (Figs. 8, 61, 62). The nerve recovery is usually incomplete in such cases and the neuroma itself may be

painful leading to functional disability. Resection of the neuroma and nerve grafting may be needed in functionally disabling cases. Grade V injury means complete discontinuity of the nerve with end bulb neuroma formation (Figs. 63–67). Nerve recovery in this case is not expected without nerve grafting or placement of a neurotube across the cut or refashioned nerve endings. One of the key roles of imaging is to measure the gap between the proximal and distal discontinuous nerve fragments for operative management. Three-dimensional isotropic imaging is often very useful in demonstrating neuroma-in-continuity (grade IV injury) and neurotmesis (grade V injury) for the benefit of the reader and the referring physicians alike. The radiologist can play an important role in accurately diagnosing Sunderland V injury in a functionally important nerve and inform the surgeon regarding the length of the gap so that an appropriate dimension allograft or autograft can be prepared prior to nerve repair. Grade VI injury shows a mixture of findings, and the degree of circumference involvement and the worst degree (I through V as above) of the nerve injury dictates the ultimate prognosis (Fig. 17, 68). The diagnostic clues of this type of injury include epineurial thickening due to direct injury, history or mechanism of external injury and imaging demonstration of internal nerve heterogeneity from hemorrhage and/or fibrosis. Another simpler way of classifying the nerve injury based on imaging and with relevance to clinical management includes, stretch or traction injury (grade I–III); neuroma in continuity (grade IV), and nerve discontinuity or avulsion (grade V) injury. The respective imaging findings in various grades of nerve injuries and their prognosis are summarized in Table 5. The nerve injury diagnostic algorithm is shown in the flow diagram. Various imaging pitfalls should be kept in mind. Magic angle artifact leads to mild increased signal intensity in the nerve at expected locations, especially where nerve makes sharp turns (Fig. 69). Thickened, hyperintense peripheral nerve on a fluid sensitive sequence is a nonspecific abnormality. History of antecedent trauma is crucial in diagnosis of traction injury. Multifocality of nerve signal and caliber abnormality or diffuse multi-nerve abnormalities suggest other possibilities of peripheral nerve pathology including inflammatory causes of diffuse neuropathy, such as autoimmune neuropathy (Parsonage–Turner syndrome), CIDP and MMN. Therefore, clinical correlation is essential in such conditions. Mass-like enlargement of the peripheral nerve can mimic peripheral nerve sheath tumors (PNST). Again, history of antecedent trauma is crucial in diagnosis. Look for classic signs of PNST—target, fascicular bag of worms, etc. Contrast examination may be used for clarification, since most PNSTs enhance, while most neuromas in continuity do not, except in the setting of recent injury, when surrounding reactive granulation tissue may enhance around the neuroma. Finally, grade III and IV peripheral nerve injuries could be misdiagnosed if close attention to fascicular anatomy and appearance is not paid. In future, diffusion tensor imaging may aid in further clarifying the diagnosis and quantification of posttraumatic nerve abnormality.

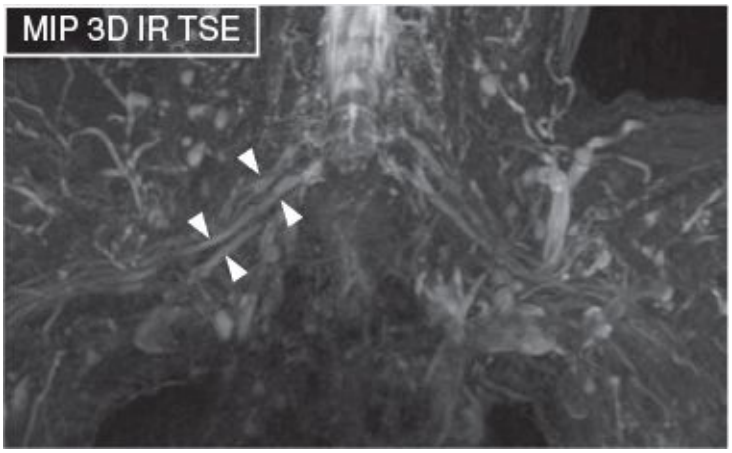

Fig. 58: Stretch injury (Sunderland grade II) of the brachial plexus in an individual with a recent motor vehicle accident. Coronal image exhibit T2 hyperintensity and mild thickening of the roots and trunks (*arrowheads*) of the right brachial plexus in the scalene triangle.

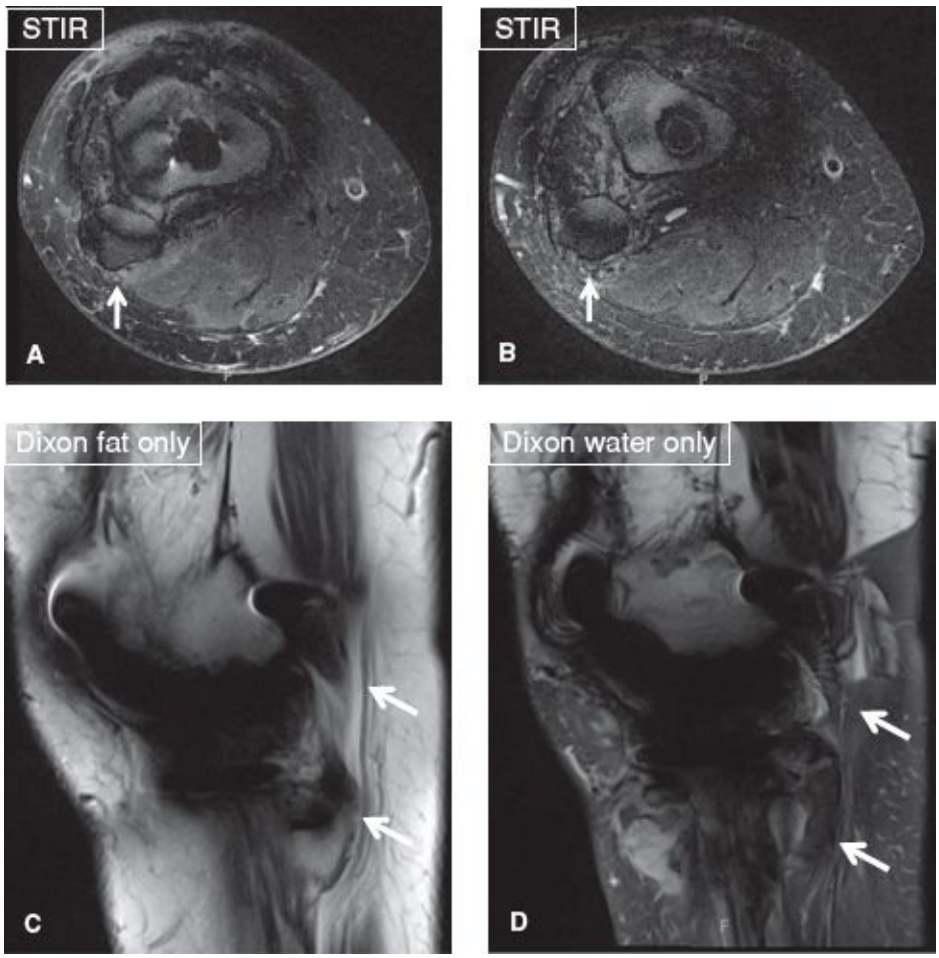

Fig. 59: Stretch injury (Sunderland grade II) to the common peroneal nerve after knee surgery. Patient presenting with anterior leg pain and mild weakness of dorsiflexion of the foot. Axial **(A, B)** and sagittal **(C, D)** images show mild hyperintensity of the common peroneal nerve (*arrows* in **A, B**) at the level of the knee joint with otherwise continuous nerve.

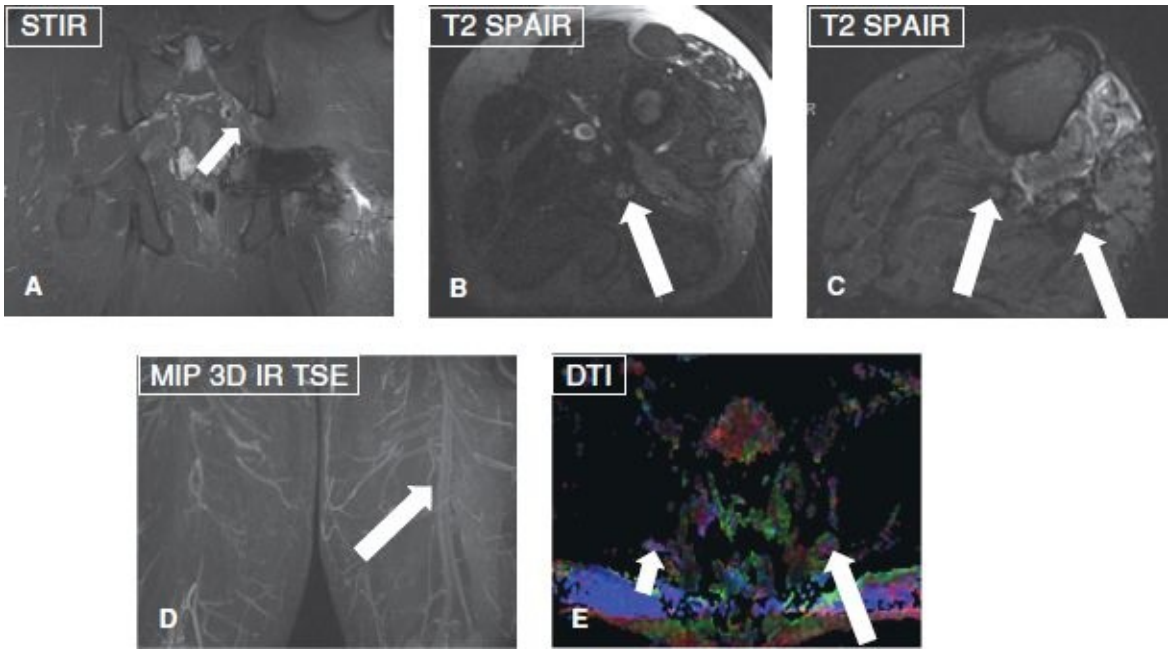

Fig. 60: Sunderland grade III injury. Coronal **(A)** image shows mildly hyperintense left sciatic plexus (*arrow*) partially obscured by the metal artifact from left hip prosthesis. Axial **(B, C)** and coronal **(D)** images show diffuse thickening and T2 hyperintensity of the left sciatic and its branches as well as extensor compartment muscle denervation change. **E:** DTI image (fractional anisotropy colored map) shows enlarged left sciatic nerve (*long arrow*) with low FA value (0.1 to 0.2) as compared to normal right-sided nerve (FA value, 0.4 to 0.5; *short arrow*). Sunderland grade III injury was confirmed on surgery.

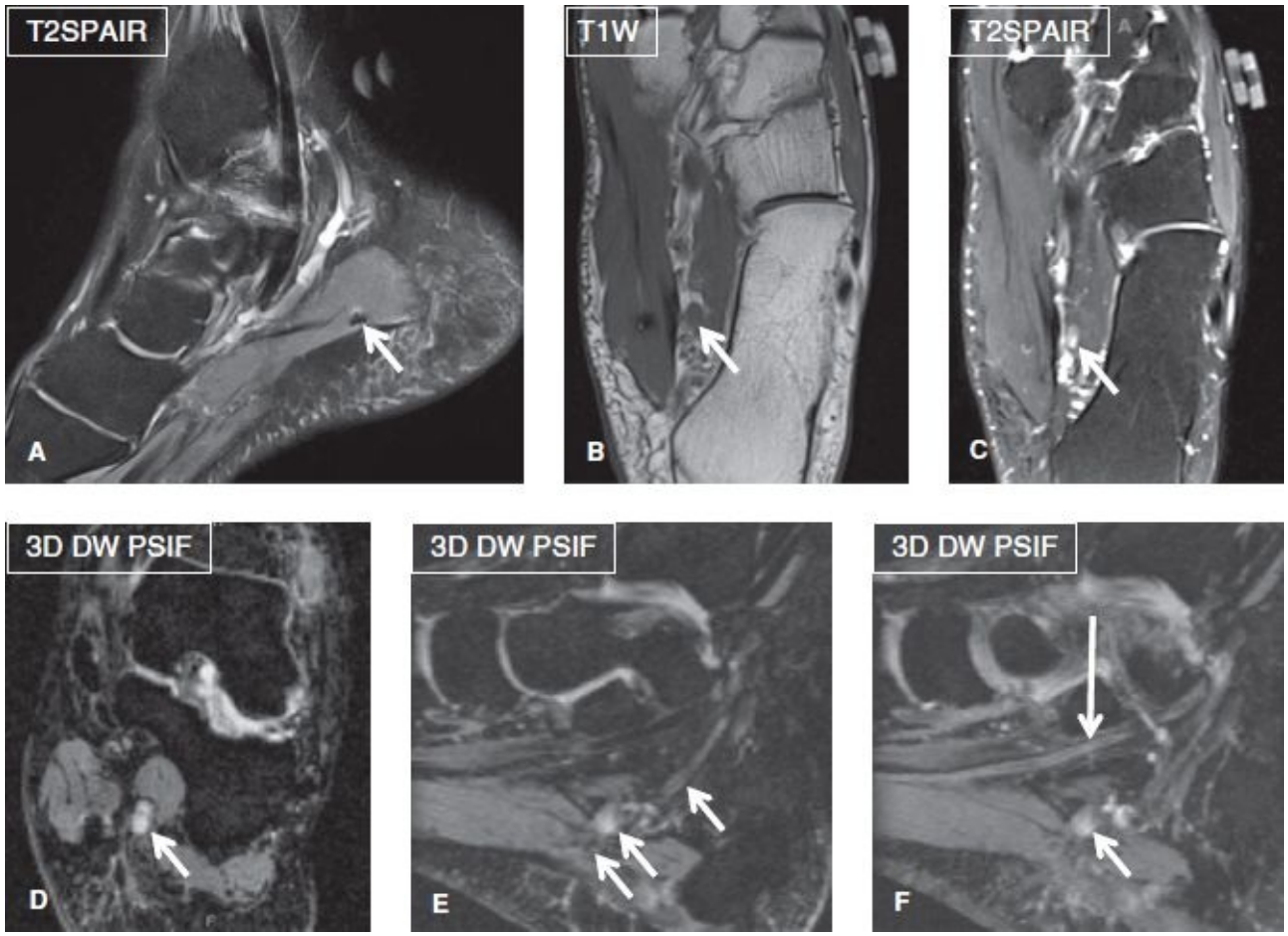

Fig. 61: Lateral plantar nerve neuroma-in-continuity (Sunderland grade IV injury) from

prior plantar fascia surgery. Sagittal **(A)** image shows susceptibility artifact from prior surgery (*arrow*). Axial **(B, C)** images show the neuroma along the course of the lateral plantar nerve between the abductor halluces and quadratus plantae muscles. Coronal **(D)** and sagittal **(E, F)** 3D reformatted images reveal a focal bulbous T2 hyperintense enlargement (*arrows*) of the lateral plantar nerve (*short arrow*) and mildly hyperintense, otherwise normal medial plantar nerve (*long arrow*).

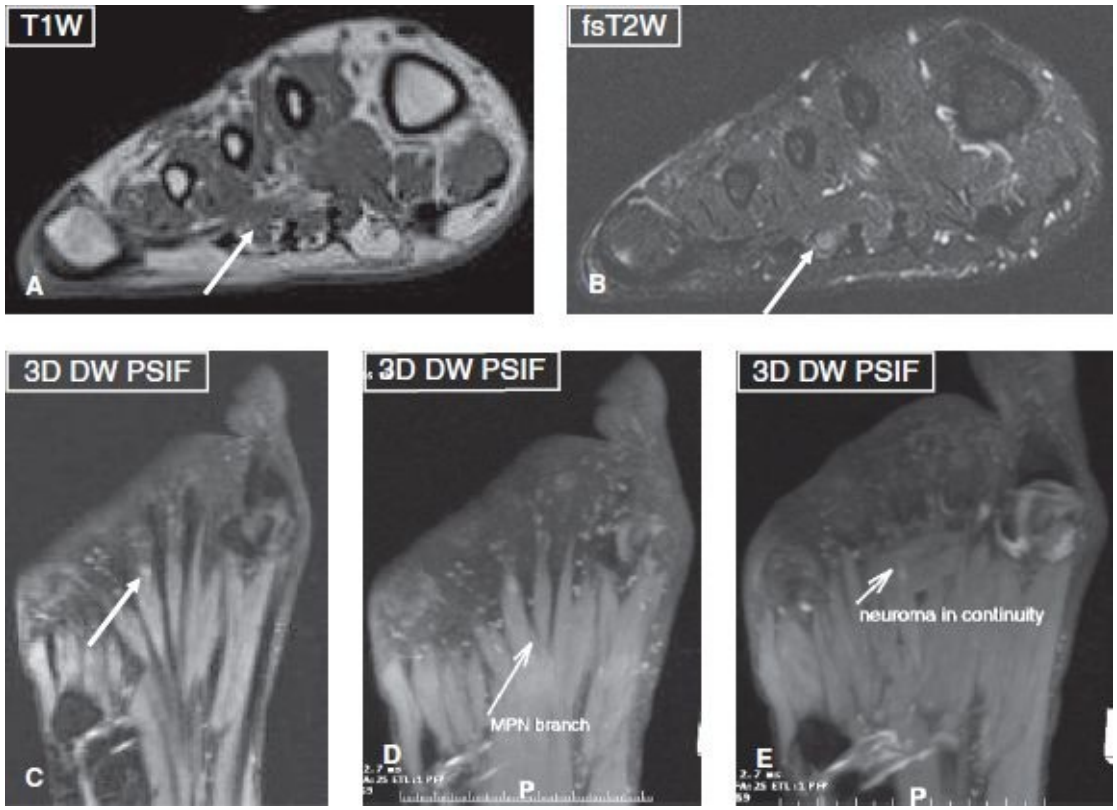

Fig. 62: Medial plantar nerve neuroma-in-continuity (Sunderland grade IV injury) from prior injury. Axial **(A, B)** and coronal **(C–E)** images show the neuroma-in-continuity along the course of the lateral most branch of the medial plantar nerve (*arrows*).

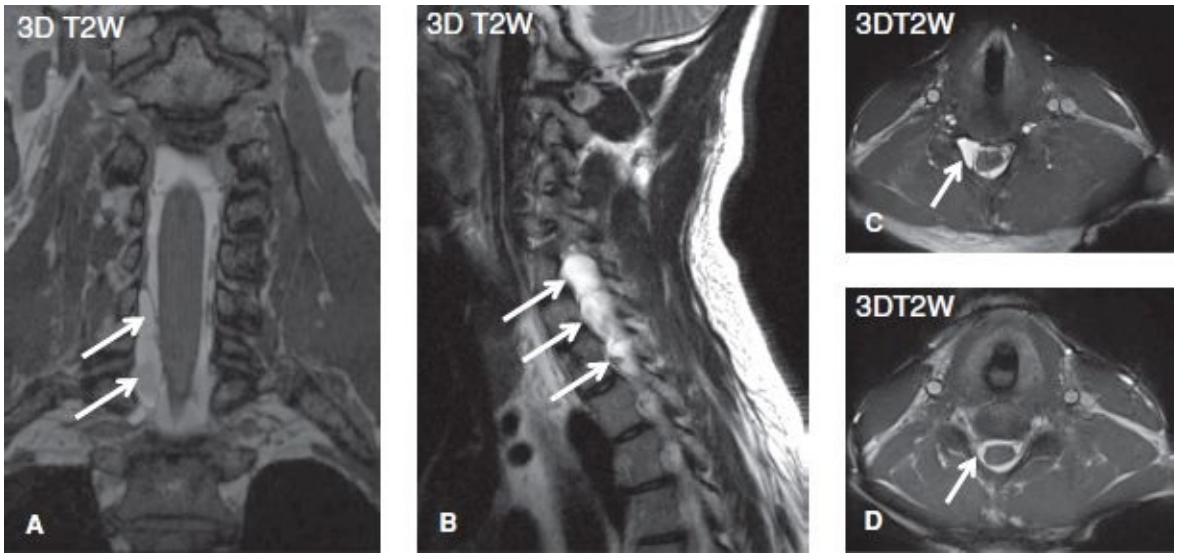

Fig. 63: Sunderland grade V injury with multiple nerve root avulsions from recent MVA. Coronal **(A)** and sagittal **(B)** reconstructed 3D T2W TSE images show multiple right-sided

lower brachial plexus (C6–T1) root avulsions with pseudomeningoceles. Axial 3D T2W steady state images confirm the pseudomeningocele (*arrow* in **C**) and absent preganglionic nerve roots (*arrow* in **D**).

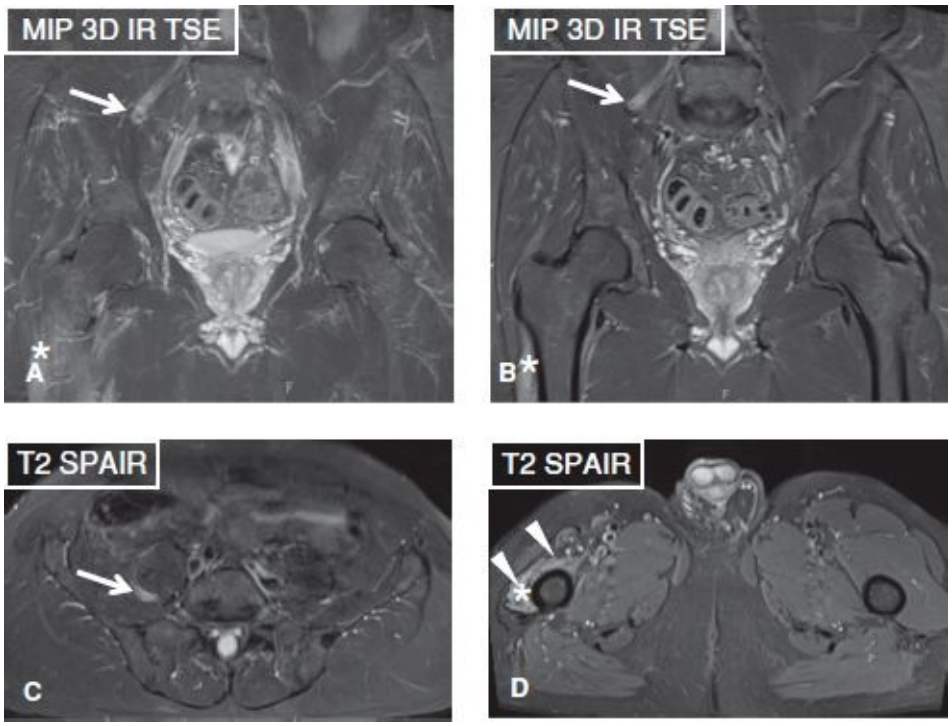

Fig. 64: Femoral nerve transection/Sunderland grade V injury. Coronal **(A, B)** and axial **(C, D)** images exhibit abrupt termination of the right femoral nerve (*arrows*). Atrophy of the anterior thigh muscles (*arrowheads*) as well as edema of the vastus intermedius muscle (*asterisk*) indicate subacute denervation.

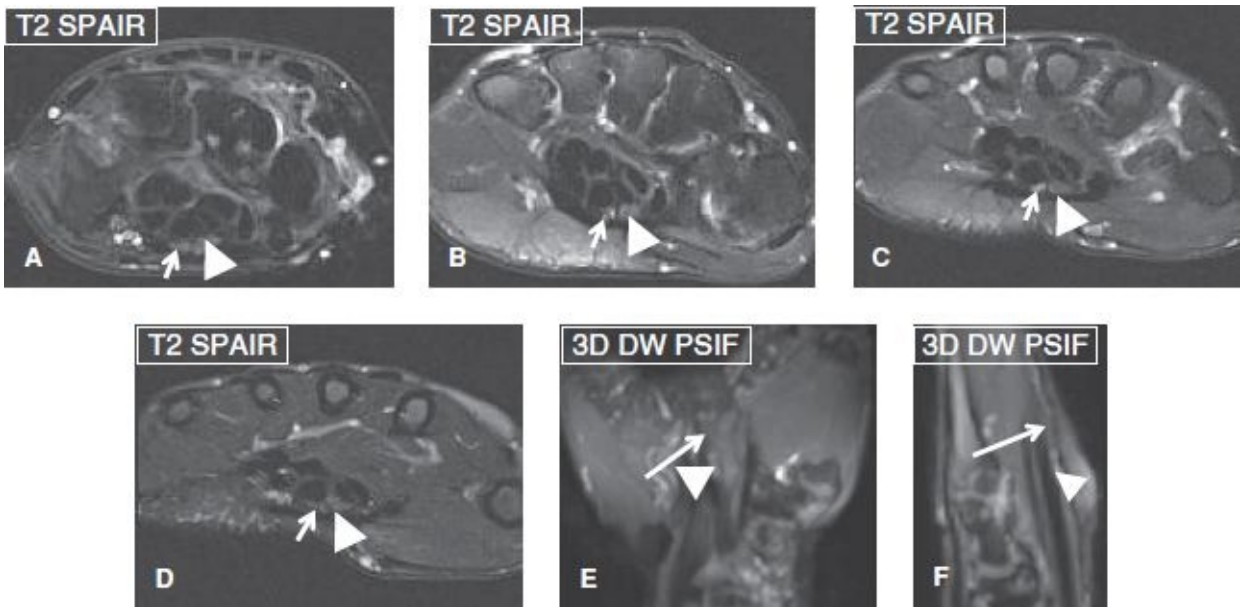

Fig. 65: Sunderland V injury/Median nerve transection during prior carpal tunnel release. Axial image **(A)** shows bifid median nerve at the level of the pisiform (*arrowhead,* radial bundle; *arrow,* ulnar bundle). Notice end bulb neuromas of the ulnar bundle (*arrow* in **B**) and normal radial bundle (*arrowhead* in **B**) with complete fluid-filled gap (*arrow* in **C**) distally. Axial image **(D)** in the hand shows normal nerve distally. Coronal and sagittal 3D images

(E, F) show the 1-cm gap (*arrows*) between the nerve endings with proximal neuromas (*arrowheads*).

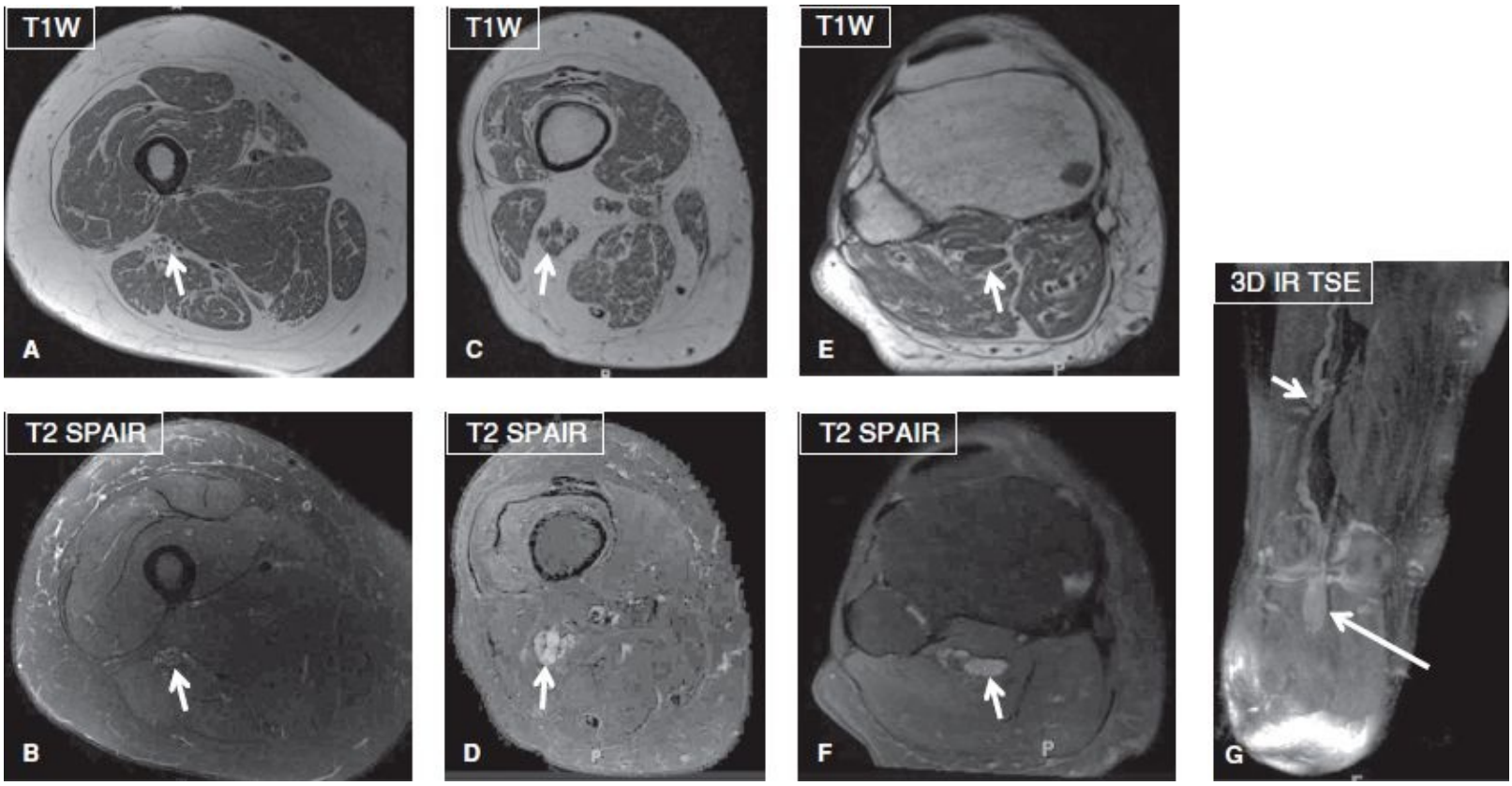

Fig. 66: Sciatic end bulb painful neuroma formation from below-knee amputation. Axial images **(A, B)** of the proximal thigh show increased intra-epineurial fat within the right sciatic nerve (*arrows*). More distal images **(C, D)** show bulbous enlargement of the common peroneal component of the sciatic nerve (*arrows*). Final axial images **(E, F)** at the level of the proximal tibiofibular joint show bulbous termination of the tibial nerve (*arrows*). Coronal image **(G)** shows both CPN (*short arrow*) and tibial (*long arrow*) neuromas.

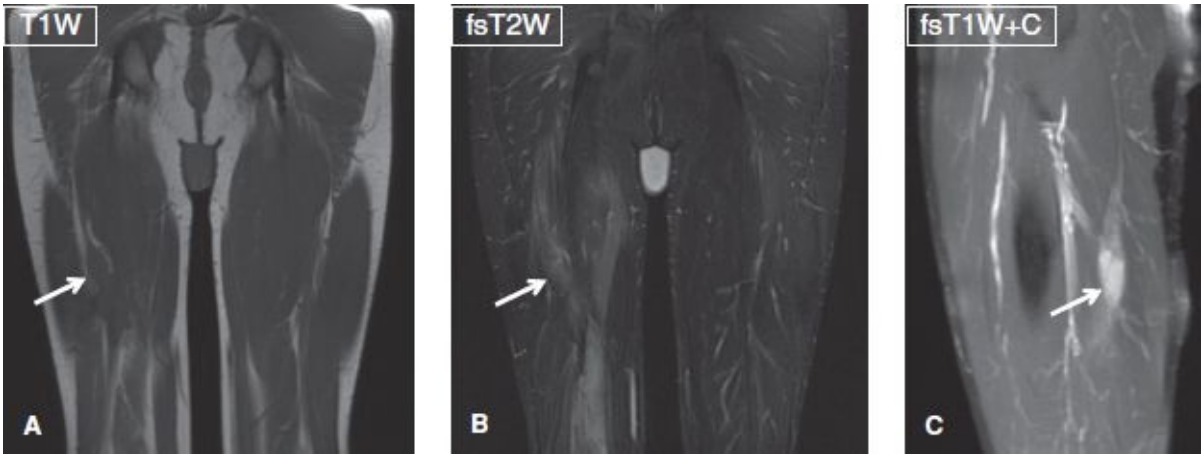

Fig. 67: Neurotmesis (Sunderland grade V injury). A young man with right leg palsy following recent gunshot wound to the right lower extremity. Coronal **(A, B)** and sagittal **(C)** images exhibit fusiform enlargement of the right sciatic nerve (*arrows* in **A, B**) in keeping with an end bulb neuroma from Sunderland grade V injury, and associated

perineuroma contrast enhancement (*arrow* in **C**), due to disruption of the peripheral blood–nerve barrier and reactive inflammatory granulation tissue.

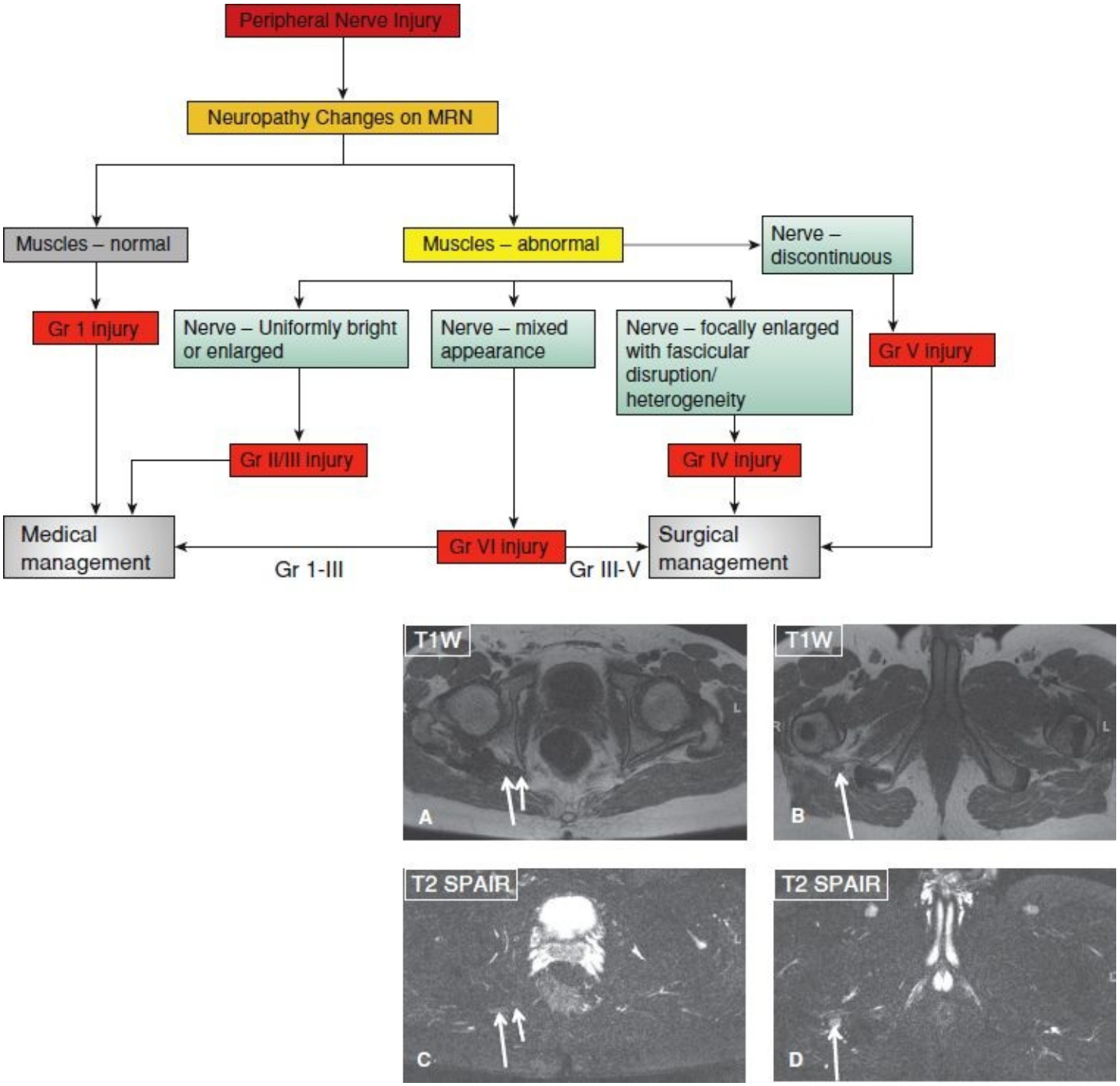

Fig. 68: Prior MVA with right acetabular posterior column fusion and hamstring repair, presenting with right foot drop and leg pain, erectile dysfunction, and depression. Axial images **(A, B)** show scar encasement of the right sciatic (*long arrows*) and pudendal (*short arrows*) nerves, while the SPAIR images **(C, D)** show enlargement and abnormal hyperintensity of these nerves reflecting Sunderland grade VI/III injury. Note thickened epineurium of the sciatic nerve.

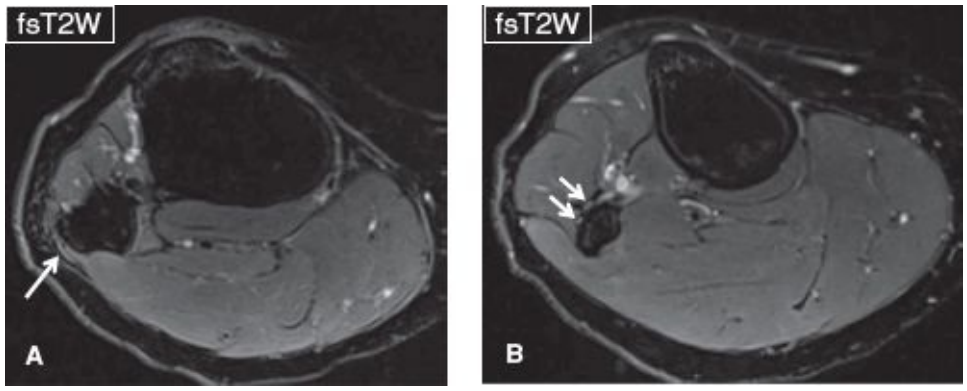

Fig. 69: Magic angle phenomenon. The common peroneal nerve (*arrow* in **A**) may normally demonstrate mild T2 hyperintensity as it courses around the fibular head, due to magic angle phenomenon. At a slightly more distal level **(B),** note the two normal isointense branches (*arrows*) of the nerve.

TABLE 3: The Sunderland classification of peripheral nerve injury

Grade	Pathology	Clinical Findings	Prognosis
I	• Mild injury • Axonal continuity between nerve and end organ preserved	Paresis and minor or complete sensory loss	Complete spontaneous recovery in wks to 4 mos
II	• Loss of axon continuity at the injured site • No disruption of the axon sheaths, endoneurium, or perineurium	Loss of sensory, motor, and sympathetic function occur distal to the lesion in the distribution of the nerve	During regeneration, the intact proximal portion of the axon grows distally at ~1 mm/day (~1 in/mo)
III	• Loss of endoneurial tube as well as axonal disruption • The perineurium and epineurium remain intact	• If all of the fascicles are involved → complete loss of motor, sensory, and sympathetic function in the autonomous distribution of the nerve • For partial lesions → the fiber composition of the injured fascicle(s) determines the type and extent of defect	• Fewer axons available for regeneration • Remaining axons sprout and descend within the fascicle but outside of their original endoneurial tubes • Usually medical management
IV	• Entire fascicle and its surrounding perineurium is disrupted and disorganized • Epineurium intact • Continuity of nerve trunk maintained	Electrical studies → no conduction across the lesion 3–4 mos from injury	• Severe fibrosis limits axon regeneration • Neuroma in continuity forms • Surgery may be required for painful or dysfunctional neuroma
V	Complete transection, with loss of continuity of the entire nerve trunk, including the epineurium	Complete loss of motor, sensory, and sympathetic function in the autonomous distribution of the severed nerve	• Functional recovery requires surgical repair • The quality of recovery depends on the degree of axon loss and disorganization of fiber pattern

EMG, electromyography; NCV, nerve conduction velocity.

TABLE 4: The essence of Seddon and Sunderland classifications of peripheral nerve injury, along with the respective MRN findings

Seddon	Sunderland	Injury	MR Neurography
Neurapraxia	Grade I	Focal demyelination	• Nerve: Increased signal +/– increased size • Muscles: Normal
Axonotmesis	Grade II	Axon damaged with intact endoneurium	• Nerve: Increased signal +/– increased size. Abnormally bright +/– enlarged fascicles • Muscles: Denervation change
	Grade III	Axon and endoneurium damaged with intact perineurium	• Nerve: Increased signal +/– increased size. Abnormally bright +/– enlarged fascicles • Muscles: Denervation change • More severe than grade II
	Grade IV	Axon, endoneurium, and perineurium damaged with intact epineurium	• Nerve: Neuroma in continuity with disrupted fascicles • Muscles: Denervation change
Neurotmesis	Grade V	Complete nerve transection	• Nerve: Gap with end bulb neuroma • Muscles: Denervation change
	Grade VI	Mixed levels of injury along circumference of the nerve	• Mixture of findings depending upon the grades of injury • Fibrosis with abrupt signal change of the nerves

TABLE 5: The MRN findings in various grades of peripheral nerve injuries, along with their treatment and prognosis

Injury (Sunderland Grade)	Nerve	Fascicles	Regional Muscles	Treatment	Prognosis
Mild stretch (I)	Increased T2 signal +/– increased size	Normal	Normal	Conservative	Good
Moderate stretch (II/III)	Increased T2 signal and size	Abnormal	Denervation change	Conservative	Good to fair
Neuroma-in-continuity (IV)	Focal nerve fusiform enlargement and heterogeneity +/– diffuse long segment enlargement	Abnormal/fascicular disruption and/or thickened perineurium may be visible around abnormal fascicles	Denervation change	Surgical	Poor
Neurotmesis (V)	Nerve gap or intervening hemorrhage and/or fibrosis/end bulb neuromas at proximal nerve segments	Abnormal and discontinuous	Denervation change	Usually surgical	Poor without surgical intervention
Mixed (VI)	Combination of findings of grades I–V/ epineurial thickening/ internal nerve heterogeneity	Abnormal	Denervation change	Usually surgical	Poor

Following nerve repair, assessment of nerve regeneration is always a difficult task. One would see susceptibility artifacts at the site of nerve repair/reconstruction or hypointense peripheral smooth or serrated marking of the nerve tube may be observed. With good regeneration, the muscle denervation changes should regress within few months and functional status should improve. Regenerating nerve sprouts are difficult to demonstrate by imaging; however, clinically, presence of advancing Tinel sign is a helpful test to detect the advancement and progression of growth of the regenerating and nerve fibers. On the other hand, MRN is quiet good for detecting nerve degeneration, which manifests as one or a combination of findings of worsening nerve hyperintensity and/or enlargement followed by atrophy and fibrosis in chronic stages, and persistent muscle denervation changes beyond the expected recovery time with worsening fatty infiltration and atrophy of the muscles. Recently, diffusion tensor imaging has been shown to be useful in this regard as a non-invasive method to evaluate nerve regeneration or response to surgery in animal models and for the median nerve assessment. Increasing serial fractional anisotropy values have been shown to correlate with neural remyelination and axonal regeneration.

Nerve Mass

A mass lesion in continuity with the nerve most commonly reflects PNST apart from the diagnosis of injury related neuroma in continuity (Fig. 8). In addition, if regional muscle denervation changes are present in the vicinity of the tumor, one should consider the possibility of a PNST. Although, uncommonly, any large mass or space occupying lesion impinging the nerve might give such denervation changes. One should look for typical imaging signs that would suggest a PNST, such as the tail sign (the mass tapers at one or both ends where the nerve enters and exits the tumor; Fig. 2), fascicular sign (enlarged nerve fibers seen in cross-section as multiple small ring-like structures, mimicking a coaxial cable), target sign (low signal centrally due to collagenous tissue with peripheral myxoid change on a fluid-sensitive sequence; Fig. 70), and split-fat sign (fat separating the tumor from adjacent muscles, best seen at tapering margins of the neoplasm indicating its slow growth consequently leading to displacement of the perineural fat planes; Fig. 26). These lesions show targetoid (Figs. 13, 41) or diffuse enhancement as compared to neuroma in continuity which typically does not show appreciable enhancement. Schwannoma is more commonly prevalent than neurofibroma, and more commonly shows cystic changes, calcification, and internal hemorrhage. Ancient schwannoma may exhibit low ADC values (Fig. 71), which may simulate malignancy. Slow growth, stability on follow-up or underlying history and genetics of schwanomatosis are useful indicators of benign diagnosis. Plexiform neurofibroma shows diffuse infiltrative mass lesion and/or associated skin thickening (Fig. 72). Plexiform neurofibroma or schwannoma may additionally show “bag of worms appearance (Fig. 27). Schwannomatosis is characterized by numerous schwannomas without bilateral acoustic neuromas (Fig. 40). It is a distinct entity from NF type II which shows acoustic neuromas and exhibits different genetic aberrations. Malignant peripheral nerve sheath tumor can occur in a sporadic fashion (older age and less aggressive) or as part of NF type I (earlier age, increased incidence, and more aggressive). It manifests with one or more imaging signs, such as large size (>4 to 5 cm), heterogeneous appearance, internal hemorrhage and/or necrosis, local tissue invasion or extra-compartmental extension, surrounding edema, heterogeneous enhancement, F18 FDG PET SUV values greater than 3–4 with increasing uptake on delayed imaging, and finally low ADC values on DTI (<1.1 mm2/s) with disrupted and disorganized tracts on tractography. One should remember that postoperatively, even after successful resection of the peripheral nerve sheath tumor, the nerve signal hyperintensity and/or mild enlargement commonly persists (Fig. 73). Contrast examination is essential to differentiate this reactive change of the nerve from recurrence of the lesion, the latter would show nodular enhancing lesion.

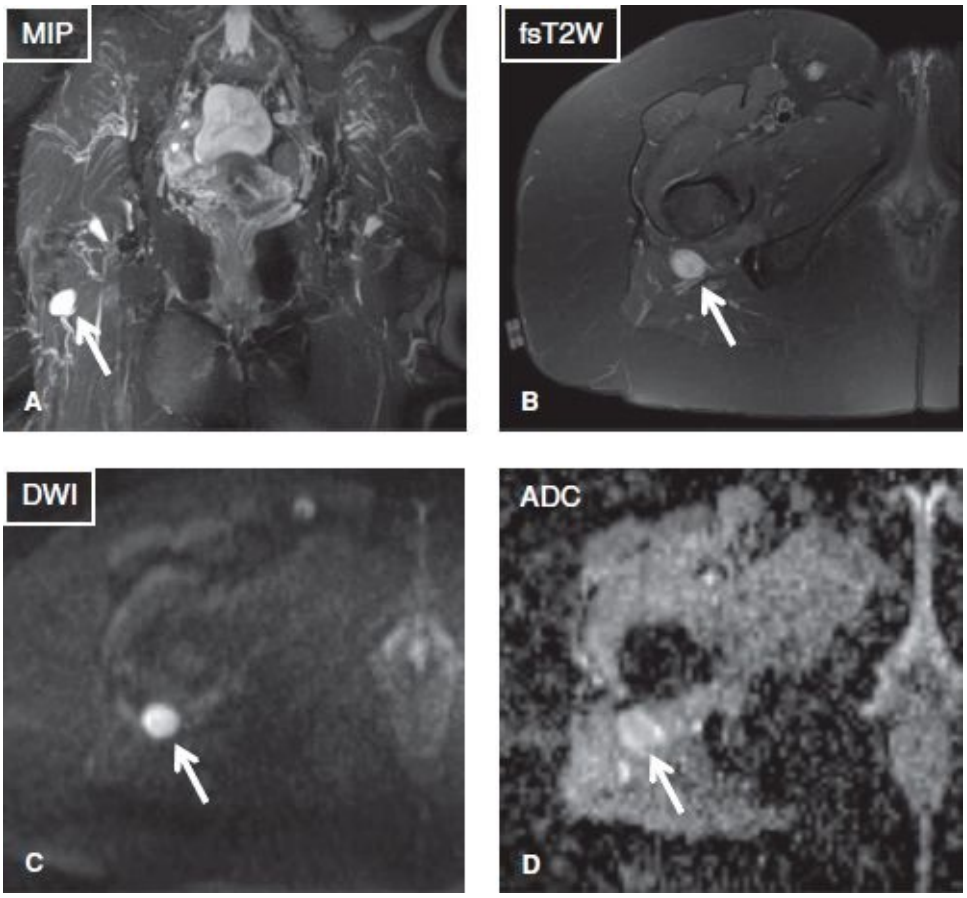

Fig. 70: Schwannoma of the sciatic nerve. Coronal **(A)** and axial **(B–D)** images demonstrate a well-circumscribed T2 hyperintense lesion with target sign (*arrows*) eccentrically located along the sciatic nerve. It shows mild diffusion restriction (ADC: 2.1 × 10−3 mm2/s).

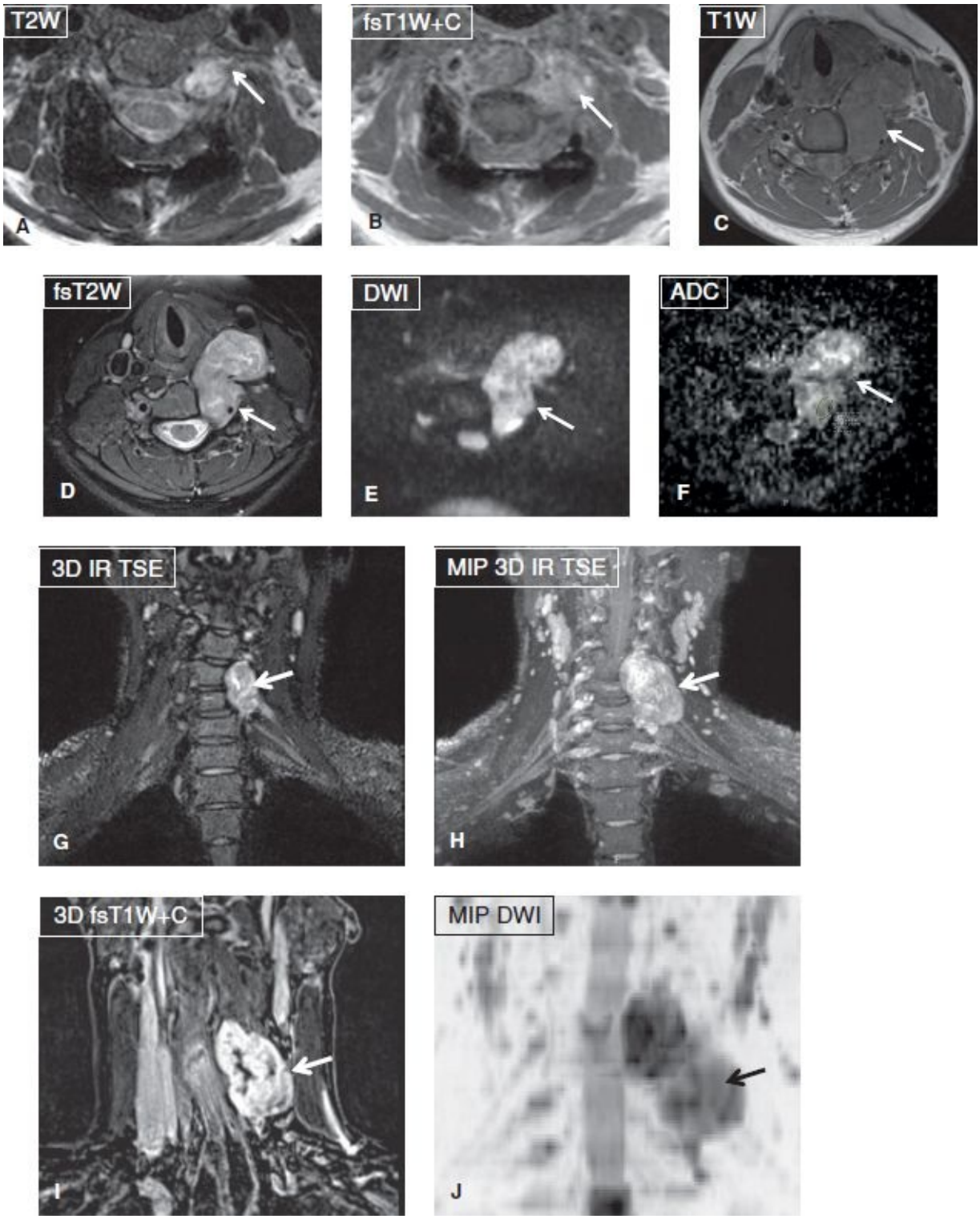

Fig. 71: Schwannoma recurrence. **A, B:** Axial images show a mildly heterogeneous schwannoma (*arrows*) in the left neural foramen, which was resected. **C–J:** Repeat scans 4 years later show a larger mass lesion (*arrows*) that has grown significantly in size, and exhibits cystic degeneration and intracanalicular expansion. The ADC values was 1.2 × 10−3 mm2/s. Ancient schwannoma may exhibit lower ADC values due to internal complexity.

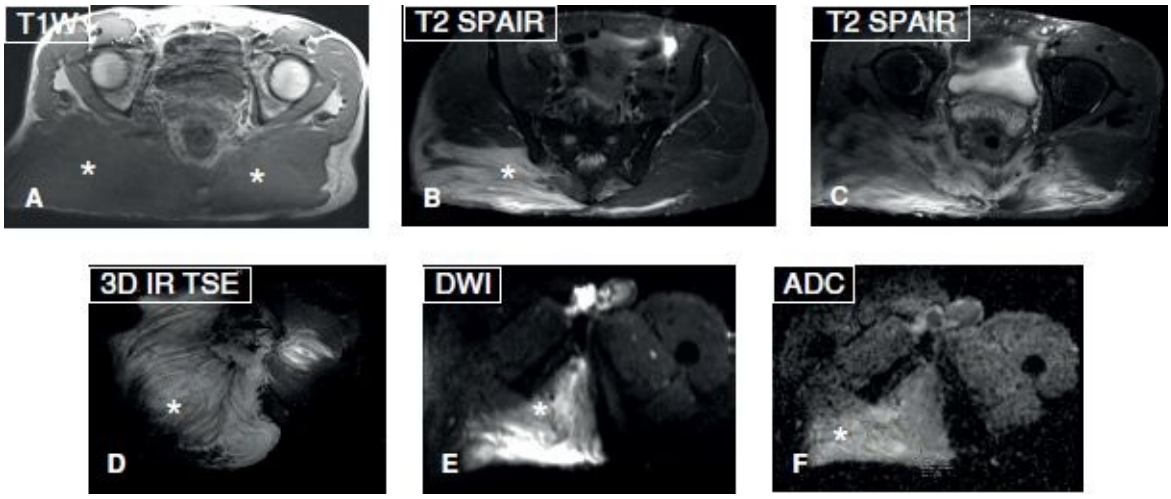

Fig. 72: Plexiform neurofibroma in a patient with NF type I. Axial images **(A–F)** exhibit a large infiltrative heterogeneous subcutaneous T2 hyperintense mass (*asterisks*), which demonstrates minimal restricted diffusion (ADC: 2.0 × 10−3 mm2/s), in keeping with a benign plexiform neurofibroma.

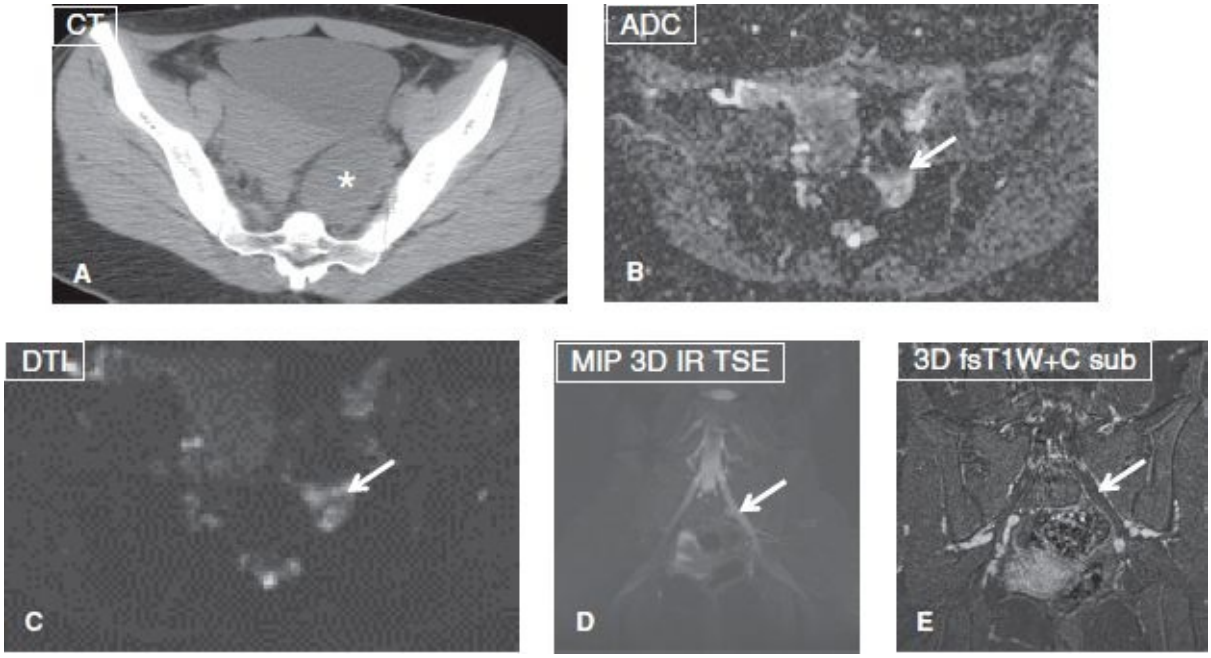

Fig. 73: Postoperative appearance of left S1 schwannoma resection. Axial CT image **(A)** shows a well-defined ovoid soft tissue lesion (*asterisk*) adjacent to the sacrum, which proved to be a schwannoma on resection. Postoperative axial **(B, C)** and coronal **(D, E)** images show no significant restricted diffusion (*arrows* in **B, C**) but there is thickening and asymmetric T2 hyperintensity of the exiting left S1 nerve root (*arrows* in **D, E**) without evidence of recurrence on the postcontrast image. This can be a asymptomatic postoperative finding.

Other lesions with typical imaging features include intraneural ganglion (Fig. 48), which appears as a multilocular cystic lesion with peripheral enhancement and T2 shine through artifact on DWI without significant diffusion restriction; lipoma, which features homogeneous fat signal, and fibrolipomatous hypertrophy, which appears as fibrofatty

enlargement of the nerve with prominent fascicular appearance ("coaxial cable" appearance on axial images and "spaghetti appearance" on longitudinal images); and perineurioma (fusiform nerve enlargement with uniform prominent fascicular pattern) (Fig. 11). FLH typically affects the median nerve, and may occur in isolation (Fig. 12) or with macrodystrophia lipomatosa. Other mass-like lesions include hematoma (history of anticoagulation or trauma, signal alterations of blood products on MRI, temporal evolution/resolution of the lesion and peripheral enhancement); Morton neuroma (perineural fibrosis leading to a pea-shaped mass lesion in the intermetatarsal space in the foot; Fig. 74, Fig. 28); prominent vascular channels, especially in syndromes like Klippel–Trenaunay–Weber syndrome, which may lead to vasculogenic sciatica (Fig. 75); and endometriosis (blood products, cyclic sciatica, patchy enhancement, chocolate cysts or other endometrial deposits in the pelvis; Fig. 10).

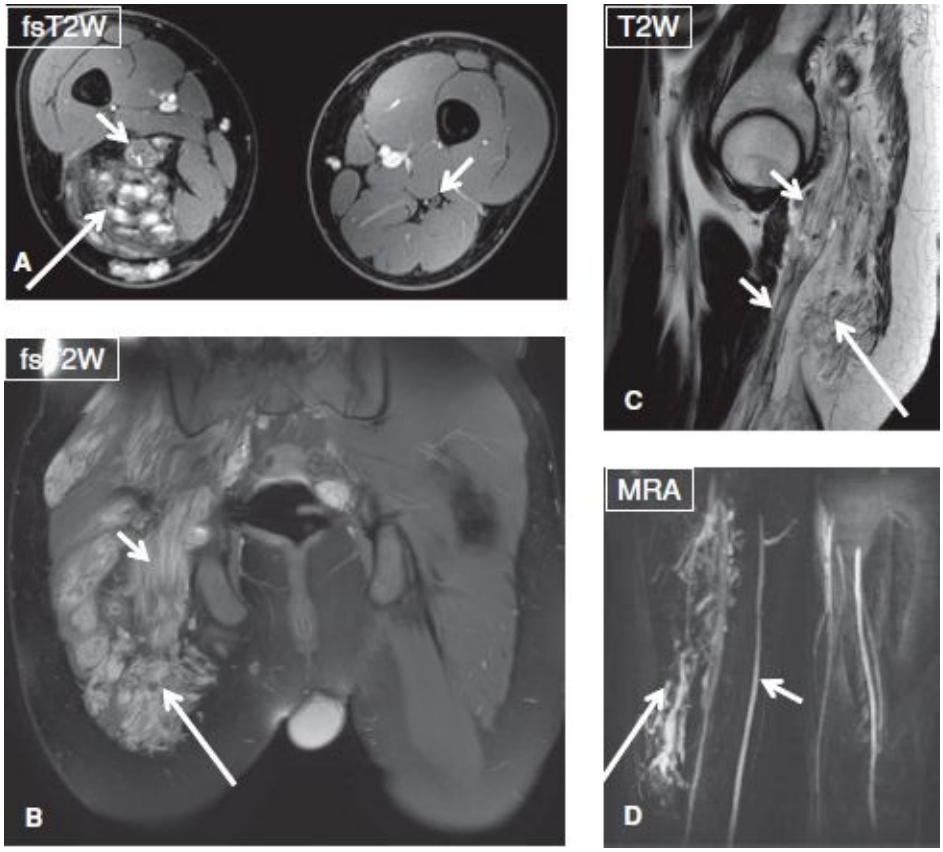

Fig. 75: Vasculogenic sciatica. Young man presenting with severe right leg pain and weakness and inability to stand for more than a few minutes. Axial **(A),** coronal **(B),** and sagittal **(C)** images show a large infiltrative polylobular venous anomaly (*long arrows*) involving the posterior compartment of the right thigh and involving the ipsilateral sciatic nerve (*short arrows*), which is markedly enlarged. MRA **(D)** image shows the venous malformation (*long arrow*) with predominant drainage along the great saphenous vein (*short arrow*).

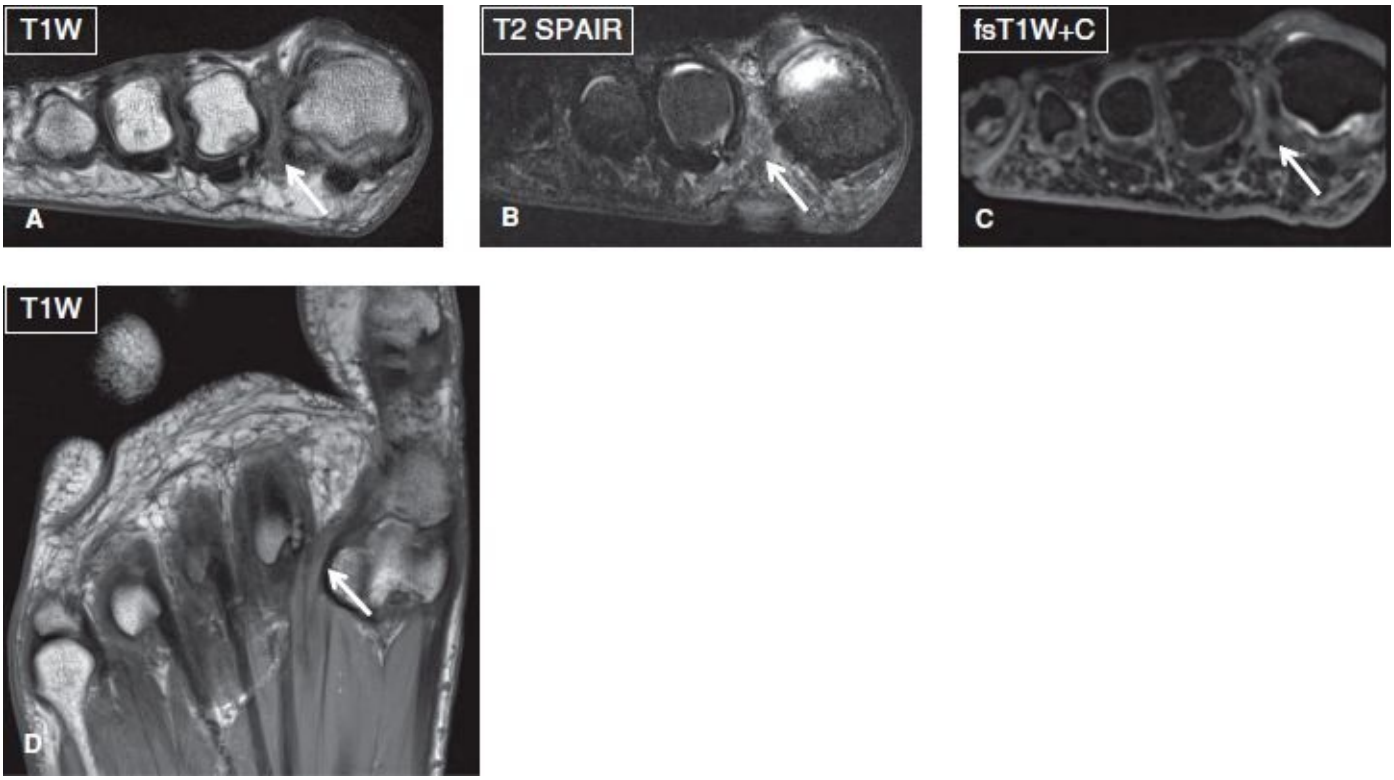

Fig. 74: Morton neuroma. Axial **(A–C)** and coronal **(D)** images show a pear-shaped intermediate signal lesion (*arrows*) between the first and second metatarsal bones, which extends into the plantar soft tissues, and demonstrates mild contrast enhancement.

To conclude, MRN is an excellent high resolution and high contrast imaging technique that not only shows the peripheral nerve in exquisite detail, but also surrounding soft tissue structures including tendons, ligaments, and muscles. Therefore, structured reporting format is essential in this domain to cover the broad spectrum of neural and regional perineural pathologies that might be encountered during systematic interpretation of these multidimensional images.

SUGGESTED READINGS

Ahlawat S, Chhabra A, Blakely J. Magnetic resonance neurography of peripheral nerve tumors and tumorlike conditions. *Neuroimaging Clin N Am.* 2014;24(1):171–192.

Chhabra A. Magnetic resonance neurography-simple guide to performance and interpretation. *Semin Roentgenol.* 2013;48(2):111–125.

Chhabra A. MR neurography. *Neuroimaging Clin N Am.* 2014;24(1):xvii.

Chhabra A, Andreisek G, Soldatos T, et al. MR neurography: Past, present, and future. *AJR Am J Roentgenol.* 2011;197(3):583–591.

Chhabra A, Lee PP, Bizzell C, et al. High-resolution 3-Tesla magnetic resonance neurography of musculocutaneous neuropathy. *J Shoulder Elbow Surg.* 2012;21(2):e1–e6.

Chhabra A, Lee PP, Bizzell C, et al. 3 Tesla MR neurography–technique, interpretation, and pitfalls. *Skeletal Radiol.* 2011;40(10):1249–1260.

Chhabra A, Subhawong TK, Williams EH, et al. High-resolution MR neurography: Evaluation before repeat tarsal tunnel surgery. *AJR Am J Roentgenol.* 2011;197(1):175–

183.
Chhabra A, Thakkar RS, Andreisek G, et al. Anatomic MR imaging and functional diffusion tensor imaging of peripheral nerve tumors and tumorlike conditions. *AJNR Am J Neuroradiol.* 2012. [Epub ahead of print]
Chhabra A, Williams EH, Wang KC, et al. MR neurography of neuromas related to nerve injury and entrapment with surgical correlation. *AJNR Am J Neuroradiol.* 2010;31(8):1363–1368.
Chhabra A, Zhao L, Carrino JA, et al. MR neurography: Advances. *Radiol Res Pract.* 2013; 2013:809568.
Mackinnon S, Dellon AL. *Diagnosis of Nerve Injury. Surgery of the Peripheral Nerve*. New York: Thieme; 1988:74–78.
Seddon HJ. Three types of nerve injury. *Brain.* 1943;66:237–288.
Seddon HJ, Medawar PB, Smith H. Rate of regeneration of peripheral nerves in man. *J Physiol.* 1943 ;102(2):191–215.
Soldatos T, Andreisek G, Thawait GK, et al. High-resolution 3-T MR neurography of the lumbosacral plexus. *Radiographics*. 2013;33(4):967–987.
Stoll G, Wilder-Smith E, Bendszus M. Imaging of the peripheral nervous system. *Handb Clin Neurol.* 2013;115:137–153.
Subhawong TK, Wang KC, Thawait SK, et al. High resolution imaging of tunnels by magnetic resonance neurography. *Skeletal Radiol.* 2012;41(1):15–31.
Sunderland S. A classification of peripheral nerve injuries producing loss of function. *Brain.* 1951;74:491–516.
Thawait SK, Chaudhry V, Thawait GK, et al. High-resolution MR neurography of diffuse peripheral nerve lesions. *AJNR Am J Neuroradiol.* 2011; 32(8):1365–1372.
Thawait SK, Wang K, Subhawong TK, et al. Peripheral nerve surgery: The role of high-resolution MR neurography. *AJNR Am J Neuroradiol.* 2012; 33(2):203–210.
Vargas MI, Viallon M, Nguyen D, et al. New approaches in imaging of the brachial plexus. *Eur J Radiol.* 2010;74(2):403–410.

APPENDIX 1: Sample Completed Structured Report: MRN of the Brachial Plexus: NORMAL

EXAMINATION: [<Order Procedure Description>]

HISTORY: [< >] year-old [<Patient Sex>] with [<Order Reason for Study>]

TECHNIQUE: High resolution MRI was performed of the brachial plexus employing MR neurography techniques on a [<3.0 or 1.5>] Tesla system using multiplanar 3D anatomical and fluid sensitive sequences. Contrast material [was/was not]

administered. [Dose]

Comparison: [< >]

FINDINGS:

Nerves:

Spinal cord: [<Normal>]

Brachial plexus: Preganglionic: [<Normal>]

Brachial plexus: Postganglionic: [<Normal>]

Muscles/Tendons:

Scalenes: [<Normal>]

Rotator cuff muscles: [<Normal>]

Other muscles: [<Normal>]

Bones:

Cervical ribs: [<Absent>]

C7 transverse processes: [<Normal>]

Marrow signal: [<Normal>]

Joints:

Cervical spine:

Alignment: [<Normal>]

Spinal canal: Developmental stenosis: [<Absent>]

Occipital-C1 and atlantoaxial (C1–C2) articulations: [<Normal>]

C2–C3: Central canal: [<Patent>]

Neural foramina: Right: [<Normal>] Left: [<Normal>]

C3–C4: Central canal: [<Patent>]

Neural foramina: Right: [<Normal>] Left: [<Normal>]

C4–C5: Central canal: [<Patent>]

Neural foramina: Right: [<Normal>] Left: [<Normal>]

C5–C6: Central canal: [<Patent>]

Neural foramina: Right: [<Normal>] Left: [<Normal>]

C6–C7: Central canal: [<Patent>]

Neural foramina: Right: [<Normal>] Left: [<Normal>]

C7–T1: Central canal: [<Patent>]

Neural foramina: Right [<Normal>] Left [<Normal>]

Sternoclavicular joints: [<Normal>]

Acromioclavicular joints: [<Normal>]

Glenohumeral joints: [<Normal>]

Thoracic Outlet/Cervicothoracobrachial Junction/Spaces:

Interscalene triangle: [<Normal>]

Costoclavicular space: [<Normal>]

Retropectoralis minor space: [<Normal>]

Vessels:

[<Within normal limits>]

Masses:

[<None>]

Other:

[<None>]

Postgadolinium Discussion: [<No abnormal enhancement>]

Impression

1. [<>]

APPENDIX 2: Sample Completed Structured Report: MRN of the Brachial Plexus: ABNORMAL

Examination: MR Neurography brachial plexus

HISTORY: 34-year-old man with MVA and right arm weakness

TECHNIQUE: High-resolution MRI was performed of the brachial plexus employing MR neurography techniques on a 3.0 Tesla system using multiplanar 3D anatomical and fluid sensitive sequences. Contrast material was not administered.

Comparison: [<None>]

FINDINGS:

Nerves:

Spinal cord: [<Mild cord edema-like signal in the posterior columns in the region of fasciculus gracilis and cuneatus at C5–C7 levels. Small fluid collection anterior to the cord from C5–C8 levels due to meningeal injury>]

Brachial plexus: Preganglionic: [<Complete avulsions of the C5–C7 nerve segments. Partial avulsion of C8 nerve segment. Pseudomeningocele C5–6 to C7–T1 right neural foramina>]

Brachial plexus: Postganglionic: [<Retracted C5–C7 nerve roots in the lower scalene triangle. Diffuse hyperintense signal and mild enlargement of the C5–C8 nerve roots, all trunks, cords, and visualized peripheral branches relative to the left side. Suprascapular nerve is partially seen and is abnormally hyperintense>]

Muscles/Tendons:

Scalenes: [<Mild edema>]

Rotator cuff muscles: [<Diffuse edema-like signal indicative of denervation change>]

Other muscles: [<Mild edema of trapezius and deltoid with adjacent fascial edema from grade I muscle strains>]

Bones:

Cervical ribs: [<Absent>]

C7 transverse processes: [<Normal>]

Marrow signal: [<Normal>]

Joints:

Cervical spine:

Alignment: [<Normal>]

Spinal canal: [<Developmental stenosis absent>]

Occipital-C1 and atlantoaxial (C1–C2) articulations: [<Normal>]

C2–C3: Central canal: [<Patent. Disc desiccation>]

Neural foramina: Right: [<Normal>] Left: [<Normal>]

C3–C4: Central canal: [<Patent. Disc desiccation>]

Neural foramina: Right: [<Normal>] Left: [<Normal>]

C4–C5: Central canal: [<Patent. Disc desiccation. Mild left facet hypertrophy>]

Neural foramina: Right: [<Normal>] Left: [<Normal>]

C5–C6: Central canal: [<Mild narrowing. Disc desiccation. Small central disc protrusion. Bilateral uncoverteral and facet arthropathy>]

Neural foramina: Right: [<Mild narrowing>] Left: [<Mild narrowing>]

C6–C7: Central canal: [<Mild narrowing. Disc desiccation. Small central disc protrusion. Bilateral uncoverteral and facet arthropathy>]

Neural foramina: Right: [<Mild narrowing>] Left: [<Mild narrowing>]

C7–T1: Central canal: [<Patent. Disc desiccation>]

Neural foramina: Right: [<Normal>] Left: [<Normal>]

Sternoclavicular joints: [<Normal>]

Acromioclavicular joints: [<Normal>]

Glenohumeral joints: [<Normal>]

Thoracic outlet/Cervicothoracobrachial junction/Spaces:

Interscalene triangle: [<Edema, otherwise normal>]

Costoclavicular space: [<Normal>]

Retropectoralis minor space: [<Normal>]

Vessels: [<Within normal limits>]

Masses: [<None>]

Other: [<None>]

Impression

1. Right brachial plexus Sunderland grade V injury involving C5–C8 nerve roots as described.

2. Small extradural fluid collection anterior to spinal cord with ascending wallerian degeneration changes of the posterior column.

3. Mild cervical spondylosis.

APPENDIX 3: Sample Completed Structured Report: MRN of the Lumbosacral Plexus: NORMAL

Examination: [<Order Procedure Description>]

History: [< >] year-old [<Patient Sex>] with [<Order Reason for Study>]

Technique: High-resolution MRI was performed of the lumbosacral plexus employing MR neurography techniques on a [<3.0 or 1.5>]-Tesla system using multiplanar 3D anatomical and fluid sensitive sequences. Contrast material [was/ was not] administered. [Dose]

Comparison: []

FINDINGS:

Nerves:

Lower cord and conus: [<Normal>]

Lumbosacral plexus: Size: [<Normal>] Signal: [<Normal>] Course: [<Normal>]

Sciatic nerve: Size: [<Normal>] Signal: [<Normal>] Course: [<Normal>]. Fascicles: [<Normal>]

Femoral and obturator nerves: Size: [<Normal>] Signal: [<Normal>] Course: [<Normal>] Fascicles: [<Normal>]

Lateral femoral cutaneous nerves: Size: [<Normal>] Signal: [<Normal>] Course: [<Normal>]

Other specific nerves in question: Pudendal/genitofemoral: [<Normal>]

Muscles/Tendons:

Psoas major: Bulk: [<Normal>] Intramuscular signal: [<Normal>]

Iliopsoas bursa: [<Normal>]

Piriformis: Bulk: [<Normal>] Intramuscular signal: [<Normal>]

Gluteal: Bulk: [<Normal>] Intramuscular signal: [<Normal>]

Greater trochanteric bursa: [<Normal>] Gluteal tendon: [<Normal>]

Hamstring tendon: [<Normal>]

Adductor: [<Normal>]

Other: [<Quadriceps femoris> <Paraspinal muscles>]

Bones:

Sciatic notches: [<Normal>]

Marrow signal: [<Otherwise normal>]

Joints:

Lumbosacral spine:

Alignment: [<Normal]

Spinal canal: Developmental stenosis: [<Absent>]

L1–L2: Central canal: [<Patent>]

Neural foramina: Right: [<Normal>] Left: [<Normal>]

L2–L3: Central canal: [<Patent>]

Neural foramina: Right: [<Normal>] Left: [<Normal>]

L3–L4: Central canal: [<Patent>]

Neural foramina: Right: [<Normal>] Left: [<Normal>]

L4–L5: Central canal: [<Patent>]

Neural foramina: Right: [<Normal>] Left: [<Normal>]

L5–S1: Central canal: [<Patent>]

Neural foramina: Right: [<Normal>] Left: [<Normal>]

Sacroiliac joints: [<Normal>]

Pubic symphysis: [<Normal>]

Hip joints: [<Normal>]

Vessels: [<Normal>]

Masses: [<None>]

Other (pelvic viscera): [<None>]

Postgadolinium discussion: [<No abnormal enhancement>]

Impression

1. [< >]

☑ APPENDIX 4: Sample Completed Structured Report: MRN of the Lumbosacral Plexus: ABNORMAL

Examiation: MR Neurography of the Lumbosacral Plexus with and Without Intravenous Contrast

History: 30-year-old woman with bilateral leg weakness and multifocal motor–sensory symptoms.

Technique: High-resolution MRI was performed of the lumbosacral plexus employing MR neurography techniques on a 3.0 Tesla system using multiplanar 3D anatomical and fluid sensitive sequences. Contrast material was administered (12 cc of intravenous gadolinium).

Comparison: [<None>]

FINDINGS:

Nerves:

Lower cord and conus: [<Normal>]

Lumbosacral plexus: Size: [<Diffusely symmetrically enlarged all nerve roots. Signal: [<Diffusely abnormally moderately hyperintense bilaterally with inconspicuous dorsal nerve root ganglia>] Course: [<Normal>]

Sciatic nerve: Size: [<Moderately enlarged bilaterally>] Signal: Abnormally diffusely moderately hyperintense>] Course: [<Developmentally split right sciatic nerve>] Fascicles: [<Prominent bilaterally with small hyperintense pseudomasses>]

Femoral and obturator nerves: Size: [<Moderately enlarged bilaterally>] Signal: [<Abnormally diffusely moderately hyperintense>] Course: [<Normal>] Fascicles: [<Mildly prominent in the femoral nerves>]

Lateral femoral cutaneous nerves: Size: [<Mildly enlarged bilaterally>] Signal: [<Moderately hyperintense bilaterally>] Course: [<Normal>]

Other specific nerves in question: Pudendal: [<Mildly enlarged and hyperintense bilaterally>]

Muscles/Tendons:

Psoas major: Bulk: [<Normal>] Intramuscular signal: [<Normal>] Iliopsoas bursa: [<Normal>]

Piriformis: Bulk: [<Normal>] Intramuscular signal: [<Normal>]

Gluteal: Bulk: [<Normal>] Intramuscular signal: [<Normal>] Greater trochanteric bursa: [<Normal>] Gluteal tendon: [<Normal>]

Hamstring tendon: [<Normal>]

Adductor: [<Normal>]

Other: [<None>]

Bones:

Sciatic notches: [<Normal>]

Marrow signal: Otherwise [<Normal>]

Joints:

Lumbosacral spine:

Alignment: [<Normal>]

Spinal canal: Developmental stenosis: [<Present>] Congenitally short pedicles at L4–L5>]

L1–L2: Central canal: [<Patent>]

Neural foramina: Right: [<Normal>] Left: [<Normal>]

L2–L3: Central canal: [<Patent>]

Neural foramina: Right: [<Normal>] Left: [<Normal>]

L3–L4: Central canal: [<Patent>]

Neural foramina: Right: [<Normal>] Left: [<Normal>]

L4–L5: Central canal: [<Patent. Mild bilateral facet arthropathy>]

Neural foramina: Right: [<Normal>] Left: [<Normal>]

L5–S1: Central canal: [<Patent. Mild facet arthropathy. Mild disc dessication>]

Neural foramina: Right: [<Normal>] Left: [<Normal>]

Sacroiliac joints: [<Normal>]

Pubic symphysis: [<Normal>]

Hip joints: [<Fibrocystic change of the right femoral head and neck junction>]

Vessels: [<Normal>]

Masses: [<None>]

Other (pelvic viscera): [<Small physiologic amount of fluid in pelvis>]

Postgadolinium discussion: [<No abnormal neuromuscular enhancement or enhancing mass lesion>]

Impression

1. Findings of diffuse symmetric polyneuropathy. Consider hereditary neuropathy, such as CMT type 1A.

2. Mild degenerative changes of lumbar spine.

APPENDIX 5: Sample Completed Structured Report for MRN of the Extremity—Generic: NORMAL

Examination: <<Order Procedure Description>>

History: [<>] year-old <<Patient Sex>> with <<Order Reason for Study>>

Technique: High-resolution MRI was performed of the [<>] employing MR neurography techniques on a [<3.0 or 1.5>]-Tesla system using multiplanar 3D anatomical and fluid sensitive sequences. Contrast material [<was>] [<was not>] administered. [<Dose>]

Comparison: [<>]

Findings:

Nerves: Size: [<Normal>] Signal: [<Normal>] Course: [<Normal>] Fascicles: [<Normal>] Variant anatomy: [<Absent>] Perineural fat: [<Normal>]

Muscles/Tendons: [<Normal>]

Bones: [<Normal>]

Joints: [<Normal>]

Vessels: [<Normal>]

Masses: [<None>]

Other: [<None>]

Postgadolinium discussion: [<No abnormal enhancement>]

Impression

1. [< >]

APPENDIX 6: Sample Completed Structured Report for MRN of the Extremity—Generic: ABNORMAL

Examination: MR Neurography of Right Thigh with and Without Contrast

History: 30-year-old woman with gradual right leg weakness over 6 months without substantial sensory symptoms.

Technique: High-resolution MRI was performed of the right thigh employing MR neurography techniques on a 3.0-Tesla system using multiplanar 3D anatomical and fluid sensitive sequences. Contrast material was not administered.

Comparison: [<None>]

FINDINGS:

Nerves:

Sciatic nerve: Size: [<Moderately diffusely enlarged from the visualized sciatic notch till immediately above its bifurcation. Signal: moderately hyperintense>] Course: [<Normal>] Fascicles: [<Uniformly enlarged>] Variant anatomy: [<Absent>] Perineural fat: [<Normal>]

[<Normal imaging appearance of saphenous nerve, common peroneal nerve, tibial nerve, medial and lateral sural cutaneous nerves, and femoral nerve branches>]

Muscles/Tendons: [<Mild right hamstring tendinosis. Denervation edema-like signal, grade II fatty replacement, and mild atrophy of the hamstring and visualized gastrocnemius muscles>]

Bones: [<Normal>]

Joints: [<Normal>]

Vessels: [<Normal>]

Masses: [<None>]

Other: [<None>]

Postgadolinium discussion: [<Diffuse homogeneous enhancement of the right sciatic lesion. Diffuse enhancement of the right hamstring and gastrocnemius muscles without fascial enhancement>]

Impression

1. Right sciatic long segment mass lesion, likely representing a perineurioma.

2. Mild hamstring tendinosis.

Index

Note: Page number followed by f and t indicates figure and table respectively.

A
Abscess, 28, 28f, 30, 30f
Accessory muscles, in wrist, 285, 288f
Acetabular cartilage lesion, 311f
Acetabular geodes, 330f
Achilles peritendinitis, 472, 472f
Achilles tendon (AT), 471–477, 471f, 473f, 474f, 475f, 476f, 500f, 501f
Acromioclavicular (AC) joint, 149, 151, 156, 157, 159f, 160f, 160t
Acromion, 151, 152f, 156, 156f, 157, 157f, 158f
Acromioplasty, 203, 203f
Adamantinoma, 82f, 98f
Adductor insertion avulsion syndrome, 73f, 314
Adductor tendon avulsions, bilateral, 316f
Adhesive capsulitis, 192–193, 193f
Adventitial bursitis, 97f
Amyloid wrist arthropathy, 274, 275f
Anconeus epitrochlearis muscle, 236f
Anderson classification, for osteochondral injuries, 382t
Aneurysmal bone cyst, 89f, 90f, 113, 113f
Angiolipoma, 100, 101f
Angiosarcoma, 120
Ankle, 439, 441f, 442f, 443
  alignment, 439, 443–444, 443f
  anterior, tendons/ligaments, 479–481, 479f–482f
  bones, 487, 487f–495f, 492–493
  fluid, 444, 444f
  image evaluation, 439
  impingement syndromes, 502–504, 505t, 506f–507f
  lateral, tendons/ligaments, 454, 456–468, 457f–469f
  medial, tendons/ligaments, 444–454, 445f–455f
  muscles, 493–494, 496f, 497f
  nerves and tarsal tunnel, 494–495, 497f
  posterior structures, 468–477, 469f–479f
  postoperative findings, 499–502, 500f–504f

sinus tarsi, 496–497, 498f, 499f
structured report, 440–441
sample, 508–509, 509–511
tibiotalar and subtalar joints, 482–487, 483f–486f
vessels, 497, 499f
Anterior cruciate ligament (ACL), 405, 406, 409, 410, 410f, 411f, 412f
complete ACL foot plate avulsion, 408f
fallen ACL sign, 407, 408f
injury, 407–409, 408f, 409f, 410f
MR drawer sign, 409, 409f
mucoid degeneration of, 406, 406f–407f
nonvisualization of, 407, 408f
PCL sign, 409, 409f
reconstruction, 429–433, 431f–433f
Segond fracture, 409, 410f
tears, 373, 407, 409, 410, 411f
Anterior interosseous syndrome, 287f
Anterior talofibular ligament (AFL), 465, 466f
Anterolateral impingement, 465, 468f, 506f
Arcuate fracture, 389, 389f
Arcuate ligament, 388f, 389
Articular cartilage, 311f, 379, 379f
Athletic pubalgia, 314, 316, 316f, 317f, 318f
Atypical lipomatous tumor, 100, 100f
Autologous osteochondral graft (OATS) procedure, 141, 142f–143f
Avascular necrosis (AVN)
of hip, 330, 332–336, 333f–338f, 336t
of humeral head, 195, 196f
of iliac bone, 338f
of talus, 493, 494f
wrist, 282, 284, 285f

B

Baker (popliteal) cyst, knee, 366, 367f, 368f
Baseball pitcher hockey goalie syndrome (BPHGS), 316, 318f
Baxter neuropathy, 497f
Benign notochordal cell tumor, 85f–86f
Benign vertebral compression fractures, 116, 118f
Biceps tendon, 177, 179f, 226, 227f, 228f, 240f
Bicipitoradial bursa, 228, 229f
Bifurcate ligament, chronic injury of, 469f

Bilateral slipped capital femoral epiphyses, 341f
Bird beak spurs, 156, 157f
Bizarre paristeal osteochondromatous proliferation (BPOP), 83f
Bone and soft tissue tumors, 69
  characteristics, 79
    fluid-containing lesions, 109, 110f
    fluid–fluid levels, 113
    lesion with cartilage, 105f, 109
    matrix, 100, 103, 105, 109–110
    periosteal reaction, 113
    T2 dark lesions, 103, 105, 106f–109f
    transition zone, 113
    uniformity, 110, 112f, 113, 113f
  extent, 113–116
  image evaluation, 69–70, 70f–74f, 75t
  location, 76, 78–79, 80f–100f
  markers, placement of, 70
  post-gadolinium discussion, 121, 124, 126
  size, 75–76, 75f–79f
  structured report, 70, 127, 128, 129, 130
Bone cyst, 113, 114f, 344f
Bone hemangiomas, 116, 120, 123f
Bone infarcts, 103, 104f, 108f, 420f, 495f
Bone involvement, by soft tissue mass, 114, 117f
Bone lymphoma, 198f
Bone marrow reconversion, extramedullary hematopoiesis and, 196, 197f
Bone metastasis, from lung carcinoma, 84f
Brachialis muscle, 226, 228f
Brachial plexus lower trunk, 537t
Breast metastases, 87f
Brodie abscess, 32, 33f, 423f, 488f
Broström procedure, 502, 503f, 504f
Bucket-handle medial meniscal tear, 373, 374f

C

Calcaneal fracture, acute, 469f
Calcaneal fractures, 492–493
Calcaneocuboid ligament, 468
Calcaneofibular ligament (CFL), 465, 465f, 466f
Calcaneonavicular coalition, 489f
Calcific tendinitis, 165, 165f–167f

Calcium hydroxyapatite deposition disease, 200f
Calcium pyrophosphate (CPPD) arthropathy, 274
Capsular rupture, ankle, 444, 444f
Carpal alignment, normal, 248f
Carpal boss syndrome, 290, 290f
Carpal tunnel syndrome, 268, 271, 271f
Carrying angle, 213
Cartilage, 131–132, 131f, 132t, 141
  pathology, imaging of, 132
    full-thickness lesions, 134, 138, 138f
    osteochondral lesions, 138, 139f–140f
    partial-thickness lesions, 132, 134, 134f–136f
    signal heterogeneity, 132, 133f, 134f
  structured report, 146, 147
  surgical repair techniques, 141, 141f–144f, 145
Cartilage defects, 136f, 380, 380f
Cartilage delamination, 138f, 380, 381f
Cartilage denudation, knee, 380, 381f
Cartilage fissures, 134f
Cartilage flap, 134f
Cartilage injury, by transient patellar dislocation, 135f
Cartilage lesions, high-grade, and patellofemoral pain, 136f
Cartilage surface fibrillation, 134f
Cat scratch disease, 239f
Cellulitis, 24–24, 25f, 26f
Charcot–Marie–Tooth disease (CMT), 116, 122f
  type 1A, 526f, 529f, 533, 533f
Chemotherapy-induced neuropathy, multiple myeloma and, 535f
Chondroblastic osteosarcoma, 348f
Chondroblastoma, 80f, 100, 110, 111f, 113, 115f, 346f, 347f, 421f
Chondrocalcinosis, 133f, 134f, 386f
Chondromalacia, 132, 380, 380f
Chondromyxoid fibroma, 100, 111f–112f
Chondrosarcoma, 99f–100f, 110, 347f, 348f
Chordoma, 86f
Chronic inflammatory demyelinating neuropathy (CIDP), 531–533
Chronic recurrent multifocal osteomyelitis (CRMO), 34, 36f
Clavicular osteolysis, posttraumatic, 161f
Common extensor tendon, 222f, 223f
Common flexor tendon (CFT), 216, 218f
Common peroneal nerve (CPN), 390f, 391f, 538t, 541f

Complex regional pain syndrome (CRPS), 487, 491f, 492
Compression fracture, of lateral femoral condyle, 418f
Cortical avulsive change, 91f, 99f
Cortical desmoid, 72f–73f, 420f
Cubital tunnel syndrome, 236, 241
Cyclops lesion, 432f
Cystic angiomatosis, 120, 125f
Cystic schwannoma, 89f

D
Degloving lesion, 30, 30f, 427f
Delaminating rotator cuff tear, 172, 174f–175f
Delayed onset muscle soreness (DOMS), 28, 29f
Deltoid ligament, 450
  acute ligament sprains, 452, 452f–454f
  deep tibiotalar ligament, 451f
  ganglion of, 456f
  sprain of, 453f, 454f
  tears of, 450, 452
  tibiocalcaneal ligaments, 451f, 452f
  tibiospring ligaments, 451f, 452f
  Weber type A fracture, 454f
De Quervain tenosynovitis, 265, 266f
Dermatomyositis, 326f, 532f
Desmoid tumor, 78f, 96f, 204f, 235f
Developmental dysplasia of hip, 304f
Diabetic femoral neuropathy, 351f
Diabetic plexopathy and neuropathy, 535f
Diffuse pigmented villonodular synovitis, 103, 107f
Diffusion tensor imaging (DTI), 12
Diffusion-weighted imaging (DWI), 11–12
Discoid meniscus, 385, 385f
Distal intersection syndrome, 266, 267f, 268f
Distal radioulnar joint (DRUJ), 245, 249f, 251, 252f
Distal radioulnar ligaments, 276, 277f
Dorsal intercalated segmental instability (DISI), 249, 250, 250f
Dorsal intercarpal ligament, 279f, 280f
Dorsal talonavicular ligament, 481, 481f–482f
Double crush syndrome, 541, 542f
Dupuytren's contracture, 290

E

Elastofibroma dorsi, 79, 92f, 100, 204f
Elbow, 211, 214f
  alignment, 213
  anterior structures, 226–228, 226f–229f
  articular, 228, 229f–232f, 231
  bones, 231–234, 232f–234f
  dislocations, 231, 231f
  image evaluation, 211, 213
  joint fluid, 213–214, 213f, 214f, 215f
  lateral structures, 218, 219f–223f, 221, 223
  medial structures, 214–218, 215f–218f
  muscles, 234, 234f–236f
  nerves, 236, 236f–238f, 238
  posterior structures, 223–225, 223f–226f
  postoperative findings, 239, 240f–241f, 241
  structured report, 212, 243, 244
  syndromes, 238–239, 239f, 240f
  vessels, 234
Empty notch sign, 410, 412f
Enchondroma, 103, 105f, 109, 346f, 421f
Endometriosis, 93f, 353f, 524f
Enthesophytes, 445, 445f
Eosinophilic granuloma, 81f, 85f, 113, 114f
Epicondyle, medial, chronic avulsion of, 218, 219f
Epidermoid cyst, 83f
Epitheliod hemangioendothelioma, 120
Erdheim–Chester disease, 116, 118f, 415, 415f
Evans osteotomy, 501, 502f
Ewing sarcoma, 82f
Excessive lateral friction syndrome (ELFS), 394
Extensor carpi ulnaris (ECU) tendon, 266, 268f
Extensor digitorum longus (EDL) tendon, 479, 481, 481f
Extensor hallucis longus (EHL) tendon, 479, 481, 481f
Extensor pollicis brevis (EPB) tendon, 263
Extensor retinaculae, 479
Extensor tendons, 263, 265f, 267f
External rotation recurvatum test, 389
Extraskeletal chondroma, 100, 112f
Extrinsic ligaments, normal, 279f

F

Fat suppression methods
chemical shift imaging, 9f, 12
Dixon type or water selective, 12, 15–16, 15f
frequency-selective fat suppression, 12, 15f
short tau inversion recovery, 14f, 16
spectral adiabatic inversion recovery, 12f, 16, 16f
Femoral articular cartilage flap, 311f
Femoral head, 330f, 338f
Femoral nerve, 351f, 352f, 530f, 537t
Femoral shaft fracture, 418f
Femoroacetabular impingement (FAI), 297–303, 298f–303f
Fibrolipomatous hamartoma, 76f, 527f
Fibromatosis, 96f
Fibroosseous capitate–hamate coalition, 281f
Fibrous dysplasia, 78f, 97f, 103, 106f
Fibrous lunotriquetral coalition, 281f
Flexor carpi ulnaris tendon, calcific tendinitis with tear, 270f
Flexor digitorum profundus (FDP) tendons, 268, 269f
Flexor digitorum superficialis (FDS) tendons, 268, 269f
Flexor hallucis longus (FHL), 444, 445, 450
Flexor pollicis longus (FPL) tendon, 268, 269f
Flexor tenosynovitis, 268, 269f
Flipped meniscus, meniscal tear, 374f, 375
Foreign body granuloma with fasciitis, 96f–97f

G

Ganglion cyst, 92f, 253f, 289, 290f, 425, 427f, 432f, 498f
Ganglion of ligamentum mucosum, 405f
Genitofemoral nerve entrapment, moderate bilateral, 539f
Geyser phenomenon, 91f, 159
Giant cell tumor, 81f, 95f, 103, 106f, 113, 115f, 290, 422f
Giant fibrocystic lesion, 300f
Gilula lines, 247, 248f
Glenohumeral (GH) joint, 149, 181–195
adhesive capsulitis, 192–193, 193f
amyloid arthropathy, renal insufficiency and, 196f
articular cartilage of, 193, 193f
denuded articular cartilage, 194f
glenohumeral ligaments, 189–193, 191f
glenoid labrum, normal, 181, 181f
inferior glenohumeral ligament, 190, 192, 192f

labral tears, 182
ALPSA lesions, 182, 183f, 184f
Bankart lesions, 182, 183f
GLAD lesion, 184, 184f
SLAP lesions, 184, 185f–187f
middle glenohumeral ligament, 189, 191f
normal MR arthrography, 191f
osteoarthritis, 193, 194f
paralabral cyst, 182, 182f, 188, 190f
pigmented villonodular synovitis, 195f
POLPSA lesion, 188, 191f
posterior peel-back lesion, 188, 188f–189f
septic arthritis, 194f
septic shoulder, 195f
sublabral sulcus, 181, 181f
superior glenohumeral ligament, 189
synovial osteochondromatosis of, 154f
thinning of articular cartilage, 193, 193f
type IV pulley injury, 181f
Glenoid labrum articular cartilage defect (GLAD), 184, 184f
Glenoid site avulsion (GAGL) lesion, 192, 192f
Glomus tumor, 84f
Gluteal minimus, 313
Gluteus maximus, 314, 315f
Gluteus medius and minimus tendon tears with bursitis, 306f
Gluteus medius avulsions, 314f
Golfer's/pitcher's elbow, 216
Gorham disease, 120
Gout, 95f, 483f
Goutalliers classification, 175f
Gracilis muscle injury, 315f
Greater trochanter fracture, benign, 342f
Greater tuberosity fracture, 196, 197f

H
Haglund syndrome, 472, 473f, 474f
Hamstring apophyseal avulsion, 324f
Hamstring avulsion, 324f
Hamstring grafts, 430
Hamstring peritendinitis, 322, 323f
Hamstrings muscles, 324

Hamstring tendon avulsion, 325f
Hawkin test, 156
Head–neck offset and alpha angle, 300f
Heel spurs, 156, 158f
Hemangioma, 71f, 100, 102f, 235f
Hemangiomatosis, 120, 123f
Hematoma, postoperative, 328f
Hemophilic arthropathy, knee, 366f
Hemorrhoid neuropathy, left inferior, 542f, 543f
Henry knot, on axial images, 446, 446f
Hereditary neuropathy, 122f, 528, 531, 535f
Heterotopic ossification, 94f, 100, 326, 326f
Hibernoma, 100, 102f
"High ankle sprain," 461, 464f
Hill–Sachs lesions, 182, 183f
Hindfoot varus, 443, 443f
Hip, 295
  alignment, 297, 297f, 298f
  angiomyolipoma, 354f, 355
  ASIS avulsion, 353f
  bones, 329–342, 329f–350f
  capsule/ligaments, 311–313, 312f–313f
  cartilage, 310–311, 310f–311f
  dysplasia, 303, 304f, 305
  FAI-related anatomy, 297–303, 297f–303f
  fluid, 305, 305f
  iliotibial band, strained, 353f
  labrum, 307–310, 307f–310f
  lipoma, 354f, 355
  liposarcoma, 354f, 355
  nerves, 349, 351f–353f, 353
  Pipkin classification, 297t
  structured report, 296, 356, 357
  trochanteric bursitis, 305–307, 305f–306f
  vessels, 342, 344, 349, 350f–351f
  viscera, 353, 353f
  visualized muscles/tendons, 313–329, 314f–328f
Hip dislocations, femoral head fractures and, 297, 297t
Hip ligament sprains, 312f
Hip osteoarthritis, 329, 329f
Hoffa's disease, chronic, 402f

Hoffa's fat pad, 134, 136f, 400, 402f, 403f
Homogeneity, on MR imaging, 110
Horizontal meniscal tear, 375, 375f
Humeral head enchondroma, 196, 198f
Hypothenar hammer syndrome, 286

I
Idiopathic myositis, 326f
Idiopathic scapulothoracic bursitis, 205f
Iliac bone fracture, nonpathologic, 343f
Iliofemoral ligament, 311
Iliopsoas bursitis, 319, 320f, 321, 321f
Iliopsoas muscle injury, 321f
Iliotibial band bursitis, 388f
Indeterminate lesions, 121, 126f
Inectious sacroilitis, 343f
Infection and inflammation, musculoskeletal, 23
  image evaluation in, 23–24
  infection (*see also* Musculoskeletal infections)
    filling of structured reporting for, 24–38
    incidental findings, 38
    post-gadolinium discussion, 38
    sample report, 65, 66
    spinal infections, 39, 39f
  inflammation/arthritis
    alignment, 51
    ankylosis, 63
    bone marrow edema, 61–62
    bony productive changes, 54, 56, 57f
    erosion/cystic change, 59–61, 60f–62f
    filling of structured reporting for, 40–50
    fluid, 51–53, 51f–53f
    incidental findings, 63, 63f
    joint space/cartilage, 58–59, 59f
    post-gadolinium discussion, 63
    sample report, 67, 68
    synovial thickening/synovitis, 53–54, 54f–56f
    tenosynovitis, 56, 58, 58f
Infectious extensor tenosynovitis, 265, 267f
Infectious tenosynovitis, 25, 27, 27f, 28f
Inferior glenohumeral ligament tear, 192, 192f

Inferior hemorrhoid neuropathy, 542f, 543
Inferior peroneal retinaculum (IPR), 456, 457f
Insall–Salvatti ratio, 394
Interdigital nerve, 538t
Intersection syndrome, 266
Intramuscular cyst, rotator cuff, 163, 164f
Intramuscular metastasis, lung adenocarcinoma and, 110, 113f
Intraosseous benign fatty lesion, 286f
Intrasubstance tears, rotator cuff, 161
Intratrabecular wrist fracture, 283f
Intrinsic ligaments, normal, 278f
Inversion ankle sprain, 465
Ischiofemoral impingement, 323f, 324f
Ischiofemoral ligament, 312
Ischiopubic ramus stress fracture, 340f
ITB (friction) syndrome, 387, 388f

J
Joint effusion
  ankle, 444, 444f
  glenohumeral, 152, 153f
  knee, 363–364, 363f, 364f
  presence of, with tumor, 106
Jumper's knee, 397, 398f, 399f
Juvenile cartilage cell implantation (JCI), 499, 501

K
Kager fat pad, 471, 472
Keel spurs, 156, 158f
Kienböck's disease, 247, 282, 285f
Kim's lesion, 188
Kimura disease, 239f
Klippel–Trenaunay–Weber (KTW) syndrome, 120, 124f, 556
Knee, 359
  anterior compartment, 392–405, 393f–406f
    alignment, 392–394
    Hoffa fat pad, 400, 402f, 403
    patellar cartilage, 397, 401f
    patellar tendon, 395, 397, 397f–401f
    plica, 403, 405f
    quadriceps tendon, 395, 395f–396f
    trochlear cartilage, 397, 401f

trochlear groove, 400, 402f
TT–TG distance, 404, 406f
autologous chondrocyte implantation, 434
autologous osteochondral transplants, 434
Baker (popliteal) cyst, 366, 367f, 368f
bone marrow stimulation techniques, 434
bones, 414–419
Erdheim–Chester disease, 415, 415f
neoplastic lesions, 417, 419, 420f–423f
osteochondral lesion, 415, 416f–417f, 417
red marrow reconversion, 414f, 415
Salter–Harris injuries, 417, 418f, 419f, 419t
sarcoid arthropathy, 415, 415f
stress injuries, 417, 417f, 418f
subchondral insufficiency fracture, 415, 416f
T1W images, 414f, 415
degloving lesion, 427f
fluid, 363–366, 363f–368f
ganglion cyst, 425, 427f
image evaluation, 359
intercondylar compartment, 405–414, 406f–414f
lateral compartment, 383, 385–387, 385f–388f
loose intra-articular bodies, 366, 367f
medial compartment, 366, 368–382, 368f–383f
multiple bursitis, 428f
muscle, 423–424, 424f
nerves, 424–425, 425f, 426f
normal MR anatomy, 361f–362f
pigmented villonodular synovitis, 364, 365f–366f
popliteal lymph node, 425, 428f
popliteofibular bursitis, 428f
posterolateral corner, 387, 388f–391f, 389–391
posteromedial corner, 382–383, 384f
postoperative, 425, 429–434, 429f–433f
structured report, 360
sample, 436, 437–438
TCL-semimembranosus bursitis, 425, 428f
vessels, 424, 424f
Köhler disease, 493
K-space profiling and bandwidth, 6–7, 8f

L
Labro-cartilage lesion, 311f
Labrum, 307–310, 307f–310f
Labrum–transverse ligament recess, 307f, 308f
L5 and S1 roots, conjoint, 527f
Langerhans cell histiocytosis, 85f
Lateral collateral ligament (LCL), 385, 387, 387f
Lateral epicondylitis, 221t
Lateral ligament complex, ankle, 465, 465f, 466f, 467f
Lateral meniscus (LM), 368, 370, 373, 383, 385, 385f, 386f
Lateral ulnar collateral ligament (LUCL), 218, 220f
Ledderhose disease, 477
Lesser tuberosity cysts, 196
Leukemia, femoral metadiaphysis, 349f
Leukemia, treated, 125f
Ligamentum teres, 312f, 313
Lipoma, 70f, 81f, 100, 103, 103f, 104f, 345f
Liposarcoma, 100, 101f
Little leaguer's elbow, 218, 219f
Little leaguer's shoulder, 196
Long head of biceps brachii tendon (LHBT), 152, 155, 155f–156f
Longitudinal meniscal tear, 373–375, 373f, 374f
Lumbosacral plexopathy, inflammatory, 542f
Lunotriquetral (LT) ligament, 252, 253f, 254–256, 254f, 256f
Lyme synovitis, 38, 38f
Lymphangiomatosis, 120
Lymphatic malformation, 109, 110f
Lymphoma, 88f

M
Madelung deformity, 279
Magic angle phenomenon, 395, 397f, 552f
Magnetic resonance neurography (MRA), 513
  brachial plexus evaluation, sagittal images, 521f
  image evaluation, 513, 517f–519f, 519–520
  nerve entrapment, 533, 536–544, 537t–538t, 538f–544f
  nerve injury, 544–553, 546f–552f
    imaging findings in various grades of, 552t
    Seddon classification, 545t, 547t
    Sunderland classification, 546t, 547t
  nerve mass, 553–556, 553f–555f

nerves, 521
enlargement and enhancement, 521–522, 523f–525f
fascicles, 528–530, 529f–531f
imaging abnormalities, 521–530
nerve signal, 522–523, 523f–527f, 526
peripheral nerves, 521, 522f
sciatic nerves, 522f
neuropathy, systemic etiologies of, 531–533, 532f–536f
peripheral nerves and skeletal muscles, 519f
regional muscle/tendon evaluation, 530–531, 531f–532f
Schwannoma of ulnar nerve, 519f
spine disease with left sciatica, 520f
structured report
MRN of brachial plexus, 514–515, 557–559
MRN of extremity, 518, 563, 564
MRN of lumbosacral plexus, 516–518, 560–562
symmetrical *versus* asymmetrical plexus appearance, 520f
Malignant peripheral nerve sheath tumor, 116, 122f
Maximum intensity projections (MIPs), 3
Mechanical tenosynovitis, 265f, 266
Medial collateral ligament (MCL), 377–379, 378f, 379f
Medial epicondylitis, 216, 239
Medial meniscus (MM), 368–377, 429
intrameniscal cyst, 369f
intrameniscal microcysts, 369f
medial oblique meniscomeniscal ligament, 368, 368f
MRI signs of degeneration, 369
normal, 368–369
posterior horn, 369
tears, 369–370
chronic degenerative tears, 375
classification of, 370f
complicated and complex, 375, 376f
horizontal, 375, 375f
longitudinal, 373–375, 373f, 374f
meniscal extrusion, 375–376
parameniscal cysts, 376, 376f, 377f
pathologic and anatomic variants, 376–377
pitfalls in evalution of, 376
radial, 370, 370f–373f, 373
Median nerve (MN), 226, 234, 236, 537t

bifid, 269, 270f, 271f
hematoma compressing, 272, 273f
intertendinous course of, 270f
lesions in, 271–272
neurotmesis of ulnar bundle of, 271, 272f
posttraumatic neuroma of, 271, 272f
Meniscal contusion, 377, 378f
Meniscal flounce, 377, 378f
Meniscocapsular injury, 382, 383f
Meniscomeniscal ligaments, 368, 368f
Mesotenons, 176, 445
Metastatic lesion, knee, 422f
Microfracture technique, 141f
Mitchell classification, of signal characteristics of necrotic bone, 334t
Monostotic fibrous dysplasia, iliac bone, 346f
Morel-Lavallée lesion, 92f, 109, 110f
Morton neuroma, 531f, 555f
MR imaging, 3. *See also specific topics*
human considerations, 3, 4f
protocols, 16
cartilage, 20, 20f
infection/inflammation, 18, 18f
metal, 20
MR arthrogram, 9f, 18
MR-guided intervention, 22, 22f
MR neurography, 12f, 13f, 14f, 20, 21f
myositis, 14f, 20
ortho, 9f, 15f, 16, 17f
tumor, 18, 19f
vascular malformation, 16f, 18–20, 19f
whole body MRI, 20
whole body MR neurography, 21, 21f
technical considerations
coil selection, 6
2D imaging pulse sequences, 7–10
3D imaging pulse sequences, 10–12
fat suppression methods, 12–16
K-space profiling and bandwidth, 6–7
phase wrap, controlling of, 6
scanner selection, 4–6, 4f–6f
Mueller–Weiss syndrome, 493, 494f, 495f

Multifocal motor neuropathy (MMN), 531, 533
Multifocal patellar chondrosis and signal alterations, 133f
Multiple myeloma, 86f–87f, 110, 113f
Multisite drilling large area technique, for cartilage repair, 141, 143f
Muscle denervation, 531f
Musculoskeletal infections, 24
  bone marrow edema, 30–34, 30f, 32f, 33f, 35f–37f
  cellulitis, 24–24, 25f, 26f
  deep lesions, 24
  delayed onset muscle soreness (DOMS), 28, 29f
  infectious tenosynovitis, 25, 27, 27f, 28f
  large drainable fluid collection, 28, 28f, 30, 30f
  large joint effusion, 38, 38f
  Lyme synovitis, 38, 38f
  necrotizing fasciitis, 27–28
  pyomyositis (infectious myositis), 28, 28f
  rhabdomyolysis, 28, 29f
  septic arthritis, 38, 39f
  septic bursitis, 25, 27f
  soft tissue edema, 24, 25f–26f
  superficial lesions, 24
Myelomalacia, and atrophic peripheral neuropathy, 529f
Myeloma lesion of right humerus, posttreatment, 125f
Myositis ossificans, 94f, 234, 234f
Myxoid liposarcoma, 73f
Myxoma, 92f

N

Navicular–cuneiform coalition, 490f
Necrotizing fasciitis, 27–28
Necrotizing myositis, 328f
Neoplastic lesions, of knee, 417, 419, 420f–423f
Nerve fascicles, 528–530, 529f–531f
Nerve hyperintensity, moderate, 526f
Nerves, normal variants, 527f
Neural fibrolipoma, 76f, 100
Neurofibroma, 116, 121f, 525f
Neurofibromatosis type-1, 79f, 530f, 536
Neuropathic (Charcot) ankle joint, 483f
Neuropathic arthropathy (NpA), 34, 38f
Neurotmesis, 549f

Nondissociate instability, 249
Non–ossifying fibroma, knee, 420f
Nora lesion, 83f
Notochordal cell tumor, benign, 85f–86f

O
Obturator externus muscle injury, 320f
Olecranon bursitis, 225, 226f
Olecranon fractures, 225, 225f
Os acromiale, 157, 158f
Osborne–Cotterill lesion, 228, 231f
Osgood–Schlatter disease, 99f, 397, 399f, 400f
Os naviculare, 446, 447f
Os peroneum, 459, 460f
Os styloideum, 290, 290f
Osteoarthritis, 135f, 137f, 138f, 329, 329f, 380, 381f, 382t, 482, 483f
Osteoblastoma, 103, 109f, 344f
Osteochondral fracture, 139f, 197f
Osteochondral lesion (OCL), 132, 138, 139f–140f, 228
  of capitellum, 229f, 230f
  of knee, 415, 416f–417f, 417
  MR imaging classification of, 229t
  of talus, 484, 485f, 486f, 487, 502f
  of talus and tibia, 486f
Osteochondritis dissecans, 139f, 140f, 381, 382t
Osteochondroma, 97f, 103, 105f, 109, 422f
Osteochondromatosis, primary, 252f
Osteoid osteoma, 88f, 98f–99f, 421f, 493, 496f
Osteomyelitis (OM), 30–32, 32f, 33f, 34, 35f, 36f, 37f, 286f, 487f, 488f
Osteonecrosis, ankle, 493, 494f
Osteopetrosis, 343f
Osteosarcoma, 74f, 117f, 196, 198f
Os trigonum, 445, 468, 469f, 470f

P
Paget disease, 79f, 196, 198f
Painful os peroneum syndrome (POPS), 459, 460f, 461, 461f
Paralabral cysts, 200, 309f, 310f
Parameniscal cysts, 376, 376f, 377f
Parosteal osteosarcoma, 116, 120f
Parsonage–Turner syndrome, 199, 200f
Particle disease, 342, 350f, 433, 433f

Patellar and trochlear articular cartilage, 397, 401f
Patellar cartilage abnormalities, multiple, 133f
Patellar chondromalacia, 133f
Patellar chondrosis, multifocal, and signal alterations, 133f
Patellar dislocation, 392, 393f
Patellar retinaculae, injuries to, 392
Patellar tendon, 392, 395, 397f–401f
Patellofemoral alignment, 394f
Patellofemoral pain syndrome, 134, 136f
Pellegrini–Stieda lesion, 378f
Perilabral recess, 307f, 308
Perineal branch pudendal neuropathy, 543f
Perineurioma, 116, 122f, 522, 524f
Periosteal chondrosarcoma, 99f–100f
Periosteal osteosarcoma, knee, 422f
Periosteal reaction, 113, 114f, 115f
Periosteal sleeve avulsion, 400f
Periostitis related to adductor avulsion, 113, 115f
Peripheral nerve sheath tumors (PNST), 426f, 536f, 546
Peroneal brevis (PB) tendon, 456–458, 458f, 459f
Peroneal tendons, 456–461, 458f, 461f, 462f
Peroneus longus (PL) tendon, 456–457, 458f, 459, 460f
Peroneus quartus muscle, 458f
Perthes disease, 334, 337f
Perthes lesion, 183f
Pes anserinus bursitis, 379, 379f
Physeal bar, 487, 491f
Pigmented villonodular synovitis (PVNS), 80f, 116, 119f, 195f, 274, 275f
  of ankle, 482, 484f
  focal extra-articular, 95f
  hip, 329, 332f
  knee, 364, 365f–366f
Pilon (tibial plafond) fractures, 492
PIN syndrome, 238
Piriformis muscle, 321
Piriformis syndrome, 321, 322f, 527f
Plantar fascia, 474, 477, 477f–479f, 501f
Plantar fibroma, 95f, 477, 479f
Plantar neuropathy, moderate medial and lateral, 539f
Plasmacytoma, 87f
Pleomorphic undifferentiated sarcoma, 105, 108, 109f

Plexiform neurofibroma, 554f, 555
Poliomyelitis, chronic, 287f
Poliomyelitis-related muscle fatty replacement, 327f
POLPSA (posterior labrocapsular periosteal sleeve avulsion) lesion, 188, 191f
Polyneuropathy, 523f
Polyostotic fibrous dysplasia, femur and iliac bone, 346f
Popliteal lymph node, 425, 428f
Popliteal vein thrombosis, 424, 424f
Popliteofibular bursitis, 428f
Popliteofibular ligament, 390f, 391
Popliteus tendon, 389, 390f
Posterior ankle bony impingement syndrome, 468
Posterior cruciate ligament (PCL), 405, 410–414, 412f, 413f
Posterior intermalleolar ligament, 470f
Posterior oblique ligament (POL), 383, 384f
Posterior peel-back lesion, 188, 188f–189f
Posterior talofibular ligament (PFL), 465, 468f
Posterior tibial tendon (PTT), 444, 446
  degeneration of, 450
  dysfunction, 501–503, 501f–502f
  os naviculare, 446, 447f
  post-traumatic synovitis and stenosing tenosynovitis, 450f
  PTT dysfunction, 450
  subluxation/dislocation, 447
  tears, 447, 448f–449f
  tendinosis, 447, 448f
  tenosynovitis, 449f
Posterior tibial tendon dysfunction, 502f, 503f
Posteromedial impingement, chronic, 240f
Post-traumatic neuroma in continuity, 523f
Prefemoral fat pad edema, 403f
Prestyloid recess, 260, 263f
Primary subcoracoid impingement, 174f
Primary synovial chondromatosis, 331f
Proton density-weighted (PDW) imaging, 9f, 68
Proximal tibiofibular joint, 391, 391f
Pseudodefect of capitellum, 228, 229f, 231
Pseudo-Madelung deformity, 281f, 282
Pubic bone insufficiency injury, 340f
Pyle's metaphyseal dysplasia, 342f
Pyomyositis, 28, 28f

Q
Quadratus femoris syndrome, 320f
Quadriceps enthesopathy, 395, 396f
Quadriceps/suprapatellar fat pad edema, 404f
Quadriceps tendon, 392, 395, 395f, 396f
Quadrilateral space syndrome, 194f

R
Radial artery thrombosis, 288f
Radial collateral ligament (RCL), 218, 220f, 276, 278f
Radial fracture, acute, 283f
Radial meniscal tear, 370, 370f–373f, 371f, 372f, 373
Radial nerve, 537t
Radial styloid impingement syndrome, 290, 291f
Radiculopathy, 543, 543f, 544f
Radiohumeral joint, 211
Red marrow reconversion, 343f
Retrocalcaneal bursitis, 472f
Retromalleolar groove, 456, 457f
Rhabdomyolysis, 28, 29f, 199, 199f
Rheumatoid arthritis, 330, 332f, 483f
Rheumatoid wrist, 274, 274f
Rice bodies, 330f
Rotator cuff, 161–175, 162f–163f
  calcific tendinitis, 165, 165f–167f
  delaminating tears, 172, 174f–175f
  Goutalliers classification, 175f
  intramuscular cyst, 163, 164f
  myotendinous junction rotator cuff tear, 167, 171f, 172
  partial RC tendon tears, 165, 167, 168f–171f
  retear, 201, 201f, 202f
  severe tendinosis, 165, 165f
  subscapularis tendon tears, 172, 172f–173f
  supraspinatus–infraspinatus tendon junction, 163f
  supraspinatus muscle atrophy, false impression of, 172, 176f
  tendinosis and tears, 163–175
Rotator cuff tears of hip, 314
Rotator interval and long head biceps brachii tendon, 175–181, 176f, 178f
  acute rotator interval injury, 176, 177f
  coracohumeral ligament, 175, 176, 178f
  long head of biceps brachii tendon, 175, 176–177, 179f–181f

superior glenohumeral ligament, 175, 176, 178f

S

Sacral insufficiency fracture, 340f
Sacroilitis, inectious, 343f
Salter–Harris classification, for injuries of physeal plate, 282, 284f, 284t
Sarcoid, 103, 107f
Scanner selection, in MR imaging, 4–6, 4f–6f
Scaphoid nonunion with advanced collapse (SNAC), 250
Scapholunate advanced collapse (SLAC), 250, 250f
Scapholunate (SL) ligament, 251–252, 252f, 254f, 255f, 256f
Scapulothoracic bursitis, 205, 205f
Scar entrapment, of left posterior superior cluneal nerve, 542f, 543
Schwannoma, 116, 120f, 551f, 552f
Schwannomatosis, 533, 536f, 555
Sciatic end bulb painful neuroma, 550f
Sciatic hyperintensity, in diabetic neuropathy, 525f
Sciatic nerve, 537t
Sciatic nerve, split, 527f
Secondary subcoracoid impingement, 173f
Septic arthritis, 38, 39f, 194f, 487f
Septic bursitis, 25, 27f
Septic carpal arthritis, 274, 276f
Septic shoulder, 195f
Seroma, 92f
Serous atrophy of bone marrow, 199f
Shepherd fracture, 470f, 471
Shouldered cartilage defect, trauma-related, 135f, 137f
Shoulder joint, 149
  acromial arch, 155–156, 156f–161f
  alignment, 151, 151f, 152f
  bones, 195, 199
  fluid, 151–152, 152f, 155
    glenohumeral joint, 152, 153f–154f
    long head of biceps brachii tendon, 152, 155, 155f–156f
    subacromial/subdeltoid bursa, 151–152, 152f–153f
  glenohumeral joint, 181–195
  image evaluation in, 149, 151
  muscles, 199, 199f, 200f
  nerves, 199
  other findings, 203–206, 204f–206f

postoperative findings, 200–203, 201f–204f
rotator cuff, 161–175
rotator interval and long head biceps brachii tendon, 175–181
structured report, 150
sample, 207, 208–209
vessels, 199, 201f
Signal-to-noise ratio (SNR), 4
Sinus tarsi, 496, 497f, 498f, 499
Sinus tarsi syndrome, 498f, 499f
Skeletal hemangiomatosis, hip, 349f
SL advanced collapse (SLAC), 250, 250f
SLAP fracture, 188, 188f
Slipped capital femoral epiphysis (SCFE), 299
Snapping hip syndrome, 322, 324
Soleus muscle, 474, 476f, 477f
Spigelian hernia, 316, 319f
Spina bifida, with valgus hip posturing, 298f
Spinal infections, 39, 39f
Spondylodiskitis, 39, 39f, 40, 41f
Spondyloepiphyseal dysplasia, 341f
Spring (plantar calcaneonavicular) ligament, 452, 454, 455f, 456f
Stellate crease, 310, 310f
Sternoclavicular joint osteoarthritis, 82f
Stieda process, 468, 469f
Stress fracture, 339f, 492f
Stress reaction, of calcaneus, 492, 492f
Stretch injury, of brachial plexus, 544f
Structured reporting, 1–2
Student's elbow, 225, 226f
Subacromial impingement, 156
Subacromial spurs, 156, 156f, 157f
Subacromial/subdeltoid (SASD) bursa, 151–152, 152f–154f
Subacute acetabular fracture, 339f
Subchondral clavicular fracture, 161f
Subchondral fractures, of naviculum and medial cuneiform, 493f
Subchondral insufficiency fracture, 338f, 339f, 415, 416f
Subchondral stress injury, 338f
Subcoracoid bursa distention, 154f
Subcoracoid bursitis, 154f
Subgluteus maximus bursitis, 306f
Subgluteus medius bursitis, 306f

Sublabral sulcus, 308
Subperiosteal abscess, 488f
Subperiosteal hematoma, knee, 420f
Subscapularis recess, small fluid collection within, 154f
Subscapularis tendon tears, 172, 172f–173f
Subtalar coalition, 489f, 490f
Subtalar joint osteoarthritis, 482, 483f
Superior gemellus muscle, calcific tendinosis of, 94f
Superior gluteal nerve neuropathy, 352f
Superior labrum anterior to posterior (SLAP) lesions, 184, 185f–187f
Superior peroneal retinaculum (SPR), 456, 462f
Superior plica, 152, 153f
Superolateral plica, 313, 313f
Superomedial plica, 313, 313f
Supracondylar process, 232
Suprascapular nerve, 537t
Supraspinatus–infraspinatus tendon junction, 163f
Supraspinatus muscle atrophy, false impression of, 172, 176f
Syndesmotic ligaments, 461, 462f–464f
Synovial chondromatosis, 154f, 329, 331f
Synovial chondrosarcoma, 80f
Synovial diverticulae, 152, 251
Synovial fringe, 214f, 231, 232f
Synovial osteochondromatosis, 110, 154f, 213–214
Synovial plicae, 403, 404f, 405f
Synovial sarcoma, 75f, 236f
Systemic lupus erythematous-related tenosynovitis, 266f

T

Talar fractures, 493
Talocalcaneal coalition, 487, 491f
Tarsal tunnel syndrome, 495–496, 497f, 539f
Tennis elbow, 221t
Teres minor muscle edema, 199, 200f
Thoracic outlet syndrome, 528, 528f, 529f
3D imaging pulse sequences, 9f, 10–12, 11f–14f
3T scanners, use of, 4–5, 4f, 5f
Tibialis anterior tendinosis, 479f
Tibialis anterior tendon, 479, 480f
Tibial nerve, 538t
Tibial plateau compression fracture, 417, 417f

Tibial tubercle to trochlear groove (TT–TG) distance, 404, 406f
Traction spurs, 156, 157f
Transient osteoporosis of hip, 336
Transverse ligament, 305, 307f
Trapezius muscle, denervation of, 200f
Trauma-related shouldered cartilage defect, 135f, 137f
Triangular fibrocartilage complex (TFCC), 245, 256–257, 256f–258f
  central perforation of disc, 259f
  disc tears, 257, 259f–261f
  grade II sprain of, 259f
  multiple carpal ligamentous injury, 261f
  Palmer classification for TFCC abnormalities, 262t
  peripheral tear, 260f
  and SL ligament injury, 261f
  tears of foveal and styloid attachments of, 260f
  type I and type II lunate facets, 258f
  ulnotriquetral ligament, 258f
Triceps tendinitis, calcific, 224f
Triceps tendinosis, 223, 223f–224f
Triceps tendon, 223, 224f, 225f
Trochanteric bursitis, 305, 305f–306f
Trochlear chondromalacia, 133f
Trochlear depth, 400, 402f
Trochlear groove, 402f
Trochlear sulcus angle, 400, 402f
Tuberculous spondylodiskitis, 40, 41f
Tunneling, 32, 33f
2D imaging pulse sequences, 7–10, 9f, 10f
Tylenol-induced myonecrosis, 328f

U

Ulnar artery aneurysm, 288f
Ulnar collateral ligament (UCL), 214, 215f, 216, 216f–217f, 240f, 241, 241f, 276, 277f
Ulnar impingement syndrome, 262, 264f
Ulnar nerve (UN), 236, 236f–238f, 272, 537t, 540f
Ulnar neuropathy, 237f–238f, 273f, 536f
Ulnar variance, 247, 248f, 249f, 262
Ulnocarpal abutment, 262, 263f–264f
Unicameral bone cyst, 72f
Unicameral cyst of calcaneus, 495f

V

Vacuum phenomenon, 386f
Valgus extension overload syndrome, 238–239
Vasculogenic sciatica, 555f
Venous malformations, 71f, 77f, 93f, 235f, 286, 289f, 424, 425f
Venous varicosities within tarsal tunnel, 498f
Vertebral compression fractures, benign *vs.* malignant, 119t
Volar intercalated segmental instability (VISI), 250, 250f, 251f
Volar intercarpal ligament, ganglion of, 280f

W
Water-selective fat saturation technique, 13f, 15
Wrist, 245
  alignment, 247–251, 247f–251f
  articular, 274–276, 274f–276f
  bones, 279–285, 281f–286f
  carpometacarpal joints, 245
  DRUJ compartment, 245
  extensor compartment, 263, 265–268, 265f–268f
  extrinsic ligaments, 276–279, 276f–280f
  flexor compartment, 268–274, 269f–273f
  fluid, 251, 252f–253f
  image evaluation, 245
  intrinsic ligaments, 245, 252–256, 253f–256f
  muscles, 285–286, 287f–288f
  soft tissue masses and other masses, 289–291, 289f–291f
  structured report, 246
    sample, 292–293, 293–294
  structure of, 245, 247f
  ulnar side, 256–262, 257f–264f
  vessels, 286–289, 288f–289f
Wrist fractures, multiple, 283f

Z
Zona orbicularis, 312